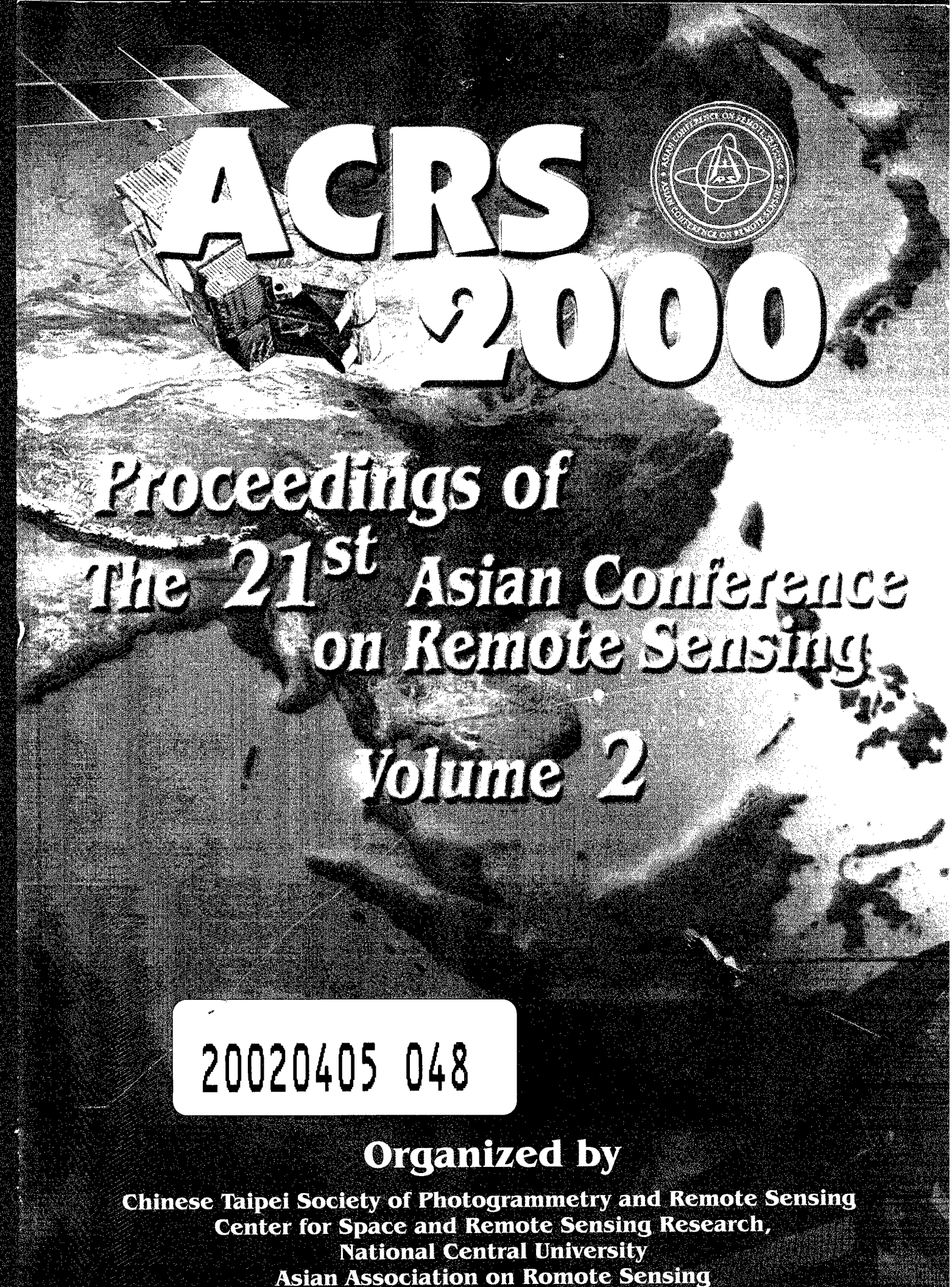


ACRS 2000

Proceedings of The 21st Asian Conference on Remote Sensing

Volume 2

20020405 048

Organized by

Chinese Taipei Society of Photogrammetry and Remote Sensing
Center for Space and Remote Sensing Research,
National Central University
Asian Association on Romote Sensing

REPORT DOCUMENTATION PAGE

Form Approved OMB No. 0704-0188

Public reporting burden for this collection of information is estimated to average 1 hour per response, including the time for reviewing instructions, searching existing data sources, gathering and maintaining the data needed, and completing and reviewing the collection of information. Send comments regarding this burden estimate or any other aspect of this collection of information, including suggestions for reducing this burden to Washington Headquarters Services, Directorate for Information Operations and Reports, 1215 Jefferson Davis Highway, Suite 1204, Arlington, VA 22202-4302, and to the Office of Management and Budget, Paperwork Reduction Project (0704-0188), Washington, DC 20503.

1. AGENCY USE ONLY (Leave blank)	2. REPORT DATE	3. REPORT TYPE AND DATES COVERED
	2000	Conference Proceedings, 4-8 December 2000

4. TITLE AND SUBTITLE

Proceedings of the 21st Asian Conference on Remote Sensing (ACRS 2000), Volume 2

5. FUNDING NUMBERS

F6256201M9011

6. AUTHOR(S)

Conference Committee

7. PERFORMING ORGANIZATION NAME(S) AND ADDRESS(ES)

Center for Space and Remote Sensing Research
National Central University
Chung-Li
Taiwan

8. Performing Organization Report Number

N/A

9. SPONSORING/MONITORING AGENCY NAME(S) AND ADDRESS(ES

AOARD
Unit 45002
APO AP 96337-5002

10. SPONSORING/MONITORING AGENCY REPORT NUMBER

CSP-001014

11. SUPPLEMENTARY NOTES

Conference held: December 4-8, 2000, Taipei International Convention Center, Taipei, Taiwan. Organized by: Chinese Taipei Society of Photogrammetry and Remote Sensing, Center for Space and Remote Sensing Research, National Central University, Asian Association on Remote Sensing. Volume 2 pages 621-1214. Volume 1 pages 1 - 620 . ISBN 957-02-7241-4.

12a. DISTRIBUTION/AVAILABILITY STATEMENT

Approved for public release; distribution is unlimited.

12b. DISTRIBUTION CODE

A

ABSTRACT (Maximum 200 words)

The 21st Asian Conference on Remote Sensing (ACRS 2000) was held 4-8 December 2000 in Taipei, Taiwan. 210 Papers are included in the proceedings, Vol. 1 & 2. Technical sessions included: Agriculture & Soil, Water Resources, Coastal Zone Monitoring, Digital Photogrammetry, Environment, Forest Resources, GIS & Data Integration, Hazard Mitigation, Image Processing, Education & Profession, Global Change, Landuse, Mapping from Space & GPS, SAR/InSAR, Oceanography, Hyperspectral & Data Acquisition Systems, and AirSAR/MASTER.

14. SUBJECT TERMS

AOARD, Taiwan, Image processing, IR sensors, Global positioning systems, Infrared technology, Hazard Mitigation

15. NUMBER OF PAGES

16. PRICE CODE

17. SECURITY CLASSIFICATION OF REPORT	18. SECURITY CLASSIFICATION OF THIS PAGE	19. SECURITY CLASSIFICATION OF ABSTRACT	20. LIMITATION OF ABSTRACT
UNCLASSIFIED	UNCLASSIFIED	UNCLASSIFIED	UL

Proceedings of

The 21st Asian Conference on Remote Sensing

Volume 2

December 4-8, 2000
Taipei International Convention Center
Taipei, TAIWAN

Organized by

Center for Space & Remote Sensing Research, National Central University
Chinese Taipei Society of Photogrammetry and Remote Sensing
Asian Association on Remote Sensing

AQ F02-06-1092

Proceedings of

The 21st Asian Conference on Remote Sensing

Volume 2

ISBN

957-02-7241-4

Copyright @2000

Center for Space & Remote Sensing Research, National Central University

Chinese Taipei Society of Photogrammetry and Remote Sensing

Asian Association on Remote Sensing

All rights reserved. Reproduction of this volume or any parts thereof (excluding quotation for use in preparation of reviews, technical and scientific papers) may be made only after obtaining the specific approval of the publishers. The publishers are not responsible for any opinions or statements made in the papers.

Published by

Center for Space & Remote Sensing Research, National Central University

Chinese Taipei Society of Photogrammetry and Remote Sensing

CONFERENCE ORGANIZING COMMITTEE

Honorary Chairman
Chao-Han Liu
(National Central University)

Secretary General of Asian Association on Sensing
Shunji Murai
(University of Tokyo)

General Chairman
A. J. Chen
(Chinese Taipei Society of Photogrammetry and Remote Sensing)

Steering Committee
Bruce Forster; John van Genderen; Armin Gruen; Chin-Chao Koh; Lim Hock; Nik Nasruddin Mahmood; Nguyen Dinh Duong; Ryutaro Tateishi; Tong Qinxi; Suvit Vibulsresth

General Vice-Chairman
S. C. Wang
(National Cheng Kung University)

Technical Committee
L. C. Chen, Chairman; C. F. Chen; K. S. Chen; T. C. Chen; Y. K. Chen; C. C. Cheng; W. H. Ho; M. K. Hsu; Y. C. Liao; Y. A. Liou; J. K. Liu; T. Y. Shih; L. C. Tsai; J. Wu

Local Organizing Committee
G. R. Liu (National Central University), Chairman; C. F. Chen; K. S. Chen; Y. A. Liou; L. C. Tsai; W. L. Wei; J. Wu

Secretariate
Mei-Yuan Lai; Wei-Ling Wei

ACRS 2000

The 21st Asian Conference on Remote Sensing

We wish to thank the following for their contributions to the success of this conference:

NATIONAL SCIENCE COUNCIL
MINISTRY OF EDUCATION
COUNCIL OF AGRICULTURE
MINISTRY OF THE INTERIOR
WATER RESOURCES BUREAU
U.S. AIR FORCE OFFICE OF SCIENTIFIC RESEARCH, ASIAN OFFICE OF AEROSPACE RESEARCH AND DEVELOPMENT (U.S. AFOSR/ AOARD)

EXHIBITORS' LIST

1. Chinese Taipei Society of Photogrammetry and Remote Sensing
2. System & Technology Corporation
3. MacDonald Dettwiler
4. Radarsat International
5. Datron/Transco Inc.
6. Intergraph Co. (Taiwan)
7. Control Signal Co. Ltd.
8. PCI Geomatics
9. ImageSat International
10. The Earth Geographic Publishing Co. Ltd.
11. Matra Systems & Information
12. Spot Image Co.
13. L-3 Communications
14. RITI Taiwan Inc.
15. Hitron Technology Inc.
16. Geoinfor Scientek Consultant Inc.
17. National Space Development Agency of Japan, (NASDA) Bangkok Office
18. Asian Institute of Technology
19. Applanix Corporation
20. China Arial Survey Co.
21. Taiwan Space Imagery Inc.
22. Hitachi Software
23. Remote Sensing Technology Center of Japan (RESTEC)
24. Productivity Group Inc.

PROGRAM OUTLINES

Date	Time	Agenda		
Dec. 4 Mon.	8:30-9:30	Registration		
	9:30-10:00	Opening Ceremony (including award presentations)		
	10:00-10:30	Coffee Break		
	10:30-11:00	Keynote Speech (1)	Possibility and Limitation of Satellite High Resolution Data Prof. Armin Gruen Institute for Geodesy and Photogrammetry, ETH	
	11:00-11:30	Keynote Speech (2)	Recent Advances in Radar Remote Sensing of Vegetation Prof. Kamal Sarabandi Department of Electrical Engineering and Computer Science, University of Michigan	
	11:30-12:00	Keynote Speech (3)	Progress of Photogrammetry and Remote Sensing Prof. Deren Li President, Wuhan Technical University of Surveying and Mapping	
	12:00-13:30	Lunch		
	13:30-15:00	TS-D1/Room 102	TS-H1/Room 101D	
	15:00-15:30	Coffee Break		
	15:30-17:00	TS-E1/Room 102	TS-I1/Room 101D	ST/Room 101C-2 Ends@17:30
	18:00	Welcome Reception		
Dec. 5 Tue.	8:30-10:00	TS-H2/Room 102	TS-M/Room 101D	SS1/Room 101C-2
	10:00-10:30	Coffee Break		
	10:30-12:00	TS-A/Room 102	TS-K/Room 101D	SS2/Room 101C-2
	12:00-13:30	Lunch		
	13:30-15:00	TS-I2/Room 102	TS-L1/Room 101D	SS3/Room 101C-2
	15:00-15:30	Coffee Break		
	15:30-16:00	Briefing by each Poster Presenter (PS-1)/Room 101D		BM-1/Room 101C-2 Ends@17:00
	16:00-18:00	PS-1/Room 101C-1 (Finger Food Provided)		
	19:00	General Meeting (1)for National Delegates only		
Dec. 6 Wed.	8:30-10:00	TS-F/Room 102	TS-J/Room 101D	BM-2/Room 101C-2 Ends@17:00
	10:00-10:30	Coffee Break		
	10:30-12:00	TS-B/Room 102	TS-N/Room 101D	
	12:00-13:30	Lunch		
	13:30-15:00	TS-C/Room 102	TS-L2/Room 101D	
	15:00-15:30	Coffee Break		
	15:30-16:00	Briefing by each Poster Presenter (PS-2)/Room 101D		
	16:00-18:00	PS-2/Room 101C-1		
	19:00	Banquet & Culture Night		
	(Technical Tour to CSRSR, one group each in Morning & Afternoon.)			

Date	Time	Agenda		
Dec. 7 Thur.	8:30-10:00	TS-E2/Room 102	TS-P/Room 101D	BM-3/Room 101C-2
	10:00-10:30	Coffee Break		
	10:30-12:00	TS-G1/Room 102	TS-O/Room 101D	BM-4/Room 101C-2
	12:00-13:30	Lunch		
	13:30-15:00	TS-D2/Room 102	TS-I3/Room 101D	BM-5/Room 101C-2 Ends@17:00
	15:00-15:30	Coffee Break		
	15:30-16:00	Briefing by each Poster Presenter (PS-3)/Room 101D		
	16:00-18:00	PS-3/Room 101C-1 (Finger Food Provided)		
	19:00	General Meeting (2) for National Delegates only		
	19:00	Students Night for Students only		
Dec. 8 Fri.	8:30-10:00	TS-I4/Room 102	TS-G2/Room 101D	
	10:00-10:30	Coffee Break		
	10:30-12:00	Closing Ceremony/Room 102 (including Best Paper Awards)		

Remarks: TS: Technical Session; SS: Special Session; PS: Poster Session, BM: Business Meeting
ST: Student Session

Session Name-Discipline Correspondence:

A	: Agriculture & Soil	J	: Education & Profession
B	: Water Resources	K	: Global Change
C	: Coastal Zone Monitoring	L 1 ~ L 2	: Landuse
D1~D2	: Digital Photogrammetry	M	: Mapping from Space & GPS
E1~E2	: Environment	N	: SAR/InSAR
F	: Forest Resources	O	: Oceanography
G1~G2	: GIS & Data Integration	P	: Hyperspectral & Data Acquisition Systems
H1~H2	: Hazard Mitigation	SS1-SS3	: Special Sessions (AIRSAR/MASTER)
I1~I4	: Image Processing	PS1-PS3	: Poster Sessions

CONTENTS

Paper List iii

Author Index xxi

VOLUME 1

Technical Session A: Agriculture & Soil

A-1 **MODELLING TEA (CAMELLIA SINENSIS (L) O. KUNTZE) YIELD USING SATELLITE DERIVED LAI, LANDUSE AND METEOROLOGICAL DATA** 1
R.M.S.S. Rajapakse, Nitin K. Tripathi, Kiyoshi Honda

A-2 **LAND DEGRADATION DUE TO HYDRO-SALINITY IN SEMI-ARID REGIONS USING GIS AND REMOTE SENSING** 7
Nasir Mahmood Khan, Yohei Sato

A-3 **ANALYSIS OF SPECTRAL CHARACTERISTICS OF RICE CANOPY UNDER WATER DEFICIENCY** 13
Chwen-Ming Yang, Muh-Rong Su

A-4 **CLIMATE CHANGE AND AGRICULTURAL FOOD PRODUCTION OF BANGLADESH: AN IMPACT ASSESSMENT USING GIS-BASED BIOPHYSICAL CROP SIMULATION MODEL** 19
Afzal Ahmed, Ryosuke Shibasaki

A-5 **THE STUDY FOR ASSESSMENT OF SUSCEPTIBILITY TO SOIL LIQUEFACTION IN TAIWAN** 23
Horng-Yuh Guo, Chih-Feng Chiang, Tsang-Sen Liu, Jiang-Liung Chu, Jen-Chyi Liu

A-6 **ON THE RETRIEVALS OF SURFACE SOIL MOISTURE FROM SIMULATED SMOS AND AMSR BRIGHTNESS TEMPERATURES** 29
Shou-Fang Liu, Yuei-An Liou, Wen-June Wang

Technical Session B: Water Resources

B-1 **IDENTIFYING OPTIMUM SITES FOR LOCATING RESERVOIRS EMPLOYING REMOTELY SENSED DATA AND GEOGRAPHICAL INFORMATION SYSTEMS** 35
K. Wan Yusof, Serwan M. J. Baban

B-2 **INTEGRATED GROUND WATER RESOURCES MAPPING IN GURGAON DISTRICT, (HARYANA) INDIA USING REMOTE SENSING AND GIS TECHNIQUES** 41
B.V.M. Rao Toleti , B. S. Chaudhary, K. E. Mothi Kumar, G. P. Saroha, Manoj Yadav, Ajeet Singh, M. P. Sharma, A. C. Pandey, P. K. Singh

B-3 **IDENTIFICATION AND MAPPING OF NEW MARU-GANGA CHANNEL IN NORTH WEST INDIA OF INDIAN SUB-CONTINENT** 47
Narpat Singh Rathore

B-4 **USING SPECTRAL MIXTURE MODELING TECHNIQUES TO DERIVE LAND-COVER PARAMETERS FOR DISTRIBUTED SEDIMENT YIELD ESTIMATIONL MODEL** 52
Enrico C. Paringit, Kazuo Nadaoka

B-5 **GROUNDWATER LEVEL FORECASTING WITH TIME SERIES ANALYSIS** 58
Miao-Hsiang Peng, Jin-King Liu, Tian-Yuan Shih

B-6 **RESERVOIR TROPHIC STATE EVALUATION USING LANDSAT TM DATA** 64
Ke-Sheng Cheng, Tsu-Chiang Lei

Technical Session C: Coastal Zone Monitoring

C-1	ANALYSIS ON THE CONVECTIVE MIXING CHARACTERISTICS OF ESTUARINE RESERVOIR BY LANDSAT TM IMAGES *Takashi Hoshi, Moon Soo Choi, Hideyuki Tonooka*	70
C-2	NEAR REAL TIME MONITORING OF TAIWAN COASTAL WATERS – A MULTIPLE SENSOR APPROACH *I-I Lin, L.S. Wen*	76
C-3	COASTAL ZONE ENVIRONMENT MANAGEMENT WITH EMPHASIS ON MANGROVE ECOSYSTEM, A CASE STUDY OF AO-SAWI THUNG KHLA, CHUMPHON, THAILAND *Surachai Ratanasermpong, Thongchai Charuppat, Dararat Disbunchong, Suwit Ongsomwang*	77
C-4	APPLICATION OF REMOTE SENSING WITH LANDSAT TM DATA FOR MANAGEMENT AND CONTROL OF MANGROVE FOREST –A CASE STUDY IN OKINAWA *Kazuhiro Sato, Munetake Kanetomi*	83
C-5	OBSERVING INTERTIDAL ZONES USING SATELLITE IMAGERY *Rigel Hian Dee Leow, Yihan Tan, Chee Yuen Wan, Christian Melsheimer*	89
C-6	CORAL REEF ECOSYSTEM CHANGE DETECTION BASED ON SPATIAL AUTOCORRELATION OF MULTISPECTRAL SATELLITE DATA *Heather Holden, Chris Derksen, Ellsworth LeDrew*	94

Technical Sessions D1, D2, D3, D4: Digital Photogrammetry

D1-1	KNOWLEDGE-BASED IMAGE ANALYSIS FOR 3D ROAD RECONSTRUCTION *Chunsun Zhang, Emmanuel Baltsavias, Armin Gruen*	100
D1-2	ORTHORECTIFICATION OF STEREO SPOT PANCHROMATIC AND RADARSAT FINE MODE DATA USING ORBITAL PARAMETERS AND DIGITAL ELEVATION MODEL *Mohd Ibrahim Seeni Mohd, Shahruddin Ahmad*	106
D1-3	HIDDEN COMPENSATION AND SHADOW ENHANCEMENT FOR TRUE ORTHOPHOTO GENERATION *Jiann-Yeou Rau, Nai-Yu, Chen, Liang-Chien Chen*	112
D1-4	DEVELOPMENT OF SOFTWARE TO CREATE A RECTIFIED IMAGE OF AN INCLINED PLANE *Ryuji Matsuoka, Naoki Shirai*	119
D1-5	AN ITERATIVE APPROACH TO ACQUIRE LINEAR FEATURES UNDER THE CONSTRAINTS OF THEIR KNOWLEDGE IN OBJECT SPACE *Shih-Hong Chio, Shue-Chia Wang*	125
D1-6	AUTOMATIC ACQUISITION OF 3D SPATIAL DATA IN CITY WITH AIR-BORNE TLS (THREE LINE SCANNER) *Yoshiaki Kagawa, Ryosuke Shibasaki*	131
D2-1	MULTI-RESOLUTION APPROACH TO RADARGRAMMETRIC DIGITAL ELEVATION MODELS GENERATION *Xiaojing Huang, Leong Keong Kwoh, Hock Lim*	135
D2-2	IMPLEMENTATION OF DIGITAL PHOTOGRAMMETRY FOR MONITORING THE TSAOLIN AREA IN TAIWAN *Yeong-Kuan Chen, Jihn-Fa Jan*	141
D2-3	TOPOGRAPHIC MAP REVISION IN DIGITAL PHOTOGRAMMETRIC ENVIRONMENT *K.S.K.Wijayawardana*	147
D2-4	GLOBAL IMAGE COMPOSITE OF ADEOS/OCTS GAC DATA *T. Hashimoto, T. Igarashi, A. Mukaida, R. Higuchi*	152
D2-5	EXTRACTION AND UTILIZATION OF GEOMETRICAL AND CONTEXTUAL INFORMATION IN VERY HIGH RESOLUTION IKONOS SATELLITE IMAGERY *Annie Hui, Soo Chin Liew, Leong Keong Kwoh, Hock Lim*	158

D2-6 THE RECTIFICATION OF HIGH RESOLUTION REMOTE SENSING SATELLITE IMAGERY 164
Chao-hsiung Wu

Technical Sessions E1, E2: Environment

E1-1 LAND COVER CHANGE AND FLUCTUATION OF LACUSTRINE WATER QUALITY IN OKUTAMA LAKE 170
Susumu Ogawa, Moe Moriyama

E1-2 VEGETATION MAPPING IN GANGES RIVER BASIN FOR GLOBAL MAPPING PROJECT 176
Mona Lacoul, Lal Samarakkon, Kiyoshi Honda

E1-3 VERIFICATION OF SURFACE TEMPERATURE FROM LANDSAT 7/ETM+ DATA 182
Yuzo Suga, Motohide Yoshimura, Shoji Takeuchi, Yoshinari Oguro

E1-4 AN EVALUATION OF DROUGHT RISK AREA IN NORTHEAST THAILAND USING REMOTELY SENSED DATA AND GIS 188
C. Mongkolsawat, P. Thirangoon, R. Suwanwerakamtorn, N. Karladee, S. Paiboonsak, P.Champathet

E1-5 INVESTIGATION OF EVAPORATE DEPOSITS ON GAVKHONI PLAYA LAKE 194
R. Ajalloeian, H.R.Pakzad, H.Safaei

E1-6 ESTIMATION OF THE METHANE EMISSION FROM WEST SIBERIAN WETLAND BY SCALING BETWEEN NOAA/AVHRR AND SPOT/HRV DATA 200
Wataru Takeuchi, Masayuki Tamura, Yoshifumi Yasuoka

E2-1 URBAN CHANGE STUDY USING RS AND GIS 204
D. Amarsaikhan, M.Ganzorig, M.Saandar

E2-2 ENVIRONMENTS TRANSITION RESEARCH IN YUSAN NATIONAL PARK AFTER EARTHQUAKE AND TYPHOON 210
Tien-Yin Chou, Chih-Cung Kao, Ying-Huei Chang

E2-3 THE CHARACTERIZATION OF VERTICAL MEAN TEMPERATURE OVER INDONESIA FROM 1994 TO 1998 216
Achmad Sasmito, Urip Haryoko, Riris Adriyanto, Nelly Florida Riama, Rosdiana

E2-4 CAPABILITY OF RADARSAT DATA IN MONSOON FLOOD MONITORING 222
Mardiana Shafiee, Azman Ahmad, Osman Kadir

E2-5 APPLYING AVHRR DATA TO ESTIMATE AND MONITOR AEROSOL OPTICAL THICKNESS 228
Tang-Huang Lin, Gin-Rong Liu

E2-6 SURFACE TEMPERATURE ANALYSIS OF URBAN AREA USING RS AND GIS 234
Myung-Hee Jo, Kwang-Jae Lee, Ji-Hyun Shin, Ae -Sook Suh, Sung-Nam Oh

Technical Session F: Forest Resources

F-1 APPLICATION AND VALIDATION OF LWCI (LEAF WATER CONTENT INDEX) TO TROPICAL SEASONAL FOREST REGION 240
Michio Anazawa, Genya Saito, Haruo Sawada

F-2 APPLICATION OF ECOSYSTEM MANAGEMENT DECISION SUPPORT SYSTEM IN SELECTING SUITABLE SITE FOR TAIWANIA 246
Su-Fen Wang, Yeong-Kuan Chen, Chi-Chuan Cheng

F-3 FOREST FIRE MONITORING WITH SPOT-4 SATELLITE IMAGERY 252
Kim Hwa Lim, Leong Keong Kwoh, Soo Chin Liew, Hock Lim

F-4 STUDY ON THE RELATIONSHIP AMONG THE MACHILUS SPECTRAL BEHAVIOR AND LIGHT INTENSITY AND PHYSIOLOGICAL ACTIVITY 258
Chinsu Lin

F-5	ANALYSIS OF FRAGMENTATION AND ANTHROPOGENIC DISTURBANCES IN THE HIMALAYAN FORESTS: USE OF REMOTE SENSING AND GIS *Subrat Sharma, L.M.S. Palni, P. S. Roy*	264
F-6	MODELING LANDSCAPE CHANGES USING LOGIT MODELS *Li-Ta Hsu, Chi-Chuan Cheng, Yu-Ching Lai*	270

Technical Sessions G1, G2: GIS & Data Integration

G1-1	IMPLEMENTATION OF A GEOGRAPHIC INFORMATION SYSTEM (GIS) TO DETERMINE WILDLIFE HABITAT QUALITY US ING HABITAT SUITABILITY INDEX *Yu Ching Lai, Walter L. Mills, Chi-Chuan Cheng*	276
G1-2	APPLICATION OF GIS TO MEASURE AND EVALUATE LANDSCAPE CHANGES *Chi-Chuan Cheng, Jihn-Fa Jan*	282
G1-3	GIS FOR VISUAL IMPACT ASSESSMENT *Zongyu Zhang, Jin Yeu Tsou, Hui Lin*	288
G1-4	INTEGRATION AND APPLICATION OF SOCIO-ECONOMIC AND ENVIRONMENTAL DATA WITHIN GIS FOR DEVELOPMENT STUDY IN THAILAND *Tran Hung, Yoshifumi Yasuoka*	294
G1-5	HARNESSING INFORMATION TECHNOLOGY FOR (GEO)MANAGEMENT AND DECISION-MAKING *Rowena Bassi Quiambao*	300
G1-6	GIS DATABASE OF THE ENVIRONMENTAL INFORMATION *Sharav Munkhtuya, Batjantsan Enkhtsetseg*	306
G2-1	APPLICATION OF GEOINFORMATICS ON MOUNTAIN LAND HAZARD MAPPING: A CASE OF ANNAPURNA HIMALAYAS, CENTRAL NEPAL. *Krishna Poudel*	312
G2-2	A SURFACE INTERPOLATION FOR LARGE-SCALE REPRESENTATION OF TERRAIN IN AN URBAN AREA *Yohko Shimura, Shaobo Huang, Ryosuke Shibasaki*	318
G2-3	DYNAMIC SPATIAL MODELING USING ROS AND CARRYING CAPACITY FOR ECOTOURISM MANAGEMENT *Kampanart Piyathamrongchai, Nitin Kumar Tripathi*	323
G2-4	A CASE-BASED URBAN PLANNING SUPPORT SYSTEM USING AN INTEGRATED COMBINATION OF GEOGRAPHICAL INFORMATION SYSTEMS AND REMOTE SENSING *Ko-Wan Tsou, Yao-Lin Chang, Yu-Ting Hung*	329
G2-5	AN IMPLEMENTATION OF 3D GIS ON WEB *Tien-Yin Chou, Lan-Kun Chung, Wen-Yuan Ku, Wei-Yuan Lo*	335
G2-6	THE MANAGEMENT SYSTEM DEVELOPMENT OF CAMPUS FACILITY INFORMATION USING WEB-BASED GIS *Myung-Hee Jo, Sung-Joong Park, Mal-Suk Kim, Yun -Won Jo*	341

Technical Sessions H1, H2: Hazard Mitigation

H1-1	INFORMATION TECHNOLO GY AND NATURAL DISAS TER MANAGEMENT IN INDIA *Alok Gupta*	346
H1-2	DETECTION OF DISASTER DAMAGE USING CHANGES OF CITY LIGHTS WITH DMSP/OLS DATA IN ASIA PACIFIC REGION *Izumi Nagatani, Genya Saito, Masafumi Kodama, Xianfang Song, Chris Elvidge*	352
H1-3	HIGH RESOLUTION REMOTE SENSING DATA & GIS TECHNIQUES IN UPDATION OF INFRASTRUCTURE DETAILS FOR FLOOD DAMAGE ASSESSMENT- A CASE STUDY *YK Srivastava, Binod Doley, Dk Pal, RK Das, S Sudhakar,S. Adiga , Kv Venkatachary, SK Srivastava*	358

H1-4	**VISUALIZATION OF WATER LEVELS FROM JERS-1 SAR IMAGES USING STRONG SCATTERS - PHITSANULOK, THAILAND -** *Takako Sakurai-Amano*	366
H1-5	**DROUGHT AND VEGETATION STRESS MONITORING IN THE ARID AND SEMI-ARID REGIONS OF THE MONGOLIA US ING REMOTE SENSING AND GROUND DATA** *Yu. Bayarjargal, Ts. Adyasuren, Sh. Munkhtuya*	372
H1-6	**INTEGRATING REMOTE SENSING AND GIS FOR FIRE HAZARD CATEGORIZATION & RES OURCE ALLOCATION** *Sunil Bhaskar*	378
H2-1	**LANDSLIDES TRIGGERED BY THE CHI-CHI EARTHQUAKE** *Hsuan Wu Liao, Chyi Tyi Lee*	383
H2-2	**DEVELOPMENT OF GIS-BASED BUILDING DAMAGE DATABASE FOR THE 1995 KOBE EARTHQUAKE** *Koichiro Umemura, Osamu Murao, Fumio Yamazaki*	389
H2-3	**AIRBORNE THERMAL IR REMOTE SENSING OF LUSHAN GEOTHERMAL FIELD** *Chi-Nan Wu, Ta-Ko Chen*	395
H2-4	**AUTOMATED DETECTION OF BUILDING DAMAGE DUE TO RECENT EARTHQUAKES USING AERIAL TELEVISION IMAGES** *Hajime Mitomi, Fumio Yamazaki, Masashi Matsuoka*	401
H2-5	**VALIDITY STUDY OF EDES APPLICATION TO TAIWAN CHI-CHI EARTHQUAKE DISASTER** *Masayuki Kohiyama, Haruo Hayashi, Norio Maki, Shin Hashitera*	407
H2-6	**ASIA PACIFIC NETWORK FOR DISASTER MITIGATION USING EARTH OBSERVATION SATELLITE (ANDES) (1) - FOREST FIRE DETECTION** *Taro Shinmura, Haruo Sawada, Izumi Nagatani*	413

Technical Sessions I1, I2, I3, I4: Image Processing

I1-1	**A NEURAL NETWORK MODEL FOR ESTIMATING SURFACE CHLOROPHYLL AND SEDIMENT CONTENT AT THE LAKE KASUMI GAURA OF JAPAN** *Pranab Jyoti Baruah, Masayuki Tamura, Kazuo Oki, Hitoshi Nishimura*	419
I1-2	**URBAN IMAGE ANALYSIS USING ADAPTIVE RESONANCE THEORY** *Supoj Mongkolworaphol, Yuttapong Rangsanseri, Punya Thitimajshima*	425
I1-3	**COLOR IMAGE ENHANCEMENT BASED ON SEGMENTATION REGION HISTOGRAM EQUALIZATION** *Sakreya Chitwong, Fusak Cheevasuvit, Kobchai Dejhan, Somsak Mitatha*	430
I1-4	**PARALLEL COMPUTING IN REMOTE SENSING DATA PROCESSING** *Chao-Tung Yang, Chi-Chu Hung*	434
I1-5	**USING COMPLETE POLARIMETRIC INFORMATION IN FUZZY NEURAL CLASSIFICATION OF SAR IMAGE BASED ON COMPLEX GAUSSIAN DISTRIBUTION** *Chia-Tang Chen, K. S. Chen*	440
I1-6	**COMPARATIVE STUDY ON MODEL FITTING METHODS FOR OBJECT EXTRACTION** *Masafumi Nakagawa, Huijing Zhao, Ryosuke Shibasaki*	446
I2-1	**SOME ADVANCED TECHNIQUES FOR SPOT 4 XI DATA HANDLING** *Nguyen Dinh Duong, Le Kim Thoa, Nguyen Thanh Hoan*	452
I2-2	**THE ANALYTIC OF REMOTELY SENSED DIGITAL IMAGE** *Xianhua Li, Dengrong Zhang, Gelong Yu, Hui Lin, Huosheng Shi*	458
I2-3	**THE STATISTICAL CORRELATION WITH INVARIANT MOMENTS FOR GEOMETRIC CORRECTION IMPROVEMENT** *Sompong Wisetphanichkij, Kobchai Dejhan, Somkid Hanpipatpongsa, Fusak Cheevasuvit, Somsak Mitatha, Chanchai Pienvijarnpong, Chatcharin Soonyeekan*	464

I2-4	**OPTIMIZATION OF ACTIVE AND PASSIVE REMOTE SENSING SYSTEMS USING INFORMATIONAL CRITERION** *Asadov Hikmat Hamid Oglu*	470
I2-5	**MULTISPECTRAL IMAGE COMPRESSION USING FCM-BASED VECTOR QUANTIZATION** *Uthai Sangthongpraow, Yuttapong Rangsanseri*	476
I2-6	**COMPARISON OF TWO TEXTURE FEATURES FOR MULTISPECTRAL IMAGERY ANALYSIS** *Pornphan Dulyakarn, Yuttapong Rangsanseri, Punya Thitimajshima*	481
I3-1	**IMAGE ANALYSIS OF REMOTE SENSING DATA INTEGRATING SPECTRAL AND SPATIAL FEATURES OF OBJECTS** *Joji Iisaka, Takako Sakurai-Amano*	486
I3-2	**A NEW APPROACH FOR AUTOMATIC DETERMINATION OF EDGE CENTER LINES IN A DIGITAL IMAGE** *Jaan-Rong Tsay*	492
I3-3	**GEOMETRIC REGISTRATION METHOD FOR 10-DAY COMPOSITE AVHRR DATA FOR ASIAN REGION** *Ts. Purevdorj, R. Yokoyama*	498
I3-4	**FEATURE EXTRACTION IN RESIDENTIAL AREAS BY KNOWLEDGE MODELLING** *His-Min Chao, John C. Trinder*	504
I3-5	**SUBBAND SAR IMAGE CODING BY USING QUADTREE DECOMPOSITION ON VARIABLE BLOCK TRUNCATION CODE** *Anmach Khawne, Somchai Omsin, Suthichai Noppanakeepong , Krit Wongrujira*	510
I3-6	**OPTIMAL POLARIZATION FOR CONTRAST ENHANCEMENT IN POLARIMETRIC SAR USING GENETIC ALGORITHM** *Ruey-Long Su, K. S. Chen, Jiancheng Shi*	516
I4-1	**A REFLECTANCE RETRIEVAL ALGORITHM FOR LANDSAT TM SATELLITE IMAGE** *C. H. Liu, E. F. Vermote*	522
I4-2	**A SYNERGISTIC AUTOMATIC CLUSTERING TECHNIQUE (SYNERACT) FOR MULTISPECTRAL IMAGE ANALYSIS** *Kai-Yi Huang*	527
I4-3	**AN EFFICIENT ARTIFICIAL NEURAL NETWORK TRAINING METHOD THROUGH INDUCED LEARNING RETARDATION: INHIBITED BRAIN LEARNING** *Joel C. Bandibas, Kazunori Kohyama*	533
I4-4	**FLOODED AREA ASSESSMENT WITH FUSED MULTI-SPECTRAL MULTI-SENSOR BY USING TEXTURE FEATURE ANALYSIS AND NEURAL NETWORK CLASSIFICATION** *Kobchai Dejhan, Sompong Wisetphanichkij, Prasit Kerdyou, Fusak Cheevasuvit , Somsak Mitatha, Chanchai Pienvijarnpong, Chatcharin Soonyeekan*	539
I4-5	**ACCURACY IMPROVEMENT OF THE LAND COVER CLASSIFICATION BY USING TRUNCATED NORMAL DISTRIBUTION** *Tsukasa Hosomura*	545
I4-6	**SELF-ORGANIZING FEATURE MAP FOR MULTI-S PECTRAL SPOT LAND COVER CLASSIFICATION** *Jen-Hon Luo, Din-Chang Tseng*	549

Technical Session J: Education & Profession

J-1	**DEVELOPMENT OF DATA SET FOR ANALYSIS OF LANDSAT TM IMAGES USING WWW BROWSER AND SPREADSHEET** *Kiyotada Sato, Ryuzo Yokoyama*	555
J-2	**SURVEY DEPARTMENT OF NEPAL: TODAY AND TOMORROW** *Krishna Raj Adhikary*	561
J-3	**TELLING STORIES OF JIN-SHAN-MIANN ADJACENT TO HSINCHU SCIENCE-BASED INDUSTRIAL PARK ON A SIMULATED ROCSAT-2 IMAGE** *Ku-Yu Chang, Chih-Li Chang*	567

J-4	**DETERMINATION OF ORIGINAL SIZE OF THE ABHAYAGIRIYA STUPA** *Siri Diyupathi Dampegama*	573
J-5	**REMOTE SENSING ACTIVITIES OF NASDA IN SOUTHEAST ASIA** *Eiichi Muto*	578
J-6	**THE EDUCATIONAL FUNCTION OF SATELLITE IMAGERY** *Shi-Ming Lu*	584

Technical Session K: Global Change

K-1	**DESERTIFICATION MAPPING OF WEST ASIA -A GIS AND REMOTE SENSING APPLICATION** *Hussein Harahseh, Ryutaro Tateishi*	585
K-2	**DEVELOPMENT FOR DATA BASE FOR ECO-SYSTEM CHANGES AND EMISSION CHANGES OF GHG USING REMOTE SENSING AND GIS IN SUMATRA ISLAND, INDONESIA** *Lilik Budi Prasetyo, Genya Saito, Haruo Tsuruta*	591
K-3	**MODELING THE EFFECTS OF RECENT LAND USE CHANGE ON THE CARBON CYCLE IN THE ZHU JIANG DELTA REGION OF SOUTHERN CHINA** *Dennis G. Dye, Thomas Hinchliffe, Curtis E. Woodcock*	597
K-4	**SATELLITE OBSERVATION OF MIGRATION ROUTES AND HABITATS OF MIGRATORY BIRDS LIVING IN WETLANDS IN EAST ASIA** *Masayuki Tamura, Hiroyoshi Higuchi*	603
K-5	**AN OPERATIONAL APPROACH FOR MAPPING BUSHFIRE HISTORY IN THE TROPICAL SAVANNAS OF NORTHERN AUSTRALIA** *Yue Zhang, Peter Whitehead, Waqar Ahmad, Carl Menges*	609
K-6	**RELATIONSHIP BETWEEN CANOPY BRDF AND PHYSICAL PARAMETERS OF 3-D STRUCTURE OF VEGETATION IN NORTHERN WETLANDS IN JAPAN** *Michiru Miyamoto, Kunihiko Yoshino, Keiji Kushida*	615

VOLUME 2

Technical Sessions L1, L2: Landuse

L1-1	CLASSIFICATION OF REMOTELY SENSED IMAGERY USING MARKOV RANDOM FIELDS *Brandt Tso, Paul M. Mather*	621
L1-2	MACHINE LEARNING METHODS TO IDENTIFY MIS LABELED TRAINING DATA AND APPROPRIATE FEATURES FOR GLOBAL LAND COVER CLASSIFICATION *Jonathan Cheung-Wai Chan, Matthew C. Hansen, Ruth Defries*	628
L1-3	DEVELOPMENT OF TRUNK-CANOPY BIOMASS AND MORPHOLOGY INDICES FROM QUADPOLARIZED RADAR DATA *Peter N. Tiangco, Bruce C. Forster*	634
L1-4	A LAND USE CHANGE STUDY USING CELLULAR AUTOMATA *Jinn-Guey Lay*	646
L1-5	IDENTIFICATION OF LANDSLIDES INDUCED BY CHI-CHI EARTHQUAKE USING SPOT MULTISPECTRAL IMAGES *Yu-Chuan Kuo, Hui-Chung Yeh, Ke-Sheng Cheng, Chia-Ming Liou , Ming-Tung Wu*	652
L1-6	DETERMINATION OF MAJOR FACTORS AFFECTING THE LAND USE/LAND COVER OF UPPER MAGAT WATERSHED. - A PRELIMINARY STUDY FOR THE LAND USE/LAND COVER CHANGE CASE STUDY OF UPPER MAGAT WATERSHED PHASE - II *Victorino A. Bato*	658
L2-1	ADDITIONAL NIGHTTIME AVHRR DATA FOR CLASSIFYING LAND COVER TYPE IN THAILAND *Chada Narongrit, Mitsuharu Tokunaga, Shunji Murai, Kaew Nualchawee, Apisit Eiumnoh, Suphat Vongvisessomjai*	665
L2-2	LAND-COVER CHANGE IN CHINA USING TIME SERIES ANALYSIS, 1982 - 1999 *Chien-Pin Lee, Stephen S. Young, Hao Chen*	671
L2-3	URBAN PLANNING AND MONITORING CHANGES USING ER MAPPER *Abdullah Mah*	678
L2-4	INVESTIGATION OF LAND USE IN RELATION TO LANDSLIDE BY USING GIS *R. Ajalloeian , R.Karami, M.Nikzad*	683
L2-5	THE STUDY OF KNOWLEDGE-BASED DATABASE ASSIST FOR URBAN LAND USE CLASSIFICATION *Fu-Jen Chien, Tien-Yin Chou*	689
L2-6	APPLICATION OF REMOTE SENSING IMAGE DATA IN THE ANALYSIS OF LAND USE MANAGEMENT OF AGRICULTURE IN CHIANAN IRRIGATION PROJECT IN TAIWAN *You Jenn Ming, Kiyoshi Torii, Yoshiaki Mori, Ryouhei Kada*	695

Technical Session M: Mapping from Space & GPS

M-1	COVARIANCE PROPAGATION IN GPS/IMU - DIRECTLY GEOREFERENCED FRAME IMAGERY *Mohamed M. R. Mostafa, Joseph Hutton, Erik Lithopoulos*	701
M-2	RADARSAT-2 MISSION: OVERVIEW AND DEVELOPMENT STATUS *Peter Meisl, Alan A. Thompson, Anthony P. Luscombe*	702
M-3	PERFORMANCE EVALUATION OF RTK GPS WITHOUT SA EFFECT *Jenn-Taur Lee, Wen-Feng Chen*	708

M-4 EFFECT OF COHERENCE ON DEMS DERIVED FROM SAR INTERFEROMETRY: A CASE STUDY OF MAYON VOLCANO, PHILIPPINES 714
Yu Tuong Thuy, Mitsuharu Tokunaga

M-5 USE OF DIGITAL TERRAIN MODELS FOR THE INFRASTRUCTURE DEVELOPMENT IN SRI LANKA 720
Nihal Wijesekara

M-6 A METHOD OF MAP MATCHING FOR PERSONAL POSITIONING SYSTEMS 726
Kay Kitazawa, Yusuke Konishi, Ryosuke Shibasaki

Technical Session N: SAR/InSAR

N-1 A MULTI-POLARIZED AND MULTI-ANGLE C-BAND RADAR SYSTEM FOR SOIL MOISTURE DETERMINATION UNDER BARE SOIL CONDITIONS 732
Shakil Ahmad Romshoo, T. Oki, K. Musiake

N-2 VERIFICATION OF INSAR CAPABILITY FOR DISASTER MONITORING - A CASE STUDY OF CHI-CHI EARTHQUAKE IN TAIWAN 738
Shoji Takeuchi, Yuzo Suga, Yoshinari Oguro, A. J. Chen, Chinatsu Yonezawa

N-3 SAR INTERFEROMETRY APPLICATIONS IN THE PHILIPPINES USING ERS-1, ERS-2 AND JERS-1: CASE STUDIES IN MAYON AND TAAL VOLCANO 744
J. H. G. Salvador, H. Kanbara,R. Abundo, M. Tsukada, K. Hirose, A. Dayao, E. Corpuz, A. Baloloy

N-4 A STUDY ON DIFFERENTIAL INTERFEROMETRY IN SUBSIDENCE 749
C. T. Wang, H. T. Wang, D. C. Chern , N. Y. Chen, L. S. Liang
Center for Space and Remote Sensing Research, National Central University, Taiwan

N-5 921 CHICHI EARTHQUAKE : PRELIMINARY INTERFEROMETRIC INTERPRETATIONS 755
B. Deffontaines, L. S. Liang, E. Pathier, C. T. Wang, B. Fruneau, C. T. Lee, D. Raymond, J. Angelier, J. P. Rudant

N-6 DOPPLER COEFFICIENT ESTIMATION FOR SYNTHETIC APERTURE RADAR USING SUB-APERTURE INTERFEROGRAM 761
Jim Min Kuo, K. S. Chen

Technical Session O: Oceanography

O-1 SEA SURFACE TEMPERATURE VARIABILITY IN THE SEAS SURROUNDING THE PHILIPPINES IN RELATION TO ENSO EVENTS 767
Erlinda E. Salamante, Cesar L. Villanoy

O-2 EL NINO SOUTHERN OSCILLATION (ENSO) IMPACT ON SEA SURFACE TEMPERATURE (SST) DERIVED FROM SATELLITE IMAGERY AND ITS RELATIONSHIP ON TUNA FISHING GROUND IN THE SOUTH JAVA SEAWATERS 772
Jonson Lumban Gaol, Djisman Manurung

O-3 DERIVATION OF AEROSOL OPTICAL DEPTH OVER THE EAST ASIAN OCEANS WITH ROCSAT-1 OCI IMAGERY 777
Shih-Jen Huang, Gin-Rong Liu

O-4 COMPARATIVE PERFORMANCE OF SST ALGORITHMS IN THE TROPICAL OCEAN USING OCTS DATA 782
K. Abdullah, M. Z. M. Jafri, N. M. Saleh, A. Bahari

O-5 THE USE OF SEAWIFS SATELLITE DATE FOR OCEAN COLOUR DETERMINATION IN FISHERIES APPLICATION 788
Mohd Ibrahim Seeni Mohd, Tadris Ahmad

O-6 CLASSIFICATION OF ALGAL BLOOM TYPES FROM REMOTE SENSING REFLECTANCE 794
Soo Chin Liew, Leong Keong Kwoh, Hock Lim

Technical Session P: Hyperspectral & Data Acquisition Systems

P-1	VEGETATION SPECTRAL FEATURE EXTRACTION MODEL *Qian Tan, Hui Lin , Yongchao Zhao , Tong Qingxi , Zhen Lanfeng*	800
P-2	HYPERSPECTRAL IMAGE COMPRESSION USING THREE-DIMENSIONAL WAVELET TRANSFORMATION *Yi-Hsing Tseng, Hung-Kuan Shih, Pai-Hui Hsu*	809
P-3	ESTIMATION OF PHOTOSYNTHETIC RATE OF PLANT FROM HYPER-SPECTRAL REMOTE SENSING OF BIOCHEMICAL CONTENT *Takahiro Endo, Toshinori Okuda, Masayuki Tamura, Yoshifumi Yasuoka*	815
P-4	MULTISCALE ANALYSIS OF HYPERSPECTRAL DATA USING WAVELETS FOR SPECTRAL FEATURE EXTRACTION *Pai-Hui Hsu, Yi-Hsing Tseng*	821
P-5	MICROWAVE HOLOGRAPHIC - IMAGING REMOTE OBJECTS USING LIGHT - MODULATED SCATTERING TECHNIQUE *Thammasak Vimonkiattikun, Jirawath Panklang , Anupong Srongprapa*	828
P-6	APPLICATION OF AIRBORNE HYPERSPECTRAL IMAGING IN WETLAND DELINEATION *Chung-Hsin Juan, Jonathan D. Jordan, Chih-Hung Tan*	834

Special Sessions SS1, SS2, SS3 : AirSAR/MASTER

SS1-1	PACRIM 2 AIRSAR DEPLOYMENT TO THE ASIA-PACIFIC REGION AUGUST - OCTOBER 2000: REPORT ON THE DATA ACQUISITION PHASE AND EARLY RESULTS *A.K. Milne, Ian J. Tapley*	840
SS1-2	THE USE OF AIRSAR DATA FOR ASSESSING THE POTENTIAL OF FUTURE SPACEBORNE SAR FOR REGIONAL ESTIMATION OF WOODLAND BIOMASS IN AUSTRALIA *A.K. Milne, N. Cronin, R.M. Lucas, C. Witte, R. Denham*	841
SS1-3	ESTIMATION OF SOIL MOISTURE WITH VEGETATED SURFACE BY MULTI-TEMPORAL MEASUREMENTS *Jiancheng Shi*	847
SS2-1	DEPLOYMENT OF THE MODIS/ASTER AIRBORNE SIMULATOR (MASTER) DURING PACRIM 2 *Ian J. Tapley, A. K. Milne*	852
SS2-2	ADVANCES IN DIGITAL ELEVATION DATASETS FOR EXPLORATION, TOPOGRAPHIC MAPPING AND DISASTER MANAGEMENT *Ian J. Tapley*	853
SS2-3	BENEFITS OF TOPSAR RADAR INTERFEROMETRY IN TROPICAL TERRAINS *Ian J. Tapley*	857
SS3-1	ANALYSIS OF POLARIZATION SIGNATURES AND TEXTURAL FEATURES FOR AIRBORNE PI-SAR IMAGES *Takahiro Yamada, Takashi Hoshi*	860
SS3-2	A STUDY OF SURFACE DEFORMATION FROM EARTHQUAKE BY DIFFERENTIAL RADAR INTERFEROMETRY *C. T. Wang, L. S. Liang, K. S. Chen, A. J. Chen*	866
SS3-3	ANALYSIS OF MULTIPOLARIZATION AND MULTI-BAND RADAR DATA OVER ILOILO CITY AND VICINITIES *Michael B. Lituanas, Jerry H.G. Salvador, Dulcisimo S. Domingo III, Aeschylus M.J. Valenzuela, Eduardo O. Claridad*	872

Poster Session PS1

PS1-01	AN INTRODUCTION OF ASTER (THE ADVANCED SPACEBORNE THERMAL EMISSION AND REFLECTION RADIOMETER) FOR THE EARTH OBSERVATION *Masatane Kato, Yuichi Maruyama, Makoto Tsukada*	877
PS1-02	PHOTOGRAMMETRIC DIGITAL DATA PROCESSING OF TSAU-LIN BIG LANDSLIDE *Hsin-Hsing Cheng*	883
PS1-03	3D DIGITAL ARCHIVING SYSTEM FOR WORLD HERITAGE *Kazuhisa Inaba, Ryosuke Shibasaki*	891
PS1-04	ON MODELING OF THE SAR-IMAGE SQUINT PARAMETER *J. Wu, C. J. Liu*	897
PS1-05	INTEGRATION OF MULTISENSOR MULTITEMPORAL SATELLITE DATA FOR AGRICULTURAL VEGETATION MAPPING *L. Zhu, R. Tateishi*	903
PS1-06	GLOBAL POSITIONING SYSTEM (GPS) *Venant B. Mugemuzi*	909
PS1-07	POST-CLASSIFICATION AND DETECTION OF SIMULATED CHANGE FOR NATURAL GRASS *Hao-Hsiung Huang, Chiao-Ju Hsiao*	915
PS1-08	CONSTRUCTION OF SATELLITE IMAGE DATA SET BY MULTISPECTRAL AND HYPERSPECTRAL SENSORS *Yuzo Suga, Kenji Takasaki, Shoji Takeuchi*	922
PS1-09	TRACKING AUTOMOBILES USING AIR-BORNE TLS (THREE LINE SCANNER) IMAGES *Ryuichi Murata, Ryosuke Shibasaki*	928
PS1-10	GEO-REFERENCING OF MULTI-SENSOR RANGE DATA FOR VEHICLE-BORNE LASER MAPPING SYSTEM (VLMS) *Dinesh Manandhar, Ryosuke Shibasaki*	932
PS1-11	A PHOTOGRAMMETRIC EVALUATION OF AN APS CAMERA *Tian-Yuan Shih, Chien-Bin Kung*	938
PS1-12	APPLICATIONS OF HYPERSPECTRAL REMOTE SENSING IN URBAN REGIONS *Sunil Bhaskaran, Bisun Datt*	944
PS1-13	IMAGE GEOMETRIC SIMULATION AND ORIENTATION MODELING FOR ROCSAT-2 *Liang-Chien Chen, Yi-Ying Wu*	948
PS1-14	SUPERVISED CLASSIFICATION OF MULTI-TEMPORAL REMOTE SENSING IMAGES *Chi-Farn Chen, Yueh-Tan Li*	954
PS1-15	COMPARING EFFECTS OF DIFFERENT SIZES OF AGGREGATION ON SPATIAL STRUCTURE OF REMOTELY SENSED DATA *Yu-Pin Lin, Tung-po Teng*	960
PS1-16	COMPUTERIZED IONOSPHERIC TOMOGRAPHY USING THE GPS/MET AND NNSS DATA *C. T. Liu, L. C. Tsai, W. H. Tsai*	967
PS1-17	SENSOR INTEGRATION FOR PERSONAL POSITIONING SYSTEM *Yusuke Konishi, Ryosuke Shibasaki*	974
PS1-18	GROUND TRUTH MEASUREMENT SYSTEM USING RC HELICOPTER *Daisuke Hongoh, Hironori Ichikawa, Koji Kajiwara, Yoshiaki Honda*	980
PS1-19	DEVELOPMENT OF THE RETRIEVAL ALGORITHMS FOR ATMOSPHERIC REFRACTIVITY FROM GPS/MET OCCULTATION *Yuei-An Liou, Cheng-Yung Huang*	984
PS1-20	AUTOMATED CARTOGRAPHIC LINE TRACKING *Pakorn Apaphant*	990
PS1-21	BIOMASS ESTIMATION BY THE STEREOPHONIC IMAGE ANALYSIS *Hiroyuki Masubuchi, Koji Kajiwara, Yoshiaki Honda*	996

Poster Session PS2

PS2-01	**OPTICAL REMOTE SENSING USING FIBER BRAGG DEVICE FOR DYNAMIC LOAD MEASUREMENTS** *C. Patimapornchai, V. Jewpraditkul, P. P. Yupapin*	1002
PS2-02	**MAPPING AND MEASURING THE TROPOSPHERE POLLUTANTS ORIGINATED FROM THE 1997 FOREST FIRE IN SOUTH EAST ASIA** *Mazlan Hashim, Kasturi Devi Kanniah, Abdul Wahid Rasib , Lim Chee Ming*	1006
PS2-03	**LAND COVER CHANGE AND LONG-TERM FLUCTUATION OF EVAPOTRANSPIRATION IN OKUTAMA** *Susumu Ogawa, Nobuaki Naito*	1012
PS2-04	**MULTISOURCE DATA FUSION – FUSING OPTICAL AND SAR DATA FOR IRRIGATED RICE AREAS IDENTIFICATION** *J. Worawattanamateekul , X. J. F. Canisius, L. Samarakoon*	1018
PS2-05	**STUDY ON LAND USE MANAGEMENT WITH GEOGRAPHIC INFORMATION SYSTEMS** *Wei-Hsin Ho, Ge-Wen Lee*	1024
PS2-06	**ASSESSMENT OF CROP PRODUCTIVITY FOR MAJOR RIVER BASINS IN ASIA USING GIS AND RS DATA** *Shiro Ochi, Shunji Murai*	1030
PS2-07	**A SYSTEMATIC APPROACH IN REMOTE SENSING EDUCATION AND TRAINING AT UNIVERSITI TEKNOLOGI MALAYSIA** *Kasturi Devi Kanniah, Mazlan Hashim, Mohd Ibrahim Seeni Mohd*	1036
PS2-08	**THE STUDY ON BIOMASS ESTIMATION IN MONGOLIAN GRASSLAND USING SATELLITE DATA AND FIELD MEASUREMENT DATA** *Hirokazu Yamamoto, Koji Kajiwara, Yoshiaki Honda*	1042
PS2-09	**INTEGRATION OF RS AND GIS TO ASSESS HUMAN IMPACT ON ECOSYSTEM CHANGE IN LLANOS AREA (VENEZUELA)** *Yanning Guan, Steven M. de Jong, Johan de Meijere*	1048
PS2-10	**THE PRODUCTION OF PHOTO BASE MAP IN TAIWAN** *Jih-Cheng Ru*	1054
PS2-11	**INTEGRATION OF WEB-BASED GIS AND ONLINE ANALYTICAL PROCESSING** *Yin Shan, Hui Lin , Wai Chee Fu*	1060
PS2-12	**THE STUDY OF PRECIPITATION EFFECTS ON AMSU AND APPLICATION OF AMSU ON TYPHOON MONITORING** *Kung-Hwa Wang*	1065
PS2-13	**PHENOLOGY DETECTION OF FOREST AREA USING SATELLITE DATA** *Asako Nagao, Koji Kajiwara, Yoshiaki Honda*	1071
PS2-14	**UTILIZATION OF LANDSAT-5 IMAGERY FOR SUGARCANE AREA SURVEY AND MAPPING IN THAILAND** *W. Hadsarang, S. Sukmuang*	1075
PS2-15	**APPLICATION OF GIS AND REMOTE SENSING TO ANALYSES LANDSCAPE STRUCTURES** *Kazuyuki Takahashi, Keitarou Hara*	1081
PS2-16	**OBSERVATIONS OF THE DAYTIME INTERNAL BOUNGARY LAYER IN ONSHORE FLOW** *N. Mohd Saleh, M. Z. M. Jafri, K. Abdullah*	1087
PS2-17	**EARTH OBSERVATION SYSTEM** *Vinai Vorrawat*	1093
PS2-18	**INTEGRATING REMOTELY SENSED DATA WITH AN ECOSYSTEM MODEL TO ESTIMATE NET PRIMARY PRODUCTIVITY IN EAST ASIA** *Wenjing Zhao, Masayuki Tamura*	1099

Poster Session PS3

PS3-01	**A R&D PROGRAM FOR PROMPT RESPONSE ABOUT FOREST-PROTECTION INFORMATION WITH PLATFORM DISPLAY SYSTEM** *Gwo-Jern Hwang, Ching-Ming Wu, Ten-Yin Chou, Joou-Shiau Lee*	1104
PS3-02	**APPLICATION OF OPTICAL REMOTE SENSING TECHNOLOGY FOR OIL PALM MANAGEMENT** *Ibrahim Selamat, Zainal Abidin Hasan, Mariamni Khalid*	1112
PS3-03	**APPROACH TO LAND-USE ANALYSIS IN HETAO IRRIGATION PROJECT OF INNER MONGOLIA, CHINA, BASED ON SATELLITE IMAGE DATA** *Takashi Kume, Kiyoshi Torii, Toru Mitsuno*	1118
PS3-04	**DROUGHT MONITORING IN ZAMBIA USING METEO SAT AND NOAA AVHRR DATA** *Kawana Nawa*	1124
PS3-05	**FOREST RESOURCES IN TAIWAN** *Jih-Cheng Ru*	1130
PS3-06	**EARTH SURFACE GEOPHYSICAL PARAMETERS DETERMINATION FROM ATSR DATA** *Yong Xue, Huadong Guo*	1136
PS3-07	**A CREEPING-TYPE LANDSLIDE OBSERVED ON AERIAL PHOTOGRAPHS FOLLOWING THE JI-JI EARTHQUAKE OF TAIWAN ON 21 SEPTEMBER 1999** *Jin-King Liu*	1142
PS3-08	**VOLCANO HAZARD MANAGEMENT USING DIGITAL ELEVATION MODEL** *D. John Prabaharan, Kasturi Devi Kanniah*	1148
PS3-09	**PROSPECT FOR THE METHOD OF URBAN SAFETY ANALYSIS AND ENVIRONMENTAL DESIGN** *Osamu Murao, Fumio Yamazaki*	1155
PS3-10	**THE DEVELOPMENT OF FOREST FIRE FORECASTING SYSTEM USING INTERNET GIS AND SATELLITE REMOTE SENSING** *Myung-Hee Jo, Myung-Bo Lee, Si-Young Lee, Yun -Won Jo, Seong-Ryul Baek*	1161
PS3-11	**CONTRIBUTION FROM REMOTE SENSING IN UPDATING BATHYMETRIC CHART** *K. Abdullah, M. Z. M. Jafri, Z. B. Din*	1167
PS3-12	**REMOTE SENSING OF TOTAL SUSPENDED SOLIDS IN PENANG COASTAL WATERS, MALAYSIA** *K. Abdullah, Z. B. Din, Y. Mahamod, R. Rainis, M. Z. M. Jafri*	1173
PS3-13	**FLOOD HAZARD MAP AND LAND DEVELOPMENT PRIORITY MAP DEVELOPED USING NOAA AVHRR AND GIS DATA** *Md. Monirul Islam, Kimiteru Sado*	1179
PS3-14	**USE OF LANDSAT IMAGES FOR THE IDENTIFICATION OF DAMAGE DUE TO THE 1999 KOCAELI, TURKEY EARTHQUAKE** *Miguel Estrada, Fumio Yamazaki, Masashi Matsuoka*	1185
PS3-15	**NATURAL-SCIENTIFIC APPROACH FOR NATURAL CONSERVATION USING GIS** *Byungyang Choi, Takekazu Koyanagi, Yuji Kuwahara, Kunio Shima*	1191
PS3-16	**GIS APPLICATION ON THE STRATEGY FOR SUSTAINABLE DEVELOPMENT IN PHITSANULOK PROVINCE** *Vicharn Amarakul, Sirirat Sangyong*	1197
PS3-17	**DYNAMIC SIMULATION OF LAND USE/COVER CHANGE BASED ON TIME SERIES SATELLITE IMAGES** *Zhongchao Shi, Ryousuke Shibasaki*	1203
PS3-18	**GROUNDWATER PREDICTION POTENTIAL ZONE IN LANGAT BASIN USING THE INTEGRATION OF REMOTE SENSING AND GIS** *Khairul Anam Musa, Juhari Mat Akhir, Ibrahim Abdullah*	1209

AUTHOR INDEX

Author	page
A :	
Abdullah, Ibrahim	1209
Abdullah, K.	782,1087,1167,1173
Abundo, R.	744
Adhikary, Krishna Raj	561
Adiga, S.	358
Adriyanto, Riris	216
Adyasuren, Ts.	372
Ahmad, Azman	222
Ahmad, Shahruddin	106,683
Ahmad, Tadris	788
Ahmad, Waqar	609
Ahmed, Afzal	19
Ajallocian, R.	194,683
Akhir, Juhari Mat	1209
Amarsaikhan, D.	204
Anazawa, Michio	240
Angelier, J.	755
Apaphant, Pakorn	990
B :	
Baban, Serwan M. J.	35
Baek, Seong-Ryul	1161
Bahari, A.	782
Baloloy, A.	744
Baltsavias, Emmanuel	100
Bandibas, Joel C.	533
Baruah, Pranab Jyoti	419
Bato, Victorino A.	658
Bayarjargal, Yu.	372
Bhaskaran, Sunil	378,944
Byungyang, Choi	1191
C :	
Champathet, P.	188
Canisius, X. J. F.	1018
Chan, Jonathan Cheung-Wai	628
Chang, Chih-Li	567
Chang, Ku-Yu	567
Chang, Yao-Lin	329
Chang, Ying-Huei	210
Chao, Hsi-Min	504
Charuppat, Thongchai	77
Chaudhary, B. S.	41
Cheevasuvit, Fusak	430,464,539
Chen, A. J.	738,866
Chen, Chi-Farn	954
Chen, Chia-Tang	440
Chen, Hao	671
Chen, K. S.	440,516,761,866
Chen, Liang-Chien	112,948
Chen, Nai-Yu	112,749
Chen, Ta-Ko	395
Chen, Yeong-Kuan	141,246
Chen, Wen-Feng	708
Cheng, Chi-Chuan	246,270,276,282
Cheng, Hsin-Hsing	883
Cheng, Ke-Sheng	64,652
Chern, D. C.	749
Chiang, Chih-Feng	23
Chien, Fu-Jen	689
Chio, Shih-Hong	125
Chitwong, Sakreya	430
Choi, Moon Soo	70
Chou, Tien-Yin	210,335,689,1104
Corpuz, E.	744
Chu, Jiang-Liung	23
Chung, Lan-Kun	335
Claridad, Eduardo O.	872
Cronin, N.	841
D :	
Dampegama, Siri Diyupathi	573
Das, RK	358
Datt, Bisun	944
Dayao, A.	744
Deffontaines, B.	755
Defries, Ruth S.	628
Dejhan, Kobchai	430,464,539
Denham, R.	841
Derksen, Chris	94
Din, Z. B.	1167,1173
Disbunchong, Dararat	77
Doley, Binod	358
Domingo III, Dulcisimo S.	872
Dulyakarn, Pornphan	481
Duong, Nguyen Dinh	452
Dye, Dennis G.	597
E :	
Eiumnoh, Apisit	665
Elvidge, Chris	352
Endo, Takahiro	815
Enkhtsetseg, Batjantsan	306
Estrada, Miguel	1185
F :	
Forster, Bruce C.	634
Fruneau, B.	755
Fu, Wai Chee	1060
G :	
Ganzorig, M.	204
Gaol, Jonson Lumban	772
Gruen, Armin	100
Guan, Yanning	1048
Guo, Horng-Yuh	23
Guo, Huadong	1136
Gupta, Alok	346
H :	
Hadsarang, W.	1075
Hanpipatpongsa, Somkid	464
Hansen, Matthew C.	628
Hara, Keitarou	1081
Harahseh, Hussein	585
Hasan, Zainal Abidin	1112
Hashim, Mazlan	1006,1036
Hashimoto, T.	152
Hashitera, Shin	407
Hayashi, Haruo	407
Haryoko, Urip	216
Higuchi, Hiroyoshi	603
Higuchi, R.	152
Hinchliffe, Thomas	597
Hirose, K.	744
Ho, Wei-Hsin	1024
Hoan, Nguyen Thanh	452
Holden, Heather	94
Honda, Kiyoshi	1,176

AUTHOR INDEX

Author	page
Honda, Yoshiaki	980,996,1042,1071
Hongoh, Daisuke	980
Hoshi, Takashi	70,860
Hosomura, Tsukasa	545
Hsiao, Chiao-Ju	915
Hsu, Li-Ta	270
Hsu, Pai-Hui	809,821
Huang, Cheng-Yung	984
Huang, Hao-Hsiung	915
Huang, Kai-Yi	527
Huang, Shaobo	318
Huang, Shih-Jen	777
Huang, Xiaojing	135
Hui, Annie	158
Hung, Chi-Chu	434
Hung, Tran	294
Hung, Yu-Ting	329
Hutton, Joseph	701
Hwang Gwo-Jern	1104
I :	
Ichikawa, Hironori	980
Igarashi, T.	152
Iisaka, Joji	486
Inaba, Kazuhisa	891
Islam, Md. Monirul	1179
J :	
Jan, Jihn-Fa	141,282
Jewpraditkul, V.	1002
Jo, Myung-Hee	234,341,1161
Jo, Yun -Won	341,1161
Jong, Steven M. de	1048
Jordan, Jonathan D.	834
Juan, Chung-Hsin	834
K :	
Kada, Ryohei	695
Kadir, Osman	222
Kagawa, Yoshiaki	131
Kajiwara, Koji	980,996,1042,1071
Kanbara, H.	744
Kanetomi, Munetake	83
Kanniah, Kasturi Devi	1006,1036,1148
Kao, Chih-Cung	210
Karami, R.	683
Karladee, N	188
Kato, Masatane	877
Kerdyou, Prasit	539
Khalid, Mariamni	1112
Khan, Nasir Mahmood	7
Khawne, Amnach	510
Kim, Mal-Suk	341
Kitazawa, Kay	726
Kodama, Masafumi	352
Kohiyama, Masayuki	407
Kohyama, Kazunori	533
Konishi, Yusuke	726,974
Koyanagi, Takekazu	1191
Ku, Wen-Yuan	335
Kuo, Jim Min	761
Kumar, K. E. Mothi	41
Kume, Takashi	1118
Kung, Chien-Bin	938
Kuo, Yu-Chuan	652
Kushida, Keiji	615
Kuwahara, Yuji	1191
Kwoh, Leong Keong	135,158,252,794
L :	
Lacoul, Mona	176
Lai, Yu-Ching	270,276
Lanfeng, Zhen	800
Lay, Jinn-Guey	646
LeDrew, Ellsworth	94
Lee, C. T.	755
Lee, Ge-Wen	1024
Lee, Chien-Pin	671
Lee, Chyi Tyi	383
Lee, Jenn-Taur	708
Lee, Joou-Shiau	1104
Lee, Kwang-Jae	234
Lee, Myung-Bo	1161
Lee, Si-Young	1161
Lei, Tsu-Chiang	64
Leow, Rigel Hian Dee	89
Li, Xianhua	458
Li, Yueh-Tan	954
Liang, L. S.	749,755,866
Liao, Hsuan Wu	383
Liew, Soo Chin	158,252,794
Lim, Chee Ming	1006
Lim, Hock	135,158,252,794
Lim, Kim Hwa	252
Lin, Chinsu	258
Lin, Hui	288,458,800,1060
Lin, I-I	76
Lin, Tang-Huang	228
Lin, Yu-Pin	960
Liou, Chia-Ming	652
Liou, Yuei-An	29,984
Lithopoulos, Erik	701
Lituanas, Michael B.	872
Liu, C. H.	522
Liu, C. J.	897
Liu, C.T.	967
Liu, Gin-Rong	228,777
Liu, Jen-Chyi	23
Liu, Jin-King	58,1142
Liu, Shou-Fang	29
Liu, Tsang-Sen	23
Lo, Wei-Yuan	335
Lu, Shi-Ming	584
Lucas, R.M.	841
Luo, Jen-Hon	549
Luscombe, Anthony P.	702
M :	
Mah, Abdullah	678
Mahamod, Y.	1173
Maki, Norio	407
Manandhar, Dinesh	932
Manurung, Djisman	772
Maruyama, Yuichi	877
Masubuchi, Hiroyuki	996
Mat, Jafei M.Z.	782,1087,1167,1173
Mather, Paul M.	621
Matsuoka, Masashi	401,1185
Matsuoka, Ryuji	119
Meijere, Johan de	1048

AUTHOR INDEX

Author	page
Meisl, Peter	702
Melsheimer, Christian	89
Menges, Carl	609
Mills, Walter L.	276
Milne, A.K.	840,841,852
Ming, Lim Chee	1006
Ming, You Jenn	695
Mitatha, Somsak	430,464,539
Mitomi, Hajime	401
Mitsuno, Toru	1118
Miyamoto, Michiru	615
Mohd, Mohd Ibrahim Seeni	106,788,1036
Mongkolsawat, C.	188
Mongkolworaphol, Supoj	425
Mori, Yoshiaki	695
Moriyama, Moe	170
Mostafa, Mohamed M. R.	701
Mugemuzi, Venant B.	909
Mukaida, A.	152
Munkhtuya, Sharav	306,372
Murai, Shunji	665,1030
Murao, Osamu	389,1155
Murata, Ryuichi	928
Musiake, K.	732
Musa, Khairul Anam	1209
Muto, Eiichi	578
N :	
Nadaoka, Kazuo	52
Nagao, Asako	1071
Nagatani, Izumi	352,413
Naito, Nobuaki	1012
Nakagawa, Masafumi	446
Narongrit, Chada	665
Nawa, Kawana	1124
Nikzad, M.	683
Nishimura, Hitoshi	419
Noppanakeepong, Suthichai	510
Nualchawee, Kaew	665
O :	
Ochi, Shiro	1030
Ogawa, Susumu	170 ,1012
Oglu, Asadov Hikmat Hamid	470
Oguro, Yoshinari	182,738
Oh, Sung-Nam	234
Omsin, Somchai	510
Ongsomwang, Suwit	77
Oki, Kazuo	419
Oki, T.	732
Okuda, Toshinori	815
P :	
Paiboonsak, S.	188
Pakzad, H.R.	194
Pal, Dk	358
Palni, L.M.S.	264
Pandey, A. C.	41
Panklang, Jirawath	828
Paringit, Enrico C.	52
Pathier, E.	755
Patimapornchai, C.	1002
Park, Sung-Joong	341
Peng, Miao-Hsiang	58
Pienvijarnpong, Chanchai	464,539
Piyathamrongchai, Kampanart	323
Poudel, Krishna	312
Prabaharan, D. John	1148
Prasetyo, Lilik Budi	591
Purevdorj, Ts.	498
Q :	
Qingxi, Tong	800
Quiambao, Rowena Bassi	300
R :	
Rainis, R.	1173
Rajapakse, R.M.S.S.	1
Rangsanseri, Yuttapong	425,476,481
Rasib, Abdul Wahid	1006
Ratanasermpong, Surachai	77
Rathore, Narpat Singh	47
Rau, Jiann-Yeou	112
Raymond, D.	755
Riama, Nelly Florida	216
Rosdiana	216
Roy, P. S.	264
Romshoo, Shakil Ahmad	732
Ru, Jih-Cheng	1054,1130
Rudant, J. P.	755
S :	
Saandar, M.	204
Sado, Kimiteru	1179
Safaci, H.	194
Saito, Genya	240,352,591
Sakurai, Amano Takako	366,486
Salamante, Erlinda E.	767
Salvador, J. H. G.	744,872
Saleh, N. Mohd	782,1087
Samarakoon, Lal	176,1018
Sangthongpraow, Uthai	476
Saroha, G. P.	41
Sasmito, Achmad	216
Sato, Kazuhiro	83
Sato, Kiyotada	555
Sato, Yohei	7
Sawada, Haruo	240,413
Selamat, Ibrahim	1112
Shafiee, Mardiana	222
Shan, Yin	1060
Sharma, M. P.	41
Sharma, Subrat	264
Shi, Huosheng	458
Shi, Jiancheng	516,847
Shi, Zhongchao	1203
Shibasaki, Ryosuke	19,131,318,446,726,891, 928,932,974,1203
Shih, Hung-Kuan	809
Shih, Tian-Yuan	58,938
Shin, Ji-Hyun	234
Shima, Kunio	1191
Shimura, Yohko	318
Shinmura, Taro	413
Shirai, Naoki	119
Singh, Ajeet	41
Singh, P. K.	41
Sirirat, Sangyong	1197
Song, Xianfang	352
Soonyeekan, Chatcharin	464,539

AUTHOR INDEX

Author	page
Srivastava, SK	358
Srivastava, YK	358
Srongprapa, Anupong	828
Su, Muh-Rong	13
Su, Ruey-Long	516
Sudhakar, S	358
Suga, Yuzo	182,738,922
Suh, Ae -Sook	234
Sukmuang, S.	1075
Suwanwerakamtorn, R.	188
T :	
Takahashi, Kazuyuki	1081
Takasaki, Kenji	922
Takeuchi, Shoji	182,738,922
Takeuchi, Wataru	200
Tamura, Masayuki	200,419,603,815,1099
Tan, Chih-Hung	834
Tan, Qian	800
Tan, Yihan	89
Tapley, Ian J.	840,852,853,857
Tateishi, Ryutaro	585,903
Teng, Tung-po	960
Thirangoon, P.	188
Thitimajshima, Punya	425,481
Thoa, Le Kim	452
Thompson, Alan A.	702
Thuy, Vu Tuong	714
Tiangco, Peter N.	634
Tokunaga, Mitsuharu	665,714
Toleti, B.V.M. Rao	41
Tonooka, Hideyuki	70
Torii, Kiyoshi	695,1118
Trinder, John C.	504
Tripathi, Nitin K.	1,323
Tsai, L. C.	967
Tsai, W. H.	967
Tsay, Jaan-Rong	492
Tseng, Din-Chang	549
Tseng, Yi-Hsing	809,821
Tso, Brandt	621
Tsou, Jin Yeu	288
Tsou, Ko-Wan	329
Tsukada, Makoto	744,877
Tsuruta, Haruo	591
U :	
Umemura, Koichiro	389
V :	
Valenzuela, Aeschylus M.J.	872
Venkatachary, KV	358
Vermote, E. F.	522
Vicharn, Amarakul	1197
Villanoy, Cesar L.	767
Vimonkiattikun, Thammasak	828
Vongvisessomjai, Suphat	665
Vorrawat, Vinai	1093
W :	
Wan, Chee Yuen	89
Wang, C. T.	749,755,866
Wang, H. T.	749
Wang, Kung-Hwa	1065
Wang, Su-Fen	246
Wang, Shue-Chia	125
Wang, Wen-June	29
Wen, L.S.	76
Whitehead, Peter	609
Wijayawardana, K.S.K.	147
Wijesekera, Nihal	720
Wisetphanichkij, Sompong	464,539
Witte, C.	841
Wongrujira, Krit	510
Woodcock, Curtis E.	597
Worawattanamateekul, J.	1018
Wu, Chao-hsiung	164
Wu, Chi-Nan	395
Wu, Ching-Ming	1104
Wu, J.	897
Wu, Ming-Tung	652
Wu, Yi-Ying	948
X :	
Xue, Yong	1136
Y :	
Yadav, Manoj	41
Yamada, Takahiro	860
Yamamoto, Hirokazu	1042
Yamazaki, Fumio	389,401,1155,1185
Yang, Chwen-Ming	13
Yang, Chao-Tung	434
Yasuoka, Yoshifumi	200,294,815
Yeh, Hui-Chung	652
Yokoyama, Ryuzo	498,555
Yonezawa, Chinatsu	738
Yoshimura, Motohide	182
Yoshino, Kunihiko	615
Young, Stephen S.	671
Yu, Gelong	458
Yupapin, P. P.	1002
Yusof, K. Wan	35
Z :	
Zhang, Chunsun	100
Zhang, Dengrong	458
Zhang, Yue	609
Zhang, Zongyu	288
Zhao, Huijing	446
Zhao, Wenjing	1099
Zhao, Yongchao	800
Zhu, L.	903

CLASSIFICATION OF REMOTELY SENSED IMAGERY USING MARKOV RANDOM FIELDS

Brandt TSO (Taiwan), Paul M. MATHER(UK)
Associated Professor, Research Centre
Operation *R&D* Division
National Defence Management College,
National Defence University,
Jong-Ho P.O. Box 90046, Taipei
Tel: +886-2-2254-8131 or +886-2-2222-2137 ext 8452, Fax +886-2-2254-8131
E-mail brandttso@kimo.com.tw
TAIWAN

Professor, Remote Sensing Society Vice President
School of Geography
University of Nottingham
Nottingham NG7 2RD England
Email paul.mather@nottingham.ac.uk
UNITED KINGDOM

KEY WORDS: Markov Random Field, Genetic Algorithm, Multisource Classification

ABSTRACT: The use of contextual information for modelling the prior probability mass function (generally called *the smoothness prior*) in the traditional statistical Bayesian classification formula has been widely adopted in recent years. Random field models, especially Markov random fields (MRF), provide a theoretical robust yet mathematical tractable way of coding multisource information and modelling such contextual behaviour. In dealing with remotely-sensed multisource data, the determination of source-weighting and MRF model-related parameters is a difficult task. We've used the genetic algorithm GA to address the parameter estimation issue in a case study over Red Sea Hill, Sudan for lithological type identification (total eight categories were involved in our classification analyses). GA has been proved in many studies to be a powerful, however cost-effective tool for searching optimal solution. The data set used for the experiment includes LANDSAT Thematic Mapper (TM) six-band and Shuttle Image Radar (SIR) L band, C band, and total power multisource data. Three kinds of MRF classification mechanisms known as Iterated Conditional Mode-ICM, Maximiser of Posterior Marginals-MPM, and Line-Process were investigated. It was shown that the incorporation of contextual information leads to impressively improved results (up to 80% of average producer's accuracy was achieved) in comparison with the output derived from traditional non-contextual maximum likelihood classifier (only around 67% of average producer's accuracy was obtained). The resulted classified imagery using context were also found to reveal more patch-like, meaningful patterns. We therefore conclude that incorporating contextual relationship in terms of MRF, with well assignments of model-related parameters and suitable classification algorithms being used, can be a powerful tool for real world, remotely-sensed imagery classification.

1. INTRODUCTION

In recent years, there has been an increasing interest in use of contextual information for modeling the prior probability density function (p.d.f.) (Derin and Elliott, 1987, Dubes and Jain, 1989, Jhung and Swain, 1996, Schistad et al., 1996, Tso and Mather, 1999). Using context to model prior probability to help the interpretation of remotely-sensed imagery is considered as a reasonable procedure, since a pixel classified as "ocean" is likely to be surrounded by the same class and more unlikely to have neighbors from categories such as "pasture" or "forest". In other words, using the concept of context, each pixel is not treated in isolation but as part of a spatial pattern. The relationship between the pixel of interest and its neighbor is therefore not considered to be statistically independent. If context information can be suitably modeled and incorporated with class-conditional p.d.f., then improved classification results can be expected(Li, 1995a, Li, 1995b)..

Discrete random field models, especially the Gibbs Random Fields (GRF) and Markov Random Fields (MRF), have been found to be useful tools for characterizing contextual information and are widely used in image segmentation and restoration(German and German, 1984, German and Gidas, 1991, Tso and Mather, 1999). This study presents some basics ideas of MRF as a framework to model prior probability (and so as to achieve MAP estimate) for remotely-sensed imagery classification.

2. THEORETICAL BACKGROUND

In the interpretation of remotely-sensed imagery, there will be a set of observed feature vectors (*e.g.* pixel gray value in different bands), d. Traditionally, each pixel r is labeled based on d_r alone without considering contextual information. Once the context is included as a *prior* information and modeled in terms of MRF, current practice is to use a Bayesian formulation to construct the *posterior energy* and to search the MAP-MRF labeling in terms of energy minimization.

2.1 Multisource Posterior Energy

Based on Bayesian formula, the posterior distribution $P(w \mid d)$ can be expressed as

$$P(w \mid d) \propto P(d \mid w)P(w) \tag{1}$$

Recall from (1) that under a pair-site MLL model, the prior probability for pixel r is

$$P(w_r) = \frac{1}{Z}\exp\left[-U(w_r)\right] \tag{2}$$

where the $U(w_r)$ is the prior energy, and is defined as

$$U(w_r) = \sum_{\{r,r'\}\in C_2} \beta\delta(w_r, w_{r'}) \tag{3}$$

where $\beta \leq 0$, and define $\delta(w_r, w_{r'})$ as a step function:

$$\begin{aligned} \delta(a,b) &= 1 \quad \text{if } a = b \\ \delta(a,b) &= 0 \quad \text{otherwise} \end{aligned} \tag{4}$$

The conditional distribution d_r given the true label w_r is often assumed to be normal. For w_r = label j, the conditional probability which can be formulated as

$$P(d_r|w_r) = \frac{1}{\sqrt{2\pi}^{\rho}\sqrt{|\Sigma_j|}} \exp\left[-U(d_r|w_r)\right] \tag{5}$$

which is the class-conditional energy. By combining (10) and (13), one obtains the posterior energy as

$$U(w_r|d_r) \propto \frac{1}{2}(d_r - u_j)\Sigma_j^{-1}(d_r - u_j) + \sum_{\{r,r'\}\in C_2} \beta\delta(w_r, w_{r'}) \tag{6}$$

The MAP estimate is equivalent to minimizing the posterior energy.

For multisource classification, in terms of simplicity, we have made a class-conditional independence assumption, *i.e.*

$$p(d_{s1}, d_{s2}, \ldots, d_{sn}|w) = p(d_{s1}|w) \cdot p(d_{s2}|w) \cdot \ldots p(d_{sn}|w) \tag{7}$$

where d_{si} is the observation from data source i. Eq. (7) means that we consider the observations from different sources to be conditionally independent. Such an assumption may not be universally valid. However, by adopting this assumption, the mathematical analysis and computation become treatable.

If we take the data-associated reliability factor into account, one simple method is to assign weighting parameters through exponential form, then Eq.(7) can be further refined as

$$P(d_{s1}, d_{s2}, \ldots, d_{sn}|w) \propto P(d_{s1}|w)^{\lambda_1} \cdot P(d_{s2}|w)^{\lambda_2} \cdot \ldots P(d_{sn}|w)^{\lambda_n} \tag{8}$$

where the λ_κ ($0 \le \lambda_\kappa \le 1$, and $1 \le k \le n$) are the data-associated reliability factor for the source k. The larger the value of λ_κ the greater the influence of data source k on the classification process. Eq. (8) indicates that multisource posterior energy can be expressed as

$$U(d_{s1}, d_{s2}, \ldots, d_{sn}|w) = \lambda_1 U(d_{s1}|w) + \lambda_2 U(d_{s2}|w) + \ldots + \lambda_n U(d_{sn}|w) \tag{9}$$

Therefore, based on (9), an alternative expression of the MAP-MRF estimation of multisource data is:

$$\hat{w} = \arg\min_{w} U(w|d_{s1}, d_{s2}, \ldots, d_{sn}) \tag{10}$$

where

$$U(w|d_{s1}, d_{s2}, \ldots, d_{sn}) \propto \sum_{k=1}^{n} \lambda_k \cdot U(d_{sk}|w) + U(w) \tag{11}$$

$U(w)$ is defined in (3). Eq. (11) can be regarded as a generalized version of (6).

The idea outlined above is mainly designed to achieve a smooth interpretation of remoteing sensing imagery. In practice, the patterns in an image are only piece-wise continuous. That is, discontinuities (*i.e.* edges between different patches) are naturally to be found within an image. In such cases, the use of a smooth interpolation operation may smear these discontinuities, causing *over-smoothing*. We are interested here in the method called *line-process*(Li, 1995b) because it allows us to mark discontinuities and minimize energy simultaneously.

The basic idea of the line-process is quite simple. Once a discontinuity (edge) between two adjacent pixels has been identified, the interaction (*i.e.* smooth interpolation operation) between these two neighboring pixels should reduced or set off, and it is reasonable to define some other potential to respond to the presence of the edge. Following this logic, the prior energy in (11) can be modified as follows:

$$U(w_r) = \beta \cdot \delta(w_r, w_{r'})(1-E_{rr'}) + V_{Err'} \tag{12}$$

2.2 Energy Minimization

Once the posterior energy model and the associated parameters have been determined, the next step is to find out the solution (*i.e.* start classification). As noted previously, a popular method of pixel labeling is to find the MAP estimate using the Bayesian formulation. The MAP approach is also equivalent to a minimum-energy solution in terms of MRF modeling. If the energy function is convex then the MAP-MRF solution can be obtained by using a search approach, such as the gradient descent technique, because there is only one minimum, which is a global one, in the solution space. However, for a non-convex energy function, the solution space may contain several local minimum. In order to obtain a truly MAP estimate, *i.e.* to find a global minimum, one has to search the full solution space exhaustively.

Three algorithms, known as *Iterated Conditional Modes* (ICM), *Maximiser of Posterior Marginals* (MPM), and Line Process have been proposed in the literature to test classification results. All three algorithms are referred to (Li, 1995b). The genetic algorithm was used for search optimal parameter assignments for the developped model.

3. EXPERIMENTAL RESULTS AND DISCUSSIONS

The study area is located within the Red Sea Hills of Sudan, The categories are shown in Table 1. Based on (12), only pair-sites cliques parameters (*i.e.* parameter β) are designated non-zero. The range of β was defined as $\beta \in [5,-5]$, $\lambda_k \in [1,-1]$and the isotropy assumption (*i.e.*, single value β, $\beta_1 = \beta_2 = \beta_3 = \beta_4$, direction independent) was made. The iterations defined for GA in each of three search experiments was 30,000, and each gene was represented by 7 bits, which results in $2^{7\cdot6}$ (= 2^{42}, where each candidate solution contains six genes in which five genes for source weighting parameter candidates and one gene for β; if a non-contextual multisource classification is performed, the search space reduces to $2^{7\cdot5} = 2^{35}$) choices in GA search space. The parameters determined by GA for both non-contextual and contextual classification are shown in Table 2(a). The parameters shown on row 2 were further used as inputs for MPM classification algorithms. The accuracy acquired is shown in Table 2(b). With the MPM classification algorithm, a range of values for the parameter k and n were tested. We

used different combinations of k and n, with k ranging from 1 to 50 and n from 100 to 500. However, no significant difference was found. The classification accuracy in most cases falls within the range of [80, 80.1].

The source-associated weighting factors and clique potential parameters in Table 2(a) show us some interesting properties. The quantity of clique potential parameters determine how strongly the labeling process for the pixel of interest is affected by its neighbours. In order to achieve a good classification result, it is worthwhile to note again that the values of clique potential cannot be chosen without thought, and GA is a suitable tool for overcoming such parameter-determination difficulty. Under the isotropic assumption, a value of -1.5828 of β was detected by GA as the best choice in terms of improving classification accuracy. When the assumption of anistropy is concerned, Table 2 row 3 shows a value of -0.8742 for the second β parameter which indicates a relatively weak contextual effect in terms of vertical orientation. The reason for the lower potential in the vertical direction might be due to the dorminant direction of between-class boundaries as lithological classes have a greater E-W than N-S extent.

The line process mechanism used here is mainly based on (12) using the first order neighbourhood system (4 nearest neighbours) to trigger parameter $E_{rr'}$. However, for parameter $V_{Err'}$, only 4-site cliques are set to be active. Therefore, the value of $V_{Err'}$ will contain 4 choices (*i.e.*, from the 1-edge case to the 4-edge cases). We further define the process rule as follows.

Within a 3 by 3 window, if a discontinuity between the centre pixel r and its upper nearest neighbour has been detected, this will trigger upper left 4 pixels to carry out line process (*i.e.*, to detect edge patterns). If the discontinuity exists between r and its right nearest neighbour, then the line process will be executed for the upper right 4 pixels. Similarly, a discontinuity between the centre pixel r and its lower nearest neighbour will trigger the lower right 4 pixels, and a discontinuity between pixel r and its left nearest neighbour will trigger the lower left 4 pixels. Compared to the contextual classification patterns without incorporating line process, the line process classification appears to generate more small patches (or holes). The presence of these small patches is mainly due to falsely-marked edges.

4. CONCLUSION

The results of a comparative study of multisource classification using MRF with different models and algorithms show that the incorporation of contextual information successfully improves classifier performance by more than 10% in terms of average producer's accuracy. However, the relative performance of ICM, and MPM does not reveal obvious differences. Although simulating annealing requires considerable computational resources, only a small improvement (around 2%) was obtained compared with the ICM algorithm. The incorporation of the line process shows no positive contribution to classification accuracy. It is also clear that, in order to achieve these improvements in classification accuracy, both the model and the associated parameters both have to be estimated objectively. We have constructed different models and successfully used GA to estimate the associated parameters. However, methods to construct more complex models and to efficiently estimate their parameters in order to achieve higher classification accuracy are still significant issues worthy of further investigation.

Information Class (Number of Pixels)
1-*Metarhyodacids (429)*, 2-*Granodiorities(43496)*,3-*Gneiss Basitic(5807)*, 4-*Volcanics (8157)*,5-*Gneiss Acidic(1998)*, 6-*Flood Plain(703)*, 7-*Quaternary Deposits(2529)*,8-*Granites(385)*

Table 1 Categories

	TM	SIR-C C-band HH, HV	SIR-C C-band Power	SIR-L L-band HH, HV	SIR-L L-band Power	Clique parameters β
Without Context	0.8346	0.6378	0.0709	0.1024	0.0709	-
Isotropic β	0.9842	0.4330	0.0078	0.0236	0.0078	-1.5828
Anisotropy β	0.8898	0.1968	0.0078	0.0236	0.0236	[1] -2.1498 [2] -0.8742 [3] -2.1498 [4] -2.5746
ICM using line process without $V_{Err\ rr''}$	0.9842	0.307	0.0394	0.0394	0.0236	β: -2.6694 V_{Err}: [1]0.3464 [2]3.4328[3]1.9216

(a)

Classification Machnism	Accuracy
Nocontext-68.17%, ICM(Isotro.)-79.24%, ICM(Anisotro.)-80.46%, MPM-80.97%, ICM(Line Process)-74.98%	

(b)

Table 2(a) Parameters Detected by GA. See Text for Details, (b) Accuracies

REFERENCES

Derin, H. and H. Elliott, 1987. Modeling and segmentation of noisy and textured images using Gibbs random fields. IEEE Transactions on Pattern Analysis and Machine Intelligence, 9(1), pp.39-55.

Dubes, R. C. and A. K. Jain, 1989. Random field models in image analysis. Journal of Applied Statistics, 16(2), pp.131-164.

Jhung, Y. and P. H. Swain, 1996. Bayesian contextual classification based on modified M-estimates and Markov random fields. IEEE Transactions on Geoscience and Remote Sensing, 34(1), pp.67-75.

Schistad, A. H., T. Taxt, and A. K. Jain, 996. Markov random field model for classification of multisource satellite imagery. IEEE Transactions on Geoscience and Remote Sensing, vol. 34(1), pp. 100-113.

Li, S. Z., 1995a. In discontinuity-adaptive smoothness priors in computer vision. IEEE Transactions on Pattern Analysis and Machine Intelligence, 17(6), pp. 576-586.

Li, S. Z., 1995b. Markov Random Field Modeling in Computer Vision. Computer Science Workbench, Editor: T. L. Kunii, Springer.

German, S. and D. German, 1984. Stochastic relaxation Gibbs distributions, and the Bayesian restoration of the image. IEEE Transactions on Pattern Analysis and Machine Intelligence, 6(6), pp. 721-741.

German, D. and B. Gidas, 1991. Image Analysis and Computer Vision. National Academy Press, USA, Chapter 2, pp.9-36

Tso, Brandt and P.M. Mather, 1999. Classification of multisource remote sensing image using a Markov Random Field. IEEE Transactions on Geoscience and Remote Sensing (TGARS), 37, pp.1255-1260

Tso, Brandt and P.M. Mather, 1999. Crop discrimination using multi-temporal SAR imagery. International Journal of Remote Sensing, 20(12), pp.2443-2460.

The 21st Asian Conference on Remote Sensing
December 4-8, 2000 Taipei, TAIWAN

MACHINE LEARNING METHODS TO IDENTIFY MISLABELED TRAINING DATA AND APPROPRIATE FEATURES FOR GLOBAL LAND COVER CLASSIFICATON

Jonathan Cheung-Wai CHAN, Matthew C. HANSEN and +Ruth S. DEFRIES

Laboratory for Global Remote Sensing Studies, University of Maryland, College Park, MD20742, USA
+ Also with Earth System Science Interdisciplinary Center, University of Maryland, College Park, MD20742, USA
Corresponding author: +1 301 405 8696 (tel), +1 301 314 9299 (fax), jonchan@glue.umd.edu

KEY WORDS: machine learning, filtering, mislabeled data, feature selection

ABSTRACT

In an effort to improve the AVHRR 1km global land cover product (Hansen, 2000), the original training data set used to derive the supervised decision tree classifier is evaluated using machine learning methods with two focuses: to identify mislabeled pixels and to optimize the input feature subset. A filtering process is formed by three data modelers: Decision Tree Classifier, Instance Based Learning and Learning Vector Quantization. Cross-validation is used to label the entire data set into correct and incorrect classification. Incorrect classified instances are considered as possible mislabels. Consensus filtering is performed and the results show that 74% of the cases identified as mislabeled agree with expert knowledge. More mislabels were identified if those chosen by either one or two of the data modelers are considered, but agreement with expert degraded to 54.2-65.5%. A wrapper approach of feature subset selection is applied to the improved data set with mislabeled training data discarded. A total of 18 features were chosen from the original 41 features. A map generated using the improved training set was compared with an expert-improved classification. Overall agreements is 53.1% and by class agreements ranged between <25% to>70%. Future efforts would be needed to address the question of what leads to the disagreements and how machine learning methods can be better tapped for operational global land cover mapping.

1. INTRODUCTION

Global land cover information is a prerequisite input to many atmospheric models that describe Earth system processes (Seller et al., 1997). In the last two decades, remotely sensed data have been increasingly utilized to monitor global land cover changes on a regular basis. Previous studies have shown success in using AVHRR data to produce global vegetation map at 1km and 8km resolutions (Hansen et al., 2000; DeFries et al., 1998). For the global land cover map at 1km resolution, only training sites that have been interpreted from fine-resolution data Landsat Multispectral Scanner System (MSS) and Thematic Mapper (TM) as containing 100% of the land covers in interest were chosen. Details of the preparation of the training data set were documented in Hansen et al. (2000). Collecting global training data set is understandably difficult considering the diversity of each land cover type. Exhaustive in-situ validations are either too expensive to get or simply physically not accessible. Mislabels in training data set due to these confinements are not uncommon. Constant efforts have been made to improve the 1km product. This paper reviews the use of machine learning techniques to identify mislabels and to optimize feature subset in the training set.

2. METHODOLOGY

Filtering mislabels in training

Weisberg (1985) suggested the use of regression analysis to identify outliers in the training data. Those cases that could not be described by the model and have the largest residual errors are outliers. Motivated by the same idea, Brodley and Friedl (1999) used *filtering* to clean out mislabeled training data. The idea is to use different learning algorithms to generate various classifiers from the training set. The classifiers form a committee of data modelers. For cases that do not conform to any model, they can be either noise or exception. Since there is no way to distinguish between noise and exception in the training set, the outliers are treated as candidate mislabels. Brodley and Friedl (1999) have shown that filtering improved classification accuracy significantly for noise up to 30%. Whether consensus filters (to throw away cases that do not follow any model) or majority filter (to throw away cases that follow most but not all models) should be used depends on the objectives of the task. In this study, two sets of training labels were used and the second set is an improved version with additional expert inputs. Mislabeled cases from the first training set identified by machine learning filtering would be compared with the improved data set.

To mark each instance as correctly or incorrectly labeled, a n-fold cross-validation is performed over the training data. The training data is subdivided into n equal parts and for each of the n parts, a classifier is generated from the other n-1 parts. After the n trials, the whole training set would be marked. We used a 10-fold cross-validation for our experiments. For the committee data modelers, we have included Decision Tree Classifier, Instance Base Learning and Learning Vector Quantization.

Decision Tree Classifiers (DTC) recursively subdivide the training set into homogenous subsets according to certain split rules. They are fast in learning and the explicit tree structures enhance interpretation of the classification process. Our experiment used C5.0, a commercial successor of C4.5 developed by Quinlan (1993). The split rule of C5.0 is made according to information gain. Details of the information gain criterion can be found in Quinlan (1993).

Instance Base Learning (IB) is described as a lazy learner as they do not process the inputs until they are requested for information (Aha, 1998). As such, they have little training costs. IB is slow when there are many attributes and as it retains the solution to a similar problem, high classification costs is expected. More about IB can be found in Aha (1992) and Wettschereck (1994). We have implemented the Instance Base Inducer of the SGIMLC++ (Machine Learning library in C++, 1996) Utilities 2.0 for our experiments. The number of nearest neighbor is set to 1.

Learning Vector Quantization (LVQ) is a supervised version of Self-organizing Maps (Kohonen, 1995). By assigning codebook representatives to each class, LVQ defines borders resembling voronoi sets in vector quantization. It is a nearest-neighbor based classifier. Experiments were performed with the LVQ_PAKv3.1 available from the Helsiki University of Technology. We assigned 100 codebook representatives to each class. The first 5,000 steps of training with self-adjusted learning rate were implemented using OLVQ1. Then, training is carried on for 200,000 steps with LVQ1

using a lower learning rate 0.05. Snapshot is taken for every 10,000 step. The step with the highest accuracy rate was chosen for the trial.

Optimal feature subset

Finding an optimal feature subset for a task can improve interpretation and reduce computing costs. Reducing computing costs is particularly important in the context of global land cover mapping considering the size of the data set we are handling. Irrelevant or correlated features are reportedly damaging to learning algorithm like decision trees (John et al., 1994). Applying feature selection will downsize input dimension with the possibility of enhanced accuracy.

Both filter and wrapper approaches can be adopted for feature subset selection. Filter approaches use only the training data in the process of evaluation but wrapper approaches incorporated the induction algorithm as part of the evaluation in the search of the best possible feature subset. Wrapper approaches are reportedly superior when applied to decision trees resulting in smaller tree sizes (better interpretative power) and higher accuracies (Kohavi and John, 1998). For our experiment, we used a wrapper approach with decision tree classifier. The induction algorithm is run on the training data set using different subsets of the original features sets. The subset with highest evaluation is used to generate a classifier.

A forward selection procedure using *best-first search* is adopted (Ginsberg, 1993). Forward selection implies an operation of addition for each expansion. The search states are nodes representing subsets of features. The idea of *best-first search* is to jump to the most promising node generated so far that has not been expanded. The search is stopped when an improved node has not been found in the previous k expansions. An improved node is defined as a node that has an accuracy of not less than x percent higher than the best node found so far. For our experiment, k and x are defined as 5 and 0.001% respectively.

3. DATA

The training data set is obtained by sampling from the AVHRR 1km global vegetation cover product (Hansen et al., 2000). A total of 37340 cases were extracted. Formation of the 41 metrics is described in details in Hansen et al. (2000). The training data is thoroughly shuffled to prevent any correlation between training and testing.

4. DISCUSSIONS AND CONCLUSIONS

	Number of cases
Expert knowledge	11732
LVQ	9058
DTC	7438
IB	5376

Table 1. Number of cases identified as mislabels

	IB	DTC
LVQ	3725	4389
DTC	3200	

Table 2. Agreements between individual data modelers

Filtering methods to identify mislabeled data

An improved version of training using expert opinion is available for comparison. With expert knowledge, 11732 cases were identified as mislabels. Table 1 shows the number of mislabels identified by each individual classifier. The number of mislabels actually represents the classification errors of each learning algorithm. IB outperformed the other two classifiers in terms of accuracy rates and hence it identified the least amount of mislabels. LVQ has the highest number of mislabels, but that is still about 2700 pixels less than expert opinions. Table 2 shows the agreements among filters and LVQ and DTC has the highest agreement. Since LVQ has the highest number of mislabels, it also has a slightly higher agreement as compared to other filters.

Number of votes	Number of cases	Cases agree with expert knowledge
One Vote	13074	7080 (54.2%)
Two Votes	6280	4115 (65.5%)
Three Votes	2517	1863 (74.0%)

Table 3. Number of mislabeled cases identified using consensus/voting filtering and the agreements with expert knowledge

1	**Maximum NDVI value**	21	Maximum Channel 3 value of 8 greenest months
2	**Minimum NDVI value of 8 greenest months**	**22**	**Minimum Channel 3 value of 8 greenest months**
3	**Mean NDVI value of 8 greenest months**	**23**	**Mean Channel 3 value of 8 greenest months**
4	**Amplitude of NDVI over 8 greenest months**	24	Amplitude of Channel 3 over 8 greenest months
5	**Mean NDVI value of 4 warmest months**	25	Channel 3 value from month of maximum NDVI
6	**NDVI value of warmest month**	26	Mean Channel 3 value of 4 warmest months
7	Maximum Channel 1 value of 8 greenest months	**27**	**Channel 3 value of warmest month**
8	**Minimum Channel 1 value of 8 greenest months**	28	Maximum Channel 4 value of 8 greenest months
9	Mean Channel 1 value of 8 greenest months	**29**	**Minimum Channel 4 value of 8 greenest months**
10	**Amplitude of Channel 1 over 8 greenest months**	**30**	**Mean Channel 4 value of 8 greenest months**
11	Channel 1 value from month of maximum NDVI	31	Amplitude of Channel 4 over 8 greenest months
12	**Mean Channel 1 value of 4 warmest months**	32	Channel 4 value from month of maximum NDVI
13	Channel 1 value of warmest month	33	Mean Channel 4 value of 4 warmest months
14	Maximum Channel 2 value of 8 greenest months	**34**	**Channel 4 value of warmest month**
15	Minimum Channel 2 value of 8 greenest months	35	Maximum Channel 5 value of 8 greenest months
16	**Mean Channel 2 value of 8 greenest months**	36	Minimum Channel 5 value of 8 greenest months
17	Amplitude of Channel 2 over 8 greenest months	**37**	**Mean Channel 5 value of 8 greenest months**
18	Channel 2 value from month of maximum NDVI	38	Amplitude of Channel 5 over 8 greenest months
19	Mean Channel 2 value of 4 warmest months	39	Channel 5 value from month of maximum NDVI
20	**Channel 2 value of warmest month**	40	Mean Channel 5 value of 4 warmest months
		41	Channel 5 value of warmest month

Table 4. List of the 41 features used for the 1km map. The 18 features in bold fonts are those selected by the feature subset selection algorithm.

Table 3 shows the results of filtering by voting. If we take all mislabels with any filter (One Vote), a total of 13074 cases were identified and 54.2% of those cases agree with expert knowledge. For majority vote filtering, i.e. at least two votes, then there are 6280 cases with higher percentage (65.5%) of agreement with expert knowledge. If consensus filtering (Three Votes) is performed, only 2517 cases were chosen. The

agreement between consensus filtering and expert knowledge is the highest (74.0%). Our finding echoed the observations from Brodley and Friedl (1999) that consensus filtering is conservative in terms of throwing away good data and majority voting are better at detecting bad data but at the risk of throwing away good data.

Our results show that filtering by consensus or by voting can be used to identify mislabeled training data with the lowest agreement with expert opinions at 54.2%. Since retaining mislabels would degrade performance, it is suggested to use majority vote since more mislabels can be identified and discarded. While we have shown that certain portion of expert opinion can be modeled by machine learning methods, more studies would be needed to address the problem concerning the disagreements between filtering by data modelers and expert knowledge.

Feature Subset Selection

The size of input dimension is extremely important when dealing with global data set since the task involves handling of millions of pixels. Our last experiment performed feature subset selection over the improved training data. We have chosen the mislabeled cases identified by majority voting (Two Votes) to be discarded. It has to be noted that there are 7612 mislabels picked by the expert that are not identified by machine learning procedures. Feature subset selection algorithm identified a subset of 18 features from the original 41 features. The input dimension is downsized by more than 50%. It will significantly reduce the processing time.

Table 4 listed the optimal features chosen by feature subset selection (FSS) algorithm. The inclusion of all NDVI metrics shows the utility of the normalized ratio in mapping global vegetative land cover. This agrees with the expert-modified tree classification where NDVI metrics were useful in mapping most cover types. Minimum annual red reflectance was also found to be important in mapping tree cover and the FSS includes it as well. Temperature bands, particularly minimum channel three, are useful in discriminating tree leaf type and leaf longevity classes. Compared to the expert-modified tree classification, an important metric missing from the FSS is the mean of the warmest four month metrics of channel 4 and/or 5 (features 33 /40 in Table 4). These metrics are useful in delineating tropical forest from woodland based on dry season land surface temperature, but are not included in the FSS output. In general, the FSS clearly retains the most important metrics, those which best generalize the data set. However, some metrics which act regionally, as just mentioned, are not included.

Map output/agreement

The overall agreement between a map generated using the training data set improved by machine learning and the expert-modified tree classification is 53.1%. Classes with the best agreement include needleleaf evergreen and deciduous forests, crops and bare ground (all >70%). The most poorly performing classes include wooded grassland, closed shrubs and grassland (all < 25%). Preserving classes with high intraclass variability such as wooded grassland can be problematic. This is highlighted here as the filtered data and FSS tree outputs resulted in an area of mapped wooded grassland of less than half that of the expert-modified map. Hansen et al. (2000) state that most training errors/confusion occurs between classes

consisting of mixtures. An example of such confusion are areas of partial tree cover such as wooded grasslands and croplands which often exist in mosaics with naturally occurring land cover types. Objectively finding the appropriate thresholds to best depict mixed cover types such as wooded grassland is a challenge and further examination is required.

Acknowledgements:

This research is supported by the NASA grants NAG56970, NAG56004, NAS596060 and NAG56364.

References:

Aha, D.W., 1992. Tolerating noisy, irrelevant, and novel attributes in instance-based learning algorithms. International Journal of Man-Machine Studies, 36:267-287.

Aha, D.W., 1998. Feature weighting for lazy learning algorithms. In Feature Extraction, Construction and Selection: A Data Mining Perspective, edited by Liu, H., and Motoda, H., Kluwer Academic.

Brodley, C.E., and Friedl, M.A., 1999. Identifying mislabeled training data. Journal of Artificial Intelligence Research, 11, pp.131-167.

DeFries, R., Hansen, M.C., Townsend, J.R.G. and Sohlberg, R., 1998. Global land cover classifications at 8 km spatial resolution: The use of training data derived from Landsat Imagery in decision tree classifers. International Journal of Remote Sensing, 19 (16), pp. 3141-3168.

Ginsberg, M., 1993. Essentials of Artificial Intelligence. Morgan Kaufmann.

Hansen, M.C., DeFries, R.S., Townsend, J.R.G. and Sohlberg, R., 2000. Global land cover classifications at 1 km spatial resolution using a classification tree approach. International Journal of Remote Sensing, 21 (6&7), pp. 1331-1364.

John, G.H., Kohavi, R., and Pfleger, K., 1994. Irrelevant features and the subset selection problem. Machine Learning: Proceedings of the Eleventh International Conference, pp. 121-129.

Kohavi, R. and John, G. H., 1998. The wrapper approach. In Feature Extraction, Construction and Selection: A Data Mining Perspective, edited by Liu, H. and Motoda, H., Kluwer Academic.

Kohonen, T., 1995. Self Organizing Maps. Berlin: Springer

Quinlan, R. J., 1993. C4.5: Programs for Machine Learning. Morgan Kaufmann.

Sellers, P.J, Dickinson, R.E., Randall, D.A., Betts, A.K., Hall, F.G., Moonney, H.A., Nobre, C.A., Sato, N., Field, C.B., and Henderson-Sellers, A., 1997. Modeling the exchanges of energy, water, and carbon between continents and the atmosphere. Science, 275, pp.502-509.

Weisberg, S., 1985. Applied linear regression. John & Wiley & Sons.

Wettschereck, D., 1994. A study of distance-based machine learning algorithms. Doctoral dissertation, Oregon State University, Department of Computer Science.

DEVELOPMENT OF TRUNK-CANOPY BIOMASS AND MORPHOLOGY INDICES FROM QUADPOLARIZED RADAR DATA

Peter N. Tiangco and Bruce C. Forster
School of Geomatic Engineering
University of New South Wales
Sydney, NSW 2052, Australia
email: z2146531@student.unsw.edu.au
B.Forster@unsw.edu.au

Abstract - The capability of microwave energy to penetrate forest vegetation makes possible the extraction of information on both the crown and trunk components from radar data. At C-band, the backscattered energy is correlated mainly with the crown constituents such as the leaves, twigs and small branches. Information on the other components beneath the canopy can be sensed through the use of bands with longer wavelengths such as the L- or P-band. The sensitivity of co-polarized and cross-polarized waves to the shapes and orientation of different tree constituents provide an added advantage in the information extraction procedure. The Trunk-Canopy Biomass Index (TCBI), which is the sum of the L-HH and C-HV backscatter, can be a measure of the total aboveground biomass as both the crown and trunk layers are taken into consideration. Owing to possible morphological variations, the relationship between TCBI and biomass is however not expected to be unique for a whole forest vegetation. It is important therefore that stand structure be first considered to allow a more accurate biomass assessment by the TCBI. An index of the relative proportions of the crown and trunk may be indicative of the approximate tree morphology. It is believed that the Trunk-Canopy Morphology Index (TCMI), which is the ratio of the L-HH to C-HV backscatter, provides a measure of tree structure. In this study, two categories are used to classify stands according to structure: the needle-leaved pines/conifers and the broad-leaved deciduous/evergreen trees. A two-stage procedure of forest biomass estimation is therefore proposed. The first stage involves the determination of the stand structure category based on the TCMI. Once the structure is known, a specific structure-dependent TCBI could then be applied for the biomass estimation process. The effectiveness of these indices is assessed by applying them to actual and modelled data interpolated from published works of other investigators. Stand structure and total aboveground biomass were found to be highly correlated with TCMI and TCBI, respectively. Comparison of the results is made difficult by the limitations in the amount of data available from the published studies and the possible errors introduced during the interpolation process. In order to verify the validity of these results, further application of these indices using AIRSAR images and adequate amount of actual and measured values from an independent study site in the Blue Mountains area in New South Wales, Australia will be conducted.

1. INTRODUCTION

The importance of quantifying and monitoring forest vegetation, given the vital productive, protective, and regenerative functions of this natural resource, is undeniable. Information on the amount and extent of vegetation provides an insight on what or how much to expect from a specific forest area in terms of these functions. From another perspective, the information can be useful in determining whether or not forest rehabilitation or other appropriate actions are needed in consideration of these three major functions.

Forest aboveground biomass, or the quantity of vegetative material per unit area, is one of the parameters recognized as a good indicator of forest condition. The use of radar remote sensing to

provide estimates of this parameter has been receiving increasing interest over recent years. This is mainly due to the ability of the radar to provide data independent of solar illumination and weather conditions. In addition, radar waves, depending on the wavelength/frequency, can be employed to scope different sections of the vegetation profile. Information on crown layer components (e.g. foliage) can be inferred from the radar backscatter at high frequency bands such as C- and X- while information pertaining to the trunks and lower branches can be obtained through the longer and more penetrative wavelengths of L- and P- bands.

Since the backscattering coefficient is influenced not only by the quantity of biomass but by how the individual components are oriented and distributed throughout the entire tree length, it is also possible to determine the general tree/stand structure based on the radar data. In fact, due to possible morphological variations between stands within a given forest area, it is recommended that the determination of the general tree/stand structure must precede biomass estimation and that radar data-based biomass equations should be formulated based on the structure. This is to avoid erroneous results will most likely be produced as it is possible to obtain different backscatter readings from two stands containing the same amount of biomass but are structurally-different.

2. SYNERGISM OF RADAR PARAMETERS FOR OPTIMUM INFORMATION EXTRACTION

The amount and quality of information which can be inferred from radar data depend on the characteristics of the target and the radar system. Important factors under the former relate to the roughness, geometric and dielectric properties of the imaged surface while under the latter are the microwave frequency/wavelength, polarization and incidence angle used in the data acquisition process. Accurate inference of vegetation properties results from the formulation of a well-established relationship between the target and the radar parameters. Being well-established implies that such a relationship is based on a complete recognition of the different scattering mechanisms present and a clear understanding of how these mechanisms relate to the radar parameters.

The advent of multi-parameter imaging radars extricated investigators from the limitations of using mono-band radar data in carrying out forest-related research. The opportunity lies in the simultaneous use of the radar parameters for optimum extraction of information from radar imagery. It is believed that a better assessment of forest resources could be achieved by utilizing a combination of the parameters. The theoretical basis for this premise and the different combinations will be presented in the following topics. Focus will be on the more controllable radar system-based components such as wavelength and polarization, with forest aboveground biomass and stand structure assessment as the particular areas of application.

2.1. Forest aboveground biomass assessment

2.1.1. Combined wavelength and polarization estimation

The total forest aboveground biomass is the summation of the biomass of the crown and bole components of all the trees in the area under consideration. Obviously, to derive an estimate of this quantity from radar data, information on both the crown and the bole should be available. A simple model of the total biomass could then be given as

$$B_{total} = B_t + B_c \quad (1)$$

where B_{total} represents the total aboveground biomass, B_t the trunk biomass, and B_c the crown biomass.

The C-band, with its relatively shorter wavelength, is sensitive to the upper layer of the vegetation such as the leaves, twigs and small branches of the crown. The more penetrative wavelength of the L-band can pass through a greater volume of the canopy and interacts with bigger structures at the lowermost canopy portion and more regularly, with the trunk and big branches. Most of the returns from the latter is from tree-ground double bounce backscattering which occurs mainly due to the

vertical orientation of the trunk with respect to the ground hence forming a corner reflector-like structure. Thus,

$$\sum_{n=1}^{N} (\sigma^{O}) = i_n \sigma^{O}_{L\cdot} + j_n \sigma^{O}_{C\cdot} \quad (2)$$

where $\sum_{n=1}^{N} (\sigma^{O})$ is the backscattering coefficient sum correlated with the total aboveground biomass; i and j are the unit vectors in x and y axes in the xy coordinate system corresponding to the backscattering coefficients of the L- and C-band, respectively.

The type of polarization employed determines the radar response to the various shapes and orientations of the scattering mechanisms within the canopy. Backscatter from cross-polarized waves tends to be related to the canopy volume rather than the lower components such as the soil and as such may be an indicator of crown biomass (ESA, 1995). Incoming vertically-polarized waves readily interact with the vertical components of the canopy. Due to the nature of its orientation, horizontally-polarized radiation tends to have a deeper degree of penetration and is less likely to be affected by canopy attenuation. The highest correlations between radar backscatter and total biomass are obtained using waves with HV- and HH- polarization: VV-polarized waves are more sensitive to the components of the crown and tend to saturate at lower total biomass levels (Dobson et al.,1995a).

Integrating the theories pertaining to the sensitivities of the different radar wavelengths and polarizations, we can deduce the following relationships:

$$\sigma^{O}(B_{t+lb}) \approx \sigma^{O}_{L\text{-}HH} \quad (3)$$

$$\sigma^{O}(B_{L+b}) \approx \sigma^{O}_{C\text{-}HV} \quad (4)$$

where B_{t+lb} refers to the biomass of the trunk and lower branches, B_{L+b} is the biomass of the leaves and most of the branches, while $\sigma^{O}_{L\text{-}HH}$ and $\sigma^{O}_{C\text{-}HV}$ are the L-HH and C-HV backscattering coefficients, respectively. Considering the above relationships, equation (2) could then be written as

$$\sum_{n=1}^{N} (\sigma^{O}) = i_n \sigma^{O}_{L\text{-}HH} + j_n \sigma^{O}_{C\text{-}HV} \quad (5)$$

where $i\,\sigma^{O}_{L\text{-}HH} + j\,\sigma^{O}_{C\text{-}HV}$ is called the Trunk-Canopy Biomass Index (TCBI). To avoid possible overestimation of total aboveground biomass, other polarization combinations of the L- and C-bands were not included in the equation as the biomass values they represent are already included in the $\sigma^{O}_{L\text{-}HH}$ and $\sigma^{O}_{C\text{-}HV}$ backscatter.

2.1.2. Saturation of radar measurements

The amount or density of the scattering components within the crown, in addition to wavelength and dielectric constant, also influences the penetration depth achieved by the transmitted energy. The influence stems from the changes in path length and the degree of attenuation imposed by the crown components on the incident radiation. As the energy travels through the canopy, it is gradually depleted by the scattering caused by dielectric discontinuities in the different canopy layers such that there is less energy available to the next layer (UNSW course notes, 1996). If we assume a continuous increase in the dimensions and amount of canopy components from left to right of a forest profile, there will be a point in the profile wherein even the longer wavelength of the L-band would no longer be able to pass through the crown layer due to attenuation.

The increase in the dimensions, amount or density of the different tree components is generally directly correlated with an increase in the total aboveground biomass. That is, as the total biomass increases in value, lesser canopy penetration is expected from the forward radiation. With L-band,

the amount of biomass at which the energy no longer passes through the canopy is called the saturation level for that band. Since the type of polarization also exerts influence on the penetration depth, the same band with different polarizations will also have different levels of saturation. These influences are illustrated in Figure 1.

Point b in Figure 1 corresponds to the amount of biomass where the sensitivity of both the L-HH and LHH + C-HV backscattering to biomass measurements becomes saturated. The saturation point for C-HV is represented by point a. The flattening of the lines beyond these points indicates that the backscattering coefficients no longer respond to an increase in biomass of the forest components. Thus, any derived relationship between biomass and backscatter would no longer be valid.

This notion of saturation has important implications for the application of radar to forest areas of high biomass. Returning to figure 1, it can be deduced that equation (5) is no longer applicable to biomass levels to the right of b. A possible solution for the estimation of biomass at ranges beyond the $\sigma^{O}_{L\text{-}HH}$ + $\sigma^{O}_{C\text{-}HV}$ saturation point is the inclusion of the backscattering from a band with a longer wavelength. Equation (5) could then be modified to

$$\sum_{n=1}^{N} (\sigma^{O}) = i_n \sigma^{O}_{L\text{-}HH} + j_n \sigma^{O}_{C\text{-}HV} + k_n \sigma^{O}_{P\text{-}HH} \qquad (6)$$

where k is the unit vector corresponding to P-band with HH polarization backscattering coefficient, $\sigma^{O}_{P\text{-}HH}$.

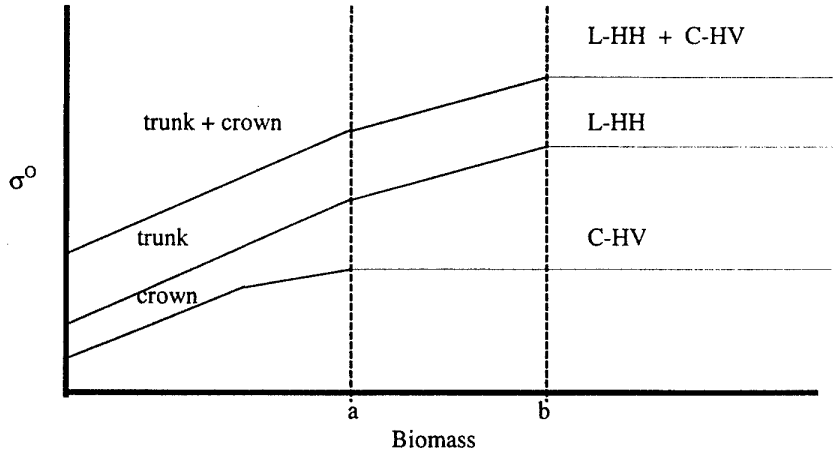


Figure 1. Sensitivities to forest components and theoretical saturation levels for C-HV, L-HH, and LHH + C-HV

2.2. Stand morphology/structure determination

In this study, two general categories are used to differentiate stands according to morphology: those composed of needle-leaved pines/conifers and broad-leaved deciduous/evergreen trees. Pines/conifers are characterized by a pattern where the bole outgrows the lateral branches thus resulting in a well-defined cylindrical trunk and a usually conical crown. The lateral branches extend up to the relatively lower portion of the central stem producing a narrow and deep crown but the bole is visible almost throughout the entire tree height due to the small size and density of the branches and the needle-like leaves. Broad-leaved trees are characterized by a less-pronounced trunk but bigger and more voluminous leaves, as well as a wider and thicker crown compared to that of the conifers. The lateral branches grow at the same rate, or even faster, than the bole and the definition of the bole can be completely lost due to repeated forking (Dobson et al., 1995a).

As radar backscattering behavior is directly influenced by the geometric properties of the target, it follows that the backscattering from stands of varying structural attributes will be relatively different. A stand of needle-leaved trees, with the small size and density of the leaves and branches as well as the long trunks of the trees, will have a strong L-HH return. On the other hand, the greater attenuation imposed by the bigger and more dense foliage components, coupled with the less conspicuous trunks, will result in a lower L-HH but higher C-HV backscatter from stands of broad-leaved trees. This change could also be related to, say, big-trunked trees and mallee or scrub type vegetation, or mangroves and trees with more conspicuous trunks. This theory is illustrated in Figure 2.

It is suggested that the above theory can be useful in the determination of tree structure. Given that the sensitivity of the L-HH and C-HV σ^o is a function of the trunk and crown components, respectively, then the true ratio of these two backscattering coefficients is a possible measure of tree morphology. This could be illustrated by the expression

$$\frac{i_n \sigma^o_{\text{L-HH}}}{j_n \sigma^o_{\text{C-HV}}} \propto \frac{\text{trunk}}{\text{crown}} = \text{TCMI} \qquad (7)$$

where TCMI is the Trunk-Canopy Morphology Index. A high TCMI implies a tree structure with more trunk and less crown component while a low TCMI indicates the opposite.

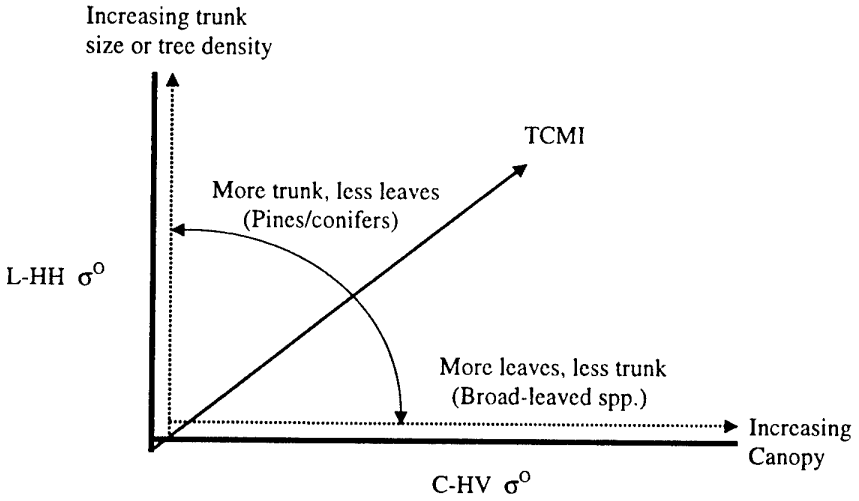


Figure 2. Sensitivity of L-HH and C-HH σ^o to stand structure properties

3. APPLICATION OF RADAR THEORY TO PUBLISHED RESEARCH

The effectiveness of the earlier presented theories, models and indices in providing measures of forest aboveground biomass and stand structure is assessed and demonstrated by applying them to actual and modelled data from published related works of other investigators. As most of the data and results from the published papers are reported in the form of graphs, interpolation was done to obtain measurements for the backscattering coefficients and the corresponding forest biomass levels.

3.1. Data Sources

Listed and individually described in Table 1 are the different studies used in the assessment of the theories and concepts previously presented. All but two of the studies involved the use of either SIR-C/X-SAR or AIRSAR system. In all of these, the HV and VH polarizations were regarded as identical and only the HV data were hence included in the analysis. The incidence angles utilized ranged from 19° - 50° and varying but closely related saturation limits were observed.

3.2. Radar backscatter versus forest biomass

All of the studies considered here, and most of the research so far reported in the literature, have correlated radar backscatter with forest biomass using single radar wavelength and polarization combinations. Although some of the forests investigated are composed of broad-leaved and mixed broad-leaved/needle-leaved species, the majority of the sites are vegetated by managed, even-aged and mono-specific coniferous stands located in temperate zones. Due to known difficulties associated with rugged topography, the different forests areas selected as study sites are located in flat to moderately-sloping areas.

In the interpolation of data from the different studies, only the L-HH and C-HV backscattering data were taken into account owing to the concepts discussed earlier. This qualification limited the number of cases considered, as only a few of the related investigations have used either or both of the L-HV and C-HV backscattering data. A maximum of 300 tons/ha was used in view of the typical saturation of radar measurements at all bands beyond this biomass level. For both L-HH and C-HV, σ° was observed to increase linearly with biomass until the saturation level for each of these wavelength-polarization combinations is reached. The TCB and TCM indices were computed based on the intensity (or true) values of the individual backscattering data i.e. not decibels. The σ° values were converted into intensity values through the formula

$$x = -\log (\sigma^\circ/10) \quad (8)$$

where x is the intensity or true value and σ° the backscattering coefficient (in decibel). No significant variation was observed between the TCBI and TCMI values within the same stand structure category from the different investigations. The similarity in the values of these indices occurred over the entire biomass range, except for some cases at low biomass levels, where inconsistent results were obtained. Factors such as strong influence of terrain/ground conditions on the radar backscatter due to low stand/crown component volume and density, may have caused these results. In general, at biomass levels below the radar saturation limits, positive linear relationships between total aboveground biomass and the two indices were observed. In comparing these index values, the effects on the data of factors such as dissimilarities in the radar systems used (e.g. viewing angle and platform altitude), discrepancies in the applied calibration methods, terrain variations, stand morphology, density and composition differences, and the possible errors introduced during the interpolation of the backscattering data and biomass levels, should however be noted.

The correlation between forest biomass and L-HH, C-HV and TCBI are presented in Table 2.

3.2.1. TCBI and total forest aboveground biomass

Table 2 indicates that in the case of C-HV, the use of TCBI (L-HH + C-HV) brought about a better correlation between radar backscatter and total forest biomass. On the other hand, in the case of L-HH, mixed results were obtained. Although much is still to be desired regarding both the number of cases and data considered, this finding is generally in support of the theory presented above (see equation (5)). Following are biomass equations derived based on linear regression analysis performed on the TCBI and biomass data from the various studies.

	Author/s	Radar System	Band/s Used	Polarization	Incidence Angle	Study Site/s	Dominant Vegetation	Saturation Limits (tons/ha)	Remarks
1.	Imhoff, 1993	JPL SAR (AIRSAR)	P-, L-, C-	HH,VV,HV	40° - 50°	a) Hawaii b)North America & Europe	a)Tropical broad-leaved evergreen b) Conifers	C- = 20 L- = 40 P- = 100	HV and VH treated as the same
2.	Souyris et al.,1995	SIR-C/X-SAR	a) L-, C- b) X-	a) HH,VV,HV b) HH, VV	26.4°	Les Landes Forest, France	Pines/conifers	50	-do-
3.	Dobson et al., 1995a	SIR-C/X-SAR	a) L-, C- b) X-	a) HH,VV,HV b) HH, VV	31°	Raco Supersite, Michigan, USA	Broad-leaved hardwoods and conifers	(multi-step approach accurate up to 250 t/ha)	-do-
4.	Dobson et al., 1995b	SIR-C/X-SAR	L-	HH, VV, HV	19° - 47°	Raco Supersite, Michigan, USA	Broad-leaved hardwoods & conifers	——	-do-
5.	Hsu et al., 1993	AIRSAR	P-, L-, C-	HH, VV, HV	45°	Les Landes Forest, France	Pines/conifers	——	-do-
6.	Dobson et al.,1992	AIRSAR	P-, L-, C-	HH, VV, HV	40° - 50°	a)Les Landes forest, France b)Duke forest, USA	Pines/Conifers	P- = 200 L- = 100	-do-
7.	Karam et al., 1995	AIRSAR	P-, L-, C-	HH, VV, HV			Pines/conifers	——	-do-
8.	Harrel et al., 1995	JERS-1 & ERS-1	L- & C-	HH & VV	45°	Les Landes forest, France	Pines/conifers(White and black spruce)	——	
9.	Christensen et al. 1990	Airborne SAR (P-3)	L-	HH, VV	42° - 49°	Duke Forest, USA	Pines/conifers	100	
10.	Moghaddam et al., 1994	AIRSAR	P-, L-, C-	HH, VV, HV	35° - 50°	Oregon, USA	Mixed hardwoods and conifers	200(for 40°-50°) 300(for °35) 150 (for 50°)	L-HH data not available from report
11.	Ranson & Sun, 1994	AIRSAR	P-, L-, C-	HH, VV, HV	25°,35°,50°	Maine, USA	Mixed hardwoods and conifers	157	L-HH data not available
12.	Ranson et al., 1995	AIRSAR	P-, L-, C-	HH, VV, HV	25°,35°,45°	Maine, USA	Mixed hardwoods and conifers	C-=100, L-=200 P- = > 200	C-HV data not available

Table 1. List and description of the different studies used in the assessment of concepts and theories

INVESTIGATOR/S	SAR Backscatter	CORRELATION COEFFICIENT			
		PINE / CONIFER Biomass (tons/ha)		BROADLEAF Biomass (tons/ha)	
		0 - 300	20 - 150	0 - 300	20 - 150
1. IMHOFF, M.L. (1993)	L-HH	0.7354	0.3140	0.8219	0.9321
	C-HV	0.6378	0.0051	0.6801	0.7926
	L-HH+ C-HV	0.6579	0.3002	0.8134	0.9326
2. KARAM, et al. (1995)	L-HH	0.7004	0.6347		
	C-HV	-0.0369	-0.2083		
	L-HH+ C-HV	0.5990	0.5571		
3. HSU, C.C. et al. (1993)	L-HH	0.8086	0.7581		
	C-HV	0.1037	0.2417		
	L-HH+ C-HV	0.6792	0.6131		
4. SOUYRIS, et al. (1995)	L-HH	0.7907	0.8764		
	C-HV	0.4919	-0.0020		
	L-HH+ C-HV	0.8268	0.8289		
5. DOBSON, et al.(1992)	L-HH	0.8731	0.9705		
	C-HV	0.7952	0.4900		
	L-HH+ C-HV	0.8769	0.8996		
6. DOBSON, et al.(1995a)	L-HH	0.4037	0.8320	0.0182	0.2317
	C-HV	0.3737	0.1329	0.4431	
	L-HH+ C-HV	0.4320	0.7759	0.5345	0.7759
7. DOBSON, et al. (1995b)	L-HH		0.7999		
8. HARREL, et al. (1995)	L-HH	0.9888	0.9879		
9.CHRISTENSEN et al.(1990)	L-HH	0.9665	0.9659		
10.MOGHADDAM, et al.('94)	C-HV*			0.9744	
11. RANSON & SUN (1994)	C-HV*			0.5113	0.6393
12. RANSON et al. (1995)	L-HH*			0.8544	0.9557

Note: * = Mixed pine and broad-leaved forest vegetation

Table 2. Correlation between forest biomass and L-HH, C-HV, and L-HH + C-HV backscatter

PINES/CONIFERS

Imhoff, 1993 : Biomass = 866.75 TCBI - 89.69 (9)
$r^2 = 0.4329$

Karam et al., 1995 : Biomass = 873.28 TCBI - 78.78 (10)
$r^2 = 0.3588$

Hsu et al., 1993 : Biomass = 1476.90 TCBI - 131.00 (11)
$r^2 = 0.4613$

Souyris et al., 1995 : Biomass = 2609.60 TCBI - 323.09 (12)
$r^2 = 0.6835$

Dobson et al., 1992 : Biomass = 1495.00 TCBI - 209.59 (13)
$r^2 = 0.7689$

Dobson et al., 1995a : Biomass = 1176.20 TCBI - 22.57 (14)
$r^2 = 0.1866$

BROAD-LEAVED STANDS

Imhoff, 1993 : Biomass = 973.50 TCBI - 74.48 (15)
$r^2 = 0.6616$

Dobson et al., 1995a : Biomass = 5396.50 TCBI - 455.58 (16)
$r^2 = 0.2857$

While the regression equation for pines/conifers generated from the results of Souyris et al. (1995) had a somewhat higher multiplicative coefficient, similarities could be observed between the equations from Imhoff (1993) and Karam et al. (1995), and from Hsu et al. (1993), Dobson et al. (1992) and Dobson et al. (1995a). The discrepancies between these groups of equations could be attributed to radar system differences and other reasons specified in Section 3.2. The differences in the equations generated for broad-leaved stands from Imhoff (1993) and Dobson et al. (1995a) are significant. However, it should be noted that the latter equation was based on four biomass values only. The highest correlation with biomass was exhibited by that from Dobson et al. (1992), with the equation explaining 77% of the biomass variation.

Given in Table 3 are the TCBI values averaged over the entire biomass range for each of the studies. A comparison of the average biomass between coniferous stands from the different studies, and between coniferous and broad-leaved stands, could be made by using these values as inputs to the corresponding biomass formulas given in equations (9) to (16).

It can be discerned from the table below that the TCBI values from the results of Imhoff (1993) and Dobson et al. (1995a) for pines/conifers and broad-leaved stands are nearly identical. This was most probably caused by the averaging process, which took into consideration the extreme values within the 0 - 300 tons/ha biomass range. Moreover, in the case of Dobson et al. (1995a), the insufficiency of available data may also have contributed to the similarity of the averaged results.

Author/s	Average TCBI Value	
	Pines/conifers	Broad-leaved stands
1. Imhoff, 1993	0.2224	0.2187
2. Karam et al., 1995	0.1761	
3. Hsu et al., 1993	0.1426	
4. Souyris et al., 1995	0.1514	
5. Dobson et al., 1992	0.2242	
6. Dobson et al., 1995a	0.1106	0.1125

Table 3. Average TCBI values for coniferous and broad-leaved stands as computed from interpolated results of different studies

3.3. Radar backscatter versus forest stand structure

Radar backscatter is mainly influenced by the geometric properties of the target. As stated above, forest stands with the same biomass but dissimilar morphology may produce different backscatter readings. Hence, radar data-based equations to estimate total aboveground biomass should be tailored according to the general structure of the forest stand. Although the importance of determining the stand structure prior to generating radar-derived estimates of forest biomass was emphasized in some of the studies (e.g. Imhoff, 1993; Dobson et al.,1995a), not one of the investigations reviewed here have considered stand structure determination through the use of radar backscattering data. In the absence of *a priori* information on stand structure, radar data-based techniques, such as the application of TCMI, is deemed essential.

3.3.1. TCMI and stand structure

The applicability of TCMI, which is the true ratio between the L-HH and C-HV backscatter, as a possible measure of stand morphology is premised on the differences in the sensitivity of the two wavelength-polarization combinations to the various tree components. Higher TCMI values are expected for conifers given their bigger trunk and smaller crown component volume compared to their broad-leaved counterpart. This theory has been proven to be generally true based on the test applied using interpolated backscatter and biomass values from related investigations albeit an overlapping of some of the values was observed. The overlaps between the conifer and broad-leaved stand TCMI points, as can be seen from Figure 3, occur at the lower and higher part of the biomass range. This is quite expected due to the minor differences in vegetation structure at low biomass levels and the saturation of radar measurements at high amounts of biomass. The usefulness of TCMI is thus at its optimum when there is a distinct difference in structure between the broad-leaved and needle-leaved trees and the backscattering data are taken at biomass levels below the radar saturation limits.

To further illustrate the usefulness of the TCMI in accounting for the difference in structure between broad-leaved and needle-leaved stands, given in Figure 3b are the graphs corresponding to those in Figure 3a but with the L-HH and C-HV data limited to those taken within a biomass range of 20 to 150 tons/ha. By adjusting the lower and higher ends of the biomass range to these levels, the probability that the broad-leaved and needle-leaved trees are more structurally defined, and that the radar measurements are less affected by saturation limits, is increased - and so is the effectiveness of the TCMI. As can be discerned from the figure, the overlapping TCMI points which exist in Figure 3a have been eliminated in the case of Dobson (1995a) and were greatly reduced in the case of Imhoff (1993). For a similar purpose, given below are the average TCMI values within the 0 to 300 tons/ha and 20 to 150 tons/ha biomass range for the different studies. The 20 to 150 tons/ha range caused a higher dynamic range between the TCMI values, and hence a better separation, of the pine and broad-leaved stands. Interestingly, the average TCMI values generated from the different investigations for pines/conifers, except those from Hsu et al. (1993), are similar though the data were taken from different study sites and conditions. The same observation holds true in the case of the values from the broad-leaved stands.

Author/s	Average TCMI Value			
	Pines/conifers		Broad-leaved stands	
	0 - 300	20 -150	0 - 300	20 - 150
1. Imhoff, 1993	3.3695	3.7013	2.5168	2.3430
2. Karam et al., 1995	3.2902	3.4119		
3. Hsu et al., 1993	5.4144	5.5431		
4. Souyris et al., 1995	3.6145	3.2267		
5. Dobson et al., 1992	3.4657	3.5937		
6. Dobson et al., 1995a	3.7642	3.9058	2.5882	2.5119

Table 4. Average TCMI values within biomass ranges of 0 to 300 tons/ha and 20 to 150 tons/ha for the different studies

4. SUMMARY AND CONCLUSIONS

The capability of microwave energy to penetrate forest vegetation makes possible the extraction of information on both the foliar and woody components from radar data. The depth of penetration, and hence the type of derivable information, is dependent upon parameters relating to both the radar sensor and the target such as the wavelength, polarization and incidence angle used, as well as the geometric and dielectric properties of the target vegetation.

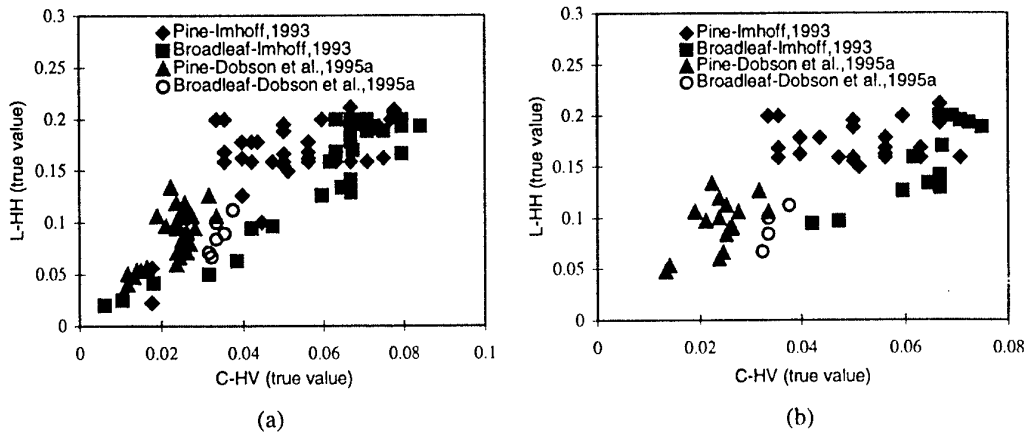


Figure 3. TCMI values within 0 -300 tons/ha (a) and 20 - 150 tons/ha (b) biomass ranges based on interpolated data from Imhoff, 1993 and Dobson et al. 1995a.

At C-band, the backscattered energy is correlated mainly with the crown constituents such as the leaves, twigs and small branches. Information on the other components beneath the canopy can be sensed through the use of bands with longer wavelengths such as the L- or P-band. The sensitivity of co-polarized and cross-polarized waves to the shapes and orientation of the different tree constituents provide an added advantage in the information extraction procedure. Given the relatively greater degree of penetration by horizontally-polarized waves and the strong interaction of the vertically-polarized energy with the vertically-oriented canopy parts, different wavelength-polarization combinations can be then used to suit the purpose of the study. In the field of forest biomass estimation, the Trunk-Canopy Biomass Index (TCBI), which is the sum of the L-HH and C-HV backscatter, can be a measure of the total aboveground biomass as both the crown and trunk layers are taken into consideration. The relationship between TCBI and biomass, however, is not expected to be unique for a whole forest vegetation owing to possible variations in morphological structure of the stands within the area. It is important therefore that stand structure be first considered to allow a more accurate biomass assessment by the TCBI parameter.

In this study, two categories are used to classify stands according to structure: the needle-leaved pines/conifers and the broad-leaved deciduous/evergreen trees. Under the first category are trees having a long main stem and a usually deep, narrow and cone-shaped crown composed of needles and small branches. Trees under the latter have a less-pronounced trunk, a wider and thicker crown with more voluminous leaves. Consequently, an index of the relative proportions of the crown and the trunk may be indicative of the approximate tree morphology. It is believed that the Trunk-Canopy Morphology Index (TCMI), which is the ratio of the L-HH to C-HV backscatter, provides a measure of tree structure.

A two-stage procedure for forest biomass estimation is therefore proposed. The first stage involves the determination of the stand structure category based on the TCMI. Once the structure is known, a specific structure-dependent TCBI could then be applied for the biomass estimation process.

The assessment of the effectiveness of the introduced theories carried out based on interpolated data from published research produced promising results. TCMI has been found to provide a good measure of the general stand structure which is deemed necessary prior to the application of biomass estimation techniques. The overlapping of the TCMI values of the needle-leaved and broad-leaved stands which occurred at both ends of the forest biomass range could be explained by the near homogeneity in structure of the stands at low biomass levels and the saturation of radar measurements at high amounts of biomass. In terms of biomass estimation, a higher correlation between TCBI and forest biomass was achieved compared to that of C-HV in all of the studies considered but mixed results were obtained in the case of L-HH. Comparison of the results is made difficult by the limitations both in the number of related studies reported in the literature and in the

amount of data available from each of the studies, inherent differences in the radar systems used, differences in the applied calibration techniques, in-situ variations (i.e., in terms of stand structure and composition, topography and other terrain features) and possible interpolation-related errors. Nevertheless, given all of these limitations, the results support the theories proposed.

To further verify the validity of the results, subsequent application of the TCB and TCM indices using extensive field data and AIRSAR images of an independent study site in the edge of the Blue Mountains National Park in New South Wales, Australia will be made.

5. REFERENCES

Dobson, M.C., F.T. Ulaby, L.E. Pierce, T.L. Sharik, K.M. Bergen, J. Kellndorfer, J.R. Kendra, E. Li, Y.C. Lin, A. Nashashibi, K. Sarabandi, and P. Siqueira, 1995a. Estimation of forest biophysical characteristics in Northern Michigan with SIR-C/X-SAR. *IEEE Transactions on Geoscience and Remote Sensing* 33(4):877-894.

Dobson, M.C., F.T. Ulaby, T. Le Toan, A. Beaudoin, E.S. Kasischke, and N. Christensen, 1992. Dependence of radar backscatter on coniferous forest biomass. *IEEE Transactions on Geoscience and Remote Sensing* 30(2):412-415.

European Space Agency, 1995. Satellite radar in agriculture : experience with ERS-1. *ESA SP-1185*, ESA Publications Division, Noordwijk, The Netherlands, 71 p.

Hsu, C.C., R.T. Shin, J.A. Kong, A. Beaudoin, and T. Le Toan, 1993. Application of theoretical model for microwave remote sensing of forest. *Proceedings of the International Geoscience and Remote Sensing Symposium,* Tokyo, Japan, 18-21 August, 2:595-597.

Imhoff, M.L., 1993. Radar backscatter/biomass saturation: observations and implications for global biomass assessment. *Proceedings of the International Geoscience and Remote Sensing Symposium,* Tokyo, Japan, 18-21 August, 1:43-45.

Karam, M.A., F. Amar, A.K. Fung, E. Mougin, A. Lopes, D.M. Le Vine, and A. Beaudoin, 1995. A microwave polarimetric scattering model for forest canopies based on vector radiative transfer theory. *Remote Sensing of Environment* 53:16-30.

Souyris, J.C., and T. Le Toan, 1995. Inversion of Landes forest biomass using SIR-C/X-SAR data: experiment and theory. *Proceedings of the International Geoscience and Remote Sensing Symposium,* Florence, Italy, 2:1201-1203.

UNSW Centre for Remote Sensing, 1996. *Microwave Remote Sensing Course Notes*, First Session, School of Geomatic Engineering, The Univ. of New South Wales, Kensington, Australia.

A Land Use Change Study Using Cellular Automata

Jinn-Guey Lay
Associate Professor, Department of Geography,
National Taiwan University
PO Box, 23-76, Taipei, Taiwan
Tel: (886)-2-23621499 Fax: (886)-2-23622911
E-mail: jglay@ccms.ntu.edu.tw
Taiwan

Key words: Spatial modeling, Land Use, Cellular Automata (CA)

ABSTRACT: Land use change is a major issue of global environment change. The modeling and projecting of land use change is essential to the assessment of consequent environmental impacts. Recent development of cellular automata (CA) provides a powerful tool for the dynamic modeling of land use change. This research adopts the spatial evolution concept embedded in CA and applies it to land use change study in Tansui Watershed. Digital land use data of two separate years were complied and analyzed using GIS software. A computer program was coded to analyze the neighborhood condition of each target cell. Summary of neighborhood conditions may reveal the dynamic process of land use change and thus enhance our understanding on transition rules, the heart of a CA.

1. Introduction

Land use activity is a linkage between human and environment. It is like a seesaw carrying human activities and environment on two opposite ends. Human activity of development is a primary driving force for global environmental changes while the changes of environment in return affects land use types. Envisioning the consequent effects of land use changes, IGBP (International Geosphere and Biosphere Programme) and IHDP (International Human Dimension Programme) co-organized a working group to set up research agenda and promote research activity for land use and land cover changes (LUCC). The working group suggested three core subjects for LUCC research, such as: situation assessment, modeling and projecting, and conceptual scaling. The ultimate goal of global change study is to assess the impacts under each possible scenario and suggest preventive actions. The modeling and projecting of land use change is essential for scenario analysis and the assessment of LUCC. Consequently, issues related to data, information, and modeling have attracted many research interests ranging from local authorities to global organizations. The importance of land use change has long been

recognized in Taiwan with many research projects undergoing. This paper presents partial result of an undergoing research, supported by National Science Council, for the study of land use change in Taiwan.

2. Cellular Automata and Land Use Change

Recent development of GIS technology enhances the analytical power needed for the study of land use and land cover change. Existing land use data are being digitized while much more data are readily created in digital format, *i.e.*, remotely sensed imagery. The development and applications of digital land use database have been successful as documented in many reports (Lay, 2000). With the help of GIS, these data can be easily overlaid and provide information needed for situational assessment. On the other hand, the methodology for predicting and modeling land use change is relatively immature. Land use change is a dynamic spatial process involves complex interactions between many factors at various spatial extents. The complexity of this dynamic process makes the creation of a comprehensive model very challenging. Recent development of cellular automata (CA) brings in a new perspective for land use change. There are increasing interests in using CA for land use study (Batty, 1998; Clarke *et al.*, 1997; White and Engelen, 1997) The concept of cellular Automata is originated from research for a *self-replicating* machine, a robot type machine equipped with visions and encoded Turing machine that can assemble a copy of itself from component parts (Firebaugh, 1988). Although such machine has not been successfully constructed, an abstract model of this self-replicating system was constructed as two-dimensional cellular automata. Cellular automata may be represented by a set of simple production rules while its outcome may mimic a very complex system (Firebaugh, 1988, p320-323). From the application side, cellular automata are dynamic model that inherently integrates spatial and temporal dimension. CA are composed of four elements as described below (White and Engelen, 2000).

- Cell space: The cell space is composed of individual cell. Theoretically, these cells may be in any geometric shape. Yet, most CA adopt regular grids to represent such space, which make CA very similar to a raster GIS.
- Cell states: The states of each cell may represent any spatial variable, *e.g.*, the various types of land use.
- Time steps: A CA will evolve at a sequence of discrete time steps. At each step, the cells will be updated simultaneously based on transition rules.
- Transition rules: These rules are the heart of a CA that guide its dynamic evolution. A transition rule normally specifies the states of cell before and after updating based on its neighborhood conditions.

This research adopts the concept of CA by analyzing the neighborhood conditions for each target cell of change. A computer program is coded to analyze the states of neighborhood of each center cell. This study used the data of Tansui Watershed as sample data for testing and

analysis. The watershed is located in northern Taiwan and the heartland of Taiwan both economically and politically. The target area of research is the plain region of this watershed, selected with elevation below 100 meters, which is about 32400 hectares of acreage. The change of land use in this area was analyzed based on the spatial condition of neighborhood. Summary of neighborhoods states is fundamental to the development of transition rules. The purpose of this analysis is to identify the relationship between land use change and surrounding environment. Findings from this analysis may reveal the dynamic process of land use change and thus enhance our understanding on transition rules, the heart of a CA.

3. Land Use Change in Tansui Watershed

With a population close to 6 millions, Tansui watershed has experienced a dramatic change during the past decades with huge amount of land use and land cover change. Land use data of the research area are available in various formats, such as: historical documents, paper maps, remotely sensed imagery, and digital data. For convenience reason, digital data are chosen as source data for this research. These data are available separately in 84 data files for each year of 1971 and 1977 in Arc/Info vector formats. The data files of each year are merged together into a big one to cover the whole research area. Since vector files tempt to result in erroneous sliver polygons thus false changes, this research converted the vector files into raster format before further process. Original data is composed of 99 categories of land use types. For the purpose of environmental change, they are reclassified into seven categories: settlement, farmland, bare land, forest, river and reservoirs, other water body, and roads. The data of two years are overlaid with each other to identify the land use change.

The overlay function is conducted using Arc View's Tabulate Area function. The change is shown in Table 1 and Table 2. As shown in Table 1, the increase of settlement is most significant with a figure near 4% or 1250 hectares. Each figure in Table 2 represents amount of change from 1971 to 1977 for each category. Based on these figures, this research therefore concentrated on investigating the change from farmland to settlement. A computer program is coded for investigating the neighborhood states of the targets cells.

Table 1: Summay of Land Use Change from 1971 to 1977

	Settlement	Farmland	Forest	River and reservoir	Other water body	Roads	Bare land
1971 acreage (hectare)	16328.97	7842.66	782.65	4194.23	827.37	590.34	1904.20
1977 acreage (hectare)	17583.53	6554.05	917.52	3532.54	733.33	800.20	2349.24
1971 percentage (%)	50.29	24.15	2.41	12.92	2.55	1.82	5.86
1977 percentage (%)	54.15	20.18	2.83	10.88	2.26	2.46	7.24

Table 2 : Summary of Land Use Change

1977 1971	Settlement	Farmland	Forest	River and reservoir	Other water body	Roads	Bare land
Settlement	46.92	1.36	0.29	0.12	0.13	0.42	1.05
Farmland	3.58	17.13	0.49	0.34	0.64	0.66	1.33
Forest	0.30	0.22	1.48	0.05	0.01	0.04	0.31
River and reservoir	0.83	0.20	0.15	9.75	0.28	0.11	1.59
Other water body	0.49	0.37	0.05	0.17	0.98	0.07	0.42
Roads	0.47	0.14	0.02	0.04	0.06	1.04	0.05
Bare land	1.56	0.76	0.34	0.42	0.16	0.13	2.49

4. Neighborhood Analysis

The states of neighborhood is summarized based on the pattern of its 8 neighboring cell regardless its orientation or sequences. Taking the example shown in Figure 1, the land use of a central cell changed from farmland to settlement, and its neighborhood are composed of one settlement cell, six farmland cells, and one forest cell. This neighborhood condition is coded as: 1610000, with each digit indicating the number of cells under each land use sequentially.

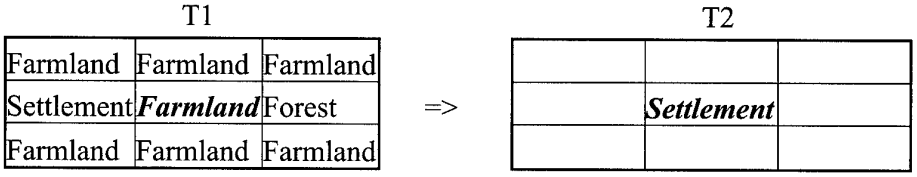


Figure1 : Illustration of Neighborhood Condition

The computer program consists of five types of query as below.

1. One to many query: showing the neighborhood statistics of target cells from one land use type to any type;
2. Many to one query: showing the neighborhood statistics of target cells from any type of land use to a particular one;
3. One to one query: showing the neighborhood statistics of target cells from one land use type to another;
4. One to many neighborhood analysis : given a neighborhood condition, showing the percentage of land use change from one type to any other;
5. Many to one neighborhood analysis : given a neighborhood state, showing the percentage of land use change from any type to a particular one.

Using function 3 of this program, the change from farmland to settlement was investigated first.

As shown in Table 3, 58% of the farmland surrounded by farmland remains farmland while 8.9% of them changed to settlement.

Table3：Settlement Change（Percentage > 1%，10M grids）

1971	1977	Settlement	Farm Land	Forest	River and reservoir	Other Water body	Roads	Bare land	No. of cells	Percen-tages (%)
Farmland	Farmland	0	8	0	0	0	0	0	451584	58.0
Farmland	Settlement	0	8	0	0	0	0	0	69116	8.9
Farmland	Bare land	0	8	0	0	0	0	0	26662	3.4
Farmland	Roads	0	8	0	0	0	0	0	14687	1.9
Farmland	Farmland	1	7	0	0	0	0	0	13478	1.7
Farmland	Other water	0	8	0	0	0	0	0	12925	1.7
Farmland	Farmland	2	6	0	0	0	0	0	10917	1.4
Farmland	Farmland	3	5	0	0	0	0	0	9482	1.2

Since an initial type of land use may result in several different land use changes, this study analyzes the various neighborhood of a particular land use change pattern type. As shown in Table 4, a farmland cell in 1971 may change to settlement in 1977 while the neighborhoods of these farmland cells may be very different. For example, sixty percent of the changed cells are surrounded by 8 farmland cells followed by the category of cells with 3 settlement cells and 5 farmland cells. These finding suggests that a land use change pattern may occur in various situations.

Table 4: Neighborhood Conditions of 1971 Farmland to 1977 Settlement (10M grids)

NEIGHBORHOOD CONDITIONS								
Settlement	Farm Land	Forest	River and reservoir	Other Water body	Roads	Bare land	Number of cells	Percen-tages (%)
0	8	0	0	0	0	0	69158	60
3	5	0	0	0	0	0	9120	8
1	7	0	0	0	0	0	6014	5.3
4	4	0	0	0	0	0	5785	5.1
2	6	0	0	0	0	0	5374	4.7
0	5	0	0	0	3	0	2154	1.9
0	7	0	0	0	1	0	1862	1.6
5	3	0	0	0	0	0	1491	1.3
0	6	0	0	0	2	0	1357	1.2

5. Conclusion

This research adopts concepts of CA to investigate land use change from a spatial evolution perspective. Factor of concern is limited to neighborhood conditions in this research. Although this approach is rather simple, yet the underneath merit lies in its ability in revealing the spatial dynamic of land use evolution. From a quantitative perspective, the prediction of future land use change may include factor of: amount of changes, rate of changes, type of changes, and location of changes. CA alone may be too simplified to predict all characteristics of changes, yet there is great possibility for CA to integrate with other methods. The creation of transition rules is but a fundamental step, yet the most challenging one, in building a comprehensive model of land use change. Findings from this research help reveal the complex process of land use change, as shown in the various changes resulted from a same pattern of neighborhood. Such finding indicates a deterministic approach of CA may not fit with real world situation. The calibration of such deficiency lends itself to many possible topics for further research.

Acknowledgement: This research is funded by National Science Council, Taiwan, Republic of China (NSC89-2750-P-002-009). The test data are provided by the Council of Agriculture, Taiwan, Republic of China.

Reference

Batty, M. 1998, Urban evolution on the desktop: simulation with the use of extended cellular automata, Environment and Planning A, 30:1943-1967.

Clarke, K.C., S. Hoppen, and L. Gaydos ,1997:A self-modifying cellular automata model of historical urbanization in the San Francisco Bay area, Environment and Planning B: Planning and Design, 24:247-261.

Firebaugh, M.W. 1988, Artificial Intelligence A Knowledge-Based Approach, Boyd and Fraser Publishing Company, Boston, 740p.

Lay, J.G., 2000, A primary study on the integration of cellular automata and GIS, Bulletin of the Chinese Geographical Society, 28:109-126.

White R., and G.Engelen,1997:Cellular automata as the basis of integrated dynamic regional modelling, Environment and Planning B, 24:235-246.

White, R., and G. Engelen, 2000, High-resolution integrated modeling of the spatial dynamics of urban and regional systems, Computer, Environment and Urban System 24:383-400.

IDENTIFICATION OF LANDSLIDES INDUCED BY CHI-CHI EARTHQUAKE USING SPOT MULTISPECTRAL IMAGES

Yu-Chuan Kuo, Hui-Chung Yeh,
Research Assistant and Post-Doctoral Research Associate
Ke-Sheng Cheng, Chia-Ming Liou, and Ming-Tung Wu,
Associate Professor and Professors
Agricultural Engineering Department/Hydrotech Research Institute,
National Taiwan University,
Taipei, Taiwan
Tel: +886-2-2366-1568, Fax: +886-2-2363-5854
E-mail: rslab@ccms.ntu.edu.tw

KEY WORDS: change detection, image rectification, kriging, remote sensing

ABSTRACT: Landuse change detection using remotely sensed images has been widely investigated. Most applications of this type involve either *image differencing* or *image classification* using multitemporal images. If multitemporal images are to be used for quantitative analysis based on their radiometric information, as in the case of change detection or landuse classification, geometric rectification and radiometric correction must be performed priori to subsequent image analyses. In particular, geometric rectification has significant effect on the accuracy of landuse change detection in areas of rugged terrain. Remote sensing image rectification is commonly done by applying a polynomial trend-mapping (PTM) model to image coordinates and map coordinates of ground control points. A major drawback of the PTM model is that it does not capture the random characteristics of terrain elevation. In this study a new anisotropic spatial modeling approach of image-to-image registration is applied to identify landslides induced by the ferocious Chi-Chi earthquake. The approach considers residuals of the PTM model as anisotropic random fields, and employs the ordinary kriging method for spatial interpolation of the residual random fields. By means of a cross validation procedure and visual check, we found that high accuracy of image-to-image registration was achieved. Band-ratioing technique was also employed for relative radiometric normalization. From the gray-level histograms of pre- and post-earthquake band-ration images, we determined the areal percentage of landuse changes in the study area. Image differencing was then performed using the pre- and post-earthquake band-ratio image pair. Finally, a gray-level threshold of the band-ratio-difference image is assigned as the value its exceeding probability equals the areal percentage of landuse change. DTM data of the study area was also used to further restrict landslide areas to steep slope areas.

1. INTRODUCTION

Change detection has been one of the major applications of remote sensing since 1960s. There are many approaches to change detection including post-classification comparison, temporal image differencing, temporal image ratioing, multifractal analysis, Bayesian probabilistic method, etc. Despite of their differences in change identification algorithms, accurate spatial registration of the various dates of imagery is a requirement for all these methods. There are essentially two different categories of image rectification approaches, the deterministic and the statistical approaches. The deterministic approach relies on data of the flight parameters and the terrain information, and is effective when types of distortion are well characterized (Richards, 1995). The statistical approach, by means of a ground-control-points (GCP) data set, establishes mathematical relationship between image coordinates and their corresponding map coordinates using standard statistical procedures. The most widely used method in this category is the polynomial trend mapping (PTM) technique that employs polynomial regression equations to relate image coordinates and their corresponding map coordinates. Although commonly applied, the PTM technique often yields significant registration errors in mountainous or rugged terrain areas. Cheng et al. (2000) proposed an anisotropic spatial modeling (ASM) approach using ordinary kriging estimation for image rectification. The approach takes into account the spatial variation structure of terrain elevation, and yields zero registration error at GCPs. For the purpose of identifying terrain changes such as landslides induced by the ferocious Chi-Chi earthquake, the ASM approach is adopted in this study.

2. STUDY AREA AND DATA

The Experimental Forest of National Taiwan University (EF-NTU) locates in central Taiwan and covers a total area of 32,781 hectares. The area is very close to the center of the Chi-Chi earthquake, occurred in September 21, 1999, and suffered severe damages. Two SPOT multispectral images, acquired on 01/04/1999 and 01/10/1999, are used in this study.

3. IMAGE REGISTRATION

In contrast to the commonly applied image-to-map registration, we perform the image-to-image registration to identify changes between two images. The reason of image-to-image registration is that the major earthquake significantly changes terrain features in many mountain areas, and selecting GCPs using maps becomes very difficult. The ordinary kriging approach of image-to-image registration is as follows.

(1). Select a set of GCPs using images acquired before and after the earthquake.
(2). Perform the first order polynomial trend mapping to map the two images.
(3). Consider the registration errors in E-W and N-S directions as two residual random fields and separately perform the anisotropic variogram modeling for each random field.
(4). Apply the ordinary kriging estimation to the residual random fields using anisotropic variograms established in step (3).
(5). Final result of the image-to-image registration is obtained by adding ordinary kriging estimates of the residual fields to the trend field estimated by PTM.

The ASM approach has the advantage of capturing local terrain variation and eliminating or reducing the distortion caused by terrain variation. Readers are referred to Cheng et al. (2000) for a complete description of the ASM approach for image registration.

An example of image-to-image registration by the ASM approach is shown in Figures 1 and 2.

4. CHANGE DETECTION

Change detection in this study involves three steps: spectral (or band) ratioing, temporal image differencing, and determination of change-no change threshold. Since images acquired before and after the earthquake have different atmospheric conditions, band ratioing analysis is performed to effectively compensate for brightness variation caused by different atmospheric conditions. Figures 3 shows that brightness of the IR image before the earthquake is lower that that of the postearthquake image. After the IR/R band-ratioing, brightness values of the two images are very close. The second step of change detection is to determine the absolute difference between the two pre- and post-earthquake (IR/R) images. Figure 5 illustrates the difference image. By comparing histograms of the two (IR/R) band-ratio images, we determine the areal percentage of changes. Finally, the change-no change threshold is determined by locating the grey level, at which exceeding probability equals the areal percentage of landuse changes, from the histogram of the difference image. Figure 6 shows an example of detected changes in the study area. DTM data are used to generates a slope image of the study area, and landslide identification is restricted only in the area with slope steeper than 18°. Up to the present, many of the identified landslide areas have been verified to by field investigations.

5. CONCLUSIONS

In this study we demonstrate that the anisotropic spatial modeling approach of image-to-image registration yields high registration accuracy in mountainous and rugged terrain areas. The band-ratioing technique yields close brightness values for two SPOT images acquired prior to and after the Chi-Chi earthquake. The multi-temporal differencing technique yields a difference image

using two (IR/R) images, and a threshold grey-level is determined for successful change detection.

REFERENCES

Cheng, K.S., Yeh, H.C., and Tsai, C.H., 2000. An anisotropic spatial modeling approach for remote sensing image rectification. Remote Sensing of Environment, Vol. 73, N0. 1, pp. 46-54.

Richards, J.A., 1995. Remote Sensing Digital Image Analyis, Springer-Verlag, Berlin, pp. 54-57.

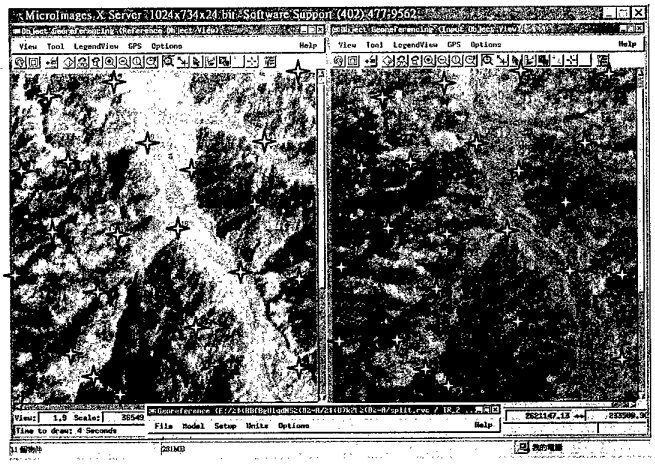


Figure 1. Image-to-image GCPs selection. (Left:pre-earthquake, Right:post-earthquake)

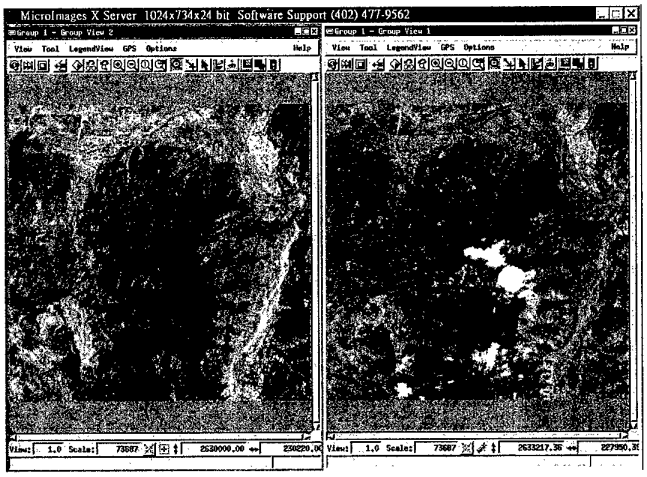


Figure 2. Result of image-to-image registration by the ASM approach.

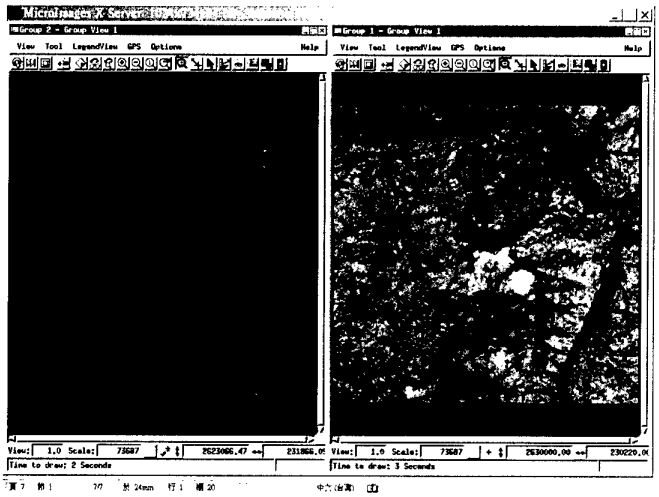


Figure 3. Pre- (left) and post-earthquake (right) IR images.

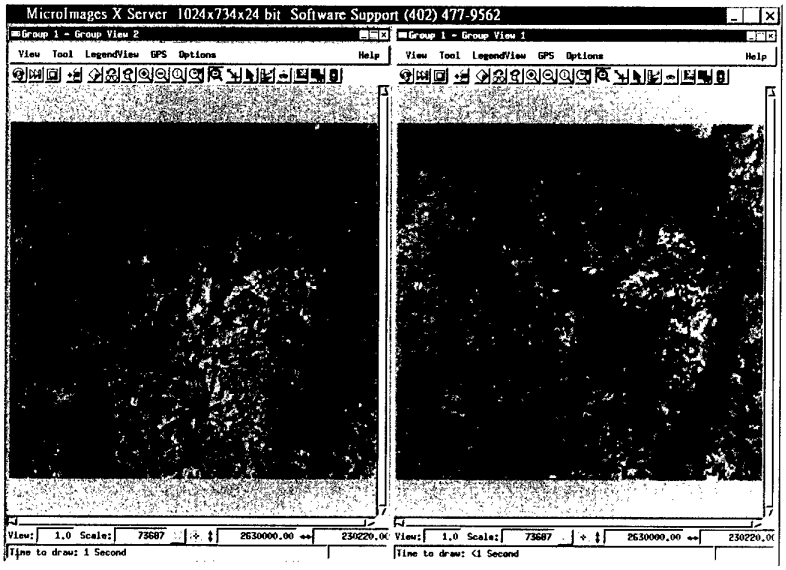


Figure 4. Pre- (left) and post-earthquake (right) band-ratioed (IR/R) images.

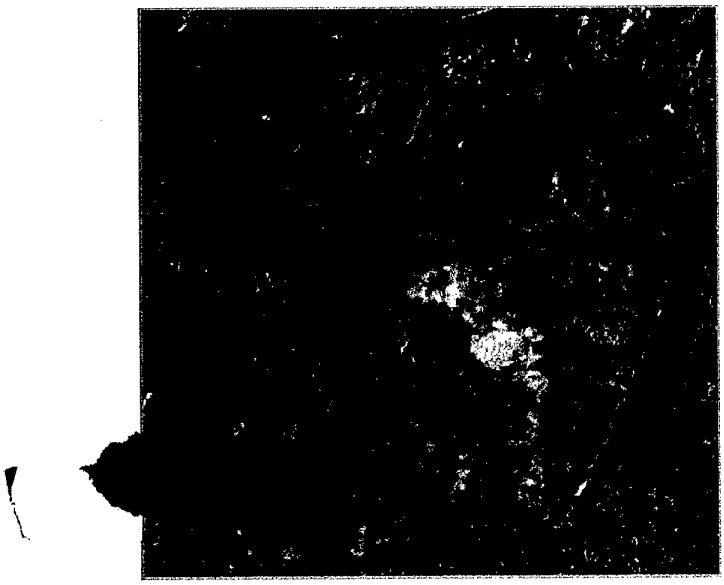


Figure 5. (IR/R) difference image



Figure 6. Image of detected changes (white areas).

DETERMINATION OF MAJOR FACTORS AFFECTING THE LAND USE/LAND COVER OF UPPER MAGAT WATERSHED. – A PRELIMINARY STUDY FOR THE LAND USE/LAND COVER CHANGE CASE STUDY OF UPPER MAGAT WATERSHED PHASE – II.

Victorino A. Bato
GIS and Remote Sensing Specialist
National Remote Sensing Center (NRSC)
Remote Sensing and Data Analysis Department (RSRDAD)
National Mapping and Resource Information Authority (NAMRIA)
Lawton Avenue, Fort Andres Bonifacio, Makati City, Philippines
Tel. No.: (632) 810-2891, (632) 810-4831 loc. 640
E-mail: victorbato@edsamail.[redacted]

KEY WORDS: Land Use Change, Land Cover Change, Magat Watershed

ABSTRACT

This study was aimed to determine the major factors which affected the land use/land cover of Upper Magat Watershed in preparation for the land use/land cover change analysis. The study area was the Upper Magat Watershed located in the Province of Nueva Vizcaya, Philippines. Land cover classification was performed on nine Landsat TM imageries taken from different dates from 1988 to 1999. The classified imageries were compared and areas with significant changes in land cover were selected as sub-areas. Analysis of the classified and raw imageries taken from different years, field pictures and histories of sub-areas pointed to four major factors which affected the land use/land cover of the Upper Magat Watershed. They were climatic conditions, human activities through agriculture, deforestation and reforestation, natural disasters like landslides from earthquakes and soil erosion.

INTRODUCTION

It is interesting to study the dynamics of land/use land cover change of an area that is agricultural, forestry and agro-forestry based. With this knowledge we can be able to predict the availability of food and resources for the coming years. We can also recommend to policy makers remedial measures if the result of our study shows that there will be problems ahead. Land use/land cover change study is a diagnostic tool for determining sustainability. It is therefore important that this diagnostic tool be done carefully and properly.

Many factors affect land use/land cover change. Economic, drought, earthquake, cropping trends, new technologies and government policies just to name a few. Each of this factor contributes with varying degree to the change dynamics of areas. A contributory factor may be applicable in one area and not in another. It is therefore important to determine which factor contributes significantly in a specific area before a full blown land use/land cover change study can be done. In the conduct of the full blown study, only the identified significant factors will be considered and the least significant ones will be removed. This procedure will ensure that our land use/land cover change study will be relevant and in the proper direction.

OBJECTIVES

The objective of this study was to determine the major factors which affected the land use/land cover of Upper Magat Watershed in preparation for land use/land cover change analysis.

STUDY BACKGROUND

Socio-economic and Physical Background

The study area was situated in the northern portion of the Philippine Archipelago covering major portions of the Province of Nueva Vizcaya. **Figure 1** shows the location map of the study site.



Figure 1. Location Map of the study site.

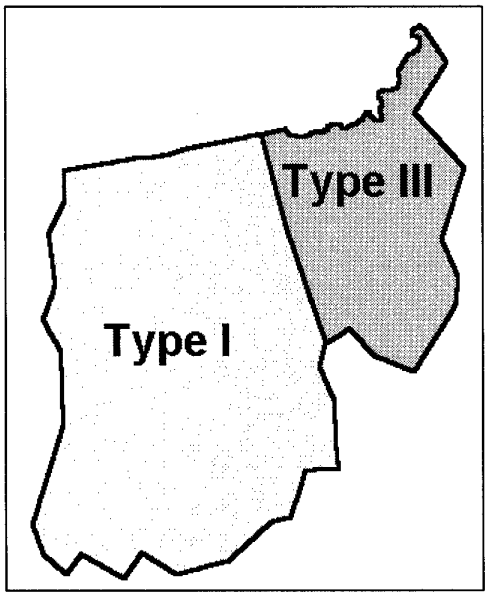


Figure 2. Climatic Map of the study site based on the Modified Coronas.

The Province of Nueva Vizcaya was composed of fifteen municipalities namely: A. Castaneda, Ambaguio, Aritao, Bagabag, Bambang, Diadi, Dupax del Norte, Dupax del Sur, Kasibu, Kayapa, Quezon, Sta. Fe, Solano, Villa Verde and Bayombong, its capitol. Its population during the 1995 survey made by the regional office of the National Statistics Office was 335,221. The economy of the study site was agricultural based. Crops like rice, corn, root crops, vegetables and fruits were the major domestic products. Farmers were also engaged in swine and cattle production.

The prevailing climate on the study site fell on two types of categories based on the Modified Coronas, type I and type II. In Type I climate, there are two pronounced seasons; dry from November to April and wet during the rest of the year. In Type II climate, seasons are not very pronounced; relatively dry from November to April and wet during the rest of the year.

The slope in the study site ranged from flat to very steep. The floodplain of the watershed was the area where most rice farming took place. The rolling and not so elevated areas were planted to upland crops, fruit trees and vegetables. Areas that were steep and/or highly elevated were mostly dipterocarp forests and some pine forests.

Concrete roads connected major municipalities of the study site. These municipalities were located on the flat lands of the watershed. Mountain trails on the other hand were the access routes to municipalities and barangays located in the highlands or areas that were separated by physical barriers like rivers and very steep mountain ridges. Mountain trails were very numerous in the watershed. Native folks and some minor ethnic groups live on very remote and steep areas accessible only through days of hike on these trails.

Historical Background on Policies

Total log ban in the Philippines was implemented around 1990 and still up to now has not been lifted. Coupled with the ban, policies like the Community Based Forest Management (CBFM), Integrated Social Forestry Program (ISFP), Community Forest Program (CFP), Forest Land Management Program (FLMP), etc began to develop to rehabilitate and improve the denuded forestlands. Sanctions like lifetime imprisonment and penalties were also imposed on violators of the law. Other than the government's Department of Environment and Natural Resources (DENR) other non-government organizations also participated in the active watch against illegal loggers.

But recently, there was a modification in the implementation of the total log ban law. This was the Sustainable Forest Management Program and one of the characteristics of this is selective logging and agro-forestry.

Historical Background on Natural Disasters

An earthquake of around intensity 7 shook the island of Luzon last 1990. This resulted to damages properties and lost lives. On the Upper Magat Watershed this resulted to the landslide of steep-unstable slopes and the siltation of Magat River and its tributaries.

The El Nino Phenomenon struck the study site and its adjoining areas from 1991 to 1995. The study site was raked among the areas in the Philippines that were severely affected by El Nino. Other than damage to crops, El Nino had also resulted to the drying of brushlands, grasslands, reduced cropping area and number per year and more occurrences of grass fires.

METHODOLOGY

Landsat TM imageries taken from different dates for ten years were used for the study. The list of imageries are presented on **Table 1**. The imageries were rectified using roads and river vector files as source of ground control points (GCPs). More than 50 GCPs were selected for each image and a root mean squared (RMS) error range of 1.5 to 1.9 was maintained for all imageries. All the imageries were classified and adjoining scenes were mosaicked.

Table 1. List of Landsat TM imageries used for the study and the date they were taken.

Landsat TM Scenes	Date Taken
116-48 and 116-49	January 31, 1988
116-48 and 116-49	April 10, 1990
116-48 and 116-49	March 30, 1992
116-49	April 2, 1993
116-48	May 20, 1993
116-48 and 116-49	August 11, 1994
116-49	March 25, 1996
116-48	July 29, 1996
116-48 and 116-49	October 22, 1997
116-48 and 116-49	January 10, 1998
116-48 and 116-9	March 18, 1999

The raw and classified imageries were examined and areas with very evident change were selected as subareas. The subareas were visited, local folks were interviewed regarding the history of the area, pictures and GPS points were taken.

Research on policies were done via interview of local government officials, library research and world wide web search.

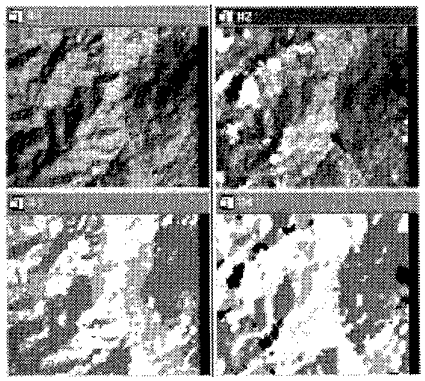


Figure 3. The effect of natural disasters on land use/land cover **(#1)** raw 1988 (before the earthquake), **(#2)** raw 1992 (after the earthquake), **(#3)** classified 1988 (before the earthquake) and **(#4)** classified 1992 (after the earthquake).

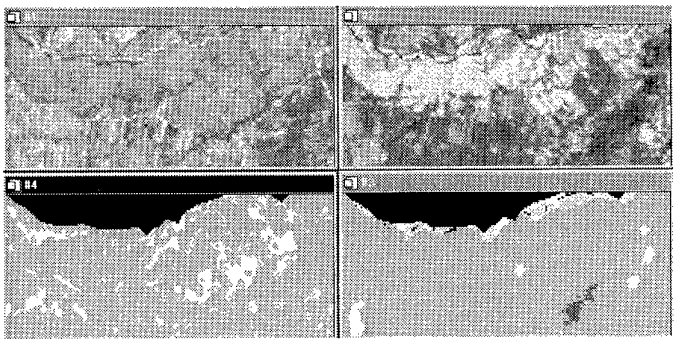


Figure 4. The effect of human intervention (agriculture) on land use/land cover **(#1)** raw 1988 (planted), **(#2)** raw 1996 (fallow), **(#3)** classified 1988 (planted) and **(#4)** classified 1996 (fallow).

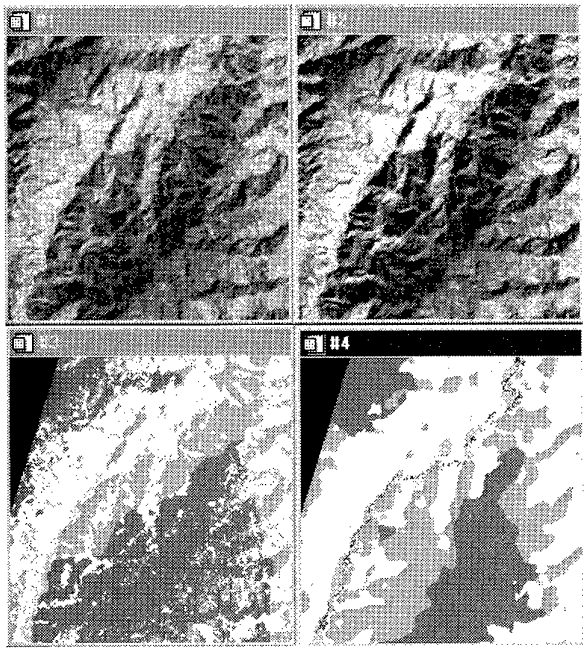


Figure 5. The effect of climate on land use/land cover **(#1)** raw 1997 (wet), **(#2)** raw 1998 (dry), **(#3)** classified 1997 (wet) and **(#4)** classified 1998 (dry).

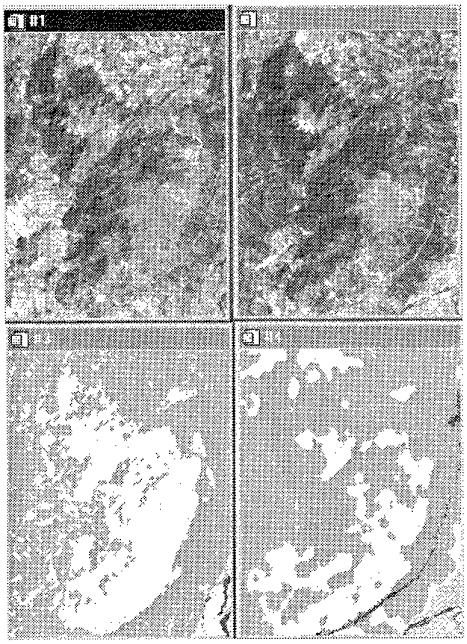


Figure 6. The effect of improvement on land use/land cover **(#1)** raw (1988), **(#2)** raw (1998), **(#3)** classified (1988) and **(#4)** classified (1998)

Legend:

- Mossy Forest
- Dipterocarp
- Brush Land
- Grassland
- Agricultural
- Built-up
- Barren Land
- Water Body

CONCLUSION

I therefore conclude that there were three major factors which affected land use/land cover of Upper Magat Watershed. They were climatic conditions, human activities through agriculture, deforestation and reforestation, natural disasters like landslides from earthquakes and soil erosion.

FURTHER STUDIES

Now that the major factors which caused change in the land use/land cover of Upper Magat Watershed has been identified, they should be considered in the land use/land cover change analysis. Spatial dimension should also be established for these factors because their activities were site specific and not applicable for the whole watershed.

REFERENCES

Climatological and Agrometeorology Branch, Philippine Atmospheric, Geophysical and Astronomical Services Administration (PAGASA), Department of Science and Technology (DOST), August 1992. Climate of the Philippines Brochure, Quezon City, Philippines.

Climatological and Agrometeorology Branch, Philippine Atmospheric, Geophysical and Astronomical Services Administration (PAGASA), Department of Science and Technology (DOST), 1997. Primer on El Nino/Southern Oscillation (ENSO), Quezon City, Philippines.

Department of Environment and Natural Resources Web Site, http:// www.denr.gov.ph

Land Use Land Cover Change (LUCC) Team, Philippine Land Use and Land Cover Change Case Study, Makati City, Philippines.

Philippine Atmospheric, Geophysical and Astronomical Services Administration (PAGASA), Rainfall and Tropical Cyclone Climatological Norms of the Philippines (1961-1990), Quezon City, Philippines.

The 21st Asian Conference on Remote Sensing
December 4-8, 2000 Taipei, TAIWAN

+ADDITIONAL NIGHTTIME AVHRR DATA FOR CLASSIFYING LAND COVER TYPES IN THAILAND

Chada Narongrit [(1)], Mitsuharu Tokunaga, Shunji Murai, Kaew Nualchawee, Apisit Eiumnoh, Suphat Vongvisessomjai

Space Technology Applications and Research (STAR) Program, School of Advanced Technologies, Asian Institute of Technology, P.O. Box 4, Klong Luang, Pathumthani 12120, Thailand
E-mail [(1)]: chadan@nu.ac.th

ABSTRACT

Nowadays, land-cover type classification using only *daytime* AVHRR data is limited by accuracy and number of land cover classes. The new method developed in this study is to investigate *nighttime* AVHRR data as an additional band for classifying land cover types with respect to improve accuracy and specify more land cover classes. The classification accuracies of various band combinations, NDVI, ordinary brightness temperatures and/or land surface temperature (LST), were comparatively assessed. Both in cool and hot seasons, overall accuracies using combination between day and night time data show better than using only daytime data. The combination of three bands of NDVI, daytime LST, and nighttime LST shows the highest accuracy. Three-band combination using only daytime shows lower accuracy than two bands using day and nighttime. Adding nighttime data obviously increases the accuracies of forest and built up classes. The nighttime data can well discriminate forest from active agriculture (or mature crops), deciduous forest in hot season from inactive agriculture (or non-mature crops), and built up from harvested or fellow agriculture. The results indicate that this approach using nighttime data behaved well as a new method for classifying land cover types at the landscape scale using AVHRR low-resolution data.

KEY WORDS: ***Nighttime NOAA-AVHRR, Land Cover Type Classification***

1. INTRODUCTION

Recently, many practical satellites have been increased to monitor land cover information around the globe. The use of high-resolution satellite data, for example, derived from Landsat-TM, and SPOT have suffered from the infrequent coverage, high data volume and high costs. Thus, recent efforts have been directed toward the use of low-resolution data (1.1 km at nadir) obtained by NOAA AVHRR sensor that provides much better temporal resolution with daily coverage (Cihlar, Ly and Xiao, 1996). For this coarser AVHRR data, a main problem is pixels containing a mixture of land cover types. The supplementation of high-resolution image is generally used to overcome this problem but this is cost consumption. Thus, the methodological challenge is to extract meaningful land cover information by using only AVHRR data. For land cover type classification, vegetation index,

computed as the pixel difference between AVHRR channels 1 and 2 reflectance divided by the sum of the two channels, is firstly used. The thermal infrared data is subsequently used. More recent research use the combination among NDVI, thermal, and ratio between these two variables. However, most of these works use only thermal data in daytime while the AVHRR sensor provides daily useful data both in day and night times. The land cover types and land characteristics can be specified by temperature difference over a time or can be described by thermal inertia, a physical variable describing the impedance to variations of temperature. High thermal inertia values lead to small changes in temperature, for a given transfer of heat (Xue and Cracknell, 1995). Water resist to the change of temperature through a time compared with other surface types. The fractional vegetation cover increases, surface temperature in daytime and temperature difference between daytime and nighttime decreases (Lambin and Ehrlich, 1997).

This study does not intend to produce a definitive land cover map, but rather attempt to investigate various band combinations of day and night time AVHRR data that can be the greatest possibility for classifying land cover types. The innovation of this research is to use nighttime AVHRR data as an additional band with respect to improve classification accuracy of land cover types derived from the AVHRR coarse resolution data.

2. DATA AND METHOD

The AVHRR images derived from the NOAA-14 passes at around 2 AM and 2 PM were selected from least cloud 3-continuous days in December 1997 (cool season) and March 1998 (hot season). Prior to image classification, the images were subjected firstly to geo-reference correction. Secondly, the images of NDVI and land surface temperature (LST) were generated. The adjusted LST equation using the split window technique (Kremer and Running, (1993), Deschamps and Phulpin (1980)) and NDVI equation in this study show as follows:

$$NDVI = (band\ 2\text{-}band\ 1)/(band\ 2+band\ 1)$$
$$LST = band\ 4 + 1.11\ (band\ 4\text{-}band\ 5) - 273, \text{ (Chada, 2000)}$$

Thirdly, The composite images of AVHRR bands 3, 4, 5, LST and NDVI were generated using maximum values. Only the NDVI images were derived from daytime data. Others were retrieved from both daytime and nighttime data. Forth, cloud remaining in MVC LST images was masked on pixels with less than 13 degree Celsius and with temperature difference between day and night less than 0 and greater than 20 degree Celsius. Next, all corrected composite images were re-scaled from 0 to 100 by relative equation:

$$\left(\frac{ActualValue - Minimum}{Maximum - Minimum}\right) * 100$$

Finally, the Maximum Likelihood classification method was used. The transected training sites or ROI (region of interest) were randomly sampled based on the overlaid digitized land use map and supplemented by recent land cover types interpreted from NDVI and temperature profiles taken from the images. At least two trainning sites and more than 150 pixels per site were labelled for seven main classes: **Water bodies (Wt):** The dam and reservoir covered by water. **Built up areas (Bu):** The urban lands have least vegetation

covered. **Field crops (Cr):** The vegetated areas grown for annual crops such as cassava, sugar cane, maize, and mixed field crops. **Paddy fields (Pa, Ph, and Pu):** The vegetated areas cultivated for rice crops. This class was labeled into three subclasses: lowland active paddy (Pa) and lowland harvested paddy (Ph) and upland paddy (Pu). **Orchards (Or):** The vegetated lands grown for fruit trees. **Para rubber (Rb):** The lands planted for para rubber tree. **Forests (Fe, Fd):** This class was labeled into two subclasses: (1) deciduous forest (Fd), the vegetative areas mostly covered by deciduous forest that somewhere mixed with the sparse evergreen forest, dry dipterocarp forest, plantation forest and disturbed forest, and (2) evergreen forest (Fe), the vegetated areas permanently covered by high density of evergreen forest.

The classified images were overlaid with the existing land use map in 1995 of Thailand classified from Landsat-TM to compute their overall accuracy (OAE, personal contact).

3. RESULTS AND DISCUSSIONS

For classified images in cool season (Figure 1), the overall accuracy assessed by the existing land use maps in 1995 were 80.64% for only daytime LST and 83.78% for combination of daytme LST (LSTd) and nighttime LST (LSTn), increased 3%. For classified images in hot season (Figure 2), the overall accuracy were 75.35% for only daytime LST and 79.40 % for combination between day and nighttime LST, increased 4%. Using only daytime data of NDVI and LSTd, Built up areas (Ba) and harvested paddy (Ph) cannot be separated. Ph in northeastern part of Thailand was mis-classified as Ba, particularly in hot season. Evergreen forest (Fe) in hot season was mis-classified as orchard (Or) and active paddy (Pa). These misclassifications were be corrected by using a combination of day and nighttime data. Because field crop (Cr) in hot season was in early planting or in harvesting period, thus, it was mis-classified as harvested paddy (Ph) and deciduous forest (Fd). The analysis between LST and two environmental factors, NDVI and elevation showed that LSTd was stronger correlated with NDVI than elevation while LSTn was fairly correlated with both NDVI and elevation (Chada, 2000). Thus, in case of Fd, its LSTd and NDVI were similarly with Cr, Ba, and Ph but its LSTn was remarkably lower than such land cover types because Fd situated on high elevation. Including channel 3 in the classifications gave good accuracy. As shown in Figure 3, the accuracy of three bands of daytime such as NDVI, band 3 and LST (81.61% in cool and 77.87% in hot season) was lower than of two bands of day and nighttime combinations such as NDVI and nighttime band 3 (82.43% in cool and 78.96% in hot), NDVI and nighttime LST (83.62% in cool and 79.85% in hot). These indicated that the accuracy was not improved by number of band but was improved by nighttime data.

The confused analysis of 7 main classes showed in Figure 4. In both cool and hot seasons, the accuracies of built up and forest were obviously increased using the combination between NDVI and LSTn. The best accuracy was obtained from paddy class. From the results, it should be explained that:

(1) Why accuracy of forest class was improved? Because forest has consistent temperature and homogenous vegetation cover whereas agricultural land has fluctuated temperature and heterogeneous vegetation cover depending on soil water regime, growing stage and land practices. In addition and more noted, the LST estimation is precisely in dense vegetated areas (Kerr et al., 1992). Daytime LST depends on NDVI and relative

humidity while nighttime not only depends on NDVI and relative humidity but depends on latitude and elevation as well (Chada, 2000). Thus, forest in high lands where temperature in nighttime decreases can be well classified even though deciduous forest was falling in hot season.

(2) Why accuracy of built up class was improved? Because temperature difference between day and night times were widest compared with other land uses. Its concrete cover has highly temperature at daytime and has rapidly decreased temperature at nighttime.

(3) Why accuracy of paddy class was the best? Typical agricultural fields in Thailand, excepting paddy fields, are smaller than each AVHRR pixel, thus, most pixels contain a mixture of land cover classes while paddy classes are less unmixed pixels.

4. CONCLUSIONS

The new method by adding nighttime data was effective to classify land cover types by improving classification accuracy, particularly of forest, paddy and built up classes. Nighttime LST can well distinguish built up from harvested land, active paddy from active filed crop or perennial crop, and forest from active paddy and lowland tree. This indicates that nighttime data can be feasibly used to classify topographically related land cover types.

ACKNOWLEDGMENT

The authors wish to express appreciation to Dr. Kiyoshi HONDA, director of ACRoRS, for contributing the AVHRR images, and to Dr. Surat Lertlum, senior researcher of ACRoRS, for his helpful knowledge in NOAA-AVHRR processing. The author sincere thanks to Dr. Supan Karnchanasutham, head of Center for Agricultural Information, for his providing the updated land use map of Thailand.

REFERENCES

Chada, N., 2000. Land Cover Type Classification in Thailand Using A Combination of Vegetation Index, Day and Night Time Thermal Bands of NOAA-AVHRR. Unpublished Ph.D. Thesis, Asian Institute of Technology, Bangkok, p. 98.

Cihlar, J., Ly, H., and Xiao, Q., 1996. Land Cover Classification with AVHRR Multichannel Composites in Northern Environments. *Journal of Remote Sensing Environment,* 58: 36-51.

Deschamps, P.Y. and Phulpin, T., 1980. Atmospheric Correction of Infrared Measurements of Sea Surface Temperature Using Channels at 3.7, 11 and 12 μm. *Boundary Layer Meteorology*, 18:131-143.

Kerr, Y.H., Lagouarde, J.P., and Imbernon, J., 1992. Accurate Land Surface Temperature Retrieval from AVHRR Data with Use of an Improved Split Window. *Journal of Remote Sensing Environment,* 41:197-209.

Kremer R.G., and Running, S.W., 1993. Community Type Differentiation Using NOAA/AVHRR Data within a Segebrush-Steppe Ecosystem. *Journal of Remote Sensing Environment,* 46: 311-318.

Lambin, E.F. and Ehrlich, D., 1997. Land Cover Changes in Sub-Saharan Africa (1982-1991): Application of a Change Index Based on Remotely Sensed Surface

Temperature and Vegetation Indices at a Continental Scale. *Journal of Remote Sensing Environment,* 61:181-200.

OAE (personal contact). *Land Use Map of Thailand in 1995*. Office of Agricultural Economics, Ministry of Agriculture and Co-Operatives, Bangkok, Thailand.

Xue, Y. and Cracknell, A.P., 1995. Advanced Thermal Inertia Modeling. *International Journal of Remote Sensing,* 16: 431-446.

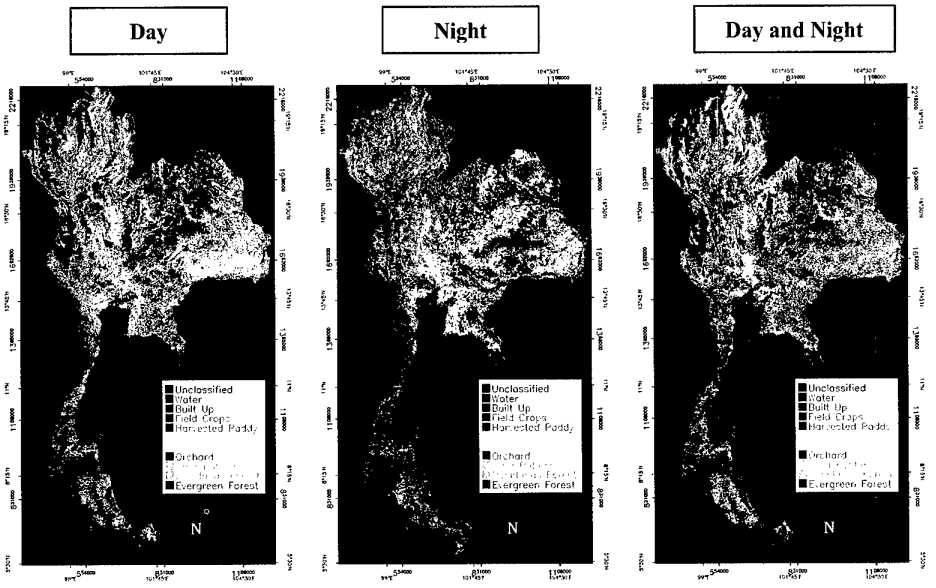


Figure 1 Classified Images in *Cool Season*

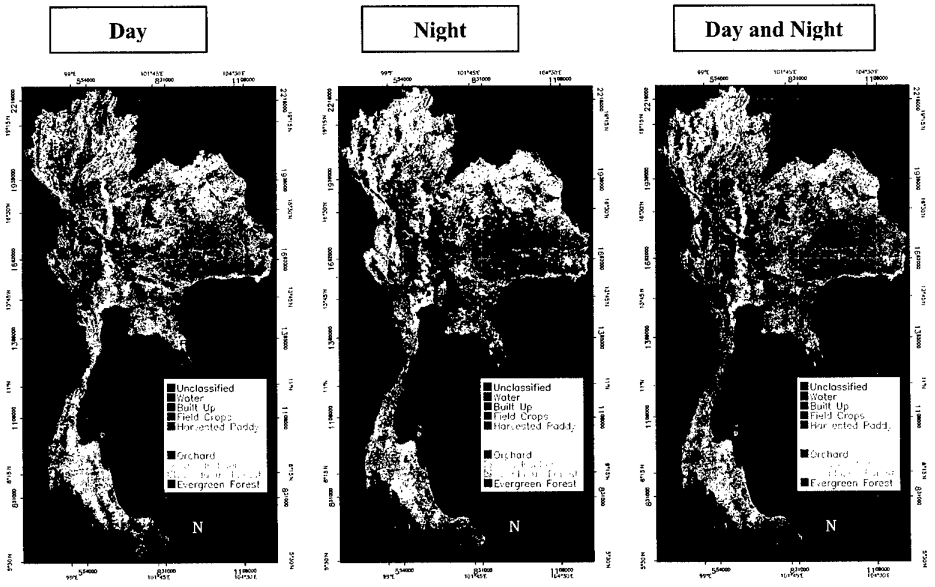


Figure 2 Classified Images in *Hot Season*

Figure 3 Comparative Accuracy of Input Bands in Hot and Cool Seasons

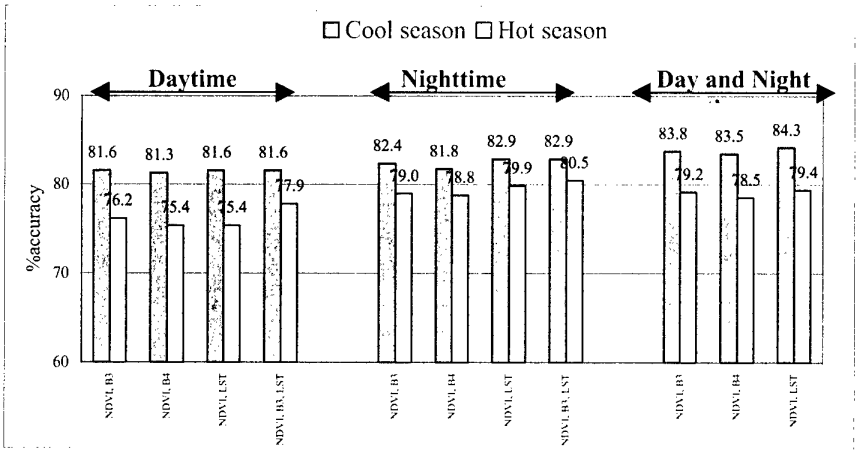
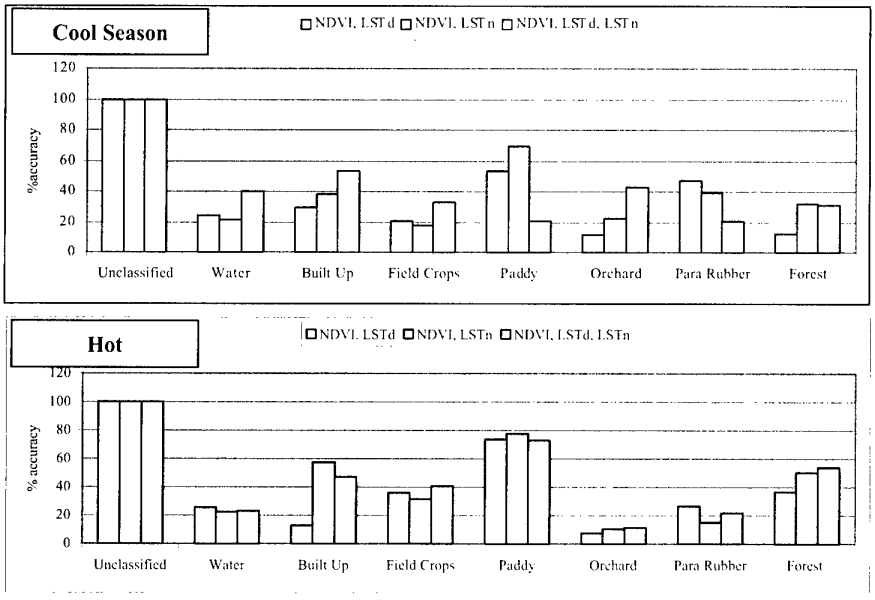


Figure 4 Accuracy Comparisons for Each Main Land Cover Types By Using Different Input Bands



The 21st Asian Conference on Remote Sensing
December 4-8, 2000 Taipei, TAIWAN

LAND-COVER CHANGE IN CHINA USING TIME SERIES ANALYSIS, 1982 - 1999

Author:
Chien-Pin Lee
GIS Business, Senior Engineer
RITI Taiwan Inc.
3F-1, 237 Sec.1, Fu-Hsin S Road,
Taipei, Taiwan, R.O.C.
E-mail: lee@mail.riti.com.tw
Tel:886-2-2325-7246 ext 292

Corresponding Author:
Stephen S. Young
Professor, Salem State College, MA
352 Lafayette Street
Salem, MA 01970, USA
E-mail: syoung@salemstate.edu
Tel: 1-978-542-6923

Hao Chen
Ph.D Candidate, Clark University, MA
950 Main St.
Worcester, MA 01610, USA
E-mail: hchen@clarku.edu
Tel: 1-508-791-4864

KEY WORDS:

Remote Sensing, Land Use, PCA, TSA, NDVI

ABSTRACT:

This study reveals some of temporal-spatial dynamics of land-cover change in China from 1982 to 1999 through Principal Components Analysis (PCA) of Pathfinder AVHRR Land (PAL) normalized difference vegetation index (NDVI) data. A more overall and newer understanding of China's land-cover change dynamic can be achieved by a longer time series analysis (TSA). The results have proved that PCA/TSA is a very effective method to identify both macro and micro factors driving the change of NDVI. Especially the thesis to paves a way to detect the impacts of extreme physical accidents and human-induced activities upon the NDVI change. The analytical results are quite exciting and satisfactory.

INTRODUCTION:

China is the world's third largest country by land area, the largest in population, and by some accounts, the third largest economy. In the past two decades, China's economy has experienced radical change, with double-digit growth rates in some years. As a result, the land use/cover change is also extensive. Rapid urbanization is leading to the loss of agricultural land. According to China's land resources management agency, the cultivatable acreage decreased by approximately 0.9% per year during the 1980s and early 1990s (Chen and Qiu, 1994). Moreover, desertification results in the gradual encroachment of originally vegetated areas. Meanwhile, some large catastrophic events, such as great floods and droughts, as well as increasing environmental pollution, may well have devastated vulnerable ecosystems, bringing about irreversible alteration of the vegetative cover. On the other hand, reforestation is, to some extent, potentially beginning to offset the negative impact of deforestation. It is apparent that the dynamic of land-cover change in China is quite complicated, because it is driven by biophysical, political, economic, and even cultural factors. China is, and will be, responsible for significant environmental changes at local to global scales (He, 1991; Young and Wang, 2000). Therefore, it is necessary to study China's land-cover change dynamic, and to find appropriate strategies to reduce the negative impacts of environmental changes.

This study reveals some of temporal-spatial dynamics of land-cover change in China from 1982 to 1999 through Principal Components Analysis (PCA) of Pathfinder AVHRR Land (PAL) normalized difference vegetation index (NDVI) data. It has been proved that unispectral time series remote sensing data can be used effectively to identify extensive and subtle changes of NDVI by means of PCA (Young, 1997). PCA is also suitable for removing noise within a multispectral image (Young, 1997). Analysis of unispectral PCA for China's vegetation change was performed by Young (1998), who averaged monthly composites to create eleven annual mean NDVI images for 1982 through 1992. He found some significant land-cover change patterns. Yet, a further study deserves undertaking, as a larger dataset with approximately 20-year coverage replaces the old dataset. A broader, updated understanding of China's land-cover change dynamic can be achieved by a longer time series analysis. Doing so, the following objectives can be expected. First, an overall spatial pattern and temporal trend of NDVI change for all of China can be gained by the yearly average NDVI value analysis and its standard variation analysis over the past two decades. Further, the difference of NDVI temporal-spatial patterns of different phenological regions can be examined. Second, using the yearly average NDVI value analysis within specific sub-regions, such as the Yangtze River Valley, the Yellow River

Valley, the Pearl River Delta and Northeast China, some more subtle but sensitive changes in vegetative cover can be ascertained, such as the impact of natural disasters as well as man-made changes.

METROLOGY:

Data

This study uses the National Oceanic and Atmospheric Administration (NOAA) / National Aeronautics and Space Administration (NASA)'s Pathfinder AVHRR Land data set with 8 km resolution (Agbu and James, 1994).

Analytical Technique

Principal Components Analysis (PCA) is an orthogonal transformation of *n*-dimensional image data that produces a new set of images. Known as components, these images are uncorrelated with one another and are ordered in terms of the amount of variance they explain in the original data set.

Framework

The purpose of this study, as addressed above, is intended to detect the temporal-spatial pattern of NDVI change in China and the possible natural and human agents responsible for these changes. Therefore, the author has designed a study framework following two main threads; that is, from macro to micro, as well as from the general to the specific, to detect these variations.

First, an overall analysis will be performed for all of China, the purpose of which is to investigate the general temporal trends and spatial distributions of NDVI within the entire country, and further to detect if there are possible regional differences in different sub-regions by means of the principal components analysis of the imagery.

Second, if regional differences in NDVI change patterns can be found, some further analyses for characteristic sub-regions will be undertaken. These sub-regions will be chosen for their physical phenological conditions, such as climate and hydrological conditions, as well as for their significance to China with respect to their agricultural importance and population characteristics.

Finally, more detailed analyses will be undertaken to further identify the impacts of natural catastrophes and human interventions upon the change of vegetation land-cover within the sub-regions through specific PCA. The study will especially focus on flood hazards and urbanization phenomena.

Study Areas

China Nation-Wide

As the third largest country in the world, China is so large that its territory spans multiple climatic zones, from the tropical and subtropical, to the temperate, to frigid zones, to the specific high-frigid climate style on high elevation plateaus. Taken as a whole, the vegetation types in China are very rich and versatile, with a nation-wide distribution geographically. In addition, with extensive human development over millennia, land use and land cover have experienced profound changes.

The study considers the entire area of China as well as its three sub-regions as the study areas, that is, Northeast China, the Yellow River Valley, and the Yangtze River Valley.

Northeast China

The northeastern area is the furthest northern part as well as the largest natural forest zone in China, where the climate is frigid and semi-humid. Natural vegetation there has been well maintained due to relatively less human development compared to the southern part of China. Biophysically, this area is an independent geographic division in terms of its climate and hydrological conditions.

Yellow River Valley

The Yellow River is the cradle of Chinese civilization. Human development, as well as the conversion of natural conditions over the past five millennia, has deeply transformed the landscape of this area. As a result, the natural vegetation coverage is much less than in ancient times, and much of the land has been converted to agricultural use. Monthly PCA/TSA was applied to this area for detecting the present-day pattern of NDVI change.

Yangtze River Valley

The Yangtze River is the longest river in China, beginning in Qinghai province located on the world's highest plateau, and crossing over almost the entire continent easterly to the sea. The Yangtze River Valley is the most vigorous and important economic zone of China. Here, the LiangHu plain of the Hubei and Hunan provinces is well known as the famous "Cereal Depository", and the city of Shanghai at the river's estuary is China's economic and financial center, playing the leading role in a new round of Chinese economic reform and development. However, the fertile Yangtze River Valley also suffers frequent natural hazards. Further, overdevelopment (its population is about 40% of the entire nation (Huang, 1994)) and unsustainable practices such as agricultural expansion by means of constructing closed levees directly cause increased soil erosion and sediment accumulation in river courses, aggravating the recurrence and magnitude of hazards (Cai, 1992). The following section of the thesis will analyze and explain the impacts of natural disasters and human-induced activities upon regional vegetation cover change through NDVI analysis.

Lake Dongting

Lake Dongting is famous for its cereal and fish production in China. Although its cropland area is just over 2% of the nation, its cereal production is 6% of the nation's total output (Huang, 1994). However, this area is also a hazard zone with very frequent floods as well as droughts. In the past 50 years this area has been subjected to 38 flood disasters, which brought huge economic losses and deaths (Li and Duan, 1997). Besides regional physical and hydrological conditions that cause flood hazards, (e.g., its lower elevations and its four big branches at the confluence of the Yangtze River), human factors have increasingly been contributing to the formation of the disasters. The most significantly negative human development is the so-called "create croplands by encroaching the lake area" phenomenon (Xiang, 1999). Due to the creation of new croplands, the lake area has dramatically shrunk 1, 659 km^2 (Wang, 1999), in turn further triggering large amounts of sediment accumulation and river course blockage, and aggravating the threat of flood disasters.

For natural hazard analysis, I concentrate on the Lake Dongting region. In the 1990s, except 1990, 1992, and 1997, floods occurred every other year. In particular, the floods of 1996 and 1998 created new historical records (Xiang, 1999). For this, the author selected the NDVI data of this area ranging from 1995 to 1999, and attempted to identify the flood accidents as well as the possible submerged extent using PCA.

Shanghai Area

Shanghai is one of China's most important economic and financial centers. Since the early 1990s, along with the opening and extensive urban construction of Pudong district, Shanghai has become the locomotive of the new Chinese economy.

Pearl River Delta

The Pearl River Delta was the first area to be developed in China upon her economic reform and opening. Because of its very tight trade and financial connections with Hong Kong, the delta has become extremely important for China. Population here is highly dense, and development activity has been very extensive. The pattern of land-cover change of this area has its own specific characteristics.

RESULTS AND DISCUSSION:

Temporal-Spatial Tendencies of NDVI Variations in China

China Nationwide

A countrywide PCA was undertaken in order to detect the overall tendencies of temporal-spatial variations of NDVI in China. Using 216 monthly Maximum value composite NDVI images from 1982 through 1999, an overall spatial pattern has been identified through component 1, which is coincident with the vegetation distribution of China (Hou, 1982). That is, in the eastern part of China, NDVI presents higher values, particularly in the southwest and northeast where natural vegetation is dense and comparatively less influenced by human activity. In the west, NDVI is much lower, where infertile deserts and high elevation plateaus are dominant. Further, the temporal curve of component 2 shows a periodic change of NDVI, which is typically influenced by the change of seasons, with a peak in July and August and a trough in December and January within each year. Based on the China Vegetation Distribution Map (Hou, 1982), it is clear that component 2 is showing natural deciduous vegetation in China. That is, in north China, especially in the northeastern area, the seasonal change of NDVI strongly corresponds to the one-peaked seasonal fluctuation characterized by the temporal curve of component 2, yet southward, the trend breaks gradually. On the

other hand, there are regions uncorrelated with this seasonal fluctuation, which reveals the regional diversity of NDVI change patterns in China. As a result, different regions command different factor composites that conduct differential temporal-spatial distributions of NDVI. Component 3 shows a different temporal and spatial pattern. It has been identified to indicate a cropping pattern, based on the temporal and spatial analysis. This is an area of wheat and rice agriculture (Hou, 1982). Therefore, on the countrywide scale, PCA is able to show the overall photosynthesis activity in China as well as showing major phenological trends involving both natural deciduous vegetation and agriculture vegetation.

Sub-regions

As is well known, component 1 generally indicates overall NDVI distribution. Therefore, the illumination below is chiefly focused on later components.

Northeast China

The temporal curve of component 2 shows a highly regular fluctuation in each year, with a peak in December and January and a trough in July and August. The spatial dimension of component 2 shows that nearly the entire region is strongly negatively correlated to the tendency of the temporal curve, which reveals that this region's NDVI variation indeed follows such a uni-peaked progression, but in the reverse direction as shown in the curve. That is, the maximum NDVI value occurs in the period of July to August instead of December to January. This pattern clearly corresponds to the pattern addressed by the temporal curve of component 2 for the entire China above. Compared to the China Vegetation Distribution Map (Hou, 1982), the pattern can be explained by the characteristics of climate, natural vegetation, and agricultural cropping structure of this region. In this region the winter is frigid, but summer's average temperature is generally over 24°C. Its adjacency to the Pacific Ocean makes the yearly average precipitation reach 700-800 mm (Liu, 1985). The natural vegetation type is forest, composed of masses of conifers and broad-leaf deciduous trees.

The Daxing'an and Changbei-shan Mountains in this area are in China's largest natural forest zone. It can be concluded that it is the specific characteristics of climate and vegetation that make this region's NDVI obviously follow the uni-peaked change pattern within one year. In summer, NDVI goes up to its maximum value along with the luxuriant growth of vegetation and increase of rainfall; in winter, NDVI declines to its harsh winter environment. On the other hand, this region's agricultural cropping structure in large part contributes to the explanation of the uni-peaked pattern as well. Restricted by temperature as well as precipitation conditions, crops in this area can only be harvested once per year. Crops are seeded in late spring, and harvested in early autumn (Liu, 1985). In late July to August, crops enter the most luxuriant growth period, which directly leads to the maximum NDVI value. It is the temporal-spatial coincidence of variations of natural vegetation and crops along with seasonal change that makes the variation of NDVI of this area concerted with the repeated uni-peaked fluctuation rhythm over years.

Yellow River Valley

The temporal curve of principal component 2 of this area exhibits a two-year period in which there are two big peaks and one small peak. The two big peaks occur in August to September, separately in each year, and the small peak grows from November of the previous year and reaches its crest in late February to March of the following year. Spatially, Weihe basin, Henan province, Anhui province, and north Jiangxu province, all located in the middle-lower reach of the Yellow River, show significant positive correlation with the temporal curve. On the other hand Shanxi[1], Inner Mongolia, Ninxia, and Shanxi[2] provinces at the upstream exhibit a negative correlation. By reference to China Vegetation Distribution Map (Hou, 1982), it is found that the former is subject to the agricultural zone with three harvests every two years. Summer and fall months ranging from May to November are the growth periods of wheat and rice, and the stage spanning November of the previous year to May of the following year is that of winter wheat (Liu, 1985). The upstream area is principally covered by semi-arid grasslands. It can be concluded that the PCA methodology can clearly pull out agricultural zones under different phenological conditions.

Yangtze River Valley

From the PCA results of Yangtze River Valley, it is concluded that the NDVI change pattern in Yangtze River Valley is significantly different from that in Northeast China and that in the Yellow River Valley. In Yangtze River Valley, both natural vegetation and corps are broadly distributed within the area. Roughly, croplands are principally found on the north side of the Yangtze River, whereas natural sub-tropical evergreen broad-leaved forests are dominant on the south side. By reference to the China Vegetation Distribution Map (Hou, 1982), the spatial dimension of

[2] Shanxi, capital is located in Taiyuan.

[3] Shanxi, capital is located in Xi'an.

component 2 characterizes the geographic distribution of natural vegetation of this area. As opposed to component 2, component 3 spatially presents almost a reverse pattern. The temporal curve of the component 3 exhibits typically two peaks per year, one of which occurs in March to April, and another in August to September. Spatially, north Hunan province around Lake Dongting, Hubei province, Anhui province, Jiangsu province, and Zhejiang province are significantly correlated to the curve. The southern part, however, generally exhibits negative or non- correlation. Referring to the vegetation distribution map (Hou, 1982), the spatial pattern is very highly coincident with the spatial distribution of rice, which, seeded in late January to February and late June to July, respectively, and harvested in May to early June and November to early December correspondingly, is the overwhelming crop type in this area (Huang, 1994 and Liu, 1985). For this, it can be concluded that component 3 represents the part of NDVI change caused by the growth of rice. In addition, the reasons that the southern part of the region presents negative or non-correlation stem from overwhelming sub-tropical natural vegetation there as well as sparse crops with three harvests in one year (Hou, 1982).

Identification of Natural and Human Factors

The temporal-spatial change pattern of NDVI is not only controlled by large-scale factors, e.g., seasonal shifts and regional agricultural cropping structures as addressed above, but also significantly influenced by some small-scale or short-term factors, especially in smaller regions or during some specific periods. In order to identify how these small-scale natural and artificial factors influence the change of NDVI, the author further applied PCA to Lake Dongting, Shanghai, and Pearl River Delta (Guangzhou Area) separately.

Flood Hazards in Lake Dongting

Floods in this area generally take place in May to July. The author therefore extracted the data series of this stage for PCA. However, the resulting components did not reveal significant NDVI change due to the influence of floods. Again, the author attempted to analyze the data series of August and September separately. As a result, the flood accidents can be clearly detected in the first component of the series in both August and September. The resulting temporal curve of the August series shows that the NDVI value of 1997 was much lower than that of any other year, and the same was true of the September series. Why could the series of May to July not identify the flood accidents, but the series for either August or September could? This involves regional climate conditions and the growth pattern of crops. During the period of late May to July, summer crops enter their harvest stage. The croplands are either uncultivated temporarily or just sparsely covered by new rice seedlings. The result is that the NDVI value of this stage is normally much lower. Hence it is difficult to distinguish the NDVI change of this stage because the NDVI of water approximates that of bare lands. Furthermore, cloud cover easily influences the imagery of this stage as well. In August and September, fall crops are normally entering their most luxuriant growth season, and their NDVI should normally approach its maximum. When floods occur, crops will generally be subject to fatal devastation. As a result, the NDVI of this stage in a flood year is much lower than its normal value. Therefore, it is concluded that August and September are the most appropriate months in which to check the NDVI change due to the influence of flooding. Further, the author attempted to delineate the possible flooded extent according to pixels' spatial correlations with the flood accident curve. The method used is to reclassify the spatial characteristic map of component 1 of the September series. Thus, possible flooded areas during 1995 through 1999 may be distinguished. As shown in Map 14, pixels in red represent the highly possibly flooded area, which are at the top 50% of positive index, showing strongly significant correlations to the curve. Pixels in yellow characterize the slightly possibly flooded area, which fall into the lower 50% of positive index, showing weak correlations to the curve. Pixels in green address the impossibly flooded area, which present no or negative correlations to the curve.

Urbanization in Shanghai Area

Shanghai's current development pattern follows a west-to-east mode. Divided by Huangpu River, the western part of the city is called Puxi, and the eastern Pudong. Puxi has been the old center of the city since 1843. Though Puxi's construction has not ever been suspended since the early 1990s, the construction focus has shifted to the Pudong district. As a result, Shanghai is once again becoming the biggest economic and financial center of China, and creating a so-called "big economic triangle" with Hong Kong and Taiwan (Zhou, 1997).

As opposed to the extensive construction in urban areas, Chongming Island, the third biggest island in China, located at the estuary of Yangtze River, is becoming the most important agricultural base of Shanghai area. The yield of Chongming Island aims at agricultural product markets. Constructing areas solely for agricultural use is its target. Meanwhile, the local government has designed and constructed a 360-hectare man-made forest garden. These policies not only maintain the original natural landscape of Chongming Island, but also make it a new resort for vacation and entertainment.

The PCA for Shanghai area is intended to detect the impacts of human development either resulting in deforestation or reforestation upon NDVI variations. Through the PCA of the series of 1982-1999 yearly average NDVI value, it is found that the continuously rising temporal curve of component 3 can well characterize the progression of urbanization. By comparison and contrast of its spatial characteristic map with its temporal curve, it is clear that urbanization is expanding around the old center of the city in a radial pattern toward the outlying areas. The central zone spatially is significantly negatively correlated to the temporal curve, whereas the spatially negative correlations of the adjacent zones with the curve are gradually dropping down. This tendency also implicitly shows a more rapid urbanization in Pudong than in Puxi, considering that Pudong was originally a large piece of undeveloped cropland in the 1980s. This urban expanding pattern is highly correspondent to the present-day Shanghai's development mode. It is apparent that urbanization is encroaching upon a large amount of croplands and natural forest cover, resulting in the dramatic decrease of NDVI value. As opposed to the development in the central urban area, Chongming Island is experiencing an utterly reverse progression. Spatially, this area is significantly correlated to the rising temporal curve, which is in keeping with its agricultural development mode and reforestation commitment (Chang, 1999).

Urbanization in the Pearl River Delta

Since the early 1980s, along with the rapid opening of China's economy, the Pearl River Delta has become one of China's most vigorous economic zones. Similar to that of Shanghai, the urbanization tendency of the Pearl River Delta can be represented by component 3. Nevertheless, the differences of these two areas are obvious, which is shown explicitly both in the temporal progress and in the spatial expanding pattern of urbanization. Over time, as shown in the temporal curve of component 3, the urbanization of the Pearl River Delta experienced a very rapid jump from 1984 to 1987. This jump corresponds to the fact that Guangzhou and Shenzhen cites were rapidly developing in this period because of the rapid growth of trade with Hong Kong. Since then, the urbanization has continued but gradually been slowing down. This tendency is partly due to the shift of China's economic focus to the Shanghai area (Yang, 1994). Spatially, as opposed to Shanghai's pattern, the urbanization in the Pearl River Delta follows a multiple-center expanding model. That is, urban areas stretch outwards separately around Guangzhou, Shenzhen, Foshan, and Huizhou and their satellite cities, such as Huadu, Chonghua, and Jiangmen. These cities typically comprise a complete, huge city collection in which cities join together seamlessly.

Conclusions

This thesis investigates the temporal-spatial change pattern of NDVI in China using PCA/TSA. The results have proved that PCA/TSA is a very effective method in which to identify both macro and micro factors driving the change of NDVI. In particular, the thesis paves a way to detect the impacts of extreme physical accidents and human-induced activities upon the NDVI change. The analytical results are quite exciting and satisfactory.

Bibliography

Agbu, P. A., and M.E. James (1994). The NOAA/NASA Pathfinder AVHRR Land Data Set User's Manual. Greenbelt, Maryland, Goddard Distributed Active Center Publication.

Anyamba, A., Eastman, J.R, and Fulk, M. (1995). NDVI Image Time Series as an Indicator of Climate Variability. Worcester, Clark University.

Anyamba, A., and Eastman, J.R. (1996). "Interannual Variability of NDVI over Africa and its Relation to El Nino / Southern Oscillation." International Journal of Remote Sensing (17): 2533-2548.

Box, E. O., and Holben, B., and Kalb, V. (1989). "Accuracy of The AVHRR Vegetation Index as a Predictor of Biomass, Primary Productivity and Net CO2 Flux." Vegetatio (80): 71-89.

Chang, S. C. (1999). Investment and Development of Chongming County.Chen, H., and Qiu, J.W. (1994). China Urbanization (Chinese). Bejjin.Eastman, J. R., and McKendry, J.E., and Fulk, M. (1995). United Nations Institute for Training and Research. Worcester, Clark Labs.

Eastman, J. R. (1999). Guide to GIS and Image Processing. Worcester, Clark Labs.

Gates, D. M., and Keegan, H.J., and Schleter, J.C., and Weidner, V.H. (1965). "Spectral Properties of Plant." Applied Optics (4): 11-20.

Goward, S. N., and Tucker, C.J., and Dye, D.G. (1985). "North American Vegetation Patterns Observed with NOAA-7 Advanced Very High Resolution Radiometer." Vegetatio (64): 3-14.

Hastings, D. A., and Emery, W.J. (1992). "The Advanced Very High Resolution Radiometer (AVHRR): A Brief Reference Guide." Photogrammetric Engineering and Remote Sensing (58): 1183-1188.

He, B. C. (1991). China on the Edge, San Francisco: China Books and Periodicals, Inc.

Hou, X. (1982). China Vegetation Distribution Map.

Huang, P. C. C. (1994). The Peasant Family and Rural Development in Yangtze Delta, 1350-1988 (Chinese), Oxford University Press.

Li, Jingbao, H. Z., Duan, Zhengliang (1997). "Hazardous Floods and Flood Disaster of Dongting Lake Area. Economy Geography (Chinese)." 169-170.

Lillesand, T. M., and Kiefer, R.W. (1994). Remote Sensing and Image Interpretation. New York, John Wiley & Sons.

Liu, H. (1985). China Geography -The Third Volume (Chinese), National Translator-Editor Embassy.

Xiang, L. (1999). "Reflection on the Hunan and Hubei '98 Flood Survey (Chinese)." Journal of China Institute of Water Resource and Hydropower Research 3(2): 80-85.

Sellers, P. J. (1985). "Canopy Reflectance Photosynthesis and Transpiration." International Journal of Remote Sensing (6): 1335-1372.

Cai, Shuming C. Z. (1992). "Strategy Against Floods and Water-logging of Middle Yangtze River (Chinese)." Chinese Academy Sciences, Geoscience Board, China Natural Disaster and Mitigation: 379-380.

Tucker, C. J., and Townshend, J,R,G,, and Goff, T.E. (1985). "African Land-cover classification using satelite data." Science (227): 369-375.

Wang Kelin, Z. C. (1999). The Mechanism of Flood and Water-logging Disaster Formation, Ecological Countermeasures of Reducing Disasters and Basin Management. Changsha, Changsha Institute of Agricultural Modernization: 1-13.

Yang, Gan Z. Q. (1994). The political economics of China reform (Chinese), Oxford University Press.

Young, S. S. (1997). The Use of Coarse-Grain, Global-Scale Remote Sensing Data to Analyze Forest Cover, Extent and Change, in China, 1982 - 1992. Department of Geography. Worcester, Clark University.

Young, S. S. (1998). Time Series Land-Cover Change Analysis Using Principal Components Analysis and AVHRR NDVI Data. Salem, Salem State College.

Young, S. S. and Wang, C.Y. (2000). "Land-cover change analysis of China using global-scale Pathfinder AVHRR Landcover (PAL) data, 1982-92." International Journal of Remote Sensing 00(00): 0000-0000.

Zhou, Q. (1997). Difference Investigation of China Area Development (Chinese), Oxford University Press.

Urban planning and monitoring changes using ER Mapper

Dr Abdullah Mah
Training & Applications Consultant
Earth Resource Mapping, Asia Pacific region

With the rapid growth in population throughout the world, it is crucial to have a well-concerted plan for urban expansion. Satellite or Airborne images give Urban planners synoptic views of large areas which allow them to lay plans for urban expansion effectively. Using December, 1990 and February, 1997 SPOT Panchromatic and Multi-Spectral imagery of the Sydney Metropolitan area, the paper demonstrates how to use ER Mapper in processing those images for urban planning and to monitor changes that took place over the 1990-1997 years.

INTRODUCTION

The study area is the Sydney Metropolitan area. SPOT Imaging Services Pty Ltd's permission to use the December, 1990 and February, 1997 SPOT Panchromatic and Multi-Spectral data of the Sydney Metropolitan area is much appreciated and acknowledged. The location map (Fig. 1) shown below covers most of the study area which is approximately 38 sq kms. The paper discusses rectification of the images, standardizing the atmospheric condition of the 2 dates imagery, change detection between the 2 dates SPOT Panchromatic and Principle Component number 1 of the 2 dates SPOT Multi-spectral imagery. A few small areas are selected to show the effectiveness of the change detection techniques applied on the 10 and 20 meters resolution SPOT Panchromatic and Multi-Spectral images.

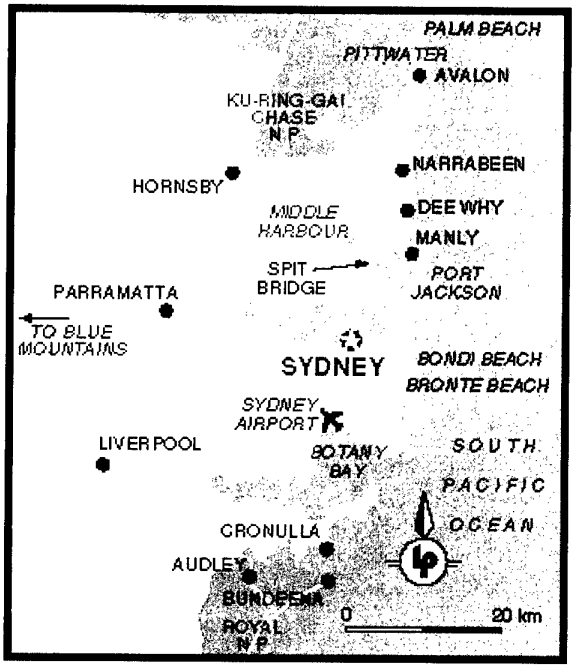


Figure 1. Location map of the study area (Sydney Metropolitan area)

PROCESSING

Rectification:
The June 1998 Orthocorrected SPOT Panchromatic image was used as the master dataset to rectify the December 1990 and February 1997 SPOT RAW images. Average RMS error of less than 0.5 is achieved for all the images (SPOT Panchromatic a RMS of 0.454 for 12/90 and 0.374 for 2/97 and SPOT Multi-Spectral 0.347 for 12/90 and 0.248 for 2/97). The common area of the 2 dates imagery was then subsetted for the study. The study area covers, Sydney in the East, Parramatta in the West, Hornsby in the North and just above Cronulla in the South (Fig. 1).

Standardizing the atmospheric condition:
The atmospheric condition was most likely to be different at the time the 2 images were taken, one in December, 1990 and the other in the February, 1997. To do change detection it is necessary to standardize the atmospheric condition of the two-date imagery. Bi-variant scattergram was used to find out the cut-off values that might have contributed by the atmosphere. The cut-off values were then used to standardize the atmospheric condition of the two-date images.

Change detection:
The recently developed Local Council Applications Wizard (LCAW) (Fig. 2) was used to carry out change detection of the Sydney Metropolitan area using the two dates SPOT Panchromatic and Multi-Spectral data. Though LCAW was developed for Local Councils to process Airphotos and Scanned maps, both Airphoto Panchromatic and SPOT Panchromatic are one band data. Similarly, both RGB Airphotos and SPOT Multi-Spectral data are 3 bands imagery. Hence, Change Detection (2 dates Airphoto Pan & Pan) and Change Detection (2 dates RGB & RGB) modules were used to carry our change detection of the 2 dates SPOT Panchromatic and Multi-Spectral data. The processing time of the change detection between the 2 dates SPOT Panchromatic was about 2 minutes and for the Multi-Spectral was about 3 minutes. Processing time for 2 dates Multi-Spectral data took longer because it uses Principle Component number one of the 3 bands Multi-Spectral data which requires statistic calculation of the datasets. All the processing steps are in-built into the LCAW and hence is very fast to process data and leaves a lot of time for the author to analyze the processed images.

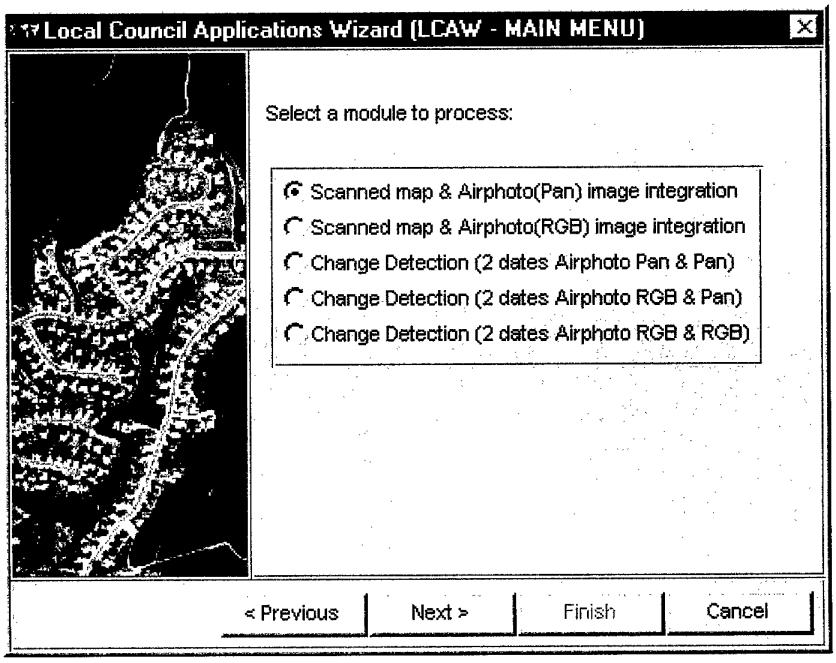


Figure 2. Local Council Applications Wizard main menu window.

SPOT Panchromatic:

Images of the original SPOT Panchromatic of December, 1990, February, 1997, change detection using Red (Feb97) and Green (Dec90), change detection subtraction and division methods are displayed in Figure 3.

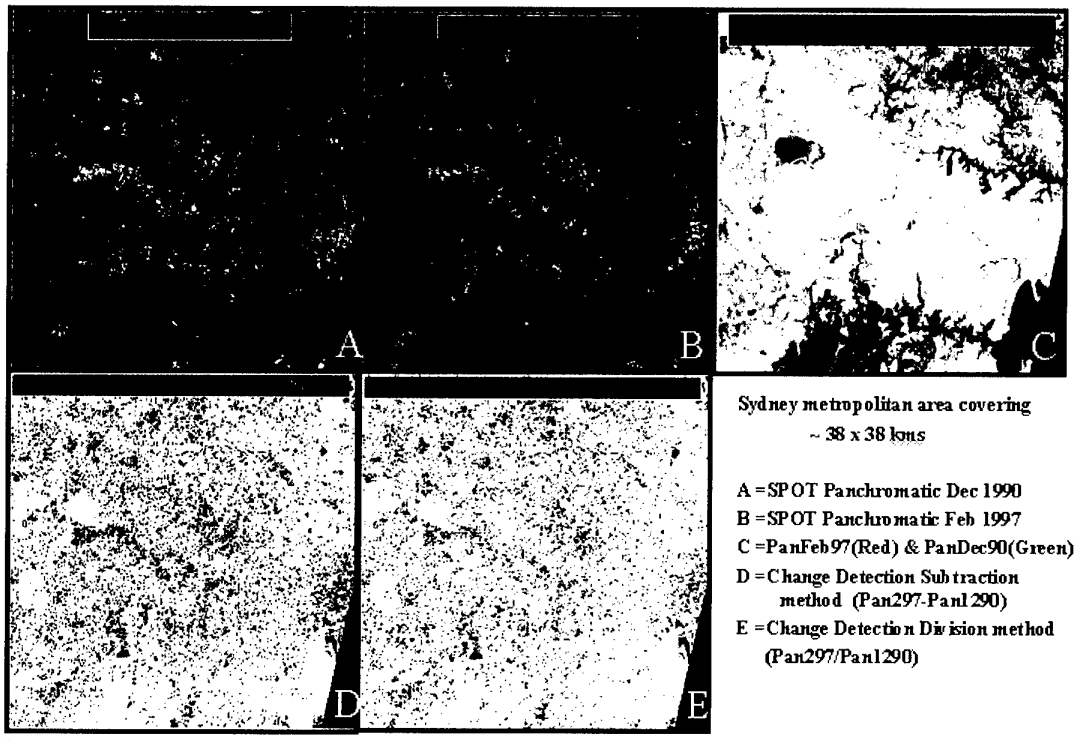


Figure 3. SPOT Panchromatic (Dec 90 & Feb 97) of Sydney Metropolitan area and change detections

Simple Red-Green combination change detection:
This is a very simple method to quickly check the changed areas by just using the Red gun for PanFeb97 and the Green gun for PanDec90. Where there are differences between the 2 dates imagery Red and Green colors are displayed and the areas where there are no differences Yellow color is displayed (Fig 3C). However, the method is only for visualization and changed areas cannot be mapped.

Change Detection – Subtraction method:
This method simply subtracts one date SPOT Pan from another (Feb97 Pan – Dec90 Pan). Using the Pseudocolor look-up-table the changed areas for the 2 dates SPOT Pan and the common areas can be mapped in three colors and changed areas can be mapped and can be converted to vector format. The changed areas of the 2 dates SPOT Pan are mapped as blue and red whereas the common areas are mapped and displayed in cyan color (Fig. 3D). The thresholds of the changed areas are defined by the step transformation where the changed areas are represented by the two extreme ends of the (Feb97 Pan – Dec90 Pan) histogram. The changed maps can then be verified with groundtruthing.

Change Detection – Division method:
This method simply divides one date SPOT Pan from another (Feb97 Pan / Dec90 Pan). Similarly, using the Pseudocolor look-up-table the changed areas for the 2 dates SPOT Pan and the common areas can be mapped in three colors. The changed areas of the 2 dates SPOT Pan are mapped as blue and red whereas

the common areas are mapped and displayed in cyan color (Fig. 3E). The thresholds of the changed areas, mainly in the two ends of the (Feb97 Pan / Dec90 Pan) histogram, are also defined by the step transformation.

SPOT Multi_Spectral:

The same process was carried out on the SPOT Multi-Spectral images of the Feb97 and Dec90 Sydney Metropolitan area (Figure 4). However, instead of comparing one band at a time, between XS1 or XS2 or XS3 of Feb97 and Dec90, PC1 of the XS123 of the Feb97 and Dec90 are used. Since Principle Component Analysis maps co-variances of the three input bands, XS1,2,3 into a new axis PC1 (Richards, 1995), it represents the common information of the three input bands. If the user wants to analyze changes in particular Visible Green, Red and Infrared, he/she can do so very easily using the LCAW.

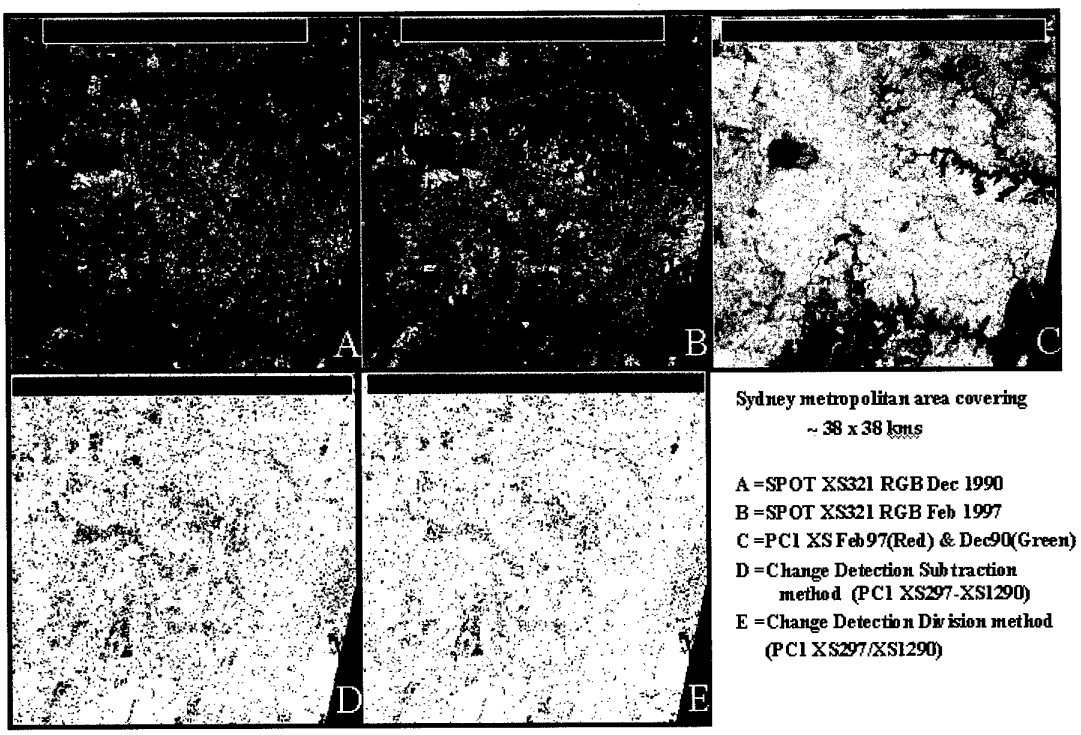


Figure 4. SPOT Multi-Spectral (Dec 90 & Feb 97) of Sydney Metropolitan area and change detections

DISCUSSION

All the simple Red, Blue color display, Subtraction and Division change detection techniques, using SPOT Panchromatic and Multi-Spectral data of the Feb97 and Dec90 render similar results. However, the Division technique on the SPOT Panchromatic does not show as clear as other techniques for the changes of the 3rd run way of the Sydney International Airport. The Subtraction technique of the Panchromatic and the PC1 of the XS123 of the Feb97 and Dec90 provide the best result. An enlarged area of the 3rd Run Way and an area in the South-West of the study are shown in Figure 5. The calculated changed areas (Red color) in the Sydney Metropolitan study area is given as 564.591 sq kilometers.

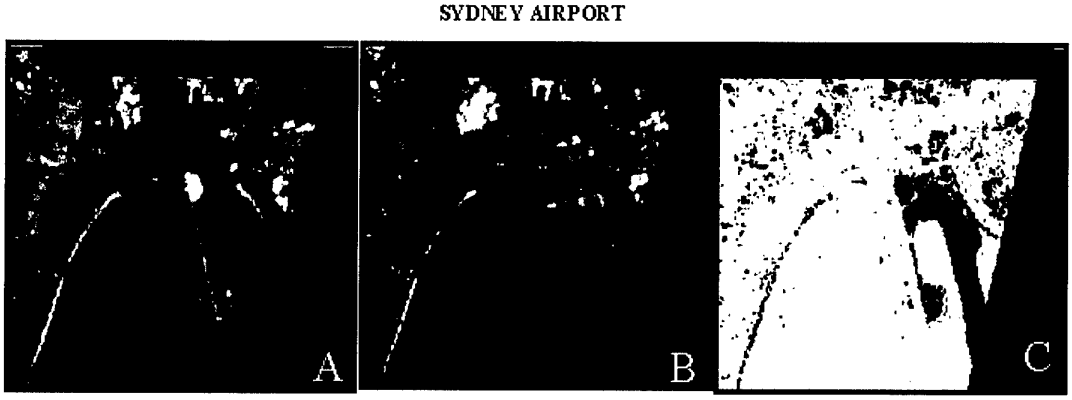


Figure 5. SPOT Multi-Spectral (Dec 90 & Feb 97) of Sydney Airport area with 3rd Run Way clearly mapped as changed area.

CONCLUSION

Multi-date temporal SPOT Panchromatic and Multi-Spectral data can be used and easily map changes that took place over the years. The multi-date datasets are required to be rectified and co-registered and is necessary to standardize the atmospheric conditions between the imagery prior to carrying out change detection. Subtraction and division change detection techniques can be applied to detect changes using either single bands or PC1 of the XS1,2 and 3. Subtraction change detection technique of the Panchromatic and the PC1 of the Feb97 and Dec90 provide the best result. Verification of the changes in the field is necessary for accuracy assessment.

REFERENCES

Richards, J. A. (1995) Remote Sensing Image Analysis (An Introduction), (2nd Edition), Springer-Verlag Publications, 340 p

INVESTIGATION OF LAND USE IN RELATION TO LANDSLIDE BY USING GIS

R.Ajalloeian (B.Sc, M.Sc, Ph.D.)
Department of Geology, Isfahan University, Isfahan-Iran
R. Karami (B.Sc, M.Sc)
Department of Geology, Isfahan University, Isfahan-Iran
M.Nikzad (B.Sc, M.Sc)
Natural Resource Organization, Isfahan-Iran

KEYWORDS: Geographic Information System (GIS), Landslide, Land use, Zonation

ABSTRACT: Similar to other developing countries, Iran is also suffering from environmental hazards. In Iran, its main reason is population pressure due to higher population growth rate and in-migration. The landslide is one example of such phenomenon that affects the household, road and etc. Under this context, the present study has been carried out to approach for better land use plan. In this regard, the role of land use change and its relation to landslide has been investigated.
Study area is Poshtkoh of Freydonshahr, which is located in southwest of Isfahan in central of Iran. From the point of view of landslide potential, this area has been detected by using geographic information system (GIS). Using the Arc Inf. Software has done this zonation. It is concluded that the most important landslide points has been occurred in the areas which was changed the land use. These changes are mainly in relation to replacement of forest to grassland and also civil activities. There are different agents that cause the landslide. For this reason, different theme maps such as raining rate map, slope map, hypsometry map and aspect map has been prepared. The final map is achieved by composing different theme maps. By using this map, it is possible to classify the area regarding to hazard rate for land use.

1. INTRODUCTION

Landslide is a world wide disaster that has murdered thousands of people and damages million dollar every year. In spite of the fact that the landslide is more manageable and more forecastable as compared with other natural calamities like earthquake and flood, there are less than one percent of the countries that have the landslide maps and few landslide stability potential maps have been prepared. In this paper authors have attempted to prepare the zonation map of the Poshtkoh area of Freydonshahr section, which located in southwest of Isfahan in relation to landslide potential by using GIS in order to land-use.

2. GENERAL

The studied region is about two hundreds kilometers far from center of Isfahan. This area is equal to 81819.8 hectares between (49 48 45 - 50 19 2) longitude and (32 37 2 - 32 53 48) latitude (figure 1). Regarding to geomorphology of area, mountains cover more of lands about 68.04% equal to 55970.5 hectares. Also hills have 11.42% equal to 9391.86 hectares and traces have 6.83% equal to 5468.6 hectares and cliffs have 13.71% equal to 11361.8 hectares of the total area.

Water-drainage of the studied project are divided in to four basins and some sub basins as follow:

Main Basin	A	B	C	D
Sub Basin	---	B1 B2 B3	C1 C2 C3	DE=DE1'DE2'DE3 DF DH

Hydrogeology factors like drainage density, waterflow regimes and etc. cause to mass movement by surface and subsurface erosions. The main rivers, because of more extensive flows, have more potential to washout the deposits and trigger the landslides. For this reasons the landslides which located in the studied area, mostly are around the rivers. Slope morphology is another factor that influences the landslide. Generally the slope alterations are divided in two categories as natural and artificial. Sometimes the rivers washout the slope-toe and unstable it. In other hand, excavations and trenches also could activate the landslides and cause to create a disaster.

One of the important factors that directly increase the landslide potential is precipitation. This phenomenon is in form of snow that is over 50% of precipitation of the area and always occurs at the winter. Eleven classes are considered for the precipitation of this area, which are between 450 to 1400 millimeters.

Destruction of grasslands in addition to land-use changes like replacement of forest and agricultural ground to building, road and other civil structure, is important factor that will cause starting the landslides. The information was collected only around the road because of difficulties to cross the mountains. Twelve important landslides were defined that we pointed them on the map with scale 1:250000.

Since preparing the zonation map of landslide and defining the critical point is via to civil planning, recognition of Poshtkoh landslides was performed by using the geographical information system (GIS) and ARCINFO software. The preparation steps of landslide zonation map are followed.

3. MODELLING OF THE MAPS OF THE AREA

After determining the landslides on the 1:250000 maps and digitizing and adding the overall description information of each one, the composition map has been prepared (figure 2). This map can be used for evaluation of various lands in studied area in relation to landslide hazard. It is necessary to mention that all of the maps must be similar in size, area and scale. The maps that were considered to compose with together are as follows:

3.1 Slope map

The slopes are classified in to seven category consist of (0% -2%), (2% - 5%), (5% - 8%), (8% -12%), (12%- 25%), (25% -40%) and (>40%) that includes 677 polygon. the slope polygon with angle greater than 40% has the most extensive area equal to 43243.8 hectares.

3.2 Hypsometry map

All of the elevation of the studied area, divided in to six classes consists of (1600m-2000m), (2000m-2400m), (2400m- 2800m), (2800m- 3200m), (3200m -3600m), (3600m- 4000m) that greatest polygon and largest area belongs to (2400m- 2800m) class, which has about 68.26 hectares area.

3.3 Climate map

Based on climatically information, four category considered for studied area consist of very humid climate with very cold winter (I.A.I), moderately humid climate with very cold winter (II.B.1), humid climate with very cold winter (II.B.2) and warm semi-humid climate with semi-cold winter (III, C, 3) .The landslides area generally belongs to (III.C.3) and (II.B.1) climates.

3.4 Geology map

From the view point of erosion, the geological formations of area has to be considered. The studied area for purposes of erosion was divided in to four classes consist of (E1), (E2), (E3) AND (E4), with regarding the strength against erosion. So that the (E2) class, has greatest area about 35500.46 hectares.

3.5 Dip-Direction map

Regarding to civil activities such as road construction, the role of dip and dip direction of geological stratums is important. This issue has to be considered in design planning. There are four main dip-direction in this area that the least area belongs to south and the most area belongs to north.

3.6 Rainfall map

Rainfall map includes seven classes consist of (450), (550), (650), (750), (850), (950) and (1050) millimeters. The least area belongs to first class (450 mm) about 283.47 hectares and the greatest area belongs to seventh class (1050 mm) about 42604.4 hectares.

3.7 Soil map

Fourteen classes have been considered that the least area belongs to seventh class that includes marl-limestone mountains with (15%) slope wash about 605.9 hectares. The largest area includes dolo-limestone and orbitoline limestone mountains with (30%) slope wash about 12266.05 hectare.

3.8 Cover crown

Six classes were considered in this classification that include (<10%), (10% - 20%), (20% - 30%), (30% - 40%), (40% - 50%) and (>50%) that the least area belongs to fifth class (40% - 50%) about 64.6 hectares and the largest area belongs to forth class (30% - 40%) about 33968.92 hectares.

4. METHODOLOGY

After plotting the landslides on map, all specifications of each one must be determine from previous maps. Then system defined 19 polygons so that the nine of them are polygons of landslides that had been studied in the field and ten remained polygons are the areas that have more potential to occur future landslide. It is interesting that the most of landslides have been occurred around the roads that points out the effect of civil activities like road, building and etc on this phenomenon.
In this stage, the information of twelve landslides must be described for the whole of area and the system automatically find the polygons that have similar characteristics that disposed them to landslide. The final echological units map is consist of a lot of polygons that each polygon has especial characteristics (figure 2). Using the GIS, this map has potential to show the properties of any land regarding to landslide hazards. Smallest polygon area in this study is 25 hectares.

5. CONCLUSION

Generally the prepared zonation map, specify the areas that have more potential to landslide, so it classify the area regarding to hazard rate for land-use. Therefore the civil operations must consider these areas and avoided them. Also the improvement activities in this area are undeniable.

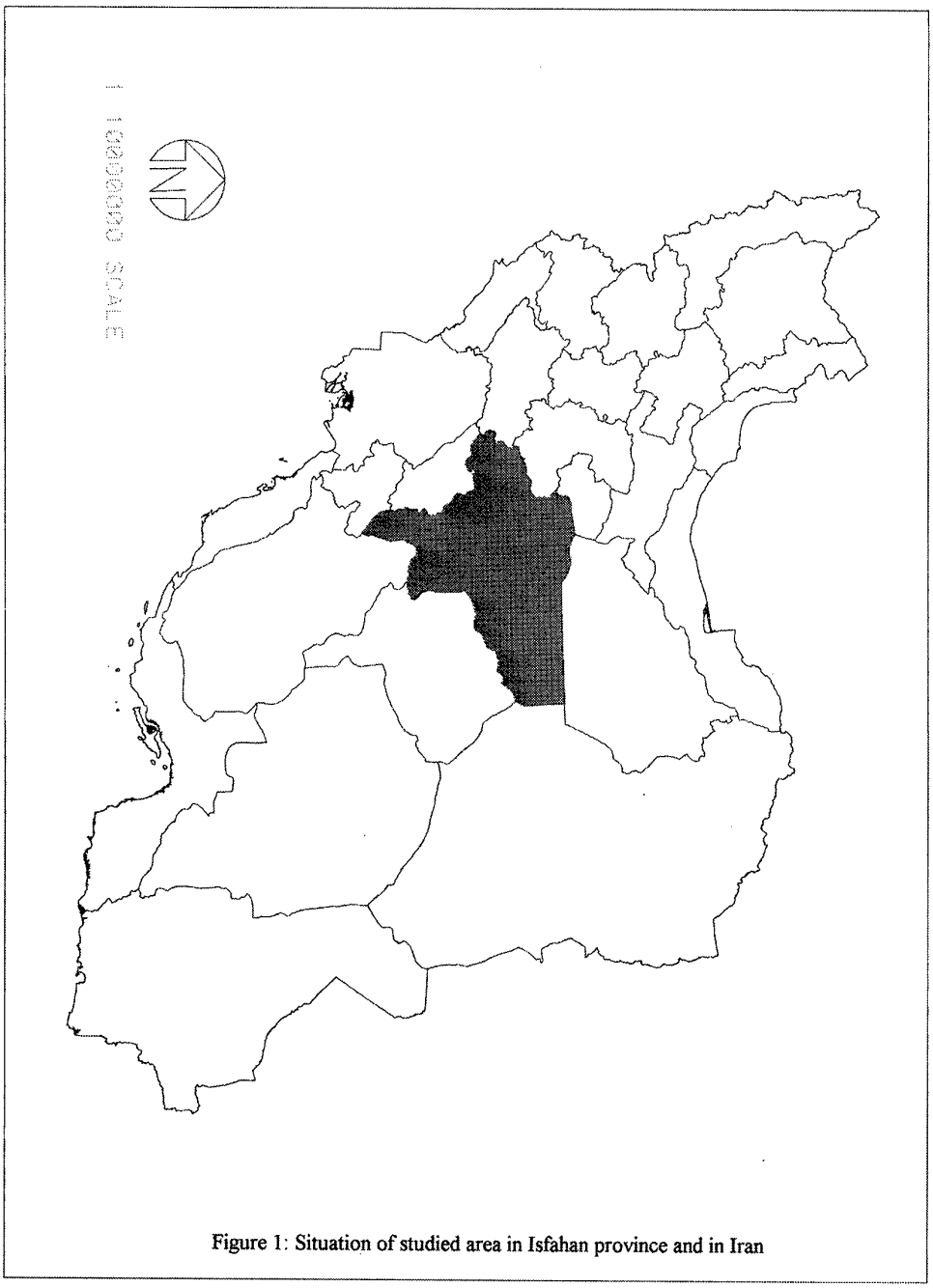


Figure 1: Situation of studied area in Isfahan province and in Iran

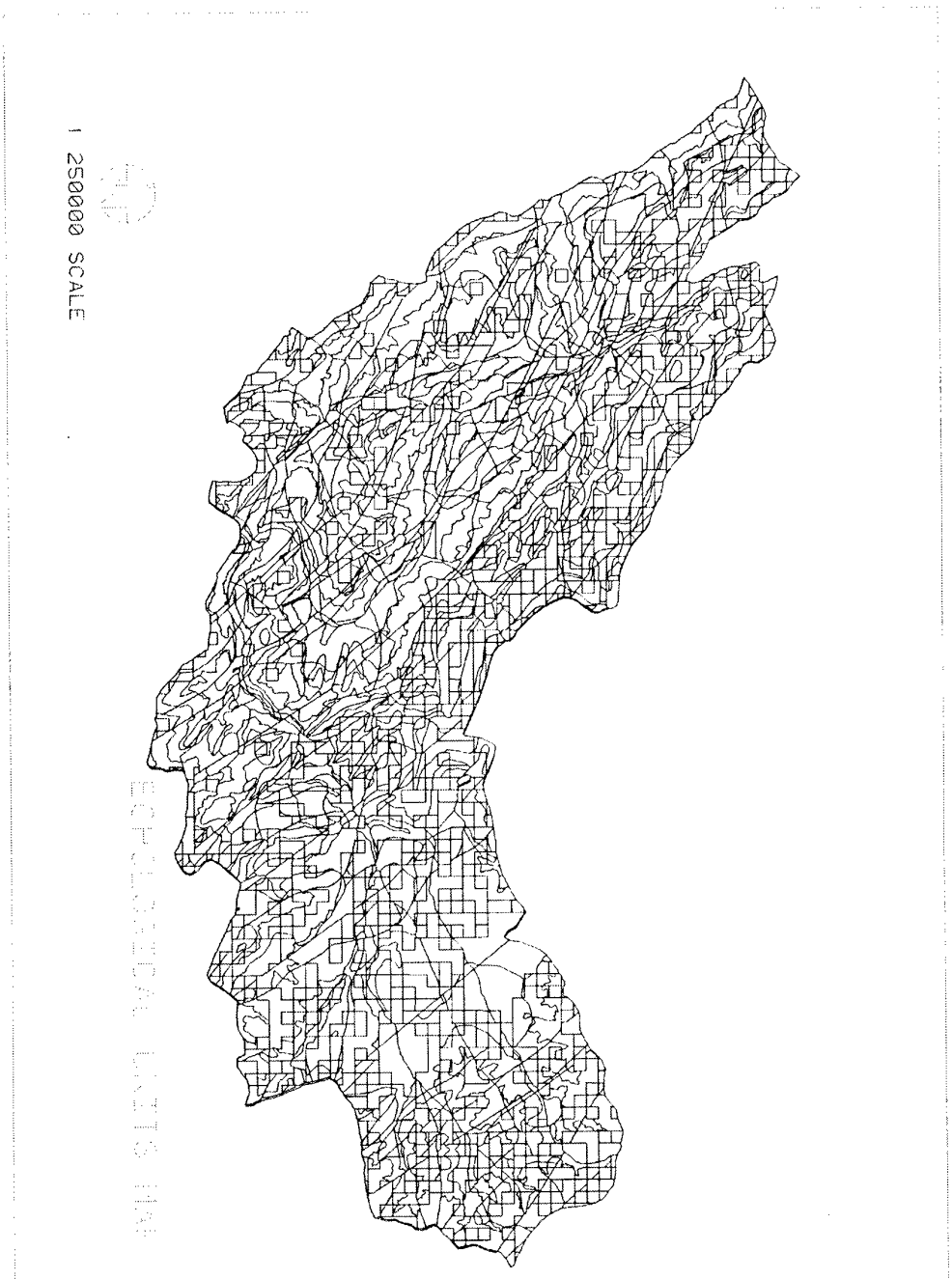


Figure 2: Composition map of Poshtkoh area

THE STUDY OF KNOWLEDGE-BASED DATABASE ASSIST FOR URBAN LAND USE CLASSIFICATION

Fu-jen Chien, Tien-Yin Chou
GIS Research Center, Department of Land Management
Feng Chia University
100 WENHWA RD., TAICHUNG, TAIWAN
TEL:(886)-4-4516669 FAX:(886)-4-4519278
fjchien@gis.fcu.edu.tw, jimmy@gis.fcu.edu.tw
TAIWAN

KEYWORD: Classification, Remote Sensing, Land use/cover, knowledge-based, GIS

ABSTRACT: The classification of urban land use/land cover requires sophisticated skill and techniques. Traditionally, it was with non-efficiency on not only upgrading the classification accuracy by simple spectral classification technology but also increasing its categories. For this reason, this study provides an urban land use/cover classification knowledge-based system by system language model which is done through AI (Artificial Intelligence) combines with the information from RS (Remote Sensing) and GIS (Geographic Information System).
This study also trends to increase urban land use/cover categories by adding with roads, water, DTM and spectral classified knowledge. The result proves to be more effective by comparing the accuracy from the consequence of knowledge-based system and the one of traditional supervised way. It can serve as a powerful tool to apply on environmental monitoring or changing detection in the future.

1. INTRODUCTION

In the past, while dealing with land use classification for urban area, quite often only gray level, texture, geometric characteristics, and the knowledge from optical spectrum bands were used to classify urban land use from satellite image. The benefit from such mean is limited in the ability of land cover classification, which can't fully describe true urban land use. With the assist the knowledge-based system, it is feasible to integrate spectral information from remote sensing and established data from GIS to set as the reference material for land use classification. Through integrated database and parameters, the related uncertainty levels data can be classified. The classification procedure must relatively fit in with true land use condition, and also have a great effect on urban land use classification. Furthermore, it will avoid the inconvenience of classification procedures towards further classification. In addition to application of the knowledge-based to develop into a better condition of Urban land use classification, the focus is how to build up the knowledge-based system with spectral information in remote sensing and the indirect data in GIS, and inference from knowledge in special domain range to make classification decision. On the other hand, it is possible to hope to promote the accuracy of image classification and trace to the condition of changes after urban land exploitation.

2. METHODOLGY

Generally, Urban land use category is complicated that needs various land use/cover classification to fit current land use/cover status. This paper applies supervised classification (maximum likelihood method) to classify conditions in land use/land cover and then join spectral characters and GIS data by knowledge-based system for increasing classification accuracy and categories. The detail steps and contents are described:

2.1 Study Area

The district of Pe-Ten in Taichung locates at the central region of Taiwan was selected as a relevant study area. The general landscape is residential and mountainous surrounding where settlements are concentrated. The area is about 62.77km^2 and population of 214,000.This region lies in a repid urbanization zone.

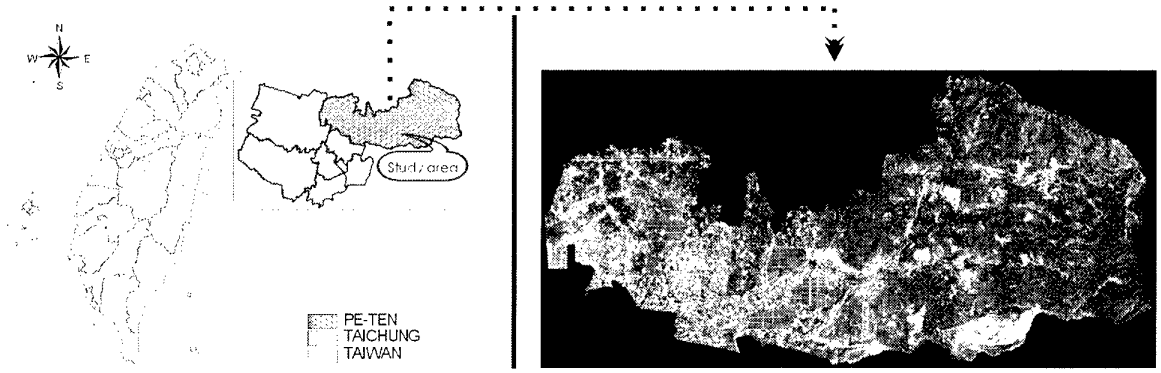


Figure1. Study Area Location

2.2 Data Sources

The main data sources are SPOT satellite images which are the main basis of spectral knowledge, while overlay with other GIS data and DTM sources to assist for knowledge-based classification. Table 1. shows the data attribute, building time and aerial photograph is only regard as an accuracy reference

Table1. Data Sources

■ Raster images ■ Vector data

Data	Resolution			Date	Data	Type	Date
	Spatial(m)	Spectral(μ m)	Radiometric				
SPOT XS	12.5m	0.50-0.59 0.61-0.68 0.79-.089	0-255	January 02,1996	Major Road	Line	About 1997
DTM	40m	-	0-255	October 01,1996	Rail Road	Line	About 1997
Aerial photograph	4m	R、G、B	0-65535	Novembe r,1998	Normal Road	Line	About 1997
SPOT PAN	10m	0.51-0.73	0-255	January 02,1996	River	Polygon	About 1997

2.3 Land Use Classification Hierarchies

According to the characteristic of urban land use/land cover in Taiwan, this research tends to classify land use categories including collecting regional factors and characteristic.

We classify five main categories, including:

1. Road: Asphalt Road, Macadam Road and etc.
2. Water: River, Ocean, Stream, Ditch, Pond, Pool and etc.
3. Barren Land: Sandy Beach, Salt Pan, Vacant Land and etc.
4. Vegetation: Forest, Grass and etc.
5. Building: Temple, Ancient Monuments, Residence and etc.

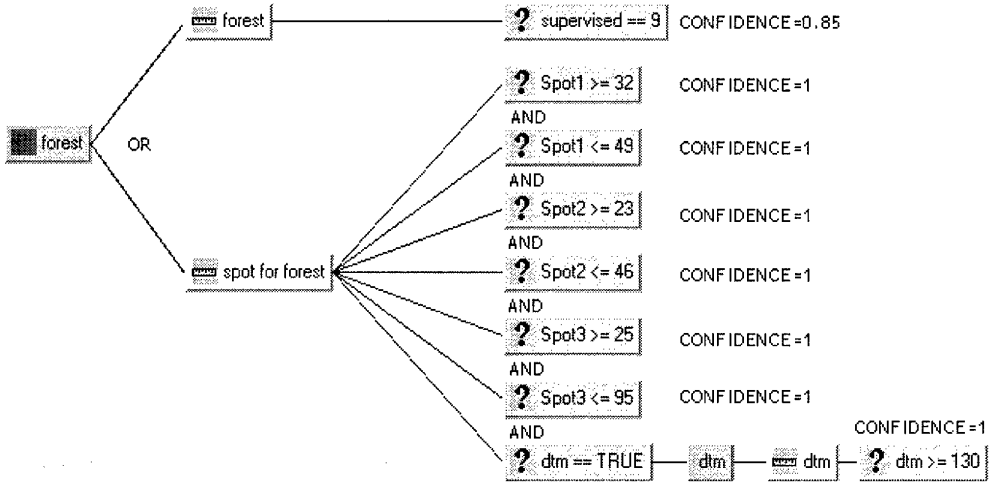
And then we subdivide five main categories into nine categories which to be hierarchies for data source of knowledge-based system so that building up knowledge-based rules.

Table 2. Hierarchies and Source

Rule	Land use Categories	Hierarchies	Data Source
1	Roads	Rail Road	Vector data
2		Major Road	Vector data
3		Normal Road	Vector data, SPOT XS(band1, band2, band3), Classification images, SPOT PAN
4	Water	River	Vector data, SPOT XS(band1, band2, band3), Classification images
5	Bare Ground	Bare Ground	SPOT XS(band1, band2, band3), Classification images, SPOT PAN
6	Vegetation	Grass	SPOT XS(band1, band2, band3), Classification images
7		Forest	SPOT XS(band1, band2, band3), Classification images, DTM
8		Agricultural Area	SPOT XS(band1, band2, band3), Classification images
9	Building	Residential Area	SPOT XS(band1, band2, band3), Classification images

2.4 Classification Experiment and Knowledge Representation

Knowledge-based system inference is a way to show the relationship among data with union or mixed forms from decision tree. Take forest catalog for example, there are three origin of it. They come from 1) supervised classified image 2) spectral knowledge and 3) DTM data. It has two major inference, one is "forest" ; the other is "spot for forest" which comes from union results. In the rule condition, it forms from a mixed case. For instance, in the spot for forest case, it has to match all rules in spot1- spot3. It will be classified into forest catalog if it conforms to its value which is greater than 130. On the other hand, every condition must have a confidence to control its accuracy. It shows a feasible way of rules by probability forms, and it also raises a flexibility of data error tolerance.



```
HYPOTHESIS {
        ID 9;
        TITLE "forest";
        SETBY 11, 12;
        COLOR 0.0905205,0.589479,0.440046;
        ENABLED 1;
}

RULE {
        ID 11;
        TITLE "forest";
        HYPOTHESIS 9;
        ENABLED 1;
        CONDITION {
                VARIABLE 14 == VALUE 9 CONFIDENCE 1;
                ENABLED 1;
        }
}

RULE {
        ID 13;
        TITLE "dtm";
        HYPOTHESIS 10;
        ENABLED 1;
        CONDITION {
                VARIABLE 16 >= VALUE 130 CONFIDENCE 1;
                ENABLED 1;
        }
}
```

```
RULE {
        ID 12;
        TITLE "spot for forest";
        HYPOTHESIS 9;
        ENABLED 1;
        CONDITION {
                VARIABLE 7 >= VALUE 32 CONFIDENCE 1;
                ENABLED 1;
        }
        CONDITION {
                VARIABLE 7 <= VALUE 49 CONFIDENCE 1;
                ENABLED 1;
        }
        CONDITION {
                VARIABLE 8 >= VALUE 23 CONFIDENCE 1;
                ENABLED 1;
        }
        CONDITION {
                VARIABLE 8 <= VALUE 46 CONFIDENCE 1;
                ENABLED 1;
        }
        CONDITION {
                VARIABLE 9 >= VALUE 25 CONFIDENCE 1;
                ENABLED 1;
        }
        CONDITION {
                VARIABLE 9 <= VALUE 95 CONFIDENCE 1;
                ENABLED 1;
        }
        CONDITION {
                HYPOTHESIS 10 == TRUE CONFIDENCE 1;
                ENABLED 1;
        }
}
```

Figure 2. Decision Diagram of Knowledge Representation

2.5 Flow diagram of Knowledge-based system

Integrating data resource with the logic of knowledge-based system, this research use a complete flow framework (Figure 3.) to show the relationships from all aspects (including theme map, GIS data, spectral knowledge, model and etc) and finally the results of knowledge-based classification feed back GIS database.

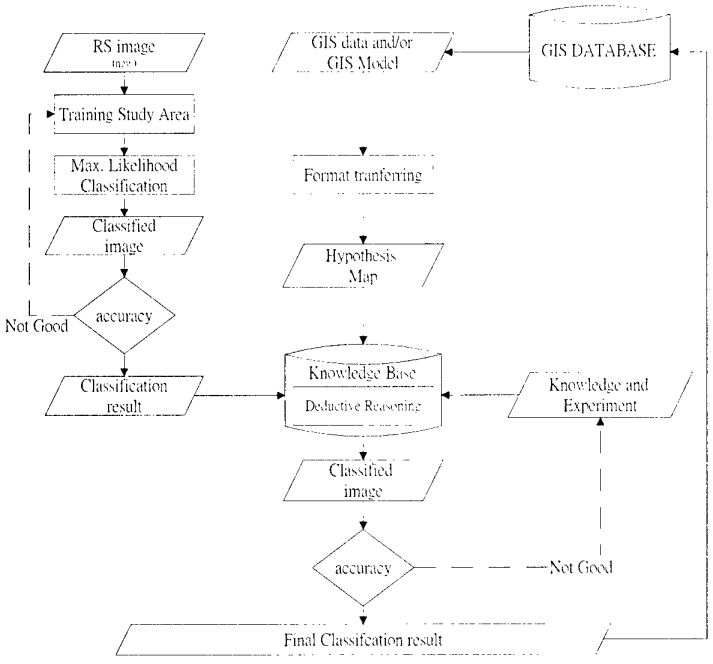


Figure 3. Knowledge-Based System with Supervised Classification Flow Diagram

3. RESULT AND DISSCUSSION

This study applies the above-mentioned knowledge-based system and adopts the maximum likelihood classifying themes and knowledge-based system classifying themes. Then, this study compared the accuracy from both ways. It concluded that the result of the maximum likelihood classification selected from sample area, the accuracy difference of each categories approach is about 21%, and the knowledge-based system classification can only reach 15%. It shows the knowledge-based system classification can low down the accuracy difference of each catalog. Furthermore, it concluded the accuracy of each category from the knowledge-based system classification is higher than one from the maximum likelihood classification. Especially for road catalog, its accuracy is the most obvious which approaches 26% with least bare ground only 2%. On the average, the accuracy of the knowledge-based system classification is 10% higher than the maximum likelihood classification. The outcome concluded find that it enhance a lot for classification by adding GIS data and spectral knowledge.

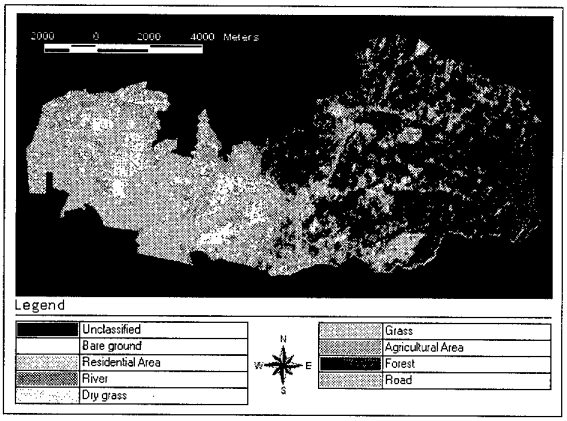


Figure4. Classification result with Maximum Likelihood Classification

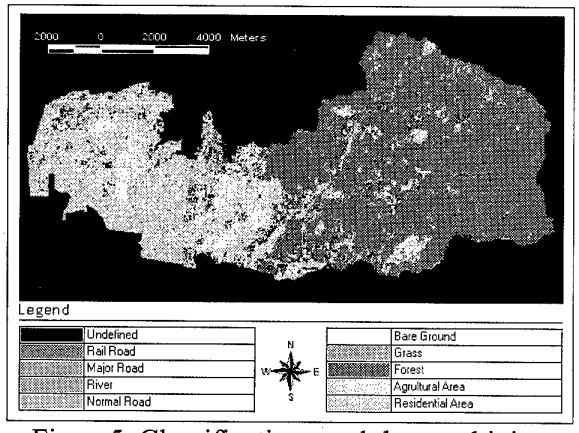
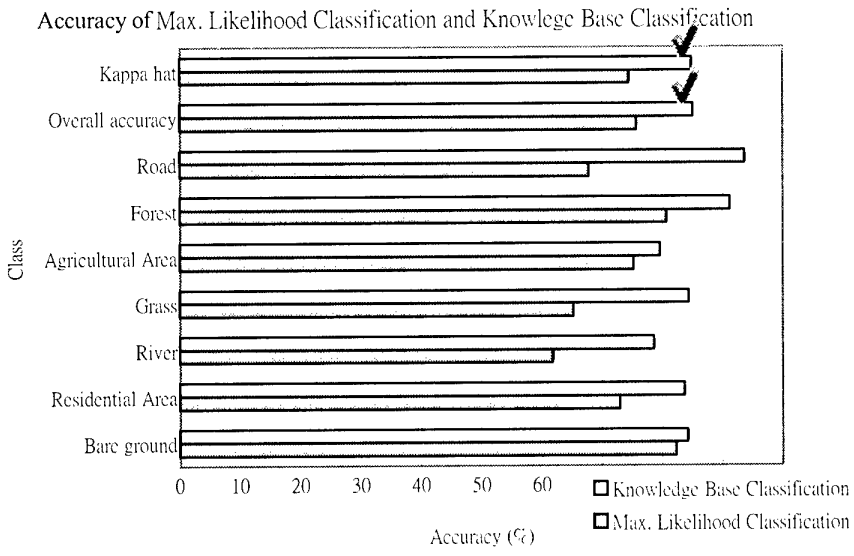


Figure5. Classification result by combining Maximum Likelihood Classification with Knowledge-Based

On the other hand, it increases the count of classifying category by GIS data. Therefore, this classification is the only effective and accurate way than traditional one. However, it still has barrier about producing null value easily by using the knowledge-based system classification. From Figure 5 it shows the null value of the knowledge-based system classification is higher than the one from maximum likelihood classification.



	Bare ground	Residential Area	River	Grass	Agricultural	Forest	Road	Overall accuracy	Kappa hat
Knowledge Base Classification	84.2	83.686	78.63	84.341	79.63	91.213	93.662	85.0517	84.825
Max. Likelihood Classification	82.254	72.962	61.82	65.235	75.268	80.691	67.825	75.7185	74.5

Figure6. The Histogram of Comparison between Maximum Likelihood and Knowledge-Based Classification Outcome

4. CONCUSION

This research superimposes supervised classification into knowledge-based system while spectral characteristics and GIS data can increase classification accuracy and categories. But we discover additionally that easily erroneous categories would cause the appearance of null values after adding spectral characters. The result can't diagnose classification categories. Two reasons probably: 1) the conditions of spectral characteristics is better too strict to easily diagnose some classification categories. 2) the supervised classification categories don't fit in with spectral characters ,and cause indetermination. The ways of solution are adding other spectral knowledge or data, for example: Landsat TM, IKONOS or aerial photography to enlarge indetermination of pixel value. In the future, it will be noticeable for classification processing. But in the view of whole aspects of urban land use/cover, the knowledge-based system not only raises classification accuracy but also increase classification categories. It is a better way to apply on environmental monitoring of urban land exploitation or environmental changing in the future.

REFFERENCES

1.Deren LI, Kaichang DI, Deyi LI., 2000.Land Use Classification of Remote Sensing Image with GIS Data Based on Spatial Data Mining Techniques. In: International Archives of Remote Sensing. Amsterdam, Vol. XXXIII, Part B3, pp.238-245.

2.A.A. ABKAR, M. A. SHARIFI., 2000.Likelihood-Based Image Segmentation and Classification: Concepts and Applications. In: International Archives of Remote Sensing. Amsterdam, Vol. XXXIII, Part B3, pp.9-16.

3.ERDAS inc., 1999. ERDAS User's Guide, pp.9-24.

APPLICATION OF REMOTE SENSING IMAGE DATA IN THE ANALYSIS OF LAND USE MANAGEMET FOR AGRICULTURE IN CHIANAN IRRIGATION PROJECT IN TAIWAN

You Jenn Ming, Kiyoshi Torii, Yoshiaki Mori, Ryohei Kada
Graduate School of Agriculture
Kyoto University
Oiwkecho, Kitashirakawa, Sakyoku, Kyoto
Te. & Fax.: (81)-75-753-6459
E-mail: Torii@kais.kyoto-u.ac.jp
JAPAN

KEY WORDS: land use , Chianan Irrigation Project , system dynamics

ABSTRACT: Wuzanto dam completed in 1930 is acting as a water source for irrigation of the area of about 150,000 ha covering T' ai-nan, and Chia-i in South Taiwan and playing a role of food supply base in Taiwan for 70 years.

We attempted an analysis of agricultural economic evaluations of land-use changes in the recent 20 years using satellite image data as well as field survey. Based on this analysis, we performed statistical analysis of agricultural production aiming at finding more effective use of this irrigation project.

1. INTRODUCTION

Farmland use has a close relationship to food production and appears to have a profound effect on the agricultural development. Therefore, understanding the change in farmland use has long been a major focus of research in Agronomy.

In previous papers, many researches have utilized map method, photo method, or econometric method for the investigation of land use. However after the rapid economic growth, the problem of land use has become more complex. In order to take account of all factors that affect land use completely, it is necessary to adopt a different approach for the analysis of land use.

In this paper we first investigate a change in cultivated land use by using remote sensing image data, and secondly, attempt to establish a model that indicates the possible change of farmland using system dynamics. The model in this study is expected to produce a result close to the reality, thus would be able to provide future reference for land management for the agricultural authority.

The paper is organized as follows: the first part is a brief description of the Chianan irrigation project and discussion of its effect on agricultural production around that area. Secondly, we analyze the change of farmland use in Chianan irrigated zone using remote sensing image data. Then we use a system dynamic model to discuss the possible changes of farmland use in Chianan zone. The last part summarizes the analysis and point out its policy implications.

2. THE CHIANAN IRRITAGION PROJECT AND ITS EFFECT ON AGLICULTURE

The Chianan irrigation project is located in the south-western part of Taiwan and was built in 1930. Its irrigated area included 50000 ha of cultivated land north of Pei-Kang river and

100000 ha of cultivated land south of Pei-Kang river (See figure1).

The Chianan irrigation project consists of 2 smaller irrigation systems: Wushanto reservoir irrigation system and Cho main canal irrigation system. The former set up a pumping station in Linnai to get water from Zhoushui river. The latter set up a dam and a tunnel in Nansei to get water from Tsengwen river. In addition, there are 100km of main line, 1200km of branch line, 7400km of little line, 960km of escape canal and 6000km of little escape canal built in the Chianan irrigation project. It was the biggest irrigation project in Taiwan during the colonial period.

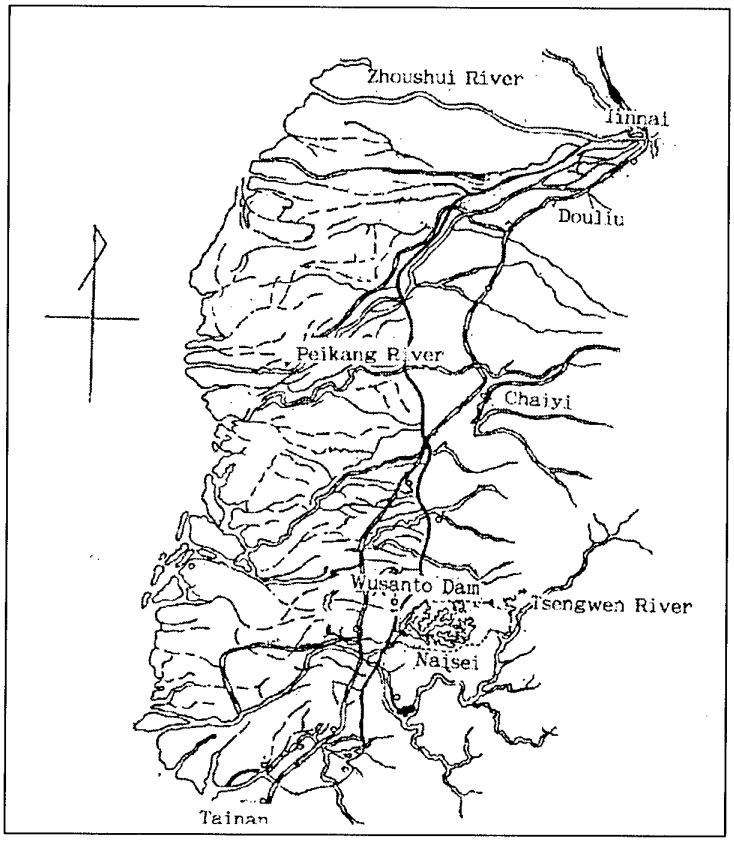


Figure 1: Chainan Irrigation Project

After the Chianan irrigation project was accomplished, there are three obvious effects on the agricultural production:

(1). Larger irrigated area: Before the building of the Chianan irrigation project, there were only 27,821 jia of irrigated area in Tainan. But after the construction, the irrigated area enlarged to 188,867 jia, which was the largest irrigated zone in Taiwan at that time.

(2). Changed upland fields into paddy fields: According to Taiwan agricultural yearbook, from 1932 to 1937, there was just little change of cultivated land in Tainan zone, but the size of paddy fields area increased twice in the same period. The reason of farmland improvement was establishment of the Chianan irrigation project.

(3). 3-year-rotation system: Since the irrigated area of Chianan irrigation project was too large to irrigate all the cultivated lands once each year, a 3-years-rotation system was adopted. This system set every 150 ha of cultivated land as one unit, then divided it into three different crop divisions. The three divisions were rice area, sugarcane area and miscellaneous crops area, and farmers took turns planting these crops in their field each year.

Owing to the above effects, quantity of crops raised and agricultural revenue increased (see table 1). Peasants who live in Chianan zone have a better living than before.

By the way, the 3-year-rotation system had been changed from 3-year-once-rice-cultivated to 3-year-twice-rice-cultivated after War II because of agricultural technological progresses such as farmland improvement, seed improvement and the construction of new irrigated facility. Furthermore, on one hand, after the rotation area has decreased and double-cropped field area has increased, the output of rice increased dramatically. On the other hand, as the national income increased, people have reduced the consumption of rice and increased the consumption of meat, vegetables and fruits. This resulted in excessive supply of rice, therefore transformation

of rice field to farmland was promoted by Taiwan's government since 1970s. Thereby, paddy field began to decrease and dry farmland increased.

In Tainan prefecture, for instance, paddy field area was 40,133 ha in 1950 and increased to 54,473 ha in 1975, and then decreased to 33257 ha in 1998. In the same time, upland field area was 31,427ha in 1950 and increased to 43,723 in 1998. Figure 2 shows the plant areas of rice, sweet potato and sugarcane were decreasing from the beginning of the 1970s, and plant areas of vegetables, fruits and corn were increasing from the 1960s.

Table 1: The production of main crops in Tainan

Item		Production		Yield per ha	
		Before	After	Before	After
Rice	Planted area (jia)	13,160	50,000	-	-
	Quantity (dan)	107,162	656,500	8.14	13.13
	Value (yen)	1,543,132,800	9,453,600,000	117,260	189,070
Sugar Cane	Planted area (jia)	31,486	50,000	-	-
	Quantity (jin)	1,379,898,838	3,882,650,000	43,826	77,653
	Value (yen)	6,374,534,650	17,860,190,000	201,600	357,200

Notes: 1jia=0.97ha; 1jin=0.6kg

Source : State government of Tainan, The general outlook of Tainan irrigation works.

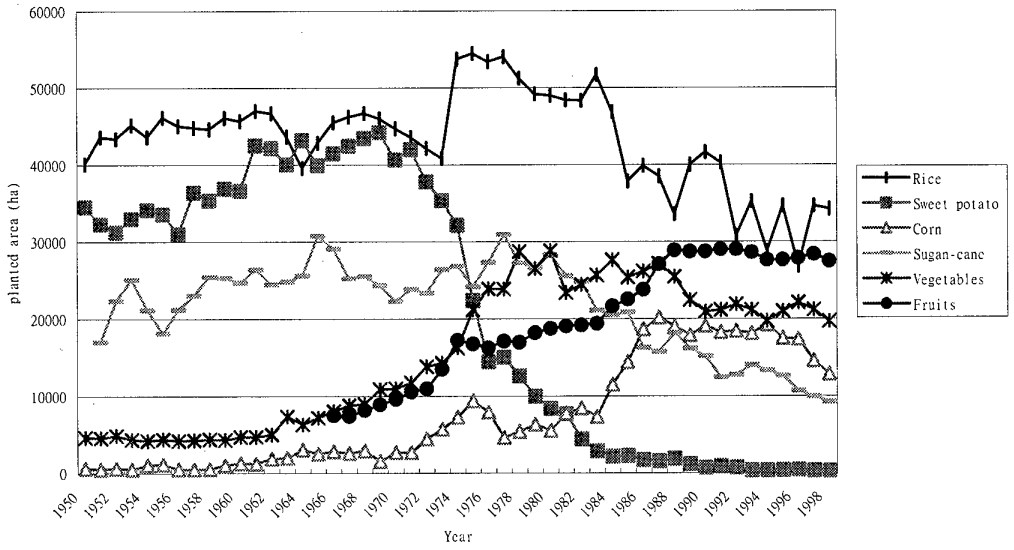


Figure : Changes of plant areas of Tainan prefecture

Due to economic growth, urbanization in Chianan zone has advanced in the last decade. Cultivated land has been transferred to commercial area or residential area etc. Figure 3 demonstrates that construction land and lands for transportation & irrigation facilities are increasing, but cultivated land is decreasing after 1980.

3. APPLICATION OF SATELLITE IMAGE DATA

As the satellite images of south Taiwan, Landsat TM, SPOT HRV and JERS-1 SAR are applicable at the Japanese receiving station and these were supplied by National Space Development Agency of Japan. The results of analysis will be given at the time of presentation.

Table 2: A list of satellite images used in the present study

Mission	Sensor	Path-Row	Obs. Date	Mission	Sensor	Path-Row	Obs. Date
Landsat	TM	118-44	21Jul90	JRERS-1	SAR	94-261	31May98
SPOT	HRV	298-304	14Oct92	〃	〃	93-262	〃
〃	〃	298-304	3Mar93	〃	〃	95-261	11Oct98
〃	〃	298-304	8Mar93	〃	〃	94-261	9Aug96
〃	〃	298-303	19Jan99	〃	〃	93-262	5Nov96
〃	〃	298-303	22Nov99	〃	〃	95-261	28Aug98
〃	PAN	298-304	9Feb99	〃	〃	94-261	2Dec94
〃	〃	298-304	26Oct99	〃	〃	93-262	27Aug.98

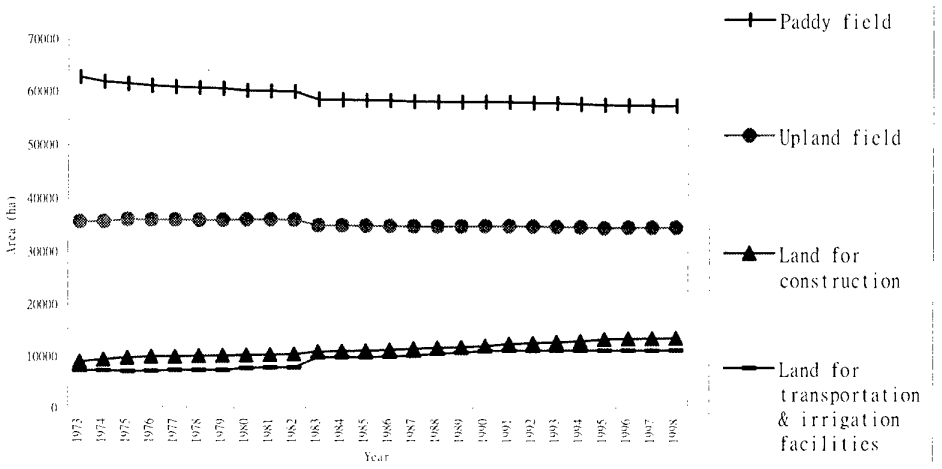


Figure 3: Changes in land use of Tainan prefecture

4. APPLICATION OF SYSTEM DYNAMICS MODELS TO THE CHANGES IN FARM LAND USE

Land use is in relevant to geographical environment and economic activities, thus different geographical environments and different regional economic activities would yield different kinds of land use.

In previous research of land use in agricultural economics, the analytical approach used most are time series model and regressive model. However, in order to understand the complex problem of land use, system dynamic approach and econometrics have been adopted increasingly. System dynamic approach is especially well disposed in nonlinear relation or while lacking part of the data, it also is suitable for analysis of long-term trend.

The system dynamic model developed in this paper is built with the graphical programming language STELLA. In the first step we stipulated the scope of research., then we consider the changes of objects (stock) depend on some factors (flow). Since these factors are influenced by others variables (converters) therefore we connect these stocks, flows and converters with a relation of feedback or infrastructures. Finally, we install coefficient for every variables according to data from the real world and then run the model.

The result from the model is compared to real life data, if they were dissimilar then there were variables that had wrong effects on the model or the coefficients installation was incorrect. Then, we revised the model and ran it again.

From the statements of former sections, it is understood that farmland transformation is the cause of urbanization and economic growth of Chianan zone. Furthermore, we assume that (1) the degree of urbanization depends on population change, and (2) economic growth is influenced by local condition (population change) and external condition (national income). The STELLA model we built for the interrelationship is shown in the following diagram.

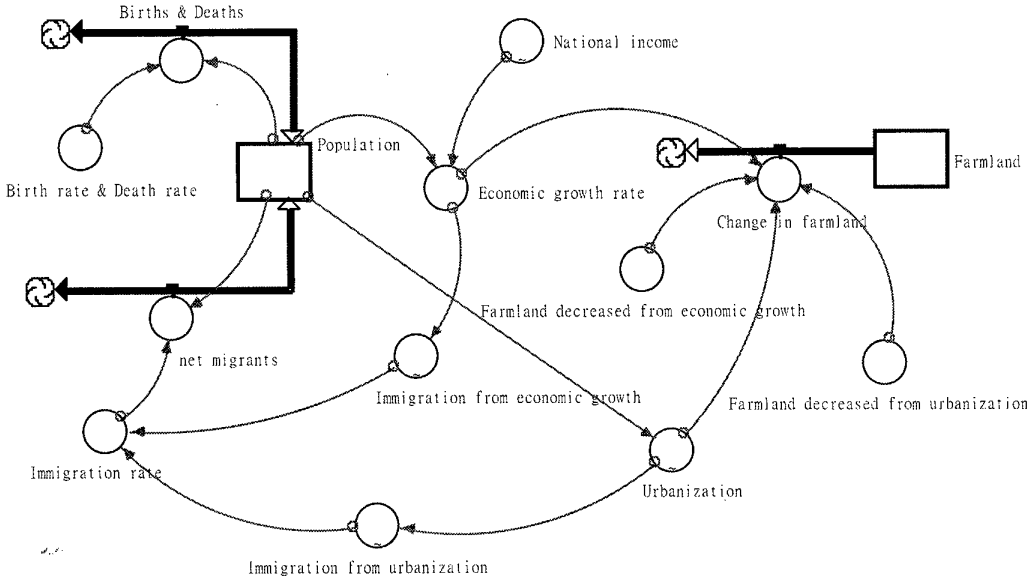


Figure 4: change in farmland

the results of our system dynamics model are shown in the Table 3 and in Figs5.. Using this model we forecast the farmland of Tainan prefecture would decrease to 90,220 ha in 2010.

Table 3: Compare forecast values with the results of remote sensing image data

Year	Forecast values	Year	Forecast Values
1991	96,898	2001	93,397
1992	96,547	2002	93,043
1993	96,196	2003	92,691
1994	95,847	2004	92,339
1995	95,501	2005	91,987
1996	95,155	2006	91,634
1997	94,806	2007	91,280
1998	94,455	2008	90,926
1999	94,103	2009	90,573
2000	93,750	2010	90,220

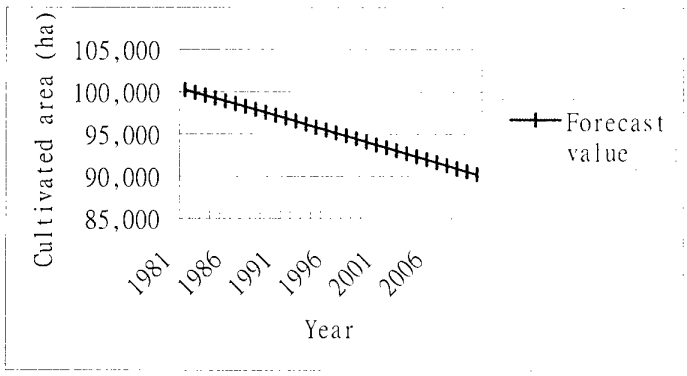


Figure 5: Forecast in farmland

5. CONCLUSION

The Chianan irrigation project has played a major role in agricultural development in Chianan zone in the past. Not only did it help raising crops production in the Chianan area but also improved the farmers' economics. However, after the high economic growth, agricultural industry began to go downhill, and the effect of Chianan irrigation project became smaller than before. Recently other than water for agriculture, it has been utilized to provide municipal water and industrial water. The Chianan irrigation project would continues to act as an important role in the economic development in Chianan zone in the future.

Fortunately, Lansat TM image data, SPOT HRV image, JERS-1 SAR image were available. Although it is far from saying that we have analyzed the imagesbfully at the present stage, we could grasp the whole framework of Chianan Irrigation Project area. We are thinking to advance analysis by dividing the area into small blocks, taking time-series data based on the images and comparing them with statistical data in future.

In order to understand the complicated relationship of modern society, interdisciplinary academic research has been receiving increased attention. This paper attempts to combine remote sensing image data and system dynamics model to the analysis of farmland use. In the future study we will focus on this approach to difference types of land user.

ACKNOWLEDGEMENT

In ending the paper, we would like to express our deep gratitude to NASDA, RESTEC in Japan and EROS Data Center in USA for satellite image data supply. This study was supported by Scientific Research Fund for Basic Researches (A)(1) of Ministry of Education Japan (Project No. 11306015, represented by Kiyoshi Torii).

REFERENCES

1.Bruce, Hannon and Matthias, Ruth. *Dynamic modeling*. New York: Springer-Verlag, 1994.

2.Bruce, Hannon and Matthias, Ruth. *Modeling dynamic economic systems*. New York: Springer-Verlag, 1997.

3. Department of agriculture and forestry Taiwan provincial government, *Taiwan agricultural yearbook*. 1950-98; State government of Tainan. *The general outlook of Tainan irrigation works*, 1933.

Covariance Propagation in GPS/IMU - Directly Georeferenced Frame Imagery

Mohamed M.R. Mostafa, Joseph Hutton, and Erik Lithopoulos

APPLANIX Corporation
85 Leek Cr., Richmond Hill, Ontario
Canada L4B 3B3
Phone: (905) 709-4600
Fax: (905)709-7153
Web: www.applanix.com
E-mail: MMostafa@applanix.com

ABSTRACT

In this paper, an error analysis for the airborne direct georeferencing technique is presented, where integrated GPS/IMU positioning and navigation systems are used in conjunction with aerial frame images for airborne photogrammetric mapping. Covariance propagation technique provides a valuable analytical tool to evaluate different parameters necessary for mapping project design and, thus, it is used to study the expected errors of ground point coordinates when derived from GPS/IMU/image data. The technical specifications of three of Applanix POS/AV airborne positioning and attitude determination systems are used in this study. Two cases are studied in this paper, namely the standard stereo model case and the single photo/DEM case. The stereo case has been already used in standard map production where the aerotriangulation step is bypassed when using direct exterior orientation information measured by the POS/AV systems during image data acquisition. The single photo case is not as widely used, yet provides more economical alternative to the stereo approach, where single photos are processed together with the available DEMs to produce orthorectified quads/images. Different sources of errors are investigated in the present study. Mainly, the effect of the exterior orientation data errors on ground point positioning errors, has been studied for different POS/AV systems and for different GPS accuracy scenarios. The error models are presented and a summary of the results is introduced. In addition to the theoretical analysis, an error analysis is performed to an airborne data set collected in northern California, where the POS/AV system was used to directly georeference aerial frame imagery. The results show that the use of POS/AV enables a variety of mapping products to be generated from airborne navigation and imagery data without the use of ground control.

RADARSAT-2 MISSION: OVERVIEW AND DEVELOPMENT STATUS

Peter MEISL, Senior Systems Engineer, Alan A. THOMPSON, Senior Systems Engineer,
Anthony P. LUSCOMBE, Senior Systems Engineer
MacDonald, Dettwiler and Associates Ltd.
13800 Commerce Parkway, Richmond, B.C. Canada V6V 2J3
Tel: (604) 278-3411, Fax: (604) 276-2856, E-mail: pm@mda.ca

KEY WORDS: RADARSAT-2, RADARSAT, SAR, Polarimetry, GMTI

ABSTRACT

RADARSAT-2, Canada's next generation earth observation satellite, is co-funded by the Canadian Space Agency (CSA) and MacDonald Dettwiler, and is the first step towards full commercialization of the RADARSAT program. The imaging sensor on the satellite is a C-band Synthetic Aperture Radar (SAR) capable of operating in a wide variety of imaging modes. All imaging modes of the current RADARSAT-1 satellite will be provided, as well as some new modes that incorporate important innovations and improvements. The horizontal co-polarization (HH) of RADARSAT-1 will be supplemented by options for vertical co-polarization (VV) and cross-polarization (HV or VH), and there will be new Quad-Polarization modes providing fully polarimetric data sets. The other major new mode is referred to as Ultra-Fine, providing swath imaging with resolution of about 3m in each dimension. Re-visit times will be reduced since all imaging modes will be available either to the left or right sides of the satellite track. This paper gives an outline of the RADARSAT-2 mission capabilities and gives an update on the development status.

1 RADARSAT-2 MISSION OVERVIEW

RADARSAT-2 is a Canadian spacecraft carrying a C-band SAR (5.4 GHz). It will provide users with advanced, commercially-available space-borne Synthetic Aperture Radar (SAR) imagery having fully polarimetric modes and resolution as fine as 3 metres. This increased capability will provide a high level of detail for research, analysis, and commercial operations in a wide variety of applications: agriculture, forestry, mapping, surveillance, environmental monitoring, natural resource exploration and management, and many dynamic ocean and sea-ice processes.

The launch is scheduled for April, 2003 and the mission duration will be 7 years.

MacDonald, Dettwiler, and Associates Ltd. (MDA) of Richmond, British Columbia, is developing the RADARSAT-2 mission in partnership with the Canadian Space Agency. MDA's design for the RADARSAT-2 mission is based on the following principles:

- Build on the RADARSAT-1 experience and infrastructure;
- Maintain continuity of data and operations from RADARSAT-1;
- Inject advanced technology into the program where this technology provides significant benefit at low risk;
- Selectively enhance components of the mission to better meet user, government, and industry needs; and
- Select capability and operational enhancements that help transition the user community to future more sophisticated missions.

In general RADARSAT-2 will operate in a similar manner as RADARSAT-1 in the areas of Mission Control, Mission Planning, and Data Collection and Processing.

2 RADARSAT-2 INNOVATIONS & IMPROVEMENTS

RADARSAT-2 offers a number of significant improvements over RADARSAT-1:

- **3-metre Ultra-Fine resolution**. This is the highest-resolution satellite SAR commercially available.
- **Left- and right-looking capability**. A significant improvement of RADARSAT-2 over its predecessor and other synthetic aperture radar satellites is its ability to image on either the left or right, nominally requiring 10 minutes to switch between either side. This capability will reduce the re-visit time for imaging opportunities of any region.
- **Fully-polarimetric imaging modes.** These modes allow the use of polarization signatures to characterize targets and support more sophisticated models of scattering from the earth's surface.
- **Solid-state Recorders for image data** capture and storage at data rates up to 400 Mbps. This offers higher capacity, flexibility and reliability than tape.
- **GPS**. This provides improved geo-location information with the data.
- **More responsive ordering**. A more flexible and faster-responding ordering and planning system.

3 RADARSAT-2 IMAGING CAPABILITIES

The RADARSAT-2 imaging modes are depicted in Figure 1 and listed in Table 1.

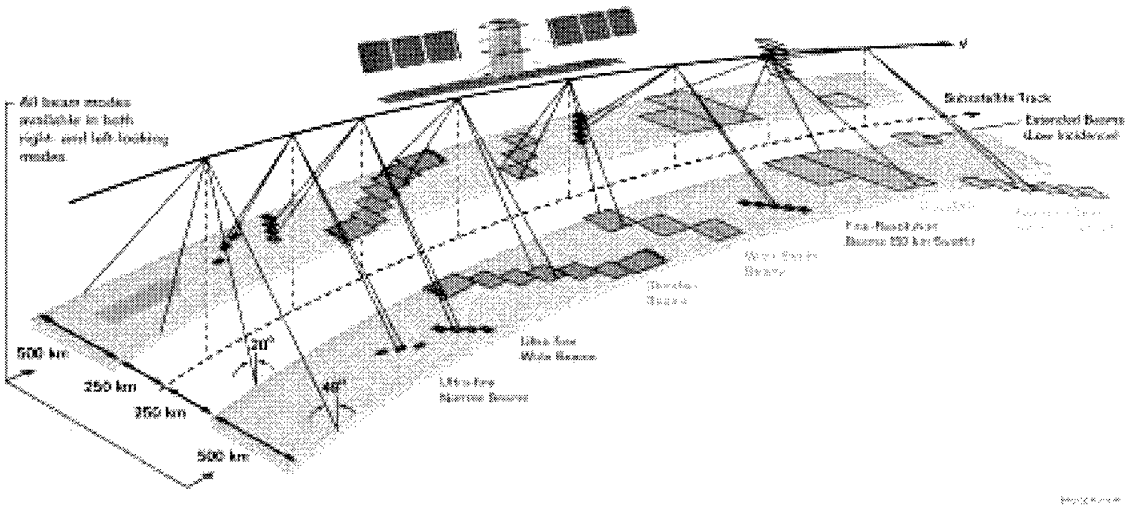


Figure 1, RADARSAT-2 Imaging Modes

The ability to continue to service the existing RADARSAT-1 customers, many of whom have a considerable infrastructure in place, is of utmost importance to the RADARSAT-2 mission. In addition to the new beam modes and features which will be offered by RADARSAT-2, all existing beam modes and product types of RADARSAT-1 will continue to be offered. Table 1 summarizes the beam modes which will be available on RADARSAT-2.

New modes which have been added include multiple polarization imaging capabilities, and Ultra-Fine 3-metre resolution modes. All RADARSAT-1 beam modes will continue to be fully

supported, and for these modes, all RADARSAT-1 image quality specifications will be met or exceeded.

Table 1, RADARSAT-2 Beam Modes.

	BEAM MODE	Nominal Swath Width	Swath coverage to left or right of ground track	Approximate Resolution: Rng x Az
RADARSAT-1 modes with Single and Dual Polarization Transmit H **or** V Receive H **or** V **or** (H **and** V)	Standard	100 km	250km-750km	25m x 28m
	Wide	150 km	250km–650km	25m x 28m
	Low Incidence	170 km	125km–300km	40m x 28m
	High Incidence	70 km	750km–1000km	20m x 28m
	Fine	50 km	525km–750km	10m x 9m
	ScanSAR Wide	500 km	250km–750km	100m x 100m
	ScanSAR Narrow	300 km	300km–720km	50m x 50m
Fully-Polarimetric modes Transmit H **and** V on alternate pulses Receive H **and** V on every pulse	Standard QP	25 km	250km–600km	25m x 28m
	Fine QP	25 km	400km–600km	11m x 9m
Selective Single Polarization Transmit H **or** V Receive H **or** V	Triple Fine	50 km	400km–750km	11m x 9m
	Ultra-Fine Wide	20 km	400km–550km	3m x 3m
	Ultra-Fine Narrow	10 km	400km–550km	3m x 3m

4 SPACECRAFT CHARACTERISTICS

4.1 SAR Sensor

The RADARSAT-2 SAR antenna will consist of a distributed network of transmit/receive modules arranged on two wings. Some of the SAR characteristics are:

- Linear FM pulse generation with bandwidths from 12MHz to 100MHz;
- Active phased array antenna,16 rows of 32 T/R modules, each feeding a subarray of 20 elements;
- T/R modules with two power settings and temperature compensation of phase and amplitude;
- Each T/R module can transmit either on H or V polarization, and can receive on both polarizations;
- Weighting: phase only on transmit; amplitude and phase on receive;
- Any subset of columns can be switched off on transmit or receive;
- Two independent receive channels used either for H and V polarizations or for separate reception on the leading and trailing antenna wings.

4.2 Data Handling

All image data is stored in high data rate (400Mbps) solid-state recorders (SSR). These have higher reliability than tape systems used in the past and will permit random image file access. The SSRs have a capacity of 2 x 128 Gbit at the beginning of the mission, decreasing to 2 x 100 Gbit at the end. They can accept data at rates up to 400 Mbps. Block Adaptive Quantization (BAQ) is used to encode signal data with a selectable wordlength (normally 4 bits I + 4 bits Q). The downlink occurs on two 105 Mbps X-band links. The high-power X-Band transmitter will be able to downlink images to ground stations having a minimum 3-metre receiving antenna.

This smaller antenna size will allow a lower "cost of entry" for new ground stations.
Encryption is available for command & control as well as for the downlink of signal data.

4.3 Position Determination

RADARSAT-2 includes on-board GPS receivers for position determination.
The absolute position will be determined to within 60m x, y, z 3σ in real time on board the spacecraft, to be downlinked with image data. This accuracy will be achieved with the onboard GPS receiver and onboard orbit models.
The RADARSAT-2 absolute position will be determined to within 15m x, y, z 3σ within 24 hours of the latest available GPS orbit data. The GPS receiver onboard will collect position measurements that will be processed on the ground to improve the accuracy.
RADARSAT-2 is yaw-steered (unlike RADARSAT-1). The yaw steering, combined with the improved attitude control of RADARSAT-2, will simplify image processing and improve image quality.

5 SPECIAL MODES

5.1 UltraFine Imaging Mode

Ultra-Fine mode is designed to provide approximately 3m x 3m resolution images covering swaths of 20km at incidence angles from 30° to 40°.
A pulse bandwidth of 100MHz is used to achieve the required resolution in range. In azimuth a "Dual-Receive" imaging technique is used to achieve the 3 m resolution.
In the Dual-Receive mode of operation, two echoes, one from each wing, are recorded for every pulse transmitted. Because the phase centres of the two receive antennas are in different positions, the two-way path length for the two simultaneous returns are different and so the two returns effectively provide separate samples along the synthetic aperture. With an appropriate choice of PRF, known as the "ideal PRF", the resulting samples will be equally spaced, and standard SAR processing techniques can be employed.
To provide the Doppler bandwidth required to achieve 3m-resolution, an azimuth beamwidth of approximately 0.5° is needed. This is achieved by using a reduced aperture or defocused beam on transmit
In order to improve sensitivity, the T/R modules can be operated at higher transmit power than in the other modes. In addition, the pulse length may be increased.
Figure 2 illustrates the Dual-Receive mode of operation. The solid line indicates one pulse transmission with two echoes; the dashed line indicates the pulse and echoes from the next pulse repetition interval.
The Dual-Receive mode is the baseline for Ultra-Fine imaging. However, conventional imaging with a broadened beam ('beam spoiling') was considered as an alternative for Ultra-Fine mode. Dual-Receive mode has the following advantages over beam spoiling:

- better sensitivity for the same power; and
- increased access at high angles because of low PRF.

Disadvantages of the Dual-Receive mode are:

- some constraints on PRFs; and
- it is unconventional.

The beam-spoiling approach is still available as a backup capability.

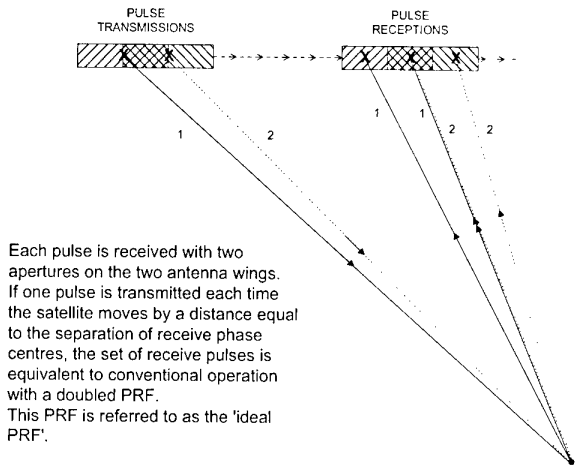


Figure 2, Dual Receive Mode Operation

5.2 GMTI Capability

RADARSAT-2 includes an experimental GMTI capability known as the Moving Object Detection Experiment (MODEX). Like Ultra-Fine mode, MODEX makes use of the Dual-Receive capability of the RADARSAT-2 antenna. This Dual-Receive capability provides two apertures aligned in the along-track direction, which is suitable for detecting moving objects. By processing the received echo data using along-track interferometric techniques and DPCA techniques, objects with non-zero radial velocities can be detected and their radial velocities can be estimated.

6 GROUND SEGMENT

To ensure the commercial success of the RADARSAT-2 mission, MacDonald Dettwiler is designing the Ground Segment in consultation with the key organizations and agencies that will be critical to the success of the mission.

Where possible, the existing RADARSAT-1 Ground Segment infrastructure will be re-used. For example the existing TT&C and Data reception facilities will be re-used. For many of the other Ground Segment functions new or upgraded components will be required.
The RADARSAT-2 Ground Segment will provide the following main enhancements to improve the operability and responsiveness to customer needs:

- **Reduced mission planning time** required for imaging requests. The RADARSAT-2 Ground Segment will be upgraded so that the time between approval of an order and time that the related commands are ready for uplink to the spacecraft is less than 48 hours for routine requests and 6 hours for emergency requests;
- **Real-time feasibility checking**. When customers' requests for imaging are placed at one of the order desks, the Acquisition and Reception Planning Subsystem will be able to detect conflicts immediately and provide feedback to the customers to assist them in finding feasible imaging times.
- **Support for the commercial operations** of RADARSAT-2. The ordering and acquisition planning system is being designed to support these operations. The experience gained with RADARSAT-1 operation is being used as a guide.
- **Automated data reception and archiving chain**. This will allow reductions in time required from image reception to distribution to the customer. After reception of the image

data, the Ground Segment will be able to produce and distribute products of any type to the customer within three hours.

- **Improved operability and maintainability** through the use of MacDonald Dettwiler's standard multi-mission Earth Observation System components, wherever feasible. These same components can be used to build or upgrade network stations for almost every civilian Earth Observation mission.

An overview of the RADARSAT-2 Ground Segment Architecture is shown in Figure 3.

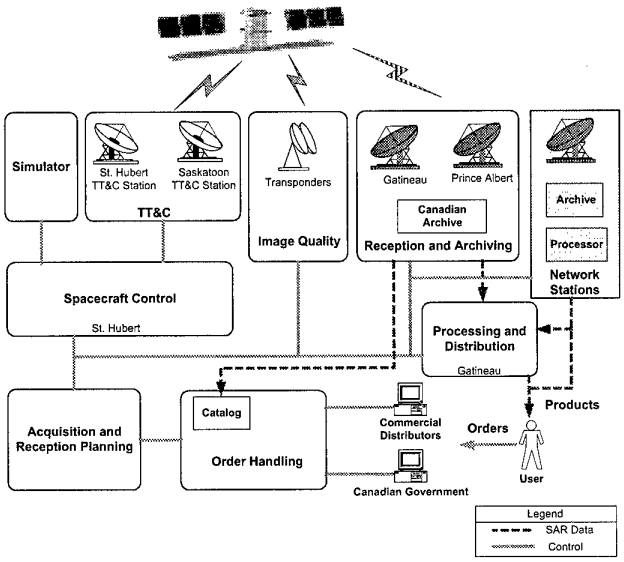


Figure 3, Ground Segment Architecture

7 DEVELOPMENT

The companies involved in building the main components of the RADARSAT-2 System are listed below.

- Alenia Aerospazio, Italy is building the spacecraft bus.
- The SAR payload is being constructed by EMS, Montreal (formerly Spar Aerospace).
- The Extendible Support Structure (ESS) is being developed by MD Robotics of Brampton, Ontario.
- In addition to being the mission prime contractor, MDA is also the subcontractor for the Ground Segment.

For updated information please refer to the RADARSAT-2 web site at radarsat.mda.ca

8 REFERENCES

[1] Apel John R., McCandless Jr. S. Walter, Reeves L. A., and Valenti E. L., July, 1999. "Application Vistas for RADARSAT-2: Oceans and Ice," IEEE 1999 International Geoscience and Remote Sensing Symposium (IGARSS), Hamburg, Germany.

[2] Luscombe, A., Oct. 1999. "Plans for Radiometric and Polarimetric Calibration of RADARSAT-2 Beams", CEOS SAR Workshop.

[3] Luscombe A., Chotoo K., and Huxtable B., July 2000. "Polarimetric Calibration for RADARSAT-2," Proceedings of IGARSS 2000.

[4] Thompson A. and Livingstone C., July 2000. "Moving Target Performance for RADARSAT-2," Proceedings of IGARSS 2000.

PERFORMANCE EVALUATION OF RTK GPS WITHOUT SA EFFECT

Jenn-Taur LEE Wen-Feng CHEN
Department of Surveying and Mapping Engineering
Chung Cheng Institute of Technology
National Defense University
Tahsi, Taoyuan
Taiwan 33509
Tel: 886-3-380-0364
Fax: 886-3-390-7810
Email: jtlee@mail.ccit.edu.tw

KEY WORDS : Global Positioning System, Selective Availability, Real Time Kinematic GPS

ABSTRACT : The policy of Selective Availability (SA) was endorsed in order to artificially widen the gap between the civilian and military positioning services. SA is an intentional degradation of the accuracy of global positioning system (GPS) horizontal positioning to 100m and height determination to 150-170m at the 95% confidence level, for standard positioning service (SPS) users. SA has been implemented since March 25, 1990, and consists of two different components.

Firstly, the so-called epsilon (ε) component consists of the truncation of the orbital information transmitted within the navigation message so that the WGS84 coordinates of the satellites cannot be computed correctly. Secondly, the so-called delta (δ) component which is achieved by dithering the satellite clock output frequency. The varying error in the satellite clock's fundamental frequency has the direct impact on both the pseudo-ranges and carrier phase observations. The variations in range have amplitudes of as much as 50m, with periods of several minutes. Fortunately, SA was discontinued on May 2, 2000 that should make GPS more responsive to civil and commercial users.

The objective of this study is to investigate the performance of real time kinematic (RTK) GPS without SA effect, since RTK GPS is widely taken in engineering and geographical information system (GIS) uses. The experiment was accomplished in an existed network that consists of 31 control points, which was surveyed with RTK GPS in addition static GPS, differential GPS, and single point positioning before and after SA effect turned off. EDM and leveling surveying was also done at the same network. Furthermore, the statistical analyses of horizontal and vertical vectors, baseline length, and height difference were completed and will be presented in the article.

1. INTRODUCTION

GPS is a dual-use system, providing highly accurate positioning and timing data for both military and civilian users. There are more than 4 million GPS users world wide, and the market for GPS applications is expected to double in the next three years, from 8 billion to over 16 billion. Some of these applications include: air, road, rail, and marine navigation, precision agriculture and mining, oil exploration, environmental research and management, telecommunication, electronic data transfer, construction, recreation and emergency response. GPS has always been the dominant standard satellite navigation system thanks to the U.S. policy of making both the signal and the receiver design specification available to the public

completely free of charge. The U.S. previously employed a technique called Selective Availability (SA) to globally degrade the civilian GPS signal. New technologies demonstrated by the military enable the U.S. to degrade the GPS signal on a regional basis. GPS users worldwide would not be affected by regional, security-motivated, GPS degradations, and businesses reliant on GPS could continue to operate at peak efficiency [Leick, 1996]. The technology that makes this extraordinary technology possible grows directly from past research investments in basic physics, mathematics, and engineering supported from U.S. Federal agencies over a period of decades.

GPS works because of super reliable atomic clocks-no mechanical device could come close. These clocks resulted from gifted physics and creative engineering that managed to package devices which once filled large physics laboratories into a compact, reliable, space-worthy device. The improved, non-degraded signal will increase civilian accuracy by an order of magnitude, and have immediate implications in areas such as car navigation, emergency services, recreation, and others. In addition to more accurate position information, the accuracy of the time data broadcast by GPS will improve to within 40 billionths of a second. Such precision may encourage adoption of GPS as a preferred means of acquiring Universal Coordinated Time (UTC) and for synchronizing everything from electrical power grids and cellular phone towers to telecommunications networks and the Internet [Teunissen, 1998]. For example, with higher precision timing, a company can stream more data through a fiber optic cable by tightening the space between data packages. Using GPS to accomplish this is far less costly than maintaining private atomic clock equipment.

2. ERROR SOURCES OF GPS

The accuracy with which a GPS receiver can determine position and velocity and synchronize to GPS time is dependent on a number of factors. GPS error sources are allocated into three categories: the space segment, control segment, and user segment. The error components that comprise these segment, as well as an estimate of the one-sigma value of each component is given in Table 1. The most dominant error source by far is Selective Availability (SA) that produces a one-sigma error of 32.3 meters. These error sources are for the civilian coarse/acquisition (C/A) code. The effective accuracy of the pseudorange value is termed the user-equivalent range error (UERE). The system UERE is the root sum square (RSS) of the individual error components. As shown in Table 1, the one-sigma UERE is reduced from 33.3 m with SA to only 8 m when SA is removed. Further reduction in the UERE can be obtained with the proposed 2nd and 3rd civilian frequencies to correct for ionospheric delay. A UERE of 6.6 m was examined to account for the ionospheric correction, as well as a UERE of 3.8 m that includes additional benefits of GPS modernization [Kaplan, 1996].

A more conservative user error budget also was examined to account for larger receiver noise and ionospheric errors. The troposphere and multipath errors also were modified to agree with the supplemental GPS Minimum Operational Performance Standards (MOPS). This error budget, shown in Table 2, results in a one-sigma pseudorange error of 12.5 m without SA. The root sum square of the receiver noise, multipath, and interchannel bias equals 5 meters which is consistent with the value in the current Wide Area Augmentation System (WAAS) MOPS. A one-sigma pseudorange error of 12.5 meters for GPS without SA was adopted by RTCA SC-159 Working Group 2 for inclusion in the WAAS MOPS. As shown in Equations (1) and (2), the magnitude of the horizontal protection level is directly related to the standard deviation of the pseudorange error. This reduction of horizontal protection level (HPL)

naturally will translate into a significant improvement in availability. The horizontal protection level is determined by HPL = SF_{max} bias (1)

Where bias = $\sigma\sqrt{\lambda}$ (2)

SF is the scale factor, λ is the noncentrality parameter of the noncentral chi-square density function, and σ is the standard deviation of the satellite pseudorange error.

Table 1 Estimated GPS C/A Code Pseudorange Error Budget

Segment Source	Error Source	GPS 1 σ Error (m) with SA	GPS 1 σ Error (m) without SA
Space	Satellite Clock Stability	3.0	3.0
	Satellite Perturbations	1.0	1.0
	Selective Availability	32.3	-
	Other (thermal radiation, etc.)	0.5	0.5
Control	Ephemeris Prediction Error	4.2	4.2
	Other (thruster performance, etc.)	0.9	0.9
User	Ionospheric Delay	5.0	5.0
	Tropospheric Delay	1.5	1.5
	Receiver Noise and Resolution	1.5	1.5
	Multipath	2.5	2.5
	Other (interchannel bias, etc.)	0.5	0.5
System UERE	Total (RSS)	33.3	8.0

Table 2 Conservative C/A Code User Pseudorange Error Budget

Error Source	GPS 1 σ Error (m) without SA
Ionospheric Delay	10.0
Tropospheric Delay	2.0
Receiver Noise and Resolution	4.8
Multipath	1.2
Other (interchannel bias, etc.)	0.5
System UERE (RSS)	12.5

Space and control segment errors remain the same (without SA).

3. METHODOLOGY OF RTK GPS

The key of RTK GPS positioning is the ambiguity solution in the movement, when the dual frequency phase measurements of master and rover stations are put together through the radio communication. If the position of master station is known, then the position of rover station is solved by double differencing algorithm, so the merits of RTK GPS are rapid positioning and cm level of accuracy [Langley, 1998; Leick, 1996].

The phase ambiguity could be resolved in a short period and only few epoch of observations, which is contributed by the full constellation of GPS satellites, the complete full wavelength of dual frequency receiver, and the advanced decoding ability. Therefore, the ambiguity function method, the fast ambiguity resolution approach, the least squares ambiguity search technique, the fast ambiguity search filter, and the on-the-fly approach are commonly adopted to gain the integer ambiguity [Abidin, 1994].

The general procedures for estimating the ambiguity are listed as the followings:
(1)initial location estimation;

(2)search space generation;
(3)phase ambiguity search;
(4)phase ambiguity verification.
Certainly, the effectiveness of phase ambiguity is related to the amount of satellite, the geometry of satellite, the location of master station, the length of baseline, the significance of multipath, the appearance of cycle slips, the carrier-to-noise ratio of observations, and so on.

4. DESCRIPTION OF EXPERIMENTS

The experiments performed on campus of Chung Cheng Institute of Technology, National Defense University. The GPS control network consisted of 31 points and the situation of control points is displayed in Figure 1. Since point A001 is considered as the fixed point for static GPS surveying, the tasks of baseline vector processing and network adjustment were done by software package. The three-dimension outcomes taken from the network adjustment are used for reference standard. Moreover, the RTK GPS accomplished over 14 points with SA and 30 points without SA. The instruments employed include Ashtech GPS receivers and Leica RTK GPS positioning system. In addition, the software packages involved GeoGenius from Spectra Precision, SKI from Leica, Excel from Microsoft, and Survey generated from this research group.

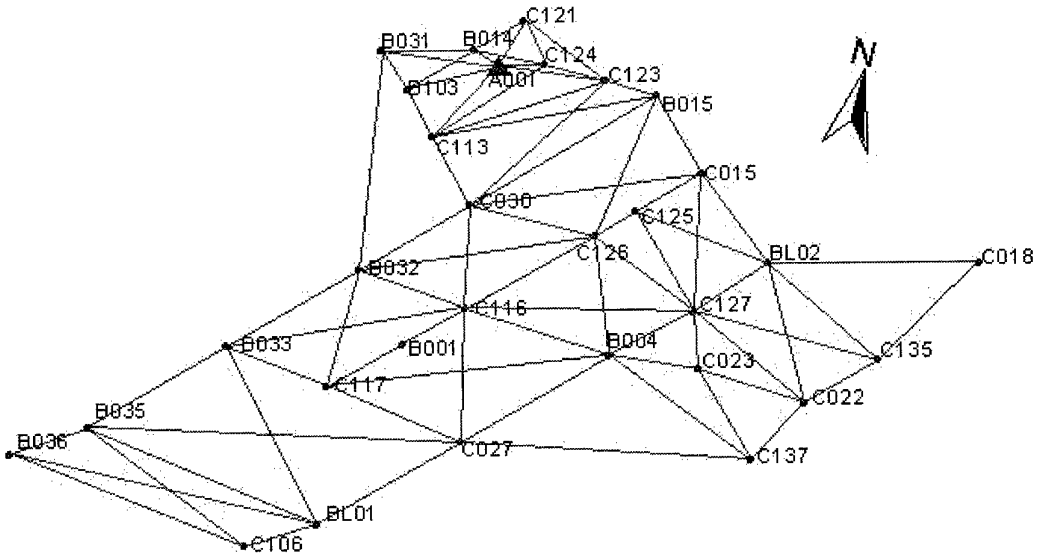


Figure 1 Experimental Network

5. PERFORMANCE EVALUATION OF RTK GPS

The evaluation tasks will be separated into RTK GPS with SA and without SA cases.

5.1 RTK GPS with SA

The static GPS surveying transacted and the outcomes are deliberated as the known facts for evaluating the capability of RTK GPS technique. Eventually, 14 points in the experimental network occupied with RTK GPS when B001 was fixed, but points B031, B033, B036, B037, and C030 were phased out during the statistical analyzing task because of no outcome appeared that may caused by the thoughtfully obstruction and the bad signal. The statistical analysis of geographical coordinates is listed in Table 3. The difference of latitude, longitude, and height does range about 1arc-second, 0.02arc-second, and 0.9m, respectively. In addition, the average deviation is around 0.1arc-second in latitude, 0.001arc-second in longitude, and 0.09m in height. In fact, the significant latitude deviation does happen in B010 and B035; the notable longitude deviation does occur in B035; the noted height deviation does appear in B035. If B010 and B035 points are not included, then the consequence may be more reasonable that is almost 1cm in horizontal vector and 2cm in vertical vector. Table 4 is the description of baseline length deviation between RTK and static GPS. The deviation range and average deviation are about 0.9m and 0.01m, respectively. The evidence of portion baseline length is not enough stability that is similar to the previous remark. Besides, the lager deviation is arisen in the longer baseline.

Table 3 Statistical Analysis of Geographical Coordinates

Point	Latitude (arc-second)	Longitude (arc-second)	Height (m)
B010	0.99989	0.00011	-0.011
B013	0.00042	-0.00041	0.003
B032	-0.00053	0.00193	0.005
B034	-0.00985	-0.00038	0.006
B035	-0.05912	0.01671	0.890
BL01	0.00006	-0.00676	-0.017
C026	0.00038	-0.00010	-0.036
C027	-0.00023	-0.00016	-0.037
C031	0.00036	0.00029	-0.015
Max	0.99989	0.01671	0.890
Min	-0.05912	-0.00676	-0.037
Mean	0.10349	0.00125	0.088
RMS	0.31745	0.00592	0.284

Table 4 Statistical Analysis of Baseline Length

Baseline	Static GPS (m)	RTK GPS (m)	Deviation (m)
B013-B032	154.606	154.674	0.067
B032-B034	194.390	194.683	0.294
B034-B035	207.985	208.076	0.091
B035-BL01	280.206	279.609	-0.597
BL01-C026	328.431	328.428	-0.003
C026-C027	144.843	144.857	0.014
C027-C031	189.289	189.307	0.018
C027-B034	210.626	210.691	0.064
Max			0.294
Min			-0.597
Mean			-0.007
RMS			0.196

5.2 RTK GPS without SA

After SA was turned off, the static and RTK GPS re-occupied the experimental network. Through the similar baseline processing and network adjustment, the outcomes of static GPS are still contemplated as the reference standard to judge the performance of RTK GPS without SA effect. The statistical analysis of TM 2° coordinates is listed in Table 4 that the deviation is less than 1cm in east and north directions and below 3cm in height, so the reliability of RTK GPS without SA is meaningful. At that time, the comparison task of RTK GPS with and without SA carried out and the estimated result is displayed in Table 6 that the discrepancy is below 3cm in east and north directions and about 10cm in height. It is compassion that only three points could evolve in the comparison because of satellite constellation and station surroundings.

Table 5 Statistical Analysis of TM 2° Coordinates

Point	E (cm)	N (cm)	H (cm)
Max	1.3	1.5	4.5
Min	-1.6	-2.2	-10.9
Mean	-0.13	0.04	-2.90
RMS	0.50	0.79	3.59

Table 6 Comparison of RTK GPS with and without SA

Point	△E (m)	△N (m)	△H (m)
B032	0.031	0.038	-0.125
BL01	-0.012	0.062	-0.144
C027	-0.027	0.047	-0.163

6. CONCLUSIONS

According to the preliminary analysis on horizontal vector, vertical vector and baseline length, the RTK GPS does denote to have the capability of static GPS technique in positioning. In other words, the RTK GPS technique is feasible, effective, and efficient for positioning and other applications, but the stableness is the most concern issue. Obviously, the reliability of RTK GPS could reach the centimeter level that is very near the order of static GPS, but the RTK GPS affected by SA on or off is also limited in centimeter level. The major difficulty of RTK GPS is the obstruction around station and the capability of radio power.

7. REFERENCES

Abidin, H.A., 1994. On-the-Fly Ambiguity Resolution. GPS World, No. 4, pp. 47-56.
Kaplan, E.D., 1996. Understanding GPS Principles and Applications. Artech House, New York.
Langley, R.B., 1998. RTK GPS. GPS World, No. 9, pp. 70-76.
Leick, A., 1996. GPS Satellite Surveying. John Wiley & Sons, Inc., New York. pp. 317-409.
Teunissen, P.J.G., 1998. GPS for Geodesy. Springer-Verlag, New York, pp. 271-318.

EFFECT OF COHERENCE ON DEMS DERIVED FROM SAR INTERFEROMETRY: A CASE STUDY OF MAYON VOLCANO, PHILIPPINES

Vu Tuong Thuy and Mitsuharu Tokunaga
Space Technology Applications and Research Program
Asian Institute of Technology
P.O. Box 4 Klong Luang, Pathumthani, 12120, Thailand
Tel: +66-2-5245577 or +66-2-5245690 Fax: +66-2-5245597
Email: rsc009994@ait.ac.th, tokunaga@ait.ac.th
THAILAND

KEY WORDS: SAR Interferometry, DEM, phase coherence

ABSTRACT: Synthetic Aperture Radar (SAR) Interferometry is a technique for obtaining the Digital Elevation Model (DEM) of the Earth surface by processing the phase difference between coincidence SAR images. Nowadays, SAR interferometry is considered as the promising technique for obtaining high resolution and quickly updated DEM. Here we present two experiments that make use of ERS1&2 Tandem data for making DEM derived from SAR Inteferometry. As the results, we show the limitation of the length of baseline for C band data, the correlation of DEM accuracy with coherence, and the correlation of DEM accuracy with NDVI.

1. INTRODUCTION

Recent years, Synthetic Aperture Radar (SAR) Interferometry has been utilized as a potential technique for obtaining accurate DEM of the Earth surface. The SAR interferometry products are becoming familiar to the applications and researches. SAR interferometry is based on the processing the phase difference between coincident SAR images. The displacement vector between two antennas is called baseline vector. Two antennas may be mounted on one aircraft and form along-track interferometry or across-track interferometry. The other way utilized in this research is repeat-pass interferometry, which is the normal implementation for satellite. If the ground objects still keep the high correlation between two times of illumination, the spatial baseline can be synthesized.

There have been several researches (Wehr A., et al., 1996, and Zebker H.A., et al., 1994) pointing out some results of the effect of phase coherence on DEM accuracy as well as analysis and utilizing of phase coherence. However, there is no any this kind of result for Southeast Asian tropical region. In this paper, besides the utilizing ERS1&2 data for investigating effect of phase coherence on DEM of Mayon volcano, we investigated the relationship between phase coherence and land cover.

2. METHODOLOGY

Table 1 – Data set used

Data	Date	Characteristics
ERS1&2 Tandem	20 and 21May 1996	Ascending
ERS1&2 Tandem	10 and 11 October 1997	Descending
Landsat TM	18 February 1994	Geocoded
DEM	Topographic map	Geocoded

In general, the processing can be separated into three parts as below:

2.1 Making DEM

- Calculation of interferograms and coherence coefficient

First, two single-complex images were coregistrated together. After coregistrating two images and resampling one to other, the complex inteferogram was calculated by using the following equation:

$$\text{Complex interferogram} = \frac{< S_1 \times S_2^* >}{\sqrt{< S_1 \times S_1^* >< S_2 \times S_2^* >}} \quad (1)$$

where s1 and s2 are single look complex values of two coregistered images,
* stands for conjugate complex,
<> stands for ensemble average

A portion of interferometric phase that are affected by the orbital fringe should be removed out of interferogram based on perpendicular component of baseline, then flattened inteferogram was formed. Along with this processing, coherence coefficient also was estimated.

- Phase unwrapping

Before doing phase unwrapping, the interferogram was filtered to reduce phase noise. Then, phase unwrapping was done following region-growing method. The low correlation area, layover area and neutral trees that were formed by the connection of residues were masked to avoid in phase unwrapping.

- Coregistration between DEM derived from topographic map and SAR slant-range

Here, GCPs were extracted from DEM derived from topographic map (DEMtopo) to precisely estimate baseline geometry, so it is necessary to coregistration between DEMtopo and SAR image. The automatically registration method is based on the cross-correlation between SAR image and simulated SAR image from DEMtopo.

- Creation of slant-range and ground-range elevation images

Based on the extracted GCPs above, least squared method was used to precisely estimate baseline geometry.

Now, we can calculate the elevetion from unwrapped phase

The equations used are listed as follow:

$$\text{Height} = h - R \quad (2)$$

According to cosine law

$$h = \sqrt{a^2 + r1^2 - 2 \times a \times r1 \times \cos\theta} \quad (3)$$

However,

$$\cos\theta = \sin(\Phi - \alpha) = \sin\Phi\cos\alpha - \cos\Phi\sin\alpha \quad (4)$$

$$\cos\theta = \sin\Phi \frac{Bc}{B} - \cos\Phi \frac{Bn}{B} \quad (5)$$

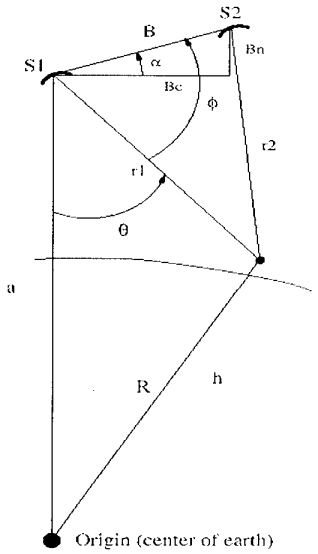
where,

$$\cos\Phi = \frac{B^2 + r1^2 - r2^2}{2 \times B \times r1} \quad (7)$$

and

$$\sin\Phi = \pm\sqrt{1 - \cos\Phi^2} \quad (8)$$

B, Bc, Bn, r1 and r2 (see Figure 1) are known values.



B	Baseline Magnitude
r1	Reference slant-range
r2	Second slant-range
h	Ground radial distance
a	Satellite radial distance
R	Center scene geocentric radius
S1	Reference satellite
S2	Second satellite
Bc, Bn	Baseline cross-track and normal component
α	Baseline orientation
ϕ	Interior angle
θ	Off-nadir angle

Figure 1 – Interferometric geometry for calculation

2.2 Investigating the effect of phase coherence on DEM accuracy

DEM derived from SAR interferometry above (DEMInSAR) was compared to DEMtopo with respect to the changes of coherence coefficient. Two-steps investigation was done. First, the profiles were taken from two DEMs and coherence image to give a figure of the trend. Then, coherence value was grouped with the interval of 0.01. With each group, the standard deviation of height difference was calculated. Last, we drew the graph of the relationship between coherence value and this standard deviation value.

2.3 Investigating the relationship between phase coherence and land cover type.

From geocoded Landsat TM images, Normalized Difference Vegetation Index (NDVI) was calculated. Like the above investigating, NDVI was grouped with the interval of 0.01. Then, the trend of coherence with respect to NDVI was investigated.

3. RESULTS AND DISCUSSION

3.1 Study area

Mayon volcano is located in the Alabay province of Philippines, 300 km SE of Manila (13°15.4'N – 123°41.1'E). The summit is about 2460 meters above sea level and base circumference is 62.8 km, encompassing the towns of Camalig, Malilipot and Sto. Domingo. Mayon has the classic conical shape of a stratovolcano. It is the most active volcano in the Philippines. The latest eruption is in February 2000 and on going.

3.2 Data processing

As mentioned above, two SAR data sets were used. The result and discussion here are demonstrated following the step in Method part.

- Making DEM

The flattened interferograms are shown in Figure 2. In 1997 data, the fringe only appears in some area in the foothill of Mayon and completely disappears in the steep slope area. With 1996 data, the result is better and we can recognize that the fringe is worse in layover area. The estimated baseline of two data sets is introduced in Table 2.

Table 2 – Estimated baseline

Data	T	C	N	Length
1996 baseline (TCN) (m)	0	-86.07	32.28	91.93
1997 baseline (TCN) (m)	0	393.98	53.97	397.66

Let us consider coherence coefficient. The coherence images are depicted in Figure 3. Compare between Figure 2 and Figure 3, we know that the higher coherence coefficient, the clearer fringe.

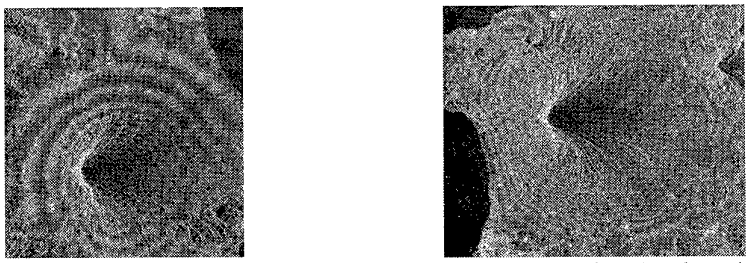


Figure 2 – Flattened interferogram of 1996 data (left) and 1997 data (right)

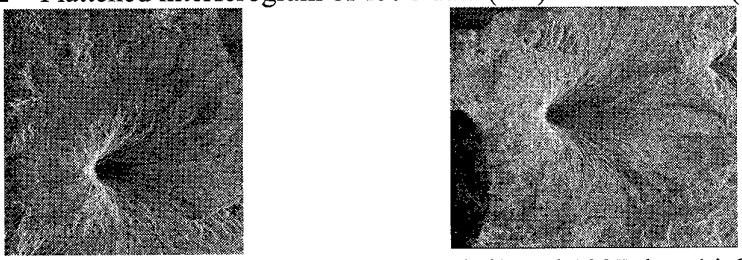


Figure 3 – Coherence image of 1996 data (left) and 1997 data (right)

As mentioned above, region-growing algorithm was used for phase unwrapping. We have done successfully with 1996 data, but failed when trying 1997 data. The reason is that the high phase noise in 1997 interferogram. Therefore, only 1996 data was used to make DEM and compared to DEMtopo.

After automatically coregistration between DEMtopo and SAR by cross-correlation analysis, a number of GCPs was extracted for precise estimation of baseline geometry. The slant-range and ground-range elevation image are shown in Figure 4. It is noted that DEMtopo should be masked with DEMInSAR to eliminate these no-information areas in comparison.

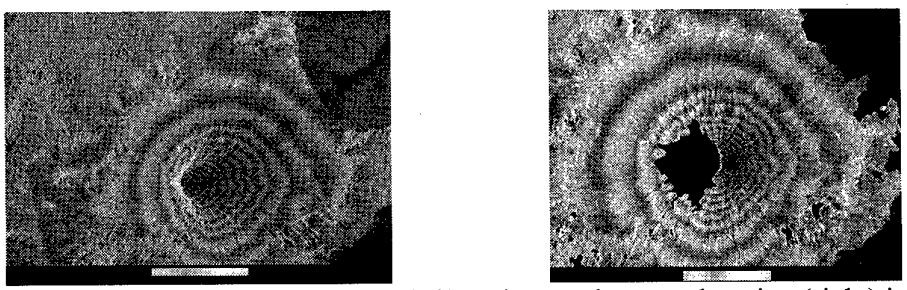


Figure 4 – 1996 slant-range elevation (left) and ground-range elevation (right) images

- Relationship between coherence and DEM accuracy

Here, by taking profile in DEMtopo, DEMInSAR and coherence images, we want to check the effect of coherence on the height difference. The result is illustrated in Figure 5. On the left side, i.e. high coherence value, two profile curves from DEMInSAR and DEMtopo are nearly coincident. On the other side, i.e. layover area with low coherence value, the profiles show the bigger differences. Then, the comparison was done more statistically. The distribution of coherence values in both data sets is illustrated in Table 3. Both data sets introduce low coherence value.

Table 3 – Statistic result of coherence value

Data	Min	Max	Mean	Stdev
1996	0.01	0.87	0.365	0.142
1997	0.01	0.85	0.255	0.138

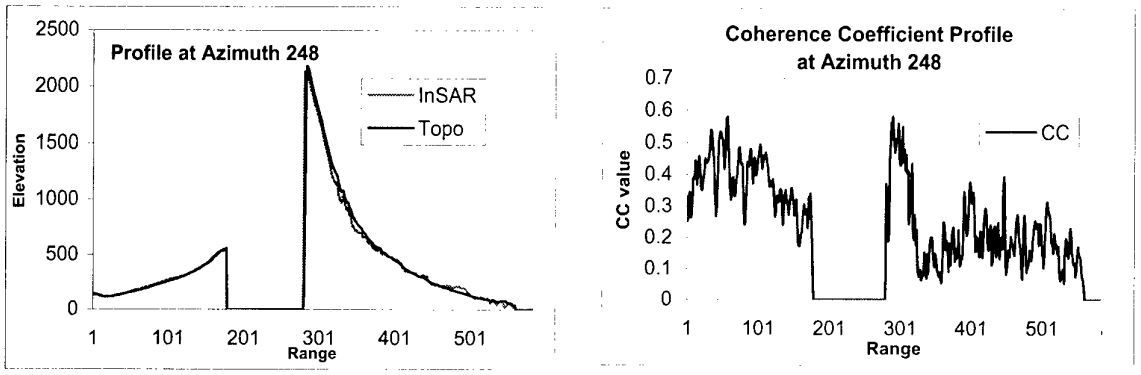


Figure 5 – Illustration of profile taken at azimuth 248
Comparison of DEMInSAR and DEMtopo (left); Coherence (right)

In Figure 6 (left), we can see that when coherence value increases, the standard deviation of height difference between two DEMs decreases quickly. This trend follows exponential function.

- Relationship between coherence and NDVI

There are many factors that affect on phase coherence. Here, we consider in land cover. We have already known that when land cover changes with the time, the coherence has the trend of decreasing. The correlation analysis between 1996 coherence, 1997 coherence and NDVI (see Table 4) shows that it is also correct here. The graph shown the trend of coherence coefficient against NDVI can be seen in Figure 6 (right).

Table 4 – Correlation analysis result

Data	96 vs 97	96 vs NDVI	97 vs NDVI
Correlation Coefficient	0.799	-0.903	-0.797

As we knew, SAR ERS1&2 data with C band and VV polarization weakly interacts to vegetation. The results from this research introduce some interesting further researches in this point.

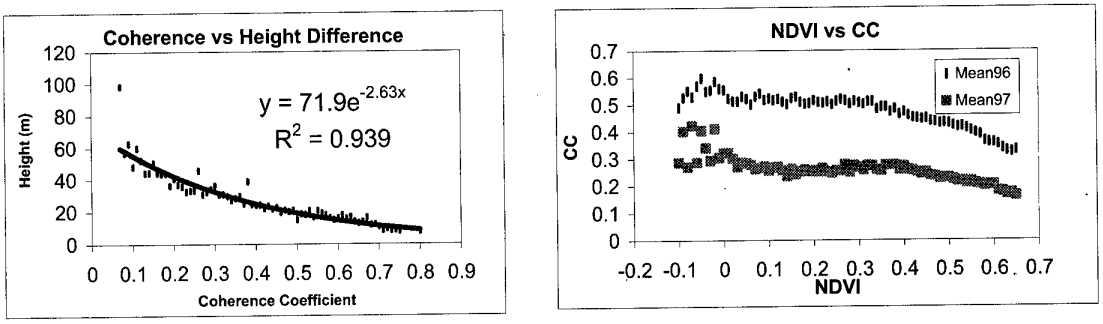


Figure 6 – Relationship between coherence and DEM accuracy (left)
Relationship between NDVI and coherence (right)

4. CONCLUSION

In this paper, ERS1&2 tandem data was used for applying of SAR interferometry in tropical Asian region. The result shows very low coherence value. However, by using 1996 data, we can make DEM using SAR interferometry. In conclusion, DEM accuracy decreases following the exponential function when coherence value increases. In addition, this paper also concluded that the coherence coefficient decreases when NDVI increases.

From this study, the results can be used for the further researches either in application site or in technique site. Phase coherence is very important in SAR interferometry research. This kind of research should be conducted for Southeast Asian region.

5. REFERENCES

Gens, R., Van Genderen, J.L., 1996. Review Articles SAR interferometry: issues, techniques, applications. Int. J. Remote Sensing, 17 (10), pp. 1803-1835.

Kenyi, L., Raggam, H., 1996. Accuracy assessment of Interferometrically derived DTMs. Fringe 1996.

Qian, Lin, Vesecky, F.J., Zebker, H.A., 1994. Comparison of elevation derived from InSAR data with DEM over large relief terrain. Int. J. Remote Sensing, 15, pp. 1775-1790.

Madsen, S.N, Zebker, H.A., Martin, J.M., 1993. Topographic Mapping Using Radar Interferometry: Processing Techniques. IEEE Trans. GE and RS, 31 (1), pp. 246-256.

Seymor, M. S., 1999. Refining Low-Quality Digital Elevation Models Using Synthetic Aperture Radar. Doctoral Thesis, University of British Columbia, Canada.

Wehr, A., et al., 1996. The effects of different land covers on the accuracy of interferometric DEM. Fringe 1996.

Zebker, H.A., Werner, C., Rosen, P.A., Hensley, S., 1994. Accuracy of Topographic Maps Derived from ERS-1 Interferometric Radar. IEEE Trans. GE and RS, 32 (4), pp. 823-836.

Zebker, H.A., Villasenor, J., 1992. Decorrelation in Interferometric Radar Echoes. IEEE Trans. GE and RS, 30 (5), pp. 950-959.

Final Report, 1999. Remote Sensing and GIS analysis for base data creation and change detection; the study on comprehensive disaster prevention around Mayon volcano in the Republic of The Philippines. *(Source Asian Center for Research on Remote Sensing)*

USE OF DIGITAL TERRAIN MODELES FOR THE INFRASTRUCTURE DEVELOPMENT IN SRI LANKA.

Nihal WIJESEKERA
Senior Lecture, Superintendent of Surveys
Institute of Surveying & Mapping, Diyatalawa
Tel: +94-57-31735 Fax: +94-57-22004
E-mail: ism_surv@sri.lanka.net
SRI LANKA

KEY WORDS: Terrain, Infrastructure

ABSTRACT: Digital Terrain Models (DTMs) have become a major constituent of geographical information processing. DTMs facilitate to model, analyse and display phenomena related to topography or similar surfaces. This paper presents an approach to use those capabilities in DTMs for the infrastructure development in Sri Lanka. The different techniques of data capturing methods are given, with a comparison, providing opportunity to select the best method that appropriate for the requirement. The theoretical basis and a number of DTM packages are described and an attempt is made to determine how best such system can cover many of the practical requirements. Some applications are mentioned where they have particular features that relate to the theme of the paper.

INTRODUCTION

A digital terrain model (DTM) can be described as a three - dimensional representation of a terrain surface consisting of X, Y, Z coordinates stored in digital form. It includes not only heights and elevations but other geographical elements and natural features such as rivers, ridge lines, etc. With the increasing use of computers in engineering and the development of fast three-dimensional computer graphics the DTM is becoming a powerful tool for a great number of applications in the earth and the engineering sciences.

DATA COLLECTION FOR DIGITAL TERRAIN MODELLING

The acquisition of accurate three-dimensional coordinates which represent the surface of the Earth is a vital stage in the process of terrain modelling. The raw data of the DTM can be captured by a number of different techniques. The particular technique used will depend on factors such as:

- The size of the area to be surveyed
- Data accuracy
- Type of information which will eventually be extracted from the model
- Availability of resources

At present, most DTM data are derived from three alternative methods.

1. Ground survey methods
2. Photogrammetric methods
3. Graphics digitizing methods

Ground Survey Methods

Ground surveys could be done with computer aided systems which may be coupled to field instruments, available from all the major manufactures, such as Kern, Zeiss Wild, Sokkia etc. Total station instruments such as Elta-2, Wild, Sokkia Set 2, Leica are common instruments used for data capturing in ground surveying method.

Since ground survey data tend to be very accurate, the accuracy of the resulting DTM is very high. Hence, it is most suitable for the small area site planning and designing. However, as this particular data collection technique is relatively time consuming and expensive its use is limited to small areas.

Photogrammetric Methods

Photogrammetric data capturing is widely used for large area projects, especially in rough terrain. Photogrammetric methods based on the use of stereoscopic interpretation of aerial photographs or satellite imagery (e.g. from the French SPOT Satellites), using suitable photogrammetric equipment such as manual or analytical stereo plotters. The accuracy of the resulting DTM depending on the sampling method and imagery that are used. The resulting DTM accuracy will be in the range of medium to high. Photogrammetric data capture is used in large engineering projects such as dams, and roads as well as nation wide data collection.

Graphics Digitizing Methods

The third alternative is the use of a very large number of topographic maps already existed in printed form. These maps are converted into a digital format by digitization. When the topographic maps are in digital format, digital map data generally occur as string or series of strings of (X,Y) coordinates with an associated Z value for the contour level.

An example of a DTM (Figure 2) constructed from an existing contour map (Figure 1) is shown below.



Figure 1 Contour map

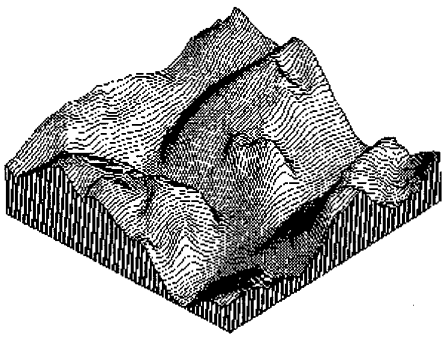


Figure 2 DTM of the area shown in Figure 1

The existing small-scale topographic maps e.g.1 inch sheets (1:63360) and 1:50000 scale maps produced by the Survey Department of Sri Lanka can be used to create DTMs with low accuracy. However, as long as users are aware of this limitation, this lower-quality data is quite acceptable in regional planning, landscaping, visualization, simulation, civil engineering projects and reconnaissance studies.

However, since large area coverage is achieved relatively at a low cost, existing topographic maps provide a compromise method of obtaining DTMs for use at medium or small scales.

Table 1 presents the three main methods which can be used to acquire the elevation data and applications of terrain models created at different scales.

Source of DTM data	Data Capturing method used	DTM accuracy	Areal coverage	Typical applications
Ground survey	Total or semi-total station	Very high	Limited to specific sites	Small area site Planning and design
Photogramme -tric measurements	Stereoplotting Machine (with or without correlators)	1 High (if from spot heights) 2 Lower (if from contours)	Large area projects, especially in rough terrain	(1) Large engineering projects:dams, reservoirs, roads, open-cast mines (2) Nationwide, especially in association with orthophotographs
Cartographic (existing topographic maps)	Either: 1 Manual digitizing 2 Semi-automatic Line following 3 Fully automatic raster scanning	Low: derived from contours on medium and small scale topographic maps	Nationwide at small scales	Aircraft simulators, Landscape Visualization, Landform Representation, military battlefield simulation

Table 1 Sources of DTM data and applications

CONSTRUCTION OF DIGITAL TERRAIN MODELS

After capturing of raw data sets, to construct a comprehensive DTM, it is necessary to establish the topological relations between the elements, as well as an interpolation model to approximate the surface behaviour. In order to do that a very large number of programme packages have been devised and written for terrain modelling and it's applications.

The general classification of terrain modelling software packages in surveying and civil engineering is illustrated in figure 3.

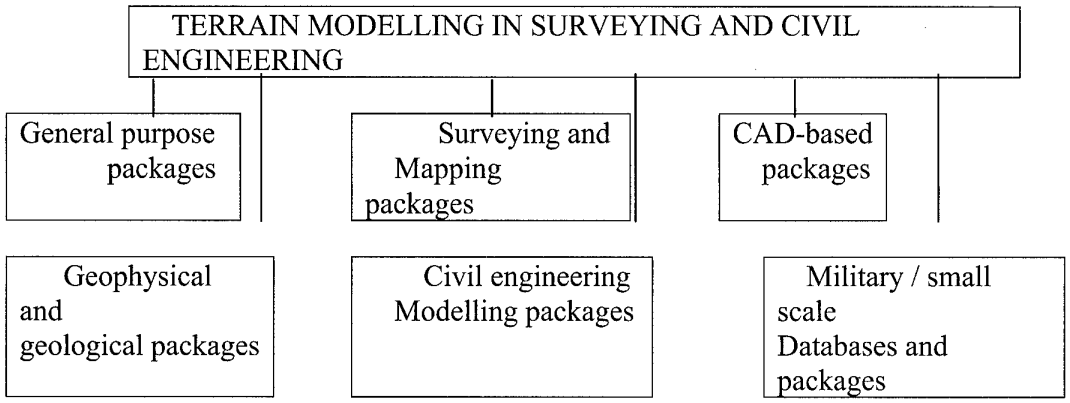


Figure 3 Classification of terrain modelling software packages in surveying and civil engineering.

APPLICATIONS

Terrain modelling is applied as a solution to a wide range of problems in the field of surveying and mapping, geology, civil and military engineering. Being Sri Lank is a developing country, much more emphasis has to be made to identify the low cost methods in infrastructure development in the country.

Terrain models which can be created by using photogrammetry and existing maps are less expensive Hence, those techniques are ideal tools to solve problems in infrastructure development.

Feasibility Studies

Feasibility study is one of the main prerequisites of any major development project. Failure of feasibility study may be the failure in the entire project giving economical & environmental hazard to the country. Traditionally a feasibility study is done by manual data capturing techniques or by simply utilizing the skill and experience of the qualified experts. The method is highly time consuming and expensive.

Having generated a ground model of the proposed area, feasibility studies and environmental impact analysis can be performed automatically once the position of the proposed site is defined. Figure 4 illustrates the use of the technique to simulate the effect of a proposed highway on an existing ground model.

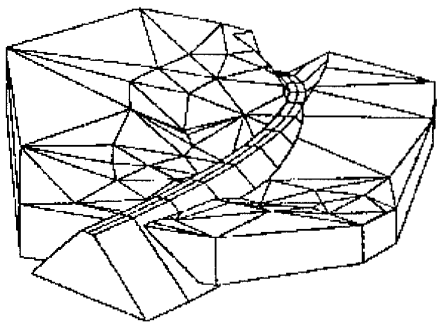


Figure 4 Simulated highway model created using the MTM Terrain modelling package

Communications Planning

In recent years use of telecommunication, radio and television, cellular and mobile telephones have increased in Sri Lanka.
The use of Terrain model data, in conjunction with computer analysis is widely use in many countries in this field. The applications are involved in the planning of communications network, rapid optimization of radio links, siting of transmitters, identification of complementary areas of coverage and prediction of areas subject to co-channel interface.
As lower accuracy DTMs could be generated with the help of photogrammetric and cartographic data capturing methods are quite suitable for the above, the method can be used in Sri Lanka to enhance the communication developments.

DTM Applications To Civil Engineering

Civil engineering is an important user of terrain modelling. The range of projects where the DTMs are used is almost endless, covering roads, railways, dams, reservoirs, canals, landscaping, land reclamation and mining, etc. The range of facilities included in the terrain modelling permits the survey and design of projects mentioned above. Apart from that, the suitable software (e.g. MOSS) can be used to produce sections, areas, volumes, setting-out information, triangulation of surfaces and contouring.

Land Settlement Programmes

Alienation of lands to the landless people is a common practice of any Government of Sri Lanka. The programme may be a small scale or a large settlement programme such as Mahaweli Development Scheme.

Settlements are done with the help of prepared plans known as Blocking Out Diagrams (BOD). (Figure 5) Traditionally these BODs are prepared by surveyors using ground survey methods considering only the topographical features available in the site.

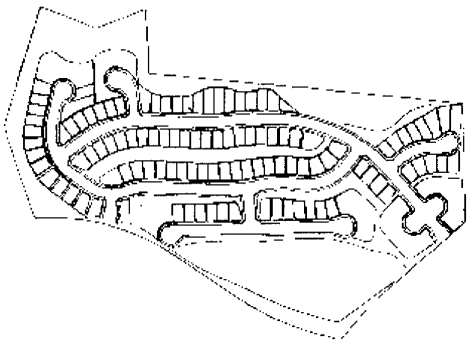


Figure 5 Blocking Out Diagram

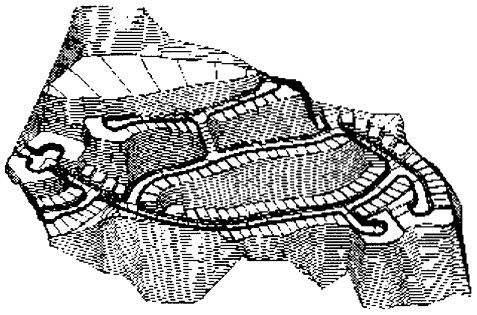


Figure 6 DTM showing the projection of design data

Due to the lack of communication with other organizations such as Electricity Board, Water Board, Telecommunication Department, Road Authorities and non availability of proper data sets, it can be seen that is a delay in providing infrastructure facilities for many years.

After preparation of the DTM of the proposed area the design (BOD) can be incorporated in to the model using Surface Modelling Programs. (eg. HASP)

The resultant model (Figure 6) can be used as a data source and a tool for the Civil Engineering, Environmental and other organizations to solve their problems, as already discussed, to develop the area.

CONCLUSION

Terrain modelling is applied as a solution to a wide range of problems in the fields of surveying and mapping, and civil engineering. For the future, the use of terrain modelling methods will continue to develop and expand into other areas of activity. Hence, introducing the technique in Sri Lanka has vital importance, because it can be used as a tool in the process of development.

REFERENCES

Burrough, P.A., 1990, Principles of Geographical Information Systems For Land Resources Assesment. Clarendon Press, Oxford.

Maguire, D.J.and Goodohild, M.F., 1992, Geographical Information Systems. Volume 1, Bath Press, Avon.

Petrie, G.and Kennie, T.J.M., 1990, Terrain Modelling in Surveying and Civil Engineering. Whittles Publishing, London, p4, p26.

A METHOD OF MAP MATCHING FOR PERSONAL POSITIONING SYSTEMS

Kay KITAZAWA, Yusuke KONISHI, Ryosuke SHIBASAKI
Ms., Center for Spatial Information Science, The University of Tokyo
Center for Spatial Information Science, Institute of Industrial Science
The University of Tokyo
4-6-1 Komaba, Meguro-ku,Tokyo 153-8505
JAPAN
Tel. +81-3-5452-6417 Fax. +81-3-5452-6417
E-mail:kitazawa@iis.u-tokyo.ac.jp

KEY WORDS: Map matching, Positioning, Human, 3D-space, gyro

ABSTRACT: To track human's movements with high accuracy in certain areas, where GPS system is not available, complimentary positioning methods are needed. Personal positioning system using a sensor of acceleration and a gyrocompass together with GPS is now being developed as one of promising methods. Accumulation of positioning errors, however, cannot be avoided. One of the solutions to reduce or modify these errors is "Map matching" technique, which modifies estimated user's position assuming that users are always along road networks.

In this paper, a method of Map Matching for Personal Positioning Systems is proposed. While it has already been in practical use for car navigation systems, its simple algorithm based on distance and direction estimation is not sufficient for tracking of man's complicated movement. In addition, matching should be done for three-dimension maps because human movement consists of both vertical and horizontal motion. The algorithm proposed in this paper combines two of the current algorithms, one of which is based on matching one's shift patterns with shapes of road network, and the other is for a frequent step-by-step adjustment of one's estimated position against outlines of objects around it. Using this integrating algorithm, we propose a new Map Matching method that would give good performance in terms of accuracy of positioning system for human movement in 3D space.

BACKGROUND

A demand for the accurate positioning technology is increasing. Though several positioning services are already in practical use, there are still some areas left to which radio waves used in such positioning systems cannot reach. Complimentary positioning methods for covering these areas are strongly needed. Though Personal Positioning System using a sensor of acceleration and a gyrocompass together with GPS to trace a person by his/her footsteps and angles is now being developed as one of promising methods, such system calculating one's

relative position always accompanies an accumulation of positioning errors. To reduce or prevent these errors to make such system as much accurate as GPS, "Map Matching" technique, which modifies user's estimated position based on the assumption that users are always along road networks on the map is combined with it.

The quite simple algorithm used in current car navigation system is not enough for Personal Positioning System. Data from sensor of acceleration and a gyrocompass such as the number of footsteps and direction is not as accurate as that from sensor of rotation and angle of wheel. In addition, while the assumption used in this algorithm that car runs always on and along roadways allows the system to reconcile the car's estimated position and correspondent point on the center line of road network described by nodes and edges in the database, complicated and various patterns of human's movement cannot be limited to the center line network of roads. For example, it is necessary for a human tracking system to determine on which side of the street or in which floor the user is now walking. (Figure 1.) As a solution of this problem, using three-dimensional database in which roads are represented by polygonal planes, a new map matching method which can cope with unsteadiness of human's movement both for vertical and horizontal direction is proposed in this paper.

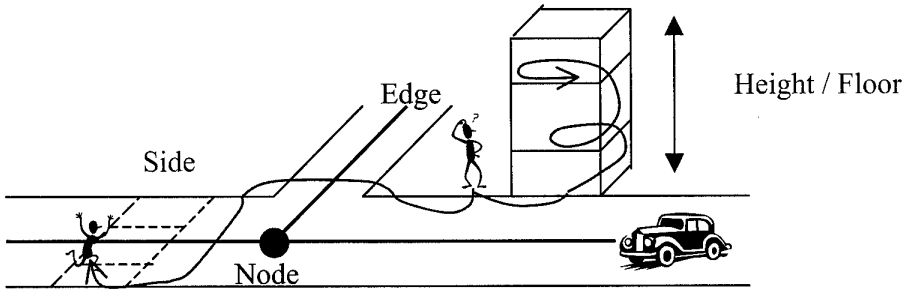


Fig. 1 Human can move more freely than cars on road networks

REVIEW:CURRENT MAP MATHICNG ALGORITHMS

As a beginning, we overview current Map Matching methods and point out their problems to highlight the differences between our approach. Current methods can be classified into two types in large. The first one makes use of distinctive features of both human's shift pattern and road networks to find a corresponding point. In other words, similarity or correlation between the trajectory up to that time (position) and alignment of the road network around is calculated to choose an edge on which user most likely exists when conspicuous change in movements such as turning at corner occurs. The clue for matching is "turn at the corner". Since this is a non-regular event, it often happens that user keeps on going straight without any turn or other distinctive movement and the time interval of matching process is prolonged consequently, which brings accumulation of errors. The other method, on the other hand, just calculates distances between the estimated position and neighboring edges in very short term. Miyata(1991)

suggests a methods with frequent calculation that enables relocation of estimated position before it goes too far away from the road networks to find correct point. Though this methods works well to avoid mismatching based on accumulation of errors, the brief algorithm designed for frequent position correction fails to modify the location if once mismatching occurs by selecting wrong edges. It has been shown in recent investigation that the mismatching occurs mainly near crossroads, that is, pros and cons of the second method are complementary to those of the first one. Then the approach we are going to take here uses both algorithms together in the process of map matching.

MAIN POINTS OF ALGORITHM

Before we describe the algorithm in detail, we would like to make some remarks on principle and basic structure of it.

Principle

We refer to either of two databases, one of which consists of point's data for boundaries of objects and polygons and the other is a network made by nodes and edges. Coordinates and time of each estimated point and each corresponding modified point are separately stored in these databases.

The estimated position at each step is put on the map as it is unless it crosses outlines of objects such as the line of a wall surface. This means we relocate the points not on a network, but on an area of the object. When an intersection is found, the current and previous position is locally modified so that the modified point comes within the correct object. This is based on the frequent modification method. Modified points are used for showing user's position immediately.

Keeping on using this algorithm, if the change of direction (angle) gets bigger than threshold, all of the points included in the trajectory from previous change to that point are globally modified. This algorithm succeeds a judgment of similarity in forms and corrects whole trajectory itself so that the point at which angle changes can fit the corner. The database of network is used in this algorithm.

Local Modification

The estimated position is locally relocated according to the angles made by tracks and an outline when they have an intersection. If the angle is smaller than threshold, we assume that this incorrect positioning is brought by drift errors of gyrocompass and rotate the current point around the former one in proportion to that angle. If the angle is bigger than threshold, the track may hit against outlines because of its error in length (distance). Relocation of the current

position is done by adjustment of the length of tracks.

Global Modification

We switch the algorithm for relocation to the global modification when sudden and sharp change of direction occurs between several steps with almost the same direction data. Searching the database of road networks for a crossroads or a curve with similar change in angle around the intersection, the edge on which user most likely locates is chosen. Compared with the shape of corresponding corner, an angle and length of tracks is modified.

ALGORITHM

The algorithm is shown in flowcharts (Figure 2, 3)
The main process of Map Matching is as follows.

(1) Coordinates and time of the currently estimated and the previous position are obtained from the storage of positional data. (x, y, z, T)

(2) Tracks expressed by a vector between these two points is calculated

(3) Errors are modified by coefficients for correction of distance and angle.
The values of these coefficients are obtained in of the previous Map Matching process.

(4)

(5) Data of the objects near the estimated position is obtained

(6) Whether the tracks cross the outlines of objects around them is checked. If there is one, we move into process 1. If not, coordinates and time of the estimated position are adopted as those of modified.

(7) Data of modified current position is obtained and added to the storage of positional data.

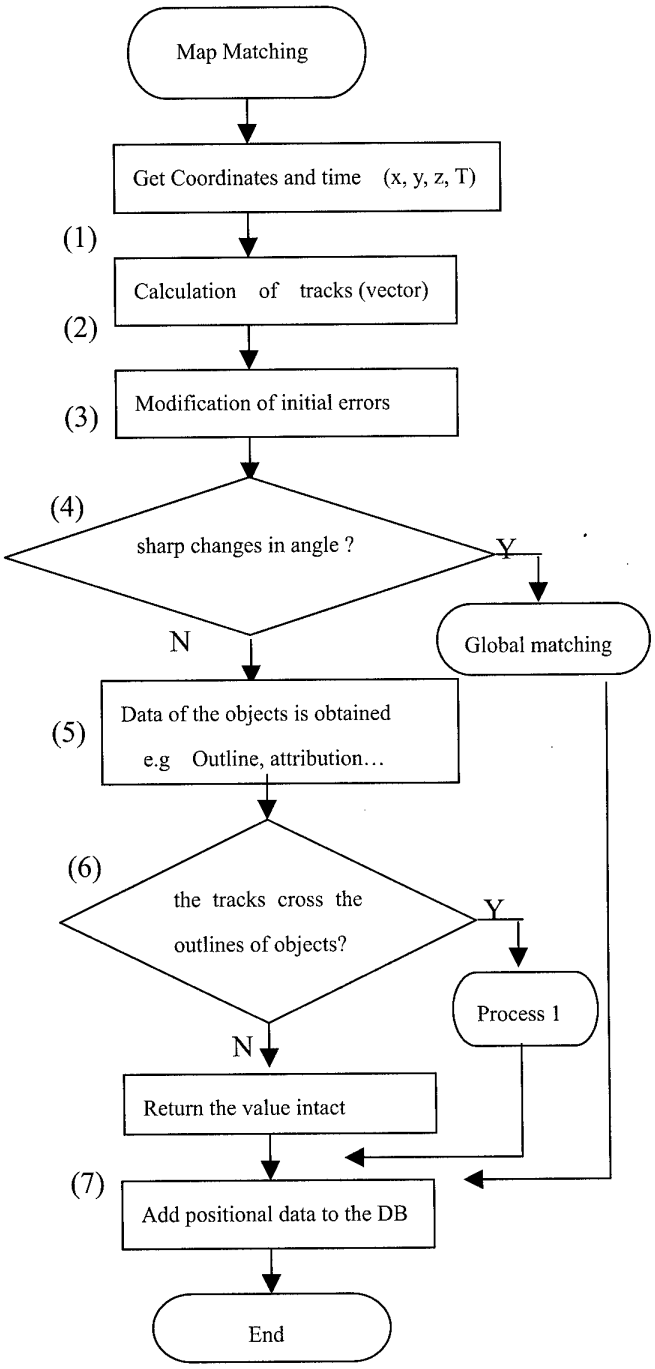


Fig.2 Flow chart of Map Matching (Main)

Next, process 1 is as follows.

(8) Whether intersection point of tracks and outlines is within the object "entrance" is checked. If so, coordinates and time of the estimated position are adopted as those of modified. If not, the whole tracks from the nearest corner are obtained.

(9) The most recent corner is detected in the tracks by calculating the angle of each step makes and comparing it with threshold. Coordinates and time of the point of the recent corner is obtained.

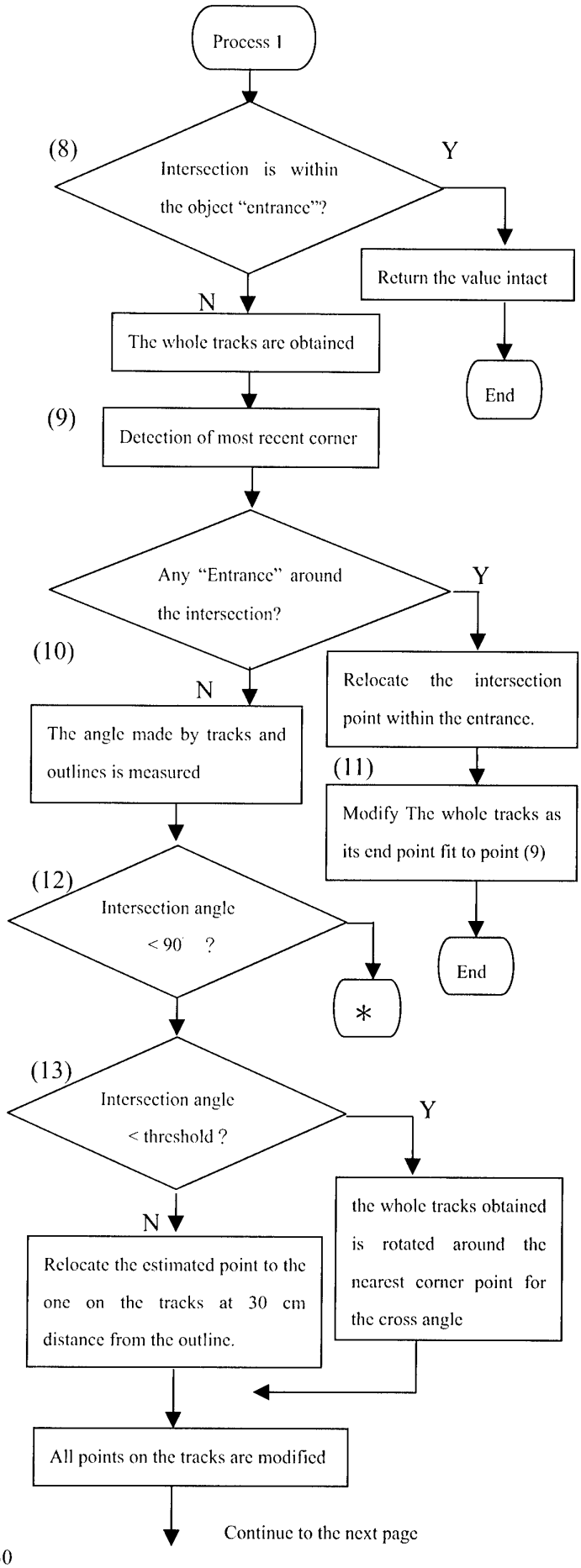
(10) Whether there is any entrance object around the intersection or on the same outline is checked. If any, the estimated point is relocated to the most nearest point within entrance area. If not, the angle made by tracks and outlines is measured.

(11) The whole tracks from the nearest corner are modified so that its end point fit to the point obtained in (9).

(12) The intersection angle is compared to right angle (90°). If the former is smaller than latter, (12) follows. If not, part of the following process change as annotation * .

(13) The angle at the intersection is compared to threshold. If the former is smaller than latter, the whole tracks obtained is rotated around the nearest corner point for the cross angle. If not, the estimated point is relocated to the point on the tracks at 30 cm distance from the outline.

* (. If the former is larger than latter, the whole tracks obtained is rotated around the nearest corner point for



(180° - the cross angle). If not, the estimated point is relocated to the point on the tracks at 30 cm from the outline.)

(14) All points on the tracks are modified.

(15) The ratio of distances of former track and that of after modification and the angle used in (13) are recorded as coefficients for correction of distance and angle.

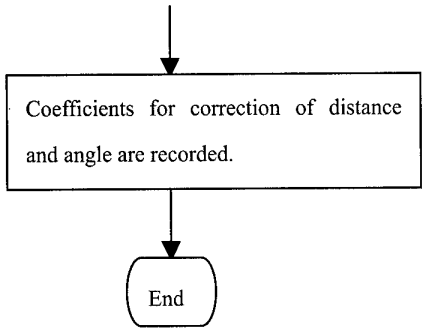


Fig. 3 Flow chart of Map Matching (Process1)

The process of Global matching is as follows.

1. Nodes and Edges around the point are obtained from network database.
2. The distance between the current and previous position and respectively each node or edge is calculated.
3. Select the nearest node if its distance is shorter than threshold, otherwise quit the process.
4. Among the edges connected to the nearest node, angle made by each edges and the nearest edge to the previous point.
5. Change the shape of tracks from the most recent point with sharp change in angle so that modified point locates on the edge with least difference in angle between the estimated one.

RESULTS AND CONSIDERATION

With the algorithm explained above, we examined the Map Matching method for tracking human's movement in three-dimensional space. The effectiveness of this series of process was tested by case studies coping with data from the Personal Positioning System and simulations with data consists of ideal value and errors measured in previous research. The results suggested that the combination approach not only be applicable to three dimensional movements but contribute raise accuracy of positioning system for human.

REFERENCES

Takeo Miyata, Kazumi Furusawa, Kosuke Thukamoto, 1991. A Method of Map Matching for Automotive Navigation. T.IEE Japan, vol.111-C, No.10, pp.83-89

Takeo Miyata, Kazumi Furusawa, Kosuke Thukamoto, 1991. A Method of Error Detection in Map Matching Technique. T.IEE Japan, vol.111-C, No.10, pp.531-532

Takeo Miyata, Yoshihiro Kimura, Kosuke Thukamoto, 1994. A Method of Map Matching Using A Low Precision Angular Sensor. Research Report: Faculty of Engineering of Ibaraki University, vol.42, pp.109-115

The 21st Asian Conference on Remote Sensing
December 4-8, 2000 Taipei, TAIWAN

A Multi-polarized and Multi-angle C-band Radar System for Soil Moisture Determination Under Bare Soil Conditions

Shakil A. Romshoo*, T. Oki** and Katumi Musiake**,

*Earth Observation Research Center, NASDA, 9-9-1, Roppongi,
Minato-ku, Tokyo, Japan
(e-mail: shakil@aab.iis.u-tokyo.ac.jp)
**Musiake Lab, IIS, University of Tokyo, B Building, 4-6-1, Komaba,
Meguro-ku, Tokyo, Japan
(e-mail: prof@hydro.iis.u-tokyo.ac.jp)

Abstract: This article is an attempt to determine the soil moisture under bare soil conditions at a field scale using a ground based C-band radar with all the three linear polarizations,i.e., HH, HV, and VV and employing 4 angles of incidence,i.e., 15^o, 23^o, 35^o and 43^o. The experiment was conducted 12 times during the year 1999 to monitor the soil moisture variation at a field scale at Chiba, Japan. The field was purposefully maintained bare and smooth. The Integral Equation Model (IEM), based on the theory of diffraction of surfaces, was used to predict the backscattering phenomena. The model is validated with the experiment data and a good agreement between the modeled and the observed backscattering coefficient is obtained at HH polarization while as the model does overestimate the backscattering at VV polarizations. Further, a sensitivity analysis of the model reveals that radar is sometimes more sensitive to the small changes in the roughness characteristics than the larger changes in the soil moisture. Under natural roughness conditions, the C-band radar, particularly with VV polarization and lower angles of incidence, should be the ideal system for soil moisture determination. Such a configuration has been found to be more sensitive to soil moisture as compared to roughness affects.

Key Words : Scattering models, backscattering coefficient, surface roughness, correlation length, wavelength, polarization

1. Introduction

Though a number of models based on experimental data have been proposed (Oh et al., 1992, Dubois et al., 1996) but for soil moisture retrieval, but the results are very limited. Further, these empirical models derived from the experimental data may sometimes lack the consistency and the universality. They may apply to surface conditions and the radar parameters that were looked at during the time of the experiments. On the other hand, the theoretical models developed have also some validity restriction as for the frequency and roughness ranges are concerned. Among the high frequency scattering models, the Kirchoff formulation (KF) is the most commonly used. For a ground surface whose standard deviation and correlation length are much smaller than the wavelength, the small perturbation method, SPM (Ulaby, 1982), which is a low frequency solution, can be used to estimate the backscattering contribution. Attempts have also been made to unite the KF and SPM to obtain a model applicable to a wide range of roughness scales or frequencies. More recently, Fung et al., 1992 has developed a surface scattering model based on the surface field integral equations called the Integral Equation Model (IEM). The IEM reduces to the SPM when the surface is smooth and to the standard Kirchhoff model when the standard deviation is much larger than the incident wavelength. In its complete version, the model describes the backscattering behavior of a random rough bare surface without any limitation on the roughness scale and frequency range.

In view of the extended validity of the IEM model and to overcome the draw of the other reported surface scattering models, we selected this model for validation of our experimental results. Besides validating the model under different surface roughness and soil moisture conditions, the simulation studies have been carried out to thoroughly understand the influences of the different

factors which influence the radar backscattering behavior.

2. Integral Equation Model

The integral equation model (Fung et al., 1992), abbreviated as IEM was used in this study to predict and understand the radar backscattering coefficient as a function of both target and sensor parameters. This model has been applied to a wide range of roughness for bare soil surfaces as well as sea surfaces (Altese et al., 1996; Chen et al., 1995). Because of complexity, it is not practical to use the complete version of the model and in the applications usually, the approximate versions are usually considered (Altese et al., 1996). The validity condition can be expressed as $k\sigma \langle 3$, where $k = 2\frac{\pi}{\lambda}$, the wavenumber; λ is the wavelength; and σ is the surface rms height. The like polarized backscattering coefficient σ^0 can be expressed as follows:

$$\sigma^0_{pq} = \frac{k^2}{2} e^{-2k_z^2\sigma^2} \sum_{n=1}^{\infty} \sigma^{2n} |I^n_{pq}|^2 [\frac{W^{(n)}(-2k_x, 0)}{n!} \tag{1}$$

Where σ^0_{pq} is the radar backscattering coefficient; p, q are vertical or horizontal polarizations; k_z= $k\cos\theta$ and k_x= $k\sin\theta$;σ is the surface rms height and $W^{(n)}(u, v)$ is the roughness spectrum of the surface related to the surface correlation function. In the above equation (4.1),

$$I^n_{pq} = (2k_z)^n f_{pq} exp_{(-\sigma^2 k_z^2)} + k_z^n \frac{[Fpq(-k_x, 0) + Fpq(k_x, 0)]}{2} \tag{2}$$

$$f_{hh} = 2R_\perp/\cos\theta \qquad f_{vv} = 2R_\parallel/\cos\theta \tag{3}$$

$R_=$ and $R_\perp$ are the Fresnel reflection coefficients for vertical and horizontal polarizations

$$F_{vv} = \frac{2\sin^2\theta}{\cos\theta}[(1 - \frac{\epsilon\cos^2\theta}{\epsilon - \sin^2\theta})(1 - R_\parallel)^2 + (1 - \frac{1}{\epsilon})(1 + R_\parallel)^2] \tag{4}$$

$$F_{hh} = [4R_\perp - (1 - \frac{1}{\epsilon}) + (1 + R_\perp)^2] \tag{5}$$

θ is the angle of incidence;

$$W^{(n)}(k_x, K_y) = \frac{1}{2\pi} \int_{-\infty}^{+\infty} \rho^n(\xi, \zeta)\, exp(-jk_x\xi - jk_y\zeta) d\xi\, d\zeta. \tag{6}$$

with

$$\sigma^0\rho((\xi, \zeta) = \langle Z(x, y)Z(x + \xi, y + \zeta)\rangle \tag{7}$$

Where$\rho(\xi, \zeta)$ is the surface correlation function, a stationary random process with zero mean and $\langle\,\rangle$denotes the ensemble average operator. In light of the previous research (Altese et al., 1996; Oh et al., 1992 and Fung et al., 1992), we assumed the correlation function as exponential which gives a better fit with the experimental data.

There are several models which convert the volumetric soil moisture to dielectric constant and vice versa (Dobson et al., 1981; Hallikainein et al., 1985). I used the the model given by Hallikainein et al., 1985 which takes into consideration the soil properties like texture and bulk density as follows:

$$\epsilon^\alpha = 1 + \frac{\rho_b}{\rho_s}(\epsilon_s^\alpha - 1) + \theta^\beta \epsilon_{fw}^\alpha - \theta \tag{8}$$

Where ϵ refers to the dielectric constant, θ is the volumetric soil moisture, α and β are the shape factor and the texture dependent coefficient respectively, ρ refers to density and the subscripts s, b, and fw refer to soil solids, bulk density and free water respectively.

3. Scatterometer Data and Field Measurements

A C-band scatterometer system was used in this study and have been described in details by Musiake et al., (1997). The Figure 1 (a) shows the van-mounted scatterometer taking measurements on the bare field. The radar system was employed at three polarizations, viz., HH, HV and VV and over four angles of incidence,i.e., 15^o, 23^o, 35^o and 43^o. Moreover, on almost every occasion of the experiment, the surface roughness and soil moisture measurements were recorded. A lazer roughness profile meter was employed to record a number of roughness measurements across and

along the field axis. The Fig 1(a) shows the lazer profiler in operation. The lazer profiler, which is driven by a stepper motor, can measure a surface profile with 1 mm horizontal resolution and 2 mm vertical accuracy. The profiler is connected to the laptop computer to record the measurements in X and Y directions. The horizontal resolution of the measurements on each occasion was maintained constant as 3 mm. Though the soil moisture measurements were recorded at the depth resolutions of 2 cm, 5 cm and 10 cm but in view of the penetration depth of the radar signals at C-band wavelength (Wilheit, 1975), only the 2 cm measurements recorded by volumetric methods were compared with the σ^0 measurement.

4. Data Analysis and Discussion

The following sections would discuss the experimental data, the relations between various surface characteristics and the radar backscattering coefficient σ^0. Also the sensitivity analysis performed would be discussed to have a thoroughly understanding of the influence of these characteristics on the radar response at different sensor configuration.

(1) Temporal Variations of σ^0

The Table 1 shows the relationships, i.e. coefficient of correlation and the slope obtained between the observed surface soil moisture and the radar backscattering coefficient σ^0. Though, the temporal relationships are reasonable for VV polarization and for all the angles of incidence but for other polarization, the relationships are week except at an incidence angle of 43^o. But this is in contrast to Sano et al., (1998) and Ulbay et al., (1979) results wherein they reported higher coefficient of correlation but compatible sensitivity of the σ^0 to soil moisture variations under varied roughness conditions. Geng et al., 1996 reported similar relationships as obtained in this experiment. The Figure 1(b-c) shows the temporal variation of the backscattering coefficient σ^0 for HH and VV polarizations and four angles of incidence employed in this experiment. The 15^o incidence angle was employed only from the 8th experiment. The dynamic range of the backscattering coefficient σ^0 during the conduct of the experiment is small especially for HH and VV polarizations. HV has comparatively better dynamic range for all the incidence angles used here. Also plotted on the figure is the temporal variation of the soil moisture. We can see on 7th experiment that despite an increase of more than 10% in the volumetric soil moisture, the backscattering coefficient has decreased by more than 5 dB for higher angles of incidence for HH polarization and a little less for 23^o incidence angle. The decrease is in response to smooth surface roughness conditions observed on 7th experiment. The decrease is obviously more at higher angles of incidence than at lower angles of incidence (Ulaby et al., 1979).

Table 1 Summary of the correlation coefficient and sensitivity of σ^0 using C-band scatterometer system over bare field

Polarization	Incidence Angle					
	23^o		35^o		45^o	
	ρ	slope	ρ	slope	ρ	slope
HH	.74	.35	.26	.11	0.28	.10
HV	.67	.47	.31	.23	.30	.22
VV	.76	.32	.62	.30	.67	.37

(2) Comparison Between Measured and Simulated Radar Data

The Integral Equation model was validated on three dates for both VV and HH polarizations. These dates are 21st May, 22nd June and 28 June. The values of the rms height have been observed as 0.34, 0.525 and 0.30 cm respectively while that of the correlation length as 14.5, 13.1, and 16 cm respectively. The simulations and observed measurements for HH polarization are plotted in Figure 1(d-e). We could get better agreement between the two at HH polarizations than at VV polarizations. The pattern is matching reasonably well for both the polarization with a decline in the σ^0 as a function of incidence angle. The exponential correlation function is assumed here.

Bracaglia et al., (1995) also reported a discrepancy when comparing the theory and experimental data over bare soils. He attributed it to the inaccuracies of the available surface models. while as Hoeben et al., reported very good agreements between the theory and the experiment for VV polarization over a range of incidence angles from 11^o to 23^o and frequency of 1-10 GHz but for 35^o angle of incidence, the deviations were quite higher than that observed here for C-band. Altese et al. (1996) also reported a wide scatter between the IEM model simulations and the ERS-1 backscattering coefficient values for VV polarization and at an incidence angle of 23^o.

(3) Sensitivity Analysis

A sensitivity of the IEM model simulations to the surface characteristics as well the radar configuration was performed to have a better understanding of the influence of these factors on soil moisture retrieval. The following subsections would deal with each of these influences separately:

The Figure 1(g-h) shows the sensitivity of the σ^0 to soil moisture variations for different frequencies, HH polarization and two angles of incidence, i.e., 23^o & 43^o on 7th experiment (28 June). The sensitivity reduces with the increase of incidence angle. For all the four frequencies tested in this analysis, a variation of soil moisture from 1% to 40% results in an increase of the backscattering coefficient values of 7 to 8 dB for HH polarization at 23^o incidence angle while as at 43^o angle, a similar change in soil moisture causes an increase in σ^0 from 5 to 6 dB depending upon the frequency. Because of the smooth nature of the surface, the σ^0 values are higher at lower angles of incidence compared to the higher ones. For VV polarization, a similar analysis results in an increase of around 8 dB for both lower (23^o) and higher (35^o) angles of incidence. For both VV and HH polarization at both lower and higher incidence angles, the sensitivity is quite high at lower values of the soil moisture and as the soil moisture increases, the sensitivity decrease.

The sensitivity analysis of backscattering coefficient to rms height has been performed for different dates. The plots in Figure 1(i-j) show the sensitivity on 21st May for HH polarization and two angles of incidence, when the soil moisture is lower (13.69%). It can be seen from the Figure that the σ^0 sensitivity to rm height is most strong of all the parameters tested during this sensitivity analysis. The sensitivity is very strong at lower values of the rms height and as the surfaces get rough and rougher, the sensitivity decreases markedly, especially for higher frequency signals. For L-band and above, the sensitivity is quite high even for rougher surfaces. The IEM model looses its validity for X-band frequency beyond the roughness values of 1.5 cm and that is reason of the discontinuity in the X-band simulations.

The sensitivity to the correlation length for different frequencies on 21st of May when the rms heigh was observed as 3.4 mm and the surface soil moisture was 16.23% for HH polarization is shown in Figure 1(k-l). Though the incidence angles do not affect the dynamic range of the change in the σ^0 as a function of correlation length, L but the magnitude of the σ^0 is lower by several decibels at higher angles of incidence than the lower angles. The polarization effects are not so marked on the correlation length sensitivity. Further, the higher frequencies are more sensitivity to the changes in the correlation length at low incidence angles than the lower frequencies with X-band showing the highest, followed by C-band, then L-band and the other one. The L-band sensitivity at higher incidence angles (43^0) is equally higher for both the polarizations. The L-band frequency shows insensitivity to the lower values of correlation length ($\langle 5cm$) for both HH and VV polarization at an incidence angle of 23^o. The 0.45 GHz frequency shows appreciable sensitivity to radar backscatter at lower values of correlation length but demonstrates week sensitivity at higher values of the parameter.

5. Conclusions

The radar backscattering coefficient σ^0 is sometimes more sensitive to small changes in roughness characteristics than to large changes in soil moisture. As observed on 7th experiment, a decrease of rms height from 5.25 mm to 3.0 mm did bring about a reduction of more than 5 dB for HH and HV polarization and a little smaller change for VV polarization, despite an increase of around 10% in the soil moisture. The small disturbances in the field, as noticed by the uprooting of weeds, can describe the surface roughness patterns and can not be assumed as constant.

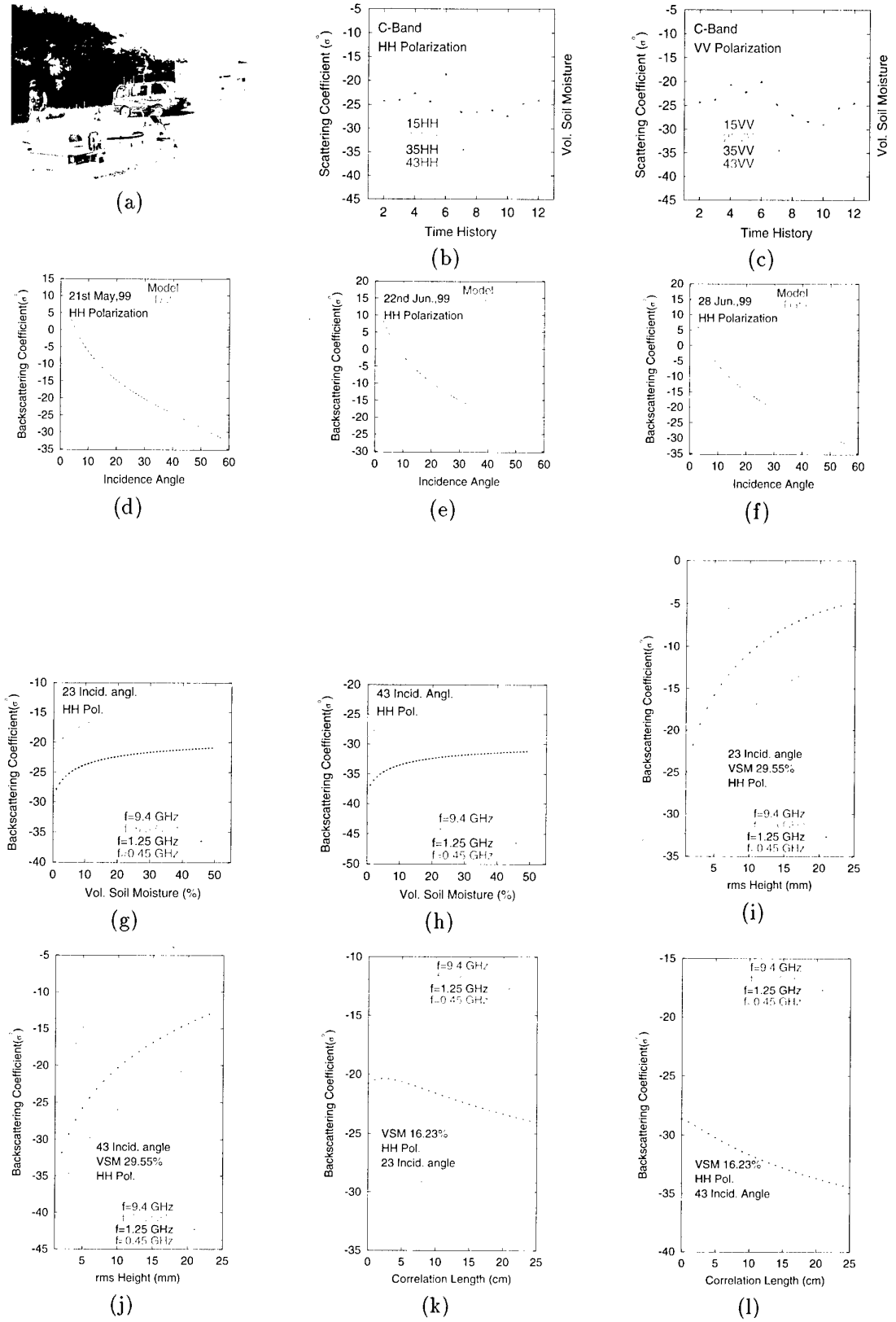


Fig. 1 This Figure is the composite of all the Figures refered in the paper: (a) shows the C-band radar system in operaton over a bare field; (b-c) shows the time history of radar observed scattering coefficient as a function of incidence angle and polarization; (d-f) shows the validation results of IEM model on differrent experiment dates; (g-h) shows the sensitivity analysis of radar to soil moisture for HH polarization and two angles of incidence; (i-j) shows the sensitivity analysis of radar to rms height for similar configuration while as the plots (k-l) show similar analysis for the correlation length

The better validation of the IEM model at HH polarization lends further confidence to the model. The disagreements between theory and experimental data at VV polarizations at higher angles of incidence may be due to the negligence of the volume scattering term in IEM model at higher angles of incidence. At higher angles, the volume scattering is expected to have an important influence at such low backscatter values.

The sensitivity analysis done for various surface characteristics have made their importance and influences on radar backscattering phenomena a lot more clear. Under smooth surface conditions, as observed in this field, the rms height has been observed to be the most sensitive parameter at lower values of the surface rms height. At higher values of rms height, for the higher frequencies, the radar backscattering coefficient σ^o gets insensitive or shows low sensitivity to the rms height at lower angles of incidence. The σ^o sensitivity to higher values of rms height is observed even at higher angles of incidence. The polarization effects are not so distinct.The L-band frequency and beyond are sensitive to rms height irrespective of the angle and the polarization.

The sensitivity to correlation length is also equally strong especially at higher angles of incidence for both HH and VV polarizations. The L-band frequency is noticed to be less sensitive to the correlation length at lower angles of incidence and insensitive to correlation length values less than 5 cm at lower angles of incidence (23^o). The 0.45 GHz frequency exhibits week sensitivity to correlation length after 5 cm. while as before that the sensitivity is appreciable.

The sensitivity to soil moisture is equally good for all the frequencies and both the angles tested here. But it is less than that for the surface rms height values.

REFERENCES

1) Altese, E., Bolognani, O and Marco Mancini (1996). Retrieving soil moisture over bare soil from ERS 1 synthetic aperture radar data: Sensitivity analysis based on a theoretical surface scattering model and field data. Water Resources Research, Vol. 32, No. 3, pp 653-661.
2) Dobson, M. C., and F. T. Ulaby (1986). Active microwave soil moisture research. IEEE Trans.Geosci. Rem. Sens., Vol. 24, No. 1, pp. 23-35.
3) Bracaglia, M., Ferrazzoli, P., and Guerriero, L., (1995). A fully polarimetric multiple scattering model for crops. Remote Sensing of Environment, Vol. 54, pp. 170-179.
4) Chen, K. S., Yen, S. K., and Huang, W. P. (1995). A simple model for retrieving bare soil moisture from radar scattering coefficients, Remote Sensing of Environment, Vol. 54, pp. 121-126.
5) Fung, A. K., Li, Z., and Chen, K.S.,(1992). Backscattering from a randomly rough dielectric surface, IEEE Trans. Geosci. Remote sens. , GE-30(2),356-369.
6) Geng, H., Hugh, Q, Gwyn, J, Brisco, B Boisvert and Brown, R.J., (1996). Mapping of soil moisture under C-band radar images. Canadian Journal of Remote Sensing,, Vol. 22, No. 1, pp. 117-126.
7) Hallikainen, M. C., F. T. Ulaby, M.T., Dobson, M. A. El-Rayes and Lin-Kun Wu (1985). Microwave dielectric behavior of wet woil- part I- Empirical models and experimental observations. IEEE Trans. Geosci. Rem. Sens., Vol. 23, No. 1, pp. 25-34.
8) Hoeben, R., Troch, P.A., Su, Z., Mancini, M., and Chen, K.S.,(1997). Sensitivity of radar backscattering to soil surface parameters: a comparison between the theoretical analysis and the experimental evidence. In Proc. International Geoscience and Remote Sensing Symposium, (IGARSS), Singapore, pp. 1368-1370.
9) Mushiake Katumi, T. Nakaegawa, M. Koike and T. Oki (1997). Soil moisture measurement using active microwave remote sensing II outdoor experiment, Journal of Japan Soc. Hydrol and water Resour., Vol. 10, No. 6, pp. 588-596.
10) Oh, Y., K. Sarabandi, and F. T. Ulaby (1992). An empirical model and an inversion technique for radar scattering from bare soil surfaces. IEEE Trans. Geosci. Rem. Sens., vol. 30, No. 2, pp. 113-123.
11) Sano, E. E. , M. S. Moran, A. R. Huete and T. Miura", (1998). C and multi-angle Ku-Band Synthetic Aperture Radar data for bare soil moisture estimation in agricultural Areas, Remote Sensing of Environment, Vol., 64, pp. 77-90.
12) Shakil, A. Romshoo, Koike, M., Nakaegawa, T., and Mushiake, Katumi (1999).Soil moisture determination under different field conditions using a scatterometer and space borne SAR systems, proceedings of the Asian Society of Remote Sensing, Vol. II, pp. 921-926, Hongkong, China.
13) Ulaby, F. T., G. A. Bradley and M. C. Dobson (1979). Microwave backscatter dependence on surface roughness, soil moisture and soil texture: Part II–bare soil. IEEE Trans. on Geosci. Electron., vol. 16, pp. 286-295.
14) Ulaby, F.T., R.K . Moore and A.K. Fung (1982). Microwave Remote sensing : Active and passive, Vol. 2, Artech House, Norwood, MA.
15) Wilheit, T. T., Jr. (1975). Radiative transfer in a plane stratified dielectric, NASA Report X-911-75-66, Goddard Space Flight Center, Greenbelt, M.D., pp 19.

VERIFICATION OF INSAR CAPABILITY FOR DISASTER MONITORING - A CASE STUDY ON CHI-CHI EARTHQUAKE IN TAIWAN -

Shoji TAKEUCHI[1], Yuzo SUGA[1], and Yoshinari OGURO[2]
[1]Professor, [2]Assistant-professor, Hiroshima Institute of Technology,
2-1-1, Miyake, Saeki-ku, Hiroshima 731-5193, Japan
Tel & Fax : (81)-82-922-5204, E-mail: sh-take@cc.it-hiroshima.ac.jp

A.J.CHEN
Professor, Center for Space and Remote Sensing Research, National Central University of Taiwan
Chung-Li, Taiwan

Chinatsu YONEZAWA
Researcher, Remote Sensing Technology Center of Japan
Roppongi First Bldg., 1-9-9, Roppongi, Minato-ku, Tokyo 106-0032, Japan

KEY WORDS : ERS/SAR, SAR interferometry, Chi-chi Earthquake, Coherence, Land displacement

ABSTRACT : The authors conducted a verification study on the capability of interferometric SAR (InSAR) technology for monitoring damages by Chi-chi earthquake occurred on Sep. 21, 1999 in Central Taiwan by using ERS-2/SAR data received at Center for Space and Remote Sensing Research (CSRSR). The items for verification are detection of damaged urban areas by building collapses, detection of land-slide areas, and extraction of land displacement patterns caused by the earthquake. We obtained positive results for supporting high capability of InSAR for detecting damaged urban areas and for extracting land displacement patterns in flat or semi-flat areas around Taichung City. On the other hand, for detecting landslide areas, InSAR did not work because of poor coherence of interferograms in mountainous regions by repeat-pass ERS-2/SAR data pairs, while SAR backscattering intensity by ERS-2/SAR was partly available for detecting land slide areas. Above results verified that InSAR by ERS/SAR is effectively used for disaster monitoring in urban or agricultural areas with flat or semi-flat topography, although InSAR is difficult to be used practically in steep mountainous areas with dense vegetation.

1. INTRODUCTION

On 21st of September in 1999 at 1:47 a.m. local time, a Ms=7.7 earthquake shook the central area of Taiwan. The epicenter was 160 km south-west of Taipei, the capital of Taiwan and near a small town Chi-chi. This is the largest earthquake on the Taiwan island in the 20th century, which caused 2470 fatalities, 11,305 injuries, 53,551 buildings totally collapsed, and 53,633 half collapsed. The total capital lost is estimated to be US $: 11.8 billions. In addition, as the results of the earthquake, wide spread landslides occurred in Central Taiwan.

Center for Space and Remote Sensing Research (CSRSR), which has been receiving SPOT data and SAR data from ERS-2 and RADARSAT operationally, started the intensive reception of SPOT data just after the earthquake, and analyzed these SPOT data to detect land slide areas as early as possible and to monitor their temporal changes (Chen and Wang, 2000). In this study, the authors studied the applicability of another data source, ERS-2/SAR data received at CSRSR, for monitoring damages or environmental changes caused by the earthquake. Currently the interferometric SAR (InSAR) technology has been one of the important and effective approaches using SAR data for disaster or environmental monitoring. Therefore, we attempted to conduct three kinds of interferometric analyses, the detection of the damaged urban areas using coherence information, the extraction of land displacement patterns using two-pass differential interferometry, and the detection of landslide areas in mountainous regions using coherence and intensity.

2. TEST SITE, DATA AND PROCESSING

The test site is located at the central area of Taiwan. Figure 1 shows ERS-2/SAR intensity image of the test site acquired on Sep. 23, 1999. The left-half areas of the image are almost flat or semi-flat areas including some urban areas, the biggest of them is Taichung City located in the upper part of the image. The right-half areas are rather steep mountainous areas, where big geometric distortions of SAR data are recognized due to foreshortening effect brought by ground height and a small incidence angle of ERS/SAR. The epicenter is indicated by a cross located in the lower-right part of the image.

Four repeat-pass ERS-2/SAR data acquired on Jan. 21, May 6, Sep. 23 and Oct.28 in 1999 were used as the test data. For interferometric processing, four data pairs were used as shown in Table 1. The table also shows nominal values of the perpendicular baseline component for each pair. The second and third data pair (pair-2 and pair-3) includes the earthquake occurrence between the times of observation, while pair-1 was acquired before the earthquake, pair-4 after the earthquake, and both pairs do not include the earthquake occurrence.

These SAR data were processed from signal data to generate multi-look intensity images, coherence images and differential interferograms using 3dSAR processor developed by Vexcel Corporation in U.S.A. The size for multi-look was 2 range pixels by 10 azimuth lines, which resolution was about 40 by 40 meters on the ground. The coherence images were generated by computing the complex correlation coefficient in a small corresponding patch using the two single-look complex (SLC) images registered each other as follows;

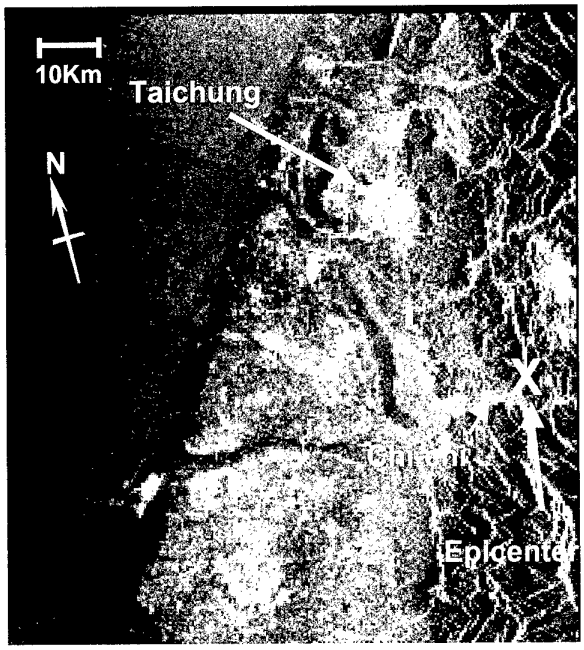


Fig.1. ERS-2/SAR intensity image (Sep. 23,1999). (©ESA/ERS 1999)

$$\text{Coherence} = \frac{\left|E(C_1 C_2^*)\right|}{\sqrt{E(C_1 C_1^*)E(C_2 C_2^*)}}$$

where C_1 and C_2 are complex values for the first and the second data, * means complex conjugate and E( ) means the expectation in the corresponding patch. The size of the corresponding patch was 2 pixels by 10 lines, which was the same as the pixel size after multi-look processing.

Table 1. Data pairs of ERS/SAR for interferometric analysis. (I: Include the earthquake, N: Not include)

Data pair	Data combination	Baseline (perp.comp.)	I or N
Pair-1	Jan. 21 - May 6, 1999	96 m	N
Pair-2	May 6 - Sep. 23, 1999	213 m	I
Pair-3	Jan. 21 - Sep. 23, 1999	309 m	I
Pair-4	Sep. 23 - Oct.28, 1999	224 m	N

The differential interferograms were generated by a rather complicated procedure, in which orbital fringes and topographic fringes are removed almost perfectly from the initial interferograms generated by computing phase differences between two SLC data which were co-registered each other precisely. The topographic fringes were removed by subtracting the simulated topographic fringes using a digital elevation model (DEM) with 100 m by 100 m pixel spacing from the real interferograms.

3. DETECTION OF DAMAGED URBAN AREAS USING COHERENCE INFORMATION

Figure 2 shows an example of the overlaid images of two ERS-2/SAR multi-look intensity images acquired on May 6 and Sep. 23, with the color assignment of red for the former and cyan for the latter. The test site is the surrounding area of Taichung City. From this image, it is almost difficult to interpret the intensity changes due to the earthquake occurrence in all urban areas located inside the image. By the report for the survey of urban damages, the urban areas in Dongshi, Puli and Wufeng located inside the image were damaged severely (Kokusai Kogyo Co. LTD.,1999). Especially in Dongshi and Puli, more than 50 percent of the buildings in the central urban areas were collapsed.

Figure 3 shows the overlaid image of two coherence images, which were obtained from the data pair-1 and pair-2 respectively. Red color was assigned to the coherence by pair-1 and cyan was assigned to the coherence by pair-2. It is clearly indicated in Figure 3 that the urban areas in Dongshi, Puli and Wufeng are colored as red, which means that the coherence by pair-2 significantly decreased compared with that by pair-1. On the other hand, in Taichung and Fengyuen there hardly seen red colors inside the urban areas. By the report, the central urban areas in these two cities were not damaged seriously by the earthquake, although point-wise damages were seen in some small parts of those sub-urban areas.

From the two figures described above, the effectiveness of the coherence information compared to the intensity information for damage detection in urban areas is definitely clear. We evaluated the changes of intensity and coherence by the normalized difference of two power data and two coherence data respectively. They are defined as follows;

$$\text{Power_ND} = \frac{\text{Power(May 6)} - \text{Power(Sep. 23)}}{\text{Power(May 6)} + \text{Power(Sep. 23)}} \quad \text{Coherence_ND} = \frac{\text{Cohrence (pair-1)} - \text{Coherence(pair-2)}}{\text{Cohrence (pair-1)} + \text{Coherence (pair-2)}}$$

All the power data were normalized by the maximum power value among all the data in the two dates. The left and right graphs in Figure 4 show the results of the evaluation of the changes in the intensity and the coherence respectively in some sample urban areas in Taichung and Nantou Prefecture. The group from Dongshi to Jungliau in the right side (attached *) is the group for severely damaged urban areas and the group from Tsautuen to Shalu in the left side is the group for non-damaged or slightly damaged urban areas. For Taichung City, the data of three sample areas were averaged. In the left graph in Figure 4, any significant separation is not seen between the damaged urban group and non-damaged urban group by Power_ND. On the other hand, in the right graph, two groups are clearly separated by Coherence_ND.

We also attempted to detect the damaged urban areas using SPOT panchromatic images acquired before the earthquake (on Feb. 9, 1999) and after the earthquake (on Sep. 27, 1999). However, in the SPOT image, it was quite difficult to interpret the image differences between damaged and non-damaged urban areas. It was also difficult to interpret the changes on spatial patterns because the resolution of SPOT panchromatic data is 10 meters and this resolution is still insufficient for detecting the changes of the shape or the size of buildings by collapsing.

Above results by the intensity and coherence of ERS/SAR verifies that the coherence is superior to the intensity as the parameter for detecting damaged urban areas by building collapse. In addition, these damaged areas are difficult to detect even by comparing two SPOT panchromatic images acquired before and after the earthquake. These facts are considered due to higher sensitivity of the coherence to ground surface changes compared with the intensity of SAR backscatter or reflection of sun light. This high sensitivity is considered to be brought by the fact that the coherence is significantly affected by phase variation and the spatial scale generating phase variation is the order of wavelength of microwave and much smaller than the ground resolution of ERS/SAR or SPOT panchromatic data.

4. EXTRACTION OF LAND DISPLACEMENT BY DIFFERENTIAL INTERFEROGRAM

We attempted to generate differential interferograms from the first three pairs indicated in Table 1. Figure 5 (a), (b),and (c) shows all of the obtained differential interferograms. The phase patterns in these interferograms indicate the phase differences due to land displacement in the slant range direction under the assumption that the phase patterns caused by orbit difference (orbital fringes) and topography (topographic fringes) are removed perfectly. For the confirmation of removal of both fringes, the phase patterns (a) by pair-1 is a key result, because this pair does not include the earthquake occurrence and so it is hardly possible to get the phase patterns due to land displacement. In fact, the phase patterns in the interferogram by pair-1 are almost flat, which supports that both fringes are almost completely removed. Another important key is the consistency of the phase patterns between the results from different data combinations. This consistency can be investigated by subtracting the interferogram by pair-2 from that by pair-3. The result is shown in Figure 5 (d). The phase patterns in the interferogram (d) are also almost flat and consistent with those by pair-1, which interval corresponds to the difference of the intervals by pair-3 and pair-2.

The investigation described above on all of the obtained intergerograms clearly supports that the differential interferometry by ERS/SAR succeeded to extract the phase patterns related to the land displacement caused by Chi-chi earthquake. However, the usable phase patterns are only available in flat or semi-flat areas. In mountainous areas, the interferograms are almost noisy and they can not bring any information about land displacement. This result clearly comes from poor coherence by ERS/SAR interferometry in mountainous areas as pointed out in the beginning of this section. Therefore the application of differential interferometry by ERS/SAR is actually limited to the areas where topography is flat or semi-flat and the vegetation cover is relatively less like urban or agricultural areas.

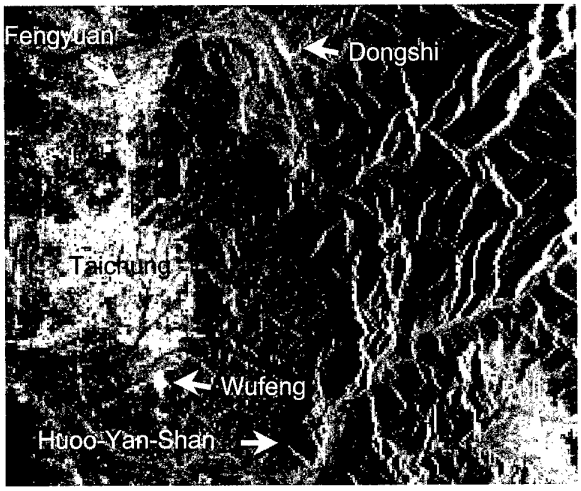


Fig.2. Overlaid image of ERS-2/SAR intensity images acquired on May 6 (Red) and Sep. 23 (Cyan).

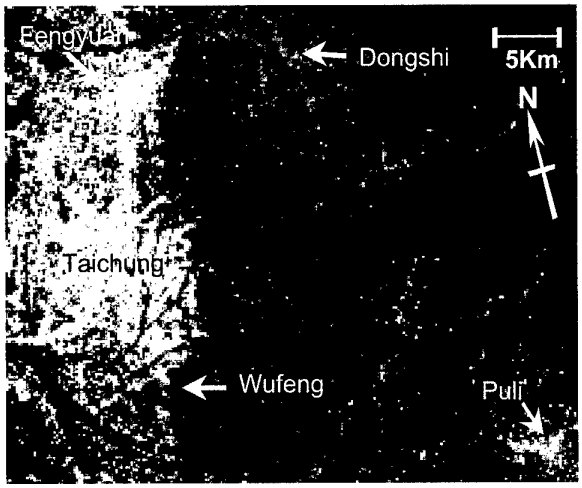


Fig.3. Overlaid image of two coherence images by pair-1(Jan.-May)(Red) and pair-2(May-Sep)(Cyan).

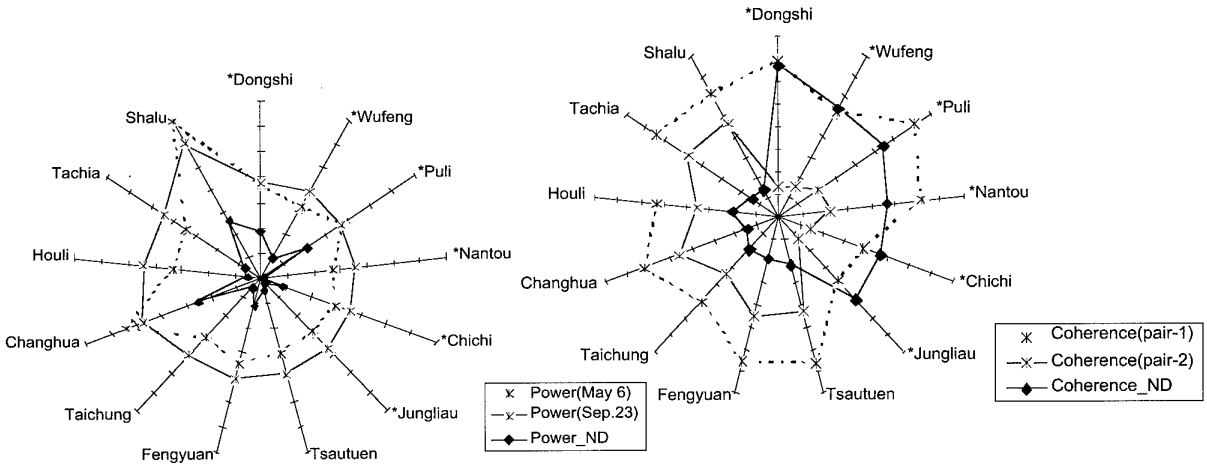


Fig.4 Results of evaluation of SAR intensity changes (left) and coherence changes (right) due to the earthquake in the sample urban areas in Taichung and Nantou Prefectures (except Changhua). (* denotes severely damaged urban group).

From the above results, the land displacement patterns due to Chi-chi earthquake are possible to extract from the differential interferograms shown in Figure 5. The amount of displacement in a slant range direction is a half of the wavelength (a half of 5.6 cm for ERS/SAR) for one cycle of phase patterns. The direction of the displacement is toward satellite if the phase values decrease toward satellite, and backward satellite if the phase values increases toward satellite. As all test ERS/SAR data were acquired in a descending orbit, the radar signals were illuminated from the right side of the images. In the interferograms of Figure 5 (b) and (c), as the phase decreases in the right direction, namely toward satellite, the directions of the displacement are all toward satellite if the left-side edge portion (actually the coastal line of the left part of the images) does not move.

Figure 6 (a), (b) and (c) show the displacement patterns obtained from the three differential interferograms in Figure 5 (a), (b) and (c) respectively. As the amount of displacement is only computed in the areas where phase unwrapping was succeeded, the displacement patterns were not obtained in almost of mountainous areas where the coherence was very poor and so the displacement fringes could be hardly obtained. In addition, the displacement patterns in Figure 6 were computed as the *relative* displacement inside the whole areas where phase unwrapping was succeeded because the displacement is possible to compute only from the relative changes of phase patterns.

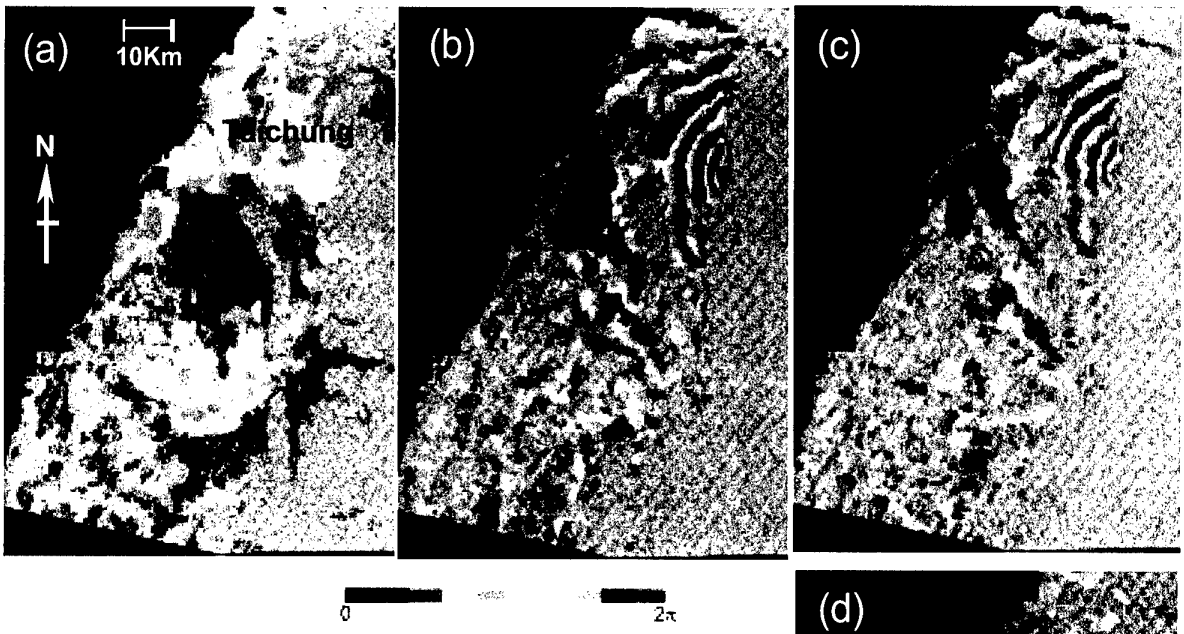


Fig.5. Differential interferograms obtained by ERS/SAR.

(a) Pair-1 (Jan. 21 – May 6, 1999).

(b) Pair-2 (May 6 – Sep. 23, 1999).

(c) Pair-3 (Jan. 21 – Sep. 23, 1999).

(d) Phase difference patterns between (b) and (c).

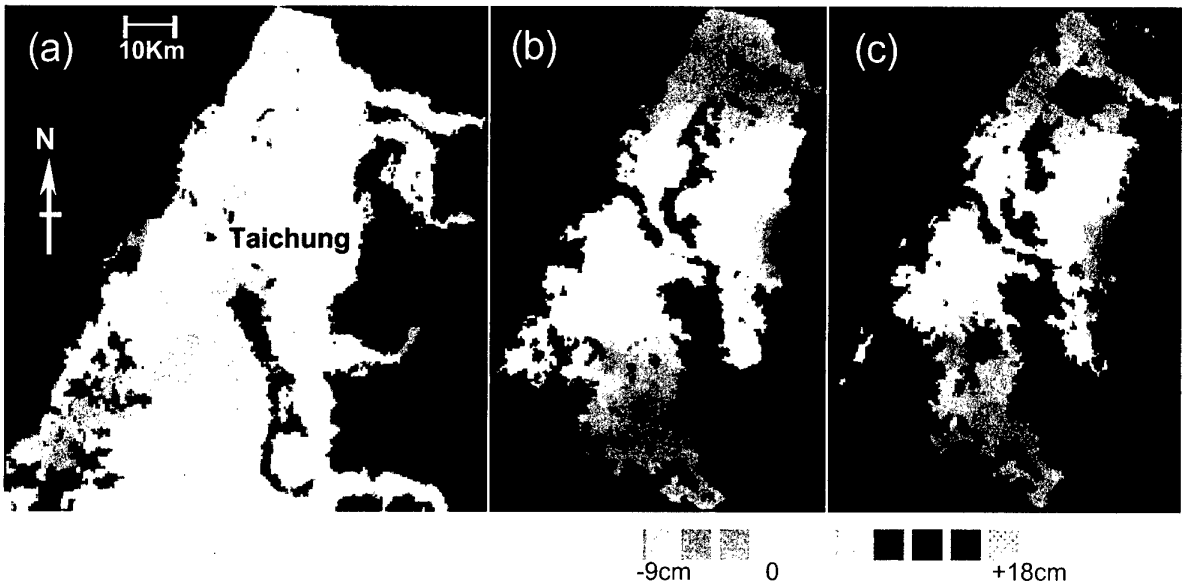


Fig.6. Displacement patterns obtained from the differential interferoframs in Figure 5.
[(a) : Pair-1, (b) : Pair-2, (c) : Pair-3]

As the displacement values in Figure 6 indicate the displacement in a slant range direction, it is necessary to convert the displacement values to those in a vertical or a horizontal direction, although it is impossible to decide either vertical or horizontal only by the interferograms. The conversion is done by the multiplication of the inverse of $\cos\theta$ (θ denotes incidence angle of SAR) for a vertical displacement and $\sin\theta$ for a horizontal displacement respectively. As θ is approximately 23 deg. for ERS/SAR, the multiplication factor is 1.09 for a vertical and 2.56 for a horizontal direction respectively. As the maximum relative displacement value seen in Figure 6 (b) and (c) is about 22 cm in a slant range, the maximum displacement value is about 24 cm for a vertical and about 56 cm for a horizontal direction. As the result of the comparison between the displacement patterns in Figure 6 and those by GPS observation (National Cheng-Kung Univ., 1999), the displacement patterns by SAR were proved to be fairly compatible to those by GPS in both of direction and amount.

5. DETECTION OF LANDSLIDE AREAS USING COHERENCE AND INTENSITY

We also attempted to detect landslide areas in mountainous regions caused by the earthquake using the change of coherence and intensity. For the extraction of coherence changes, the coherence images by pair-1 and pair-4 were compared each other. The reason why these two pairs were used was that there might be some possibility for coherence increase in landslide areas after the earthquake because forest vegetation was almost lost due to the landslide. However, the result was that coherence by pair-4 (after the earthquake) was extremely low in mountainous regions and still same as that by pair-1 (before the earthquake). This result indicates some limitation of InSAR by C-band SAR in steep mountainous regions. On the other hand, it was found that the intensity by SAR multi-look images partly decreased in landslide areas after the earthquake. Therefore, some of the landslide areas were possible to be detected using these intensity changes, although the landslide areas in the slopes facing to radar illumination were hardly detected due to a big foreshortening effect in ERS-2/SAR images. This result indicates that backscattering intensity is partly available to detect landslide areas even in mountainous regions.

6. CONCLUSION

As the first result of this study, the coherence information was proved to be an effective parameter to detect damaged urban areas by the earthquake, which has been also verified by another case study for The 1999 Great Hanshin-Awaji Earthquake (Yonezawa and Takeuchi, 1999). The consistency between the two case studies seems quite important and valuable because it clearly enhances that SAR observation in which a good interferometreic condition is maintained is significantly important for disaster monitoring by SAR data. The second result suggested that differential interferometry by ERS/SAR is possibly effective to extract land displacement by an earthquake together with some limitation. In flat or semi-flat areas where main land covers are occupied by urban or agricultural lands, the differential interferogframs obtained by ERS/SAR brought reasonable displacement information caused by the earthquake. The third result suggested an essential limitation of C-band InSAR in steep mountainous regions. The first two successful results clearly enhance the importance of interferometric SAR for disaster or environmental monitoring using space-borne SAR data.

REFERENCES

Chen A.J. and Chien Ying Wang. 2000. Using SPOT Imageries to Monitor Landslides in Chi-chi earthquake. Presented At International Workshop 2000 in HIT on Generation of Advanced Earth Environmental Information.

Kokusai Kogyo Co., LTD. 1999. Record of Great Taiwan Earthquake on September 21, 1999 (in Japanese).

National Cheng-Kung University. 1999. Satellite Geoinformatics Research Center, 921 Chi-chi earthquake damaged area satellite control points displacement map, http://www.sgrc.ncku.edu.tw,

Yonezawa,C. and S.Takeuchi. 1999. Detection of Urban Damage Using Interferometric SAR Decorrelation. Proceeding of IGARSS'99, pp925-927.

SAR INTERFEROMETRY APPLICATIONS IN THE PHILIPPINES USING ERS-1, ERS-2 AND JERS-1: CASE STUDIES IN MAYON AND TAAL VOLCANOES

Salvador, J.H.G.[1], Kanbara, H.[2], Abundo, R.[1], Tsukada, M.[3],
Hirose, K.[3], Dayao, A.[4], Corpuz, E.[5]and Baloloy, A.[5]

[1]Senior Science Research Specialist, Mines and Geosciences Bureau
North Avenue, Diliman, Q.C. 1104 Philippines. Email: bernards@pacific.net.ph

[2]Senior Geologist, Nippon Mining and Metals Co. Ltd.
7-10 Toranomon 2-chome, Minatoku-Tokyo, Japan. Email: kanbara@tankai.co.jp

[3]Earth Remote Sensing Data Analysis Center
Forefront Tower 3-12-1 Kachidoki Chuo-ku Tokyo 104, Japan. Email: hirosc@ersdac.or.jp

[4]Mines and Geosciences Bureau Regional Office No. 5 Daraga, Albay, Philippines

[5]Philippine Institute of Volcanology and Seismology
C.P. Garcia Avenue, U.P Diliman Campus, Diliman, Q.C. 1104, Philippines

KEY WORDS: Interferometry, Mayon Volcano, Taal Volcano

ABSTRACT

SAR Interferometry studies were conducted in Mayon and Taal Volcanoes in the Philippines. In Mayon, we used the ERS-1 and ERS-2 data. In Taal, we used the JERS-1 SAR data. In both cases, differential SAR interferograms were successfully generated.

For Mayon Volcano, we applied the three-pass method. Three ERS-1 datasets dated 1993/11/17, 1993/10/13 and 1997/10/10 were utilized. The baseline perpendiculars are –21m for first pair and –156m for the second pair. Two coherence maps and two interferograms were used. Further processing produced a differential interferogram. The result was refined using a "helper phase". The measured displacement along the southwest flank of the volcano amounted to 6cm and roughly coincides with the tiltmeter record in the Mayon Observatory.

We also applied the two-pass method to the available pair of ERS-2 data dated 1999/03/20 and 1999/08/07. The baseline perpendicular is 105m. A coherence map and interferogram was generated. A DEM was integrated to produce a differential interferogram. The measured displacement along the southwest flank of Mayon Volcano is up to 30cm. Later in February 2000, the volcano erupted.

For Taal Volcano, the three-pass method was applied to the JERS-1 data dated 1995/11/15, 1995/02/24 and 1995/12/29. The baseline perpendiculars are 171m for first pair and 741m for the second pair. The resulting differential interferogram shows displacement of more than 10cm along the southwest flank of Taal Volcano.

1. INTRODUCTION

Recent technological advances in radar image analysis show those interferometry techniques using SAR data is able to detect changes in the earth's surface in the order of one to several mm. The principle of SAR interferometry is explained in many documents such as Dixon (ed., 1995), Gen and Van Genderen (1996), Fujiwara and Tobita (1999), and Tanaka and Nakano (1997). The technique was used

to detect surface changes due to earthquakes (Massonnet et al., 1993), volcanic activity (Massonnet et al., 1995) and glacier movements (Goldstein et al., 1993) among others. The application of SAR interferometry to study deformations in the Mayon and Taal Volcanoes in the Philippines is the subject of this paper. In Mayon, we used the ERS-1 and ERS-2 data. In Taal, we used the JERS-1 SAR data. In both cases, differential SAR interferograms were successfully generated.

This paper presents some results of the three-year Joint Study called RP-ERSDAC Remote Sensing Project. This collaboration project involves the Earth Remote Sensing Data Analysis Center (ERSDAC) of Japan, the Philippine Mines and Geosciences Bureau (MGB), the Philippine Institute of Volcanology and Seismology (PHIVOLCS) and the Philippine National Oil Company-Energy Development Corporation (PNOC-EDC). The project is part of ERSDAC's "***Technology Development for Phased Array type L-band Synthetic Aperture Radar (PALSAR) data***": ERSDAC designated Nippon Mining & Metals Co., Ltd. (NMM) as the contractor to implement the work.

2. BRIEF GEOLOGIC SETTING OF THE STUDY AREAS

Taal Volcano near Manila and Mayon Volcano in Albay belong to the Philippine Mobile Belt described by Gervacio (1966, 1971). To the east of the study areas, we find the west subducting Philippine Trench. To the west, we find the east subducting Manila Trench. In between, we find the 1,200-km-long left-lateral strike-slip Philippine Fault cutting across the Philippine Archipelago (Aurelio, 1997). Two volcanic rows, the western and the eastern belts, correspond to these sinking plates. The western belt runs from Mindoro Island to the Verde Island Passage. This belt includes Taal and Pinatubo Volcanoes. The eastern belt corresponds to the Philippine Sea Plate. It runs from the Bicol Peninsula in Luzon down to Mindanao. It includes Mayon and Bulusan Volcanoes.

2.1 Mayon volcano

Mayon Volcano is an active volcano with highest elevation of about 2,462masl. It has a long history of eruptions. The first recorded was in 1616 and the latest in February 2000. It has erupted 45 times. The most destructive took place on February 14, 1814, killing at least 1,500 people (Moore and Melson, 1969). The eruption cycle is from 10 to 12 years. It erupted in the years 1928, 1938, 1947, 1968, 1978, 1987,1993. During the last eruption, more than 5,000 people were evacuated.

2.2 Taal Volcano

Taal Volcano, located 40-km southeast of Manila, is one of the most active volcanoes in the world. It is composed of between two and four coalesced lake-filled calderas with a central active volcanic center called the Volcano Island. The volcanic center has erupted about 40 times since 1540. Major eruptions occurred in 1574, 1911, and 1965 resulting in several thousand deaths. Taal Volcano has been restless since early 1991, with earthquake swarms, new steaming, and rise in temperature of the main Crater Lake.

In 1994, an intrusion of magma was observed underneath Taal near the Crater Lake. The Crater Lake's water temperature rose and high temperature volcanic gas were emitted. The gas contained much SO_2 and the water in the crater lake became strongly acidic. The earthquake swarm concentrated in the Crater Lake and in the Calawit district in the vicinity. By this activity, the southeast part of the Volcano Island upheaved by about 15cm. Presently, Taal volcano is Alert Level Zero, meaning there is no danger of the eruption.

3.0 Differential SAR Interferometry

For this study, we used the repeat pass method that utilized two spatially close radar observations of the same area separated in time and using only one antenna or two different sensors having nearly identical radar system parameters. The repeat pass method can be "two-pass" or "three-pass". The former needs a digital elevation model (DEM) data to simulate the topographic fringe. The latter has the advantage of removing the topographic fringe element by using two interferograms.

Four JERS-1 SAR images for Mayon and eight for Taal were accumulated during the six and a half years period from 11 February 1992 (JERS-1 satellite launch) until 12 October 1998 (JERS-1 stopped). Since then, the ERS SAR was used to continue observing the study area. The ERS data is being received at the Chung-Ii station (Space and Remote Sensing Research Center, National Central University) in Taiwan.

Generally, the suitable pairs for SAR interferometry are those where the baseline perpendicular (Bp) distance and the acquisition interval are both short. These data were prioritized and selected. From them, we generated the initial interferograms. We processed the data using the VEXCEL 3D SAR Processing Software Ver. 2.27 in the Unix Platform. The DEM in each study area was digitized from existing topographical maps published by National Mapping & Resource Information Authority (NAMRIA) of the Philippines.

For Mayon Volcano, we applied the three-pass method on the first set of data pairs. Three ERS-1 datasets dated 1993/11/17, 1993/10/13 and 1997/10/10 were utilized. We also applied the two-pass method to the second set of ERS-2 data pair dated 1999/03/20 and 1999/08/07 and a DEM. For Taal Volcano, the three-pass method was applied to the JERS-1 data dated 1995/11/15, 1995/02/24 and 1995/12/29. Global Positioning System (GPS) measurements were made over Mayon Volcano during 1997 to 1999. However, time and space does not allow presentation of the GPS measurement data and results in this occasion.

4. Results and Discussions

The surface of the earth is said to have changed whenever $\lambda/2$ (2.8cm) was changed along the look direction of the satellite. The phase difference, which was obtained from the phase-unwrapping processing from 2π radian, was converted into the amount of change or deformation.

4.1 Mayon Volcano

The three-pass method was applied to the first three ERS-1 datasets dated 1993/11/17, 1993/10/13 and 1997/10/10. The Bp is –21m for first pair and –156m for the second pair. Two coherence maps and two interferograms were produced. The area with high coherence was near the city and along the southwest the foot of the Mayon Volcano. This area corresponds to the lava flow and the pyroclastic flow deposited during the eruptive activity in 1993 or 1984. In this area with high coherence, it is thought that vegetation is scarce or the area is almost bare ground.

Further processing produced a differential interferogram. The result was refined using a "helper phase". About 6cm displacement was measured along the southwest flank of the volcano near the crest. This measured displacement roughly coincides with the tiltmeter record from January 1993 to December

1997 from the Mayon Rest House Observatory. For the water tube tiltmeter data the line A-C indicates the direction towards the summit of the volcano while the line A-B is perpendicular to line A-C. The rising curve of the A-C line shows that the crest rose gradually although there is a period when the meter broke down.

We applied the two-pass method to the second set consisting of ERS-2 data dated 1999/03/20 and 1999/08/07. The Bp is 105m. A coherence map and interferogram were generated. A DEM was integrated to produce a differential interferogram. The measured displacement along the southwest slope of Mayon Volcano is up to 30cm (fig1). It is viewed that this corresponds to some magmatic movements underneath the volcano. Later in February 2000, the volcano erupted.

In general, the changes between 1999/08/07 and 1999/03/20, and between 1993/11/17 and 1997/10/10 were detected using SAR interferometry technique. The results show that in the former, the vicinity of the crest expanded by about several cm. In the latter, the slope dilated not the crest. The amount of the change cannot be quantitatively evaluated from the data of the tiltmeter meter alone. However, the amount of change obtained as a result of SAR interferometry is thought to be the one being affirmed by the tiltmeter record. This is further collaborated by the GPS measurement results obtained over Mayon Volcano during 1997 to 1999. However, time and space does not allow presentation of the GPS data and results in this occasion.

3.2 Taal Volcano

The DEM generated for Taal volcano has a size of 9km by 9km. Since this size was too narrow to be utilized by the processing software, the DEM was not used and the three-pass method was applied on the JERS-1 data. Three data dated 1995/11/15, 1995/02/24 and 1995/12/29 were utilized. The Bp is 171m for first pair and 741m for the second pair. The resulting differential interferogram shows displacement of more than 10cm along the southwest flank of Taal Volcano. There was also some subsidence near the southwest lakefront going towards the crater. For now, we do not have observation data to verify this detected amount of change.

6.0 Summary and Conclusions

We examined the application of SAR interferometry to study deformations in the Mayon and Taal Volcanoes in the Philippines. We used the JERS-1 SAR and ERS SAR data. We applied the differential interferometry technique to detect surface change in both volcanoes. We used the repeat pass method (two- or three-passes). In both cases, differential SAR interferograms were successfully generated.

In Mayon, both two- and three passes were applied. Both methods succeeded in detecting surface deformation in limited areas. The first set using three ERS-1 datasets dated 1993/11/17, 1993/10/13 and 1997/10/10 shows displacement along the southwest flank of the volcano amounting to 6cm. This roughly coincides with the tiltmeter record in the Mayon Observatory.

We also applied the two-pass method to the second set of ERS-2 data dated 1999/03/20 and 1999/08/07. The measured displacement along the southwest flank of Mayon Volcano is up to 30cm.

In the first dataset, the vicinity of the crest has expanded by about several cm. In the second set, it is the slope that expanded and not the crest. It is viewed that the expansion of the slope in the second set represents magmatic movements underneath the volcano. Later in February 2000, the volcano erupted.

We successfully generated interferograms using the JERS-1 SAR data for Taal Volcano. For Taal Volcano, the three-pass method was applied to the JERS-1 data dated 1995/11/15, 1995/02/24 and 1995/12/29 The resulting differential interferogram shows displacement of more than 10cm along the southwest flank of Taal Volcano.

As a whole, while the technique may have successfully produced differential interferogram, we still need to refine our methods. Much research is still necessary.

References

Aurelio, M., Barrier, E., Gaullon, R., and Rangin, C., 1997,Deformation and Stress States along the Philippines Fault: Implications to Wrench Fault Tectonics, Journal of Asian Earth Sciences, Vol.15, and Nos. 2-3, p.107-119.

Dixon, T. H. ed., 1995,SAR Interferometry and Surface Change Detection. RSMAS Technical Report TR95-003. Report of a Workshop held in Boulder, February 3-4,1994. 97pp., Colorado.

Fujiwara, S., and Tobita, M., 1999, SAR interferometry techniques for precise surface change detection. Journal of the Geodetic Society of Japan, Vol.45, No.4, p.283-295, (in Japanese).

Gervacio, F.C., 1966,A Study of the Tectonics of the Philippines Archipelago, The Philippines Geologist. Vol. XX, no.2, p.51-75. Reprinted in the Journal of the Geological Society of the Philippines, 1995. Vol. L, no.3, p.149-167.

Gervacio, F.C., 1971,Geotectonic Evolution of the Philippines, Journal of the Geological Society of the Philippines", vol.25, p.18-38.

Gens, R. and Van Genderen, J. L., 1996, SAR interferometry - issues, techniques, applications. Int. J. Remote Sensing, Vol. 17, No.10, 1803-1835.

Massonnet, D.,and Rabaute, T., 1995. Radar interferometry: Limit and Potential. IEEE Transactions on Geoscience and Remote Sensing. Vol.31, p454-464.

Massonnet, D., Rossl, M., Carmona, C., Adragna, F., Peltzer, G. and Rabaute, T., 1993, The displacement field of the Landers Earthquake mapped by radar interferometry. Nature,vol.364,p.138-142.

Moore, J. G., and Melson, W.G., 1969, Nuees ardentes of the 1968 eruptions of Mayon Volcano, Philippines, Bulletin Volcanologique, Vol. 33, p.600-620.

Tanaka, A., and Nakano, T., 1997, Some problems on displacement field mapped by SAR interferometry. Journal of the Seismological Society of Japan, "Jishin", vol.50, p.89-99, (in Japanese).

The 21st Asian Conference on Remote Sensing
December 4-8, 2000 Taipei, TAIWAN

A Study on Differential Interferometry in Subsidence

王志添[1] 王顯達[2] 陳滌清[3] 陳乃宇[4] 梁隆鑫[5]
C. T. WANG[1], H. T. WANG[2], D. C. CHERN[3], N. Y. CHEN[4], L. S. LIANG[5]

KEY WORDS: Differential Interferometry、Subsidence

ABSTRACT： In this study, the technique of differential interferometric synthetic aperture radar (DInSAR)was used to locate the displacement field and to estimate the terrain subsidence of a 45 km x 25 km coastal area, Ton-Kang, southwestern Taiwan. We performed a three-pass differential interferometry from three SAR images from ERS1 and ERS2, dated Jan. 31, 1996, Feb. 1,1996, and May 16, 1996, respectively. The first two images were taken in tandem mode and thus preserving relatively high coherence, from which a DEM was generated with reasonable accuracy except for some mountainous areas. The third image was taken later, and was used to find possible displacement filed during that period through the differential process.

The subsidence of this area has been the subject of an extensive GPS study (Central Geological Survey) from November 1996 to July 1997. Comparison between GPS measurements and DInSAR results are quite favorable both in the pattern of subsidence and in its magnitude (about 2cm/month). We conclude that, given suitable SAR images, the DInSAR technique can be a useful tool for monitoring the earth surface displacement even for a subtropical, densely vegetative area like Taiwan.

1 Assistant Research Scientist, CSRSR, National Central University
2 Professor, CSRSR, National Central University
3 Professor, CSRSR, National Central University
4 Associate Research scientist, CSRSR, National Central University
5 Technician, CSRSR, National Central University

1. Introduction

Radar interferometry is a technique for extracting three-dimension information of the Earth's surface by using the phase content of the radar signal as an additional information source derived from the complex radar data. It was first used in observation of the surface of Venus and the Moon. Zebker (Zebker, 1992) and Madsen (Madsen, 1993) presented the practical results of observations with side-looking airborne radar. Zebker (Zebker, 1994) presented accuracy of using ERS1 interferomtry to estimate DEM. Goldsten (Goldsten, 1988) used phase unwrapping to solve the phase discontinuity of the interferogram. Bone (Bone, 1991) made use of mask of local phase discontinuity to unwrap phase. Regarding application of displacement filed, Gabtiel (Gabtiel, 1989) estimated displacement using differential interferometric synthetic aperture radar (DInSAR). Massonnet (Massonnet, 1993) studied earth deformation using differential interferometry due to earthquake. Carnec (Carnec, 1996) gave detail analysis of accuracy of displacement using the DInSAR technique.

There are now many major research groups actively involved in developing SAR interferometric techniques and their applications. In the U.S.A., most of the research is going on at JPL, where Zebker and others (Zebker, 1992/1994) are working on both airborne and satellite SAR interferometry. In Canada, research is mainly carried out by CCRS focusing on airborne systems, and is now also starting on satellite systems since the successful launch of RADARSAT1. In Europe, some of the major research centres specializing in SAR interferometry including Hartl's team at Stuttgart, Germany, Prati and Rocca's research group in Milan, Italy, Vetrella's team at CO.RI.S.T.A., Naples, Italy and groups at the RSL, Zurich, Switzerland, CNES, Toulouse, France, as well as several in the Netherlands such as FEL-TNO, University of Delft, ITC and research groups in several other countries. ESA has set a special interest group on ERS-1 SAR interferometry called ERS-1 FRINGE group.

The main objective of the study is to estimate the ground surface displacement fields using the differential interferometric synthetic aperture radar (DInSAR). The study area is located in the southwestern coast of Taiwan because of dense aquarium there that actively extracts ground water in quite large scale. The estimation by means of DInSAR will be validated by comparing with the GPS ground measurements. In the following section, we describe our data sets, followed by the data processing. We show how to fine-tune the base line based on the interferogram and how to establish a model between differential interferogram and the ground surface displacement field. Section 4 presents some experimental with discussions. Finally, a summary is given to conclude the paper.

2. Data Description

ERS1 and ERS2 are the earth resource satellites and are developed by ESA (European Space Agency). The ERS missions consist of a series of remote sensing satellites to be launched in the 1990s. The first of the series, ERS1, was launched in July 1991. The second of the series, ERS2 was launched in April 1995, in order to ensure the long-term continuity of the data which is essential

for many of its operational applications as well as for research purpose. These satellites are devoted entirely to remote sensing from a polar orbit and will make a substantial contribution to the scientific study of our environment. Both of the satellites have the same specifications of SAR instruments. The ERS satellites have Sun-synchronous, near polar, quasi-circular orbits with a mean altitude of 785 km and an inclination of 98.5 degree. For ERS2 a 35-days cycle is currently foreseen coverage the entire mission. Total of the coverage is 501 orbits over the world.

The Satellite Remote Sensing Lab. of CSRSR have acquired and processed the ERS satellites since October 1993. Then in 1996, cooperated with ESA, CSRSR acquired ERS1 and ERS2 Tandem Mode Mission data over most of the south and east of Asia.

The test site of this study is in Southwestern Taiwan, which belongs to ERS1 and ERS2 track 232 and frame 3159(figure 1). To begin, we select the SAR pairs according to the base line information from ESRIN. The base line is best around 100m for our purpose. It turns out that the base line of the first pair is 106 m formed from 31 January 1996 and 1 February 1996. The other pair base line is 2 m from 31 January 1996 and 16 May 1996. The detail parameters regarding these pairs are given in Table 1.

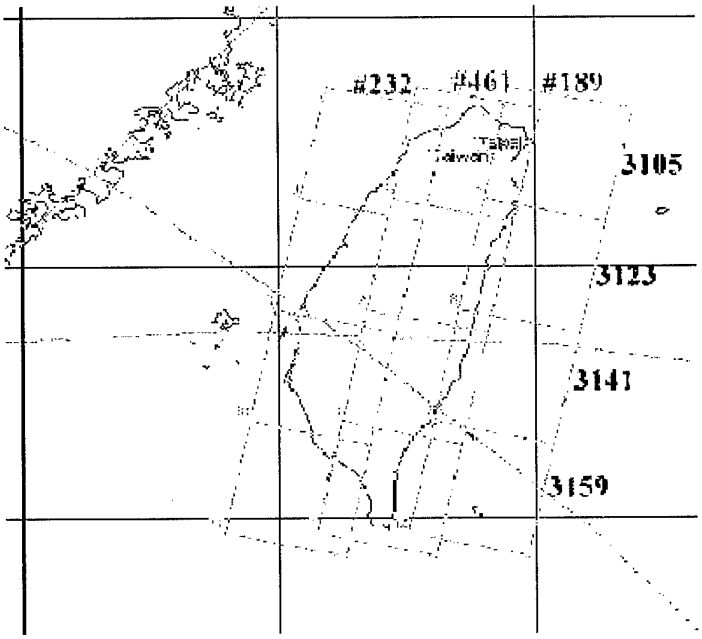


Figure 1、 Coverage map of ERS1/2 over Taiwan

Table 1. Parameters of interferometry SAR pairs:

Mater	Slave	Time Interval	B_|_	B//
96/01/31	96/02/01	1 day	106m	56m
96/03/06	96/03/07	1 day	-68m	-55m
96/04/11	96/04/10	1day	-95m	-45m
96/01/31	96/05/16	105 days	2m	59m
96/01/31	96/04/11	70 days	9m	17m
96/04/11	96/05/16	35 days	-11m	39m

3. Data Processing

The data processing is taken from single look complex image for each scene, and each was identified by a location in latitude and longitude and by date with ground areas of approximately 100 Km x 100 Km with pixel spacing of 7.9 m at slant range and 3.9 m at azimuth. The data are in complex format, with 16-bits representations for each of the real and imaginary parts. One complex scene has 4900 range elements and 26000 azimuth lines with a total size of about 500 MB.

For purpose of demonstration, we performed a three-pass differential interferometry, using three SAR images from ERS1 and ERS2, dated Jan. 31, 1996, Feb. 1, 1996, and May 16, 1996, respectively. The first two images are taken on two consecutive days in tandem mode, thus having relatively high coherence. For urban area the average coherence is about 0.4 and displays clear fringe (Figure2). A DEM was firstly generated from this pair. Fairly good accuracy can be obtained except for high relief areas. The third image was taken much later, 105 days apart, and was used to produce the displacement filed during that period. For urban area the average coherence is about 0.2 with observable fringe pattern. Because the satellites are very close to each other, the base line is only 2 meters (Figure 3).

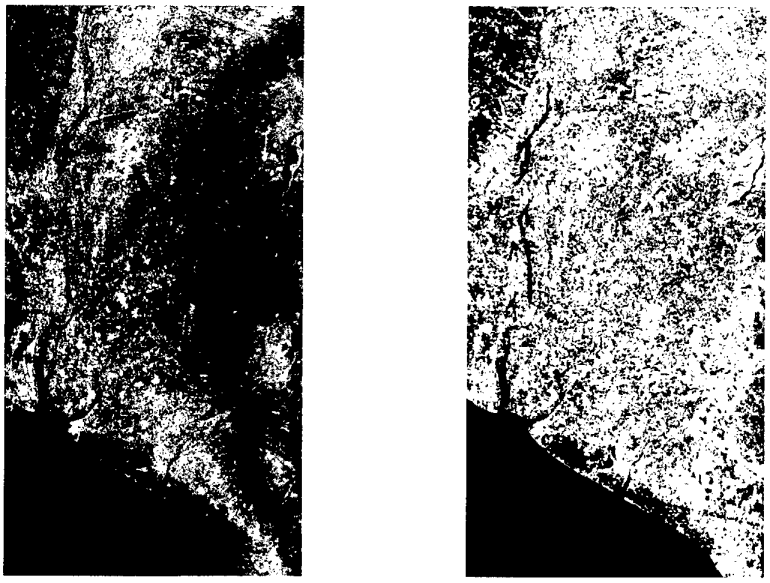


Figure 2 Interferogram and Coherence map of pair 01.31/02.01

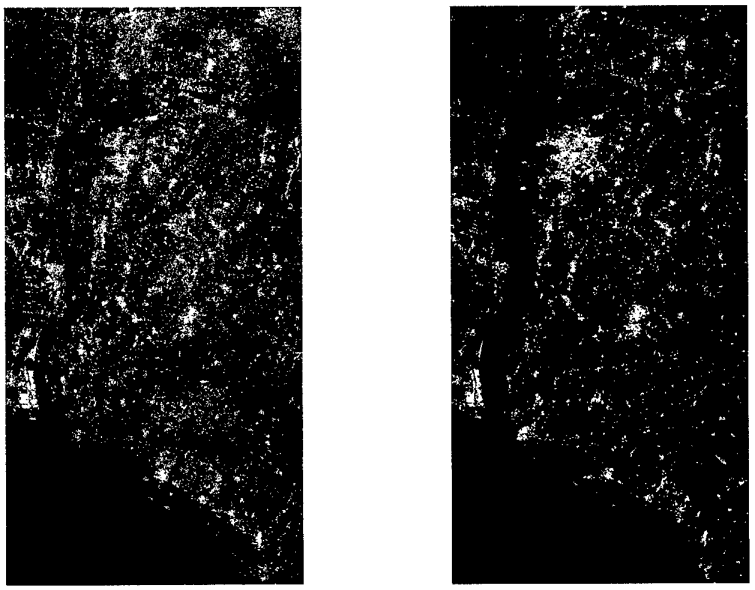


Figure 3 Interferogram and Coherence map of pair 01.31/05.16

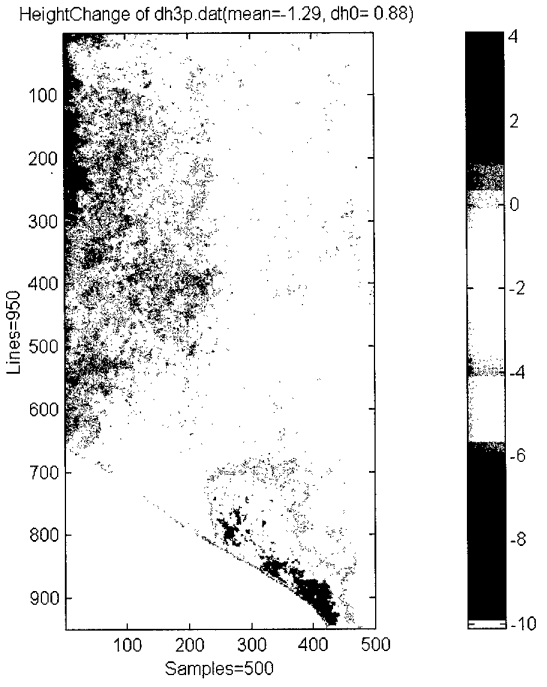


Figure 4 Subsidence from Differential Interferometry

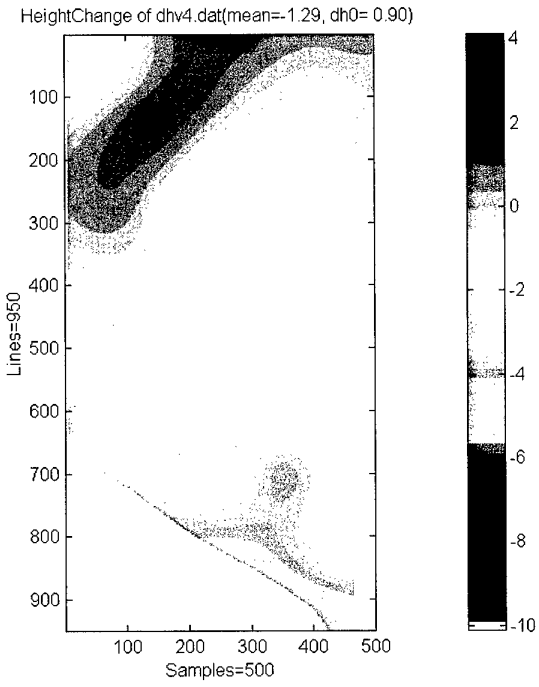


Figure 5 Subsidence from GPSs

4. Experimental Results:

In this study, the technique of differential interferometry was used to find the displacement field and to estimate the terrain subsidence of a 45 km x 25 km coastal area, Ton-Kang, southwestern Taiwan. The subsidence of this area has 48 GPS measurement points. The distances of GPSs are from 5 Km to 10 Km. The time difference is about 8 months. Over the test area, southwestern region is subsidence while the northeastern region is arising.(侯進雄, 1998). For comparison, we interpolated and scaled the GPS data same with time difference of test pairs (Figure 5).

It is shown from the comparison that the DInSAR results are consistent with GPS measurements, both in the pattern of subsidence and in its magnitude (about 2cm/month).

5. Summary

(1) We conclude that, given suitable SAR images, the differential interferometry can be a useful tool for monitoring the earth surface displacement even for a subtropical, densely vegetative area like Taiwan.

(2) Atmospheric effect should be taken into account in forming the interferogram and subsequent process, because, heavy cloud, for example, can cause the phase shifts resulting appreciable error in displacement estimation.

(3) For long-term and large area subsidence monitoring, DInSAR provides cost-effective and yet practical tool which is complementary and supplementary to ground GPS surveys.

(4) RADARSAT has more choices of beam modes which can release limitations of ERS series satellites having high incidence angle causing several layovers over mountain area, and should be considered as another data sources.

Acknowledgement

This research was partly supported by NSC 88-2612-E-008-003. CSRSR, National Central University supported ERS1、ERS2、SPOT images and assistants. Central Geological Survey supported the GPS data of subsidence over test area.

6. References

1.侯進雄、費立沅、賴典章(1998),屏東平原之 GPS 測量調查研究,屏東平原地下水及水文地質研討會論文集,pp.239-251.

2.Goldsten, R.M., Zebker, H. A., and Werner, C. L.(1988), Satellite radar interferometry: Two-dimensional phase unwrapping, *Radio Science*, Vol. 23, No. 4, pp. 713-720.

3.Gabtiel, A. K., Goldstein, R. M., and Zebker, H. A.(1989), Mapping small elevation changes over large areas: Differential radar Interferometry, *j. Geophys. Res.*,. Vol. 94, No. B7, pp. 9183-9191.

4.Bone, D. J.(1991), Fourier fringe analysis: the two-dimensional phase unwrapping problem, *Applied Optics*, Vol. 30, No. 25, pp. 3627-3632.

5.Zekber, H. A., and Villasenor, J.(1992), Decorrelation in interferometric radar echoes, *IEEE Trans. Geosci. Remote Sensing*, Vol.30., No. 5, pp.950-959.

6.Madsen, S. N., Zebker, H. A., and Martin, J.(1993), Topographic mapping using radar interferometry: Processing techniques, *IEEE Trans. Geosci. Remote Sensing*, Vol. 31, No. 1, pp. 246-256.

7.Massonnet, D., Rossi, M., Carmona, C., Adragna, F., Peitzer, G., Feigi, K., and Rabaute, T.(1993), The displacement field of the Landers earthquake mapped by radar interferometry, *Nature*, Vol. 364, No. 8, pp. 138-142.

8.Zekber, H. A., Werner, C. L., Rosen, P. A., and Hensley, S.(1994), Accuracy of topographic maps derived from ERS-1 interferometric radar, *IEEE Trans. Geosci. Remote Sensing*, Vol. 32, No. 4, pp. 823-836.

9.Zekber, H. A., Rosen, P. A., Goldstein,R. M., Gabriel,A., and Werner,C. L. (1994), On the derivation of coseismic displacement fields using differential radar interferometry: The Landers earthquake, *J, Geophy.*, Vol. 99, No. B10, pp. 19.617-19.634.

10.Carnec. C., Massonnet, D., and King, C.(1996), Two examples of the use of SAR interferometry on displacement fields of small spatial extent, *Geophy. Res.*, Vol. 23, No. 24, pp. 3579-3582.

The 21st Asian Conference on Remote Sensing
December 4-8, 2000 Taipei, TAIWAN

921 CHICHI EARTHQUAKE : PRELIMINARY INTERFEROMETRIC INTERPRETATIONS

Deffontaines B.[1], Liang L.S.[2], Pathier E.[1], Wang C.T. [2], Fruneau B.[3], Lee C.T.[4], Raymond D.[1], J.Angelier[1] and Rudant J.P.[3]
Centre National de la Recherche Scientifique ESA 7072, and Université Pierre et Marie Curie,Paris, France,
Remote Sensing Center Chungli, National Central University, Chungli, ***TAIWAN***
Université de Marne-La Vallée, ***France***
Contact : benoit.deffontaines@lgs.jussieu.fr

Keywords : Chichi Earthquake, 921, Neotectonics, Active Faults, SAR-ERS, Interferogram, Foothills, Taiwan.

Abstract
Taiwan island displays active tectonics expressed by high seismicity. The 921 Chichi earthquake (M_w= 7.3 - Foothills, Western Taiwan), occured last 21st September 1999 at 1 :47am. By SAR-ERS interferometry, we show herein the deformation field in the western side of the active Chelungpu thrust fault (Taichung area) induced by the Chichi earthquake. It shows a slight subsidence, with a maximum displacement of 30cm. This new methodology combined to precise GPS measurements, field work (trenching, fault and syndeposits analyses), geophysics, sismologist and morphotectonic works, lead to a better knowledge of active faults in Taiwan.

Introduction
Taiwan is located on plate boundaries between *both* Philippine and Eurasian plates to the East and West respectively. This island shows a spectacular compressional tectonics, underlined by a recent mountain range culminating almost at 4.000m. Otherwise, the present deformation is also expressed by high seismicity, including the last destructive Chichi earthquake (21.09.99), and by less known slow deformations, partly recorded by G.P.S methods. Our aim in this paper is to better know the deformation field within the Chichi area, so we have carried out SAR interferometric studies in the western part of Taiwan (Taichung cities and surrounding areas).

After a brief review of Taiwan geodynamical setting, and Western coastal plain geological features, we present herein three new and complementary SAR interferogram of the studied area, evidencing the tectonic deformation linked to the earthquake. One may notice the major contribution of these results for a better knowledge of natural hazards of tectonic origin in this densely populated area.

Taiwan geodynamical setting (fig 1)
To the NE of Taiwan, the Philippine plate subducts towards the Northwest beneath the Eurasian plate into the Ryukyu arc-trench system. Contrasting to the S of Taiwan, where the Philippine plate, bounded by the Luzon volcanic arc, overrides towards the West the South China Sea oceanic crust into the Manilla trench. This latter subduction is transformed northward and onshore into a collision between Philippine and Eurasian plates. Therefore Taiwan is an accretionary prism linked to this collision. The obliquity between the Chinese continental margin (Eurasian plate) and the Luzon volcanic arc (Philippine plate) involves a progressive migration towards the South of the active collision (e.g. Biq, 1972; Bowin *et al.*, 1978; Wu, 1978; Suppe, 1981; Ho, 1986). A present 70 mm/yr northwestern relative motion between Philippine and Eurasian plates, predicted by Seno *et al.* (1977, 1993) has been recently raised to 81 mm/yr according to GPS measurements (Yu *et al.,* 1997).

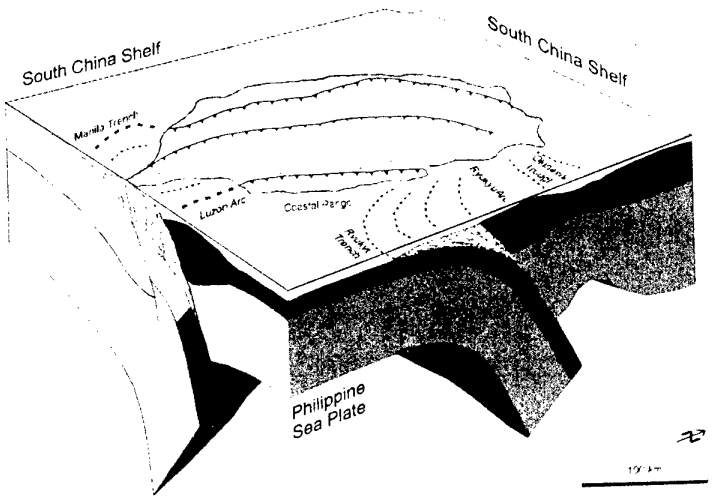


Fig. 1. Taiwan geodynamical setting
The Philippine Sea Plate subduct under the Eurasian plate to the NE and is overriding the Eurasiatic plate to the SW (from Angelier 1986-99).

SAR interferometry data acquisition and processing (table 1)

With the aim of detecting deformations linked to Chichi earthquake, we have analysed the western Foothills of Taiwan, in the Taichung area, by the means of SAR interferometry. This method has already been used for recording and measuring ground "fast" motions linked to earthquakes (normal and strike-slip faults, volcanic eruptions, and landslides (Massonnet & Feigl, 1998). But it is the first time that a thrust to be studied with this methodology. The problem with Chichi earthquake is to get good base line (distance between the two satellites orbits) in order to get rid of topographic artefacts. Unfortunately, with SAR-ERS2 the dates close to the September 21st are of poor base lines which imply to take into account longer time interval before and after the 921 quake. Consequently, an interferogram with a long time interval between the two images involve a coherence loss. Nevertheless, weak ground motions have been already characterized by the means of interferograms with long intervals (until 3 years) either in desert areas like Iceland (Vadon & Sigmundson, 1997), within towns like Paris (Fruneau & al. 1998) or within a compressive environment in Tainan (Taiwan, Deffontaines et al., 2000). In Taiwan, SAR interferometry use for ground motion measurements is difficult because coherence problems induced by extensive tropical vegetation, water stretches, rice and tea crops. In this context, the Foothills is nevertheless a good target because this area is rather low relief, with several important towns connected by wide suburbs, so favourable to a coherence preservation, during a long time (Deffontaines et al., 2000).

The Taichung studied area is covered by several ERS-SAR 2 frame (descending and ascending orbits). Among the frames, we have selected, with the help of ORBISCAN$_{©}$ (CNES) software several pairs of interferometrable images (track 232 and frames 3123, see table 1 for parameters).

Processing of the images had been done using the DIAPASON$_{©}$ (CNES) software which lead to interferogram where the effects of satellite geometry and topography are removed using 80m ground resolution digital terrain model (hereafter DTM).

Date(1st)	Date(2nd)	Difference	V or parallel Baseline/	H-Perpendicular Baseline/
99/02/25	99/09/23	210 days	39m	36m
99/05/06	99/01/21	105days	-96m	-91m
99/10/28	99/09/23	35 days	219m	91m
99/05/06	99/09/23	140 days	213m	54m
99/05/06	99/10/28	175 days	-6m	37m

Table 1 : Characteristics of the different ERS-2, 3123/232 interferograms realized

Results and interpretation (Fig.2A-B, 3, 4, 5)

On the amplitude image (Fig.2A), one may notice Taichung and surrounding city buildings (white pixels), fish ponds, rice fields and rivers (black pixels), Taiwan strait and vegetation onshore (grey pixels). From the processing of interferometrable image pairs, we have carried out calculation of several interferograms (e.g. Fig.3, 4 and 5) and coherence images (e.g., Fig. 2B). White pixels on the coherence image correspond to coherent points on the two radar images such as urbanized areas. The corresponding interferogram (Fig.) and fringes on the western down-faulted block of the Chelungpu fault (Chichi earthquake). The rather low base line of the pair (100m in the specific area of Taichung) linked with low relief, logically suppresses fringes, due to topographic artefacts for example to DTM errors. Otherwise, with the aim of avoiding the hypothesis of parasitical fringes occurrence generated by atmospheric effects, we have to carried out other interferograms with independent pairs of images (work in progress).

So without parasitically effects, the interferograms (fig.4) shows particularly a serie of 10 complete fringes to the W of the Chelungpu fault. We interpret these fringes as corresponding to a present displacement witness.

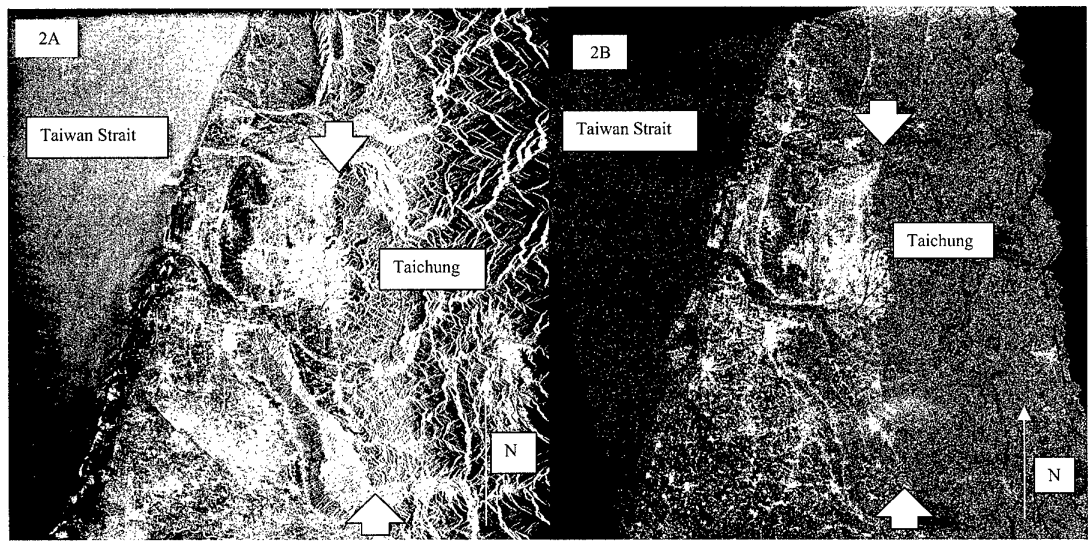


Fig.2A : Amplitude image of the Taichung area (23/09/1999 - SAR-ERS) ; 2B : Coherence image of the Taichung area (02/25 ~ 09/23 pairs). White pixels = coherent points (e.g. : urbanized areas), black and grey ones = not coherent (sea water, and vegetation).

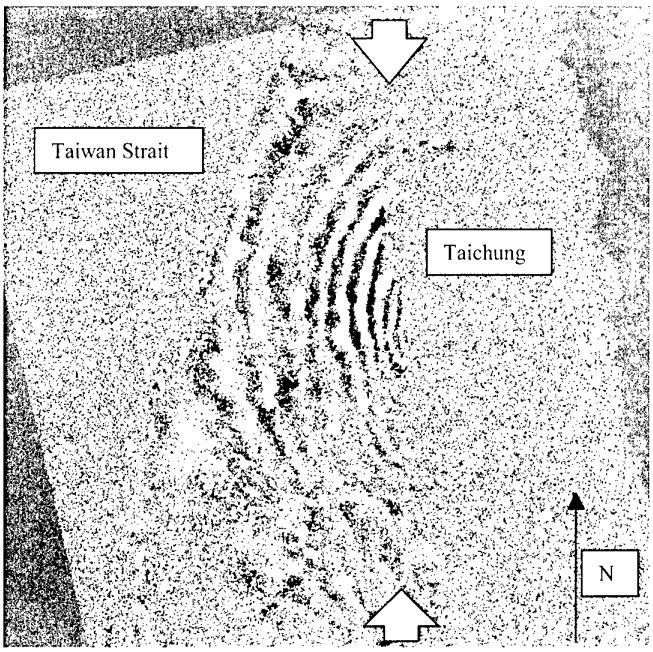


Fig. 3 : Non ortho-referenced interferogram (02/25 ~ 09/23) of the Taichung area
Note the 10 fringes in the western down-faulted block of the Chelungpu active Fault (location between white arrows)

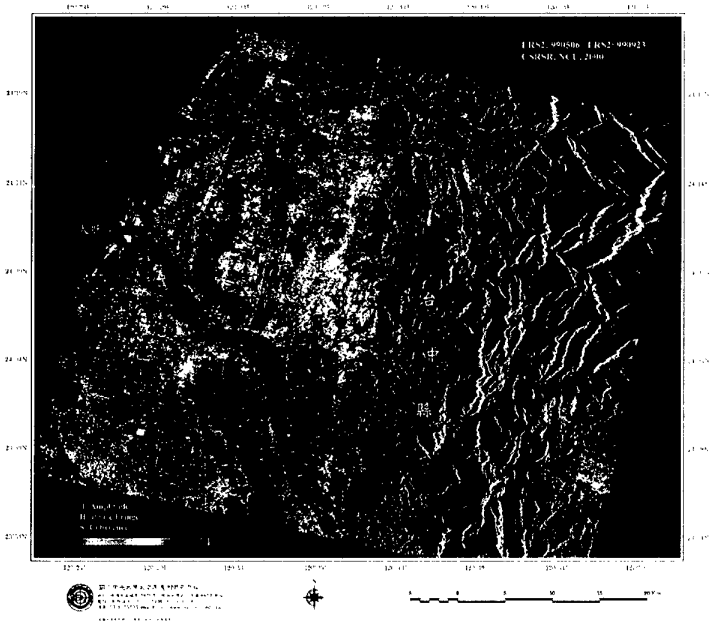


Fig. 4: Ortho-referenced interferogram (05/06 ~ 09/23) of the Taichung area
(Intensity : Amplitude, Hue : Phase - interferogram, Saturation : Coherence)

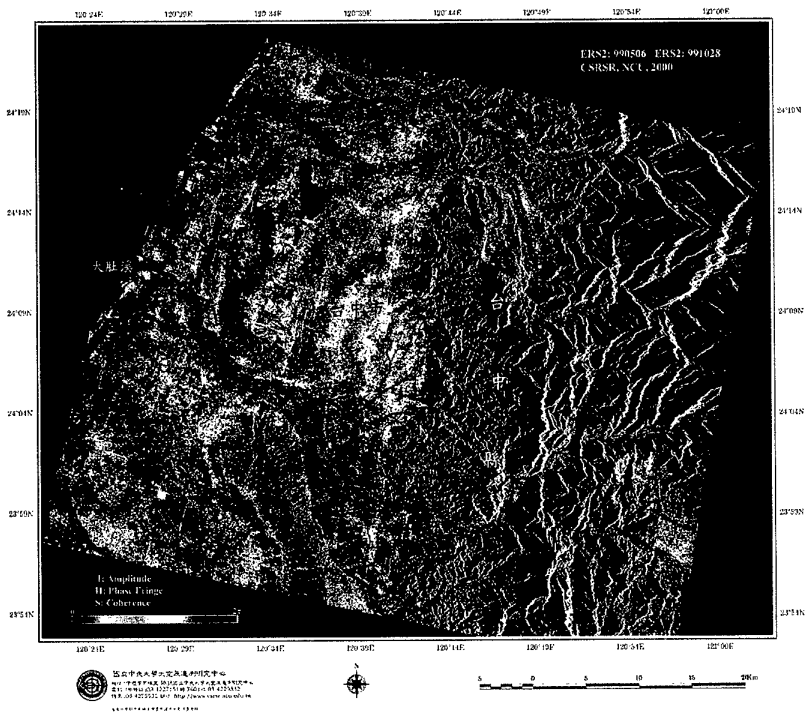


Fig. 5: Ortho-referenced Interferogram (05/06 ~10/28) of the Taichung area
(Intensity : Amplitude, Hue : Phase - interferogram, Saturation : Coherence)

One may notice on fig. 2B and consequently on Fig. 3, 4 and 5, the absence of interpretable interferometric data on the eastern side of the Chelungpu Active Fault due to the large amount of displacement, the large destructions of buildings, the differenciate relief and the luxuriant vegetation. In contrast, the western down-faulted block displays almost 10 fringes interpreted herein as deformations due to the Chichi earthquake as the high base line, and the low relief of the studied area avoid classical topographic artefacts. The coherence of the three independant interferogram shown here lead also to minimize atmospheric artefacts.

On the Taichung basin, the calculated interferograms shown here, present coherent 10 to 11 phases variation modulo 2Π. As the radar wavelength of SAR-ERS2 is 2.8cm, the down-faulted side of the Chelungpu thrust reaches almost 30cm of subsidence linked to the 921 Chichi earthquake. In order to get both horizontal and vertical component of this deformation, we have taken GPS data into account (work in progress with Yu S.B.). Our preliminary results combining both interferogram and GPS data show the pretty good accordance and highlight the complementarity. Especially, one may notice the interest of interferograms which show spatially the maximum area of deformation of the Western block of the Chelungpu active fault in east Taichung city, within a gap of GPS stations. The maximum of subsidence area revealed by SAR interferograms is coherent to the maximum of destructions of buildings in the city. This is closely linked to the geometry of the fault which is not a uniform fault plan and present several re-etrent (Deffontaines, 2000). The further direction of studies deal with the vertical variation of water-table which also might produce centimetric ground deformation on interferograms (work in progress).

Conclusions

The preliminary interferograms linked to 921 Chichi earthquake (Taiwan) reveal spatially the western deformation field of the Chelungpu Active Fault. It is the first example of interferogram linked to active thrust in the world studied by SAR interferometry. Such studies of active deformation within high anthropic area such as the Taichung county (third city of Taiwan) shows how important is this interferometric approach to better locate, characterise, quantify and modelize natural hazards due to tectonic effects. This interferometric approach had to be combined with classical field data (trenching, and morphotectonic studies), and with GPS, levelling, geophysics and seismological approach in order to better constrain the active faults of Taiwan.

Acknowledgments

This research has been done with various supports from the Taiwan-France cooperation program supported by the French Institute in Taipei (IFT), the National Science Council (NSC), the Ministry of Education of Taiwan, the French National Center of Spatial Studies (C.N.E.S) and the European Spatial Agency (E.S.A.) and within a collaboration between University Pierre and Marie Curie and the National Central University (Chungli) and the remote sensing of NCU-Chungli.

References

Angelier J., Chu H.T., Lee J.C., Hu J.C., Lu C.Y., Mouthereau F., Font Y., Deffontaines B., Chow J.D., Tsai Y.B., Chan Y.C., Lin T.J., 2000. How can geologists efficiently contribute to seismik risk mitigation ? The ChiChi earthquake case, Taiwan, Taiwan Natural Mitigation, Taipei, 21-26/05/2000.

Biq C.C., 1972. Dual trench structure in the Taiwan-Luzon region. Proc. Geol. Soc. China 15:65-75

Bowin C., Lu R.S., Lee C.S. and Schouten H., 1978. Plate convergence and accretion in the Taiwan-Luzon region. Am. Assoc. Pet. Geol. Bull., 62: 1645-1672.

Deffontaines et al. 1995 TEA colloquium Chungli

Deffontaines B., Lee J.C., Angelier J., Carvalho J., Rudant J.P. 1994: New geomorphic data on Taiwan active orogen: a multisource approach, Jour. Geophys. Res, 99, B10: 20,243-20,266.

Deffontaines B., Lacombe O., Angelier J., Chu H.T., Mouthereau F., Lee C.T., Deramond J., Lee J.F., Yu M.S., Liew P.M., 1997. Quaternary transfer faulting in Taiwan Foothills: Evidence from a multisource approach, Tectonophysics, 274, 1-3: 61-82.

Deffontaines B., Fruneau B., Pathier E., Raymond D., Lee C.T., Angelier J., Wang H.T., Rudant J.P., 2000. Long time SAR Interferometry for detection active ground motions: The Tainan anticline (SW Taiwan), Taiwan Natural Mitigation, Taipei, 21-26/05/2000.

Deffontaines, C.T. Lee, E. Pathier, J.Y.H. Yu, B. Fruneau, H.H. Chen, L.S. Liang, A.J. Chen, S.K. Chen, D. Raymond, C.L. Tseng, J.P. Rudant, Y.B. Tsai, J. Angelier, C.P. Chang, T.Y. Chang, F.C. Li, C.T. Wang, H.H. Hsi, 2000. preliminary interferometric results on 921 chichi earthquake (central taiwan). Proc. Int. Workshop on annual commemoration of Chichi earthquake, Vol1. Science aspect 18-20/09/2000, 105-110.

Delcaillau B., Deffontaines B., Floissac L., Angelier J., Deramond J., Souquet P., Chu H.T., Lee J.F., 1998. Morphotectonics in the Western fold-and thrust belt of Taiwan: an integrated analysis of the Pakuashan anticline, Geomorphology, 24 : 263-290.

Fruneau B., Rudant J.P., Obert D., Raymond D. (1998) Small displacements detected by SAR interferometry on the city of Paris (France). Proceeding of the 2nd International workshop on retrieval of bio- and geo- physical parameters from SAR data for land applications, 21-23 October 1998, Noordwijk, The Netherlands, p.557-563.

Ho C.S., (1986). A synthesis of the geologic evolution of Taiwan. Tectonophysises, 125: 1-16.

Huang C.Y., Wu W.Y., Chang C.P., Tsao S., Yuan P.B., Lin C.W., Yuan X.K. (1997). Tectonic evolution of accretionary prism in the arc-continent collision terrane of Taiwan. Tectonophysics, 281, 31-51.

Massonnet D., Feigl K., (1998). Radar Interferometry and its application to changes in the earth's urface . Reviews of Geophysics, 36, 4: 441-500.

Okada Y., (1985). Surface deformations due to shear and tensile faults in a half-space, Bull. Seism. Soc. Am., 75 : 1135-1154.

Seno T., 1977. The instantaneous rotation vector of the Philippine Sea plate relative to the Eurasian plate. Tectonophysics,42:209-226.

Seno T., Stein S., Gripp A.E., 1993. A model for the motion of the Philippine Sea Plate consistent with Nuvel-1 and geological data, Jour. Geophys. Res., 98 : 17.941-17.948.

Suppe, J, 1981. Mechanics of mountain-building and metamorphism in Taiwan: Mem. Geol. Soc. China, 4, 67-89.

Vadon H., Sigmundsson F., (1997). 1992-1995 crustal deformation at Mid-Atlantic ridge, SW Iceland, mapped by radar interferometry. Science, 275, 194-197.

Wang and Liang Juillet 2000 Interferometric results on Chichi earthquake.

Wu F.T., (1978). Recent tectonics in Taiwan. J. Phys. Earth, 26, S265-S299.

Yu S.B., Chen H.Y., and Kuo L.C., 1997, Velocity field of GPS stations in the Taiwan area, Tectonophysics, 274 : 41-59.

Doppler Coefficient Estimation for Synthetic Aperture Radar Using Sub-Aperture Interferogram

Jim Min Kuo, K. S. Chen
Institute of space Science, National Central University, Chung-Li, Taiwan
TEL:866-3-4227151 ext.7644; FAX: 866-2-22450943
E-mail: jmguo@mail2000.com.tw; dkschen@csr900.csrsr.ncu.edu.tw

KEY WORDS: *Synthetic Aperture Radar, Sub-Aperture Interferogram, chirp signal*

ABSTRACT
A moving target will change the doppler coefficients of the received signal of Synthetic aperture radar(SAR), so we need to compute the coefficients, then we can obtain the moving targets speed or avoid smear of SAR images. This paper describes a new approach for estimating the doppler coefficients. Our approach uses the sub-aperture *Interferogram* scheme to estimate the doppler coefficients. Closed-form expressions are derived, and simulation results show this method can estimate the coefficients accurately. Less computation and a smaller amount samples of the signals are the characteristics of the Sub-Aperture Interferogram than other algorithms.

1. Introduction

Synthetic aperture radar (SAR) uses match filters to process the chirp signal to produce an accurate, high resolution images. A presence of moving targets, however, induces unwanted phase variations, resulting image degradations due to range migration. In addition, smeared and ill-positioned images with respect to the stationary background are caused as well. Hence, an estimate of the moving target relation to the antenna is necessary in order to improve the SAR images[1]. On the other hand, these estimates allows us to determine the moving targets velocity. The later is the purpose of this paper.

There are many works on how to estimate the phase coefficients. Based on the fact that the moving target and stationary background induce different doppler spectra, a detecting method was proposed in [2]. The method requires the use of a high pulse repetition frequency (*prf*) and performs poorly as the moving targets have a small range velocity components. Soumekh et al.[3] described the relation of the phase coefficients and the center frequency of doppler spectrum based on the short time Fourier transform (STFT). But as is well known, in STFT the resolution was limited either in time or in frequency domain, and it suffers from smearing and side-lobe leakage. Some methods use regression on the unwrapping signal phase [4] to estimate the polynomial phase coefficients of a constant amplitude signal, which requires to use a phase unwrapping algorithm prior to coefficient estimation. The algorithms is based on accumulate the phase difference, but it can be fooled by spare, rapidly changing phase values, and phase unwrapping errors cause inaccurate coefficient estimates. Another method by maximum likelihood estimation[5], it performs well at low SNR, but its cost is high computational complexity.

An estimation algorithm based on sub-aperture interferometric scheme and phase shift measurement to estimate the doppler coefficients is proposed in this paper. This paper also addresses the relation of target speed with the phase shift. Basically, the phase of the observed sequence is model as a polynomial embedded in white noise, which implies that, first, select an appropriate sub-aperture size and then segment recorded data to a finite number of subsets with the same size. Second, we can estimate the doppler parameters from the phase shift.

The presentation of the paper is as follows. First the problem of moving target velocity estimation in SAR signal is stated. Then a SAR signal model of a moving target velocity estimation is given in section Ⅱ. Then a method for estimate doppler parameters is proposed in

section Ⅲ, which based on the application of interferometric scheme. And simulation results is shown in section Ⅳ. Finally, a conclusion is provided.

2. SAR Signal Model of A Moving Target

A moving target will alter the coefficients of the phase function of observed signals and target motion is generally unknown. When a conventional SAR processing algorithm is applied to scene with moving targets, the images of a moving targets are typically mislocated and smeared due to phase errors induced by the motion. The relation between antenna and a moving target can be express as a function of time and distance[1],[3].

$$g(t) = A(t)\exp\left\{-j\frac{4\pi}{\lambda}\vec{R}(t)\right\} \tag{1}$$

Where A(t) is the amplitude of the signal, $\vec{R}(t)$ is the distance vector between target and antenna, and λ is the wave length of SAR. This magnitude of $\vec{R}(t)$ will be denoted as $\left|\vec{R}(t)\right|$. For small time variations, $\left|\vec{R}(t)\right|$ is large relative to the magnitudes of the velocity and acceleration vectors, and neglecting terms higher than t^3 in a Taylor series expansion of the magnitude, then we can obtain the expansion:

$$\left|\vec{R}(t)\right| = \left|\vec{R}\right| + \frac{\vec{R}\bullet\vec{V}t}{\left|\vec{R}\right|} + \left\{\frac{\vec{V}\bullet\vec{V}}{\left|\vec{R}\right|} + \frac{(\vec{R}\bullet\vec{V})^2}{\left|\vec{R}\right|^3}\right\}\frac{t^2}{2} \tag{2}$$

where V is the velocity contains both radar and moving target. We denote the moving target velocity vector as (v_x,v_y), which is the components of moving target velocity in range and azimuth respectively, and the along track's speed of the radar symbolized as U. The relation of moving speed to antenna speed can be expressed as:

$$(v_x, v_y)=(aU, bU) \tag{3}$$

Where (a,b) is the dimensionless of target's velocity scaled to the speed of the radar, and Normally, |a| and |b| <<1. From above mention we can assume that (a, b) is nearly constant during the integration time in the azimuth.

Using equation (2) and (3), (2) can be rewritten as follows:

$$\left|\vec{R}(t)\right| = \left|\vec{R}\right| + aUt + \frac{(1-b)^2U^2}{\left|\vec{R}\right|}\frac{t^2}{2} \tag{4}$$

Let Ut=y, the magnitude in (4) can be rewritten as followers:

$$\left|\vec{R}(y)\right| = \left|\vec{R}\right| + ay + \frac{(1-b)^2y^2}{2\left|\vec{R}\right|} \tag{5}$$

Using equation (1) and (5), the received signals can be written as:

$$g(y) = A(y)\exp\left\{-j\frac{4\pi}{\lambda}\left[\left|\vec{R}\right| + ay + \frac{(1-b)^2y^2}{2\left|\vec{R}\right|}\right]\right\} \tag{6}$$

This is a signal of the linear FM form. Where A(y) will be considered a nuisance parameter and will not be estimated.

3. Estimation of the Chirp Signal Coefficient

From section Ⅱ, we know SAR signal is a typical chirp signal and in general, is blurred by noise. We use a discrete-time polynomial phase signal model for the source signal, the measured data are assumed to consisted of signal and noise,

$$g(y) = A(y)e^{-j\psi(y)} * n(y) \qquad 0 < y \le T * r \tag{7}$$

where $\psi(y)$ is the phase of the signal, y_0 is the initial point, T denote the total number of samples and r is sample spacing on the synthetic aperture of SAR, and n(y) denote multiply noise, it can be assumed as a zero mean white Gaussian noise[4,5,6]. The phase of the chirp signal is

$$\psi(y) = f_0 + f_1 y + f_2 y^2 \tag{8}$$

where f_0, f_1, f_2 are its initial phase, initial frequency and frequency rate, respectively. The principle value of the phase function of the measured signal can be expressed as

$$\begin{aligned} \angle g(y) &= \arctan\left(\frac{image\{g(y)\}}{real\{g(y)\}}\right) \\ &= \psi(y) + \angle n(y) \\ &\overset{def}{=} ARG(g(y)) \end{aligned} \tag{9}$$

where $-\pi \leqq \angle g(y) \leqq \pi$, it can be computed from the data.

With the recorded data set of M elements, we generate a finite number of subsets with the same size N, what we call sub-apertures, by sequentially not overlapping each other.

SA_j denote the j-th sub-aperture; and sub-aperture sizes is express as ΔY for convention, it is equal to samples N multiply sample spacing, $\Delta Y = N * r$. Based on the above-mentioned, the interferometric phase is come from (j+1)-th sub-aperture signal interfere with j-th sub-aperture signal, which is denote as $\phi_j(y)$:

$$\begin{aligned} \phi_j(y) &= \{f_0 + f_1((j+1)\Delta Y + y) + f_2((j+1)\Delta Y + y)^2\} \\ &\quad - \{f_0 + f_1(j\Delta Y + y) + f_2(j\Delta Y + y)^2\} + \phi_{j_n}'(y) \\ &= f_1\Delta Y + (2j+1)f_2\Delta Y^2 + 2f_2\Delta Y y + \phi_{jn}'(y) \qquad j = 0,1,2,3.... \end{aligned} \tag{10}$$

Where $\phi_{jn}'(y)$ is the phase noise sequence and $0 < y \le N * r$ for a sub-aperture. Follow equation (10) we can obtain:

$$\phi_{j+1}(y) = f_1\Delta Y + (2j+3)f_2\Delta Y^2 + 2f_2\Delta Y y + \phi_{(j+1)n}'(y) \tag{11}$$

We use ERS SAR as the simulation system, to illustration it. We will assume that the electromagnetic behavior of the moving targets is similar to one point scatter response. The magnitude of the slant range is 8.4848e+005km, aircraft altitude is 800000m, azimuth sample spacing is 3.990574m and total samples is 1068, aircraft ground speed is 6.699028e+03m/sec, platform heading is 192.036610832947° and radar wavelength is 0.056666m, target heading is 161°, target speed is 9m/sec.

Some of the interferometric phase ϕ_j are shown in Figure 1. By this procedure the phase history from curve transform to linear and then the phase shift between $\phi_{j+1}(y)$ and $\phi_j(y)$ are constant. Compare equation (10) and (11), we can obtain the phase shift:

$$\begin{aligned} \Delta\phi(y) &= \phi_{j+1} - \phi_j \\ &= 2f_2\Delta Y^2 + \phi_n''(y) \end{aligned} \tag{12}$$

From equation (12) we can estimate a frequency rate f_{2i} in every subsets of the measured signal:

$$f_{2i} = \frac{\Delta\phi(y) - \phi_n''(y)}{2\Delta Y^2} \tag{13}$$

Using equation (13) and after some manipulations, one can obtain the following estimate for the frequency rate $\hat{f}_2$:

$$\hat{f}_2 = \frac{1}{M-2}\sum_j \frac{1}{N}\sum_i f_{2i} \tag{14}$$

Once $\hat{f}_2$ is available, then substitute it to the below equation

$$\tilde{\psi}(y) = f_2 y^2 \tag{15}$$

Follow the above-procedure of (10), we can obtain

$$\tilde{\phi}_j(y) = (2j+1) f_2 \Delta Y^2 + 2 f_2 \Delta Y y + \phi'_{jn}(y) \qquad j = 1,2,3.... \tag{16}$$

Some of the interferometric phase $\tilde{\phi}_j$ are shown in Figure.2. Compare equation (10) with (16), we know the phase difference between $\tilde{\phi}_j$ and ϕ_j is

$$\begin{aligned} \Delta\hat{\phi}_j(y) &= \phi_j(y) - \tilde{\phi}_j(y) \\ &= f_1 \Delta Y + \tilde{\phi}''_n(y) \end{aligned} \tag{17}$$

From the equation (17), we can estimate the value of the frequency f_{1i}:

$$f_{1i} = \frac{\Delta\hat{\phi}(y) - \tilde{\phi}''_n(y)}{\Delta Y} \tag{18}$$

The last result of $\hat{f}_1$ is

$$\hat{f}_1 = \frac{1}{M-2}\sum_j \frac{1}{N}\sum_i f_{1i} \tag{19}$$

In the next section we show how to use this method for estimating a moving target speed in SAR.

4. Simulations

We use ERS SAR as the simulation system, the parameters were the same as previous case, except that moving target speed, target heading, and sub-aperture size.

For convenience, we reference equation (8) to rewritten (6) as a type chirp signal form

$$\begin{aligned} g(y) &= \exp\left\{-j\frac{4\pi}{\lambda}\left[|\vec{R}| + ay + \frac{(1-b)^2 y^2}{2|\vec{R}|}\right]\right\} + n(y) \\ &= \exp\left\{-j\left[\frac{4\pi|\vec{R}|}{\lambda} + \frac{4\pi a y}{\lambda} + \frac{2\pi(1-b)^2 y^2}{\lambda|\vec{R}|}\right]\right\} + n(y) \\ &= \exp\left\{-j\left[f_0 + f_1 y + f_2 y^2\right]\right\} + n(y) \end{aligned} \tag{20}$$

We assume that a moving target heading is 161°, moving speed vary from 0.1m/sec to 30m/sec and the sub-aperture size is 39.90574m. We can to estimate the coefficient of $\hat{f}_2$ and $\hat{f}_1$ by follow the procedure of sub-aperture interferometry method described in section Ⅲ. The relational frequency rate f_2 and estimate result of $\hat{f}_2$ is display in Figure.3, we can find the estimate results agree very well with the truth coefficient. The frequency f_1 and estimated results of $\hat{f}_1$ is display in Figure.4. To observed the variation of Figure.4, we find when that $f_1\Delta Y$ is larger than2π then $\hat{f}_1$ is deviant. Which is caused by the original signal is wrapped by 2π, and therefore the limit of interferometric approach is that the absolute value of $2f_2\Delta Y^2$ and $f_1\Delta Y$ have to be smaller than 2π. In addition, we can obtain the minimum velocity of moving targets is restricted within the resolution of phase of SAR.

In last, we summarize, the estimation procedure consists of six steps:

Step 1: Select a appropriate sub-aperture size and then segment recorded data to a finite number of subsets with the same size.

Step 2: transform $\{\angle g(y)\}$ into $\{\phi_j(y)\}$ by equation (10).

Step 3: evaluate the phase difference by equation (12).

Step 4: use equation (13) to estimate $\hat{f}_2$;

Step 5: Once $\hat{f}_2$ is available, follow equation (16) to obtain $\{\tilde{\phi}_j(y)\}$;

Step 6: evaluate the phase difference between $\{\phi_j(y)\}$ and $\{\tilde{\phi}_j(y)\}$, to obtain $\hat{f}_1$;

5. Conclusion

In this paper, we have developed an algorithm for estimate the coefficients of chirp signal. Through some analysis, we proved the relation of a phase difference of a series subsets' interferometric signals with the coefficients of chirp signal. In this algorithm, the coefficients $\hat{f}_2$ and $\hat{f}_1$ are contrary to the sub-aperture size ΔY. So sub-aperture sizes selection is a trade-off between the target velocity and noise.

We finally applied the algorithm to estimate the target speed of a simulation data of ERS SAR signals. Computer simulation results agree very well with the theoretical performance derived. And we find that the cost of computation is fewer and only need a small amount of samples of the data compare to some other methods.

Current, this algorithm is confined to use the principle value of the phase function, so to overcome this restriction, it could be to estimate the higher-speed's target and support a lower SNR of a signal.

Refferences

[1] J. Patrick Fitch, "*Synthetic Aperture Radar*," New York : Springer-Verlag , 1988.

[2] R.K. Raney, "Synthetic aperture imaging radar and moving target," *IEEE Trans. Aerospace and Electronic Systems,* Vol. AES-7, pp. 499-505, 1971.

[3] Soumekh Mehrdad, "Fourier array imaging," Englewood Cliffs, N.J : PTR Prentice-Hall, c1994.

[4] Slocumb, B.J.; Kitchen, J., "A polynomial phase parameter estimation-phase unwrapping algorithm," ICASSP-94: IEEE International Conference on Acoustics, Speech, and Signal Processing, vol. 4, pp. 129 -132, 1994.

[5] Besson, O.; Ghogho, N.; Swami, A., "Parameter estimation for random amplitude chirp signals ," IEEE Transactions on Signal Processing, vol. 47, pp 3208 –3219,1999.

[6] Jong-Sen Lee, Karl W. Hoppel, "Intensity and phase statistics of multilook polarimetric and interferometric SAR imagery", IEEE Transactions on Geoscience and Remote Sensing v 32 n 5 p 1017-1027, Sept 1994.

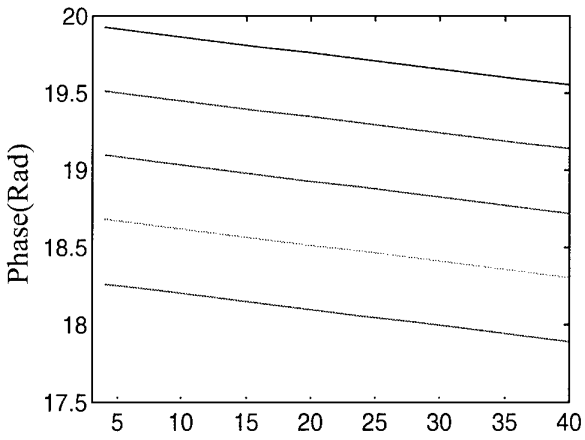


Figure.1. The histories of some interferometric signals phase from the original signal

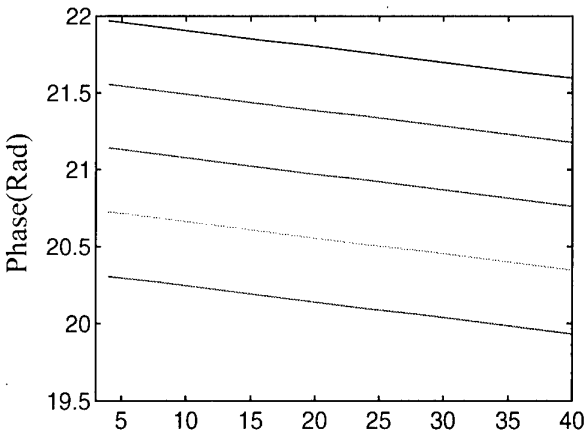


Figure.2. The histories of some interferometric signals phase from the dechirped signal

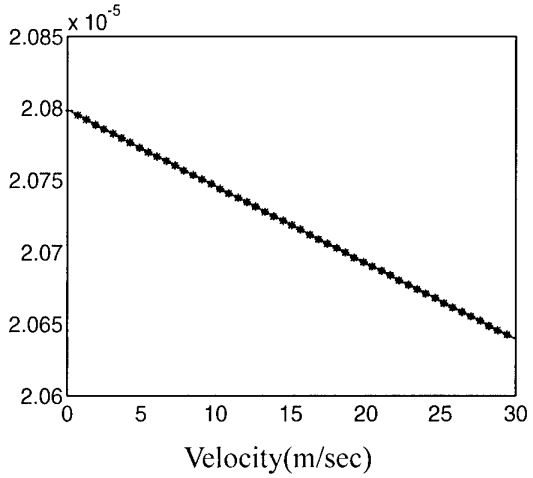


Figure.3. The frequency rate f_2 and estamate results $\hat{f}_2$.

f_2: solid line, "★": $\hat{f}_2$

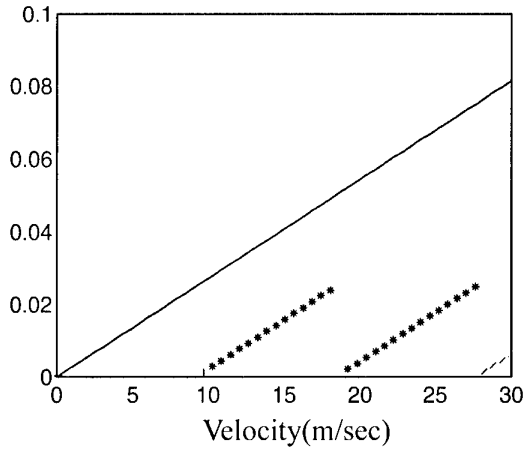


Figure.4. The frequency f_1 and estimate result $\hat{f}_1$.

f_1: solid line, "★": $\hat{f}_1$

The 21st Asian Conference on Remote Sensing
December 4-8, 2000 Taipei, TAIWAN

SEA SURFACE TEMPERATURE VARIABILITY IN THE SEAS SURROUNDING THE PHILIPPINES IN RELATION TO ENSO EVENTS

[1]Erlinda E. Salamante and [2]Cesar L. Villanoy
Marine Science Institute, University of the Philippines
Velasquez Street, Diliman, Quezon City, Philippines 1101
Tel no.: (63-2) 922-3944; Fax no.: (63-2) 922-3959
E-mail: [1]lindae@msi01.cs.upd.edu.ph; [2]cesarv@msi01.cs.upd.edu.ph

KEY WORDS: sea surface temperature, El Niño Southern Oscillation (ENSO), Empirical Orthogonal Functions (EOF)

ABSTRACT

Sea surface temperature (SST) of the Philippine, Celebes, Sulu and South China Seas (SCS) was analyzed using time-domain Empirical Orthogonal Functions (EOF) to describe the spatial, temporal and interannual variability existing within the different basins. The satellite-derived monthly SST distributions were obtained from the Earth Observing System Data and Information System (EOSDIS) at the Jet Propulsion Laboratory (JPL). The SST images extracted were from September to August of the following years: 1991 to 1992, 1995 to 1996 and from 1997 to 1998. These data sets were used to represent weak ENSO, non-ENSO and strong ENSO, respectively. The first three EOF modes were compared to investigate the SST variability in relation to ENSO. For the first mode, the SST patterns during non-ENSO are similar with those of ENSO years, although the temperature difference, between the Philippine and the South China Seas, for the latter is smaller compared to the former. This mode shows that the advection of cold water from the north in the SCS weakens during strong ENSO. The Philippine Sea, on the other hand, is characterized by weak latitudinal temperature gradient and homogeneous warm water at the southern portion. The second mode exhibits strong interannual variations. The basin-wide circulation in the SCS during strong ENSO weakens and the cold upwelled water off Vietnam during normal year did not developed as ENSO occurs. The third mode is dominated by the interaction of the SCS water and the Pacific water west of Luzon strait.

INTRODUCTION

The ENSO event is one of the natural phenomenon which affects both regional and global climate. On the average this event occurs about once every 3 to 4 years. It typically lasts from 1 to 1.5 years and is known to be accompanied by an interannual see-saw in the tropical sea level pressure between the eastern and western hemispheres called the Southern Oscillation (Thurman, 1998a).

Though it is already a common notion that SST during ENSO is measurably higher in the Equatorial Eastern Pacific than normal, many aspects of the oceanic changes considerably vary in every occurrence of this event. Much research and analyses are needed to explore and adequately understand the possible dominant physical processes at work during the various phases of ENSO. This study explores the possible influence of this phenomenon to the SST variability within the Philippine, Celebes and Sulu seas as well as in the SCS.

METHODS

The satellite images of monthly-derived SST were downloaded from the NOAA/ NASA AVHRR Ocean Pathfinder SST website (http://podaac.jpl.nasa.gov/sst). The images downloaded were from 1988 to 1998, but only those years with almost continuous monthly data were included (i.e. January 1991 to November 1993 and January 1995 to August 1998), three years worth of monthly SST data representing weak ENSO, non-ENSO and strong ENSO conditions were selected based on the Southern Oscillation Index (SOI) for 1991 to 1998. The SST images extracted were from September to August of the following years: 1991 to 1992, 1995 to 1996 and from 1997 to 1998, respectively.

Each monthly image extracted has a spatial resolution of 9 km x 9 km and represents monthly averaged SST data. The missing values were interpolated using weighted fill method . The mean for each month was calculated and used as reference to derive the monthly SST anomaly fields. The output generated was then decomposed in terms of orthogonal functions to describe the spatial and temporal variability, utilizing EOF in a time domain application. The EOF computation/ analysis was done using the scatter matrix method (Emery and Thomson, 1997b).

DISCUSSION OF RESULTS AND FINDINGS

Monthly mean SST images

The SST variations in the SCS during non-ENSO are primarily influenced by the monsoon and surface current circulation. The Pacific, on the other hand, is generally affected by a complex near-surface wind-driven circulation (Kendall, 1989 as cited by Masumoto et al., 1991c). These major forces, which drive the circulation of the SCS and the Pacific, as well as dominant mechanisms, which influence the SST per se, are the significant aspects that should be considered in analysing the effect of ENSO. Moreover, determining the cause of this phenomenon also entails the identification of certain mechanisms that are consistent with the vast quantity of evidence of the oceanographic and meteorological changes coincident with this event.

The SST images exhibit distinct seasonal variation. During winter, the SST variations with weak and non-ENSO events are similar, and the SCS is dominated by cooler temperature to the north and northwest against warmer temperatures to the south and southeast. The intrusion of cold water from the north expands southward against the diminishing warm water in October, reaching its maximum dispersion off Vietnam in February. After this month, the inflow of warm water from the southern extremities starts to cover a greater part of the SCS and the southern portion of the Philippine Sea. By July, the cold water is completely eroded and the entire basins are completely covered with warm water. During this month, maximum SST in the SCS is higher by 0.4°C during non-ENSO compared with weak ENSO, while the minimum temperature in the Philippine Sea during weak ENSO is recorded to be lower by 1.4°C compared with non-ENSO year. The low SST to the north and west is largely induced by evaporation associated with the strong northeasterly wind (Chao et al., 1996d).

The northeast monsoon weakens from February to March. As of April, weak transition from cold to warm water starts to prevail within the whole basin. Higher temperatures covered a greater part of the SCS and the Philippine Sea with temperatures as high as 32.85°C recorded for the month of July at the northwestern part of Luzon, compared with non-ENSO. A weaker and more southerly southwest monsoon, from June to August, can highly be attributed to the eastward wind stress anomalies associated with a weak northerly component (Chao et al., 1996d).

Sea surface temperature within the Sulu and Celebes Seas obtained from the satellite images, only show a handful of distinct variations as well as significant similarities during normal and ENSO years. The surface temperature within the former basin is estimated to reach only as high as 26°C up to 30°C, during non-ENSO. The same minimum temperature exists during weak ENSO but the water is much warmer by 1°C. During ENSO event, the estimated temperature ranges from 27°C to 31°C. The maximum temperature, during non-and weak ENSO is observed in May, but with strong ENSO it dominates the basin only after two months. On the other hand, surface temperature in the Celebes Sea only ranges from 29°C up to 30°C for the three given conditions, all throughout the year.

EOF Analysis

The EOF decomposition of SST data, for the three ENSO phases, yields three dominant modes. On the average, the three modes accounted 71%, 7% and 5% of the total variations, respectively.

The first mode, shows typical spatial pattern associated with the monsoon. It is dominated by the intrusion of cold water from the northeast that reaches southward off the southern coast of Vietnam: (~9°N) during non-ENSO, north of 14°N during weak ENSO and north of 23°N during ENSO. The Philippine Sea is characterized by weak latitudinal temperature gradient and homogeneous warm water at the southern portion up to 18°N. The amplitudes of the first mode, which is identical for the three data sets, are characterizes by almost uniform positive values throughout the year - weakening during southwest monsoon months (i.e. from June to September).

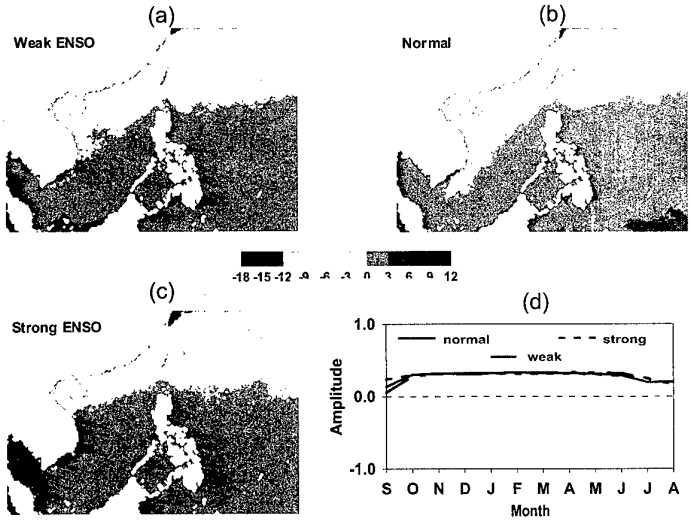


Figure 1. Spatial distributions (a, b and c) and seasonal amplitudes (d) of the 1st EOF mode.

For the three periods considered, the first mode, shows typical spatial pattern associated with the monsoon. With or without ENSO, for both the SCS and the Philippine Sea, there exists a north to south temperature gradient - with a decreasing temperature from the north. The weaker signal given during the southwest monsoon suggests that the north to south gradient pattern (which is very prominent during the northeast monsoon) diminish with the onset of this season. Reduced inflow of cold water in the northern extremities, during strong ENSO, can be associated to the anomalous southerlies or southwesterlies in the SCS during ENSO, which opposes the mean wintertime northeasterly flow that advects cold and dry air off the Asian continent (Klein et al., 1999e). This eventually lead to the reduction in the wind speed and occurrence of cold-air outbreaks, for that reason, the latent and sensible heat flux in the northern portion of the SCS as well as in regions northeast of the Philippines were also reduced.

The second mode exhibits strong interannual variations. The spatial variability of temperature in the Philippine Sea is smaller during period of non-ENSO compared with ENSO years. The basin-wide circulation in the SCS during strong ENSO, on the other hand, seems to weaken as the temperature difference between the northern and southern portion of the basin is very distinct. The cold upwelled water off Vietnam during normal year did not also developed as ENSO occurs. Its monthly amplitudes during non-ENSO, are symmetrical with the seasonal variations. However, periods with weak and strong ENSO indicate a reversal of the amplitude values as compared with non-ENSO. Period with weak ENSO also shows the same temporal variability as that of strong ENSO, however the negative amplitude only extended up to October. The negative amplitude and the negative anomalies in the northern part of the SCS and Philippine Sea, during strong ENSO, can be associated to the weak transition of northeast monsoon (Wu et al., 1998f).

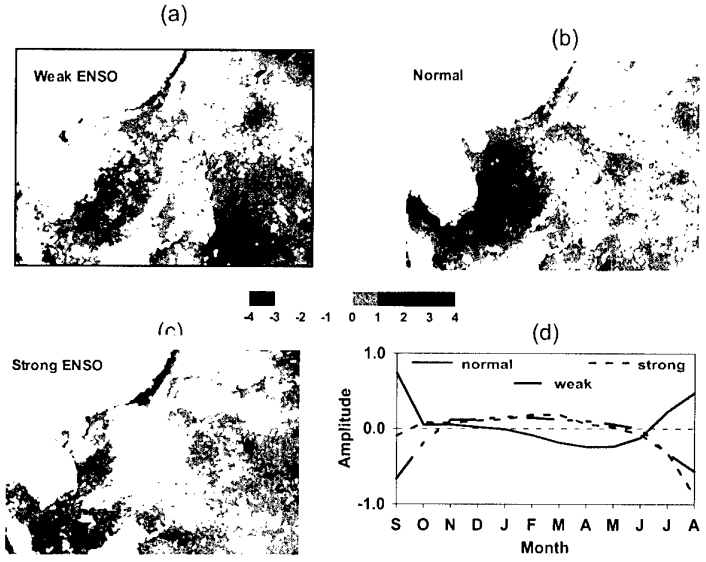


Figure 2. Spatial distributions (a, b and c) and seasonal amplitudes (d) of the 2nd EOF mode.

The third mode highlights the formation of a warm/ cool pool in the northwestern part of Luzon (centered at 16.4°N, 118.3°E) during strong ENSO. This spatial pattern may already be affected by noise due to some undefined patterns, particularly during weak ENSO. The feasible reason behind the formation of warm water on this area, during strong ENSO, is quite hard to define. Whether this feature was caused by the occurrence of ENSO or by processes of a large-scale origin, requires further investigation. In terms of its amplitude, this mode only shows one significant feature during non-ENSO, which is the appearance of the extreme negative amplitude in July. This features may be an indication of a northeastward warm current off the southern coast of China (Chao et al., 1995g) during winter.

The results of the EOF analysis within the Sulu Sea and Celebes Sea are not that distinct compared with the SCS and the Philippine Sea. Since the two basins are partly bounded by land, land masking highly influences the result of the analysis. Though the spatial and temporal patterns in these two regions are quite hard to define, the characteristics of their surface temperature can still be compared based on the satellite images. Surface temperature in the Sulu Sea is much warmer compared to the Celebes Sea since the primary source of the water in the former basin comes from the SCS while the latter is primarily influence by the Mindanao current. And in general, since the water in the SCS is distinctly colder than the Pacific (Shaw, 1991h), it is expected that water in the Sulu Sea is colder than the Celebes Sea.

SUMMARY AND CONCLUSION

The seasonal, temporal and internannual variations of sea surface temperature, highlighting its association to the ENSO event, in the water surrounding the Philippines was examined by performing an EOF analysis. Satellite-derived monthly SST images of the area were used as the principal basis. The images were classified into three periods, representing specific year with strong, weak and non-ENSO. Results from the first three EOF modes reflect various significant characteristics linking the SST variations to the ENSO event, such as reduced inflow of cold water in the northern extremities, reduced upwelling and weak seasonal variation. It was also observed that the dominant spatial pattern in the South China Sea can be associated with the northeast monsoon. Distinct latitudinal difference exists in the Philippine Sea with or without ENSO. Lastly, sudden change in the prevailing local wind system in the SCS during ENSO primarily affects the circulation in the basin and results in the warming of the upper ocean.

REFERENCES

Chao, S. Y., P. T. Shaw, and J. Wang, 1995g. Wind Relaxation as a Possible Cause of the South China Sea Warm Current. J. Oceanography, 51, pp. 111-132.

Chao, S. Y., P.T. Shaw, and S.Y. Wu, 1996d. El Niño Modulation of the South China Sea Circulation. Prog. Oceanog., 38, pp.51-93.

Emery, W. J. and R. E. Thomson, 1997b. Data Analysis Methods in Physical Oceanography. Gray Publishing, Tunbridge Wells, Kent, pp.319-340.

Klein, S.A., B.J. Soden. and N.C. Lau, 1999e. Remote Sea Surface Temperature Variations during ENSO: Evidence for a Tropical Atmospheric Bridge. J. Climate, 12, pp. 917-932.

Masumoto, Y. and T. Yamagata, 1991c. Response of the Western Tropical Pacific to the Asian Winter Monsoon: The Generation of Mindanao Dome. J. Phys. Oceanogr., 21, pp.1386-1398.

Shaw, P.T., 1991h. The seasonal variation of the intrusion of the Philippine Sea water into the South China Sea. J. Geophys. Res., 96, pp. 821-827.

Thurman, H. V., 1998a: Introductory Oceanography, 7th. Ed. Macmillan Publishing Company, New York, pp.185-212.

Wu, C.R., P.T. Shaw and S.Y. Chao, 1998f. Seasonal and interannual variations in the velocity field of the South China Sea. J. Oceanogr., 54, pp. 361-372.

EL NIÑO SOUTHERN OSCILLATION (ENSO) IMPACT ON SEA SURFACE TEMPERATURE (SST) DERIVED FROM SATELLITE IMAGERY AND ITS RELATIONSHIP ON TUNA FISHING GROUND IN THE SOUTH JAVA SEAWATERS

Jonson Lumban Gaol, and Djisman Manurung
Academic staff, Marine Science and Technology Department,
Faculty of Fisheries and Marine Science, Bogor Agricultural University
Kampus IPB Darmaga, Bogor 16680, Indonesia
Tel: (62)-251-621211 Fax: (62)-251-622907
E-mail: jonsonl@mailcity.com
INDONESIA

KEY WORDS: ENSO, SST, Imagery, Tuna, Fishing Ground.

ABSTRACT: El Niño Southern Oscillation (ENSO) impact on sea surface temperature (SST) derived from satellite imagery in the south Java seawaters has been investigated. The ENSO years is defined as the years that fall during El Niño events and the standard deviation of the Southern Oscillation Index <= -1.5. Therefore, the ENSO year in this paper is 1998 and non-ENSO year is 1996. SST monthly mean for the years of 1996 and 1998 is estimated from AVHRR LAPAN (Indonesia) receiver. Monthly mean SST values during Non-ENSO years along the south Java seawaters are higher than that of the ENSO years with the average different of 1.7°C. Total big eye tuna catch in 1996 and 1998 are 30.401 fish and 42.209 fish respectively. On the other word, big eye tuna catch during ENSO year is higher than that Non-ENSO year.

1. INTRODUCTION

1.1. Background

The South Java seawater is one of the important tuna fishing ground in the world. Japan Fisheries Agency has observed sea surface temperature (SST) and current by using BT and long line drift in the south of Java since 1960s (Mizuno, 1995). SST is one of important parameter on oceanographic factors that allow a forecast of fish distributions. ENSO event are changes in SST, change in vertical, thermal structure of the ocean and altered coastal and upwelling current. Generally, in Indonesian Seawaters, correlation between fish catch and ENSO consistent in the time and space domain (Pariwono, 1996).

The Southern Oscillation is an inter-annual see-saw in tropical sea level pressure between the eastern and western hemisphere, with center action located over Indonesia and the tropical South Pacific Ocean (Philander, 1997; Quin *et al.*, 1987). The Southern Oscillation index is the sea level pressure different between Darwin (12.4°S, 130.9°E) in northern Australia and Tahiti (17.5°S, 149.67°W) in the South Pacific Ocean with a high negative value indicate a warm event and a high positive value indicate a cold event (also referred to La Niña). However, it is important to note that there is not a one-to-one correspondence between the occurrence of Southern Oscillation events and El Niño events.

The scientific community uses the term El Niño Southern Oscillation (ENSO), combination of El Niño (ocean component of ENSO) and Southern Oscillation (atmospheric component of ENSO), to identify cases of warm eastern and central equatorial Pacific Sea Surface Temperature (SST) anomalies (Philander, 1990; Trenberth, 1991; Quin *et al.* 1987; Bigg, 1986).

ENSO events occur irregularly at intervals of 2-7 years, at an average of about 3-4 years. They typically last 12-18 months and affect weather, climate, marine ecosystems, terrestrial ecosystems, and economies worldwide (Polis, 1997). The ENSO event of 1997/1998 is recognized to be the strongest ENSO in recorded history. It is causing a very long drought in Southeast Asian Countries and in Australia with severe economic consequences. In the United States, ENSO has caused heavy rain and increasing number of typhoons and hurricanes in the eastern Pacific Ocean compared to non-ENSO years.

Studies about ENSO's impacts on SST in Pacific Ocean have been numerous. Meanwhile, very few studies have been conducted in Indonesian Seawaters, and specifically in the south Java seawaters. The objective of this study is to investigate the impact on ENSO evidences on SST derived from satellite imagery in the Java Sea and it's surrounding and its relationship on tuna catch.

2. METHODOLOGY

The study sites were the fishing ground of "PT Perikanan Samudra Besar" fishing fleet in the south Java seawaters (Fig. 1). There are 10 tuna fishing vessel operated in this area every day. Tuna catch data were obtained from daily logbook for period 1996 and 1998. These data are compiled in the gird of 1° longitude and latitude and are plotted in map.

SST data are derived from satellite imagery from the LAPAN (Indonesian Agency for Aerospace) local area coverage for 1996 and 1988 in the south Java seawaters. Twelve boxes are selected around the south Java seawaters for study areas.

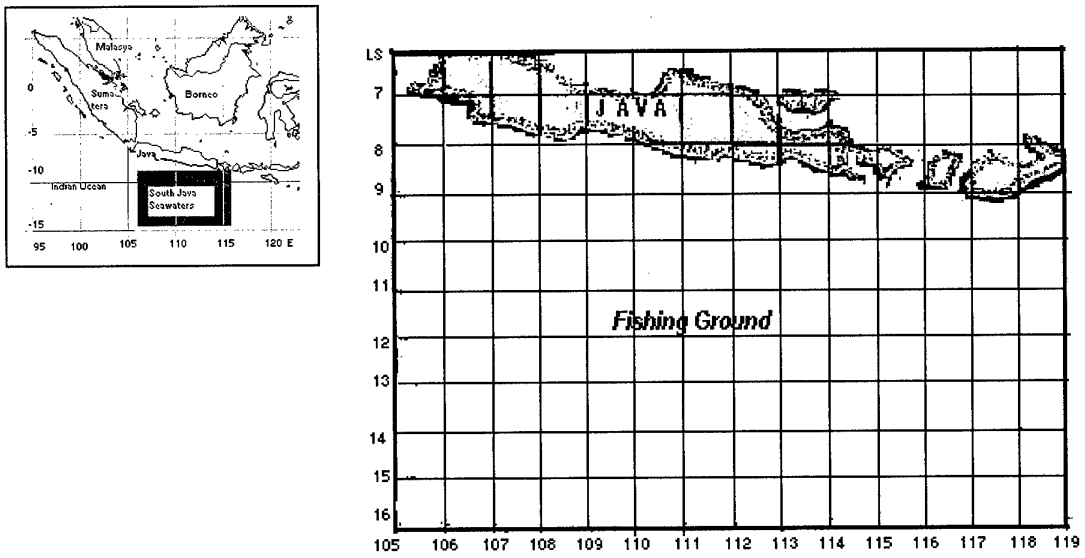


Fig. 1. Map of study area in the South Java Seawaters.

SST for AVHRR LAPAN local area coverage is estimated using formula McMillan and Crosby: SST = TW4 + 2.702 (TW4-TW5) -0.528-273.0 °C, where TW4 and TW5 are channel-4 and channel-5 of NOAA-AVHRR.

ENSO year herein are defined as years with standard deviation value of Southern Oscillation Index (SOI) <= -1.5 (Fig. 2). The determination for this value is based on the literature of ENSO years, which fall into above SOI range. Therefore, in this study, ENSO year is 1998 and non-ENSO year is 1996. Descriptive statistic is used to compare monthly mean SST during ENSO years versus non-ENSO years. T-test is used to test the statistical significant of monthly mean of ENSO years versus non-ENSO years.

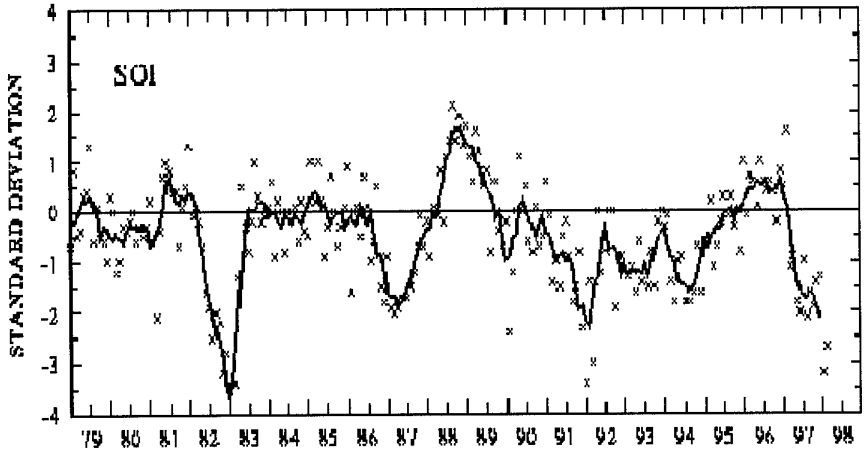


Fig. 2. Standard Deviation of Southern Oscillation Index for Determining ENSO Years.

3. RESULT AND DISCUSSION

3.1. SST in the South Java Seawaters

Monthly mean SST for each station of twelve selected stations during non-ENSO and ENSO years are presented at Table 1. The average of SST from all selected twelve stations range from 26.0°C to 28.5°C for non-ENSO years and from 25.9 °C to 27.1°C during the ENSO year.

Table 1. SST Mean Data During the Non-ENSO Years Versus ENSO Year in the South Java Seawaters.

Stations	Non-ENSO year (1996)	ENSO year (1998)
1	26.0	25.9
2	27.5	25.8
3	28.5	27.1
4	28.0	26.3
5	28.0	25.9
6	28.0	26.7
7	27.5	26.2
8	28.0	26.4
9	29.0	26.4
10	28.0	25.9
11	28.0	26.1
12	28.5	25.6

The monthly mean SST plots for each station during non-ENSO and ENSO years are presented in Figure 3. In general, monthly mean SST value in the south Java seawaters for the Non-ENSO year is higher than that of the ENSO year with the average different of 1.7°C. The lower monthly mean SST during ENSO year could be connected to the cold front shifted to the north in South Pacific, east of Australia. That cold front affecting the south Java seawaters by passing Arafuru Sea.

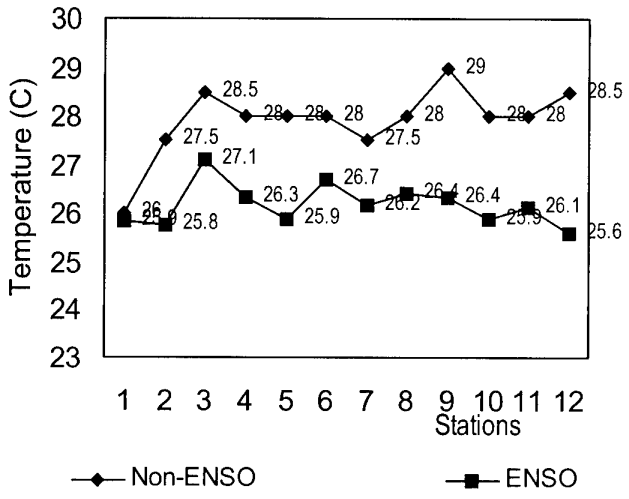


Fig. 3. SST Average Non-ENSO (1996) versus ENSO Year (1998).

The minimum value of monthly mean SST of twelve stations in the south Java seawaters occur in July for non-ENSO and ENSO years. This result is coherent with the study conducted by Pariwono (1995) that found SST minima in Java Sea occur in July to September.

In July to September, SST near Bali Island is lower than that it's surrounding. This phenomenon known as indicator of upwelling process.

3.2 Tuna Catch in South Java Seawaters

Based on the "PT Perikanan Samudra Besar" tuna fishing vessels catches, big eye tuna is the dominant catches beside yellow fin tuna in south Java seawater in 1996 and 1998. Total big eye tuna catch for each month is shown in Table 2. Total tuna catches in 1996 and 1998 are 30,401 fishes and 42,209 fishes respectively. On the other word, the big eye tuna catch in ENSO year is higher than that non-ENSO year.

Table 2. Total Big Eye Tuna Catches in 1996 (Non-ENSO year) and 1998 (ENSO year) for Every Months

Month	ENSO, 1998 (fishes)	Non-ENSO, 1996 (fishes)
February	1564	2627
March	1617	2316
April	1821	2332
May	27577	2746
June	2814	2234
July	2572	1875
August	1565	1739
September	1117	1247
October	863	1403
November	699	11882
Total	42,209	30,401

The highest big eye tuna catch in south Java seawaters in 1998 is related to the lower SST in ENSO year. Temperature changing in ENSO year can directly affect the abundance of big eye. In ENSO year is predicted that big eye tuna move up to sea surface because temperature in deeper water is too cold.

In 1996, the higher tuna catches occur for period of May, June and July, with maximum catches (2814 fishes) in June. In 1998, the higher catches occur for period February, April, May and June, with maximum catches in May (2746 fishes) (Fig 2).

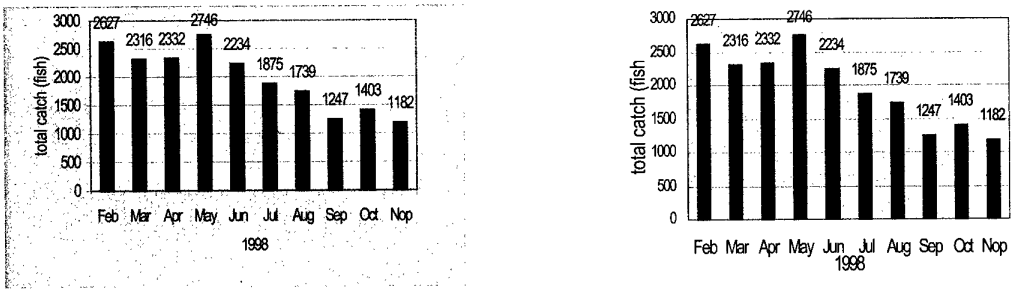


Fig. 2. Big eye monthly catches in the south Java seawaters in 1996 and 1998 respectively.

The monthly migratory pattern of big eye in Indian Ocean was deduced by use of 1967-1985 catch data of Japanese tuna long line fishery (Mohri *et al.*, 1997). During the southern hemisphere winter season, from April to September, the big eye tuna are generally distributed in the high latitude area of Indian Ocean. However, some big eye tuna also occur in the waters north the Madagascar in June, and off Java in July.

The catches pattern of big eye in 1996 and 1998 (Fig. 3) in south Java seawaters is coincided with the study conducted by Mohri *et. al,* 1997, who found that the higher big eye catches occur for period of February, May, June and July.

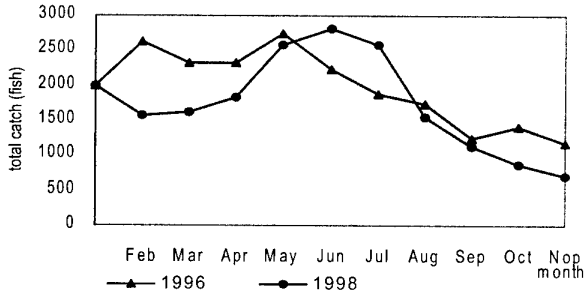


Fig. 3. The pattern tuna catch in the south Java seawater in 1996 and 1998.

4. CONCLUSION

Defining ENSO years as the years that fall in standard deviation of Southern Oscillation Index <= -1.5, the SST monthly mean in the south Java seawaters range from 25.9 to 27.1°C for non-ENSO year and 26.0°C to 28.5°C during the ENSO year.

Monthly mean SST value in the south Java seawaters ENSO years are lower than that of the non-ENSO year with the average different of 1.7°C.

Total tuna catch in 1996 and 1998 are 42,209 fishes 30,401 fishes respectively. Therefore, big eye tuna catch in ENSO year is higher than that non-ENSO year.

REFERENCES

Bigg, G. R. The Oceans and Climate. Cambridge University Press. Cambridge. 1996. 266p.

Mizuno, K., 1995. Variabilities of Thermal and Velocity Field in the Vinicy of North of Australia Basin with Regard to the Indonesia Trough flow. In: Proceeding of International Workshop the Trough flow Studies in Around Indonesian Waters. BPPT. Indonesia.

Mohri, M., E. Hanamoto, M. Nemoto, and S. Takeuchi, 1997. Fishing Season, Fishing Ground and Migratory Pattern of Big Eye Tuna in the Indian Ocean as Seen from Tuna Long Line Catches. In Japan Fisheries Bulletin, pp 1-5.

Pariwono, J.I : Effect of El-Nino Southern Oscillation (ENSO) on Fish Catch in Indonesian. Bogor Agricultural University, pp. 20-25.

Philander, S. G., 1990. El NIÑO, La Nina, and the Southern Oscillation. Academic Press, Inc. San Diego, pp. 12-25.

Polis, G. A., S. D. Hurd, C. T. Jackson, and F. S. Pinero, 1997. El NIÑO Effects on the Dynamics and Controls of an Island Ecosystem in the Gulf of California. Ecology. Vol. 78. No.6. pp. 1884-1897.

Quinn, W. H., V. T. Neal, and S. E. Antunez de Maloyo, 1987. El NIÑO Occurrences over the Past Four and Half Centuries. J. of. Geophys. Res. Vol. 92, pp. 14449-14461

Trenberth, K. E., 1991. General Characteristics of El Nino-Southern Oscillation. *In:* Glantz, M. H., Katz, R. W., and Nicholls, N. (eds). Teleconnections Linking Worldwide Climate Anomalies. Cambridge University Press. Cambridge, pp.13-42.

Derivation of Aerosol Optical Thickness over the East Asian Oceans with ROCSAT-1 OCI Imagery

Shih-Jen Huang* and Gin-Rong Liu**
*Institute of Space Science
National Central University
320 Chung-Li, Taiwan
Email: huang@sun4.oce.ntou.edu.tw
** Professor, Center for Space and Remote Sensing Research
National Central University
320 Chung-Li, Taiwan
Email: grliu@csrsr.ncu.edu.tw

KEY WORDS: aerosol optical thickness, dust storm, ocean color imager (OCI)

ABSTRACT The goal of this study is to derive the Aerosol Optical Thickness (AOT) pixel-by-pixel over ocean with ROCSAT-1 OCI imagery. The result shows that there is a high correlation between the AOT assessed from our procedure and from the SeaWiFS' operational atmospheric correlation package, SeaDAS, revealing that our method is acceptable. In the future study, OCI imagery and our procedure can be used to derive AOT distributions for the monitoring of the air quality and dust storm which comes from the northwestern and northern Mainland China.

1. INTRODUCTION

The atmosphere contains suspended particles, ranging in size from about 10^{-3} μm to about 20 μm, called aerosols. These aerosols are produced directly by natural processes and human activities. Natural aerosols include volcanic dust, sea spray, and its particulate product etc. Aerosols not only scatter but also significantly absorb the incoming solar radiation covering the entire spectrum (Liou, 1980).

Since these particles can scatter and absorb the radiance, the atmospheric aerosols directly influence the radiance reflected to space. Aerosol also provides cloud condensation nuclei that lead cloud formation and affect the earth radiation budget. In general, the Aerosol Optical Thickness (AOT) is one indicate of aerosol optical properties. The AOT over the ocean with measurements from the Advance Very High Resolution Radiometer (AVHRR) (Rao et al. 1989, Ignatov et al. 1995) and become routinely operation in the National Oceanic and Atmospheric Administration (NOAA).

In the recent years, the ground in situ measurements and the retrieved aerosol optical properties using air- and space born sensors (King et al., 1999). The global aerosol optical property monthly composite images are retrieved from two near-infrared bands (765 and 865nm)

of Sea-viewing Wide Field-of-view Sensor (SeaWiFS) (Wang et al., 2000). In this paper, the ROCSAT-1/OCI images will be used to estimate the AOT and to draw out the time variation of AOT adjacent Taiwan area.

2. METHODOLOGY

The primary goals of Ocean Color Imager ROCSAT-1, which was successfully launched on January 27 1999, are to measure the middle and low latitude ocean color and generate ocean bio-optical property products (Li et al., 1998). However, when we retrieve the ocean surface signal from measured radiance at the satellite sensors, the atmospheric effects must be removed. Studies show that the atmospheric correction removes almost more than 90% of the observed radiance at visible wavelength measured at the satellite sensor.

The OCI bands are similar to the SeaWiFS channels, but lack the 412 and 765nm bands (Liu et al., 1999). In this study, we developed an algorithm called OCITRAN. It uses two OCI bands (670 and 865nm) radiance to determinate the air mass character and sea surface albedo. After the air mass character is decided, we can estimate the aerosol size distribution and get the Angstrom exponent. Therefore, the AOT of OCI bands can be found because of the Angstrom exponent, which is related to the wavelength dependence of the AOT.

3. RESULTS

To validate the AOT algorithm, two SeaWiFS data sets are input to our algorithm and SeaDAS respectively. Those images covering the Taiwan area and the northern South China Sea were acquired at 0423z, March 25 and 0414z, April 16, 1999. The ground resolution was about 1.1x1.1km at nadir. In order to study the AOT variance, 14 OCI images covering the Taiwan area (Table 1) are used.

In order to validate the AOT retrieved algorithm, we compare the result of this algorithm and that of SeaWiFS operational model SeaDAS with two SeaWiFS data sets. The result shows that the AOT estimated by our algorithm and the SeaDAS model has a rather good consistency. Their correlation coefficients are 0.87 and 0.89 for two data sets, respectively. And their standard deviations are 0.0264 and 0.0267 (Figure 1). We also use the AERONET (AErosol RObotic NETwork) in situ measurement data at Anymon and Chinhae in Southern Korea to examine the AOT derived from OCI data. The AERONET program is a worldwide ground-based remote sensing aerosol network. Its goal is to assess aerosol optical properties and validate satellite retrievals of aerosol optical properties. Owing to the constraint of ROCSAT-1 mission and cloud contamination, there are only 3 data pairs for OCI and AERONET data. Their acquisition time are May 13 0603z, Oct. 24 0517z, and Nov. 2 0129z. The derived AOT from OCI 865nm band compared with the Aeronet measurement data is shown in Figure 2. Their correlation coefficient is 0.995 and standard deviation is 0.0069. Therefore, the AOT algorithm in this study is feasible.

For the purpose of understanding the variation of AOT on the East Asian Ocean, we selected 14 OCI images (from March 1999 to June 2000) around Taiwan area and process them with our algorithm. The AOT was taken 1°x1° space average under clear sky condition. The Figure 3 shows the fluctuation of average AOT located on (23N, 119E) near Penghu. The higher AOT observed in March and May. The lower AOT value appeared in June. According to the report of the environment information of China, the Mainland's dust storm happened on April 3-4, 1999 and March 22-23 and 27, 2000. The pattern of Figure 3 is similar to the dust storm existence time but has some time lag. Perhaps the high AOT value has some relationship with the dust storm.

4. CONCLUSION

From the comparison of SeaWiFS data, the results of this study have high correlation with those of SeaDAS. The AOT also agrees with the AERONET in situ data. We will find more data pairs of OCI and AERONET measurements to validate our algorithm in the future. However, the algorithm developed in this study is capable to retrieve the AOT. According to our result, the seasonal fluctuation of AOT can be revealed clearly with OCI data. The serious aerosol will occur in spring and fall. It shows that the Mainland's dust storm may affect the atmosphere constituent around Taiwan area. Because of its 35° inclination and on-board memory space limitation, ROCSAT-1 OCI can not take image in same area during short period. Hence, we will try to map the aerosol distribution and monthly aerosol variation with multi-temporal OCI images in next study.

ACKNOWLEDGEMENTS

The SeaWiFS data, used in this study, were provided by the Goddard DAAC, NASA, USA. The OCI data were provided by the OCI Data Distribution Center, NSPO, Taiwan. This study was supported by the NSPO, NSC, with the grant of NSC89-NSPO-A-OCI-019-01-02.

REFERENCES

[1] Ignatov, A. M., L.L. Stowe, S. M. Sakerin, and G.K. Korotaev, 1995: Validation of the NOAA/NESDIS satellite aerosol product over the North Atlantic in 1989. J. Geophy. Res. Vol. 100, No. D3, pp.5123-5132.

[2] King, M.D., Y.J. Kaufman, D. Tanre, and T. Nakajima,1999: Remote sensing of tropospheric aerosols from space: Past, present, and future, Bull. Am. Meterolo. Soc., 80, pp.2220-2259.

[3] Li, H.W., C.R. Ho, N.J. Kuo, S.J. Huang, and W. P. Tsai, 1998: ROCSAT-1/OCI—A low-latitude covering spaceborne ocean color sensor. 5th Inter. Conf. On Remote Sensing for Marine Coastal Environments, San Diego, California, 5-7 Oct. 1998, pp.245-251.

[4] Liou, K. N., 1980. An introduction to atmospheric radiation, Academic Press, New York, pp.234-292.

[5] Liu, G.R., S.J. Huang, T.H. Kuo, W. J. Chen and C. Y. Tseng, 1999. The atmospheric effect correction of the Ocean Color Imager of ROCSAT-1-simulations and using SeaWiFS data as the example, TAO, Supplementary Issue, 99-114.

[6] Rao, C.R.N., L.L. Stowe, and E.P. McClain, 1989: Remote sensing of aerosols over the oceans using AVHRR data Theory, practice and applications. Int. J. Remote Sensing, Vol. 10, No. 4, pp.743-749.

[7] Wang, M.H., S. Bailey, and C. R. McClain, 2000. SeaWiFS provides unique global aerosol optical property data. EOS, Trans. AGU, Vol. 81, pp.197-202.

Table 1. The observation time of OCI images covering Taiwan area.

Date	UTC	Date	UTC
1999/3/26	0205z	2000/2/19	0215z
1999/5/17	0211z	2000/3/22	0411z
1999/6/8	2321z	2000/3/29	0115z
1999/7/13	0710z	2000/5/5	0754z
1999/8/19	0713z	2000/5/8	0707z
1999/9/2	0122z	2000/6/4	0139z
1999/10/10	0717z	2000/6/26	0831z

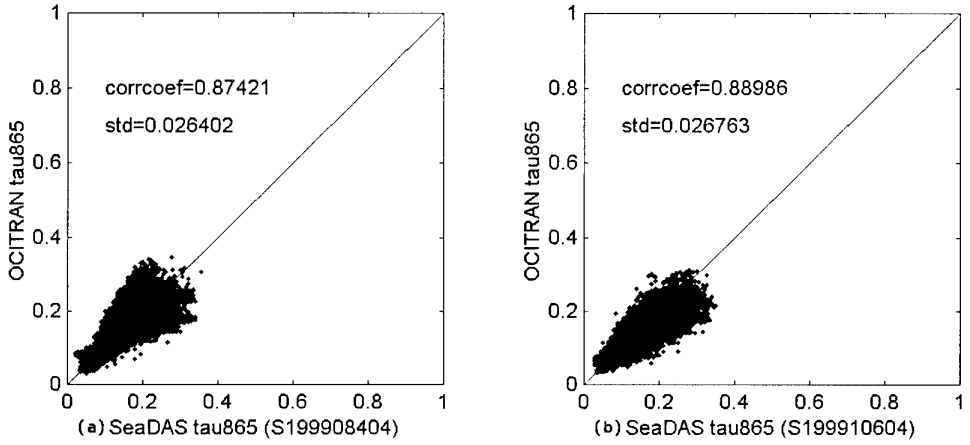


Figure 1. The Comparison of aerosol optical thickness derived from SeaWiFS data by the OCITRAN and the SeaDAS models.

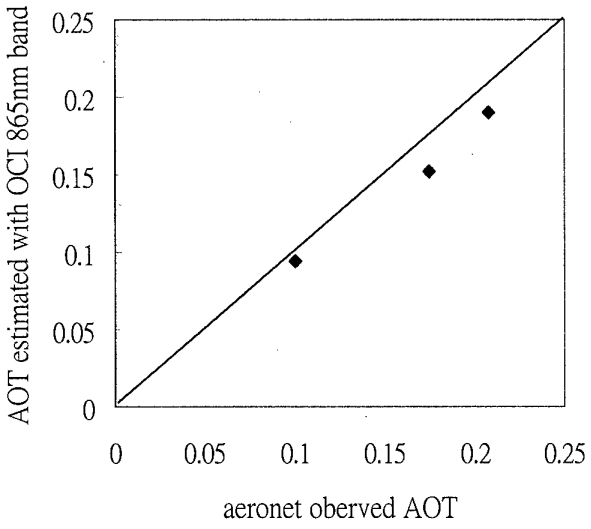


Figure 2. The comparison of aerosol optical thickness at 865nm band derived from OCI data and Aeronet data observed on Southern Korea (Corrcoef=0.995, std=0.0069).

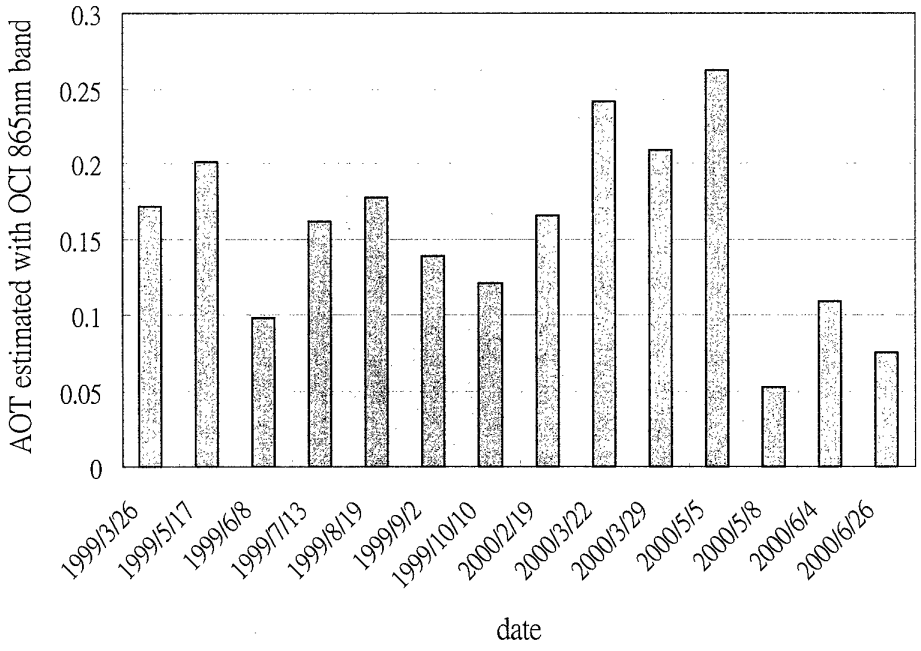


Figure 3. The variation of averaged aerosol optical thickness retrieved from OCI 865nm band around Penghu (23N, 119E).

COMPARATIVE PERFORMANCE OF SST ALGORITHMS IN THE TROPICAL OCEAN USING OCTS DATA

K. Abdullah, M. Z. MatJafri and N. M. Saleh
Universiti Sains Malaysia
11800 Penang, Malaysia
Tel: 604-6577888 Fax: 604-6579150
E-mail: khirudd@usm.my, mjafri@usm.my, nasirun@usm.my

A. Bahari
Malaysian Meteorological Service
46667 Petaling Jaya
Selangor, Malaysia
Tel: 603-7569422 Fax: 603-7550964 E-mail: alui@kjc.gov.my

KEY WORDS: algorithm, emissivity, sea surface temperature, transmittance

ABSTRACT

A two-channel algorithm for measuring sea surface temperature (SST) using non-regression coefficients was applied to the Ocean Colour Temperature Scanner (OCTS) data from the Advanced Earth Observation Satellite (ADEOS). The algorithm is based on the fact that the recorded infrared signal at the sensor is composed of three terms, namely, the surface emission, the upwelling radiance emitted by the atmosphere, and the downwelling atmospheric radiance that is reflected at the sea surface. This algorithm requires the atmospheric transmittance values of two thermal bands. In this study the transmittance function for each band was modeled using the MODTRAN code and radiosonde data. The expression of transmittance as a function of zenith view angle was obtained for each channel through regression of the MODTRAN output. The in-situ data (ship collected SST values) were used for verification of results. Contour maps of the in-situ SST values were generated because clouds covered the measured locations. Cloud contaminated pixels were masked out using the standard procedures. The cloud free pixels were extracted and converted to brightness temperature values and then substituted in the proposed algorithm. The appropriate transmittance value for each channel derived earlier was then assigned in the calculation. The correlation coefficients and the root-mean-square deviations between the computed and the ship-collected values were determined. The results were also compared with the results from OCTS multichannel sea surface temperature (MCSST) algorithm. The performance of this algorithm is comparable with the established OCTS algorithm. SST map was created and comparison with the OCTS algorithm generated map was made.

1.0 INTRODUCTION

Sea surface temperature (SST) algorithms have been determined by two basic techniques: i) regression between coincident satellite brightness temperatures and surface measurements, and ii) theoretical atmospheric transmission model with a set of representative vertical profiles of atmospheric temperature and absorbing constituents is used (Barton 1995). Various algorithms for performing this task have been developed; these include the single infrared channel method, the multichannel method and the multiangle method. The operational SST algorithms using AVHRR

data established their coefficients through regression techniques. Recently, the MCSST algorithm has been developed by NASDA for OCTS data using similar approach.

Application of regression technique requires a sufficient amount of coincident in-situ data with the remotely sensed data. The requirement is not easily achievable in the equatorial region due to unfavorable sky conditions. Therefore in this study, the algorithm that has been derived theoretically which does not require in-situ SSTs for calibration was used. This algorithm is designed to measure SST using thermal images from any satellite. The purpose of this study is to test our developed algorithm using OCTS data sets. The performance of this algorithm was compared with the NASDA MCSST and in-situ data.

2.0 DATA SETS

Three OCTS TI level 1B scenes covering the South East Asia region were selected based on availability of cloud free pixels. They were captured (daytime) by ADEOS satellite on 22 March 1997, 21 April 1997 and 13 June 1997. In-situ SST data collected by sea cruises (under the Voluntary Observing Ship Programme of the World Meteorological Organization) on these dates were supplied by the Malaysian Meteorological Service.

3.0 DATA CALIBRATION

The conversion from digital number, DN, to radiance, L (mW cm^{-2} str^{-1} μm^{-1}) was performed using the information given by NASDA. The radiance values were converted to brightness temperature values, T (K), for band 10, 11 and 12 of OCTS data by using the published conversion table (table IX of Shimada 1998). Analysis of the tabulated values for the temperature range from 273 K to 315 K, showed that the relationship could be accurately described by the polynomial equation

$$T_i = a_o + a_1 L_i + a_2 L_i^2 + a_3 L_i^3 \qquad (1)$$

The coefficients were determined through regression.

4.0 CLOUD MASKING TECHNIQUES

The thermal infrared bands were used because the near infrared bands contained some noise problems. Three techniques were employed, (a) the infrared threshold test or gross cloud check, (b) the spatial coherence technique, and (c) the channel difference (Saunders and Kriebel, 1988). For each image date, several small sub-scenes (channels 10,11,12) containing clouds and cloud free water pixels were extracted for detailed study using each technique mentioned above. Digital numbers (DN) were used in the analysis instead of brightness temperature values to simplify the data processing. After the data were passed through the series of tests described earlier, the combined cloud masks were finally obtained.

5.0 SEA SURFACE TEMPERATURE ALGORITHM

Based on the radiative transfer equation in the atmosphere for a cloud free atmosphere under local thermodynamic equilibrium, a single channel algorithm can be derived for measuring sea surface temperature for infrared band i.

$$T_s = Ti + (T_i - T_a) b_i/a_i + D(T_i)(1-a_i-b_i)/a_i \qquad (2)$$

where T_i = brightness temperature of band i
T_a = temperature of atmosphere
$D(T_i) = L_i/[dL/dT(T_i)]$
$a_i = \varepsilon_i\tau_i$
$b_i = (1 - \tau_i)(1 + \tau_i - \varepsilon_i\tau_i)$
ε_i = emissivity of sea water in band i
τ_i = atmospheric transmittance

By writing the equation for another band j, a split window expression or dual-channel algorithm (Abdullah 1994) for measuring sea surface temperature, T_s can finally be obtained

$$T_s=T_i + \frac{(a_jb_i+b_ib_j)(T_i - T_j)}{(a_ib_j - a_jb_i)} + \frac{[b_jD(T_i)(1- a_i - b_i) - b_iD(T_j)(1- a_j - b_j)]}{(a_ib_j - a_jb_i)} \quad (3)$$

The algorithm requires two environmental parameters, (i) the atmospheric transmittance and (ii) the emissivity of seawater. The transmittance was modelled using the MODTRAN code. Radiosonde data acquired on the dates of OCTS scenes were used in the MODTRAN calculation for the atmospheric model. For each channel, the view angle from the top of the absorbing atmosphere was varied in steps of 5 degrees from 0 to 65 degrees. The average transmittance values and their corresponding zenith angles were noted. Inspection of the results suggests that the relation can be approximated by the expression

$$\tau(\theta)=t_o + t_1\cos(\theta) + t_2\cos^2(\theta)\ \ t_3\cos^3(\theta) \quad (4)$$

where θ is the satellite zenith angle at the pixel location. The coefficients were determined from regression analysis.

Various emissivity values have been used in SST retrieval algorithms. The earlier algorithms used $\varepsilon = 1$. Singh (1984) assumed 0.98 in his calculation. The spectral dependence of emissivity, where ε_4=0.992 and ε_5=0.989 was considered by Becker and Li (1990).

6.0 COMPUTATION OF SEA SURFACE TEMPERATURE

Equation (3) can be used for atmospheric correction at any satellite angle or on a pixel-by-pixel basis. Cloud free seawater pixels for bands 10, 11 and 12 were extracted for SST retrieval. The digital numbers were converted to brightness temperatures and their corresponding zenith angles were calculated. The emissivity was assumed to be 0.96 (the value given in the MODTRAN manual for 12μm) in both bands. Appropriate transmittance function derived earlier was used for each image date. Having determined the transmittance as a function zenith angle and the emissivity for seawater for each band, equation (3) can be applied to measure SST

7.0 COMPARISON WITH NASDA MCSST ALGORITHM

The Multichannel Sea Surface Temperature algorithm developed by NASDA (Sakaida et al. 1998) is expressed as

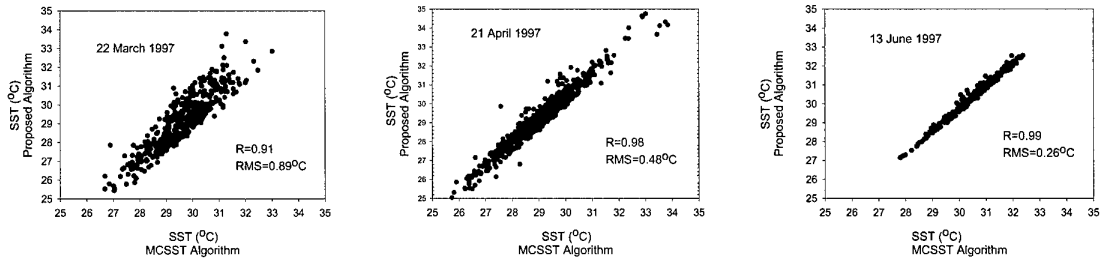
$$MCSST = c_o+c_1T_{11}+c_2(T_{11}-T_{12})+c_3(T_{11}-T_{10})+c_4(1/\cos\theta-1)(T_{11}-T_{12})+c_5(1/\cos\theta-1)(T_{11}-T_{12}) \quad (5)$$

The coefficients c_o to c_5 were taken from the table provided in the report.

The SST values computed using the proposed algorithm were then compared with the values retrieved using the MCSST algorithm. The outputs from these algorithms were correlated. The RMS deviations of the computed values using the proposed algorithm from the MCSST outputs were estimated. Table 1 and the set of graphs in Figure 1 show the results of the analysis. With these data sets the present algorithm has shown comparable performance with the established algorithm produced by NASDA.

Table 1 Comparison of proposed algorithm with MCSST

	R	RMS (°C)
22 March 1977	0.91	0.89
21 April 1977	0.98	0.48
13 June 1977	0.99	0.26



(a) (b) (c)

Figure 1 Comparison of the proposed algorithm with the MCSST algorithm (a) 22 March1997, (b) 21 April1997and (c) 13 June 1997

8.0 VALIDATION OF RESULTS

The in-situ data collected within the region of interest were used for verification of the retrieved SST values. From the analysis, unfortunately, we discovered that all the in-situ points were located on cloudy pixels. Measured SST values were interpolated spatially by plotting contour maps of the in-situ data. These maps were used to verify the computed SST values. The locations of the cloud free pixels were determined and the corresponding in-situ values were read from the map. The 22 March 1997 and 21 April 1997 cloud free pixels areas occurred within the generated contour maps. The results of the verification using the proposed algorithm and the MCSST algorithm are listed in Table 2. Figure 2 shows their scatter plots.

Table 2 Verification results from the present study

	Proposed algorithm (RMS, °C)	MCSST (RMS, °C)
22 March 1997	1.27	1.10
21 April 1997	1.24	1.18

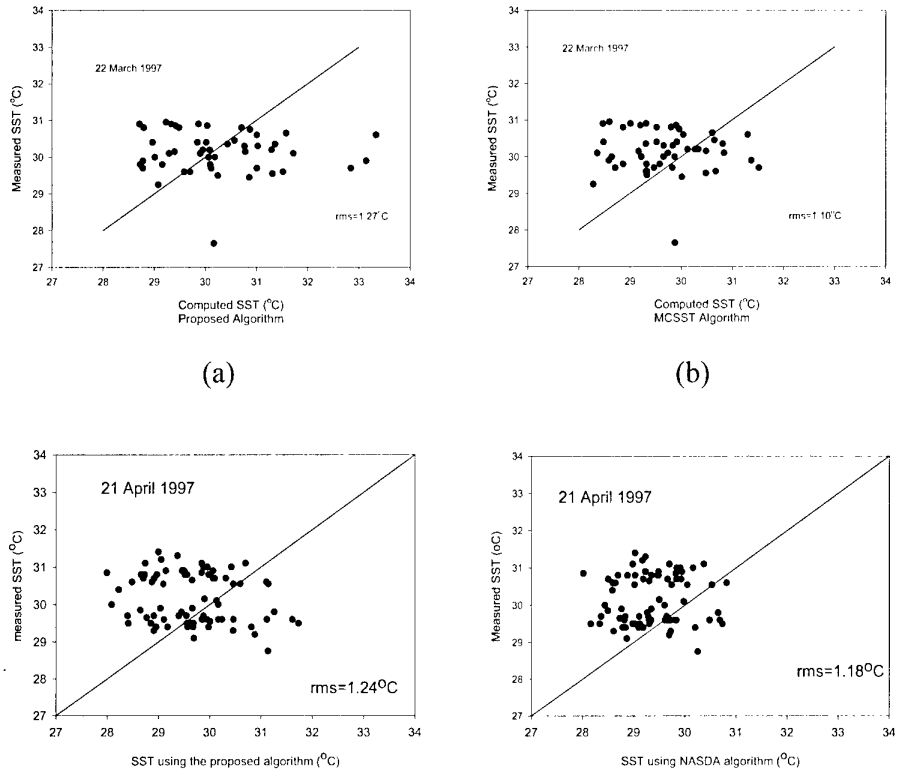


Figure 2 Comparison of computed SST values with the measured values (a) the proposed algorithm (22/3/1999), (b) MCSST algorithm (22/3/1999), (c) proposed algorithm (21/4/1999) and (d) MCSST algorithm (21/4/1999)

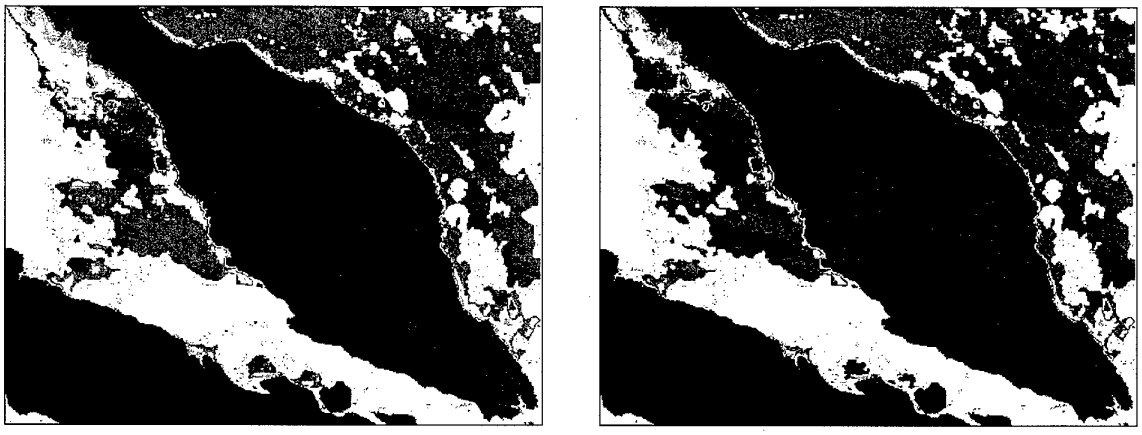
9.0 GENERATION OF SST MAPS

Both algorithms were applied to the thermal infrared bands to generate SST maps. The land and cloud areas were masked out. Figure 3 shows the generated SST maps for the image date of 21 April 1997 using the two algorithms. Similar SST patterns are shown by both images.

10.0 CONCLUSION

The results of the study indicated that the performance of the developed algorithm is comparable to the established NASDA MCSST algorithm. However, this algorithm requires only two thermal infrared bands instead of three bands used by NASDA. This algorithm takes into account of the local atmospheric condition. The retrieved SST values are highly correlated with the NASDA MCSST computed values. The computed values using the proposed algorithm deviated by a small amount from the MCSST retrieval values. The typical SST values in the studied region were between 28°C to 31°C. However very little points having these values were used in NASDA calibration analysis and some of these points showed higher in-situ values than the computed values. At higher temperatures, proposed algorithm gave slightly higher values than those computed using NASDA MCSST. Based on the analysis, proposed algorithm is capable to produce reliable results. The present study has indicated that it is possible to use this algorithm globally. It requires the knowledge of the atmospheric transmittance at the study location.

Coincident SST values are needed for more accurate verification. This will be verified by pursuing further research.



(a) (b)

Figure 3 SST maps on 21 April 1997 using (a) the proposed algorithm and (b) NASDA algorithm (colour code: blue 28-29°C, green 29-30°C, yellow 30-31°C, orange > 31°C, white for cloud and brown for land areas)

Acknowledgments

This study is partially supported by NASDA through the joint NASDA-ESCAP project. Thanks are extended to RESTEC, the Universiti Sains Malaysia and the Malaysian Meteorological Service.

References

Abdullah, K., 1994. The use of satellite data in studying geophysical and biological aspects of coastal waters. PhD Thesis, University of Dundee.

Barton, I. J., 1995. Satellite derived sea surface temperatures: Current status. Journal of Geophysical Research, 100: 8777-8790.

Becker, F. and Li, Z. L., 1990. Towards a local split window method over land surfaces. *International Journal of Remote Sensing*, 11:369-394.

Sakaida, F., Moriyama, M., Murakami, H., Oaku, H., Mitomi, Y., and Kawamura, H., 1998. The sea surface temperature product algorithm of the Ocean Colour Temperature Scanner (OCTS) and its accuracy. *Journal of Oceanography*, 54: 437-442.

Saunders, R. W. and Kriebel, K. T., 1988. An improve method for detecting clear sky and cloudy radiances from AVHRR data. *International Journal of Remote Sensing*, 9: 123-150.

Shimada, M., 1998. A cal/Val Report on the OCTS version 3 product.

Singh, S. M., 1984. Removal of atmospheric effects on a pixel by pixel basis from the thermal infrared data from instruments on satellites. The Advanced Very High Resolution radiometer (AVHRR). *International Journal of Remote Sensing*, 5: 161-183.

THE USE OF SEAWIFS SATELLITE DATA FOR OCEAN COLOUR DETERMINATION IN FISHERIES APPLICATION

Mohd Ibrahim Seeni Mohd and Tadris Ahmad
Department of Remote Sensing, Faculty of Geoinformation Science and Engineering
Universiti Teknologi Malaysia, 81310 Skudai, Johor, Malaysia
Tel : (607) 5502969 Fax : (607) 5566163 E-mail : mism@fksg.utm.my, amir_ahmad@lycos.com

ABSTRACT

Several studies have explored the possibility of using remote sensing data for marine and oceanography applications in Malaysia. These include satellite bathymetry, suspended sediment and sea bottom features mapping. Remote sensing of ocean colour in the coastal zone is currently used to map a chlorophyll concentration. Through analysis of satellite data over long time of periods, a suitable algorithm can be test and evaluated in responsed to different seasons and environment. This research intends to study on the algorithm development using SeaWiFS data with the hope to improve the results. In – situ data were collected at the time of satellite pass in Terengganu coastal area during 20 to 22 June 2000. This data will be used with SeaWiFS data acquired during this period to calibrate and validate relevant algorithm. The preminilary result shows the correlation between normalised water leaving radiance (nLw) at 443 nm and chlorophyll concentration. At this wavelengths, as chlorophyll concentration increases, absorption will also increases. The R--squared value for the correlation of above parameters is 0.96. Further investigation will be carried out to evaluate the RMSE between the in-situ measurement and the chlorophyll concentration calculated using the SeaWiFS data. This research would be beneficial to the Fisheries Department to determine potential fishing grounds.

Keywords : SeaWiFS satellite data, normalised water leaving radiance(nLw) at 443nm, fish distribution, concentration of chlorophyll

INTRODUCTION

The research includes the identification of regression coefficient through a modification of existing algorithm which is suitable to Malaysia coastal waters. The suitable algorithms will be used to estimate the concentration of chlorophyll using the satellite data. Time series satellite images are required for the analyses with in – situ data obtained simultaneously . This quantitative technique can be used to monitor the variability of chlorophyll spatially and temporally.

The study will be conducted in the coastal waters of Terengganu located between 5^0 - $6^0 30'$ N and 102^0 - 104^0 E (Figure 1). The east coast of Peninsular Malaysia has a complex oceanic characteristics due to the monsoon winds which have a significant effect on the chlorophyll distribution.

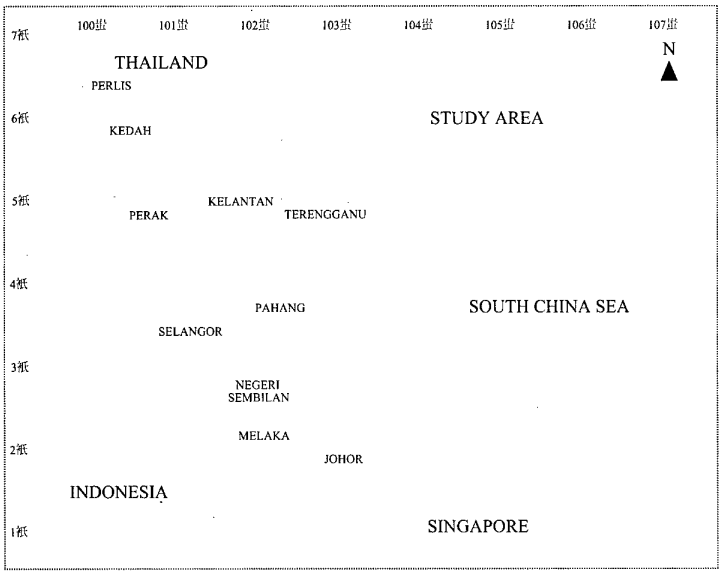


Figure 1: Location of map study area.

MATERIALS AND METHODS

This study was carried out using SeaWiFS satellite data which was taken simultaneously with in – situ measurement. SeaWiFS data was supplied by HRPT (High Resolution Picture Transmission) station at National University of Singapore. The raw level 1A data was processed using SEADAS image processing to extract normalised water leaving radiance (nLw). The influence of molecular scaterring from atmosphere is corrected by employing an atmospheric correction procedured, referred as Gordon and Wang algorithm(Wang 1994). It is necessary to normalised the radiance by the incoming solar irradiance to eliminate sun zenith angle effects and atmospheric effects.

Chlorophyll concentration was quantitatively estimated using an algorithm proposed by Robert Frouin from Scripps Institute for Oceanography. However the algorithm has been modified prior to regional variability.

$$\text{pigment} = 10^{(A - B * \text{NDPI})} \qquad (1)$$

$$\text{NDPI} = \left[\frac{R443}{R490}\right] - \left[\frac{R565}{R490}\right]$$

C = phytoplankton concentration
A and B = regression coefficient (site – spesific)

The algorithm above then has been iterated to retrieve the regression coefficient.

Log Chl = A (NDPI) – B (2)

RESULTS

SeaWiFS data taken on 20 June 2000 over Terengganu coast of Malaysia was available on compact disc. Sea – truth of chlorophyll had been taken at 4 stations by Unipertama 7 and Unipertama 3 ships .

The values of normalised water leaving radiance at several bands corresponding to chlorophyll concentration are given in table 1.

Table 1. Normalised water leaving radiance (nLw) and chlorophyll concentration for several points along the on – shore to off shore ship track.

Station	nLw 443	nLw 490	nLw 555	Chlorophyll
1	0.285	0.685	0.617	0.146
2	0.526	1.025	0.678	0.138
3	0.741	1.254	0.895	0.117
4	0.749	0.815	0.405	0.121
5	0.195	0.496	0.323	0.075
6	0.155	0.413	0.237	0.089
7	0.109	0.326	0.177	0.113
8	0.251	0.454	0.230	0.063

Figure 2 presents a relationship between the normalised water leaving radiance (nLw) at 443 nm and chlorophyll . When the chlorophyll concentration increase, there is more absorption in the blue and the nLw at 443 nm should decrease.

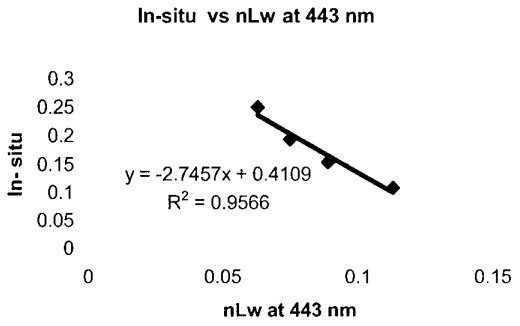


Figure 2: Relation between chlorophyll concentration and normalised water leaving radiance at 443 nm (blue wavelength) observed by Unipertama 7 cruise.

Figure 3 allows a comparison of chlorophyll determined from in - situ with the chlorophyll concentration as estimate from the SeaWiFs data. Results show that the chlorophyll

concentration derived from satellite image is generally larger than that derived from in-situ measurement at some stations. The CAL-P6 algorithm uses a sixth-order polynomial of the ratio of radiances at 490 nm and 555 nm proposed by Kahru and Mitchell (1999) also show a significant overestimation by SeaWiFS at high chlorophyll concentration.

The details about comparison of the value are shown in table 2. The root-mean-square error (RMSE) of chlorophyll concentration is about 0.050 mgm^{-3}. Validation of the SeaWiFS-derived chlorophyll values with 7 concurrent in - situ measurements showed high correlation $r^2 = 0.75$.

Table 2. Sea truth measurement and the calculated amout of chlorophyll concentration using satellite data.

Station	Chlorophyll concentration from in-situ measurement	Chlorophyll concentration estimated by satellite
1	0.146	0.080
2	0.138	0.083
3	0.117	0.104
5	0.075	0.114
6	0.089	0.116
7	0.113	0.116
8	0.063	0.118

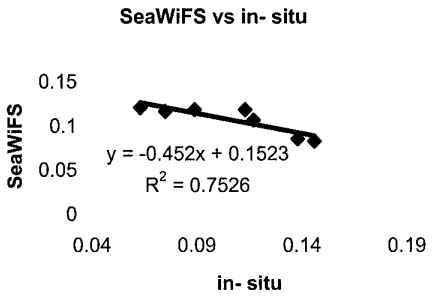


Figure 3: A good relationship between the sea truth measurement and satellite data for estimating chlorophyll concentration value($r^2 = 0.75$).

CONCLUSIONS

Site specific algorithm have been derived from the nLw at 443, 490, 555 using modified Frouin algorithm . The regression coefficient for A and B are 0.22 and 0.89 respectively. Although the results are encouraging , further in – situ measurements need to be done to compare the variability of the chlorophyll distribution before and after the monsoon seasons. The avaibility to relate

chlorophyll concentration to optical characteristic is seriously impaired by the relatively small quantity of coincident in – situ measurement during satellite overpass.

In general, chlorophyll with high concentration was distributed around the coast line compared to area far from the coast. However from the study some of the area which is far from the coast has a high chlorophyll concentration. This phenomena happen due to a strong current that move the chlorophyll patchines from coastal area. Moreover the effect of upwelling is more marked when upwelling occurs on coastlines with a continental shelf. When upwelling occurs along a coastline, the upwelled water which carry the floating chlorophyll tend to move away from the coast. The monsoon winds have a significant effect on the current circulation in the South China Sea. According to Nasir *et al.* 1996, from July to September 1996, the net current flow near the coast of Kuala Terengganu is toward the southwest direction.

The movement of the current can be detected clearly when observe the map of chlorophyll distribution using satellite image(Figure 4). The result of the study reveals that the chlorophyll concentration pattern of 0.104 – 0.129 mgm^{-3} can be used as a tracer for the current movement.

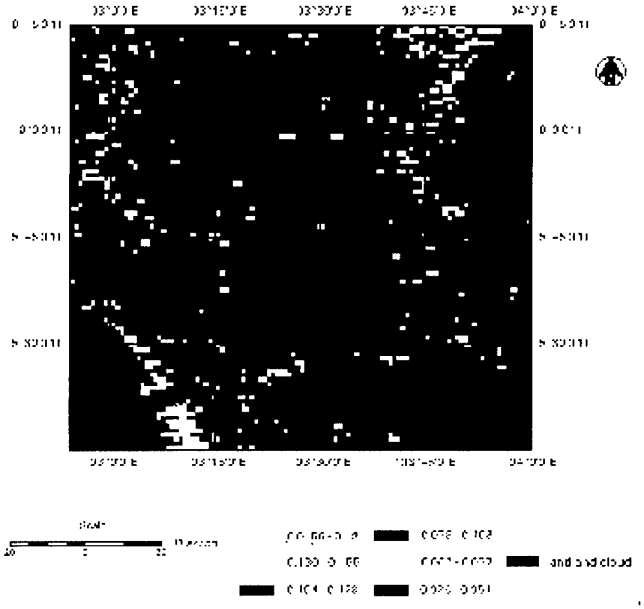


Figure 4:Chlorophyll concentration distribution estimated using SeaWiFS satellite data.

ACKNOWLEDGEMENTS

The authors would like to thank the SeaWiFS Project (Code 970.2) and Distributed Active Archive Center (Code 902) at the Goddard Space Flight Center,Greenbelt MD 20771 for the production and distribution of these data respectively. These activities are sponsored by NASA's Mission to Planet Earth program. Thanks are also due to CRISP of NUS for supplying LAC data. The contribution from technical staff of Universiti Teknologi Malysia and Universiti Putra Malaysia Terengganu are duely acknowledge.

REFERENCES

Fougnie, B., Deschamps, D. Y. and Frouin, F.(1999)."Vicarious Calibration of the POLDER Ocean Colour Spectral Bands using In – situ Measurement." IEEE Transactions on Geoscience and Remote Sensing. **37 (3)**. 1567-1574

Kahru, M. and Mitchell, B.G. (1999). "Empirical chlorophyll algorithm and preliminary SeaWiFS validation for the California Current." International Journal Of Remote Sensing. **20**. 17.

Nasir, M. S., Camerlengo, A. L. & Wan, H. K. (1996). "Coastal Current in the Northern Region of the East Coast of Peninsular Malaysia." Sains Malaysiana. **26 (2)** .5-14.

Wang, M. and Gordon , H . R . (1994). "A Simple, moderately accurate, atmospheric correction algorithm for SeaWiFS." Remote Sensing of Environment. **50**. 231 – 239.

The 21st Asian Conference on Remote Sensing
December 4-8, 2000 Taipei, TAIWAN

CLASSIFICATION OF ALGAL BLOOM TYPES FROM REMOTE SENSING REFLECTANCE

Soo Chin LIEW, Leong Keong KWOH, and Hock LIM
Centre for Remote Imaging, Sensing and Processing
National University of Singapore
Blk. SOC1 Level 2, Lower Kent Ridge Road, Singapore 119260
Tel: (65) 8745069 Fax: (65) 7757717 email: liew_soo_chin@nus.edu.sg
SINGAPORE

KEY WORDS: Ocean color, reflectance, algal blooms, phytoplanktons, classification

ABSTRACT A technique for classification of phytoplankton bloom types from remote sensing reflectance is described in this paper. Several minor algal bloom events were sighted and their characteristics reflectance signatures were collected using a handheld spectrometer during a series of sea-truth water sampling campaigns carried out from Dec 1996 to Dec 1999 in coastal waters around Singapore. Reflectance spectra of two additional algal bloom classes were also collected during two field trips to the Manila Bay. In order to assess the potential of utilizing satellite ocean color sensors for algal bloom detection and classification, reflectance data for the SeaWiFS and future MERIS sensor spectral bands were simulated from the in-situ radiance data. An algorithm based on the singular value decomposition (SVD) technique was then applied for classification of algal bloom types from the simulated satellite sensor reflectance data. The results show that all the eight algal bloom classes can be distinguished from the clear sea water reference sample. The average accuracy of classification using this technique for all the classes are 98.6% (for MERIS) and 96.6% (for SeaWiFS), in comparison to 87.5% (MERIS) and 73.8% (SeaWiFS) if the reflectance values are used.

1. INTRODUCTION

Phytoplantons (or algae) constitute the base of the marine food web. However, algal blooms may cause harm by shading other aquatic life, depleting the dissolved oxygen content, and causing paralytic or diarrhetic shellfish poisoning (Richardson 1997). It is important to monitor occurrences of algal blooms due to their strong social, economic and health impacts. Satellite remote sensing measurement of ocean color provides a tool complementary to in-situ sea-truth measurements for algal bloom monitoring. As the individual phytoplankton pigments are characterized by their unique light absorption features, this property allows detection and identification of algal blooms by ocean color remote sensing technique (Cullen et al. 1997, Kahru and Mitchell 1998, Sathyendranath et al. 1994),

Currently, the SeaWiFS sensor on board the Orbview 2 satellite (launched October 1997) provides ocean color data with about 1-km resolution. It has six bands in the visible region and two in the near-infrared region. Each band has a 20-nm bandwidth. The recently launched MODIS sensor on board the NASA's Terra satellite has eight ocean color bands in the visible spectral region, with 10 nm bandwidth. The other recent sensor was the OCTS onboard the Japan's ADEOS satellite launched in August 1996. ADEOS ceased operation in June 1997 when the ADEOS satellite stops its operation. It was the first second-generation ocean color sensor after the 10 years gap since NASA's CZCS. Future planned ocean color sensors include the NASDA's ADEOS2-GLI and ESA's ENVISAT-MERIS. These future sensors have more wavelength bands, all with about 10 nm bandwidths. With the availability of these ocean color satellites, it is foreseeable that satellite ocean color data will play an increasingly important role

in the monitoring of algal blooms. Algorithms for algal bloom detection and for classification of algal bloom types will be required.

In this paper, we describe a method of detecting and classifying algal bloom types based on the singular value decomposition technique. Satellite remote sensing reflectance signatures for several types of algal blooms were simulated using in-situ reflectance data measured during a series of water sampling campaigns around Singapore and in Manila Bay. The satellite sensors tested are SeaWiFS and MERIS.

2. ALGAL BLOOM CLASSES

Sea-truth water sampling campaigns were carried out from Dec 1996 to Dec 1999 in coastal waters around Singapore (Lin et al. 1999, Liew et al. 2000). In-situ reflectance spectra from sea water surface were acquired using a portable spectroradiometer. Several minor algal bloom events were sighted and their characteristic reflectance signatures were collected during this period. The classes of algal blooms observed include: Trichodesmium (a type of cyanobacteria); Chain forming diatoms; Chochlodinium (naked dinoflagellate); Dinoflagellates predominantly Dinophysis caudata; Diatoms (Rhizolenia Sp.); and mixture of chain forming diatoms (Skeletonema type) with some armoured dinoflagellates. Two additional algal bloom classes were collected during two field trips to the Manila Bay. One trip was carried out during the algal bloom episode (mainly Ceratium and Pyrodinium Bahamense) in Aug 1998, and the other in March 2000. Although there was no report of red tide during the later trip, results of water sampling in Manila Bay indicated that there were signs of increasing phytoplankton counts. A class of sea water reference spectra for sea water samples with low chlorophyll and low suspended solids was also collected during the regular water sampling field trips.

Altogether eight algal bloom classes and one reference sea water class are used in the analysis. The nine classes of spectra are tabulated in Table 1.

Table 1: The nine classes of reflectance spectra from algal blooms and reference sea water

Class	Description
1	Clear sea water reference (Singapore)
2	Trichodesmium (Singapore)
3	Chain forming diatoms (Singapore)
4	Cochlodinium (Singapore)
5	Ceratium and Pyrodinium Bahamense (Manila Bay)
6	Dinoflagellates (mainly Dinophysis caudata) (Singapore)
7	Diatoms (Rhizolenia Sp.) (Singapore)
8	Chain forming diatoms (Skeletonema) with some armoured dinoflagellates (Singapore)
9	Protoperidinium and Ceratum (Manila Bay)

3. SPECTRAL REFLECTANCE SIGNATURES OF ALGAL BLOOM CLASSES

Spectral reflectance refers to the ratio of the detected radiance reflected from a target surface to the total incidence irradiance. In this project, a handheld spectrometer (GER 1500) was used to measure the radiance reflected from the sea surface. The detected radiance from the sea surface was normalized by the radiance reflected off the surface of a reference white plate to obtain the reflectance of the sea surface. The spectrometer has 512 wavelength channels covering the wavelength from 350 nm to 1050 nm, with a wavelength resolution of 2 nm.

From the collected spectra, SeaWiFS and MERIS data are simulated according to the band specifications shown in Table 2. The simulation is done by integrating the spectrometer radiance

within each specified wavelength window to obtain the desired radiance for the corresponding SeaWiFS and MERIS channels. A flat spectral response curve is assumed for each of the satellite sensor channels. Only the channels in the visible region (400 nm to 760 nm) are considered in the simulation. Hence, the first 6 bands of the SeaWiFS sensor and the first 10 bands of the MERIS sensor are simulated. The simulated SeaWiFS and MERIS spectral reflectance data for the reference sea water and the eight algal bloom classes are shown in Fig. 1. Each spectrum shown in Fig. 1 is the mean of a set of spectra corresponding to the reference sea water and each of the algal bloom classes. The spectra have been normalized so that each of them has a mean value of zero and a variance of one. In this way, the magnitude of reflectance has no influence on the normalized spectra, and the shapes of the spectra can be compared directly.

Table 2: Spectral bands of the SeaWiFS and MERIS sensors

MERIS															
BN	1	2	3	4	5	6	7	8	9	10	11	12	13	14	15
BC	412.5	442.5	490	510	560	620	665	681.25	705	753.75	760	775	865	890	900
BW	10	10	10	10	10	10	10	7.5	10	7.5	2.5	15	20	10	10
SeaWiFS															
BN	1	2	3	4	5	-	6	-	-	-	7	-	8	-	-
BC	412	443	490	510	555	-	670	-	-	-	765	-	864	-	-
BW	20	20	20	20	20	-	20	-	-	-	40	-	40	-	-

Note: BN = Band Number, BC = Band Centre (nm), BW = Band Width (nm)

It can be seen that the MERIS spectra of the eight algal bloom classes are quite distinct from each other. For many algal bloom types, the spectra can be differentiated visually from their shapes around the chlorophyll absorption band at 670 nm. In comparison, the SeaWiFS does not have spectral bands beyond 670 nm. Hence, it is expected that SeaWiFS will fare poorer in terms of accuracy in classification of the algal bloom types.

4. CLASSIFICATION OF ALGAL BLOOMS FROM REFLECTANCE

An algorithm based on the singular value decomposition (SVD) technique (Danaher and Omongain 1992) has been developed for the detection and classification of algal bloom types from reflectance data. This algorithm is a type of supervised classification technique. In this algorithm, a "key vector" $V_i(\lambda)$ for each algal bloom class labelled by the subscript i is first determined from the reflectance spectra of the algal bloom class of interest measured during the field trips. This key vector acts as a sort of template for this class of algal bloom. A given measured spectrum $R(\lambda)$ to be classified is then "matched" to this key vector using the dot-product operation to give a key value w_i. Mathematically, the dot-product operation is represented by the formula:

$$w_i = \sum_{\lambda} R(\lambda) V_i(\lambda) \tag{1}$$

Ideally, if the spectrum $R(\lambda)$ belongs to class-i, then w_i=1, otherwise w_i=0. Using a training set of spectra of known classes, the key vector for each of the nine classes (8 algal bloom classes + 1 reference sea water class) are obtained using the singular value decomposition technique. The key vectors are then matched to each of the unknown spectra $R(\lambda)$ to be classified, using the dot-product operation. In this way, each spectrum is transformed into a vector of nine key values. The results of supervised minimum distance classification in the key value space are shown in Tables 3 and 4 for the SeaWiFS and MERIS sensors respectively. For comparison, the results of supervised minimum distance classification using normalized spectral values of the respective sensors are shown in Tables 5 and 6.

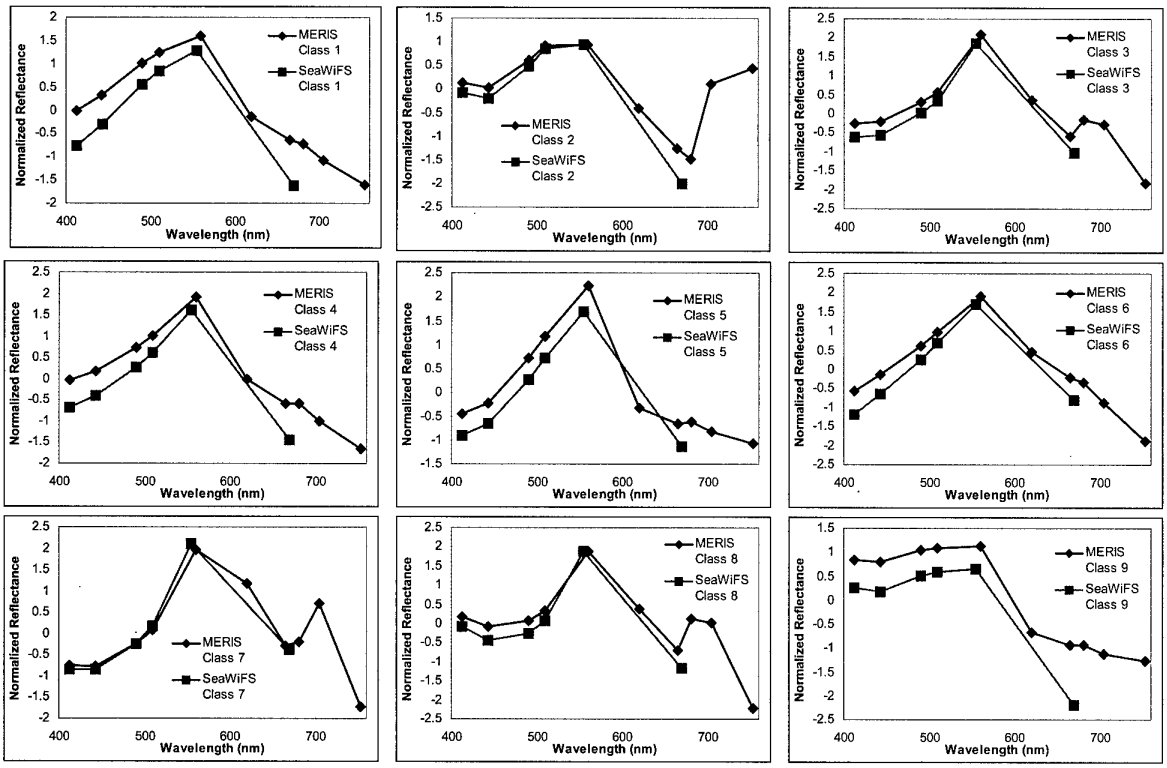


Figure 1: Simulated SeaWiFS and MERIS spectra for the reference sea water class (class 1) and the 8 algal boom classes (Class 2 to 9)

Table 3: Minimum distance classification in the key value space for SeaWiFS

		Assigned Class (%)									
		1	2	3	4	5	6	7	8	9	Total (%)
Actual Class	1	100	0	0	0	0	0	0	0	0	100
	2	0	69.6	0	0	0	0	0	0	30.4	100
	3	0	0	100	0	0	0	0	0	0	100
	4	0	0	0	100	0	0	0	0	0	100
	5	0	0	0	0	100	0	0	0	0	100
	6	0	0	0	0	0	100	0	0	0	100
	7	0	0	0	0	0	0	100	0	0	100
	8	0	0	0	0	0	0	0	100	0	100
	9	0	0	0	0	0	0	0	0	100	100

Average Overall Accuracy **96.6 %**

Table 4: Minimum distance classification in the key value space for MERIS

		Assigned Class (%)									
		1	2	3	4	5	6	7	8	9	Total (%)
Actual Class	1	100	0	0	0	0	0	0	0	0	100
	2	13.0	87.0	0	0	0	0	0	0	0	100
	3	0	0	100	0	0	0	0	0	0	100
	4	0	0	0	100	0	0	0	0	0	100
	5	0	0	0	0	100	0	0	0	0	100
	6	0	0	0	0	0	100	0	0	0	100
	7	0	0	0	0	0	0	100	0	0	100
	8	0	0	0	0	0	0	0	100	0	100
	9	0	0	0	0	0	0	0	0	100	100

Average Overall Accuracy **98.6 %**

Table 5: Minimum distance classification in the normalized spectral value space for SeaWiFS

		Assigned Class (%)									
		1	2	3	4	5	6	7	8	9	Total (%)
Actual Class	1	97.5	2.5	0	0	0	0	0	0	0	100
	2	4.35	91.3	0	0	0	0	0	0	4.35	100
	3	0	2.5	42.5	5.0	0	0	37.5	0	12.5	100
	4	0	20	0	50	20	10	0	0	0	100
	5	0	0	0	0	77.8	22.2	0	0	0	100
	6	0	0	0	0	10	90	0	0	0	100
	7	0	0	0	0	0	0	100	0	0	100
	8	0	0	0	0	0	0	50	25	25	100
	9	0	10	0	0	0	0	0	0	90	100

Average Overall Accuracy: **73.8%**

Table 6: Minimum distance classification in the normalized spectral value space for MERIS

		Assigned Class (%)									
		1	2	3	4	5	6	7	8	9	Total (%)
Actual Class	1	100	0	0	0	0	0	0	0	0	100
	2	0	69.6	0	0	0	0	0	0	30.4	100
	3	0	0	57.5	15	0	0	15	2.5	10	100
	4	20	0	0	60	0	20	0	0	0	100
	5	0	0	0	0	100	0	0	0	0	100
	6	0	0	0	0	0	100	0	0	0	100
	7	0	0	0	0	0	0	100	0	0	100
	8	0	0	0	0	0	0	0	100	0	100
	9	0	0	0	0	0	0	0	0	100	100

Average Overall Accuracy: **87.5%**

The accuracy of minimum distance classification using the normalized spectral reflectance values of the SeaWiFS sensors is only 73.8%. With four additional bands of the MERIS sensor, the accuracy improves to 87.5 % (see Tables 5 and 6). This improvement is expected, as the additional bands are located around the chlorophyll-a absorption band at 670 nm, which helps to discriminate between the algal bloom classes. The transformation of the reflectance spectra into the key value space using a simple matrix multiplication operation improves the classification accuracy to 96.6% and 98.6% for SeaWiFS and MERIS respectively (see Tables 3 and 4). It is noted that for both SeaWiFS and MERIS sensors, the spectra from eight out of nine classes are correctly classified after transformation into the key values. The only class that performs poorly is class 2 (Trichodesmium).

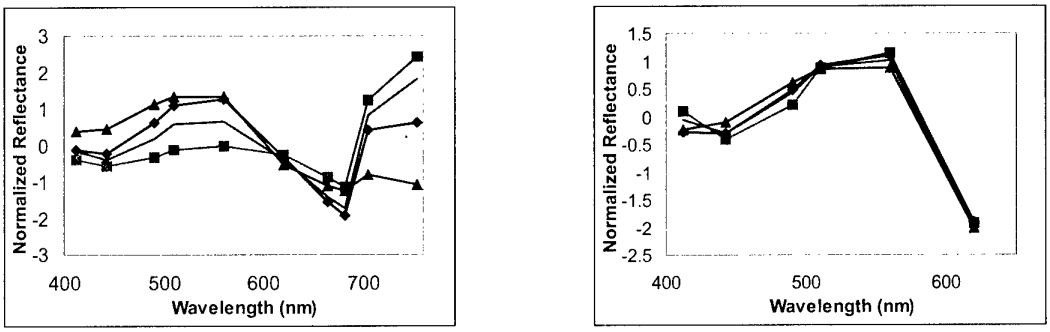


Figure 2: Samples of MERIS (left) and SeaWiFS (right) reflectance spectra of class 2 (Trichodesmium)

Samples of the reflectance spectra of class 2 (Trichodesmium) are shown in Fig. 2. For MERIS, all the class 2 reflectance spectra have similar shapes in the shorter wavelength (<650 nm) region. The variation is greater in the longer wavelength region. Hence, it is expected that some spectra be misclassified. For SeaWiFS, the within class variation is smaller. However, the class 2 spectra shape is very similar to class 9 and hence many spectra are misclassified as class 9.

5. CONCLUDING REMARKS

We have presented a technique for classification of algal blooms types from remote sensing reflectance. This technique is based on a linear transformation of the normalized reflectance spectra into a "key value" space. The success of this technique depends on the availability of spectral reflectance signatures of known algal bloom classes. The key vectors required for constructing the transformation matrix are derived from this set of reflectance signatures. The present database of algal bloom signatures used in this study have been accumulated during a 3-year period of water sampling in Singapore waters and in the Manila Bay. The classification technique is tested on the simulated data for the current SeaWiFS and future MERIS ocean color sensors. The simulated data are constructed from in-situ radiance data measured using a handheld spectrometer. Atmospheric effects are not included in the simulation. Hence, it is assumed that atmospheric correction has been done before the classification technique is applied. This study show that the spectral bands of the current SeaWiFS sensor is sufficient for algal bloom classification, while the MERIS sensor provides certain advantages in identifying different algal bloom types.

ACKNOWLEDGMENTS

The authors acknowledge support from SPOT Asia Pte. Ltd, in the form of a grant awarded by the Regional Institute of Environmental Technology (RIET) under the Asia-EcoBest Work Programme '99. Some of the data used in this study were obtained during field trips conducted with partial funding from the National Space Development Agency of Japan (NASDA) through a joint NASDA-ESCAP project entitled "National capacity building for sustainable environment and natural resources management through research and studies on the uses of ADEOS data". The authors would like to thank Dr Michael Holmes of the Department of Biological Sciences and the Tropical Marine Science Institute (TMSI), National University of Singapore (NUS); Dr Serena Teo of TMSI, NUS; Dr Karina Gin of the Department of Civil Engineering, NUS; and Dr. I-I Lin (currently at the National Centre for Ocean Research, National Taiwan University) for their contributions in the water sampling field trips in Singapore. The assistance rendered by Prof. Rhodora Azanza and Ms Arlynn Gedaria of the Marine Science Institute, University of Philippines at Diliman during the field trips in Manila Bay is gratefully acknowledged.

REFERENCES

Cullen, J. J., A. M. Ciotti, R. F. Davis, and M. R. Lewis (1997), Optical detection and assessment of algal blooms, Limnology and Oceanography, 42(5), 1223-1239.

Danaher, S. and E. Omongain (1992), Singular value decomposition in multispectral radiometry, Int. J. Remote Sens. 13, 1771-1777.

Kahru, M. and B. G. Mitchell (1998), Spectral reflectance and absorption of a massive red tide off southern California, Journal of Geophysical Research 103(C10), 21601-21609.

Liew, S. C., I-I Lin, H. Lim, L. K. Kwoh, M. Holmes, S. Teo, S. T. Koh, and K. Gin (2000), Tropical algal bloom monitoring by sea truth, Paper presented at 28th International Symposium on Remote Sensing of Environment, 27 - 31 March, 2000, Cape Town, South Africa.

Lin, I-I, S. C. Liew, H. Lim, L. K. Kwoh, M. Holmes, S. Teo, S. T. Koh and K. Gin (1999), Classification of Tropical Algal Bloom Types By Sea Truth Spectral-Radiometric Data, Proc. 20th. Asian Conference for Remote Sensing, 22-25 November 1999, Hong Kong, China.

Richardson, K. (1997), Harmful or Exceptional Phytoplankton Blooms in the Marine ecosystem. Adv. Mar. Biol. 31, 301-385.

Sathyendranath, S., F. E. Hoge, T. Platt, and R. N. Swift (1994), Detection of phytoplankton pigments from ocean color: improved algorithms, Applied Optics 33, 1081-1089.

The 21st Asian Conference on Remote Sensing
December 4-8, 2000 Taipei, TAIWAN

Vegetation Spectral Feature Extraction Model

Qian Tan , Hui Lin

Dept. of Geography & Joint Lab. For Geoinformation Science ,

The Chinese University of Hong Kong , Hong Kong

Tel: (+852)-26098105

E-mail: tanqian@cuhk.edu.hk

Yongchao Zhao , Tong Qingxi , Zhen Lanfeng

Lab. Of Remote sensing Information Sciences ,

Institute of Remote Sensing Applications ,CAS , Beijing , 100101 , China

Key words : vegetation, hyperspectral, spectral feature extraction

Abstract :

A new spectral feature selection and extraction model(***for vegetation only!***)--- Vegetation Spectral Feature Extraction Model （VSFEM） is presented . A lot of vegetation field spectrum analyzed , 8 vegetation spectral feature positions are acquired , through which a series of feature parameters are achieved .

1. Introduction

Spectral feature extraction were mostly from or for target classification .

Principle Component Analysis (PCA) is used by most people . This method produces a new series of images , put in order by information content (or variance) . Relationships among images are essentially removed . With forward principle components , most information content can be seen , which is the optimal result for minimum mean square error . Green (1988) developed PCA , who applied MNF (Minimum Noise Fraction) so as to make every component after MNF transform in order by signal-to-noise ratio (S/N) from large to small , instead of variance . Jia (1999) developed PCA to segment PCA to make feature extraction , whose classification and display result has made some progress . Though PCA can compress and extract information with minimum mean square error , information of principle component images is hard to explain directly according to spectrum , moreover , sample distribution not considered , it's uncertain to get optimal classification result . After realizing this problem , Fukunaga (1970) proposed a new transform method , that was , to find an transform matrix , who satisfied the formula , $T(S_1+S_2)T^{-T}=I$, in which Si is the correlation matrix of class i . This method is effective when differences of average values are small and covariance play a key role , but for common situation , is ineffective (Foley , 1975) . Kazakos (1978) put forward a feature extraction algorithm ---linear scalar extraction , making minimum classification error probability for two classes of multi-dimension normal distribution . This method can find an optimal vector to get minimum classification error probability , but when more than one feature is required , this method has no power . After considering within-class and between-class distance , Richard (1986) posed a feature extraction method---Canonical Analysis (CA) , Lee (1993) raised a feature extraction method based on decision boundary .

This paper puts forward VSFEM(Vegetation Spectral Feature Extraction Model) , which is very different from above methods . VSFEM aims at vegetation spectral feature extraction , from or for controlling vegetation spectral curves , through an amount of analysis of field vegetation spectral curves to get some regularity . Compared to above methods , VSFEM pay much attention to target spectral reflection of biological and physical features , not thinking feature extraction just as pattern recognition or information compression of a branch of mathmatics .

2. Study Area and Data Collection

Study Area

A study area near Changzhou city, Jiangsu Province, China was chosen for collecting ground data . The study focused on vegetation , which included principle types of agricultural crops and trees in the study area , such as , rice , maize , peanut , sweet potato , cotton ,soybean , cabbage , carrot , etc .

Data Collection

During the period from late August(middle season in vegetation growing circle) to mid-October(later season in vegetation growing circle), 55 field vegetation spectral data were acquired from 20 sites in Changzhou by SE-590 ---a portable field spectroradiometer . At the same time , some biochemical parameters , such as chlorophll concentration , leaf area index(LAI) were measured . Data were collected in nadir orientation of the radiometer and at about 45° solar zenith angle. Four scans at a time were averaged as the final spectra in each measurement. In addition , the data were collected from 11:00 to 13:00 .

When trees were measured , branches with leaves were picked down and laid on the ground. The specific parameters of SE-590 Portable Field Spectroradiometer are shown as follows:

Wavelength: 400 – 1100 nm **Spectral resolution : 4.0 nm** **Sample channels: 252** **Field of view:15^0**

3. Methodology

3.1 Vegetation Spectral Feature Extraction Model

There are some special features, such as "green peak", "red valley" and "NIR platform", in the curve of the reflectance, reflectance intensities of these featured positions vary remarkably or regularly with the species or growth periods. So, it is possible that we design special parameters that are good tokens of curve shape of different species or growth stages. Moreover , if we want to discuss correlation between spectra and vegetation biochemical properties, we also need to find some special spectral parameters. For this case, we define eight special positions(feature position) and design many parameters(feature parameter) like NDVI to discuss the species and property(including the growth stage) difference of typical vegetation in Changzhou. All the eight feature positions as M, B, G, Y, R, V, I1 and I, and some feature parameters are shown in ***fig.1*** . This figure shows a typical spectral curve R(λ) .The definition of 8 feature positions as shown in ***fig.1*** and their agorithms are as follows:

1). Absorption peak in purple-blue band-M(λ_M , R_M): The position where the reflectance is the minimum in the wavelength range of <500nm:

$$R_M=MIN(R(\lambda\in 380\text{-}500nm)) , \lambda_M=\lambda_i(R(\lambda_i)=R_M)$$

2). Absorption edge of blue waveband (blue edge)-B(λ_B , R_B): the turning point of the spectral curve in the range of 500-550nm, defined as the maximum point in the first-order derivative value in the same waveband region:

$$\lambda_B=\lambda_i(R'(\lambda)=MAX(R'(\lambda\in 450\text{-}550nm)) , R_B=R(\lambda_B)$$

3). Reflectance peak of green band(green peak)-G(λ_G , R_G): the maximum position of reflectance band from 500-600 as:

$$R_G=MAX(R(\lambda\in 500\text{-}600nm)) , \lambda_G=\lambda_i(R(\lambda_i)=R_G)$$

4). Absorption edge of yellow waveband(yellow edge)-Y(λ_Y , R_Y): the turning point of the spectral curve in the range of 550-650nm, defined as the minimum point in the first-order derivative in this range:

$$\lambda_Y=\lambda_i(R'(\lambda)=MIN(R'(\lambda\in 550\text{-}650nm)) , R_Y=R(\lambda_Y)$$

5). Absorption peak in red band(red "valley")-R(λ_R , R_R): where the reflectance is the minimum in the red band of 600-720nm:

$$R_R=MIN(R(\lambda\in 600\text{-}720nm)) , \lambda_R=\lambda_i(R(\lambda_i)=R_R)$$

6). Red edge-V(λ_V , R_V): the turning point of reflectance curve within waveband of red-NIR, the maximum point of the first-order derivative spectral curve in 670-780nm:

$$\lambda_V=\lambda_i(R'(\lambda)=MAX(R'(\lambda\in 670\text{-}780nm)) , R_V=R(\lambda_V)$$

7). Start site of the NIR platform-I_1(λ_{I1} , R_{I1}): the transition point between the red slope in wavelength >760nm and the NIR platform. It is also defined as the first joining point of the spectral curve and its continuum curve in range of 670-800nm as shown in fig 5.4.A. Its arithmetic is:

$$\lambda_{I1}=\lambda_i(Rcr(\lambda\in 670\text{-}800nm)) , R_{I1}=R(\lambda_{I1})$$

8). Maximum point of reflectance in NIR of 780-950-I(λ_I , R_I):

$$R_I=MAX(R(\lambda\in 780\text{-}950nm)) , \lambda_I=\lambda_i(R(\lambda_i)=R_I)$$

In order to get the green peak G and the red "valley" R, they are also defined as the zero points of the first-order derivative spectra $R'(\lambda)$ in the range of 500-600 and 600-720nm, respectively. Thus we get $G'(\lambda_{G'}, R_{G'})$ and $R'(\lambda_{R'}$, $R_{R'})$ as:

$$\lambda_{G'}=\lambda(R'(\lambda\in 500-600nm)=0)$$

$$\lambda_{R'}=\lambda(R'(\lambda\in 600-720nm)=0)$$

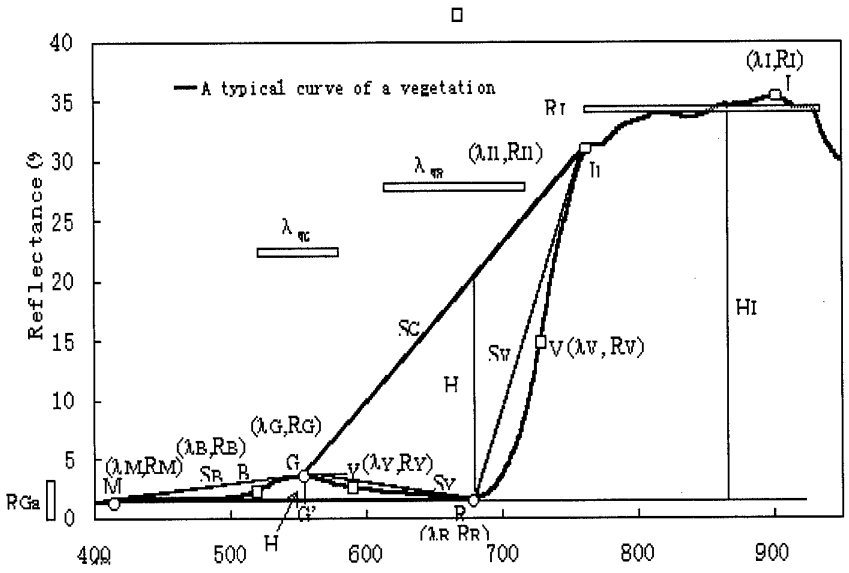


Fig 1. sketch of 8 feature positions and some feature parameters for the green vegetation in Changzhou
The reflectance is about Rice measured in Aug. 31 at Changzhou. The parameters and positions labeled in this sketch are defined in the text.

As shown in ***fig.1***, the eight special positions determine, on the whole, shape and spectral feature of reflectance spectra of vegetation in visible-near infrared band. It is distinct that the multi-line MBGYR determines the feature of green peak while the multi-line $GYRVI_1$ determines the general shape of red absorption peak. Line I_1I can be looked upon as the representation of NIR platform. As shown in ***Table 1*** , these 8 positions almost keep constant with outer changes while their corresponding reflectivity intensities vary greatly .Thus there is some possibility that we can use a variety of these 8 special positions and their relations to represent spectral change of different vegetation.

In order to figure out the correlative variety of these special position and therefore to show the changing rules of reflectance spectra with vegetation species, we designed some parameters(feature parameters) on the base of the 8 special positions according to the spectral features in ***fig 1***. They are:

1). The coordinate of 8 feature position M, B, G, Y, R, V, I_1, I and two accessorial positions as G' and R': (λ_P , R_P). where the subscript P is the name of these positions, λ is the wavelength and R is the reflectance. Obviously, there have 20 such parameters and in general we have G'≈G and R'≈R.

2). Slope of blue edge-S_B: the slope of line MG.

$$S_B=(R_G-R_M)/(\lambda_G-\lambda_M)$$

Thus it approximately determines the curve of MBG.

3). Slope of yellow edge-S_Y: the slope of line RG. It approximately determines the character of curve GYR:

$$S_B=(R_G-R_R)/(\lambda_G-\lambda_R)$$

4). Slope of the incline among bands of red-NIR-S_V: the slope of line RI_1 , it is a representation of curve RVI_1:

$$S_V=(R_{I1}-R_R)/(\lambda_{I1}-\lambda_R)$$

5). Slope of the continuum-S_C: the slope of line GI_1. It generally reflects the background feature of the absorption peak $GYRVI_1$:

$$S_C=(R_G-R_{I1})/(\lambda_G-\lambda_{I1})$$

6). Net height of green peak-H_G: the distance between G and line MR in the dimension of reflectance. It generally equals to the net reflectance of the background-removed green peak and is the reflection of reflectance

peak MBGYR:

$$H_G = R_G - ((R_R - R_M)/(\lambda_R - \lambda_M) \times (\lambda_G - \lambda_R) + R_R)$$

7). Net depth of red absorption "valley"-H_R: the distance between R and line GI_1 in the dimension of reflectance. It's can be looked upon as background-removed depth of red absorption peak and reflects the feature of peak $GYRVI_1$:

$$H_R = (R_G - R_{I1})/(\lambda_G - \lambda_{I1}) \times (\lambda_R - \lambda_G) + R_G - R_R$$

8). Net height of infrared platform-H_I: the difference between the averaged reflectance of NIR platform and the reflectance of point R. It can be substituted by the reflectance difference of R and the midpoint of line I_1I and reflects the feature of platform I_1I:

$$H_I = (\sum((R^i + R_{i+1}) \times (\lambda_{i+1} - \lambda_i)/2))/\Delta\lambda - R_R \approx (R_{I1} + R_I)/2 - R_R,$$

where $\lambda_i \in \lambda_{I1}$-930nm, $\Delta\lambda$ is the width of NIR=$930 - \lambda_{I1}$.

9). FWFH of green peak-λ_{wG}: generally represents the width of green peak. It is approximately calculated as the horizontal interval between points B and Y:

$$\lambda_{wG} \approx \lambda_Y - \lambda_B$$

10). FWFH of red absorption peak-λ_{wR}: the reflection of the width of red "valley". It is calculated as the half width of continuum-removed red "valley" and can be replaced as the horizontal interval of line YV:

$$\lambda_{wR} \approx \lambda_V - \lambda_B$$

11). Averaged reflectance of NIR platform-R_{Ia}: can be substituted by the reflectance average of I_1 and I:

$$R_{Ia} = (\sum((R_i + R_{i+1}) \times (\lambda_{i+1} - \lambda_i)/2))/\Delta\lambda \approx (R_{I1} + R_I)/2 = H_I + R_R$$

where $\lambda_i \in \lambda_{I1}$-930nm, $\Delta\lambda$ is the width as $930 - \lambda_{I1}$.

12). Area of green peak-A_G: the integrated area under curve MBGYR. It is the embodiment of green peak intensity and can be approximately substituted by the area under multiline MBGYR:

$$A_G = (\sum((R_i + R_{i+1}) \times (\lambda_{i+1} - \lambda_i)/2))$$

$$\approx [(\sum(R_p + R_{p+1}) \times (\lambda_{p+1} - \lambda_p)/2)), p = M,B,G,Y]$$

where $\lambda_i \in \lambda_M$-λ_R.

13). Pure area of green peak-$A_{G'}$: the integrated area enveloped by curve MBGYR and line MR. It is the net intensity of green peak and obviously can be replaced by the area of polygon MBGYRM:

$$A_{G'} = A_G - ((R_M + R_R) \times (\lambda_R - \lambda_M)/2)$$

$$\approx [(\sum(R_p + R_{p+1}) \times (\lambda_{p+1} - \lambda_p)/2)], p = M,B,G,Y]$$

$$-((R_M + R_R) \times (\lambda_R - \lambda_M)/2)$$

where $\lambda_i \in \lambda_M$-λ_R

14). Net area of red absorption peak-A_R: the area enclosed by curve $GYRVI_1$ and line GI_1. It can estimate as the area of polygon GYRVI1G:

$$A_R = S_{GYRVI1G}$$

Other parameters can also be gotten if necessary. For instance, after removing the continuum, the 5 most intensive peaks can be extracted from the continuum-removed(named as λdi with i increasing with intensity decrease) and normalized continuum-removed results(λci).

It should be pointed out that the usually applied parameters in vegetation study such as NDVI, red edge λ_{re} and red

edge slope dr_{re} could also be obtained from these parameters as follows:

$NDVI=(R_{I1}-R_R)/(R_{I1}+R_R)$, $\lambda_{re}=\lambda_V$, $dr_{re}\approx S_V$

Therefore, the definition of eight feature positions not only reflects the general feature of the reflectance data, but also can get many high-information-content feature parameters that may have good relationships with some property parameters of vegetation such as chlorophyll concentration.

3.2 Analysis for Effectiveness of VSFEM---Relative Stability of Position

To study characteristics of the above feature positions and parameters , especially to study relationships between feature positions and vegetation types , as well as action of feature parameters for reflecting vegetation parameters . Based on above definitions and algorithms , more than 100 spectral data of about 20 types of vegetation in Chang Zhou were analyzed to get spectral feature positions and parameters.

Table 1 gives principle results , from which we can see that ,

under the research conditions of the experiment , all feature positions , especially 8 feature positions are stable , these positions are : M : 404, B : 525 , G : 556 , Y : 573 , R : 671 , V : 723 , I1 : 758 , I : 900nm , take I position as example , which has the largest change range , for 62 samples at different time and place , its confidence width is 6.4nm , others less than 3nm , even for standard deviation , are less than 6nm generally . This kind of confidence interval has been super than spectral resolution of many instruments .

Table 1 feature position statistics result based on 62 samples

Feature position	samples	average(nm)	Standard deviation	Relative error(%)	95%confidence(nm)	Range of 95% confidence(nm)	Width of 95%confidence (nm)
λ_B	62	524.7	1.04	0.20	0.3	524.5 - 525.0	0.5
λ_G	62	556.2	3.67	0.66	0.9	555.3 - 557.1	1.8
λ_I	62	900.7	12.77	1.42	3.2	897.5 - 903.8	6.4
λ_{I1}	62	758.3	7.01	0.92	1.7	756.5 - 760.0	3.5
λ_M	62	403.9	2.72	0.67	0.7	403.3 - 404.6	1.4
λ_R	62	671.4	2.40	0.36	0.6	670.8 - 672.0	1.2
λ_V	62	723.4	9.80	1.35	2.4	720.9 - 725.8	4.9
λ_Y	59	573.2	0.81	0.14	0.2	572.9 - 573.4	0.4

3.3 Rediscussion for VSFEM---Reduction of Some Feature Positions

In addition , we calculate the correlation coefficients between different bands for all the spectral vegetation data measured by Se590 to show the independence of the bands and to select the most information-containing band group in order to indicate more efficiently the difference among different vegetation species , through which we can prove the effectiveness of VSFEM .

$$S=\begin{vmatrix} r_{11}, r_{21}, \ldots, r_{i1}, \ldots, r_{n1} \\ r_{12}, r_{22}, \ldots, r_{i2}, \ldots, r_{n2} \\ r_{1j}, r_{2j}, \ldots, r_{ij}, \ldots, r_{nj} \\ r_{1n}, r_{2n}, \ldots, r_{in}, \ldots, r_{nn} \end{vmatrix}$$

where S is the correlation coefficient matrix of all bands, r_{ij} is the absolute value of correlation coefficient between

band i and band j. Obviously:

$$r_{ij}=r_{ji}=|L_{ij}/SQRT(L_{ii}\times L_{jj})|$$

where L_{ij} is the covariance between band i and band j.

Fig. 2 is the simulated image of the correlation coefficient matrix among 187 bands that is calculated on the base of 71 vegetation . Curves in **Fig. 2** are isolines , from diagonal line to outside , the values are 0.9999,0.999,0.99,0.95,0.9,0.5,0.3 and 0.1 in the order .

From **Fig. 2** we can see that ,

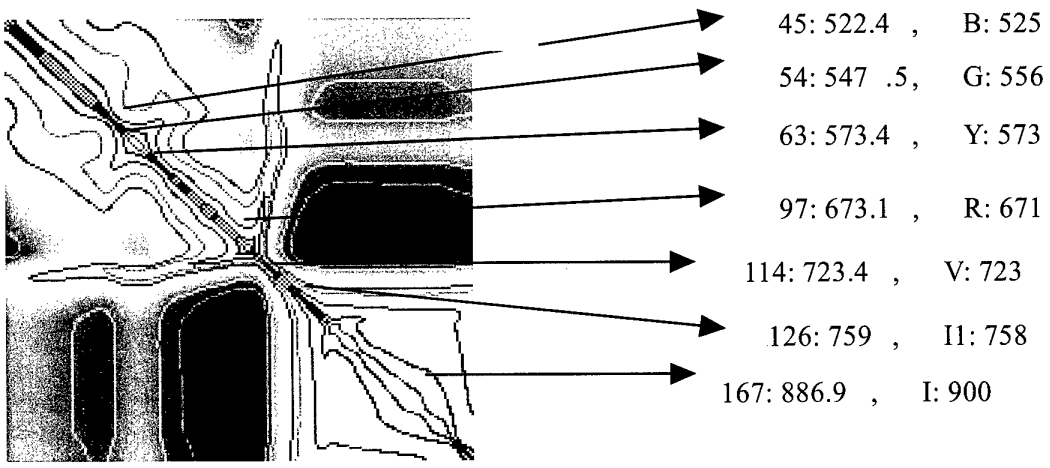
Except band 100(band number of Se590) to 126 , for vegetation , correlation coefficient are all very high (more than 99.99% generally) , that is to say, it's practical for band reduction .It shows two high-correlative platforms of 400-670nm and 760-950nm respectively, which means within these two regions , a few bands are enough to extract vegetation information . Moreover , around 550nm and 670nm , there are relatively wider areas . It's unnecessary to subdivide bands in these regions . but between 675nm---775nm and around 522nm and around 573nm , correlation coefficient are low generally . This shows more information here and bands should be subdivided . compared to 8 feature positions referred before , we can get that , for vegetation research , those regions that should be subdivided are just blue edge B , yellow edge Y and red edge V, while those regions that needn't be subdivided are blue absorption valley M , green peak G , red absorption valley R , and NIR platform I . In **Fig. 2** , position B , Y and V are located in the center of narrow regions of isolines , while M , G , R , I in the center of broad regions . The arrows in **Fig. 2** explain this clearly .

Table 2 lists correlation matrix of 8 feature positions , from **Table 2** , we can get priority order for 8 feature positions : first , select two positions with minimum correlation coefficient (absolute value) , remove these two bands and those bands with highest correlation coefficient with them , then , select repeatedly for the rest bands until we get to band number we predetermine.

Table 2 correlation coefficient of 8 feature positions (bands)

Corresponding feature position	M	B	G	Y	R	V	II	I
Wavelength(nm)	404.7	522.4	544.7	573.4	673.1	723.4	759.0	890.1
404.7		0.8890	0.8952	0.8372	0.4575	0.8408	0.6561	0.6117
522.4	0.8890		0.9895	0.9925	0.7071	0.8265	0.5520	0.5185
544.7	0.8952	0.9895		0.9812	0.6161	0.8785	0.6364	0.6035
573.4	0.8372	0.9925	0.9812		0.7455	0.7960	0.5053	0.4758
673.1	0.4575	0.7071	0.6161	0.7455		0.3313	-0.0230	-0.0366
723.4	0.8408	0.8265	0.8785	0.7960	0.3313		0.9020	0.8806
759.0	0.6561	0.5520	0.6364	0.5053	-0.0230	0.9020		0.9947
890.1	0.6117	0.5185	0.6035	0.4758	-0.0366	0.8806	0.9947	

Fig. 2 The simulated images of the correlation coefficient matrix among 187 bands(400-950nm) of Se590



from **Table 2** , we can get priority order for 8 feature positions : first , select two positions with minimum correlation coefficient (absolute value) , remove these two bands and those bands with highest correlation coefficient with them , then , select repeatedly for the rest bands until we get to band number we predetermine.

4. Conclusion

According to above analysis , we find out that:

1. Through lots of analysis on field vegetation spectral data, A new spectral feature selection and extraction model(for vegetation only!)--- Vegetation Spectral Feature Extraction Model （VSFEM） is presented , with which 8 spectral feature positions are suggested to control vegetation spectral curves . Those feature positions are 404(M), 525(B) ， 556(G) ， 573(Y) ， 671(R) ， 723(V) ， 758(I1) ， 900nm(I) .
2. It is reasonable to select feature positions as best bands. However, the feature positions and bandwidths for different feature are not the same. As a result, the accurate positions of G, R, M, I are not necessary. They should change in a proper range, such as I and M which could use a broader band.
4. According to the correlationship among bands, the bands could be removed are: I, M, B, Y and G. As for band R 、V 、I1, they should not be removed . If subdivision allowed , it's proper to subdivide red edge(R—V—I1) , moreover , we can subdivide around B and Y position .

Anyway , above results are acquired through spectral data by Se590 and some other conditions , we cannot reject absolutely new results under higher spectral resolution and other conditions .

REFERENCES

1. 茅亚澜，多光谱遥感波段选择问题的研究，中国科学院摇遥感应用研究所硕士学位论文，1981 年 10 月。
2. 尼曼，模式分类，科学出版社，1988 年 7 月第一版，128-262。
3. 刘建贵，高光谱城市地物及人工目标识别与提取，中国科学院遥感应用研究所博士学位论文，1999 年 8 月。
4. 童庆禧、田国良、茅亚澜，多光谱遥感波段选择方法的研究，宇航学报，1983 年 4 月，No.2, 1-13。
5. 童庆禧等，多光谱遥感波段选择方法研究，宇航学报，1983 年 4 月 No.2。
6. 王传善，多光谱遥感之最佳波段选择，空间科学学报，1985 年 1 月，Vol.5, No.1, 45-52。
7. Boardman, J. W., and Kruse, F. A., 1994, "Automated spectral analysis: a geological example using AVIRIS data, north Grapevine Mountains, Nevada." , Proceedings, ERIM Tenth Thematic Conference on Geologic Remote Sensing, Environmental Research Institute of Michigan, Ann Arbor, MI, p. I-407 - I-418.
8. Fukunaga,K., Koontz,W.L.G., 1970, "Application of the Karhunen_Loeve expansion to feature selection and ordering." , IEEE Trans. Comput., Vol. C-19,No.4,pp311-318,Apr.1970.
9. Green, A. A., Berman, M., Switzer, P, and Craig, M. D., 1988, "A transformation for ordering multispectral data in terms of image quality with implications for noise removal", IEEE Transactions on Geoscience and Remote Sensing, v. 26, no. 1, p. 65-74.
10. Jia,Xiuping, Richards,J. A.,1999, "Segmented principal components transformation for efficient hyperspectral remote-sensing image display and classification.", IEEE Trans. On Geosci. And Remote Sensing, Vol.37, No.1, 538-542, Jan. 1999.
11. Kazakos,D.,1978, "On the optimal linear feature." , IEEE Trans. Inform. Theory, Vol. IT-24,No.5,pp651-652,Sept. 1978.
12. Lee, C. and Landgrebe, D. A.,1993, "Feature extraction based on decision boundaries.", IEEE Trans on P.A.M.I. Vol. 15, No.4, April 1993.
13. Richards,John A., Remote Sensing Digital Image Analysis, An Introduction, Spriger-Verlag,1986.

Acknowledgement

The authors wish to thank Laboratory of Remote Sensing Information Sciences , Institute of Remote Sensing Applications for providing the data and their sincere help .

The 21st Asian Conference on Remote Sensing
December 4-8, 2000 Taipei, TAIWAN

HYPERSPECTRAL IMAGE COMPRESSION USING THREE-DIMENSIONAL WAVELET TRANSFORMATION

Yi-Hsing TSENG, Hung-Kuan SHIH, Pai-Hui HSU

Department of Surveying Engineering
National Cheng Kung University, Tainan, Taiwan, R.O.C.
E-mail: tseng@mail.ncku.edu.tw

KEY WORDS— Hyperspectral Image, Image Compression, 3-D Wavelet Transformation, Classification

ABSTRACT—A three-dimensional (3-D) wavelet compression method for hyperspectral images is proposed. This method applies a separable 3-D wavelet transformation (WT) to hyperspectral datacubes resulting in wavelet coefficients for 3-D multi-resolution image representation. The coefficients are then compressed using the optimal scalar quantization. Finally, Huffman coding is applied to save storage space. Experimenting on an AVIRIS image is performed with various combinations of wavelet banks, transformation levels, and quantization intervals. The decompressed images are evaluated objectively and subjectively, based on signal-to-noise ratio (SNR) and classification accuracy measures, respectively. The results show that a two-level 3-D WT offers a compressed ratio (CR) in between 20 and 150, which would be suitable for most applications. A comparison of two wavelets shows that the db3 wavelet outperforms the db1 wavelet based on both objective and subjective evaluations. The results also show an interesting phenomenon in which classification accuracy does not drop in response to an increase in information loss. Information loss caused by image compression possesses two different effects: image roughing due to quantization and smoothing due to decomposition. In this data set, image smoothing promotes classification accuracy, while image roughing reduces classification accuracy.

1. INTRODUCTION

Hyperspectral images provide much richer and finer spectral information than traditional multispectral images, however the volume of generated data is dramatically increased. Image compression will be essential for economical of distribution when spaceborne hyperspectral data are regularly available. Image compression reduces storage requirements, network traffic, and therefore improves efficiency. However, the satisfactory image compression requires a large compression ratio and a small amount of information loss. A lossless compression is the best choice as long as the compression ratio is acceptable, but it usually cannot offer a satisfactory compression ratio due to the limitation of image entropy. Typical hyperspectral data, such as images obtained with the Airborne Visible/Infrared Imaging Spectrometer (AVIRIS), are stored as 16-bit words, and have an average entropy of about 9 bits/pixel (Ryan and Arnold, 1997). Therefore, in most cases, lossless hyperspectral image compression hardly achieves a compression ratio greater than 2. To obtain significant image compression, lossy compression is preferable to a lossless compression. Under these circumstances, preserving the most useful information when compressing an image to an acceptable size becomes the central issue of hyperspectral image compression (Qian et al., 2000).

Hyperspectral data sets are referred to as *datacubes* because of their 3-dimensional (3-D) nature (two spatial dimensions and one spectral dimension). Conventional image compression techniques explore useful information within the two spatial dimensions. Among these techniques, wavelet transformation (WT) has been proven to be very efficient for 2-D image coding (Antonini et al., 1992). Compared to the popular method, discrete cosine transform (DCT), WT extracts not only frequency information, but also spatial information. For multispectral image compression, band images are usually compressed separately with a 2-D image coding technique, so that spectral redundancy will not be explored. A hybrid scheme was proposed to solve this problem using a two-step transformation (Markas and Reif, 1993). First, a spectral transformation, such as principal component transformation (PCT) or DCT, is applied to decorrelate spectral information. Second, 2-D image compression is applied to each transformed component. Removing spectral redundancy is achieved by compressing the subordinate components more than the dominant components. Although the hybrid scheme, in a sense, may be one of the most suitable methods for hyperspectral image compression, it does not fully take the advantage of the 3-D nature of hyperspectral data. A 3-D WT is therefore proposed to simultaneously explore the most representative information in the spatial and spectral dimensions. Figure 1 shows a block diagram of this 3-D wavelet compression method.

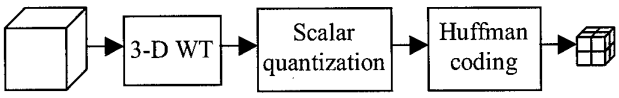


Fig 1. 3-D wavelet compression process.

2. 3-D WAVELET TRANSFORMATION

A wavelet transform (WT) decomposes a signal into a series of smooth signals and the associated detailed signals at different resolution levels (Mallat, 1989). At each level, the smooth signal and associated detailed signal have all of the information necessary to reconstruct the smooth signal at the next higher resolution level. The transformed signal has both time and frequency information from the original signal and provides a good representation for coding. The WT application to image compression has shown promising results (Antonini et al., 1992).

A multiresolution WT involves two functions: a *mother wavelet* ψ and a *scaling function* ϕ. Let the normalized scale factor be 2^j and the translation be $k \cdot 2^j$ (where $j, k \in \boldsymbol{Z}$), then the dilated and translated wavelets will be:

$$\psi_{j,k}(x) = 2^{-j/2}\psi(2^{-j}x - k) \tag{1}$$

Also, the dilated and translated scale functions will be:

$$\phi_{j,k}(x) = 2^{-j/2}\phi(2^{-j}x - k) \tag{2}$$

For fixed j, the $\phi_{j,k}$ are orthonormal. The spaces V_j spanned by the $\phi_{j,k}$ describe successive *approximation spaces*, $\ldots V_2 \subset V_1 \subset V_0 \subset V_{-1} \subset V_{-2} \ldots$, each with resolution 2^j. For each j, the $\psi_{j,k}$ span a *detail space* W_j which is exactly the orthogonal complement in V_{j-1} of V_j:

$$V_{j-1} = V_j \oplus W_j \tag{3}$$

It has been proven that any scaling function is specified by a discrete filter called a *conjugate mirror filter*. The causality $V_{j+1} \subset V_j$ is verified using a conjugate mirror filter:

$$\phi_{j+1,k} = \sum_n h_{n-2k}\phi_{j,n} \qquad \text{in which} \quad h_{n-2k} = \left\langle \phi_{j+1,0}, \phi_{j,n-2k} \right\rangle \tag{4}$$

Similarity, the causality $W_{j+1} \subset V_j$ is verified by:

$$\psi_{j+1,k} = \sum_n g_{n-2k}\phi_{j,n} \qquad \text{in which} \quad g_{n-2k} = \left\langle \psi_{j+1,0}, \phi_{j,n-2k} \right\rangle \tag{5}$$

The *scaling coefficients* $\langle f, \phi_{j,k} \rangle$, denoted by a_{jk}, characterize the projection of f onto V_j. The *detailed coefficients* $\langle f, \psi_{j,k} \rangle$, denoted by d_{jk}, describe the information lost when going from an approximation of f with resolution 2^{j-1} to the coarser resolution 2^j. If $f(x) \in L^2(\mathbf{R})$, it can be decomposed into a series of smooth signals and the associated detailed signals at different resolution levels:

$$A_j f = \sum_k a_{jk}\phi_{j,k}; \qquad D_j f = \sum_k d_{jk}\phi_{j,k} \tag{6); (7}$$

Based on (4) and (5), one obtains

$$a_{jk} = \left\langle f, \phi_{j,k} \right\rangle = \sum_n h_{n-2k} \left\langle f, \phi_{j-1,n} \right\rangle; \qquad d_{jk} = \left\langle f, \psi_{j,k} \right\rangle = \sum_n g_{n-2k} \left\langle f, \phi_{j-1,n} \right\rangle \tag{8); (9}$$

Substituting (8) and (9) into (6) and (7) respectively:

$$A_j f = \sum_n h_{n-2k} A_{j-1} f; \qquad D_j f = \sum_n g_{n-2k} D_{j-1} f \tag{10); (11}$$

The multiresolution WT can be implemented using a two-channel perfect reconstruction filter bank as shown in (10) and (11). The first channel is a low-pass filter h and the second channel is a high-pass filter g. The WT of a signal can be obtained by repeatedly applying the two-channel filter bank to the signal in a pyramidal scheme. A separable 3-D WT can be computed by extending the pyramidal algorithm. Suppose the spatial dimensions are labeled x and y, and z denotes the spectral dimension. The decomposition can be performed sequentially; by first convoluting the x-direction, followed by the y and z directions. Figure 2 shows a one-level 3-D WT.

Figure 3 shows the eight data blocks resulting from a one-level image cube 3-D WT. Three-letter labels are marked on each data block to denote the filter type in the x, y, and z directions. L denotes a low-pass filter and H denotes a high-pass filter. The block in the top-left corner is the low-frequency portion of the image cube. The other blocks are filtered at least once with a high-pass filter and therefore contain high-frequency components in one of the directions. The low-frequency block can be further decomposed into eight more blocks. The WT yields a good representation of the original image for compression purposes. The low-frequency component of WT contains about 90% of the total energy in most cases. Different blocks and different levels of resolution can be coded in different ways to improve compression results.

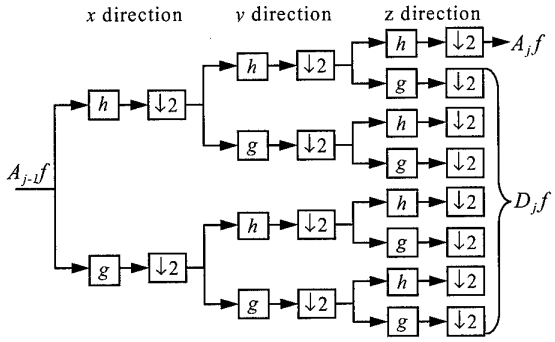


Fig. 2. One level of 3-D decomposition.

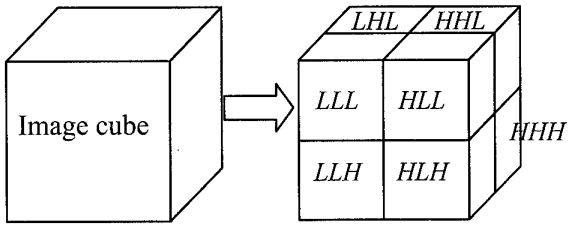
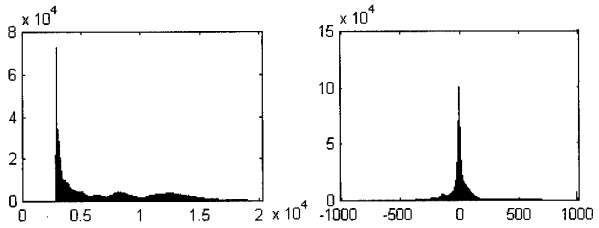


Fig. 3. The eight data blocks resulting from the first level image cube 3-D WT.

3. Optimal Scalar Quantization

The purpose of quantization is to reduce data entropy by decreasing the data precision. A quantization scheme maps a large number of input values into a smaller set of output values. This implies that some information is lost during the quantization process. The original data cannot be recovered exactly after quantization. A quantization strategy design must balance the compression achievement and information loss. One of the criteria for optimal quantization is minimizing the mean square error (MSE) given a quantization scale. The quantization scale is not necessarily uniform, and for most data sets the optimal quantization scale is not uniform. In this study, wavelet coefficients were compressed using the optimal scalar quantization scheme proposed by (Lloyd, 1957) and (Max, 1960), which is commonly called the Lloyd-Max quantization.

The data blocks resulting from the 3-D WT are represented by floating point values and consist of two types of data: the *LLL* block, which preserves most of the energy; and the other high-resolution data blocks, which contain the sharp edge information. Figure 4 shows the histograms of a typical *LLL* data block and a typical high-resolution data block. The *LLL* block obviously has a much larger data range than the high-resolution data blocks. It is therefore reasonable to apply a large quantization scale for the *LLL* block and a relatively small scale for the other blocks. In this study, we used 256 intervals for the *LLL* block and less than 32 intervals for the other blocks.



(a) (b)

Fig. 4. The histograms of (a) a typical *LLL* data block and (b) a typical high-resolution data block.

4. Huffman Coding

The final step in the compression process is coding. Huffman coding (Huffman, 1952) is a minimum redundancy coding. It assigns fewer bits to the values with a higher frequency of occurrence and more bits to the values with a lesser frequency of occurrence. Based on the occurrence frequency of each quantization level, a hierarchical binary coding tree structure brings by sequentially finding the lowest two frequencies as tree branches and adding each low frequency pair as a new node for the next level. Huffman coding allows reforming the data to be optimized in less space than the original data.

Because each data block is quantized into different numbers of quantization levels, the coding process should be performed for each data block separately. Compared with equal-length coding, Huffman coding can easily save more than 50% of the required memory space without losing any information.

5. TEST DATA AND EVALUATION

5.1 Test Data

The test data is an AVIRIS image downloaded from the web site (http://dynamo.ecn.purdue.edu/~biehl/MultiSpec/) of Purdue University. The image size is 145×145 pixels with 220 bands, and the pixels are stored as 16-bit words. The storage size is about 9.3 mega-bytes. Figure 5 shows a perspective picture of the image cube. The image was taken in 1992, covering the Indian Pine Site 3, an agriculture area. The ground truth is also available for image classification evaluation. There are 16 land cover classes, in which some classes may be grouped into single landuse types. For example, corn, corn-min, and corn-notill belong to the corn landuse type, but due to the differences of crop canopies they are categorized into three different land-cover classes. Classes of a same group tend to possess similar spectral properties, so that it is usually difficult to differentiate them in a multispectral image. This data set was especially provided to show the application potentials of hyperspectral images.

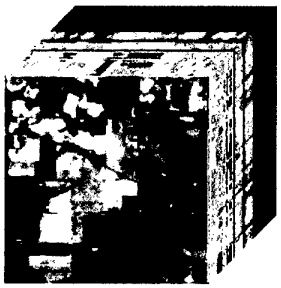


Fig. 5. A perspective picture of image cube of the test data.

5.2 Evaluations of Image Compression

There are two ways to evaluate the quality of decompressed images: the objective and subjective evaluations. The objective method measures the amount of information loss or preserved by comparing decompressed images with the original one. The amount of information loss may be defined as mean square error (MSE), or the amount of preserved information can be described as cross correlation (CC) or signal to noise ratio (*SNR*) etc. Although MSE and CC objectively gauge the image difference, they are sensitive to strong signals. For most images with textures, *SNR* is an ideal assessment of how much the original signal preserved after a compressed image is recovered from compression, and is commonly applied for the evaluation of image compression. Therefore, in this paper, *SNR* is used as an objective measure to evaluate the performance of the developed algorithm.

The subjective evaluation is a measure of the performance of decompressed images on certain applications, for example visualization, feature extraction, or classification etc. Because image classification is a common application of a remotely sensed image, the classification results of the original and decompressed images are therefore compared to obtain subjective measures. Supervised classification using maximum-likelihood classifier is applied for the classification test. All samples of the ground truth data are used as training data, and they are also used as reference data for accuracy assessment. Theoretically, all spectral bands of image should be involved in the classification process. However, due to the insufficiency of training samples, classification will be failed if all spectral bands are used. In order to reduce the number of feature space dimension, only the first 30 principal components of image are extracted and used for classification. When the original image is applied, the resulted overall accuracy of classification is 89.39%.

6. EXPERIMENTAL RESULTS

Two selected wavelet filter candidates were employed for the 3-D WT. They are the Daubechies_1 (db1) (i.e. the Hard) and Daubechies_3 (db3) (Daubechies and Micchelli, 1994). Because the Daubechies scaling function ϕ and wavelet ψ have the supports $[0, 2p\text{-}1]$ and $[-p+1, p]$ (p denotes the vanishing moments), the db1 filters have the supports [0,1] and [0,1] and the db3 filters have the supports [0,5] and [-2,3]. The Lipschitz regularity of the db1 wavelet ψ is about 0.3 and the db3 wavelet ψ is Lipschitz 1.08. This means that the db3 wavelet ψ is continuously differentiable, whereas the db1 wavelet ψ is not. The choice of an optimal wavelet is a trade-off between the number of vanishing moments and its support size (Mallat and Hwang, 1992). A high amplitude wavelet coefficient occurs when the wavelet has a support that overlaps a brutal transition like an edge, which should thus be as small as possible to reduce the quantization error. In addition, over smooth regions, the wavelet coefficients are small at fine scales if ψ has enough vanishing moments to take advantage of the large Lipschitz regularity. However, the support size of ψ increases proportionally to the number of vanishing moments. For large classes of natural images, it has been observed numerically that the distortion rate is optimized with wavelets having three or four vanishing moments. Therefore, to obtain optimal results, the db3 wavelet was adopted. The db1 wavelet was applied for comparison because of its computation simplicity.

A four-level 3-D wavelet decomposition was applied to the test image with the db1 and db3 wavelets respectively. For each decomposition level, we used 256 quantization intervals for the *LLL* block and tried 0, 4, 8, 16, and 32 intervals for the other blocks, in which 0 interval means that the data block is ignored. With various combinations of using different decomposition levels and quantization intervals, objective measures (*SNR*) and subjective measures (classification overall accuracy, OA) are presented versus compression ratio (*CR*).

In order not to make complicated combinations, only data blocks from the highest decomposition level were kept, i.e. data blocks from the lower decomposition levels were always ignored. Therefore, for *CR* less than 20, a one-level decomposition was applied with the five-quantization intervals on high-resolution blocks to obtain five combinations of compression, which is denoted as the level 1 result. To take a two-level decomposition, high-resolution blocks in the first level were discarded and same five combinations were made for data blocks in the second level to obtain the results from level 2. The results from level 3 and 4 were obtained after the fashion of the previous combinations. Figure 6 shows compression ratios achieved with respect to different combinations, which reveals a clue to determining an appropriate decomposition level. The first decomposition offers a *CR* less

than 20. It cannot produce a *CR* greater than 10 if one does not discard the high-resolution data. Generally speaking, for most applications, the appropriate *CR* range should be between 10 and 100. It is not necessary to compress an image by a factor of more than 100. The second decomposition offers a *CR* in between 20 and 150. Therefore, the level-2 combinations are good choices for hyperspectral image compression. Figure 6 also shows the fact that the db1 wavelet offers a higher *CR* than the db3 wavelet under the same decomposition and quantization combinations. This fact, however, is not the key factor for judging compression performance.

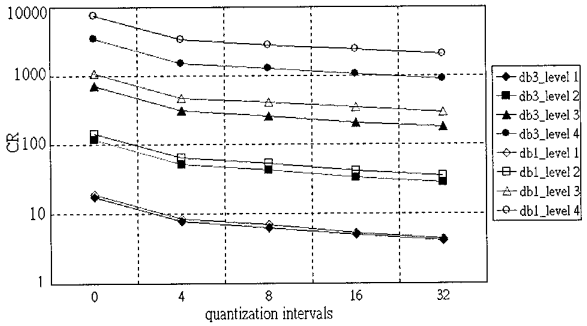


Fig. 6. Compression ratio versus different combinations of filters, decomposition levels, and quantization intervals.

Figure 7 (a), (b), (c), and (d) show the objective measures of the 1, 2, 3, and 4 level results, respectively. Comparing the db1 and db3 wavelet performance, two concluding remarks can be made. First, the db3 wavelet outperforms the db1 wavelet at a given *CR* based on the objective evaluation. Second, the *SNR* drops rapidly in the first decomposition level, but after that, the decrease becomes lesser with respect to the rapid increase in *CR*. Concerned with practical applications, the first conclusion implies that the db3 wavelet is a better choice than the db1 wavelet. Figure 8 (a), (b), (c), and (d) show the subjective measures of the level 1, 2, 3, and 4 results respectively. Based on a subjective evaluation, the db3 wavelet also obviously outperforms the db1 wavelet. In the level-4 combinations, decompressed images were even not converged in the classification process.

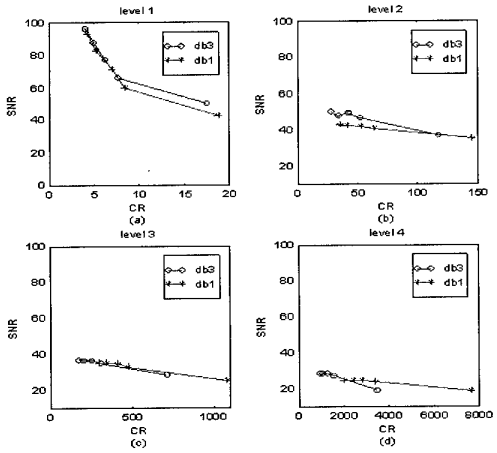


Fig. 7. The *SNR* measures of the 4 different level combinations versus compression ratio. (a) level 1. (b) level 2. (c) level 3. (d) level 4.

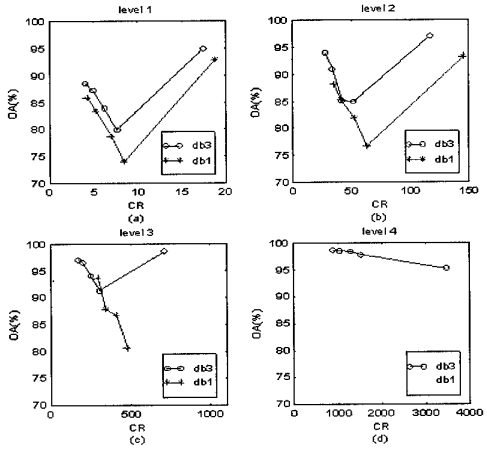


Fig. 8. The classification accuracy measures of the 4 different level combinations versus compression ratio. (a) level 1. (b) level 2. (c) level 3. (d) level 4.

An interesting phenomenon can be observed in Figure 8. OA Values do not decrease in response to the increase in information loss. In each decomposition level, the OA reduces when the number of quantization intervals drops, but it suddenly goes up to a level even higher than the original data when the number of quantization intervals goes to zero (i.e. ignoring all high-resolution data). This phenomenon still has us puzzled. A reasonable explanation is that information loss caused by image compression possesses two different effects: image roughing and smoothing. When the number of quantization intervals drops, the image is roughed. However, if all of the high-resolution data are ignored, the image is smoothed by wavelet decomposition. Hsieh (Hsieh, 1998) demonstrated that spatially smoothing a hyperspectral image improves the classification accuracy. The phenomenon can be explained in response to Hsieh's conclusion. The OA went up to 99% when a four-level decomposition was applied. The reason it reached a higher accuracy than Hsieh's demonstration was due to the 3-D smoothness. However, one should take a conservative view of this conclusion, because the spatial reference data distribution strongly affects classification accuracy. Land-cover classes of ground truth in the test data set are distributed as blocks, and so are Hsieh's data sets. Under this circumstance, the fact that smoothing images increases the classification accuracy (and vice versa) can be expected. However, this will not be true if the class data are not distributed as blocks.

7. CONCLUSION

An efficient scheme for hyperspectral image compression using 3-D wavelet transformation (WT) was developed. This scheme simultaneously explores useful information in the spatial and spectral dimensions and fully takes advantage of the 3-D nature of hyperspectral data. The 3-D WT yields a good representation of an image cube for compression purposes. The low-frequency WT component contains about 90% of the total energy in most cases. Various blocks and resolution levels can be coded in various ways to improve compression results. Using two-level wavelet decomposition offers compression ratios between 20 and 150 that are appropriate for most applications.

Both objective and subjective evaluations confirm that the db3 wavelet outperforms the db1 wavelet at a given *CR*. This implies that the db3 wavelet is a better choice than the db1 wavelet for the proposed scheme.

The subjective measure does not decrease in response to an increase in information loss. Information loss caused by image compression possesses two different effects: image roughing and smoothing. Smoothing the image promotes classification accuracy, while roughing the image reduce classification accuracy. Generally speaking, 3-D image compression is a sort of 3-D hyperspectral data feature extraction. However, how 3-D features contribute to classification requires further investigation.

ACKNOWLEDGEMENT

We thank the National Science Council, ROC, for the support of this research project: NSC89-2211-E006-084.

REFERENCES

Antonini, M., Barlaud, M., Mathieu, P. and Daubechies, I., 1992. Image Coding Using Wavelet Transform. *IEEE Transactions on Image Processing*, 1(2):pp. 205-220.

Daubechies, I. and Micchelli, C.A., 1994. Ten Lectures on Wavelets.*SIAM.*

Hsieh, P.F., 1998. Classification of High Dimensional Data. Ph.D. Thesis, Purdue University.

Huffman, D.A., 1952. A Method for the Construction of Minimum Redundancy Codes. *Pro. IRE*, 40:pp. 1098-1101.

Lloyd, S.P., 1957. Least Squares Quantization in PCM. *IEEE Trans. Info. Theory*, IT-28:pp. 129-137.

Mallat, S. and Hwang, W.L., 1992. Singularity Detection and Processing with Wavelets. *IEEE Transactions on Information Theory*, 38(2):pp. 617-643.

Mallat, S.G., 1989. A Theory for Multiresolution Signal Decomposition : The Wavelet Representation. *IEEE Transactions on Pattern Analysis and Machine Intelligence*, 11(7):pp. 674-693.

Markas, T. and Reif, J., 1993. Multispectral Image Compression Algorithms. *Data Compression Conference, DCC '93.*,:pp. 391-400.

Max, J., 1960. Quantizing for Minimum Distortion. *IRE Trans. Info. Theory*, IT-6(1):pp. 7-12.

Qian, S.E., Hollinger, A.B., Williams, D. and Manak, D., 2000. Vector Quantization Using Spectral Index-Based Multiple Subcodebooks for Hyperspectral Data Compression. *IEEE Transactions on Geoscience and Remote Sensing*, 38(3):pp. 1183-1190.

Ryan, M.J. and Arnold, J.F., 1997. The Lossless Compression of AVIRIS Images by Vector Quantization. *IEEE Transactions on Geoscience and Remote Sensing*, 35(3):pp. 546 -550.

The 21st Asian Conference on Remote Sensing
December 4-8, 2000 Taipei, TAIWAN

Estimation of Photosynthetic Rate of Plant from Hyper-spectral Remote Sensing of Biochemical Content

Takahiro ENDO*, Toshinori OKUDA**, Masayuki TAMURA**, and Yoshifumi YASUOKA*

*Institute of Industrial Science, University of Tokyo
4-6-1 Komaba, Meguro-ku, Tokyo, 153-8503 Japan
Tel: (81)-3-5452-6410 Fax: (81)-3-5452-6415
E-mail: tendo@iis.u-tokyo.ac.jp
**National Institute for Environmental Studies
16-2 Onogawa, Tsukuba, 305-0053 Japan

KEYWORDS: hyperspectral remote sensing, carbon absorption, photosynthetic rate, chlorophyll, nitrogen

ABSTRACT

Carbon absorption of plant is one of the essential parameters in assessing terrestrial ecosystem functions with respect to global warming. It is, however, not easy to measure carbon absorption directly on the ground. In this study remote sensing method was investigated to estimate photosynthetic rate of plant from the measurement of biochemical content. If net photosynthetic rate may be estimated, carbon absorption and NPP can be predicted. Firstly, we measure the relationship between biochemical concentrations and parameters of "Blackman" photosynthetic model. Secondly, we measure the relationship between biochemical concentration and hyperspectral characteristics. High-resolution reflectance over a range of 333 -2507nm with resolution of about 1.5-10 nm and net Amax (maximum assimilation rate) - photon flux density (PFD) were measured respectively by the GER 2600, LI-6400. Also, chlorophyll *a*, chlorophyll *b*, chlorophyll *a+b* and nitrogen concentrations were quantitatively analyzed from in situ measurement of cucumber's fresh leaves that were cultivated to have different biochemical concentration in a greenhouse chamber. Correlation between saturated Amax and chlorophyll *a* and nitrogen concentration was r^2=0.90, and 0.91, respectively. Both chlorophyll *a* and nitrogen concentrations were estimated by the first derivative spectral reflectance (RF') of fresh leaf. RF' at 678.011nm correlated best with chlorophyll *a* concentration (r^2=0.81). RF'at 732.122nm correlated best with nitrogen concentration (r^2=0.86). Finally, net Amax at given PFD was estimated by the photosynthetic rate model. A correlation between the actual net Amax and the estimated net Amax was r^2=0.74.

1. INTRODUCTION

In recent years, remote sensing has made a rapid progress in developing methods to estimate of a number of essential forest ecosystem variables, such as leaf area index (LAI), absorbed fraction of photosynthetically active radiation, canopy temperature, and plant community type. These variables are useful for predicting ecological fluxes. Further insights to ecosystem function, such as biochemical fluxes and processing require additional variables. The prospect of biochemical composition of plant canopy is relevant to the potential elucidation of biochemical fluxes, such as nitrogen cycle and carbon cycle components. A kind of terrestrial ecosystem function is descried as an enormous sink of carbon. The terrestrial vegetation can assimilate carbon dioxide, a kind of greenhouse gas, through photosynthesis, which is a basic process for biochemical fluxes. Photosynthetic rate, which is a kind of biosynthesis, depends on biochemical content in leaf and environmental condition, such as temperature, water and light condition. For example, in case of interspecies, a single leaf with high photosynthetic rate has high biochemical concentration, such as chlorophyll or nitrogen concentration.

Estimation of optical and biochemical properties of fresh leaves have been reported, especially using short-wave infrared wavelengths. Lee F. Johnson et al.[1] found correspondence between the first derivative spectral reflectance from the Airborne Visible/Infrared Imaging Spectrometer (AVIRIS) and concentrations of both chlorophyll and total nitrogen (R^2=0.71 and R^2=0.85, respectively) along a vegetation transect in Oregon. Paul J. Curran et al.[2] also used the first derivative reflectance of AVIRIS data to predict chlorophyll, nitrogen, lignin, and cellulose concentrations (R^2=0.96 R^2=0.94 R^2=0.93, and R^2=0.61, respectively) at a slash pine

plantation, Florida.

The objective of this study is to estimate net photosynthetic rate based on physiological parameters. Our study examines whether chlorophyll and nitrogen concentrations could be estimated using spectral reflectance and net photosynthetic rate could be estimated by estimating chlorophyll and nitrogen content at the single leaf in the laboratory darkroom and the greenhouse chamber. We tried to investigate net photosynthetic rate models suitable for remote sensing and to statistically analyze relationship between parameters of photosynthetic rate model and biochemical concentrations of fresh leaves. Finally, the authors estimated the net photosynthetic rate using spectral reflectance of fresh leaves measured by a hyperspectral spectrometer.

2. PHOTOSYNTHETIC RATE MODELS

2.1. Light-Photosynthetic Rate Curve

At present, several net photosynthetic rate models have been developed based on the physiological properties in the plant physiological studies. There are mainly two groups of models based on either the photon flux density (PFD) or CO_2 concentration. One set of models defines PFD as incident light energy, while the other models define CO_2 concentration and rate of electron transport system in the leaf. The estimation of net photosynthetic rate of the latter group of models is more accurate than that of the former. But, these parameters can't be directly measured using remote sensing data. Hence, the authors selected the former set of models, such as " light-photosynthetic rate model ".

The light-photosynthetic rate models are mainly three types; (1) the Michaels-Menten type models; (2) the asymptotic exponential equation type models; (3) the Blackman type models[3]. Based on a review of the available literature, the Blackman type was the best fit to an actual net photosynthetic rate. The Michaels-Menten type doesn't fit to the actual photosynthetic rate, when incident light energy is low. In case of using the asymptotic exponential equation type, the slope of the curve raises slowly in the region of curve inflexion. The Blackman type model estimated the actual fresh leave's photosynthetic rate more effectively from low incident light energy levels to high incident light energy levels. So, the authors selected the Blackman type.

2.2. Blackman Type

The "Blackman type" estimation model of net photosynthetic rate of a fresh leaf has five parameters. Amax, the maximum assimilation rate same as maximum photosynthesis rate is estimated as in Eq. (1):

$$A\,max = \frac{\phi PFD + A\,max' - \sqrt{(\phi PFD + A\,max')^2 - 4A\,max'\phi\theta PFD}}{2\theta} - R \qquad \cdots \text{(1a)}$$

$$A\,max' = A\,max_{sat} - R \qquad \cdots \text{(1b)}$$

where, Amax [μmol CO_2 m^{-2} s^{-1}] is the maximum assimilation rate, PDF [μmol photon m^{-2} s^{-1}] is Photon Flux Density, Amax' [μmol CO_2 m^{-2} s^{-1}] is the gross maximum photosynthetic rate, θ is the convex value of this model's curve, which stands for the Rubisco activity level. Rubisco is the enzyme that traps CO_2 gas from atmosphere into Calvin cycle. Φ is the initial slope of the curve under low incident level. $Amax_{sat}$ is the saturation value of the Amax-PFD curve, R [μmol CO_2 m^{-2} s^{-1}] is the respiration rate of flesh leaf.

As a result of literature reviews, $Amax_{sat}$ and R have high correlation with chlorophyll and nitrogen content. These two parameters can be estimated by hyperspectral characteristics. θ and Φ is said to be within a range of 0.7-0.95 and 0.04-0.06, respectively. But, we used the measured value in this study, as we had the results of experiment.

3. MATERIALS AND METHODS

3.1. Plant Materials and Measurements of Leaf Reflectance and of Light-Photosynthetic Rate Curve

Cucumber seeds were planted into a plastic pot and maintained for 28days in a greenhouse chamber. These plants were cultivated under two different conditions in order to make leaves with different concentration

of chlorophyll, nitrogen, and so on. While conditions for one series was most suitable with regard to light condition, water condition, and nutrient condition, the other series was cultivated under shade that cut off incident light at 50% by a shade curtain. After 28 days, there were some distinct characteristics between the two. In the first series, Height of cucumber plants was higher, and color of leaf was greener.

Leaf reflectance measurement was carried out in a laboratory darkroom and a greenhouse chamber using the Geophysical Environment Research Field Portable Spectrometer (GER-2600). The GER-2600 records radiation in 650 channels over 350-2500 nm wavelength range. Leaf reflectance is a ratio of foliar radiance to white board's radiance. The reference radiance is defined as the radiance of a white-board made from $BaSO_4$. Light source used in the darkroom case was the standard halide lamp, and in the greenhouse chamber case the sunlight is the incident light.

The fresh leaf's light-photosynthetic rate curve was measured by the portable photosynthesis system (LI-cor, LI-6400). This instrument can control all environmental variables, such as CO_2, H_2O concentration of both input flux and output flux, leaf surface temperature and an incident light. Also the LI-6400 is able to measure stomatal conductance and evapotranspiration. In this experiment, we measured net photosynthetic rate with photon flux density ranging from 0 to 2000 [$\mu mol\ m^{-2}\ s^{-1}$].

3.2. Measurements of Chlorophyll and Nitrogen Concentration, Leaf Area, and Dry Mass of Leaf

The leaf area was determined prior to pigment analysis. Leaf area was determined as the result of the following steps. First step was to cut a fresh leaf, second step was to photocopy the fresh leaf by a copying machine, third step was to import monochrome image of leaf into PC, final step was to measure leaf area using the software-NIH Image, version. 1.62, distributed by National Institute of Health, USA. After photocopying, the cut leaf was dried for 48hrs in the drying machine at 80 °C, and then the weight of the dried leaf was weighed.

The chlorophylls were extracted in 100 % DMS (*N,N'-dimethylformamide*) with a leaf disc of 1.0 cm diameter. Extractable efficiency of DMS is stronger than that of acetone[4]. The absorption of the extract at 663.8 nm and 646.8 nm were measured with a HITACHI, U-1000 spectrophotometer. Chlorophyll *a*, chlorophyll *b* and chlorophyll *a*+*b* concentration (μg /ml) are calculated by Eq. (2):

$$\text{Chl a } (\mu g / ml) = 12.00A^{663.8} - 3.11A^{646.8} \quad \cdots \quad (2a)$$

$$\text{Chl b } (\mu g / ml) = 20.78A^{646.8} - 4.88A^{663.8} \quad \cdots \quad (2b)$$

$$\text{Chl a + b } (\mu g / ml) = 17.67A^{646.8} + 7.12A^{663.8} \quad \cdots \quad (2c)$$

where $A^{663.8}$ and $A^{646.8}$ are the absorbance at 663.8 nm and 646.8 nm wavelength, respectively.

The nitrogen concentration was determined using the NC-90A (Sumika Chemical Analysis Center), that can detect total nitrogen and carbon content in the sample. The calibration curve was obtained with the analytical standard acetanilide as a standard reagent. Total nitrogen content was determined as Eq. (3):

$$\text{Total nitorogen (mg)} = 6.77E^{-6} * \text{area} - 6.18E^{-3} \quad (R^2 = 0.999) \quad \cdots \quad (3)$$

where area is the measured peak area of total nitrogen.

4. RESULTS AND DISCUSSION

4.1. Correlation Between Biochemical Content and Model's Parameters

Correlation between the measured saturated Amax and chlorophyll *a* concentration per unit area was high with a coefficient of determination of R^2=0.91. There was linear correlation between saturated Amax and chlorophyll *a* concentration per unit area, as saturated Amax value increased in proportion to chlorophyll *a* concentration. But chlorophyll *a* concentration per unit mass didn't correlate with saturated Amax. Furthermore, both chlorophyll *b* concentration per unit area and its per unit mass didn't correlate with saturated Amax. R didn't correlated for chlorophyll *a* concentration per unit area or chlorophyll *a* concentration per unit mass.

However, R had the best correlation with saturated Amax. Also total nitrogen concentration per unit area very much correlate with saturated Amax, R^2=0.91. But total nitrogen concentration per unit mass didn't correlate with saturated Amax. Figure 1 shows correlation between saturated Amax and chlorophylls per unit area (left diagram) and between saturated Amax and total nitrogen concentration per unit area (right diagram).

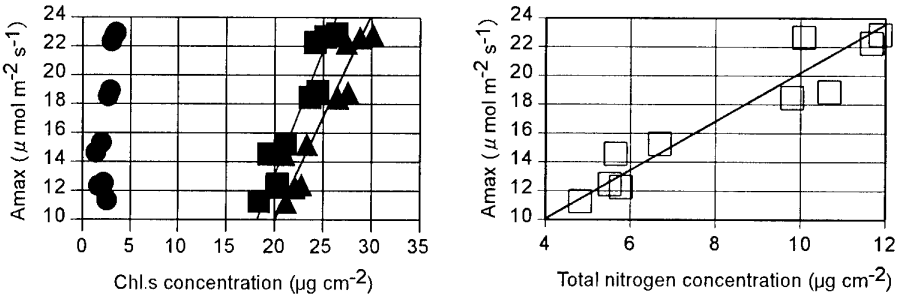


Figure 1. Correlation between saturated Amax and chlorophylls concentration per unit area (left) and total nitrogen concentration per unit area (right); ■ stands for chlorophyll *a*, ● stands for chlorophyll *b*, ▲ stands for chlorophyll *a*+*b*, □ stands for total nitrogen

4.2. Relationship between biochemical concentration and leaf reflectance

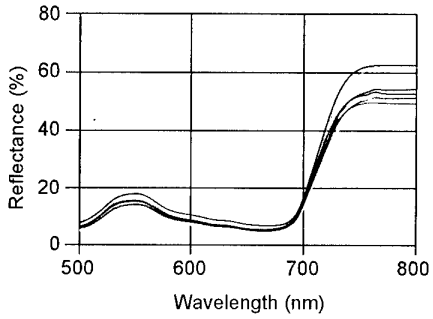


Figure 2 shows result of spectral reflectance curves of cucumber leaves in greenhouse chamber. The curves had common characteristics. There was the first positive peak called as the green peak driven by chlorophylls and carotenoids at 550 nm. There was a negative peak identified by absorption band of chlorophyll *a* at 680 nm. Moreover, these curve had red edge region and plateau region depending on its leaf structure over 700 nm. This reflectance curve is a typical reflectance curve of leaf.

Figure 2. A reflectance of cucumber's leaves in the greenhouse chamber

Three methods were examined to estimate chlorophyll *a* concentration per unit area from spectral reflectance; (1) a correlation between chlorophyll *a* concentration per unit area and spectral reflectance at one single wavelength; (2) a correlation between chlorophyll *a* concentration per unit area and ratio of spectral reflectance at two different wavelengths; (3) a correlation between chlorophyll *a* concentration per unit area and the first derivative spectral reflectance at one single wavelength.

A range of wavelength was selected between 500 nm to 800 nm to remove the effect of water and sensor noise. As the result from these methods, coefficient of determination of the method using spectral reflectance at one single wavelength was low over all ranges of wavelength in the greenhouse chamber. This result is shown in Figure 3 (left). Distribution of coefficient of determination between chlorophyll *a* concentration per unit area and the ratio of spectral reflectance at two different wavelengths is shown in Figure 3 (right). The ratio became higher than that of spectral reflectance at one single wavelength. Also the ratio became high, when either denominator or numerator was selected as spectral reflectance at absorption band of chlorophyll *a*. The coefficient of determination between the first derivative spectral reflectance and chlorophyll *a* concentration per unit area is shown in Figure 4. There were three peaks. The first peak was due to pigments like chlorophylls and carotenoids. The second peak was absorption band of chlorophyll *a*. The third peak is due to the structure of leaf.

The authors found that two methods were effective to estimate chlorophyll *a* concentration per unit area using hyperspectral data. Moreover, it is important to select the best method based on the measurement condition. In case of the experiment in the greenhouse chamber, the best method was the first derivative spectral reflectance.

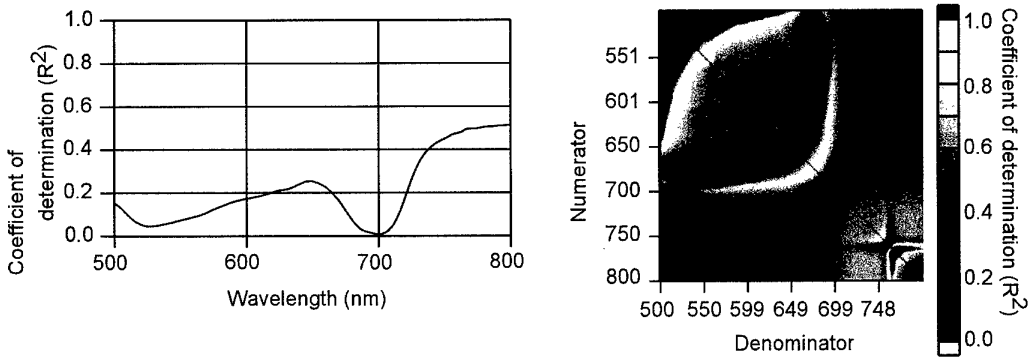


Figure 3. Coefficient of the determination between chlorophyll *a* concentration per unit area and spectral reflectance at one single wavelength in the greenhouse chamber (left) and distribution of coefficient of determination between chlorophyll *a* concentration per unit area and ratio of spectral reflectance at two different wavelengths (right) in the greenhouse chamber

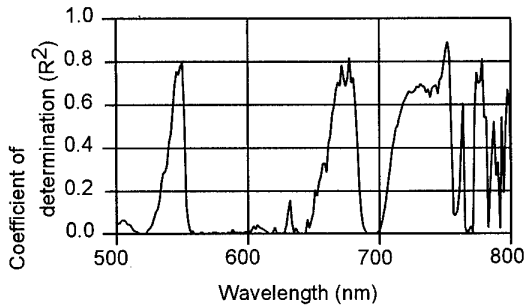


Figure 4. Coefficient of determination between the first derivative spectral reflectance and chlorophyll *a* concentration per unit area

4.3. Evaluation of Net Photosynthetic Rate

In this study, the first derivative spectral reflectance was considered best to estimate chlorophyll *a* concentration per unit area. This process model was obtained based on both relationship between saturated Amax and chlorophyll *a* concentration and between chlorophyll *a* concentration and the first derivative spectral reflectance. Model's parameters were estimated as shown in Eq. (7).

$$\text{Chl_a}\ (\mu g\ cm^{-2}) = -191.61\ RF'(678.01nm) + 35.07\ [R^2 = 0.81] \quad \cdots\ (7a)$$

$$A\max_{sat}\ (\mu mol\ m^{-2}\ s^{-1}) = 1.55\ \text{Chl_a} + 17.75\ [R^2 = 0.90] \quad \cdots\ (7b)$$

$$R\ (\mu mol\ m^{-2}\ s^{-1}) = -4.36E-2\ A\max_{sat} + 5.85\ [R^2 = 0.56] \quad \cdots\ (7c)$$

$$A\max'\ (\mu mol\ m^{-2}\ s^{-1}) = A\max_{sat} - R \quad \cdots\ (7d)$$

Chlorophyll *a* concentration per unit area could be estimated with R^2=0.81 using the first derivative spectral reflectance at 678.01 nm and then saturated Amax could be estimated with R^2=0.90 by the estimated chlorophyll *a* concentration. Also R can be estimated by saturated Amax, and finally, Amax' was calculated by saturated Amax and R. The Light-photosynthetic rate curve was drawn. We estimated net photosynthetic rate at PFD condition that is same as that in greenhouse chamber. The relationship between measured net photosynthetic rate and estimated net photosynthetic rate is shown in Figure 7. Coefficient of determination was 0.74.

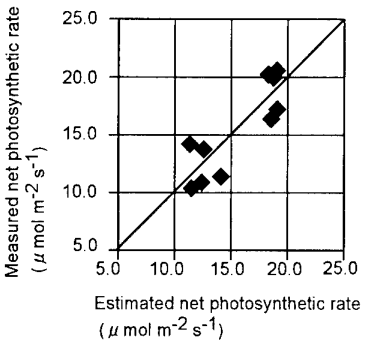


Figure 7. Correlation between measured net photosynthetic rate and estimated net photosynthetic rate

6. CONCLUSION

It is important to estimate parameters of a terrestrial ecosystem function to solve the global environmental issues. Hyperspectral remote sensing is a new technology, which is most useful to estimate biochemical parameters. This study investigated whether it is possible to estimate net photosynthetic rate from hyperspectral remote sensing. It was found that the net photosynthetic rate could be estimated by chlorophyll *a* concentration per unit area with hyperspectral data. Also, the net photosynthetic rate could be estimated by nitrogen concentration per unit area a similar equation that is a little bit different in respect of selected wavelength at 732.122 nm. The saturated Amax could be estimated with chlorophyll *a* or nitrogen concentration per unit area measured by hyperspectral data. Further, the saturated Amax could be used to estimate the respiration. Then our process model could estimate net photosynthetic rate with coefficient of determination of 0.74. We've suggested a new method to estimate CO_2 uptake based on the estimated chlorophyll or nitrogen concentration per unit area.

In future, it will be necessary to examine relationship between physiological variables and model's parameters to net photosynthetic rate at canopy and community scale. Furthermore Blackman type will be modified to accommodate in consider effects of temperature and water stress and so on. Then biochemical variables of a terrestrial ecosystem like lignin and cellulose will be estimate using hyperspectral imager at canopy and community scale.

ACKNOWLEDGMENTS

This work was supported by two divisions of NIES - the natural vegetation conservation research team of the global environment division; the information processing and analysis section of the social and environmental system division.

REFERENCES

1. Lee F. Johnson, Christine A. Hlacka, and David L. Peterson, "Multivariate Analysis of AVIRIS Data for Canopy Biochemical Estimation along the Oregon Transect ", *REMOTE SEN. ENVIRON.*, **47**, pp. 216-230. 1994.
2. Paul J. Curran, John A. Kupiec, and Geoffrey M. Smith, "Remote Sensing the Biochemical Composition of a Slash Pine Canopy", *IEEE TRANSSACTION ON GEOSCIENCE AND REMOTE SENSING*, **35**, NO. 2, MARCH, pp. 415-420. 1997.
3. Blackman FF, "Optima and limiting factors", *Annals of Botany*, **19**, pp. 281-295. 1905.
4. R. J. Porra, W. A. Thompson and P. E. Kriedeman, "Determination of accurate extinction coefficients and simultaneous equations for assaying chlorophylls *a* and *b* extracted with four different solvents: verification of the concentration of chlorophyll standards by atomic absorption spectroscopy ", *Biochi. mica et Biophysica Acta*, **975**, pp. 384-394. 1989.

Multiscale Analysis of Hyperspectral Data Using Wavelets for Spectral Feature Extraction

Pai-Hui Hsu Yi-Hsing Tseng
Department of Surveying Engineering,
National Cheng-Kung University
No.1 University Road, Tainan, Taiwan
Tel:+886-6-2370876 Fax: +886-6-2375764
Email: p6885101@sparc1.cc.ncku.edu.tw
TAIWAN

KEY WORDS: Hyperspectral Data, Spectral Feature Extraction, Wavelet Transform

ABSTRACT: The purpose of feature extraction is to abstract substantial information from the original data input and filter out redundant information. In this study, we transfer hyperspectral data from the original-feature space into a scale-space plane using the wavelet transform to extract the significant spectral features. The wavelet transform can focus on localized signal structures with a zooming procedure. The absorption bands are thus detected with the wavelet transform modulus maxima, and Lipschitz exponents are estimated at each singularity point of the spectral curve from the decay of the wavelet transform amplitude. The local frequency variances provide some useful information about the oscillations in the hyperspectral curve for each pixel. Various types of materials can be distinguished by the differences in the local frequency variation. This new method generates more features that are meaningful and is more stable than other known methods for spectral feature extraction.

1. INTRODUCTION

Multispectral imagery has been used for earth observation since the 1960's. Many effective methods of spectral data analysis have been developed for various applications. Although multispectral imagery has proved to be useful for earth observation, it frequently failed to differentiate similar land cover reflectance due to its low spectral resolution. Imaging spectrometry was developed to acquire images with high spectral resolution, which are commonly called hyperspectral images. These images typically have several hundred spectral bands, and so enable the construction of detail reflectance spectrum for each pixel (Lillesand and Kiffer, 2000). A typical example is the image obtained by the Airborne Visible/Infrared Imaging Spectrometer (AVIRIS) developed by NASA JPL which has 224 contiguous spectral channels covering a spectral region form 0.4 to 2.5 μm with 10 nm bandwidth. Theoretically, using hyperspectral images should increase our abilities to identify various material types. However, the data classification approach that has been successfully applied to multispectral images in the past is not as effective with hyperspectral images. Most of the traditional methods for classification are statistically based on decision rules, which are determined by the known training samples. As the number of dimensions in the feature space increases, subject to the number of bands, the number of training samples needed for image classification also increases. If the number of training samples is insufficient, which is quite common in hyperspectral data cases, the statistical parameter estimation becomes inaccurate. The classification accuracy first grows and then declines as the number of spectral bands increases, which is often referred to as the Hughes phenomenon (Hughes, 1968).

In order to improve the classification performance, some of the approaches are based on statistical theory to extract important features from the original hyperspectral data prior to the

classification processing. The goal of employing feature extraction is to substantially remove the redundant information without sacrificing significant information. Some proposed feature extraction methods are compared by the classification performance (Hsu and Tseng, 1999), such as principal component analysis (Schowengerdt, 1997), discriminant analysis feature extraction (Tadjudin and Landgrebe, 1998), and decision boundary feature extraction (Lee and Landgrebe, 1993). These methods are referred to as statistic-based feature extraction.

Due to the high spectral resolution of hyperspectral images, it becomes possible to analyze the diagnostic absorption and reflection characteristics of an object over narrow wavelength intervals. For example, the spectral reflectance curves of healthy green vegetation manifests a "peak-and-valley" configuration (Lillesand and Kiffer, 2000). The absorption and reflection characteristics are often related to the internal structure of the materials. Some approaches were proposed to locate and characterize these subtle spectral details. Piech et. al. (1987) used the symbolic descriptions of spectral features, called fingerprints, as quantitative indices of the absorption bands to distinguish various materials. Derivative analysis (Demetriades-Shah et. al., 1990; Philpot, 1991; Tsai and Philpot, 1997) of hyperspectral data makes use of the fact that the derivative of a function tends to emphasize changes irrespective of the mean level (Tsai and Philpot, 1998). Techniques that can detect more meaningful spectral features that are related to physical attributes are called physical-related feature extraction methods.

In this study, we attempted to transform the spectral data from the original feature space into a scale-space plane using the wavelet transform. The wavelet transform (WT) can focus on localized signal structures with a zooming procedure (Mallat, 1997). The local frequency characteristics such as the *Lipschitz exponents* provide some useful information about the oscillation of the spectral curve for each pixel. Different types of materials can be distinguished by the differences in the local frequency variation. The method we propose in this study is called the *modulus maxima feature extraction* (MMFE) method. In this method, the features are extracted according to the wavelet transform modulus maxima. This new method generates features that are more meaningful and is more stable than other known methods for spectral feature extraction. The fingerprints of spectral curve, the derivative analysis and the wavelet transform are also referred to as multiscale feature extraction because they can emphasize local spectral features in the scale-space plane from course to fine scale

2. MULTISCALE FEATURE EXTRACTION METHODS

Generally speaking, a feature is any attribute that can be extracted from the measurement data. Features may be numerical, symbolic, or both. For remote sensing data, the molecular absorption bands of water and carbon dioxide cause deep absorption features that complete radiation block transmissions. These spectral regions were avoided for traditional earth surface remote sensing (Schowengerdt, 1997). However, hyperspectral data produces laboratory-like curves with spectral resolution sufficient to describe the essential absorption features of many materials. This spectral analysis characteristic has also renewed interest in extracting physical spectral features in contrast to statistical approaches. One of the earliest physical feature extraction specifications for hyperspectral data was the calculation of image "residual" spectra for mineral detection and identification (Schowengerdt, 1997). This method emphasizes the absorption bands of different minerals relative to an average signature without absorption features. Multiscale methods are used to extract spectral features from course to fine scales. Thus the physical meaning of a spectral curve can be surveyed at different scales. A method of symbolic description called absorption band fingerprints for hyperspectral data was developed by Piech and Piech (1987,1989). The fingerprints are a representation based on a scale space filter for the hyperspectral data. In this method, a scale space image is a set of progressively

smoothed versions produced by convoluting the original spectral curve with a LoG filter. As the smoothing scale increase, features of the curve disappear until only a dominant spectral shape remains. A plot of the points of inflection within the scale space image results in a fingerprint. The net result of the scale space analysis of a hyperspectral data curve is a sequence of triplets. Each triplet describes a spectral feature and contains important measures directly related to the area contained within the spectral feature and the left and right inflection points of the spectral feature. Another method proposed to reduce the effects of atmospheric scattering and absorption on spectral signatures is derivative analysis. The derivatives are estimated using a finite divided difference approximation algorithm with a finite band separation, $\Delta\lambda = \lambda_{i+1} - \lambda_i$ (Tsai and Philpot, 1997). The derivatives not only emphasize subtle spectral details, but also minimize illumination and atmospheric effects. Thus, derivatives are well suited to extract spectral features relating to specified target properties. A common disadvantage of this method is its extreme sensitivity to noise. For this reason, the derivative computation is typically coupled with spectral smoothing (Tsai and Philpot, 1999).

In this study , the wavelet transform was applied to extract physical features. The wavelet transform can focus on localized signal structures with a zooming procedure. The local frequency characteristics, such as the Lipschitz exponents, provide useful information about the oscillation of the spectral curve for each pixel. In the next section, we briefly introduce the basic theory of wavelet transform and then explain the MMFE method theory.

3. WAVELET-BASED FEATURE EXTRACTION

3.1 Wavelet Transform

The continuous wavelet transform (CWT) which decomposes signals over dilated and translated wavelets was first introduced by Grossmann and Morlet (1984). The wavelet transform of a function $f \in \mathbf{L}^2(\ )$ is defined by

$$Wf(u,s) = \langle f, \psi_{u,s} \rangle = \int_{-\infty}^{+\infty} f(t) \frac{1}{\sqrt{s}} \psi^*(\frac{x-u}{s}) dx \qquad (1)$$

where $\psi_{u,s}(x)$ is obtained by introducing a scale factor s and a translation factor u to the mother wavelet function $\psi(x)$:

$$\psi_{u,s}(x) = \frac{1}{\sqrt{s}} \psi\left(\frac{x-u}{s}\right) \qquad (2)$$

The wavelet transform $Wf(u,s)$ is a function of the scale and the spatial position x. It measures the variation in f in the neighborhood of u, whose size is proportional to s. When the scale s varies from its maximum to zero, the decay of the wavelet coefficients characterizes the regularity of f in the neighborhood of u. This is the essential idea in detecting the absorption band position from the reflectance spectra.

3.2 Modulus Maxima of Wavelet Transform

A wavelet ψ with n vanishing moments can be written as the n^{th} order derivative of a function θ, that is $\psi = (-1)^n \theta^{(n)}$, thus the resulting wavelet transform is a multiscale differential operator:

$$Wf(u,s) = s^n \frac{d^n}{du^n} (f * \bar{\theta}_s)(u) \qquad (3)$$

Suppose the convolution $f * \bar{\theta}_s(u)$ averages $f(x)$ over a domain proportional to s. Let $\psi_1 = -\theta'$ and $\psi_2 = \theta''$ be two wavelets, thus the wavelet transforms, $W^1 f(u,s)$ and $W^2 f(u,s)$, are respective to the first and second derivative of $f(x)$ smoothed by

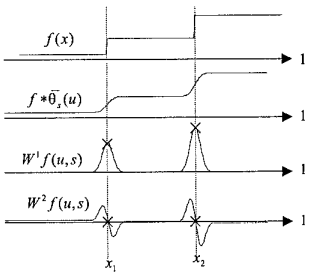


Figure 1. The positions of the local maxima of and the zero-crossing of

$f * \bar{\theta}_s(u)$. For a fixed scale, the local maxima of $W^1 f(u,s)$ and the zero-crossings of $W^2 f(u,s)$ will correspond to the inflection points of $f * \bar{\theta}_s(u)$ (figure 1). For all scales, the local maxima points of $W^1 f(u,s)$ can be connected as a set of maximal lines in the scale-space plane (u, s). Similarly, the zero-crossings of $W^2 f(u,s)$ define a set of smooth curves that often look like fingerprints. By detecting the positions of the local maxima or zero-crossings from a coarse to fine scale, we can obtain the positions of the singularities of a signal. These two methods are very similar, but the local maxima approach has several important advantages (Mallat and Hwang, 1992). The smoothing function θ can be viewed as the impulse response of a low-pass filter. An important example often used in signal processing is the Gaussian function. In this study, the wavelet is defined as the first derivative of the Gaussian function.

3.3 The Estimation of Lipschitz Regularity

To characterize the singular structure of a signal, it is necessary to quantify local regularities precisely. Lipschitz exponents provide not only uniform regularity measurements over time intervals, but also pointwise Lipschitz regularity at any point v of a signal. The relationship between the decay of the wavelet transform amplitude across scales and the pointwise Lipschitz regularity of the signal was described by Jaffard (1991). He proved a necessary and sufficient condition in the wavelet transform for estimating the Lipschitz regularity of f at a point v. Assume that the wavelet ψ has n vanishing moments and n derivatives with a fast decay. If $f \in \mathbf{L}^2(\ )$ is Lipschitz $\alpha \le n$ at v, then there exists $A > 0$ such that $\forall (u,s) \in \ \times\ ^+$,

$$|Wf(u,s)| \le A s^{\alpha+\frac{1}{2}} \left(1 + \left|\frac{u-v}{s}\right|^{\alpha}\right) \qquad (4)$$

In order to simplify the above condition, we assume that ψ has a compact support equal to $[-C, C]$. The cone of influence of v in the scale-space plane is the set of points (u, s) such that v is included in the support of $\psi_{u,s}(t) = \frac{1}{\sqrt{s}}\psi(\frac{t-u}{s})$ (Mallat, 1997). Since the support of $\psi(\frac{t-u}{s})$ is equal to $[u - Cs, u + Cs]$, the cone of influence of v is defined by $|u - v| \le Cs$. This is illustrated in Figure 2. Since $|u - v| \le Cs$, the conditions (4) and (5) can be written as

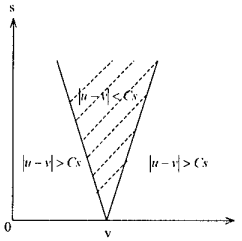


Figure 2. The cone of influence in the scale-space.

$$|Wf(u,s)| \le A' s^{\alpha+\frac{1}{2}} \qquad (5)$$

which is equivalent to the uniform Lipschitz condition given by Mallat (1997). In this study, we assumed that all modulus maxima converging to v are included in a cone. The potential singularity at v is isolated. Function f is uniformly Lipschitz α in the neighborhood of v if and only if there exist $A > 0$ such that each modulus maximum (u, s) in the cone satisfies (6). In order to estimate the Lipschitz exponent we rewrite (5) as $\log_2 |Wf(u,s)| \le \log_2 A + (\alpha + \frac{1}{2}) \log_2 s$. The Lipschitz regularity at v is thus the maximum slope of $\log_2 |Wf(u,s)|$ as a function of $\log_2 s$ along the maxima lines converging to v.

4. EXPERIMENTS

4.1 Test data

The test data are a set of hyperspectral data delivered from AVIRIS. The data has 220 spectral bands from 0.4um to 2.5um with about 10 nm spectral resolution. The spectral curves of three different materials are shown in

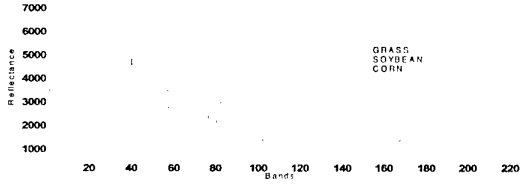
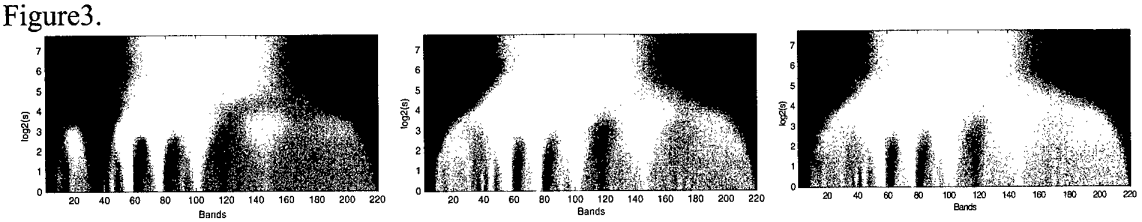


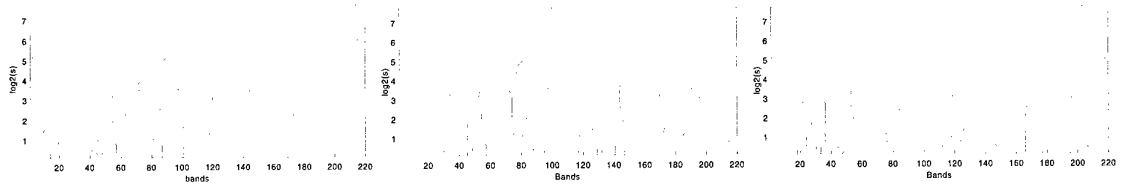
Figure 3. Three kinds of hyperspectral curves from AVIRIS images.

Figure3.



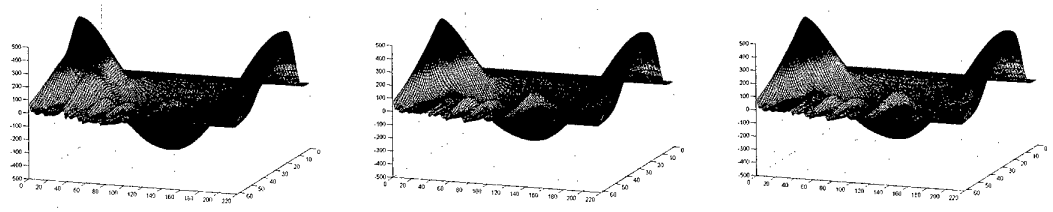
(a) grass (b) soybean (c) corn

Figure 4. $Wf(u,s)$, wavelet transform of the spectrums,



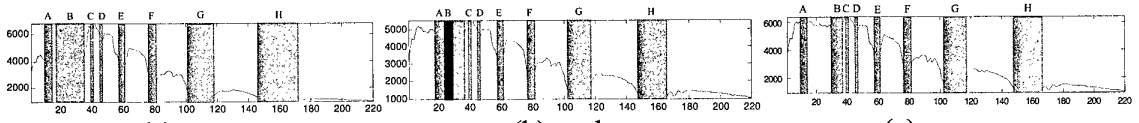
(a) grass (b) soybean (c) corn

Figure 5. The modulus maxima of $Wf(u,s)$



(a) grass (b) soybean (c) corn

Figure 6. 3D view of $Wf(u,s)$



(a) grass (b) soybean (c) corn

Figure 7. The spectral features extracted by modulus maxima of $Wf(u,s)$

4.2 Wavelet Transform Modulus

Figures 4(a), (b) and (c) show the wavelet transform $Wf(u,s)$ of the spectral curves with respect to the three materials. They were calculated with $\psi = -\theta'$, where θ is a Gaussian function. The position parameter u and the $\log_2$ of scale s vary respectively along the horizontal and vertical axes. Black, gray and white points represent positive, zero and negative wavelet coefficients respectively. Figures 5(a), (b) and (c) show the results of extracting modulus maxima from $Wf(u,s)$. It can be seen that all singularities can be detected easily along the maxima line from coarse to fine scales. The maxima lines detected along the scale space correspond to the main absorption bands of the spectral curve. The 3D views of the wavelet transform are respectively shown in figures 6(a), (b) and (c). The absorption bands create large amplitude coefficients in their cone of influence. In figure 7(a), (b) and (c), eight absorption spectral features are marked with gray rectangles $A\cdots E$. The left and right borders of the rectangles are determined by the maxima lines. The converged position of a maxima line with negative wavelet coefficients correspond to the left border of a rectangle, then the right border of the rectangle will be determined by the next maxima line with positive wavelet coefficients. Because the spectral curves of these three materials are very similar in shape, the extracted spectral features C, D, E,

F, and *G* almost have the same positions (See table 1.). However, these three materials can be differentiated using the features *A*, *B*, and *H*, which are represent small variations of the spectral curves.

4.3 Lipschitz Exponent

Figure 8 shows the results of Lipschitz exponents calculated at each singularity point for the test data. Because the Lipschitz regular α was estimated under the assumption of the compact support wavelet ψ with one vanishing moment, the values of α should satisfy $0 \le \alpha < 1$ for isolated singularity. The negative Lipschitz exponent values indicate the corresponding points possessing high-frequency oscillations in their neighborhood.

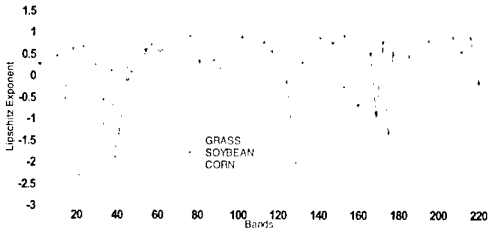


Figure 8. . The Lipschitz exponents calculated at each singularity point for the test data.

The spectral curves for soybean and corn shown in figure 5 look quite similar in shape and their main absorption bands corresponding to the low-frequency components are nearly the same. However, one would easily discover the differences when a scale factor is introduced to overlap these two curves. Figure 9 obviously shows that the high-frequency variations in the corn spectrum are larger than the soybean spectrum in the 21st, 76th and 153rd bands. Therefore, these two different materials can be distinguished easily with the Lipschitz exponents. Table 1. shows that the spectral features *C, D, E, F,* and *G* have the same positions in spectral curves, but their Lipschitz exponents are different. The variations will be useful to distinguish a spectral curve. For example, the grass spectral curve at the right boder of *E* feature is smoother than the other two curves at the same location, so its Lipschitz exponent is larger than the other two.

Table1. Results of spectral absorption positions

bsorption features		A		B		C		D		E		F		G		H	
parameters		L	R	L	R	L	R	L	R	L	R	L	R	L	R	L	R
grass	band	9	14	18	36	39	41	45	47	57	61	76	81	101	118	146	172
	Lips. exp..	0.756	-0.174	0.669	0.777	-2.800	-1.283	0.116	-0.350	0.618	0.555	0.752	0.281	0.826	0.852	0.898	0.854
soybean	band	18	37	23	29	39	41	45	47	57	61	76	81	102	117	147	166
	Lips. exp.	0.614	0.116	0.670	0.251	-1.894	-1.286	-0.122	0.079	0.710	0.560	0.911	0.320	0.909	0.553	0.760	0.492
corn	band	9	14	29	37	39	41	45	47	57	61	76	81	102	117	147	166
	Lips. exp.	-0.106	-0.319	0.411	-0.17	-1.71	-1.300	0.255	-0.216	0.857	0.553	0.400	0.293	0.827	0.547	0.805	0.571

5. DISCUSSION

The high spectral resolution of hyperspectral data provides the ability for diagnostic identification of various materials. In order to increase the classification performance, feature extraction is pre-processed to substantially remove the redundant information without sacrificing significant information. In this study, we transferred the hyperspectral data into the scale-space plane using the wavelet transform to extract important spectral features. The wavelet transform can focus on localized signal structures by scaling and dilating a wavelet. The absorption bands of spectral curves are thus detected automatically by the wavelet transform modulus maxima, and the Lipschitz exponents are estimated at each singularity point in the spectral curve from the decay of the wavelet transform amplitude. The local frequency variances provide useful information about the oscillations in the hyperspectral curve for each pixel.

Various materials can be distinguished by the differences in the local frequency variations. This new method generates features that are more meaningful and is more stable than other known methods for spectral feature extraction. In particular, the method proposed in this paper will be helpful for spectral analysis that reduces the multidimensional hyperspectral data to a smaller number of essential features that can be both automatically processed and physically interpreted.

ACKNOWLEDGMENTS

The authors would like to thank the National Science Council of Republic of China, for support of this research project: NSC88-2211-E006-084.

REFERENCE

Demetriades-Shah, T.H., M.D. Steven and J.A. Clark, 1990. High Resolution Derivatives Spectra in Remote Sensing. Remote Sens. Environ, 33, pp. 55-64.

Grossmann, A. and J. Morlet, 1984. .Decomposition of Hardy functions into square integrable wavelets of constant shape. SIAM J. Math, 5 , pp.723-736.

Hsu, P.H. and Y.H. Tseng, 1999. Feature Extraction for Hyperspectral Image. Proceedings of the 20th Asian Conference on Remote Sensing, Vol. 1, pp. 405-410.

Hughes, G.F., 1968. On the Mean Accuracy of Statistical Pattern Recognizers. IEEE Transaction on Information Theory, IT-14, pp. 55-63

Jaffard, S., 1991. Pointwise smoothness, two microlocalisation and wavelet coefficients. Publications Mathematiques, 35.

Lee, C. and D. Landgrebe, 1993. Feature Extraction and Classification Algorithms for High Dimensional Data. TR-EE 93-1, Purdue University.

Lillesand, T.M. and R.W. Kiffer, 2000. Remote Sensing and Image Interpretation, Fourth Edition, John Wiley & Sons, Inc.

Mallat, S. and W. L. Hwang, 1992. Singularity Detection and Processing with Wavelets. IEEE Transactions on Information Theory, 38(2), pp. 617-643.

Mallat, S., 1997. A wavelet tour of signal processing, ACADEMIC PRESS.

Philpot, W.D., 1991. The Derivative Ratio Algorithm: Avoiding Atmospheric Effects in Remote Sensing. IEEE Transactions on Geoscience and Remote Sensing, 29(3), pp.350-357.

Piech, M.A. and K.R. Piech, 1987. Symbolic representation of hyperspectral data. Applied Optic, 26(18), pp. 4018-4026.

Piech, M.A. and K. R. Piech, 1989. Hyperspectral interactions: invariance and scaling. Applied Optic, 28(3), pp.481-489.

Richards, J.A., 1993. Remote Sensing Digital Image Analysis: An Introduction. Springer-Verlag Berlin Heidelberg, Second Edition.

Schowengerdt, R.A., 1997. Remote Sensing: Models and Methods for Image Processing, Academic Press.

Tadjudin, S. and D. Landgrebe, 1998. Classification of High Dimensional Data with Limited Training Samples. PhD Thesis and School of Electrical & Computer Engineering Technical Report TR-ECE 98-8, Purdue University.

Tsai, F. and W. Philpot, 1997. Derivative Analysis of Hyperspectral Data for Detecting Spectral Features. IGARSS '97, Remote Sensing - A Scientific Vision for Sustainable Development,Vol.3, pp.1243-1245.

Tsai, F. and W. Philpot, 1998. Derivative Analysis of Hyperspectral Data. Remote Sens. Environ, 66, pp.41-51.

The 21st Asian Conference on Remote Sensing
December 4-8, 2000 Taipei, TAIWAN

Microwave holographic- imaging remote objects using light-modulated scattering technique

Thammasak Vimonkiattikun[1], Jirawath Panklang[2], Anupong Srongprapa[3]

[1,2]Department of Electronic Engineering, Faculty of Engineering
[3]Applied Microwave Research Laboratory(AMRL)
Department of Applied Physics, Faculty of Science
King Mongkut's Institute of Technology Ladkrabang, Bangkok 10520,
Tel (66-2)3269980 ext. 213/214, fax: (66-2)3269981, ksanupon@kmitl.ac.th,
Thailand

KEY WORDS: Image Processing, Microwave, Holography, Digital Signal Processing, Remote Sensing,Modulated Scattering.

ABSTRACT

Modulated scattering technique is mostly used for measuring microwave fields with less perturbation to obtain near – field antenna pattern, such a technique can also bc used for microwave holography.A computerized system for recording and reconstruction of microwave hologram at 9.2 GHz X-band frequency is described. A small dipole loaded by MRD 721 photodiode is suspended by thin balsa post at some distance along symmetric Z-axis of the fixed illuminating pyramidal horn antenna. The scattering cross-section of the dipole was modulated by 50 KHz optical signals guided to the diode through a plastic optical fiber. Low-intensity microwave was transmitted to a remote object via a free space and then reflected from object surface. Both the outgoing and backward wave excited the scattering wave, originated from the dipole,then propagated back to the same antenna and mixed with the synthetic off-axis internal reference wave providing by a programmable microwave phase shifter. The object was scanned 1/3 of wavelength stepwise in both X and Y directions, perpendicular to Z-axis, generating 128x128 sampling. For each object position, the output current of the mixer was preamplified and coherently measured at the modulated frequency using a lock-in amplifier to form hologram intensity signals. Fresnel diffraction approximation is used in digital reconstruction from stored hologram data to yield the two- dimensional image of the object.The distance between antenna, scatterer and object plane was allowed to varied. The higher resolving power of system compare with the Rayleigh limit for a conventional hologram has been demonstrated.

1. INTRODUCTION

As a mean of seeing through optically opaque medium, various application areas of microwave holography (Tricole,1977) are possible such as all-weather remote sensing, medical diagnosis, buried objects locator, etc. In ordinary system the microwavefield scattered from a stationary object coherently illuminated from a stationary transmitter is mapped over a prescribed hologram recording aperture by means of a detector that is scanned over the aperture. The simplest one need a fixed reference beam to interfere with the object wave and creates wavefield pattern that can be measured by intensity sensitive detector. The more advance one uses coherent phase-locked receiver with local oscillator acting as synthetic internal reference beam. Normally, with regards to the actual size of the conventional probing detector for low intensity application, the detected wavefield is considerably disturbed.

This problem can be overcome by using modulated scattering technique, where the original ones measured the field using a scatterer which may be mechanically (Cullen and Parr,1955), electrically (Richmond,1955) or optically (Iizuka,1963) modulated with synchronous detection of the modulated scattered signal. Orme and Anderson (Orme,1973) used spinning dipole technique of Cullen and Parr in their high resolution microwave holographic imaging of the objects obsured by dielectric media. In the work described here, a system similar to Orme and Anderson's, has been used to perform two-dimensional image of remote metallic objects. Now, the scatterer,in the form of a selected high speed photodiode, is modulated optically via a plastic fiber (Hajnal,1987) and the system is computerized for creating arbitrary internal reference beam angle, scanning control, data collecting and performing image reconstruction digitally.

2. OFF-AXIS SCANNING SOURCE / RECEIVER MICROWAVE HOLOGRAPHY

In some situations where microwavefield can be appropriately described as scalar quantity, scalar diffraction theory of light wave can be used. It is well known in physical optics that light which passes through an aperture or reflects from a plana reflector is fully described by the phase and amplitude distribution in the aperture/or reflector area. According to The Huygens' principle, this is sufficient to reconstruct the light wave at any point behind the aperture (or infront of the reflector). If we describe phase and amplitude in the aperture plane z = 0 by the complex function F(x,y),we obtain for the wave f(x,y,z) which develops behind the aperture (Born and Wolf,1964)

$$f(x,y,z) = F(x,y)*G(x,y,z) \tag{1}$$

where the symbol * denotes convolution and G is a sperical wave of wavelength λ originating in the aperture plane. Thus $G = e^{j2\pi/\lambda}/r$ with $r = \sqrt{x^2+y^2+z^2}$, which becomes in Fresnel's approximation $r = z + \sqrt{(x^2+y^2)/2z}$ giving the function f(x,y,z) to be found from a Fresnel's transform of F(x,y). Figure.1 represents the general geometric set up of the scanning-source/receiver microwave hologram recording. Here, a point source, a sensor (or detector), and an object are located at 3 consequetive planes denoted by source plane, sensor plane and object plane respectively. Spherical wave emitted from point source at P_1 (x,y,z) propagates to a point P_2 (ζ,η,o) on finite extended object at object plane. The reflected wave from point P_2 propagates to sensor at position P_3 (u,v,w). If sensor and point source are scanned coincidently,(i.e. x = u , y = v) the reflected wavefunction at sensor plane are given by

$$a(x,y,w) = a_0(x,y,w)\exp\{-j\phi(x,y,w)\}$$

$$= A_4 \exp\{jk_2(w+z)\}\times \int_{-\infty}^{\infty}\int_{-\infty}^{\infty} D(\zeta,\eta)\exp\left[jk_2\left\{\frac{(x-\zeta)^2+(y-\eta)^2}{2wz/(w+z)}\right\}\right]\partial\zeta\partial\eta \tag{2}$$

which is recognised as the diffraction field at plane z' = wz /(w+z) distant from the object for the situation of conventional holography. The Rayleigh resolution limit of the system is then given by

$$\delta = \frac{\lambda wz}{D(w+z)} \tag{3}$$

(instead of $\frac{\lambda w}{D}$) where D is the hologram dimension.

At the sensor position there is also reference planewave field b(x,y) whose direction of propagation make an incident angle θ to the normal of the plane.Thus

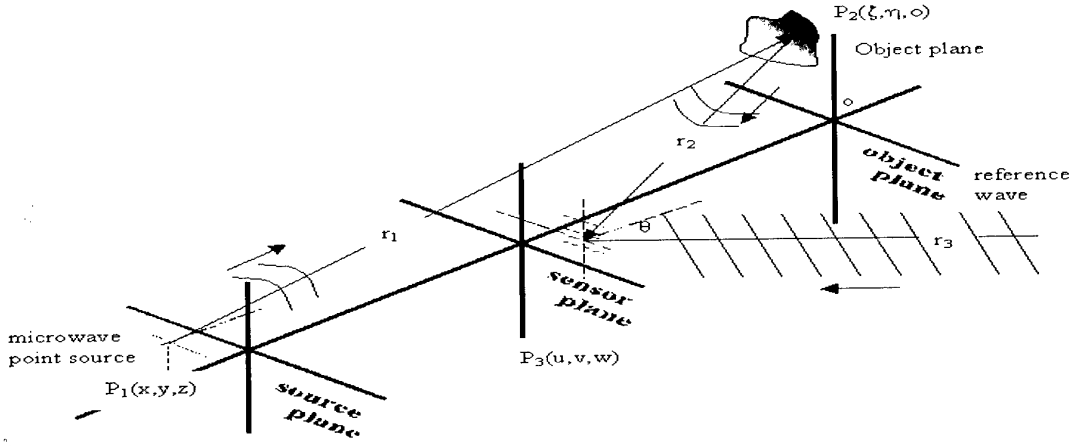


Figure 1. Recording Image data hologram of object using microwave

$$b(x,y) = b_0 \exp(-j2\pi\alpha x) \tag{4}$$

where α is spatial frequency of wavefront in the x direction which is equal to $\frac{\sin\theta}{\lambda}$,

$\lambda = 2\pi/k$ is wavelength, and b_0 is the field amplitude.

If the total wave function is C(x,y) and regards w as a constant, the intensity at sensor is

$$I(x,y) = C(x,y) \times C^*(x,y) \tag{5}$$

$$= (a+b)(a+b)^* = |a|^2 + |b|^2 + a^*b + ab^* \tag{6}$$

$$= \left\langle |a(x,y)|^2 + b_0^2 + b_0 a(x,y)\exp[j2\pi\alpha x] + b_0 a^*(x,y)\exp[-j2\pi\alpha x] \right\rangle \tag{7}$$

Image reconstruction process concerns with the modification of the reconstructed reference plane wave b*(x,y) by the intensity distribution I(x,y) to be b*(x,y)×I(x,y).Fresnel's transform of the term $b_0^2 a^*(x,y)$ corresponds to the real image wavefield of the object at the image plane.There is also a direct illuminating field E(u,v,w) which remain constant,as the sensor and source are scanned together.This term do not alter the results derived above significantly.

3. MODULATED SCATTERING MICROWAVE HOLOGRAPHIC SYSTEM

A schematic diagram of the system is shown in Figure 2. Experimental positions arrangement of the pyramidal microwave antenna, dipole scaterrer and object are shown in Figure 3. Both the antenna radiating field and the synthetic off-axis reference wave providing by a programmable movable short phase-shifter are fed by a single 10 mw. 9.2 GHz. Gunn oscillator. Direct illuminating wave and the object wavefield excite the 2 cm.-long MRD 721 photodiode, optically modulated at 50 KHz. via a fiber optic cable, to produce modulated scattering wave travelling back to the same antenna and combines with the reference wave at the mixer. Synchronous demodulation of the mixer signal output after amplification by a low-noise preamplifier is done by using a lock-in amplifier to produce hologram intensity signals. In this computerized-controlled prototype system,the source and scatterrer are stationary while the

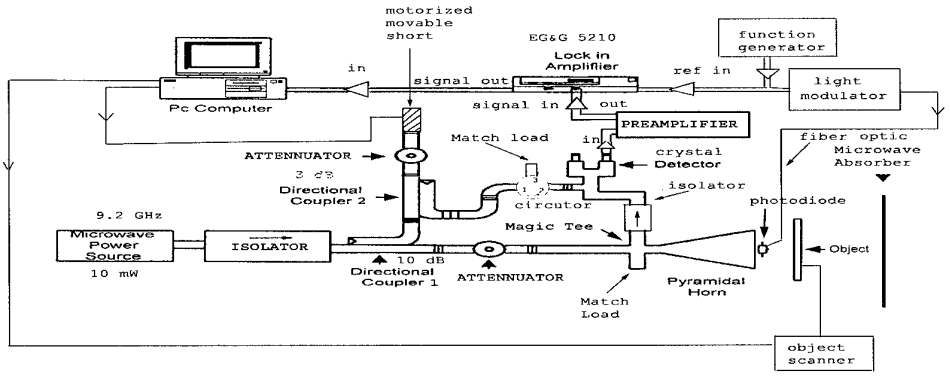


Figure. 2 Schematic diagram of microwave holographic system

object is scanned 1/3 of wavelength stepwise in both x and y direction generating 128×128 sampling signals associate with each position. Fresnel diffraction approximation is used in digital reconstruction from stored hologram data to yield the two-dimensional image of the object.

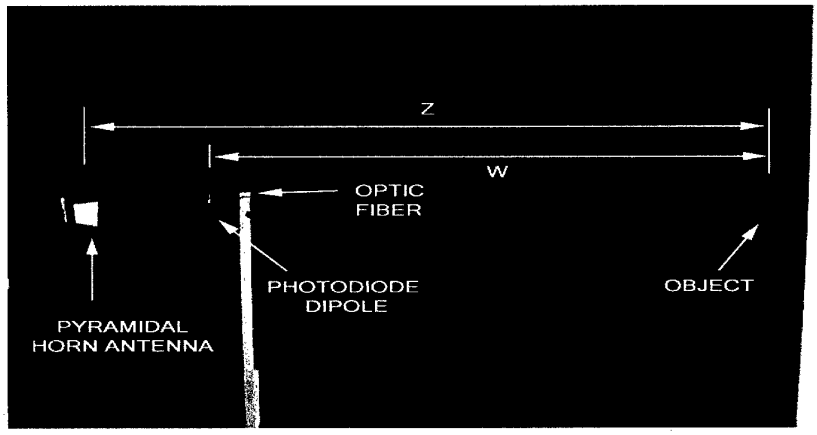


Figure. 3 Relative position between microwave antenna, dipole and object

4. EXPERIMENTED RESULTS

The system was successfully used to image flat metallic objects of various shape and size at different synthesized reference wave incident angle θ and limited distance, bound by the size of the existent small anechoic chamber 3.5×3.5×3.5 m^3 together with the degrading ratio S/N of the signal, but not too short to violate the Fresnel approximation. Some of the results are shown in Figure 4 for donut-shape object (for z = 288 cm., w = 211.5 cm., θ =44.3°) and dumbbell-shape object (for z = 288 cm., w = 249.5 cm., θ = 44.3°). Figure 5 shows the full width-half maximum of the image field intensity distribution of a 20 cm. diameter plate (for which z = 288 cm., w = 249.5 cm., θ = 44.3°). Consider this case as an example, the theoretical resolution limits are 5.44 cm. and 2.92 cm. for the conventional and source-receiver type hologram respectively. The estimated difference between actual object size and full width-half maximum of 2.7 cm. implies that the resolving power of the system that has been developed is significantly better than conventional system.

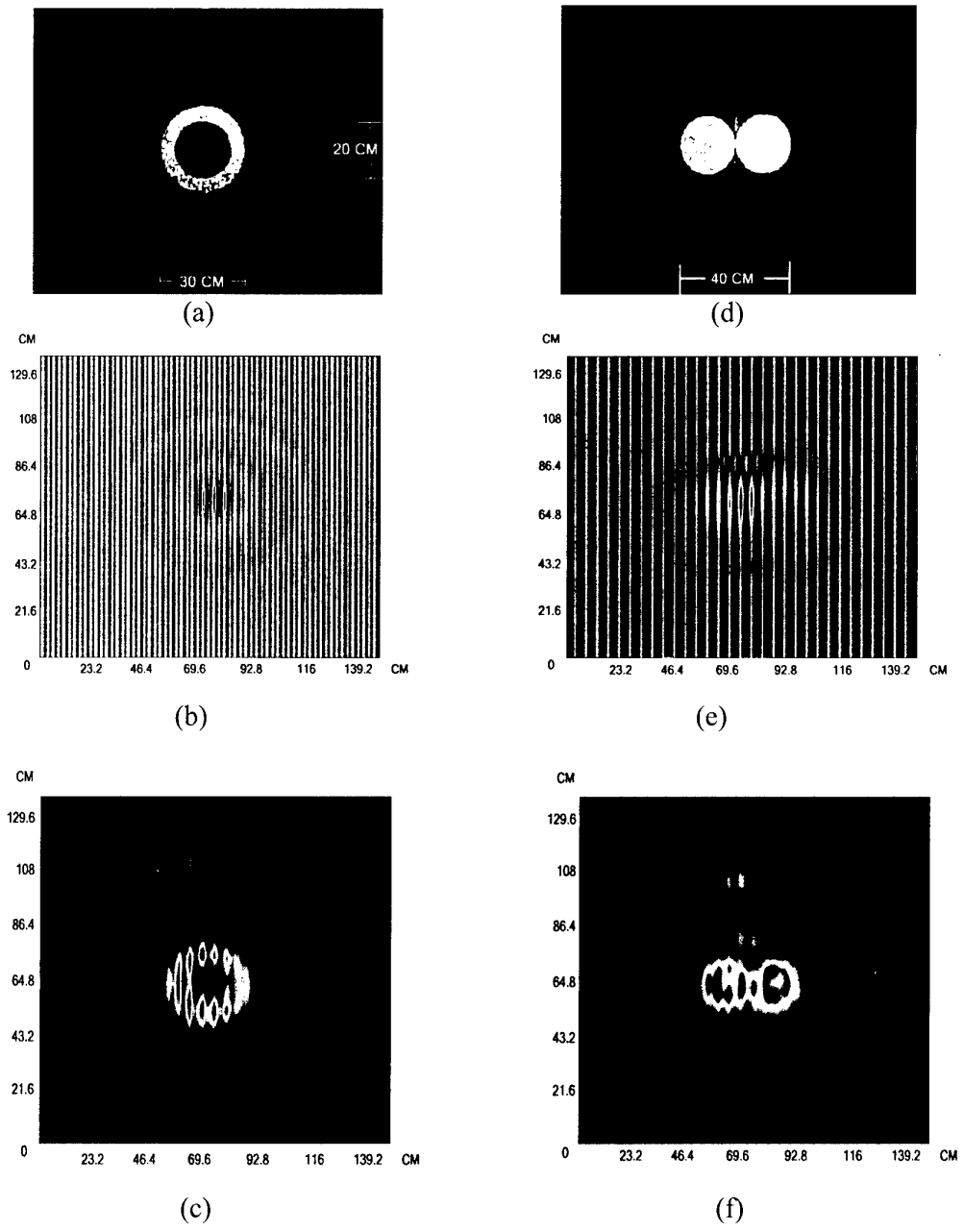
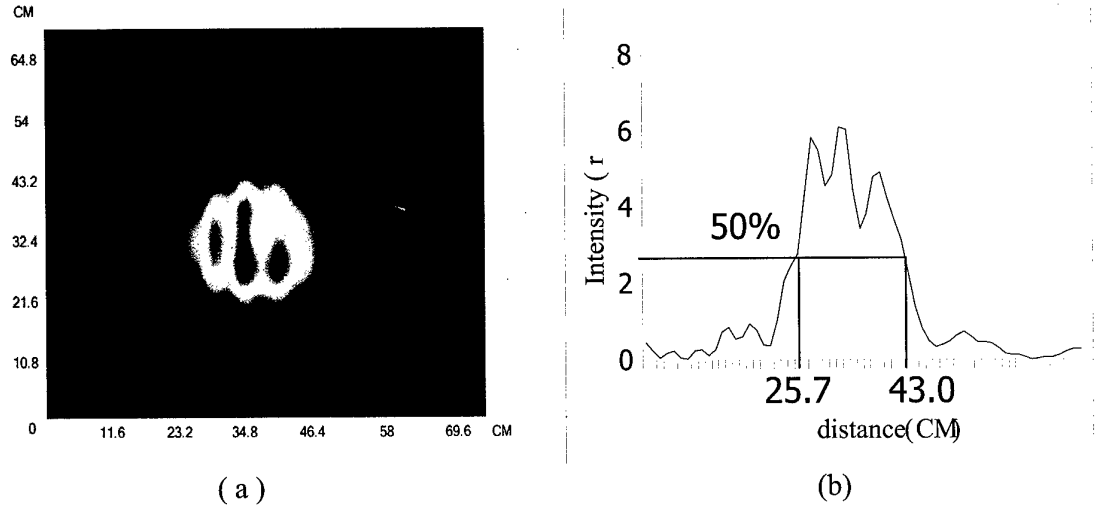


Figure. 4 Examples of the experimented results for : (a) donut-shape metallic plate objects with (b) its corresponding microwave hologram.and its image(c), (d) dumbells-shape metallic plate object with (e) its corresponding microwave hologram and its image (f).



(a)

(b)

Figure. 5 (a) microwave image of a 20 cm diameter flat metallic plate with (b) its corresponding estimate size from full width-half maximum intensity distribution.

5. CONCLUSIONS

A technique for obtaining two-dimensional microwave holographic images of objects using light-modulated scatterer has been described. Images of different target shape using the technique have been presented. The higher resolving power of the system compare with the Rayleigh limit for a conventional holography has been demonstrated.

6. ACKNOWLEDGEMENTS

The research described in this paper was carried out by the Applied Microwave Research Laboratory, King Mongkut's Institute of Technology Ladkrabang, under a contract with the Thailand National Electronics and Computer Technology Center (NECTEC). We are also grateful for financial assistance from the NECTEC.

REFERENCE

Born, M., and Wolf, E ., 1964. Principle of Optics., New York.

Cullen, A.L., and Parr, J.C., 1955. A new perturbation method for measuring microwave field in free space., Proc. IEE, 102B, pp.836-844.

Hajnal, J.V.,1987., Compound modulated scatterer measuring system., Proc. IEE, 134H(4), pp. 350-356.

Orme,R.D., and Anderson,A.P., 1973. High resolution microwave holographic technique : application to the imaging of objects obscured by dielectric media., Proc. IEE, 120(4),pp. 401-406.

Richmond J.H., 1955. A modulated scattering technique for measurement of field distributions. IRE Trans. on Microwave Theory and Techniques., ;V. MTT-3,pp. 13-15.

Tricoles, G. and Farhat, N. H. , 1977. Microwave holography: applications and techniques, Proc. of the IEEE.,65(1),pp. 108-120.

The 21st Asian Conference on Remote Sensing
December 4-8, 2000 Taipei, TAIWAN

APPLICATION OF AIRBORNE HYPERSPECTRAL IMAGING IN WETLAND DELINEATION

Chung-hsin Juan[1], Jonathan D. Jordan[1], and Chih-Hung Tan[2]
[1]Agricultural and Biological Engineering Department, University of Florida
PO Box 110570, Gainesville, Florida 32611-0570,USA
Tel: +1 (352) 3928030 Email: crs@ufl.edu
[2] Agricultural Engineering Research Center
196-1, ChungYuan Rd., ChungLi
Tel: (886)-3-4521314 Email:chtan@aerc.org.tw
TAIWAN

KEY WORDS: Hyperspectral image, Wetland delineation, Wetland Vegetation Mapping, Remote sensing

ABSTRACT: The study site is located in Fort Drum Marsh, Indian River county, Florida, where the main vegetation types are sawgrass (*Cladium Jamaicense*) and cattail (*Typha domigensis*) with some floating vegetation and scattered clusters of bushes and trees. A complete hyperspetral imaging mission for hyperspectral imaging was performed in May, 2000. The mission included the preparation of ground targets and calibration panels, the aerial imaging flight, and the ground truth trip. The mounted hyperspectral imaging sensor has 64 wavebands from 399.2 nm to 920.5 nm. The ground truth work included taking spectral reflectance measurements by a hand-held radiometer, multi-spectral images by a multi-spectral imager, measurements of leaf area indices (LAI) by a LAI meter in the locations where only one interested plant species grew in the surrounding area. After the hyperspectral image was rectified and spectrally calibrated, the pixels of the ground truthing points were extracted from the images and then their spectral reflectances were compared with the ground spectral reflectances acquired by the spectral radiometer. The results demonstrated noticeable differences in the spectral reflectances of different wetland plant species. Therefore, wetland could be delineated into species level using aerial hyperspectral imaging.

1. INTRODUCTION

Wetland vegetation species are very sensitive to the environmental changes, and vice versa wetland vegetation species may be a good indicator of the environmental changes. As the concerns of wetland protection grow, wetland delineation is also getting more important. In freshwater marsh, both cattail (Thyha, spp.) and sawgrass (Cladium jamincese) can grow in similar geomorphological and geographical locations and may mix together, but sawgrass tends to be found in lower nutrient level conditions (Kadlec and Knight, 1996). Therefore, the spatial distribution of the cattail and sawgrass in freshwater marshes are monitored by the

government agencies routinely. However, both of the species looked very similar from a distance and hardly identified without close observations, and thus wetland delineation to the specie level usually needs more intensive tasks in field trips. In order to save the time and labor consuming filed work in identifying different species, remote sensing was employed as an ideal and convenient tool to serve this purpose (Doren, 1999).

The most frequently used conventional remote sensed data were either satellite images or airborne color infrared (CIR) photos and images (Madden, 1999; Welch, 1996). The satellite data mostly have not enough high spatial resolution to differentiate detailed ground information. Although the airborne CIR photos and images may have enough spatial resolution, they may have too broad spectral wavebands to identify two similar color looking species. Therefore, as to properly delineate wetlands of the study purpose, airborne hyperspectral images would fit the needs in terms of both spatial and spectral resolutions.

The main goal of this study is to use ground-based and airborne remote sensing tools to study the feasibility of delineate wetlands at species level. The mission of the aerial hyperspectral imaging have three stages: 1) Preparations before aerial hyperspectral imaging, 2) Setup during aerial imaging, and 3) Ground truthing.

2. MATERIALS AND METHODS

2.1 Study Area

The study site is located in the Fort Drum marsh, upper St. John's River basin, in Indian River county, Florida (27E35'12"N, 80E41'17"W, Figure1). It is the headwater of the St. Johns River. The site is a freshwater marsh with cattail and sawgrass as the dominant vegetation species. The desired imaging area with the illustration of the mission plan was also show in Figure 1.

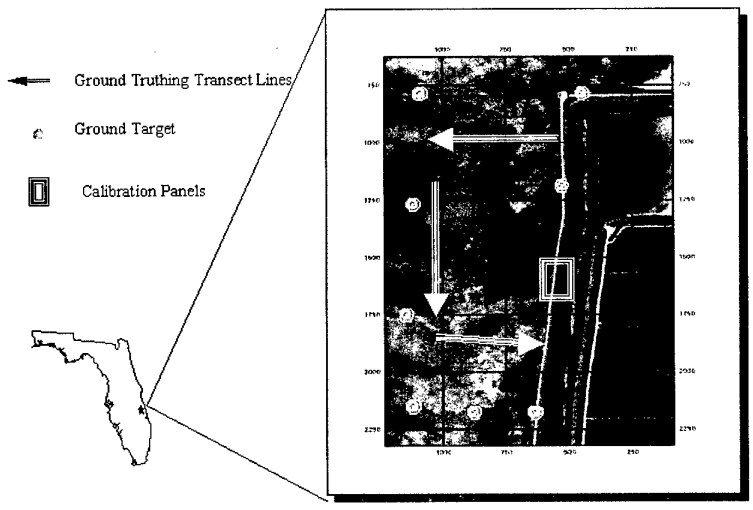


Figure 1. The location of the study site and the illustration of the mission plan.

2.2 Mission Plan for Aerial Hyperspectral Imaging

The employed hyperspectral imager in this study is band-adjustable and can have 128 wavebands in maximum. Due to the limitation of the transfer rate and the storage capacity, to get more wavebands will be traded off by less available imaging area and larger pixel size. In this study, 64 wavebands with the pixel size of 1 meter with a range from 399.2 nm to 920.5 nm were selected.

2.2.1 Preparations of Ground Targets and Calibration Panels Before Aerial Imaging

To utilize the aerial hyperspectral images usually has two main problems of concerns. First, due to the current data transferring speed and storage capacity of storage devices, many hyperspectral imagers are pushbroom imaging systems. Because the instability of the airplane, to keep the imager scanning ground areas exactly along the designated route is difficult and usually results in more possible distortion than fixed-frame imagers (Lee and et al, 2000). Second, the hyperspectral imager measures reflected radiances of ground objects, which may change with respect to incoming radiances and may be hardly compared with other images of the same objects but different light conditions. More useful measuring unit to represent the signatures of measured objects is the ratio of the reflected radiance of an object to the incoming radiance. Therefore, during the aerial imaging, a set of white bright ground targets and a set of calibration panels with different gray levels all the way from visible wavebands and infrared wavebands were necessary to be properly placed in the desired imaging area.

Because the imaging area was a marsh, the ground targets needed to be water-proof, floatable, and anchorable in the marsh. One meter by one meter white foam boards coated with plastic films were used as ground targets, because they were water-proof, floatable and more resistant to bending stress with plastic films. Two wood sticks cross each other were affixed on the back of each white foam board to increase its resistance to winds and waves. A fishing line with 100 lbs resistance was tied up onto the wood frame and linked to a concrete block served as an anchor. An airboat trip was taken in the Ft. Drum Marsh before the imaging day to place the ground targets and record their coordinates using a code differential GPS unit (Model Pathfinder Pro XR, Trimble Navigation, California).

There are few companies that make calibration panels with large sizes and different well-reflected gray shades. Those calibration panels are very nice but sometimes beyond the budgets of research centers at university and local government levels. Therefore, some other alternative materials were used. We examined cloths of their spectral reflectance ratios using a hand-held spectral radiometer (Model GER-1500, Geophysical & Environmental Research, New York) in local textile stores and found out some black, white and white-meshy fabrics with the same reflectance ratios from blue waveband through near infrared wavebands. Then, we sewed those fabrics and attached them on black tarpaulins to make five durable calibration panels with the size of 3.7 meter by 3.7 meter and the

relative reflectance ratios of 4%, 10%, 25%, 45%, and 56%, respectively.

2.2.2 Setup for Aerial Hyperspectral Imaging

The preferred imaging day would be on or near the days when the LandSat 7 satellite would visit the study area in order to seek the potential of applying the results of airborne hyperspectral images to satellite images. Usually, spring is less clouded in Florida. Thus, the imaging day was considered around April 25 or May 11, 2000, which days the LandSat 7 satellite would visit on. The calibration panels and some extra ground targets were placed on the dike of the Ft. Drum Marsh before aerial imaging on the imaging day. The imaging was desired to do two different directions in order to avoid the shadows of the airplane and some clumps. One imaging was from north toward south, the other was from west to east.

2.2.3 Ground Truthing

Another airboat trip was made to do the ground truthing. Based upon the results of the unsurprised classification of the 1999 airborne image, there were some classes of that the spectral characteristics were not able to identified. According to the classification of the 1999 image, the desired ground truth points were pre-selected. The actual ground truth points might be changed as the field situations. At each point, first, the geo locations was first measured by the GPS unit. Then, the plants and were identified as well as the growth situation. The spectral reflectance, leaf area indices (LAI) were also measured using the spectral radiometer and a LAI meter (Model SunScan canopy analysis system, Detla-T Devices, Cambridge, England). At and around the ground truth points, digital video images at four narrow wavebands of 550 nm, 698nm, 798 nm, and 850 nm were recorded by a multi-spectral imager (Model MultiSpec Agro-Imager, Optical Insights, Arizona).

3. RESULTS AND DISCUSSION

Ten ground targets were placed in the marshes on April 29, 2000. The aerial imaging was performed on May 12, 2000, and the field ground truthing was completed on May 17, 2000. The hyperspectral images were rectified by a piecewise rectification procedure. By observing the straight dike along the flight direction, the hyperspectral image was subset into several images for rectifications using polynomial functions, and then mosaiced together afterwards. By this special procedure, the root mean of square errors was 4.7 meter.

The spectral reflectance ratios of cattail and sawgrass have a little bit but still distinguishable difference (Juan and Shih, 1997). The ground spectral radiometer measurements of several different species was normalized (Tan, 1998) and displayed in Figure 2. The hyperspectral image was spectrally calibrated using the measured spectral characteristics of the calibration panels. The pixels at the ground truthing locations with known vegetation species were exacted and shown in Figure 3. The spectral reflectances ratios of different species were obvious in both Figure 2 and Figure 3 except sawgrass and

cattail. In Figure 2, the difference between sawgrass and cattail was noticeable but insignificant, where the difference between sawgrass and cattail was significant. When cattail dies off, the dead leaves fall down and layer above the water surface but not break down at once. Therefore, the aerial images viewing from top to down showed more spectral influence of dead leaves of cattail than the spectral radiometer measurements from the side view.

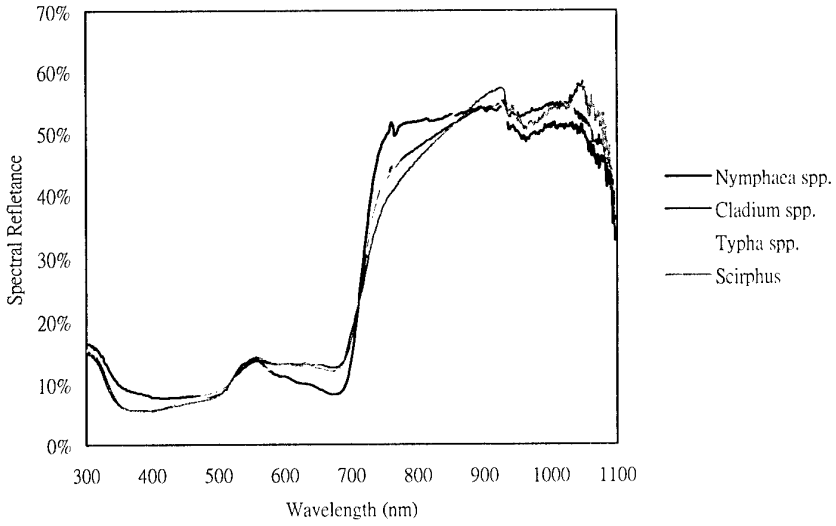


Figure 2. Spectral Refletance Ratios of Different Wetland Vegetation Species Measured by Ground Spectral Radiometer

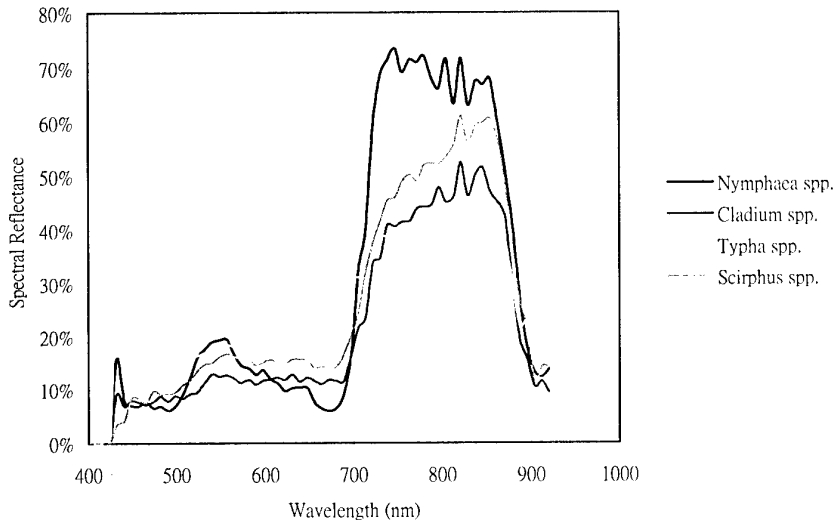


Figure 3. Spectral Reflectance Ratios of Different Wetland Vegetation Species From the Spectrally Calibrated Hyperspectral Image

4. CONCLUSSION AND CONTINUING WORK

The aerial hyperspectral imaging was shown to be a considerable technique to delineate wetland. More analysis will be done to evaluate the most sensitive wavebands to identify different plant species. In addition, subpixel classifications from satellite images from the results of the hyperstral images will be also attempted.

5. ACKOWLEDGEMENTS

The authors would like to address their appreciations to the Institute of Technology Development, Stennis Space Center, NASA for their kindly offer of the hyperspectral imager and the aerial imaging flight. They'd also like to express their sincere thanks to St. John's River Water Management District the assistance in field trips. Furthermore, we'd like to show our gratitude to Mr. Orland Lanni in the Center for Remote Sensing for his efforts in making the calibration panels. At the end, they'd like to honor Dr. Sun-Fu Shih, the former director of Center for Remote Sensing, who passed away in June, 2000 during the ongoing of this research.

REFERENCES

Doren, R. F., K. Rutchey, and R. Welch, 1999. The Everglades: a perspective on the requirements and applications for vegetation map and database products. Photogrammetric Engineering and Remote Sensing, 65 (2) pp. 155-161.

Juan, C. H. and S. F. Shih, 1997. A Lysimeter System for Evapotranspiration Estimation for Wetland Vegetation. Soil Crop Sci Soc. Florida Proc. 56, pp. 125-130.

Kadlec, R. H. and R. L. Knight, 1996. Treatment Wetlands. CRS, Boca Ration, Florida, pp. 447 – 448.

Lee C., H. J. Theiss, J. S. Bethel, and E. M. Mikhail, 2000. Rigorous Mathematical Modeling of Airborne Pushbroom Imaging Systems. Photogrammetric Engineering and Remote Sensing, 66 (4) pp. 385-392.

Madden, M., D. Jones, and L. Vilchek, 1999. Photointerpretation key for the Everglades Vegetation Classification System. Photogrammetric Engineering and Remote Sensing, 65 (2), p. 171-177.

Tan, C. H., 1998. Regional Scale Evaptranspiration Estimation Using Vegetation Index and Surface Temperature from NOAA Satellite AVHRR Data. Doctoral Dissertation, Univesity of Florida, pp. 64.

Welch, R., 1996. GPS, image processing and GIS techniques for coastal wetland mapping applications. International Archives of Photogrammetry and Remote Sensing, 31 (B4) pp. 931-933.

PACRIM 2 AIRSAR DEPLOYMENT TO THE ASIA-PACIFIC REGION AUGUST - OCTOBER 2000: REPORT ON THE DATA ACQUISITION PHASE AND EARLY RESULTS

Professor A. K. Milne
Office of Postgraduate Studies
The University of New South Wales
Sydney, NSW, 2052, Australia
Telephone: 61 2 9385 2731 Facsimile: 61 2 9385 3733
Email: t.milne@unsw.edu.au

Dr. I. Tapley
Cooperative Research Centre for Landscape Evolution and Mineral Exploration
CSIRO Division of Exploration and Mining
Private Mail Bag
Wembley, WA, 6014, Australia
Telephone: 61 8 9333 6263 Facsimile: 61 8 9383 9179
Email: i.tapley@per.dem.csiro.au

Abstract.
PACRIM 2 is a NASA sponsored science mission to advance the development of polarimetric and interferometric radar in Pacific rim countries including South Pacific island nations, New Zealand, Australia, Papua New Guinea, Indonesia, Malaysia, Cambodia, Vietnam, Philippines, Taiwan, South Korea, Japan and the United States.

AIRSAR is an airborne synthetic aperature radar which can be operated in three modes; polarimetric SAR (POLSAR) provides high quality polarimetric data in three frequencies; cross-track interferometric SAR (XTI or TOPSAR) allows precision digital elevation information of the earth's surface to be obtained; and along-track interferometric SAR (ATI) can be used to detect ocean current movements.

In addition data will be collected by a second instrument, the MASTER or MODIS/ASTER airborne simulator. This is a multispectral imaging scanner with 50 channels, 25 in the visible shortwave infrared (0.4-2.5 um), 15 channels in the mid-infrared (3-5 um) and 10 channels in the thermal infrared (7-13 um).

The AIRSAR system was previously flown in Australia in 1993, and in ten countries in the Asia-Pacific region in 1996. In this latter deployment called PACRIM, POLSAR and TOPSAR data were collected over some 120 sites in the region.

Data acquired during this PACRIM mission will be analysed by Principal Investigators in each of the countries involved, supported by American and Australian scientists, in seven scientific research areas. These are forestry and vegetation, geology and tectonic processes, interferometry, disaster management, coastal analysis, agriculture, and urban and regional development.

This paper will present an overview of the recent mission with examples of data collected during the deployment.

The 21st Asian Conference on Remote Sensing
December 4-8, 2000 Taipei, TAIWAN

THE USE OF AIRSAR DATA FOR ASSESSING THE POTENTIAL OF FUTURE SPACEBORNE SAR FOR REGIONAL ESTIMATION OF WOODLAND BIOMASS IN AUSTRALIA

A.K. Milne[1], N. Cronin[1], R.M. Lucas[1], C. Witte[2] and R. Denham[2]

[1]School of Geography, the University of New South Wales, Sydney, NSW, 2052.
[2]Forest Ecosystem Assessment and Planning, Queensland Department of Natural Resources, Resource Sciences Centre, 80 Meiers Road, Indooroopilly, QLD, 4068

Corresponding author A. K. Milne
Office of Postgraduate Studies, The University of New South Wales
Sydney, NSW, 2052, Australia
Telephone: 61 2 9385 2731 Facsimile: 61 2 9385 3733
Email: t.milne@unsw.edu.au

KEY WORDS:

ABSTRACT

With the expected launch of polarimetric spaceborne Synthetic Apaerture Radar (SAR) sensors over the next few years, namely ENVISAT ASAR (C band) and PALSAR (L band), there is an opportunity for regional estimation of forest and woodland biomass in Australia. However, due largely to political pressures, there is an increasing need to provide reliable estimates of Australia's greenhouse gas emissions resulting from changes in vegetation biomass within a relatively short timeframe. For this reason, the use of existing Landsat-based methods for biomass estimation is likely to continue, despite the known limitations of optical sensors for this purpose and the demonstration internationally of the benefits of SAR. This approach is, however, justified given the uncertainty in the potential use of future SAR sensors.

To address this uncertainty, research was undertaken to investigate how current airborne SAR sensors may be used to assess the potential of future SAR sensors for biomass estimation. This was undertaken by comparing relationships established with above ground/component biomass and NASA JPL AIRSAR data with those established with existing spaceborne SAR data at similar wavelengths and polarisations.

The study was conducted in an area near Talwood, southern Queensland. Ground estimates of above ground and component biomass were generated by applying a range of allometric equations to tree size measurements collected, in 1998 and 1999, from 44 fixed and variable area plots. Relationships were then established between total/component biomass and Japanese Earth Resources Satellite (JERS1) SAR L band HH, Space Shuttle Imaging Radar (SIR-C) SAR C band VV and L band VV, and NASA JPL AIRSAR C band VV, L band VV and fully polarimetric P band data, all acquired over the period 1994 to 1996.

The study indicated of C, L and P band data at all polarisations occurred at an above ground biomass of approximately 20-30 Mg ha^{-1}, 60 Mg ha^{-1} and 80-100 Mg ha^{-1} respectively. Different SAR wavelengths were also shown to interact with different components of the biomass. Furthermore, the saturation levels and relationships observed were relatively consistent between sensors. The study concluded that the AIRSAR can be used to determine the likely potential of future spaceborne SAR sensors for biomass estimation. Furthermore, the added benefits of using SAR for biomass estimation, and hence for better quantifying greenhouse gas emissions from land use change and forestry, were demonstrated.

1. INTRODUCTION

Although a number of studies have demonstrated relationships between SAR data and vegetation biomass, the majority have focused on forests in tropical regions and the northern hemisphere. The research presented in this paper addresses the potential of SAR for quantifying the total above ground biomass (TAGB) of Australia's *Eucalyptus* woodlands.

2. SPECIFIC OBJECTIVES

The study aimed to determine whether

a) statistically significant relationships exist between polarimetric C, L and P band data and component (leaf, branch and trunk) biomass, and
b) relationships are consistent regardless of whether TOPSAR and SIR-C SAR C- and L-band data are used.

The research formed part of a pilot study aimed at determining whether a more rigorous investigation into the use of SAR for biomass estimation was warranted. For the study, only historical SAR data sets were available.

3. STUDY AREA

The study was conducted in Queensland where, for the period 1990 to 1995, 56 % (1 million ha) of the total area of native woody vegetation clearance in Australia has occurred, averaging 268,060 ha yr^{-1}. The study region, near Talwood (28°29'S, 149°28'E) supported extensive areas of open woodland consisting largely of Poplar Box (*Eucalyptus populnea*), Silver-leaved Ironbark (*E. melanaphloia*), Belah (*Casuarina cristata*), Brigalow (*Acacia harpophylla*) and White Cypress Pine (*Callitris glaucophylla*). Common understorey species included Wilga (*Geijera parviflora*) and Sandalwood Box (*Eremophila mitchelli*). Due to the complex nature of land use and management practices, the landscape consisted of a mosaic of cleared fields and woodland communities in various stages of degradation and/or regeneration.

4. METHODS

Space Shuttle Imaging Radar (SIR-C SAR; C-and L-band VV polarisations), and NASA JPL TOPSAR (C-band HH, L-band VV and fully polarimetric P-band) were available for the study area for the years 1994 and 1996 respectively. Pre-processing included georeferencing of all SAR data to Australian Map Grid (AMG) coordinates, resampling to a pixel resolution of 12.5 m, and converting data to the backscatter coefficient (σ^o), defined as the average radar cross section per unit area of the individual scattering elements. For display purposes, σ^o was expressed in decibels (dB).

5. FIELD DATA COLLECTION

In October, 1998, field data were collected from 29 plots sited in woodlands in varying states of degradation and/or regeneration. In June, 1999, a further 14 plots were established largely in areas of younger regeneration. Although the field and remotely sensed data were collected several years apart, the rates of growth within these woodlands are relatively low and changes in biomass over the intervening periods were not considered to be substantial. Woodlands cleared or degraded since 1994 were not sampled.

Sampling was undertaken using fixed area plots in the early regeneration woodlands and variable area plots, sampled using the prism wedge method [1], in older regenerating and intact, albeit degrading, woodlands. The AMG co-ordinates of the centre of plots were obtained using a Global Positioning System with an accuracy of ± 10 metres. All trees > 3 cm diameter (D, at c 30 cm) were measured for D (at both 30 cm and 130 cm). Trees with D < 3 cm (at c 30 cm) were counted and their height (H, cm) was estimated. All trees measured were identified to genus or species. For selected genera/species, relationships were established between D and H. For all trees in each plot, the TAGB and component biomass was estimated using allometric equations [2,3], which required D and/or H as input, for *Eucalpytus* and understorey species. In all calculations, a bias correction factor was applied to avoid systematic bias when antilogging estimates to arithmetic units [4]. As allometric equations for biomass estimation were unavailable for *Casuarina cristata* and *Callitris glaucophylla*, the few plots containing these species were excluded from the analysis. For all plots, the component biomass was scaled-up to generate an estimate of component biomass per hectare (Mg ha^{-1}). For regions centred on each plot location, SIR-C SAR and TOPSAR data were extracted, averaged and related to component biomass.

6. RESULTS

Relationships between biomass components

Pearson's product moment correlation coefficients (r) indicated significant relationships (at the 0.01 level) between TAGB and all biomass components (branch, trunk and leaf), and between branch and trunk biomass. The leaf biomass was related to branch biomass at the 0.05 level, although the relationship with trunk biomass was insignificant.

Relationships between biomass and SAR data

Relationships between both SIR-C SAR and TOPSAR data and component biomass (including TAGB) were investigated initially on the basis of the correlation coefficient between the log of both the backscatter coefficient (σ^o, dB) and estimated biomass. When establishing relationships, data for low biomass pastures were included.

Correlation coefficients between SIR-C SAR C- and L-band data with leaf, branch, trunk and TAGB were significant at the 0.01 level, with the strongest relationship observed between L-band VV data and TAGB (Table 1). L-band VV backscatter was related more closely to the woody (i.e., branches and trunks) rather than the leaf biomass. The relationships between C-band VV data and all components of the biomass were comparatively weak, with the exception of the relationship with leaf biomass.

The correlation coefficients between TOPSAR C-, L- and P- band (all polarisations) and all biomass components were also significant at the 0.01 level (Table 2). P band backscatter (all polarisations) was more strongly related to TAGB, and also branch and trunk biomass, compared to L band VV and C band HH backscatter. The weakest relationship with woody (trunk and branch) biomass was observed with C band HH backscatter. The strength of the relationship with leaf biomass was similar for all wavebands.

Log	SIR-C Backscatter (dB)	
	C VV	L VV
1.1 TAGB	0.66	0.81
Branch	0.61	0.74
Trunk	0.59	0.70
Leaf	0.54	0.51

All figures significant at the 0.01 level (two tailed).

Table 1: Pearson's correlation coefficients (r) between the logarithm of component biomass and SIR-C SAR C- and L-band backscatter.

Log	TOPSAR Backscatter (dB)					
	C HH	L VV	P HH	P VV	P HV	P TP
1.2 TAGB	0.61	0.85	0.91	0.85	0.91	0.90
Branch	0.58	0.79	0.86	0.81	0.86	0.85
Trunk	0.51	0.77	0.84	0.79	0.82	0.83
Leaf	0.48	0.54	0.48	0.45	0.45	0.48

All figures significant at the 0.01 level (two tailed).

Table 2: Pearson's correlation coefficients (r) between the logarithm of component biomass and TOPSAR C-, L- and P-band backscatter.

The lowest dynamic range was observed for TOPSAR C band HH (-9.3 to -21.6; range -12.3 dB) and L band VV (-44.8 to -28.2; range –16.6) data and the largest for P band HV data (–18.9 to - 45.9 dB; range 27.0). Saturation of both SIR-C SAR and TOPSAR C- and L-band data occurred at approximately 20-30 Mg ha^{-1} and 50-60 Mg ha^{-1} respectively. P-band saturation (all polarisations) occurred at 80-100 Mg ha^{-1}.

7. DISCUSSION

The results indicated the greater interaction of L- and P-band microwaves with the woody components of the biomass compared to C-band microwaves. The relationship between C-band and woody biomass is more likely to have resulted from the inherent relationships of leaf with branch, trunk and TAGB. Microwaves at both L and P band were related almost equally with both the trunk and the branch biomass. The correspondence in these relationships was attributed partly to the similarity in the size range and orientation of branches and trunks. However, the inherent relationship between branch and trunk biomass leads to uncertainties as to the interaction of these wavelengths with different vegetation components.

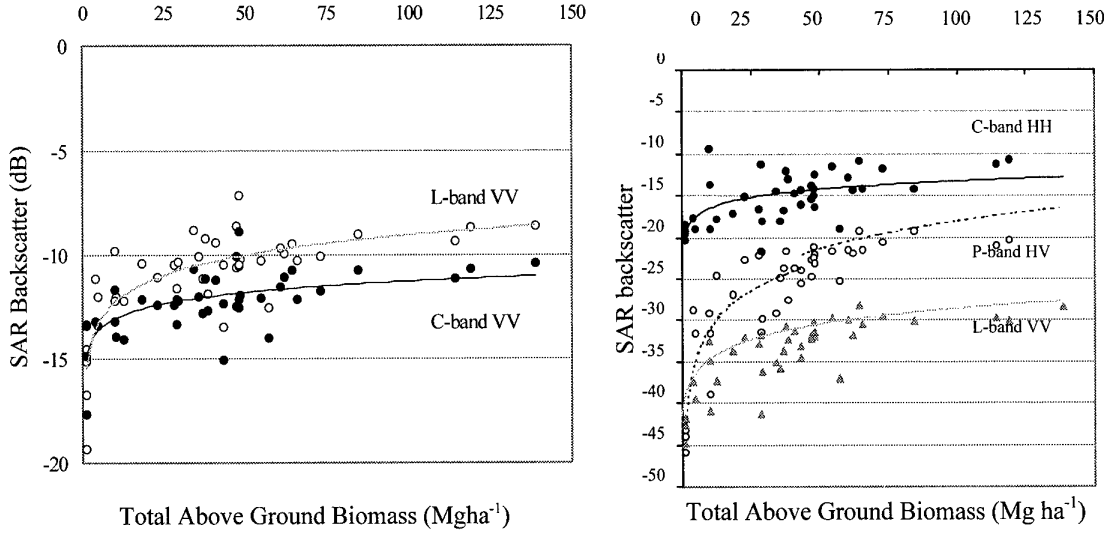


Figure. 1: Relationship between TAGB and a) SIR-C SAR C- and L band backscatter and b) TOPSAR C-, L- and P-band backscatter

Unlike previous studies (e.g., [5]), where different P-band polarisations were related to differential scattering by trunks and branches, differences in the P-band backscatter at three polarisations were not noticeable in this study. This similarity was again attributed to the overlap in the size distribution/orientation of these components and a lack of layering within the uneven aged woodlands.

The TAGB saturation levels for both TOPSAR C-band HH and SIR-C SAR C-band VV and TOPSAR L-band VV and SIR-C SAR L-band VV were similar at 20-30 Mg ha^{-1} and 50-60 Mg ha^{-1} respectively. Studies in Injune suggest a saturation of c 60-80 Mg ha^{-1} in the relationship with JERS-1 SAR L-band HH data. In spatially quantifying the TAGB of woodland vegetation, P-band HH data seems optimal due to the observed strength in the relationship with TAGB, the higher limit of biomass saturation (100 Mg ha^{-1}), and the greater dynamic range of the data.

8. CONCLUSIONS AND FUTURE WORK

Polarimetric C, L and P band data can be related to TAGB and different biomass components with varying degrees of significance. The better relationships were established using TOPSAR data. The main similarities in using TOPSAR and SIR-C SAR were the strength of the relationships between C- and L-band data and component mass, and the TAGB saturation levels for both C-band and L-band data. The study suggests that single-band SAR may be used to quantify the TAGB of woodlands in Australia, although better results are likely to be obtained using polarimetric SAR. This capacity will be fully tested using PACRIM AIRSAR data collected in August, 2000.

9. ACKNOWLEDGMENTS

The authors thank the Bureau of Resource Sciences and the Australian Greenhouse Office, the Australian Research Council and the Queensland Department of Natural Resources for financial and logistical support.

10. REFERENCES

[1] Beers T., and Miller, C., "Point Sampling: Research Results, Theory and Applications", Purdue University, Agricultural Experiment Station Lafayette, Research Bulletin, vol. 786, August 1965.

[2] Burrows, W.H., Compton, J.F., Hoffman, M.B., Back, P.V., and Tait, L.J., "Allometric relationships and community biomass estimates for some dominant eucalypts and associated species in Central Queensland woodlands", unpublished.

[3] Harrington, G., "Estimation of above ground biomass of trees and shrubs in *Eucalyptus populnea* F. Muell. woodland by regression of mass on trunk diameter and plant height", Australian Journal of Botany, vol. 2, pp. 135-143, 1979.

[4] Beauchamp, J.J., and Olsen, J.S., "Corrections for bias in regression estimates after logarithmic transformation", Ecology, vol. 54, pp. 1403-1407, 1973.

[5] Beaudoin, A., Le Toan, T., Goze, S., Nezry, E., Lopes, A., Mougin, E., Hsu, C.C., Han, H.C., Kong, J.A., and Shin, R.T., "Retrieval of forest biomass from SAR data", International Journal of Remote Sensing, vol. 15, pp. 2777-2796, 1994.

Estimation of Soil Moisture with Vegetated Surface by Multi-Temporal Measurements

Jiancheng Shi

Institute for Computational Earth System Science

University of California, Santa Barbara
Tel: 805-893-2309, Fax: 805-893-2578, E-mail: shi@icess.ucsb.edu

INTRODUCTION

During recent years, theoretical modeling and field experiments have established the fundamentals of active microwave remote sensing as an important tool in determining physical properties of soil. The ability to estimate soil moisture in the surface layer to an approximately 5 cm depth by microwave remote sensing has been demonstrated under a variety of the topographic and land cover conditions (Engman *et al.*, 1995). Despite the promise, its application to hydrological and agricultural sciences has been hampered by natural variability and the complexity of the vegetation canopy and surface roughness that significantly affect the sensitivity of radar backscattering to soil moisture.

Although experiments demonstrated radar sensitivity to soil moisture variation more than two decades ago (Ulaby, 1974), an operational algorithm for mapping soil moisture distribution has not been developed because of the effects of the surface roughness and vegetation cover. The inversion of soil moisture information from radar backscatter became more rigorous after the availability of multi-polarization radar data. Several algorithms have been developed for measuring bare surface soil moisture quantitatively using either dual-polarization L-band SAR image data (Dubois et al., 1995, Ulaby et al., 1996 and Shi et al., 1997) or three-polarization SAR measurements (Oh et al., 1992). The algorithms had been applied to a series of L-band SIR-C and JPL/AIRSAR image data successfully by using VV and HH polarization (Dubois 1995 and Shi 1997). However, all those algorithms were under the surface scattering consideration. They used the weighted combinations of the different polarization signatures to minimize the effect of surface roughness so that soil moisture can be directly inferred from SAR image data. The effect of vegetation cover has not been included in current available algorithms. It is clear that vegetation cover will cause an under-estimation of soil moisture and an over-estimation of surface roughness when we apply the algorithm for bare surface soil moisture estimation to vegetation covered regions.

A polarimetric SAR backscatter measurements, by using eigenvalues and eigenvectors of the covariance matrix, can be decomposed to into three components based on the scattering types - (1) an odd number of reflections, (2) an even number reflections, and (3) a cross-polarized scattering power [Van]. It can be written as

$$\mathbf{T} = \lambda_1 \mathbf{K}_1 \mathbf{K}_1^{*T} + \lambda_2 \mathbf{K}_2 \mathbf{K}_2^{*T} + \lambda_3 \mathbf{K}_3 \mathbf{K}_3^{*T} \qquad (1)$$

Where λ and $\mathbf{K}$ are eigenvalues and eigenvectors. * is a conjugate operator for a complex number and T is a transpose operator for a vector. The subscript 1, 2, and 3 represents the decomposed odd, even, and defuse components, respectively. This decomposition technique allows us to obtain the estimation of single and double reflection components of backscattering coefficients for VV and HH polarization.

In this study, we evaluate the usage of the decomposition theory in application of estimating soil moisture for vegetated surface with the temporal fully polarimetric L-band SAR measurements. Using the decomposed scattering measurements from JPL/AIRSAR image data, we evaluated their usage to reduce the vegetation effect on estimation soil moisture under configurations of a single-frequency (L-band) and multi-pass with a same incidence.

RELATIONS THE COMPONENTS IN BACKSCATTERING MODEL AND THE DECOMPOSED SCATTERING COMPONENTS

In consideration of a more general natural vegetated surface, we construct our first-order physical based scattering model as a discontinuous vegetated backscattering model. This model can be written as

$$\sigma_t^{pp} = f_v\sigma_v^{pp}(\theta) + f_v\sigma_{sv}^{pp}(\theta)$$

$$+ f_v\sigma_s^{pp}(\theta)L_{pp}^2 + (1-f_v)\sigma_s^{pp}(\theta) \qquad (2)$$

Where f_v is the fraction of vegetation cover in a given pixel. $L_{pp}^2 = \exp\left(-2\kappa_e^{pp} d\sec(\theta)\right)$ is the double pass attenuation factor. κ_e is the volume extinction coefficient depending on the polarization configurations. d is the thickness of the vegetation layer and θ is the radar incidence angle. The superscript or subscript *pp* represents polarization configuration for either VV or HH. The subscript *t, v, s*, and *sv* are for total, volume, surface, and surface-volume interaction terms. The direct volume scattering and the surface-volume interaction scattering terms in (2) can be written as

$$\sigma_v^{pp}(\theta) = 0.5\kappa_s^{pp}\left(1-L_{pp}^2\right)/\kappa_e^{pp} \qquad (3)$$

and

$$\sigma_{sv}^{pp}(\theta) = 2\kappa_s^{pp} dR_{pp}L_{pp}^2 \qquad (4)$$

Where κ_s^{pp} is the volume scattering coefficient. R is the surface reflectivity. Both varies with the polarization parameter *pp*.

Since both volume extinction and scattering coefficients are strongly depended on the number density, shape and size parameters, as well as orientation or structure of the vegetation canopy, in addition to canopy thickness, it would be extremely difficult to estimate the surface scattering component or soil moisture from a limited SAR measurements.

By comparison of backscattering components in (2) and the decomposed scattering components in (1), we can approximately write

$$\sigma_1^{pp}(\theta) \approx f_v\sigma_v^{pp}(\theta) + \sigma_s^{pp}(\theta)\left(1-f_v+f_vL_{pp}^2\right) \qquad (5)$$

$$\sigma_2^{pp}(\theta) \approx f_v\sigma_{sv}^{pp}(\theta) \qquad (6)$$

Where subscript number 1 and 2 represent the single and double reflection components.

Advantage of (2) is that it represents a general case of natural surface. It can be applied to both the fully vegetated surface (continuous layered vegetation when $f_v = 1$) and the bare surface (when $f_v = 0$).

DATA ANALYSIS UNDER MULTI-TEMPORAL MEASUREMENTS CONFIGURATION

The temporal variability of surface roughness and vegetation cover are generally at much longer time scale than that of soil moisture. Unless there is a human activity we may reasonably assume that both surface roughness and vegetation cover are same at time interval from a few days to a week. The change in SAR measurements between the repeat passes, therefore, is resulted from the change of ground dielectric properties or soil moisture. Under this configuration, using two repeat pass polarimetric SAR measurements, we can write the difference of the first components

$$\sigma_1^{pp1} - \sigma_1^{pp2} = (\sigma_s^{pp1} - \sigma_s^{pp2})(1 - f_v + f_v L_{pp}^2)$$
$$= \sigma_1^{pp1}(1 - \sigma_s^{pp2}/\sigma_s^{pp1})(1 - f_v + f_v L_{pp}^2) \quad (7)$$

and the ratio of the second components by (4) as

$$\sigma_2^{pp2}/\sigma_2^{pp1} = R_{pp2}/R_{pp1} \quad (8)$$

Where the number after pp in either superscript or subscript represents the first and second SAR measurements. At L-band, the surface roughness parameter RMS height is small in comparison of the incidence wavelength so that we could approximate the polarization amplitude as that in the small perturbation model - α_{pp} which are only depends only on the surface dielectric constant ε_s and incidence angle θ. Where α_{pp} is given by

$$|\alpha_{hh}|^2 = \left[\frac{(\varepsilon_s - 1)}{(\cos\theta + \sqrt{\varepsilon_s - \sin^2\theta})^2}\right]^2 = R_{hh} \quad (9)$$

As we noticed in (9), the polarization amplitude is exactly same as the surface reflectivity for HH polarization. Under assumption of the surface roughness do not change between two SAR measurements, we have

$$\sigma_s^{hh2}/\sigma_s^{hh1} = |\alpha_{hh2}|^2/|\alpha_{hh1}|^2 = R_{hh2}/R_{hh1} \quad (10)$$

Furthermore, using (7), (8) and (10), we obtain

$$\sigma_s^{hh1}(1 - f_v + f_v L_{hh}^2)$$
$$= (\sigma_1^{hh1} - \sigma_1^{hh2})/(1 - \sigma_2^{hh2}/\sigma_2^{hh1}) \quad (11)$$

and

$$f_v \sigma_v^{hh} = (\sigma_1^{hh2} - \sigma_1^{hh1}\sigma_2^{hh2}/\sigma_2^{hh1})$$
$$/(1 - \sigma_2^{hh2}/\sigma_2^{hh1}) \quad (12)$$

Therefore, we can decompose or directly estimate the volume and surface scattering components by (11) and (12) for HH polarization measurements.

The SAR data used in this study was from the Washita '92 experiment. During the experiment from June 10-18, 1992, a time series of spatially distributed hydrologic data focusing on soil moisture and evaporative fluxes were collected. At the same time, the AIRSAR sensor aboard the NASA DC-8 aircraft collected a sequence of 6 L band radar images over an agricultural test site located just outside the watershed. The Washita '92 experiment was conducted immediately following a series of heavy rainfalls that ended on June 9. Thereafter, no more rain occurred throughout the entire series of the AIRSAR flights, thus allowing observation of a drying-down sequence. From any two of 6 sequence SAR measurements, we can estimated the surface and volume backscattering components using (11) and (12). Furthermore, the relative change in dielectric property of any pair from 6 sequence SAR measurements can be estimated by (10).

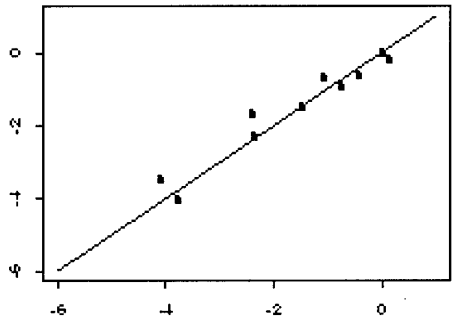


Figure 1. Comparison of the normalized cross product of the decomposed even reflection components with that of reflection coefficients calculated from field measurements data.

REFERENCES

[1] E. T. Engman and N. Chauhan, " Status of Microwave Soil Measurements with Remote Sensing", *Remote Sensing Environ.,* vol 51, no. 1, pp. 189-198, 1995.

[2] F. T. Ulaby, J. Cihlar, and R. K. Moore, "Active Microwave Measurement of Soil Water Content", *Remote Sensing Environ.,* (3):185-203, 1974.

[3] P. C. Dubois, J. J. Van Zyl, and E. T. Engman, "Measuring soil moisture with imaging radar", *IEEE Trans. Geosci. and Remote Sens.,* vol. 33, no. 4, pp. 195-926, 1995.

[4] F. T. Ulaby, P. C. Dubois, and J. J. Van Zyl, "Radar Mapping of Surface Soil Moisture", J. of Hydrology, 184, 57-84, 1996.

[5] J. Shi, J. Wang, A. Hsu, P. O'Neill, and E. T. Engman, "Estimation of bare surface soil moisture and surface roughness parameters using L-band SAR image data", In press, *IEEE Transactions on Geoscience and Remote Sensing, 1997.*

[6] Y. Oh, K. Sarabandi, and F. T. Ulaby. "An empirical model and inversion technique for radar scattering from bare soil surface", *IEEE Trans. Geosci. Remote Sens.,* vol. 30, no. 2, pp 370-381, 1992.

[7] S. R. Cloude, "Uniqueness of target decomposition theorems in radar polarimetry", in *Direct and inverse methods in radar polarimetry: Part 1,* Kluwer Academic Publishers, Dordrecht, pp. 266-296, 1992

[8] J. J. van Zyl, Application of Cloude's target decomposition theorem to polarimetric imaging radar data, *Submitted to PIERS Progress in electromagnetics research symposium,* 1993.

The 21st Asian Conference on Remote Sensing
December 4-8, 2000 Taipei, TAIWAN

DEPLOYMENT OF THE MODIS/ASTER AIRBORNE SIMULATOR (MASTER) DURING PACRIM 2

Dr. I. Tapley
Cooperative Research Centre for Landscape Evolution and Mineral Exploration
CSIRO Exploration and Mining, Private Mail Bag No 5, Wembley, Western Australia 6913
Telephone: 61 8 9333 6263 Facsimile: 61 8 9383 9179
Email: i.tapley@per.dem.csiro.au

Professor A. K. Milne
Office of Postgraduate Studies
The University of New South Wales, Sydney, NSW, 2052, Australia
Telephone: 61 2 9385 2731 Facsimile: 61 2 9385 3733
Email: t.milne@unsw.edu.au

ABSTRACT

PacRim2 was a NASA-sponsored science mission conducted in the Pacific Rim region during the period August-October 2000. While the primary objective of the mission was to collect POLSAR and TOPSAR datasets with the AIRSAR instrument, a second objective was to collect MASTER datasets to advance the development and application of MODIS and ASTER datasets currently being recorded on NASA's TERRA Earth Observation System AM-1 platform. As the name suggests and the wavelengths indicate, MASTER is the simulator instrument for these two spaceborne sensors (http://terra.nasa.gov/).

When suitable weather conditions prevailed, PacRim2 provided investigators with the opportunity to collect high spatial resolution, multispectral visible, reflected IR, mid-IR and thermal IR datasets in 50 narrow-band channels over the ranges of 440-965nm, 1.63-2.43 microns, 3.08-5.33 microns and 7.7-13.0 micros respectively, from a single instrument. In addition to spectral reflectance information regarding land cover, soil properties, water quality and rock mineralization, the availability of fully calibrated thermal data in ten wavelengths will permit the calculation of surface temperature and surface spectral emittance. The latter relates to the composition of the surface and is often used for surface constituent mapping, particularly that of silicate mineralogy. The separation of temperature and emissivity can be affected using published algorithms or the ENVI image processing software package that now has an option of three utilities to convert thermal data sets from radiance to emissivity and temperature. A simple ENVI add-on tool also permits the precision ortho-rectification of MASTER data using the positional information from the Applanix GPS/INS, a digital elevation model and the full MASTER camera model.

This paper will expand on the MASTER datasets and examine their applications for:

- Validation of ASTER and MODIS datasets;
- Mapping of geological structures, rock units and minerals;
- Soil properties, vegetation composition and crop discrimination;
- Mapping coastal zone resources, rainforests and mangroves;
- Environmental impact studies; and
- Inventory of coral reefs.

The 21st Asian Conference on Remote Sensing
December 4-8, 2000 Taipei, TAIWAN

ADVANCES IN DIGITAL ELEVATION DATASETS FOR EXPLORATION, TOPOGRAPHIC MAPPING AND DISASTER MANAGEMENT

Dr. Ian J. Tapley
CRC for Landscape Evolution and Mineral Exploration
CSIRO Exploration and Mining, Private Bag No.5, Wembley, Western Australia 6913
Telephone: 61 8 9333 6263 Facsimile: 61 8 9383 9179
Email: i.tapley@per.dem.csiro.au

SUMMARY

1. Background

The production of digital elevation models (DEMs) is an expanding aspect of photogrammetry and a new and rapidly developing technology, radar interferometry. The growing availability of DEM data is opening new possibilities to earth scientists whether they be geologists, geomorphologists or pedologists. The land surface has long been recognized as the basis to which all geoscientific observations are tied. Only recently, however, have the technologies been developed to produce topographic data of large areas with sufficient horizontal and vertical resolution to meet the requirements of detailed spatial analysis. Earth scientists in the past have often been constrained by using a mosaic of existing DEMs that were derived by different resolutions and datum. The results were mostly inhomogeneous, inconsistent and, consequently, not comparable. Improved aerial photogrammetry (stereoscopy) through state-of-the-art Soft Photogrammetric Digital Workstations, and interferometric synthetic aperture radar, has meant that topography has gained a whole new meaning in spatial studies. Large-area DEMs with consistent quality and high precision can now be produced. NASA's recent Shuttle Radar Topography Mapping Mission (SRTM) ensured that high-resolution topographic data for the majority of the earth's surface will be available to all users within two years (http://www.jpl.nasa.gov/srtm/). In the Pacific Rim, TOPographic Synthetic Aperture Radar (TOPSAR) datasets were acquired over selected sites during the PacRim1 (1996) and PacRim2 (2000) AIRSAR missions for the purposes of advancing the understanding of radar technology, in particular that of radar polarimetry and radar interferometry. Details describing sites covered during these missions can be found on the JPL AIRSAR web page (http://airsar.jpl.nasa.gov/).

With the advent of geographical information systems (GIS) DEMs can be used together with other spatial datasets such as geological information, airborne magnetics, gamma-ray spectroscopy and hyperspectral datasets. The DEM provides a basic spatial reference system and images and vector data can automatically be draped over the DEM for more advanced analyses. Software packages such as ESRI's Spatial Analyst and 3D Analyst (http://www.esri.com/software/arcview/extensions/spatext.html), and IDL's RiverTools (http://www.rsinc.com/rivertools/index.cfm) includes tools for generating geomorphometric models such as slope, and modelling of drainage basins.
Freeware packages on the Internet such as:
LandSerf (http://www.geog.le.ac.uk/jwo/research/LandSerf/index.html),
MicroDem (http://www.nadn.navy.mil/Users/oceano/pguth/website/microdem.htm),
GRASS http://www.baylor.edu/~grass/index2.html and
DiGem (http://member.aol.com/oconrad/dgm/dgm_main.htm)
can also be downloaded for visualizing and performing analysis of generic elevation datasets.

2. Current Capabilities

2.1 Stereo Photogrammetry

Aerial photography

Precision DEMs are now being acquired by commercial groups using soft photogrammetric digital workstations, such as the HELAVA system. Stereo aerial photographs used for generating the DEM are either purchased from an archive or reflown if the existing photographs are unsuitable. In addition to the DEM, digital imagery of the aerial photos can be projected or draped over the terrain data to form an orthoimage. For example, using 1:86 000 scale photography scanned at 15μm, the resultant product has a ground resolution of 1.2 m and height accuracy of 3-5 m, depending on accurate ground calibration and quality of the stereo model.

SPOT-PAN

DEMs can be produced from SPOT-PAN image stereopairs through stereoplotting and automatic correlation. The cross-track pointing capability of SPOT allows the second image of the stereo pair to be acquired as little as 2 days after the first with base-to-height ratios of 0 to 1. McMullen Nolan and Partners have shown that when using high contrast imagery with minimal time difference between the images forming the stereo pair, an optimal base:height ratio of 0.7 and suitable ground survey information, SPOT DEMs of low relief terrain typically achieve 7-12 m RMSE horizontal and vertical errors.

RADARSAT

Stereo pairs for DEM generation are created using one of RADARSAT's Fine, Standard, Wide or ScanSAR Narrow beam modes. The finest resolution of 8x8 m horizontal and 15-20 m vertical for 50 m postings is provided in the Fine beam mode but it covers the smallest area (50 km width). These products are suitable for a variety of applications at map scales smaller than 1:100,000. Further details regarding stereo accuracy and costs for each mode can be viewed at http://www.vexcel.com/radar/stereo.dem.html

ASTER

The Advanced Spaceborne Thermal Emission and Reflection Radiometer mounted on the TERRA spacecraft launched in December 1999 obtains high-resolution (15 to 90 square metres per pixel) images of the Earth in 14 different wavelengths of the electromagnetic spectrum, ranging from visible to thermal infrared light (http://asterweb.jpl.nasa.gov/).

Unlike the other instruments aboard TERRA, ASTER will not collect data continuously; rather, it will collect an average of 8 minutes of data per orbit. All three ASTER telescopes (VNIR, SWIR and TIR) are pointable in the cross-track direction. Given its high resolution and its ability to change viewing angles, ASTER will produce stereoscopic images and detailed terrain height information. Stereo data have a spatial resolution of 15 m and the base:height ratio, based on the nadir and back view (at 27.6 degrees off nadir, along track), is 0.6. Standard product DEMs will come in two basic modes, relative and absolute. Both are produced using automated, correlation-based, commercial softcopy photogrammetric software. Both modes will have a X-Y resolution of 30 m and a vertical resolution (smallest Z increment measured) of 1 m. Absolute DEMs require user-supplied ground control points (GCPs). Based on pre-launch studies, with 4 or more GCPs/scene with XYZ accuracies of 5-15 m, RMSE xyz accuracies of 7-30 m for the absolute DEMs are predicted.

Standard product DEMs from ASTER are produced at no charge, but production plans are limited to only one 60x60 km scene per day. The idea is that users with their own soft copy photogrammetric software will be able to produce their own DEMs when the stereo data become available. The data are of sufficient quality to allow for 15 m posting by users with their own software, and will be available at no charge from early July 2000. The overall mission plan is to acquire and archive a global data set between 82 degrees North and South of cloud free stereo over a period of 2 and 5 years. The nominal maximum number of stereo pairs that can be acquired/day is 771, but this maximum will probably not be realized; and no more than about 350 scenes/day will be processed.

2.2 Radar interferometry

Radar interferometry is an innovative technique that enables very high-resolution topographic maps of the earth's surface to be generated using spaceborne and airborne radar instruments. The technique has the advantages of automatic processing of the data, and operation in cloud, smoke and rainfall conditions, night and day. A transmit antenna mounted on a spacecraft or plane illuminates the terrain with a radar beam that is scattered by the surface. This radar echo has two components: amplitude (brightness) and phase (distance to the target). Two receive antennas with a fixed baseline record the radar echo from slightly different positions resulting in two different radar images. The two signals received at both ends of the baseline (referred to as the interferometric baseline) show a phase shift due to differing lengths of the signal paths. The phase difference, determined by effectively subtracting the measured phase at each end of the baseline, is sensitive to both viewing geometry and the height of the terrain. If the viewing geometry is known to sufficient accuracy, then the topography can be inferred from the phase measurement to a precision of several metres. The accompanying amplitude information is measured to construct a radar image showing details describing the surface's roughness and dielectric properties.

Interferometric data can be generated from either single-pass or repeat-pass systems. Single-pass systems such as the TOPSAR and SRTM instruments use the two-antenna system, as described above, to record both images simultaneously. Repeat-pass interferograms are generated from separate passes over the same target such as from the European ERS-1 and ERS-2 systems http://www.eurimage.com/.

TOPSAR (TOPographic Synthetic Aperture Radar)

The JPL TOPSAR system is a 5cm wavelength, C-band interferometer operating on NASA's DC-8 research aircraft as an adjunct to the polarimetric Airborne Synthetic Aperture Radar (AIRSAR) system. TOPSAR is implemented via two antennas flush-mounted nearly vertically on the left side of the aircraft with a 2.6 m baseline spacing. The boresights of the antennas are depressed 45° with respect to the horizontal. The lower antenna is used for transmission whereas both antennas are used for reception. The height accuracy of TOPSAR digital elevation models has been shown by Madsen et al (1995) to be 1 m RMSE in flat terrain and 3 m in mountain areas with a 2 m RMSE overall. Typical data acquisitions are for areas of 10 km across-track (range direction) and 60 km along track (azimuth direction). The output of high precision TOPSAR datasets is accomplished by comprehensive navigational systems to determine the precise position of the DC-8 aircraft, and full motion compensation algorithms in the TOPSAR processor to accommodate large translational and altitude perturbations during the data recording process (Madsen et al, 1995). Apart from the digital elevation data, L- and P-band polarimetric and Cvv data are also recorded. All datasets are registered and the radar data ortho-corrected using the DEM.

SRTM (Shuttle Radar Topography Mapping Mission)

The SRTM recorded both radar images simultaneously using two antennas – a transmitting and receiving antenna in the cargo bay of the Shuttle Endeavor, and a second receiving antenna at the tip of a 60 m deployable mast. Both radar and phase data were recorded in C-band (5.56 cm) and X band (3.1 cm) frequencies. During the 11-day mission, data were acquired along 225 km wide swaths imaging all of Earth's land surface between 60° north and 56° south latitude, with data points spaced every 1 arcsecond of latitude and longitude (approximately 30 m). X-band coverage occurred along narrow 50 km wide swaths and cover 40% of the area mapped by the C-band data. The absolute horizontal and vertical accuracy of the C-band data will be 30 m and 16 m, respectively. Relative height accuracy will be 10 m. However, data of these specifications will not be readily available for public use. Within 2 years, data spatially degraded to 90x90 m horizontal resolution but retaining the initial height accuracy, will be available at the low cost of regridding the data to a 1°x1° area. The policy for distributing the higher resolution data is currently not clear. However, it is expected that data over politically insensitive areas will be accessible. X-band DEM data of the narrower 50 km wide swath have a horizontal resolution of 30 m and relative and absolute height accuracies of 6 m and 16 m, respectively. These data will be unclassified and available for public use from the German Aerospace Centre. Both C and X-band datasets will be geometrically corrected and projected to the WGS84 datum. Extensive information describing the data products and their availability is available on the SRTM Home Page (http://www.jpl.nasa.gov/srtm/) and DLR Home page (http://www.jpl.nasa.gov/dlr-mirror/srtm/).

SELECTED READING

Madsen, S. N., Martin, J.M. and Zebker, H.A. 1993. Analysis and Evaluation of the NASA/JPL Across-Track Interferometric SAR System. IEEE Trans. Geosci. Remote Sensing, vol. 33, no 2, pp. 383-391.

Thompson, T.W., Zebker, H.A., Carande, R.E., Rosen, P.A., Madsen, S.N., Hensley, S., Rodriguez, E., van Zyl, J.J., Martin, J.M. and Miller, T.W. 1994. NASA/JPL TOPSAR Interferometric SAR. NASA/JPL Imaging Radar Homepage, http://southport.jpl.nasa.gov/topsardesc.html

Van Zyl, J.J., Zebker, H.A., Hensley, S., Haub, D. and Wiesbeck, W., 1995. The new dual frequency (C- and L-Band) TOPSAR airborne interferometric SAR. http://www.jpl.nasa.gov/techreport/1995/95-0530.rfr.html

Burgman, R., Rosen, P.A. and Fielding, E.J., 2000. Synthetic aperture radar interferometry to measure Earth's surface topography and its deformation. Annual Review Earth Planet Science 2000, 28:169-209.

The 21st Asian Conference on Remote Sensing
December 4-8, 2000 Taipei, TAIWAN

BENEFITS OF TOPSAR RADAR INTERFEROMETRY IN TROPICAL TERRAINS

Dr. Ian J. Tapley
Cooperative Research Centre for Landscape Evolution and Mineral Exploration
CSIRO Exploration and Mining, Private Mail Bag No 5, Wembley, Western Australia 6913
Telephone: 61 8 9333 6263 Facsimile: 61 8 9383 9179
Email: i.tapley@per.dem.csiro.au

SUMMARY

TOPSAR (TOPographic Synthetic Aperture Radar) is an aircraft-mounted radar interferometer that uses radar and interferometry to rapidly produce high-resolution topographic maps of the earth's surface. Such is the precision that in many applications, this radar technique has the potential of being a viable alternative to conventional photogrammetric techniques that use aerial photography. For example, when operating in the 40 MHz bandwidth, TOPSAR height measurements are made for every 4.63 x 3.3 m posting along a flight swath 10 km wide and typically 60 km long. In low relief terrains, sub-metre height accuracy's are typical whilst in high relief areas, height differences of 3-5 m are resolved. The process needs no gridding or interpolation as required for digital elevation models (DEMs) generated from stereo pairs of optical imagery. In addition, the technique has the advantages of automatic processing of the data, and operation in cloud, smoke and rainfall conditions, night and day. Thus radar interferometry is very appropriate for operations in humid tropical climates that normally prohibit the successful acquisition of optical products such as aerial photographs and SPOT-PAN imagery. TOPSAR has been developed by NASA-JPL as a proof of concept and a pre-cursor for future spaceborne missions including the highly successful February 2000 Shuttle Radar Topographic Mapping Mission (SRTM) (http://www-radar.jpl.nasa.gov/srtm/).

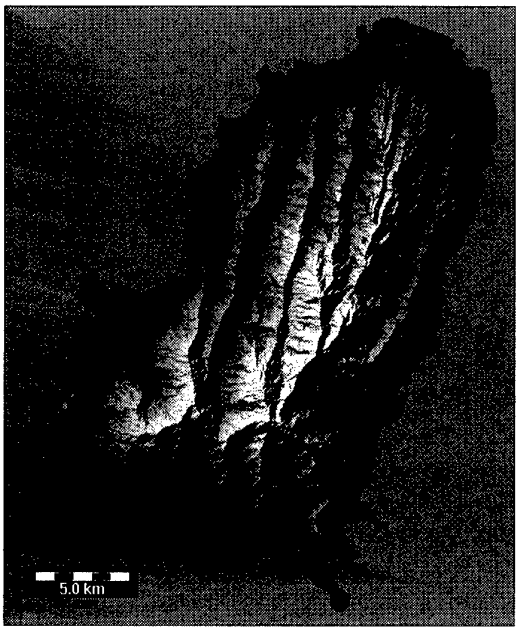
TOPSAR operates in C-band (5.56 cm wavelength) using the phase difference information captured from the VV-polarization signals received at two antennas mounted on the fuselage of NASA's DC-8 research aircraft. It effectively replaces the C-band polarimeter instrument in the existing AIRSAR hardware (Zebker et al, 1992), but the remaining L- and P-band systems are undisturbed and operate together with the TOPSAR hardware. Therefore, the combined instrument produces simultaneous L- and P-band fully polarimetric plus C-band VV polarization backscatter images in addition to the topographic product.

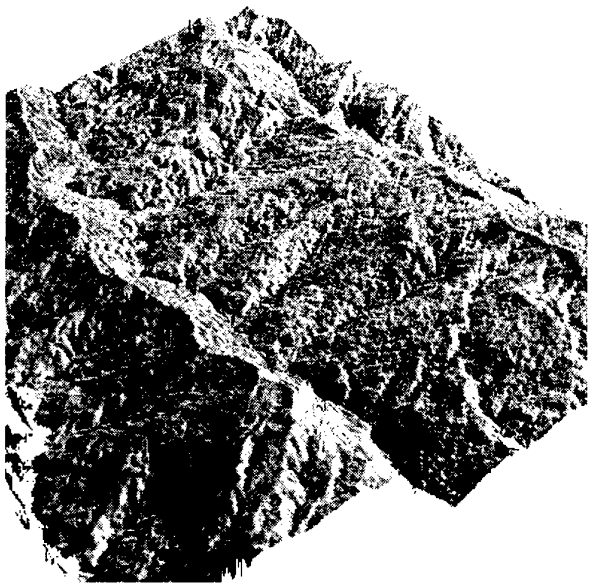
The output of high precision TOPSAR datasets is accomplished by comprehensive navigational systems to determine the precise position of the DC-8 aircraft, and full motion compensation algorithms in the TOPSAR processor to accommodate large translational and altitude perturbations during the data recording process (Madsen et al, 1995). Because the TOPSAR processor outputs the data with uniform x and y 5 m spacings, it recognizes and compensates for intrinsic distortions in the signal such as foreshortening. Areas of layover in high relief areas are also recognized, discarded and filled in by linear interpolation.

Apart from the digital elevation data, L- and P-band polarimetric and Cvv data, the TOPSAR data package also includes a local incidence angle image and an image of the correlation between the interferometric channels to assess the relative height accuracy of the data (van Zyl et al, 1995). All datasets are registered and projected to groundrange. The C-band digital elevation information is used to geometrically resample the radar images to correct for the

effects of topography on the radar imaging geometry. All radar images are radiometrically corrected by taking into account the effects of topography as described by van Zyl et al (1993).

During the PacRim AIRSAR missions in 1996 and 2000 quality TOPSAR datasets were collected in the humid-tropical environments of Papua New Guinea, Indonesia, Malaysia, Brunei, Cambodia, Vietnam, Philippines, Taiwan and South Korea. The accuracy of the data lends itself to generating precision geomorphometric and structural detail in these regions. A shaded relief image (below left) and 3D perspective image (below right) highlight foliation and trends within a metamorphic core complex masked by a canopy of tropical vegetation in Papua New Guinea. It is evident that the top of the vegetation canopy conforms to the underlying topography that, in turn, is controlled by geological features and geomorphic processes. The majority of the short wavelength C-band radar backscatter is from the canopy surface thereby providing a reasonably accurate digital elevation product of the terrain.





Apart from the obvious benefits of generating large-scale topographic maps and hydrological modelling, TOPSAR image-map products are most useful for: mapping geology and landforms; planning geochemical sampling strategies during mineral exploration programs; designing access routes for roadways, pipelines and powerlines; planning and rehabilitating minesites; and modelling and designing management strategies for natural disasters including tsunamis, lahars and flooding. Examples of these applications will be described using TOPSAR data collected during the PacRim AIRSAR deployments.

REFERENCES

Madsen, S. N., Martin, J.M. and Zebker, H.A. 1993. Analysis and Evaluation of the NASA/JPL Across-Track Interferometric SAR System. IEEE Trans. Geosci. Remote Sensing, vol. 33, no 2, pp. 383-391.

Thompson, T.W., Zebker, H.A., Carande, R.E., Rosen, P.A., Madsen, S.N., Hensley, S., Rodriguez, E., van Zyl, J.J., Martin, J.M. and Miller, T.W. 1994. NASA/JPL TOPSAR Interferometric SAR. World Wide Web, NASA/JPL Imaging Radar Homepage, http://southport.jpl.nasa.gov/topsardesc.html

van Zyl, J.J., 1993, The effect of topography on radar scattering from vegetated areas, IEEE Trans. Geosci. Remote Sensing, vol. 31, no. 1, pp. 153-160.

Van Zyl, J.J., Zebker, H.A., Hensley, S., Haub, D. and Wiesbeck, W., 1995. The New Dual Frequency (C- and L-Band) TOPSAR Airborne Interferometric SAR. http://www.jpl.nasa.gov/techreport/1995/95-0530.rfr.html

Zebker, H.A., Madsen, S.N., Martin, J., Wheeler, K.B., Miller, T., Lou, Y., Alberti, G., Vetrella, S. and Cucci, A., 1992. The TOPSAR Interferometric Radar Topographic Mapping Instrument. IEEE Transactions on Geoscience and Remote Sensing, Vol. 30, No. 5, pp. 933-939.

ANALYSIS OF POLARIZATION SIGNATURES AND TEXTURAL FEATURES FOR AIRBORNE PI-SAR IMAGES

Takahiro YAMADA
Graduate School of Science and Engineering,
Ibaraki University
4-12-1 Nakanarusawa, Hitachi, Ibaraki, 316-8511, Japan
Tel: (81)-294-38-8235, Fax: (81)-294-38-5282
E-mail: yamada@fukushima-nct.ac.jp

Takashi HOSHI
Professor, Department of the Computer and Information Sciences,
Faculty of Engineering, Ibaraki University
4-12-1 Nakanarusawa, Hitachi, Ibaraki, 316-8511, Japan
Tel: (81)-294-38-5133, Fax: (81)-294-38-5282
E-mail: hoshi@cis.ibaraki.ac.jp

KEY WORDS: Polarization Signature, Textural Feature, PI-SAR

ABSTRACT: For high resolution SAR images, the influences of the factors that can be ignored for usual SAR images, such as the shadows of buildings and trees, have to consider. In this paper, the influences of the factors particular to high resolution images for polarization signatures and textural features, and the changes by the differences of wavelength are analyzed using PI-SAR images.

1. INTRODUCTION

Recently, resolution of remote sensing image data has been higher, and the tendency has been seen not only for visible sensor images but also for Synthetic Aperture Radar (SAR) images. For the observations of earth using SAR, to observe the detailed physical properties for the surfaces has been possible by polarimetry technique, and various products have been reported [1],[2]. Analysis of polarization signatures, one of general methods for the analysis of polarimetric SAR images, has been expressed in many papers and shown its availability [3]. Textural analysis has also been carried out for polarimetric SAR [4],[5]. However, it is scarcely discussed that changes polarization signatures and textural features caused by improvement of the resolution.

In this study, the influences carried by the shadows of buildings and trees that have never been considered in usual resolution polarimetric SAR (SIR-C and so on) are analyzed using airborne PI-SAR (Polarimetric and Interferometric SAR) high resolution images. In general resolution SAR images, the shadow effect should be considered for the analysis of mountain areas. For these images, the shadows of buildings and trees had been ignored because their sizes were smaller than limits of resolutions. However, unusual surface patterns are formed clearly due to the fine shadow included the analysis areas using higher resolution images. The influences of back-scattering coefficients for the patterns are compared using polarization signatures and the influences of image structures are analyzed using textural features. For PI-SAR data, the resolution varies according to the frequency band (X-band or L-band), so that the resolutions are transformed the same value and the differences among wavelength are also discussed.

2. PI-SAR DATA

PI-SAR is one of airborne SAR developed by CRL and NASDA for the purpose of observing

earth environment and watching disasters [6],[7]. Its observation frequency band are X-band (9.55 [GHz]) and L-band (1.27 [GHz]), and the resolutions vary according to the wavelength; 1.5 [m] and 3.0 [m] respectively. In distributed PI-SAR data products, there are SSC (Single-look Slantrange Complex), MGA (Multi-look Groundrange Complex), and MGP (Multi-look Groundrange Polarimetric) formats. In this study, MGP format data was selected because this format data has full-polarimetric information. For each pixel, the polarization information expressed by 10 byte data.

As the object areas, vegetation area and residential area were mainly extracted. In these areas, though shadows of trees and buildings appear scarcely, the changes of pattern influenced by the shadows should be considered for high resolution sensor like PI-SAR. The overview of PI-SAR data used in this study is shown in Table 1, and the sizes of extracted areas are shown in Table 2 respectively. Fig.1 shows the positions of these areas in used scene.

Table 1: Overview of used PI-SAR data

Subject	X-band data	L-band data
Frequency [GHz]	9.55	1.27
Azimuth resolution [m]	1.5 / 3.0	3.0
Range resolution [m]	1.5 / 3.0	3.0
Data format	Multi-look Grouondrange Polarimetric	
Observation site	Tsukuba, Japan	
Acquisition date	1997. 9. 30	

Table 2: Sizes of extracted areas (Unit: pixels)

Name of area	Azimuth orientation	Range orientation
Paddy field	140	140
Vegetation area	160	160
Residential area	170	130

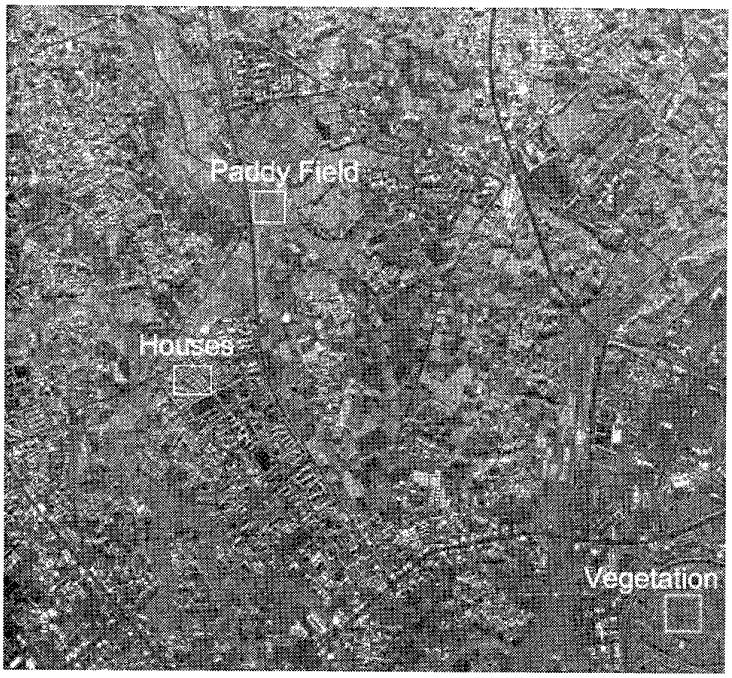


Fig.1: Extracted areas in Tsukuba site (X-band HH polarization image)

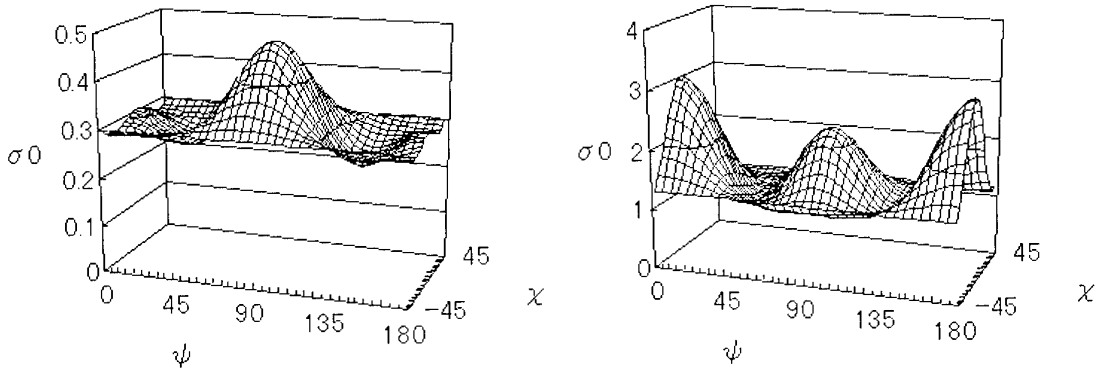
© Communication Research Laboratory 1999.

3. ANALYSIS OF POLARIZATION SIGNATURES FOR THE TARGETS

The first, complex scattering matrices were derived from PI-SAR MGP data for each pixel to make polarization signatures that indicate the polarization properties of scattering intensity of microwave for the target. Next, the complex scattering matrices were transformed Mueller matrices constructed by real number elements, and obtained matrices were averaged in homogeneous area to reduction influences of speckle noises. Generally, polarization signatures are obtained from averaged Mueller matrices. Polarization signature diagrams represent the value of polarization signatures graphically, and these shapes characterize the targets [1]~[3],[8].

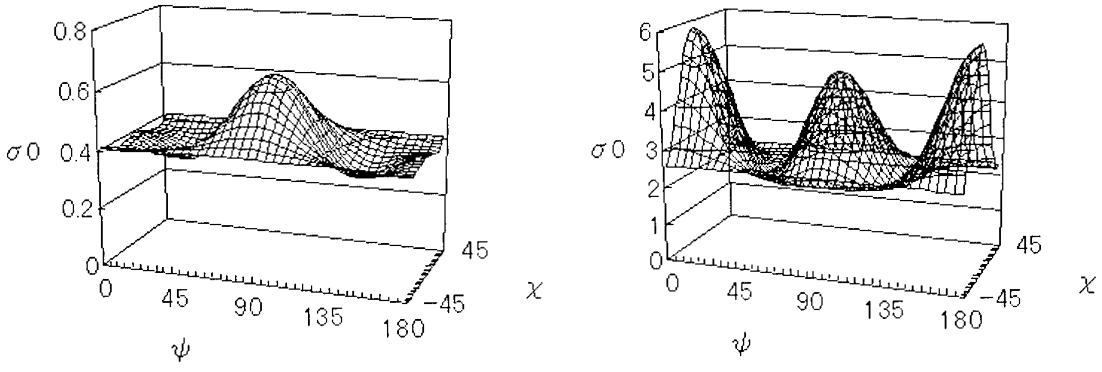
In SAR images, it is well known to undergo the influences of shadows that appear scarcely in the images obtained by the sensor observing directly below. Particularly, in high resolution SAR image, including the shadows in extracted sample areas is liable to occur. In the following description, the fluctuations of polarization signatures between the area including shadows and the area excluding them are investigated [9].

Fig.2 shows the polarization signature diagrams of vegetation area and residential area including shadows, and Fig.3 shows the ones of the same areas excluding them. These diagrams were obtained from high resolution X-band data, and combination of polarization was co-polarization. Although influence of shadows for the shape of polarization signature diagrams was little, it was found that the reciprocity value of σ^0 for including shadows area was smaller than for excluding shadow area. Then we estimated the polarization signature ratio of including shadow to excluding one. Fig.4 shows that the dependence of the ratio of σ^0 was small, and it was nearly certain.



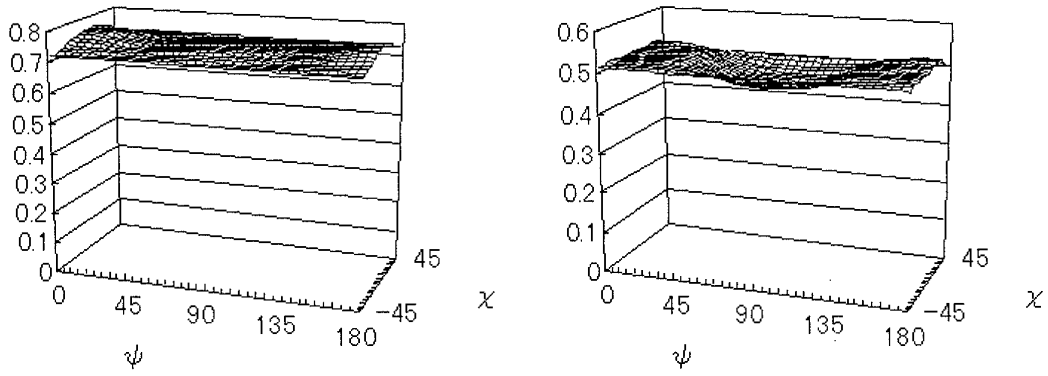
(a) Vegetation area (b) Residential area

Fig.2: Polarization signature diagrams for extracted area including shadows



(a) Vegetation area (b) Residential area

Fig.3: Polarization signature diagrams for extracted area excluding shadows



(a) Vegetation area (b) Residential area

Fig.4: The polarization signature ratio of including shadow to excluding one

4. ANALYSIS OF TEXTURAL FEATURES FOR THE TARGETS

In the next place, we estimated textural features from the same areas analyzed polarization signatures. For PI-SAR data, it is difficult to compare as it stands because the resolutions depend on the observation frequencies (X and L-band). Hence two kinds of sub-images were compared for X-band data. One of them was the features derived from normal pixel spacing images, another one was derived from thinned out images to match the resolution to L-band image data. Furthermore, features of thinned out X-band images are compared with the features of L-band normal pixel spacing images [10].

In this study, GLCM (Gray Level Co-occurrence Matrix) method was used to estimate textural features. In this method, textures are defined from distances and directions of neighbor two pixels. Some textural features derived by this method are proposed, Angular Second Moment (ASM), Contrast (CON), Entropy (ENT), and so on [9],[11],[12]. Each element of GLCM is expressed as $P(i, j, d, \theta)$, and it is changed into probability variable $p(i, j, d, \theta)$ by equation (1) to derive the textural features.

$$p(i,j,d,\theta) = \frac{P(i,j,d,\theta)}{\sum_{i=0}^{N-1}\sum_{j=0}^{N-1} P(i,j,d,\theta)} \tag{1}$$

Where N is the size of GLCM (in this study, N is set 16), i and j are number of line and column for the remarkable element in GLCM, d is the distance of two pixels to define the texture, and θ is the direction of them. ASM, CON, and ENT are derived Equation (2) to (4).

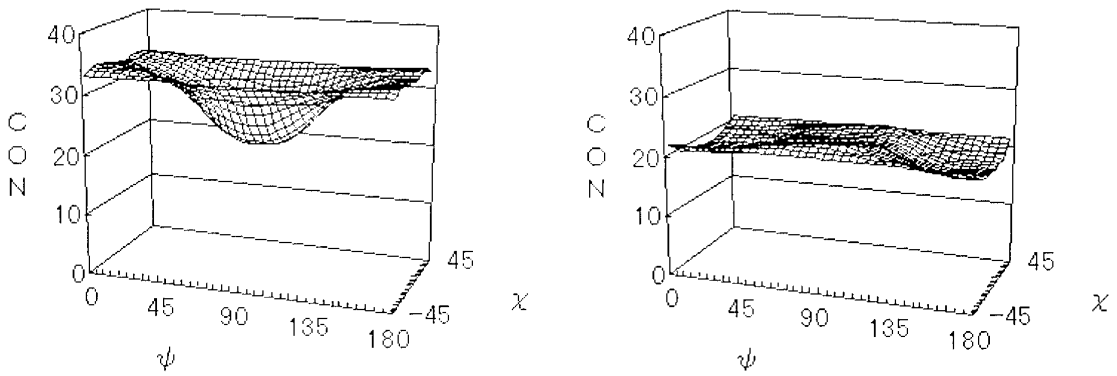
$$ASM = \sum_{i=0}^{N-1}\sum_{j=0}^{N-1} p^2(i,j,d,\theta) \tag{2}$$

$$CON = \sum_{n=0}^{N-1} n^2 \left\{ \sum_{|i-j=n|} p(i,j,d,\theta) \right\} \tag{3}$$

$$ENT = -\sum_{i=0}^{N-1}\sum_{j=0}^{N-1} p(i,j,d,\theta)\log p(i,j,d,\theta) \tag{4}$$

Polarization properties of textural features are expressed in the same co-ordinates as polarization signatures. Fig.5 shows the polarization properties of contrast for residential area derived from X-band data, (a) shows for normal pixel spacing image and (b) shows for thinned out image.

To analyze the difference by frequency band, the feature property diagram for the same area of L-band normal pixel spacing image data is shown Fig.6.



(a) Normal pixel spacing image data (b) Thinned out image data

Fig.5: Polarization properties for X-band residential area image

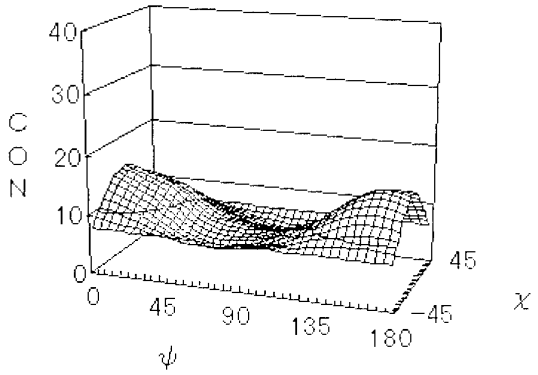


Fig.6: Polarization property diagram for residential area of L-band normal pixel spacing image

5. DISCUSSIONS

The first, fluctuations of polarization signatures caused by including shadows in partial area are considered. Back-scattering for the shadow is much smaller, so that the elements of Mueller matrix are also smaller wholly. Hence, averaged values of the elements are smaller than the area excluding shadows relatively. Therefore, values of σ^0 become smaller, too. On the other hand, the shapes of polarization signature diagrams are preserved because back-scattering for shadows depend on the polarization scarcely.

Next, the polarization properties of textural features are considered. For the textural features like contrast that depend on the intensity of the change of gray level in partial area, feature values decreased for thinned images. Especially, in the residential area, though the minimum value was around VV polarization for normal pixel spacing images, the minimum was around HH polarization for thinned images. Hence, we found differences of the pattern caused by resolution appear in the same area images, and these influence polarization properties. Textures were changed by the wave-length, we consider that was caused by the relationship between wave-length with the size and arrangement of targets.

6. CONCLUSIONS

In this study, the fluctuations of polarization signatures and textural features for the situation including shadow in the objective areas using high resolution PI-SAR images. For polarization signature, the value of σ^0 decreased relatively by including shadow, dependence on polarization was

preserved. On the other hand, for textural feature, the change appeared in the polarization properties. Therefore, to analyze high resolution SAR images, the rate of shadow in objective area should be considered. For more land-cover pattern, this research is needed to advance.

ACKNOWLEDGMENT

The authors would like to thank Dr. Masaharu FUJITA, Professor of Tokyo Metropolitan Institute of Technology, Makoto SATAKE and Dr. Tatsuharu KOBAYASHI, Senior research official of Communications Research Laboratory, Ministry of Posts and Telecommunications, offered the data of PI-SAR.

REFERENCES

[1] H. A. Zebker and J. J. van Zyl: "Imaging Radar Polarimetry: A Review," Proc. IEEE, Vol.79, No.11, pp.1583~1606, 1991.

[2] F. T. Ulaby and C. Elachi: "Radar Polarimetry for Geoscience Applications," Artech House, Inc., 1990.

[3] J. J. van Zyl, H. A. Zebker, and C. Elachi: "Imaging radar polarization signatures: Theory and observation," Radio Science, Vol.22, No.4, pp.529~543, 1987.

[4] T. Hoshi, T. Yamada, and M. Fujita: "Analysis of Textural Feature Using SIR-C Polarimetric Image Data," Trans. IEICE, Vol.J82B, No.2, pp.283~291, 1999.

[5] T. Yamada and T. Hoshi: "Application of Polarization Signatures and Textural Features to Classification of Polarimetric SAR Images," Proc. NAGANO magel '99, pp.81~84, 1999.

[6] T. Kobayashi, S. Uratsuka, A. Nadai, T. Umehara, M. Satake, H. Sawada, N. Mitsuzuka, G. Takao, S. Ishibashi and M. Shimada: "Forest observation by high resolution airborne dual-frequency SAR," Proc. Joint Conference of JSPRS and RSSJ, pp.563~564, 1999.

[7] N. Sudo, M. Furuya, A. Iwashita, H. Shimoda, T.Sakata, T. Matsuoka, S. Uratsuka, M. Satake, T. Kobayashi, T. Umehara, A. Nadai, H. Meno and H. Masuko: "The land cover classification by airborne high-resolution multi-parameter synthetic aperture radar," Proc. Joint Conference of JSPRS and RSSJ, pp.559~562, 1999.

[8] Y. Yamaguchi: "Fundamentals of Polarimetric Radar and Its Applications," Realize, Inc., 1998.

[9] T. Yamada and T. Hoshi: "Analysis of the surface polarization properties using high resolution airborne PI-SAR data," Proc. The 27th Conference of RSSJ, pp.163~166, 1999.

[10] T. Yamada and T. Hoshi: "Investigation of the polarization properties of textural features for the high resolution airborne PI-SAR images," Proc. The 28th Conference of RSSJ, pp.43~44, 2000.

[11] R. M. Haralick, K. Shanmugam, and Its'hak Dinstein: "Textural Features for Image Classification," IEEE Trans. Systems, Man, and Cybernetics, Vol.SMC3, No.6, pp.610~621, 1973.

[12] T. Hashimoto and M. Matsuo: "One Method of Texture Analysis of Synthetic Aperture Radar Images," Technical Report of IEICE, Vol.IE86-88, pp.33~40, 1986.

The 21st Asian Conference on Remote Sensing
December 4-8, 2000 Taipei, TAIWAN

A Study of Surface Deformation From Earthquake by Differential Radar Interferometry

C. T. WANG[1] , L. S. LIANG[2] , K. S. CHEN[3] , A. J. CHEN[4]

KEY WORDS : Differential Interferometry 、Synthetic Aperture Radar 、Surface Deformation 、Earthquake

ABSTRACT : We present a mapping of the surface deformation resulting from the 921 earthquake in Central Range of Taiwan using data acquired from ERS/2 high-resolution synthetic aperture radar(SAR) imagery. SAR data sets acquired in January 21 , May 6 , September 23 and October 28 1999 were processed by differential interferometric technique to generate interferograms from which the deformation is assessed. The coherence between these pairs of interferograms were evaluated for quality check. In addition, the atmosphere effects on the coherence were reduced using sereral sets of interferograms. It is shown that the deformation derived from the interferograms are compared well with GPS measurements by Central Geological Survey (CGS) with interferometric baseline even more than 200m. Results also indicate that the subsidence more than 10cm on the west side of fault area in Taichung is detectable by differential interferometric SAR. It is concluded in this study that the InSAR technique provides a promising tool for detecting crustal deformation by earthquake

1.Assistant Researcher of CSRSR, National Central University
2.Technician of CSRSR, National Central University
3.Professor of CSRSR, National Central University
4.Professor of CSRSR, National Central University

1.Introduction

The purpose of this paper is to utilize the technique of interferometric synthetic aperture radar (IFSAR) to extract information about the crustal deformation after earthquake using the phase content of the complex SAR images, and to detect the land subsidence and crustal movement in Taiwan. SAR not only obtains the radar scattering coefficient of the land cover, but also carries the phase information about the target when a pair of data is conherently processed. The phase has two major parts: the character of the land cover itself and the distance between radar and the target. A single phase echoes essentially bears no information. Therefore, we must have at least one image pair with the same measuring direction and near the same measuring position to examine the difference of echos. If the character of the land cover changes little during the period of images taken, we can ignore the influence of phase caused by it, and then get the radar Interferometric map, produced by the difference of the measuring distance. We then calculate the difference of the distance by using the Interferometric image pairs, and furthermore we use the differential interferogram map with the same area but at different time to calculate the height and the crustal movement. On the development of the relative technology and application, many scholars abroad had researched in this aspect, and the result can be found in many academic periodical. Decorrection in interferometric radar echos has been demonstrated by Howard A. Zebker in 1992 [2]. S. N. Madsen uses airborne synthetic aperture radar interferometry to produce topographic mapping by NASA DC-8 plane in 1993 [3]; and he also presented that accuracy of topographic maps derived from

ERS-1 interferometric radar in 1994 [4]. R. M. Goldsten announced satellite radar interferometry: two-dimensional phase unwrapping in 1988 [5]. D. J. Bone published Fourier fringe analysis: the two-dimensional phase unwrapping problem in 1991 [6]. While the application of surface displacement, A. K. Gabtiel ever presented mapping small elevation changes over large areas: differential radar interferometry in 1989 [7]. Massonnet used a map by radar interferometry to check the displacement field of the Landers earthquake in 1993 [8]. Zebker also used differential radar interferometry to derive coseismic displacement in 1994 [9]. Carnec explained two examples of the useage of SAR interferometry on displacement fields of small spatial extent in 1996 [10].

According a report of Central Weather Bureau (CWB), a major earthquake (M_L=7.3) has occurred near the small town Chi-Chi in the Nantou County, Taiwan, at 1:47 a.m. local time on September 21, 1999 (17:47 GMT on 20 September). The epicenter was 12.5 km northwest the Sun-Moon lake. The focal depth is 8 km. The death toll has exceeded 2100 and is mounting during the first week after the main shock. The Chi-Chi earthquake essentially was resulted from a major reverse fault, the Chelungpu Fault, trending N-S to NNE-SSW, one of the major trust faults in the deformation front of the fold-and-thrust belt of the Taiwan orogenic belt. The movement of the earthquake produced a linear zone of surface ruptures, extending about 80 km long from north to south. According to the in-situ t field investigations, the surface break shows large vertical as well as horizontal displacements, ranged from 1 to 8 meters, along the fault line as a consequence of the Chi-Chi earthquake.

When we reviewed the epicenter distribution during this century, we will get a conclusion that there is a main earthquake zone, which extends to the southeast direction from HouLong (in MiaoLi County), passing through MiaoLi city, SanYi, ZhuoLan, DongShi, PuLi, SunMoon Lake, and then turning to the southwest direction, passing through ZhuShan, MeiShan, JiaYi, XinYing, Tainan, and forming a wide arc curve seismic zone. This arc curve seismic zone surrounds roughly a stable foundation, which hides in shallow underground of BeiGang, TaiXi, and PengHu. This zone is called BeiGang highlands; it is exactly located in the core area of the inner side in the arc curve seismic zone; relatively, the epicenter of the area distributes fewer, and the earthquake also happens fewer. When the Philippine plate subducts towards the North beneath the Eurasian plate, BeiGang highlands hinder Taiwan island from moving west, as a result, there are some activities of trust faults and earthquakes in the front of mountains; this is the reason that most active faults distribute in the front of mountains[1]. This paper reports the analyzed results for the case of 921 Great Earthquake using differential interferometric SAR technique. Qualitative and quantitative assessments were discussed and compared to field GPS survey.

2. Data Description

In respect of data sources, there are two ways to acquire interferometric SAR pairs: dual pass and dual antenna. Currently, satellite SAR belongs to dual pass, while airborne system such as JPL AIRSAR is kind of dual antenna. This study makes use of ERS SAR data. ERS1 and ERS2 are both earth source satellite, developed by European Space Agency (ESA). They pass over Taiwan at 10:28 am and 10:20 pm. The Center for Space and Remote Sensing Research at National Central University has received and archived quite a large volume of ERS1/2 radar image data since 1993m, providing a very valuable database for interferogram measurement in Taiwan.

We choose the central mountainous area of Taiwan for testing. The ERS satellite

orbit no.232, frame 3123 (Figure. 1) was selected to form the image pairs according on the base line term for interferometry provided by ESA. Then, based on the date for the 921 Great Earthquake, data of 21 Jan、6 May、23 Sep and 28 Oct 1999 were singled out for use. The perpendicular and horizontal components of the base lines of these data sets is given in Table 1.

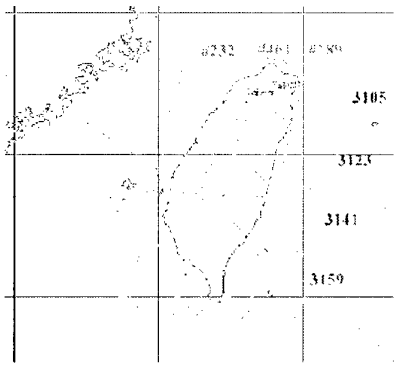


Figure. 1 : Coverage map of ERS2 over Taiwan

Table 1. : the image pair of ERS2 interferometry

The date of the master image	The date of the slave image	The interval of the date	Perpendicular base line	Horizontal base line
99/05/06	99/01/21	105	-96m	-91m
99/10/28	99/09/23	35	219m	91m
99/05/06	99/09/23	140	213m	54m
99/05/06	99/10/28	175	-6m	37m

3. Data Processing Procedure

The orbit and the observing angle of the ERS satellites are known to be fixed. Hence, it is well suitable for the Interferometry measurements. In another words, it is quite a stable dual pass or repeat pass system. We processed the ERS2 raw signals of these four images (21 Jan、6 May、23 Sep and 28 Oct) with single look complex(SLC) product. Their coherence maps are respectively displayed in Figure.2 to Figure.5. Noted that the signal data being processed are in complex form, with 16-bit representations for each of the real and imaginary parts, so we can preserve the original phase information. The pixel spacing in slant range and azimuth are 7.9 meters and 3.9 meters, respectively. First we processed the pair of 21 Jan and 6 May before earthquake, and 23 Sep and 28 Oct after earthquake. In view of these two pairs of interference fringes, it can be clearly observed that they are correlated to each other, and there is little atmosphere inference. The differential interference fringes implies the presence of the surface deformation by earthquake. It is noted that the spacing of the fringes is obviously in connection with the base line; great base line has great spacing and vise visa.

We proceed in the way called "Three Pass" by using image from May 6 as reference scene before earthquake, and matching that with 23 Sep and 28 Oct to produce two interferogram images removing the earth curved surface and topography inference. At this point, we still keep working in slant rage coordinate, so that we can subtract with the interferogram images (May 6 and Jan 21) directly to generate two interferometric phase images due to surface deformation, (6 May, 23 Sep) and (6 May, 28 Oct) (Figure.6 and Figure.7). Finally, we perform phase restoration in tenth of pixel accuracy to get the surface deformation.

The next step is the image pairs matching each other by conjugate points. Since the orbits are nearly parallel, this kind of images are similar to each other in the geometric characteristic. The conjugate points is best uniformly distributed over the study area and the required number depends on the terrain relief. For this study, about 100 were used. The rms error registration is about 0.1 pixel. Then, the single look complex data is resampled, followed by a 2x10 running window to reduce the speckle noise. The method phase unwrapping is then applied to produce the image of the change of the topography. In this way, the phase error of the interferogram caused by coregistration might be minimized.

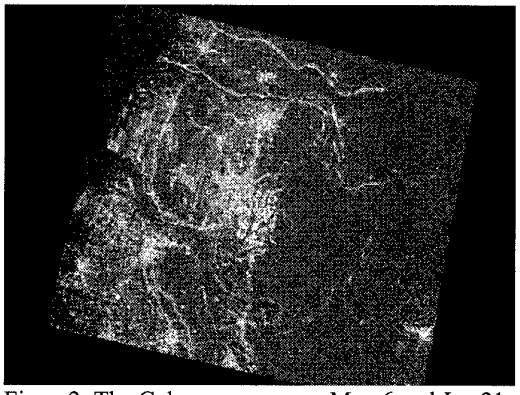


Figure2: The Coherence map on May 6 and Jan 21

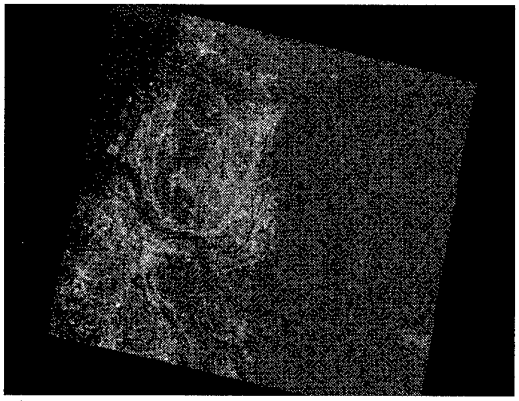


Figure3: The Coherence map on May 6 and Sep 23

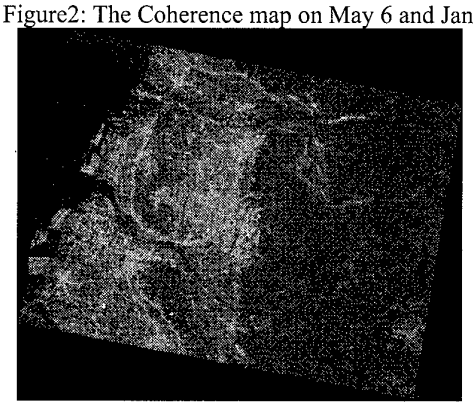


Figure. 4: The Coherence map on May 6 and Oct 28

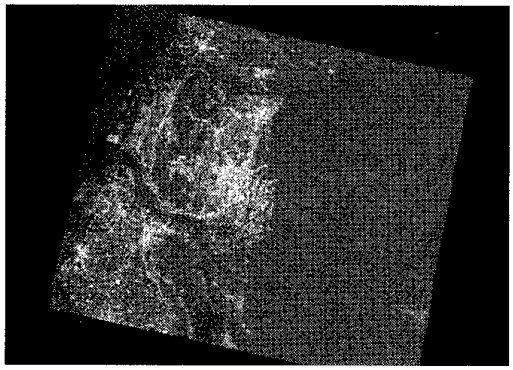


Figure. 5: The Coherence map on Sep 23 and Oct 28

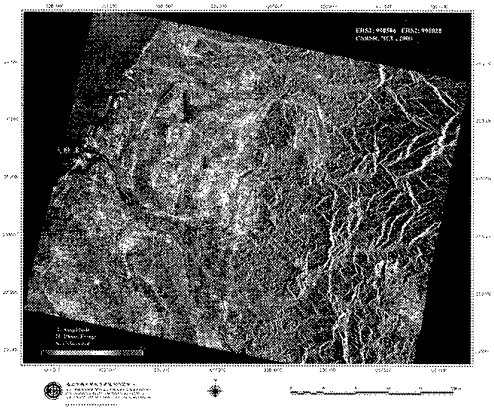


Figure. 6: The differential interferogram on May 6 and Sep 23

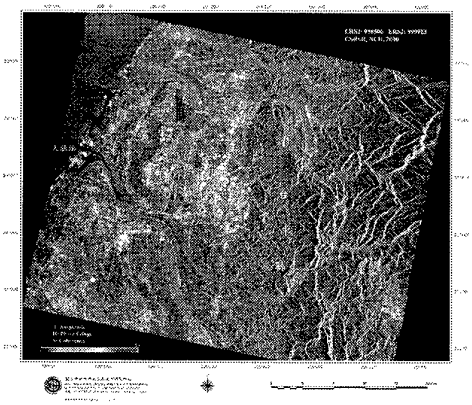


Figure. 7: The differential interferogram on May 6 and Oct 28

4. RESULTS AND DISCUSSIONS

From the coherence maps, there is no interference fringe in the sea due to the lack of coherence. In plain area including town and the suburb area, the vertical component of the base

line is about 6 meters with average coherence of above 0.2, in spite of the longest time interval of 175 days (between 6 May and 28 Oct). Similarly, for the time interval of 140 days between May 6 and Sep 23, the vertical component of the base line is about 213 meters with average coherence of above 0.2. These may be acceptable for purpose of interferometric detection. By differential interferometry we further get a series of subsidence maps in Taichung city. A maximum scale of about 18 cm after earthquake was estimated, which compare fairly well with GPS measurement [1].

To make sense of the comparison, we carefully investigated and checked the GPS measurement along fault broken zone. From the great earthquake resulted in the obvious bulge along the Chelungpu fault, we calculated the measurement of the fault broken zone which has both historical meaning and practical value that leads the Central Geological Survey(CGS) to give every effort to survey the fault belt (zone). In order to make sure the position of the surface rupture of fault, CGS has confirmed the position of outcrop by in-situ field measurements. Trimble 4000 SSi receiver was used in the survey of the fault broken line(zone) by means of fast static survey method, with one or two the GPS stake set by CGS as reference station. Processing along the fault zone by 4 or 5 moving GPS station was conducted with receiving signals sampled at every 5 seconds for 8 to 15 minutes. Depending on the field of view of the GPS station, each critical outcrop had been measured except in mountainous area where it was difficult, if not impossible, to be tracked. After data taken, the base line precision was confirmed to be under 10 cm [10] for the distance in between 3 and 60 kilometers from reference station.

The GPS network measurement shows that between the north Tunzijiao fault and Yuanli it arises 4 to 8 cm in vertical displacement component; it descended 11 to 22 cm in the west of ChangHua fault. Among the east of ChungHua fault, the west of Chelungpu fault, and the south of Caotun, a 18 to 22 cm decending was observed. And in the north of Caotun, there was a 8 to 18 cm descending, while between the east of Chelungpu fault and Shuangdong fault, it arises 1.5 to 4 meters. It was even greater near the Chelungpu fault; in the east part of Shuangdong fault appears about 1 meter arising; and the position of geography center of Taiwan moved 2.3 meters in northwest direction with descending of 63 cm in vertical

To this end, it may be recalled that the differential interferometry is measuring movemen in centimeter scale. When the vertical displacement is too large such as those analyzed above, the interferometric coherence was almost lost, making the deformation detection very difficult. The Chelungpu fault, for example, presented a displacement amount to meters. C band system like ERS is not appropriate. We must consider the radar system of the L band like JERS-1 having longer wavelength.

5. Summary

Some conclusions are reached based the case study in this paper:

(1)The most severe land subsidence of Taichung city was estimated to be about 18 cm. Comparison with the GPS surveying data confirms that the InSAR and GPS results have in the same sinking tendency, suggesting that the differential interferometry has great potential for detecting the displacement in large area.

(2) If the displacement is too large in vertical part, the coherence of the image pairs is too low, then we can't detect possible surface deformation. A system with longer wavelength might be a solution. Besides, the phase noise due to the vegetation cover can be reduced.

(4) The influence of atmospheric and ionospheric effects in interferogram should be taken into account. One solution is using GPS network observations to remove such effetes. Another way is to increase the numbers of monitoring. In this paper, the ERSs' data are all in descending mode, the change in distance being in slant range. Thus, it is not possible to separate the horizontal and perpendicular component. If we acquire the data in ascending mode data in the

future, we may analyze the components of change.

(5) The complete detecting task of long-term and large area of surface deformation depends greatly on continuity of the image data receiving. Also, a large volume of SAR data archive is essential for long term displacement monitoring as well as short term displacement by natural disaster such as earthquake. The GPS survey is good for a point by point, but not cost effective for extensive area. The interferometric SAR technique and GPS are complementary and supplementary to each other.

(6) The ground resolution of ERS satellite series is 20 meters now, and its incident angle is fixed to 23°, so image of mountainous area has many layovers and shadows. We should have choice for higher resolution and flexible incident angle, such as Radersat-1 or Radersat-2, to minimize the amount of layovers and shadows.

Acknowledgement

We would like to thank Dr. Kuo-Fong Ma (Institute of Geophysics, National Central University, Chung-Li, Taiwan, ROC), Dr. Shui-Bei Yu (Institute of Earth Science, Academia Sinica, Nankang, Taiwan, ROC), the GPS surveying data after earthquake was supplied by the Central Geological Survey (CGS). We are also indebted to all the staff members of CSRSR who processed ERS and SPOT images used in this study.

6. References

1. Zhao-Xia Chen(1999), the survey reports of 921 earthquake and geology, Central Geological Survey, Department of Economy, Taiwan.

1. Goldsten, R.M., Zebker, H. A., and Werner, C. L.(1988), Satellite radar interferometry: Two-dimensional phase unwrapping, *Radio Science*, Vol. 23, No. 4, pp. 713-720.

2. Gabtiel, A. K., Goldstein, R. M., and Zebker, H. A.(1989), Mapping small elevation changes over large areas: Differential radar Interferometry, *j. Geophys. Res.*, Vol. 94, No. B7, pp. 9183-9191.

3. Bone, D. J.(1991), Fourier fringe analysis: the two-dimensional phase unwrapping problem, *Applied Optics*, Vol. 30, No. 25, pp. 3627-3632.

4. Zekber, H. A., and Villasenor, J.(1992), Decorrelation in interferometric radar echoes, *IEEE Trans. Geosci. Remote Sensing*, Vol.30., No. 5, pp.950-959.

5. Madsen, S. N., Zebker, H. A., and Martin, J.(1993), Topographic mapping using radar interferometry: Processing techniques, *IEEE Trans. Geosci. Remote Sensing*, Vol. 31, No. 1, pp. 246-256.

6. Massonnet, D., Rossi, M., Carmona, C., Adragna, F., Peitzer, G., Feigi, K., and Rabaute, T.(1993), The displacement field of the Landers earthquake mapped by radar interferometry, *Nature*, Vol. 364, No. 8, pp. 138-142.

7. Zekber, H. A., Werner, C. L., Rosen, P. A., and Hensley, S.(1994), Accuracy of topographic maps derived from ERS-1 interferometric radar, *IEEE Trans. Geosci. Remote Sensing*, Vol. 32, No. 4, pp. 823-836.

8. Zekber, H. A., Rosen, P. A., Goldstein, R. M., Gabriel, A., and Werner, C. L. (1994), On the derivation of coseismic displacement fields using differential radar interferometry: The Landers earthquake, *J, Geophy.*, Vol. 99, No. B10, pp. 19.617-19.634.

9. Carnec. C., Massonnet D. and King C.(1996), Two examples of the use of SAR interferometry on displacement fields of small spatial extent, *Geophy. Res.*, Vol. 23, No. 24, pp. 3579-3582.

10. Hui-Zheng Zhang(1999), the survey reports of 921 earthquake and geology, Central Geological Survey, Department of Economy, Taiwan.

ANALYSIS OF MULTIPOLARIZATION AND MULTI-BAND RADAR DATA OVER ILOILO CITY AND VICINITIES

Michael B. LITUAÑAS, Jerry H.G. SALVADOR, Dulcisimo S. DOMINGO III,
Aeschylus M.J. VALENZUELA and Eduardo O. CLARIDAD
Mines and Geosciences Bureau
North Avenue, Diliman, Quezon City, 1104, Philippines
Tel/Fax: (632) 928-8544 email: totic@pacific.net.ph

KEYWORDS: AirSAR, Modified Rayleigh Criterion, relief

ABSTRACT

This research report is the synthesis of the image analysis and the result of the field verification using AirSAR data obtained over southeast Iloilo and northern Guimaras Island.

Iloilo generally has a flat relief. Broad alluvial plains stretch along the land. The coastal zone has several active tidal flats. Within the vicinities there are many gently sloping, low relief hills. In three test areas, we showed that multi-band radar data could help approximate the surface relief of materials in the field by describing the relief in terms of surface roughness calculated from the Modified Rayleigh Criterion. Such relief correlates with signatures in the radar image. We also showed closely the patterns of lineation in the Oton coast image correlating it with field observation deducing some of the process that took place in the past. In northern Guimaras, we identified and mapped several lithologies using the radar image.

We showed the AirSAR image's usefulness for geomorphologic terrain mapping. We identified three landforms namely, the fluvio-denudational landform, the fluvial landforms, and the fluvio-marine landforms.

1.0 INTRODUCTION

The use of multi-band and multi-polarized imaging radar data for geologic applications is new in the Philippines. Filipino researchers got the chance to use the multi-band and multi-polarized radar data upon participation to the Pacific Rim (PACRIM) airborne synthetic aperture radar (AirSAR) Mission in 1996. AirSAR is a 3-frequency, 4-polarization, SAR system – a multi-parameter system - carried on-board a DC-8 aircraft made by the National Aeronautics and Space Administration- Jet Propulsion Laboratories (NASA-JPL). One of the target areas is the southeastern coast of Iloilo and Guimaras Island. The report is the synthesis of the image analysis and field verification results of the AirSAR image taken over the southeastern coast of Iloilo and of Guimaras Island. Field inspection was conducted last April 15 to 19, 1999 by personnel from the MGB-Central and its Region 6 Office. This research is a sub-project under the major project entitled "Analysis of AirSAR and TopSAR Datasets for Resource Management and Development Planning Activities". The project's developmental objective is to "promote the use of remote sensing technology for various applications relating to resource management and developmental planning activities. The purpose of this study is coastal environment and geologic studies. We used the data to: 1) geologically map Iloilo City and the surrounding coastal areas in reference to the major lithologic and structural units, and 2) study the coastal environment and the impact assessment of flood-prone areas.

2.0 DESCRIPTION OF THE STUDY AREA

The study area is located in the southeastern coast of Panay Island and the northern part of Guimaras Island. From northeast to southwest, the major towns and cities in Iloilo are Dumangas, Zarraga, Leganes, Jaro, Iloilo City, and Oton. South of Iloilo City and separated from it by the Iloilo Strait is Guimaras Island. Panay and Guimaras Islands are portions of Visayas Islands that are found in the Central Philippines.

The AirSAR swath image has dimensions of 40.5km x 8.5 km, with the land area along coastal Iloilo is roughly 265 sq. km while that in Guimaras is roughly 32 sq. km (Figure 1).

Iloilo is a flat to almost flat relief of broad and poorly drained alluvial plain. Alluvial deposits of river and beach deposits of Recent age (GOP, 1996) comprise this wide plain. Cabatuan Formation underlains the plain with a series of sandstone, siltstone and mudstone. Much of the alluvial plain is cultivated for agricultural rice. The major cities and towns are also built on this plain. The major river systems in the Iloilo area are the Jalaud River in the northeast, the Jaro River and Iloilo River in the

southwest. The last two rivers pass through Iloilo City. The coast has tidal flats and are used as fish pens and ponds.

In Guimaras, the study area ranges from sea level to 100m elevation. The area has many low relief hills and gentle slopes wherein forest covers the rolling hills. A diorite body intrudes the dominant limestone lithology (Abundo, et al, 1998). Quaternary alluvium is abundant along the coast. The dominant land uses are similar to that in Iloilo.

3.0 METHODOLOGY

3.1 Field Investigation and Data Integration

We produced preliminary maps after some preliminary interpretations were made. We conducted a fieldwork in Iloilo and Guimaras to verify the features observed in the AirSAR image and the accuracy of our preliminary maps and mapped the geologic and the geomorphologic terrain of Iloilo and Guimaras. We compiled all field data and updated all our preliminary maps. We compared and updated maps with the reference geologic and geomorphologic maps. The results of the image analysis, field investigation and data integration are presented in this report.

3.2 Image Processing

We used the Environment for Visualizing Images software (ENVI) version 3.1 to analyze the AirSAR data. We decompressed and synthesized all data of C-, L- and P-bands HH, VV, and HV polarizations, with an additional "total available power" band, from the Stokes Matrix compression. We corrected 12 bands all synthesized data, from slant to ground range and registered the corrected data to the map using ground control points (GCPs) from global positioning system (GPS) measurements in the field. The registered image is shown in figure 1. The C-, L- and P- bands were assigned to the Red-Green-Blue (RGB) color composite, respectively. We visually interpreted the image for geologic and geomorphologic features. From the main registered image, we selected three test areas for analysis namely, 1) in Dumangas, 2) in Oton and 3) in northern Guimaras (Figures 2,3 and 4). Using the subset command in ENVI, we created output files, enhanced each subset using interactive stretching and the lee filter and then interpreted each image.

4.0 RESULTS AND DISCUSSION

4.1 Geologic and Geomorphologic Investigations

Quaternary Alluvium underlains Iloilo and composed of unconsolidated sand, silt, pebbles, and cobbles with broken shells and foraminefera. These are found on the floodplains, along the coast coasts and mouths of the rivers. Pebble- to cobble sized deposits predominate along the Oton coast and Guimaras Island inlet bay areas. The **Dingle Limestone** in Dumangas occurs as 25m low hill, and set against flat alluvial plain background. It is cream to gray in color, hard but fragmental in portions and has interbeds of coarse-grained sandstone. The **Buenavista Limestone** in Guimaras outcrops along the northwest coast, buff to gray-brown in color, appears massive and fossiliferous with some hexacorals partly replaced with calcite. It gently dips to the northwest with typical karst feature. The **Guimaras Diorite** composed of the minerals hornblende, feldspar (some show pinkish alterations), plagioclase (at times replaced by silica) vuggy quartz and pyrite disseminations. When weathered it shows oxidation and alteration to clay minerals. The outcrops in the northern and western part of Guimaras are low-lying hills, mounds and peaks ranging in elevation from 150m to 200m (Calomarde, 1987).

We identified homogenous landform association related to terrain characteristics using the parameters: genesis, relief and sediment type. First is the "fluvio-denudational landform", an alluvial and slope debris association (Javelosa, et al, 1994) from the base of western range of Panay Island to gently sloping alluvial plains, and cultivated for rice and floodplain areas used as fishponds. Second is the "fluvial landform" mainly by river actions. Northeast of Iloilo City, relief morphology is flat/almost flat where point bars, natural levees, backswamps and abandoned channels exist. The gentle slopes and high suspended load to bed ratio of sediments in the river system favor the meandering nature of the rivers. Alluvial, channel and overbank complexes, channel floodplain associations and natural levee are also observed within city limits. General relief is flat/almost flat. The third is "fluvio-marine landform" due by interaction of fluvial and marine processes along the coast, 10km northeast of Iloilo City. These are mostly active tidal flats, some are used as salt beds, and are gently sloping towards the Iloilo Strait marked by the wide tidal and fluvial channels in other areas.

In Figure 1,"broad fluvial-denudational landform" is in red color at the left side of the image. The high backscatter of agricultural crops in C-band is responsible for the red color. Fluvial landforms in bluish white delineate the river dominated areas. The dark sinuous patterns are meandering channels of main rivers and their tributaries. The fluvial-marine landforms have the active and relict tidal flats as salt beds and marine cultures. The tidal flats appear as dark colored areas with bright linear features of fish pens.

In terms of impact assessment for flooding hazard, the fluvio-marine environment is prone to frequent flooding mainly due to its low relief and geomorphologic setting. The next area prone to flooding is the fluvial environment. The rivers carry the flood waters and spills it over its banks. This area includes Iloilo City. We also noted the transgression of the sea inland to form inland tidal flats in Oton.

4.2 Image Processing Analysis on Test Areas Observations

Surface roughness is measured in centimeters and determined by textural features comparable in size to the radar wavelength, such as leaves and twigs of vegetation and sand, gravel and cobble particles (Sabins, 1987). The Dingle Limestone (blue outline) in Dumangas test area (Figure 2) shows a bright area in relatively dark areas. Its surrounding plain has agricultural crops and gravel (Lituanas, 1999) with actual size range of 2cm to 15cm of the AirSAR sensors, and show up as bright areas in C- and L-band but darker in the P-band. The limestone produces a backscatter related to its topographic relief. Thus, it shows up as a bright area in all 3 bands. Using Table 1, an object has to be >18.64cm to be rough and exhibit a bright response for the P-band. Anything that is <18.64cm will show up either as intermediate (gray color) or smooth (black). By contrast, if L- and C-bands are used, an object needs only be >1.56cm and 6.85cm to be rough and exhibit the same response. Since the vertical size range of the agricultural crops and the gravel is 2cm and 15cm, they also show up as bright areas in L-band and more so in the C-band. Thus, marking the limestone hill will be difficult in the C- and L-bands but not in the P-band. In the P-band, the hill is outlined by its bright response against the dark response of the alluvial plain with its vegetation and gravel.

In Oton test area (Figure 3), bright areas in the center image are newly developed urban areas. The rectangular-shaped, light toned objects on the right are agricultural areas. The dark areas in the upper part are land submerged in water due to the sea's transgression inland forming tidal flats. The beach area of sand and gravel deposit shows uniform intermediate response to the L-HH band, bright in C-HH band and dark in the P-HH band. Using Table 1, we can deduce the beach sand deposits in the range of 1.21cm and 6.8cm (intermediate). Pebble- sized sands and cobbles have composite size range of 0.4 cm to 25.6cm. These form a series of micro-ridges that lie sub-parallel to the curve of the coastline as outlined. It can be deduced that these are series of deposition of sediments parallel to the coastline caused by the interaction of the land and the sea. The relative uniformity of the size range is due to the winnowing effect of the waves. This explains the relatively uniform intermediate response in the L-HH image. Multi-band radar is useful in estimating surface relief of materials. We can state some of the process that took place in the past by observing closely the patterns of lineation on the coast, and correlating it with field observation.

The Guimaras test area (Figure 4) provides the radar data for lithologic terrain mapping. Geologic structure and erosional characteristics of underlying rocks control the topography. The Buenavista Limestone (50m to 80m el.) in white outline, exhibits a pitted texture of karst topography (Sabins, 1987) and has some bedding that forms asymmetric ridge. The beds dip gently to the northwest. On the lower right of the image is the Guimaras Diorite identified in the field as quartz diorite porphyry. It has a higher relief than the limestone, producing a bright backscatter and shows no definitive pattern. On the upper part is the Quaternary alluvium that exhibits a fine texture, dark gray color and forms as fringe on the northwest side of the limestone.

5.0 SUMMARY AND CONCLUSIONS

In the test areas, we demonstrated that multi-band radar data could help approximate the surface relief of materials in the field by describing the relief in terms of surface roughness derived from the Modified Rayleigh Criterion. Such relief correlates with signatures in the radar image. By observing closely the patterns of lineation in the Oton coast image and by correlating it with field observation, we could deduce some of the process that took place in the past.

We demonstrated that L-band radar is useful for recognizing major lithologic terrain in a tropical environment such as in Guimaras. These are (1) the Buenavista Limestone - karstic, gently dipping and fossiliferrous limestone in north and northwest

Guimaras (2) the Guimaras Diorite – as low-lying hills and mounds in northern and central parts; (3) and the Quaternary Alluvium – the sediments along the coast, along river deltas and active tidal flats.

We also showed that AirSAR image is useful for geomorphologic terrain mapping. We identified three landforms namely, the fluvio-denudational, the fluvial and the fluvio-marine landforms. Lastly, by comparing the present image with an existing reference map, we can detect changes in the land cover and in the geomorphologic setting of the area. In terms of impact assessment for flooding hazard of the three terrain, the fluvio-marine environment is prone to frequent flooding mainly due to its low relief and geomorphologic setting. The next area prone to flooding is the fluvial environment.

6.0 ACKNOWLEDGMENT

We thank the DOST-PCASTRD for the generous financial support to this project. We also thank our colleagues at the MGB Central Office and Regional Office No.6, personnel from NAMRIA and UP-TCAGP for joining us in the field. We also appreciate Mr. Bobby Crisostomo of NAMRIA for his leadership in this project.

7.0 REFERENCES

Abundo, R.V., Parringit, E., Domingo III, D.S. and Lituanas, M.B., 1998. AirSAR Capability to Geomorphology and Geologic Mapping Application. *Proceedings of the 19th Asian Conference on Remote Sensing*, pp. J-2-1 – J-2-5, Manila, Philippines.

Calomarde, R.I., 1987a. Geology and Geomorphological Terrain Classification of the Guimaras Island, Iloilo City. Mines and Geosciences Development Services Regional Office No. 06, Iloilo City, Philippines.

Evans, D.L., Farr, T.G., Van Zyl, J.J., Zebker, H.A., 1988. Radar Polarimetry: Analysis and Applications. *EEE Transactions on Geoscience and Remote Sensing,* **26**, pp.774-789.

Geology of the Philippines,1996. Unedited version. Mines and Geosciences Bureau.

Hewson, R.D and Taylor, G.R., 1995. AirSAR Imagery as an Ancillary Data Set for Geological Mapping and Fowlers Gap, Western New South Wales. *Proceedings of the International Workshop on Radar Image Processing and Applications held in the UNSW, Sydney in November 6-8, 1995.*

Javelosa, R.,1994. Report on the Quaternary Geological and Geomorphological Survey of Iloilo City. Mines and Geosciences Bureau, Quezon City, Philippines.

Sabins, Jr., F.F.,1987. *Remote Sensing: Principles and Interpretation*, 2nd ed. (New York: W.H. Freeman and Company).

8.0 TABLE AND FIGURES

Table 1. Summary of the calculation results for the AirSAR bands using the Modified Rayleigh Criterion (Peake and Oliver,1971) at a look angle of 56^0. Values are in cm. H refers to the vertical height of the object

Category	C-band	L-band	P-band	Signature as observed In the image
Smooth	H< 0.275	H<1.21	H<3.28	Dark
Intermediate	1.56<H<0.275	6.85<H<1.21	18.64<H3.28	Shades of gray
Rough	H>1.56	H>6.85	H>18.64	Bright white

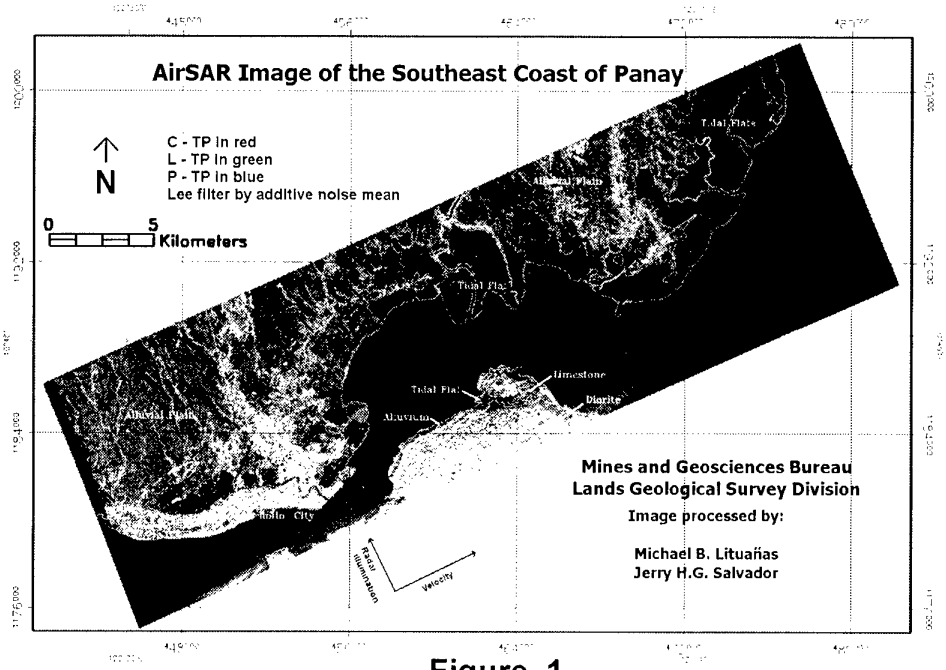


Figure 1

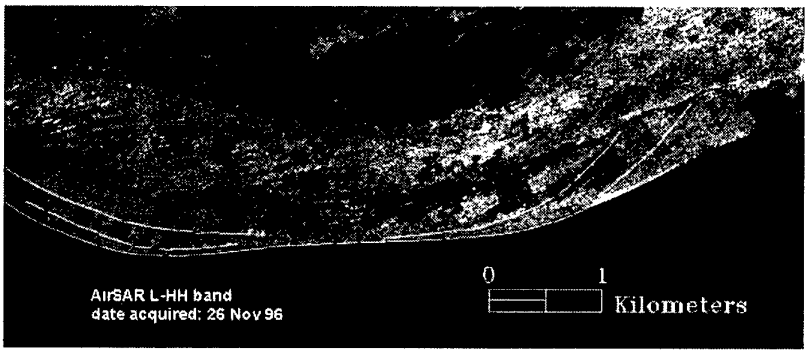


Figure 3: Oton Coastline

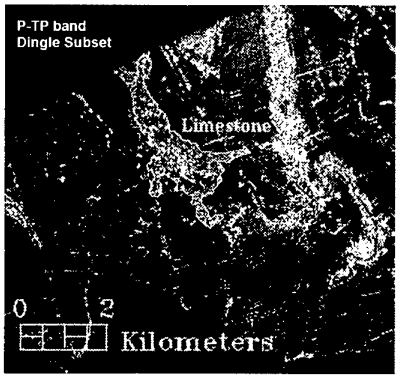


Figure 2: Dingle Limestone

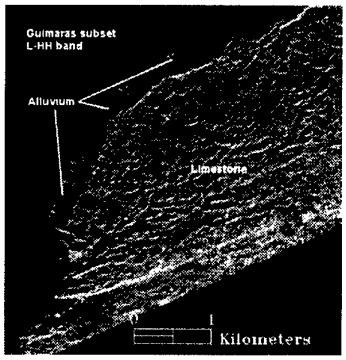


Figure 4: Guimaras Diorite

An introduction of ASTER (The Advanced Spaceborne Thermal Emission and Reflection Radiometer) for the Earth observation

Masatane KATO, Yuichi MARUYAMA, Makoto TSUKADA
Earth Remote Sensing Data Analysis Center (ERSDAC)
3-12-1, Kachidoki, Chuo-ku, Tokyo 104-0054
Tel:(81) –3-3533-9380 Fax: (81)-3-3533-9383
E-mail: kato@ersdac.or.jp, maruyama@ersdac.or.jp, tsukada@ersdac.or.jp
JAPAN

KEYWORDS: ASTER, VNIR, SWIR, TIR, EOS, Global Mapping, Stereoscopic data

ABSTRACT : ASTER, the successor to the Japanese Earth Resources Satellite-1 (JERS-1) launched in 1992, is a high-resolution multi-spectral imaging sensor, developed by MITI (Ministry of International Trade and Industry) , covering from visible to thermal infrared region. ASTER Project is a joint project carried out by MITI/ERSDAC and NASA to contribute the extensive understanding of the Earth as a system through NASA's EOS (Earth Observing System) Program. ASTER was successfully launched from Vandenberg Air Force Base on December 18th, 1999 as a one of the sensors of the 'TERRA' satellite of EOS Flagship. After launch, ASTER ICO(Initial Check-Out) were conducted by ASTER three projects, Instrument/Science/GDS(Ground Data System) project. The function check for ASTER sensors were carried out by ASTER Instrument project, the calibration/validation for the data processing/scheduling algorithm by ASTER Science project, and the performance check for all ground data systems by ASTER GDS. ERSDAC is involved with the ASTER Mission operation and data processing and distribution. The acquired data are processed in ASTER GDS (Ground Data System) at ERSDAC as various data products from level-1A to level- 4. Users of ASTER can confirm the data acquisition and make a request through the following web site.
http://www.ersdac.or.jp
ERSDAC coordinated the public solicitation of researchers to use ASTER data, called ASTER Announcement of Opportunity (ASTER AO). Any and all researchers, scientists, and research organizations are welcome to submit research proposals for non-profit and peaceful purposes to use ASTER data. They will be privileged to obtain a certain amount of ASTER data and to submit the data acquisition requests (DAR). ASTER data will be distributed to all users on a nondiscriminatory basis for peaceful purposes in consistent with national laws and regulations.

1. INTRODUCTION

ASTER Program is to make contribution to extend the understanding of local and regional phenomena on the Earth surface and its atmosphere through EOS Program, a comprehensive each observation program led by NASA of USA and is executed jointly by the Ministry of International Trade and Industry, Japan (MITI) and NASA. MITI has the responsibility of the development and operation of a sensor which is called ASTER (Advanced Spaceborne Thermal Emission and Reflection Radiometer) and the ASTER Ground Data System, while NASA has the responsibility for the development and operations of the platform. Both parties have the

responsibility for the ASTER data processing, distribution and archive.
In order to execute this joint project, ASTER Science Project along with ASTER Science Team, ASTER Instrument Project, and ASTER Ground Data System Project have been established.

2. ASTER INSTRUMENT

ASTER is a high-resolution multi-spectral imaging sensor with visible-near infrared, short wavelength infrared and thermal infrared spectral bands. ASTER was launched on December in 1999 as the one of the sensors of the NASA's 'TERRA' which was the first satellite of the EOS program.

Table 1 'TERRA' Orbit Parameters

Item	Specification
Orbit	Sun Synchronous
Local time at equator	10:30±15min.am
Altitude range	705 km at equator
Inclination	98.2° ± 0.15°
Repeat cycle	16 days (233 revolutions / 16 days)
Distance between adjacent orbits	172 km
Orbit period	98.9 min
Mission life	6 years
Sensors on 'TERRA'	ASTER: Advanced Spaceborne Thermal Emission and Reflection Radiometer CERES: Clouds and the Earth's Radiant Energy System MISR : Multi-angle Imaging SpectroRadiometer MODIS : MODerate-resolution Imaging Spectroradiameter MOPITT: Measurements Of Pollution In The Troposphere

ASTER is comprised of 3 subsystems, VNIR (Visible and Near Infrared Radiometer), SWIR (Short Wavelength Infrared Radiometer), TIR (Thermal Infrared Radiometer). The main characteristics of ASTER are;

(1) **High spectral resolutions**: 3 bands over VNIR region, 6 bands over SWIR region and 5 bands over TIR region.

(2) **High spatial resolution**: VNIR 15m, SWIR 30m and TIR 90m.

(3) **Along track stereoscopic data acquisition capability**: Base/Height=0.6.

(4) **Cross track pointing capability**: VNIR ±24° , SWIR ±8.55° , TIR ±8.55° . The swath of ASTER is 60 km and narrower than the orbital spacing (172 km). It can, however, observe the entire globe by using this pointing capability. Although the repeat cycle of 'TERRA' is 16 days, the global observation cycle of ASTER is 48 days due to its swath. ASTER can perform an emergency observation within 5 days (worst case) using the ±24° pointing capability of VNIR.

Although the mission operation of ASTER is mainly in daytime because of an optical sensor, TIR can observe the thermal emissivity in nighttime and if temperature of a target such as lava is high enough, it is observed by SWIR as well. Table 2 shows main characteristics of ASTER.

Table 2 Main characteristics of ASTER

Item	Specification
Spatial resolution	VNIR: 15m(Bands 1-2, 3N&3B*) 0.52 - 0.86 μm SWIR: 30m(Bands 4-9) 1.60 - 2.43 μm TIR : 90m(Bands 10-14) 8.125 - 11.65 μm
Base-to-height ratio of stereoscopic capability	0.6 (along-track)
Swath width	60 km
Pointing function in cross-track direction	VNIR: ±24 deg. (Bands 1-3) SWIR: ±8.55 deg. (Bands 4-9) TIR : ±8.55 deg. (Bands 10-14)

3. MISSION OPERATION

The operation of the ASTER will be affected by various constraints such as duty cycle (average 8 minutes/orbit) and pointing frequencies. Moreover, many possible combinations of the observation modes complicate the data acquisition scenario. Therefore, it is necessary to optimize the operation scenario for efficient data acquisition during the 6-year mission period.
There are three data acquisition request categories; DAR (Data Acquisition Request), STAR (Science Team Acquisition Request) and ETR (Engineering Team acquisition Request).

(1) DAR: DARs correspond to the bcal observations requested from individual investigators selected through authorized process by ASTER Announcement of Opportunity (AO)

(2) STAR: STARs correspond to the observations requested from ASTER Science Team and are divided into three sub-categories; Global Mapping (GM), Regional Monitoring (RM) and Local observation

1) Global Mapping (GM) is to make a global data set comprised of a single set of images covering the entire global land surface using all channels including stereo, of each subsystem. For GM, a global prioritization map is shown in Fig.1.

2) Regional Monitoring (RM) is to make regional data sets necessary to perform a large area and/or multi-temporal analysis of a region such as a study over several years of the advance.

3) Local Observation is to observe a spatial and time limited target (Ex. Volcano eruptions of Mt. Usu/ Mt. Miyake, Flooding at Nagoya in Japan this year etc.) .

(3) ETR: ETRs correspond to the observations requested from ASTER Instrument Team for the check of the health and safety and the performance of the Instrument including on board calibration data acquisition.

The scheduling for mission operation is established once a day using the ASTER Scheduler algorithm based on the prioritization of the data acquisition requests. Prioritization is done considering the factors such as user category and observation category. The schedule is fixed

27 hours before the start of the observation day.

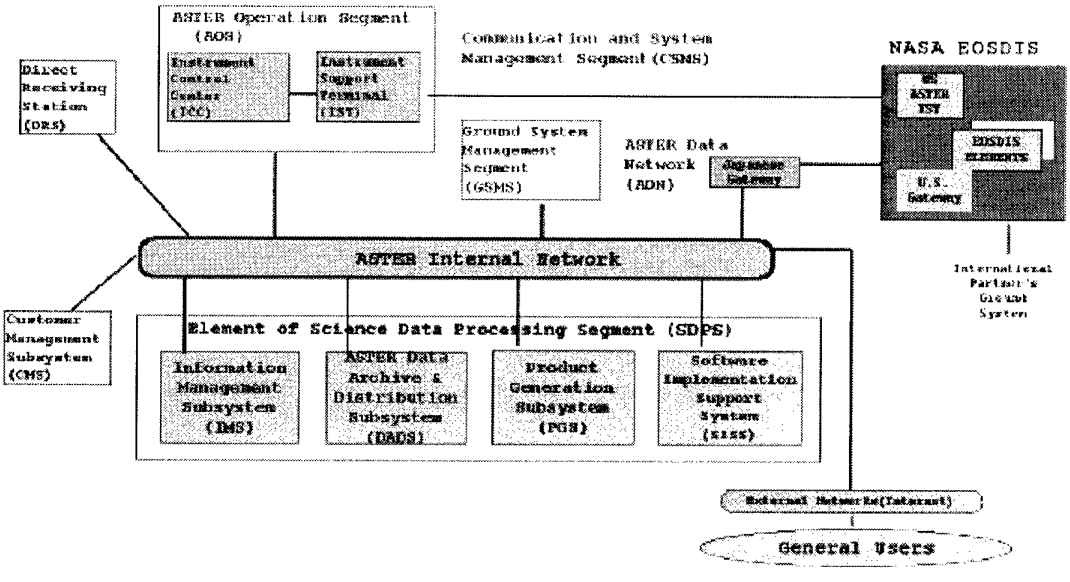
4. ASTER DATA PRODUCTS

The ASTER data products, such as Radiance registered at sensor, Surface radiance, Surface temperature, Surface emissivity, Surface reflectance, Radiance registered at sensor with ortho-photo correction, Digital elevation model (Relative) and so on, are developed by ASTER Science Team and distributed by ASTER GDS(Ground Data System).

5. ASTER GROUND DATA SYSTEM

ASTER Ground Data System (ASTER GDS) , located at ERSDAC in Japan, is the ground system for ASTER operation, data processing, data archiving and distribution. The ASTER GDS plays an important role in the sensor operation by ASTER Operation Segment (AOS) and data processing by Science Data Processing Segment (SDPS), and network and manage entire ASTER GDS by Communication and System Management Segment (CSMS) and requires close coordination with NASA/GSFC(Goddard Space Flight Center) / EOSDIS (EOS Data and Information System). ASTER GDS has important interfaces with the users by Information Management Subsystem (IMS) as well as with the United States. Configuration of ASTER GDS is comprised with 3 segments that are shown in Figure 1.

Figure 1 Configuration of ASTER



6. ASTER IMAGES OBSERVED IN ICO PERIODS

After launch, some ASTER images were observed in the Initial Check-Out phase. Two ASTER images, one is VNIR image at San Francisco in USA and another TIR image at Rift Valley in

Ethiopia, are shown in Figure 2 and Figure 3 respectively. VNIR images in San Francisco, whose ground resolution is 15m, make it possible to discern Golden Gate Bridge, buildings, streets, and golf courses, etc. On the other hand, TIR images in Rift valley show distinction between rocks such as andesite and basalt based on the emissivity.



Figure 2 VNIR Image in San Francisco,USA

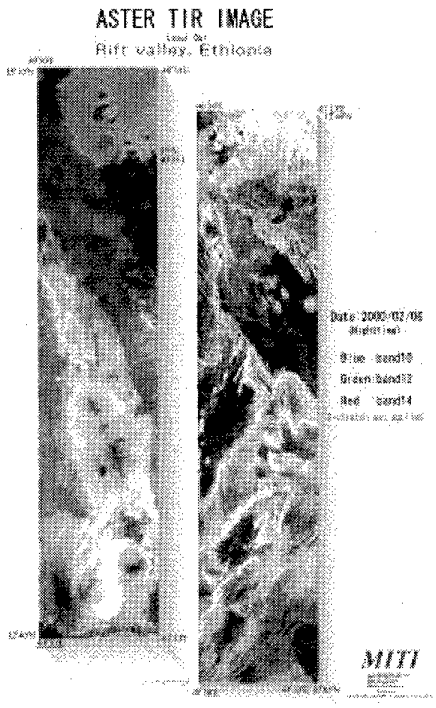


Figure 3 TIR Image in Rift Valley in Ethiopia

5. ASTER ANNOUNCEMENT OF OPPORTUNITY

ERSDAC coordinates the public solicitation of researchers to use ASTER data, called ASTER Announcement of Opportunity (ASTER AO). Any and all researchers, scientists, and research organizations are welcome to submit the research proposals for non-profit and peaceful purposes to use ASTER data. They will be privileged to obtain a certain amount of ASTER data and to submit the data acquisition requests (DAR). ASTER AO has already started and proposals will be accepted over the WWW (http://astweb.ersdac.or.jp/ao/) and through regular mail (Post).

6. DATA POLICY

ASTER data is distributed according to IEOS (International Earth Observing System) Data Exchange Principles in consistent with national laws and regulation, i.e.;

- All ASTER Data is available for peaceful purposes to all users on a non-discriminatory basis and in a timely manner.
- All ASTER Data is available for the designated users at the lowest possible cost for

non-commercial use on the following categories: Research, Application, and Operational Use for the Public Benefit. For purposes other than above, the specified data is made available in accordance with terms and conditions to be established by the Data Providing Agency.

7. CONCLUSION

ASTER Program is executing ASTER GDS Project as well as NASA and ASTER Instrument Project intensively in cooperation with ASTER Science Project along with ASTER Science Team. The contribution to making clear the process of an environmental change on global scale and to forecasting the future of a global environment by ASTER data observed after launch, depends on the results of research in various fields by not only academic users but also practical users.

8. ACKNOWLEDGEMENTS

The author is also grateful to NASA and MITI for their support in the EOS and ASTER programs.

9. REFERENCES

1. T. Kawakami, "ASTER Program Overview", *Proc. SPIE,* Vol.3502, pp23-29, 1998.

Photogrammetric Digital Data Processing of Tsau-Lin Big Landslide

Hsin-Hsing Cheng

Engineer, Water Conservancy agency No.501, Li-Ming rd Taichung Taiwan
Tel:886-4-2501217 Fax:886-4-2523223 E-mail:chh@wca.gov.tw

abstract

After the serious 921-Tsau-Lin Earthquake, it's necessary and urgent to know the landslide condition and to handle the effectiveness of the silted earth mass on its upper and lower stream channel. Those data have been urgently concerned about engineering field. To integrate the aerial photogrammetric photograph, GIS and image processing software, and modeling 3-D image, drown range delineation, the overtopping height calculation and the storage water volume etc., we can finish the preprocessing operation. Next, to create the 10m*10m resolution DTM of the site before and after the earthquake. Finally, to overlap that coverage's we have finished, we can get the reliable volume of landslide.The purpose of this article is to make a complete introduce the results and some important procedures how we utilized the scientific technique of aerial photogrammetry, image processing and geographic information system etc. Finally, we made a real and complete record about the important digital information of Tsau-Lin landslide.

Key words: landslide, digital photogrammetry, digital terrain model (DTM).

1.Introduction

A largest earthquake of this century in Taiwan occurred on September 21, 1999 and caused deaths of more than 2,000 human lives and loss of billions dollars worth in houses, buildings, roads, bridges and dams. This disastrous earthquake also induced 2,365 landslides and soil mass movements with total area of 14,000 ha. After the serious earthquake of central Taiwan, the biggest one, landslide dammed the Chin-Shui-Chi River and formed Tsau-Lin reservoir, it's necessary and urgent to know the landslide condition and to handle the effectiveness of the silted earth mass on its upper and lower stream channel and the mud disaster that may caused owing to the silted earth mass. Those data have been urgently concerned about by both research institute and engineering field such as: the location, area and the volume of the silted earth mass, the drown range of water, the over flow height, and the storage water volume. To integrate the aerial photogrammetric photograph, GIS and image processing software, and modeling 3-D image, drown range delineation, the over flow height calculation and the storage water volume etc., we can finish the preprocessing operation. Next, to create the 10m*10m resolution DTM of the site before and after the earthquake. Finally, to overlap that coverage's we have finished, we can get the reliable volume of silted earth mass.

The purpose of this article is to make a complete introduce the results and some important procedure how we utilized the scientific technique of aerial photogrammetry, image processing and geographic information system etc. and quickly to handle the field situation and processed the relative

digital data. Finally, we made a real and complete record about the important digital information of Tsau-Lin landslide. The emergency treatment project to reduce the disaster can be determined helpfully and rapidly.

2.The history of Tsao-Ling landslide.

According to the documents, the Tsao-Ling landslides were decided by seismic and intense rainfall factors, the another factors were topography, soil, geology, and active fault zones.

An unusual series of events illustrating the formation and destruction of a landslide dam has been documented for the Tsao-Ling landslide in central Taiwan. This case demonstrates just how complex natural dam processes can be. In June 6,1862, a major earthquake triggered a landslide that dammed the Chin-Shui-Chi River. In 1898, the natural dam failed for unknown reasons. In December 17, 1941, a major earthquake formed another landslide dam, 140 m high, at the same location. In August 10, 1942, heavy rainfall caused reactivation of the landslide and the natural dam increased in height form 140 to 217 m. In May 1951, several days of intense rainfall led to the overtopping and failure of the natural dam. In the subsequent flood, 154 people were killed and 564 homes damaged. On August 15,1979, heavy rainfall again activated the landslide, which dammed the river with a natural barrier 90 m high. Heavy precipitation continued, and 9 days later, the landslide dam was overtopped and failed, causing severe flooding (Costa and Schuster 1988).

In September 21,1999, Richter scale 7.3 earthquake formed landslide dam again, the detailed landslide data were gathered rapidly by integrating aerial photogrammetry and GIS. The main data of Tsao-Ling Landslide are shown follow ：a. Deposit Height of Upstream：50m (EL.539.6m), b. Area of Upstream Watershed：162Km^2, c. Landslide Area：620ha, d. Deposit Distance：5Km, e. Landslide Volume：126 million M^3(Cut) and 150 million M^3(Fill), f. Lake Volume：46 million M^3, g. Overtopping Elevation：EL.539.6m, h. Second pond volume：4.99 million M^3 for EL.520.4 overtopping, 3.4 million M^3 for EL.515 overtopping.

3. Processing of created DTM of before and after landslide

In order to compare the surface deformation before and after landslide, it's
rapid method to create the high resolution Images and DTM of the site, before and after the earthquake. We can compare, overlap, and calculate with these digital data conveniently and precisely. The detailed flow chat is shown as figure 1.

3.1 Photogrammetry

Photogrammetry was invented in 1851 by Laussedat, and has continued to develop over the last 140 years. The development of photogrammetry has passed through the phases of plane table photogrammetry, analog photogrammtry, analytical photogrammetry, and has now entered the phase of digital photogrammetry (Konecny, 1994). In analytical photogrammetry, the computer replaces some expensive optical and mechanical components. The resulting devices were analog/digital hybrids. Analytical aero-triangulation, analytical plotters, and ortho-photo projectors were the main developments during this phase. Outputs of analytical photogrammetry can be topographic maps, but

can also be digital products, such as digital maps and DEMs. Digital photogrammetry is photogrammetry as applied to digital images that are stored and processed on a computer. Digital images can be scanned from photographs or can be directly captured by digital cameras. Many photogrammetric tasks can be highly automated in digital photogrammetry (e.g., automatic DEM extraction and digital ortho-photo generation) (IMAGINE Tour Guide 1998). A strip of photographs consists of images captured along a flight line, normally with an overlap of 60%~70%, with a sidelap of 20%~30%(figure 2, figure,3). Especially for mountain area the overlap and sidelap more will be better. Strips and exposure points have been calculated so that the specifications concerning overlapping and total ground coverage is being fulfilled.

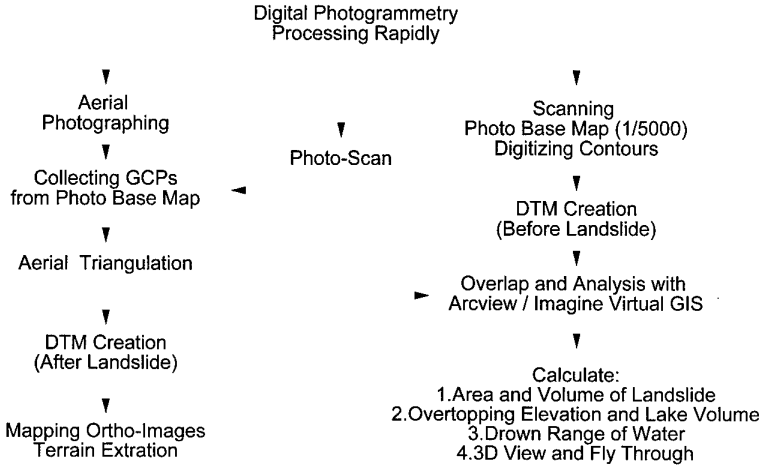


Figure 1 、processing flow chat

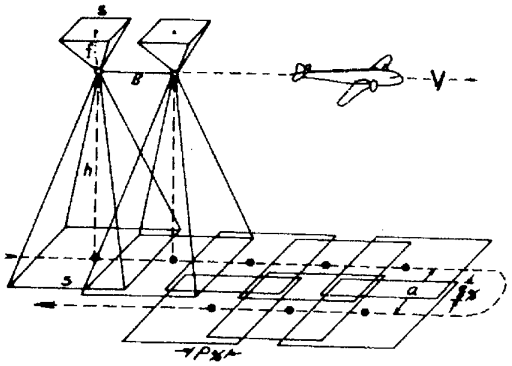


Figure 2 、strip of photographs desigh

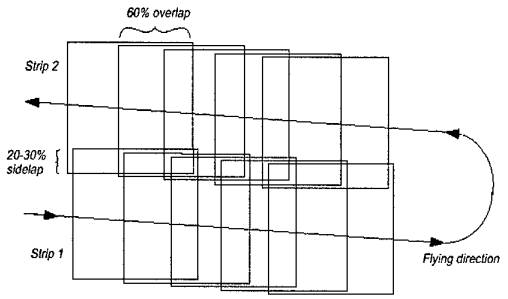


Figure 3 、overlap and sidelap area (IMAGINE Tour Guide 1998)

In July 1975, the Executive Yuan approved a project for producing large -scale photo base map covering all of Taiwan. Aerial photo and mapping works are executed by the Agricultural and Forestry Aerial Survey Institute , Taiwan Forestry Bureau(RU, 2000). So, we have many existing base maps and aerial photos about the Tsao-Ling landslides to be applied. When the earthquake occurred, the Agricultural and Forestry Aerial Survey Institute have captured full disaster area color photo in late two or three days by good weather. The Tow-Lin survey company have completed creating DTM and

Maps in two days rapidly. Next we used these digital data integrating GIS and RS tools to obtain landslide area, volume, water volume, 3D view, and overtopping elevation, etc. Image measurement and calculations must be done rapidly and effectively in the emergency situation. Therefore there are needs to automate the measurements and to develop an effective user interface.

Each photograph or image that is exposed has a corresponding image scale associated with it. The image scale expresses the average ratio between a distance in the image and the same distance on the ground. It is computed as focal length divided by the flying height above the mean ground elevation.

$S_h = f/H-h$ S_h：Photo-Scale of Point h、H：Flying Height f：Focus length of Camera

This emergency tasks of aerial photographing with zeiss RC10 cameras, focus length 135.04mm, 1/10000 photo scale. The cameras that are used for aerial photographing are designed exclusively for that purpose. According to the single hardcopy color films that is approaching the real sight, we can interpreter and check the magnitude and area of landslide site rapidly, and we can also take a simple measurement for obtaining the location, situation, and disaster area information with the photo scale instantly.

3.2 Images Scan、mapping and ortho-photo

Though digital cameras have developed much the latest years they still cannot compete with the resolution of analogue cameras when it comes to aerial images. Thus the images has to be scanned to digital format before they can be used in digital photogrammetry applications. Photogrammetric quality scanners are special devices capable of high image quality and excellent positional accuracy. The required pixel resolution varies depending on the application. Aerial triangulation and feature collection applications often scan in the 10 to 30 micron range. Orthophoto applications often use 15 to 30 micron pixels. Color film is less sharp than panchromatic, therefore color ortho applications often use 20 to 40 micron pixels (IMAGINE Tour Guide 1998). Scanning aerial color film with high resolution following the procedure of mapping images, ortho-photo, and triangulation, stereo-pair model calculation by Tow-Lin company with high technology and computer, it's very efficiently. These task facilities as follows：

(1) VEXCEL Ultra Scan 5000：20 micron pixels resolution

(2) Leica SD2000 analytical

(3) VirtuoZo Digital Images Workstation

(4) SGI Octane work station with 144G Disk Array

3.3 Results of Arial Triangulation

Owing to Earthquake-caused surface ruptured, and we can not survey the exact coordinate by GPS at the landslide site immediately, so we used 1998 (1/5000) 1980 (1/10000) photo base map to calculate the control points of the coordinate and height for triangulation. The results of Arial Triangulation are shown at Table 1.

Table1 、Results of Arial Triangulation

	TM2			error		
Number of Points	X-axis	Y-axis	elevation	X-axis	T-axis	elevation
A1	213357.202	2609402.837	323.592	-2.798	2.837	0.142
A2	212194.921	2609081.358	779.789	0.921	1.358	-0.311
A3	211974.992	2609272.138	756.735	2.992	-1.862	-0.615
A4	212692.065	2607412.883	427.478	0.065	0.883	-0.122
A6	217875.808	2609152.702	764.273			
A7	218260.828	2607654.870	522.190	-1.172	-5.130	-0.160
A8	217933.711	2608797.932	715.870	5.711	-2.068	0.770
A9	217967.963	2609634.568	856.824	-0.037	2.568	0.324
A10	216852.131	2607677.368	570.688	0.131	-2.632	0.588
A14	213390.126	2606605.351	656.569	0.126	-2.649	0.569
A16	212066.016	2609884.016	916.938			
A17	213910.384	2610729.050	330.253	-1.616	1.050	0.253
A18	218056.550	2606098.051	710.411			
A19	216305.210	2606227.056	1251.897	1.210	3.056	-1.103
A20	218156.072	2610030.099	960.040	-3.928	2.099	0.040
A21	220518.394	2607676.490	573.625	-1.606	0.490	-0.375

3.4 Created DTMs of before and after landslide

With the 10- m pixel size resolution that is enough to demonstrate the deformation of the landslide surface which is better than the existing DTM of 40- m resolution of Taiwan. For improving the accuracy and efficient, we have created the DTM of before and after landslide with 1998, 1/5000 photo base maps, with the same coordinate system and pixel resolution.

4. Applications of Photo-Images and DTM

We used these digital data integrating GIS and RS tools to obtain landslide area, volume, water volume, 3D view, and overtopping elevation, etc. Image measurement and calculations must be done rapidly and effectively in the emergency situation, by using IMAGINE VITUAL GIS and ARCVIEW GIS 之 3D model. The results of cut and fill area of the landslide shown as Figure 4. Overtopping Elevation and Water Volume can be calculated with RS tools, results shown as table 2, table 3 and figure 5. Applied the 3-D view and fly through also.

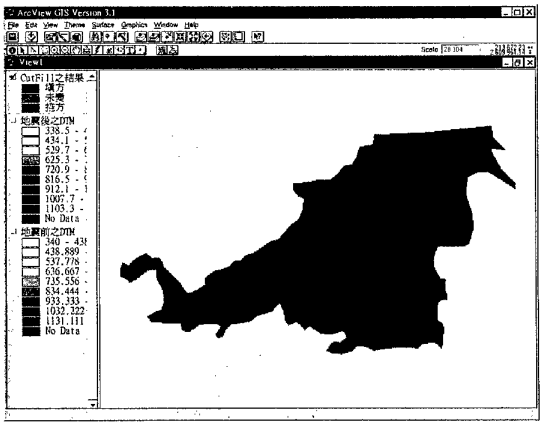


Figure4 calculation of the volume of landslide by Arcview 3D Analysis

(Blue : cut, Red :fill)

Table2、Modeling prediction of Volume and overtopping elevation of Dammed lake

Water elevation	Volume(m^3)	
527	28430.0	
528	29706.7	
529	31020.6	
530	32360.6	
531	33726.3	
532	35123.8	
533	36573.1	
534	38083.4	
535	39603.1	
536	41161.8	
537	42741.9	
537.5	43543.6	
538	44352.8	
538.5	45169.2	
539	45992.8	
539.6	46824.3	overtopping

Table3、Modeling prediction of Volume and overtopping elevation of second pond

Water Elevation	Volume(m^3)	
500.00	454,889	
505.00	1,123,360	
506.00	1,300,289	
507.00	1,489,370	
508.00	1,693,369	
509.00	1,908,209	
510.00	2,132,709	
511.00	2,368,199	
512.00	2,614,969	
513.00	2,872,049	
514.00	3,140,039	
515.00	3,419,429	Overtopping after Channeled
516.00	3,708,899	
517.00	4,011,479	
518.00	4,325,979	
519.00	4,652,739	
520.00	4,993,049	
520.40	overtopping	Original

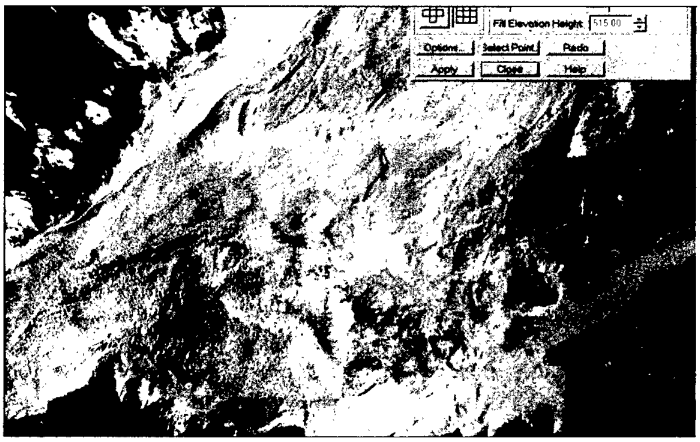


Figure 5 modeling submerged area and water volume by Erdas Imagine Virtual GIS water layer model



Figure 6 landslide full 3-D view

5. discussions

5.1 Because of the complex and variation of landcover in the mountainous area, differences between digital surface model (DSM) and digital terrain model must be suitful treated (Chen, 1999). Owing to the surface and feature of landslide area are clear, bright, and outshine, it's helpful to automatic feature based matching. Especially, the elevation will be accuracy more than other tree or creek area so that the widely Tsao-ling landslide area elevation measurement is very accuracy for calculating the overtopping height.

5.2 Photogrammetry is suitable and available for large disaster area mapping. In this case it just takes two days to complete entire landslide area mapping tasks.

5.3 The aerial photos were digitized with high resolution, and automatic aerial triangulation, automatic matching, 3-D stereo mapping were performed to apply digital photogrammetric mapping techniques to improve the accuracy of DTM while maintaining high-quality product and low-cost.

5.3 The results of photo automatic matching depend on photos likelihood, less ratio of base line and flying height, tone, and scanned resolution (Chen, 1999). The relations between Photo-Scale and Map-Accuracy are shown as Table 4.

Table 4、Relations between Photo-Scale and Map-Accuracy (Petrie 1990)

Photo scale	resolution @ 40 1 p/mm	Altitude of flight(m)	Map scale	Photo/map	Interval of Contours (m)
1:3000	0.075 m	450	1:500	6x	0.5
1:5000	0.125 m	450	1:1000	5x	1
1:10000	0.25 m	1500	1:2500	4x	2
1:25000	0.625 m	3750	1:10000	2.5x	5
1:50000	1.25 m	7500	1:50000	1x	10
1:80000	2.0 m	12000	1:100000	0.8x	20

5.4 The Taiwan Datum 1997 (TWD97) coordinate system is not used in this plan at the pre-period processing. The coordinates of control points are surveyed by GPS after 921 Chi-Chi earthquake. But in the late processing of the Tsao-lin digital data, we have added GPS data and have improved the accuracy.

6. Conclusions

6.1 We have successfully and rapidly integrated RS、Aerial photogrammetry、GIS、GPS to obtain digital data about the landslide. By Using produced DEM data, and arcview 3D Analyst model and Erdas Imagine Vitural GIS. We have estimated the total landslide area about 620 ha, a volume of about126 million m^3 (figure 1), storage water volume of the upstream about 46 million m^3 with overtopping EL.539.6m, the second pond volume about 3.14 million m^3 with overtopping EL.515m.

6.2 In addition to orthoimages, photogrammetry can also provide other geographic information such as a DTM, topographic features, and line maps reliably and efficiently. Photogrammetry produces accurate and precise geographic information from a wide range of photographs. Any measurement taken on a photogrammetrically processed photograph reflects a measurement taken on the ground. Rather than constantly go to the field to measure distances, areas, angles, and point positions, photogrammetric tools allow for the accurate collection of information from imagery. Photogrammetric approaches for collecting geographic information save time and money, and maintain the highest accuracy.

6. Reference

1、Taiwan provincial water bureau (1979) The history of Tsao-Ling landslide.

2、Ho, wei-sin (1995) Aerial photogrammetry.

3、Yeong-Kuan Chen, Jihn-Fa Jan, Yin-Lin Wu, Kuen-Sheng Yeh (1999) Automatic Matching of DTM for Forested Mountain Areas The 18th Symposium on survey and applications.

4、IMAGINE Tour Guide (1998) Photogrammetry and IMAGINE Orthobase, Chapter 2, pp.7-50.

5、Petrie, G..(1990), Photogrammetric Methods of Data Acquisition for Terrain Modeling, in Terrain Modeling in Surveying and Civil Engineering, Eds. G. Petrie, T. J. M. Kennie, Whittles Publishing, pp.26-48.

6、Ru, j. c. (2000), Production of photo base map in Taiwan, The 4th Symposium on GPS Technology, pp.181-193

7、Costa and Schuster (1988), The formation and failure of nature dams, Geological Society of America Bulletin, v.100, pp 1054-1068.

3D Digital Archiving System for World Heritage.

Kazuhisa INABA and Ryosuke SHIBASAKI
Centre for Spatial Information Science and
Institute of Industrial Science, The University of Tokyo
4-6-1, Komaba, Meguro-ku, Tokyo 153-8505, JAPAN
Tel and Fax:+81-3-5452-6417
E-mail; inaba@skl.iis.u-tokyo.ac.jp

Abstract

Currently to survey the remains like World Heritage, traditional surveying methods such as plane table surveying are used. But surveying is labor-demanding and, more importantly, not always appropriate to record objective data because these methods can only record objects which are supposed to be important by the surveyors. In addition, dynamic changes of the remains due to the excavation is hard to record with the traditional surveying method.

In this research, two new kinds of surveying methods --Laser scanner/CCD Camera system and Digital Video Camera with GPS/Gyro--are adopted. 3D spatial data with textural data will be obtained by Laser scanner and by CCD Camera respectively. For areas which are difficult to survey with the laser scanner system, Digital Video Camera with GPS/Gyro is applied which allows 3D data acquisition from sequential image from digital video. The Factorization method is used to estimate the motion of the digital video camera. To improve accuracy of the Factorization, camera position and attitude data from Gyro and GPS are used as complementary data.

We have conducted a field test of Suzaku-mon in Nara, Japan with the laser scanning system, and Tyle in Lebanon with the both system. In this paper, we discuss mainly about the matching methods of Laser Scanner with CCD Camera data and implementing methods for Factorization using Gyro and GPS.

Introduction

In surveying of the remains like World Heritage, traditional surveying methods such as plane table surveying are used. But this type of surveying is labor-demanding and time-consuming. And more importantly, not always appropriate to record objective data because these methods can only record objects which are supposed to be important by the surveyors. In addition, dynamic changes of the remains due to the excavation is hard to record with the traditional surveying method.

Aerial photogrammetic methods are also used. But it takes so much time that we can't check the result because excavation of the remains is going.

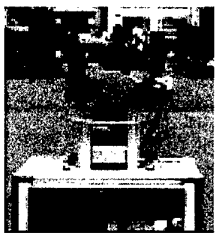
In other cases, Remains are going to be ruined or removed because of the construction such as the highway or building. With these kinds of changes, remains cannot be restored even if re-surveying for remains come to be required. Also from the viewpoint of preservation of remains, survey should be done as objectively as possible. At same time, digital technology enables us to distribute or share digital information very efficiently. We should explore the possibilities of other uses for digital data such as visualization or entertainment to people.

3D Digital Archive System has been developed for the improvement of the surveying. This system should give us labor/time saving., objective record and easy view of output. With this system, we can observe and measure the remains using PC in laboratory, not in the site.

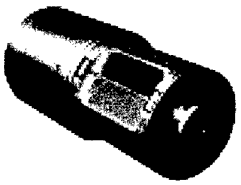
Measurement devices or simply Hardware

Two new kinds of data acquisition techniques are introduced in this research. One is Laser scanner/CCD Camera system and another is Digital Video Camera with GPS and 3 axial gyroscopes. The merit of Laser scanner/CCD Camera system is obtaining not only point data but also texture data, which make point data more visible or easier to interpret or handle. For example, checking of the registration of different images or views becomes easier than with only 3D point data. The demerit of this system is insufficient flexibility in moving from place to place. For the areas which are difficult to survey with the laser scanner system, Digital Video Camera with GPS/Gyro is applied which allows 3D data acquisition from sequential image of digital video. The Factorization method is used to estimate the motion of the digital video camera. To improve accuracy of the Factorization, camera position and attitude data from Gyro are used as complementary data. The GPS data will be used for record the position of the objects.

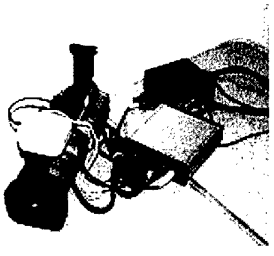
The pictures of the measurement devices which we used shown in



a) 3D scanner used in Nara



b) RIEGL 3D scanner



c) Digital Video Camera with GPS/Gyro

Figure1. Measurement devices

figure 1. Machine in figure 1a was used in Nara and owned by Shibasaki laboratory, CSIS, Univ. of Tokyo. This can obtain the point and texture data of the object. Picture1b shows RIEGL 3D scanner which can obtain additionally intensity data of laser. This intensity data will be useful for the image registration in dark places such as inside of the room. Figure-1c shows Digital video camera with GPS/Gyro sensor.

Applications

We have conducted a preliminary field test of Suzaku-mon (Suzaku-mon gate) in Nara, Japan with only laser scanning system, and a large-scale field survey of Tyre in Lebanon with the both system.

In Lebanon, we have conducted surveying for 4 sites, street area (Al Baas area), Hippodrome area, underground tomb (Ramali area) and City area. Because the construction of expressway has been planned in Ramali area, it is necessary to obtain and preserve the data.

Al Baas, Hippodrome and City site are outside. But Ramali is underground tomb and the inside is too dark to obtain true color image. Reflectors for survey are installed on walls and ceiling and intensity image of laser scanner will be used for range image registration, because it is difficult to find feature points in laser reflection intensity images without such the reflectors.



a) True color image b) Range image (colores with distance) c) Intensity image

Figure2. Image data of sensor

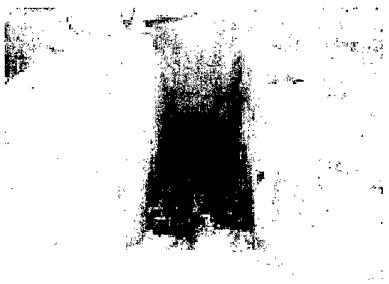


Figure3. Underground tomb in Ramali

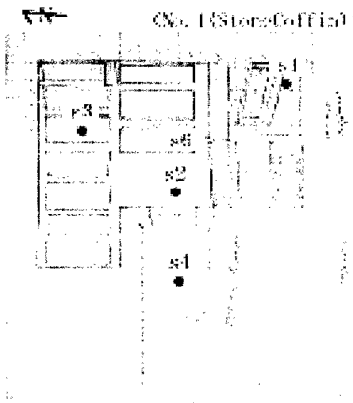


Figure4. Example of arrangement of survey points (Ramali area)

Image Registration System

Image Registration System among data sets from Laser system and 3D products from Digital video is being developed. But at present, Image Registration System between data from the laser scanning system and the digital video system is not completed. Then in this paper we discuss about the system for the data from laser system.

Algorithm

Figure5 shows the flow of the algorithm of Image Registration System for laser range data. Image Registration System has two parts, coarse registration and fine tuning.

Firstly, the coordinate of feature points will be selected manually in true color images. In the laser system, each coordinate on true color image should have spatial coordinate. Then the corresponding points will be selected and least square method with equation 1 will be applied to calculate the transformation between center of different survey points.

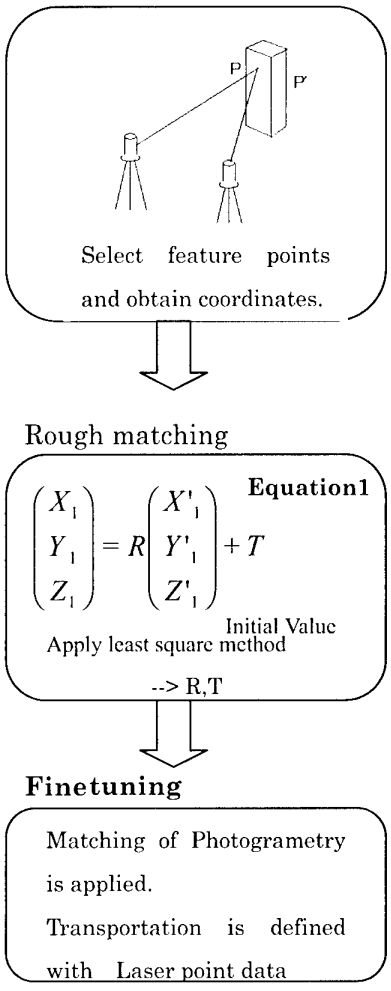


Figure5. Flow of the algorism fo image registration matching

Secondly, the output of previous registration will be used as initial conditions for more accurate estimation of transformation parameters with photogrammetric techniques. Since true color image have many feature points, high accuracy of matching is expected. The

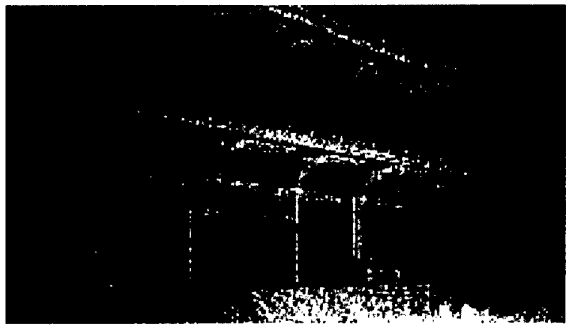


Figure6. Results of coarse registration of range images.

relative transformation calculated with the photogrammetric technique will converted to absolute value with Laser scanner data.

Output

Figure6 shows the output of first step of the Image Registration System for laser data. Since error is still left to some extent, fine tuning is needed.

Improvement of Factorization

The factorization method is used to estimate the motion of the digital video camera. (for the detail, Kanade, 19**) With the motion data of camera, stereo matching will be conducted to build 3D model. But the output of this method is not always good especially for building.

Outline of the algorithm of how to incorporate the data from Gyro into factorization is summarized in Figure6. We will report test results in the conference..

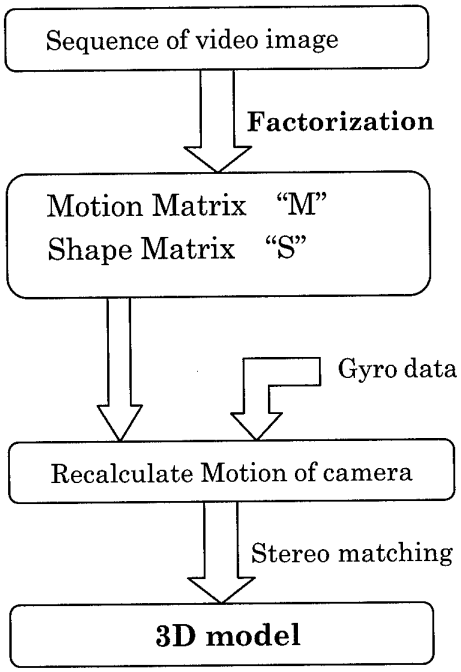


Figure7. Outline of algorism for Improvement of Factorization

Discussions and Conclusions

We discussed about the algorithm for the matching of data from Laser/CCD system. The same matching algorithm can be applied to registering laser data and 3D data generated from digital video data with factorization and stereo matching technique. At present, we are still processing Tyre data which are obtained by the survey in Lebanon this September. The results of generating 3D model of the Tyre remains will be reported in the conference.. We will also report the detail and test results of the algorithm for improvement of factorization using gyro data.

References

[1] Conrad J. Poleman and Takeo Kanade. A Paraperspective Factorization Method for Shape and Motion Recovery. CMU-CS-93-219 1993.

[2]Joao Costeira and Takeo Kanade. A Multibody Factorization Method for Motion Analysis. CMU-CS-TR-94-220
[3]JSPRS. Analysis for photogrammetic

The 21st Asian Conference on Remote Sensing
December 4-8, 2000 Taipei, TAIWAN

ON MODELING OF THE SAR-IMAGE SQUINT PARAMETER

Joz WU, Chia-Jun LIU
Center for Space and Remote Sensing Research
National Central University
Chungli 320
Tel: (886-)3-4227151-7626 Fax: (886-)3-4254908
E-mail: jozwu@csrsr.ncu.edu.tw
TAIWAN

KEY WORDS: Modeling, Squint Angle, Optimization, Accuracy.

ABSTRACT: By using radargrammetric (range/Doppler) equations for an SAR image, radar's trajectory polynomial modelings require statistical evaluation in order to determine the model optimality. Thus, a least-squares estimation technique, a parametric significance hypothesis testing, and the necessary optimization criteria are introduced, in detail enough for a basic algorithmic understanding. A second-order polynomial expansion is then employed to describe the time-varying squint-angle parameter. Experiments with an airborne SAR image reveal that the time dependence of an imaging radar squint parameter can have an impact on planimetric position accuracy, as would be expected. Capability to adequately model airborne/spaceborne SAR orientation parameters still merits research and development.

1. INTRODUCTION

A proper geometric image processing frequently relies on a sound functional model. For a side-looking SAR (synthetic aperture radar) image, consisting of sequential, scanned range-lines, a sound functional model again depends on some time-varying parameter descriptions. In most instances, time polynomial expansions can be used to describe the radar antenna's positions/velocities along a flight path (Lee et al., 2000; Tannous and Pikeroen, 1994; Toutin and Gray, 2000). This is logically done because the unknown position/velocity parameters explicitly exist in the radargrammetric (range and Doppler) equations. Other geometric parameters, such as the squint angle, the pixel spacing and the near-range slant delay, are less obvious as far as their time-dependent modelings are concerned.

This paper addresses a time polynomial modeling for the squint parameter and reports the planimetric accurary gain that can be expected. The least-squares estimator is statistical in nature, therefore sufficient control point coordinate measurements should be made available in an airborne SAR-image. Following a brief introduction of the necessary analytic equations, estimation results will be presented and analyzed.

2. ANALYTIC RELATIONSHIPS

In order to understand what our parameter estimation algorithm does, it is of interest to give the next relevant relationships.

2.1 Functional and Stochastic Models

For the geometric SAR-image processing, the range and Doppler (radargrammetric) conditions are of fundamental importance (Curlander et al., 1987; Dowman, 1992; Gelautz et al., 1998; Leberl, 1979):

$$R_{ji}=[(X_i-X_{oj})^2+(Y_i-Y_{oj})^2+(Z_i-Z_{oj})^2]^{\frac{1}{2}} \tag{1}$$

$$R_{ji}\sin\tau=u_x(X_i-X_{oj})+u_y(Y_i-Y_{oj})+u_z(Z_i-Z_{oj}) \tag{2}$$

$$R_{ji}=M_b r_{i,j}+R_n \tag{3}$$

where R_{ji} (m) is the slant range between the radar antenna position (X_{oj}, Y_{oj}, Z_{oj}) at station j and the object-space target position (X_i, Y_i, Z_i) at point i; see Figure 1 for notation illustrations (Wu and Lin, 2000). The squint angle τ (deg) is such as interpreted in Figure 2, where the instantaneous along-track antenna unit velocity (u_x, u_y, u_z) is also shown. In Eq. (3), M_b (m/pixel) stands for the pixel spacing. $r_{i,j}$ (pixels) is the i-th cross-track, pertaining to station j, image coordinate measurement. R_n (m) represents a constant slant range delay.

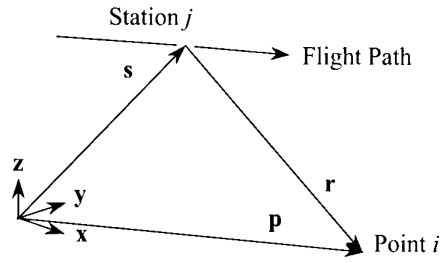


Figure 1. Range vector **r** and position vectors **s** and **p** in a given topocentric rectangular system of coordinates denoted by unit vectors **x**, **y**, **z**

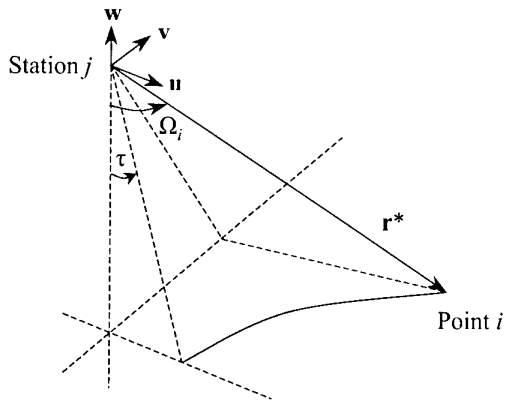


Figure 2. Range vector **r*** in a radar antenna system of rectangular coordinates defined by unit vectors **u**, **v**, and **w**; squint angle τ and off-nadir look angle Ω_i after Leberl (1976)

The along-track image coordinate measurement is denoted by t_j (pixels, or seconds), serving as an argument. The trajectory parameters $X_{oj}(t)$, $Y_{oj}(t)$ and $Z_{oj}(t)$ are further expanded in polynomials:

$$X_{oj} = a_0 + a_1 t_j + a_2 t_j^2 + a_3 t_j^3 \tag{4a}$$

$$Y_{oj} = b_0 + b_1 t_j + b_2 t_j^2 + b_3 t_j^3 \tag{4b}$$

$$Z_{oj} = c_0 + c_1 t_j + c_2 t_j^2 + c_3 t_j^3 \tag{4c}$$

The polynomial coefficients/parameters (a_k, b_k, c_k) with $k = 0, 1, \ldots$, will be estimated in a least-squares sense, and be individually checked for their significance by using statistical hypothesis testings. Recapitulating, we now have unknown parameters ($\tau, M_b, a_k, \ldots, b_k, \ldots, c_k, \ldots$) and image point measurements ($\ldots, r_i, t_j, \ldots$) in our functional model. The measurement error variance-covariance matrix then serves as the accompanying stochastic model.

2.2 Time-Varying Squint Parameter

As a logical consequence, the squint angle τ is expanded in a second-order polynomial, leading to an extension of the underlying functional model:

$$\tau(t_j) = \tau_0 + \tau_1 t_j + \tau_2 t_j^2 \tag{5}$$

Here, the fixed-order polynomial modeling is rather tentative. One may notice from Eq. (4) that higher-order time polynomial terms can give rise to numerical stability problems. The acceptance of any initial convergent parameter solution is statistically based on the global model chi-square distribution test (Leick, 1995), at an α % significance level.

3. LEAST-SQUARES ESTIMATION

If the preceding functional and stochastic models are correct, a least-squares method yields the adjusted parameters/measurements that are the best linear unbiased estimates (Koch, 1999).

3.1 Parameter Corrections and Measurement Residuals

To begin with, the nonlinear equations (1-4) have to be linearized to form a system of error equations, of which the expansion point is at the available measurements and parameter approximations:

$$\mathbf{Bv} + \mathbf{Ax} = \boldsymbol{l} \quad \text{with} \quad \sigma_0^2\mathbf{Q} \tag{6}$$

where the $n\times n$ coefficient matrix **B** contains the partial derivatives of Eqs. (1-4) with respect to the $n\times 1$ measurement vector $(\ldots, r_i, t_j, \ldots)$. The $n\times 1$ vector **v** stands for the measurement residuals $(\ldots, v_{r_i}, v_{t_j}, \ldots)$. Analogously, the $n\times u$ design matrix **A** contains the partial derivatives with respect to the u unknown parameters. The $u\times 1$ vector **x** represents the parameter corrections $(d\tau, dM_b, da_k, db_k, dc_k)$ with k = 0, 1, 2, 3. The $n\times 1$ vector $\boldsymbol{l}$ is the reduced observation vector. The measurement error covariance matrix is denoted by $\sigma_0^2\mathbf{Q}$, where σ_0^2 is the a priori unit weight reference variance. A least-squares method, which requires a minimization of the quadratic form $\mathbf{v}^T\mathbf{Q}^{-1}\mathbf{v}$, produces the parameter corrections and the measurement residuals, as follows:

$$\mathbf{x} = \mathbf{Q}_x\mathbf{A}^T(\mathbf{BQB}^T)^{-1}\boldsymbol{l} \tag{7a}$$

$$\mathbf{v} = \mathbf{Q}_v\mathbf{B}^T(\mathbf{BQB}^T)^{-1}\boldsymbol{l} \tag{7b}$$

where the $u\times u$ scaled covariance matrix $\mathbf{Q}_x$ and the $n\times n$ scaled covariance matrix $\mathbf{Q}_v$ refer to the parameter correction vector **x** and the measurement residual vector **v**, respectively. The covariance matrices can be obtained by using the law of error propagation. Both Leick (1995) and Mikhail (1976) detailed the derivation of $\mathbf{Q}_x$ and $\mathbf{Q}_v$ so that their explicit expressions are not repeated here. The **v**-vector quadratic form can lead to the a posteriori estimate $\hat{\sigma}_0^2$ of a unit weight reference variance. The same **v**-quadratic form also leads to a chi-square (χ^2) test statistic:

$$\hat{\sigma}_0^2 = \mathbf{v}^T\mathbf{Q}^{-1}\mathbf{v}/(n-u) \tag{8}$$

$$\chi^2_{n-u,\alpha/2} < \frac{\mathbf{v}^T\mathbf{Q}^{-1}\mathbf{v}}{\sigma_0^2} < \chi^2_{n-u,1-\alpha/2} \tag{9}$$

where n–u represents the degree of freedom. α is a chosen significance level, e. g. at 5%, used to create the lower and upper bounds of the inequality equation (9), in the course of a global model hypothesis testing. If this testing fails, an analyst can state that, with a 1–α confidence level, the functional and stochastic models (1-4) are not in order.

3.2 Optimal Parameter Selection

Another statistical testing can be utilized to validate parametric significance when trajectory polynomial modelings, such as described in Eq. (4), are involved. For any element x of a parameter correction vector **x** (7a), an F-distribution test statistic can be given as the term on the left-hand side of the following inequality equation (Zhong, 1997):

$$\frac{xq_x^{-1}x}{\hat{\sigma}_0^2} \geq F_{1-\alpha;1,n-u} \tag{10}$$

where q_x denotes the scaled variance of x. The F-distribution has (1, n–u) degrees of freedom. Upon choosing a significance level α, the upper critical value $F_{1-\alpha;1,n-u}$ is read from an F-distribution look-up table. If the test quantity $xq_x^{-1}x\hat{\sigma}_0^{-2}$ fulfills the inequality relationship (10), this parameter element x is considered to be insignificant. After its deletion, the new parameter set will have u–1 elements. The measurement vector and its error covariance matrix remain unchanged.

A repeated least-squares adjustment is performed by using the algorithmic equations (6-7). New u–1 parameter corrections and new n measurement residuals are estimated. Their acceptance is based on the required global model test, as indicated in Eq. (9). The following minimum criteria, all related to the quadratic form of the estimated measurement residuals (Zhong, 1997), serve as the optimization indices in order to distinguish between the old/previous and new/current estimation results:

$$\hat{\sigma}_0^2 = \mathbf{v}^T\mathbf{Q}^{-1}\mathbf{v}/(n-u) \quad \rightarrow \quad \min \tag{11a}$$

$$V_p = (n+u)\hat{\sigma}_0^2 \quad \rightarrow \quad \min \tag{11b}$$

$$AIC = n\ln(\mathbf{v}^T\mathbf{Q}^{-1}\mathbf{v}) + 2u \quad \rightarrow \quad \min \tag{11c}$$

where Eq. (11a) is identical to Eq. (8). If the new model has a better performance than the old one, the search for another possible insignificant parameter continues. This means that the significance testing, Eq. (10), will be invoked. If, on the other hand, the previous model produces more optimal results than the current model does, the old/previous functional model represents the sought-after model solution.

4. EXPERIMENTATION AND ANALYSIS

4.1 Airborne Chaochou SAR-Image

The airborne SAR-image over a 5.0 km×14.0 km area near the Chaochou town, Figure 3 on the last page, was a result of the Canadian CV-580 GlobeSAR campaign in Taiwan, near the end of October, 1993 (INTERA, 1994). The nominal flying height was 7.1 km above a mean sea level, with the airplane cruising at ~120 m/s (240 knots). A ground range resolution was ~4.0 m; an azimuth resolution was ~4.0 m, too.

Ground control/check point coordinates (X_i, Y_i, Z_i) were digitized/interpolated from the available 1:5000 topographic photo-maps. The corresponding image point line/pixel coordinates were measured, using the ERDAS/Imagine software utilities. All the coordinates were independently measured by three operators. The averaged coordinate measurements were accepted and prepared in an input data file. In our radargrammetric processing, the measurements were treated as being independent and identically distributed.

4.2 Significant Parameters

For the monoscopic Chaochou SAR-image, its space resection deals with the determination of radar antenna's orientation parameters. With regard to the range/Doppler and the trajectory modeling equations (1-4), significant polynomial coefficients can be identified by following the stage-by-stage significance testing and the optimality assessment algorithm, in terms of Eq. (10-11). The results are given in Table 1, according to which the optimal set of parameters produced at the second stage will have been selected.

4.3 Planimetric Accuracy

When the SAR-image orientation parameters are made available, they can be used for each image point to determine its planimetric ground coordinates $(X_i,\ Y_i)$ where the Z_i-coordinate is assumed to be known. This point-by-point space intersection is conducted for the 30 independent check points, leading to the accuracy results in Table 2. It is made clear that a single-valued variable squint angle is more suitable than a constant zero squint. The root-mean-square errors also indicate that a tentative second-order polynomial modeling (5) of the squint parameter has the highest accuracy level, in terms of the planimetric point positioning with the airborne Chaochou SAR-image.

Table 1. Iterative optimal determination of significant orientation parameters for the Chaochou SAR-image

	Stage-1	Stage-2	Stage-3
Parameter set : (besides τ and M_b)	$a_0, \ldots, a_3$ $b_0, \ldots, b_3$ $c_0, \ldots, c_3$	$a_0, \ldots, a_3$ $b_0, \ldots, b_3$ c_0, c_1, c_3	a_0, a_1, a_3 $b_0, \ldots, b_3$ c_0, c_1, c_3
Parameter having a maximum F-test statistic	c_2	a_2	-
Minimum criteria :			
$\hat{\sigma}_0^2$	0.38	0.26	0.29
V_p	98	67	75
AIC	630	575	592
Optimization	No	Yes	No

5. SUMMARY

The SAR-image range/Doppler equations are introduced so as to recognize the geometric squint parameter. Before embarking on a polynomial modeling of the squint angle, a least-squares estimation algorithm and a parametric significance testing methodology are briefly given. They serve as a sufficient processing tool in order to obtain an optimal set of radar's orientation parameters. In studying the space resection/intersection of the airborne SAR Chaochou image, a second-order polynomial description of the squint parameter yields an improved Easting coordinate accuracy of ± 4.8 m and an improved Northing accuracy of ± 5.3 m.

Table 2. Planimetric point accuracy in relation to the squint, τ, parameter modeling

	Root-mean-square errors	
	X/Easting (m)	*Y*/Northing (m)
τ (= 0.0 deg)	± 6.2	± 7.1
τ as a variable (= -0.38 deg)	± 5.4	± 6.1
τ modeled by using a 2nd-order polynomial: τ_0 = -0.053 deg $\tau_1 = 3.26\times10^{-3}$ deg/pixel $\tau_2 = 2.44\times10^{-6}$ deg/pixel^2	± 4.8	± 5.3

Based on the positive experimental outcome, some future SAR-image processing schemes are itemized here: (1) automated setting of a polynomial expansion order for the squint angle; (2) possibility of a first-order range-dependent modeling of the pixel-spacing parameter; (3) application of the proposed methodology to spaceborne Earth resources SAR imagery.

ACKNOWLEDGMENTS

The writers are indebted to the Council of Agriculture for sponsoring the 1993 GlobeSAR campaign. Thanks also go to Mr. C.-T. Wang of the NSC Satellite Remote Sensing Laboratory for pre-processing the SAR image.

REFERENCES

Curlander, J.C., Kwok, R., Pang, S.S., 1987. A post-processing system for automated rectification and registration of spaceborne SAR imagery. International Journal of Remote Sensing, 8(4), pp.621-638.

Dowman, I., 1992. The geometry of SAR images for geocoding and stereo applications. International Journal of Remote Sensing, 13(9), pp.1609-1617.

Gelautz, M., Frick, H., Raggam, J., Burgstaller, J., Leberl, F., 1998. SAR image simulation and analysis of alpine terrain. ISPRS Journal of Photogrammetry and Remote Sensing, 53(1), pp.17-38.

INTERA, 1994. GlobeSAR CV-580 campaign to Taiwan 1993 final report. Intera Information Technologies Ltd., Ontario, Canada, 56p.

Koch, K.R., 1999. Parameter Estimation and Hypothesis Testing in Linear Models. Springer-Verlag, Berlin.

Leberl, F., 1976. Imaging radar applications to mapping and charting. Photogrammetria, 32, pp.75-100.

Leberl, F., 1979. Accuracy analysis of stereo side-looking radar. Photogrammetric Engineering and Remote Sensing, 45(8), pp.1083-1096.

Lee, C., Theiss, H.J., Bethel, J.S., Mikhail, E.M., 2000. Rigorous mathematical modeling of airborne pushbroom imaging systems. Photogrammetric Engineering and Remote Sensing, 66(4), pp.385-392.

Leick, A., 1995. GPS Satellite Surveying. John Wiley & Sons, Inc., New York.

Mikhail, E.M., 1976. Observations and Least Squares. University Press of America, Lanham, Maryland.

Tannous, I., Pikeroen, B., 1994. Parametric modeling of spaceborne SAR image geometry. Application: SEASAT/SPOT image registration. Photogrammetric Engineering and Remote Sensing, 60(6), pp.755-766.

Toutin, Th., Gray, L., 2000. State-of-the-art of elevation extraction from satellite SAR data. ISPRS Journal of Photogrammetry and remote Sensing, 55(1), pp.13-33.

Wu, J., Lin, D.-C., 2000. Radargrammetric parameter evaluation of an airborne SAR image. Photogrammetric Engineering and Remote Sensing, 66(1), pp. 41-47.

Zhong, D., 1997. Robust estimation and optimal selection of polynomial parameters for the interpolation of GPS geoid heights. Journal of Geodesy, 71(9), pp.552-561.

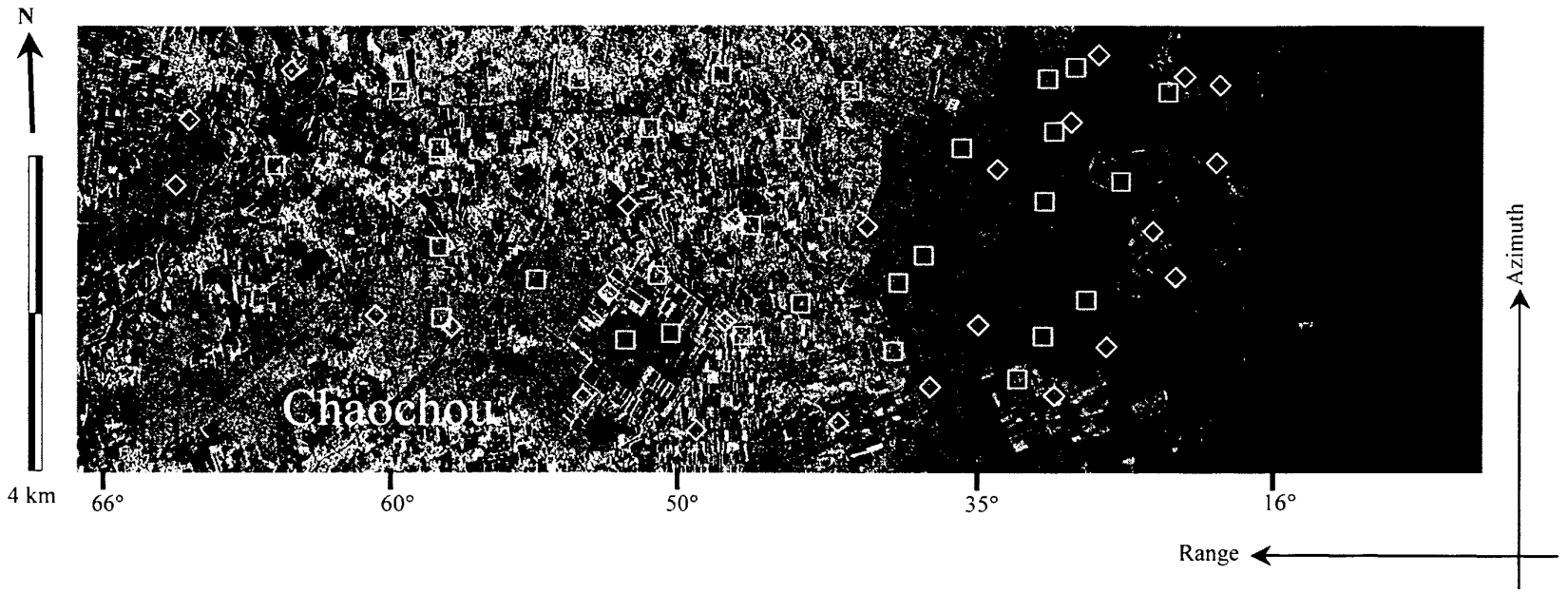


Figure 3. Airborne Chaochou SAR-image (*C*-band, *HH*-polarization, ten-look) in slant-range projection, on 30 October, 1993; 30 control points shown by (◇), and 30 check points by (□); terrain heights varying between 4.0 m and 84.0 m

INTEGRATION OF MULTISENSOR MULTITEMPORAL SATELLITE DATA FOR AGRICULTURAL VEGETATION MAPPING

L. ZHU and R. TATEISHI
Center for Environment Remote Sensing (CEReS), Chiba University
1-33, Yayoi-cho, Inage-ku, Chiba, 263-8522
Tel: (81)-43-290-3850 Fax: (81)-43-290-3857
E-mail: zhulin@ceres.cr.chiba-u.ac.jp
JAPAN

KEY WORDS: Data Fusion, Transition Probability, Vegetation Dynamics Indicator

ABSTRACT: Efficient integration of temporal, spectral and spatial resolution information is important for accurate mapping of agricultural areas. In this study, a new temporal fusion classification (TFC) model is presented for classification of agricultural vegetation, based on statistical fusion of single source multitemporal satellite images. In the proposed model, the temporal dependence of multitemporal images is taken into account by estimating transition probabilities from the change pattern of vegetation dynamics indicator (VDI). For integration of multisensor multitemporal satellite data, an extended multisensor temporal fusion classification (MTFC) model is proposed, concerning both temporal attributes and reliability of multiple data sources. The feasibility of the new method is verified by using multitemporal Landsat TM and ERS SAR satellite images, and experimental results show improved performance than the conventional method.

1. INTRODUCTION

The effective agricultural mapping and monitoring are required for a variety of applications ranging from general inventory requirements to ecological studies. Remote sensing has shown great potential in agricultural mapping and monitoring due to its advantages over traditional procedures in terms of cost effectiveness and timeliness in the availability of information over larger areas (Murthy *et al* 1998). Automated interpretation of satellite images for agricultural area mapping is relatively complicated due to spectrum similarity of agricultural crops. Fusion techniques have been adopted for crop discrimination to provide increased interpretation capabilities and more reliable results since data with different characteristics are combined. The efficient fusion measure depends on the better understanding of characteristics of sophisticated multisource data and selecting the optimal interpretation algorithm. Advanced analytical or numerical data fusion techniques are imperative for the integration of temporal, spectral and spatial resolution information.

The aim of this study is to incorporate the temporal dependence of multitemporal image data into the fusion algorithm by estimating transition probabilities theoretically and reasonably from the change pattern of VDI, and consequently enhance the interpretation capabilities; moreover, to integrate multisensor multitemporal satellite data effectively, i.e., both the temporal attribute and the reliability of multiple data sources are concerned.

2. METHODOLOGY

2.1 Temporal Data Fusion Based on a Bayesian Formulation

Let us consider that two multispectral remote sensing images acquired at time t_1 and t_2 on the same area are examined. Let us suppose that a pixel of the multispectral image acquired at time t_1 and a spatially corresponding pixel of multispectral image acquired at time t_2. These pixels are characterized by the m-variate observation feature vectors X_1 and X_2, respectively. Let ω_i (i=1, 2, ..., n) and v_k (k=1, 2, ..., n) be the set of possible land cover classes at time t_1 and t_2 respectively, if we classify each couple of pixels independently of any other on the basis only of its feature vectors X_1 and X_2, based on the Bayes rule, it requires that the couple of classes (ω_i, v_k) be selected that provides the maximum likelihood $L(\omega_i, v_k)$, according to Swain (1978) and by applying some transformations, the likelihood function that will be used in the decision rule takes the following form:

$$L(\omega_i, v_k) = P(\omega_i \mid X_1) P(v_k \mid X_2) \frac{P(v_k \mid \omega_i)}{P(v_k)} \tag{1}$$

2.2 Determination of Transition Probabilities

According to formula (1), we can see that only transition probabilities $P(v_k \mid \omega_i)$ represent the temporal dependence of multitemporal images. Formerly, when we incorporated temporal aspect to the fusion model, transition probabilities were always decided empirically (Solberg *et al* 1994). It should be more reasonable to decide transition probabilities using the change pattern of VDI, e.g., Normalized difference vegetation index (NDVI) for optical data and backscattering coefficient for SAR data. We can use the change of VDI to represent crop seasonal differences, or land use change of terrain categories. For the consecutive pair of images, let us define the change index (CI) using VDI derived from multitemporal images like following,

$$CI = DN_2 - DN_1 \tag{2}$$

Here, DN_2 and DN_1 are the pixel digital numbers of VDI at time t_1 and t_2, respectively. Let us name the change pattern of VDI, which are calculated from the training data set and decided by

the predetermined thresholds, as the estimated change pattern (ECP). Thus, the ECP of VDI can be defined as:

$$\begin{aligned}&\text{If } \xi_2 \le CI \le \xi_1, \text{ then } ECP = 0\\ &\text{If } CI > \xi_1, \text{ then } ECP = 1\\ &\text{If } CI < \xi_2, \text{ then } ECP = -1\end{aligned} \tag{3}$$

Here, ξ_1 and ξ_2 are the predetermined thresholds to decide the estimated change pattern (ECP) of VDI from time t_1 to time t_2, the determination of ξ_1 and ξ_2 will be discussed afterward. The change pattern of VDI, which are calculated directly from the classification processing of images and defined as the same as formulation (3), are named as the actual change pattern (ACP). By comparing the prepared ECP to the ACP, the transition probabilities $P(v_k \mid \omega_i)$ are defined as follows:

$$\begin{aligned}&\text{If } \omega_i = v_k \text{ and ACP=ECP, then the transition probabilities } P(v_k \mid \omega_i) = 1\\ &\text{If } \omega_i = v_k \text{ but ACP} \neq \text{ECP, then } P(v_k \mid \omega_i) = \alpha \frac{P(\omega_i \mid X_1)}{P_1(\max)} \frac{P(v_k \mid X_2)}{P_2(\max)}\\ &\text{If } \omega_i \neq v_k \text{ and ACP} \neq \text{ECP, then } P(v_k \mid \omega_i) = 0\\ &\text{If } \omega_i \neq v_k \text{ but ACP=ECP, then } P(v_k \mid \omega_i) = \beta \frac{P(\omega_i \mid X_1)}{P_1(\max)} \frac{P(v_k \mid X_2)}{P_2(\max)}\end{aligned} \tag{4}$$

Here $P_1(\max)$ and $P_2(\max)$ are the maximum *a posteriori* probabilities among the different classes at time t_1 and t_2, respectively. α and β are user-specified constants, which control the degree of consistency between the multitemporal data.

2.3 Multisensor Data Fusion Modelling

For integration of multisensor multitemporal satellite data, let us consider the m-variate observation feature vectors of Landsat TM data X_T^t and the set of possible land cover classes C_i^t (i=1, 2, ..., n) related to time t (t=1, 2, ..., p), also the d-variate observation feature vectors of ERS SAR data X_S^g and the set of possible land cover classes E_i^g (i=1, 2, ..., n) related to time g (g=1, 2, ..., q). For each data source, it is suggested to allow different data sources to be weighted differently according to some measure of their reliability (Benediktsson and Swain 1992). Thus, the likelihood function that both the temporal attribute of single-source data and the reliability of multi-source data are concerned can be derived to take the following form:

$$L(c) = P(C^1, C^2, ..., C^p \mid X_T^1, X_T^2, ..., X_T^p)^{\lambda_T} \; P(E^1, E^2, ..., E^g \mid X_S^1, X_S^2, ..., X_S^g)^{\lambda_S} \tag{5}$$

$$P(C^1,C^2,...,C^p \mid X_T^1,X_T^2,...,X_T^p)=\frac{P(C^1 \mid X_T^1)...P(C^p \mid X_T^p)P(C^2 \mid C^1)...P(C^p \mid C^{p-1})}{P(C^2)P(C^3)...P(C^p)}$$

$$P(E^1,E^2,...,E^g \mid X_S^1,X_S^2,...,X_S^g)=\frac{P(E^1 \mid X_S^1)...P(E^g \mid X_S^g)P(E^2 \mid E^1)...P(E^g \mid E^{g-1})}{P(E^2)P(E^3)...P(E^g)} \quad (6)$$

Here, λ_T and λ_S, $0<\lambda_T$, $\lambda_S<1$ represent the reliability factors associated with the temporal data fusion performance on multitemporal Landsat TM data and ERS SAR data, respectively.

3. EXPERIMENT

3.1 Study Area

The study area is located in the region of Zhangwu County, a typical agricultural area of Liaoning province in the northeast part of China. The image size is 1024 x 1024 pixels, corresponding to 25.6 x 25.6 km^2, with geographical coordinates from 42^{0}22′6″N to 42^{0}35′50″N in latitude and from 122^{0}12′56″E to 122^{0}31′50″E in longitude.

Zhangwu's economy is oriented toward agriculture, producing mainly crops such as corn and grain, as well as soybean, wheat, pachyrhizus, peanut, and tobacco. The main crop season in this area is from April to October, including the driest month July. The ground survey trip was carried out in July 1999. The classification of the following land cover classes is considered: corn, paddy, soybean, wheat, meadow, poplar, pine, bare land, urban, water, dried area and deforest area.

3.2 Data Acquisition and Preprocessing

In this study, two Landsat TM images and two ERS-1 SAR images were applied for investigating the performance of multisensor temporal fusion model. The multitemporal Landsat TM images collected on 19 May 1994 and 23 August 1994 were selected mainly because these are the best available cloud-free scenes in the crop season. Relative radiometric correction was performed on multitemporal Landsat TM images so that both the influences of atmospheric conditions and sun elevation angle were removed (Oguma and Yamagata 1997). The two ERS-1 SAR images were acquired on 14 July 1994 and 9 September 1994. For the preprocessing of SAR images, the 16-bit data were firstly converted to 8-bit data. Then, two passes of filtering were performed in order to reduce inherent noise, the first filtering was done by using 3 by 3 median filter, the second iteration using 5 by 5 mean filter. The multitemporal TM and SAR images were co-registered and resampled to 25m pixel size, then geometrically corrected in UTM projection using the nearest neighbor method. The RMS error less than 1 pixel was yielded. Only six channels of TM data were used except the thermal channel 6. NDVI data was

extracted and scaled to integer value from 0 to 200 to be used as VDI. For temporal data fusion of ERS SAR data, we used the digital value of SAR backscattering coefficient directly as VDI.

3.3 Parameter Selection

How to decide the thresholds ξ_1 and ξ_2 is very important. It is essential that the specification of ξ_1 and ξ_2 should make the classes to be more easily separated. For different classes to be classified, VDI exhibit different change directions and magnitudes. We firstly derived the VDI values of different classes from the training data set of multitemporal satellite data, then we calculated CI values between all the same classes and different classes, finally, we deliberated the results and selected the most appropriate thresholds to try to separate all CI values into three groups evenly: increasing, decreasing and constant. We can easily decide the thresholds and divide these values into three groups. For Landsat TM data, we decided the thresholds as ξ_1=13 and ξ_2=-1, and for ERS SAR data, we decided the thresholds as ξ_1=12 and ξ_2=-2.

α and β are user-specified parameters which control the degree of consistency between the temporal data, they were determined experimentally with respect to the overall classification accuracy. Through an inspection of these results, the optimal choice (α_{TM}=0.6 and β_{TM}=0.0) was made that the classification performance was best, and the optimal choice of α_{SAR} and β_{SAR} respect to classification accuracy is α_{SAR}=0.7 and β_{SAR}=0.0. For the determination of reliability factors λ_T and λ_S, in our MTFC model, λ_T and λ_S do not simply represent the reliability of different data sources, but the reliability of the proposed TFC model applied on multiple source data. Thus, the determination of λ_T and λ_S rely on classification results of the TFC model for multitemporal Landsat TM and ERS SAR data.

4. RESULTS AND DISCUSSION

The performances of the proposed TFC technique are assessed and compared with the conventional Maximum Likelihood Classification (MLC) method. To provide a reference for comparison, the single period images are first analyzed separately, the performances of the MLC method are 73.3% and 73.1% correct for the May 1994 and August 1994 Landsat TM data, respectively, and 24.5% and 22.1% correct for the July 1994 and September 1994 ERS SAR data, respectively. The results of multitemporal classification are substantially better than either of single period performances. The results demonstrated by the proposed TFC method show an overall accuracy of 89.0% and 39.6% for Landsat TM and ERS SAR data, respectively, these are truly better than the MLC method of 85.5% correct performance for TM data and 39.1% correct performance for SAR data. Moreover, 10 of the all 12 classes show improved accuracy using the proposed TFC model compared to the MLC method for Landsat TM data. The results indicate that the proposed TFC method can be applicable for multiple source satellite data which

have different characteristics. Furthermore, the computation time using the TFC method is less than half of the time used by the MLC method.

For multiple source classification of multitemporal Landsat TM and ERS SAR images, the proposed multisensor temporal fusion classification (MTFC) model shows improved 89.1% correct performance, compared to an overall accuracy of 88.9% derived by the simple combination temporal fusion classification (SCTFC) model which ignores the reliabilities of different data sources, and much better than the MLC method of 86.4% correct performance.

5. CONCLUSION

We proposed a new method based on the Bayesian formulation and try to integrate multisensor multitemporal satellite data for accurate mapping of agricultural area. This is a statistical method based on multisensor multitemporal data fusion, which takes into account the temporal dependence of images and the reliabilities of different data sources. In the proposed TFC model, the class-dependent likelihood of multitemporal data are calculated, respectively, and the transition probabilities are estimated from the change pattern of VDI between the same and different classes of images, then the Bayes optimal classification is performed by maximizing the set of the class-dependent likelihood and the transition probabilities. The proposed TFC model was further extended and can be applied for classification of optical and SAR satellite images. This method can also be used as an alternative method for change detection of land cover and land use. Experimental results showed that the fusion model is robust and can improve the classification accuracy, moreover, reduce the dimensionality of the probability functions used and facilitate the computation over time.

References:

Benediktsson, J. A., and Swain, P. H., 1992, Consensus theoretic classification methods. *I.E.E.E. Transactions on Systems, Man, Cybernetics*, **22,** 688-704.

Murthy, C. S., Raju, P. V., Jonna, S., Abdul Hakeem, K., and Thiruvengadachari, S., 1998, Satellite derived crop calendar for canal operation schedule in Bhadra project command area, India. *International Journal of Remote Sensing*, **19,** 2865-2876.

Oguma, H., and Yamagata, Y., 1997, Study on effective observing season selection to produce the wetland vegetation map. *Journal of the Japan Society of Photogrammetry and Remote Sensing*, **36,** 5-16.

Schistad Solberg, A. H., Jain, A. K., and Taxt, T., 1994, MultiSource classification of remotely sensed data: fusion of Landsat TM and SAR images. *I.E.E.E. Transactions on Geoscience and Remote sensing*, **32,** 768-777.

Swain, P. H., 1978, Bayesian classification in a time-varying environment. *I.E.E.E. Transactions on Systems, Man, Cybernetics*, **SMC-8,** 879-883.

GLOBAL POSITIONING SYSTEM (GPS)

Venant Balwegirira Mugemuzi,
Land Surveyor & GIS, Surveys & Mapping Division,
P. O. Box 9201,
Dar Es Salaam,
Telephone: 255 22 2121894
Fax: 255 22 2138962
E-mail: SMD@raha.com
TANZANIA.

Key Words: Survey marks, Control surveys, Funds & GPS

Abstract

Developing Countries have experienced a low pace of mapping their land, lack of up-to-dated maps for planning and execution of new projects and programmes. The question of timely data collection is still an issue taking in to consideration traditional technology of surveying, which is still dominant.
Lack of precise controls, to tie the subsequent survey works like cadastral surveys, hydrographic Surveys, engineering activities, ground photographic controls, topographic mapping and other uses, is a setback to many programmes and projects in Tanzania and some other developing countries. The geodetic framework of the past has been decimated following beliefs that the pillar mark positions of underground goldfields.
Following the authorisation to use GPS for activities other than Military purposes, more survey projects can be executed within a short time and the aforementioned programmes and projects can be executed accurately and timely by using the new technology of Global Positioning System (GPS). World Geodetic System (WGS84), as a multipurpose system, has done marvellously especially when the World is entering the new millennium by determining the position of any point on the earth instantaneously. Ships and aircraft track their location, velocity and time through GPS.

1.0 Introduction

Tanzania is located on the East Coast of Africa and south of the Equator. Its extends from meridians 30^0 to 39^0 East of Greenwich and 1^0 to 11^0 south of Equator.
The country is covered with the area 939,704 sq.kms. Mount Kilimanjaro with a permanent ice cap is 6,340mitres above sea level and the highest mountain in Africa, and in the deep trough-like depression within the Great Rift Valley of East Africa is Lake Tanganyika, lies the world's second deepest lake.

2.0 Land Surveying in Tanzania

The United Republic of Tanzania came into being on 26 April 1964 following the merger of Zanzibar Islands and Tanganyika Mainland. However, matters relating to Surveys and Mapping are not a Union affair. Hence there are two separate departments dealing with surveying and mapping one in the Islands and the other in the Mainland. Throughout my paper, the name Tanzania is used to refer to the mainland unless otherwise stated.
Tanzania is divided into 20 administrative regions. Every region has a regional land surveyor being a member of regional advisory committee to support a Regional Administrative Secretary (RAS) on land Surveying matters. This survey officer is responsible to legal and technical

matters related to surveying land for that particular region. Also every region is divided into Districts, at the moment we have 104 district covering the whole country.
Surveys and Mapping being an organisation in the Ministry of Lands, Human Settlement Development usually prepare good plans for execution of projects. Such projects are related to cadastral surveys, ground photographic control surveys, hydrographic surveys. Other projects like engineering surveys are mostly taken by private firms.

3.0 Control surveys in Tanzania

The traditional technology of data collection is still dominating 90% of the whole country and the controls are passive where monuments are used to extend new surveys. Control points are categorised by orders, from zero order, which is highest accuracy to 5th order. These categories are varying in their naming, monumentation, spacing, and specified accuracies. Method commonly applied before GPS technology was hierarchical triangular network (horizontal co-ordinates, attained cm-dm precision). The observations start by astronomical observations and base measurements, then employed other methods depending on which available survey equipment. E.g.Triangulation was employed when theodolites were available, trilateration was employed when Electromagnetic Distance Measurement (EDM) were available, traversing as well employed when theodolites and EDM are both available or total stations nowadays. The network established since colonial era, very few points are still existing. Sometimes it is hardly to locate any control point in the area of 50 square kilometres to the area outside the township instead of the normal required of one control point within two square kilometres or lesser than to cover the whole country. Some of the monuments were decimated and some are suffering from radio-waves construction made very nearby on which mostly preferred on the highest terrain.

3.1 Survey Marks

The monuments, which are known as survey marks, are trigonometric stations, pillars, benchmarks, boundary beacons, Iron pins in concrete (IPC), wooden pegs, whether above or below the surface of the ground on which it is fixed. Either can be placed or set-up by or under the direction of a land surveyor for purpose of any survey (Silayo, 1985). In all classes of Surveying in Tanzania survey marks giving the exact position plannimetric and height for main survey station should left on the ground. These vary from temporary ones, such as wooden pegs used in setting out works, to permanent ones, such as triangulation pillars and fundamental benchmarks.
The usefulness of a survey depends on the precision with which these marks are located, their permanence, the accuracy of their fixation and positional restoration should then be removed or damaged.

3.2 Problem of decimating Survey Marks

There exist a wrong belief among some tribes in Tanzania that underneath the survey marks such as pillars there is wealth of minerals such as gold, diamond, copper extra. Such people in the case of mining their assumption causes to remove, destroy displacement or alter the position of, or defacing, mutilating, obliterating the survey marks. Also development activities such as road construction and agricultural activities destroy the survey marks. A research carried out in various towns and cities in Tanzania about two decades ago gave the results that between 5% and 20% of ground monuments are destroyed every year in urban areas (Blashut T.J., 1979).
Intervisibility between the ground marked control points is oftenly lost permanently by new construction along the line of sight or blocked temporarily by parked cars causing delay in new

surveys. City traffic and construction excavations causes ground movements that lead to the displacement of survey marks.

4.0 Impact of limited funds on executing projects

Planned projects remain uncompleted for long time, and cause some conflict when being late on implementation. For example any cadastral survey in Tanzania by the law require to use town planning proposed drawings to guide any demarcation which is being done. But town-planning drawings are normally prepared using outdated base maps with neither field verification nor any details are being picked in the site. This brings about conflict with cadastral plans due to lack of parcel/plots conformity after field survey. Instead of starting with, Planning, Surveying, Building and Occupation (PSBO) we are falling in Building, Occupation, Planning and Surveying (BOPS) popularly known as squatter upgrading.
Densification of controls as a base for any subsequent survey requires enough money for monumentation and field execution especially in the traditional survey environment either aerial survey projects which are required for ground photo controls in the case of base maps preparation or field completion need enough money which are not available.

4.1 High demand of surveyed land

Demand for surveyed parcels of land in urban areas is very high for example in Tanzania, is increasing daily due to people migrating to urban centres from rural areas seeking employment and better social amenities and natural increase of population. Lack of funds for surveying parcels of land in time and the awareness of people to own the surveyed and register land, have been noticed as one major problem.

5.0 Global Positioning System (GPS)

The Global positioning System was developed to replace the U.S. Navy Navigational Satellite System (NNSS), also called TRANSIT or DOPPLAR System. This System was composed of six satellites orbiting at altitudes of about 1100 km with near circular polar orbits. The TRANSIT System was developed by the U.S. Military, primarily to determine the positions by co-ordinates of vessels and aircraft. Civilian use of this Satellite system was eventually authorised, and the system became used worldwide both for Navigation and Surveying. The GPS was developed to replace the TRANSIT system because of two major shortcomings in the earlier system.

1. The main problem with TRANSIT was the large time gaps in coverage. Since normally a satellite would pass overhead every 90 minutes, users had to interpolate their position between "fixes" or passes.
2. The second problem with TRANSIT system was its relatively low navigation accuracy.

In contrast, GPS answers the questions "what time, what position, and on what velocity is it?" Such questions are answered quickly, accurately, and inexpensively anywhere on the globe at any time. Remondi (1991).

5.1 Space Segment (Satellite Constellation)

The Space Segment of the system consists of 24 GPS satellites. In-order to provide a continuous global positioning capability, a scheme to orbit a sufficient number of Satellites, to ensure that at least four were always electronically visible, was developed for GPS. **Figure 1** shows the system consists of constellation of 24 satellites (21 satellites constellation with 3 active on-orbit spaces) in six evenly spaced orbital planes placed in circular 12 - hours orbits inclined at 55^0 to

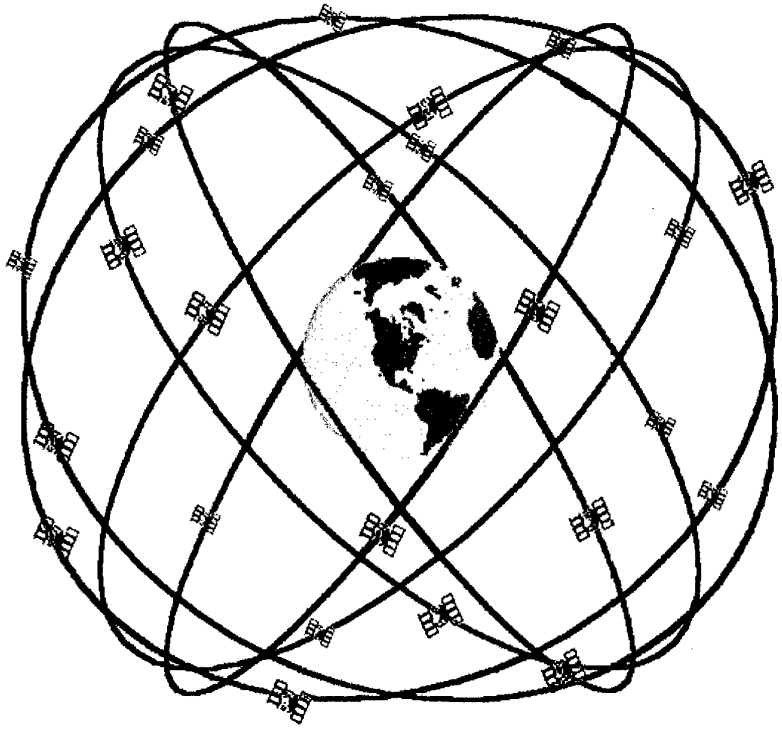
equatorial plane. In any event, this constellation provides a minimum of four satellites in good geometric position at any of the 24 hours of a day anywhere on the earth's surface. Depending on selected elevation angle, there is often more than the minimum number of satellites available to enable the receiver to compute the position, velocity and time. Four GPS satellite signals are used to compute positions in three dimensions and the time offset in the receiver clock. It is during these periods of 4 satellites and above that Surveyors perform any method of GPS Surveys **Figure 2**. In fact, assuming a 10^0 elevation angle, there are brief periods where up to 10 GPS Satellites are visible on the earth's surface.

5.2 Global Positioning System is a solution technology

Advancement of space technology lead to develop Global Positioning System (GPS), although it was intended to be used to different purposes in army activities. The alternative of surveying is another reported a timely breakthrough to rescue the aforementioned problems. It is a multipurpose system, which has done marvellously especially when the World is entering the new millennium by determining the position of any point on the earth instantaneously. Ships and aircraft track their location, velocity and time through GPS. GPS is the best for networking, provided the space between antenna of the receiver and sky is clear and at least four satellites are available. That measurement provides World Geodetic Co-ordinates (WGS84) in three dimensional co-ordinate systems that is fixed to the earth and has its origin at the centre of the earth. During measurement requires occupying at least three local known points for our case in Tanzania of UTM co-ordinate system to be used to determine parameters for transforming from WGS84 to the mapping plane.

5.3 World Geodetic System of 1984 (WGS 84).

The struggle to tie different regional datums and the advent of Satellite-based positioning systems assert the need for a global geodetic reference system.
World Geodetic System 84(WGS84) in the determination of true shape of the earth through mapping as the regional datums and the advent of Satellite-based positioning Systems, asserts the need for a global geodetic reference system.
The reference ellipsoid of WGS84 is essentially that of the International Union of Geodesy and Geophysics (IUGG) Geodetic Reference System 1980 (GRS80) with some minor changes. The International geodetic community at the IUGG's 17th quadrennial meeting, held in Canberra, Australia in 1979, as best representing the size and shape of the earth adopted this ellipsoid.
World Geodetic System has a long history starting in the early 1960s, when the United States Department of Defense introduced the WGS60. It was created from a global Database of conventional geodetic measurements, satellite observations, data from High-Precision Short-Range Navigation (HIRAN), Airborne trilateration, or range measuring systems developed during and after World War II. In the years following the introduction of WGS60, the accuracy and number of satellite observations greatly increased and led to the development of WGS66 and subsequently WGS72.
WGS72 was initially adopted as the Conventional Terrestrial System (CTS) for describing the orbits of the Global Positioning System (GPS) Satellites in their navigation messages (signals). But as with WGS60 and WGS66, the accuracy of WGS72 eventually was found wanting. WGS72 was superseded by WGS84 and has been used for GPS navigation messages since January 1987.



GPS Nominal Constellation
24 Satellites in 6 Orbital Planes
4 Satellites in each Plane
20,200 km Altitudes, 55 Degree Inclination

Figure 1. Space Segment (Satellite Constellation by Dana)

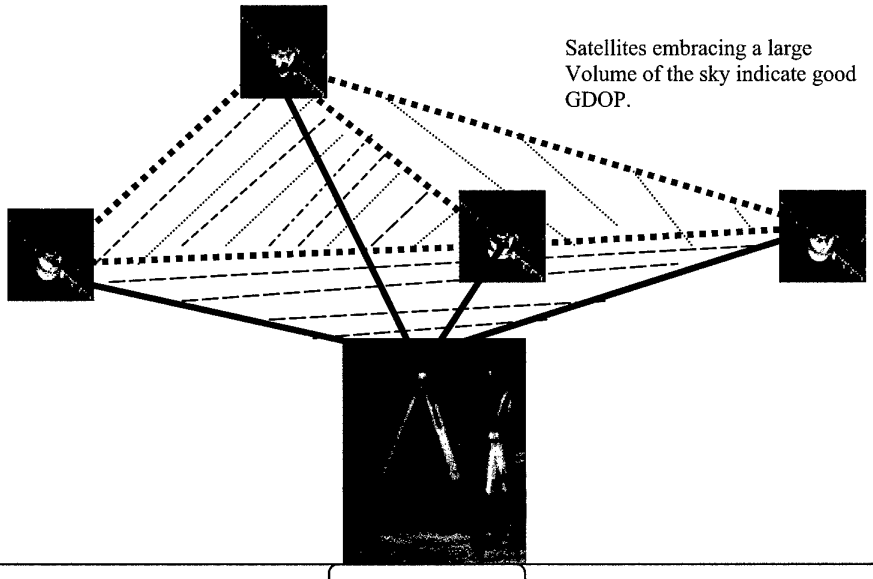


Figure 2: Measurements of code phase arrival times from at least four satellites are used to estimate four unknown: position in three dimensions (X, Y, Z) and GPS time (T).
By V.B.Mugemuzi

5.4 GPS Technology in Tanzania

The first time Tanzania introduced GPS receivers, was in 1992 under the Urban Sector Engineering Project (USEP) part of which covered the topographical mapping of nine Cities in Tanzania. The said project was executed jointly by three Companies Viak AS, Blom AS and Norconsult AS all of them from Norway with the collaboration to Surveys and Mapping Division (SMD) of the Ministry of Lands and Human Settlements Development. Since then many projects have been done to increase controls in WGS84 using GPS receivers available at SMD. The long-term aim is to cover the whole country. The recent ICAO project, to establish WGS84 Controls at the airports in Tanzania, aims to provide a very precise geometrical reference for Tanzania majors Airports. This task will serve as a backbone for future surveys and the future GPS-based navigation infrastructure. The actual survey consisted of GPS measurements at 8 main airports in Tanzania; two of them are first order points located at Dar es Salaam and Mbeya airports. The remaining six are located at Kilimanjaro, Zanzibar, Mtwara, Dodoma, Mwanza and Kigoma airports. The distribution intends to provide precise co-ordinates in the international reference frame (ITRF/WGS84). The points provide important navaid positions as well as the position and orientation of the runways. NeSA B.V. from the Netherlands did the fieldwork in co-operation with the Tanzania Directorate of Civil Aviation and the full participation of Tanzanian Surveys and Mapping Division.

6.0 The Immediate Need of Tanzania

As mentioned above, Tanzania is already close to WGS84 through the ICAO project. The main thrust now is to use this basic framework to densify GPS Control networks. In order to improve on this framework, some primary levelling and gravimetric observations are urgently need to complete basic parameters for computing the reference spheroid. Local resources can not accommodate this work which rightly puts Tanzania on the Global System now termed the Global Village Reference Frame. The intended goals will be achieved through joint global efforts upon addressing such existing pressure, where moral and material support are required. The scientist congregation at Taipei, not only discussing modern technology among of members attending the conference, but further to open the eyes for investors to collaborate on projects like control densification and chances of education to accelerate surveys and mapping activities in Tanzania.

Thank you for paying attention.

References

1. **Alfred Kleusberg, 1992.** Precise Differential Positioning and Surveying, Department of Surveying Engineering, University of New Brunswick
2. **B. Hofmann-Wellenhof, H. Lichtenegger and J. Collins, 1992.** GPS theory and Practice
3. **Jan Van Sickle, 1996.** Global Positioning System (GPS) for Land Surveyors.
4. **Venant B. Mugemuzi, 1991.** The question of preserving Survey marks in Tanzania. A paper presented on the technical committee of former Ardhi Institute then University College of Lands and Architectural Studies - Dar es Salaam Tanzania.
5. **Venant B. Mugemuzi, 1999.** Accelerating Cadastral Survey Processes to Improve Up-to-date Digital Parcel Information in Tanzania. Professional Masters Degree report in GIS for Cadastral Applications. ITC, Enschede, The Netherlands.
6. **Venant B. Mugemuzi, 2000.** Interpretation of WGS84 and Advantages. A paper presented on the Tanzania Aeronautical Information Service Officer's Association (TAISOA) being the 2nd Annual General Meeting (AGM) held on 14 April 2000 in Dar Es Salaam.

POST-CLASSIFICATION AND DETECTION OF SIMULATED CHANGE FOR NATURAL GRASS

Hao-Hsiung HUANG and Chiao-Ju HSIAO
Associate Professor and Graduate Student
Department of Land Economics
National Cheng-Chi University
64, Sec. 2, Tzu-Nan Road, Wensan, Taipei, Taiwan
Tel: (886)-2-29379261, Fax: (886)-2-2939-0251
E-mail: hhh@nccu.edu.tw and g8257016@grad.cc.nccu.edu.tw
TAIWAN

KEY WORDS: Supervised Classification, Change Detection

ABSTRACT: Natural healthy grass and varnished grass all appear green under a visible band, and generally not to be distinguishable. But this does not apply to the near infrared wave testing which is useful in determining the health conditions of plants. Experiments have been designed and executed, therefore, using both normal color slides and color infrared slides to take both natural health and varnished grass at a close distance. Then, the slides were scanned and transformed to obtain digital images for comparison. Observing the changes on the brightness value, determining the differences in healthy plants and varnished grass, and then studying all the above results for reference in order to improve the credibility on plant testing in the future. Variables are controlled and fixed in the whole process to provide an ideal remote sensing environment and to increase the accuracy of the experiment.

1. INTRODUCTION

When investigating the characteristic of the ground area with remote sensed images, one should keep in mind that to minimize unwanted spectral variability as well as to maximize this variability when the specific application requires it (Lillesand, 2000). According to this, in order to test the accuracy of change detection using postclassification comparison, such as temporal effects and spatial effects are minimized in this research. The methods, experimental design, results and their analyses are discussed respectively in the following sections.

2. METHODOLOGY

2.1. Image Classification

In general, image classification involves three procedures, supervised classification,

unsupervised classification, and hybrid classification. Supervised classification with Gaussian maximum likelihood classifier has been used to simplify the study and improve the accuracy. Base on the maps, images, pictures that could represent the particle category are taken as samples for training sites. To calculate the statistics of the mean, variance, variance-covariance matrix on every training sites, and then come up with the classification according to the produced equation and appropriate wave band formula.

Gaussian maximum likelihood classifier is one of the most used formulas in supervised classification. First, the brightness value of every category, wave band from the image is set as norm and then the operator determine the numbers of categories in the picture. And training sites are picked and selected in each picture. Using the brightness value of the picture in training sites, calculating the mean and covariance matrix within each wave band in each category. And then apply the result to the equation of possibility, and calculus then figure out the possibilities of the item to each category. Finally, classify according to the maximum likelihood.

2.2. Change Detection

To detect the changes on the ground area or gather the changes in a short period of time can only rely on the remote sensing image data. Change detection is to compare and contrast the two images with symmetrical positions, and use image-handling technique to analyze the reformed area. There are many methods to detect the reformation, such as Image Differencing Method, Multi-Date Composite Image Change Detection, and Post-Classification Comparison Change Detection...etc. The Post-Classification Comparison Change Detection is to classify the rectified images separately from two periods of time, giving appropriate marks to different particles on the surface of the ground. Then, compare and analyze the classified images from the two periods to figure out the change-detecting matrix, and finally construct the change map.

3. EXPERIMENTAL DESIGN

This research is to investigate the light wave reaction on the real green grass. Normal color slides and color infrared slides have been used to closely take the same area. Flow chart of the experiment is shown in Fig.1.

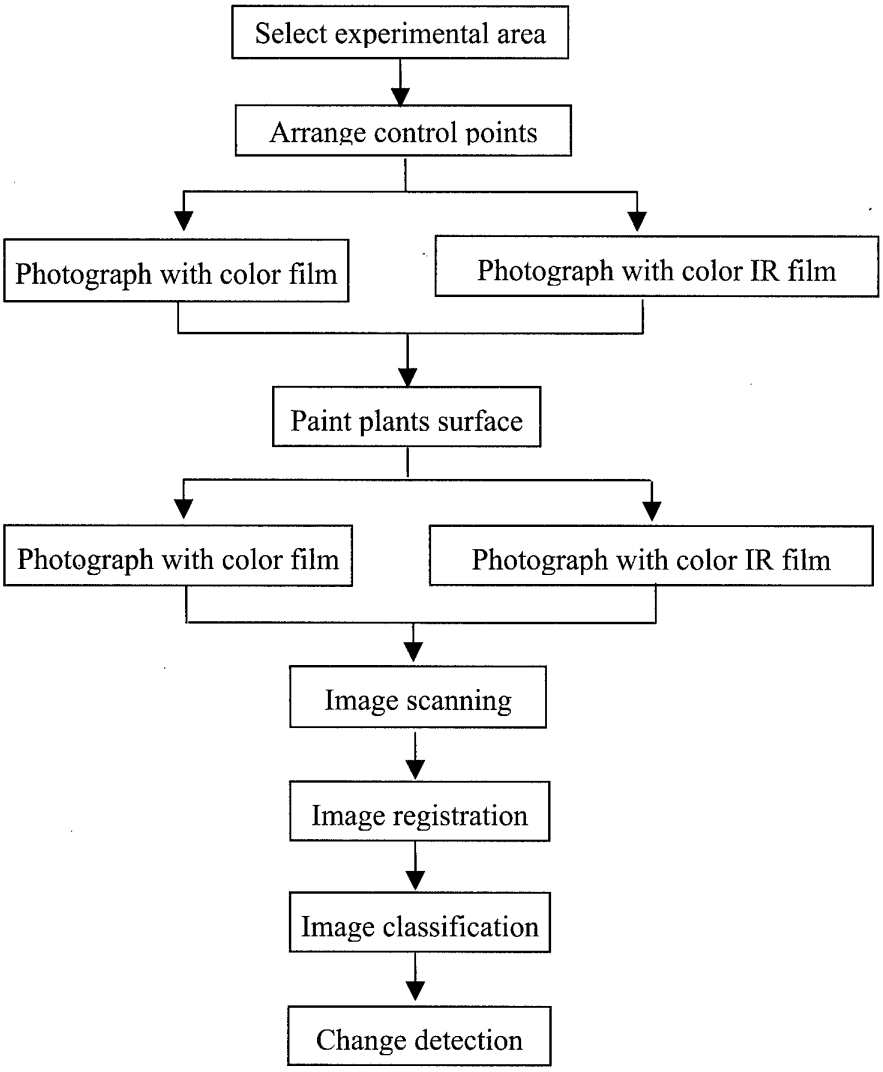


Figure 1 Flow chart of the experiment

3.1. Image Acquisition

Healthy green grass has a strong reflection in the near infrared region. Therefore, they appear bright red on color infrared images. However, varnished grass often shows low reflection rate in the near infrared area, thus it appears dark red on the color infrared image. According to this, change of the environment has been simulated. A normal color film has been put in one 50mm single lens camera, and a color infrared film has been put in another 50 mm single lens camera. Control points have also been set up around the experimental area. To observe the reflection difference on both healthy and false green plants, four small areas are varnished in green. A pixel size of 400dpi was used for scanning. Four digital color images were generated in the size of 450 x 210, and processed as described in the succeeding sections.

3.2. Image Registration and Image Classification

Four images were registered by the use of ground control points. One of the four images has been used as the master image. The other images were then geometric registered to each other. ER Mapper software was used to do the supervised classification with Gaussian maximum likelihood algorithm.

3.3. Change Detection

Following registration and classification, two classified images were produced. One image was classified healthy grass without any change, and the other one was classified varnished grass. Post-Classification Comparison was then employed to detect the differences between the two images. Change maps have been complied to display the specific nature of the changes between the two classified images.

4. OUTCOME ANALYSIS

4.1. Color Infrared Image

Images of healthy grass without any change and of varnished grass are shown respectively in Fig. 2 and Fig. 3. The white circles shown in these images are control points used in image registration. Healthy vegetation shown in Fig.2 reflects strong infrared wave before change. Some grass have been painted and then exposed dark red as shown in Fig.3. Because of the painted grass have low reflection in the IR region.

4.2. Supervised Classification

Classified images of healthy grass without any change and of varnished grass are shown respectively in Fig. 4 and Fig. 5. Four blue spot with red ring shown in these images are control points. Healthy vegetation appears to be green tone, painted grass shown in Fig.5 appears red tone, and unclassified pixels shown in both Fig.4 and Fig.5 appear to be black tone.

4.3. Change Detection Matrix

Post-classification change detection used in this research provides "from-to" information. A change detection matrix is shown as below. Note in the table that the pixels without change are located along the major diagonal of this matrix. Note also in the table that the producer's accuracy of painted grass class is only 20.29%, the omission error is 79.71%. The user's accuracy of painted grass class is 15.17%, the commission error is 84.83%. The overall

classification accuracy of this error matrix is 62.82%. Kappa analysis is a discrete multivariate technique of use in accuracy assessment (Congalton and Mead, 1983). K_{hat} computation incorporates the of-diagonal elements as a product of the row and column marginal. Computation of the K_{hat} statistic may also be used to compare two similar matrices(consisting of identical categories) to determine if they are significantly different. The K_{hat} computation of the error matrix is 17.34%, and it means that the two classified images have significantly difference.

Categories		**Image categories without change (from)**				
		Unclassified pixel (0)	Healthy grass (1)	Painted grass (2)	Control point (3)	Total
Image categories with change (to)	Unclassified pixel (0)	51461	22922	2146	0	76529
	Healthy grass (1)	5018	6924	755	1	12698
	Painted grass (2)	2215	1931	755	76	4977
	Control point (3)	0	3	65	228	296
	Total	58694	31780	3721	305	94500

Producer's Accuracy
Unclassified pixel = 51461/58694 = 86.21%
Healthy grass = 6924/31780 = 21.79%
Painted grass = 755/3721 = 20.29%
Control point = 228/305 = 74.75%

User's Accuracy
Unclassified pixel = 51461/76529 = 67.24%
Healthy grass = 6924/12698 = 54.53%
Painted grass = 755 / 4977 = 15.17%
Control point = 228/296 = 77.03%

$$\kappa_{hat} = \frac{N\sum_{I=1}^{R} X_{II} - \sum_{i=1}^{r}(x_{i+} \times x_{+i})}{N^2 - \sum_{i=1}^{r}(x_{i+} \times x_{+i})}$$

where r is the number of rows in the matrix
x_{ii} *is the num*ber of observations in row i and column i
x_{i+} x_{+i} are the marginal totals for row i and column i
N is the total number of observations

$$\sum_{i=1}^{r}(x_{i+} \times x_{+i}) = 76529 \times 58694 + 12698 \times 31780 + 4977 \times 3721 + 296 \times 305 = 4913945263$$

$(94500 \times 59368 - 4913945263)/(94500^2 - 4913945263) = 17.34\%$

Figure 2 Color IR image without change

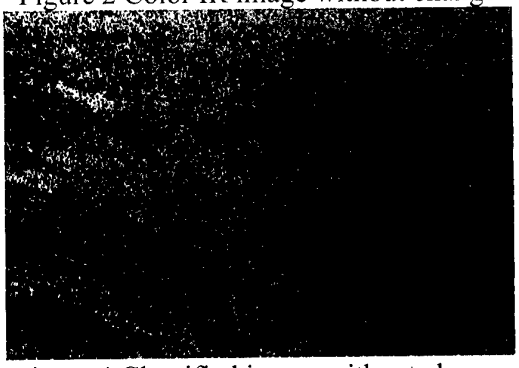


Figure 3 Color IR image with change

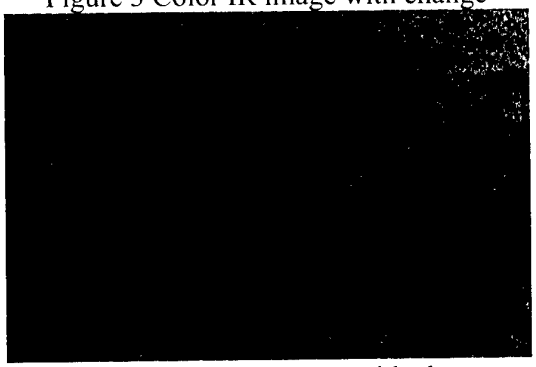


Figure 4 Classified image without change

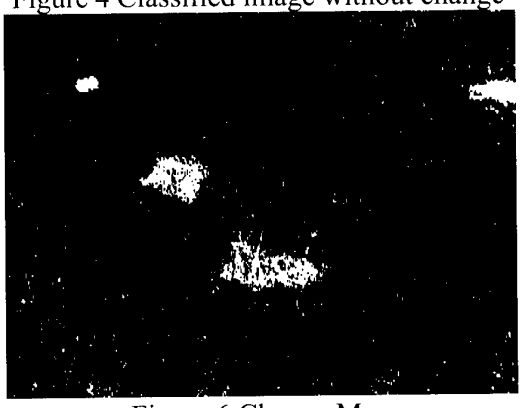


Figure 5 Classified image with change

Figure 6 Change Map

5. SUMMARY

Spectral variability has been controlled as possible as in this research to simulate an ideal remote sensing environment. The visual appearance of the change map was so good that one can easily distinguish any change by the use of post-classification change detection method. Furthermore, utilizing such a simple camera has provided considerable convenience for remote sensing experiment. On the other hand, the accuracy of registration influences the quality of classification. As the same reason, a classification with high quality indicates that change detection has excellent results.

6. REFERENCE

1.Augenstein, E., D. Stow, and A. Hope, 1991, "Evaluation of SPOT HRV-XS Data for Kelp Resource Inventories," Photogrammetric Engineering & Remote Sensing,57(5):501-509

2.Chavez, P. S., Jr., 1986. Digital merging of Landsat TM and digitized NHAP data for 1:24,000 scale image mapping, Photogrammetric Engineering & Remote Sensing, 52(10), pp. 1637-1646.

3.Jensen, J. R. and S. Narumalani, 1992,"Improve Remote Sensing and GIS Reliability Diagrams, Image Genealogy Diagrams, and Thematic Map Legends to Enhance Communication," International Archives of Photogrammetry and Remote Sensing,6(B6):125-132.

4.Jensen, J. R., D. J. Cowen, S Narumalani, J. D.Althausen, and O.Weatherbee,1993a,"An Evaluation of Coast Watch Change Detection Protocol in South Carolina," Photogrammetric Engineering & Remote Sensing,59(6):1039-1046.

5. Jensen, J. R. 1996. Introductory digital image processing: A remote sensing perspective, Prentice Hall.

6. Jensen, J. R., E. W. Ramsey, J. M. Holmes, J. E. Michel, B. Savitsky, and B. A. Davis 1990. Environmental Sensitivity Index (ESI) Mapping for Oil Spills Using Remote Sensing and Geographic Information System Technology, International Journal of Geographical Information Systems, 4(2), pp. 181-201.

7. Lillesand, T. M., and R. W. Kiefer. 2000. Remote Sensing And Image Interpretation, 4th ed., John Wiley & Sons.

8.Rutchey, K. and L.Velcheck, 1994,"Development of an Everglades Vegetation Map Using a SPOT Image and the Global Positioning System," Photogrammetric Engineering & Remote Sensing,60(6):767-775.

9.Walkey, J. A., "Development of a Change Detection Tool for Image Analysts," M.S. Thesis, University of Wisconsin-Madison, 1997.

CONSTRUCTION OF SATELLITE IMAGE DATA SET BY MULTISPECTRAL AND HYPERSPECTRAL SENSORS

Yuzo SUGA[1], Kenji TAKASAKI[2] and Shoji TAKEUCHI[1]
[1]Professor, [2]Assistant, Hiroshima Institute of Technology,
2-1-1, Miyake, Saeki-ku, Hiroshima 731-5193, Japan
Tel & Fax : (81)-82-922-5204, E-mail: ysuga@cc.it-hiroshima.ac.jp

KEY WORDS : NOAA/AVHRR, SeaWiFS, MODIS, Landsat-7/ETM+, Regional Monitoring.

ABSTRACT : Hiroshima Institute of Technology (HIT) has established the ground receiving station that has capabilities to capture and process the x-band down link data from earth observation satellite. This study deals with the construction of satellite image data set used to map the environmental information using several kinds of data from NOAA/AVHRR, SEASTAR/SeaWiFS, TERRA/MODIS, Landsat-7/ETM+, SPOT-1,2/HRV and SPOT-4/HRVIR captured in HIT ground station. This satellite image data set is constructed for the purpose of environmental information mapping from the wide area to the local area scale using the different spatial and spectral resolutions such as multispectral and hyperspectral sensor data. In this paper, some preliminary results are presented to demonstrate the capability for land and sea environmental monitoring using the data set produced by the initial operation of HIT ground station.

1. INTRODUCTION

Since 1980's NOAA/AVHRR data have been widely used for monitoring of earth environment in global scale. For regional scale, AVHRR sensor still has been only one practical data source to be used to monitor land and sea environment, such as the distributions/conditions of vegetation, sea surface temperature (SST) and to monitor disaster phenomena such as forest fire or volcano eruption. On the other hand for local scale, Landsat-5/TM and SPOT/HRV have been main data sources for land cover mapping, land cover change detection, and disaster monitoring etc. Nowadays, some new sensors are going to be available in global and regional scale, i.e. SEASTAR/SeaWiFS and TERRA/MODIS. The spatial resolution of these sensors are moderate and compatible to that of AVHRR, however, the number of spectral band is significantly increased, especially for MODIS sensor. By these new sensors, the spectral information is significantly enhanced compared with that by conventional AVHRR sensor and therefore, they are highly expected to extract more plentiful and accurate environmental information in global or regional scale.

Recently Hiroshima Institute of Technology (HIT) has established the ground receiving station that has capabilities to capture and process the x-band down link data from various earth observation satellites, SeaWiFS, MODIS, Landsat-7/ETM+, and SPOT-1,2/HRV and SPOT-4/HRVIR. In this paper, we report the present status for receiving and processing of these satellite data and some preliminary results by data analysis of these satellite data to evaluate their capabilities for monitoring land and sea environment.

2. SENSOR SPECIFICATIONS AND POSSIBLE SENSOR COMBINATIONS

The sensor specifications for AVHRR, SeaWiFS, MODIS and ETM+ are summarized in Table 1 to 4. As the wavelength characteristics of SeaWiFS and MODIS, it is pointed out that bandwidths are generally narrower than those of AVHRR and ETM+ as well as that number of band is much bigger. For example,

Table 1. Specification of NOAA-14,15/AVHRR.

Band No.	Wavelength Region (μm)	Spatial Resolution
1	0.58 – 0.68	1.1 Km
2	0.725 – 1.1	1.1 Km
3	3.55 – 3.93 or 1.58 – 1.64 (N-15 only)	1.1 Km
4	10.3 – 11.3	1.1 Km
5	11.5 – 12.5	1.1 Km

Table 2. Specification of SEASTAR/SeaWiFS.

Band No.	Wavelength Region (μm)	Spatial Resolution
1	0.402 – 0.422	1.1 Km
2	0.433 – 0.453	1.1 Km
3	0.480 – 0.500	1.1 Km
4	0.500 – 0.520	1.1 Km
5	0.545 – 0.565	1.1 Km
6	0.660 – 0.680	1.1 Km
7	0.745 – 0.785	1.1 Km
8	0.845 – 0.885	1.1 Km

Table 3. Specification of TERRA/MODIS.

Band No.	Wavelength Region (μm)	Spatial Resolution
1	0.620 –0.670	250 m
2	0.841 – 0.876	250 m
3	0.459 – 0.479	500 m
4	0.545 – 0.565	500 m
5	1.230 –1.250	500 m
6	1.628 – 1.652	500 m
7	2.105 – 2.155	500 m
8	0.405 –0.420	1 Km
9	0.438 – 0.448	1 Km
10	0.483 – 0.493	1 Km
11	0.526 – 0.536	1 Km
12	0.546 – 0.556	1 Km
13	0.662 – 0.672	1 Km
14	0.673 – 0.683	1 Km
15	0.743 – 0.753	1 Km
16	0.862 – 0.877	1 Km
17	0.890 – 0.920	1 Km
18	0.931 – 0.941	1 Km
19	0.915 – 0.965	1 Km
26	1.360 – 1.390	1 Km
20	3.660 – 3.840	1 Km
21	3.929 – 3.989	1 Km
22	3.929 – 3.989*	1 Km
23	4.020 – 4.080	1 Km
24	4.433 – 4.498	1 Km
25	4.482 – 4.549	1 Km
27	6.535 – 6.895	1 Km
28	7.175 – 7.475	1 Km
29	8.400 – 8.700	1 Km
30	9.580 – 9.880	1 Km
31	10.780 –11.280	1 Km
32	11.770 – 12.270	1 Km
33	13.185 – 13.485	1 Km
34	13.485 – 13.785	1 Km
35	13.785 – 14.085	1 Km
36	14.085 –14.385	1 Km

* Saturation level is smaller than previous band.

Table 4. Specification of Landsat-7/ETM+.

Band No.	Wavelength Region (μm)	Spatial Resolution
1	0.45 – 0.52	30 m
2	0.53 – 0.61	30 m
3	0.63 – 0.69	30 m
4	0.78 – 0.90	30 m
5	1.55 – 1.75	30 m
6	10.4 – 12.5	60 m
7	2.09 – 2.35	30 m
8	0.52 – 0.90	15 m

the band-1 of AVHRR corresponds to the band-6 of SeaWiFS as a wavelength region. However, the bandwidth for AVHRR is 0.1 μm, while that for SeaWiFS is 0.02 μm and five times narrower than AVHRR because the band-6 of SeaWiFS is designed to extract spectral signatures caused by absorption by chlorophyll. Therefore, the conventional vegetation index parameter like NDVI is still expected to be improved by replacing AVHRR band-1 with SeaWiFS band-6.

Among the four sensors listed in Table-1 to 4, ETM+ is special due to its much higher resolution and narrower swath, which has been used mainly for monitoring local areas. However, as the first seven bands of MODIS almost corresponds to the wavelength regions by ETM+, there might be some possibility to use both sensor data as the complement data in spatial resolution and swath. For example, the up-scaling of land cover information using Landsat-5/TM and NOAA/AVHRR was attempted (i.e.

Takeuchi and Inanaga, 2000) and proved to be effective for monitoring wide areas more accurately even if both spectral information is not compatible each other. Therefore, up-scaling using TM/ETM+ and MODIS band-1 to 7 is expected to bring more accurate monitoring capability by the combined utilization of multiple sensor data.

SeaWiFS is originally designed to extract some physical parameters for oceanic applications, like water quality and chlorophyll content using visible band information. Therefore, one of the standard ways for sensor combinations will be the combined use of visible bands from SeaWiFS with the thermal bands from AVHRR, the former brings water quality and chlorophyll content and the latter sea surface temperature (SST). In addition, due to its capability for non-saturated observation of land areas, the similar combination might be effective for land environmental monitoring. For example, NDVI by SeaWiFS might be better than that by AVHRR as described previously, or, the enhanced vegetation index (EVI) is possibly extracted from band-1/2, 6, and 8 of SeaWiFS, while it is impossible by AVHRR data. The latter approach is also possible for MODIS band-1 to 3 (Justice *et al,* 2000 and Huete *et al*, 2000). These multiple sensor combinations are expected to enable to achieve more accurate land environmental monitoring in regional scale.

3. DATA RECEPTION AND PROCESSING IN HIT

At a moment, HIT has two antenna systems, a 7.3 meters Transportable Ground Station (TGS) antenna and a 13 meters antenna, the latter was just established in March this year. Currently SeaWiFS and MODIS are received by the 7.3 meters antenna and Landsat-7/ETM+ and SPOT-1,2, and 4 are received by the 13 meters antenna. In addition, NOAA/AVHRR is received by a 1.2 meters antenna system.

Landsat-7/ETM+ data are processed soon after reception in the 13 meters antenna system. As the products, Raw, Level-0, Level-0R, Level-1R and Level-1G are archived. The format of Level-1R is HDF only and those for Level-1G are HDF, FAST and GeoTIFF. SPOT-1, 2 and 4 data are also processed in the 13meter antenna system and Level-1B with CAP format is archived as the SPOT data product. For NOAA/AVHRR, raw AVHRR data are converted to NOAA/NESDIS Level-1B format. For SeaWiFS and MODIS, all data are archived in HDF format.

4. SOME PRELIMINARY RESULTS

We preliminary evaluated the spectral information by AVHRR, SeaWiFS, MODIS, and ETM+ data. AVHRR, SeaWiFS, and MODIS data were acquired on the same day (Aug. 4, 2000). ETM+ was acquired on July 22, 2000, almost same season as that for the formers. Figure 1 shows AVHRR false-color composite image, in which red and blue are assigned to band-1 and green for band-2. As there are only two bands for visible and near-infrared regions, there is no other way to enhance spectral information except NDVI, which will be discussed later.

On the other hand, as SeaWiFS has total eight bands in the same wavelength regions, there might be various band combinations to enhance spectral information in land areas as well as in water areas. Figure 2 shows an example for such an enhanced false-color composite image. In Figure 2, red is assigned to the enhanced image by the computation of (B6-B1)/(B6+B1), where B1 and B6 are data values for band-1 and band-6 respectively. This image enhances the difference of reflectance in band-1 (blue-color region) and band-6 (red-color region). The other two color components, green and blue, are assigned to band-8 (near-infrared) and band-4 (green-color region) respectively. Therefore the color image in Figure 2 includes all information from blue, green, red and near-infrared regions. The result clearly indicates the differences between forested land covers and urban/agricultural land covers, while in AVHRR image these differences are not identified so clearly.

Figure 3 shows an example of MODIS false-color composite image acquired on the same day as AVHRR and SeaWiFS. The color assignment is that red is assigned to band-6, green to band-2, and blue to band-1. Band-6, 2 and 1 correspond to band-5, 4 and 3 of ETM+ respectively. Figure 4 shows the false-color of ETM+ in the color assignment similar to MODIS, namely red is assigned to band-5, green to band-4 and blue to band-3. Both images indicate similar color tones for similar land covers. This result suggests that there might be a possibility to use both data as a complement data set as described in section 2.

Figure 5 shows an enhanced color image using principal component analysis (P.C.A.) for eight bands data only in water areas. The colors are assigned to the first three principal components, red to PC-1, green to PC-2 and blue to PC-3. The image clearly shows the differences in water quality between the water in Pacific Ocean and the water in coastal regions or Seto Inland Sea. Figure 6 shows the color image for sea surface temperature (SST) derived from AVHRR on the same day. It is clearly seen from both images that the boundary for two different water quality in Figure 5 corresponds to the boundary for two different temperature regions in Figure 6, namely between inner or coastal water areas with lower temperature and the warm ocean current (Kuroshio) with higher temperature. This result suggests that the combined use of visible information from SeaWiFS and thermal information from AVHRR is very effective for monitoring sea surface environmental conditions.

Figure 7 and 8 show the comparison of NDVI images derived from AVHRR and SeaWiFS data respectively. As described in section 2, there might be a possibility to improve NDVI parameter by using SeaWiFS band-6 as a visible band. The comparison of Figure 7 and 8 supports this improvement. In Figure 7 it is rather difficult to discriminate the differences between forested land covers and agricultural land covers (see Kyushu region in Figure 7). On the other hand, in Figure 8, it is very easy to discriminate these differences. The observation seasons of both images are summer and rice is planted in almost agricultural areas and it is almost a peak condition for rice-growth in this season. Therefore, the result of Figure 7 and 8 clearly supports that NDVI derived from SeaWiFS is more effective than that by AVHRR for monitoring vegetative conditions.

5. CONCLUSION

Some preliminary results on the evaluation of spectral information for regional land and sea environmental monitoring using NOAA/AVHRR, SeaWiFS, MODIS and Landsat-7/ETM+ were presented in this paper. These preliminary results support that the data from above new sensors are capable to monitor land and sea environmental conditions more accurately in regional scale if the sensors are combined each other. From now we will develop the combination methods for above sensors to establish effective data sets based on HIT ground receiving facilities, and also conduct various kinds of feasible studies for land and sea environmental monitoring around the Japan Islands.

REFERENCES

Takeuchi, S. and A. Inanaga, 2000. Scaling-Up of Land Cover Information by Using Multiple Resolution Satellite Data. *Adv. Space Res.* Vol.26, No.7, 1127.

Justice, C., J.Townshend, E.Vermote, et al. 2000. Preliminary Land Surface Products from the NASA Moderate Resolution Imaging Specroradiometer (MODIS). Proceedings of *IGARSS' 2000 Symposium.*

Huete, A., K.Didan, Y.Shimabokuro, L.Ferreira, and E.Rodriguez. 2000. Regional Amazon Basin and Global Analysis of MODIS Vegetation Indices: Early Results and Comparisons with AVHRR. Proceedings of *IGARSS' 2000 Symposium.*



Fig.1.NOAA-14/AVHRR False-Color.
(Red:B1, Green:B2, Blue:B1)



Fig.2. SeaWiFS Enhanced False-Color.
(Red:(B6-B1)/(B6+B1), Green:B8, Blue:B4)



Fig.3. MODIS False-Color.
(Red:B6, Green:B2, Blue:B1)

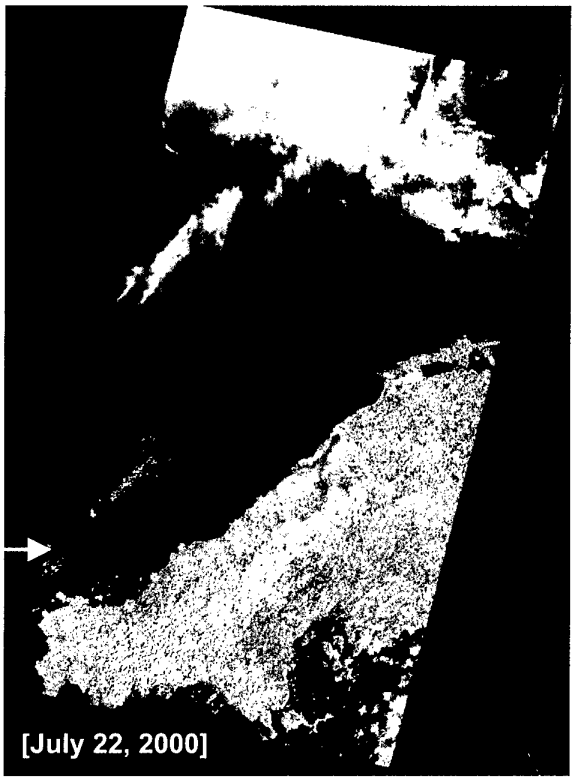


Fig.4. Landsat-7/ETM+ False-Color (Path:112).
(Red:B5, Green:B4, Blue:B3)

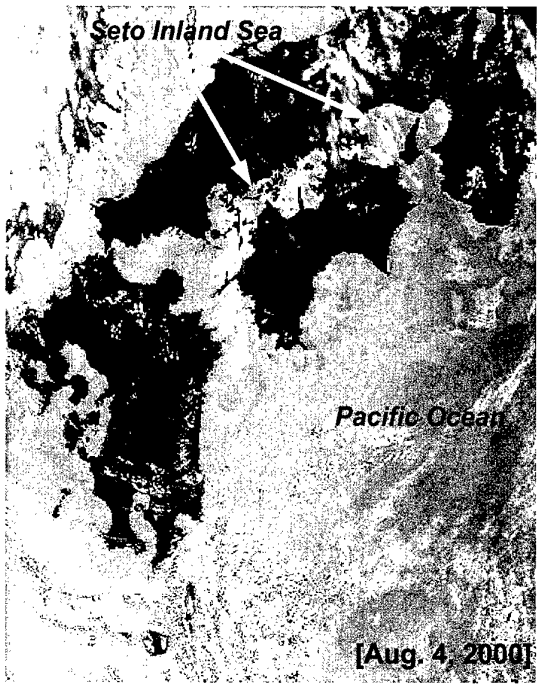


Fig.5. SeaWifs Enhanced False-Color by P.C.A. (Red:PC-1, Green:PC-2, Blue:PC-3)

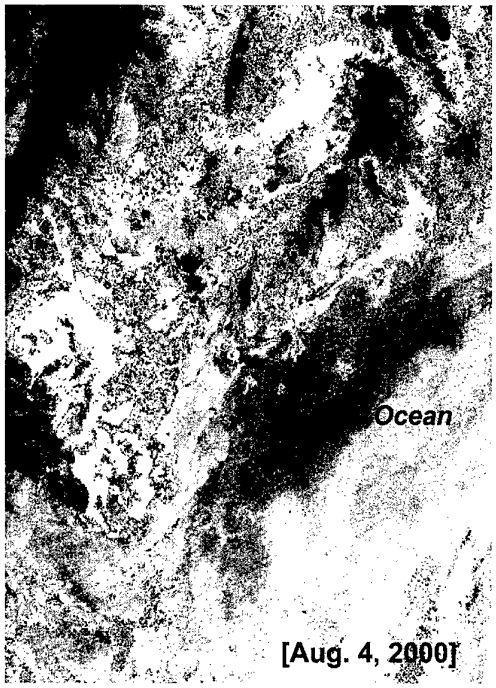


Fig.6. NOAA-14/AVHRR Sea Surface Temperature (SST) - Color.

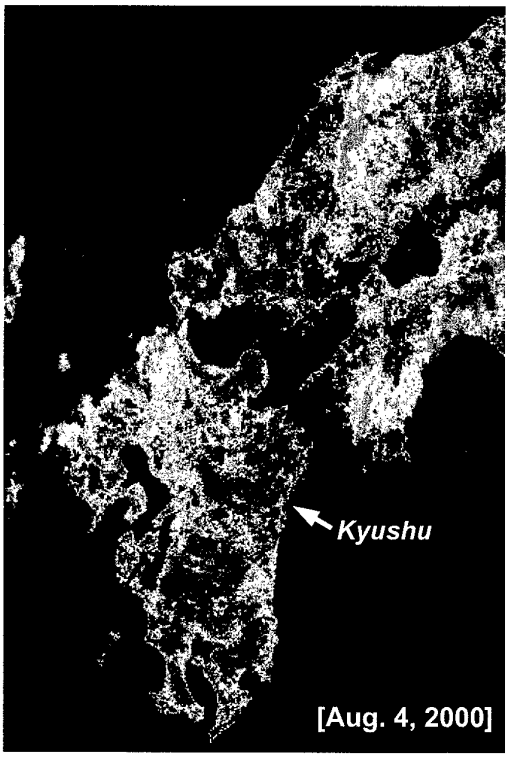


Fig.7. NOAA-14/AVHRR NDVI-Color. [NDVI = (B2-B1)/(B2+B1)]

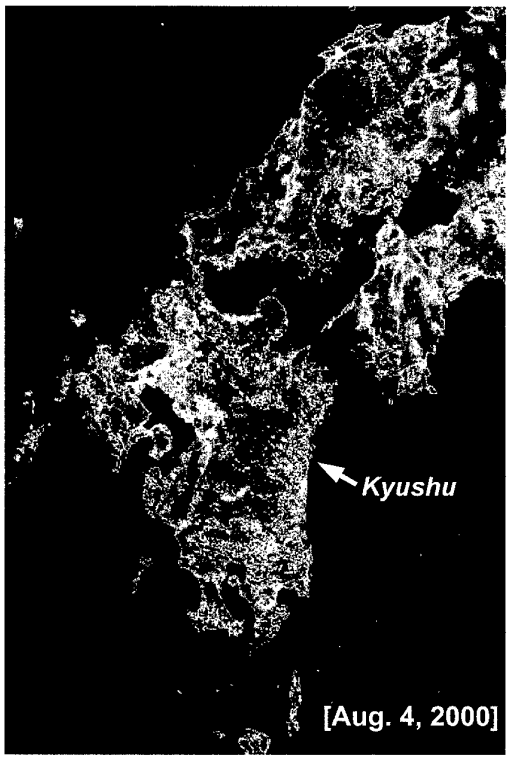


Fig.8. SeaWiFS NDVI-Color. [NDVI = (B8-B6)/(B8+B6)]

Tracking Automobiles using Air-borne TLS (Three Line Scanner) Images

Ryuichi MURATA, Ryosuke SHIBASAKI
Center for Spatial Information Science (CSIS)
University of Tokyo
4-6-1 komaba, Meguro-ku, Tokyo 153-8505, Japan
Tel&Fax: +81-3-5452-6417
E-mail: rmurata@iis.u-tokyo.ac.jp

KEYWORDS: TLS (three line scanner), air-borne sensor, ITS, object tracking

ABSTRACT: Acquiring traffic data such as number of cars, speed distribution, number of illegal parking cars accurately and quickly is needed for ITS (Intelligent Transport System). ITS is expected to mitigate traffic jam and to improve management of limited road resources. Currently, as a common practice, only limited traffic data are collected; vehicles are counted using roadside ultra-sonic sensors. Finding traffic accidents depends on the witness's notice, patrol of road administrative officers, and monitoring with roadside cameras. TLS (Three Line Scanner) is an air-borne sensor consisting of three parallel one-dimensional CCDs mounted on the imaging plane. It obtains seamless high-resolution images (5-10cm on the ground) with three viewing directions (fore, nadir, aft) simultaneously mainly to generate 3D spatial data accurately. In addition, the high-resolution imagery can be applied to observe running cars, speed and parking cars on the street since TLS scans the same road surface with a time interval with approximately 10 seconds. This paper describes methodologies and the results of applying TLS imagery to the tracking of automobiles.

1. Introduction

ITS (Intelligent Transport System) society will spread in near the future. ITS is expected to operate traffic flows and to provide efficient road administration. But generally, acquiring traffic data depends on roadside ultra-sonic detectors, cameras, witness's notices or patrols of road administrative officers. Traffic data acquired with such devices are basically point-based and fail to represent spatial distribution. It is quite necessary to develop a method of acquiring traffic data such as number of cars, speed distribution, finding accidental vehicles accurately and quickly over large areas. The high-resolution imagery of TLS (Three Line Scanners) can be applied to the observation of running cars, their speed and parking cars on the street because TLS can scan the same road surface and objects with a time interval with approximately 10 seconds.

2. TLS system

2.1 TLS principle

TLS (Three Line Scanner) is an air-borne sensor consisting of three parallel one-dimensional CCDs mounted on the imaging plane (Fig.1 and Fig.2). It obtains seamless high-resolution images (5-10cm on the ground) with three viewing directions (fore, nadir, aft) simultaneously mainly to generate 3D spatial data accurately with RTK-GPS and INS.

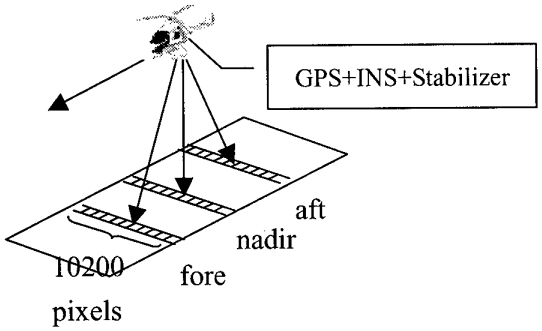


Fig.1: Method of TLS image Acquiring

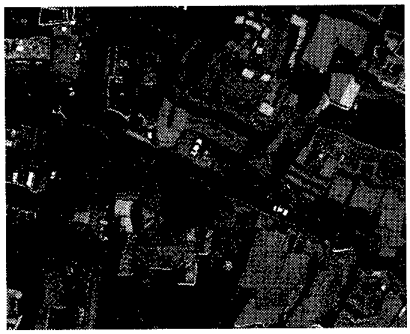


Fig.2: Plain TLS image

2.2 TLS performance

Table1: system specification of TLS

CCD	Number of pixel/line	10200 pixels
	Pitch of pixel	7 um
Number of CCD		3(monochrome), 1(RGB)
Number of shading		12 bit
Lens	Distance of focus	60mm
Angle of stereo		21°
Frequency		500 line/second

2.3 TLS characteristics

Characteristics of TLS are summarized as follows.

1. Seamless high-resolution images (5-10cm on the ground, about aerial photograph class) can be obtained with three different viewing directions (fore, nadir, aft). Easy to create ortho-image from TLS images because TLS images are "line-projection" and less distorted

than conventional aerial photo-images, which is point-projection image.

2. Much less ground control point is needed since RTK-GPS and INS can estimate the sensor position and attitude accurately.
3. TLS system records digital data directly, which enable users to easily process and analyze them on the real-time basis and help minimize processing errors.
4. Multi-spectrum images can be acquired by replacing the filters and sensors.

3. Automobile tracking method

We examined two automobile tracking methods using TLS gray scale image.

3.1 brightness difference from a pair of images

Since moving objects on the road are only automobiles, it is possible to track automobile objects using differential image from a pair of image covering the same area at the different times (Fig.3). We calculate object's speed by dividing the ground distance of centroids of each object by time difference. Fig.3 shows a result of tracking a white bus. But any automobiles whose color is similar to road surface are not tracked. In addition, we can't apply this method to track standing automobiles due to a traffic jam or an accident.

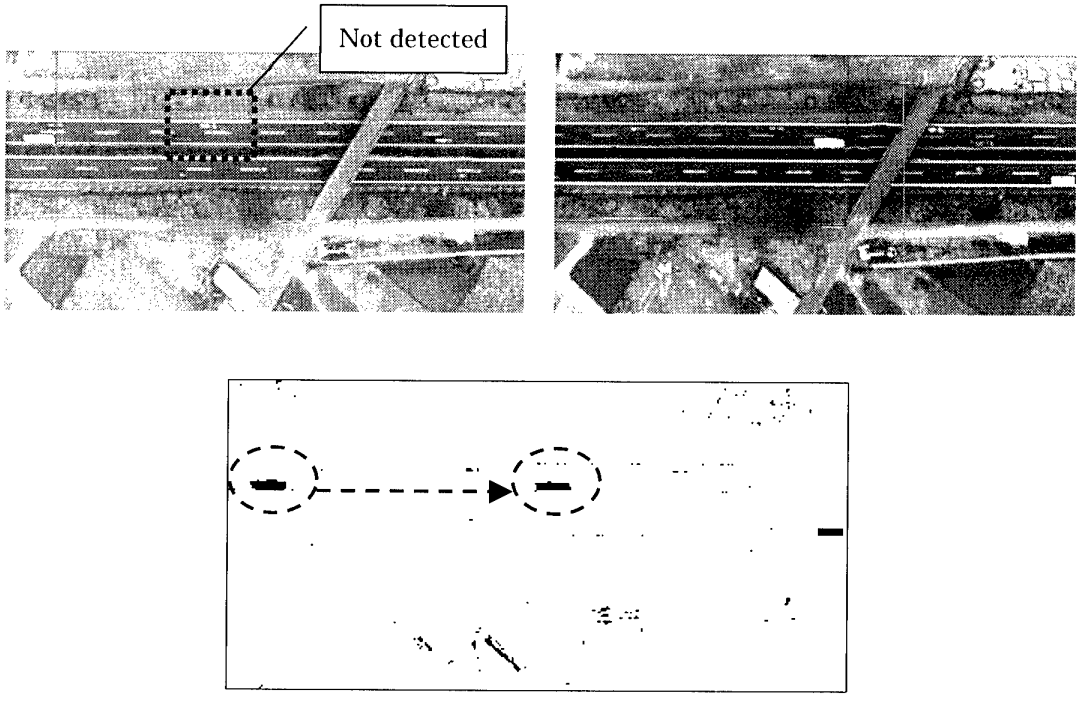


Fig.3: Differential image and a pair of image covered the same area at the different times

3.2 Template matching

In order to track stopping automobiles, I used template matching method using Hausdorff distance. First operation in the processing is edge detection from TLS image. Secondary is making a proper size rectangle template according to altitude of a platform or image resolution since all automobiles in aerial images have rectangular shape. Last one is affine transformation of TLS image and template matching. We narrowed down the operation image area to roads to improve the accuracy of the matching.

The distance between the each pixel of the template and the nearest TLS edge point defines the Hausdorff distance. We detected template position whose summation of each points Hausdorff distance is under set threshold as automobile object.

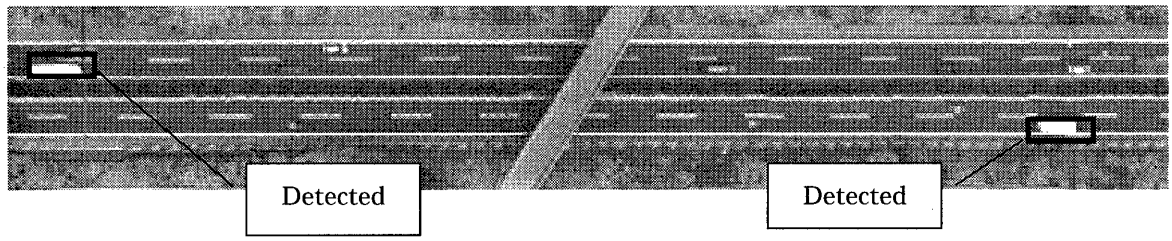


Fig.4: Detected objects by template matching

4. Conclusions

This study show that it is possible to track automobiles using TLS gray scale image. Differential image method depends on brightness of TLS image, so automobiles whose colors are similar to those of road surfaces were not tracked. It is difficult to detect edge in template matching method since the test image is experimental with no enough quality. Further studies are required to improve the accuracy of tracking objects using color image and high resolution image from the TLS.

References

Shunji Murai, Yositaka Matsumoto, Li Xun, 1995, stereoscopic imagery with an air borne three-line scanner (TLS), ISPRS commission V, Intercom mission Workshop, pp20-25

Michihiro Murao, Yasuyuki Matsushita, Katsushi Ikeuchi, Masao Sakauchi, 2000, Visualization of traffic Conditions for Drivers, UM3'2000 session D, p22

GEO-REFERENCING OF MULTI-SENSOR RANGE DATA FOR VEHICLE-BORNE LASER MAPPING SYSTEM (VLMS)

Dinesh MANANDHAR, Ryosuke SHIBASAKI
Centre for Spatial Information Science, The University of Tokyo
4-6-1, Komaba, Meguro-ku, Tokyo 153-8505, JAPAN
Tel / Fax No: 88-3-5452-6417
e-mail: {dinesh,shiba}@skl.iis.u-tokyo.ac.jp

KEY WORDS: Mobile Mapping, Range Data, Sensor Calibration, INS / GPS

ABSTRACT: Laser mapping has become quite popular in recent days due to it's capability of providing information directly in three dimension. However, the present laser mapping systems are either air-borne or ground-based (on a static platform). We cannot achieve detail information from air-borne system, though it has it's own suitability for applications like DEM generation. Ground based static systems are not suitable for larger area mapping purpose.

The vehicle-borne laser mapping system (VLMS) use laser scanners for three dimensional data acquisition, CCD cameras for texture information, GPS, INS and odometer for positioning information. The data obtained by this system could be a good resource for developing urban 3-D database, which has numerous applications in the field of virtual reality, car navigation, computer games, planning and management.

In this paper, we discuss about the system architecture of VLMS, calibration of sensors, integration of all these sensors and positioning devices for direct geo-referencing.

1 INTRODUCTION

The mobile mapping technology has been developed since late 1980's. The development of the mobile mapping system became possible due to the availability of GPS signal to the civilian community. This system is capable of observing the objects at closer range, thus giving greater details. As per our knowledge, so far, the vehicle based mobile mapping system are based on CCD cameras (in combination with video camera in some cases) for data acquisition. Combination of GPS with either INS or Gyro is used for navigation purpose. For reference of some of these systems, refer GPS-VanTM (Bossler et al, 1991), VISAT-Van (Schwarz et al, 1993, Li et al, 1994), TruckMapTM (Pottle, 1995), KiSS (Hock et al, 1995), GPS Vision (He, 1996) and GeoMaster (Tamura et al, 1998).

In our system, we have used laser scanners as the main data acquisition device. The system is supplemented by CCD cameras for texture information and as usual combination of GPS, INS and odometer is used for position and attitude information.

2 SYSTEM CONFIGURATION

The mobile mapping system is shown in figure 1. It consists of four CCD cameras, four laser scanners, Hybrid Inertial Survey System (HISS) which consists of DGPS, INS and electronic odometer for position and orientation data.

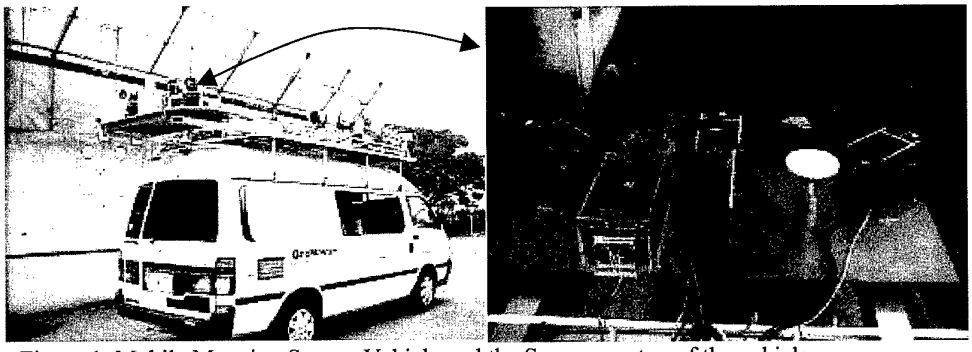


Figure 1. Mobile Mapping Survey Vehicle and the Sensors on top of the vehicle

2.1 HISS (The GPS/INS Integration)

The Hybrid Inertial Survey System (HISS) is the integration of GPS, INS and Odometer. The integrated system has an accuracy of about one-meter in horizontal plane. The system once initialized can work either on DGPS/INS mode or Odometer/INS mode. The switching between the two modes is automatic, which is based on PDOP (if PDOP > 4.0) and number of visible satellites (if no. of sat < 4). The preference is always given to DGPS/INS mode. We have conducted some tests to see the behavior of the DGPS alone and DGPS/INS results at stationary mode (while the vehicle is not moving). For details on HISS and it's field test results, refer (Tamura et al,1998).

2.2 Laser Scanner

Four laser scanners are fixed on top of the vehicle at four different directions as shown in figure 1. The purpose of using four units is to capture the data from different viewing angle so that as much of data can be extracted as possible even when the target is occluded by pedestrians or moving vehicles. The laser scanner head rotates around it's head (shown in figure 2). It provides the distance from the laser head to the target. This distance is later converted into 3-D coordinates. The configuration of laser scanner is given in Table 1.

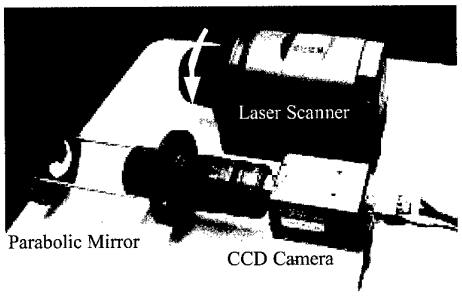


Figure 2. CCD and Laser sensor units

Meas. Distance Range	50m(reflection rate 20%)
Accuracy of Range Measurement	3cm(1)
Scanning Range	300°
Angular Range Step	0.25°
Frequency	10Hz

Table 1. Laser Scanner configuration

2.3 CCD Camera

Four CCD cameras are used with parabolic reflecting mirrors. Each unit of CCD camera and Laser scanner are housed in a single frame. Table 2 shows the configuration of the CCD camera.

Photograph Element	1/2 inch color CCD
Resolution	659x494
Output	RGB
Trigger shutter	1/60 1/10000
Lens Mount	C mount

Table 2. Configuration of CCD Camera

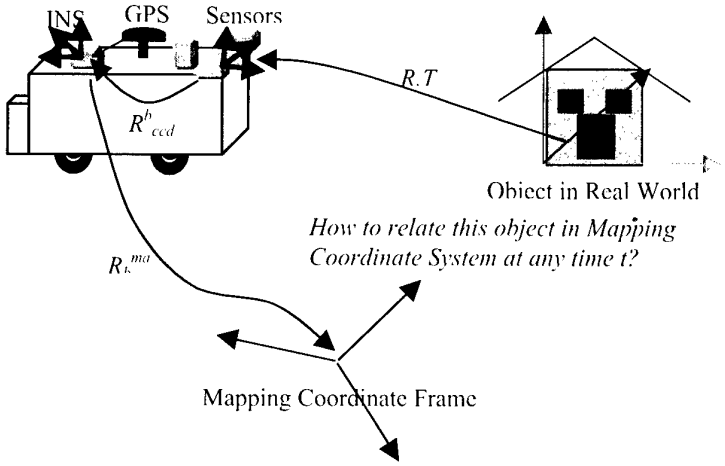


Figure 3. Illustration of Geo-referencing

3 GEO-REFERENCING

In mobile mapping, the vehicle is continuously moving or the position of the vehicle is changing with respect to time. Besides, every sensor and device has it's own local coordinate system. For example, GPS output is based on WGS84 coordinates system, Laser data is based on it's own local coordinate system, the origin of which lies at the laser scanning head and so on for other sensors and devices. The major problem is to identify the spatial position of the objects scanned by the laser at any time while the vehicle is moving with reference to a common coordinate system, which is called Geo-referencing. It involves the integration of all the sensors and devices to a common coordinate system, which is the (local) mapping coordinate system. The integration process mainly involves the computation of fixed rotation and shift vectors between the INS body and sensors. As the GPS and INS are physically located in two different places, we also need to know the shift vector between the GPS and INS. Refer (Manandhar and Shibasaki, 2000) for details on individual sensor calibration.

The general mathematical model (Cramer et al., 1998) for direct geo-referencing when the GPS and INS are physically offset is given in equation 1.

$$\vec{X}_p^{map} = \vec{X}_{gps}^{map} + R_b^{map}[R_{ccd}^b \vec{x}_p^i + \Delta\vec{X}_{ccd}^b - \Delta X_{gps}^b] \qquad \text{Equation 1}$$

where, $\vec{X}_p^{map} = \begin{bmatrix} X_p \\ Y_p \\ Z_p \end{bmatrix}^{map}$ Equation 2 Any object point vector at time t in mapping coordinate system

$\vec{X}_{gps}^{map} = \begin{bmatrix} X_{gps} \\ Y_{gps} \\ Z_{gps} \end{bmatrix}^{map}$ Equation 3 GPS measured point vector at time t in mapping coordinate system

R_b^{map} A variable, 3 x 3 Rotation Matrix at time t from INS body (INS coordinate system) to Mapping Frame. This is direct observation value at time t by INS. The HISS system is calibrated so as to give the output in WGS84 coordinate system.

$$\vec{x}_p^i = \begin{bmatrix} x_p \\ y_p \\ -f \end{bmatrix}^i \qquad \text{Equation 4}$$

Image vector in Image Coordinate System

$$\Delta\vec{X}_{ccd}^b = \begin{bmatrix} \Delta X_{ccd} \\ \Delta Y_{ccd} \\ \Delta Z_{ccd} \end{bmatrix}^b \qquad \text{Equation 5}$$

Offset from INS to the CCD in body frame, obtained by direct measurement.

$$\Delta\vec{X}_{gps}^b = \begin{bmatrix} \Delta X_{gps} \\ \Delta Y_{gps} \\ \Delta Z_{gps} \end{bmatrix}^b \qquad \text{Equation 6}$$

Offset from INS to GPS in body frame, obtained by direct measurement.

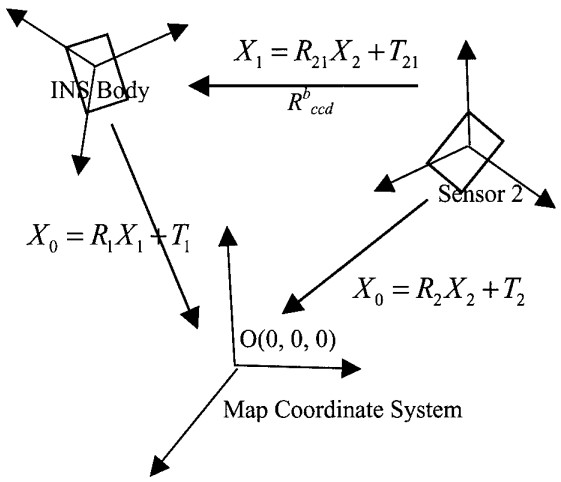


Figure 4. Illustration of computation of Fixed Rotation between the Sensor and INS

R^b_{ccd} A fixed, 3 x 3 Rotation Matrix between CCD camera and INS body in INS coordinate system. The computation of this rotation matrix is given below:

We get rotation matrix and shift vector between the CCD and local coordinate system from outdoor camera calibration. During the calibration process we observe the GPS/INS position together with acquisition of the calibration target images. We have defined a local coordinate system for measuring the calibration targets by the total station. While defining the local coordinate system, the orientation of the x, y, and z-axis were set following the map coordinate system, so that the rotation between the two coordinate systems is a 3x3 unit matrix. Thus we can approximate that the rotation between the CCD camera and the local coordinate system is the rotation between the CCD camera and mapping coordinate system. The transformation from local coordinate system to mapping coordinate system is given by equation 7. This is a two-dimensional affine transformation.

$$\begin{bmatrix} X \\ Y \end{bmatrix}_{MapCoordinateSystem} = \begin{bmatrix} a & b \\ d & e \end{bmatrix} \begin{bmatrix} x \\ y \end{bmatrix}_{\substack{TotalStation \\ LocalCoordinateSystem}} + \begin{bmatrix} c \\ f \end{bmatrix} \qquad \text{Equation 7}$$

The initialization process of INS aligns the horizontal plane and finds the north direction and the output is calibrated to give the rotation with respect to the map coordinate system. Thus the rotation output from the HISS (INS/GPS) is the rotation from the INS body to the Mapping coordinate system.

Now, we have both the rotation of the CCD camera and INS body with respect to the mapping coordinate system. From this two information, we can compute the fixed rotation between the CCD and INS with respect to mapping coordinate system by using the three equations illustrated in figure 4.

Since, we need to geo-reference laser coordinates, we have to know the relation between the laser coordinate system and the mapping coordinate system. However, one major problem in

outdoor experiment is to identify a specific reflected laser from the object point (or calibration target). The laser data we get is just a cloud of points and it's too difficult to know which particular point or points is the one reflected by the target. Thus in order to overcome this problem, we based our integrated calibration on CCD calibration. We converted the laser coordinate system to CCD coordinate system (image coordinate system) with some assumptions. This is achieved by using the equations 8 and 9.

$$X_{ccd} = R^{ccd}_{laser} X_{laser} + T^{ccd}_{laser} \qquad \text{Equation 8}$$

$$\text{where, } \vec{X}_{laser} = \begin{bmatrix} 0 \\ r\cos\theta \\ r\sin\theta \end{bmatrix} \qquad \text{Equation 9}$$

In this system, the laser and CCD camera are housed in the same frame. Thus, both of these two sensors rotate together with respect to INS and other devices. We assumed that the imaging plane of CCD and Laser are orthogonal to each other and from the coordinate systems defined for laser and CCD, we can write the rotation from laser to CCD as [0 0 –90] along X, Y and Z axis. The shift between the laser and CCD are physically measured.

Thus we modify equation 1 to equation 10. We use this equation to compute every object coordinate measured by laser with respect to the map coordinate system.

$$\vec{X}^{map}_{p} = \vec{X}^{map}_{gps} + R^{map}_{b}[R^{b}_{ccd}[R^{ccd}_{laser} X_{laser} + T^{ccd}_{laser}] + \Delta\vec{X}^{b}_{ccd} - \Delta X^{b}_{gps}] \qquad \text{Equation 10}$$

Using above mathematical model for geo-referencing, we have integrated laser range data from three sensors. The fourth sensor, which is placed vertically up on top of the vehicle is used for deriving the horizontal profile of the vehicle.

4 RESULTS AND DISCUSSIONS

Table3 shows the results of the integrated calibration of the sensors and the positioning devices.

Sensors to INS	Roll	Pitch	Yaw	Tx	Ty	Tz
Sensor 1	-0.476	-0.982	44.659	-0.437	-0.965	0.110
Sensor 2	0.100	-0.474	90.727	-0.562	-0.236	0.150
Sensor 3	-0.125	-1.037	134.389	-0.423	0.480	0.100

Table 3: Computation Results of Fixed Rotation and Shift Vectors from Sensors to INS body

The range data taken by each of the laser scanner is shown in figure 5. The orientation of scanners is approximately at 45 degrees to each other. Scanner 2 is the middle scanner, which captured most of the data. We can see some occluded regions in range data taken by scanner 2 due to trees. The region of occlusion is more prominent in scanner 1 and scanner 3 data sets. However, when we combine all these three data sets, we can recover part of the occluded region.

5 CONCLUSION AND FUTURE WORK

We have developed a Vehicle-borne Laser Mapping System (VLMS), which is capable of acquiring data in three dimensions. This data can be further processed for use in urban 3-D GIS. The future work includes segmentation of these laser data so that we can classify the objects into buildings, trees (vegetation), road surfaces and other classes.

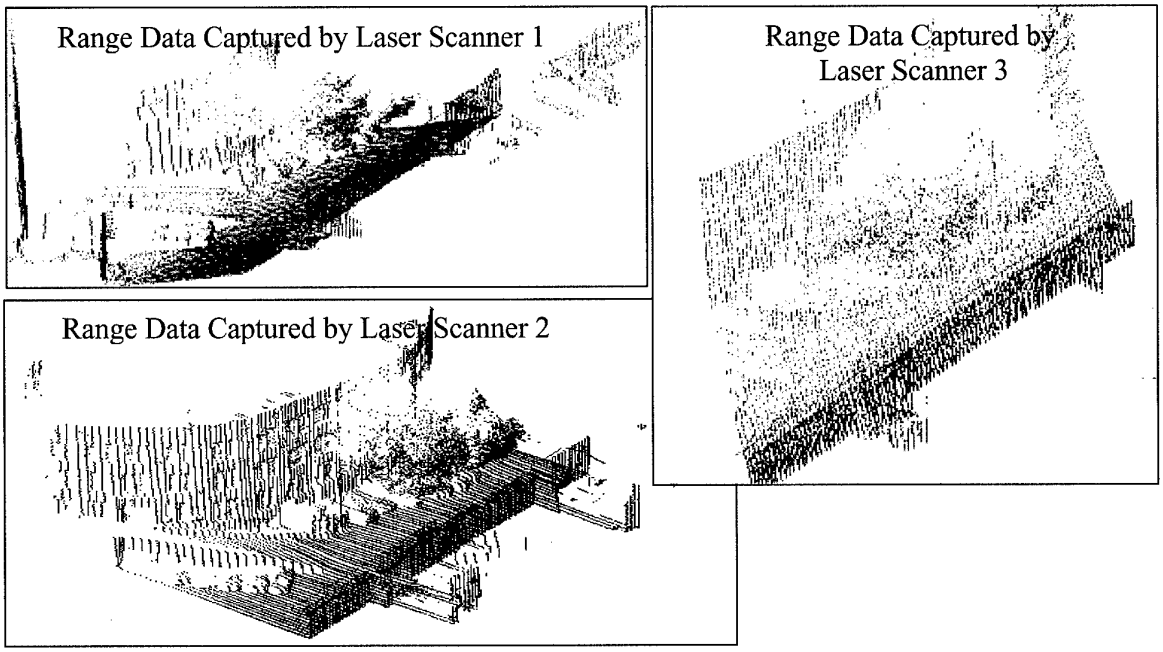


Figure 5: Plot of Laser Range Data from each of the scanners.

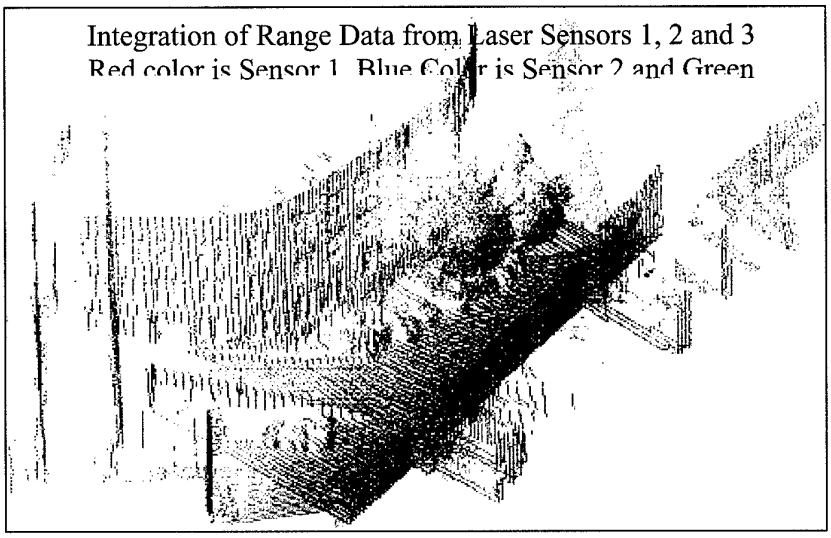


Figure 6: Integration of Laser Range Data from Three different sensors

REFERENCES

1 Bossler, J.D., Goad, C.C., Johnson, P.C., and Novak, K., 1991, GPS and GIS map the nation's highways, GeoInfo Systems, March 1991, p.27-37

2 Haala, N., Stallman D., Cramer, M., Calibration of Directly Measured Position and Attitude by Aerotriangulation of Three Line Airborne Imagery, e-mail: Norbert.Haala@ifp.uni-stuttgart.de

3 He, G., 1996, Design of a mobile mapping system for GIS data collection, IAPRS, Vol. XXXI, part B2, pp.154-159

4 Hock, C., W. Caspary, H. Heister, J. Klemm, and H. Sternberg 1995, Architecture and design of the kinematic survey system KiSS, Proc. of the 3rd Int Workshop on High Precision Navigation, Stuttgart, April, p. 569-576

5 Li, R. Mobile Mapping – An emerging technology for spatial data acquisition, http://shoreline.eng.ohio-state.edu/ron/teaching/894a/paper1.htm

6 Manandhar, D., Shibasaki, R., 2000, Prototype Development for Vehicle based Laser Mapping System (VLMS), IAPRS, 16-23 July, Amsterdam, Vol XXXIII, part B2, pp. 359-366

7 Pottle, D., 1995, new mobile mapping system seeds data acquisition, GIM, Vol 9, No. 9, p51-53

8 Schwarz, K.P., H.E. Martell, N.El. Sheimy, Ron Li, M.A. Chapman, and D. Cosandier 1993, VISAT – A mobile highway survey system of high accuracy. Proc. of the IEEE vehicle navigation and information systems conference, October 12-15, Ottawa, pp. 476-481

9 Tamura, T., Kitagawa, T., Tsuji, K., Uchida O., Shimogaki, Y., 1998, The GPS/INS integration and kinematic photogrammetry for mobile mapping system, International Archives of Photogrammetry and Remote Sensing, Hakodate, Vol. XXXII, part 5, pp. 824-829

A PHOTOGRAMMETRIC EVALUATION OF AN APS CAMERA

Tian-Yuan SHIH and Chien-Bin KUNG
Department of Civil Engineering
National Chiao-Tung University
1001 Ta-Hsueh Road, Hsin-Chu, Taiwan
E-mail: tyshih@cc.nctu.edu.tw

KEY WORDS: Resolution, Calibration

ABSTRACT: APS (Advanced Photographic System) is a new camera format recently introduced to the market. The APS formatted camera's photogrammetric potential is tested in this study with practical experiments. The photographic resolution is first evaluated with the USAF optical test pattern-resolving power chart. Then a test field is used for the evaluation of the metric properties. After the photographic development, the photographs are scanned and the image coordinates are then measured in a digital environment. In comparison to Wild P32 metric camera, significantly larger distortions were found with the tested Kodak Advantix 2100 Auto camera.

1. INTRODUCTION

The Advanced Photographic System (APS) is a new commercial photographic system developed by the alliance of Cannon, Kodak, Fuji, Minolta, and Nikon. The objective of APS development is to provide a more reliable commercial photographic system with better quality. Although APS is not expected to replace the commonly used 135 format camera completely, it is hoped that the APS format camera will eventually share a significant portion of the market.

The effective exposure area of traditional 135 format film is 24mm 36mm. While the film size of APS is smaller, 16.7mm 30.2mm, the image quality is not reduced. A newly developed film technique made this possible. With smaller film size, cameras can be made more compact. Usually the APS camera is 20% smaller than its 135 format counterpart. This may not be an advantage for close-range photogrammetric applications, because the photo scale is smaller for the same object distance and focal length.

There are three photo formats available in the APS system. As listed in Table 1, each photo format has a different aspect ratio. Accordingly, each photo format has different magnification scales. In this study, H format is selected.

Table 1: APS Photo Format Specification

Name	Aspect Ratio	Format (mm)	Magnification
C	2:3	4 6 (102 152)	6.1
H	9:16	4 7 (102 178)	6.1
P	1:3	4 12 (102 305)	10.1

A low-end APS camera, Kodak Advantix 2100 AUTO, is used in this study. The focal length is 25 mm with maximum aperture f/5.4. Because the APS film is designed that it will not to be accessed by the user, the photo coordinate measurements are performed with the developed photo, not the film.

2. THE RESOLUTION

LPM (lines per millimeter) is frequently applied for measuring the resolution of an imaging system. In this study, a printed standard chart is posted onto a vertical wall as the reference for evaluation. In this chart, there are groups of bars with different widths and four different colors, namely, black, red, blue, and yellow. The developed paper prints are scanned with 300, 600, 1000, and 1500dpi with a desktop flatbed scanner. The evaluation is performed on the screen of a personal computer. When the three lines cannot be differentiated, the LPM number is obtained from the look-up table printed on the reference chart. Then, the largest LPM value among all groups is taken to compute the LPM value of the photo.

$$\text{LPM photo} = \text{LPM chart} \times (D - f_0) / f_0 \quad (4\text{-}1)$$

Where D is the distance between the camera and the chart; f_0為 is the focal length of the camera.

Table 2: The Resolution of Kodak Advantix 2100 AUTO I (300dpi)

Distance (cm)	LPM chart	LPM photo	Photo Scale
100	0.891	34.7	1 : 6.20
120	0.707	33.2	1 : 7.37
150	0.629	37.1	1 : 9.27
180	0.500	35.5	1 : 11.11
240	0.354	33.6	1 : 14.51

Table 3: The Resolution of Kodak Advantix 2100 AUTO II (600dpi)

Distance (cm)	LPM chart	LPM photo	Photo Scale
100	1.000	39.0	1 : 6.20
120	0.794	37.3	1 : 7.37
150	0.707	41.7	1 : 9.27
180	0.561	39.8	1 : 11.11
240	0.397	37.7	1 : 14.51

Table 4: The Resolution of Kodak Advantix 2100 AUTO III (1000dpi)

Distance (cm)	LPM chart	LPM photo	Photo Scale
100	1.000	39.0	1 : 6.20
120	0.891	41.9	1 : 7.37
150	0.707	41.7	1 : 9.27
180	0.629	44.7	1 : 11.11
240	0.445	42.3	1 : 14.51

Table 5: The Resolution of Kodak Advantix 2100 AUTO IV (1500dpi)

Distance (cm)	LPM chart	LPM photo	Photo Scale
100	1.000	39.0	1 : 6.20
120	0.891	41.9	1 : 7.37
150	0.707	41.7	1 : 9.27
180	0.629	44.7	1 : 11.11
240	0.445	42.3	1 : 14.51

From tables 2, 3, 4, and 5, it is observed that there are differences among the photos taken with different object distances, while the scanning resolution is the same. However, if the number is normalized with photo scale, the resolution is about the same. It is also observed that the LPM improves with higher scanning resolution. But, the LPM remains the same after certain scanning resolution. That is, after certain scanning resolutions, the resolution of the photo itself becomes the governing factor.

3. THE TEST FIELDS

3.1 The NCKU Test Field

The NCKU test field is established indoors. The targets in the field are designed for close-range applications. There are three depth levels, as shown in Figure 1. The first and the second level each consist of several hanging metal strips. The targets are adhered to the strips. The targets of the third level are directly stuck onto the wall. The three dimensional coordinates of each target are determined with both total station and photogrammetric means. In the current experiment, several photos were taken from different angles with Kodak Advantix 2100 AUTO. Four of them are selected for further measurement and analysis.

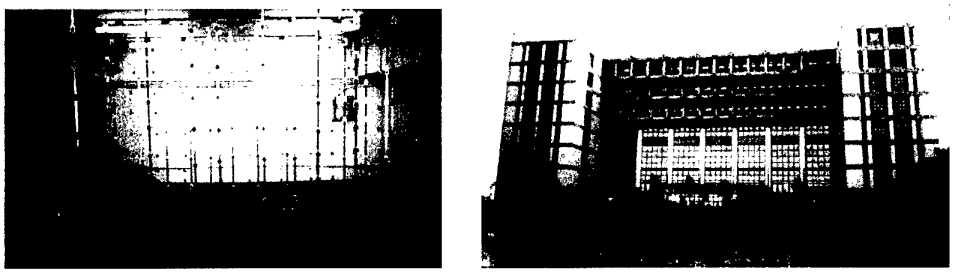


Figure 1: The NCKU (left) and NCTU (right) Test Field

3.2 The NCTU Test Field

An outdoor test field is established on the campus of National Chiao-Tung University, Hsin-Chu. A building as shown in Figure 1 is used as the object. Natural points, such as the corner of windows, are selected as targets. The object coordinates are measured with both the conventional surveying method with a total

station and the photogrammetric method with a Wild P32 metric camera. In this study, four projective stations are established, from the left to right, namely, STA1, STA2, STA3, and STA4.

4. THE PHOTOGRAMMETRIC EVALUATION

Based on collinearity equation, the relationship between image and object space can be described. The correction terms implemented to model the deviation between the ideal and the real optical systems, and named as the additional parameters. According to Brown (1971), the physical distortion can be described with radial, decentering, and affine distortions. The program UNBASC1 (Moniwa, 1972), which includes the interior parameters (x_0, y_0, c) and distortion parameters (K_1, K_2, K_3, P_1, P_2, A, B) is used in this study. This program does not have the gross error detection scheme implemented. Therefore, three times the amount of the RMSE is used as the threshold for screening the residuals. In order to avoid the spreading effect of gross errors, the gross errors are removed one at a time.

4.1 The NCKU Test Field

The image coordinates are measured with WINDIG program on an Intel-based personal computer. Each point is measured three times and the root mean square errors (RMSE) are listed in Table 6.

Table 6: The Measuring Repeatibility of Image Coordinates, NCKU Test Field

Photo	# of repetitions	# of Points	RMSE x		RMSE y	
			mm	pixel	mm	pixel
2	3	82	0.0369	0.436	0.0495	0.585
3	3	84	0.0326	0.385	0.0373	0.441
5	3	115	0.0304	0.360	0.0325	0.384
7	3	106	0.0283	0.334	0.0266	0.314
Sum	3	387	0.0318	0.375	0.0364	0.430

From Table 6, the RMSEs of the image coordinate measurement are all less than one pixel (about 0.0847mm). With the space resection, some gross errors are found. After cross-examination (cross-examination) between photos, it is suspected that the locations of these points have been displaced after determination of reference coordinates. The RMSE values also change with additional parameter sets. When all distortions are considered, the residuals become the smallest.

In the space intersection stage, different stereopairs result in different RMSE values (Table 7, 8). Because stereopair 3-7 has the longest base length, and stereopair 2-3 has the shortest object distance, these two pairs have better base/height ratio, and, therefore, have better accuracy. Meanwhile, the farther the points are, the

worse the result. The points on the wall have the lowest accuracy. This is because the larger the object distance, the smaller the photo scale, and then the larger the measurement error. The farther points have relatively worse geometry. That is, the larger the base/height ratio.

Table 7: The RMSE of Image Coordinates after Adjustment with UNBASC1, NCKU Test Field, Photo 2

Additional Parameters	# of control points	# of gross errors	Image coor. RMSE(mm)	
			x	y
None	57	1	0.077	0.065
Radial	56	2	0.062	0.062
Decentering	57	1	0.075	0.063
Film	57	1	0.062	0.053
All	56	2	0.039	0.047

Table 8: Space Intersection Accuracy with UNBASC1, NCKU Test Field (With all three distortion models; in mm)

Photo Pair	# of Control Pts	# of Check Pts	# of Gross Error	B/D Value	Control Pts RMSE			Check Pts RMSE		
					X	Y	Z	X	Y	Z
2 and 3	42	7	1	0.28	1.0	1.0	4.0	1.1	1.0	3.0
2 and 5	43	8	1	0.14	1.0	1.0	7.0	1.4	2.7	10.0
2 and 7	21	7	0	0.15	4.0	2.0	13.0	3.0	2.0	14.0
3 and 5	53	8	0	0.10	5.0	3.0	19.0	1.1	1.2	10.4
3 and 7	26	7	0	0.38	1.0	1.0	4.0	0.7	1.7	3.3
5 and 7	53	7	1	0.25	1.0	1.0	5.0	0.7	0.7	3.2

4.2 The NCTU Test Field

Four photos are taken for the NCTU test field, namely 21, 22, 23, and 24. The photo scale is about 1/500. Scanned with 300 dpi and measured with WINDIG three times, the RMSE is about 0.03 mm for both x and y. The intersection accuracy is listed in Table 9.

Table 9: Space Intersection with Photo 21 and 24, NCTU, UNBASC1, 300 dpi (in mm) (B/D ~ 0.24)

Additional Parameters	# of Control Points	# of Check Points	# of Gross Errors	RMSE on Control Points			RMSE on Check Points		
				X	Y	Z	X	Y	Z
None	46	28	0	67	79	172	83	84	193
Radial	44	28	2	40	60	137	73	82	180
Decentering	45	28	1	63	63	148	83	69	178
Film	46	28	0	60	59	155	79	69	176
All	45	28	1	33	43	124	53	54	144

5. CONCLUDING REMARKS

1. Regarding the digitization of image coordinates, the scanning/digitizing approach proved to be a good replacement for conventional comparator. The scanning resolution of 450 dpi provides slightly smaller RMSE than 300 dpi. There is also an improvement in the object coordinate determination by the photogrammetric process. The image coordinates are digitized on a Wild BC-3 analytical plotter with the original negative. It is found that the additional parameters are more effective for the enlargement/scanning approach, than for the direct measurement with the negative. Apparently, additional distortions are introduced in the enlargement/scanning procedure.
2. Based on the simulation, it can be concluded that the longer the focal length, the larger the photo scale, and in turn, the better the geometry and accuracy.
3. Comparing the simulation with the experiments, simulation concluded better accuracy. This is understood by the fact that only random errors are considered in the simulation; while the real case suffers with the systematic errors.
4. Comparing the results from APS and Wild P32, P32 has longer focal length and larger image format. The lens distortion with P32 is smaller as well. Although a 6.1 times enlargement is performed with the APS photo before the scanning, the Wild P32 still provides better accuracy.
5. When the photo scale is about 1/500, the relative accuracy from APS photos can reach 1/500 of the average object distance. For the current study, the base/height ratio is limited by the surroundings of the test fields. Accuracy may be further improved if the geometry can be improved.

REFERENCES

Brown, D.C., 1971. Close-Range Camera Calibration, Photogrammetric Engineering, 37:855.

Edmund, 1978. USAF 1951 Resolving Power Chart, Edmund Scientific Co., Barrington, New Jersey, U.S.A.

Moniwa, H., 1972. Analytical Camera Calibration for Close-Range Photogrammetry, MscE thesis, Department of Surveying Engineering, Univ. of New Brunswick.

Wolf, P.R., 1983. Elements of Photogrammetry, 2nd Ed., McGraw-Hill

APPLICATIONS OF HYPERSPECTRAL REMOTE SENSING IN URBAN REGIONS

Sunil BHASKARAN* and Bisun DATT

School of Geography
Faculty of Science and Technology
University of New South Wales, 2052,
Australia
Tel : +61-2-9385 5537
Fax :+61-2-9313 7878
***Email :** z2240167@student.unsw.edu.au

KEY WORDS: Complex, Urban Scenes, Spatio-temporal, Phenological

ABSTRACT

This paper examines the potential application of hyperspectral remote sensing for the analysis of complex urban scenes. Urban areas go through phenological changes (just the same way as a vegetation cycle), that have a spatio-temporal dimension, which is important to understand for various applications and land management related issues. However the study of urban areas is a complex process since they are characterised by the presence of numerous surface materials in relatively small regions. The features in these urban scenes contribute to the reflected radiance and are difficult to detect by coarse sensors.

Hyperspectral sensors have the highest potential for mapping complex urban ecosystems mainly attributed to their fine spectral resolution. This study uses Hymap data which has 124 spectral bands.This paper describes the compilation of a spectral library of urban surface materials, which is then used for calibrating an airborne hyperspectral image of a selected scene in Perth, Australia. The spectral library was also used for identifying pure pixels in the image, identification of image derived endmembers, and for spectral unmixing to decompose this image into abundance of individual surface materials. A georeferenced map showing the distribution of surface materials was generated.

INTRODUCTION

Urban areas are typified by intricate mixtures of materials ranging from concrete, wood, tiles, bitumen, metal, sand, and stone. The Spatial distribution of these materials is not regular and is compounded by rapid temporal changes that occur in the urban landscape over a very short period of time. Besides they have a high object density which leads to errors in the multispectral classification (Hornstra et al, 1999). Hyperspectral sensors with their high spectral resolutions carry contiguous information about the urban landscapes and enable quantification of surface features, particularly for classifications based on the material composition. The creation of spectral library for urban surface

materials can assist in the sub-pixel analysis and has the potential to diminish some of the limitations posed due to spatial resolution. Hyperspectral imagery has been widely used for vegetation studies and geologic mapping but very little has been done for urban surface (Bing et al, 1998). This paper examines the potential to use hyperspectral remote sensors for the classification of urban features.

Study Area and Data Collection

An urban area in Perth, Western Australia was selected for investigation. Image data was obtained by HyMap, an airborne imaging spectrometer developed in Australia. HyMap data is available in 124 contiguous bands over the 450-2500 nm wavelengths, with a spatial resolution of 5-metre (Cocks et al, 1998). The HyMap was most appropriate for this study due to its superior signal to noise ratio and high spatial and spectral resolutions.

Methodology and Analysis (Fig. 1)

A laboratory spectroradiometer (FieldSpec) was used to measure reflectance of urban surface materials over the 450-2500 nm wavelengths. Samples of building materials were collected including bitumen, concrete, tiles, roofing material, brick, etc. For each sample 10 scans were taken and averaged. The spectra were imported into the ENVI image analysis software for compilation of a 'Spectral library'. Of the 124 bands in the HyMap image, 6 bands in the major water absorption regions near 1450 and 1930 nm were found to be bad bands. These 6 bands were excluded and the remaining 118 bands retained for further analysis. The spectral library consisting of 2150 nm bands was resampled to the 118 HyMap bands. The reflectance image was first classified with the Spectral Angle mapper (SAM) algorithm in ENVI. For this classification the entire spectral library (70 endmembers) was used and the classified image produced abundance of pure pixels matching the library endmembers. The result of SAM revealed that nearly 70% of the image was unclassified. Several library endmembers did not match any pixel spectra. This result showed that

1) The image contains many mixed pixels
2) There may be other pure pixels for which no library spectra were available

The next step of the analysis was to determine the endmembers from the image itself and to use these for:

1) Identifying all pure pixels in the image
2) Unmixing the mixed pixels

The image was first transformed using the minimum noise fraction (MNF) transform, in order to remove noise in the data, determine the inherent dimensionality of the image, and to speed up the subsequent computer processing. The forward MNF with rotation was used and eigen values greater than 1 were retained. The pixel purity index (PPI) was run on the MNF image to separate the pure pixels from the mixed pixels. The PPI was run with 2000 iterations using a threshold of 3 standard deviations. The n-dimensional visualizer was then used with the PPI image to extract image end-members.

The image end-members were compared to the library spectra to identify some of the end-members. Several image end-members were not identified since their library spectra were not available. The image derived end-members were exported into a spectral library.

The SAM classifier was run again with the image derived spectral library. Linking the new SAM image and the PPI image showed that the SAM did identify all pure pixels in the image. The reflectance image was finally unmixed using ENVI's linear unmixing procedure and the image derived spectral library. The resulting image produced classes showing abundance of the image derived endmembers.
Comparison of unmixing and SAM results with true colour RGB image of the scene showed that the unmixing and SAM procedures showed accurate locations of natural and man-made materials.

Results

The main findings were that :

- There are more endmembers in an urban scene compared to vegetated or agricultural landscapes
- Not all urban endmembers can be easily represented in a laboratory spectral library.
- Useful to derive image endmembers and use it for unmixing or spectral matching.
- However laboratory spectral library is still useful for identification of image derived endmembers.

The detailed spectral analysis carried out in this study reveals that complex urban scenes can be analysed accurately with hyper-spectral imagery. Further work is continuing and will look at the use of spectral techniques of derivative analysis, as well as use of neural networks for quantitative analysis and classification of heterogenous urban images.

ACKNOWLEDGEMENTS

The authors are grateful to Terry Cox and Peter Cox of HyVista Corporation, Australia for providing the HyMap image data.

Cited References:

1.Cocks, R.Jensen, A.Stewart, I.Wilson, T.Sheilds, 1998. The HyMap Airborne Hyperspectral Sensor: The System, Calibration and Performance. (Paper presented at 1rst EARSEL Workshop on Imaging Spectroscopy, Zurich, October.

2.T.J Hornstra, M.J.P.M Lemmens, G.L. Wright, 1999. Incorporating intra-pixel reflectance variability in the multi-spectral classification process of high resolution satellite imagery of urbanized areas. Vol. 28, No. 2, December.

3. Z. Bing, L. Jiangu, W. Xiangjun, W Changshan, 1998. Study on the classification of Hyperspectral Data in urban area. SPIE Vol. 3502.0277-786x/98.

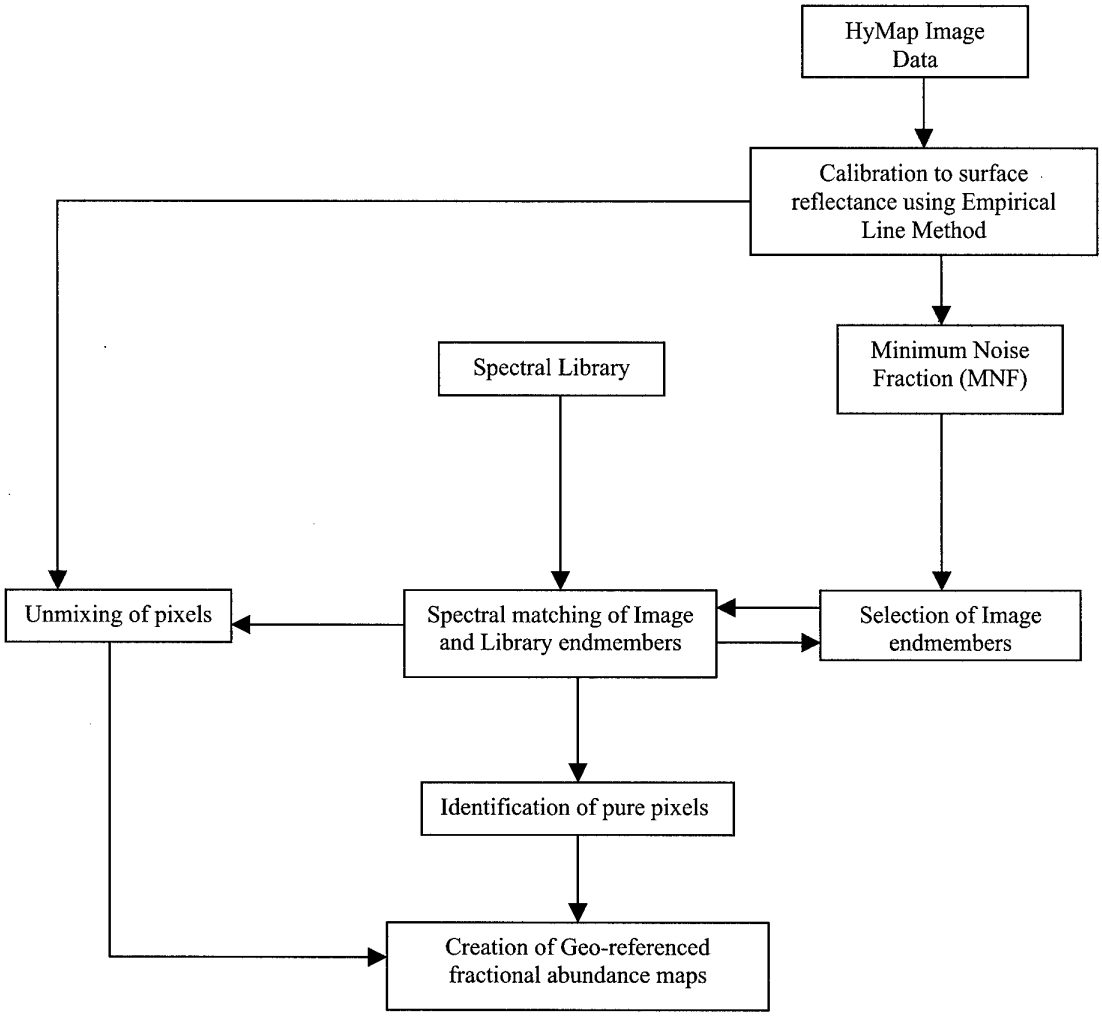


Fig. 1 Methodology and Analysis

IMAGE GEOMETRIC SIMULATION AND ORIENTATION MODELING FOR ROCSAT-2

Liang-Chien CHEN and Yi-Ying WU
Center for Space and Remote Sensing Research
National Central University
Chung-Li, TAIWAN
Tel: +886-3-4227151 ext. 7622
Fax: +886-3-4254908
E-mail: lchen@csrsr.ncu.edu.tw

KEY WORDS: Image Simulation, Orientation Modeling, ROCSAT-2

ABSTRACT: The objective of this investigation is to propose a scheme to model the orientation parameters for ROCSAT-2 satellite. Due to the unavailability of the satellite imagery, a geometric simulation for ROCSAT-2 is also included. Four major components are included in the simulation procedure. The first is to perform the transformations between related coordinate systems. The second component establishes the satellite-flying model to describe the orbit and attitude variations. The third one is to form ROCSAT-2 images. Finally, we include systematic and random errors in the orbital and attitude data for simulating the ephemeris. In the orientation modeling, the ephemeris data with systematic and random errors are use to construct the approximate imaging geometry. Then ground control points are used to fine-tune the exterior orientation parameters. Experimental results indicate that the systematic errors may be mostly compensated while the random errors consistently influence the positioning accuracy.

1. INTRODUCTION

ROCSAT-2 is a sun synchronous remote sensing satellite, which is scheduled to launch in early 2003. It flies 890km in height on a plane with 98.99° inclination angle. The off-nadir look angle may reach 45° in the along-track and cross-track directions [NSPO, 2000]. The pushbroom imager on board has 12,000 pixels per line, for panchromatic band each with 2m-ground coverage. Thus, the swath is 24km nadir and the FOV is about 1.5°. The multi-spectral imager includes 4 bands namely blue, green, red, and near IR. The ground resolution for multi-spectral imagery is 8m nadir. In this investigation, we only use panchromatic imagery to validate the geometric simulation and processing.

Since the trend is to integrate remotely sensed information and other data in geographic information systems, geometric correction for satellite imagery is required. In addition, ROCSAT-2 has a capability of stereoscopic observation by collecting along-track or cross-track stereopairs. Thus, generation of digital terrain models (DTMs) is possible. No matte what in the generation of DTMs or performing

orthorectification, a modeling for precision orientation parameters is always the first step [Chen & Chang, 1998]. The objective of this investigation is to propose a scheme to model precision orientation parameters.

The imagery of ROCSAT-2 is not available at the moment. Thus, we need to simulate ones for validation of the geometric process. Since the point is for the geometric processing, the radiometric unsoundness is not considered. In addition, we ignore the building effect during imaging due to the unavailability of digital building models.

2. IMAGE SIMULATION

The proposed procedures for image simulation are shown in fig.1. Given 6 elements for a satellite, namely right ascension, inclination (orbital plane with respect to equator), argument of perigee, semi-major axis and eccentricity of earth ellipsoid, and true anomaly, by assigning the initial time, we can determine the position of the satellite at a given instant [Tseng, 1983].

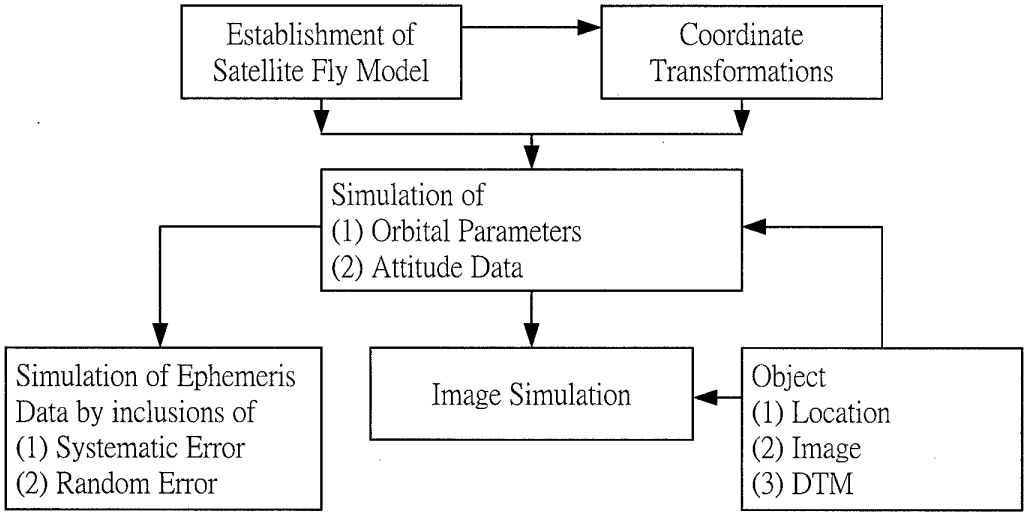


Figure 1. Proposed Scheme for Image Simulation

In order to simulate orientation parameters, transformations between following coordinate systems are considered:

(1) Attitude Reference System and Local Orbital Reference System
(2) Local Orbital Reference System and WGS84
(3) WGS84 and ECI (Earth Center Inertia)
(4) WGS84 and GRS67 (GRS67 is being replaced by WGS84 in Taiwan)
(5) GRS67 and Geographic System (Longitude, Latitude, Height)
(6) Map projection (Geographic System and 2 $^{\circ}$ Transverse Mercator)

When the satellite location is determined with respect to time, we may begin with image simulation for a target area. We need to calculate the attitude angle according to the target position with respect to satellite's. Then an image simulation may be performed by Top-Down approach as shown in fig. 2. Two major steps are included:

(1) Calculation of observation vector for each CCD detector.

(2) Determination of the grey value for each CCD detector by corresponding the object point and image pixel using Top-Down ray tracing in an iteration way.

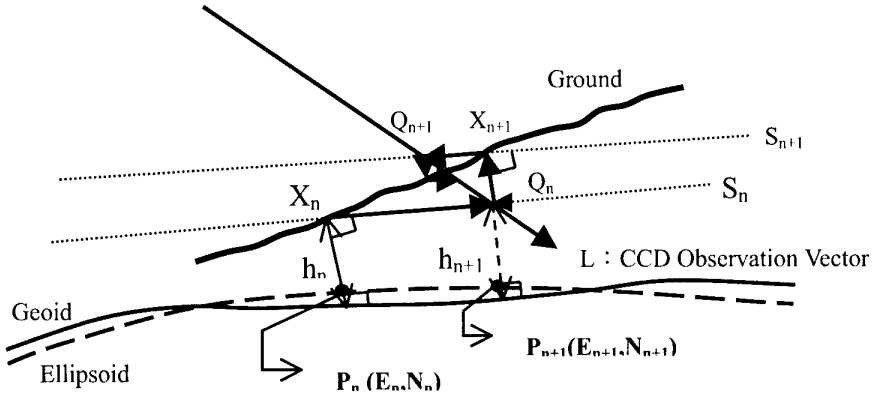


Figure 2. Image Simulation by Ray Tracing

Considering the errors of ephemeris data for ROCSAT-2, we include systematic and random errors to complete the simulation. The scale of the systematic error may be selected according to the satellite specification. On the other hand, random error is not well known at the moment. We consider the following factors: (1) random error are fully random and independent, (2) each component corresponds to half-pixel coverage on ground, i.e., 1m.

3. PRECISION ORIENTATION MODELING

We will provide a procedure to model the precision orientation for monoscopic images. The procedures are stated as follows:

(1) Establishing the approximate orbital parameters using ephemeris data.

(2) Apply ground control points (GCPs) to determine the deviation between each observation vector and GCP, shown in fig.3 .

(3) Considering 3 or more GCPs, the orbital parameters are corrected according to the collinearity condition, as shown in eq.1.

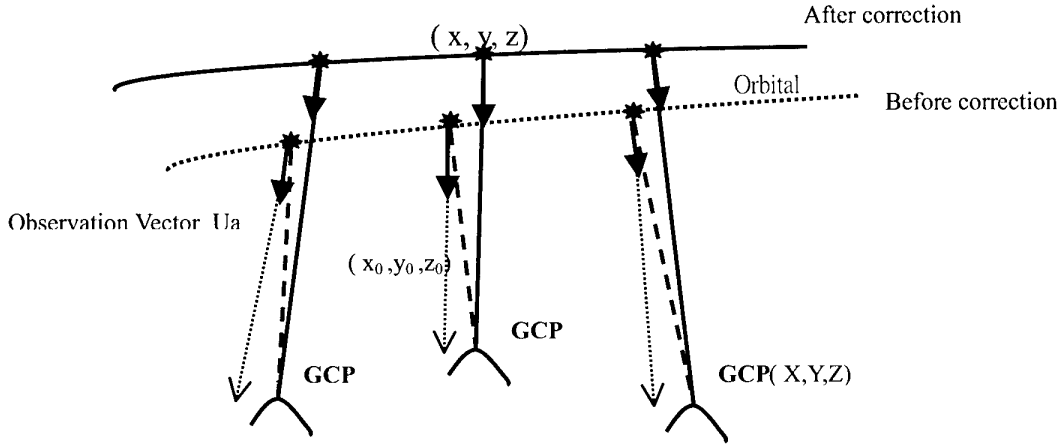


Figure 3. Illustration of Orbit Correction

$$\frac{x(t) - X}{u_x} = \frac{y(t) - Y}{u_y} = \frac{z(t) - Z}{u_z} \qquad \text{.....(1)}$$

where $x(t) = x_0 + a_0 + a_1 * t$

$y(t) = y_0 + b_0 + b_1 * t$

$z(t) = z_0 + c_0 + c_1 * t$

(4) Applying Least Squares Filtering method to fine-tune the orbit, by eq. 2. We use Gaussian for covariance function in this study.

$$\rho_k = \vec{v}_k \, [\Sigma_k]^{-1} \, \vec{\varepsilon}_k \qquad \text{.....(2)}$$

ρ : x , y , z three direction

ρ_k : correction is k direction

$\vec{v}_k$: covariance vector between interpolated point and each GCP

Σ_k : covariance matrix formed by GCPs

$\vec{\varepsilon}_k$: residual vector

(5) Considering the extremely high correlation between orbital parameters and pitch and roll angles, we only correct yaw angle. Due to its very small field of view, i.e., about 1.5 degrees, the correlation between the orbit parameters [x(t), y(t)] and the attitude data(pitch, roll) are extremely high. This coupling phenomenon implies that systematic errors in pitch and roll will be compensated for by the orbit parameters x(t) and y(t), respectively. Accordingly, only the orbit parameters need to be considered in this investigation. However, the behavior of yaw is quite different. We observed that the yaw data does not significantly correlate to any other orientation parameters in the geometric reconstruction of the ROCSAT-2 images. Thus, corrections of yaw data must be taken into account.

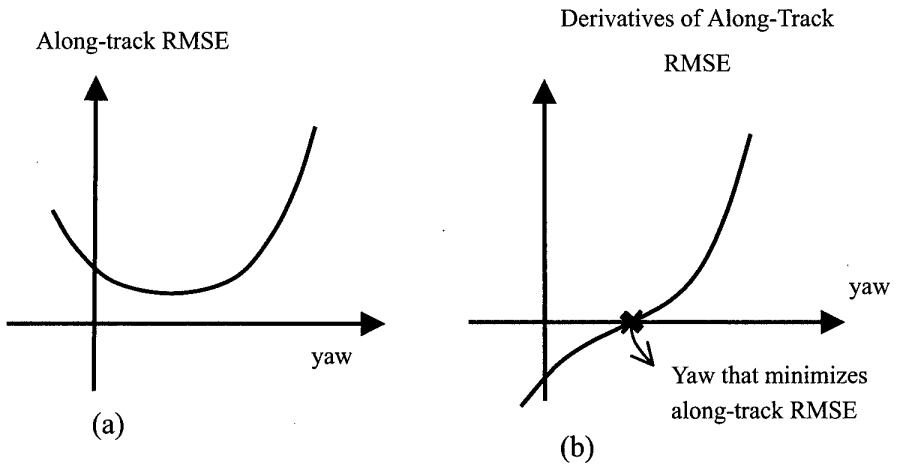


Figure 4. Correction of Yaw Angle

Theoretically, having calibrated the orbital parameters, systematic errors in yaw angle would be reflected on the along-track component of the root-mean-square error (RMSE) for the GCPs. Thus, the RMSE could be used to fine-tune the yaw data. Referring to fig. 4(a), for any given yaw angle, we can get an along-track RMSE on the image plane for GCPs, then the RMSE derivative with respect to the angle in fig. 4(b). Therefore, the along-track RMSE and its derivative for GCPs may be expressed as functions of the yaw angle. Then, given a reasonable range of yaw angles, we can use a bisection method (Gerald and Wheatley 1994) to find the root of the derivative function and get the most probable value of the yaw angle that minimizes the along-track RMSE for the GCPs.

4. EXPERIMENTAL RESULTS

We simulate two images based on the assumed orbit and orthorectified aerial images for the target area. The resolution of the orthoimage is 1m*1m(fig.5).A simulated DTM with 1m*1m is also prepared(fig.6).The orbit passes the Strait near Taiwan. The attitude angles for each of the images are:

Image1: roll=14.33125 °, pitch=13.29759 °, yaw=0°

Image2: roll=15.81852 °, pitch=-10.50034 °, yaw=0°

Fig.7 and fig.8 represent the two simulated images.

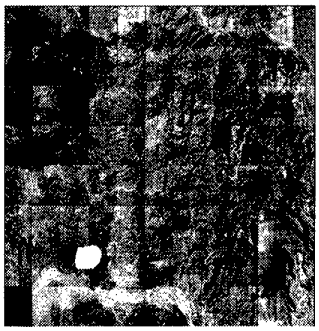


Figure 5. Target Image

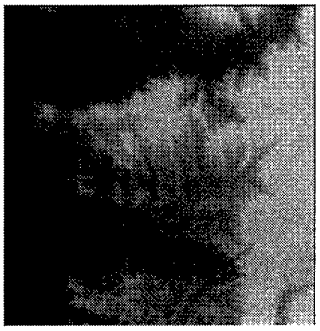


Figure 6. Target DTM

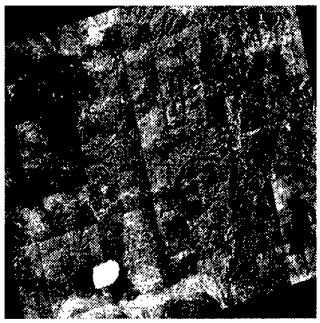


Figure 7. Simulated Image1

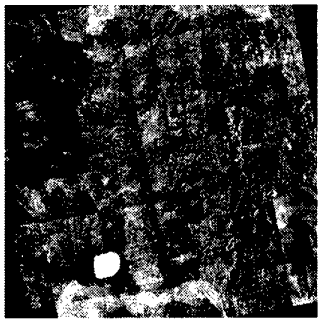


Figure 8. Simulated Image2

Considering different combinations of systematic and random errors, the accuracy analyses for 5 GCPs are summarized in Table1. In which,121 checkpoints are analyzed. The systematic errors are not linear in terms of sampling time. The random

errors are Gaussian distributed. It is observed that the systematic errors are well compensated. While random errors behave differently. This is what it reflects the characteristics of "Random".

Table1. Error Analyses by Checkpoints

Error Inclusion		RMSE(m)	
Type	Quantity(each component)	E	N
Systematic position	450m	0.53	0.25
Systematic Attitude	30"	0.13	0.20
Systematic Position + Attitude	450m 30"	0.41	0.13
Random Position	1m	1.08	1.00
Random Attitude	0.25"	1.34	1.28
Random Position + Attitude	1m 0.25"	1.34	1.60
Systematic and Random(Position + Attitude)	Systematic:450m 30" Random:1m 0.25"	1.33	1.60

5. CONCLUSIONS

We developed a scheme to simulated ROCSAT-2 Images. The scheme considers the satellite flying characteristics and imaging behaviors. Systematic and random errors are simulated in the scheme. A scheme for modeling precision orientation parameters is also established. Experimental results indicate that systematic errors may be compensated while random errors are still kept random. The RMSE from ground checkpoints reflects the random errors of inclusion consistently.

Only panchromatic images are simulated and tested. For multi-spectral images, the geometric behavior is expected to be similar. Because this investigation only concerns about the geometrical property, the simulated images do not consider the radiometric characteristics. Further investigation on radiometry is suggested.

REFERENCES

1. Chen, L.C., and Chang, L.Y., 1998, "Three-Dimensional Positioning Using SPOT Stereostrips with Sparse Control", Journal of Surveying Engineering, ASCE, Vol.124, No.2., pp.63-72
2. Gerald, C.F., and Wheatley,p.p.,1994,"Applied Numerical Analysis", Addison -Wesley Publishing Co., Reading, Mass.
3. NSPO, 2000,"ROCSAT-2 Satellite Property " , http://www.nspo.gov.tw/e40/welcome.htm
4. Tseng, C.Y., 1983, "Remote Sensing of the Atmosphere: Principles and Applications ", Wen -Ying Qc871.T83, TAIWAN. (in Chinese)

The 21st Asian Conference on Remote Sensing
December 4-8, 2000 Taipei, TAIWAN

SUPERVISED CLASSIFICATION OF MULTI-TEMPORAL REMOTE SENSING IMAGES

Chi-Farn Chen Yueh-Tan Li
Center for Space and Remote Sensing Research
National Central University
Chung Li, TAIWAN
Tel: 886-3-4227151-7624, Fax: 886-3-4254908
e-mail: cfchen@csrsr.ncu.edu.tw

KEY WORDS: multi-temporal remote sensing images, supervised fuzzy classification

ABSTRACT: This paper presents a supervised approach for classifying multi-temporal remote sensing images. One major disadvantage to use the supervised classification of multi-temporal data is that each image is required to select its training data, even the images cover the same area. An attempt to use the fuzzy training method to avoid repeated selection of training data in each image is proposed here. Theoretically, the fuzzy training method is able to deal with the problem of mixture of training classes, therefore, the classification map generated from first-period image can be automatically becoming the fuzzy training sites for second-period image. The proposed approach is tested by a series of simulated multi-temporal images. The results indicate that the method presented here has great potential to extend to the practical applications.

1. INTRODUCTION

In processing of multi-temporal remote sensing images, accurate and convenient classification is among one of difficult tasks in practical applications (Baber, 1985). This study aims to use supervised algorithm to classify multi-temporal images. One major procedure of using supervised algorithm is the collection of training data that is relatively time-consuming and labor-intensive (Lillesand, 2000). Furthermore, the image responses may change due to variability in time and space within the multi-temporal images (Richards, 1993). Therefore, the problem that faces the supervised classification of multi-temporal images is that the training data has to be repeatedly selected for each image within the multi-temporal remote sensing data (Schowengerdt,1997). For this reason, a concept is proposed: choosing training set and finishing classification in first-period image, then the training data of the following period images would be automatically generated from the first-period classification image. The most difficult part of the study is that the class positions, numbers, and contents may change in the following-period images. Thus it would generate the complicated mixture of the training classes when it attempts to automatically select the training data for second-period image. This study uses the fuzzy training method (Wang, 1990) to overcome the mixing problem of training classes. Basically, the fuzzy approach allows the heterogeneity to exist within the training sites and may contain mixing classes in the training data. Consequently, the change of class positions and contents in second-period images can be tackled by the characteristics of the fuzzy training data, while the detection of change of class numbers leave a key problem in the process of automated selection of training data. This problem is studied and the

solutions are obtained from a series of analysis of fuzzy means and covariance matrix of the training data. A series of simulated data are tested, and the results indicate that the proposed fuzzy training method has the potential to automatically classify multi-temporal remote sensing images.

2. Method

The following section 2.1 discusses the fuzzy training method and the section 2.2 present the multi-temporal supervised classification.

2.1 Fuzzy training

Basically, the fuzzy training method is the training procedure of supervised fuzzy classification. In this procedure, the conventional mean and covariance parameters of training data are represented as a fuzzy set. The following two equations (Equ.1 and Equ.2) describe the fuzzy parameters of the training data:

$$\mu_c^* = \frac{\sum_{i=1}^{n} f_c(x_i) x_i}{\sum_{i=1}^{n} f_c(x_i)} \qquad \text{(Equ.1)}$$

$$\Sigma_c^* = \frac{\sum_{i=1}^{n} f_c(x_i)(x_i - \mu_c^*)(x_i - \mu_c^*)^T}{\sum_{i=1}^{n} f_c(x_i)} \qquad \text{(Equ.2)}$$

where μ_c^* is the fuzzy mean of training class c, Σ_c^* is the fuzzy covariance of training class c, x_i is the vector value of pixel i, $f_c(x_i)$ is the membership of pixel x_i to training class c, n is the total number of pixels of the training data. In order to find the fuzzy mean (Equ.1) and fuzzy covariance (Equ.2) of every training class, it must know the membership of pixel x_i to training class c first. In this study, the membership function is defined based on the conventional maximum likelihood classification algorithm with fuzzy mean and fuzzy covariance.

$$f_c(x_i) = \frac{P_c^*(x_i)}{\sum_{j=1}^{m} P_j^*(x_i)} \qquad \text{(Equ.3)}$$

where

$$P_c^*(x_i) = (2\pi)^{-N/2} \left|\Sigma_c^*\right|^{-1/2} \exp\left[-\frac{1}{2}(x_i - \mu_c^*)^T \Sigma_c^{*-1}(x_i - \mu_c^*)\right]$$

$f_c(x_i)$ is the membership of pixel x_i to class c, $P_c^*(x_i)$ is the maximum likelihood probability of pixel x_i to class c, m is the number of classes, n is the number of the bands. These equations would ultimately produce the fuzzy mean and fuzzy covariance for each training class. Consequently, the membership values would be used to describe the mixing

classes in every training site.

2.2. The supervised fuzzy classification of multi-temporal images

As long as the necessary fuzzy mean and fuzzy covariance of each training class are calculated from the procedures described at the previous section 2.1, a fuzzy supervised classification can be implemented at first-period image of multi-temporal data. Accordingly, the membership values of each pixel calculated from Equ.3 can be used to generate a classification map. Then the classification map is overlaid with second-period image, and the positions of the classes can be used as the reference to collect the training data. However, the problem always arises when second-period image has some variations in the class positions, contents, and numbers. The fuzzy training method with the capability to mix the training classes, in fact, would successfully manage the variation of the class positions and contents as long as the class numbers stays the same. It appears that the class numbers of second-period image has to be decided before the fuzzy supervised classification can be applied to second-period image. The values of fuzzy covariance and fuzzy mean of training data actually provide some answers to the problem of the class numbers. Accordingly, the threshold techniques are used to obtain the change of the class numbers. A high fuzzy covariance threshold will suggest an increase of the class numbers, while a high distance threshold between different fuzzy means will indicate a decrease of the class numbers. Therefore, with the class numbers known, the fuzzy training and classification will bring back to train and classify second-period image.

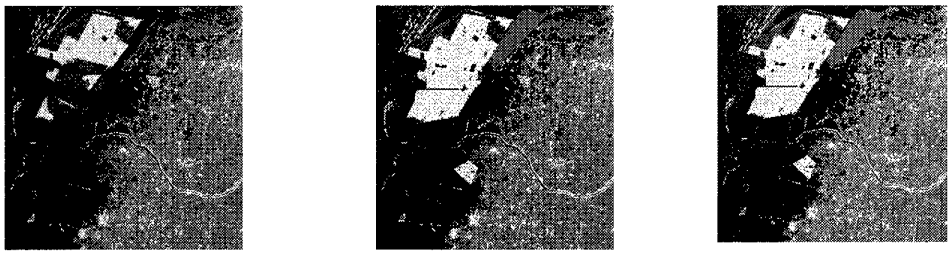
3. Test Data and the Results

The class variation of second-period image basically can be grouped into class positions, contents, and numbers. Their possible combination would be summarized to five cases, which is described as follows.

class variation	Class numbers	Class contents	Class positions
Case 1	no-change	no-change	change
Case 2	no-change	change	no-change
Case 3	no-change	change	change
Case 4	increase	change	change
Case 5	decrease	change	change

A series of images to simulate above five cases is generated for testing the proposed method. The following is the testing results and their discussions.

Case 1:

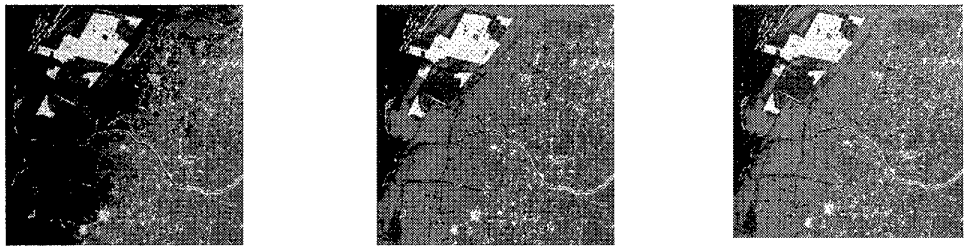


(a) (b) (c)

Fig.1 (a) simulated 1st-period image; (b) 2nd-period image (case 1); (c) classification image

Case 1 represents the situation with 'no-change' in both class numbers and class contents, but 'change' in class positions. The testing results are showing in Figure 1. The visual inspection (Fig.1(b) and (c)) and 96% overall accuracy indicate a successful classification.

Case 2

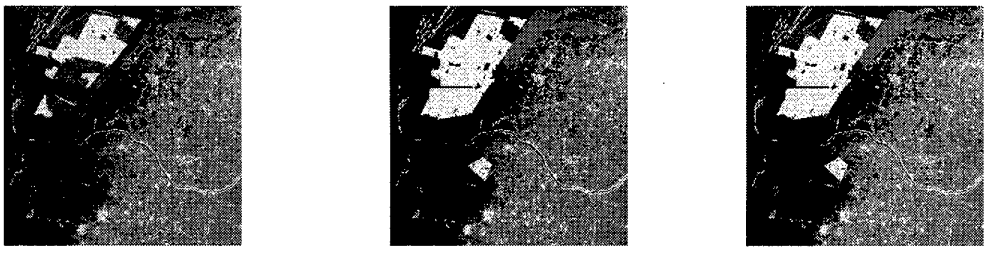


(a) (b) (c)

Fig.2 (a) simulated 1st-period image; (b) 2nd-period image (case 2); (c) classification image

Case 2 represents the situation with 'no-change' in both class numbers and class positions, but 'change' in class contents. The testing results are showing in Figure 2. The visual inspection (Fig.2(b) and (c)) and 98% overall accuracy indicate a successful classification.

Case 3

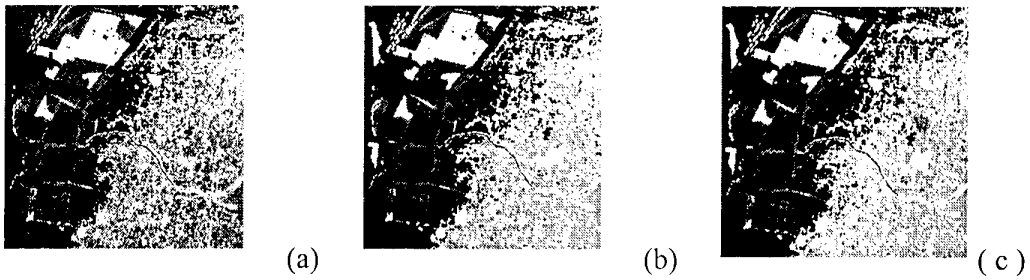


(a) (b) (c)

Fig.3 (a) simulated 1st-period image; (b) 2nd-period image (case 3); (c) classification image

Case 2 represents the situation with 'no-change' in class numbers, but 'change' in both class contents and class positions. The testing results are showing in Figure 3. The visual inspection (Fig.3(b) and (c)) and 99% overall accuracy indicate a successful classification.

Case 4

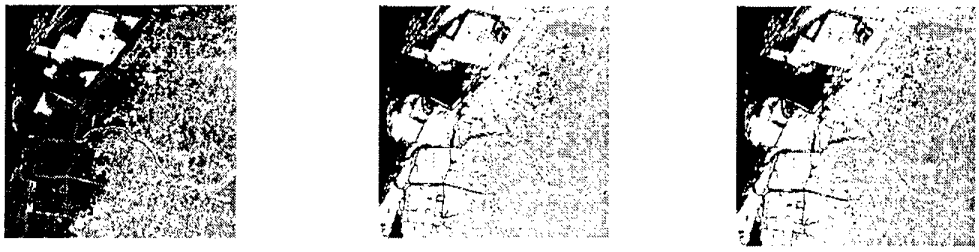


(a) (b) (c)

Fig.4 (a) simulated 1st-period image; (b) 2nd-period image (case 4); (c) classification image

Case 4 represents the situation with 'increase' in class numbers, and 'change' in both class contents and class positions. The testing results are showing in Figure 4. The visual inspection (Fig.4(b) and (c)) and 97% overall accuracy indicate a successful classification.

Case 5



(a) (b) (c)

Fig.5 (a) simulated 1st-period image; (b) 2nd-period image (case 5); (c) classification image

Case 5 represents the situation with 'decrease' in class numbers, and 'change' in both class contents and class positions. The testing results are showing in Figure 5. The visual inspection (Fig.5(b) and (c)) and 99% overall accuracy indicate a successful classification.

4. Conclusion

This study proposes a supervised fuzzy classification for multi-temporal remote sensing images. The class variation between multi-temporal images normally requires the selection of training data for every image when performing classification. An automatic procedure to generate the training data for multi-temporal image classification is presented here. The procedure combines the classification map from first-period image and the fuzzy training method to automatically collect the training data for second-period image. A series of simulated images are created for testing the proposed method. Their results suggest that the practical application of the method to the multi-temporal remote sensing images can be expected.

REFERENCES

Baber, M. L., D. Wood, and R. A. McBride, 1985. Classification of Corn and Soybeans Using Multitemporal Thematic Mapper Data. Remote Sensing of Environment, Vol. 16,

pp.175-181.
Lillesand, T. M., and R. W. Kiefer, 2000. Remote Sensing and Image Interpretation. 4th edition, John Wiley & Sons, Inc,.
Richards, J. A., 1993. Remote Sensing Digital ImageAnalysis: An Introduction. 2nd Ed., Springer-Verlag Berlin Heidelberg.
Schowengerdt, R. A., 1997. Remote Sensing: Models and Methods for Image Processing . 2nd Edition, Academic Press, pp. 522.
Wang, F., 1990. Fuzzy Supervised Classification of Remote Sensing Images. IEEE Trans. on Geoscience and Remote Sensing, GE-28(2), pp. 194-201.

COMPARING EFFECTS OF DIFFERENT SIZES OF AGGREGATION ON SPATIAL STRUCTURE OF REMOTELY SENSED DATA

Yu-Pin LIN[1*], Tung-po TENG[2]

[1]Association Professor, Department of Landscape Architecture

Chinese Culture University

55, Hwa-Ken Rd. Yangming Shan, Taipei, Taiwan 11114

Tel: 011-8862-2862-6433 Fax: 011-8862-2861-7507

E-mail: eales@staff.pccu.edu.tw

[2]Graduate student, Graduate institute of Geography

Chinese Culture University

TAIWAN

KEY WORDS: Aggregation, Spatial structure, Variogram, NDVI, Remote sensing

ABSTRACT: Remote sensing data can be aggregated to evaluate, model and monitor in environment and ecology from local to lager scaled region. The effects of aggregated data sometimes also display on the output of models or the results of monitoring. Meanwhile, variograms provides a model of the spatial correlation of data within a statistical framework, including spatial covariance functions and a means of quantifying the commonly observed relationship. Therefore, this study performed isotropic and anisotropic experimental variograms in 12.5m, 25m, 37.5m, and 50m resolutions NDVI data from a Spot image at three different land-cover sites that were an almost pure grass, a mixed grass and shrub, and a broad forest within the yangmingshan national park in Taiwan to evaluate the impact of aggregation on the spatial structure at different land-cover sites. The results indicated that the experimental variograms of the NDVI data in the above four different resolutions displayed identical spatial structure in both isotropic and anisotropic directions at the pure grass site. At the mixed grass and shrub site the NDVI experimental variograms in the 12.5m, 25m, 37.5m, and 50m resolutions displayed a similar spatial tendency but different spatial variations. The experimental variograms of NDVI of these four resolutions at the broad-forest site displayed different spatial patterns and spatial variations in both isotropic and anisotropic directions. The experimental variograms of the 25 m and 50 m resolutions of the broad forest site displayed a similar tendency. Moreover, the 12.5 m and 37.5 m resolutions NDVI data of the broad forest site exhibit a similar pattern on their variograms.

1. INTRODUCTION

Remote sensing data can be aggregated to evaluate, model and monitor in local or global environmental and ecological study. However, the aggregations of data increase each pixel size of

data and reduce the number of pixel in a sampling site. Moreover, these aggregated data are often referred to having a coarser spatial resolution (Bian and Butler, 1999). The effects of aggregated data sometimes also display on the output of models. Therefore, many scientists recently focused on these data aggregation effects to evaluate different aggregation methods.

The normalized different vegetation index (NDVI) calculated by remote sensing data can be used to evaluate monitor the spatial and temporal vegetation change. Meanwhile, the NDVI is preferred to the simple index for global vegetation monitoring (Lillesand and Kiefer, 2000). Moreover, NDVI data are useful to identify land cover categories through the seasonal variation of greenness (Loveland et al, 1991 and Cihlar et al. 1996). In biophysical remote sensing, greenness can be measured in terms of the normalized different vegetation index (NDVI) that uses radiances or reflectances from a red channel around 0.66 and a near-IR channel around 0.86 μ m (Lo and Faber, 2000).

A great deal of collected environmental data, high spatial continuity, indicate that points that are closer in given direction display higher correlation values than those that are separated farther (Lin and Change, 2000). The above spatial structure analysis may be affected by aggregated data. Variography is usually performed by determine the estimated variogram of the data collected in time and space. Variogram provides a model of the spatial correlation of data within a statistical framework, including spatial and temporal covariance functions (Lin and Change, 2000). Not surprisingly, these models are defined in terms of the correlation between any two data points separated by either spatial or temporal distances. Variogram has been applied in many fields such as soil pollution, air pollution, hydrology, ecology, and remote sensing. These techniques have also recently been applied to characterize the spatial variability of pollutants and environmental monitoring.

This study performed isotropic and anisotropic experimental variograms in 12.5m, 25m, 37.5m, and 50m resolutions NDVI data from a SPOT image at three 0.1407 km^2 different land-cover sites that are an almost pure grass, a mixed grass and shrub, and a broad forest within the Yang Ming Shan National Park in Taiwan to evaluate the impact of aggregation on the spatial structure at different land-cover site.

2. MATERIALS AND METHODS

In order to analyze the aggregation effects on different resolutions the 12.5m, 25m, 37.5m, and 50m resolutions NDVI data calculated from the aggregated SPOT images at three different 0.1407 km^2 land-cover sites that are an almost pure grass, a mixed grass and shrub, and a broad forest within the Yang Ming Shan National Park in Taiwan. These level 10 SPOT images were from the center for space and remote sensing research of the national central university in Taiwan. The three selected areas are displayed in Fig 1. The aggregated NDVI maps are displayed in Fig. 2. Moreover, the experimental variograms of NDVI data were calculated within GS+ (Gamma Design, 1995).

2.1 Greenness Index

High reflectance in the near-infrared part of the spectrum, together with chlorophyll absorption in the red wavelengths, is typical, green vegetation (Gates et al. 1965, O'neill, 1996). Vegetation areas will generally yield high value for either index because of their relatively high near-IR reflectance and low visible reflectance (Lillesand and Kiefer, 2000). The NDVI expresses the difference between the incident radiation reflected by photosynthetically active pigments in green leaves, and that portion reflected on the near-infrared part of the spectrum (Jelinski and Wu, 1996). NDVI is defined as:

$$NDVI = \frac{NIR - RED}{RED + NIR} \tag{1}$$

where NIR and RED are wavelengths in the reflective infrared (~0.65-0.90 μ m) and red (~0.60-0.65 μ m) bandwidths, respectively (Quattrochi and Luvall, 1999). Thus NDVI is bounded ratio that varies between –0.1 and 0.1, with only active growing vegetation having positive values typically between 0.1 and 0.6 (Jelinski and Wu, 1996).

2.2 Spatial Structure

Variography is initiated by the grouping of the available pair-values into a number of lags or distance classes in accordance with their in between distances. Variograms provide a means of quantifying the commonly observed relationship where by samples close together will tend to have more similar values than samples farther apart. The variogram γ (h) is defined as:

$$\gamma(h) = (1/2)Var[Z(x) - Z(x+h)] \tag{2}$$

where h is the lag distance separating pairs of data points, *Var* is the variance of the argument. Z(x) is the value of the regionalized variable of interest at location x, and Z(x + h) is the value at the location x + h.

An isotropic experimental variogram γ *(h), is given by:

$$\gamma^*(h) = 1/[2n(h)] \sum_{i=1}^{n(h)} [Z(x_i + h) - Z(x_i)]^2 \tag{3}$$

where γ *(h) is variogram for interval lag distance class h, n(h) is the number of pairs separated by the lag distance h.

An anisotropic experimental variogram is defined as:

$$\gamma^*(h,\theta) = 1/[2n(h,\theta)] \sum_{i=1}^{n(h,\theta)} [Z(x_i + h,\theta) - Z(x_i)]^2 \tag{4}$$

where θ is the angle of a principal axis.

For anisotropic analyses the principal axis is the base axis from which the offset angles are calculated. Offset angles are 0°, 45°, 90° and 135° clockwise from the base axis (Gamma Design, 1995). The axis of 0° is defined from the north-south axis. The points aligned sufficiently close to one or another of

these angles with 22.5° tolerance are included in the anisotropic analysis for that angle.

The main features of a typical variogram are three-fold: (1) range, (2) sill, and (3) nugget effect. Range is the distance at which the variogram reaches its maximum value. Paired samples whose in-between distance is greater than the range is uncorrelated. This means that range is regarded as a measure of the spatial continuity of the investigated variable. Sill, as the upper limit of the variogram which tends to level off at large distances, is a measure of the population variability of the investigated variable generally, the higher the sill, the greater the variability in the population. The nugget effect is exhibited by the apparent jump in the variogram at the origin, a phenomenon that may be attributed to the small-scale variability of the investigated process and/or to measurement errors.

3. RESULTS AND DISCUSSION

3.1 Statistics concerning Aggregation sizes

The aggregation processes were based on the 12.5m, 25m, 37.5m, and 50m NDVI resolutions of three different land cover sites. Table 1 summarizes the descriptive statistics relating to the aggregate results. Table1 presents the statistics on the aggregation of the pure grass, mixed grass-shrub and broad forest sites. The statistics, mean, standard deviation, minimum and maximum, of the NDVI data were almost identical to those of the above four resolutions at the pure grass site as listed in Table 1. Meanwhile, The statistics, mean, standard deviation, minimum and maximum, of the NDVI data were different to those of the above four resolutions at the mixed grass-wood and wood sites as listed in Table 1. Comparison revealed the statistics of the aggregated NDVI data in the above four resolutions at the pure grass site display more consistently than those at the mixed grass-shrub and broad forest sites.

3.2 Experimental Variogram

Experimental variograms of the above four resolution NDVI at the three different land cover sites were calculated at same active lag and lag interval. The experimental variograms are isotropic experimental variograms displayed in Fig. 2. Fig. 2(a) displays the experimental variograms of the aggregated NDVI data at the pure grass site in 12.5m, 25m, 37.5m and 50m resolutions. These experimental variogram show that the spatial structures of the above four NDVI resolutions displayed almost identical pattern in isotropic formation. The experimental variograms of the 25 m and 50 m resolutions of the wood site displayed a similar tendency. Moreover, the 12.5 m and 37.5 m resolutions NDVI data exhibit a similar pattern on their variograms, as illustrated in Fig. 2(b). Meanwhile, the four resolutions of NDVI data at the mixed grass-shrub site displayed different tendencies and variations on their experimental variograms, as displayed in Fig. 2(c). These results illustrated that the aggregation size effect on the isotropic spatial structure varies on different land covers in this study

area.

The anisotropic formation analysis results illustrated that the experimental variograms of the four resolutions on the pure grass site at 0°, 45° and 135° directions displayed a similar tendency, as presented in Figs. 3(a), (b) and (c). Similar to the isotropic formation analysis Figs. 4(a), (b) and (c) indicated that the experimental variograms at 0°, 45° and 135° directions on the 25 m and 50 m resolutions of the broad forest site displayed a similar tendency. Moreover, on this broad forest site the 12.5 m and 37.5 m resolutions NDVI data exhibit a similar pattern on their variograms at 0°, 45° and 135° directions, as illustrated in Figs. 4(a), (b) and (c). Meanwhile, the four NDVI resolutions data at the mixed grass-shrub site displayed different tendencies and variations on their experimental variograms at 0°, 45° and 135° directions, as displayed in Figs. 5(a), (b) and (c). These results indicated that the aggregation size effect on the anisotropic spatial structure varies on different land covers in this study area.

4. CONCLUSION

This study has demonstrated isotropic and anisotropic spatial structures in 12.5m, 25m, 37.5m, and 50m resolutions NDVI data from a Spot image at three different 0.1407 km^2 land-cover sites that were an almost pure grass, a mixed grass and shrub, and a broad forest within the Yang Ming Shan National Park in Taiwan to evaluate the impact of aggregation on the spatial structure at different land-cover sites. The results indicated that the experimental variograms of the NDVI data in these four different resolutions displayed identical spatial structure in both isotropic and anisotropic directions at the grass site of Yang Ming Shan National Park. At the mixed grass-shrub site of this study area the NDVI experimental variograms in the 12.5m, 25m, 37.5m, and 50m resolutions roughly displayed a similar spatial tendency but different spatial variations. The experimental variograms of NDVI of these four resolutions at the broad-forest site of this study area displayed different spatial patterns and spatial variations in both isotropic and anisotropic directions. The experimental variograms of the broad forest site in the 25 m and 50 m resolutions displayed a similar tendency. Moreover, the 12.5 m and 37.5 m resolutions NDVI data exhibit a similar pattern on their variograms. However, the aggregation effect displayed significantly on the mixed grass-shrub and the broad forest sites in this study.

5. REFERENCES

Bian, Ling and R. Butler, 1999. Comparing Effects of aggregation methods on statistical and spatial properties of simulated spatial data, Photogrammetric Eng. & Remote Sensing, 65 (1), pp. 73-84.

Cihlar J. et al., 1996, Land Cover Classification with AVHRR Multichannel composites in Northern Environments, Remote Sensing Environ. , 58, pp.36-51.

Gamma Design Software, 1995. GS+: Geostatistics for the environmental sciences. Version 2.3.

Gamma Design Software, Plainwell, MI.

Gates, D.M. et al., 1965, Spectral properties of plants, Applied Optics, 4, pp.11-20.

Jelinski, D.E. and J. Wu, 1996,The modifiable areal unit problem and implications for landscape ecology, Vol. 11, No. 3, Landscape Ecology, pp.129-140.

Lillesend, T.M. and R. W. Kiefer, Remote Sensing and Image interpretation, John Wiley & Suns, Inc., Fourth edition, New York, p.724.

Lin, Y.P. and T. K. Chang, 2000. Simulated annealing and kriging method for identifying the spatial patterns and variability of Soil heavy metal, Journal of Environmental Science and Health, Part A - Toxic/Hazardous Substance & Environmental Engineering, A35 (7), pp.1089-1115.

Lin, Y.P., Chang, T.K., 2000. Geostatistical Simulation and Estimation of the Spatial Variability of Soil Zinc. Journal of Environmental Science and Health, Part A - Toxic/Hazardous Substance & Environmental Engineering A35 (3), pp. 327-347.

Lo, C. P. and B.J. Faber, 1997, Integration of landscape thematic mapper and census for quality of life assessment, Remote Sens. Environ., 62, pp.143-157.

Loveland, T. R. et al., 1991, Development of a land cover characteristics database for the conterminous U.S., Photogrammetric Eng. & Remote Sens., 57, pp.1453-1463.

O'neill A.L., 1996, Satellite-derived vegetation indices applied to semi-arid shrublands in Australia, Australian geographer, 27(2), pp.185-199.

Quattrochi, D.A. and J. C. Luvall, 1999,Thermal infrared remote sensing for analysis of landscape ecological processes: methods and applications, 14, Landscape Ecology, pp.577-598.

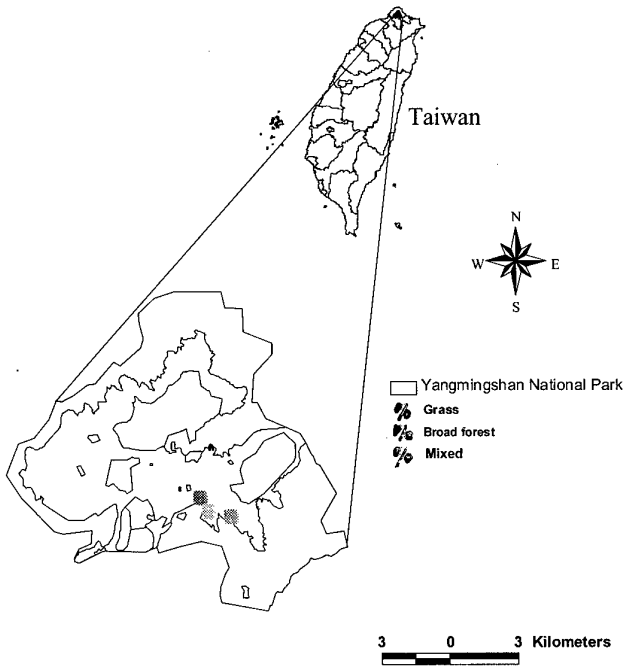
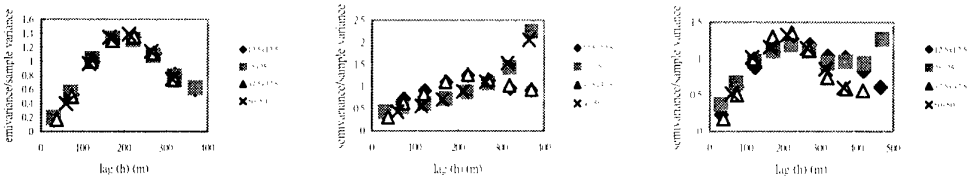
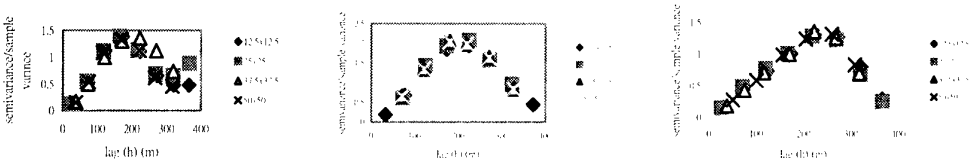


Figure 1. Locations of Study area



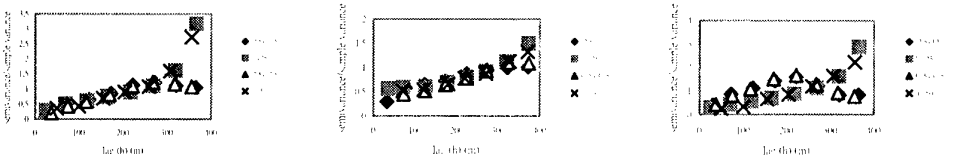
(a) (b) (c)

Figure 2 Experimental variograms of (a) the pure grass site; (b) the broad forest site; (c) the mixed grass-shrub site.



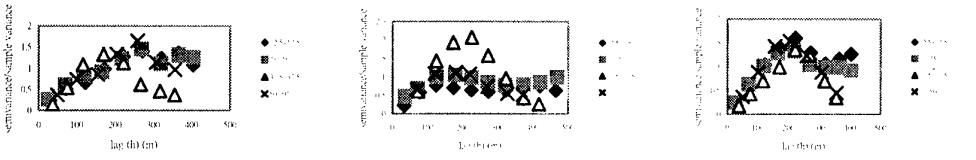
(a) (b) (c)

Figure 3 Experimental variograms of the grass site at (a) 0°; (b) 45°; (c) 135°.



(a) (b) (c)

Figure 4 Experimental variograms of the broad forest site at (a) 0°; (b) 45°; (c) 135°.



(a) (b) (c)

Figure 5 Experimental variograms of the mixed grass-shrub site at (a) 0°; (b) 45°; (c) 135°.

Computerized Ionospheric Tomography Using the GPS/MET and NNSS Data

C. T Liu[1], L. C Tsai[2, 1], and W. H. Tsai[1]
[1] Institute of Space Science, National Central University (NCU), Chung-Li, Taiwan
[2] Center for Space and Remote Sensing Research, NCU, Chung-Li, Taiwan
TAIWAN

Abstract

We have implemented the Multiplicative Algebraic Reconstruction Technique (MART) algorithm to the ionospheric electron density inversion from measured total electron contents (TECs) through radio observation of the Global Positioning System (GPS) signals and the Naval Navigation Satellite System (NNSS) transit signals to reconstruct two-dimensional ionospheric structures. We are also going to compare with the tomography results and show good agreement for both of the Global Positioning System / Meteorology (GPS/MET) and the Low-latitude Ionospheric Tomography Network (LITN) programs.

1. Introduction

The mathematical justification for tomographic reconstructions have been deeply rooted in the Radon transform [*Radon, 1917;Dean, 1983;Kak and Slaney, 1988*]. In a tomographic application, projections in as many directions as practicable and feasible are usually measured. The Fourier slice theorem [*Bracewell, 1956*] tells us how the two dimensional Fourier transform space of the object function is being filled by each such measured projection. Only when the Fourier space is completely filled can one hope to find a unique object function. Combine the theory of image reconstruction and the computerized processing ability, we may get the high-resolution image. Methods of computerized ionospheric tomography (CIT) from satellite radio measurements have been under development in more than ten years. The earlier experiments were conduced by receiving satellite signals from ground-based stations. In June 1994, National Central University also built up the Low-altitude Ionospheric Tomography Network (LITN). Furthermore, a recent mission termed the Global Positioning System/Meteorology (GPS/MET) program used a low Earth orbiting (LEO) satellite (the MicroLab-1) to receive multi-channel GPS carrier phase signals (~1.5GHz and ~1.2GHz) and demonstrate active limb sounding of the Earth's atmosphere and ionosphere.

In this paper, the LITN and GPS/MET programs will be described and some initial

ionospheric tomography result will be presented. In section 2, section 3, the technical details of GPS/MET and LITN will be discussed. In section 4, the multiplicative algebraic reconstruction technique (MART) will be described and some of derived tomography results will be presented. Some future works for imaging the ionosphere will be summarized in section 5.

2. The basic technique of GPS/MET

Since the mid-1960s, the radio occultation technique has been used to study the properties and structure of the atmospheres of Venus, Mars, some other outer planets and many of their moons [*Kliore, et. Al, 1965; Lindal, et. Al, 1979, 1981, and 1987*]. In 1993 the University Corporation for Atmospheric Research (UCAR) organized a proof-of-concept experiment on a 735-km low Earth orbiting (LEO) satellite (the MicroLab-1 satellite) to receive GPS signals and demonstrate active limb sounding of the Earth's atmosphere and ionosphere by radio occultation techniques. In the geometrical optics approximation as shown as Figure 1, a ray passing through the ionosphere is refracted according to Snell's law due to the vertical gradient of electron density and hence the refractive index n. The overall effect of the atmosphere can be characterized by a total bending angle α, an impact parameter a, and a tangent radius r_t as defined in Figure 1. During an occultation, the variation of α with the impact parameter a can be given by Snell's law when local spherical symmetry is assumed and can be expressed by

$$a(a) = -\int_{r_t}^{r_{GPS}} da + \int_{r_t}^{r_{LEO}} da \approx -2a\int_{r_t}^{\infty} \frac{1}{\sqrt{r^2 n^2 - a^2}} \frac{d\ln(n)}{dr} dr \ .$$

And then, using the Abel integral transformation under a spherically symmetrical assumption, the corresponding refractivity at a tangent radius r_t can be expressed in term of $a(a)$ and the impact parameter a as

$$n(r_t) \approx Exp\left(\frac{1}{p} \int_{a_t}^{\infty} \frac{a(a)}{\sqrt{a^2 - a_t^2}} da \right),$$

where $a_t (= n(r_t) r_t)$ is the impact parameter for the ray whose tangent radius is r_t.

Actually, the GPS frequencies bending in the ionosphere is so small. Even during the daytime and near solar maximum, the absolute magnitude of the bending angle does not exceed 0.03° for both of L1 and L2 GPS frequencies [*Hajj and Romans, 1998;*

Schreiner et al., 1999] in the F-region. Applying the Abel transformation, as is similarly done with inversions through bending angles with an assumption of local spherical symmetry, the electron density can then be given by the following integral equation:

$$n_e(t_t) = -\frac{1}{\pi}\int_{r_t}^{LEO} \frac{dT(r)/dr}{\sqrt{r^2 - r_t^2}}\,dr \quad .$$

We note that the derived electron density from the Abel integral transform can be used an initial condition for the MART algorithm described in later section.

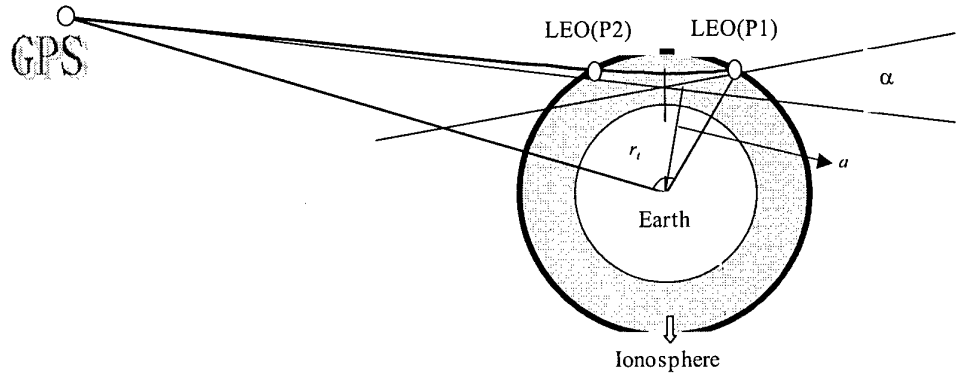


Figure 1. Illustration of the geometry of the GPS-LEO occultation problem for ionosphere observations, where p1 is an occulting LEO point, p2 is an auxiliary LEO point with the same impact distance of p1, α is the bending angle, r_t is the ray's tangent radius, and a is the impact parameter.

3. The Low-Latitude Ionospheric Tomography Network (LITN)

The LITN consists of a chain of six stations. Each station receives and records signals transmitted by the Naval Navigation Satellite System (NNSS). The receiver measures the Doppler shifts of the 400 and 150 MHz signals from NNSS due to the ionosphere, from which total electron content (TEC) can be deduced. As presented in Figure 2, it shows the geographic location of the six stations. The six receiving stations are Manila (121°E, 14.6°N), Baguio (121°E, 16.4°N), Kaohsiung (121°E, 22.5°N), Chungli (121°E, 25°N), Wenzhou (121°E, 28.0°N), and Shanghai (121°E, 31°N). The chain spans a range of 16.4° in latitude within 1° of 121°E longitude or a distance of more than 1800 km along the surface of the Earth. Geomagnetically, the visible region extends from 25° in the north and to just south of the magnetic equator in the south, with the northern equatorial anomaly region completely nested inside.

Referring to Figure 2, for any given path p at any station, the measured phase difference Ψ between the signals at the two frequencies is related to the slant TEC C_s for that path by (Leitinger et al., 1975)

$$\Psi+\Phi_0=DC_s,\ C_s=\int_p N_e ds$$

where N_e is the electron density, Φ_0 the unknown initial phase for a given receiver,and D is a proportional constant. Only when Φ_0 is found, can one obtain the absolute TEC from the measured data Ψ. To determine Φ_0 [*Leitinger et al. 1975*] proposed a two-station procedure.

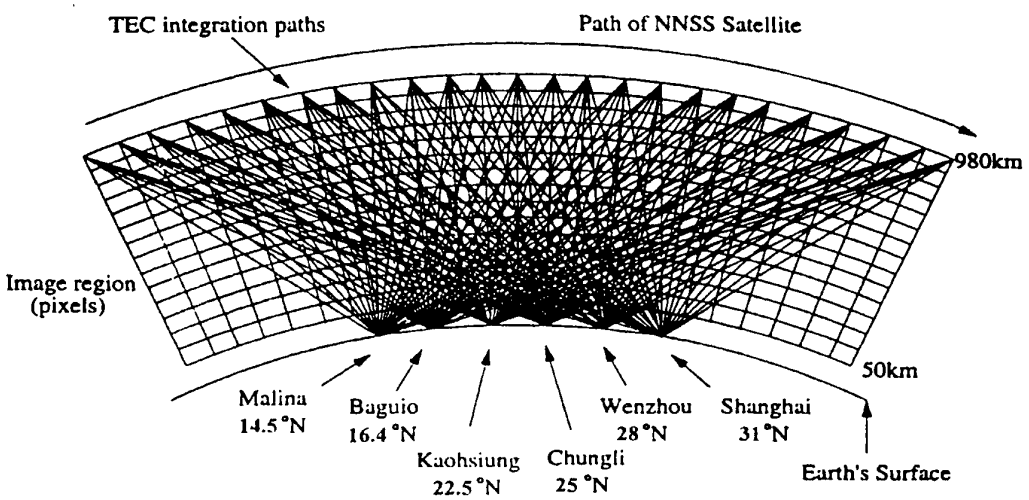


Figure 2. A vertical cross section depicting scanning of radio rays as one Naval Navigation Satellite System (NNSS) satellite passes overhead of six receiving stations on the ground.

4. The MART algorithm for CIT reconstruction and their results

With the initial constants determined, the absolute slant TEC can be obtained from the data. We start by considering the slant TEC along any path p between a transmitter and a receiver. For tomographic applications, the TEC along some path p is approximated by a finite sum of segment of the integral

$$C=\int_p N_e ds \qquad (1)$$

The TEC along some path p is approximated. This is carried out by dividing the two dimensional ionosphere into a set of n pixels and denoting the electron density in the j-th pixel by x_j. Then for the i-th path, equation (1) can be approximated by

$$C_i = \sum_{j=1}^{n} A_{ij} X_j \,, \quad where \;\; i = 1, 2, ..., m \,.$$

or in matrix notation:

$$C = AX \,, \qquad (2)$$

where A is a matrix whose element denote the length of the path-pixel intersections for each path. Note that C and X are column vectors for absolute slant TEC and electron density. A is an $m \times n$ matrix where m is the number of TEC values from all paths at all receiving sites. The elements in A depend on the geometry of the paths and can be computed once the experimental configuration is fixed. The task of CIT is to invert the equation (2) to obtain the electron density vector X.

Raymund(1994) reviewed the CIT reconstruction algorithms proposed by various investigators. One of the most commonly used algorithms is Algebraic Reconstruction Technique, or ART, having an additive correction and first introduced in CIT by Austen *et al.* (1988). This is an iterative procedure for solving the equation (2). A modified version of ART is the so-called multiplicative ART (MART) algorithm in which the correction in each iteration is obtained by making a multiplicative modification to X as

$$x_j^{k+1} = \left(\frac{C_i}{\langle a^i, x^k \rangle} \right)^{\lambda_k a_j^i} \cdot x_j^k \,, \quad j = 1,2, ..., n.$$

shown as the following equation (*Raymund et al., 1990*).
where λ_k are relaxation parameters such that $0 < \lambda_k < 1$. In this paper, the MART algorithm has been applied to the data (absolute slant TECs) to reconstruct the ionosphere as the examples of Figures 3 and 4.

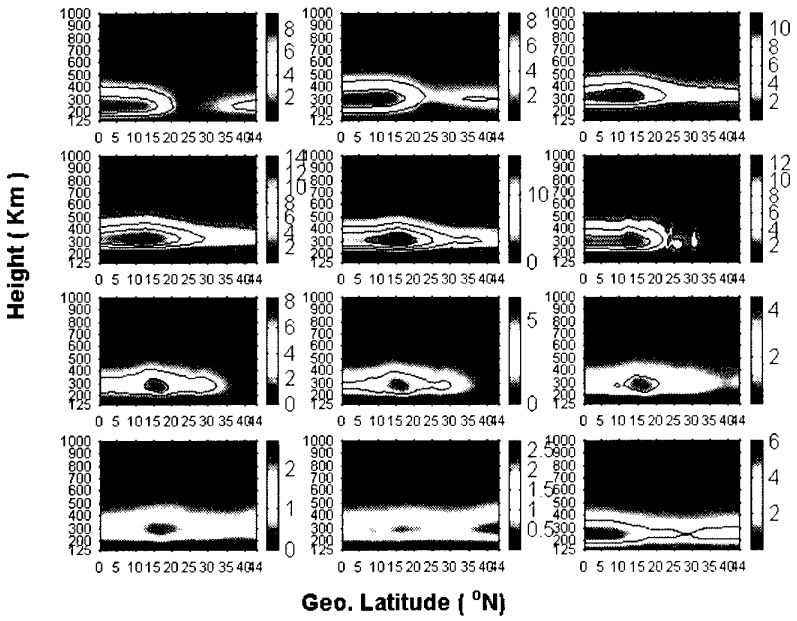


Figure 3. The electron density contour reconstructed by LITN on Aug. 28, 1995.

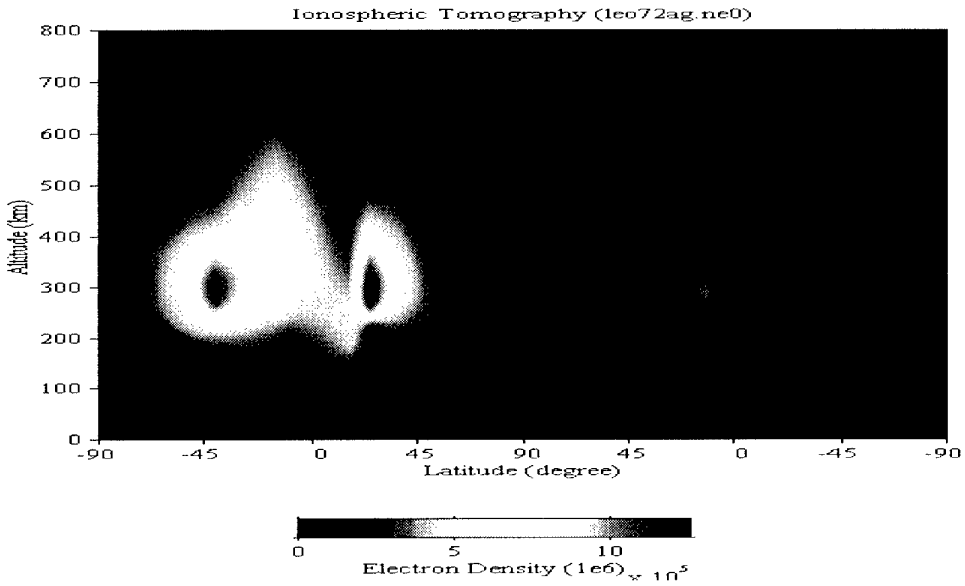


Figure 4. Ionospheric tomography by GPS/MET from 05:00 to 06:39 UT on the 10th of Feb., 1997. We note that the period of GPS satellite orbiting the Earth is about 100 minutes. Furthermore, the left part of this figure (–90°~90° at the x-axis) is dayside tomography; and the right part (90°~-90° along) is night side tomography.

5. Conclusion and future work

We note that, using the GPS/MET to reconstruct the ionosphere, it is hard to observe the Es layer. One of the probable reason is the LEO' s GPS signal observation using a low sampling rate at 0.1 Hz. Furthermore, the initial guess in MART algorithms is very important. The initial value in LITN is used to adopting the prediction of IRI-90 model. However, the GPS/MET occultation observation gives us another way to retrieve the initial electron densities from the Abel integral transform. We hope to get more accurate reconstruction of the ionosphere by the assistant of GPS/MET.

References

C. R. Huang, C. H. Liu, H. C. Yeh and W. H. Tsai, The low-latitude ionospheric tomography network (LITN)-initial results, Journal of Atmospheric and Solar-Terrestrial, 1997

C. R. Huang, C. H. Liu, K. C. Yeh, K. H. Lin, W. H. Tsai, H. C. Yeh, and J. Y. Liu, A study of tomographically reconstructed ionospheric images during a solar eclipse, Journal of Geophysical Research, VOL. 104, NO. A1, pages 79-94, January 1,1999

T. D. Raymund, J. R. Austen, S. J. Franke, C.H. Lin, J. A. Klobuchar, and J. Sralker, Application of computerized tomography to the investigation of ionospheric structures, Radio Science, Volume 25, Number 3, Pages 771-789, September/October 1990

T. D. Raymund, S. J. Franke, and K. C. Yeh, Ionospheric tomograph: its limitations and reconstruction methods, Journal of Atmospheric and Terrestrial Physics, Vol. 56, No. 5, pp. 637-657, 1994

Antonio Rius, Giulio Ruffini, and August Romeo, Analysis of Ionospheric Electron Density Distribution from GPS/MET Occultations, Transactions on Geoscience and Remote Sensing, Vol. 36, No. 2, March 1998

William S. Schreiner, Sergey V. Sokolovskiy, Christian Rocken, and Douglas C. Hunt,Analysis and Validation of GPS/MET radio occultation data in the ionosphere, Radio Science, Volume 34,Number 4, Pages 949-966, July-August 1999

L.-C. Tsai, W. H. Tsai, W. S. Schreiner, F. T. Berkey, and J. Y. Liu, Comparisons of GPS/MET Retrieved Ionospheric Electron Density and Ground Based Ionosonde Data

Sergey V. Sokolovskiy, Inversions of Radio Occultation Amplitude Data, Radio Science, Volume 35, Number 1.Pages 97-105, January-February 2000.

The 21st Asian Conference on Remote Sensing
December 4-8, 2000 Taipei, TAIWAN

Sensor integration for Personal Positioning System

Yusuke KONISHI, Ryosuke SHIBASAKI

Center for Spatial Information Science, Institute of Industrial Science, University of Tokyo

4-6-1 Komaba, Meguro-ku, Tokyo 153-8505, Japan
Tel & Fax : (81)-3-5452-6417

E-mail : konishi@skl.iis.u-tokyo.ac.jp

KEY WORDS:
positioning system, personal system, sensor, gyrocompass

ABSTRACT

To realize monitoring system of human activity and transportation, or to provide the positional information services, it is necessary to develop the positioning technologies which can estimate user's position and activities. As before, positioning systems using GPS or PHS were typical system as personal positioning system. However, the personal navigation systems using GPS or PHS need improvement in respect of availability, time-resolution and positioning accuracy. It is strongly demanded to develop personal positioning systems which can estimate one's position continuously and with high time-resolution, especially in urban area where the positioning systems using GPS or PHS can't work correctly. In this paper, we make a proposal of a personal positioning system which consists of some sensors.

1 Introduction

To realize monitoring system of human activity and transportation, or to provide the positional information services, it is necessary to develop the positioning technologies which can estimate user's position and activities. Recently, many researches are being conducted on the personal positioning system, and many personal or hand-held positioning systems using GPS or PHS were being proposed.

However, the personal navigation systems using GPS or PHS need improvement in respect of availability, time-resolution and positioning accuracy. GPS accuracy and reliability is limited in the area where the sufficient signal from GPS satellites can not be received, for example, in the valley between buildings, underground shopping malls, and so on. Similarly, the positioning systems using PHS can't work correctly in the area where the signal from the base-stations can not be received, and the positioning accuracy is about dozens meters which is insufficient to use for personal positioning system. It is strongly demanded to develop the complementary positioning systems which can

estimate one's position continuously and accurately, especially in urban area where the positioning systems using GPS or PHS can't work correctly.

In the case of car navigation, some complementary positioning systems were already developed and reached practicable level. They are realized by counting number of wheel rotations, sensing steering angles, and matching positioning trajectory to map. On the other hand, there is no effective complementary positioning system for human under the present circumstances, although the development is strongly demanded.

In this paper, we make a proposal of a personal positioning system consists of some sensors which can complement GPS or PHS in urban areas.

2 Positioning System

2.1 Hardware

This system consists of some sensors and a note-PC. The outline of this system is illustrated in Figure 1.

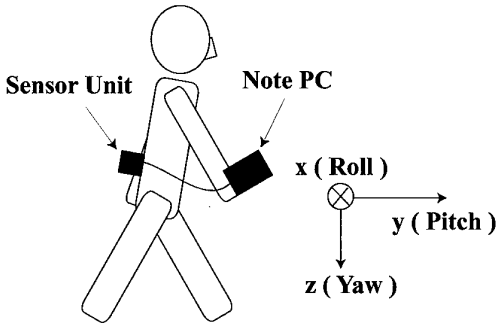


Figure 1: Hardware

The sensor unit illustrated in Figure 1 consists of a pocket-size gyrocompass which can measure three-dimensional posture angle and acceleration (Japan Aviation Electronics, JIMS-30S), a magnetic sensor which can measure three-dimensional magnetic field (Honeywell, HMR2300), a digital barometer (Yokogawa M&C, MU101-AM1P), and a GPS receiver (Trimble, Lassen-SK8). The sensor unit is fixed to the lower back of a user, and signals are processed by the note-PC.

2.2 System

Sub-systems are constructed by the combinations of the sensors illustrated in 2.1. As subsystems, we propose Pedometer System, Direction Finder, Height Finder, and GPS. This personal positioning system is constructed by the effective combinations of these sub-systems. The concept of this system is illustrated in Figure 2.

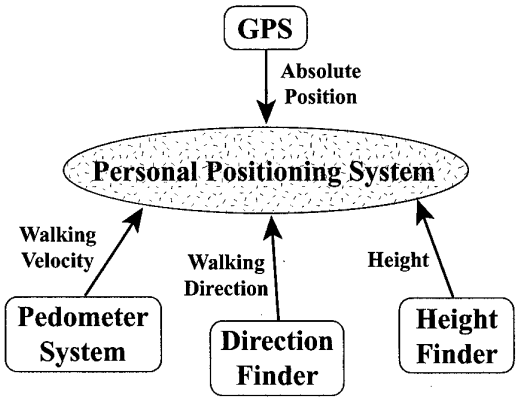


Figure 2: Concept of system

In developing this system, we focused the motion of walking human's pelvis, and number of steps, length of a step, and walking direction are listed as important parameters of human's walking. Therefore, we construct the Pedometer System to estimate number of steps and length of a step, the Direction Finder to estimate walking direction, and the Height Finder to estimate vertical movement.

Finally, this personal positioning system is constructed by the combination of these complementary sub-systems and GPS which can estimate absolute position.

3 Sub Systems

3.1 Pedometer System

In developing this system, we focused the motion of walking human's pelvis.

3.1.1 Algorithm

At first, we measured the motion of pelvis when user walks 6 meters in 10 steps by the gyrocompass which is fixed to the lower back of a user. The time-series data of rotation angles around each axes measured by the gyrocompass are illustrated in Figure 3. The axes are defined in Figure 1.

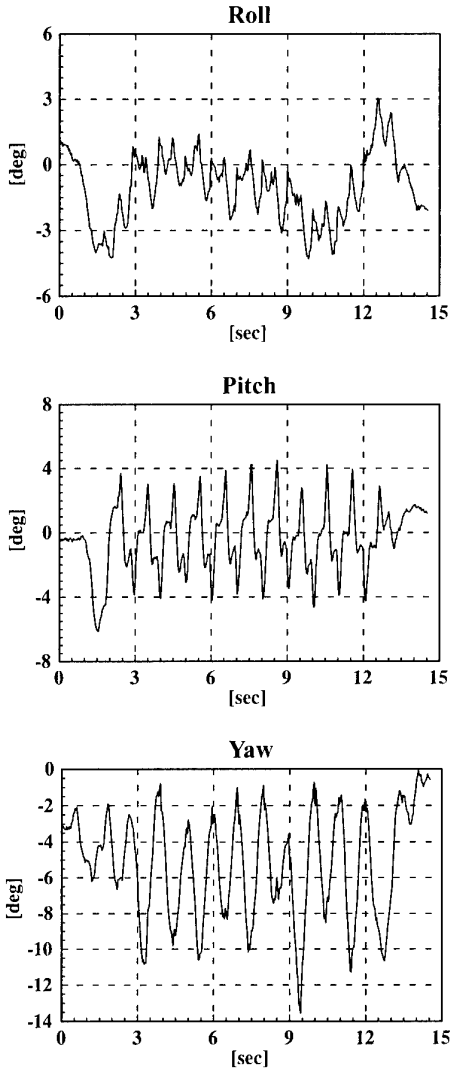


Figure 3: The motion of walking human's pelvis measured by the gyrometer

The experimental data illustrated in Figure 3 shows that number of steps is corresponding to number of waves which appeared in time-series data of pitch angle. Therefore, number of steps can be estimated by the time-series data of pitch angle measured by the gyrocompass.

Additionally, we measured the motion of pelvis when an identical user walks 14 meters in 22 steps, 20 steps and 17 steps. The each time-series data of pitch angle are illustrated in Figure 4.

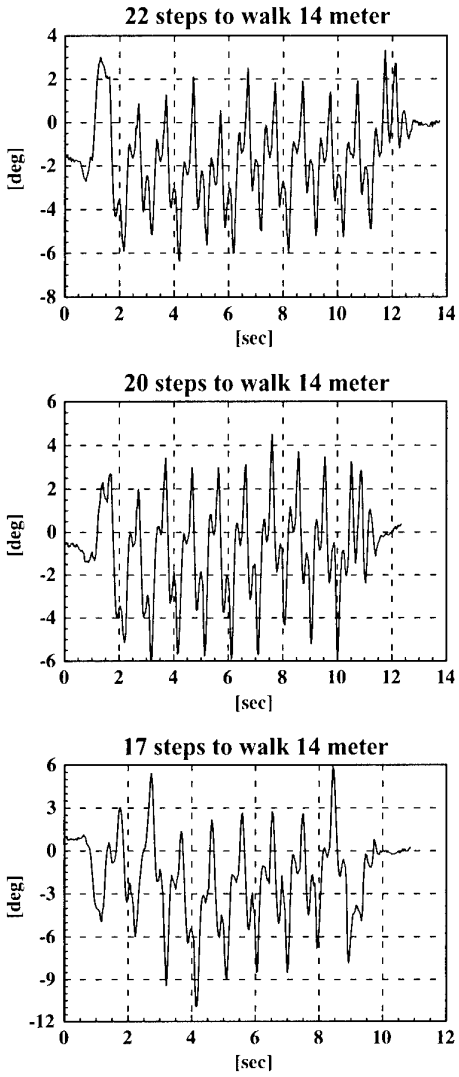


Figure 4: The time-series data of pitch angle whose forms change as number of steps

The relationship between width of changing pitch angle and length of a step which is computed by Figure 4 is illustrated in Figure 5.

The experimental data illustrated in Figure 5 shows that length of a step is computed by the time-series data of pitch angle measured by the gyrocompass.

Therefore important parameters of human's walking which includes number of steps and length of a step can be computed by the time-

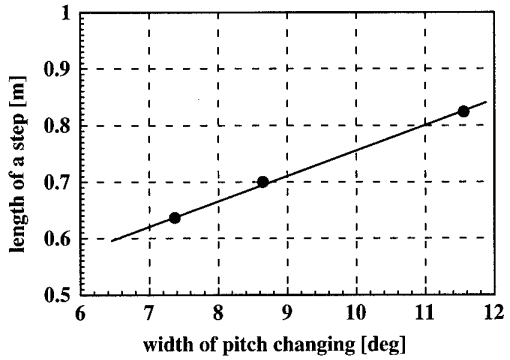


Figure 5: The relationship between width of changing pitch angle and length of step

series data of the motion of pelvis measured by the gyrocompass.

3.1.2 Experiment

To prove applicability of this system, we examined how accurately this system can compute the walking distance. Each four subjects walks 15 meters in three different length of a step, and each walking distances are estimated by the Pedometer System. In this experiment, we use the same parameters to estimate length of a step from width of changing pitch angle. The experimental results is illustrated in Figure 6.

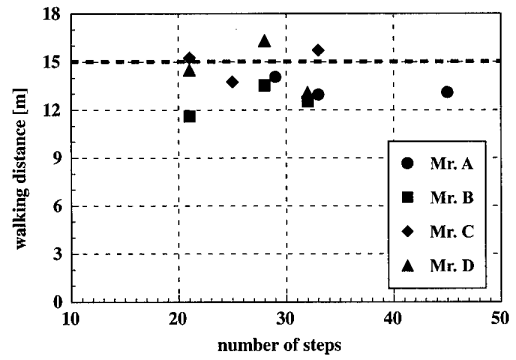


Figure 6: The relationship between number of steps and estimated walking distance

The experimental data illustrated in Figure 6 shows that the accuracy of estimated walking distance is different from each subjects. This means that we can improve the accuracy by setting up different parameters for each subjects.

3.2 Direction Finder

The time-series data of yaw angle measured by the gyrocompass has an important characteristic, gradual drift of the origin. The time-series data measured by the gyrocompass in a stationary state is illustrated in Figure 7.

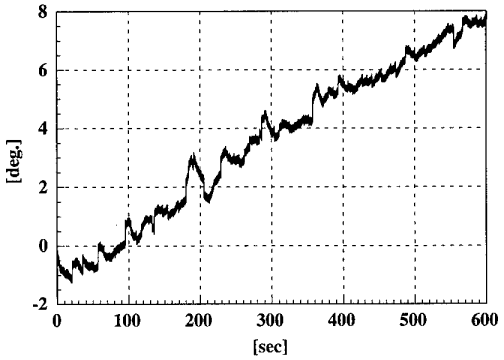


Figure 7: The time-series data of yaw angle when the sensor is stable

Drift of the origin illustrated in Figure 7 is observed about 1 degree per minute as an average value, and about 3 degrees per minute as the biggest value. Because of this characteristic, estimate of direction by using only gyrocompass is very difficult.

The other hand, the magnetic sensor is so sensitive that the measured data is easily affected by disturbance of magnetic field. The magnetic sensor which is adopted for this system can measure three-dimensional magnetic field by each x, y, and z axes' magnetic sensors. Offset of the origin and difference of sensitivity between each axes are occurred by the characteristics of each axes' sensor and the disturbance of magnetic field around the magnetic sensor. The concept of these error is illustrated in Figure 8; this figure shows measured data of geomagnetic field when the magnetic sensor is rotated 360 degrees in horizontal plane.

To estimate the amount of offset of the origin and difference of sensitivity between each axes illustrated in Figure 8, we measured the magnetic field in 5 typical places of human activity in urban area; in an open space, beside a prefab, beside a ferroconcrete pole, in an elevator, and on an narrow corridor. In each places, we measured magnetic field when the magnetic sensor

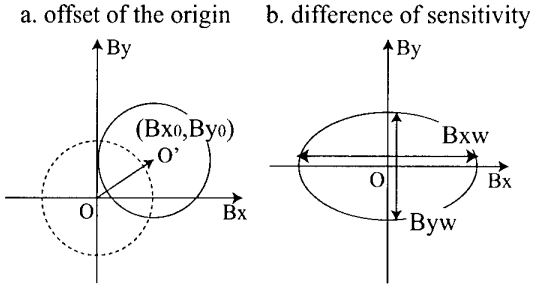


Figure 8: The characteristics of magnetic sensor

is rotated 360 degrees in horizontal plane. Offsets of the origin computed by the measured data is illustrated in Figure 9, and difference of sensitivity between each axes computed by the measured data is illustrated in Table 1.

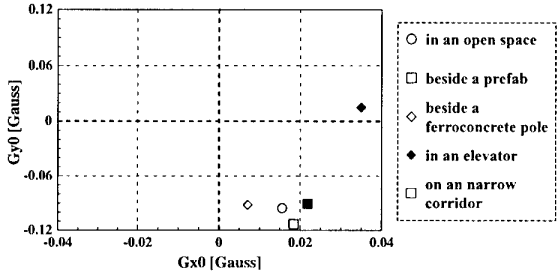


Figure 9: Offsets of the origin in each places

Table 1: Differences of sensitivity in each places

	difference of sensibility (B_{yw}/B_{xw})
on an open space	1.52
beside a prefab	1.50
beside a ferroconcrete pole	1.54
in an elevator	1.42
on an narrow corridor	1.74

Offset of the origin illustrated in Figure 9 and difference of sensitivity between each axes illustrated in Table 1 shows that there is disturbance of magnetic field in some specific places. In other words, the walking direction computed by the measured data of magnetic sensor has disturbance in some specific places where there is disturbance of magnetic field.

Then, we realize Direction Finder by combination of magnetic sensor and gyrocompass. The disturbance of estimated direction computed by measured data of magnetic sensor can be complemented by the time-series data of yaw angle measured by gyrocompass. This combination of magnetic sensor and gyrocompass can realize continuous and stable estimate of walking direction.

3.3 Height Finder

To monitor human activity in the underground shopping malls, buildings, and so on, the vertical movement is also important. However, the Pedometer System can estimate only horizontal movement, especially movement of walking. So, it is necessary to develop the Height Finder which can estimate vertical movement. In this system, we use barometer for estimate of vertical movement.

4 Conclusions

We proposed the Pedometer System for estimate of walking velocity, the Direction Finder for estimate of walking direction, and the Height Finder for estimate of vertical movement, which can complement GPS as personal positioning system. It is expected that this system can get one's positional information continuously and in high time-resolution.

5 Future works

5.1 Sub-systems' future works

We have some future works about each sybsystems.

5.1.1 Pedometer System

To improve the accuracy of estimated walking velocity, it is necessary to develop the algorithm to set up different parameters for each users. We are now developing some mechanism to set up different parameters for each users; the parameters are estimated by the time-series data measured by the sensors when user walks several times in the same distance, or the

parameters are automatically improved while user using the positioning system.

5.1.2 Direction Finder

We have to develop the algorithm which can estimate walking direction by the combination of gyrocompass and magnetic sensor. It is also necessary to do many detailed examination to examine the characteristics of magnetic field in each places in urban area.

5.1.3 Height Finder

We have to develop the algorithm which can estimate vertical movement by using barometer. And, it is also necessary to develop the algorithm to estimate the horizontal movement by using estimated vertical movement, for example, movement by using an escalator.

5.2 Future works

At first, it is necessary to develop an algorithm which can automatically distinguish modes of activity, like walking, running, going up or down stairs, standing, sitting, and so on. And it is also important to develop an algorithm which can automatically identify the modes of transportation, like by elevator, escalator, car, bus, trains, and so on. If these algorithms are developed, and the positioning system can estimate one's modes of activity and modes of transportation in real-time basis, the utility value of positional information will be more higher.

Next, it is necessary to combine this personal positioning system with map matching technology. It is expected that the combination is especially effective in buildings, underground shopping malls, and so on.

After discussing about these ideas, we will conduct detailed experiments to prove the accuracy and availability of this personal positioning system.

References

[1] Hideo KAWAI, Haruyoshi IWAMOTO and Koji TORII, 1988. A Route Navigational Composite System of Pedometer and Azimuth Compass for Human. T.IEICE, J71-A-11, pp.2054-2062.

[2] Takayuki TAKAHASHI, Hirofumi OSAWA, Akihiro SUZUKI and Hikaru INOOKA, 1995. An Improved Algorithm and Implementation for the Ambulatory Measuring System of Human Gait. T.SICE, 32-7, pp.1057-1064.

[3] Koichi SAGAWA, Atsushi INA, Takayuki TAKAHASHI, Tadashi ISHIHARA and Hikaru INOOKA, 1998. Estimation of Human Moving Behavior by Using Acceleration and Air Pressure. T.SICE, 35-2, pp.184-190.

Ground Truth Measurement System using RC Helicopter

Daisuke HONGOH, Hironori ICHIKAWA, Koji KAJIWARA, Yoshiaki HONDA.

Center for Environmental Remote Sensing, Chiba University
1-33 Yayoi-chou, Inage-ku, Chiba, 263-8522, JAPAN
Tel: +81-43-290-3845 Fax: +81-43-290-3857 E-mail: d-hongoh@ceres.cr.chiba-u.ac.jp

Keyword: RC helicopter, BRDF, NDVI

1.Introduction

Monitoring with data got by artificial satellites is very useful to know some changes in earth environment. But data got by artificial satellite don't show true value correctly, because that data have many noises that effect of aerosol and sensor angle etc. Therefore local observation is very important to relate characteristic of state of ground and date got by artificial satellite.

To know effect of sensor and sun angle, we need to observe BRDF (Bi-directional Reflectance Distribution Function).

$$\text{BRDF} \quad f_r(\theta_i, \phi_i; \theta_r, \phi_r) = \frac{dL_r(\theta_r, \phi_r)}{dE_i(\theta_i, \phi_i)}$$

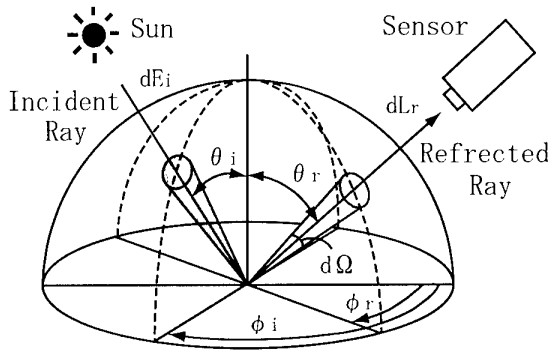


Fig1.BRDF

Some systems of BRDF observation had made by some studies in the past. But those systems have some problems that it's too big to carry or able to measure in only frat area, because BRDF observation needs many data got from deferent angles around the target.

Therefore in this study we thought RC helicopter (radio control helicopter) is vary useful platform of BRDF measurement, and we have developed observation system using RC helicopter since 1999. We tested this system in Mongolian grassland in August 1999, and proved this system is available for BRDF measurement.

2.Objective

To measure some areas with measurement system using RC helicopter in deferent condition of plant, and compare data, and consider the correspondence ability of this measurement system in some situation.

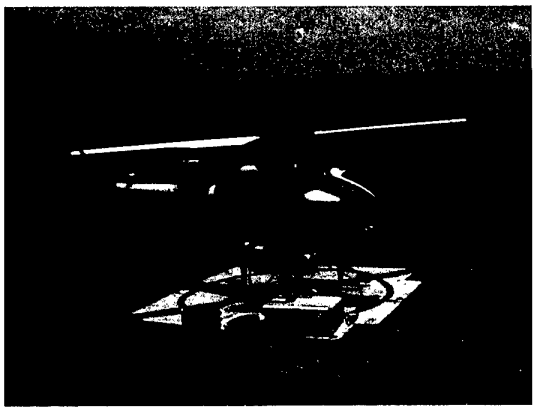


Fig2.RC helicopter

3.Instruments

The RC helicopter that we use in this study is actually for industrial product (RMAX YAMAHA Fig2), and used for sprinkling agricultural chemicals. This RC helicopter has hovering

system to keep its position by using GPS. And Fig3 shows measurement instruments that this RC helicopter has.

・Spectrometer

It is multi spectral spectrometer that has dual port, and it can select the sensor view angle from 20 degrees to 1 degree. And it can get both data, the data of the target and that of white at the same time.

・Digital Camera

It is 6 million pixels digital camera that can change lenses. Images are recorded into PC card and one HD card that can have 1 GB data can take pictures 160 times.

・Measurement condition monitoring system

It can monitor on earth by CCD camera and BS system.

・Laser range profiler

It can measure the distance up to 200 m at 50 cm accuracy.

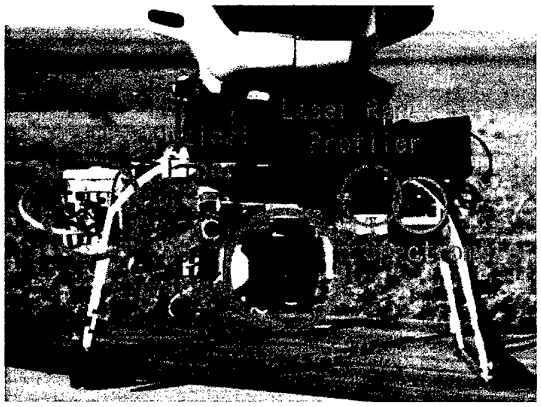


Fig3.Instruments

4.Method

The observation using RC helicopter need 2 kinds of flight pattern to measure.

First, changing the view range of the sensor, we observe to calculate minimum area that shows typical characteristics around observation area. Because to get the typical data of the observation area, we must observe a fully wide range so that local characteristics may not become big, but the observation range had better be as little as possible when we do observation in limited time. We call it representative area. We use NDVI to decide representative area.

NDVI=(NIR-RED)/(NIR+RED)

RED: Reflectance (580-680nm)

NIR: Reflectance (725-850nm)

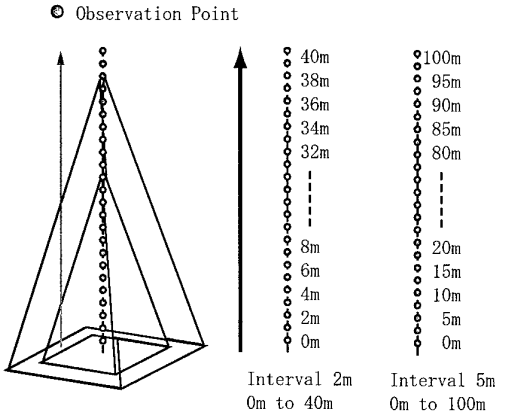


Fig4. Flight pattern of representative area measurement

Next, We set flight altitude from value of representative area. And RC helicopter fly and get data keeping same distance from the target, and sensors can keep watching same target using information of RC helicopters position. Fig5 shows the flight pattern of BRDF measurement. It has 2 lines of flight routine that principal line and vertical line, because change of reflectance data that measured toward sun direction is largest than other data, and data that measured toward perpendicular from sun direction is most different from data measured toward sun direction.

This measurement needs 15 minutes from start to end getting data every 34 points. In this situation we can observe in almost same condition

of sunlight, because the sun moves less than 3 degrees. The distance from RC helicopter to the target is 30m in lowest safety altitude think over emergency.

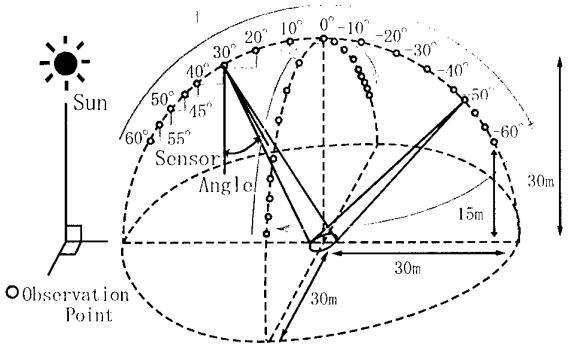


Fig5.Flight pattern of BRDF measurement

5.Observation

We carried on this system and observed in US and Canada since May 31 until July 9, 2000. Fig6 shows places and target we measured. Fig7 to 10 are results of measurements using RC helicopter. (a) is data of grassland in Mongolia that got in August 8, 1999. (b) is data of grassland in Montana that got in June 22, 2000. (c) is data of conifer forest in Victoria that got in June 28, 2000. And the sun elevation angle are (a)35.41° (b)66.17° (c)64.35°

Fig6.Measurment place and target

Place	Latitude	Longitude	Taget
Arizona	N31.60326	W110.50222	Yellow Grassland Tree
New Mexico	N32.59027	W106.84436	Desert
Kansas	N39.10101	W86.60814	Glassland
Montana	N46.89415	W133.43759	Glassland Bush Bloadleaf Forest Conifer Forest
Victoria	N48.61708	W123.72346	Conifer Forest
Oregon	N44.25141	W122.21037	Conifer Forest

Fig7 shows results of representative area measurement. Change of NDVI for altitude when data were got is small in every situation. Therefore we set distance from RC helicopter to the target is 30m.

Fig8 shows spectral data of each area. Those graphs are data of backward scan, and plotted every sensor angles.

Fig9 shows data of reflectance of RED and NIR of principal line and vertical line, and those data plotted every sensor angles.

Fig10 are digital image of measurement area.

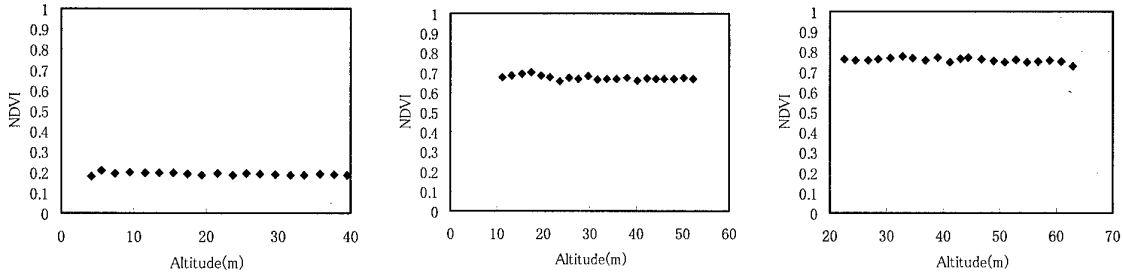
6.Conculusion

The spectral data of grassland in Montana and forest in Victoria show characteristic of reflectance of plants that NIR is high and RED is low as opposite to data of Mongolian grassland that shapes like gentle slope, because plants of Mongolian grassland are smaller than other place in quantity.

In grassland area, reflectances of NIR of backward scan are getting higher as sensor angle is getting higher, and reflectance of forward scan are low reflectance. In forest area, change reflectance is irregular, because construction of canopy is complex. And reflectance of RED of grassland in Montana and forest in Victoria don't change as sensor angle changed as opposite to Mongolian grassland.

In this observation, we could get some good data using this measurement system in grassland and forest area. We hope to get many data in deferent situation, and compare in time series. And to limit number of data got in one flight is remained problem.

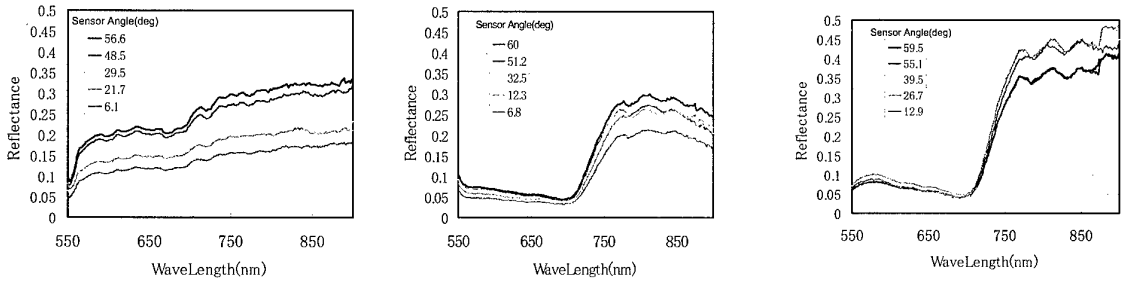
This work has been supported by CREST (Core Research for Evolutional Science and Technology) of Japan Science and Technology Corporation (JST). And we are very grateful to many staffs of US, Canada and Mongolia.



(a) Grassland in Mongolia *(b) Grassland in Montana* *(c) Conifer forest in Victoria*

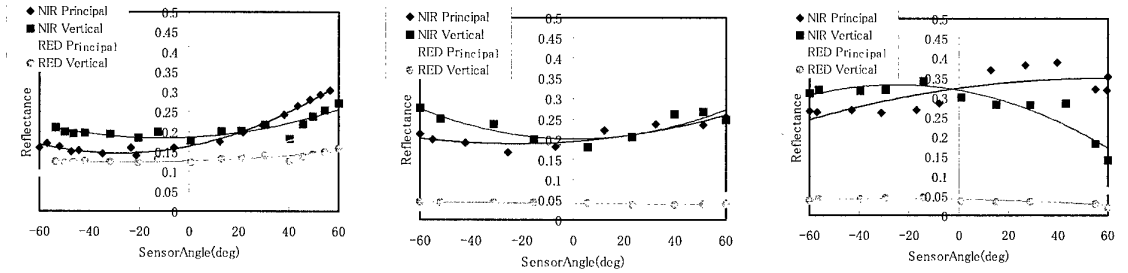
Sun elevation angle:35.41deg *Sun elevation angle:66.17deg* *Sun elevation angle:64.35deg°*

Fig7.NDVI and Altitude of RC helicopter



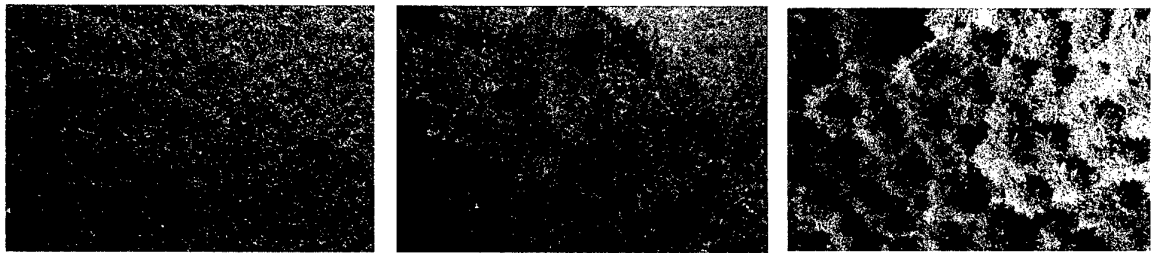
(a) Grassland in Mongolia *(b) Grassland in Montana* *(c) Conifer forest in Victoria*

Fig8.Rflectance and wavelength every sensor angle



(a) Grassland in Mongolia *(b) Grassland in Montana* *(c) Conifer forest in Victoria*

Fig9.Reflectance of RED and NIR every sensor angle



(a) Grassland in Mongolia *(b) Grassland in Montana* *(c) Conifer forest in Victoria*

Fig10.Digital Images

Development of the Retrieval Algorithms for Atmospheric Refractivity from GPS/MET Occultation

Yuei-An Liou and Cheng-Yung Huang
Center for Space and Remote Sensing Research, and Institute of Space Sciences
National Central University, Chung-Li, Taiwan, 320.
Phone: +886-3-4227151 ext. 7631 ; Fax: +886-3-4254908 ; email: yuei an@csrsr.ncu.edu.tw

KEY WOEDS: GPS/MET, Occultation, Refractivity

ABSTRACT

The Global Positioning System/Meteorology (GPS/MET) occultation experiment demonstrates the use of GPS in obtaining ionospheric electron density profile and other atmospheric profiles like refractivity, temperature and pressure. This paper describes the GPS/MET occultation technique and the method of data analysis. It also presents an inversion algorithm for extracting bending angles and the atmospheric refractivity profiles from GPS/MET occultation using the Abel inversion technique. Some GPS/MET retrieval results e.g. bending angle profile, refractivity profiles are presented here for illustration. A slight change in refractivity profile slope at tropopause around 15 km is noticed. High resolution global observation of refractivity could be useful in climate studies. Consequently, we may comfortably state that the occultation technique promises to open up new ways to monitor global atmospheric refractivity and the other variables of the neutral atmosphere like temperature and pressure for the studies of meteorology, climate and ionosphere.

Introduction

GPS/MET program was established in May, 1993 by the University Cooperation for Atmospheric Research (UCAR) to demonstrate active limb sounding of the Earth's neutral atmosphere and ionosphere using the radio occultation technique (Ware et al. 1996), which was first developed to investigate planetary atmosphere and ionosphere by JPL and Stanford University. The retrieval algorithm is mainly based on Abel's transformation. This method helps us produce an accurate all weather round-the-clock global refractive index profile, temperature, pressure and density profiles from several km above the ground level to about 40 km or more. Hence the GPS/MET technique has a large potential to monitor climate change, to improve weather forecasting and to provide low cost ionospheric data.

When the LEO receiver, tracks a GPS satellite as it occults the Earth's atmosphere, the arrival time of the GPS signal at the receiver is delayed because of the refractive bending and slowing of the signal as it traverses the atmosphere. When GPS signal transected the planetary ionosphere and atmosphere during an occultation, height profiles of ionospheric and atmospheric parameters could be retrieved from the observed phase path increase and amplitude variations. Under the fundamental assumption in GPS/MET occultation that Earth's atmosphere is spherically symmetric, all the atmospheric parameters, like refractive index, pressure, density and temperature, are functions of radius only. By measuring the change in the carrier phase over the

entire occultation event, the atmospheric refractivity index can be determined as a function of altitude. Hence this occultation technique was used to infer ionospheric electron density profiles (Hajj and Romans, 1998; Rius et al., 1998), and temperature and pressure profiles of the neutral atmosphere (Ware et al., 1996; Rocken et al., 1997; Kursinski et al., 1997). Temperature and pressure profiles can be derived through a downward integration using the known linear relationship between refractivity and density of dry air, the gas law, and the assumption of the hydrostatic equilibrium.

Data Processing Technique

Derivation of the Doppler shifted frequency

Basic observable in GPS/MET occultation is the phase change of the radio signal between the transmitter and the receiver. Each GPS satellite broadcasts two L-band signal of frequency 1575.42 MHz (L1) and 1227.60 MHz (L2). In GPS/MET occultation, the phases $\varphi(t)$ of carrier L1 and L2 are measured and recorded as function of time. The GPS/MET L1 and L2 excess phase data can be used to derive the Doppler–shifted frequencies. Note that the solutions are obtained by solving the high rate GPS data (50 Hz). Through the calibration process the sum of neutral and ionospheric delay is isolated. When the delay due to ionosphere is determined, it is differenciated to obtain the extra Doppler-shift introduced by the medium to obtain the bending angle of the GPS signal, α, as a function of the asymptote miss distance "a". Assuming a spherically symmetric atmosphere in the surroundings of occultation, the extra Doppler shift, Δf and can be written as

$$\Delta f = \frac{f}{c}[(\vec{v}_g \cdot \vec{e}_g - \vec{v}_l \cdot \vec{e}_l) - (\vec{v}_g \cdot \vec{e} - \vec{v}_l \cdot \vec{e})] \qquad \ldots\ldots(1)$$

Where f is the operating frequency, c is the velocity of light, v_g and v_l are the velocity of GPS and LEO satellite respectively, e_g and e_l are unit vector of signal transmitted by GPS and that of signal received by LEO respectively.

Smooth the Doppler-shifted frequencies

The computed Doppler-shifted frequencies are contaminated when the GPS signals occult through the atmosphere. Hence they have to be smoothed by some low-pass filters in some way before further processing. In smoothing data we have used here constrained matrix smoothing method similar to linear constrained matrix inversion method (Twomey, 1977).

$$\vec{f}_s(t_1,t_2,\cdots,t_n) = \left[\vec{I} + \vec{S}^t\vec{\Gamma}\vec{S}\right]^{-1} \times \vec{f}_d(t_1,t_2,\cdots,t_n) \qquad \ldots\ldots(2)$$

where S, I, Γ, f_d and f_s are the constraint smoothing matrix, unitary matrix, weighting function, Doppler-shifted frequency and the smoothed Doppler-shifted frequency respectively. Superscripts 't' and '–1' denote the matrix transpose and inverse. The measure used in this study is to minimize the sum of squares of the third derivatives of the unsmoothed vector f_d with respect to time "t" (Twomey, 1977). The smaller the sum of squares of the third derivative, the smoother the function. So the S matrix can be represented as

$$\overline{S} = \begin{vmatrix} 0 & 0 & 0 & 0 & 0 & 0 & 0 \\ -1 & 2 & -1 & 0 & 0 & 0 & 0 \\ 1 & -3 & 3 & -1 & 0 & 0 & 0 \\ 0 & 1 & -3 & 3 & -1 & 0 & 0 \\ 0 & 0 & 1 & -3 & 3 & -1 & 0 \\ 0 & 0 & 0 & 1 & -3 & 3 & -1 \\ 0 & 0 & 0 & 0 & -1 & 2 & -1 \end{vmatrix} \qquad \text{.....(3)}$$

The values of the weighting function Γ are selected according to the smoothness required and the amplitude of the noise of the unsmoothed data.

Derivation of bending angles and impact distance

The atmospheric bending angle profile is calculated from the measured time series of phase path increases and of the satellite velocities and positions. Knowing the positions and the velocities of the GPS and LEO satellites during the occultation event, the Doppler shift equation is solved for two GPS carrier frequencies separately in order to calculate the bending angles α_1 and α_2 as function of the impact parameters a_1 and a_2. The atmospheric bending α angle is then obtained by the linear correction method of Vorob'ev and Krasil'nikova (1993) as:

$$\alpha(a) = \frac{f_1^2 \alpha_1(a) - f_2^2 \alpha_2(a)}{f_1^2 - f_2^2} \qquad \text{.....(4)}$$

Further, for a spherically symmetric atmosphere the impact distance on both the GPS and LEO sides must be equal. This condition leads to

$$r_g \sin(\alpha_0 + \alpha_1) = r_l \sin(\beta_0 + \beta_1) \qquad \text{.....(5)}$$

At each occultation epoch, equation (4) and (5) may be solved for angles α_1 and β_1 , Since r_l, r_g and α_0, β_0 are precisely known from the ephemerides of the satellites (Fjelbdo et al., 1971). Once knowing α_1 and β_1, calculation of the impact distance $a = r_l \times \sin(\alpha_0 + \alpha_1)$ and the bending angle $\alpha = (\alpha_1 + \beta_1)$ is straightforward. This procedure results in $\alpha(t)$ and a(t).

Ionospheric corrections

Before arriving at the LEO all L1 and L2 signals must go through the Earth's dispersive ionosphere either once or twice. Depending upon the perigee altitude, time of day and year, the ionosphere may have significant effects on the observed phases and bending angles. To obtain the refractivity profiles of the neutral atmosphere, the ionospheric effects must be removed. First of all the Doppler shifts of the two GPS carrier frequencies are calculated. The contribution of the neutral atmosphere to the Doppler shift was estimated by differentiation of the linear corrected phase path increase. The ionospheric contribution is then the difference between the total Doppler shift and the neutral Doppler shift. The corrected ionosphere–free bending angle profile is plotted in Figure (1) along with the uncorrected L1 and L2 bending angle profiles for comparison. These curves show the significance of ionospheric corrections, especially above the middle atmosphere. Even after correction the corrected bending angle profiles show some small

fluctuations above 45 km. Based on the relatively strong signal to noise ratio in the 10 to 45 km height range it is likely that these fluctuations are real and might have caused by gravity waves. At higher altitude the strong fluctuations are likely due to the free electron density fluctuations in the ionosphere.

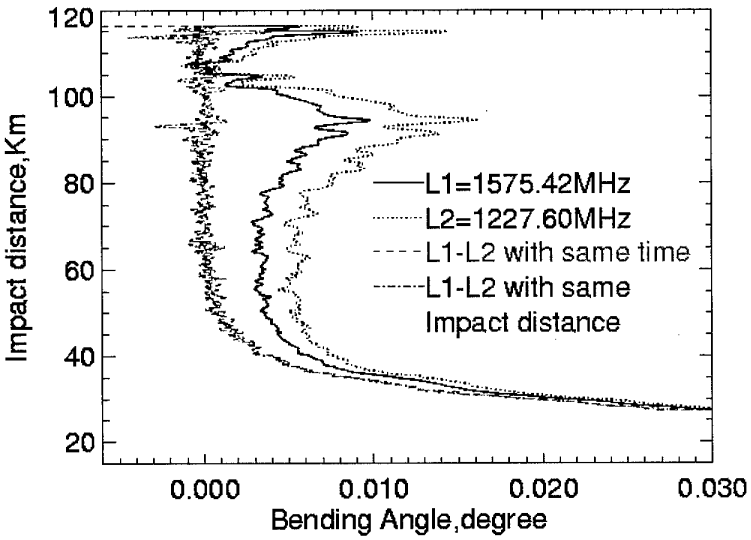


Figure 1. Bending angle vs Impact parameter before and after ionospheric correction

Abel inversion to retrieve the index of refraction

For the spherically symmetric atmosphere, the Abel integral equation gives a relationship between bending angle $\alpha(a)$ and refractive index n(a) (Phinney and Anderson, 1968; Fjeldbo et al., 1971)

$$n(a_0) = \exp\{\frac{1}{\pi}\int_{a_0}^{\infty}\frac{\alpha(a)\,da}{\sqrt{a^2 - a_0^2}}\} \qquad .....(8)$$

where $a_0 = n(a_0) \times r_0 = n(r_0) \times r_0$ (r_0 is the radial distance of the radio path at the perigee point B from the Earth). Thus once the numerical function $\alpha(a)$ is calculated from the Doppler-shifted frequencies, then the above equation yields the refractive index "n" at a_0 or r_0. By varying a_0, we can obtain the refractivity index profile $n(a_0)$ or $n(r_0)$. The retrieval is based on Abelian integral inversion. The Abel integration (8) transform $\alpha(a)$ to n(a). In practice one has to stop the integration at some altitude, where the ray impact distance is a_{top}. Hence equation (8) becomes

$$n(a_0) = \exp\{\frac{1}{\pi}\int_{a_0}^{a_{top}}\frac{\alpha(a)da}{\sqrt{a^2 - a_0^2}}\}\ \exp\{\frac{1}{\pi}\int_{a_{top}}^{\infty}\frac{\alpha(a)da}{\sqrt{a^2 - a_0^2}}\} \qquad .....(9)$$

By choosing a_{top} =90 km, the second exponential term of the above equation may be set to one, since the atmosphere above such a high altitude is so tenuous that $\alpha(a)$ is virtually zero. This

selection would not deteriorate the retrieval results below ~60 km. Figure (2) shows the retrieved profiles of refractivity by our scheme labeled as NCU with those from the UCAR scheme. It is evident from the figure that our results agree fairly well with UCAR results.

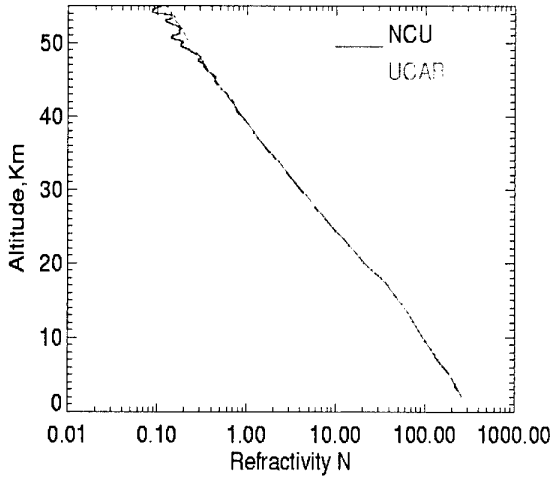


Figure 2. Retrieved profiles of refractive index

Results and Discussion

Figure (1) shows a plot of bending angle versus impact distance. It is evident that the ionospheric effect can not be ignored for the purpose of tropospheric research. Figure (2) shows our retrieved refractivity profile from the GPS/MET occultation. It is evident that the slope is changed at tropopause height, around 15 km. This supports strongly the earlier results. In the lower part of the troposphere, atmospheric defocusing, turbulence and inhomogeneity, especially when associated with unpredictable water vapor distribution, cause weak signal-to-noise ratio and multipath. Multipath, if it occurs, undermines the applicability of the Abel equation, causing larger errors in refractivity and temperature retrievals. Severe multipath makes the occultation phase measurements and the retrievals fail. The multipath problem primarily associated with water vapor limits the applications of the GPS/MET sounding in the lower troposphere. Recently using the principles of wave optics, Gorbunov and Gurvich (1998) applied the diffraction correction method to the multipath problem. Their results are encouraging, although this method does not work out for all multipath cases. Further studies are still desired to effectively improve the GPS/MET retrievals in the lower troposphere.

Conclusions

We have presented here a short overview of the GPS occultation technique to touch upon the key issues and aspects of the basic retrieval technique. Although many attempts have been made in developing effective retrieval algorithms of GPS radio occultation data, many issues remain to be

unaddressed. Basic conclusions came from all those studies that GPS radio occultation data has the potential to improve significantly the accuracy of global and regional analysis and weather prediction. Neutral atmospheric bending angles and refractivity are the two forms of the GPS radio occultation data that appear most suitable for data assimilation in GPS radio occultation. In the derivation of bending angles in the lower atmosphere and to assimilate refractivities in the upper atmosphere, we assumed the region a spherically symmetric one while it is obvious that the assumption of spherical symmetry in the ionosphere can never be an accurate one. Hence, further studies are needed to resolve the problem.

Acknowledgements

We are grateful to NSC, ROC, and ONR, USA, for their financial support under grants NSC 89 2111-M-008-059 and N00014-00-1-0528, respectively.

References

Fjeldbo, G. F., Kliore, A. J. and Eshleman, V.R., 1971. The neutral atmosphere of Venus as studied with the Mariner V radio occultation experiments. Astronomical Journal, **76**, 123-140.

Gorbunov, M. E. and Gurvich, A.S., 1998. Algorithms of inversion of Microlab-1 Satellite data including effects of multipath propagation. Int. J. Remote Sensing, 19, 2283-2300.

Hajj, G. A. and Romans, L.J., 1998. Ionospheric electron density profiles obtained with the Global Positioning System: Results from the GPS/MET experiment. Radio Science, **33(1),** 175-190.

Kursinski, E. R., Hajj, G. A., Hardy, K. R., Schofield, J. T. and Linfield, R., 1997. Observing Earth's atmosphere with radio occultation measurements. J. Geophys. Res., **102**, 23429-23465.

Rius, A., Ruffini, G. and Romeo, A., 1998. Analysis of ionospheric electron density distribution from GPS/MET occultations. IEEE Trans. Geoscience and Remote Sensing, **36**, 383-394.

Rocken, C., Anthes, R., Exner, M., Hunt, D., Sokolovskiy, S., Ware, R., Gorbunov, M., Schreiner, W., Feng, D., Herman, B., Kuo, Y. –H. and Zou, X., 1997. Analysis and validation of GPS/MET data in the neutral atmosphere. J. Geophys. Res., **102**, 29849-29866.

Twomey, S., 1977. Introduction to the Mathematics of Inversion in Remote Sensing and Indirect Measurements. Elsevier/North Holland, pp 243.

Vorob'ev, V. V. and Krasil'nikova, T. G., 1993. Estimation of the accuracy of the atmospheric refractive index recovery from Doppler shift measurements at frequencies used in the NAVSTAR system. Phys. Atmos. Ocean., **29,** 602-609.

Ware, R., Exner, M., Feng, D., Gorbunov, M., Hardy, K., Herman, B., Kuo, Y., Meehan, T., Melbourne, W., Rocken, C., Schreiner, W., Sokolovoskiy, S., Solheim, F., Zou, X., Anthes, R., Businger, S. and trenberth, K., 1996. GPS sounding of the atmosphere from Low Earth Orbit : Preliminary Results. Bull. Am. Meteorol. Soc., **77**, 19-40.

AUTOMATED CARTOGRAPHIC LINE TRACKING

Pakorn APAPHANT, Ph.D.
Researcher, Remote Sensing Division
National Research Council of Thailand
196 Paholyotin Rd., Jatujak, Bangkok 10900
Tel. (66)-2-940-6997 Fax. (66)-2-579-5618
E-mail: pakorn@pop.nrct.go.th
THAILAND

KEYWORDS: Line tracking, Line extraction, Skeletonization

ABSTRACT: Line is often regarded as one of the most valuable features in a map. Cartographic line tracking tools found in most commercial software typically are semi-automated process. This research studied and purposed an automatic method. It consists of line thinning, and line following steps. The algorithm has been examined using several scanned contour maps. An experimental result is also included herein.

INTRODUCTION

The simplest and perhaps the most useful feature in a map is line. This feature contains some essential structural information which is useful for further analysis. Although the line extraction process requires basic understanding of computer vision, many researchers in cartography have tried to study and applied them to their own discipline. Some researchers are interested in detecting lines directly from an original image (Apaphant and Bethel, 2000), while the others concentrate in tracking this feature from a line image. Except for extracting important information from an image, one of their common goals is to reduce memory space. Recently, there are many line tracking tools available in commercial GIS software. However they are semi-automatic process which can be tardy and expensive. Some tools even create artifacts. Hence the automation of the process can definitely bring considerable benefits to users of GIS system.

To track lines in a line image, two basic steps, i.e., skeletonization and line following, are required. Some research have emphasized developments only on the individual steps. Skeletonization is the process that reduces thick lines into single pixel wide lines. All 256 possible surrounding conditions for the pixel of interest were employed for decision-making of line thinning (Cohan and Landy, 1985). Nevertheless, their methods produced poor results in some specific cases. The medial axis method detected skeletons based on the maximum distance from all edges of the original line (Peuquet, 1981). This method could not be assured that the information of the original medial axis is always held. Line following is the process that identifies the series of coordinates in each individual thinned line. It is categorized into two approaches (Rosenfeld and Kak, 1982). The scan-line based method search for an object by scanning either row-by-row basis or column-by-column basis (Peuquet, 1981). The object-based method typically first detected endpoints of lines (Greenlee, 1987)(Moore, 1992). The individual objects are then followed from the beginning node of the objects through the ending node of the objects. Motivated by these problems, an automated line tracking is proposed in this paper. This method improves and assembles the two basic steps into one suite, without human intervention.

SKELETONIZATION

Thinning , also called *Skeletonization*, is the process that reduces thick lines into lines with single pixel thickness. It reduces data to be stored while brings out the structure of the pattern. The remaining pixels of each object form a line-string on the medial line of the original object. Since there are many possible applications of thinning, it is difficult to design criteria that will satisfy all applications. In cartography and GIS applications, two criteria are often required. Firstly, the removal must not change continuity of an original objects. This means that the removal operator must not create any discontinuity or holes. Secondly, the shape of an object must be preserved. However, due to the flawed computer decision during thinning, some small holes may be created. This problem can be addressed by a procedure so called *Gap filling*. It searches for the pixels which appear to be gaps and replaces them with object pixels. For the sake of completeness, this thinning algorithm is therefore itemized into two steps which are, thinning and gap filling.

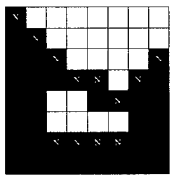


Figure 1: North border segments (N)

The proposed algorithm is based on the peeling approach. The thickness of a line is reduced by one unit at a time on each border of an object until its skeleton remains. We first define a border point of an object as a point whose adjacent point in its eight neighbors is not an object point. We divide the border points into four types i.e., north, south, west, and east borders. For instance the object points with character "N" in Figure 1 are the north border points. Another terminology often employed in this thinning algorithm is *an obese point*. A point, *p,* is a candidate for *an obese* if originally there is only one region adjacent to *p* based on the four neighboring definition. If point *p* is removed and that one region is still preserved then *the p* is called *an obese point*. This thinning process begins with iteratively deleting only the boundary segments which are obese points, on the north, south, east, and west borders consecutively. For example, in the first iteration, all north border points categorized as obese points are marked for deletion and then simultaneously removed for the entire image. After that, the thinned image and the original one are compared pixel by pixel for the entire image. If they are exactly the same, the iteration is stopped and the skeleton is obtained from the result of this pass. Otherwise the original image is updated. And the updated image is thinned along the south border and then compared. If the thinning process is still required, the same procedure performs on the east and west directions consecutively. After the updating, if the skeleton image is still not received, the next iteration is then continued with the same procedure. The iteration should stop when there are no further deletions. Note that change of thinning order may cause slightly different on the final result. Figure 2 illustrates the thinning procedure. Figure 2B is the output from thinning the north obese segments of the original one (Figure 2A). Figure 2C is the thinning result after the first iteration. And Figure 2D is the skeletons.

The point removal process may create small gaps in some places. To preserve the continuity of the lines, these gaps must be filled. They are converted to object points, if found. A general problem which often occurs in other algorithms is bridging between adjacent object. It is taken care in this

study by not allowing gaps between parallel lines to be filled. It can be noticed that this proposed algorithm produces the reducing object pixels systematically. Using this approach, the number of iterations for thinning an object is approximately on half of the objects thickness measured in pixel units. The resulting figure should be a line drawing retaining continuity and shape information of the original one. These thinned lines are spatially placed along the medial regions of the original objects. They therefore conform closely to the original but thinner (Figure 3).

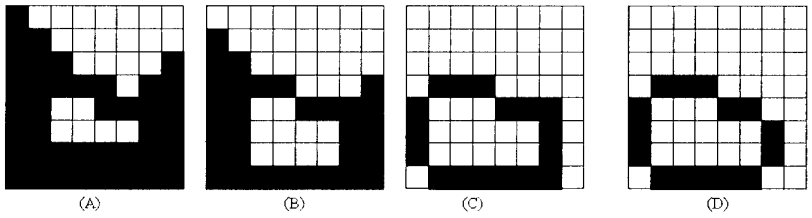


Figure 2:Thinning procedure

LINE FOLLOWING

It is possible to express a line as an equation if its geometry is simple and can be defined by simple mathematics equation. Unfortunately, most lines in cartography applications have complex geometry. In addition, database queries in geographic information systems are mostly framed in terms of the coordinates of figures in the map. A curved cartographic line is then often expressed by a string of consecutive head-to-tail vectors. These vectors are normally retrieved using line following technique. It identifies the series of coordinates in the individual lines. This process would be complicate if the ending nodes of each line-string were unknown. Therefore node marking is a required preprocess for the line following.

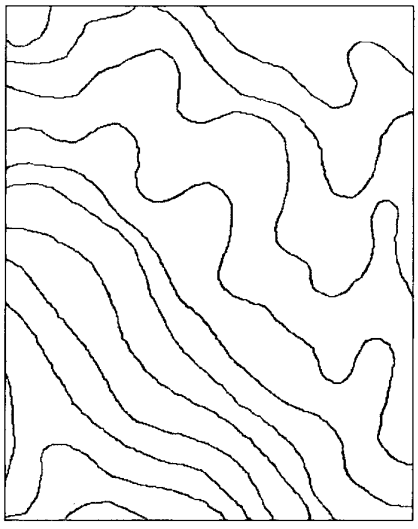


Figure 3: Skeletons overlaid on the original scanned portion

One method to build up a vector by coordinates is to begin with the endpoints and then find coordinates of the individual lines between these two points. Hence, after lines are thinned, node detection is performed on every object pixel. The decision rule, whether or not a pixel is a node, is based on some characteristics of the 256 possible combinations the eight connected neighboring pixels. Firstly the number of object pixels in the eight neighbors, denoted as $N(x)$, is introduced. The number of object pixel to background pixel transitions in the eight neighbors cyclically, denoted as $T(x)$, is also employed in this rule. Actually there are three types of node pixel. They are the isolated node, the junction node, and the terminated node. Generally, the isolated nodes are black spots in an image. Only the terminated nodes and the junction nodes may be the ending points of the line-string. It should be noted that a junction node may be the ending points of several line-strings. If the pixel of interest is denoted by x, the following rules are applied.

1. If $N(x) = 0$, x is an isolated node.
2. If $N(x) < 3$ and $T(x) = 2$, x is a terminated node.
3. If $N(x) > 2$ and $T(x) = 2$, x is a junction node.
4. If $T(x) > 5$, x is a junction node.

Once the coordinates of all nodes are obtained, the line following may simply launch. From the node list, the first node is retrieved and the line string of this node is then tracked until the other end is reached. The process is iterative for the entire node list. An ambiguity can occur when a line intersection is met. In this research, a decision is automatically made which direction to follow.



Figure 4: A portion of the scanned contour map

EXPERIMENTS

A portion of a scanned contour map sheet with scale of 1:50,000 was used in this experiment (Figure 4). It covers an area in the northern part of Thailand. The chosen part is compromised of several types of terrain data including rivers, mountains, ridges, and etc. The minimum elevation is

480 meters while the maximum elevation is 941 meters Contour lines are very dense. The original line thickness falls between 5 to 11 pixels. For the sake of simplicity, all contour annotations and other text appeared in the original scanned image were removed before this tracking algorithm performed. It can be noticed that some features in the original image are poorly defined. In addition there are some breaks in lines appearing on the original image. The grayscale scanned image was threshold to black and white image to differentiated the object pixels from the background pixels.

The output image after thinning and gap filling could be accepted in a certain regions. Some breaks in lines still appeared in the output. In general, the thinning operators worked very well on a contour map. All lines become single pixel wide features. The node marking algorithm then was employed for finding all types of nodes in the thinned image. Each thinned line then was followed on a line by line basis from its starting node until its ending nodes was reached. Note that there was no action taken on the isolated nodes.

In order to apply this contour data for use in constructing a digital elevation model or DEM, the elevation attribute data for these contour lines were noted. The individual contour lines were tagged with an elevation attribute. These XYZ contour line points could be used in several ways to build a DEM. Taken as random spot heights they can be processed into a TIN. A constant shade rendering is shown in Figure 5.

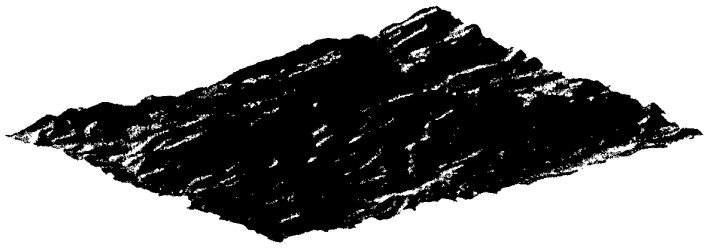


Figure 5: A shaded rendering of the terrain model

CONCLUSIONS

This paper has described an automatic line tracking technique for contour imageries. It integrates two crucial steps into one suite. The thinning operators can preserve shape of the object while it does not create any artifact or holes. At the end, the algorithm generates the series of coordinates of the thinned lines between two detected endpoints. Using this approach, memory space required to store the data can be reduced while most distinct patterns are retained. Several experimental results imply that this approach offers an alternative method of automatic line tracking.

REFERENCES

Apaphant, P. and Bethel, J., 2000. In: International Archives of Photogrammetry and Remote Sensing, Amsterdam, The Netherlands Vol. XXXIII, Part B3, pp.267-273.

Greenlee, D. D., 1987. Raster to vector processing for scanned linework. Photogrammetric Engineering and Remote Sensing, Vol.53, No.10, pp.1383-1387.

Landy, M. S. and Cohen, Y., 1985. Vectorgraph coding: Efficient coding of line drawing. Computer Graphics and Image Processing, Vol. 30, pp.331-344.

Moore, L. R., 1971. Software for cartographic raster to vector conversion. In: International Archives of Photogrammetry and Remote Sensing, Washington, D.C., Vol. XIV, No.5, pp.335-345.

Peuquet D. J., An examination of techniques for remote formatting digital cartographic data/part 1: The raster to vector process. Cartographica, Vol.18, No. 1, 1981, pp.34-38.

Rosenfeld, A. and Kak, A. C., 1982. Digital Picture Processing(2^{nd} edition), Academic Press, Vol. 2, pp.55-163.

Biomass Estimation by The Stereophonic Image Analysis

Hiroyuki MASUBUCHI, Koji KAJIWARA, Yoshiaki HONDA.

Center for Environmental Remote Sensing, Chiba University
1-33 Yayoi-cho, Inage-ku, Chiba, 263-8522, JAPAN
Tel:+81-43-290-3845 Fax:+81-43-290-3857
E-mail:hiroyuki@ceres.cr.chiba-u.ac.jp
JAPAN

Key Words: Stereophonic image, Biomass, Grass Height

1.Intoroduction

These days, an environmental problem becomes serious. It is important to grasp a change in the plant in the earth scale. The change in the plant is a great influence an environment. Other side, a detailed remote sensing is becoming available because of a satellite's ability improved more high resolution and many channels. Our laboratory has been analyzing satellite data for the estimate biomass in processing. And we have been getting real biomass data by the observation on any places. The methods of observation are biomass measurement and other measurement using car, tower, RC Helicopter. In the biomass measurement, we measure the dry weight, grass height, spectral reflectance in detail on the small cell 1 square meter. In the other measurements, we measure the spectral reflectance and picture on the large area. We want to measure any samples and quickly. But on the biomass measurement, we have to crop grass for a long time. It is heavy work. And we can't crop grass, if we measure it for long run. It needs method to know biomass by the non-contact.

2.Objective

A study of method to estimate biomass using the stereophonic images analysis.

3.Stereophonic Images Measurement System

3D scanner and Stereophonic image are available to measure the height of object by non-contact. 3D scanner can measure correct height and dimension detail. However it needs long time for measuring and it is not easy to move. Other way, the height accuracy using the stereophonic image is lower than 3D scanner. But system is simple and mobility. And it is practicable other observation. Therefore stereophonic image was selected.

Figure 3.1 shows the Stereophonic image measurement system. It has two digital cameras, spectrometer, white board for the reference of spectrometer.

Digital camera is CAMEDIAC-3030ZOOM, OLYMPAS has 3 million pixels CCD and it has non-compress image storage mode (TIFF). It will able to get high-resolution image.

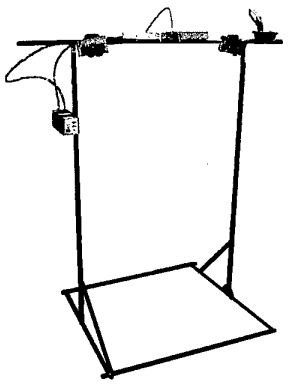


Fig.3.1 Stereophonic image measurement system

Equation 3.1 means the accuracy of height. L is height of camera, f is focal length, ΔCCD is pitch of pixel on CCD, B is camera distance.

$$accuracy = \frac{L^2}{fB}\Delta CCD \quad (3.1)$$

The accuracy of height is lower 2mm is better because of low grass at Mongolia. So for, camera distance is 1050mm.



Fig.3.2 images

4.Measurement

4.1.Measurement Work Sequence

Biomass measurement work sequence has 5steps. At first, it makes the cells on ground. Cell size is 1 square meter. Measurement target is inside a cell. 2nd, the spectral reflectance and stereo image are gotten, and grass is measured height. 3rd, All grass is cropped. 4th, grass is dried into an oven for 72 hours. At last, measure the dry grass weight.

4.2.Observation Site

In June 2000, we had observation in North America then in august we had observation in Mongolia.

In North America

We visited to Tucson-Arizona, LusCruces-New Mexico, Conza-Kansas and Missoula-Montana. The observation data has a wide variety of environment.



Fig.4.1 Observation site in North America

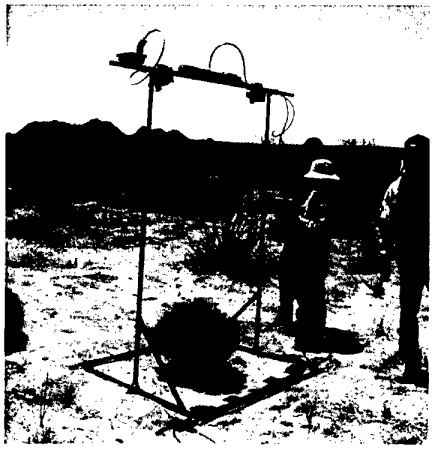


Fig.4.2 Measuring in North America

In Mongolia

We had observation in Mandalgob for 280km south of Ulanbator.



Fig.4.3 Observation in Mongolia



Fig.4.4 Measuring in Mongolia

5.Analysis

5.1.Estimate grass height

Figure 5.1 shows process flow for the estimate grass height. At first, it compensates distortion of images. Then height map is calculated by the parallax error using a based mapping method of stereo matching. In addition, it makes the vegetation cover image by the extract vegetation from compensated image using principal component analysis. The height map part of vegetation cover and the height map part of ground

(it is the other vegetation cover) are made with height map and vegetation cover image. The ground height map has many holes by the part of vegetation cover. So, there are estimate from pixels around the hole. The height map of vegetation is made difference in height between vegetation and ground. Figure 5.2-5.8 show the images are made by each process.

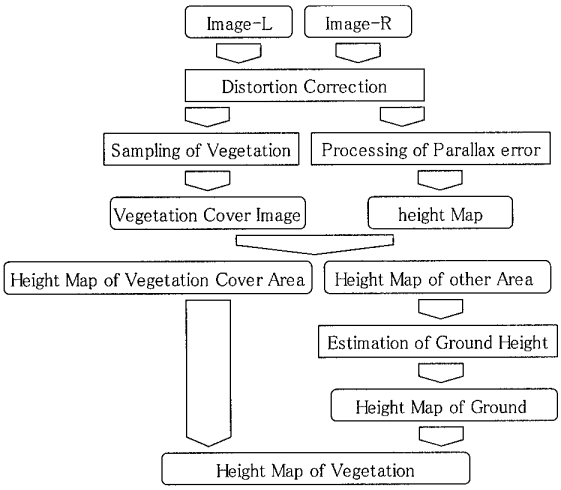


Fig.5.1 Process Flow

5.2 Estimate Biomass

The equation of translation from volume to biomass is liner function as weight density (k) is constant.

$$Biomass = volume \times k \quad (5.1)$$

Figure 5.9 shows that the vegetation volume calculated from the height map of vegetation. Table 5.1 shows the compared result and true value.

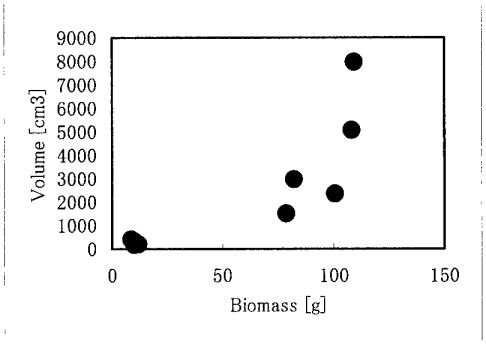


Fig.5.9 Estimated Volume-Biomass

Table5.1 Result

Cell No.	Volume [cm3]	Biomass [g]	Estimated Biomass [g]	Error [%]
JC01	7972	109.33	215.244	96.9
JC02	2975	82.08	80.325	2.1
JC03	5076	108.03	137.052	26.9
JC04	2361.97	100.74	63.77319	36.7
JC05	1515.7	78.54	40.9239	47.9
B00	180.5	9.92	4.8735	50.9
B01	253	10.08	6.831	32.2
B02	207	11.86	5.589	52.9
B03	341	10	9.207	7.9
B04	420	8.58	11.34	32.2

6.Conclusion

We estimate biomass from stereophonic image. But their results have error. As for main cause of error is equation of translation volume to biomass. Weight density is needs to fix better using many processed data and need to consider grass height. In addition, it is necessary for inspect height map and vegetation cover image because error is multiplied. It will become better precision of the estimate biomass by improved algorithm.

This work has been supported by CREST (Core Research for Evolutional Science and Technology) of Japan Science and Technology Corporation (JST). And we are very grateful to many staffs at US and Mongolia

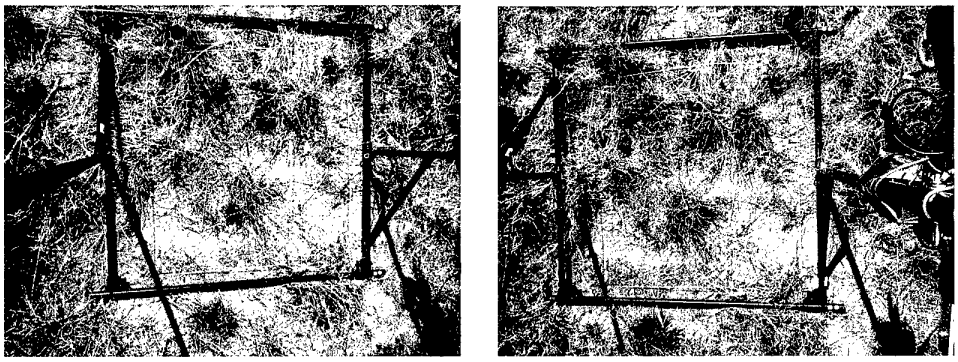


Fig.5.2 Digital Camera Image (L : Left R : Right)

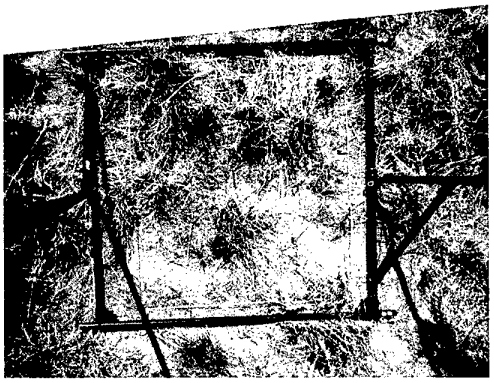


Fig.5.3 Compensated Image

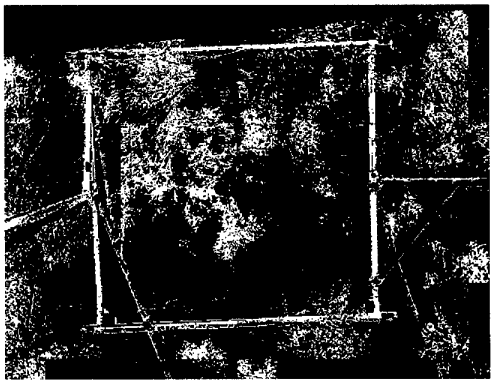


Fig.5.4 Vegetation Cover Image

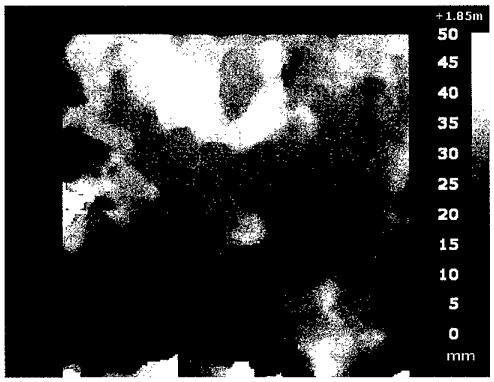


Fig.5.5 Height map

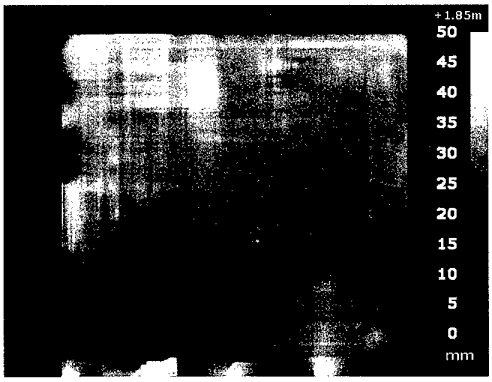


Fig.5.6 Height map of Estimated Ground



Fig.5.7 Height map part of Vegetation cover

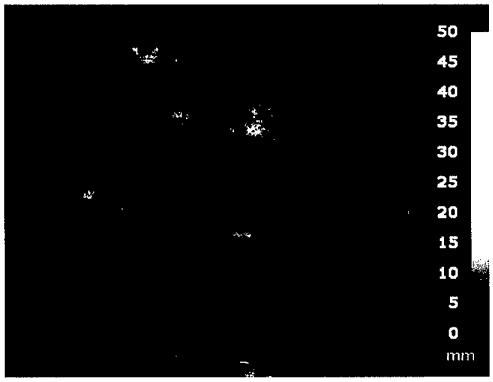


Fig.5.8 Height map of vegetation (Result)

Optical Remote Sensing Using Fiber Bragg Device For Dynamic Load Measurements

C. Patimapornchai[1], V. Jewpraditkul[2] and P.P.Yupapin[3]

[1] Department of Control System and Instrumentation Engineering, Faculty of Engineering
[2] Department of Physics, Faculty of Science
King Mongkut 's University of Technology Thonburi, Bangkok 10140, Thailand
[3] Lightwave Technology Research Center (**LTRC**), Department of Applied Physics
Faculty of Science, King Mongkut 's Institute of Technology Ladkrabang
Bangkok 10520, Thailand, Tel: 7373000 ext. 6271/6213, Fax: 3269981
Yupapin.Preecha@kmitl.ac.th

ABSTRACT

This work is the feasibility study of the dynamical load sensors, using optical remote measurement scheme. The optical sensing head is designed consisting of a fiber grating then spliced i.e. connected to a length of transmitted single mode fiber. The other end of the transmitted fiber is connected to the signals processing unit known as an optical time domain reflectometer (***OTDR***). The sensing head is sandwiched between a pair of sensing device buffer, where the applied loads can be applied on the sensing head. The measurement relationship between the reflected light intensity and applied loads are the subject of the investigation.

INTRODUCTION

Optical devices have been widely used either in sensors and communications [1-3]. An optical device known as fiber grating has also been investigated and used in both areas [4]. The use of such a device for temperature sensor has been reported [5], where grating was attached between two different materials where their thermal expansion effect the chane in grating period introducing the temperature measurement. The simultaneous measurement of temperature and strain was investigated [6], where two different physical parameters could be observed and measured using scch a siple and low cost technique. The use of fiber grating for the measurement of alternative current (ac) was reported by [7], the multimode laser diode was employed to relatively measure the change in modulated frequency respecting to the change in drived current. Fiber grating was also used in communication and signal processing system, to complement the idea of all fiber communication and networks [8].

The measurement relationship between the dynamical applied loads and output light intensity is detected by using ***OTDR***, where the long length of single mode fiber is shown the remote sensing sense [9]. The measurement errors contributing by either small vibration or temperature changes are also our subject of this investigation. The remote sensing sense and the dynamical measurement are also the major objectives of this work. The application for fluid flow rate and transported load may be discussed.

2. OPERATING PRINCIPLES

When coherent light from source enters into an optical system and sensing element as shown in Fig. 1, the coupled light from one end of the sensing fibers is reflected into the launching source, the other is reflected to the optical detector, P_r, which is expressed as [9]

$$P_r = \sin^2[2\int_0^z C(z)dz] \tag{1}$$

The coupling coefficient from equation (1) is given as

$$C(z) = 3.26\,\delta^{1/2}/a(z)[V(z)]^{5/2} \tag{2}$$

$$V(z) = a(z)\,k\,(n_1^2-n_2^2)^{1/2} \tag{3}$$

$$\delta = 1-(n_2/n_1)^2 \tag{4}$$

and $k = 2\pi/\lambda$. Where a is the coupling fiber radius, n_1 and n_2 are core and cladding refractive indices of the coupling fibers, respectively. λ is light source wavelength.

The change in grating period, Λ, is formed the change in Bragg wavelength as

$$\lambda_B = 2\,mn_c\Lambda \tag{5}$$

where λ_B is Bragg wavelength, m = 1, 2, 3.....is the reflection grating wavelength order. n_c is fiber optic refractive index and G is Bragg grating period.

When force is applied on he sensing unit that the change in grating period occurs inducing the change in output reflected light, P_r, which is observed by detector.

3. EXPERIMENT

The experimental system set up may be used an optical sytem or OTDR. A coherent light from a laser diode with wavelength of 1.31 micron is employed then launched into a length of a single mode fiber as shown in Figure 1, in the measurement system by the ***OTDR***, before entering into a sensing unit i.e. fiber Bragg device or fiber grating. The return signals either from the applied loads or fiber end itself is detected then seen on the ***OTDR*** monitor. The change in output signal intensity relating to the applied loads is observed respecting to the sensing head position, with dynamical and real times processing. The bulky signal detection using grating and the scanning detector are also our subject to be investigated.

The measurement relationship between the dynamical applied loads and output light intensity is detected by using ***OTDR***. The reflected light output from sensing unit is splitted and observed by using bulky grating before entering into detector. The change in output light intensity may be relatived to he change in applied loads.

4. DISCUSSION AND CONCLUSION

The research work is being continued in progress that the expected experimental scheme and results should be realized by the conference time.

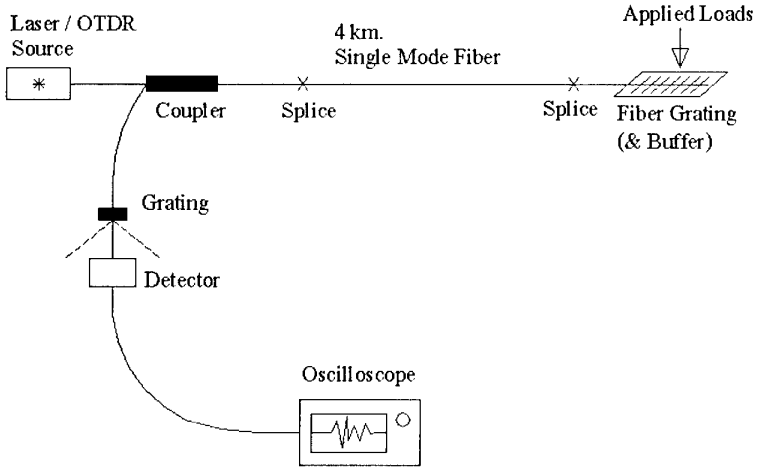


Figure 1 Illustrates of the experimental system use for dynamic load measurement.

The dynamic measurement means the measurement is taken place when load is in under movement condition. For examples, the measure of fluid in plastic pipe, the measurement of transported vehicles in the traffic.

5. ACKNOWLEDGEMENT

The authors are pleased to acknowledge support from National Science and Technology Development Agency of Thailand (**NSTDA**) by way of a research scholarship to Ms. C. Patimapornchai.

6. REFERENCES

1. Udd, E., 1991. Fiber optics sensors : An introduction for engineers and scientists, John Wiley & Sons, Toronto, pp. 443-445.
2. Wright, J.V.,1986. Wavelength dependence of fused couplers. Electron. Lett., **22**, pp. 320-321.
3. Gonthier, F. *et al,* 1987. Investigation of power oscillations along tapered monomode fibers measurements and analyses of fields in fused tapered single mode fiber couplers. Appl. Opt., **26**, pp. 444-449.
4. Hill, K.O. and Meltz, G., 1997. Fiber Bragg Grating Technology Fundamentals and Overview. Journal of Lightwave Technology, **15**(8), pp. 1263 – 1276.
5. Jung, J. et al, 1999. Fiber Bragg grating temperature sensor with controllable sensitivity. Appl. Opt., **38**(13), pp. 2752 – 2754.

6. Jung, J. et al, 2000. Simultaneous measurement of strain and temperature by use of a single fiber Bragg grating written in an erbium: yttbium – doped fiber. Appl. Opt., **39**(7), pp. 1118 – 1120.
7. Ferreira, L.A. et al, 1999. Demodulation of fiber Bragg grating sensors based on dynamic tuning of a multimode laser diode. Appl. Opt., **38**(22), pp. 4751 – 4759.
8. Mayer, E. and Basting, D., 2000. Excimer – laser advance aid production of fiber grating. Laser Focus World, April, pp. 107 – 110.
9. Raknoi, P. and Yupapin, P.P., 2000. Optical remote measurement technique using loop-mirrors sensing fibers, *Science Asia*, (in press).

.....

MAPPING AND MEASURING THE TROPOSPHERE POLLUTANTS ORIGINATED FROM THE 1997 FOREST FIRE IN SOUTH EAST ASIA.

Mazlan Hashim, Kasturi Devi Kanniah, Abdul Wahid Rasib and Lim Chee Ming
Department of Remote Sensing
Faculty of Geoinformation Science and Engineering
Universiti Teknologi Malaysia
81310 Skudai, Johor, Malaysia.

KEYWORDS: remote sensing, AVHRR, forest fire, aerosols, gases, atmospheric pollutants.

ABSTRACT: The massive forest fire in Indonesia in 1997 affected the whole Asian region by transporting large quantity of smoke plume with Malaysia bearing the brunt due to being nearer, wind direction and weather conditions. In this study, AVHRR (Advanced Very High Resolution Radiometer) satellite data were used to detect and subsequently map the five primary sources of fire pollutants namely Carbon monoxide (CM), Sulphur dioxide (SO_2), Nitrogen dioxide (NO_2), Ozone (O_3) and particulate matter less than 10 micron ((PM10) in Peninsular Malaysia. A multi regression analysis was used in this study to establish a statistical relationship between *atmospheric pollutants* (ppm) readings recorded at 5 stations around the Peninsular and *reflectance values* from AVHRR data. This model, based on 5 samples was then applied to all the pixels in the image covering the whole Peninsular Malaysia. The obtained values are in parts per million (ppm) for all the constituents except for PM10 in ug/cu.m.

1. INTRODUCTION

In Southeast Asia, currently it has become evident by estimates from satellite remote sensing data that biomass burning play an important role in air pollution and atmospheric chemistry. Palm oil plantations in Riau and other Sumatera provinces are the main source of the fires as many companies use fire as a cheap method to clear the land for the next planting season (UNEP, 1999). Combustion products of biomass burning include various hazardous gases such as carbon dioxide, carbon monoxide, nitrous oxide, oxides of sulphur, methane, non-methane hydrocarbons, nitric oxide and various types of atmospheric particulates.

Gases and aerosols are very efficient at scattering sunlight. Scattering of solar radiation by aerosols can limit human visibility in the troposphere; this is the phenomenon known as haze. Some aerosols, especially black carbon particles created by fires, efficiently absorb sunlight and results in heating of the atmospheric layer, whilst, scattering properties cause a redistribution of radiation including losses back to space. In the lower atmosphere, aerosols and gases can modify the size of cloud particles which changes how the clouds both reflect and absorb sunlight thus, modifies the radiative budget. The 1997 and also the subsequent fire scenarios (1998, 1999 and Mac 2000) have affected the whole Asian regions with Malaysia bearing the brunt due to being nearer to Sumatera, wind directions (Monsoon Seasons) and weather conditions. In Malaysia, the main pollutant that is contributing to the haze is PM10, besides CM, SO_2, NO_2 and O_3 (Vadivale 1997). Pollutants from forest fire can be hazardous to the environment and human health.

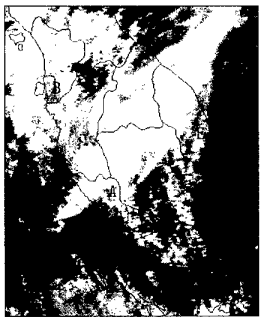
The ability to detect the extent and amount of the forest smoke plume during early stages of the disaster would greatly assist in the emergency response planning by responsible teams. Many studies have been conducted using remote sensing technique to map or measure the forest fire constituents (Kaufmann et al (1990), Cahoon Jr. et al (1994) and etc. used AVHRR data to estimate the particulates and trace gases originated from forest fire in Brazil, China and South America respectively. Satellite remote sensing can determine the distribution and total content of the pollutants over large areas. Coarse spatial and high temporal resolutions of AVHRR

sensor onboard NOAA (National Oceanic and Atmospheric Administration) satellites made it possible to detect and monitor the fast spread of fire emissions over countries, regions or even continents continuously.

In this study NOAA AVHRR data were used to map and measure the spatial distribution of PM10, CO_3, NO_2, O_3, and SO_2 on 17, 28 and 29 of September, 1997 (period of thick haze episode) over Peninsular Malaysia. The current study is an extension of previous work that looked at the determination of haze in API (Air Pollution Index) units (Asmala, 1997).

2. DATA AND TECHNIQUE

Channels 1 and 2 of AVHRR (short wavelength; 0.58- 1.10 μm) were selected to be used in the extraction of fire emission constituents information. Atmospheric molecules and other tiny particles that are much smaller in diameter than the wavelength of the interacting radiation are efficiently diffuse the radiation. The effect of Rayleigh scatter is inversely proportional to the forth power of wavelength and therefore there is much stronger tendency for short wavelengths to be scattered by this scattering mechanism than long wavelengths (Lillesand and Kiefer 1994). Hence, the contribution of measured radiance at the top of the atmosphere from the path radiance is larger for shorter wavelengths. Smoke originated from wild forest fire is not observable in the mid IR (2.2 μm) due to the large ratio of wavelength to the size of the particles. Kaufman (1993) also used sun photometer/ radiometer in the 0.44-1.03 μm range to make measurements of the path radiance and the aerosol optical thickness from the ground.



	Monitoring stations	Geographical location	
		Longitude	Latitude
A	Kuala Lumpur	101°42.274' E	03°08.286' N
B	Prai	100°24.194' E	05°23.890' N
C	Pasir Gudang	103°53.637' E	01°28.225' N
D	Bukit Rambai,	102°10.554' E	02°15.924' N
E	Bukit Kuang	103°25.826' E	03°16.260' N

Figure 1. Location of the 5 atmospheric constituents monitoring stations (shown by letters A, B, C, D and E).and their corresponding geographical locations. Fire emission constituents (ppm level) data were provided by Alam Sekitar Malaysia Berhad (ASMA).
(Source: Ahmad and Hashim, 1999).

2.1 METHOD

All the procedures followed to map and obtain the amount of fire emission constituents were performed using the ERDAS Imagine (Digital image processing software) and SPSS softwares.

(i) Data calibration

Raw digital numbers (DN) of channels 1 and 2 of AVHRR data were first converted into percent albedo values. Such conversion is important because the resulting reflectance compensating for the in-orbit degradation of DN as a result of weather changes before and after the launch of AVHRR sensor into the space. The conversion of DN to radiance governs the following relationship.

$$Ai/ii = Si/iiC + Ii/ii \quad (1)$$

where, $A_{i/ii}$ is the percent albedo measured by AVHRR channels (channels 1 and 2 in this study), C is the input data value in counts (DN) and Si/ii and Ii/ii are respectively the slope and intercept values for bands 1 and 2. These calibration coefficients were obtained from Rao and Chen, 1998. These values are updated at NOAA/NESDIS in the 1B data stream at approximately one- month intervals.

Table 1. The Si and Ii values for AVHRR channels 1 and 2

Satellite	Si	Ii	S_2	I_2
NOAA- 14	0.1318	-5.4050	0.1657	-6.7938

(Source: Rao and Chen, 1998)

(ii) Geometric correction

Image to image registration technique was carried out to register all the 3 calibrated images (dated 17, 28 and 29 September, 1997) to a master image. The master image is a digital map of the corresponding area captured originally by digitizing a topo map and then rasterized to 1 km grid size to match the NOAA AVHRR LAC data.

(iii) Atmospheric correction

The atmospheric correction for this study was performed using radiative transfer model with ground truth parameters like temperature, relative humidity, atmospheric pressure, visibility and height from sea level and zenith angle (satellite parameter) determined from historic data (Table 2). An assumption of a Lambertian surface was made because it considers a perfect diffusion and therefore facilitate the calculation. Reflectance values (after compensating for scattering and absorption of atmosphere) were obtained after performing the sequence of the following calculations;

(i) estimation of *total optical thickness*, (ii) estimation of *atmospheric transmittance*, (iii) estimation of *total irradiance* at the surface of the earth, (iv) estimation of the *path radiance*, (v) estimation of the *radiance sensed by the sensor* and, (vi) estimation of the *reflectance*.

$$R_{\text{channeli}} \frac{L_S - L_P}{\frac{1}{\pi} T_\theta E_g} \qquad (2)$$

where,

R channel = reflectance after compensating for atmospheric attenuation, L_s = radiance sensed by the sensor, L_p= path radiance, T_θ= atmospheric transmittance at θ zenith, E_g= global irradiance reaching the surface of the earth.

Table 2. Ground-truth parameters used in radiative trasfer model to estimate the reflectance values of AVHRR data.

Parameters	Averaged value
Satellite zenith angle (°)	36.52
Temperature (° C)	27.28
Relative humidity (%)	83.40
Atmosphere pressure (mbar)	1011.86
Visibility (km)	3.74
Altitude from sea level (m)	14.16

(Source: Asmala Ahmad and Mazlan Hasim, 1999)

(iv) Cloud masking

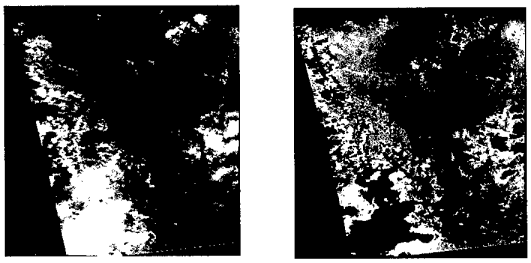
It is necessary to identify and separate the cloud pixels from non- cloud pixels for the retrieval of smoke plume originated from forest fire. This is because of the enormous errors arising from cloud contamination when deriving atmospheric pollutants present in the smoke plume. In this study a simple technique (Q technique) which was proposed by Saunders and Kriebal (1988) was used.This technique is based on the ratio between the reflectance in the NIR and visible bands of AVHRR data.

$$Q = NIR / Visible \quad (3)$$

Q values over cloud pixels are close to unity due to quite similar Mie scattering effects of the reflectance for both channels (Franca and Cracknell, 1995).

(v) Extraction of haze constituents

The measurement of space-borne remote sensing of gases and aerosol particles in this study is based on an assumed relationship between the ground measured aerosols and the spectral path radiance. Path radiance is detected by AVHRR sensor above a non-reflective surface and is the result of backscattering to space by particles and molecules in the atmosphere (Kaufman 1993). The amount of each of the 5 atmospheric constituents acquired at the 5 monitoring stations (dependent variables) and the calibrated reflectance from satellite data (independent variables) at the corresponding locations were used to establish empirical relationships between the aerosol and the scattered spectral path radiance. A multiple regression analysis (using both channels 1 and 2 of AVHRR) was carried out to predict some of the common but not validated assumptions about the spatial distribution and estimation of the amount of the particles over Peninsular Malaysia. The best model based on the best regression coefficients (r^2) for each of the constituents was selected to be applied to every pixel of images dated 17, 28 and 29 of September 1997. The regression line/model expresses the best prediction of the dependent variable (haze constituents) at other locations all over Peninsular Malaysia.



(a) (b)

Figure 3. Cloud masking using Q technique, (a) image of Peninsular Malaysia before cloud masking and (b) after cloud masking.

3. RESULTS AND DISCUSSION

Table 3 shows the best model derived from multi regression analysis for each of the atmospheric pollutants. All the five pollutants reveal a good relationship where the r^2 is exceeding 0.7. However, SO_2 exhibits the strongest relationship between satellite reflectance and sulphur readings and this is followed by NO_2, O_3, CM and PM 10. These models were then applied on calibrated images to map the spread and the amount of these pollutants over Peninsular Malaysia.

The ppm values for CM, SO_2, NO_2 and O_3 and ug/cu.m value for PM10 observed over Peninsular Malaysia versus the regressed computed values using both bands 1 and 2 is shown in figure 4. Meanwhile, figure 5 shows the spread of the pollutants over Peninsular Malaysia. All the pollutants except for PM10 not been seen at unhealthy levels. When the measured level of

each of the four pollutants were converted to a scale index (Air Pollution Index), they respectively reveal a value of less than 50 which is a good Malaysian air quality index. However, for PM10 156.84 ug/cu.m (exceeds API value of 100) indicates this pollutant is an indicator of an unhealthy condition. PM 10 was identified as the main pollutant driving the atmospheric pollution during the fire in 1997 in Malaysia and is the concern of many people because it is respirable and can cause diseases like asthma attacks, chronic bronchitis, decreased lung function and etc.

4. SUMMARY

Remote sensing data can be used for mapping air pollutants over large areas with minimum cost and time. The regression analysis using air pollutant readings obtained from observations stations and satellite reflectance shows good correlation for all the pollutants. Of all the five pollutants, PM10 was identified as the most hazardous pollutant present over Malaysian atmosphere during the 1997 forest fire scenario in South East Asia. The high level of this pollutant could also be contributed by construction activities and unpaved roads. The ongoing study using more sample points is anticipated to further improve the results of the study.

REFERENCES

1. Asmala Ahmad and Mazlan Hashim, 1997, Determination of Haze from remotely sensed data: some preliminary results, Proceedings of 18th Asian Conference on Remote Sensing 1997 in Kuala Lumpur, 20-24 October 1997, R-11-1- R-11-6, Asia Associate in Remote Sensing.

2. Cahoon Jr., D.R., Stocks, B.J., Levine, J.S., Cofer III, W.R., dan Pierson, J.M., 1994, "Satellite Analysis of the Severe 1987 Forest Fires in northern China and Southeastern Siberia." *Journal of Geophysical Research.* 99(D9) ; 18,627 - 18, 638.

3. Franca, G.B., and Cracknell, A.P., 1995, A simple cloud masking approach using NOAA AVHRR daytime data for tropical areas, IJRS, Vol.16, No.6, 1697-1705.

4. Kaufman, Y.J., Tucker C.J.,dan Fung, I., 1990, "Remote Sensing of Biomass Burning in the Tropics." *Journal of Geosphysical Research.* 95 (D7) ; 9927-9939.

5. Kaufman, Y.J, 1993, Aerosol Optical thickness and atmospheric path radiance, Journal of Geophysical Research, 98, 2677-2692.

6. Lillesand, T M., and Kiefer R W., 1994, Remote Sensing and Image Interpretation, John Wiley & Sons, Inc.

7. Rao, N.C.R and Chen, J., 1998, Calibration updates for the visible and near infrared channels of the Advanced Very High Resolution Radiometer on the NOAA- 14 spacecraft, http://140.90.207.25:8080/EBB/ml/niccal2.html
(date of access: 08 December 1999).

8. UNEP (1999). Levine, J.S., Bobbe, T., Ray, N., Singh, A. and R.G. Witt., Wildland Fires and the Environment: a Global Synthesis. UNEP/DEIAEW/TR.99-1.

9. Vadivale, M., 1997, http://www.geocities.com/HotSprings/2188/hazemma.html
(date of access: 09 March 2000).

Table 3. Best model derived from multi regression analysis for each of the atmospheric pollutants.

Atmospheric pollutants	*Best regression coefficients (r^2)*	*Model*
Nitrogen dioxide (NO_2)	0.879	y = -1.614 x 10-2(DN1) + 1.511 x 10-2(DN2) + 4.148 x 10-3) + 0.005
Carbon monoxide (CO_3)	0.806	y = -0.534(DN1) + 1.604(DN2) + 0.112)
Sulphur dioxide (SO_2)	0.991	y = 0.005352(DN1) - 0.006247(DN2) + 0.007604
Ozone (O_3)	0.864	y = -0.005738(DN1) - 0.0005142(DN2) + 0.05224
PM 10	0.778	y = 146.903(DN1) - 99.071(DN2) + 88.984

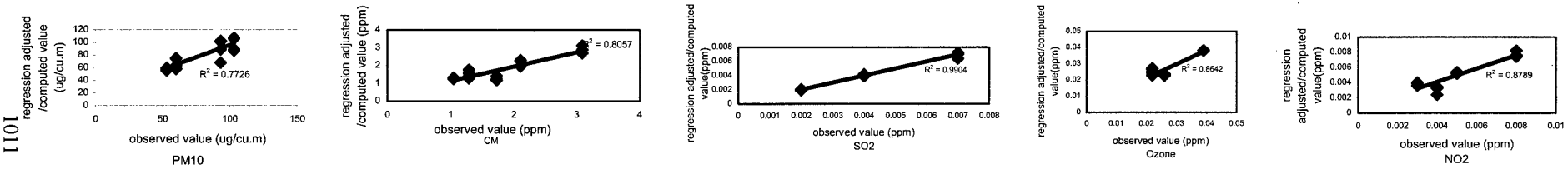


Figure 4. The relationship between observed value and regression adjusted computed values (channels 1 and 2) for the five pollutants originated from forest fire emission.

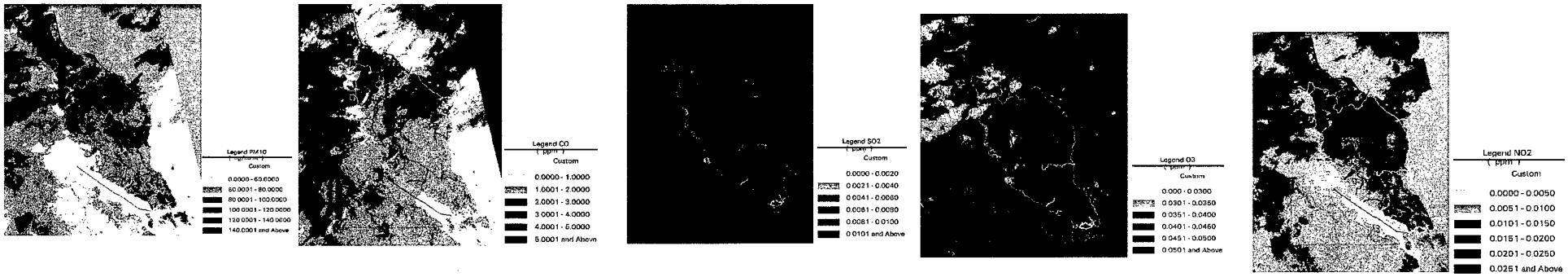


Figure 5. The spread and amount of PM 10 CM, SO_2,O_3 and NO_2 over Peninsular Malaysia during September, 1997.

LAND COVER CHANGE AND LONG-TERM FLUCTUATION OF EVAPOTRANSPIRATION IN OKUTAMA

Susumu Ogawa* and Nobuaki Naito**
Faculty of Geo-Environment Science, Rissho University
1700 Magechi, Kumagaya, Saitama, 360-0194 Japan
Phone: +81-48-539-1652 Facsimile: +81-48-539-1632
E-mail: *ogawa@ris.ac.jp; **981w00037@ris.ac.jp

KEY WORDS: water balance, remote sensing, Landsat TM, forest, paddy fields

ABSTRACT: Land cover change and fluctuation of evapotranspiration were examined in Okutama using Landsat TM data. Most land cover was composed of forest in Okutama. Forests had changed the constitution of evergreen and deciduous trees, while agricultural fields had decreased for the examined period. The long-term water budget from 1959 to 1997 in this basin showed that annual mean evapotranspiration increased and runoff ratio decreased. The short-term water budget showed that the monthly mean evapotranspiration fluctuation in May, July and October changed for that period. Such change may be caused by the decrease of the paddy fields and the change of its forest constitution.

1. INTRODUCTION

In Okutama good conditioned forest for drinking water has been kept for stable river flow and Ogouchi Reservoir. However, relationship between land cover change and water budget is still unknown. Therefore, in this paper runoff fluctuation with land cover change in Okutama was examined by two-date satellite data for land cover change and water budget for 39 years. Moreover, the forest state of drinking water was confirmed to make the future plan for forest management (Aoyama, Nishikawa & Murai, 1990; Kazama, Tada & Sawamoto, 1996; Sado & Wei, 1996; Sado, 1996).

2. MATERIALS AND METHOD

2.1 Data Used and Observation Stations

Objective area is located over upper stream catchment above the Okutama Lake: Ogouchi Reservoir. Two date satellite data were used for land cover classification and each area calculation. Watershed separation was carried out with digital elevation models '25,000' and '50m-mesh' by the Geological Survey Institute, Japan. Water budget was obtained from hydrological data from 1959 to 1997 in Okutama. Dam-inlet observation station is located at the Ogouchi Dam, while rainfall observation stations are located at Tabayama, Kosuge, Ochiai, and

Okutama (Fig. 1; Waterworks Bureau, Tokyo Metropolitan Government, 1959-1997). For calculation of evapotranspiration meteorological data at Tokyo and Chichibu Local Meteorological Observatories were used (Meteorological Agency, 1968-1997). The objective watershed was determined semi-automatically with GIS software from digital elevation models '50m-mesh' by the Geological Survey Institute.

2.2 Water Balance

From annual rainfall and dam-inlet flow rate in long-term observation at the Ogouchi Reservoir, annual evapotranspiration was obtained by the next equation.

$$\frac{dS}{dt} = P - Q - E \tag{1}$$

where S is the watershed storage, t time, P precipitation, Q flow rate, and E evapotranspiration. For long-term observation, the left hand of Equation (1) should be ignored. Therefore, annual evapotranspiration becomes the difference between annual precipitation and flow rate. In this area groundwater is not used and watershed area is small. Thus, short-term water budget method (Suzuki, 1985) was also applied for monthly evapotranspiration by the calculation of difference between precipitation and flow rate each rain.

2.3 Penman's Method

Daily evapotranspiration each land cover is calculated from meteorological data with the Penman's method.

$$E = \frac{\Delta}{\Delta+\gamma} Q_n + \frac{\gamma}{\Delta+\gamma} f(u)(e_a^* - e_a) \tag{2}$$

$$Q_n = \frac{R_n}{L_l} \tag{3}$$

$$R_n = R_s(1-\alpha_s) + \varepsilon_s R_{ld} - R_{lu} \tag{4}$$

$$R_{ld} = \varepsilon_a \sigma T_a^4 \tag{5}$$

$$\varepsilon_a = 1.24\left(\frac{\varepsilon_a}{T_a}\right)^{1/7} \tag{6}$$

$$R_{lu} = \varepsilon_s \sigma T_s^4 \tag{7}$$

where $\Delta = (de^*/dT)_T$, $\gamma \equiv c_p P/\varepsilon l$, Q_n the available energy flux in mm/day, $f(u)$ the wind function in mm/day · hPa, u the mean wind speed in m/s, e_a* the saturation water vapor pressure in hPa, e_a the vapor pressure in hPa, R_n the net radiation in W/m^2, L_l the latent heat of vaporization (=2.454×10^{6}J/kg), R_s the global short-wave radiation in W/m^2, α_s the albedo of the surface, R_{ld} the downward long-wave or atmospheric radiation in W/m^2, R_{lu} the upward long-wave radiation in W/m^2, ε_s the emissivity of the surface(= 0.97), ε_a the atmospheric emissivity, σ the Stefan-Boltzmann constant (=5.67×10^{-8}Wm^{-2}K^{-4}), T_a the air temperature in K, T_s the surface temperature in K.

Here, daily evapotranspiration for forest only was calculated. The albedo was cited from the empirical values (Kotoda, 1986).

2.4 Land Cover Classification

Land cover was classified into seven categories, urban area, paddy fields, vegetable fields, evergreen forest, deciduous forest, grass, and water body from two-date Landsat TM with supervised classification. From these results area ratios each land cover were obtained. The ground truth was carried out in 1999 and 2000.

3. RESULTS AND DISCUSSION

3.1 Land Cover Change

Land cover classification in 1984 and 1995 was carried out. Table 2 shows the area ratios each land cover. The forest area in 1984 was 92.8 % of the total watershed, while that in 1997 increased to 97.2 % by 4.4 %. The agricultural area decreased from 2.9 % to 1.5 % during the same period. These results coincide with *'Agricultural Field Area Statistics'* in trend as shown in Figure 2.

3.2 Long-term Water Budget

Figure 3 and Table 3 show the results of water budget from 1959 to 1997. Annual evapotranspiration and runoff ratio were calculated from annual precipitation and dam-inlet flow rate during the same period. The annual precipitation has constant trend, while the annual evapotranspiration increased 490 mm on average during 1959 and 1967 to 524 mm during 1988 and 1997. However, runoff ratio decreased for the same period as shown in Figure 4. These results seem to relate the increase of forest and the decrease of agricultural fields in area.

3.3 Estimated Evapotranspiration

Evapotranspiration was estimated by three ways, water budget, pan observation, and the Penman's method. Table 4 shows these results on average by three periods: 1968-1977, 1978-1987, and 1988-1997. Through all three methods, annual evapotranspiration has increase trend. However, the ratio of its increase equals between the pan observation and Penman's method, which are controlled by meteorological factors, while that of water budget is smaller than these two. That is, the results of water budget may be controlled by land cover change, which seems to be tree species change or the increase of forest and the decrease of agricultural fields.

3.4 Short-Term Water Budget

Figure 5 shows the results of short-term water budget. Monthly evapotranspiration fluctuated each period, 1959-1967, 1968-1977, 1978-1987, and 1988-1997. The results show that the monthly evapotranspiration decreased in trend in May and October, and increased in July. These months coincide with the periods of seeding, mid-term drying, and final drying in paddy fields (Makino, Ogawa & Saito, 1999). Therefore, the fluctuation of the monthly evapotranspiration may be the results of agricultural water use change with the policy of paddy field reduction.

4. CONCLUSION

From hydrological and satellite data, annual water budget and evapotranspiration in the upper Tama River were analyzed to conclude the next items.

(1) From satellite data in 1984 and 1997, forest area increased from 92.8 % to 97.2 %, while agricultural fields decreased from 2.9 to 1.5 %.

(2) As a result of long-term water budget from 1959 to 1997, annual precipitation was constant, annual evapotranspiration increased moderately, but runoff ratio decreased in trend. It seems to be caused by forest constitution change or the increase of forest area and the decrease of paddy fields.

(3) As a result of short-term water budget, monthly evapotranspiration changed with corresponding to seeding, mid-term drying, and final drying in paddy fields. Therefore, the fluctuation of the monthly evapotranspiration may be the results of agricultural water use change with the policy of paddy field reduction.

ACKNOWLEDGEMENT: The authors thank Waterworks Bureau in Tokyo Metropolitan Government for their hydrological data. We also greatly appreciate to Dr. Genya Saito, Mr. Naoki Ishituka, and Dr. Takuhiko Murakami at National Institute of Agro-Environmental Sciences, and Ms. Ikuyo Makino at Tokyo Institute of Technology for their cooperation.

REFERENCES

Aoyama, T., H. Nishikawa, and H. Murai, *Journal of Remote Sensing Society of Japan*, 20, 2, 539-551, 1990.

Kazama, S., T. Tada, and M. Sawamoto, *Annual Journal of Hydraulic Engineering,* 40, 323-328, 1996.

Sado, K. and R.Wei, *Annual Journal of Hydraulic Engineering,* 40, 323-328, 1996.

Sado, K., *Journal of Japan Society of Hydrology & Water Resources,* 9, 2, 188-197, 1996.

Waterworks Bureau, Tokyo Metropolitan Government, *Annual Report of Ogouchi Reservoir Management,* 1959-1997.

Meteorological Agency, *Meteorological Monthly,* 1968-1997.

Suzuki, M., *Journal of Japan Society of Forest,* 67, 4, 115-125, 1985.

Kotoda, K., Estimation of River Basin Evapotranspiration, *Environmental Research Center,* The University of Tsukuba, 1986.

Statistics and Information Department, Economic Affairs Bureau, Ministry of Agriculture and Forestry, *Agricultural Field Area Statistics,* 1973-1999.

Makino, I., S. Ogawa, and G. Saito, *Annual Journal of Hydraulic Engineering,* 44, 283-288, 1999.

Table 1 Satellite data used

Satellite	Date
LandsatTM	1984/10/26; 1997/10/30

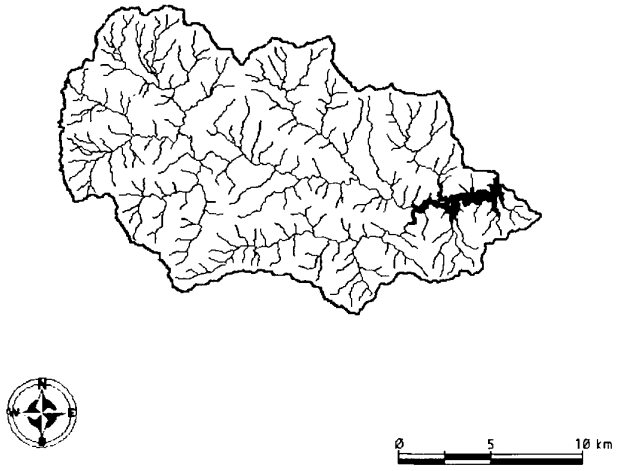


Figure 1 Okutama and its observation stations

Table 2 Land cover area rate in Okutama using LandsatTM (Unit:%)

Year	Forest	Urban Area	Grass	Paddy Field	Vegetable Field	Water
1984	92.8	0.4	2.6	2.1	0.8	1.3
1997	97.2	1.0	0	1.0	0.5	1.3

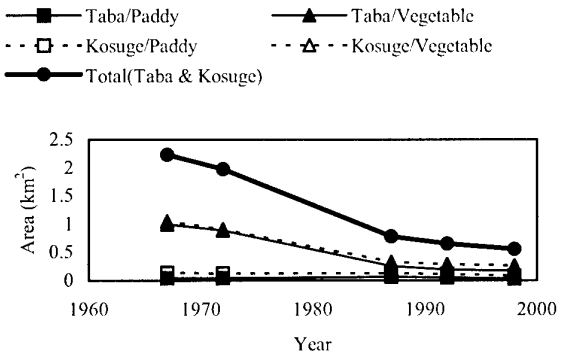


Figure 2 Agricultural area ratio in Okutama

Table 3 Annual mean hydrological observation results

Period	Precipitation	Discharge	Evapotranspiration	Runoff ratio
1958-1967	1550mm	1060mm	490mm	0.68
1968-1977	1582	1067	515	0.67
1978-1987	1551	1013	538	0.64
1988-1997	1658	1135	524	0.67

Table 4 Annual mean evapotranspiration with water balance, pan evaporation, and Penman's method

Period	Water Balance	Pan Evaporation	Penman's method
1968-1977	515mm	760mm	655mm
1978-1987	538	768	662
1988-1997	524	792	683

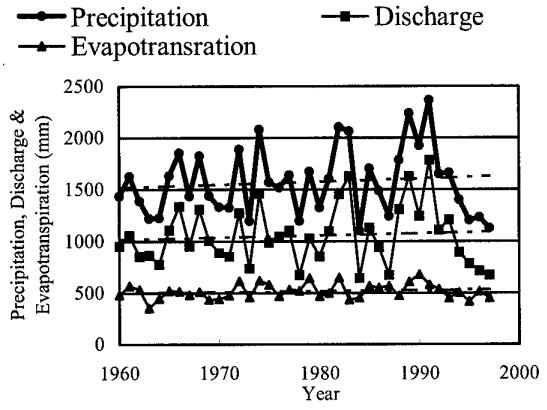


Figure 3 Water balance in Okutama

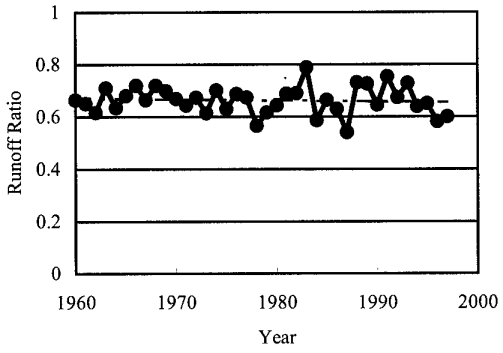


Figure 4 Runoff ratio in Okutama

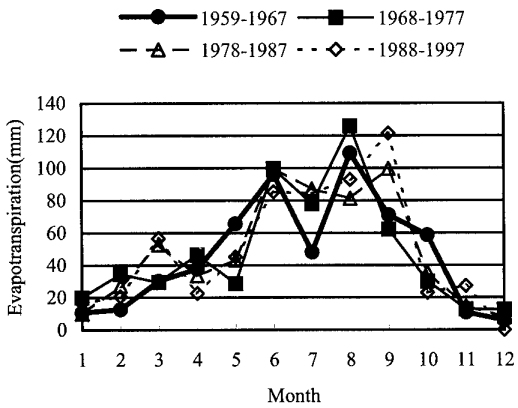


Figure 5 Monthly evapotranspiration in Okutama

MULTISOURCE DATA FUSION- FUSING OPTICAL AND SAR DATA FOR IRRIGATED RICE AREAS IDENTIFICATION

Jirathana WORAWATTANAMATEEKUL
Canisius X.J.F.
Lal SAMARAKOON
Asian Center for Research on Remote Sensing
Asian Institute of Technology
P.O.Box 4 Klong Luang, Pathumthani 12120
Tel: (66)-2-524-6148 Fax: (66)-2-524-6147
E-mail: jirathan@ait.ac.th
THAILAND

KEY WORDS: Data Fusion, Principal Component Analysis,Thematic Combination

ABSTRACT: Food security has become a global key issue, and this is a major concern particularly to Asian region due to rapid expansion of Asian population. In many countries of the region, accurate evaluation of food production and estimation is not possible due to lack of information. Further, insufficient or obsolete information hampers timely solutions when there is a decrease in production, and introducing appropriate solutions for increase productivity. One of the basic information that is not available in most of the countries in Asian region is the cultivated area that could keep the planers well informed of the future harvest, and prepared for food crisis in advance. This paper examined the potential of satellite remote sensing in estimating irrigated paddy cultivated areas in a test site in Indonesia. Due to frequent cloud cover in this area solely rely on optical sensor data is a limiting factor of using satellite data for mapping. Attempt was made to integrate SAR data acquired during growing period with optical data to overcome this limitation. Data from JERS-1, optical and SAR data was used for the study. Applying various fusion methods, it was found that combination of vegetation index, average intensities of SAR, and principal component of optical data gives the optimal solution for the test area. Results proved data fusion from different sources acquired in various stages irrespective to their source could satisfactorily be used in estimating irrigated paddy area under cultivation.

1. INTRODUCTION

Data fusion means a very wide domain and it is rather difficult to provide a precise definition. Several definitions of data fusion have been proposed. Pohl and Van Genderen (Wald, 1999) defined " image fusion is the combination of two or more different images to form a new image by using a certain algorithm" which is restricted to image. Hall and Llinas (Wald, 1999) defined "data fusion techniques combine data from multiple sensors, and related information from associated databases, to achieve improved accuracy and more specific inferences that could be achieved by the use of single sensor alone". This definition focused on information quality and fusion methods. According to these definitions, it could imply that purposes of data fusion should be the information obtained that hopefully should at least improve image visualization and interpretation.

There are several fusion approaches, generally, fusion can be divided into three main categories based on the stage at which the fusion is performed namely: pixel based, feature based and decision based. In pixel based fusion, the data are merged on a pixel-by-pixel basis. Feature based approach always merge the different data sources at the intermediate level. Each image from different sources is segmented and the segmented images are fused together. Decision based fusion, the outputs of each of the single source interpretation are combined to create a new interpretation.

Although there are many data sources for the purpose of fusion, this study was mainly dedicated to only remote sensing data fusion and their visualization with the following possibilities; multitemporal and multisensor data fusion. Several remote sensing data have been acquired and some possible fusion techniques were applied to these data to generate image fusion results. Results of fused data were demonstrated and interpreted in terms of its usefulness in irrigated rice field identification.

2. TEST AREA AND DATA USED

Semarang is the selected test area and located in Central part of Java Island, Indonesia. This area is predominated by paddy rice. Both optical and SAR data were used in this study. Figure 1 shows false color composite of JERS-OPS data of test area, table 1 present satellite data descriptions used in the study.

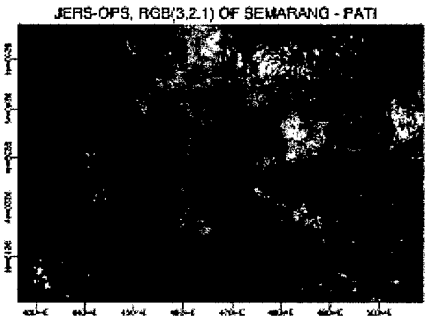


Figure 1: False Color Com posite Image of the Test Area

Table 1: Descriptions of Remote Sensing Data Used

Satellite	Sensor	Date
JERS-OPS	Visible-NIR	24/8/96
JERS	SAR	29/09/96
JERS	SAR	12/11/96
JERS	SAR	24/03/97

3. METHODOLOGY

All remotely sensed data both optical and SAR data required systematic corrections. The data distributor normally provides this step. Speckle reduction by applying speckle specific filter is the next process applied to SAR data to reduce the data noise while retaining the information. Subsequently, 16 bit SAR data were converted to 8 bit data to be able to compare with 8 bit

optical data. In the optical side, the data were necessary to go through atmospheric correction step. Then, both optical and radar data were coregistered in order to be fused together. Finally, the visualization step presents results of fusing data. Figure 2 shows general steps in fusion process.

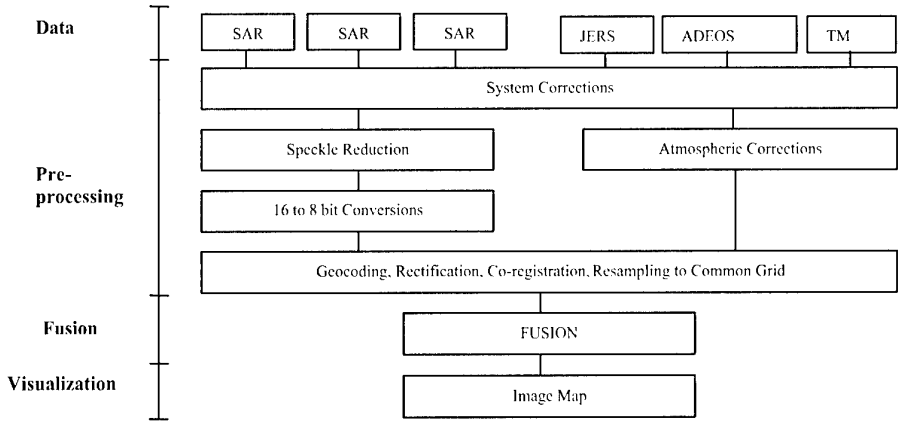


Figure 2: Data Fusion Process

Figure 2 shows general steps in data fusion process. However, it is necessary keeping in mind that the previous steps in the flow are crucial for the succeeding steps and therefore to the overall accuracy of the image map. Selection of data for fusion is very important as fusing inappropriate data could deteriorate information content.

All optical and SAR data were pre-processed and coregistered into the same coordinate system. At the fusion step, we applied several fusion techniques and compared the fused results. Those techniques are overlay, principal component analysis (PCA) and thematic combinations.

3.1 Overlay

Overlay of multi temporal data and display in different color channel of RGB. This technique is suitable to apply to single frequency or single polarization data like SAR. Not only this technique renders some colors to the interpreter but it also present changes during the acquisition period of the multidate data.

3.2 Principal Component Analysis

The purpose of applying principal component analysis (PCA) is to reduce the dimensionality of input data into a smaller number of output channels. It is more suitable to multi spectral data where each spectral band is always highly correlated. In PCA, the most information of input will be transformed into the first component and the information content decreases with increasing of the number of PCA component. As indicated in Figure 3, there is a scatter diagram plot of the original gray level value in band A and band B. Superimposed on these original axis is the new axis (axis I and axis II) which defined the direction of the first and the second principal components. PCA is the relationship that transforms the original value from band A/band B coordinate system to the new axis (axis I/axis II) system (Lillesand et al., 3rd Edition) and it is the linear relationship (see figure 3).

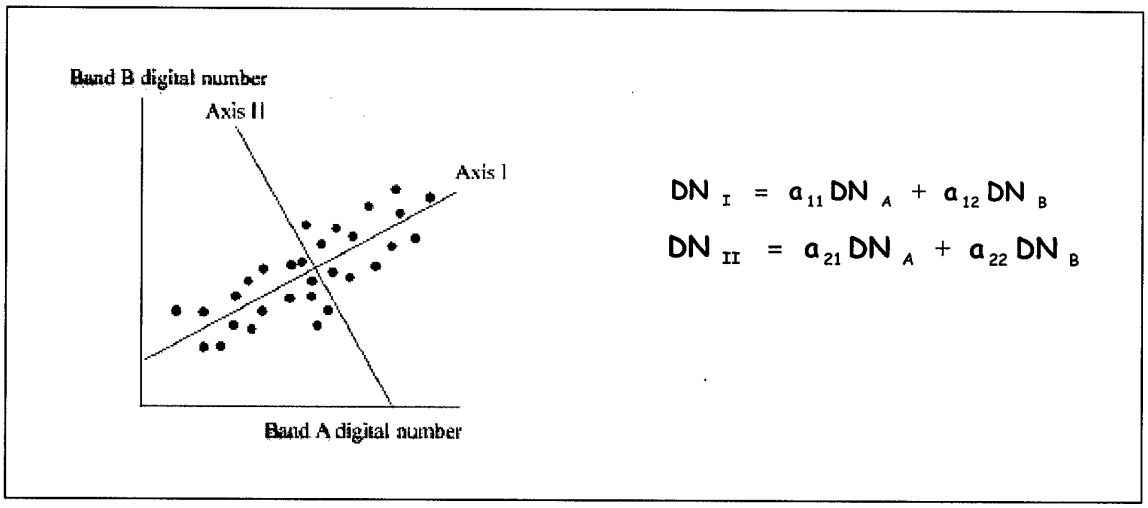


Figure 3: Graphical representation of Principal Component Analysis (PCA)

3.3 Thematic Combinations

The purpose of thematic combination is to combine the information rather than the base data. By this mean, the source data are not necessary converted to one common format (e.g. resampling to one resolution) before deriving information and therefore less information are lost. In this study, information was derived from optical and SAR data sources separately and each technique was evaluated using the correlation coefficient. NDVI image, PCA of JERS-OPS and average of multitemporal SAR data were investigated for the purpose of irrigated rice area identification.

4. RESULTS

Results from applying the above fusion techniques are demonstrated and interpreted to show the derived information.

Overlay three SAR images not only render different colors related to different information but also provide changes information. In the RGB image (figure 4), gray, white and dark color represented no changes area (during Sep'96 to Mar'97) meaning that the bright white color in the image demonstrated a stable land use which has been no changes during such period. In this image, those are settlements (indicated by red circle). Another primary colors, Red, Green and Blue represented changes (changes of backscattered energy) area. Red color indicated the object that gave higher backscatter in September than in November and March. Green and Blue color are followed the same rule. Green indicated the area where the object provided higher backscatter in November while lower in September and March. Blue represented the area containing the object that gave high backscatter in March and low backscatter in September and November. Usage of cropping calendar in this area will help in more detailed interpretation.

Principal components derived from JERS-OPS multispectral data (3 bands) were demonstrated in figure 5. The first component (PC1) contained highest variance (indicated by more variation of gray levels) and therefore contained most information compared to the succeeding components PC2 and PC3. Thus PC1 were then used as one theme for thematic combinations instead of using 3 bands of optical data.

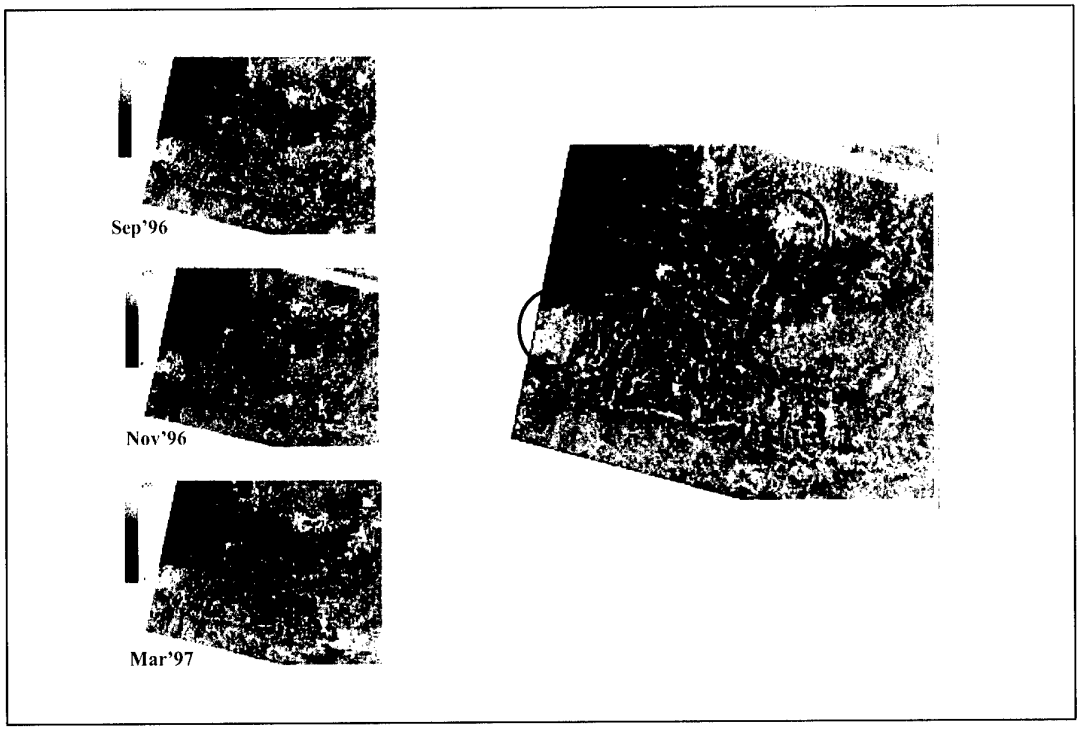


Figure 4: Show original multitemporal Images (Sep'96, Nov'96 and Mar'97) and their overlay result in RGB channel

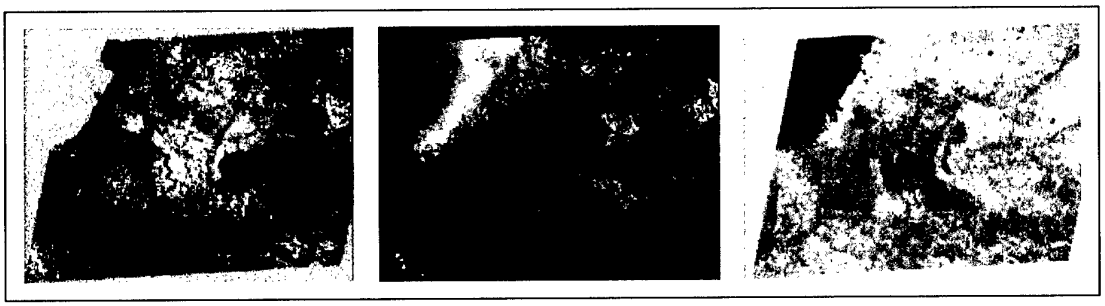


Figure 5: Principal Components of JERS-OPS data from left to right PC1, PC2 and PC3

Figure 6 shows the information derived from JERS-OPS and JERS-SAR namely, NDVI image, the first principal component and average of three date SAR images respectively. NDVI value will determine how much green vegetation presented in a particular area. In the NDVI image presented here the lowest area NDVI is indicated by blue color and the highest indicated by red color. Same as PC1 image the lowest value is ranged from blue to the highest in red color. Average SAR images is presented in gray scale image where dark meant lowbackscatter and bright meant high backscatter.

All the information (figure 6) derived from both OPS and SAR were then be the input bands for the classification process. Unsupervised method was applied 2 times and the result is shown in figure 7. This classified image result was checked and it had the correspondence with the field information.

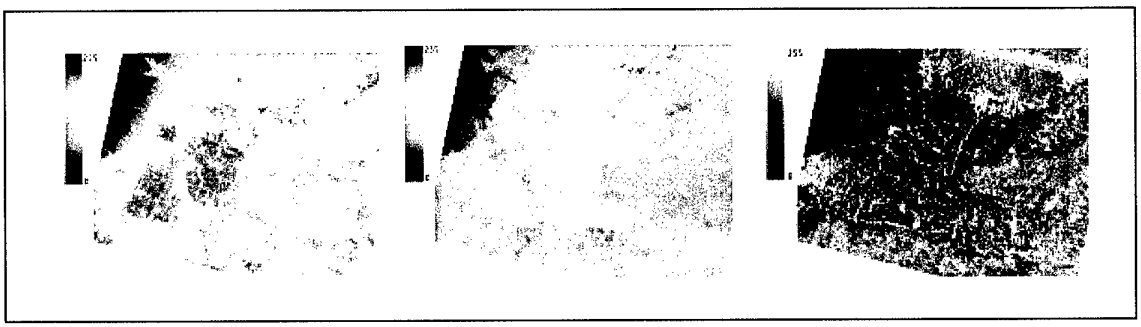


Figure 6: From left to right: NDVI image, PC1 image and average of 3 SAR images

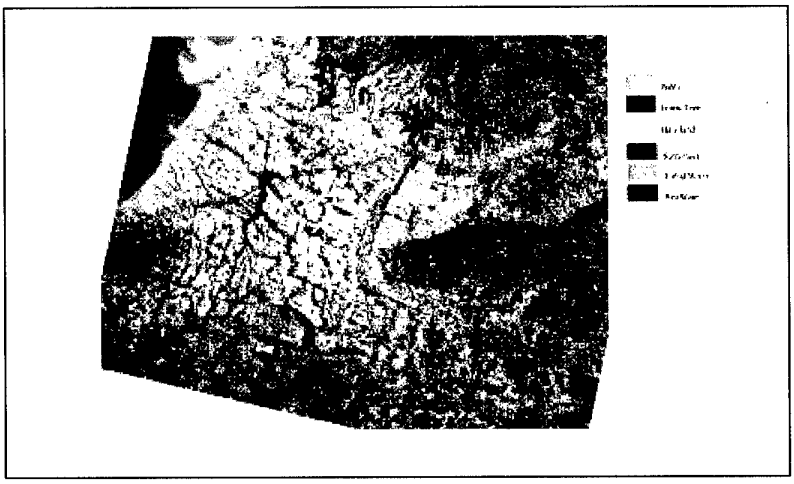


Figure 7: Unsupervised classification result

5. CONCLUSION

Combining of data from different sources using thematic combination seems to be the most appropriate technique because less information were lost. However, the information obtained from this study still requires more field information to verify the applicability of fusion technique presented here. Further, fusion among multi sensor and multi systems could require more parameters for instance satellite geometry, spectral band width etc. complexing the interpretation.

6. REFERENCES

Lillesand M.T., Kiefer W.R., Remote Sensing and Image Interpretation, 3rd Edition, P572, John Wiley & Sons, Inc, New York.

Soldberg, A. H., 1994, Multisource classification of Remotely Sensed Data: Fusion ofLandsat TM and SAR Images, IEEE Transactions on Geoscience and Remote Sensing Vol.32 No.4 July 1994 pp768-776.

Wald L., 1999, Some Terms of Reference in Data Fusion, IEEE Transactions on Geoscience and Remote Sensing Vol.37 No.3 May 1999 pp1190.

Study on Land Use Management with Geographic Information Systems

Wei-Hsin Ho
Professor, Department of Land Economics,
National Chengchi University,
64, Chih-nan Rd., Sec. 2, Wenshan, Taipei , Taiwan
E-mail:whh@nccu.edu.tw
and Ge-Wen Lee
Ph. D. Candidate Student, Department of Civil Engineering,
National Chiao Tung University,
Hsin-Chu, Taiwan
E-mail:bearlee@cc04.ccit.edu.tw

KEY WORDS: Land Use, Geographical Information Systems, Potential Areas of Slope Disease

ABSTRACT: Geographic Information Systems (GIS) have powerful tools to the analysis of spatial data and the management of land information. The article concentrates on how GISs can improve the land use management. The first step was to design a database based upon the requirements of land use management. Owing to the widely scope of land use management, the requirement analysis specifies on the delineation of development potential areas and development constraint areas for land use. Secondly, a fundamental toolbox was established under PC ARC/INFO and Visual Basic Ver. 6.0. Finally, a application system was constructed on the foundation of the fundamental toolbox. The Nantou County, a mountainous county in central Taiwan, which has abundant natural resources, was selected as the study area. In addition, a set of rules derived in this investigation was applied to predict the potential areas of slope disease. Results of the case study confirm the design of database and the application system. The experiences of the case study indicate the open system and the modulation design are useful to develop a flexible system. Metadata is important to describe the content and usage of database. Moreover, metadata can assist the interface design of the software.

1. INTRODUCTION

Geographic Information system (GISs) is a novel technology widely used to survey the land use problem. The GIS adopts the numerical methods and spatial analysis tools to delineate the land use. The methods can yield the same results after repeatedly applying the same procedures. Moreover, they reduce the manpower and time consumption for the delineation of land use. In

contrast with the manual methods, the GIS is the most economic and objective methods.

This article describes a pilot study to land use management with GIS. The investigation designed a delineation system of land use with a GIS software (PC ARC/INFO) and a high-level language (Visual Basic). Also constructed herein is a database to implement the delineation of land use. For the effective usage of the database, the metadata which described the attribute definition, code meaning, data quality and production information of maps was generated while the maps were input to the database. Finally, a case study about potential was conducted to evaluate these designs.

2. SYSTEM DESIGN

2.1 System Framework

The analysis system of land use consists of a module based software, databases and metadata. The fundamental analysis software was designed by PC ARC/INFO SML language. Some tools embedded by the graphic user interface were written by Visual Basic. These tools offer the functions of project management and data management. Visual Basic produces not only a friendly environment for the users, but also effective tools to integrate all the elements in the system. Figure 1 shows the relation between the elements.

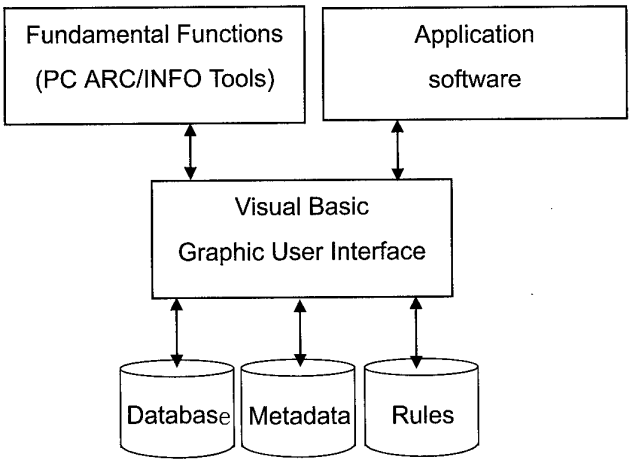


Figure 1 The Framework for the Delineation System of Land Use

2.2 System Operation

The system has two operation modes: project management mode and case study. The project management mode can generate a project directory and store the results in the directory. The case study mode provides a relatively easy means of testing the system tools case by case. Under the graphic user interface, the users can select the interest coverage and input the proper parameters.

3. DATABASE

3.1 Database Organization

The database has three sub-databases such as geographic and land use database, project database and test database. Herein, a tree structure was designed to manage these data. The graphic and geographic database including the land use data is the primary database for the system. This database consists of sixteen coverage items such as land use, geology, soil, water system, road system, boundary line, forest map, and national park map, coastal conservation map, slope map, relic place map, natural ecological protection map, water quality and water quantity conservation map. The project database stores the data generated from each individual project. The test database is a temp directory for the data generated from the system test. The following paragraphs describe data processing and the contents of the geographic and land use database.

3.2 Data Source and Gathering

Three types of data were used in the database: the coverage obtained from Construction and Planning Administration, digital topographic maps published by Interior of Ministry, and 40m by 40m Digital Elevation Model (DEM) supplied by Center for Space and Remote Sensing Research, National Central University.

The processes, transferring the source data to database, include generalization, aggregation, and reclassification. The generalization of coverage is to eliminate the unwanted attributes and graphic entities in the coverage. The aggregation of features in the coverage was to combine the data with the similar characteristics to the same category. The reclassification of features in the coverage set the new category for the selected data according to the specified conditions. While the data are input to the database after the above processes, the description data that are relevant to the data should be established sequentially.

3.3 Metadata

The metadata offered by the database greatly benefits the understanding of the data users. In addition to the database description, the metadata can support the functions of analysis tools, for example, attribute selection (Ho, 1997). The metadata not only enhance the understanding of the users, but also assist the item selected in the analysis system. Figure 2 presents an example of usr interface created from metadata. The elements of metadata include database description file, project description file, attribute list file, code table list, code table, map boundary file, project list file, coverage list file, coverage description file, the results list file, description file of the results and map symbol description file. .The detail description of metadata can be found in Ho (1998).

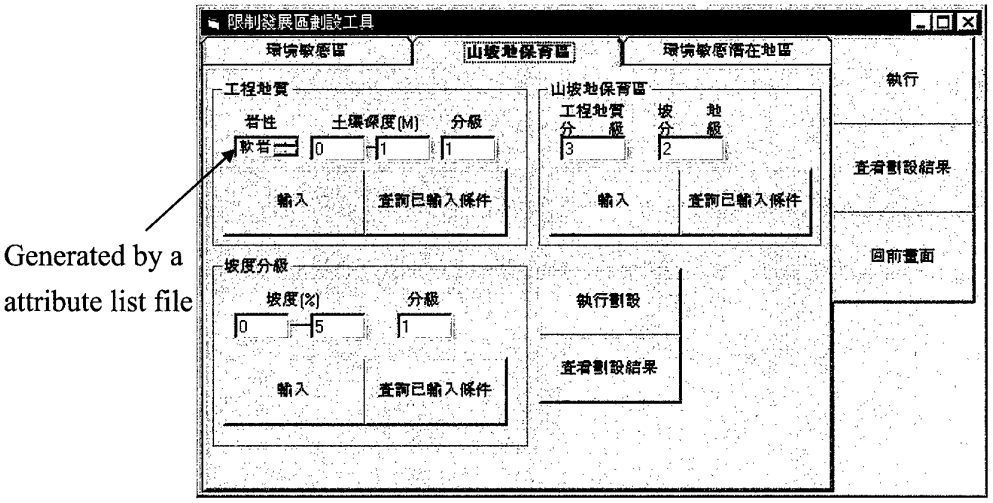


Figure 2 An example of user interface creating from metadata

4. CASE STUDY

4.1 Study Area

The study area for potential areas of slope disease is the Nantou County, a mountainous district in the central Taiwan. Owing to the weakened geologic formation at some areas in the county, the natural disease occurs annually. Notably, the pollution and environmental damage are slight because the primary land use is agriculture and forestry.

4.2 Rules of Delineation

Figure 3 displays the procedures and the rules to delineate the potential areas of slope disease. The rules derived from the construction laws, The White Book of Construction Planing Strategy, and reports of Construction and Planning Administration (1993) and Chen (1993). The construction laws referred Yiin(1997).

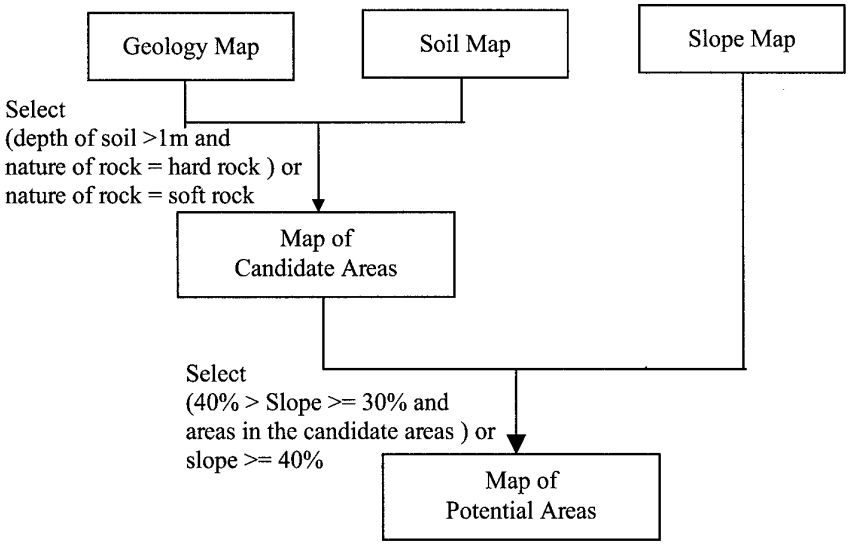


Figure 3 The procedures and rules for the case study

4.3 Results

Figure 4 represents the potential areas of slope disease in this case study. Some disease areas of 921 earthquake in 1999 just located nearby the predict areas in Figure 4. Although the rules conducted in this case study were not novel, the system had the capability to find out the similar areas on real disease areas. More rigorous investigation should achieve more exactly prediction.

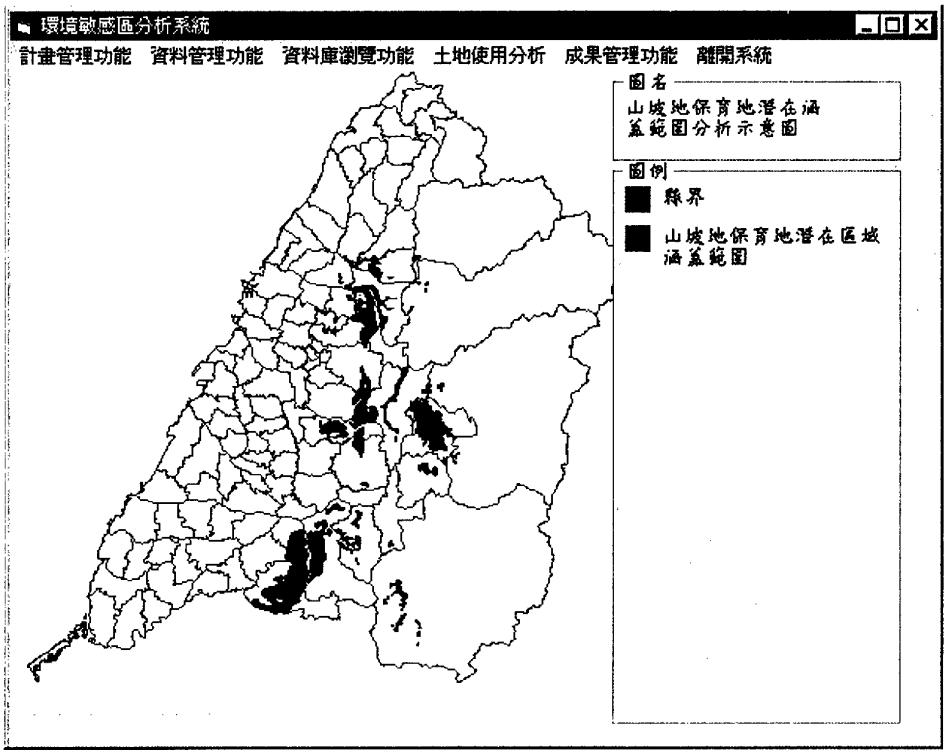


Figure 4 The potential areas of slope disease

5. CONCLUSION

The application system integrates four major components for identifying the suitable land use: (1) a geo-referenced database, (2) a fundamental toolbox for basic analysis of land use, (3) three subsystems for specific purpose and (4) a system for geographically displaying. Implementing such system provides the following advantages.

- The graphical interface allows the user to easily evaluate the type of land use.
- The system makes it easy to understand and prepare the required data for land use.
- The system's generic structure can be applied in different study areas and different evaluations.
- The system's modular structure is easily enhanced or modified with additional models.

Except for the above benefits of the delineate system, the case study presented herein provides an interesting result that the potential areas of slope disease is similar to the recently disease on the study area, for example 921 earthquake. This result indicates the opportunity that more advanced study about these rules can achieve more exactly areas of such disease. Moreover, the case study proves that GIS is a useful technology to land use management.

ACKNOWLEDGEMENT

The Authors would like to thank the National Science Council of the Republic of China for financially supporting this research under Contract No. NSC87-2621-P004-004.

REFERENCES

Chen, R. C. et. al 1993. Study on the Project of Conservation Area in The Science-based Industrial Park, Report of Hsinchu Science-based Industrial Park, Hsinchu, Taiwan, R.O.C. (by Chinese)

Construction and Planning Administration (CPA) 1997. An Overview of the Construction and Planning Administration, Construction and Planning Administration, Ministry of Interior, Republic of China, http:\\www.cpami.gov.tw\~unalis\introduce\e-index.html.

Construction and Planning Administration (CPA) 1993. Environmentally Sensitive Areas delineation and Land use Suitable Analysis in Taiwan (The North and The South Areas), technical report of Construction and Planning Administration, Ministry of Interior, R.O.C. (by Chinese)

Construction and Planning Administration (CPA) 1996. The White Book of Construction Planing Strategy, edited by Construction and Planning Administration, Ministry of Interior, Republic of China. (by Chinese)

Council of Agriculture (COA) 1997. Starting A New Era for Agriculture: Environment, edited by Council of Agriculture, Republic of China, 1997, http://www.coa.gov.tw/en/e5.htm.

Environmental System Research Institute (ESRI) 1991. Surface Modeling with TIN, ARC/INFO User's Guide 6.0" edited by Environmental System Research Institute, Inc.

Ho, Wei-Hsin 1997. Study on the Support System for the Land Use and Land Conservation (II), NSC Project Research Report, NSC86-2621-P004-004, Taipei, R.O.C. (by Chinese)

Ho, Wei-Hsin 1998. Study on the Support System for the Land Use and Land Conservation (III), NSC Project Research Report, NSC87-2621-P004-004, Taipei, R.O.C. (by Chinese)

The Coalition of Wetland Protection 1997. What is the wetland, edited by The Coalition of Wetland Protection, Republic of China, http://www.wetland.tw.com. (by Chinese)

Yiin, J. H. 1997. The Compilation and Analysis of the Construction Laws, published by Sun-Min, Inc, Taipei, R.O.C. (by Chinese)

The 21st Asian Conference on Remote Sensing
December 4-8, 2000 Taipei, TAIWAN

ASSESSMENT OF CROP PRODUCTIVITY FOR MAJOR RIVER BASINS IN ASIA USING GIS AND RS DATA

Shiro OCHI and Shunji MURAI
Institute of Industrial Science, Univ. of Tokyo
JAPAN
ochi@iis.u-tokyo.ac.jp, murai@rs.iis.u-tokyo.ac.jp

KEY WORDS: NPP, Crop production, NDVI, Remote Sensing, GIS

ABSTRACT: The land use / land cover has been dramatically changed in Asian countries in the last a few decades caused by the population pressure. Generally, the forested lands have been converted to agricultural lands, as well as the productivity has been improved because of irrigation, chemical fertilizer, mechanization and so on. The agricultural production has increased for many years in the region to support the population. However, there arises a doubt that there must exist a limit of sustaining the regional population based on agricultural production. In this study, the estimation of agricultural production reflecting the current land use / land cover in the major river basins in Asia, has been investigated.

The agricultural production is considered to be a part of Net Primary Production(NPP) on the agricultural land. The NPP can be estimated using Photosynthetically Active Radiation(PAR) and NDVI, that can be derived from Satellite data. The distribution of agricultural land can be seen in the land use/land cover map. The NPP on the agricultural land of major river basins in Asia was estimated with these dataset. Moreover, by integrating the result of the agricultural NPP with the statistics of country based crop production, the conversion efficiency of agricultural production from agricultural NPP was made. Finally, per capita productivity is analyzed in the region.

1. Introduction

By the UN announcement, world population reaches 6 billion in October 1999. According to the FAO statistics, the crop production has increased corresponding to the population increase in the last 40 years. However, optimistic forecasting of crop production can not be expected, because there are limit of suitable crop land, limitation of productivity and shortage of water resources. Monitoring, estimating and forecasting crop production are quite important for the management of world, regional or local food demand and supply balance. A method to monitor and estimate per capita productivity using remote sensing data and Geographic Information System(GIS) is applied in this study for the region of major river basins in Asia.

2. Processing flow and data used

Figure-1 shows the flow of data processing in this study. There are three kind of source data. Map data include (1) Digital Elevation Model(DEM), (2) River Network Map and (3) Administration Boundary. Statistical data include (4) Agricultural Production and (5) Population. Satellite Data include (6) Land Cover data, (7) Normalized Vegetation Difference Index(NDVI) and (8) Photosynthesis Active Radiation (PAR) Data.

Crop Land Suitability map is generated using DEM based on information of land altitude and slope gradient. Drainage model was generated using DEM(GTOPO30) and River Network Information. The drainage model can extract catchment area of major rivers in Asia such as Amur river, Yellow river, Yangzhu river, Mekong river, Ganges river and Indus river. And the drainage model has consistent flow direction in each pixel from top stream to the bottom of the river. By using the drainage model, each pixel can be identified where is the catchment of the pixel and where to flow to the down stream(Ochi and Shibasaki, 1999). Net Primary Productivity(NPP) is estimated using NDVI and PAR data(Monteith, 1977).

Crop production analysis is made using administrative boundary, statistics of agricultural production

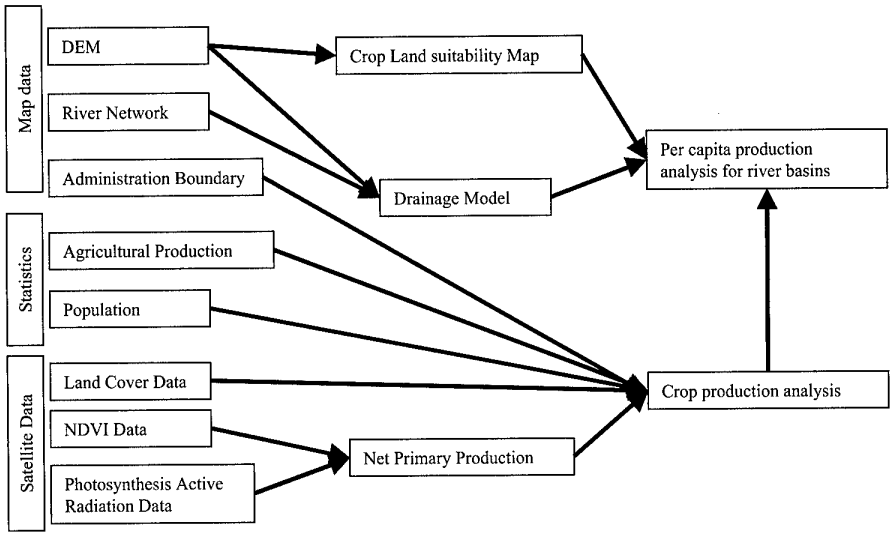


Figure-1 Flow of Data Processing

and population, land cover data and NPP. Finally, per capita crop production analysis is made using crop land suitability map, drainage model and the output of crop production analysis. The detail of the source data is described as follows:

(1) Digital Elevation Model(DEM): GTOPO30, which is 30 second arc resolution(approx. 1km resolution) produced by U.S. Geological Survey(USGS). The data can be downloaded from internet URL : http://edcdaac.usgs.gov/gtopo30/gtopo30.html.

(2) River Network and (3) Administrative boundary map: Rasterized River Network image is generated from Digital Chart of the World(DCW) using ARC/Info - "linegrid" - command. The DCW data can be downloaded from internet URL: http://www.nima.mil/publications/guides/dtf/dcw.html.

(4) Agricultural Production: Agricultural production data is retrieved from FAOSTAT Agricultural Data URL: http://apps.fao.org/. In this study, "cereal production" is used to represent agricultural production.

(5) Population data: CIESIN(Consortium for International Earth Science Information Network) provides 5 minutes population data which were interpolated from the population census in 1994. The CIESIN URL is http://www.ciesin.org/.

(6) Land Cover Data: Land cover data were retrieved from USGS Global Land Cover Characteristics Data Base retrieved at the URL: http://edcwww.cr.usgs.gov/landdaac/glcc/glcc_na.html. There are 6 maps in different schemes in the data base, and IGBP Legend map was used in this study.

(7) NDVI Data: Monthly NDVI data from January 1982 to December 1993 were composed using 8km resolution 10 days composite data set given as NOAA/NASA Pathfinder AVHRR Land Data Set.

(8) PAR Data: One degree monthly Photosynthesis Active Radiation(PAR) data from January 1979 to December 1989 were provided using TOMS satellite data(Dye et al, 1993). In this study, interpolated 8km resolution averaged monthly PAR data were used in order to calculate NPP of 1981 to1989.

3. Methodology and Output

3.1 Estimation of Net Primary Productivity

Monthly Net Primary Productivity(NPP) can be estimated using NDVI and PAR data by "production efficiency approach" proposed by Goward and Huemmrich(1992) and Ruimy, Saugier and Dedien(1994).

$$NPP = \varepsilon \int fAPARdt \qquad \cdots\cdots\cdots\cdots\cdots (1)$$

NPP : [gDM/m2/time], ε : efficiency[g/MJ], $fAPAR$: Function of Absorbed PAR [MJ/m2]

$$fAPAR = -0.08 + 1.075 \text{ x NDVI} \qquad \cdots\cdots\cdots\cdots (2)$$

ε is 1.5 for global average.

The annual total NPP can be estimated as follows:

$$NPP = 0.5 \int_{i=1}^{12} f_{APAR}(NDVI_i) \times PAR_i \qquad \cdots\cdots\cdots (3)$$

By using this formula, annual total of Net Primary Productivity(NPP) from 1981 to 1989 was generated. The output was verified using existing study concerning the global NPP and the regional NPP. Table-1 and Table-2 show the comparison of Global NPP versus our study and Regional NPP versus our study respectively(Ochi and Murai,1999). By comparing with other studies, the adopted method in our study for estimation of NPP is acceptable for the purpose of our study goal, though there have been no reference data.

Table –1 Verification of Global NPP

Model	GNPP(g ton DM/year)
Whittaker(1979)	115.6
Lieth(1977)	106.0-125.8
Box(1989)	122.9
Gotoh(1993)	110.2
Ochi/Murai(1999)	119.4

Table-2 Verification of Regional NPP

	NPP(g ton)
Africa	22.9
North/Central Americ	19.1
South America	30.3
Eurasia	38.6
Oceania	8.5
Total	119.4

3.2 Correlation between Global NPP and Cereal Production

Figure-2 shows the relationship between Global NPP derived by this study and world Cereal Production prepared by FAO. The correlation factor(R) of the two items is 0.91 in the period from 1982 to 1990. However, the correlation become worse when the data from 1991 to 1993 are involved. It is said that the NDVI data and PAR data include some noise due to the aerosol caused by Mt. Pinatubo Eruption of 1991 therefore the data after the eruption are not adequate for the use. It was found that the NPP can be used for the estimation of crop(or cereal) production.

3.3 Change of NPP in major river basins in Asia

By overlaying USGS/IGBP cover map with global NPP map, NPP from each land cover category can be extracted. Figure-3 shows that changes of NPP from 1982 to 1990 in major six river basins in Asia ; Amur,

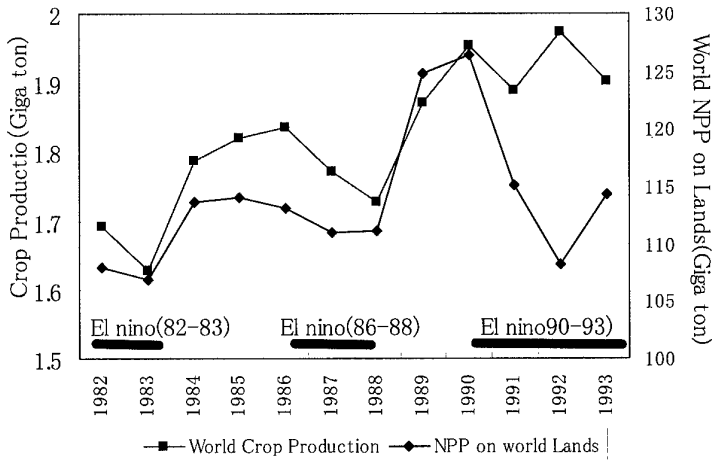


Figure-2 Correlation between NPP and World Crop(Cereal) Production

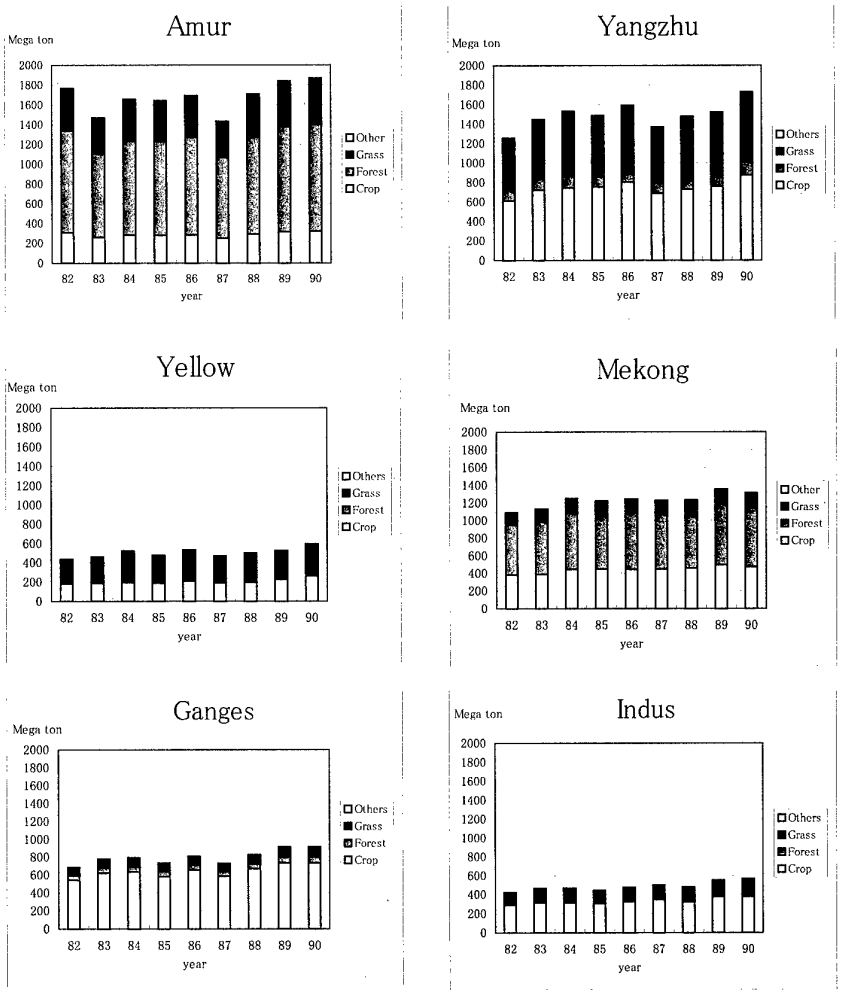


Figure-3 Changes of NPP in major river basins in Asia

Yellow, Yangzhu, Mekong, Ganges and Indus. NPP are mainly produced in the crop and grass land with high

population density in the Yangzhu, Yellow, Ganges and Indus river basins. On the contrary, NPP are produced in the forested area in Amur and Mekong river basins where population density is not so high. NPP of crop land are more stable than NPP of other land covers.

4. Analysis and simulation

4.1 Per capita productivity

Per capita productivity is defined for each pixel as follows. 1) Catchment area for a pixel along a river is defined using drainage model . 2)Accumulated population in the catchment area is calculated for the pixel. 3)Accumulated Cropland NPP(CNPP) in the catchment area is calculated for the pixel. 4)Per capita productivity is calculated by dividing the accumulated CNPP by the accumulated population for the pixel. 5)Per capita productivity is calculated for all pixels of the six major river basins in Asia.

Figure-5 and Table-3 show the per capita productivity – relation between accumulated CNPP and accumulated population - from the upper stream of the river basin to the bottom of the basin for these six river basins. The slope of the regression line means per capta productivity. Per capita production is an indicator to evaluate the potential or population carrying capacity, because the indicator can show how much cropland NPP is produced/consumed for one person in the basin. So, if the per capita productivity is big, it means that the basin is more rich than the basin with small per capita productivity.

$$\text{CNPP} = a \times \text{Population} \quad \cdots\cdots\cdots\cdots (4)$$

where a: per capita CNPP

Figure-4 Relation between CNPP and Population in 6 Major River Basins in Asia

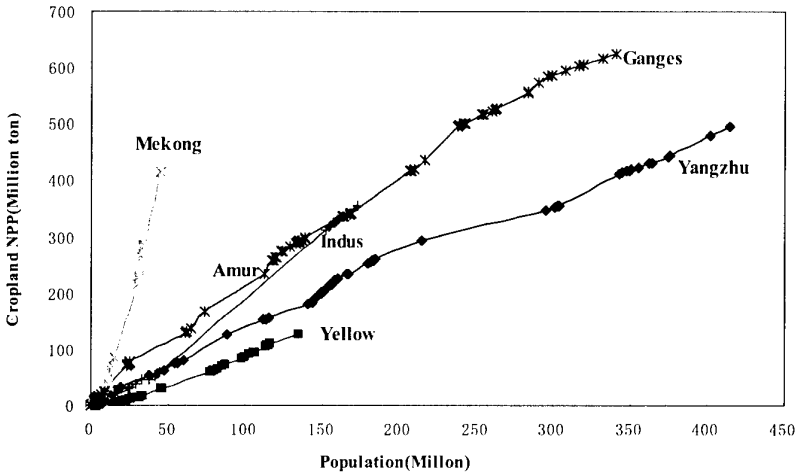


Table-3 Per capita productivity for 6 major river basins in Asia

Basin	Per capita CNPP (ton/cap)	Productivity
Mekong	9.09	High
Amur	3.46	Medium
Indus	3.46	Medium
Ganges	1.93	Low
Yangzhu	1.22	Low
Yellow	0.95	Low

4.2 Simulation

Carrying capacity based on crop(cereal) production were estimated for these six river basins as shown in

Table-4. Cropland areas were measured from USGS/IGBP land cover map for each river basin. Potential cropland was estimated by assuming if a half of existing forested area were converted to cropland. Because the Mekong and Amur river basins remain large amount of forest land, these two basins have more potential of cropland rather than other four basins where most land of the basins are already used for cropland or grassland. "Potential of per capita productivity" means that how many population can be supported by one unit of C-NPP in case one unit of C-NPP can support the same population realized in Yangzhu river basin(820 persons per ton of C-NPP). The current population was measured from CIESIN population data. The output shows that Mekong river basin can support about 13.9 times of the current population in the basin. On the contrary, Yangzhu river and Yellow river basin can support about 1.2 and 1.3 times respectively of the current population in the basins.

Table-4 Population Carrying Capacity in Six Major River Basins

Basin	Cropland area (1000sq.km)	Potential cropland* (%)	Potential of per capita productivity (%)	Current Population (million)	Potential Population (million)	
Mekong	266.1	159	745	45.2	535	(1185%)
Amur	233.3	314	284	60.6	540	(892%)
Indus	370.7	101	174	172.8	302	(175%)
Ganges	638.3	104	158	340.2	558	(164%)
Yangzhu	617.4	108	100**	414.2	447	(108%)
Yellow	151.9	105	77	135.2	109	(81%)

Remarks : * a half of forest land is assumed to be converted to cropland

** per capita CNPP is assumed same as of Yangzhu River Basin

5. Conclusions and Further Studies

In this study, Satellite RS and GIS are used to estimate NPP and Population Capacity in major river basins in Asia. Most of the input data can be down loaded through internet or access-free CD-ROM. The procedure can work to other regions in the world in any scale from local to global, and can be applied using updated satellite data. The result shows that Mekong and Amur River basins have the highest population carrying capacity under the above-mentioned assumptions, while Yangzu and Yellow River basins are saturated. In the previous study about global population carrying capacity, it was not clear how many, where and how people can survive on the land. The output is very useful to understand the future status of the population distribution in the region and to plan the strategy for land use/agricultural development.

There remain some problems to be solved in the procedure. Firstly, in the algorithm to estimate NPP using NDVI and PAR, ε (efficiency parameter) is set to 1.5 as a global average. However, the efficiency is considered to vary depending on the climate condition and vegetation type. Secondly, it was assumed that per capita productivity for all river basins in Asia can attain to the level of Yangzhu river basin in the simulation procedure. However, per capita productivity must have unique value depending on the region specified by the climate, cultivation style etc. The regional characteristics of per capita productivity should be investigated through further studies.

Reference:

Dye, D.G., Goward,S. and Eck, T.F., Global Solar Radiation Data Set for Global Primary Production Studies, Proceedings of SEIKEN SYMPOSIUM-Vol.12 " , pp41-47, 1993.

Goward, S.N. and Huemmrich, K.F., Vegetation Canopy PAR Absorptance and the Normalized Difference Vegetation Index: An Assessment Using the SAIL Model, Remote Sensing of Environment, 39, pp119-140, 1992.

Monteith, J.L., Climate and the efficiency of crop production In Britain, Philophical transactions of the Royal Society of London, Ser. B, 281, pp277-294, 1977

Ochi,S. and Murai, S., , " Analysis of relationship between NPP and Population carrying capacity for major river basins in Asia, Proceedings of 9th SEIKEN Forum "Global Environment Monitoring from Space", pp258-262, 1999.

Ochi,S, and Shibasaki, R., Algorithm for Generating Drainage Direction Matrix using DEM(GTOPO30) and DCW, Journal of the Japan Society of Photogrammetry and Remote Sensing, Vol38, No.3, pp60-68,1999.

Ruimy, A., Saugier, B. and Dedien, G., Methodology for the estimation of terrestrial net primary production from remote sensed data, Journal of Geophysical Research, 99, pp5266, 1994.

The 21st Asian Conference on Remote Sensing
December 4-8, 2000 Taipei, TAIWAN

A SYSTEMATIC APPROACH IN REMOTE SENSING EDUCATION AND TRAINING AT UNIVERSITI TEKNOLOGI MALAYSIA

Kasturi Devi Kanniah, Mazlan Hashim and Mohd Ibrahim seeni Mohd
Department of Remote Sensing
Faculty of Engineering and Geoinformation Science
Universiti Teknologi Malaysia
81310 Skudai
Johor, Malaysia

KEY WORDS: Systematic education, Training, Research, Remote Sensing, Technology integration.

ABSTRACT

The current approach that has been adopted in remote sensing teaching environment in Universiti Teknologi Malaysia (UTM) is presented in this paper. A systematic formulation of syllabus that addresses cognitive learning issues, the integration of remote sensing with other related technologies, opportunities to conduct research, undergoing training and promoting the technology to others are viewed as systematic approach in remote sensing education and further discussed in this paper. Suggestions are also made to have knowledge fusion between remote sensing and related technologies. Research shows that UTM has adopted near systematic approach with rooms for improvement. With the Memorandum of Understanding signed between UTM and Malaysian Centre for Remote Sensing, further development in the aspects of human resource development , technology transfer, research, consultation, and data and information exchange is expected to happen in remote sensing.

1. INTRODUCTION

Remote Sensing is a rapidly growing technology and is one of the important spin offs in the space research. Remote Sensing is always viewed as a discipline that is integrated with other disciplines such as photogrametry, GIS and computer science. As with the introduction of remote sensing and related technologies, education plays a pivotal role in its widespread adoption. This is because education is a medium that channels knowledge and understanding of concepts and applications of the technology using the formal system of school, college or university. In addition, education also provides opportunities for the learners and teachers to conduct research and training activities.

Systematic review is a uniquely powerful mechanism for teaching, and they offer teachers a new opportunity to model rational and effective use of information (Robert et al, 1997). In the context of remote sensing, systematic education is reviewed as the integration of remote sensing with other related technologies such as GIS, GPS, Photogrammetry and computer science. Integration of satellite based remote sensing with photogrammetry and GIS has enhanced its capabilities in the areas of resource management and solving environmental or spatial related problems very rapidly and efficiently in comparison to exploiting just one of the technology alone. Remote sensing and photogrammetry provide a means of creating and revising data in GIS. Satellite data is an essential component in GIS as data to be stored, analyzed, retrieved at will and produced end products that are used to solve problems. Therefore, it is worthwhile to treat remote sensing as an integrated disciplines of photogrammetry GIS and computer technology. In addition to that, systematic education must also cover research into new areas, appropriate training activities to both the learners and teaching/ academic staff in related fields, and promotion/ awareness of the technology to other remote sensing society or other communities. The combination of all the 4 above mentioned aspects are considered here as a systematic approach in remote sensing education.

Remote sensing education had fairly a late start in Malaysian universities due to the lack of expertise, facilities and the late realization of the technology (Mohd Ibrahim Seeni Mohd, 1993). Remote sensing had its prominent step in Malaysia via a general Memorandum of Understanding (MOU) that was signed between the Australian government, Department of Science and Malaysian Ministry of Science, Technology and Environment in December 1985 (Forster, 1993). Malaysian Centre for Remote Sensing (MACRES) was established via the memorandum and this emerged the needs for education, research and training.

In UTM, education in remote sensing and related technologies has its origin from the undergraduate programme in Land Surveying at the Faculty of Surveying and Real Estate (now called Geomatic Engineering at the Faculty of Geoinformation Science and Engineering) (Mohd Ibrahim Seeni Mohd, 1993). Remote sensing has been taught as a compulsory subject as well as an optional subject in this course since 1983. However, with the increasing importance given to remote sensing and related technologies in order to fulfill the human resource development needs of the country, a four year undergraduate programme was started in May 1997 at the faculty leading to the B.Sc. (Remote Sensing) Degree. To date only UTM offer B.Sc in remote sensing in Malaysia. Whilst, the postgraduate programmes in remote sensing have been offered since 1986. The Department of Remote Sensing at UTM was established in July, 1998. However, the concept and application of remote sensing technology has already been implemented in UTM as early as 1986 via the establishment of the Centre for Remote Sensing (CRS) which has objectives to provide courses and training at undergraduate and postgraduate levels in remote sensing, facilities for staff to carry out research , consultation services and training for users from government, semi-government and private sectors. The department consists of 8 full- time lecturers, one tutor and three laboratory assistants. In addition to that, the course is also supported by lecturers from other departments at the faculty such as the departments of Geomatics and Geoinformatics. The central mission of the department and CRS is to achieve excellence in teaching, research and professional activities in applied remote sensing and related technologies , and to promote the awareness of the technology within the remote sensing community and outside world.

2. EDUCATION

2.1 Undergraduate Programme

Department of Remote Sensing provides education and training in remote sensing to a group of undergraduate students. Student intake was begun in May 1997 with the intake of 28 students. Currently introductory and advanced level remote sensing and GIS are taught to 136 students from year one to four. The first batch will graduate in the year of 2001. The entrance requirements for the B.Sc. (Remote Sensing) course are, to have passed the Sijil Pelajaran Malaysia (equivalent to Cambridge O level exams) with credits in stipulated subjects. The study period for the course is 8 semesters (4 years) and the maximum allowed study period is 12 semesters.

2.1.1 Curriculum

The curriculum of Bachelor of Science (Remote Sensing) was modified by UTM upon the consent of National Remote Sensing Committee (NRSC) and also based on the curriculum of similar programs at over sea institutions. A total of 128 credits are needed in order to fulfill the requirements to be awarded the Degree of Bachelor of Science (Remote Sensing). The credits come from 7 study sections. The composition of the study sections is shown in Table 1.

Table 1. Subjects and the corresponding credits for the B.Sc (Remote Sensing) course at UTM.

Course subjects	Number of subjects	Number of credits	Percentage
Main core remote sensing	6	24	18.7
Core Remote Sensing	15	45	35.2
Science of Mapping and Surveying	2	6	4.7
Computer Science	3	9	7.0
Mathematics, Physics and Statistics	4	12	9.4
Selective subjects (subjects 3m)	3	9	7.0
General subjects	12	23	18.0
Total	45	128	100

Source: Department of Remote Sensing, 2000.

Integration of remote sensing with other related technologies/ disciplines such as GIS, photogrammetry and computer science also essential to acquire complete benefits of this technology. However, in most universities in Malaysia the separation between remote sensing and GIS departments are apparent and the students from the Department of Remote Sensing are not well exposed to the technology of GIS and students in GIS programs do not receive enough knowledge and sufficient training in image processing. Therefore, knowledge fusion between GIS and remote sensing or photogrammetry needs to be conducted and all students from both departments must be exposed to the technologies at undergraduate levels. However, students can be given choice to select either one of these technologies or integration of both during their final year projects. In this way, upon the completion of their studies the students will have a complete knowledge fusion of remote sensing and related technologies and skill which ensures prospective job opportunities.

2.1.2 Training

Training provides the students with practical skill that can be used to solve problems in the real world. Remote sensing at undergraduate levels rely on a mixture of theory and practical applications. Weekly laboratory exercises for every subject are designed to complement recent lecture topics in order to create a seamless teaching environment. The classroom training objectives for students include the development of skills in the use of remote sensing data for the purpose of: knowledge of image acquisition methods, data merging, image rectification, image enhancement, image classification, and image algebra, the use GIS including the knowledge of the characteristics of spatial data and spatial data handling systems, data acquisition, analytical operations and construction of output products, analysing remotely sensed data and applying GIS tools to address issues in natural resource management and environmental monitoring.

At the Department of Remote Sensing, UTM, laboratory assignments are conducted using imagery from the local region so that students will be familiar with the study sites and encouraged to conduct necessary ground truthing. Besides that, students are also trained to use data collecting equipments like radiometer and hand held GPS or other conventional methods of data collecting such as boat for oceonographic applications.

The final year (4^{th} year) students in this course will also be participated in independent undergraduate projects which carry 5 credits towards the end of the semester. This requirement encourages students to experiment the learnt theory and remotely sensed imagery or GIS techniques to topics of personal interest to them. In addition, the department has also arranged industrial training for students besides the classroom practical/ laboratory training. This industrial training is formulated to expose students to the aspects of remote sensing, GIS and other related

technologies that are practiced in government departments and private sectors, to give opportunity to students to experience the real working environment, to relate both the learning process and the real working environment and to have a good relationship between university and industries with the objective to have job placement for students upon the completion of their course.

The training locations are at government or private departments/ agencies that have the application of remote sensing in their daily activities. This includes, the utilization and extraction of geospatial data using remote sensing data, integration of remote sensing with GIS technology and other related technologies. Among the agencies/ departments are; the Malaysian Centre for Remote Sensing, Department of Agriculture, Department of Forestry, Department of Meteorology, South East Asian Fisheries Development Centre (SEAFDEC), Department of Environment, Forest Research Institute of Malaysia (FRIM), Institute of Mineral Research, Institute of Fishery, Malaysian Agricultural Research and Development Institute (MARDI), Palm Oil Research Institute of Malaysia and other private companies.

2.2 GRADUATE COURSE

In addition to the 4 year undergraduate programme the department also offers Master (both by Research and Taught Course) and Doctoral programmes in Remote Sensing to support the needs of the country in this field. Currently, there are 13 graduate students had registered and undertaking their research in various fields. At present, only master course through research and PhD are available at the department. Master through taught course requires a minimum of 5 candidates to start the course. The specification of the postgraduate courses at the department is summarized in Table 2.

Table 2. The requirements for M.Sc and PhD at the Department of Remote Sensing, UTM

Requirements	*M.Sc (Taught course)*	*M.Sc (Research)*	*PhD*
Admission requirement	A relevant bachelor degree recognized by the university	A relevant bachelor degree recognized by the university	A relevant master degree recognized by the university
Total credit hours	24 (taught subjects) 6 (master's project)	30	90
Subjects	Courses offered within interfaculties	Own thesis topic	Own thesis topic
Study Period (years)	2	2	3-4

Some of the present research works by the students areas follow : Mapping topography using SAR Interferometry techniques, Extraction of coastal zone information using SAR, Potentional of Radar data for estimation of soil moisture, Remote sensing and Hydrological modeling in flood prediction studies, Extraction of sea grass information, Remote sensing for sea Oil spill studies, Haze determination from NOAA AVHRR, Landsat TM and Radarsat SAR data Fusion for improving landcover classification and GIS for oil spill monitoring.

3. RESEARCH

Innovations, new understanding and advancement in remote sensing will only occur when great amount of effort put towards research activities. The initiation of this field of research began as early as 1986. At present staff and postgraduate research projects span as diverse as marine applications, topographical mapping, vegetation mapping, hydrological analysis, spatial variability studies and natural hazards monitoring. The development in the field of research and also consultation activities are greatly supported and enhanced by the well-equipped centre. Amongst the facilities available at the centre are PCI EASI/PACE (v6.1), PCI (v6.3), ILWIS, ERDAS-Imagine, ER-Mapper, Ergo Vista (Image processing), Digital Photogrammetric Workstation, ARC

INFO, ARC VIEW, MapInfo, WinGis (GIS), Hand held GPS, Gamman Trimble (GPS) and other facilities such as Radiometer, LOWTRAN, MODTRAN, PcGiant,Autocad, Quicksurf, Surveying equipments and a library. Refer to the departmental homepage at http://.rs.fksg.utm.my for some of the major research projects that have successfully been completed by the staff at the Department of Remote Sensing.

The department and CRS proactively involve in many new projects in order to achieve innovations, new understanding and advancement in remote sensing. Among others are Development of Direct satellite data Readout for daily monitoring of haze and coastal environments, Integration of remote sensing and GIS for oil palm spatial variability studies, Ocean Variability studies using SEAWIFF data, Generation of Spectral signature database and Videogrammetry system for ship building, repair and maintenance. Funding for these projects come from the Ministry of Science, Technology and Environment via Intensified Research in Priority Areas (IRPA), Contract research and etc.

Links have also been made with external organisations both for development of research and funding. UTM proactively involves with foreign organisations to undertake joint research projects. It started to have collaboration with Japanese Society for the promotion of Science (JSPS) since 1991 which was scientists exchange programme and from 1999 the both institutions has taken part in cooperative projects. Their focus is mainly to study the variability of ocean condition that involving application of SeaWifs data and ADEOS satellite. Besides that, UTM also involve with British universities like University College London under Committee for International Cooperation in Higher Education (CHICHE) scheme to undertake topographical mapping in Malaysia using SAR data. Through these collaborative/ bilateral projects UTM aims not only to exchange techniques and skills but also to produce graduate students.

4. CONSULTANCY

The centre has been offering consultancy services since 1990 to many local government, and private user agencies and also to some foreign agencies like Bintan Resort Management Pte. Ltd. The areas of consultancy services rendered by CRS can be grouped into; Water depth mapping, Seagrass mapping, Sea surface temperature mapping, Coastline variation mapping of Peninsular Malaysia, Coral reefs mapping, Land use mapping, Estimation of water volume in reservoirs, Modelling of sedimentation in reservoirs, Pipeline corridor mapping analysis, and Digital Mapping.

5. AWARENESS AND PROMOTING ACTIVITIES

5.1 Seminar, workshop, short courses

Any new technology will not expand without promotion. The department and centre has a strong commitment to promoting awareness of remote sensing and GIS throughout the academic and commercial sectors. This is achieved both through presentation of papers at conferences and hosting specific conferences at UTM. There were 2 seminars/ conferences had been hosted in UTM. The first was "The South East Asian Regional Conference on Education and Research in Remote Sensing" held in 1993. This was followed by "The Integration of Remote Sensing and GIS for Applications in South East Asia seminar hosted by UTM in 1995. Since the adoption of the technology many papers have been presented by specialist staff and postgraduate students at various National and International GIS and RS conferences. (for detail information refer to the departmental homepage at (http://rs.fksg.utm.my).

The department and centre for remote sensing also offer short training courses. The first short course ran in 1992 for personnel from government agencies and other user departments and it

was proved to be successful. The first short course was mainly on the application of remote sensing for marine studies. However, realizing the lack of remote sensing basic knowledge among many user departments, this programme has been extended to include courses on the basics of remote sensing to form a strong foundation among the users of the technology. The department has run 5 courses until 1999 on a yearly basis. The ever-increasing number of participants from year to year (from only 10 in 1995 to 25 in 1999) (Department of Remote Sensing, UTM, 2000) shows the realization of the importance of this technology in many aspects of resources development in developing countries like Malaysia. The 2 months short course covers many parts on RS, GIS, Photogrammetry and other related fields as diverse as the basic concepts, application, field data collection and finally the presentation of the output.

6. SUMMARY

The major objective of the Department of Remote Sensing, and Centre for Remote Sensing at UTM is to produce qualified graduates or trained professionals in Remote Sensing and related technologies to fulfill the needs of National Remote Sensing Committee in order to overcome the Natural Resource Management problems in Malaysia. The approach that has been adopted and implemented in higher educational institutions in Malaysia like UTM can be said as near systematic approach as it has met the conditions used to define the term systematic. However there is still room for improvement. First of all the integration between GIS and other related technologies should be further enhanced. This can be achieved by having a mutual understanding between those departments or sections that are available at the same university or employing staff who has wider experience is such fields. UTM has always take effort towards research into new areas and promoting this rapidly growing technology to remote sensing community via hosting seminars, workshops and short courses.

ACKNOWLEDGEMENTS

My whole hearted thanks go to all the staff at the Department of Remote Sensing, UTM, to academic staff from other local universities and The Malaysian Ministry of Education for providing me data and guidance to complete this paper.

REFERENCES

1. Dowman, I.J., 1993, Trends in Remote Sensing Education and Research in Europe, Proceedings of The South East Asian Regional Conference on Education and Research in Remote Sensing, June 28-30, 1993, Universiti Teknologi Malaysia, Malaysia

2. Mohd Ibrahim Seeni Mohd, 1993, Remote Sensing Education and Research at Universiti Teknologi Malaysia, Proceedings of The South East Asian Regional Conference on Education and Research in Remote Sensing, June 28-30, 1993, Universiti Teknologi Malaysia, Malaysia

3. Forster, B.C., 1993, Remote Sensing Education and Human Resources for Malaysia, Proceedings of The South East Asian Regional Conference on Education and Research in Remote Sensing, June 28-30, 1993, Universiti Teknologi Malaysia, Malaysia.

4.Robert G.B., Mary O'Keefe., Mark C., and Henderson, 1997, Using Systematic Reviews in Clinical Education, Annals of Internal Medicine 1 June 1997. 126:886-891.

The 21st Asian Conference on Remote Sensing
December 4-8, 2000 Taipei, TAIWAN

The study on biomass estimation in Mongolian Grassland using satellite data and field measurement data

Hirokazu YAMAMOTO, Koji KAJIWARA, and Yoshiaki HONDA
Center for Environmental Remote Sensing, Chiba University.
1-33, Yayoi-cho, Inageku, Chiba, 263-8522
Tel : +81-43-290-3835 Fax : +81-43-290-3835
E-mail : kath@ceres.cr.chiba-u.ac.jp
JAPAN

KEY WORDS : Biomass Estimation, NOAA AVHRR LAC, Field Measurement Data

***ABSTRACT**: It is said that earth environment is affected by changing vegetation biomass. So, it is needed the analysis of physical parameter of vegetation in the wide area by using satellite data, which has middle spatial resolution (approx. 1km^2). In this study, biomass is estimated on a large scale using NOAA AVHRR LAC data received in Mongolia and field measurement data.*

As the result, we found that it is able to estimate vegetation biomass without influence of cloud contamination and vegetation growth in case of more than 5 days composite of NOAA AVHRR LAC data. And we could estimate biomass in the wide area until less than 10% error.

1. Introduction

Carbon is one of the most important element on the earth, and it can become with key word of the mechanism of earth fluctuation. Also, it is said that vegetation has the important role of the carbon circulation of biosphere-lithosphere-atmosphere. Therefore, it is needed for environment monitoring to understand plant productivity globally.. Many research have done to the estimation of vegetation amount using satellite data which has characteristics of high frequency and middle spatial resolution such as NOAA AVHRR in recent years.

EOS-AM1(Terra) satellite has launched successfully, and MODIS is expected to the understanding of global dynamics. Japan also has plan of launch satellite, ADEOS-II GLI, ADEOS –III SGLI, but there are no methodology of calibration and validation for the above mentioned middle resolution satellite. We already tried the acquisition of various kinds of ground based data in Mongolian grassland in comparison with the satellite data scale, and we succeeded in estimating the relation between vegetation index and vegetation cover ratio (VCR) obtained by the mobile measurement system (Yamamoto *et al.*,1997). However, actually, such these data have not been applied to satellite data using the model obtained from field measurement data.

2. Objective

The aim of this study is the following items.

To construct ,of biomass estimation model which can be calibrated from the relationship between vegetation index – vegetation cover ratio – biomass using the field experiment data

To apply the field data to satellite data.

To evaluate the derived satellite biomass estimation by using meteorological station data in Mongolia.

3. Method

3.1 The Study Area and Data

The study area of field measurement and satellite data is Mongolian grassland. Figure.1 shows the range of this study area of field measurement. Field measurement data we used in this study was acquired in summer from 1995 to 1998(Table.1). NOAA AVHRR LAC data received at Ulaanbaatar in Mongolia was used as satellite data. Table.2 shows acquisition date and time of AVHRR data used in this study.

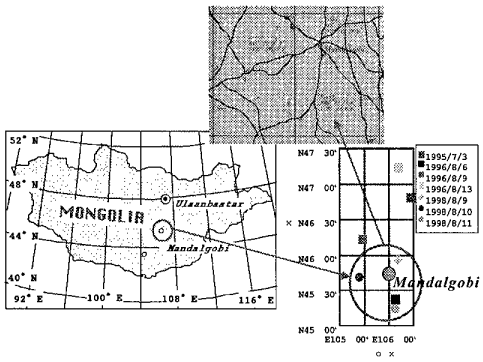
3.2 Analysis of Field Measurement Data

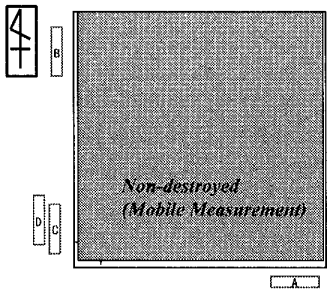
The mobile measurement system is quick measurement system for acquisition of the various kinds of ground information over a large area such as the scale of satellite data. Sensor height from the ground is approximately 2 m. Optical axis of this system is adjusted to become parallel and being fixed to always measure nadir. Spectrometer measures in the visible and near-infrared region (350nm- 1050nm) with 512 channels. Observation item is spectral reflectance and ground digital image for vegetation cover ratio. In this study, vegetation cover ration is defined as the proportion of the green plant that is viewed in nadir direction from the sensor to ground surface.

The biomass measurement is cutting all the grass (green leaf) inside of 1m^2 area with the hand, and wet grass

weight and dry grass weight by using drying machine for 8.5 hours is measured. And this system is also able to acquire nadir ground digital image, spectral information, and grass height. System is designed the same as mobile measurement system. In this study, 58 good biomass measurement points obtained from August 3 to August 9, 1998 in Site.1 were analyzed. And 5 points data had been obtained in August 10, 1998 in Site.2 and 3 points data had been obtained in August 11 in Site.3. Observation items are spectral reflectance, ground images, and biomass(wet and dry grass weight, and grass height). In this study, biomass is defined as the weight of sufficient dried up grass which is green and fresh matter on the ground.

Calculation of vegetation coverage ratio is derived from digital images using RGB pattern method and hue and intensity method (Yamamoto *et al.*,1997).





* D area is daily grass cutting area
* A, B and C area are weekly grass cutting area.

Figure.1 The study Area

Table.1 Acquisition date and time of field measurement data in this study

Date	Time	Number of Points
1995/7/3	13:40-17:52	65
1996/8/7	12:03-13:53	100
1996/8/8	11:02-17:22	10
1996/8/14	15:44-17:30	100
1998/8/9	09:47-11:23	104
1998/8/9	11:39-13:21	105
1998/8/9	14:15-15:54	105
1998/8/9	16:15-17:52	93
1998/8/10	15:18-16:02	44
1998/8/10	12:15-14:01	109
1998/8/10	16:36-16:59	28
1998/8/11	12:04-13:15	55
1998/8/11	14:43-15:02	22
1998/8/2 1998/8/11	9:25 17:05	67

Table.2 NOAA AVHRR LAC in this study

	Date	Time(GMT)
1996's Data	1996/7/30	5:51:58
	1996/7/31	5:39:36
	1996/8/1	7:10:23
	1996/8/2	5:18:00
	1996/8/2	6:59:12
1998's Data	1998/8/6	5:13:41
	1998/8/6	6:52:33
	1998/8/6	8:35:12
	1998/8/7	5:03:05
	1998/8/7	8:23:34
	1998/8/8	4:52:34
	1998/8/8	6:30:36
	1998/8/8	8:12:26
	1998/8/9	6:19:39
	1998/8/9	8:01:10
	1998/8/10	6:08:36
	1998/8/10	7:49:46
	1998/8/11	5:57:35
	1998/8/11	7:38:20
	1998/8/12	5:46:40
	1998/8/12	7:27:07
	1998/8/13	5:35:55
	1998/8/13	7:15:52

3.3 Satellite Data Processing

In this study, NOAA-14 AVHRR LAC data received at Ulaanbaatar in Mongolia was used. It is able to calculate reflectance from NOAA AVHRR LAC data (Mather,1998). The accuracy of the reflectance is about 0.1%. NOAA/NESDIS (NOAA's National Environmental Satellite Data and Information Service) is opened for acquisition of the latest information of gain and offset for calibration. It is said that calibration coefficient is changeable for sensor deterioration, and so on (Brest *et al.*, 1992; Rao *et al.*,1994) . In this study, the latest gain and offset was used every date of acquisition.

Geometric correction was conducted using automatic acquisition of GCPs. This method can generate GCP data automatically by matching the coastline data (Shimoda *et al.*,1998, Hashimoto *et al..*,1993). In this study, residuals on image is less than 0.4 pixels, and map projection is Latitude/Longitude Grid system (WGS84) and resampling method is nearest neighbor.

Atmospheric correction was conducted by 6S code, which is focused on visible and near infra-red region (Vermote *et al.*, 1997). In this study, LUT method (Lei *et al.*,1998) was used. At first, LUT is calculated for each Sun-Target-Sensor geometry condition. GTOPO30 which has approx. 1km resolution is used as height above sea level . And high reliable data (AeroNet) is used as optical thickness (Optical thickness @550nm was re-calculated.), which was measured at Mandalgobi in Aug. of 1998. These data are obtained every day, and it is varied from 0.036 to 0.071. Therefore, in this study, 0.071 is used for 6Scode. Table.3 shows input parameters

for 6S code.

Table.3 Input Parameters for 6S

Atmospheric Model	Midlatitude Summer
Aerosole Model	Continental Model
Solar Zenith Angle	0,10,20,30,40,50,60,70 [deg]
Satellite Zenith Angle	0,10,20,30,40,50,60,70[deg]
Relative Azimuth Angle	0,20,40,60,80,100,120,140,160,180[deg]
Height avobe Sea Level	0.0,0.5,1.0,1.5,2.0,2.5,3.0 [km]

3.4 Analysis of Meteorological Station data

15 meteorological stations are located at flat and homogeneous grassland in eastern part of Mongolia (Figure.2). Acquisition date is from the beginning of June to the end of September every 10 days. Observation items are ground image by photographs, wet and dry grass weight, and grass height. Cutting area is 1m ×1m, and cutting method is almost same as field biomass measurement. Dry weight is the grass weight dried by sun for a few days. In this study, meteorological station data was used as evaluation of estimated biomass in the wide area and construction of VCR-Biomass model.

In model construction, using 4 corners of the clipping area as control point, affine transformation method was conducted to the non-vertical digitized photograph. After this process, the RGB Pattern method and Hue and Intensity method were conducted to the image. 270 good points of 420 measurement points were used as VCR data. And then VCR-Biomass model was constructed by simple linear regression between this VCR data and biomass data of meteorological station.

In evaluation of estimated biomass, as above-mentioned, corrected reflectance of satellite sensor is calculated each channels, therefore NDVI is derived from these reflectance data. Moreover, biomass map in the wide area can be calculated by using biomass estimation model derived from field experiment data. The following equation was used as accuracy of the estimated biomass:

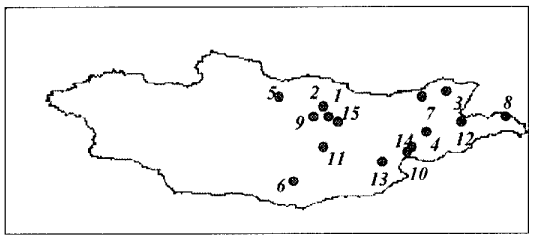
$\varepsilon = (T-M)/T \times 100$

ε : Relative Error

M: Estimated Biomass

T: Meteorological Station Data (15 Stations) ··· (1)

Moreover, the estimation biomass was evaluated every composite period. The influence of the plant growth for composite period was also evaluated.



No.	Station Name	Latitude(N deg)	Longitude(E deg)
1	Baruunurt	46.68	113.28
2	Bayanchadmani	48.23	106.28
3	Bayandelger	45.73	112.37
4	Bayanuul(Onou)	49.12	112.68
5	Bulgan(Orkhon)	48.80	103.55
6	Dalanzadgad	43.58	104.42
7	Dashbalbar	49.55	114.40
8	Khalkhgol	47.62	118.62
9	Khustai	47.80	105.92
10	Maanit	47.30	107.48
11	Mandalgobi	45.77	106.28
12	Matad	47.15	115.67
13	Sainhand	44.90	110.12
14	Tumenthogt	45.60	112.20
15	Yamag(Uhanbartar)	47.79	106.63

Figure.2 The Distribution of 15 Meteorological Stations in Mongolia

4. Result

4.1 Biomass Estimation Model Using Field data and Meteorological Station Data

Figure.3 depicts example of averaged spectral reflectance obtained by mobile measurement. It is clearly that enough amount of data was collected in the wide area, and it can be said the representative reflectance on a satellite scale. NDVI was calculated from convolved reflectance to NOAA AVHRR spectral resolution. The left side of Figure.4 shows relationship between NDVI and vegetation cover ratio (VCR). It is good correlation between VCR and NDVI. Therefore they are able to be constructed NDVI-VCR model on a satellite scale. This model can be obtained by simple regression analysis, and it expressed as the following formula:

VCR = 0.9375 NDVI-0.0830 (R = 0.847)

VCR : Vegetation Cover Ratio ···(2)

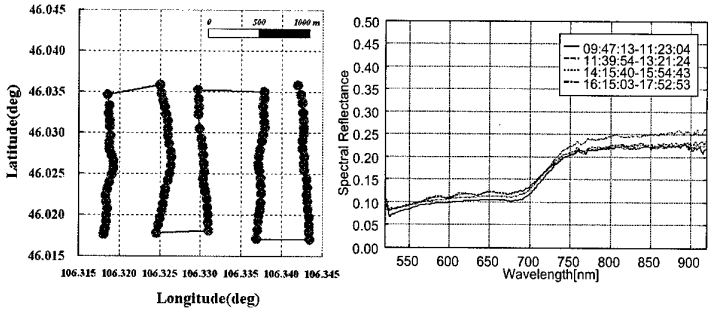


Figure.3 Example of Averaged Spectral Reflectance obtained by Mobile Measurement

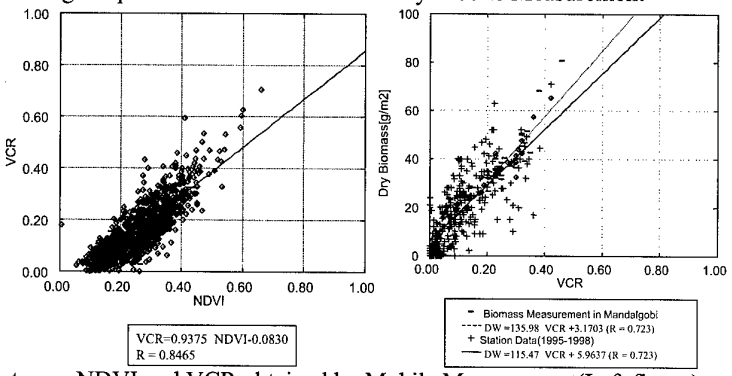


Figure.4 Relation between NDVI and VCR obtained by Mobile Measurement(Left figure)
Relation between VCR and Biomass obtained by Field Measurement
and Meteorological Station(Right figure)

Moreover, the following simple linear regression equation is expressed with vegetation cover ratio (VCR) and biomass :

DW = 135.98 VCR+3.1703 (R = 0.723)
DW : Biomass (g/m^2)
VCR : Vegetation Cover Ratio (VCR) … (3)

In case of using meteorological station data:

DW = 115.47 VCR+5.964 (R = 0.723)
DW : Biomass (g/m^2)
VCR : Vegetation Cover Ratio (VCR) … (4)

Using formula (2) and (3), biomass estimation model by simple linear regression of field measurement data is expressed as:

DW = 127.481 NDVI-8.116
DW: Biomass(g/m^2) … (5)

Similarly, biomass estimation model using meteorological station data is expressed derived from formula (2) and (4):

DW = 108.25 NDVI-3.620
DW : Biomass(g/m^2) … (6)

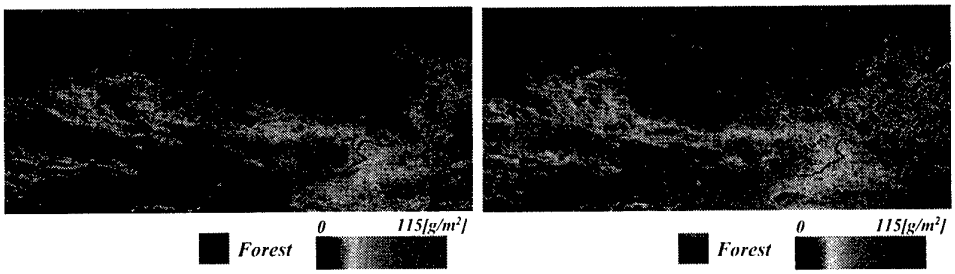


Figure.5 Biomass estimation using 5days composite NOAA AVHRR LAC(1996) (left)
Biomass estimation using 8days composite NOAA AVHRR LAC(1998)(right)

4.2 Evaluation of Estimated Biomass for Composite Period

Therefore, estimation biomass in the whole Mongolian grassland is made by equation (5) or (6). Figure.5 depicts estimated biomass derived from model of field measurement data.

Left figure of Figure.5 is the result of 5 days composite of 1996 and right figure shows 8 days composite of 1998. Left figure of Figure.6 shows the relative errors of the average of all 15 meteorological stations for 5 days composite of 1996. The influence of plant growth is not appearing with the 5th days when composite is completed. Right figure of Figure.6 is the relative errors of the average of all 15 meteorological station composite for 1998 year 8 of days. Relative error becomes 0% to the 4th days ,and after the 5th days, it becomes to negative.

Therefore, it is clear that composite data can be reflected the vegetation quantity without the influence of the plant growth, if cloud cover removal is completed with 5 days composite. This result shows that 10 days composite data and monthly composite data which are used generally may not reflect actual vegetation quantity.

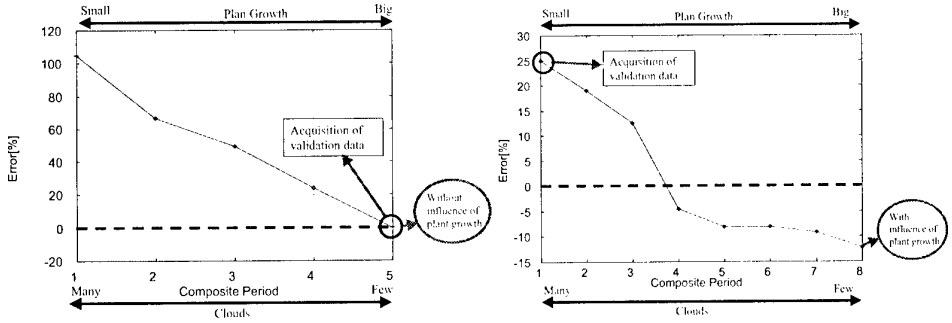


Figure.6 Averaged Relative Error versus Composite Period of NOAA AVHRR LAC data(left is 1996's, right is 1998's)

4.3 Biomass Estimation Using Field Data and Satellite Data

The evaluation of the relative error was carried out only by using 5 days composite data (1996) in this research, because it was confirmed that 1998 composite data has the influence of plant growth.

Left figure of Figure.7 shows the error of the estimated biomass by field measurement model on the map. The relative error is 0.45%, and extremely high accuracy with Mandalgobi. Mandalgobi meteorological station may be periphery close to field measurement site. However, a relative error is growing up in the place which is distant from Mandalgobi.

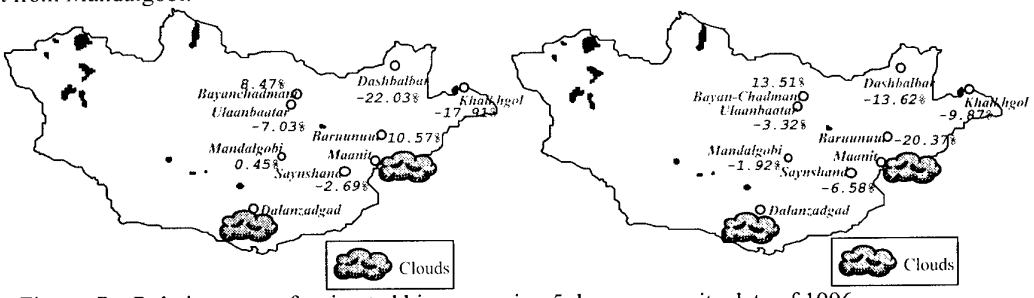


Figure. 7 Relative error of estimated biomass using 5 days composite data of 1996
(Filed Measurement Model, Left figure)
Relative error of estimated biomass using 5 days composite data of 1996
(Meteorological Station data Model, Right figure)

4.4 Biomass Estimation Using Meteorological Station Data and Satellite Data

Right figure of Figure.7 shows the relative error of estimated biomass of 5 days composite data of 1996 using meteorological station data model on the map. The accuracy is -1.92% in Mandalgobi. The accuracy is less than biomass estimated by field measurement model, but Ulaanbaatar are -3.32%. Relative error at the place

among Ulaanbaatar and Mandalgobi. is within about 10 %.

5. Conclusions

In this study, we estimated biomass in the wide area using field measurement data and satellite data, NOAA AVHRR LAC data., and evaluated the estimated biomass using meteorological station data. As the result, it is able to conclude the following items.

It is developed the methodology of field experiment strategy (Mobile Measurement, Biomass Measurement) for footprint of satellite sensor scale, and NDVI-Biomass model is constructed with vegetation cover.

Both of field measurement data and meteorological station data can be applied to NOAA AVHRR LAC data, and it can estimate biomass on a large scale.

It is able to estimate biomass in the wide area by using NOAA AVHRR LAC data and field data with high accuracy. The error ratio of biomass estimation is less than approx. 10% between Ulaanbataar and Mandalgobi. Moreover, LAC data should be less than 5 days composite, because more than 5 days composite data has capability of influence of plant growth in the Mongolian grassland.

Acknowledgments

This work has been supported by CREST (Core Research for Evolutional Science and Technology) of Japan Science and Technology Corporation (JST). And we are very grateful to many staffs of Dundgobi local government and The Information and Computer Center in Mongolia.

References

[1]Hashimoto, T. and Murai., S., Geometric Correction of NOAA AVHRR Imagery in accordance with the number of GCPs., Journal of the Japan Society of Photogrammetry and Remote Sensing, Vol.36, No., 1993.(in Japanese)

[2]Honda, Y., Kajiwara, K., Yamamoto, H., Hashimoto, T., Takagi, M., and Takamura, T., Project for Establishment of Plant Production Estimation Using Remote Sensing, Proceeding of The International Symposium on Global Change in East Asia - Vegetation Monitoring -, p.113-127, 1998.

[3]Lei, L., Koide, M., Iikura, Y., and Yokoyama, R., Correction of atmospheric effects on AVHRR imagery by 6S code, The Remote Sensing Society of Japan ,Journal of The Remote Sensing Society of Japan,Vol. 18, No. 2, p.51-64, 1998.

[4]Mather, P. M., Computer Processing of Remotely-Sensed Images, NOAA Polar Orbiter Data (POD) User's Guide, November 1998 revision Section 3.3, p.202-206, 1998.

[5] Shimoda, H., Fukue, K., Cho, K., Matsuoka, R., Hashimoto, T., Nemote, T., Tokunaga, M., Tanba, S., and Takagi, M., Development of a Software Package for ADEOS and NOAA Data Analysis, Proceedings of the IGARSS'98, Vol.2, Int03, ISBN, 0-7803-4406-5, 1998.

[6] Tucker, C. J., Red and Photographic Infrared Linear Combinations for Monitoring Vegetation, Remote Sensing of Environment., Vol. 8, p.127-150, 1979.

[7] Vermote, E. F., Tanre, D., Herman, M., and Morcrette, J. J., Second Simulation of the Satellite Signal in the Solar Spectrum 6S An over view, IEEE Trans. Geosci. Remote Sensing, Vol. 35, No. 3, p.657-686, 1997.

[8] Yamamoto, H.,Kajiwara, K., Honda, Y.:The Estimation of Vegetation Coverage Ratio by Car Survey --- The Experience in Mongolian Grassland ---, Proceeding of the Symposium of the Japan Society of Photogrammetry and Remote Sensing,241-244, 1996.(in Japanese)

[9] Yamamoto, H., Honda, Y., Kajiwara, K., Okano, C., Huang, S. and Matsuoka, .:The Analysis of Field Data Measured in Grassland for Biomass Monitoring Using Satellite Data, Journal of the Japan Society of Photogrammetry and Remote Sensing, Vol.36, No.4, 1997.(in Japanese)

The 21st Asian Conference on Remote Sensing
December 4-8, 2000 Taipei, TAIWAN

INTEGRATION OF RS AND GIS TO ASSESS HUMAN IMPACT ON ECOSYSTEM CHANGE IN LLANOS AREA (VENEZUELA)

[1]Yanning GUAN (China), [2]Steven M. de JONG, [3]Johan de MEIJERE (Netherlands)
[1]Institute of Remote Sensing Applications, Chinese Academy of Sciences,
P. Box 9718, Beijing 100101, China
Tel: 86-10-64889540
E-mail: gyn@hrs1.irsa.ac.cn
[2]Center of Geoimformation, Wageningen University and Research Center
[3]International Institute for Aerospace Survey and Earth Sciences

KEY WORDS: landscape ecology, ecosystem change, human impact, probability model, flooding savanna, integration of RS and GIS.

ABSTRACT: Landscape ecology emphasizes large areas and ecological effects of the spatial patterning of ecosystem. Recent developments in landscape ecology have emphasized the important relationship between spatial patterns and many ecological processes. Quantitative methods in landscape ecology link spatial patterns and ecological processes at broad spatial and temporal scales. In turn the increased attention on temporal change of ecosystem and human impact has highlighted the need for quantitative methods that can analyze patterns, determine the importance of spatially explicit processes, and develop reliable model. This research applies quantitative methods to assess the human impact on ecosystem temporal change in the flooding savanna area. Remote sensing offers the temporal change of ecosystem on landscape characteristics and disturbed by human. GIS as an important tool use in ecosystem temporal change analysis, landscape fragmentation analysis, and a probability model was developed to assess the relationship between ecosystem change and anthropogenic variables. The results are calculated in different scales.

1. Introduction

Landscape processes are dynamic and various climatic, lithological, landscape and anthropological factors contribute to significant spatial and temporal variability in environmental phenomena. Recognition, interpretation and mapping of the variability of process controlling variables and land conditions are imperative for assessing impact on ecological environment of human being and implementation of effective natural resources management.

Remote sensing image analyses systems and Geographic Information System (GIS) show great functionality for the integration of a wide variety of spatial information supporting tasks such as natural resource management, regional planning, and environmental monitoring. Current remote sensing programs are based on a variety of sensors that provide temporal and spatial earth observation on a global scale, thereby offering the opportunity for analyses of various phenomena synoptically from local to global scales. These attributes make remote sensing appealing for application to landscape ecology. GIS offers efficient tools for handling, manipulating, analyzing and presenting spatial data. Working in an integrated remote sensing and GIS environment allows taking advantage of both GIS and remote sensing image analysis techniques.

Remote sensing and GIS are powerful tools for the integration of a wide variety of spatial information applying tasks such as natural resource management and environmental change monitoring. Remote sensing

technology and GIS offer the ability to facilitate ecosystem change investigations leading to a more complete understanding of human impact on the ecosystem. The research gives the approaches to derived the ecosystem temporal change and landscape fragmentation analysis by integrated remote sensing and GIS, and to model the human impact on the ecosystem change.

2. The Study Area

The flooding savannas of the Llanos area, which cover around 16,000 km^2, are in the west central part of Venezuela, and occupy portions of Guarico, Cojedes, Portuguesa, Barinas and Apure States. The study area is in the Apure and locates in the central of Llanos.

In 1967, there was a serious flooding in Apure, where about 50,000 km^2 were inundated. The government carried out a project named "Modulos of Apure" to control flooding and improve the hydrologic management of the region. There are 188, 000 ha of modulated area constructed. The advantages of the project were evident when productivity indexes of the modulated savannas under rational management were compared against the indexes of the natural savanna under traditional management. A series of dikes have been built for experiment. The dikes are more or less perpendicular to the riverbanks, and parallel to each other. The area closed by these dikes and riverbanks is called a 'module'. A module can be defined as: "a sector of savanna that has been provided with low earth dikes to retain rainfall water in order to maintain green pastures throughout the year. These dikes have also the additional use as communication ways (roads)" (Gisele, 1998).

The construction of dikes has had an enormous effect on the economy of the Apure area. It not only impacts the local economy situation, but also affects the ecosystem in numerous ways. Change in hydrological factors, such as increased or decreased spate frequency and magnitude, change in frequency of drying events or shortening of drying, can affect the ecosystems extremely. The faunas characterised by extraordinarily rapid development. Similarly, biotic communities of the module area are disturbed. The stability of the habitats in these disturbed ecosystems may, in some case, provide a refuge for many species on other hand the construction of dikes led to an increase in influences on ecosystem by human being.

3. Research Methodology

The framework for remote sensing application in landscape ecology must be considered in reference to both the spatial and temporal condition. The individual research question associated with space, time and dynamics. (Quattrochi, D.A., and Pelletier, R.E., 1990) An appropriate data collection design can be employed within the scope of an investigation to provide answers to the specific landscape questions under consideration. For to assess the human impact on the ecosystem change these questions are not all-encompassing and should be addressed. The landscape processes associated with the landscape spatial and temporal dynamics should be observed and measured.

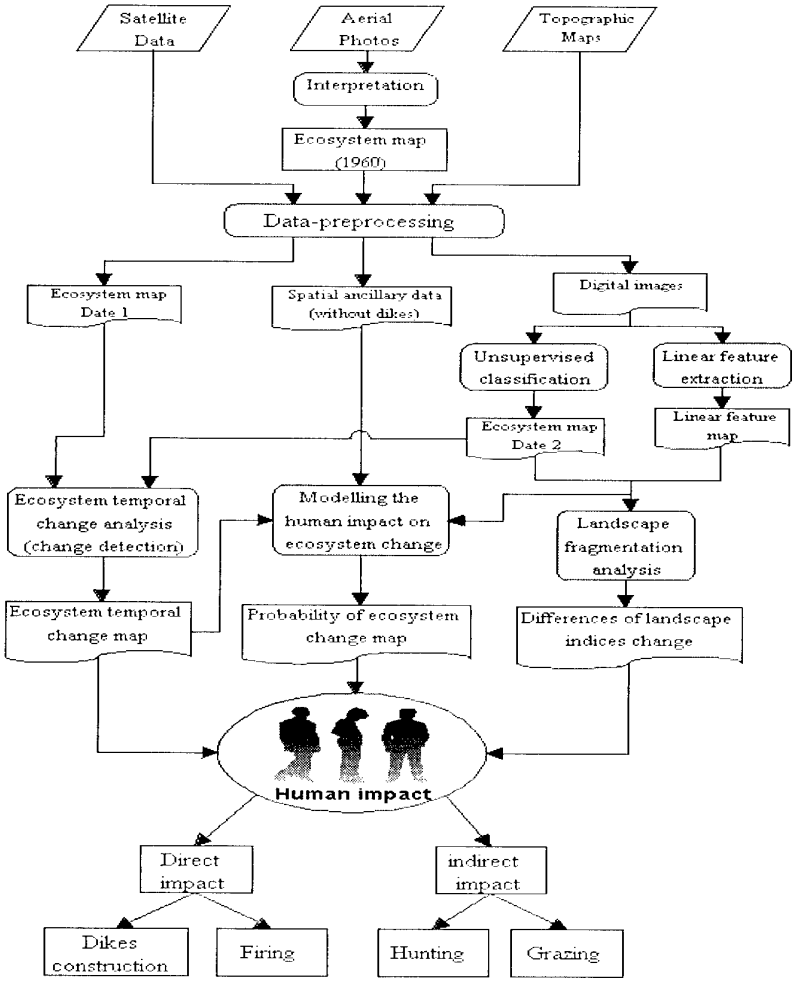


Figure 1 Methods of implemented integrated GIS and RS assess to human impact in the Llanos area

To take into account the landscape ecological characteristics in the study area and the research question and the limitation of available data, the framework of implemented methods in this research is:

- Constructing the spatial ancillary database including road map and residential area map etc.
- Interpreting the ecosystem map from Landsat TM.
- Employing the change detection technique to derive the ecosystem temporal change 1960 to 1988.
- Extracting the main human impact factor — dikes by using knowledge based and fuzzy classification.
- Carrying out the landscape fragmentation analysis in different scales — to calculate the landscape pattern index that correlated with the degree of human manipulation of landscape in GIS environment to compare the spatial difference of landscape change in modular area and non-modular area.
- Applying GIS to model the human impact on ecosystem change to take into account the anthropogenic factors such as distance to dikes etc.

Figure 1 gives an overview about implemented methods of integrated GIS and remote sensing to assess human impact in the study area.

4. Results

Temporal changes in a landscape could include change in (1) patch number, (2) patch size, (3) number and type of corridors, (4) number and type of dispersal barriers, (5) probability and spread of disturbance. (Turner, 1988) The emphases in this study are 1,2,4 and 5.

The change detection is a technique that detects the changes between two data sets, the Ecosystem map 1960 and the Ecosystem map 1988 pixel by pixel. The implementing of the post-classification is a program in GIS environment (ARC/INFO). Based on the results of landscape change detection, the Ecosystem change map, the area of ecosystem temporal change can be identified.

The patch number and the total boundary length in 1988 increase enormously comparing with in 1960, the average patch size is shrinking. The construction of dikes is the dissection, dissect or subdivide of the landscapes into sections. Fragmentation predominates in the present phases of landscape change.

Analysis of the landscape type change, the River forest and the Hyper-seasonal savanna, which dominated the study area and relative stable comparing with the other types. However, it is remarkable that the area of Hyper-seasonal savanna inundated by water is more than the Semi-seasonal savanna, and the Semi-seasonal savanna is the lower part in the study area. The trend of the landscape change indicates the landscape transformation that is not a natural process.

Using GIS the overlay analysis function, the ecosystem map 1960 was intersected with the dike map. The patches that were dissected by dikes were reselected. The areas of each landscape type were counted as disturbed by the construction of dikes. For the landscape types within the study area, the frequencies of disturbance are more than 80%.

The landscape indices represent the quantify aspects of spatial pattern that can be correlated with the spatial process. One of the indices, the fractal dimension is shown to be correlated with the degree of human manipulation of the landscape. The fractal dimension is an index of the complexity of shapes on the landscape. If the landscape is composed of simple geometric shapes like squares and rectangles, the fractal dimension will be small, approaching 1.0. If the landscape contains many patches with complex and convoluted shapes, the fractal dimension will be large. The fractal dimensions of 20 coverage were calculated in various scales for the modulated area and non-modulated area (Table 1).

Table 1 The fractal dimension on multi-scales in the modulated area and non-modulated area

Scale	Modulated area Fractal dimension		Non-modulated area Fractal dimension	
	1960	1988	1960	1988
Patch area >0. 5 ha	1.200	1.406	-	1.402
Patch area > 5 ha	1.196	1.390	1.086	1.386
Patch area > 10 ha	1.214	1.372	1.086	1.346
Patch area > 25 ha	1.216	1.244	1.126	1.368
Patch area > 50 ha	1.156	1.016	1.100	1.306

In the non-modulated area, the fractal dimensions increase from 1960 to 1988 in multi-scale. These differences of the landscape indices between the two periods illustrate the natural fragmentation processes. The patches were fragmented to small pieces and the shapes of the patch became more complex.

In the modulated area, the fractal dimensions increase from 1960 to 1988 on the patch scales of: patch area >0. 5 ha, patch area > 5 ha, patch area >10 ha and patch area >2 5 ha. The differences indicate the natural fragmentation processes on the four patch scales as well. In the contrast, the fractal dimension decreases from

1960 to 1988 on the patch scale large than 50 ha. The change shows an opposite direction of the natural fragmentation process. The shape patch became simple like square and rectangle. It is anthropogenic process that can be associated with the construction of dikes.

The landscape properties is highly scale dependent (Keitt,T.H. 1997). Ecological studies more often have a spatial component and include landscape scale parameters (Baker W. And Cai Y., 1992). The results show that on the scale of patch area > 50 ha. Landscape indices captures major features of pattern — the effects of the construction of dikes. The landscape indices are sensitive to the calculation scale (O'Neill, R.V.; Hunsaker, C.T.; et al. 1996).

An ecosystem change assessing model is developed by using GIS and logistic regression analysis. The logistic regression model has been studied the Mt.Graham red squirrel habitat (Pereira, J.M.C., and Itami, R.M., 1991), crane habitat (Herr,A.M., and Queen, L.P., 1993) and bobwhite habitat (Roseberry,J.L.,et.al.1994). The logistic regression analysis can contain numeric as well as categorical data. The change of ecosystem is the dependent variable. The independent variables included the environmental variables (ecosystem units) and anthropogenic variables. (eg. Distance to dike) Using GIS function the shortest distances will be measured between the ecosystem change and anthropogenic features. The land use anthropogenic features (dikes etc.) are extracted from TM.

The logistic model and the probability of ecosystem change developed in this study is represented in the following:

$$Y = c_0 + c_1 dist.dike + ... + c_n dist.residental.area + c_m dist.airport + ...$$

$$P = \frac{e^y}{e^y + 1}$$

Where Y is the exponent of the logistic equation;
P is the probability ecosystem change at a particular location.

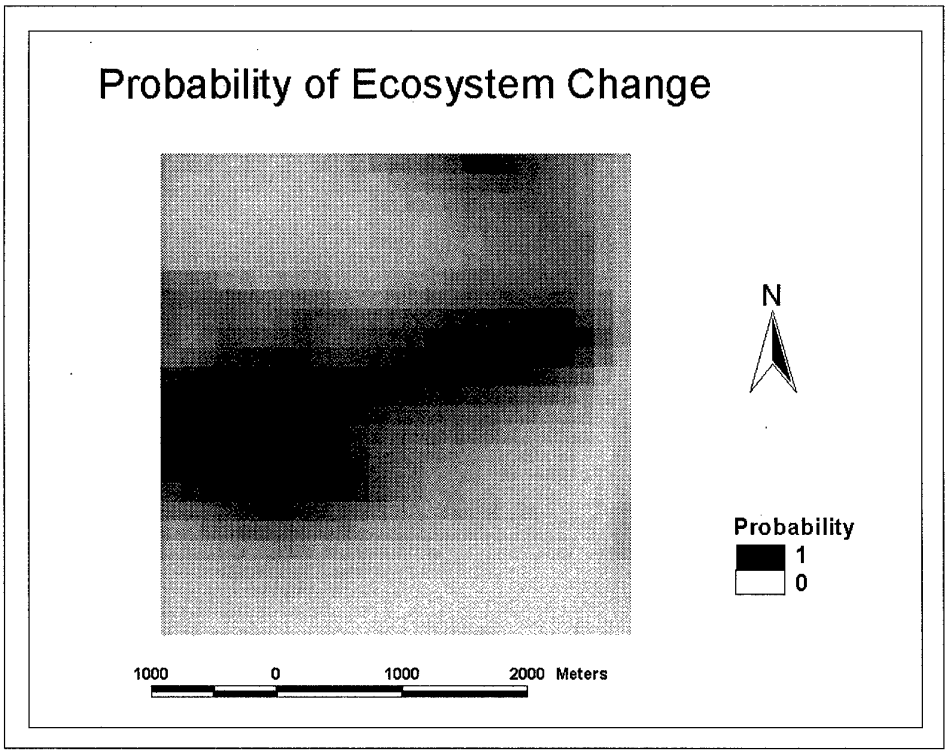
The output probability values range from 0 to 1 indicating 0 to 100 percent probability of ecosystem change. The result can be illustrated by GIS in a digital map.

The descriptive statistics of the anthropogenic independent variables are the Distance to dike, Distance to residential area, Distance to main road, Distance to dirt road, Distance to path and Distance to airport. The ecosystem change map as the dependent variable is only having two codes, 0 is non-changed and 1 is changed. The dependent and the independent variables are exactly identical in location and pixel size.

Applying the logistic model, which the pixel size is 150m by 150m and the sample area is 30pixel by 30pixel, assessed the ecosystem change probability. A raster format was used for it is more effective at presenting spatially continuous phenomena than is a vector format. The result is a probability of the ecosystem changing effected by the anthropogenic factors (Figure 2).

5. Summary

In general agreement with the ground truths, the models suggested that the construction of the dikes have the unique directional influence on the ecosystem change. Close to the dikes, the probabilities of the ecosystem change increase. This may suggest the construction of the dikes is the human disturbances that are widely spread in the Llanos modular area, and roads, airport and the residential sites provided the important impacts for the ecosystem change as well. This study should contribute to understand the human impact on the



flooding savanna in Llanos area.

Figure 2 The probability of the ecosystem changing effected by the anthropogenic factors

The structure and function of a landscape can be perceived differently at different scales, and it is important for the observer to decide upon appropriate scales for a study. To develop the GIS model, not only the sample scale effects the result of model; the cell size also influences the model establishing. This is the particular issue of modelling in the GIS environment.

References

Baker W. And Cai Y., 1992. The r.le programs for multiscale analysis of landscape structure using the GRASS geographical information system. Landscape Ecology, vol.7(4), p291-302.

Gisele, C. L., 1998. GIS support for SWOT analysis applied to land evaluation, Msc. thesis of Wageningen Agriculture University, the Netherlands.

Herr,A.M., and Queen, L. P., 1993. Crane nabitat evaluation using GIS and remote sensing, *Photogrammetric Engineering & Remote Sensing,* 59(10): 1531-1538.

Keitt, T. H. et. al., 1997. Detecting critical scales in fragmented landscapes, http://life.csu.edu.au/consecol /vol1/iss1/art4/

Pereira, J.M.C., and Itami, R.M., 1991. GIS-based habitat modeling using logistic multiple regression: a study of the Mt. Graham red squirrel, *Photogrammetric Engineering & Remote Sensing*, 57(11) 1475-1486.

Quattrochi, D.A., and Pelletier, R. E., 1990. Remote sensing for analysis of landscapes: an introduction, *Quantitative Methods in Landscape Ecology*, ed. Turner, M. G., and Gardner, R.H. 53-76.

Roseberry, J. L., et.al.1994. Assessing the potential impact of conservation reserve program lands on bobwhite habitat using remote sensing, GIS, and habitat modeling, *Photogrammetric Engineering & Remote Sensing,* 60(9): 1139-1143.

THE PRODUCTION OF PHOTO BASE MAP IN TAIWAN

Jih-cheng RU
Director, Agricultural and Forestry Aerial Survey Institute
No 61-3, Chao-chou Street, Taipei, Taiwan
Tel: (886)-2-23931837 Fax: (886)-2-23931870
E-mail: nn240918@ms19.hinet.net
TAIWAN

KEY WORDS：Aerial Photo, Photo Base Map, Orthophoto Mapping Method

ABSTRACT： In July 1975, the Executive Yuan (Cabinet) approved a project for producing large-scale photo base maps covering all of Taiwan. The mapping project is sponsored by the Ministry of Interior with the assistance of Council of Agriculture, but the actual mapping work is executed by the Agricultural and Forestry Aerial Survey Institute, Taiwan Forestry Bureau. The photo base maps were made from aerial photos through the orthophoto mapping method. At the end of 1999, the completed photo base maps can be divided into two systems. The analog mapping system with a total of 15,160 sheets included：(1) Base maps of the first edition 3,773 sheets, the second edition 2,000 sheets, and the third edition 2,400 sheets. (2) Forest maps of national forest 37 working circles 3,731 sheets. (3) Coastal area maps 3,256 sheets. The digital mapping system with a total of 1,580 sheets included：(1) Base maps 856 sheets. (2) Forest maps 604 sheets. (3) Others 120 sheets . These completed photo base maps are widely used by the people of all sectors and has won nation-wide acclamation because of their delicacy and accuracy. Besides, the photomaps provided more and clear ground features. It has made an outstanding contributions to the promotion of aerial survey mapping work and national economic development in Taiwan.

1. PREFACE

The land surveying works of Taiwan are divided into three parts：(1) Revision of basic control points. (2) Production of photo base maps in Taiwan areas. (3) Resurveying of cadastral maps. In order to meet the needs of national economic reconstruction, The Agricultural and Forestry Aerial Survey Institute has been actively developing its aerial survey and remote sensing business. Now, The Institute possesses two aerial survey airplanes, digital mapping and resource inventory instruments, as well as the most experienced technicians to perform the aerial photography, mapping and resource inventory works.

2. PHOTO BASE MAP

2.1 Definition

The digital photo base map is storing the spatial data of the global surface in the computer by means of digital form. The geometric data of the point, line, and area on the base map are expressed by the coordinate system. It is enable to provide the GIS applications.

2.2 Theory of Mapping

central projection photo→differential rectification→orthographic projection photo

2.3 Map Accuracy

(1) The differences of x and y coordinates between the map and ground should be < 0.5 mm on the map.

(2) The differences of z value between the map and ground should be < 1/4 of the contour line interval.

(3) The shift of contour line should be < 1/3 of the contour line intervals in the flat land below 15 degree and < 1/2 of the contour line intervals in the slope land over 15 degree.

(4) The accuracy of digital terrain model is the same as the regulated contour line shifting.

3. MAP PROJECTION AND COORDINATES SYSTEM

The map projection is based on the Two Degree Zone Transverse Mercator Projection. Central meridian 121^0 East Longitude, y coordinate shift to west 250,000 m., scale ratio of central meridian is 0.9999.

3.1 TWD 67

The Geodetic Reference System determined by the International Association of Geodesy and International Geophysical Union in 1967 was used for the coordinate calculation of the Taiwan photo base map. The data are as follows：

Earth ellipsoid parameters：long radius a = 6,378,160 m　short radius b = 6,356,774.7192 m
flattening f = (a-b)/a = 1/298.25

Geodetic datum：based on the first order triangulation point named Fu-tse-shan.
Longitude $120^0$58'25.975"　Latitude $23^0$58'32.340"
The azimuth to Tou-chi-shan = $323^0$57'23.135"

Elevation datum：Taiwan Island based on the mean sea level of Kee-lung.
Pescadores based on the mean sea level of Ma-kung.

3.2 TWD 97

In 1997, the Ministry of Interior announced the TWD 97 based on the determinations of International Association of Geodesy and International Geophysical Union in 1997. The data are as follows：

Earth ellipsoid parameters：long radius a = 6,378,137 m short radius b = 6,356,752.31414 m

flattening f = (a-b)/a = 1/298.25722210

GPS elevation survey：The elevation got from GPS survey is the height of ellipsoid. It should be deducted the geoid undulations to obtain the orthometric height.

4. PHOTO BASE MAP PRODUCTION

4.1 Analog Mapping System

From the fiscal year 1976 to 1999, the analog photomap production reached a total of 15,160 sheets. The details are as follows：

Table 1 Production of Analog Maps

Fiscal Year	Areas	Completed Sheets	Scale
1976-1982 (Base map)	Taiwan, Pescadores	3,209 564	1/5,000 1/10,000
1983-1987 (Base map 1st revision)	Taiwan (western urban areas)	2,000	1/5,000
1985-1989 (Coastal map)	Taiwan (coast region)	3,256	1/1,000
1987-1999 (Forest map)	National forest (37 working circles)	3,731	1/5,000
1989-1995 (Base map 2nd revision)	Taiwan (western urban areas)	2,400	1/5,000
Total		15,160	

4.2 Digital Mapping System

From the fiscal year 1995 to 1999, the digital photomap production was 1,580 sheets. The details are as follows：

Table 2 Production of Digital Maps

Fiscal Year	Areas	Completed Sheets	Scale
1995-1999 (Base map)	Tai-chuug,Nan-ton,Chang-hua, Yun-lin,Chia-yi,Kao-hsiung, Ping-tung	856	1/5,000
1997 (Photomap)	NTU Experiment Forest Erh-chung spill way	80 40	1/5,000 1/1,000
1997-1999 (Forest map)	National forest 6 working circles	604	1/5,000
Total		1,580	

5. DIGITAL MAPPING PROCEDURES

5.1 Flight Plan

(1) Formulate the aerial photography implementation project (includes：areas to be photographed, flight routes, flight altitude, photo scale, photo end lap and side lap requirements, weather

condition etc.)

(2) Application for aerial photography. (Ministry of Interior)

(3) Application for special flight .(Ministry of Communication)

5.2 Ground Control Targeting

Prior to aerial photography, the ground targets must be placed on the control points in the areas to be photographed. The white rectangular plastic sheets are laid out around each control point to form a landmark in the shape of a cross or the letter Y or T. This will facilitate the identification of the location of the control points to be shown on the photographs.

5.3 Aerial Photography

Aerial photography is implemented by the Agricultural and Forestry Aerial Survey Institute in cooperation with the Aeronautic Team of the Ministry of Communication. Two aircrafts, Super King Air Beechcraft 200 and Beechcraft 350 with GPS navigation are used to take the aerial photographs for mapping purposes. The camera used are Zeiss RMK TOP series, focus 15/23 and 30/23. The flying crew consists of a pilot, a copilot, a cameraman, a supervisor and a mechanician.

5.4 **Photo Processing**

Black/White Aerial Film Processor and Color Aerial Film Processor are used for photo processing.

5.5 Ground Control Survey

There are two ground control survey systems. One is horizontal and the other is vertical. Trimble SSI and Trimble 4700 are used for the horizontal control survey and the Wild 2002A digital level is used for the elevation surveys based on the benchmarks on the known elevation point.

5.6 Photo Scanning

There are two instruments employed for digital photo scanning . One is Photogrammetric Workstation (PS-1) used for individual films, resolution ranges from 7.5, 15, 22.5, 30, 60, 120, 240 micron. The other is Photogrammetric Workstation (PS-TD) used for both roll films and individual films, resolution ranges from 7, 14, 21, 28, 56, 112, 224 micron.

5.7 DTM Recording

Ground DTM = 40m x 40m or 20m x 20m by manual

Cover DTM = 9m x 9m by automatic Match-T Program

5.8 Measurements and Triangulation

Aerial triangulation is a triangulation survey based on aerial photographs to minimize ground survey work. Each aerial triangulation block consists of about 200 maps. The control points along the boundaries of the triangulation block are GPS surveyed, but the control points inside the block are measured from photographs. With the aid of a computer---Zeiss C-100 Planicomp Analytical Steroplotter, the PAT-M-43 program is used for aerial triangulation computation. All the measurements on aerial photographs are adjusted and tied to the ground coordinates.

5.9 Contour Line Plotting

Zeiss P33/PC Digital Analytical Stereoplotter is used for the contour line; break line; hydrograph and spot height plotting.

5.10 Orthophoto Production

The Intergraph ImageStation is employed for contour lines plotting and orthophoto production. The orthophotographs are rectified and printed based on the digital terrain data measured from the stereo model.

5.11 Field Photo Identification

The orthophotos are field identified by the field team to add the names of places, buildings, administrative boundaries, road categories and numbers, landmarks, species of forest, crops and so forth.

5.12 Map Manuscript Compilation

The compilers are checking orthophotos and contours to ensure that are matched properly. The map corners, map borders and grids are then plotted on the orthophotos and annotations are made on the overlay of orthophotos.

5.13 Field Editing

In addition to examination at each working stages, one-tenth of the completed photomaps are selected for field editing to check if the position and elevation of ground features shown on maps meet a standard map practices, and whether the annotations and features are correct.

5.14 Drafting

The maps are drafted on different coverage's such as the contour line layer, annotation layer, image layer and so forth. The negatives of composite map film are made through the MapSetter 5000.

5.15 Photo Map Printing

The Gordon contact printer is used for the black and white photomap printing. The color map printing is carried out by the 401 mapping factory, Combine Service Force.

6 MAP DISTRIBUTIONS AND UTILIZATION

All the finished photomaps are stored and saled by the Agricultural and Forestry Aerial Survey Institute upon request. The uses of photo base maps include：

(1) Planning for agricultural production, forest management, resource development and land use.

(2) Serving as a basis for the planning of various economic projects like highways, railways, airports, harbors, telecommunication facilities, oil pipelines, industrial zone and mine field.

(3) Supplying the basic data for regional planning, urban development, land taxation, local construction and population censuses.

(4) Administration management by the government and civilian agencies.

7. FUTURE DEVELOPMENT

(1) Establishmen of the basic control points in the central mountain areas.

(2) Study on the production of 1/5,000 map by using the IKONOS satellite images with 1 m resolution

(3) Introduce the Synthetic Aperture Radar (SAR) to overcome the weather problem.

8. CONCLUSION

In order to meet the tendency of digital mapping system, the Institute purchased the advanced aerial survey airplane with GPS navigation and RMK TOP aerial cameras, digital mapping instruments year by year. From the trial to mass production, it is really a journey to undergo all the hardships.

At present, 15,160 sheets of analog photomaps and 1,580 sheets of digital photomaps have been completed. These completed photo base maps are widely used by the people of all sectors and have won nation-wide acclamation because of their delicacy and accuracy. It has made an outstanding contributions to the promotion of photomap production and national economic development in Taiwan.

REFERENCES：

Intergraph, July 1993.ImageStation Stereo Display (ISSD) User's Guide.

ZEISS, August 1996.AutoScan (TD) User's Guide

Ministry of Interior, Executive Yuan., September 1996. Mapping Standard for Digital Photo Base Map.

INTEGRATION OF WEB-BASED GIS AND ONLINE ANALYTICAL PROCESSING

SHAN Yin, LIN Hui
Department of Geography, The Chinese University of Hong Kong
{shanyin, huilin}@cuhk.edu.hk
FU Wai Chee
Department of Computer Science and Engineering,
The Chinese University of Hong Kong
adafu@cse.cuhk.edu.hk

KEY WORDS: Spatial OLAP, Web-based GIS, Data Mining

ABSTRACT:

Nowadays, huge volume of geo-referenced data has been available to geographers and other scientists. This data-rich environment is considerably different from the data-poor environment when Geographic Information System (GIS) originated. Furthermore, although Web-based GIS improved the accessibility, simple query and retrieval function of Web-based GIS cannot meet the need of geographers and other scientists. On-Line Analytical Processing (OLAP) occurs to facilitate the decision-maker to gain insight from large treasury of data, instead of drowning in the sea of unmeaning data. We believe that OLAP should be integrated into GIS so that we can make the most of the geographic data.

In this paper, we would give a very brief introduction to OLAP, Web-based GIS and related techniques first. Then the system architecture for integrating OLAP and Web-based GIS is proposed. Subsequently, spatial OLAP server is examined. We take a prototype system, which is under development, targeting on facilitating users' access to OLAP function through Internet, as an example. A conclusion is given at last.

With the advance of Web technology, Web-based GIS has already become one of the focuses of GIS research. Many Web-based GIS systems have been built around the world. Even some commercial software packages are now available which make the construction of Web-based GIS systems easier than ever (ESRI, 2000a, 2000b). However, most Web-based GIS systems have limited analysis functions, let alone mining knowledge interactively from the precious geo-referenced data. Web-based GIS with OLAP style makes geo-referenced data more understandable to users, which leads to detection of implicit but valuable patterns and associations possible.

Furthermore, huge volume of data is now available. Traditional GIS is only a good repository of geographical information, rather than helping scientist to gain insight from these data. Spatial OLAP and other data mining technique can meet this end. Spatial OLAP help scientist observe these geo-referenced data from different perspective and various levels of concept hierarchy.

Introduction

Data mining and knowledge discovery in databases is relatively a new field of study. It can be understood as the discovery of interesting, implicit, and previously unknown knowledge from large databases (Frawley, 1991). Spatial data mining is a promising field of data mining, which intends to extract implicit knowledge from spatial database. Some researches have been conducted in this field with good outcome. (Ester, 1997; Kroperski, 1996; Lu, 1993). Issues covered in these researches include spatial generalization, spatial clustering, spatial association detection and spatial classification.

OLAP is an indispensable part of spatial data mining, focusing on the end user's analytical requirements and computation process necessary to fulfill them. Just like OLAP, the popular operations of spatial OLAP are slicing and dicing, pivoting, roll-up and drill-down. Obviously, these interesting functions cannot be found in current Web-based GIS systems. We believe that OLAP should be integrated into Web-based GIS so that the capability of web-based GIS system will be improved greatly.

Architecture of Integrated System

The architecture of the integrated system is depicted in figure 1 in a brief way. This is a multitier structure. Concisely, it consists of three tiers. Presentation Tier publishes data through Internet and gathers requests from users. Service Tier processes request and generates response while Data Management Tier is the repository of geographical information.

As a Web-based system, users can access geographical information through Internet using popular Internet browser. Web Server communicates with Internet Map Server. Internet Map Server retrieves geographical information from Spatial Database and transform into appropriate format before sending the data to a Web Server. Some complicated requests which cannot be handled by Internet Map Server, such as drilling

down and rolling up, are handed to Spatial OLAP Server for processing. Spatial OLAP Server processes data retrieved from Spatial Database, combining with hierarchy information and maybe materialized data, to get the results and the then transfers to Internet Map Server for publishing through Internet.

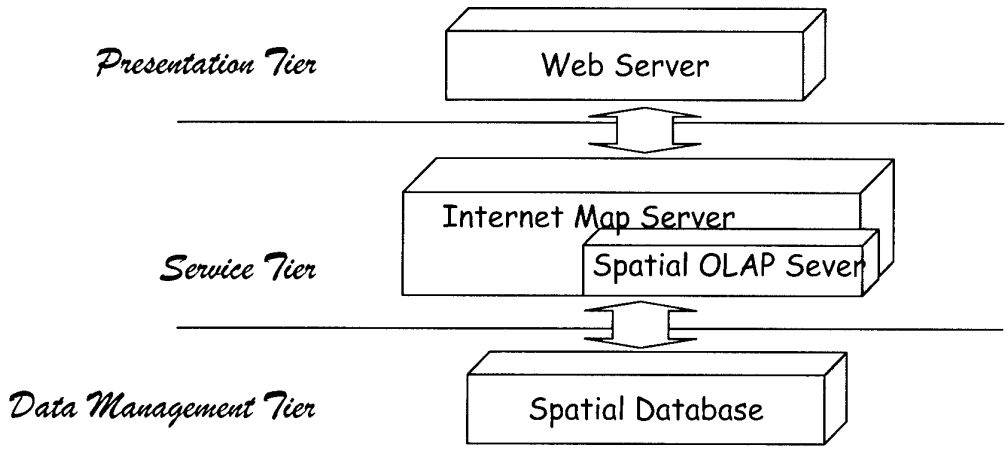


Figure 1. Architecture of Integrated System

The general architecture seems easy to understand. Even some commercial packages are available for some of the services mentioned above which can accelerate system construction. Microsoft IIS, ArcIMS and ArcInfo are good examples for these services respectively. However, Spatial OLAP Server deserves more attention. We would focuses on it in next section.

Spatial OLAP Server

The main requirements of OLAP server include supporting multiple users, handling huge volume of data efficiently as well as supporting rich OLAP operations. Multiple users access is very common nowadays, especially to network applications. Typical OLAP operations are roll-up, drill-down, slice and dice, pivot. Spatial OLAP server should implement all of these functions. Generally OLAP runs against very large dataset. Hence efficient and effective access methods are critical. Furthermore, when it comes to spatial data, the situation becomes more complicated (Egenhofer, 1994).

To access spatial dataset efficiently, many methods and models have been proposed from the perspective of databases (Egenhofer, 1994; Aref, 1991). In addition to these kinds of effort, materialization of view (Harinarayan, 1996; Stefanovic, 1993) and indexing are very promising fields. In (Harinarayan, 1996), a lattice framework is

presented to express dependency among view. With the help of this framework, a greedy algorithm is developed to choose proper views to materialize so that response time is shortened. Stefanovic (1993) improves the algorithm above according to the characteristics of spatial measures. Indexing on summary tables (subcubes of the data cube) would enhance the efficiency of query further, Gupta (1997) propose algorithm for index selection for OLAP which takes efficient use of space into consideration. We would employ these achievements in our system.

Regarding data storage, the spatial data and its attribute are managed by geographical information systems in our system. The non-spatial data, metadata and concept hierarchy are stored in relational DBMS (RDBMS). Spatial OLAP server manages the materialized view which can shorten response time greatly. Data cube, which is constructed and managed by OLAP server, makes it possible for users to observe data from various concept levels. There are two major direction in implementing OLAP Servers, namely Relation OLAP (ROLAP) and Multidimensional OLAP (MOLAP). ROLAP extend traditional relational server to support multidimensional view while MOLAP utilize a direct way, such as, multidimensional array, to manage multidimensional information. ROLAP integrates naturally with existing technology and standards, which is reliable and scalable whereas MOLAP provide efficiency in storage and operations because of its direct representation of multidimensional data. (Zhao 1997; Shoshani, 1997) The former is adopted in our system

Conclusion

Spatial OLAP is a fresh but promising field of research. Its integration with Web-based GIS is an even more interesting area. Web technology makes spatial OLAP more accessible to decision maker. Spatial OLAP equips Web-based GIS important functions for decision support. So far there many questions to them remain open, such as automatic construction of concept hierarchies, data integration, incremental update of spatial data cube.

References

1. Aref, Walid G., et al., 1991. Extending a DBMS with Spatial Operations. In: Advances in Spatial Databases, Proceedings of Symposium on Large Spatial Databases, SSD'91.
2. Egenhofer, M. J., 1994. Spatial SQL: a query and presentation language. IEEE Transactions on Knowledge and Data Engineering, Volume: 6 No. 1, Feb. 1994

pp.86-95.

3. Erik, T., 1997. OLAP Solutions: Building Multidimensional Information Systems, Wiley, US.
4. ESRI, May 2000a (Access Date). The ArcIMS 3 Architecture. Available at: http://arconline.esri.com/arconline/whitepapers.cfm?PID=6
5. ESRI, May 2000b(Access Date). ArcIMS 3 Features and Functions. Available at: http://arconline.esri.com/arconline/whitepapers.cfm?PID=6
6. Ester, M., 1997. Spatial Data Mining: A Database Approach. In: Advances in Spatial Database. SSD'97 Berlin.
7. Frawley, W. J., et al., 1991. Knowledge Discovery in Databases: An Overview. In: Knowledge Discovery in Database. Edited by Piatetsky-shapiro, G., et al., AAAI/MIT Press, Menlo Park, CA
8. Gupta, H., Harinarayan, V., Rajaraman, A., Ullman J. D., 1997. Index Selection for OLAP. In: 13th International Conference on Data Engineering, pp.208-219.
9. Harinarayan, V., Rajaraman, A., and Ullaman, J. D., 1996. Implementing data cubes efficiently. In: Proc. 1996 ACM-SIGMOD Int. Conf. Management of Data, Montreal, Canada, June 1996, pp205-216.
10. Koperski, K., et al, 1996. Spatial Data Mining: Progress and Challenges. In : Proceedings of SIGMOD'96 Workshop, Data Mining and Knowledge Discovery (DMKD'96), Montreal, Canada, June 1996.
11. Lu, W., et al., 1993. Discovery of General Knowledge in Large Spatial Databases. In: Proc. of 1993 Far East Workshop on Geographic Information Systems (FEGIS'93), Singapore, June 1993, pp. 275-289
12. Stefanovic, N., 1993. Design and Implementation of On-Line Analytical. In: Processing of Spatial Data. M.Sc. Thesis, Computing Science, Simon Fraser University, Canada. Available at: http://db.cs.sfu.ca/sections/publication/theses/theses.html
13. Shoshani, A., 1997. OLAP and statistical databases: similarities and differences. In: Proceedings of the sixteenth ACM SIGACT-SIGMOD-SIGART symposium on Principles of database systems. pp.185 - 196
14. Zhao, Y., et al., 1997. An array-based algorithm for simultaneous multidimensional aggregates. In: Proceedings of the ACM SIGMOD international conference on Management of data, pp. 159 - 170.

THE STUDY OF PRECIPITATION EFFECTS ON AMSU AND APPLICATION OF AMSU ON TYPHOON MONOTORNING

Kung-Hwa Wang
Meteorological Satellite Center, Central Weather Bureau
64, Kung Yuen Rd. Taipei,100
Tel:(2)2349-1238 Fax: (2)2349-1259
E-mail: peter@msc.cwb .gov.tw
TAIWAN

KEY WORD: AMSU, microwave, precipitation typhoon

ABSTRACT: AMSU (Advanced Microwave Sounding Units) is a new instrument on NOAA series. A forward model was developed and it included emission and scatter mode. From simulation of this radiation transfer model many characters of AMSU are understood. Total water vapor (TWV) retrieval algorithm was improved and validated with RAOB data. Improved results from estimated TWV compared to RAOB data are clear. AMSU Brightness temperatures (TB) have some relationship with rain rate. There is almost not any evidence shows that the relationship is existing among observed AMSU data and rain rates. AMSU is a very good tool to make typhoon structure more clear, and it is easier to identify center of typhoon than before.

1. Introduction

After NOAA-15 is operating from 1998, AMSU data is the most interesting data in ATOVS data sets. Because it was a new instrument in TIROS-N series, not so many utilization reports were published. Pre-study and research were performing in NESDIS/NOAA and relative association before satellite was lunched. The advantage of AMSU has not effectes by not rain cloud. The specification of AMSU was published in NESDIS User's Guide (Goodrum etc, 1997). Norman Grody (1999) described some useful AMSU retrieval algorithms. Which include TWV, rain identification, scattering index, and Liquid Water Contents (LWC) and it is worldwide use.

AMSU-A is a multi-channel microwave radiometer that is be used for measuring global atmospheric temperature profiles and provide information on atmospheric water in all of its forms (with the exception of small ice particles, which are transparent at microwave frequencies) from the NOAA 15 spacecraft and following series. AMSU-A is a cross-track, line-scanned instrument designed to measure scene radiance in 15 discrete frequency channels which the calculation of the

vertical temperature profile from about 3 millibars (45 Km) pressure height to the Earth's surface.

AMSU-B is a 5 channels microwave radiometer. The purpose of the instrument is to receive and measure radiation from a number of different layers of the atmosphere in order to obtain global data on humidity profiles. It works in conjunction with the AMSU-A instruments to provide a 20 channel's microwave radiometer. AMSU-B scan patters and geometric resolution translate to a 16.3 Km diameter cell at nadir at a normal altitude of 850 Km.

2. Development of AMSU forward model

2.1 The background of moded's development

RTTOV-7 was released recently, it seems is the best AMSU forward model. On 1999 JAN. , NOAA-15 is running on orbit for a while and the data is routing receiving. Before using AMSU data, the characteristics of AMSU should be make clear. Except FASCOD3P (Fast Atmosphere CODE version 3 Plus) was in hand, no other's model could be used. FASCOD3P is a line by line model and very precise model, because it is so complicate that uneasy to apply on real data and it is uneasy to modify the codes to fit the requirement of research. A radiation transfer model, which combines emission and shattering modes in microwave bands, is needed. Develop a forward model by myself is the last choice at that circumstance.

In this forward model, which the absorption coefficients of Oxygen, water vapor, ozone and liquid water are adapted from Liebe (1985) and Rosenkranz (1998). Scattering model is used Eddington Approximation, and the coding was developed by Kumerrow (1994). In cloudy and raining condition, the most uncertainty factor is cloud physical, which include cloud height, vertical distribution of liquid water contents, water vapor, rain and ice. Those cloud parameters usually can not be obtained by observe system routinely. CIMSS provided a cloud model in this model, which is a simulation model from hurricane Bonnie (98238).

In order to demonstrate the effects of precipitation on AMSU upward radiance, the parameters of cloud model, which includes water vapor, liquid water content (LWC) and precipitation was normalized as function of surface rain rate. Dependding on surface rain rates and cloud top temperature, cloud types were classified into 9 categories. Each of these 9 categories has different vertical distribution of hydrogen. For different absorption line coefficient there are a little different transmittance in microwave frequencies. About liquid water absorption line, because of coefficients of Kummerrow's are divided into two groups, there is a gap at 100GHz. So Leibe's coefficient is used in this model.

2.2 Validation of the model

A satellite pass in 15-NOV-1998 was chosen as real data. All RAOB data under satellite pass were collected and treated as model's input parameters. Assumed all data set were under clear condition, and surface emissivity was set to same value over ocean, and AMSU channel 5 was chosen for comparison because channel 5 is less effect by surface situation. The compared result of estimated TB and satellite observed TB is shown on Fig. 1. Most of the data is distributed along a line, but some of the point scatter from the strength line, which are caused by precipitation and surface emissivity. This model is can be used for AMSU data simulation.

2.3 Characteristics of AMSU data on precipitation and liquid water content

With different rain rate and maintain other parameters in same situation, then we may get the variance of TB that has effectes by rain rate. AMSU channel 1-4 and channel 15-17 are change significant with rain rate from 0 to about 30mm/hr. AMSU channel 1,2 and 15,16, 17, those are surface channel, and has effecte by precipitation. The effects of LWC on AMSU upward radiance are similar features as effect of precipitation. It is found that the influences of precipitation and LWC have similar intensity on AMSU.

Having 2343 Km swath width, local zenith scan angle of AMSU is up to 57 degree, so the limbs correct is needed for further retrieval process. From the simulation of the AMSU forward model, TB of AMSU channel 1 and 2 are increasing when local zenith angle is increasing, others are decreasing. Sea surface is cold to AMSU channel 1 and 2, surface component is decreasing when local zenith scan angle is increasing, then upward TB of channel 1 and 2 are increasing. TB of other channels decreasing with scan angle increasing is caused by optical depth is increasing.

3. Improvement of total water vapor retrieval

After AMSU data was available, research group of Dr Grody (1999) announced a few algorithms for AMSU instrument to retrieve sea ice, water vapor, cloud liquid water (LWC), rain identification and snow cover. Those algorithms have great contribution on global hydrogen retrieval by AMSU in preliminary stage. The accuracy of TWV could not fit the requirement of local weather services, such as in Taiwan area and tropical area. In this situation, an improved algorithm of TWV retrieval was developed.

In order to reduce the influence of surface emissivity to TB of AMSU, nine RAOB data on island and near Taiwan area were selected. TWV is estimated from those RAOB data and it was regarded as ground truth. Most of the water vapor is located under 3000 meter, so low level WV is very close to TWV. When satellite

observed AMSU data pass over those islands RAOB data were collected as well. From the scattering diagrams between TWV and TB of each AMSU channel, AMSU channel 1, 2 and 16 have better correlation with TWV. So channel 1, 2, and 16 of AMSU were chosen for retrieval. Linear multiple regression function was estimated from above TB of channels and collocated RAOB data. Then TWV can be retrieved from AMSU data set. Estimated results are shown on Fig. 2. 3. Statistically it is shown that this improved method is obviously better than original one and the spatial resolution is increased either.

4. Monitoring Typhoon by AMSU

When typhoon is severe, there is almost not problem to identify the center of typhoon. When typhoon or tropical cyclone is weak, or the eye of typhoon is masked by cirrus cloud, it is very difficult to identify the center of cyclone. Traditionally base on the cloud bands of the cyclone to track the eye of typhoon, such as Dvorak (1982). This identification skill strongly depends on the experience of the weather analyst. When center of typhoon is unclear, the forecast of moving direction of typhoon could be missed. Identify center of typhoon is a very important issue in tropical and subtropical area weather services.

Viewing from vertical distribution of AMSU weighting function, each channel of AMSU-A can present vertical structure of temperature at specific level. It is shows in Fig. 4. Viewing the vertical structure over a cross line that passes through center of typhoon. The surface warm core of typhoon and cold core at high altitude is significant. Weak typhoon is shows on Fig. 4. The low-level warm core still is very easy to be identified. Not only center of typhoon, but also the strength of typhoon could be defined also. Further more researches are keep on going.

5. Conclusion

A developed forward model is presented that could be used in real data simulation and widely used in research. Not only clear sky but also cloudy or rain could be a simulation tool also. Using AMSU data on weather analysis was mentioned in this research, such as using AMSU may provide total water vapor or low level water vapor and typhoon tracking successfully. The relation between AMSU and wind speed is an interesting and useful article in weather forecast, and it will be next research object. The original design purpose of AMSU is not used for precipitation retrieval. Actually, the correlation between rain rate and AMSU observed TB is poor, but rains still affect upward radiance of AMSU surface channel. Removing rain effects on AMSU data utilization, or getting more precise surface emissivity to retrieval rainfall information from AMSU is another task in the near future.

Since AMSU data was available two years passed, and NOAA-16 was lunched also. AMSU is not a new instrument any more, and other new microwave instruments are in progressing, which means microwave remote sensing may create a new window for satellite weather service.

6. Reference

Dvorak, V.F., 1982: A technique for the analysis and forecasting of tropical cyclone intensities from satellite pictures. NOAA Tech. Memo. NESS 36, Dept of Comm.

Goodrum, Geoffrey, Katherine B. Kidwell, Wayne Winston, 1997, NOAA KLM USER's GUIDE, NOAA/NESDIS

Grody, Norman, Fuzhong Weng and Ralph Ferraro, 1999, Technical Proceedings of The Tenth International ATOVS Study Conference, Boulder CO

Kummerow, C. L. Giglo,1994: A passive microwave technique for estimating rainfall and vertical structure information from space, Part I: algorithm description, J. of Appl. Meteo. , 33, 3-18.

Liebe, H. J. , 1985, An updated model for millimeter wave propagation in moist air, Radio Science, 20, 1069-1089.

Rosenkranz, P. W., 1998, Improved rapid transmittance algorithm for microwave sounding channels, International Geoscience and Remote Sensing Symposium (IGARSS'98), Seattle, WA

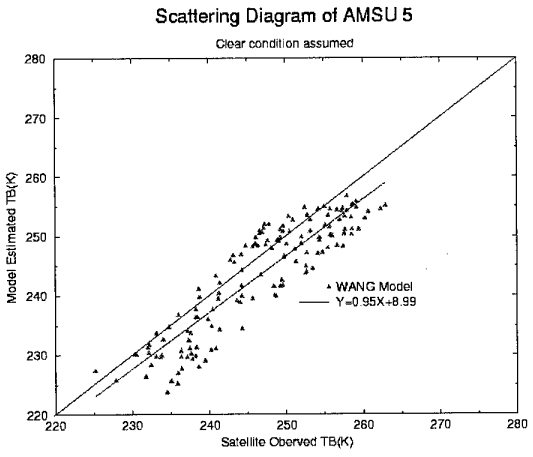


Figure 1. Scattering diagram of estimated TB and satellite observed TB. Data are almost linear distribute along a line. Some points disperse from central line are caused by unknown precipitaion and surface emissivity.

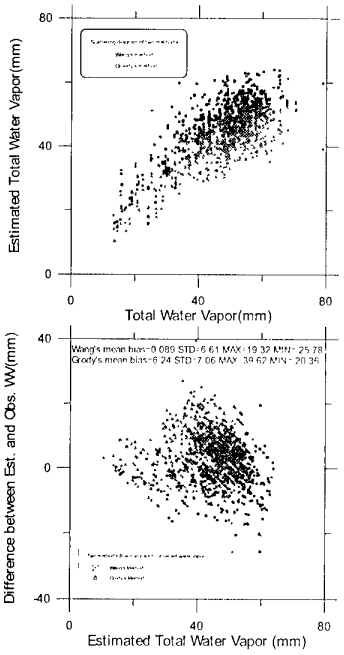


Figure 2. Scatter diagram of two result of Grody's and Wang's TWV with RAOB's TWV. Lower graphic is the difference between these two algorithm and RAOB's results

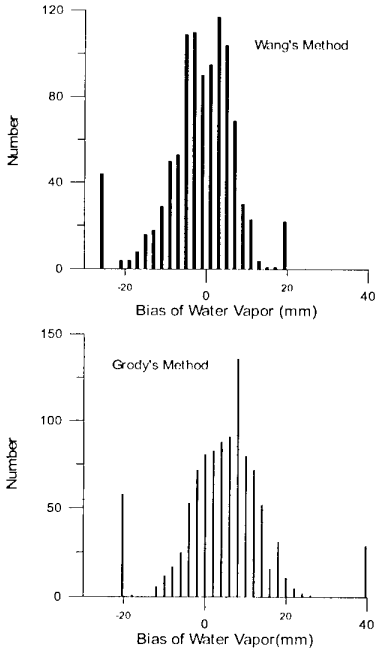


Figure 3. Histogram of two results of Grody's and Wang's TWV algoritms

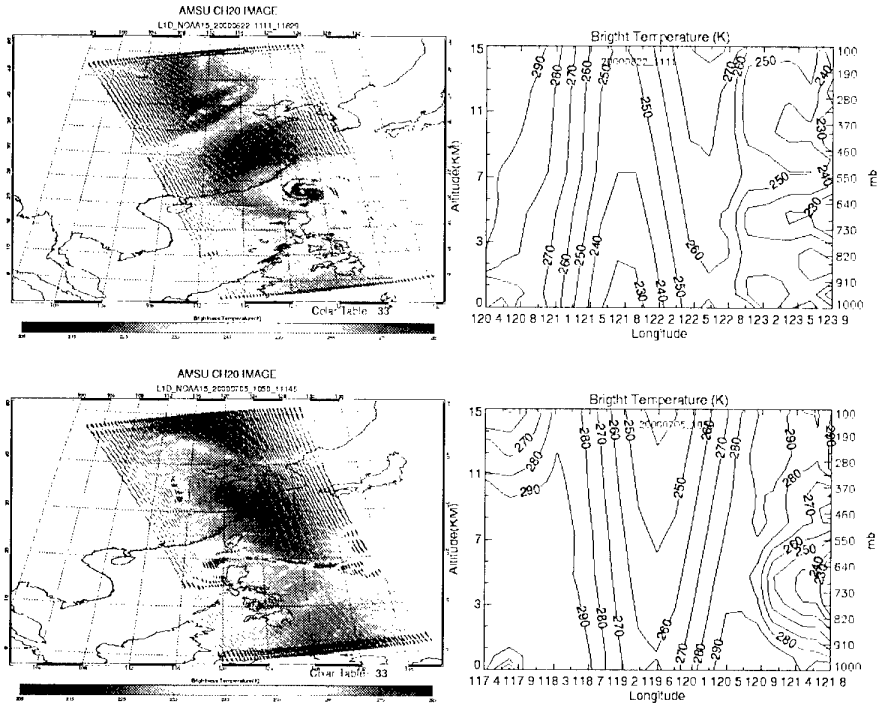


Figure 4. Upper left are sever Typhoon Bilis (0010), announced eye of typhoon is located on 22.2N, 122.2E. Upper right is structure of typhoon center. Lower left is weak typhoon Kaitak(0004), announced eye of typhoon is located on 18.7N, 120.7E

The 21st Asian Conference on Remote Sensing
December 4-8, 2000 Taipei, TAIWAN

Phenology Detection of Forest Area Using Satellite Data

Asako NAGAO, Koji KAJIWARA, Yoshiaki HONDA
Center for Environmental Remote Sensing, Chiba University
1-33 Yayoi-cho, Inage-ku, Chiba city, Chiba, 263-8522
Tel: (81)-43-290-3845 Fax: (81)-43-290-3845
Email: nagao@ceres.cr.chiba-u.ac.jp
JAPAN

KEY WORDS: Forest, Remote Sensing, Phenology, Reflectance, NDVI

ABSTRUCT: Detecting Phenology of forest area using satellite data is effective way for the global environmental problems. We have established an observation tower in a forest area and been gotten ground truth data. By using these data, we decide the active period of forest area, and we could check satellite data how accurate data can detect this period.

1. INTRODUCTION

Global environmental problems, for example, greenhouse effect, Extinction of tropical rain forest, desertification have relevance to forest resource deeply and it is more and more necessary to monitor the condition of environment with a big scale and real time by satellite data. This method makes it possible to estimate vegetation amount of forest area but active period of forest area depends on the period of photosynthesis and we need to specify the time when photosynthesis is going active.

2 OBJECTIVES

To specify the period of forest is in active, it is important to detect the time when forest starts and finish their activities throughout the year. After all we need to know a germination period and the period when leaves fall and compare it with satellite data.

3 MEASUREMENT SYSTEM OF GROUND TRUTH DATA

For ground truth data, we have established an observation tower in Yatsugatake forest area, Kobuchizawa, Yamanashi Pref., Japan.(Fig.1) On the tower, we have set up spectrometer, CCD camera which catch the image of same place of spectrometer, and camera.(Fig.2)

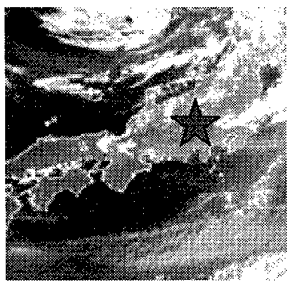


Fig.1 Measurement Site

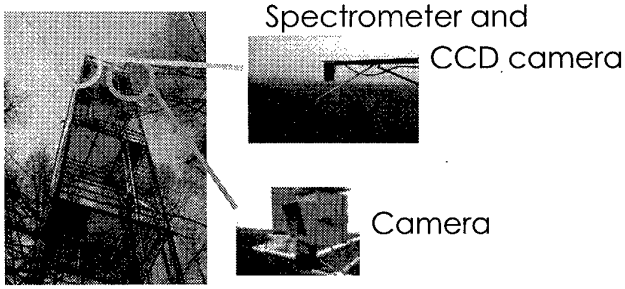


Fig.2 Measurement System of Observation Tower

The observation tower is about 25m tall and the camera and the spectrometer has been set at top of the tower. The camera takes photo once a day, and spectrometer and CCD camera take data since 6:00 until 18:00 every 15 minute. Measurement system of spectrometer is as follows (Fig.3).

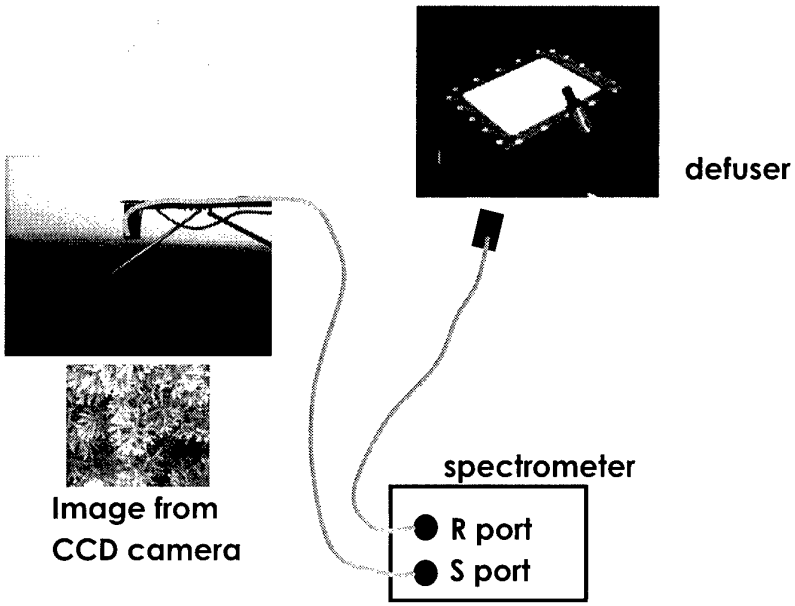


Fig.3 Measurement System of Spectrometer on the Tower

4 GROUND TRUTH DATA

4.1 CCD camera image and camera image

CCD camera data and camera data shows as follows(Fig.4). From these data, we can specify the condition of increasing of vegetation.

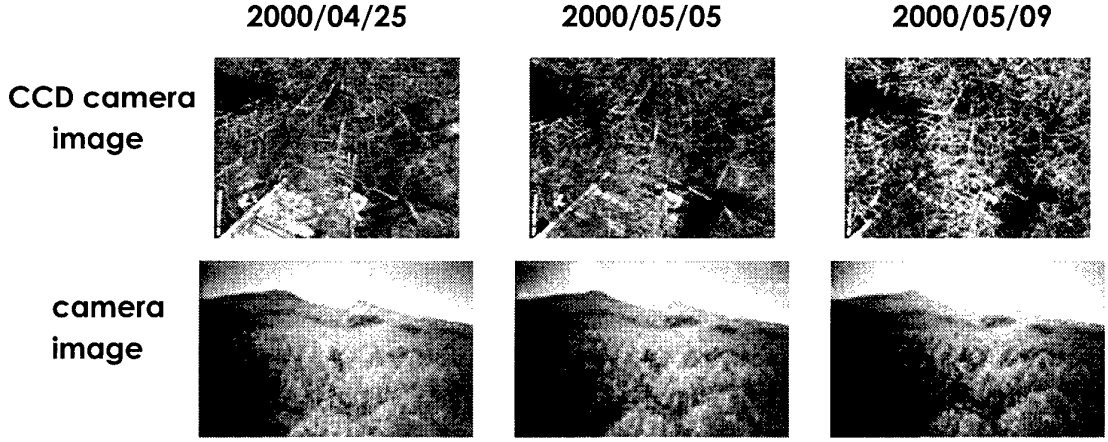


Fig.4 CCD camera image and Camera image

4.2 Spectrometer Data

Spectrometer is used to know the reflectance of leaves. Leaves show its reflectance highly at NIR, so we can know the time when leaves come out from

spectrometer. By using this data, we have checked the value of NDVI. NDVI shows the amount of vagetation and it would be showed as follows:

$$NDVI = (NIR - RED) / (NIR + RED) \qquad (2.1)$$

This width of RED and NIR is depending on the sensor of satellite, but this time we use these values based on NOAA / AVHRR data. That is:

RED: 580-680nm NIR : 725-850nm

This figure(Fig.5) shows the change of NDVI at Yatsugatake forest area in April 1st until May 15th this year.

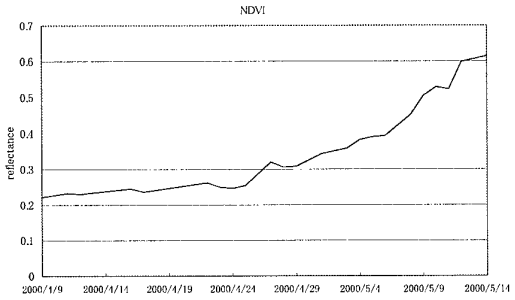


Fig.5 Change of NDVI of spectrometer at Yatsugatake

4.3 Satellite Data

For satellite data, we used NOAA/AVHRR data. NOAA/AVHRR data have 1km/pixel resolution and we used it of Yatsugatake Area for two months(Fig. 6).



Fig.6 Satellite(NOAA/AVHRR) data

4.4 Result of analysis

For image data (CCD camera image and camera image), to extract the amount of vegetation, we used irvep program(Ichikawa, 2000). And for spectrometer data and satellite data, we calculated the values of NDVI for two months. The result of vegetation amount by each of the image data(CCD camera and camera) show as follows(Fig.7.1), and the result of NDVI(spectrometer data and NOAA/AVHRR data) shows as follows(Fig.7.2) :

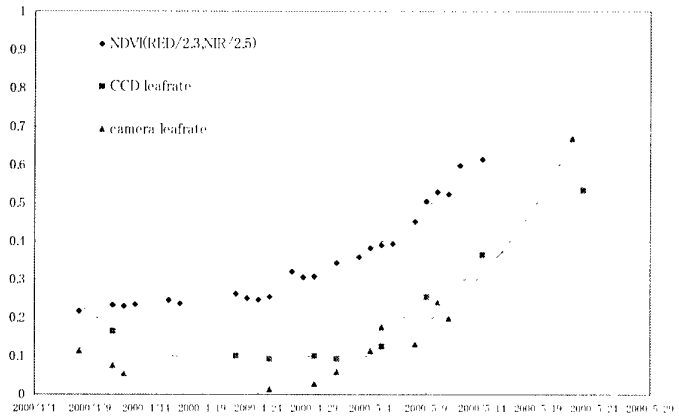


Fig.7.1 Changes of Vegetation amount of CCD camera, camera and NDVI of spectrometer data

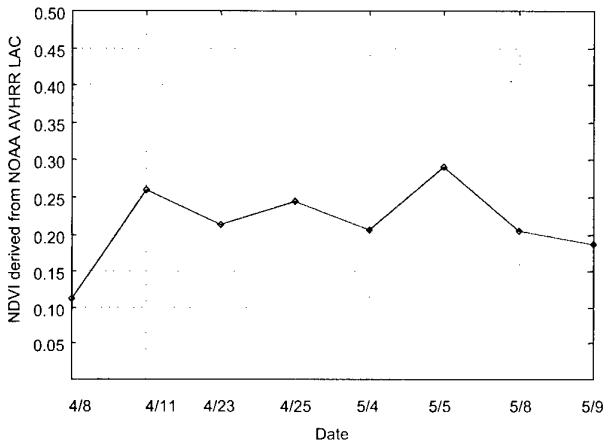


Fig7.2 NDVI of NOAA/AVHRR data

5. CONCLUTION AND PROBLEMS FOR THE FUTURE

Looking at the graph(Fig. 7.1), we can know the difference of recognition period by each of measurement system(camera, CCD camera, spectrometer). And the value of NDVI of NOAA/AVHRR is not so big compare with ground truth data(Fig.7.2). It is to say, NOAA/AVHRR data doesn't show accurately and it is clear that there is a gap between satellite data and ground truth data.

We can guess the reason why satellite data didn't show bigger value than ground truth data is because of the vapor and dust in the air over Japan. And these problems make it more difficult to specify phenology of forest area.

And, the data which we have used this time was only two months, so we have to check the past data and continue our research with a long period after this, and know the difference according to the year.

ACKNOWLEDGEMENT

This work has been supported by CREST (Core Research for Evolutional Science and Technology) of Japan Science and Technology Corporation (JST).

The 21st Asian Conference on Remote Sensing
December 4-8, 2000 Taipei, TAIWAN

UTILIZATION OF LANDSAT-5 (TM) IMAGERY FOR SUGARCANE AREA SURVEY AND MAPPING IN THAILAND

W. Hadsarang[1] & S. Sukmuang [1]
[1]The Office of Cane and Sugar Board, Ministry of Industry, Thailand
Tel : (662) 2023291-4 Fax : (662) 2023293
E-mail Address : wimonlak@narai.oie.go.th

KEYWORDS : Landsat, GIS, remote sensing, sugarcane

ABSTRACT

A visual interpretation of Landsat-5 (TM) imagery at a scale of 1:500,000 by the Procom-II projection system was initiated for a survey of selected sugarcane plantations in Thailand in the 1997/98 growing season. The study covered 48 provinces with a total area of 955,255.85 hectares (giving the equivalent production of 42.20 million tons of sugarcane). The Landsat-5 (TM) imagery was shown to be a promising tool for surveying and mapping. The area covered by sugarcane was separated from other crops by a false color composite and it was possible to delineate these in the district level at 1:50,000 map scale. There was a significant difference between the on site survey and visual interpretation. The problem concerning this technique is the clearness of the imagery. During the high sugarcane season, the geographic sectors always have high humidity and cloudy skies hindering image capture, therefore interpretation was accomplished later in the year when the atmosphere was clearer.

INTROCUCTION

Geographic information system (GIS) is recognized as an important tool for geographical surveys and has been applied in agronomic surveys, such as those for sugarcane (Jhoty et al., 1994). The technique has been used in a number of countries such as Australia (Lee-Lovick and Kirchner, 1990, 1991, Lee-Lovick et al., 1992), South Africa (Platford, 1990) and Mauritius (Jhoty et al., 1994). Thailand started a remote sensing project after collaborating in a natural resources survey with NASA in September 1971. The necessary project infrastructure was completed by 1981 and its application for agronomic purpose have been conducted for cassava and sugarcane since 1995. Each year in October, the Office of Cane and Sugar Board, Ministry of Industry must predict the official yield and subsequent price of sugarcane, so that quotas and milling allocations can be set before milling begins in November / December. The total amount of production will influence the price of sugarcane. This paper reports on the results of an application of Landsat-5 (TM) imagery to predict the plantation area of sugarcane and discusses the complication of this technology by comparing it with on-site surveys.

MATERIAL AND METHODS

Imagery from landsat-5 (TM) using film with 4^{th} ,5^{th} and 3^{rd} (red, green and blue) false color composite bands in the ratio 1:500,000 was used. Translation was achieved using a single-band compositor projector (Procom II, Gregory Geoscience Ltd., Canada). The interpretation was confirmed by field surveys using a Global Positioning System (GPS). The drafting film was transferred to a computer system by Scanner (Calcomp Ltd., U.S.A). Using Microstation software, Intergraph Raster Binary (IRASB) and Intergraph Raster Continuous (IRASC) data in the form of vectors was obtained. The plantation area of sugarcane was calculated using software Modular GIS Environmental Analysis (MGA) and Modular GIS Environment (MGE)

systems. The map of Thailand (1:50,000) for plotting, was supplied by Royal Thai Survey Department, Ministry of Defense. The results were compared with the on-site surveys of the Office of Agricultural Economics, Ministry of Agriculture and Co-operatives.

RESULTS AND DISCUSSIONS

Visual interpretation of the false color composite was capable of differentiating sugarcane plantation area from other crops such as eucalyptus, pineapple and cassava when the 4th, 5th and 3rd band (red, green and blue) were applied (Figure 1). Using this technique the sugarcane growing area was transcribed onto a map of Thailand at a scale of 1:50,000.

Estimates of the plantation area by visual interpretation and on-site surveys (Table 1) were unfortunately not comparable. The plantation area determined by on-site survey is the one adopted by the Office of Agricultural Economics, Ministry of Agriculture and Co-operatives. The on-site survey was mainly achieved by using a database of cane growers' registration records, together with interviews in some areas. The registration database was established in 1986, with updated in 1988 and 1992 but these updates only include the addition of new registrants. The lack of continuous updating and ongoing confirmation of the validity of records explains the discrepancy between the two methods.

The results have been instrumental in encouraging the Office of Cane and Sugar Board to review the sugarcane growers' registration. Application of a Global Positioning System (GPS) confirmed the visual interpretation, confirming the observations that the sugarcane plantation area is decreasing.

The most serious problem encountered by visual interpretation was lack of clarity of the imagery. Sugarcane planting is always at the same time of year, resulting in a high density of leaves and foliage, resulting in a high absorption of light during July/August, but in this period, the sky is always cloudy (Figure 2a), hindering transmission of wavelengths between the visible and infrared preventing penetration to the object. As a result, the imagery for this study was taken from December/January when it was less cloudy (Figure 2b).

As a result of this study, the Ministry of Industry has improved the computerized system including software. The application of data in the microwave region (RADAR) is also being studied. The announcement of the sugarcane plantation area and production in the near future will consider both visual interpretation and on-site surveys.

REFERENCES

Jhoty, I.; Chung, Maryse, Ah Koon, D.; Deville, J. & Ricaud, C. (1994). Digital terrain modelling for the siting of a centre pivot irrigation system in sugarcane. In L.O. Fresco, L. Stroosnijder, J. Bouma & H. van Keulen (eds). The *Future of the Land: Mobilizing and Integrating knowledge for Use Options. John Wiley & Sons Ltd., New York.*

Lee-Lovick, G. & Kirchner, L. (1990). The application of remotely sensed (Landsat TM) data to monitor the growth and predict yields in sugarcane. Proc. Austr. Soc. Sug. Cane Technol., pp 65-72.

Lee-Lovick, G. & Kirchner, L. (1991). Limitation of Landsat TM data in monitoring growth and predicting yields in sugarcane. Proc. Austr. Soc. Sug. Cane Technol., pp 124-130.

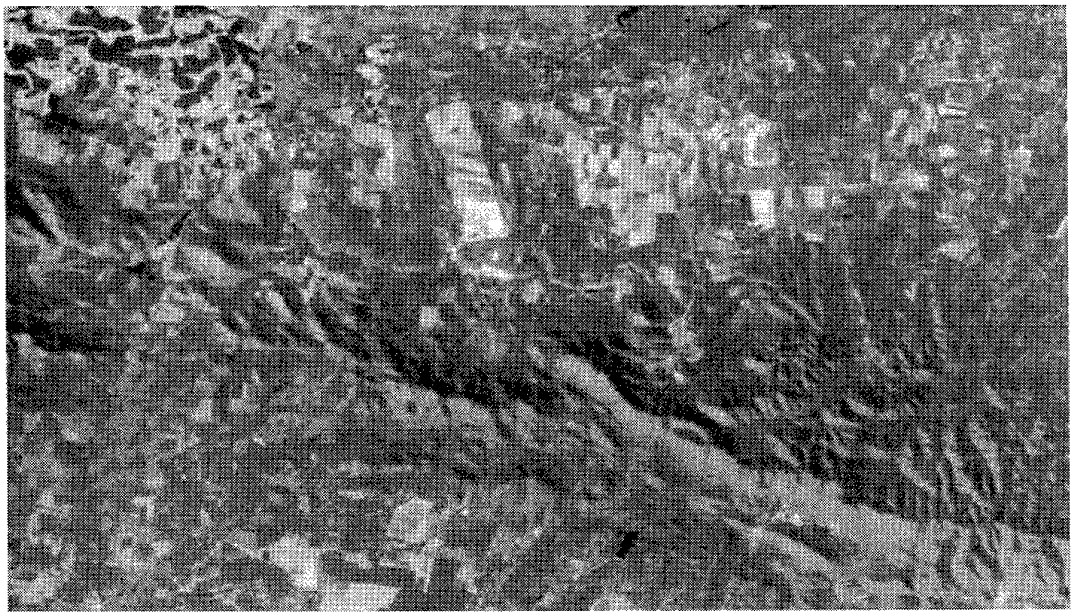
Lee-Lovick, G.; Saunders, M.; Willcox, T. & Bent, M. (1992). The establishment of a geographic information system in the Bundaberg district. Proc. Austr. Soc. Sug. Cane Technol., pp 107-115.

Platford, G.G. (1990). A geographic system for use in the sugarcane industry. Proc. S. Afr. Sug. Technol. Ass., pp 83-87.

Table 1. Comparison of estimated sugarcane planted area between the imagery interpretation and on-site survey in 1997/98 growing season.

Provinces	Sugar cane area from the Imagery interpretation (hectares)	Sugar area from the on-site survey (hectares)	Discrepancy (%)
Northern region			
Lampang	5,958.00	6,144.96	-3.14
Chiang mai	174.40	617.92	-254.31
Chiang rai	562.45	140.64	75.00
Uttaradit	12,716.96	15,244.16	-19.87
Sukhothai	36,246.00	30,178.56	16.74
Phrae	1,336.12	4,381.60	-227.93
Phitsanulok	26,910.00	10,139.20	62.32
Kamphaeng phet	69,559.00	73,130.56	-5.13
Tak	3,210.00	1,791.20	44.20
Phichit	6,262.00	5,626.56	10.15
Nakhon sawan	59,005.00	62,540.48	-5.99
Phetchabun	20,179.00	6,798.24	66.31
Central plain region			
Kanchanaburi	87,101.00	120,337.12	-38.16
Ratchaburi	27,953.00	51,539.04	-84.38
Nakhon Pathom	9,456.80	15,784.00	-66.91
Suphan Buri	62,499.00	70,429.12	-12.69
Sing Buri	4,428.32	4,792.00	-8.21
Ang Thong	4,083.00	3,886.88	4.80
Chai Nat	7,757.00	6,002.08	22.62
Lop Buri	34,769.76	33,219.68	4.46
Saraburi	9,788.00	6,173.28	36.93
Uthai Thani	10,163.00	18,572.48	-82.75
Prachuap Khiri Khan	7,409.40	12,331.36	-66.43
Phetchaburi	3,778.62	5,948.32	-57.42

Provinces	Sugar cane area from the Imagery interpretation (hectares)	Sugar area from the on-site survey (hectares)	Discrepancy (%)
Eastern region			
Chon Buri	17,350.00	34,795.20	-100.55
Chachoengsao	3,485.00	13,140.16	-277.05
Prachin Buri	2,001.00	1,189.60	40.55
Rayong	3,201.00	7,410.08	-131.49
Chanthaburi	3,323.00	4,059.52	-22.16
Sakaeo	19,366.00	9,316.80	51.89
North-Eastern region			
Udon Thani	85,960.11	81,346.88	5.37
Nongkhai	4,266.00	1,004.16	76.46
Sakon Nakhon	5,912.00	3,087.52	47.78
Nakhon Phanom	531.60	2,489.60	-368.32
Khon Kaen	66,847.88	43,420.48	35.05
Loei	15,203.00	16,804.64	-10.54
Chaiyaphum	69,182.80	65,947.36	4.68
Maha Sarakham	9,608.00	2,585.76	73.09
Kalasin	27,626.00	10,759.84	61.05
Roiet	4,863.09	1,475.52	69.66
Yasothon	3,669.60	783.84	78.64
Buriram	17,122.92	11,882.72	30.60
Nakhon Ratchasima	69660	65,948.80	5.33
Mukdahan	8,139.00	11,771.68	-44.63
Ubon Ratchathani	120.90	-	-
Amnat Charoen	188.00	-	-
Nong Bua Lam Phu	5,951.00	4,943.52	16.93
Surin	372.00	258.40	30.54
TOTAL	**955,255.73**	**960,171.52**	**-0.51**

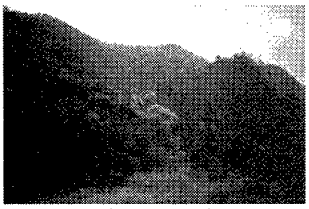




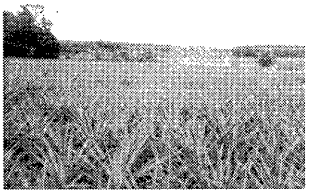
A:SUGARCANE



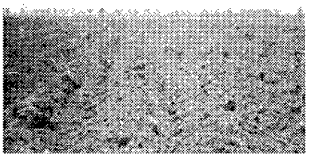
B:EUCALYPTUS



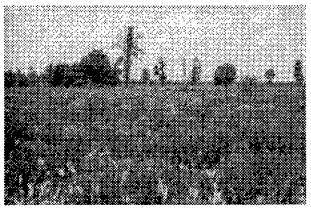
C:FOREST



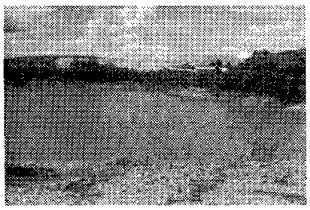
D:PINEAPPLE



E:BARE SOIL

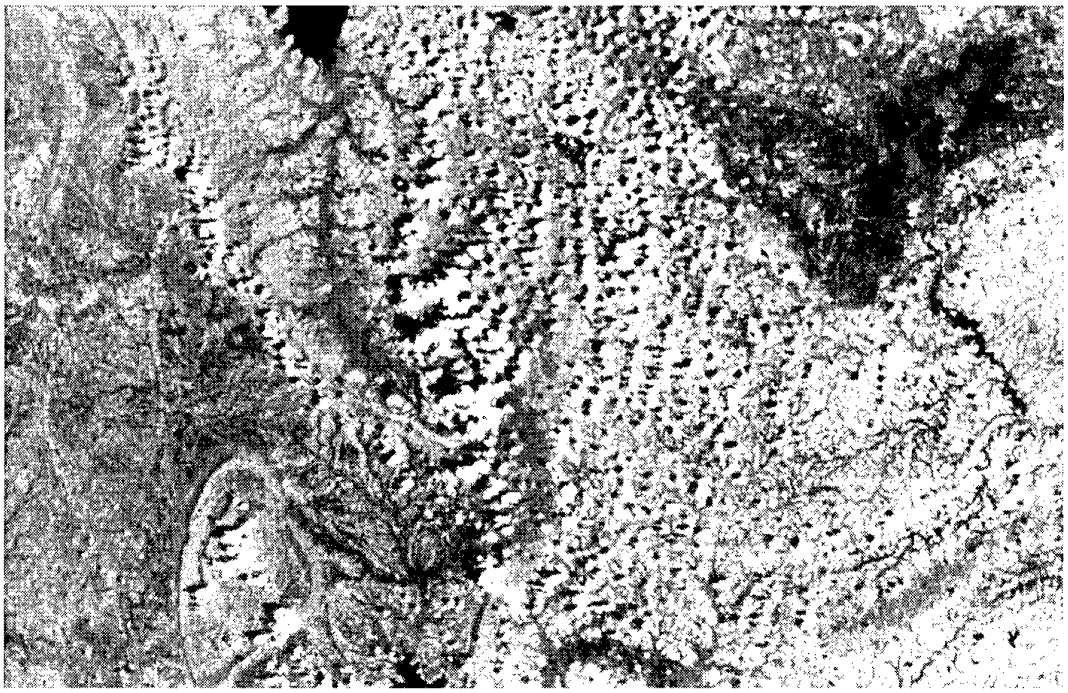


F:CASSAVA

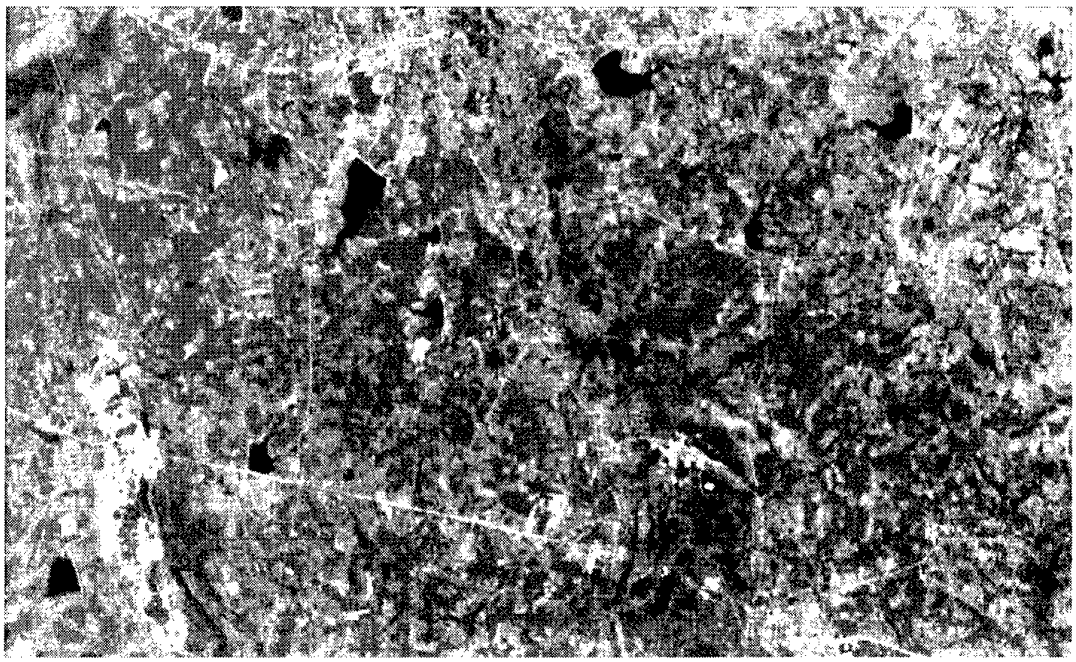


G:PRECIOUS STONE MINING

Figure1. False color composite and its interpretation



(a) cloudy



(b) less cloudy

Figure2. Imagery From LANDSAT-5 (TM) at different cloudy levels

The 21st Asian Conference on Remote Sensing
December 4-8, 2000 Taipei, TAIWAN

APPLICATION OF GIS AND REMOTE SENSING TO ANALYSES LANDSCAPE STRUCTURES

Kazuyuki Takahashi[1] and Keitarou Hara[2]

Graduate School of Business Administration and Information Science,
Tokyo University of Information Sciences,
1200-2 Yatoh-cho, Wakaba-ku, Chiba 265-8501 Japan
[1]kazuyuki@rsch.tuis.ac.jp, [2]hara@rsch.tuis.ac.jp
Tel: +81-43-236-4628 Fax: +81-43-236-2601

KEY WORDS: landscape classi-cation, regional planning, remote sensing, GIS

ABSTRACT

Landscape structure of Sakura-city, central Japan was analysed using GIS and remotely sensed data in order to examine the methodology of landscape classi-cation and e®ectiveness of utilization of GIS and remote sensing. Sakura-city is situated on the fringe of the Tokyo metropolis and urban development has been done in the suburb/rural areas. Following -ve landscape types were classi-ed on the basis of the topographic features and land cover types derived from Landsat TM data: 1. Marsh landscape, 2. Lowland rural landscape, 3. Upland rural landscape, 4. Yatsuda rural landscape, and 5. Urban landscape. Ecotopes (the minimum units of landscape) were de-ned by topographic features (altitude and inclination of slope) and land cover types. Then the characteristics of each landscape type were examined according to the composition of ecotopes. The e®ectiveness in the use of GIS and remotely sensed data was veri-ed by this study as follows: Firstly, unbiased classi-cation could be carried out using digital terrain and land cover data. Secondly, the resolution of the TM data coincides with the scale of the landscape analysis. Thirdly, the latest information of land cover could be obtained from the area concerned where the rapid urbanization is promoting.

1. INTRODUCTION

Rising public concerns on natural environment have accelerated needs in recent years to implement, as part of any development projects, speci-c measures to preserve our environment. The conservation of natural environment should not stop at simply protecting one ecosystem. As pointed out by Forman & Godron (1986) and by Forman (1995), it is essential to tackle this issue from a wider perspective - to conserve an overall landscape that represents composites of many ecosystems.

Many researchers have classi-ed the natural environment by landscape types to come up with indicator to evaluate environment (Blankson & Green, 1991; Bunce, 1996). Landscape classi-cation systems proposed so far tried to extract landscape elements based on topographic features and land use. These previous systems tended to have unclearly de-ned judgment criteria, which resulted in inconsistent evaluation between researchers. Reasons for such inconsistency included: 1) the ambiguity of the classi-cation criteria themselves, and 2) di®erences between individual researchers on de-ning topographic boundaries. Meanwhile, with the rapid progress in accumulation and improvement of digitized geographic data, the level of availability of topographic and land use information has improved substantially in Japan. For more rational land use and for implementing suburban and urban planning in a manner following natural landscapes more closely, it is necessary to introduce a standardized landscape classi-cation method which yields consistent classi-cation results independent of a person doing the job.

We examine for use in landscape classi-cation methods the generation of standard algorithms such as for handling digital terrain models (DTM) and Landsat TM data in order to attain the standardization mentioned above.

2. STUDY AREA

Landscape structure of Sakura City in Chiba Prefecture in central Japan was analyzed in this study. Sakura is located at the center of the Shimousa upland in the northern part of Chiba Prefecture. Around Lake Inbanuma located in the northwest part of Sakura, a marshy lowland spreads and this lowland together with the Shimousa upland forms an inter-winding complicated topography. At the head of rivers, a rural landscape speci¯c to this region, called the Yatsuda paddy ¯elds, spreads in tree-branch shapes. Being only 40 kilometers away from the center of Tokyo, there is a rapid housing land development around Sakura Station and other commuter train stations along JR and Keisei commuter train lines. Needs are therefore high for development harmonious with the nature.

3. METHOD

3.1 Analysis System

The Environmental Data Analysis System at the Tokyo University of Information Sciences was used in the landscape analyses. The hardware and software composition is given below:

Hardware:
- SUN S-7/300U
- Gateway GP6-450, 700

Software:
- ARC/INFO Ver7.2.1
- ERDAS IMAGINE Ver8.3.1
- ArcView Ver3.2

3.2 Data for Analyses

Data used for analyses are listed below:

- Digital Map 50m Grid (Geographical Survey Institute)
- Landsat TM data (14th April 1997)
- Urban Planning Map
- Actual Vegetation Map
- Surface Geology Map

3.3 Landscape Types

The basic data were scrutinized and well examined before landscape analyses. The landscape types for use in the classi¯cation were then de¯ned, taking into consideration the topographic conditions and land use types in Sakura. As discussed by Hara (2000), the following landscape types were chosen to describe the landscape of Sakura. Each landscape type is also described subsequently: Marsh landscape, Rural landscape (Lowland rural landscape, Upland rural landscape, Yatsuda rural landscape), Urban landscape.

1) Marsh Landscape

Covers Lake Inbanuma and surrounding areas. This landscape, which consists of the open water area of the lake and its shore areas covered by reed (Phragmites communis) and other plant communities. This landscape maintains a high level of natural environment.

2) Rural Landscape

i. Lowland rural landscape:

Mostly °at and marshy lowlands with an altitude of less than 10 meters. The scenery is mostly paddy ¯elds and there is no housing. Rice paddies are transformed to dry paddies in winter for cultivation of other crops. Some ¯elds are also laid abandoned.

ii. Upland rural landscape:
Typical upland farm village landscape on upland with altitudes of 10 to 40 meters. Mainly farmhouses and dry farmlands, mixed with oak forests and other secondary forests.

iii. Yatsuda rural landscape:
At upstream of small rivers, paddy fields with narrow widths spread along the streams, forming paddy shapes called Yatsuda. In contrast with the paddy fields around Lake Inbanuma, some paddy fields in this region remain wet throughout the year. These Yatsuda paddy fields and the slope forests surrounding these paddies are classified as the Yatsuda rural landscape.

3) Urban Landscape
This landscape covers both those residential areas going back many years and the relatively newly developed housing areas. In terms of composition, the majority was developed in years after the mid-1960s.

3.4 Method of Classification

Figure 1 shows the decision tree followed in executing the landscape classification. In this classification method, independent topographic elements were extracted and used for classification. For the differentiation of lowlands and uplands, the altitude of 20 meters from the sea level was used as the threshold borderline.

4. RESULTS AND DISCUSSIONS

4.1 Landscape Map

Figure 2 shows the results executed by the landscape classification method described above. Digital data are treated automatically on the GIS system in accordance with the analyses algorithm, so whoever executes the classification, the outcome should be the same. In this way, the standardization of the classification is achieved. Results for each landscape type were examined by using the units called ecotopes.

4.2 Extraction of Ecotopes

There are different views on what the minimum units of landscapes should be. For the purpose of our discussions, we will use the concept "ecotope" which is the minimum unit combining topographic features and land use.

Remote sensed satellite data and DTM were used for the extraction of ecotopes. Based on the ISODATA method in accordance with procedures of Hara (1997), LandstatTM data covering the entire area of Sakura, detected on April 14th 1997 (referred to herein as TM970414), were classified for land cover types and 13 elements extracted. These are: Water (open water), Marsh (marsh), Paddy (paddy field), Grass (grassland), Scrub (scrub), Forest_b (broad-leaved forest), Forest_c (conifer forest), Urban_g (urban district with many trees), Urban_o (urban district), Urban_f (factory and industrial area), Field (field), Bare_o (bare land), and Bare_c (bare land covered concrete).

From DTM for Sakura, altitudes and inclination of slopes were calculated and landscapes of the entire Sakura City area were classified into four broad types including lowland, upland and slope areas by topographic features. From these two sets of information, a total of 52 ecotopes were defined. Table 1 shows these extracted ecotopes.

4.3 Method of Evaluation

A map of areas representing these 52 ecotopes was placed as an over-layer on the landscape classification map, and percentage of each ecotope in respective landscape areas were

calculated. Tables 2-1 to 2-5 summarize the results for each landscape.

4.4 Discussions

For each landscape classi ed in this study and the percentages of ecotopes which constitute such landscape, the following observations were made: In the marsh landscape, lowland open water area representing a wetland element accounts for more than 90% of the area. In the urban landscape, the urban element accounts for 70% of the area whereas there are topographic element variations in the relevant area. The reclaiming of the lowland by land lling for urban development is considered a factor behind such variations. In the lowland rural landscape, a number of grasslands are found among the lowland paddy eld elements and among the vegetation elements, caused by abondanment of paddy elds. The upland rural landscape is made up of diversi ed elements, including vegetation elements such as broad-leaved forests and conifer forests, as well as elds and urban districts with lots of trees. It is interesting to note that Yatsuda which comprises of paddy elds and vegetation elements are in fact a landscape made up of wet paddies and secondary forests remaining along the slopes. As shown, the landscape classi cation method which is based on the classi cation algorithm under this study proves to give rational classi cations.

5. CONCLUSION

This study examined a method of landscape classi cation which uses remote sensed data and GIS. We have shown that the classi cation method based on our classi cation algorithms can produce standardized classi cation results. Our next step will be a comparison of this method with the existing methods including the ones utilizing the multi-variate analysis, with a view to develop a landscape classi cation system adaptable for use at di®erent localities.

ACKNOWLEDGEMENT

This study was conducted as part of Sakura City's Natural Environment Survey Project. We owe a lot to the sta® members of the Department of Conservation of Natural Environment at Sakura City, the Chiba Prefecture Environment Foundation and to the members of the Survey Team. Hereby we would like to make acknowledgement of their contribution and express our sincere thanks.

REFERENCES

Blankson, E. J. & B.H. Green. 1991. Use of landscape classi cation as an essential prerequisite to landscape evaluation. Landscape and Urban Planning, 21: 149-162.

Bunce R. G. H. 1996. ITE Merlewood Land Classi cation of Great Britain. Journal of Biogeography, 23: 625-634.

Forman, R. T. T. 1995. Landscape Mosaics, The Ecology of Landscapes and Regions, 632pp. Cambridge University Press, Cambridge.

Forman, R. T. T. & M. Godron. 1986. Landscape Ecology, 619pp. John Wiley & Sons Inc, New York.

Hara, K. 1997. Macroscale analysis of landscape pattern in Chiba City. In " Conservation of Regional Biodiversity - Surveys of Spceies Communities and Ecosystems in Chiba City - " (ed M. Numata), 193-206. Shinzansha, Tokyo. (In Japanese with English summary)

Hara, K. 2000. Landscape of Sakura-City. In " Natural Environment of Sakura City " (ed. Sakura Natural Environment Survey Group), 585-591, +7pp Sakura City. (In Japanese)

Table 1.
Ecotope types based on landform and landcover

Ecotope Group	Landform			
	Ⅰ	Ⅱ	Ⅲ	Ⅳ
Marsh element type				
Open Water	water-1	water2	water3	water4
Marsh	marsh-1	marsh-2	marsh-3	marsh-4
Paddy element type				
Paddy	paddy-1	paddy-2	paddy-3	paddy-4
Vegetation element type				
Grass	grass-1	grass-2	grass-3	grass-4
Scrub	scrub-1	scrub-2	scrub-3	scrub-4
Broadleaf tree forest	forest_b-1	forest_b-2	forest_b-3	forest_b-4
Conifer forest	forest_c-1	forest_c-2	forest_c-3	forest_c-4
Urban element type				
Green Urban	urban_g-1	urban_g-2	urban_g-3	urban_g-4
Ordinary Urban	urban_o-1	urban_o-2	urban_o-3	urban_o-4
Factory	urban_f-1	urban_f-2	urban_f-3	urban_f-4
Field element type				
Field	¯eld-1	¯eld-2	¯eld-3	¯eld-4
Bare element type				
Ordinary Bare	bare_o-1	bare_o-2	bare_o-3	bare_o-4
Concrete	bare_c-1	bare_c-2	bare_c-3	bare_c-4

Ⅰ. Altitude(m) ($0 \leqq a \leqq 10$), Inclination(dgree) ($0 \leqq s < 5$)
Ⅱ. Altitude(m) ($10 \leqq a \leqq 20$), Inclination(dgree) ($0 \leqq s < 5$)
Ⅲ. Altitude(m) ($20 \leqq a \leqq 45$), Inclination(dgree) ($0 \leqq s < 5$)
Ⅳ. Altitude(m) ($0 \leqq a \leqq 45$), Inclination(dgree) ($s \geqq 5$)

Table 2-1. Composition of each ecotope element type in the marsh landscape

Ecotope Group	Area(ha)	%
Marsh element type	239:58	96:67
water-1	239.58	96.67
Paddy element type	4:25	1:71
Vegetation element type	1:58	0:64
Urban element type	0:91	0:37
Field element type	0:34	0:14
Bare element type	0:65	0:26
Total	247:85	100:00

Table 2-2. Composition of each ecotope element type in the urban landscape

Ecotope Group	Area(ha)	%
Marsh element type	13:63	0:59
Paddy element type	0:36	0:02
Vegetation element type	480:49	20:67
grass-3	130.52	5.62
others	349.97	15.05
Urban element type	1586:53	68:26
urban_g-3	255.63	11.00
urban_o-1	179.84	7.74
urban_o-2	266.40	11.46
urban_o-3	531.48	22.87
urban_o-4	127.03	5.47
others	226.14	9.73
Field element type	79:01	3:40
Bare element type	163:68	7:04
Total	2324:24	100:00

Table 2-3. Composition of each ecotope element type in the lowland rural landscape

Ecotope Group	Area(ha)	%
Marsh element type	44:30	2:12
Paddy element type	1121:58	53:72
paddy-1	1110.82	53.20
others	10.76	0.52
Vegetation element type	594:83	28:49
grass-1	352.40	16.88
scrub-1	123.58	5.92
others	118.85	5.69
Urban element type	130:33	6:24
Field element type	42:30	2:03
Bare element type	153:93	7:36
Total	2087:84	100:00

Table 2-4. Composition of each ecotope element type in the upland rural landscape

Ecotope Group	Area(ha)	%
Marsh element type	38:88	0:88
Paddy element type	0:95	0:02
Vegetation element type	2555:57	57:68
grass-3	560.42	12.65
forest_b-3	331.99	7.49
forest_c-3	498.00	11.24
others	1165.16	26.30
Urban element type	1079:85	24:37
urban_g-2	511.43	11.54
urban_o-3	214.53	4.84
others	353.89	7.99
Field element type	75:82	1:71
Bare element type	676:38	15:27
bare_o-3	479.95	10.83
others	196.43	4.44
Total	4430:71	100:00

Table 2-5. Composition of each ecotope element type in the Yatsuda rural landscape

Ecotope Group	Area(ha)	%
Marsh element type	19:68	1:54
Paddy element type	278:64	21:83
paddy-2	143.82	11.27
others	134.82	10.56
Vegetation element type	836:17	65:51
grass-2	126.05	9.88
grass-4	105.31	8.25
forest_b-4	73.22	5.74
forest_c-4	117.11	9.18
others	414.48	32.46
Urban element type	53:27	4:18
Field element type	8:51	0:67
Bare element type	77:86	6:10
Total	1276:32	100:00

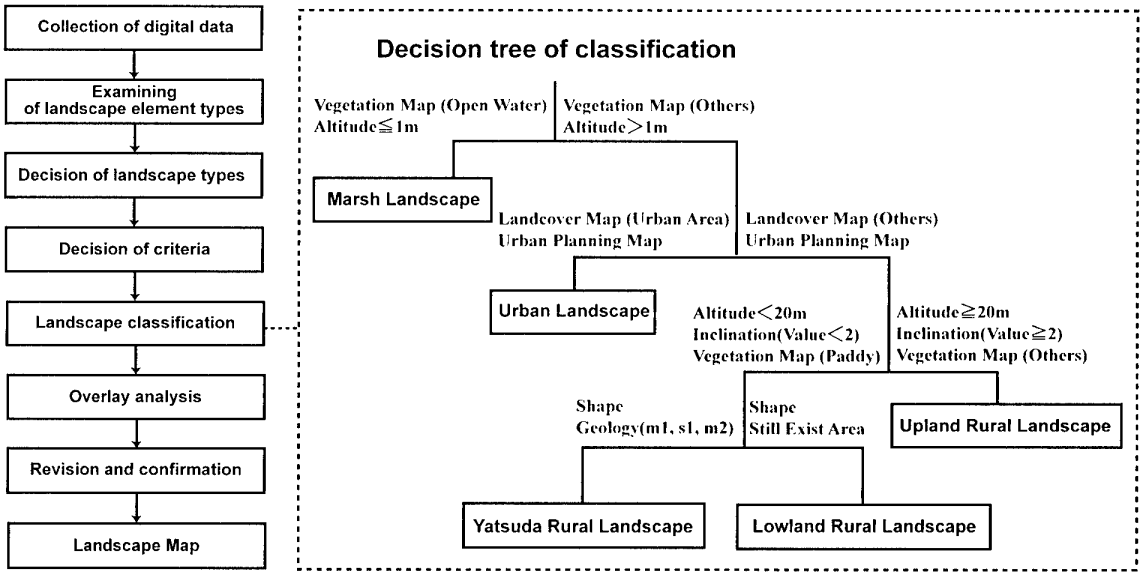


Figure 1. Landscape classification method (modified from Hara, 2000)

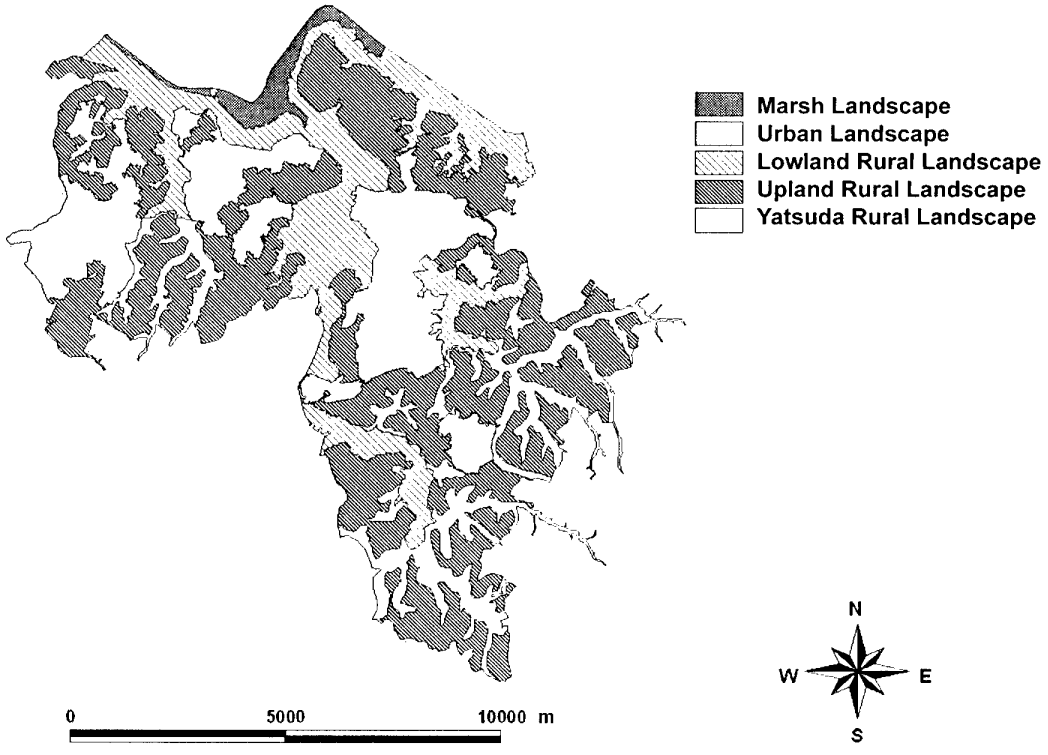


Figure 2. Landscape classification map (modified from Hara, 2000)

OBSERVATIONS OF THE DAYTIME INTERNAL BOUNDARY LAYER IN ONSHORE FLOW

N. M. Saleh, M.Z. MatJafri and K. Abdullah
School of Physics, Universiti Sains Malaysia
11800 Penang, Malaysia
Telephone: 604-6577888ext3676 Fax: 604-6579150 E-mail: nasirun@usm.my

KEYWORDS: Internal Boundary Layer, Mast, Wind Speed, Potential Temperature

ABSTRACT

One of the most important characteristics of the atmospheric environment in coastal regions is the internal boundary layer (IBL), formed when air flows across the surface discontinuity between land and water. Since the two surfaces rarely have the same temperature and almost always exhibit a difference in aerodynamic roughness, an interface is created. A study to investigate the development and behavior of the IBL by using the atmospheric data acquisition Tethersonde System in coastal area of Sufolk, during the periods of onshore wind flow. A data set from a 16m mast deployed near the coast to correlate with features observed in the tethersonde data. A new method to improved the utility of the measured tethersonde data has been developed which is shown to produce consistent results. A best-fit straight line to wind speed and potential temperature profiles are used to determine the evolution of the IBL at a distance of 850m from the shoreline. The data collected during periods of IBL development has shown that the atmosphere below 110m is divided into three main layers: The lower is the adjusted surface boundary layer; The middle is the transition layer and; The upper is s region of free atmosphere. It is also found that the IBL heights obtained lay the same population as Hsu's (1988) observations, which ranged over fetch-lengths of 30m to 6000m.

1. INTRODUCTION

One of the principle areas of meteorology at the coastal sites, has been on the growth of the convective thermal internal boundary layer, mainly concerning the influence of this boundary layer on coastal pollution from industrial sites. This study considers the development of Internal Boundary Layer (IBL) which develops when air flows and the air above the ground surface. This horizontal thermal discontinuity principally arises since the two surfaces rarely have the same temperature and almost always differ in aerodynamic roughness, resulting in an interface.

In this research a boundary layer height (ZIBL) is determined by using the wind speed, potential temperature profile. The best fit straight line is introduced onto the wind speed and potential temperature profile to which the boundary layer is determined. The IBL determined is informatively integrated with the specific humidity and the atmospheric stability characteristic of the study area.

In this study a 16m mast is set up (120m from the coastline) to monitor the fresh onshore flow at the coastal areas. However, data collected from instruments supported on a cable of a tethered balloon, which can be systematically raised and lowered in the free atmosphere, is used to study the atmospheric behavior further inland at (about 850m from the coastline). Therefore, to used this kind of data will not be a straight forward process as a specific method has to be developed in order to present and interpret the data. As such the mast data (as shown in formula below) is used to correct the tethersonde data(formula below) and thus minimize the tethersonde data of large variation from the mean.

$$\mathbf{U_c = U_T - U'(t)}$$

U_c = The tethesonde wind speed
U_T = The tethersonde correction wind speed
U' = The correction factor, t is the time lag.

The internal boundary layer obtained from this study is compared with some works that had been conducted at different coastal areas.

2 METHOD TO DETERMINE THE IBL HEIGHT.

2.1 Best Fit Straight Line.

The thickness of the IBL was defined as the height above the ground, where logarithmic profiles of wind speed and potential temperature were intersect and abrupted, that is, separated by a distinct change of vertical slope for both wind speed and potential temperature profile. In practice, the thickness of the IBL was determined by means of finding the intersection of the best fit straight lines on the wind speed and the potential temperature profile (refer figure 1).

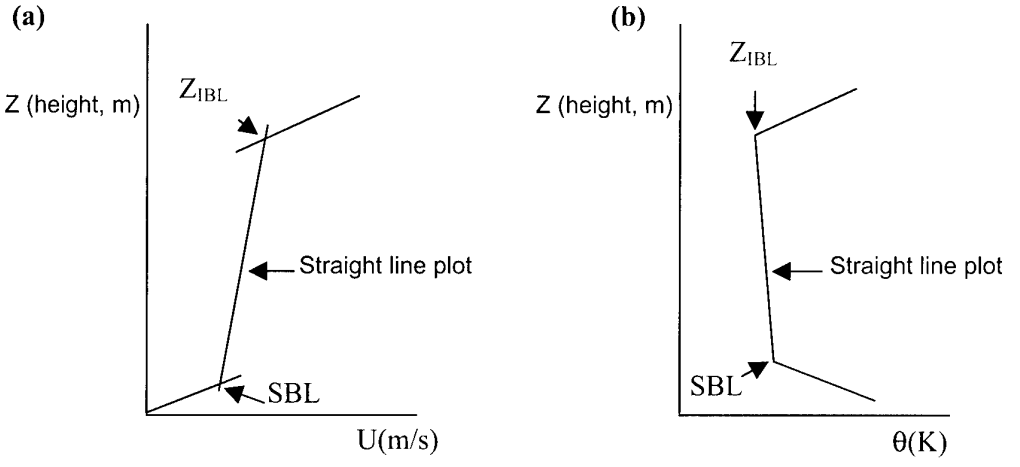


Figure 1 : Schematic diagram of straght line drawn on. (a) wind speed and (b) potential temperature profile.

To put it briefly, the sketching of the straight line to form the slope from the profile points can be accomplished utilising two methods; the first takes into consideration the maximum points from the profile as the slope boundary between the lower and upper slope points and; secondly, if the maximum points are scattered below and far from the other points, especially to the lower profile, thereupon the maximum points that are scattered are not taken into consideration as the boundary for the sketching of the straight line.

3. RESULTS

3.1 Internal Boundary Layer, 30th. June 1994.

Method as mention above was fitted to the wind speed profile for the data taken on the 30th. of June 1994. A total of seven hourly (from 11:06 until 18:00) average wind speed data profile were plotted. Two intersecting points were obtained representing the adjusted SBL and the top was the internal boundary layer height. Both height layers are tabulated in table 1.

Time	adjusted surface layer (m)	Z_{IBL} (m)
11:06-12:07	14	@
12:08-13:o6	19	72
13:06-14:05	41	95
14:06-15:00	35	73
15:01-15:52	52	92
15:59-17:06	25	70
17:07-18:00	22	75

Note; @ no sign of wind speed variation on the profile.

Table 1: The Adjusted surface and Internal Boundary Layer Height from the wind speed profile on 30th. June 1994.

The results showed that the adjusted layer height increased during the mid afternoon and decreased during the evening. No sign of wind speed variation at the upper level between time period of 11:06 to 12:07 was observed. This made marking the point of intersection between the lines difficult. However, the profile clearly revealed the existence of the adjusted layer near 17m at this time period. The adjusted layer increased in height with time until mid afternoon and it is at its maximum height (52m) during time period between 15:01 to 15:52 and but decreased later in the evening. The ZIBL was first obtained from the 12:08-13:06 wind speed profile at 72m height and increased to 95m for the data taken between 13:06 to 14:05. The wind speed profile varied greater during this time period. This corresponded to the lower level wind speed increase with time. The ZIBL decreased to 73m during time period 14:06 to 15:00 and increased to 92m high between 15:01 to 15:52. The wind speed increase with height at and above this level

(Z_{IBL}) was mainly caused by the active marine air flow inland. The increased of potential temperature at this (Z_{IBL}) provided evidence of marine air flow activity.

Later in the day between the time period of 15:59 to 17:06 and 17:07 18:00 the Z_{IBL} decreased to 70m and 75m respectively. There was no clear evidence of the potential temperature change with height at this level. However, the specific humidity decreased sharply over small ΔZ at this level .The air above the IBL was dry. Angevine et.al., (1994), explained that the synoptic subsidence appeared to be the primary controller of the strength of the potential temperature increase with height and the boundary layer height. The subsidence associated with high pressure near the surface caused significant drying above the boundary layer and strengthen the inversion, and also directly suppressds boundary layer growth.

The same method, the best fit straight line, was applied to the potential temperature profile to determine the IBL height. It shows the ZIBL is at 96m during the early hour (11:06-12:07) and which decreased during the mid afternoon. The ZIBL was at its maximum height (96m) between the time period 15:59 to 17:06. Table 2 shows the ZIBL variation with height on the 30th. of June 1994 from the potential temperature profile between the time period 12:08 to 13:06, showed no sign of an inversion layer corresponding to the Z_{IBL} layer.

Time	adjusted surface layer (m)	Z_{IBL} (m)
11:06-12:07	25	96
12:08-13:06	28	@
13:06-14:05	36	95
14:06-15:00	46	94
15:01-15:52	57	85
15:59-17:06	37	96
17:07-18:00	28	82

@ no sign of ZIBL from the profile.

Table 2: The Adjusted surface Internal Boundary Layer Height from the potential temperature profile on 30th. June 1994.

The adjusted layer was observed to develop at 25m during the late morning hours (11:06-12:07) and increased by 3m one hour later. The height of this layer continued to increase during the mid afternoon. This was associate with the intense ground heating as high temperature reading was recorded at 6m mast level . The temperature variation displayed in the figure corresponded to the solar radiation which was effected by the present of the cumulus cloud. The adjusted surface layer revealed a further increase in height (by 21m) which indicated it's maximum height (57m) between 15:01 to 15:52.

The Z_{IBL} was marked to have occurred between highest (96m) during the morning hour (11:06 to 12:07) and lowest (82m) during the evening (17:07 to 18:00). No significant Z_{IBL} height was observed for the potential temperature profile for the data between 12:09 to 13:06. It reflected a decreasing tendency at upper layer, except a 10m inversion layer was observed at approximately 60m height. The Z_{IBL} obtained from the potential temperature was slightly higher compared to the Z_{IBL} obtained from the wind speed profile.

3.2 Intercomparison of the Internal Boundary Layer Heights.

There are many other IBL studies that have been conducted along the coastal area. Interestingly some of these studies have been carried out at different fetches (X). It is the intention of this section to compare the Z_{IBL} that was obtained in this study to those found in the literature. Three different studies (Ogawa & Ohara, (1985), Smedman & Hogstrom, (1983) and Druilhet et. al., (1982)).who their studies at different places and at a different fetches will be used as a guide to observed the Z_{IBL} growth with fetch distance.

Table 3 highlight the Z_{IBL} obtained from this study (30th. June 1994, as a function of stability) and studies that have being conducted by the people mentioned above.

Table 3

The Tabulation of the Z_{IBL} against fetch (X)

X (m)	Z_{IBL} (m)
30	8[a]
90	11[a]
160	24[a]
850 *(Our study)*	*74*[d]
1000	79[c]
1500	76[b]
2000	105[c]
3000	123[c]
4000	138[c]
5000	151[c]
6000	162[c]

Note:

[a] = from Ogawa and Ohara, (1985)

[b] = from Smedman and Hogstrom, (1983)

[c] = From Druilhet et. al., (1982)

[d] = Obtained Z_{IBL} from stability function (30th. June 1994)

From table 3 it can be observed that the Z_{IBL} obtained as a function of stability on the 30th. June 1994 is significantly correlated to the ZIBL growth with fetch conducted from the other studies . The Z_{IBL} growth presented statistically by Hsu (1988) when he formularised the boundary layer height from the three different studies mentioned above as $\mathbf{ZIBL = (1.91 \pm 2 \times 0.38)\, X^{1/2}}$

The Z_{IBL} obtained as a function of stability on the 30th. of June was in the increasing slope of the Internal Boundary Layer height with fetch (lies in the range between 30m to 6000m downwind distance).

4. DISCUSSION.

Two methods had been used to obtained the thickness of the adjusted Surface Boundary Layer (SBL) and the Internal Boundary Layer (Z_{IBL}); the first from the best fit straight line drawn on the wind speed and potential temperature profile and the SBL and Z_{IBL} was obtained from which the two straight lines intersect and abstrupt and; the second was determined as a function of stability (Richardson number). The layer of separation between the bottom and the top layer can be seen when there is an abstrupt change on the profile behavior. The top of the Z_{IBL} was determined when fresh incoming onshore flow on top of the land surface atmospheric layer. The corresponding potential temperature behavior at the top of Z_{IBL}, which displayed an inversion characteristic gave evidence of this fresh onshore wind.

Data on 30/6 were examined in order to investigate the Z_{IBL} growth. This was done by using both methods. The result explained showed the existence of the Internal Boundary Layer height on 30/6/94 during the summer of 1994. Comparatively the Z_{IBL} that was obtained lay within the increase slope of the Internal Boundary Layer height proposed by Hsu (1988).

5. REFERENCES

Druilhet, A., Herrada, A., Pages, J. P., and Saissac, J., (1982). Etude experimentale de la couche limite interne associee a la brize de mer. Boundary Layer Meteor., 22, 511-524.
Hsu, S. A. (1988). Coastal Meteorology. 260pp. ISBN 0-12-357955-4. Academic Press Inc. London.
Ogawa, Y. and Ohara, T., (1984). The Turbulent Structure of the Internal Boundary Layer near the coast, Boundary Layer Meteorol. 31, 369-384.
Smedman, A. S. and Hogstrom, U., (1983). Turbulent Characteristic of a shallow Convective Internal Boundary Layer. Boundary Layer Meteorology, 25, 271-287.

EARTH OBSERVATION SYSTEM

Vinai VORRAWAT
National Research Council of Thailand
196 Pahonyothin Road, Bangkhen, Bangkok 10230, Thailand

KEY WORDS: Earth, observation system

ABSTRACT: The JERS-1 observation system can be divided into space segment and ground segment the space segments is JERS-1 satellite. The ground segment includes the tracking and control system a data acquisition and processing system. JERS-1 can carry two pieces of observation equipment, the synthetic aperture radar (SAR) and optical sensor (OPS) which composed of two radiometer the visible and near infrared radiometer (VNIR) and short wave infrared radiometer (SWIR) JERS-1 composed of these observation equipment. Mission data recorder (MDR), Mission data transmission (MDT) and subsystems for solar paddle, attitude and orbit control and thermal control. The satellite revolves in 96 minutes around the earth. It makes 15-1/44 revolutions per day and returns to the same orbit every day.

1. INTRODUCTION

When 8 GHz band receiving subsystem is used to receive a JERS-1 signal and checking the operation of a receiving system the subsystem is operated either through remote control by an antenna subsystem or local control by the controller of a 8GHz band main receiver. The subsystem does not require much complicated operation and can be set to most operating modes of the subsystem through remote control, enabling the subsystem unattended during normal operation.this paper descries outlines of the operation procedures for startup of the whole subsystem, receiving the signals and stopping power base on fig 1 for details refer to the operation introduction in relevant equipment. 8 GHz band main low noise The status can only be checked by the antenna subsystem.8 GHz band frequency down converter (X-D/C) (S/X –D/C) set the power on/off control switch to remote. The X-D/C status can be also checked at the antenna system. 8 GHz band main receiver (X-RX). The normal operation mode is remote (remote control from the antenna subsystem.) 8 GHz band main receiver (X-RX). The normal operation mode is remote (remote control from antenna system) . The following element should preferably be monitored during reception a reception level (AGC level.) angle error voltage. Lock status and the X-RX status can be also checked at the X-RX status can be also check at the antenna system. 8 GHz band receiving system. The receiving subsystem operations check using the X-cal before reception is not necessary unless otherwise specified. However recommences that the check be perform as it is an effective way of ensuring the reception.

X-LNA : 8 GHz Band Low-noise amplifier
X-D/C : 8 GHz Band frequency down converter
X-RX : 8 GHz Band main receiver

- These procedures may not be performed.

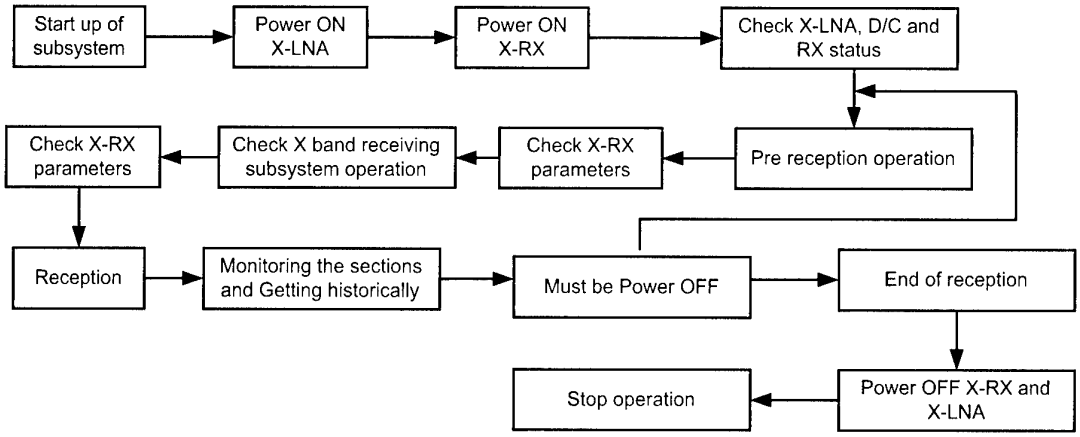


Figure 1 Flow Chart Overall Operation Procedure

2. OPERATION

Table 1. Lists the operation precautions for each equipment

No.	Equipment name
1.	8 GHz band low-noise the status can only be checked by the antenna subsystem.
2.	8 GHz band frequency down converter (X-D/C) (S/X-D/C) - Set the power ON/OFF control switch to REMOTE - The X-D/C status can be also checked at the antenna subsystem.
3.	8 GHz band main receiver (X-RX) - The normal operation mode is REMOTE (remote control from the antenna subsystem) - The following items should preferably be monitored during reception - Reception level (AGC level) - Angle error voltage - Lock status - The X-RX status can be also checked at the antenna subsystem.
4.	8 GHz band test equipment (X-CAL) - Before reception, check that the test signal output is OFF. - The status can be also checked at the antenna subsystem .
5.	8 GHz band receiving subsystem - The receiving subsystem operation checks using the X-CAL before reception is not necessary unless otherwise specified. - However, NEC recommends that the check be performed, as it is an effective way of ensuring the reception.

3. TROUBLESHOOTING

3.1 Abnormal condition

The section descries the abnormal conditions and troubleshooting of troubles in the receiving subsystem as well as associate with other subsystem. To find and handle troubles in each equipment, refer to relevant pages of the manual for each equipment.

Abnormal condition

No image output on the quick looks equipment after a passage of the satellite arrival time.

<Assumption>

The antenna is oriented to the arriving satellite, the programmed tracking operation normal and the predicted value for the orbit correct.

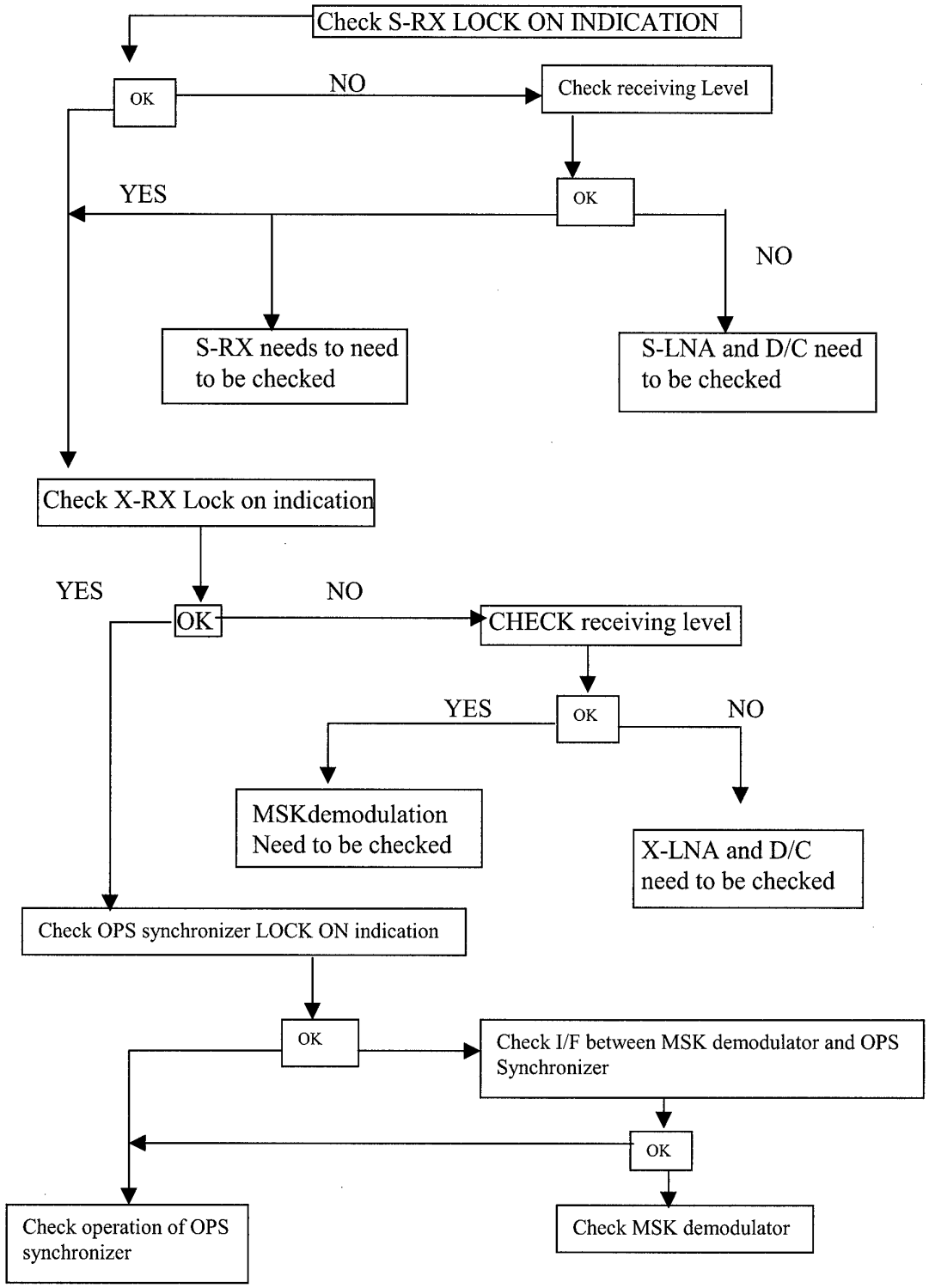


Figure 2 Flow chart for troubleshooting

3.2 Abnormal condition 2

The satellite reception is performed normally but the operation fails with a testing equipment.

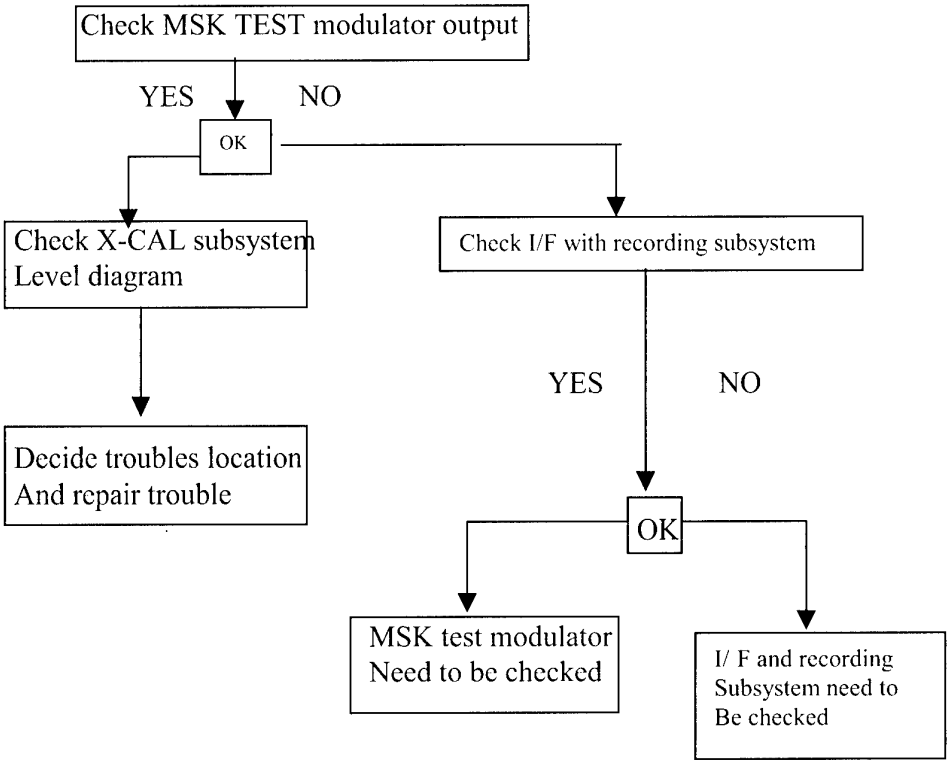


Figure 3 Flow chart for Troubleshooting

3.4 Measure in case of trouble

When a trouble is detected the instructions below:

- Turn off the power of the equipment in trouble installed in the antenna center ring; The D/C and U/C should be powered off at the main receiver.
- Inspect the equipment in trouble according to the maintenance manual for that equipment, and notify NEC of the details of the trouble.

Level control

Proposes of the Test

To confirm the control function of output level

Performance objective

(a) Control by means of the step attenuator.

(b) Remote control can be performed at the operation room.

(c) Output level

Range: -110 dBm (1 dB step).(This level is calculated on condition that the test RF signal is supplied to 8 GHz Band Low noise Amplifier input terminal.)

Setting: The deviation is less than 2-dB accuracy

(d) Test Equipment

signal generator : HP– 8863 A

Power meter : HP- 436 A

Controller in the 8 GHz band main receiver

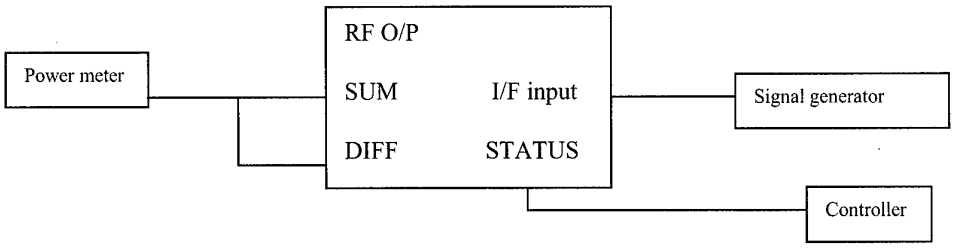


Figure 4 Measurement (X-BAND) 8150MHz and 8350 MHz

Test procedure

Step 1 set the signal generator as follows

Frequency 140 MHz

Level –7 dBm 1 dB (50 ohm)

Step 2 Supply the signal to TEST UP CONVERTER.

Step 3 set controller as table 1

Step 4 Measure the output at "RF OUT PUT SUM" connector.

(i) The level at LNA input terminal is 35 dB (nominal) less than the output level at "RF OUTPUT SUM" connector of MSK TEST UP CONVERTER.

(ii) The level at " RF OUTPUT DIFF" is 9 dB (nominal) less than have "RF OUTPUT SUM"

Table 1 Controller Parameter setting

ITEM	PARAMETER
CONTROL MODE	LOCAL
OUTPUT	ON
FREQUENCY	8150M or 8350M
LNA INPUT LEVELS	70-110dBm the Level more than –70dBm and the level less than 110dBm are set at –110dBm.
LEVEL CONTROL (X-BAND)	output frequency 8150 MHz

LNA INPUT LEVEL (dBm)	U/C OUTPUT LEVEL (dBm)	ATTENUATION (dB)
-70	-35.93	0
-71	-36.97	1.04
-72	-37.92	1.99
-73	-38.94	3.01
-74	-39.96	4.03
-75	-40.97	5.04
-76	-41.94	6.01
-77	-42.99	7.06
-78	-44.00	8.07
-79	-45.06	9.13
-80	-46.16	10.23
-90	-56.16	20.23
-100	-66.13	30.20
-110	-76.21	40.28
Maximum deviation +0.28dB at –110 dBm –0.01 dB at –72 dBm 0.29 dBp-p		

LEVEL CONTROL (X-BAND)	Output frequency 8350 MHz	
LNA INPUT LEVEL (dBm)	U/C OUTPUT LEVEL (dBm)	ATENUATION (dB)
-70	-35.80	0
-71	-36.83	1.03
-72	-37.77	1.97
-73	-38.81	3.01
-74	-39.81	4.01
-75	-40.84	5.04
-76	-41.84	6.04
-77	-42.87	7.07
-78	-43.89	8.09
-79	-44.90	9.10
-80	-55.85	10.13
-90	-65.85	20.05
-100	-65.85	30.05
-110	-75.85	40.05
Max deviation 0.13dB at 80dB -0.03dB at 100dB 0.16 dBp-p		

REFERENCE

Reception and recording facility MOS-1 Thailand Station
Maintenance Test Data, NEC Corporation, March 1995
Training Manual (in Thailand) on Reception and Recording Facility
(MOS-1 Thailand Station), November 1987, NEC Corporation Tokyo, Japan

INTEGRATING REMOTELY SENSED DATA WITH AN ECOSYSTEM MODEL TO ESTIMATE NET PRIMARY PRODUCTIVITY IN EAST ASIA

Wenjing ZHAO, Masayuki TAMURA
Social and Environmental System Division, National Institute for Environmental Studies
16-2 Onogawa, Tsukuba, Ibaraki 305-0053, Japan
Tel: +81-298-50-2589 Fax: +81-298-58-2645
E-mail: zhao.wenjing@nies.go.jp, m-tamura@nies.go.jp

KEY WORDS: Remotely Sensed Data, Ecosystem Process Model, Net Primary Productivity

ABSTRACT: This paper describes a method of integrating remotely sensed data with an ecosystem model to estimate NPP in East Asia. Principles of forest biogeochemical cycles (FOREST-BGC) are used for simulating biological processes affecting NPP, such as photosynthesis, respiration, and transpiration. Input requirements for the ecosystem process model are: (1) land cover types and leaf area index from remote sensing data; (2) daily meteorological data such as maximum and minimum air temperature, incoming short-wave radiation, precipitation, and humidity; and (3) water holding capacity of soil. By incorporating the above data sources concerning all major environmental variables affecting plant growth and development, a map showing the distribution of annual NPP in East Asia in 1998 has been produced.

1. INTRODUCTION

Net primary Productivity (NPP) is a key component of the terrestrial carbon cycle, and defined as the net amount of new carbon absorbed by plants per unit space and time (Liu et al., 1999). Estimation of NPP accurately at regional or global scales is very important in studies of global climate. Liu et al. (1997) developed a Boreal Ecosystem Productivity Simulator (BEPS) based on the Forest BioGeochemical Cycles (FOREST-BGC) model (Running et al. 1988). Although the BEPS model has improved the original FOREST-BGC model for a regional scale by adding remote sensing inputs, robustness of the BEPS model should be verified for other area (or other land cover types) such as East Asia region, because it was just developed and validated for boreal ecosystem. Therefore, the primary objective of this study are: (1) to develop a model for estimating NPP in East Asia base on BEPS model, (2) to show the NPP distribution in East Asia region.

2. STUDY AREA

The study region of East Asia encompasses a 10^8 km^2 (11040 pixels$\times$9000 lines) area bounded by 66° N-9° S latitude and 78° -170° E longitude (Figure 1). The climatic zone of this area ranges from subfrigid zone in the north to tropical zone in the south. Land cover types includes boreal forest, grassland, crops, needle forest, broadleaf forest, and tropical rainforest.

3. MODEL

The model is based on BEPS model (Liu et al., 1997), which consists of three parts: remotely sensed and meteorological inputs, ecosystem process model, and NPP output (Figure 2). The BEPS model uses principles of the Forest BioGeochemical Cycles (FOREST-BGC) model (Running et al., 1988) for quantifying the biophysical processes governing ecosystems productivity. The BEPS model modified original model in the following aspects: (1) implement of a more advanced photosynthesis model with a new temporal and spatial scaling scheme (Chen et al., 1999); (2) inclusion of an advanced canopy radiation model to describe the specific boreal canopy architecture; and (3) adjustments of biophysical and biochemical

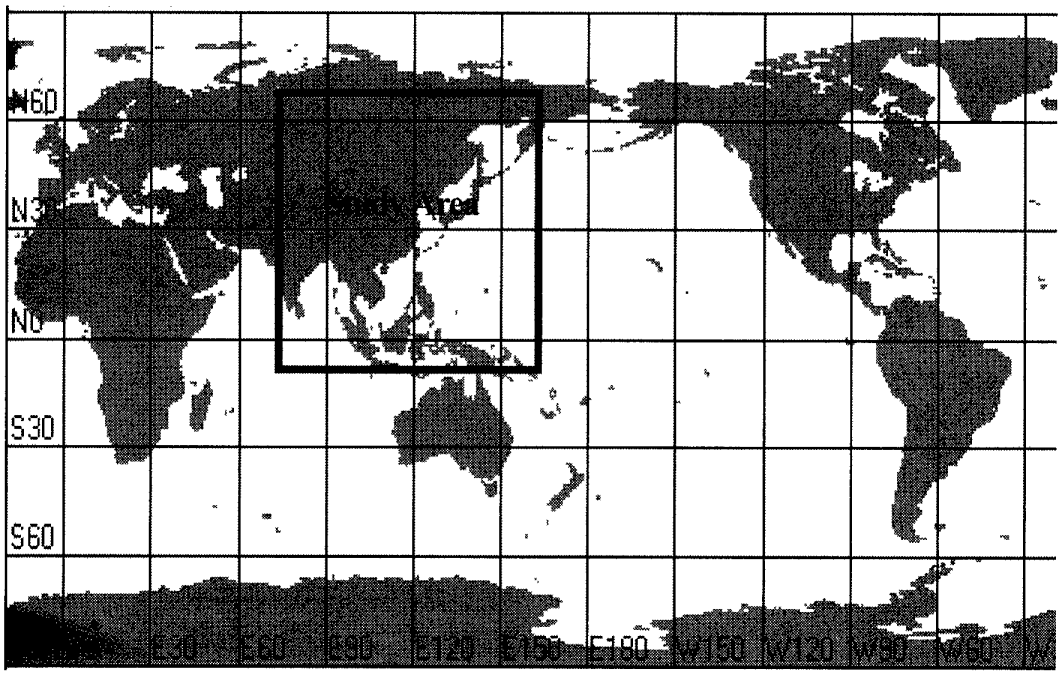


Figure 1. Location of study area bounded by 66° N-9° S latitude and 78° -170° E longitude.

parameters for the main boreal land cover types. The BEPS model are then modified when we use it in East Asia because its limitation of specific region for boreal ecosystem. They are: (1) more flexible land cover types map (Myneni et al., 1997) for global application is adapted; (2) more robust algorithm of estimating Leaf Area Index (LAI) from remotely sensed data (Myneni et al., 1997) for global application is adapted; (3) adjustments of biophysical and biochemical parameters according to the land cover types in East Asia. The remotely sensed inputs are land cover types and LAI, and the meteorological inputs are temperature, precipitation, humidity, and radiation. The temporal interval is daily for meteorological data, 10 days for LAI, and annual for land cover. The model computes daily NPP pixel by pixel ($1km^2$) assuming vegetation and environment conditions were uniform within each pixel, and then accumulates daily NPP to annual NPP.

4. INPUT REQUIREMENTS FOR THE MODEL

4.1 Land Cover Types

Theoretically, the relationship between NDVI (Normalized Difference Vegetation Index) and LAI depends on the land cover types. However, Loveland et al. (1991) pointed out that traditional land cover classifications based on botanical, ecological or functional metrics may be unsuitable for LAI estimation, because these classifications are not necessarily based on NDVI-LAI considerations. For instance, if several canopies have a similar or a nearly similar NDNI-LAI relationship, information on such land covers is redundant for the estimation of LAI (Myneni et al., 1997). Therefore, Myneni et al. (1997) developed a new land cover classification for global application to estimate LAI from NDVI. They classified global land covers into six types depending on their canopy structure. The structural attributes of these land covers were parameterized in terms of variables that the radiative transfer models admit. The six land cover types are: (1) grasses and cereal crops; (2) shrubs; (3) broadleaf crops; (4) savanna; (5) broadleaf forests; and (6) needle forests. In this study, we incorporate these land cover types into our model to resolve the limitation of specific region in BEPS model.

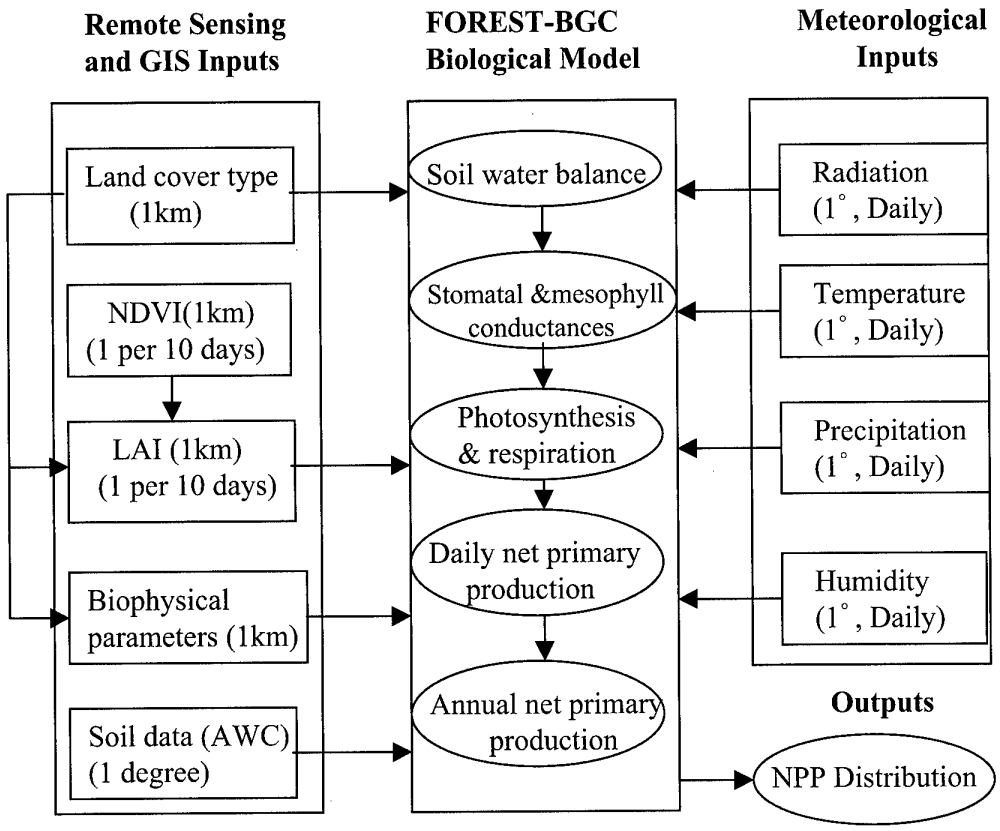


Figure 2. Framework of estimation NPP showing the major modeling steps, the input requirements, and the data's spatial resolutions and temporal intervals prior to simulation. (Modified from Liu et al., 1997)

4.2 Leaf Area Index

LAI is a key parameter to integrate remotely sensed data with an ecosystem model. The LAI was estimated from NOAA/AVHRR 10-day composite NDVI by using the NDVI-LAI algorithm developed by Myneni et al. (1997). Similar LAI images were calculated in this study for each 10- (or 11-) day period in 1998 by using the 10- (or 11-) day NDVI composites. Atmospheric corrections were performed to NOAA/AVHRR channel 1 and 2 using 6S code before using them to estimate NDVI. The NDVI composites were produced from single-day co-registered images by using the maximum NDVI criterion to obtain cloud-free pixels.

4.3 Daily Meteorological Data

The meteorological data required by the inputs of ecosystem model include daily maximum and minimum air temperatures, incoming short-wave radiation, precipitation, and specific humidity. These data were obtained from National Center for Atmospheric Research (NCAR), USA. The gridded data were 6-hourly forecasts by the National Meteorological Center (NMC) of NCAR, using their global spectral model (the MRF model). For the maximum and minimum air temperatures, the maximum and minimum of the four 6-hourly readings were used as the daily maximum and minimum air temperatures. For the incoming short-wave radiation and precipitation, the sums of the four 6-hourly readings were used as the daily total. For the specific humidity, the average of the four 6-hourly readings was used as the daily specific humidity. The gridded data were bilinearly interpolated for each pixel of $1km^2$ to match the remote sensing data because their resolutions are so coarse (approximately 1-degree intervals).

4.4 Soil Data

Soil data (Soil Water Holding Capacity) was downloaded from a free access web site of Center for Global Environmental Research (CGER) of National Institute for Environmental Studies (NIES) (http://www-cger.nies.go.jp/grid-j/gridtxt/grid18.html). This data set shows the global distribution of soil water holding capacity, at field capacity for the top soil (0-30cm), with a 1-degree latitude/longitude spatial resolution, and was derived from information on soil type and texture (FAO Soil Map of the World). This data was also bilinearly interpolated for each pixel of 1km^2 to match the remote sensing data.

5. RESULTS AND DISCUSSION

5.1 Annual NPP

Annual NPP in1998 was estimated using the above model, and the distribution map of NPP over the East Asia region in 1998 is shown in Figure 3. Except ocean, lake, and barren pixels (NPP of these areas are set to

---------- Please place figure 3 here ----------

0 according to land cover map), the mean NPP over the study region was calculated to be 511 g C m^{-2} yr^{-1} in 1998. The mean NPP of grasslands and cereal crops were the smallest (443 g C m^{-2} yr^{-1}), followed by that of needle forests (467 g C m^{-2} yr^{-1}), shrubs (504 g C m^{-2} yr^{-1}), savannas (538 g C m^{-2} yr^{-1}), and broadleaf crops (579 g C m^{-2} yr^{-1}). The mean NPP of broadleaf forests (671 g C m^{-2} yr^{-1}) were the largest. It is very difficult to validate our modeled NPP because of the lack of field measurement data. However, we can obtain some NPP data from NPP Database, which provided by Oak Ridge National Laboratory Distributed Active Archive Center in the web site (http://www-eosdis.ornl.gov/NPP/npp_home.html). The NPP database contains documented field measurements of biomass and estimated NPP for terrestrial sites worldwide, compiled from published literature and other extant data sources. From this web site, we found that some field measurements of NPP in some Country of East Asia such as Russia, India, Japan, Malaysia, Indonesia, and Thailand. The NPP values range from 26 g C m^{-2} yr^{-1} to 2793 g C m^{-2} yr^{-1}, and very closed our modeled result, which ranges from 6 g C m^{-2} yr^{-1} to 2210 g C m^{-2} yr^{-1}, even though the filed measurements are rather old (from 1947-1981).

5.2 Seasonal Variations of NPP

Figure 4 shows the seasonal NPP distributions in East Asia region in 1998. In the north area, the NPP became very low in period 1 (Jan. - Mar.) and period 4 (Oct. - Dec.) because the average daily air temperature is almost lower than 5℃ in this area during these periods, and then make plant growth stop. However, in the south area, the NPP in period 2 (Apr. - Jun.) and period 3 (Jul. - Sep.) was lower than periods 1 and 4. This is because the average daily air temperature is always higher than 5℃ through a year, and periods 2 and 3 are rainy seasons, then have not enough solar radiation for plant photosynthesis in this area. The peak of NPP occurred in period 3 in the north area and in period 4 in the south area, respectively.

---------- Please place figure 4 here ----------

6. CONCLUSION

The method of integrating remotely sensed data with an ecosystem model to estimate NPP in East Asia was described. By incorporating the remote sensing data, daily meteorological data and soil data concerning all major environmental variables affecting plant growth and development, the distribution map of annual NPP

in East Asia region in 1998 was produced. The mean NPP of grasslands and cereal crops were the smallest (443 g C m^{-2} yr^{-1}), followed by that of needle forests (467 g C m^{-2} yr^{-1}), shrubs (504 g C m^{-2} yr^{-1}), savannas (538 g C m^{-2} yr^{-1}), and broadleaf crops (579 g C m^{-2} yr^{-1}). The mean NPP of broadleaf forests (671 g C m^{-2} yr^{-1}) were the largest. The results also showed the difference of seasonal variation of NPP between the north and south areas.

7. ACKNOWLEDGMENT

We thank Dr. Liu J. and M. J. Chen of Canada Center for Remote Sensing for providing the BEPS code and very useful suggestions to use it. We also thank Dr. R. B. Myneni of Boston University and Dr. R. R. Nemani of University of Montana for providing NDVI-LAI algorithm and global land cover map, soil NDVI map and soil type map.

8. REFERENCES

Chen J. M., J. Liu, J. Cihlar, and M. L. Goulden, 1999. Daily canopy photosynthesis model through temporal and spatial scaling for remote sensing applications. Ecological Modelling, 124, 99-119.

Liu J., J. M. Chen, J. Cihlar, and W. M. Park, 1997. A process-based boreal ecosystem productivity simulator using remote sensing inputs. Remote Sensing of Environment, 62, 158-175.

Liu J., J. M. Chen, J. Cihlar, and W. Chen, 1999. Net primary productivity distribution in the BOREAS region from a process model using satellite and surface data. Journal of Geophysical Research, Vol. 104, No. D22, 27735-27754.

Loveland T. R., J. W. Merchant, D. O. Ohlen, and J. F. Brown, 1991. Development of a land cover characteristic data base for the conterminous U. S.. Photgramm. Eng. Remote Sens., Vol. 57, 1453-1463.

Myneni R. B., R. R. Nemani, and S. W. Running, 1997. Estimation of global leaf area index and absorbed par using radiative transfer models. IEEE Transactions on Geoscience and Remote Sensing, Vol. 35, No. 6, 1380-1393.

Running S. W., and J. C. Coughlan, 1988. A general model of forest ecosystem processes for regional applications, I, Hydrological balance, canopy gas exchange and primary production processes. Ecological Modelling, 42, 125-154.

A R&D Program for Prompt Response about Forest-Protection Information with Platform Display System

Gwo-Jern Hwang [1] *Ching-Ming Wu*[2] *Ten-Yin Chou*[3] *Joou-Shiau Lee*[4]

[1]*Taiwan Forestry Bureau (TFB),#2,Sec.1.Hang-Chows.Rd.Taipei Taiwan 100*

[23]*Geographic Information System Research Center, Feng Chia University*

[4]*The Department and Graduate Institute of Forestry, National Chung-Hsing University.*

E_mail: n1206153@pagic.net

ABSTRACT: The Taiwan Forestry Bureau (TFB) is the major agency, which is authorized to manage the national forest. TFB has been a research for forest fire precaution and rescue from 1999.

In that research, the forest patrolman is equipped with radio interphone, GPS receiver, and potable Laser gun. The forest patrolman traces route can be recorded by GPS receiver and key in different code when he comes across various forest disasters. In case of fire emergence, interphone can be used to report to rescue center immediately and transmitted the coordinates of fire location and it's boundary, which are identified by Laser gun. The control system in the rescue center will compute the area and overlay the fire position on digital map. When fire-fighting team arrive the scene, digital video is using to catch the image of the fire development and ISM BAND Microwave Radio System is used to transmit to the rescue center.

1. Original of the Research

Forest, the land of nature, not only for its rich resources, but also it affects related to our natural economy and livelihood. However, fire emergence, plant blight, illegal cutting and unlawful cultivation happen in the forest, endanger the circumstance from peaceful and quiet. If we cannot prevent and control those factors, they will threat the forestry development and increase water and soil erosion rate. Therefore, 210 protection-management offices were set up by TFB. Besides, 450 protection-management areas were delineated from forest location, traffic, construction, residents' distribution and the disasters over the years (1998 TFB.) . The protection-management officers have the obligation to patrol and report for rescue on time, and reduce the disasters and damage to minimum.

Nevertheless, it is still a difficult task to patrol and manage the mountainous area without a vast expanse. The office usually know the result after the patrolmen come back from the field and fill-up the report forms step by step, which is useless to prevent from disasters. Once disaster happened, the patrolmen only can describe the situation in the scene, and the executive officers fill the report and submit to higher level. Because the return-time is always delayed or the message is possible error, the commander may instruct wrong direction from the scene, therefore, the emergency rescue timing will be delayed.

2.Research Content

In this research, we aim at the disadvantages of the currently forest patrol system and disasters return-report to draft the improvement, moreover, we plan 3 targets:

2.1 The patrolmen's position is located and displayed on digital map immediately

2.2 The present disaster scene images can be transmitted and displayed on the digital map platform immediately

2.3 The report of the forest-protection form can be inquired and transmitted by Internet.

Ordinarily, every patrolman has one hand-held GPS receiver that could record the trace automatically by keyboard operation. The GPS receiver could record the disaster coordinates and assign a code, and transmit the disaster coordinates and scene images to the office or the rescue center. The system can also perform the distance measurement by laser gun, record the digital photography by video, and transmit images by microwave radio. GIS module was used to develop the monitor platform on digital-maps. It can also analyze the exact data through maps overlay for topographic chart, cadastral chart, forest chart, disaster location images, area measure, the plant feature, and the scene situation, etc.

3.Major Techniques

3.1 Digital Map

In the past, the disaster location was only displayed on the paper maps that pieced up on the wall of the disaster rescue center. Besides, only the officers who were familiar with local environment could search the location on the maps quickly. When the disaster expanded, or it is necessary for a mobile rescue center, paper maps have some problems, such as it is difficult to carry and handle, the information is insufficient, the update speed is too slow, etc. This research engages in creating a Digital Map by digitizing, editing, and coordinates transformation to build forest topographic chart and advanced automatic mapping technology (Yang long-shi, 1998).

3.2 Geography Information System (GIS)

GIS includes hardware, software, spatial and attributes data link, and data analyze integration, such as topological data structures database management and spatial analysis. The users can build, collect, and save points, lines, polygon, and the changes of landforms (spatial data); as well as business forms, reports, measurement, diagrams (attribute data). The maps can be saved in different layers' contents, make it easy to draw, display, inquire, save and distribute. This research program to analyze and create different statistics data. After that, the result can be displayed by 3D, and the result were applied to business management, resources management, ground exploitation, maps management, production management, diseases control, environmental protection, etc.

After the skills of GIS are applied generally, the system builders can combine with Object-Oriented Programming to build executable software; or build some business GIS functions by GIS module. The users do not have to buy the complete set of GIS software since it's common windows based, and it offers the GIS functions through Internet（Fig.1）. Thus, it effectively develops the functions of support and decision to execute the business of forest protection (Zhong lan-kun, 1999).

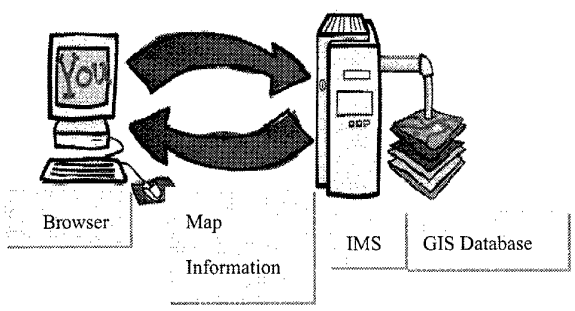


Fig.1 Structure of WWW-GIS

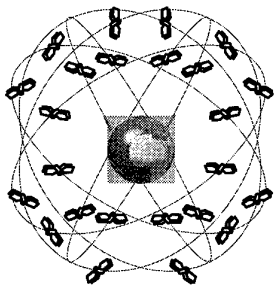


Fig.2 GPS constellation

3.3 Global Positioning System (GPS)

GPS is used to measure the time and distance by satellites (Fig.2) , and offers the global, all-weather, three-dimensional space, three-dimensional speed, continuous, immediately high precision navigation message (Liu ji-yu, 1993). The research only gather the message of the GPS's electromagnetic wave with the GPS receiver and calculate precisely the coordinates of the object's position, timing, and ranging by the theory of fore intersection at any movement and any place.

Presently, GPS is widely popularized to different business in the world. Those application include mounting, traveling, hunting, engineering, disaster protection, mapping, natural resource exploration, land development, space expand, scientific research, earth crust monitor, precise geodesy, intelligent transportation, vehicle navigation, and GIS investigation, etc.

"GPS User's Unit" indicates the GPS receiver, engine chip, or the processing board in the computer module (Fig.3 User's Unit) . Those shape and size is quite different. The precise Geodesy type is bigger and heavier than the engine chip that is similar as a stamp.

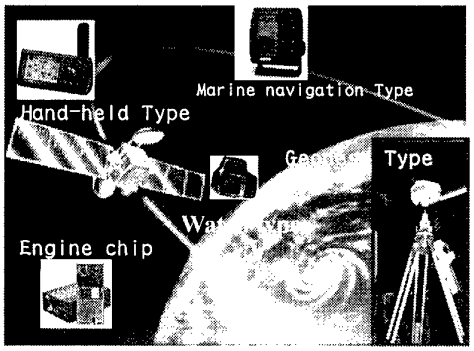


Fig.3 GPS User's Unit

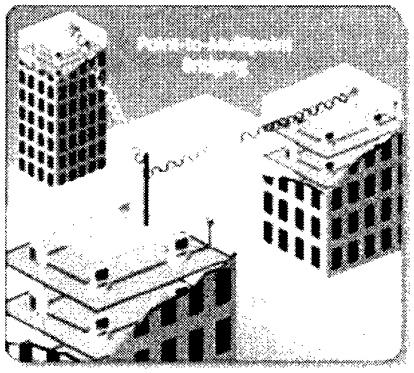


Fig.4 Wireless radio Internet technique

3.4 Radio Imagine Transmitting

Internet technologies shorten human range and create a convenient life style. The problems that is derivative from the Internet cable would be urgent to solve, such as massive wiring engineering, long interval of system setting up, maintenance of the old fashion or damage set, etc. Fortunately, the wireless radio Internet technique (Fig. 4) is exploited and overcome those problems on time.

4.Research projects

4.1 System Structure

The system can be installed on every Forest Protection-Management Offices and their workstations in the future. It is necessary to consider about the simple setting up, easier operation, quicker maintenance, etc. By using the system (Fig.5) the patrolmen record the coordinates of their patrol path into the hand held GPS receiver (Fig.6) automatically (Chou Ten-Yin) and enter the coincident definition code from the key board when they come across the illegal cutting, unlawful cultivation, collapse areas, etc.

4.2 The Interface in System

The systems include complete data transmitting and receiving interface (Fig.7). It can be installed in anyone compatible x86 computer, to transfer data mutually by transmitting interface. It is probable to install in notebook computer, so that rescuers can operate with the equipment in forest calamity region. Due to this reason, the design to establish in individual

operating system in computer, is different from the dispersed structure (N-Tier) ◦ This individual operating system can keep best mobility and simplification, even if necessary, to set up temporary rescuing control commander to support rescuing work with installing one set of equipment.

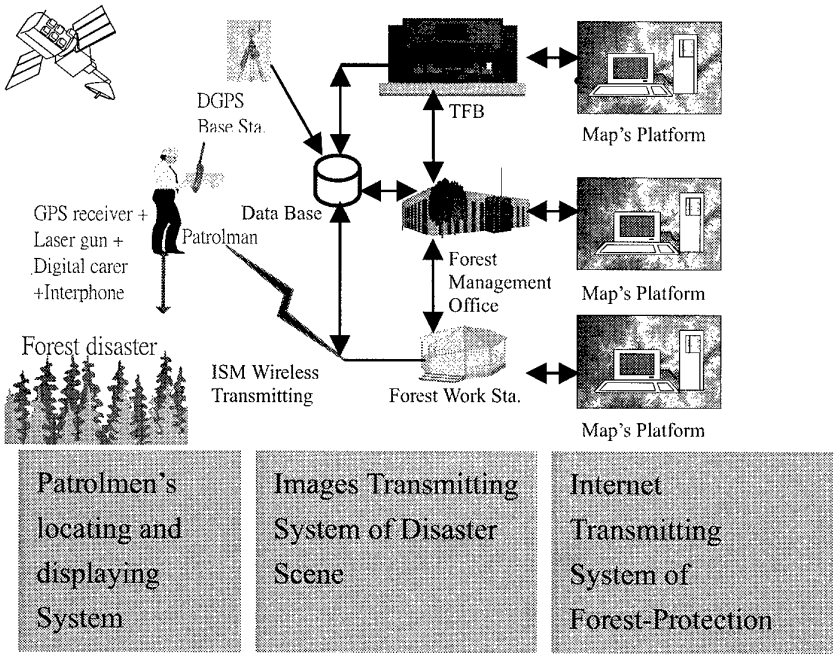


Fig 5 System Structure Chart

The report of the can be inquired and transmitted by.

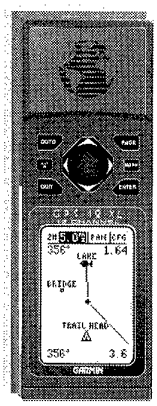


Fig.6 Hand-Held GPS receiver

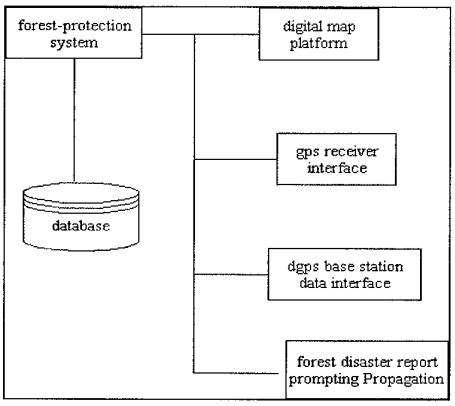


Fig. 7 system interface diagram

4.3 The System Functions

This research performs the whole system to an executive file, which is operated independently. This system can be carried to install in any computer or Notebook computer. The following functions are included:

The Functions of Digital Map

Digital maps operate the system mainly. The digital map has the followed functions:

4.3.1 The Overlay of Map Layers

At anytime, the system combine forest topographies and forest cadastral maps as basic map, and then join in the administrative district map (Fig 8), hydrographic map, gradient map, imaging map, forest patrol-trail map (show as Fig 9) and forest calamity place coordinates etc, to construct an integrated GIS on the map layers for rescuing.

4.3.2 Basic Operation

The Basic functions of digital map are enlargement, reduction, displacement and revolution.

4.3.3 Information Inquiring

While clicking mouse on digital map screen, the system will display the clicked point interrelated information immediately, or one can key-in some data in inquiry item to filtrate the place and information which is required.

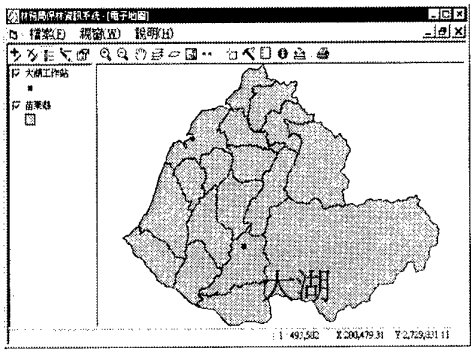


Fig.8 Administrative district map

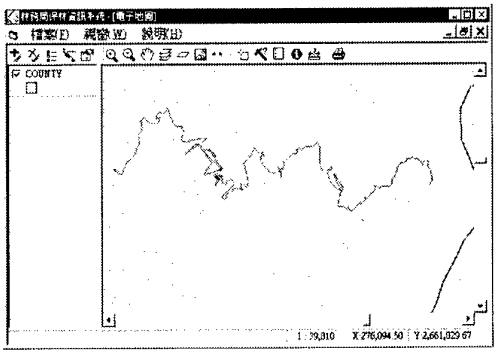


Fig. 9 Forest patrol-trail map

4.3.4 Map Printing

Printing the map in needed scale from plotter for analyze and consulting.

4.4 The Sub-system Function for Forest Patrol

4.4.1 The Essential Maintenance Data of Forest Patrolmen

Includes the ID, name, department of forest patrolmen, which would be identify and match the transmitted coordinates.

4.4.2. The Data Receiving of Portable GPS Receiver

The system provide two ways to get GPS data, one can immediately transmit the coordinates information which obtain from GPS receiver to forest workstation computer by radio modem, or download GPS data to computer from GPS receiver directly, when coming back to the office.

4.4.3. The Sub-system Function of Forest Disaster Prompting Propagation

4.4.3.1. The Forest Disaster Prompting Propagation Data Maintaining

This operation includes forest disaster information, calamity region coordinates, instant scene pictures etc. The collecting information will be distinguished in primary file and detailed files. The primary file record essential information of calamity region, the detailed files record post-conduction after forest calamity.

4.4.3.2. The Forest Disaster Prompting Propagation Data Transmitting

This system compress recorded files to transmit the data by Internet or compact disks.

4.4.3.3. The Identification Number Maintenance of Forest Disaster

This operation includes each type of forest disaster identification number.

4.4.4 The Sub-system Function of Forest Disaster Prompting Propagation

4.4.4.1 The Forest Disaster Prompting Propagation Data Maintaining

This operation includes forest disaster information, calamity region coordinates, instant scene pictures etc. The collecting information will be distinguished in primary file and detailed files. The primary file record essential information of calamity region, the detailed files record post-conduction after forest calamity.

4.4.4.2 The Forest Disaster Prompting Propagation Data Transmitting

This system compress recorded files to transmit the data by Internet or compact disks.

4.4.4.3 The Identification Number Maintenance of Forest Disaster

This operation includes each kind of forest disaster identification number.

4.4.5 DGPS Base Station Establishment

This research project intent to promote the positioning accuracy, to establish a DGPS base station in Tahu Forest Work Station, receiving GPS message for whole time in everyday, and link with main system, so get the better differential correction value in computer. While hand-held GPS receiver's data of the patrolman has been linking to computer, the patrolling trail correction data has been done automatically.

Before establishing GPS base station, the base station setup the Leica system 300 GPS receiver, in the mean while also setup same model instrument in 5 known coordinate control point located around the base station within 3 kilometers, while performing static GPS surveying more than one hour, then post-process the GPS observations with Leica Ski software to get the local coordinate of Tahu base station.

4.4.6 Web inquiring forest calamity

Through the network to display the forest calamity, then establishing the common sense of protect forest.

4.4.7 Forest calamity scene real time transmitting

This research employ 2000 series, 2.4-2.4835GHz ISM frequency band local radio network （Industrial Science Medicine Frequency Band）. The transmitting speed reaches 2 Mbps, even if transmitting place is far as 25 km, still can reaches 1 Mbps.（1999 翔益） This equipment transmission can provide more economical, tolerable than cable network. It always proceed transmitting stable no matter how weather situation. So user can understand calamity situation from browser through network facilities.

When patroller propagate forest calamity, the control commander instantly dispatch Van rescuing troops. The rescuer take forest calamity photo with AXIS 2100 digital camera （Fig. 10）. The captured images are compressed to ZIP files with JPEG file type, transmitting to the nearest T1 network control center of forest management office by OMNI-Directional Antenna, WLD2000SA Wireless LAN Unit. The control commander can understand forest calamity development area and rescuing situation with browser software in computer.

Intent to develop effectively radio local network benefit, this research just run an enterprise investigate on-the-spot to choose 3 proper places as relay-station in Tahu region, will key-in coordinates and jurisdiction region to setup its data base. Then if it is successful to carry out the functions of display, inquiring, transmission, etc presently. This system will be an established basis for forest calamity relay station in future



Fig, 10 AXIS 2100 Digital Camera

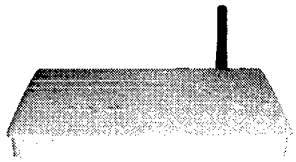


Fig.11 WLD2000SA Wireless Connector

5.Conclusion

5.1 This research had run an demonstration in Tahu Work Station, employ palm GPS receiver just proceed simple operating procedure, to record patrolling trail and time, effectively improve management.

5.2 This system posse completes function to easily operating.

5.3 This system display or inquire patroller trail, effectively modify and manage patrolling route, completely eliminate patrolling blind angle.

5.4 Ordinarily every patroller possess one GPS receiver displaying Chinese, while finding forest calamity in patrolling, recording calamity place coordinate and setup identified number, immediately transmitting calamity place coordinate, area, forest plantation, scene image to control commander with laser range finder, digital camera and, micro wave wireless radio for making a strategic decision.

5.5 This system process receiving GPS message to record patrolling trail, forest identification number, extend inspecting forest administration to fulfill investigating national forest information.

5.6 This system can improve management efficiency for forest administration; the executing achievement can be as a reference for revising policy.

6. Reference Articles

6.1. TFB（1998）, Forest Protection, Briefing of TFB, P.16~21.

6.2. Yang, L.S., Wu,C.M.（1998）E-Map Design, Cartography Conference, P.58-67.

6.3 Shih,P.H.,（1997）Geographic Information Systems,P.63~65

6.4 Chung,L.K.,（1999）。The Evolution of GIS,P.7.2~7.30。

6.5 Lieu, J.Y.,（1993）The Principles and Applications of GPS, P163~164

6.6 Jeng. C.L.,（1999）The Fundamentals and Applications of GPS, P197~198

6.7Lee, C.T.,（1999）The Introduction of Internet, P23~24

6.8Chou,T.Y.,Cheng, S.P.,（1995）The Study of Real Time Vehicle Navigation & Tracing System, The 14th Conference of Surveyor Engineering & Application,P.159-172。

6.9 Steve Dye, Dr. Frank Baylin,（1997）,The GPS Manual Principles and Application, P.143-144

6.10 Chen,H.Y.,1996,.4, Decision Support for Agricultural Land Management, The Second International Symposium on Systems Approaches for Agriculture Development, IRRI,.Los Banos,.Philippines,.13P。

6.11 Chou Tien-yin, Yen Mei-lin, Chen Cheng-jane, 1995, 5, Land Use Monitoring and Management for DerChi Reservoir Watershed, Hong Kong University Geoinformatics '95 Hong Kong.

APPLICATION OF OPTICAL REMOTE SENSING TECHNOLOGY FOR OIL PALM MANAGEMENT

Ibrahim.S , Zainal Abidin Hasan & Mariamni Khalid

ABSTRACT

Recent advances in remote sensing technology and applications, with concurrent advances in global positioning systems (GPS) and the ubiquitous use of geographic information systems (GIS), have provided a powerful analysis tool for precision agriculture. These advances have also led to intense informational requirements. Image-based remote sensing may provide the timely, spatially distributed information on crop and soil conditions that is needed to implement precision agriculture. The aim of this paper is to investigate the relationship between Landsat Thematic Mapper (TM) relative radiance and phenology of oil palm for commercial estates in Selangor, Malaysia. This study focused on estimating oil palm phenology with special emphasis to planting age (1- >20 years) and Leaf Area Index (LAI) to spectral radiance via multiple linear regression models. The carrier (predictor) variables that was considered for multiple regression are the six Landsat TM bands, Shadow Canopy Index (SI), Bare Soil Index (BIO), Normalised Vegetation index (NDVI), Advanced Vegetation Index (AVI), planting densities, soil units and relief. The relative radiance recorded by Landsat TM for oil palm was negatively correlated with stand age. Middle Infrared wavebands (MIR) band 7 and 5 showed high correlation (> 0.74) and more discriminating power (Lambda Wilk's coefficient) to discriminate the oil palm age classes. However, the visible and Near Infrared bands displayed insignificant correlation (< -0.05). Nevertheless, it is concluded that the developed regression model was able to produce reasonably accurate oil palm age classes at estate level from satellite image.

1.0 INTRODUCTION

Oil palm has become an important crop in Malaysia. The country is the world's largest exporter of palm oil. Within a relatively short period the planted areas under oil palm have increased tremendously from 54,656 hectares in 1960 to 300,800 hectares in 1970 and 1.98 million hectares in 1990. In 1993, the total area under oil palm was estimated to be 2.2 million hectares (Primary Industries Department of Malaysia, 1998). Oil palm cultivation in Malaysia is largely based on the estate management system and organised smallholders under The Federal Land Development Authority (FELDA), Federal Land Consolidation and Rehabilitation Authority (FELCRA), The Rubber Industry Smallholders Development Authority (RISDA) and the State Economic Development Corporation (SEDCs). This has enabled a better utilisation of resources as well as the application of advanced management and planning techniques throughout most of the industry.

Because of the importance of oil palm to the country, accurate and reliable information is needed for oil palm management, especially on plant quality, phenology, health and yield prediction. However, in the context of Malaysia, lack of data, cost effective and timely processing of information for oil palm management planning are major constraints which hold up decision making. Currently data collection for oil palm planning and management depend mainly on traditional methods of sample surveys in the field. The main task of Malaysian agriculture agencies is to improve the reliability, timeliness and cost effectiveness of data collection techniques. Remote sensing was identified as an effective recent agricultural crop information for the global oil palm plantation industry planning (MACRES, 1998).

In Malaysia, the usefulness of remote sensing in crop management has not been intensively explored. Remote sensing in conjunction with a land information system is believed to be a good technique to assist the Malaysian Agriculture Planning Unit and estate managers in making fast decisions.

Therefore, based on the importance of oil palm to the country and the lack of reliable, timely and cost effective data, a study of application of satellite images to plantation information management and planning is justified. The aim of this paper is to elaborate the relationship between Landsat TM radiance and the phenology of oil palm on commercial estates in Selangor, Malaysia (Tuan Mee and Balau Estate), especially the ability to characterise age since field planting and to acquire knowledge on producing oil palm vigour map from remote sensing.

2.0 METHODOLOGY

2.1 Study area

Balau and Tuan Mee estates are situated at Semenyih and Kuala Selangor, respectively, in the state of Selangor, Malaysia They were selected as study areas because of the availability of the ground-surveyed data supplied by Applied Agriculture Research Sendirian Berhad (AARSB), the agriculture adviser to both estates. Balau Estate is relatively flat with less than 17 degree slope whereas Tuan Mee Estate is undulating with 10 to 20 degree slopes.

2.2 Landsat imagery

The Landsat TM scene used was path 127 row 58 for 6 March 1996, bands 1,2,3,4,5 and 7, pre-processed by the ground station to level 4 (radiometrically corrected and across track geometric correction applied) (Figure 3.2 and Figure 3.3). The imagery was supplied by the Malaysian Centre for Remote Sensing (MACRES) who acquired it from Thailand's ground receiving station. The Landsat TM imagery was atmospherically adjusted using the dark-pixel subtraction method (Foody, 1997). Dark object subtraction methods are based on the assumption that within an image some pixels will lie in areas of complete shadow and so any radiance measured from them by the sensor must be attributable to the atmosphere requisite that image has been radiometrically calibrated.

2.3 Pixel sampling

A simple stratified sampling scheme (Gallego, 1995) with strata based on oil palm age was used to extract the Landsat TM spectral radiance values. A sample of 373 and 757 pixels, each 30 X 30 m were distributed randomly were selected from Balau and Tuan Mee Estate, respectively. Samples were selected based on visual interpretation of the Landsat-5 image, the topographic map, and oil palm years planting map. A number of considerations were taken into account during the sampling procedure: 1: The location of training areas near the boundary of different planting stages was avoided. 2: Extreme care was taken to prevent the selection of training areas within or near to shadow areas.

3.1 DISCRIMINANT ANALYSIS OF LANDSAT TM SPECTRAL RADIANCE ON OIL PALM PLANTATION

The relative strength of the relationship between oil palm age classes and the radiance data acquired from Landsat TM bands were examined. The Wilks's Lambda coefficients (Johnston 1978, Klecka 1980, and Boyd *et. al.* 1996) adopted from discriminant analysis in SPPS were used to analyse the relative importance of six Landsat TM bands as discriminating variables. The magnitude of the Lambda coefficient is inversely related to the ability of wavebands to discriminate between classes (Boyd *et. al.* 1996). Table 3.1 shows the rank order of the six individuals Landsat TM bands according to discriminant analysis. It illustrates that the data acquired by band 5 and band 7 (middle infrared, MIR) of both the study sites showed a considerably more discriminating powers, with band 7 providing the highest.

Landsat TM	Wilks's Lambda(a)	Correlation (r_s)	Wilks's Lambda(b)	Correlation (r_s)
TM1	0.665	-0.71683	0.856	0.09857
TM2	0.381	-0.70300	0.806	-0.01492
TM3	0.371	-0.65986	0.809	-0.14758
TM4	0.864	-0.50710	0.772	-0.06242
TM5	0.283	-0.79930	0.459	-0.84384
TM7	0.273	-0.73718	0.383	-0.65027

Table 3.1: Discriminant analysis for TM bands and age classes for Tuan Mee Estate (a) and Balau Estate (b). Spearman rank correlation coefficients ($p < 0.05$) *between radiance and age is also shown (source: ibrahim, 2000)*

The Spearman rank correlation coefficient (r_s) of each Landsat TM bands was calculated. The visible and near infra red bands displayed insignificant correlation ($p < 0.05$). The relationships obtained from the data acquired in MIR bands were stronger and statistically more significant than those achieved in the visible (band1, band 2 and band 3) and near infrared band (NIR) (band 4). The highest correlation coefficients between oil palm age classes and TM radiance were obtained from TM7 and TM5 [(r_s = -0.737 and –0.799 (Tuan Mee), r_s = -0.650 and –0.844 (Balau Estate)], respectively which were significant at the 99% confidence level. A study by Boyd *et. al.* (1996) also found that Landsat TM band 5 and 7 showed higher Spearman rank correlation coefficient and better power to discriminate tropical regenerative stages in even-aged forest. The effects of interrelated factors such as scattering within leaves, canopy shadow, chlorophyll absorption, canopy transpiration and under storey reflectance (McWilliam *et al.* 1993) can be used to explain the relationships resulting from data acquired in respective TM Wavebands and oil palm age classes. However, the influence of each factor may be changed due to the canopy development of oil palm. Other factors that influence the relationship may be oil palm management practices in pruning, harvesting, fertilising and weeding of the respective study areas. TM bands had higher discrimation power and Spearman rank correlation coefficients between oil palm age and Landsat TM wavebands for Tuan Mee than Balau Estate. The result will be discussed in section 3.3.

The information provided by MIR bands 7 and 5 can be used effectively by incorporating other image processing techniques such as Advanced Vegetation Indices (AVI), Bare Soil Indices (BIO) and Shadow Indices (SI). The combination of the information provided by data acquired in the Landsat TM bands and its indices it is believed can strengthen the correlations obtained between the remotely sensed image and oil palm age classes and properties.

The study also illustrates that, of the indices, the Soil Index had the strongest Spearman rank correlation coefficients over the whole 1-26 or 4-21 year age range at 99% confidence level (r_s = -0.78 and –0.82 for Tuan Mee and Balau estate, respectively). Other indices such as NDVI and the Advanced Vegetation Index had insignificant correlations and an inability to discriminate between age classes (r_s = 0.47 and -0.05 for Tuan Mee Estate and r_s = 0.13 and –0.01 for Balau Estate). However, the Spearman rank correlation coefficient for the Shadow Index (SI) was strong at Tuan Mee (rs = 0.70) and weak for Balau (rs = 0.02).

3.2 Spectral response and the development of oil palm canopy

A decrease in relative radiance with stand age was identified in all Landsat TM bands (table 3.1). McMorrow (1995) found the same trend for Landsat TM spectral response of oil palm stand age classes in Sabah Malaysia, and that oil palm spectral response was most age-sensitive for stands less than 5 years old. In this study, oil palm spectral radiance was also most age-sensitive for younger stands, between 1 to 4 years old (figure 3.1). The higher discriminatory power and significant

correlation at Tuan Mee relative to Balau Estate is explained by the fact that in the age range was 4 to 21 years old, whereas at Tuan Mee Estate it is between 1 to 26 years old, so Balau estate excludes the young stands that have the stronger correlation between age and radiance.

The factors explaining the spectral response of vegetation are numerous. They include interaction of radiation with the plant canopy, under storey plant effects, attenuation coefficient for radiation in the canopy and it's underlying soil background (Price and Bausch 1995). Corley (1973) explained that oil palm canopy closure starts at 4 years old and canopies reach a constant size by 9 to10 years old. The percentage of incident light intensity below canopy is a function of LAI: $\text{Log } I = -0.44\ L$

where I is light intensity below the canopy and L is leaf area index (Corley 1973). Light intensity below the canopy is important because although the leaf area will be constant by 9 to 10 years old, by 20 years old the change of leaflets horizontal angle increases from 20 degrees to probably 40 to 60 degrees (Corley, 1973). The leaflets angle becoming less horizontal and more vertical and thus it mean that the canopy gap fraction is greater and so the ground cover contributes more.

The magnitude of the contribution of the canopy and soil are indicated in figure 3.3. Based on the contribution of the canopy and soil to the relative Landsat TM radiance, 6 types of oil palm plantation spectral response were identified: (1). One year old after planting, (2). 2 years old after planting, (3). 3 years old after planting, (4). 4 to 8 years after planting, (5). 9 to 19 years old after planting and (6). More than 20 years old after planting. The factors operating at each stage are:

1. At 1 to 3 years old, the oil palm canopy LAI development increases rapidly and at the same time the contribution of soil and under layer vegetation decrease, i.e. as crown diameter increases.
2. The LAI expands gradually until 8 years old.
3. The LAI reaches a constant at 9 to 10 years old, depending on the genotype and oil palm management practices. The contribution of oil palm canopy, soil and under-storey vegetation is believed to be equal at 9 to 19 years old.
4. The leaflet angles are believed to increase up to 60^{o} (starting at 20 years old) and allow more light penetration to under-storey vegetation and soil.
5. After 21 years old, the under-storey vegetation is believed to increase rapidly and at the same time the soil effect reduces until constant under-storey vegetation was achieved depending on oil palm plantation management practices

The unsupervised classification based on a ratio of the Shadow Index and Bare Soil Index from were computed. It contained 5 classes: (1) 1 year old oil palm after planting, (2) 2 years old after planting, (3). 3 years old after planting, (4) 4 to 8 years old after planting and (5) 9 to 26 years old after planting. The accuracy of the TM image classification was visually compared against the age map complied from AARSB maps. The results were acceptable and useful, however further study are required especially on data calibration and spatial variability of Landsat TM data.

4.0 Conclusions

This study has investigated the usefulness of remote sensing for estimating oil palm age and leaf area index (LAI) using Landsat TM data and its indices in the Malaysian oil palm plantation system. The following summaries can be made from this study:

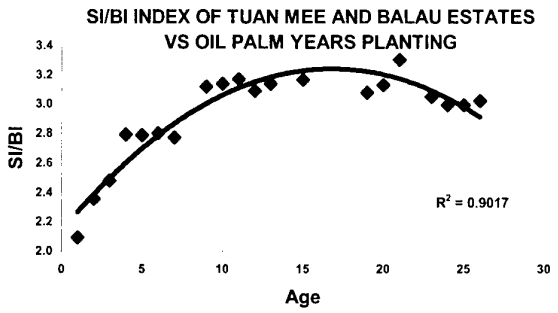


Figure3.1: The magnitude of the contribution of the oil palm canopy and soil

1. Middle Infrared (MIR) wavebands of Landsat TM (band 5 and 7) for both estates contained considerable discriminating power and provide stronger relationships with oil palm age classes than data acquired in visible and near infrared wavebands. Similarly, it was found that the inclusion of MIR wavebands in multiple linear regression model 1 improves statistical significance. When all Landsat TM wavebands were included in the multiple regression analysis, band 5, 7 and 1 (Balau Estate) and band 5, 4, 3, 1 and 7 (Tuan Mee Estate) were found to be statistically significant as predictor variables for oil palm age class estimation.

2. Balau Estate had less relative error in oil palm age estimates in all models (model 1, 2 and 3) than Tuan Mee Estate. The regression analysis of oil palm age classes of Tuan Mee Estate needed more predictor variables compared to Balau Estate. This is believed to be due to the wide range of oil palm planting density and the terrain complexity of Tuan Mee Estate.

3. Although the main aim of this study is to estimate oil palm age classes from spectral Landsat TM wavebands it was found that spectral indices could better discriminate oil palm age classes. Multiple regression models including indices SI, BIO and AVI with Landsat TM bands produced less error in age estimates at Tuan Mee.. They are recommended for plantations with similar complex terrain and a wide range of planting densities.

4. Landsat TM bands and its indices in conjunction with GIS information can provide a reasonably accurate estimation of oil palm age at estate level. The planting density predictor variable improved the error of oil palm age estimation for both estates. Planting density can influence canopy development and, especially the age at which the oil palm canopy starts to close. Higher planting density causes canopy closure at an earlier age so that the regression line (constant) suggested should be steeper. The planting density variable should be investigated by developing separate regression models for low and high density blocks.

5. The approach developed in the present study agrees with the view that the all features of the biosphere cannot be measured directly from satellite data. However by using an underlying functional relationship between variable under investigation and secondary variable that can be measured by satellite sensor, a model can be developed that predicts the desired information.

5.0 REFERENCES

BOYD D.S., FOODY D.S, CURRAN P.J., LUCAS R.M. HONZAK M. (1996) *An assessment of radiance in Landsat TM middle and thermal infrared wavebands for the detection of tropical forest regeneration. International Journal of Remote Sensing, 17, 294-261*

CORLEY R.H.V.,*(1973) Effects of plant density on growth and yeild of oil palm. Expl. Agric, 9: 169-180.*

JOHNSTON R. J., *(1978), Multivariate statistic analysis in geography (London: Longman).*

MCMORROW J.M.*, 1995. Relation of oil palm spectral respone to stand age. International Journal of Remote Sensing, 16, 3203-3209*

GALLEGO *1995 SAMPLING PROCEDURES, FRANCE GDTA 25-65*

MCWILLIAM A. L. C., ROBERTS , J. M., BACRAL., O. M. R., LETITAO, M. V. B. R., DE COATA, A. C. L., MAITELL, G. T., AND LAMPARONI, C. A. G. P., 1993*, Leaf area indices and above-ground biomass of terra firme rain forest and adjacent clearings in Amazonia. Functional Ecology, 71, 310-317*

PRICE J. C., and BAUSCH W. C., 1995 *Leaf area estimation from visible and near infrared reflectance data. Remote Sensing and Environment. 52: 55-65.*

APPROACH TO LAND-USE ANALYSIS IN HETAO IRRIGATION PROJECT OF INNER MONGOLIA, CHINA, BASED ON SATELLITE IMAGE DATA

Takashi KUME, Kiyoshi TORII and Toru MITSUNO
Graduate School of Agriculture
Kyoto University
Oiwakecho, Kitashirakawa, Sakyoku, Kyoto
Tel. & Fax.: (81)-75-753-6459
E-mail: zak@kais.kyoto-u.ac.jp
JAPAN

KEY WORDS: Land use analysis, Inner Mongolia irrigation project

Abstract: Hetao irrigation district is a large-scale irrigation area, which takes 294,000,000 m^3 of water annually (just less than 300 m/sec) from the Yellow River and covers 500,000 ha of agricultural field with. While this area has the history of irrigated agriculture since the time before Christ, a full-scale irrigation product was started about 100 years ago. At present, the project is said to be in a critical situation due to serious problems of water shortage and saline soil in addition to decrepitude of irrigation facilities.

In the present study, we analyzed land-use changes in the respective irrigation blocks in recent years using satellite image data to grasp the actual state of irrigation in this big project and to find a clue for solving problems in future. We present outline of the results.

1. INTORDUCTION

Land-use analysis in a large-scale irrigation area is a very useful method for cropping, improvement in agricultural production, environmental assessment and irrigation-drainage planning.

Irrigation-drainage system is indispensable in arid and semi-arid areas such as Hetao irrigation district (Fig. 1) selected in this study. Agriculture without irrigation is not effected in arid and semi-arid areas where evapo-transpiration exceeds precipitation. However, inappropriate irrigation has caused soil salinization problem all over the world and this is one of the serious problems to be solved as quickly as possible. Hetao irrigation district is no exception in this aspect and the soil salinization problem is also found in this area. To solve the problem, the areas with soil salinization must be specified. However, specification of the areas with soil salinization consumes much labor, time and cost in large-scale irrigation areas such as Hetao. Thus, utilization of satellite image data, which offer monitoring

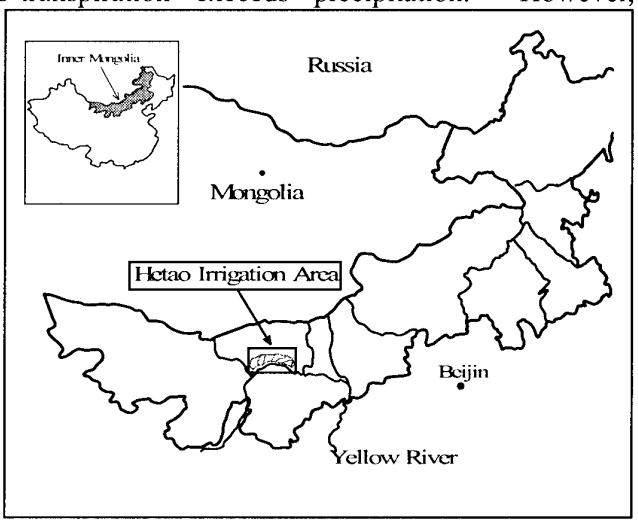


Fig. 1 Inner Mongolia

in extensive areas and time-series analysis, becomes very effective.

The study area where we attempted land-use analysis based on satellite image data is Linhe City. We performed supervised classification (the most-likely classification method) and unsupervised classification to identify dunes and salinized areas in this district.

Soil salinization in arid and semi-arid areas is likely to result in desertification in future. In Hetao irrigation district in particular, Wuliangpuhe Desert is approaching from the west and continuation of irrigated agriculture in this area will consequently prevent desertification of Inner Mongolia. In this study, we attempted to grasp the situation in the salinized areas spreading around the irrigation district.

2. STUDY AREA

Hetao irrigation district (Fig. 2) is located in Yellow River basin, Inner Mongolia, China, and it is 250 km in width from east to west and 50 km in length from north to south and its altitude is between 1019 and 1050 m. It has the east-to-west inclination between 1/5000 and 1/8000 and the north-to-south inclination between 1/4000 and 1/8000. It has the area of about 1,100,000 ha including 514,000 ha of agricultural area and 482,000 ha of the agricultural area corresponding to 93% are irrigated by Yellow River. Agriculture is impossible in this area without irrigation water from Yellow River. The annual precipitation in this area is between 130 and 200 mm increasing from west to east and the annual evapo-transpiration is between 2000 and 2400 mm. The highest temperature in summer is 38 ℃ and the lowest temperature in winter is –38 ℃.

Irrigation in this area has a long history since the time before Christ. In 1900, eight large irrigation canals were completed and the irrigation area from Yellow River became around 700,000 ha. After 1901, the Ching dynasty continued to expand irrigation area. Since the founding of People's Republic of China in 1949, Hetao irrigation district was improved rapidly. The Yellow River embankment was completed in 1950 and the irrigation area was expanded to 270,000 ha with construction of release sluice.

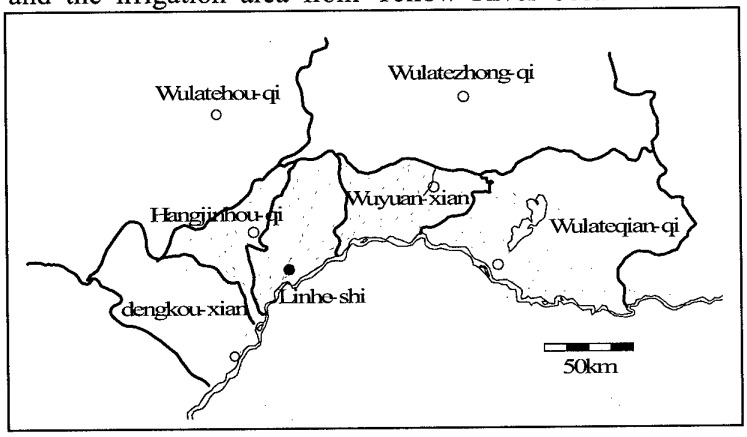


Fig. 2 Hetao rrigation district

The irrigation area continued to expand subsequently reaching 480,000 ha in 1975. However, with expansion in the irrigated area, soil salinization in Hetao irrigation district has become a serious problem coupled with long-standing irrigation and various problems. In 1997, flow in Yellow River was cut from the river mouth to the point 700 km upstream raising a problem of water shortage. In Hetao irrigation district, salt accumulation is detected in 476,000 ha corresponding to 50% of the irrigated land of 1,100,000 ha. While salt once accumulated cannot be eliminated unless it is leached by a large amount of precipitation or irrigation water, the annual rainfall in Hetao irrigation district is extremely small as 180 to 200 mm as mentioned previously and, together with the water shortage in Yellow River, there is not sufficient water for leaching.

In this difficult situation, Hetao irrigation district has tasks of crop production with economized irrigation and rehabilitation of salinized ground. We examined distribution of dunes and salinized areas by the land-use analysis using remote sensing image data as the first step to solve these problems.

3. MATERIALS AND METHOD

As satellite image data, Landsat TM data (spatial resolution: 30m x 30m, path-row: 129–32 , date of observation: 1989/9/17) were used.

The result of image classification was used to analyze land uses in Hetao irrigation district according to the following procedure.

(1) All satellite image data were geometrically corrected based on the GCP obtained by the field survey (2000/8/11, 12) using the analysis software.

(2) Subset image around Linhe City was extracted referring to Inner Mongolia Maps (published by Inner Mongolia Map Pub.).

(3) Supervised and unsupervised classifications were performed with five training classes of water, dune, urban area, vegetation and saline soil (including naked ground).

(4) From the results of classification, areas were calculated and compared with the results of the field survey.

Table 1 shows the detailed classifications performed in the present study; three classification in total including two supervised classifications and one unsupervised classification.

Table 1 Decision rules

	Parametric Decision Rule	Non-Parametric Decision Rule	Other Decision Rule
Supervised classification 1	Maximum Likelihood	Multi Level Slice	×
Supervised classification 2	Maximum Likelihood	×	×
Unsupervised classification	×	×	ISODATA Method

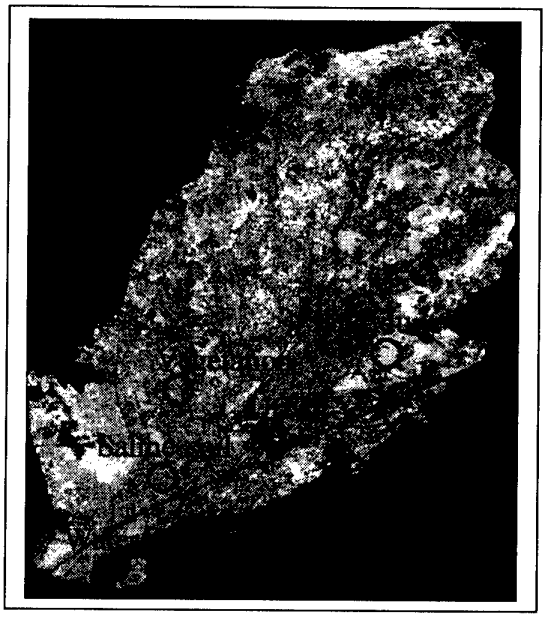


Fig.3 Signatures in Linhe

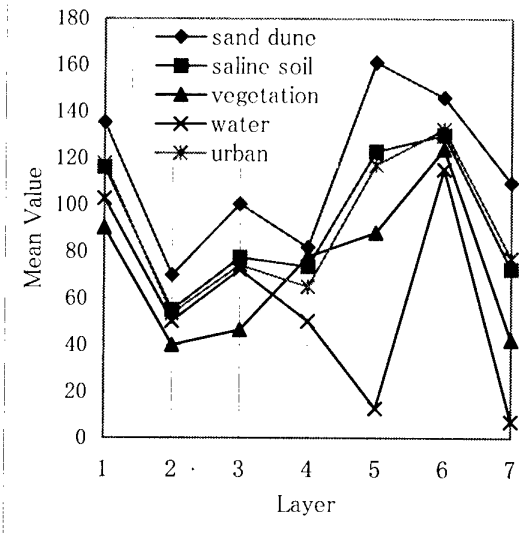


Fig4 Reflection characteristics(CCT value)

In the supervised classification 1, parametric most-likely classification method was employed for unclassified areas following the nonparametric classification. In the supervised classification 2, only parametric most-likely classification was performed. For unsupervised classification, ISODATA method was used.

Fig. 3 shows the areas extracted as training data for dune, salinized soil (including naked soil), vegetation, water and urban area based on the satellite image of the area. All the areas underwent ground-truth in the present survey.

Fig. 4 shows the mean spectral reflection characteristics of the respective bands in the training area.

4. RESULTS AND DISCUSSION

Figs. 5 to 7 show the results of the supervised classifications 1 and 2 and unsupervised classification mentioned previously. Table 2 shows the areas (ha) of the respective classes in the results of classification in Figs. 5 to 7. Here, we discuss the most-likely classification method applied generally. In the area of about 247,000 ha in Linhe, 8,556 ha (3.46%) were classified into dune and 96,532 ha (39.1%) were classified into the saline soil; the area amounting to 42.56% is the land of dunes and saline soils not covered with vegetation.



Fig5 Supervised classisification1



Fig6 Supervised classisification2

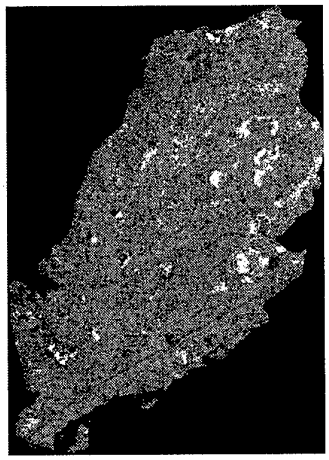


Fig7 Unsupervised classification

Table2 Result of classification

Method	Sand dune (ha)	Saline soil (ha)	Vegetation (ha)	Water (ha)	Urban (ha)	Others (ha)	Total (ha)
Supervised classification 1	8556	96532	111967	13763	3009	13135	246963
Supervised classification 2	7218	97158	111884	13600	3642	13460	246963
Unsupervised classification	14458	92745	98986	8135	26602	6037	246963

Figs. 8 and 9 show the areas coinciding to both the result of extraction of dunes and the result of extraction of dunes and saline soils (including naked soils) from Figs. 5 and 6. Table 3 shows the results. Comparison of Tables 2 and 3 reveals decreases in dunes and saline soils. These are the results of extracting the areas common to Figs. 5 and 6.

While the result of classification of saline soil is considered to include large areas of naked land, a diagram of naked land = saline soil is true in many areas in Hetao irrigation district

and detailed classification is difficult. Moreover, as our analysis utilizes the block where a part of dunes, saline soils and houses are made of alluvial soil distributed in the whole Hetao irrigation district, it is very difficult to classify them in detail.

Table2 Result of classification

Method	Sand dune (ha)	Saline soil (ha)	Vegetation (ha)	Water (ha)	Urban (ha)	Others (ha)	Total (ha)
Supervised classification 1	8556	96532	111967	13763	3009	13135	246963
Supervised classification 2	7218	97158	111884	13600	3642	13460	246963
Unsupervised classification	14458	92745	98986	8135	26602	6037	246963

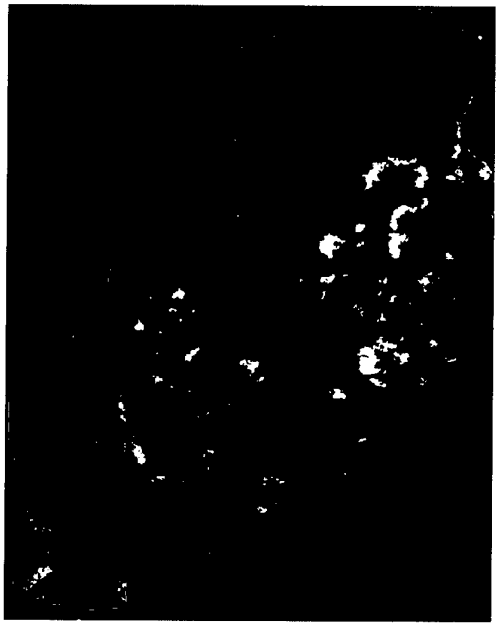


Fig8 Extracted image of sand dune

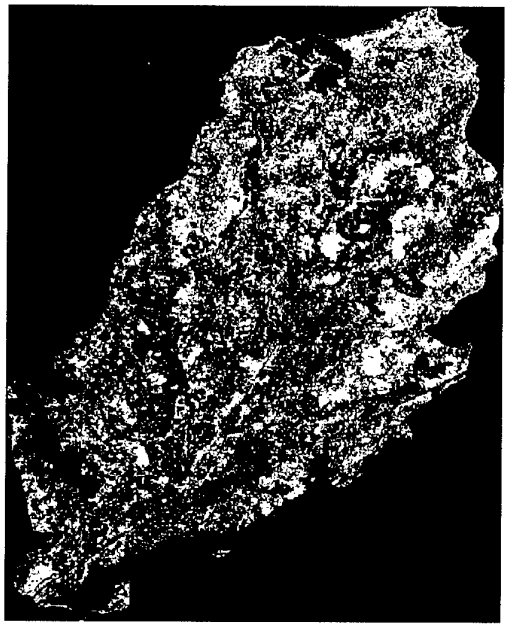


Fig9 Extracted image of sand dune and saline soil

Table3 Result of after extract

Sand dune (ha)	Sand dune (%)	Saline soil (ha)	Saline soil (%)
7211	2.9	93056	37.7

It is seen from Fig. 9 that soil salinization in Hetao irrigation district tended to increase from the south with the main canal (irrigation) to the north with the main drainage canal. In Linhe City, three irrigation canals (Yongji canal, Gangji canal, Fengji canal) out of eight big canals were constructed already in 1900 and inappropriate irrigation at that time was considered to accelerate soil salinization resulting in presence of numerous dunes in comparison to the vicinity of Linhe.

5. CONCLUSION

Following results were obtained by the analysis.

(1) It was necessary to combine the result of detailed ground truth in analysis for accurate classification of saline soil and naked soil.

(2) It would be possible to grasp land cover changes in dunes and saline soils accurately by performing time-series analysis of satellite images in various seasons by supervised classification.

Irrigation and drainage canals are set up like arteries and veins in Hetao irrigation district and combination of satellite image analysis and canal net analysis will permit more accurate analysis of dunes and saline soils as well as analysis of their changes. We would like to subdivide the district into smaller blocks and perform analysis for the respective blocks of irrigation canals and their vicinities, drainage canals and their vicinities and water-rich areas by preparing DEM showing altitude.

ACKNOWLEDGEMENT

In ending the paper, we would like to express our deep gratitude to Inner Mongolia Scientific Technology Association, Inner Mongolia Agricultural College and Hetao Irrigation District Authority for their cooperation in survey and field trip, Professor emeritus Kinzo Nagahori of Okayama University, Professor Takao Amaya of Gifu University and Professor Takeo Akae of Okayama University for their useful advice and NASDA, RESTEC in Japan and EROS Data Center in USA for satellite image data supply. The survey in Hetao Irrigation District was supported by Scientific Research Fund for Basic Researches (A)(1) of Ministry of Education (Project No. 11306015, represented by Kiyoshi Torii).

REFERENCES

(1) Wang, lun, ping. , Study on Irrigation-Drainage system and prevention of Alkali-saline soil in Hetao irrigation area, Inner Mongolia.

(2) T. Amaya, Study on agriculture and livestock farming productivity based on grassland soil in Inner Mongolia, China: Bulletin of Agriculture, Gifu University No.61

(3) K. Nagahori, Study on development of alkali-saline soil in Hetao irrigation area, Inner Mongolia, China: Bulletin of Environmental Scie. & Tech, Okayama University

(4) T. Akae, Study on irrigation agriculture and saline accumulation problem in Hetao irrigation area, Inner Mongolia, China: Bulletin of Environmental Scie. & Tech., Okayama University

(5) T. Kume, Study on development of saline soil and Irrigation-Drainage system in Hetao irrigation area: 1999, Master Thesis, Gifu University

(6) ERDAS FIELD GUIDE, ERDAS Inc., pp.213-258

DROUGHT MONITORING IN ZAMBIA USING METEOSAT AND NOAA AVHRR DATA

Kawana Nawa
Remote Sensing Unit
Zambia Meteorological Department,E-mail: knawa@yahoo.com
Fax/Phone: (260-1) 252728/251889, P.O. Box 30200, Lusaka, Zambia

1. KEY WORDS

Satellite rainfall estimates, Rainfall deficits, Meteosat, NOAA,

2. ABSTRACT

Rainfall is of crucial importance for all life in Zambia not only because it is a resource for human and livestock but also because it is the major limiting factor to plant growth. Between 80 to 90% of agriculture in Zambia is rain-fed and as a result, any falls in the required amounts need to be identified as quickly as possible to enable decision makers take necessary measures to avoid catastrophe in human, plant and animal life. Rainfall in Zambia is highly irregular in space and time which makes cultivation difficult since small differences in the amounts and timing of rain received at a site may determine the success or failure of critical stages in Vegetation development and hence crop production. Determination of areas of rainfall deficit can be greatly improved by using satellite rainfall estimates.
Rainfall measurements have traditionally come from a network of raingauges which in the past years have dwindled in number. Since raingauge measurements are only valid for a small area in the immediate vicinity of the instrument, use of Geo-stationary satellites such as the Meteosat and polar orbiting satellites such as the NOAA series, provide data at a resolution sufficient for monitoring of rainfall events at a much wider scale. Currently different rainfall information is produced and disseminated to various users ranging from farmers, researchers to decision makers.

4. INTRODUCTION

Throughout much of Africa, rainfall is the most important meteorological factor in determining agricultural production and hence economic well being on a local or national scale. Accurate, real-time information on rainfall should therefore be valuable in providing an overview of the development of the current rainy season, and highlighting areas where drought or crop shortfalls are likely. Unfortunately, the raingauge network in Zambia is too sparse to provide this overview and is still reducing further as government funding on public services continues to be small.
The use of rainfall estimates based on satellite data should be of great benefit. In particular, Meteosat thermal infrared imagery can be used in detecting CCD's (an indicator of convective cloud activity) at different thresholds. The CCD images are used in a number of algorithms to give useful quantitative rainfall estimates. These estimates can easily be produced in near real-time and give full area coverage irrespective of the remoteness of a region given the temperal and spatial characteristics of the Meteosat satellite. Complementary information on vegetation and seasonal large scale flooding can be derived from NOAA-AVHRR satellite.

The problem remains of how to communicate this information to local institutions that need to use it. We argue in favour of local reception facilities – they provide more timely information, ensure local staff are familiar with remote sensing technology, improves their scientific background, promotes technical independence of local institutions and can provide information not usually available from international dissemination centres. Locally produced information has a better chance of reaching a wider local user base and is more flexible to varying user demands.
Aiming at improving this situation a joint project took place between the TAMSAT group, Department of Meteorology at the University of Reading, UK and the Zambian Meteorological Department (ZMD). Zambia was suitable for simple rainfall estimation algorithms based on Meteosat Thermal Infra-Red (TIR) imagery and ZMD had the basic technical capacity (Meteosat and NOAA-AVHRR receivers) already in place.

The Aims of the Project were:
- To refine rainfall related information from station and satellite data.
- To implement an operational system of dissemination of agro-meteorological information to a user community along the principles of sustainability and independence. Such a system was designated ZAMIS (Zambian AgroMeteorological Information System).

5. The Zambian Agrometeorological Information System (ZAMIS)

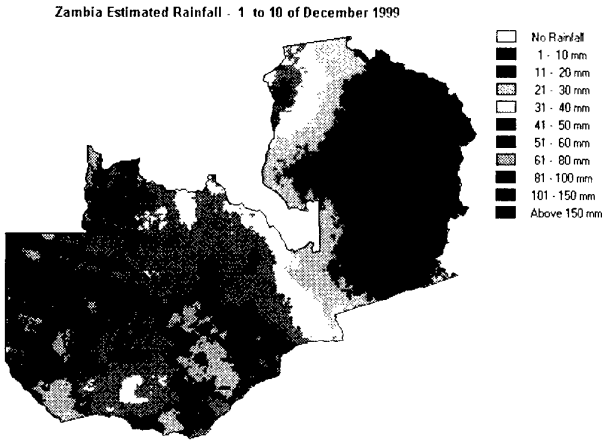
5.1 **ZAMIS Design :**The design of the ZAMIS obeyed the following requirements:
- that it should be adaptable to take account of changing user requirements;
- that the hardware and software used should be inexpensive and easily maintained
- that the staff involved should understand the limitations and benefits of the methodologies
- that the staff involved should be capable of developing new output products as appropriate

5.2 **Software Development :** From the operational sources of raw data, there was a need to produce a very specific set of information outputs using particular methodologies and algorithms. Given the requirements for flexibility, ease of maintenance and low cost, instead of developing a software package to deal with this need in a specific way, the system was built by breaking down the processing task into a sequence of small modular units, each coded in a third party (low cost or free) GIS/IP software macro language and some programs provided by TAMSAT. A scripting language (AWK) is used as a "software glue" to define, control and automate the sequence of processing modules. The AWK scripts have embedded all the required coefficients – e.g. calibration coefficients for rainfall occurrence and estimates, geographic region definitions, settings for image format conversions, etc,. Since all scripts are ASCII, updating and modification of settings and coefficients is a trivial task. IDRISI is the GIS/IP used at ZMD, but any with an ASCII macro language will do (e.g. IDA/WinDisp).

5.3 **System Outputs:** From an input consisting of sets of dekadal raingauge data, daily and dekadal images of storm cloud duration (CCD), plus NOAA-AVHRR day time and night time imagery, the system is able to produce a set of outputs such as:

Ten day rainfall estimates: These are derived from a weighted average of gauge and satellite data (Grimes et al, 1999): A set of gauge rainfall values is interpolated by block kriging thus deriving a map of rainfall and a map of the associated uncertainty (error variance). A regression model provides an estimate of rainfall and associated error from an image of CCD output by a Meteosat. A combined estimate is derived as a weighted average of the two above estimates. The weights are a function of the uncertainty in each component – where the gauge network is sparse, the gauge derived estimate has higher error and hence smaller weight than the satellite estimate. The combined estimate therefore is weighted more heavily by whatever component is locally more accurate.

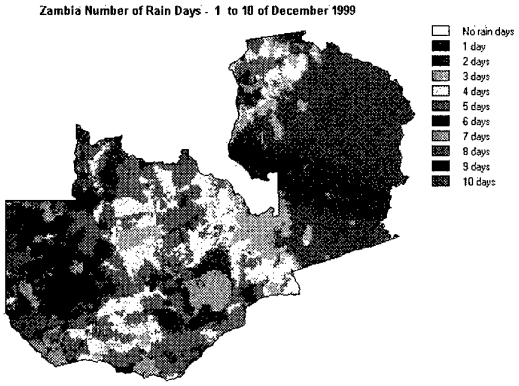
Figure 1



Rainfall Estimate for dekad 1, December 1999

Number of rain days in dekad: Although the amount of rainfall from Satellite Estimates is less reliable on a daily time step as compared to decadal, it can provide useful information on the probability of rainfall having occurred.
A logistic model was derived relating probability of rainfall above 0 to amount of daily CCD, calibrated on years of historical data. This model derives an image of probability of rainfall from an image of daily CCD. From the images of probability of rainfall we derive categorical images of rainfall occurrence by thresholding at a given probability level, i.e. set pixels to 1 if above this threshold, set to 0 if below. The threshold is derived according to criteria of optimal discrimination of rain/no-rain.
From these daily rainfall occurrence images we can trivially derive images of number of rain days per dekad or month. The quality of estimates of consecutive dry periods is under investigation.

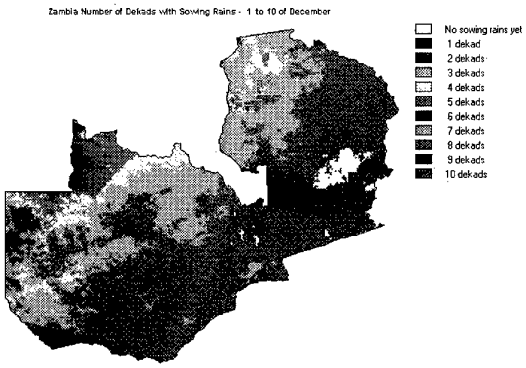
Figure2



Number of Rain Days in dekad 1, December 1999

Sowing rains occurrence: These are derived from the above as areas where it rains more than 25mm from 4 or more rain days in a dekad (ZMD internal definition). These are used to monitor the onset of the growing season and produced up to end of December.

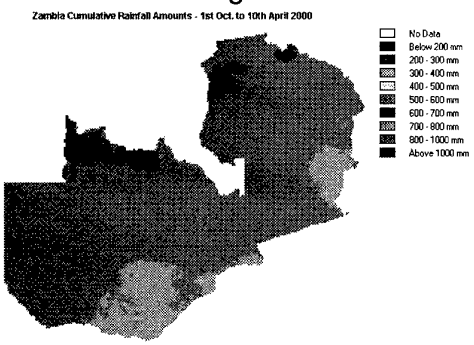
Figure 3



No. of Dekads with Sowing Rains, dekad 1 December 1999

Cumulative rainfall: Derived from the ten day rainfall images.

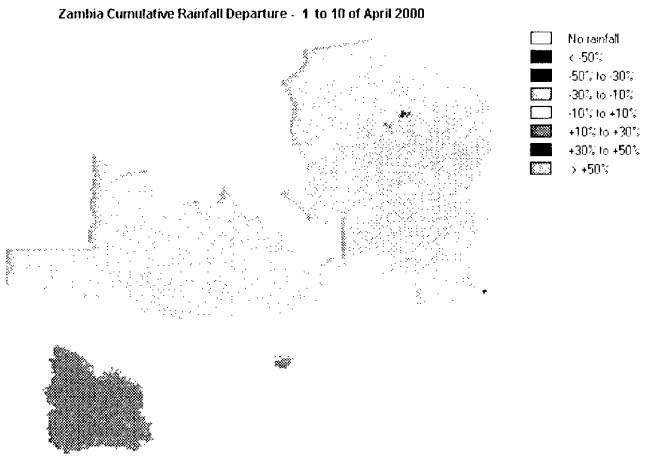
Figure 4



Cumulative Rainfall from 1st October 1999 to April 10, 2000

Cumulative Rainfall Departure: Derived from the rainfall images and climatological rainfall images.

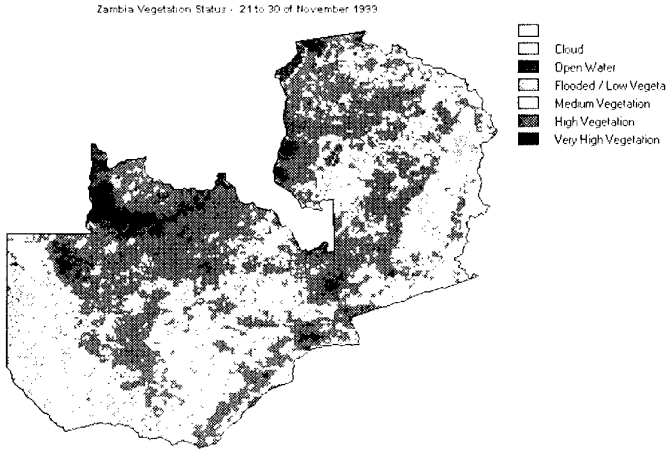
Figure 5



Cumulative Rainfall Departure from normal 1 to 10th April, 2000

Vegetation index, NDVI: Derived from the NOAA data by the usual combination of NIR and Red reflectances. These are produced consistently with the rainfall outputs (same window, resolution)

Figure 6



Zambia Vegetation Status 21- 30th November 1999

6. Users: The users of our information range from Government Institutions (like Disaster Management Unit, Ministry of Agriculture, Department of Water Affairs e.t.c), International Organisations like FEWS, farming community, researchers from local and International Universities, Non Governmental Organisations, Zambia Electricity Supply Company, Regional Organisations involved with management of regional water bodies like Zambezi River Authority.

This information has been well received by users who have used it in various ways like agriculture, water management, research, disaster management e.t.c. Most of the users have been very active and have helped in refining our products by giving us feed

back and suggestions on how best to improve our information to suit their needs. One particular example is one in which a non-governmental organisation (Program Against Malnutrition) asked for rainfall data normally represented at a national scale broken down to administrative districts. This suggestion was incorporated into our dekadal tasks and the product has proved more helpful to the NGO whose work is mainly at district level. Another example was one in which FEWS asked for Excel plots of point extracted values from a cumulative rainfall image against the normal. This helps them in verifying independent field reports.

7. Validation: National Early Warning Cards are usually sent to Meteorological and part time Rainfall reporting Stations. At the end of every dekad, fully completed cards are then sent back to us containing all the rainfall amounts for that dekad and comments on agriculture performance. We then use the rainfall reports to improve the accuracy of Rainfall Estimates and the Agriculture performance reports to independently validate data that we produce.

8. Dissemination: Given widespread access to e-mail the maps (JPEG) derived from the system are sent as e-bulletins (Word files) via e-mail. Web versions are prepared and we hope to have them available soon. All data is produced in a regular lat-long grid (20 pixels/degree) covering most of the Zambezi Catchment.

9. Training: The installation of the AMIS was accompanied by an extensive training program. Given the need for sustainability it was crucial for the operators to be fully familiar with the background, the methodologies and the software the system had been implemented in. Depending on the initial status of the staff, training also included basic programming principles and algorithms. The choices made for software (IDRISI+AWK) provided a very shallow learning curve allowing the operators to quickly build up significant amounts of work and a good confidence level.

10. Conclusion: The temporal and spatial resolution of satellite derived information has practically proven in this particular case to be more handy and timely to decision makers to make well informed decisions on time. A steady stream of quality data has been accumulating and we hope to benefit in future from improved calibrations and refinement in the interpretation of NOAA-AVHRR data. We hope in particular to start the usage of the produced rainfall and vegetation related data in applications such as rainfall-runoff models for flood warning and river management. We have been archiving data and would like to invite other institutions to participate in cooperative applied research ventures.

References

Grimes, D.G., E. Pardo and R. Bonifácio, 1999, Optimal Areal Rainfall Estimation using raingauges and satellite data, *Journal of Hydrology*, 222, 93-108,
Nawa.,K 2000, Drought Monitoring in Zambia using Meteosat and AVHRR Data.

FOREST RESOURCES IN TAIWAN

Jih-Cheng RU
Director, Agricultural and Forestry Aerial Survey Institute
No 61-3, Chao-chou Street, Taipei, TAIWAN
Tel：(886)-2-23931837 Fax：(886)-2-23931870
E-mail:nn240918@ms19.hinet.net
TAIWAN

KEY WORDS：Aerial Photo, Forest Resources, Forest Growing Stock, Biodiversity.

ABSTRACT：The island-wide forest resource inventory has been implemented three times since 1945. Each time the aerial photographs were used for stereo-interpretation, trans-plotting and plot sampling. During the period from July 1990 to June 1993, a total of 32,730 aerial photographs taken by the Agricultural and Forestry Aerial Survey Institute were used for the 3rd island-wide forest resource inventory. The object of this paper is to introduce the process in aerial photography and present status of the forest rsources in Taiwan.
Forest is the largest ecosystems in land area. The biodiversity and global climate change are closely related to the forest. During this time, the forest resource conservation and sustained yield management play an important role in the nation's policy.

1. INTRODUCTION

Four hundred years ago, Taiwan was called "Ihla Formosa "--the beautiful island--for its lustrous landscape. Forests have not only been the home of abundant flora and fauna but also protected the national land, provided the water resource for our daily life and recreation sites. All our basic necessities such as food, water, clothing, housing, transportation, education and recreation are closely related to the forests. Forest resources include the timber resource, water resource, biological resource, recreation resource and other ecological resources etc.

2. AERIAL PHOTOGRAPHY

The island-wide forest resource inventory has been implemented three times since 1945. Each time the aerial photographs were used for stereo-interpretation, trans-plotting , plot sampling, and data compilation. Prior to the implementation of the island-wide forest resource inventory, aerial photography must be taken covering all of Taiwan. During the period from July 1990 to June 1993, a total of 32,730 aerial photos in panchromatic film, focal length 6", at scale of

1/17,000-1/20,000 taken by the Agricultural and Forestry Aerial Survey Institute were used in the 3rd island-wide forest resource inventory.

The flight line spacing is 2.5 km interval divided into 78 flying lines, north-south covering the entire island. The forward overlap is 60%-90%; side overlap 30%. Among these photographs, a total of 286,925 photo points and 3,996 ground plots were selected by double sampling for computations of land-use, forest area, timber volume, forest soil, wildlife and recreation, forest land classification. The photo base maps both B&W and color at scale of 1/5,000 and 1/10,000 were used as a base map for trans-plotting and field survey.

Investigating works included：

1. Photo point interpretation
2. Ground plot Investigation
3. Land use type trans-plotting
4. Forest soil Investigation and soil map production
5. Wildlife and recreation resources inventory
6. Establishment of GIS and database
7. Establishment of forest land classification

3. TIMBER RESOURCES

3.1 Forest Land Area

According to the data of the third aerial survey of forest resources in 1995, there are 2,102,400 hectares of forest land occupying 58.53% of the total island base (3,591,500 hectares). The non-forest land area 1,489,100 hectares occupying 41.47%. Among the forest land areas, the conifer forests occupy 438,500ha., or 20.86 %, conifer and hardwood mixed forests 391,200ha., or 18.61 %, hardwood forests 1,120,400ha., or 53.29 % and bamboo forests 152,300ha., or 7.24%. (Table 1)

Table 1 Forest Land in Taiwan

Land classification	Area (ha)	Percentage (%)
Forest land	2,102,400	58.53(100.00)
Conifers	438,500	12.21(20.86)
Conifers & hardwoods	391,200	10.89(18.61)
Hardwoods	1,120,400	31.19(53.29)
Bamboo	152,300	4.24(7.24)
Non-forest land	1,489,100	41.47
Total	3,591,500	100.00

Among the forest land area, of which the natural forest is 1,527,500ha, occupying 72.7%,

plantation forest is 422,600ha occupying 20.1%, and bamboo forest 152,300ha occupying 7.2%. (Table 2)

Table 2 Forest Land by Major Forest Type

forest type	Area (ha)	Percentage (%)
Natural forest	**1,527,500**	**72.7**
Natural conifers	220,100	10.5
Spruce, Fir	27,100	1.3
Hemlock	52,600	2.5
Cypress	48,500	2.3
Other conifers (pine included)	91,900	4.4
Mixed forests	331,600	15.8
Hardwoods	975,800	46.4
Plantation	**422,600**	**20.1**
Conifers	218,400	10.4
Mixed forests	59,600	2.8
Hardwoods	144,600	6.9
Bamboo	**152,300**	**7.2**
Total	**2,102,400**	**100.0**

Table 3 Forest Land by Major Ownership

Ownership	Area(ha)	Percentage(%)
National land (aborigines reserves incl.)	1,869,492	88.92
Public land	46,782	2.23
Private land	186,126	8.85
Total	2,102,400	100.00

Table 4 Forest Growing Stock by Major Forest Type

forest type	growing stock ($1000m^3$)	Percentage (%)
Natural forest	**310,533**	**86.56**
Natural conifers	91,770	25.58
Spruce,Fir	10,564	2.94
Hemlock	31,490	8.78
Cypress	29,045	8.10
Other conifers (pine included)	20,671	5.76
Mixed forests	94,608	26.37
Hardwoods	124,155	34.61
Plantation	**47,676**	**13.29**
Conifers	34,065	9.50
Mixed forests	4,793	1.34
Hardwoods	8,818	2.46
Bamboo	**535**	**0.15**
Total	358,744	100.00

3.2 Ownership of Forest Land

The ownership of forest land can be divided by national, public and private land. The national ownership including aborigines reserves, accounts for 88.92%, while the public and private ownership only 11.08%.(Table 3)

3.3. Forest Growing Stock

The estimated forest growing stock of the whole island is 358,744 thousand cubic meters, this number breaking down into 310,533 thousand cubic meters of natural forest or 86.56%, 47,676 thousand cubic meters of plantation or 13.29%, 535 thousand cubic meters of trees in bamboo forest or 0.15%. The average forest growing stock per hectare of the whole island is 203 cubic meters in natural forest, 113 cubic meters in plantation. (Table 4)

3.4 Forest Type

The forest in Taiwan supports a very rich flora. Under the influence of the climate, humidity and altitude, forest types can be divided into tropical, warm, temperate, and frigid forest zones. There are more than 200 species with high economic value, such as Taiwan zelkova, Formosan michelia, Stout camphor tree, Griffith's ash, Taiwan red cypress, Taiwan yellow cypress, Taiwan hemlock, and Taiwania just to mention a few. The excellent timber of Taiwan red cypress and Taiwan yellow cypress is well known in the world. Many plantations are established mainly with Japanese cedar, China fir, Taiwania, Taiwan red cypress, and Taiwan Acacia. Under the favorable environments, trees survive and are quickly established.

The main forest types in Taiwan are briefly described as follows:

Spruce-fir type: Spruce and fir are major trees and grow in pure stand of the most inaccessible region. They are found at elevation above 2,500 meters.

Hemlock type: This is one of the most significant conifer types. It is distributed between 2,000 and 3,000 meters above the sea level, usually mixed with fir at higher elevations but with pine or temperate hardwoods at lower elevations.

Cypress type: This is the most valuable species in Taiwan. It is composed of red and yellow cypress (*Chamaecyparis* spp.). They are found between 1,500 and 2,800 meters above the sea level, and either in pure stand or mixed stands.

Pine type: It is found at elevation between 300 and 2,800 meters, being in the most easily accessible area of the natural conifer forests. The Taiwan red pine has a wide range with good stocking.

Miscellaneous conifer type: China fir and Japanese cedar are exotic species and usually planted even-aged pure stands. This forest type also includes other native conifers, mixed mostly with hardwoods. They seldom exist as pure stand.

Conifer-hardwood mixed type: It is distributed between the temperate hardwood zone and

the conifer zone. Elevation ranges from 1,500.to 2,100 meters.

Hardwood type: Distributing at elevations ranging from the sea level to 2,000 meters, this is the most easily accessible forest in the low elevation. The major species are members of Lauraceae and Fagaceae .

Bamboo type: This type is common throughout the island. The large pure stand of *Phyllostschys* spp. is found only in the central part of the island at the intermediate altitudes. The important Ma Bamboo (*Sinocalamus latiflorus*) is found at elevations below 1,300 meters, however, Makino Bamboo (*Phyllostachys makinoi*), at elevations from 100 to 1,000 meters and Moso Bamboo (*Phyllostachys edulis*), from 1000 to 1,600 meters.

4. WATER RESOURCE

Water is a finite resource. Fresh water is one of the most precious resources in the world. Rainfall is the main source of water for Taiwan. The average annual rainfall is 2,500 mm. and ranges from 1,100 mm. to 4,980 mm. It is 3.44 times of the world average and rank at 19 of the world's abundant rainfall countries. Owing to the dense populations, the rainfall per capita is only 4,107 cubic meters, which is less than a sixth of the world average and become the country of water shortage.

Taiwan is very mountainous with a central axis stretching from north to south. The concentrated precipitation makes 55% of the rainfall flow into the sea that cannot be used effectively. Fortunately, there are 2,102,400 hectares of forest land covering the island, which can postpone the surface run off into the sea. Besides, the forest soils have the function of reserving water and purifing the water quality. According to the research, the capability of the forest water conservation is 26% higher than the farmland. Therefore, water fosters forests and forests conserve water resources.

5. BIOLOGICAL RESOURCE

Because of the unique natural environment, Taiwan has an estimated 150,000 to 200,000 species of organisms. The relatively well known are 4,200 species of vascular plants, 61 species of mammals, 460 species of birds, 150 species of freshwater fish, 81 species of reptiles, 32 species of amphibians, 400 species of butterfly and more than 20,000 species of insects. The poorly known are fungi, bacteria and nematodes. Therefore, Taiwan can be said a huge living natural museum, All of their habitats are forest and its surroundings, such as natural forests, plantations, bamboo forests, coastal shelters, swamps and mangroves etc. Therefore, forest is the homeland of organism.

6. RECREATION RESOURCE

The forest distribution of Taiwan from the seacoast to the elevation 3,952m of Yu-shan. The vertical distribution has lots of biodiversity. No matter the natural forests or plantations, are the best places for outdoor recreations. At present, there are 20 forest recreation areas and 5 millions visitors annually. The recreational income has more than the value of timber production.

7. OTHER ECOLOGICAL RESOURCES

Under the complexity of topography and unique environments, Taiwan is one of the highest biodiversity areas in the world. In order to protect the rare flora, fauna and ecosystems resources, 39 nature reserves with the areas of 390,000ha have been set up by the Taiwan Forestry Bureau since 1974. There are 6 national parks in Taiwan of which 95% of the land areas are in the national forest. The stock of biodiversity in Taiwan, as anywhere, provides components most suited to that region, and in part unique. Thus about a fourth of the organisms found in Taiwan occur nowhere else on Earth. Understanding, protecting, and sustainably utilizing this island's biodiversity, protecting Taiwan's natural resources are our responsibility. Therefore, strong efforts have been made to conserve the biodiversity of Taiwan.

8. CONCLUSION

Forest is a renewable resources. If properly managed, it continues to grow and provides benefits to society and mankind forever. But forest construction is a long-term enterprise, which cannot be accomplished in a single day. The forestry practice in Taiwan has been changed from the simple reforestation and harvesting to all-out ecosystems management basis. We believe that the foresters would contribute significantly to the sustainable future of Taiwan.

REFERENCES :

Taiwan Forestry Bureau, The Third Forest Resources and Land Use Inventory in Taiwan,December 1995

Peter H. Raven, The Living World : Key to Sustainability, May 2000

EARTH SURFACE GEOPHYSICAL PARAMETERS DETERMINATION FROM ATSR DATA

Dr. Yong XUE and Huadong GUO
Professors, Laboratory of Remote Sensing Information Sciences
Institute of Remote Sensing Applications
Chinese Academy of Sciences
No.3, Datun Road, Chaoyang District, PO Box 9718, Beijing 100871, China
Tel: (86)-10-64889540 Fax: (86)-10-64889786
E-mail: y.xue@unl.ac.uk; guohd@irsa.irsa.ac.cn
CHINA

KEY WORDS: ATSR, Albedo, Temperature, Emissivity, Remote Sensing

ABSTRACT: The paper discusses determination of the Earth's geophysical parameters from ERS satellite Along-Track Scanning Radiometer (ATSR) data. This paper focuses on Earth's surface Albedo, temperature and emissivity. Land surface temperature (LST) and land surface emissivity retrieval by use of ATSR data was discussed in the paper. SST data is from Rutherford Appleton Lab, Oxford. In this paper, results of Earth's surface Albedo, Land surface temperature (LST) and land surface emissivity in UK and surrounding areas are presented. The ATSR SST data set has been shown to be useful in helping to estimate the geophysical parameters over the large space scale.

1. INTRODUCTION

Until very recently all Earth resource satellites have had near-nadir looking radiometers. However, off-nadir looking radiometers are now operating (SPOT, ATSR) and future scanning and pointable systems are being planned (AATSR). These systems have off-nadir and multiple view angle capabilities, which permit one to consider the intriguing possibility that off-nadir and multiple view angles, may provide a more accurate estimate of hemispherical reflectance than a nadir view angle only.

ERS-2 and ERS-1 carry onboard Along Track Scanning Radiometer (ATSR) which has a unique feature of viewing the Earth's surface from two different angles, i.e., 0° (nadir) and 55° (forward) and in multi-spectral mode. The dual angle and multi-spectral observations from ERS-1 ATSR has been shown to be useful not only affecting corrections for sea surface temperature but also in helping to estimate the moisture and temperature structure of the lower boundary (Mathur *et al.* 1993). Sea surface temperature (SST) retrieval from satellite IR observations is always perturbed by the attenuation of the IR signal reaching the satellite sensor due to water vapour along with CO_2 and Ozone gases present in the intervening atmosphere. Therefore, the major efforts for retrieving the SST from satellite data is always concentrated towards a reasonable estimate of this perturbation. For the estimation of land surface temperatures the situation is quite different. Much less work has been done for land surface temperature (LST) than for sea surface temperature because LST is generally not homogeneous within a pixel and land surface emissivity may be quite different from unity and also dependent on the channel. There have been several attempts to achieve this goal under different conditions of the atmosphere (Xue and Cracknell 1996, Mutlow *et al.* 1994, Sobrino *et al.* 1993, 1994). In this paper, land surface temperature (LST) and land surface emissivity retrieval by use of ATSR data is discussed firstly.

The visible and near-infrared reflectances were derived from ERS-2 ATSR-2 spectral bands by using atmospheric radiative transfer model developed by Xue and Cracknell (1995). The narrow-band reflectances are combined into a measure of surface albedo by use of a weighted averaged scheme. The schemes were applied to the land and sea areas in UK.

2. EARTH'S SURFACE TEMPERATURE DETERMINATION FROM SATELLITE DATA

For a cloudfree atmosphere under local thermodynamic equilibrium and a Lambertian Earth surface, the signal recorded in channel i of a satellite that observes the Earth's surface under a zenithal angle θ can be written as follows:

$$I_{sat} = I_{surf} + I_{atm} + I_{refl}. \quad (1)$$

I_{sat} is the total radiance received by the sensor on the satellite, I_{surf} represents the contribution to the received radiance resulting from surface emission, I_{atm} represents the contribution to the received radiance resulting from the upwelling radiance emitted by the atmosphere towards the sensor and I_{refl} is the downward atmospheric radiance emitted by the atmosphere that is reflected upward at the Earth's surface and attenuated in its path to the sensor.

A multi-channel split-window equation has been obtained by the solutions of Equation (1) for two channels (i=11 and i=12, which are for the 11μm channel and the 12μm channel respectively). The basis of the double viewing angle method is to use two different absorption path lengths at one wavelength. A same multi-angle split-window equation also can be obtained by the solutions of Equation (1) for nadir- and forward-view. Following equation illustrates both situations:

$$T_s = A_{0,\theta} + A_{1,\theta} T_\theta^{11} + A_{2,\theta} T_\theta^{12} \quad (2)$$

where $A_{0,\theta}$, $A_{1,\theta}$ and $A_{2,\theta}$ are the local split-window coefficients, which depend on the surface emissivity and the atmospheric state (Becker and Li 1990, Sobrino *et al.* 1991).

The formulae of multi-channel and multi-angle split-window should be chosen with caution. We used the formula from Becker and Li (1990) for nadir-view ATSR data. For two view angles at one wavelength Sobrino *et al.* (1993) was used. Based on above equation, We used

$$T_s = A^{11}_{0,\theta} + A^{11}_{1,\theta} T_\theta^{11} + A^{11}_{2,\theta} T_\theta^{11} \quad (3)$$

where

$$A^{11}_{2,\theta} = -(\alpha_0 + \alpha_1 + \alpha_2 \Delta\varepsilon_\theta^{11}) + \alpha_1 (0.075\varepsilon^{11} + 0.90) \quad (4)$$

$$A^{11}_{0,\theta} = 1.274 + 273.15(1 - A^{11}_{1,\theta} - A^{11}_{2,\theta}) \quad (5)$$

$$A^{11}_{1,\theta} = \beta_0^{11} + \beta_1^{11} + \alpha_0 + \alpha_1 + (\alpha_2 + \beta_2^{11})\Delta\varepsilon_\theta^{11} - (\beta_1^{11} + \alpha_1)(0.075\varepsilon^{11} + 0.90) \quad (6)$$

for 11μm channel and

$$T_s = A^{12}_{0,\theta} + A^{12}_{1,\theta} T_\theta^{12} + A^{12}_{2,\theta} T_\theta^{12}$$

where

$$A^{12}_{2,\theta} = -(\alpha_0 + \alpha_1 + \alpha_2 \Delta\varepsilon_\theta^{12}) + \alpha_1(0.075\varepsilon^{12} + 0.90)$$

$$A^{12}_{1,\theta} = \beta_0^{12} + \beta_1^{12} + \alpha_0 + \alpha_1 + (\alpha_2 + \beta_2^{12})\Delta\varepsilon_\theta^{12} - (\beta_1^{12} + \alpha_1)(0.075\varepsilon^{12} + 0.90) \quad (9)$$

$$A^{12}_{0,\theta} = 1.274 + 273.15(1 - A^{12}_{1,\theta} - A^{12}_{2,\theta}) \quad (10)$$

for 12μm channel. $\Delta\varepsilon_\theta^{11} = \varepsilon_0^{11} - \varepsilon_\theta^{11}$ and $\Delta\varepsilon_\theta^{12} = \varepsilon_0^{12} - \varepsilon_\theta^{12}$.

The solution of the simultaneous equations (2), (3) and (7) gives the surface temperature (T_s) and the surface emissivities for the 11μm channel (ε^{11}) and for the 12μm channel (ε^{12}).

3. EARTH SURFACE ALBEDO

The three main mechanisms by which the terrestrial atmosphere perturbs measurements of ground reflectance from space are as follows: (1) the aerosol and molecular backscattering changes the measured target reflectance, (2) for nonuniform sites the measurement is altered by the contribution of the target background and (3) the bidirectional properties of the target reflectance are partially smoothed out by the atmospheric scattering processes (Tanré *et al.* 1979). The study of these different atmospheric effects has been considerably developed (Fraser and Kaufman 1985, Kaufman 1982, Odell and Weinman 1975, Steven and Rollin 1986). Atmospheric models assuming the ground to be uniform and Lambertian have been studied extensively (Tanré *et al.* 1979).

The inference of surface spectral reflectance using visible observations is complicated mainly because of scattering effects, especially aerosol scattering effects. The aerosol optical thickness depends on aerosol characteristics (size distribution and refractive index) and on aerosol total loading. Ångström suggested a single formula for aerosol scattering optical thickness generally known as Ångström's turbidity formula given by the following: $\tau_\Lambda^\lambda = \beta\lambda^{-\alpha}$. In this formula, β is called Engstrφm's turbidity coefficient, a is the wavelength exponent and λ is the wavelength (Iqbal 1983). The problem arises of how to estimate the values of the parameters β and α.

A variety of techniques, the doubling or adding method, the successive orders of scattering, the iteration of the formal solution, the invariant imbedding method, the method of X and Y functions, the method of discrete ordinates, the spherical harmonics method, the method of expansion in eigenfunctions and the Monte Carlo method, have been developed for computing the intensity and polarisation of multiple-scattered light (Hansen and Travis 1974). The aim of the paper by Xue and Cracknell (1995) was to find an operational method which relies on multiple view angle observations or multiple solar zenith angle observations of the surface to accomplish part of this task in a routine manner. In the paper they attempted a solution to the problem of the retrieval of surface reflectance from satellite radiance measurements based on a solution of the radiative transfer equation introduced by Chandrasekhar (1960) and developed further by Kondratyev (1969). The problem defined for a horizontally stratified atmosphere is sufficient to cover most applications for light scattering in planetary atmospheres. The scattering was assumed to involve no change of frequency within the visible region.

From Xue and Cracknell (1995), spectral downcoming radiation flux and upgoing radiation flux can be calculated. At the Earth surface, $\tau^{\lambda} = 0$, which gives

$$F_2^{\lambda}(0) = \frac{b - a}{(1 - A)b + (Ab - a)e^{(a-b)\varepsilon\tau_0^{\lambda} m_r}} E_0^{\lambda} \cos\theta \qquad (11)$$

for a downcoming global radiation flux and

$$F_1^{\lambda}(0) = \frac{A(b - a)}{(1 - A)b + (Ab - a)e^{(a-b)\varepsilon\tau_0^{\lambda} \sin\theta'}} E_0^{\lambda} \cos\theta \qquad (11)$$

for a upgoing global radiation flux. A is the surface albedo. The E_0^{λ} is the solar spectral irradiance at the top of atmosphere, $a = \sec\theta$ and $b = 2$; ε is the backscattering coefficient, typically 0.1. The solar zenith angle is calculated from latitude, longitude and time and θ' is the zenith angle of the sensor. The atmospheric optical depth (τ_0^{λ}) is determined by the turbidity state of the atmosphere. The details on how to derive the Albedo and reflectance from ATSR dual view visible band data can be found from Xue and Cracknell (1995).

4. TESTS AND RESULTS

The date and time of the ATSR data were 2nd August 1995 and 11:00 GMT. The area is located in the middle of UK. In this area there are land and sea surfaces. The algorithms have been used to calculate reflectances and albedo from dual view ATSR visible band data. Figure 1 (a) shows the Earth's surface albedo. Figure 1 (b) gives Earth Surface temperature (LST and SST) in °K. Figures (c) and (d) show the land surface emissivity for 11μm and 12μm channels respectively. Cloudy areas (white plot) were not calculated.

The 1995 is the hottest year since first global temperature recording in 1860 from the Meterological Office, UK. The sunny and exceptionally hot weather which began at the end of July lasted through the first three days of August with the temperature exceeding 33°C (306 degK) daily at several places. August 1995 was, averaged over the whole United Kingdom, probably the hottest and sunniest on record, and one of the driest (Eden 1995). In Fig. 1(a), we can see that the temperatures in most areas are around 30°C. Some areas in Midland are higher than 36°C. The surface temperature determined from satellite data is the instantaneous effective surface temperature. The temperature from weather forecasting is the air temperature at 1 m height. The black plots are cloudy areas. From Fig. 1 (b) and (c), we can see that the emissivity is not very close to unity. The values of the emissivity is around 0.97 - 0.99 for the 11μm channel and 0.96 - 0.98 for the 12μm channel. This agrees with the result of Taylor (1979) that the surface in agricultural areas behaves almost like a black body ($\varepsilon = 0.97$). It will be noticed that the emissivity for the 11μm channel is greater than for the 12μm channel.

5. CONCLUSIONS

An accurate determination of the surface properties is therefore essential to obtain the various terms of the energy budget: the reflected solar flux - knowledge of the emissivity and the temperature; the upward longwave flux - knowledge of the emissivity and the surface temperature; the heat and water fluxes are the turbulent sensible and latent heat fluxes, both depending on the surface temperature (Xue *et al.* 1998, 2000a, b).

The paper demonstrated that ATSR-2 data can be used to determine the Earth's surface Albedo, temperature and emissivity. The approaches are simple methods to remove the atmospheric effects

from visible and thermal band data. For a non-Lambertian surface, the bidirectional properties of the ground surface should be taken into account. The narrow-band reflectances are combined into a measure of surface albedo by use of a weighted averaged scheme.

6. ACKNOWLEDGEMENT

The author thanks Professor D. T. Llewellyn-Jones and the RAL, Oxford, for supplying the ATSR data.

7. REFERENCES

Becker, F., and Li Z. L., 1990, Towards a local split window method over land surfaces. *International Journal of Remote Sensing*, **11**, 369-393.

Chandrasekhar, S., 1960, *Radiative Transfer* (New York: Dover Publications).

Eden, P. 1995, Hot, dry, and sunny - a record-breaking month. *Weather Log*, August, 1995.

Hansen, J.E., and Travis, L.D., 1974, Light scattering in planetary atmospheres. *Space Science Reviews,* **16**, 527-610.

Iqbal, M., 1983, *An Introduction to Solar Radiation* (Toronto, Canada: Academic Press).

Kondratyev, K. Ya, 1969, *Radiation in the Atmosphere* (New York: Academic Press).

Mutlow, C. T., Zavody, A. M., Barton, I. J., and Llewellyn-Jones, D. T., 1994, Sea-surface temperature-measurements by the along-track scanning radiometer on the ERS-1 satellite - early results. *Journal of Geophysical Research-Oceans*, **99**, 22575-22588.

Sobrino, J. A., Coll, C., and Caselles, V., 1991, Atmospheric correction for land surface temperature using NOAA-11 AVHRR channel 4 and 5. *Remote Sensing of Environment*, **38**, 19-34.

Sobrino, J. A., Li, Z. -L., Stoll, M. P., and Becker, F., 1993, Determination of the surface temperature from ATSR data. *Proceedings of 25th International Symposium on Remote Sensing of Environment held in Graz, Austria, on 4th-8th April, 1993* (Ann Arbor, ERIM), pp II-19-II-109.

Sobrino, J. A., Li, Z. -L., Stoll, M. P., and Becker, F., 1994, Improvements in the split-window technique for land surface temperature determination. *IEEE Transactions on Geoscience and Remote Sensing*, **32**, 243-253.

Tanré, D., Herman, M., Deschamps, P.Y., and De Leffe, A., 1979, Atmospheric modelling for space measurements of ground reflectances, including bidirectional properties. *Applied Optics,* **18**, 3587-3594.

Taylor, S. E., 1979, Measured emissivity of soil in the Southeast United States. *Remote Sensing of Environment*, **8**, 359-364.

Xue, Y., and Cracknell, A. P., 1995, Operational bi-angle approach to retrieve the Earth surface albedo from AVHRR data in the visible band. *International Journal of Remote Sensing*. **16**, 417-429.

Xue, Y. and Cracknell, A. P., 1996, The Earth's surface temperature. In *The Determination of Geophysical Parameters from Space*, edited by N. E. Fancey, I. D. Gardiner and R. A. Vaughan (Edinburgh: SUSSP Publications; London: IOP Publishing), pp. 209-240.

Xue, Y., Lawrence, S. P., Llewellyn-Jones, D. T., and Mutlow, C. T., 1998, On the Earth's surface energy exchange determination from ERS satellite ATSR data: Part 1. Long-wave radiation. *International Journal of Remote Sensing*, Vol. 19, No. 13, pp2561-2583.

Yong Xue, David T. Llewellyn-Jones, Sean P. Lawrence, and Mutlow, C. T., 2000, On the Earth's surface energy exchange determination from ERS satellite ATSR data: Part 2. Short-wave radiation. *International Journal of Remote Sensing* (In print).

Yong Xue, David T. Llewellyn-Jones, Sean P. Lawrence, and Mutlow, C. T., 2000, On the Earth's surface energy exchange determination from ERS satellite ATSR data: Part 3. Turbulence heat flux of open sea. *International Journal of Remote Sensing* (In print).

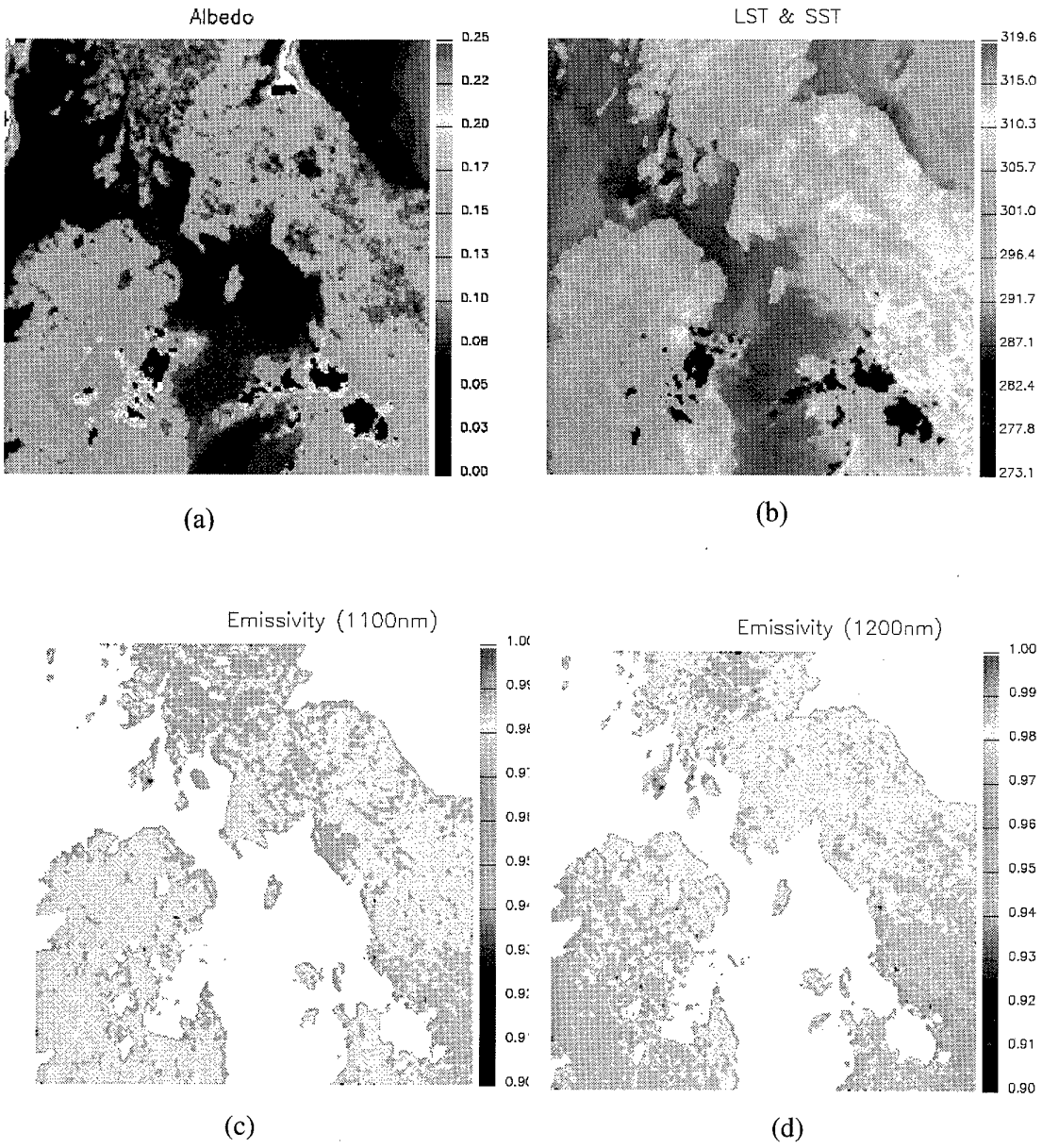


Figure 1 Geophysical parameters derived from ATSR data in UK and surrounding area. The date and time of the ATSR data were 2nd August 1995 and 11:00 GMT. The unit for Land Surface Temperature (LST) and Sea Surface Temperature (SST) is °K.

The 21st Asian Conference on Remote Sensing
December 4-8, 2000 Taipei, TAIWAN

A Creeping-type Landslide Observed on Aerial Photographs Following the Ji-Ji Earthquake of Taiwan on 21 September 1999

Jin-King Liu
Research Scientist and Head of Mineral Resources Department
Energy and Resources Laboratories, Industrial Technology Research Institute
Hsin-Chu 310, TAIWAN
JKLiu@itri.org.tw

ABSTRACT

At 01:47 of 21 September 1999, a disastrous earthquake known as Ji-Ji Earthquake with a magnitude of 7.3 struck central Taiwan. Casualties and damages include more than 2505 persons killed, 8700 persons injured, 10000 buildings totally damaged, and 7500 buildings partially damaged.

Earthquake-triggered landslides were interpreted both by using SPOT images taken on 27 September and aerial photographs taken from 21 September to 27 September. Scars of land surface are depicted conspicuously on both color aerial photographs and color composite images. Conventional manual method of interpretation was adopted with a modification of on-screen approach for directly obtaining a dataset suitable for subsequent GIS processing. A total of more than 10 thousand landslides were observed on SPOT images within a week and, on contrast, more than 20 thousand landslides were obtained by 1400 air-photos in one month.

Landslides with a small amount of surface creeping would give little clues on images and photographs. A close-look and enlargement of high resolution image is required to observe such a type of landslide. In this study, a creeping-type landslide of more than 100 hectares were observed using aerial photographs in a scale of 1/17000. For a visualization of the change of this landslide, stereo-pairs both prior to and aft the event were also registered, rectified, and processed to obtain ortho-photos, contours, and DTMs. The existence of this creeping-type landslide was further proved by field observations. It is concluded that it is possible to detect and identify creeping-type landslide by using aerial photographs especially when multi-temporal and high-resolution images are used for a close study on the characteristics of landform change.

KEY WORDS: Ji-Ji Earthquake, creeping, landslide, aerial photographs

1.INTRODUCTION

At 01:47 of 21 September 1999, a disastrous earthquake known as Ji-Ji Earthquake with a magnitude of 7.3 in Richter scale (as announced by Central Weather Bureau) struck central Taiwan (Figure 1). The surface rupture accompanied the Ji-Ji Earthquake, epicenter at latitude 23.85° and longitude 120.78° , extends 105 kilometers along an existing active fault, known as Che-Long-Pu Active Fault. Casualties and damages include more than 2505 persons killed, 8700 persons injured, 10000 buildings totally damaged, and 7500 buildings partially damaged.

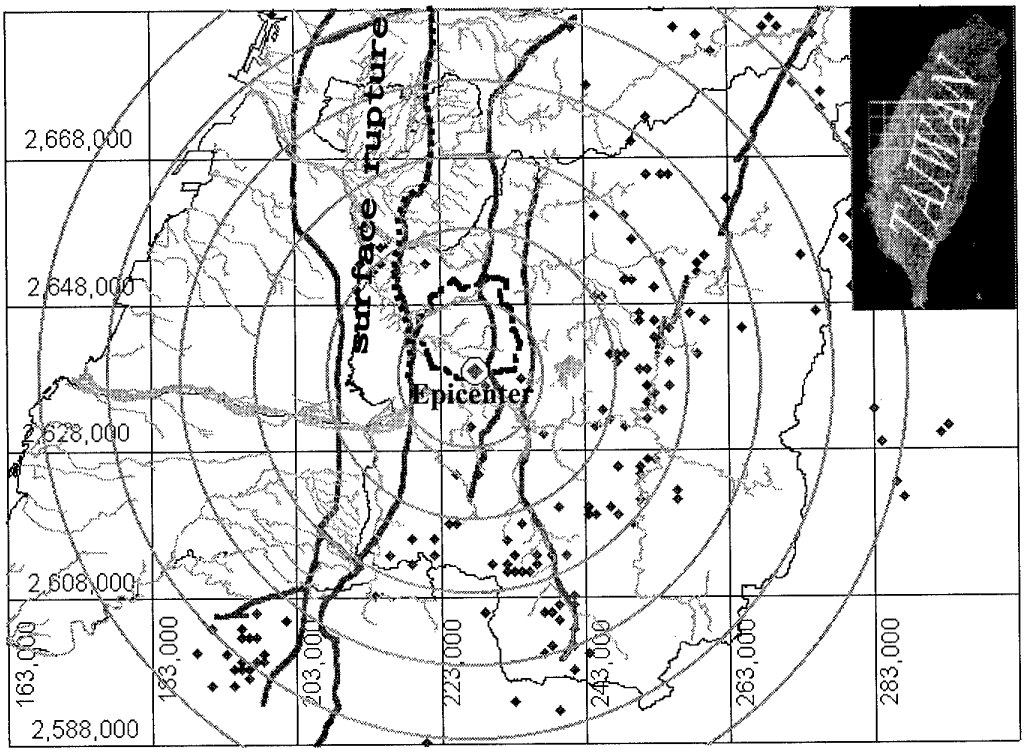


Figure 1 The location of the epicenter of Ji-Ji Earthquake(N23.85° , E 120.78°). The surface rupture extended 105 km from the west of the epicenter to the north of Ta-Chia River in TaiChung County. The major faults and after-shocks happened within one month with magnitude greater than 4 in this area are also shown on the map.

2.INVENTORY OF LANDSLIDES BY REMOTE SENSING

Earthquake-triggered landslides were enumerated both by using SPOT images taken on 27 September and by aerial photographs taken in 7 days from 21 September to 27 September. Scars of land surface are depicted conspicuously on color aerial

photographs as well as on color composite images because on the places of the landslides there are no vegetation and fresh rocks are exposed. Conventional manual approaches of interpretation are adopted with a modification of on-screen approach for directly obtaining a landslide dataset suitable for subsequent GIS processing. Aerial photographs in a scale of 1/17000 were digitally-scanned in 600 dpi for this purpose.

A total of more than 10 thousand landslides were observed on SPOT images within a week (Figure 2) and, on contrast, more than 20 thousand landslides were obtained by photo-interpretation using 1400 aerial photographs in one month.

(Coordinate system used in this study is a transverse Mercator projection with central meridian in longitude of E121 degrees and a swath from E120 to E123 degrees, covering the Taiwan Island.)

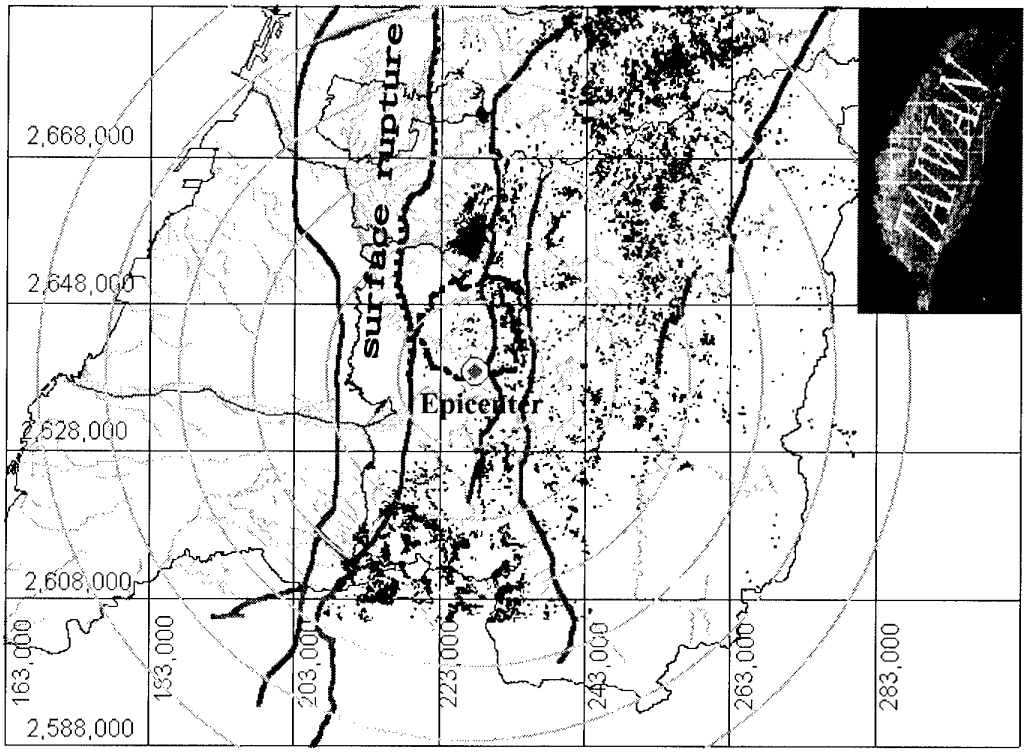


Figure 2 Landslides triggered by Ji-Ji Earthquake as interpreted from SPOT images taken within one week after the main shock.

3.A CREEPING-TYPE LANDSLIDE

Landslides with a small amount of surface creeping would give little clues on images and photographs, as shown in Figure 3. The place indicated by capital letter A shows no clear evidence of landslide. However, the field pictures (Figure 4) showed a disturbance of ground surface materials of the area. A close-look with scrutiny for the

image with high resolution reveals a tensional linear cracks extending 1300m from point C to D. This indication gives a clue for further inspection of the photographs under stereoscope. The linear zone of the extensional crack shows clearly in the enlargement of the image. As depicted in Figure 5, roads along the crack zone were destroyed, this corresponding to a deformation zone in the field with more than 5 meters in width.

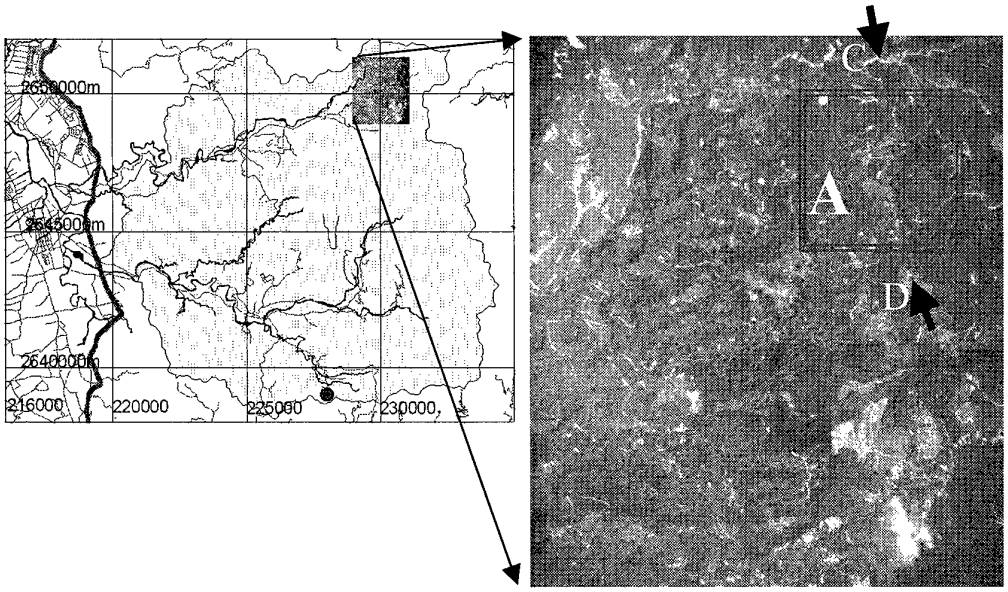


Figure 3 In a synoptic view of aerial photograph taken on 26 September 1999, landslides with exposed scars are conspicuous. However little clues can be found for a creeping type of landslide indicated at A.

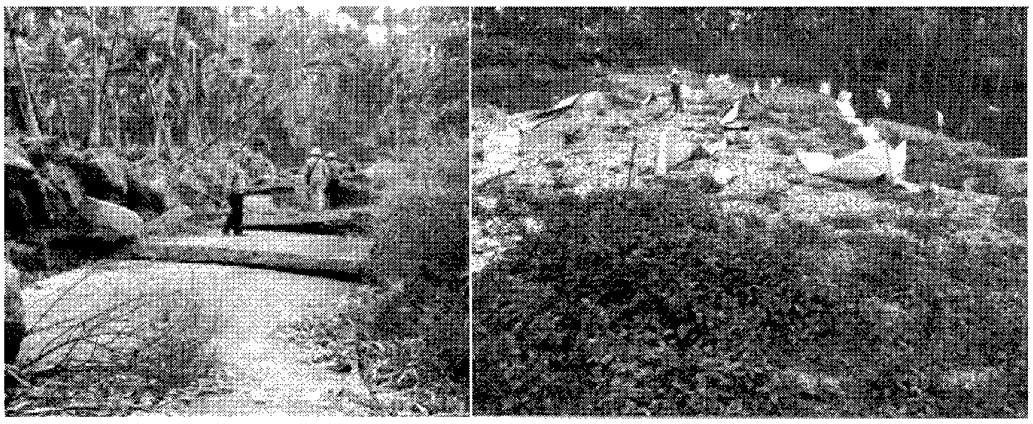
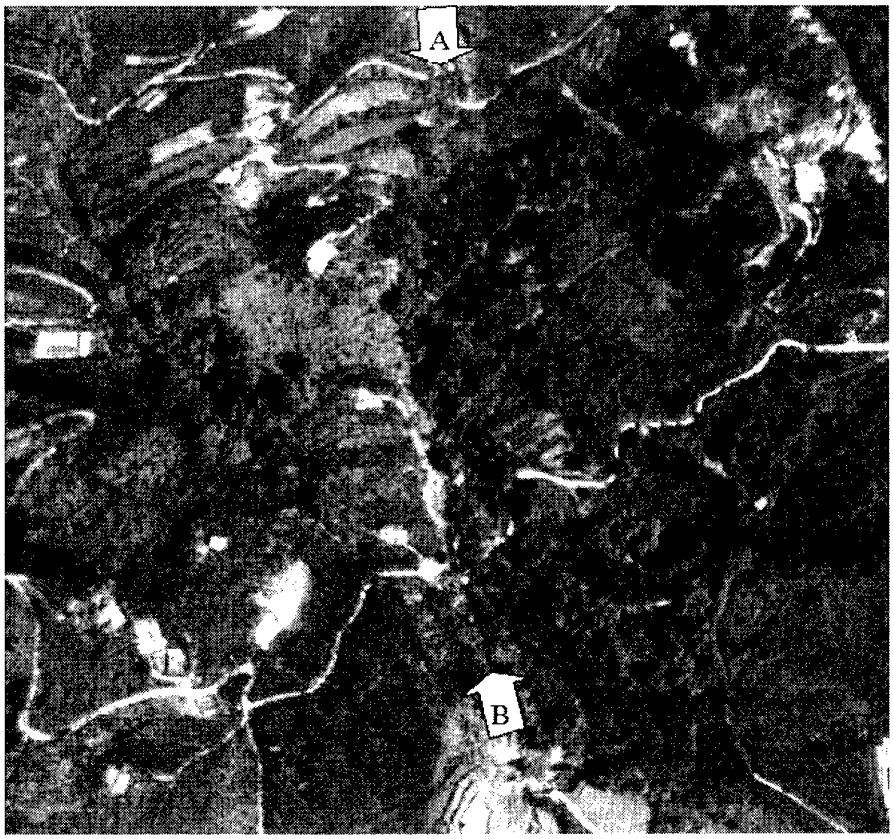


Figure 4 Field pictures show that the lands surface are disturbed by a creeping process in the area indicated at A in Figure 3. Though this is hardly can be clearly identified by aerial photo-interpretation.



Fugure 5 An enlargement of the crack zone, the area is also indicted in the rectangle of Figure 3.

For a visualization of the change of this landslide, stereo-pairs both prior to and aft the event were also registered, rectified, and processed to obtain ortho-photos, contours, and DTMs (Figure 6). The sequence of the event is clearly exposed and the extent of the disturbed area of ground surface materials can be interpreted from the 3d images. The creeping-type landslide with an area of more than 100 hectares were thus observed. And, the existence of this creeping-type landslide was further proved by field observations (Figure 4).

4.DISCUSSION AND CONCLUSION

Generally speaking, earthquake-triggered landslides are easily enumerated by using satellite images or aerial photographs as the scars of land surface are depicted conspicuously on the places of the landslides, where there are no vegetation and fresh rocks are exposed. It is also possible to detect and identify creeping-type landslide by using aerial photographs especially when multi-temporal and high-resolution images are used for a close study on the characteristics of landform change.

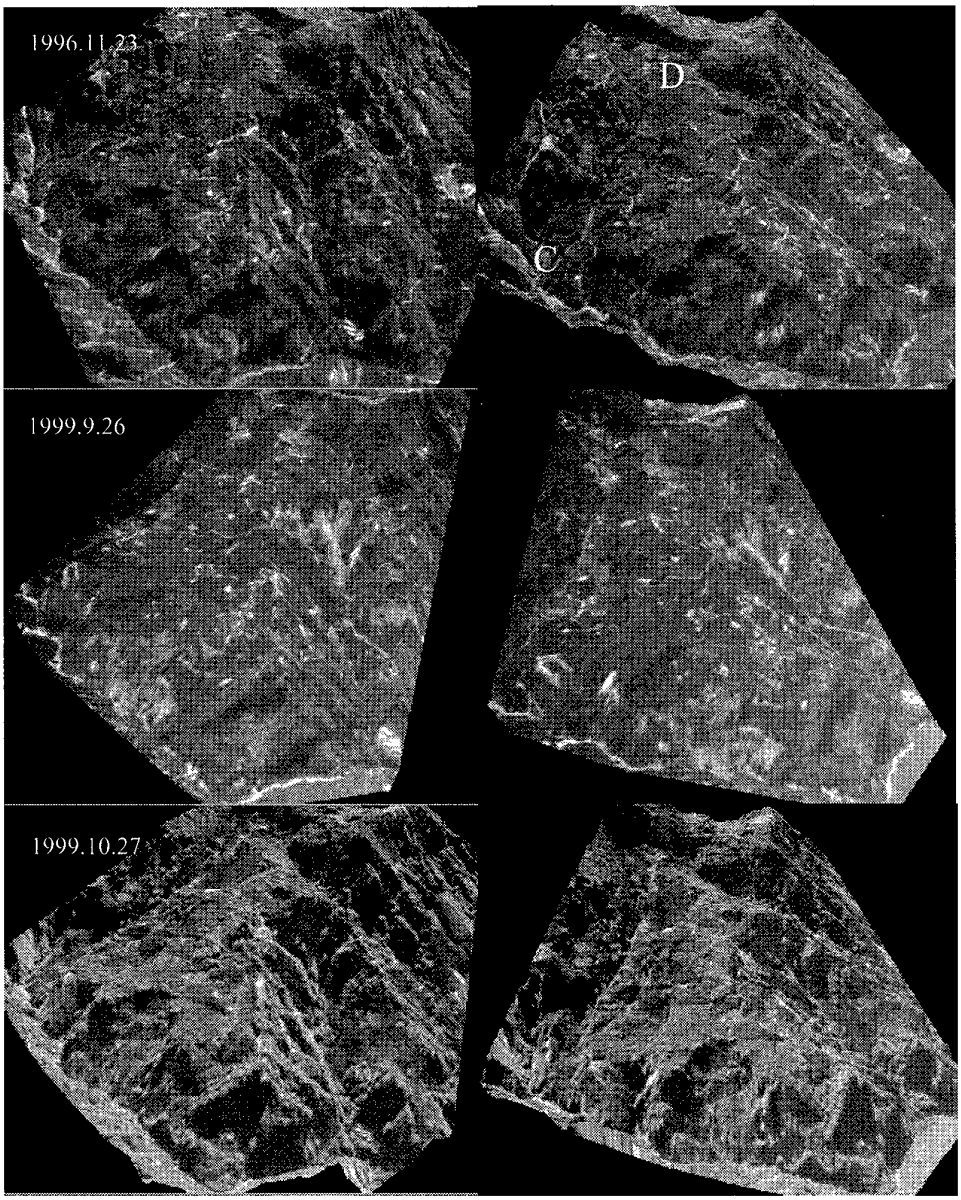


Figure 6 A sequence of the landform change prior to and aft the Ji-Ji Earthquake as simulated by merging orthophotos and DTMs of the Hon-Tsai-Ping study area.

5.REFERENCES

ERL (1999) Final Report on the investigation of landslides triggered by 921 Ji-Ji Earthquake and a general mitigation proposal. By Energy and Resources Laboratories, ITRI. 31 March 2000.

VOLCANO HAZARD MANAGEMENT USING DIGITAL ELEVATION MODEL

[1]D.John Prabaharan and [2]Kasturi Devi Kanniah
[1]School of Spatial Science, Curtin University of Technology, Perth,
W.Australia – 6845
jdp27@yahoo.com
[2]Department of Remote Sensing
Faculty of Engineering and Geoinformation Science
Universiti Teknologi Malaysia, 81310 Skudai
Johor, Malaysia
Email: kdk21@yahoo.com

KEY WORDS: GIS, DEM, mudflow, flow path, velocity, discharge rate, traveling time.

ABSTRACT

GIS is being recognized as having applications for volcanic hazard assessment in early 90's. In this study digital terrain model within GIS environment was used to model the mudflow in Kawah Ijen volcano, Indonesia. With 36 million m^3 of acidic water in its crater lake, Kawah Ijen is recognized as a potential threat to the surrounding population and properties. Using DTM, which was created by interpolating contours, two major mudflow paths were identified. Even a minor mudflow originated from the lake will flow through these paths. The topographic characteristics such as flow path's bed slope, width and depth were used to estimate the velocity and quantity of mudflow. The Manning formula with coefficient of 0.15 was used for calculating the velocity and quantity of mudflow.

1. INTRODUCTION

Volcanoes generate a wide variety of phenomena that can alter the earth's surface and atmosphere and endanger people and property. During the past 15 years volcanic activity killed more than 29000 people, forced over 830000 to flee from their homes and caused economic losses in excess of $3 billion (Simkin and Siebert, 1994). Countries like Indonesia which lies at the junction of three major plates with a population of 150 million face the greatest overall threat (Suryo et al, 1985). Most volcanoes related to deaths are associated with highly explosive eruptions involving pyroclastic flows and mudflows.

A flow composed of relatively small rock particles dominantly sand and silt size particles (less than 2 millimeters in diameter) are often called as mudflow. Mudflows have sediment concentration as great as debris flows and their sediment composition typically consists of at least 50% sand; silt and clay sized particles. Mudflows contain high concentration of rock debris to give them the internal strength necessary to transport huge boulders as well as buildings and bridges and to exert extremely high impact forces against objects in their paths (USGS, 1998).

Among the factors cause mudflow hazards, eruption through volcanic crater lakes represent a unique hazard because of the danger posed by the storage of large volume of water in proximity to near surface magma bodies the degree of hazard is proportional to the volume of water in the lake. This study is related to this category of mudflows. Eruptions in crater lake settings can result in deadly mudflows as seen at Mt. Ruapehu (New Zealand), Mt.

Kelut (Indonesia) and etc (Oppenheimer, 1993). The most frequent reason for lake breakouts is the overflow of lake water across the dam and subsequent erosion and rapid down cutting into the loose volcanic rocks.

Since the impact posed by mudflow hazards is severe, it is vital to monitor, improve or lessen the impacts by utilizing GIS. Modeling the path of mudflow is fundamental to understand the areas affected by mudflow. The contribution of GIS in mudflow disaster ranges from identifying areas at risk, monitoring and forecasting hazards, to warning the possibly affected people or responsible teams to take precautions. All these strategies can be performed by utilizing the input, data analysis, modeling and display capability of GIS. This study was carried out by digitizing and interpolating the contours of Kawah Ijen area to create a DEM. Subsequently the DEM was used to identify the major mudflow paths that would carry the mud to the surrounding areas in a GIS environment. The velocity and quantity of mudflow from the crater lake was also estimated using hydraulic models.

2. STUDY AREA

In this study, Kawah Ijen crater lake was selected because it is one of the largest and most active lakes that contain huge quantity of water. Any eruption through this lake would expel the water and create deadly mudflow that can claim hundreds of lives and properties (Oppenheimer, 1993). It contains about 36 million cubic meters of steaming, sulphurous acidic water. The floor is covered completely by a warm lake with the temperature ranges from 27 - 42°C. The outlet of the crater lake is located in western side that becomes the upper course of Banyupait - Banyuputih rivers. The size of the crater is about 960m x 600 m and has the surface area of $41x10^4$ m^2 and 200 m deep. Kawah Ijen is placed on the summit of Mt. Ijen which is located in east Java. Ijen is one of the active volcanoes situated towards the eastern side of Ijen caldera The location of Mt. Ijen is shown in figure 1.

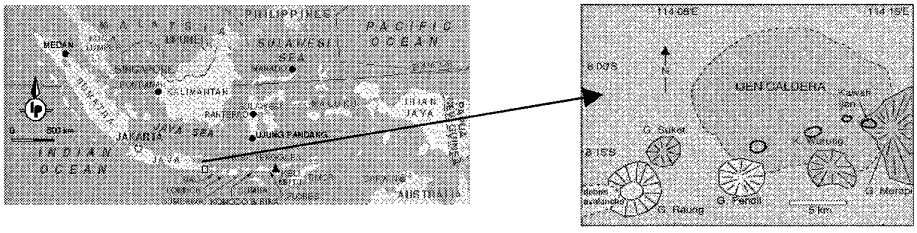


Figure 1 shows the location of Mt. Ijen in East Java, Indonesia and its aproximate outline of Ijen caldera.
(Source : http://www.lonelyplanet.com/dest/sea/graphics/map-indo.htm).

3. DATA

For the above purposes the below data sets and methods were utilized.

(i) Toposheet map of Kawah Ijen area with a scale 1: 50,000 and Landsat 5 Thematic Mapper (TM) scene of Kawah Ijen dated on 5th October 1994 with World Referencing System of Path and row of 117/166.
(ii) Arc info version 7.1 and Arc view 3.0 GIS software packages, Imagine image processing software 8.3 (all run on windows network system) and Microsoft excel.

4. METHODOLOGY

4.1 Flow path derivation

Firstly, a DEM was created by digitizing and interpolating contour map of Kawah Ijen area (1:50,000 scale). Subsequently, the DEM was used for deriving the mudflow direction. The direction of the flow is determined by finding the steepest descent, or maximum drop from each cellThe flow direction was found by Arcinfo "flow direction" command. The next step was to find the flow path. The flow accumulation process was utilized to find the gravity driven flow path.

The flow accumulation function calculates accumulated flow as the accumulated weight of all cells flowing into each down slope cell in the output grid. Cells with a high flow accumulation are areas of concentrated flow. The flow path was identified using 'stream network' and 'connects stream' functions available in arcinfo. The important flow paths were converted into arc coverage using arcview on screen digitization facility to drape over the DEM.

4.2 Estimation of Velocity and Quantity of Mudflow

In hydraulic flow routing the equation of motion for an open channel mudflow are

$$\partial Q/\partial t + (\partial QV/\partial x) + gA(\partial y/\partial x) = gA\,(S_x - S_f) \qquad (1)$$

where, x - the longitudinal distance along the meandering channel, t – time, A - wet cross sectional area, y - flow depth, V - average velocity (over cross - sectional wetted area), Q - the Quantity of discharge (=VA), S_x- channel slope ($S_x = \tan\theta$ = bed slope), S_f - Term which takes into account energy dissipation.

For the case with zero lateral inflow, the friction slope is

$$S_f = S - \partial y/\partial x - V/g\,\partial V/\partial x - 1/g\,\partial V/\partial t \qquad (2)$$

where, S_f - Slope friction, S - Bed slope, $\partial y/\partial x$ - Surface slope of flow materials, $V/g\,\partial V/\partial x$ - Convective acceleration, $1/g\,\partial V/\partial t$ -Temporal acceleration.

The kinematic wave method assumes that the inertia terms of Eq.(2) are negligible and that the friction equals the bed slope S. Momentum conservation is approximated by assuming steady uniform flow, and routing is accomplished by combining the continuity equation. Typically either the manning or Chezy equation is used to find the velocity. The Chezy (3) and Manning (4) equations are:

$$V = C\sqrt{RS} \qquad (3)$$

$$V = (1.486/n)\,R^{2/3}\,S^{1/2} \qquad (4)$$

where C and n are friction coefficients, S is the friction slope, and R is the hydraulic radius (area divided by wetted perimeter). Both give velocity in meters per second if area and wetted perimeters are input using square meter and meter units. The applicability of the manning formula to hyper concentrated flows has been used successfully by Laenen and Hansen (1988), Takahashi (1985), Public Work Research Institute(1988) and Vignaux and Weir (1990).

The channel geometry (flow depth and width, cross sectional area, wetted perimeter, hydraulic radius and slope) was calculated using the DEM. In nature, the flow paths do not have a perfect shape of triangular or trapezoidal. Therefore, in this study each cross-section was examined carefully and assumed to fit either to triangular, trapezoidal, circular or rectangular shape. The most appropriate formulae were selected in accordance to the channel shape for calculating the area (A), wetted perimeter (P), hydraulic radius (R) and top width (B).

The Manning coefficient of n can be predicted using Strickler equation. The Strickler equation to predict n is

$$n = 0.41\ D^{1/6} \qquad (5)$$

where, D - is the median grain size (m).

The mudflow grain size assumed is 2 mm (USGS1998). The calculated n is 0.15 (This co-efficient is well agree with the viscous co-efficient of lahar found by Macedonio et al (1992) for muddy flow and by Costa (1997) for hydraulic modeling for lahar hazard study at Cascades volcanoes. The velocity and quantity of discharge are calculated for various flow depths using manning formula in the Microsoft excel.

Table 1 shows the velocity of mudflow for 60,000 m^3 and 90,000 m^3 of lake water discharge. The calculated velocity for 90,000 m^3 of discharge is shown in italic.

Distance along flow path, l (m)	103	1640	3800	4700	7905	10800
Distance between two cross sectional areas (m)	1537	2160	900	3250	2850	
Calculated velocity V(m/s)	28.5/*31.0*	24.0/*26.0*	18.0/*20.0*	14.5/*17.0*	15.2/*17.5*	14.0/*15.5*
Average velocity (m/s)	26.25/*28.5*	21.0/*23.25*	16.25/*18.75*	14.85/*17.25*	14.6/*16.5*	

5. RESULTS AND DISCUSSION

5.1 Mudflow path

Analysis of flow path and visualization of the terrain will lead to the understanding of the mudflow origin and flow direction of the mud. This is shown in Figure 2 where two major mudflow paths were derived from DEM. Mudflow is most likely to flow on the west and Northwest of Kawah Ijen volcanic flank. Flow path A (Banyoeputih river) originates from Ijen Crater's outlet and flows towards the west of the volcano flank. It passes West of Mt. Blade and crosses in between Blawan- Kidoel and Kaligedang areas. Pelanggan and Blawan settlements that are located in Blawan Kidoel area are in proximity to the major mudflow route. Thus, any mudflow hazard from Kawah Ijen would affect the people and properties of these settlements. Whilst, flow path B starts from the Northeast of Ijen volcano's flank and in proximity to Blaoe settlement that is located approximately 0.25 km from this flow path. This shows that the mudflow hazard originated from Kawah Ijen would seriously affect this settlement area. The flow path crosses the Kaligedang area and flows into Sengon River. In accordance to the satellite image of this area, there are valuable natural forest and horticulture plantations like tea and coffee in Blawan Kidoel and Kaligedang areas. Obviously, these resources would be destroyed by vigorously moving mudflow. These two major mudflow paths identified from DEM are also exactly coinciding with the mudflow hazard map prepared by volcano survey team of Indonesia in 1990 (Sumberdaya, 1990).

5.2 Quantitative analysis of mudflow

Wholesale ejection of lake water (36 million m^3) would not be expected in on go. However, even a fraction of water that rushes through the outlet is capable of creating mudflow. The **hydraulic radius and velocity** depict a linear relationship where the increase in the hydraulic radius (which is a function of flow path cross sectional area and wetted perimeter) is accompanied by a steady increase in the velocity. This is shown in figure 3i (a-f). For example at the distance of 4.7 km from the Crater Lake (figure 3id) the mudflow achieves a velocity of 16 m/s when the hydraulic radius extent to 12.4 m. Meanwhile, the relationship between **discharge rate and the velocity** of mudflow reveals that as the quantity of discharge increases the velocity also increases in a non- linear fashion (Figure 3ii (a-f)) For example near to the outlet, when the discharge rate increases from 20,000m^3/s, 60,000 m^3/s and 90,000 m^3/s the mudflow travels rapidly at a velocity of 22 m/s to 28.5m/s and 31 m/s respectively. The higher rate of velocity near the outlet could be due to the steep slope at the volcanic flank. It is gradually decreasing when mudflow approaching the downhill side, mainly due to the slope of the topography. At the distance of 4700m the velocity of mudflow is comparatively lower because the flow path's width is wider than that of other areas. The velocity of mudflow is mainly depending upon the characteristics of topography such as slope and the quantity of discharge of water from the Crater Lake (figure 3(iii)).

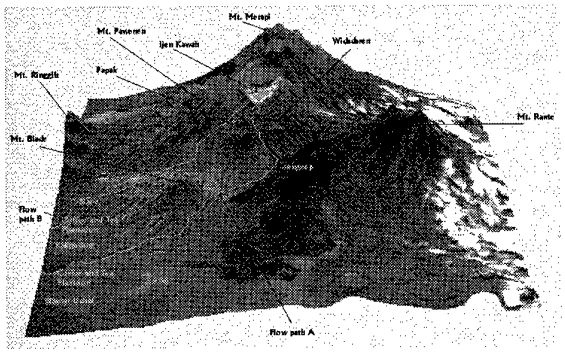
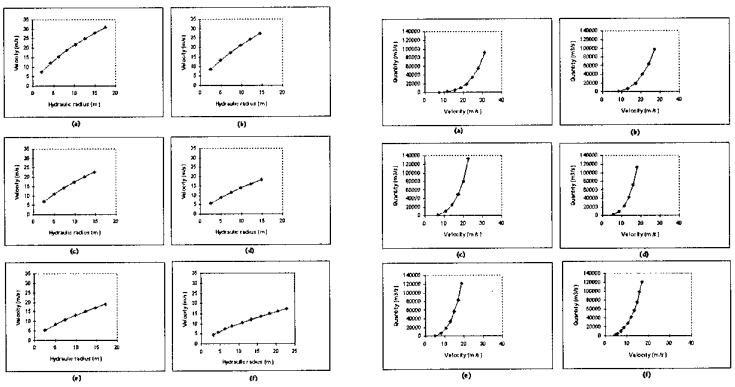
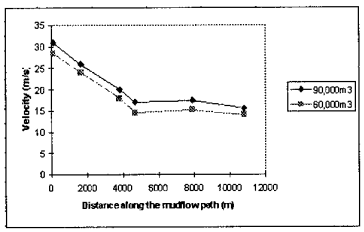


Figure 2 shows the major mud flow paths. Flow paths and Landsat TM image (RGB:4 3 2) overlaid onto DEM to visualise the flow path in a 3D perspective view.



(i)

(ii)



(iii)

Figure 5 (i) to (f) Shows the relationship between the hydraulic radius and the velocity of mudflow at several areas along the flow path at various distances, Surface Profile a) in outlet area, 0.103 km distant from the crater lake, b) 1.64 km, c) 3.8 km, d) 4.7 km, e) 7.95 km, f) 10.8 km from the crater lake. Figure 5 (ii) shows the relationship between discharge rate and velocity of the mudflow at several cross sectional areas along the major mudflow path. Surface profile (a) nearer (0.103km) to the outlet of Kawah Ijen Crater Lake. (b) 1.64 km, (c) 3.8 km, (d) 4.7 km, e) 7.95 km. (f) at 10.8 km from the Crater Lake. Figure 5 (iii) shows the velocity of mudflow along the flow path.

6. CONCLUSION

Mudflow modeling of Ijen kawah volcano using DEM within a GIS environment is found to be useful in providing information pertinent to mudflow hazard. The velocity of the mudflow is directly proportional to the cross-sectional area of the flow path, hydraulic radius and bed slope of flow path and inversely proportional to the wetted area perimeter. Meanwhile, as the quantity of water discharge from the Crater Lake increases the velocity of mudflow also increases. Information pertinent to the routes of flows can provide precautionary measurement against mudflow hazards. In mudflow analysis, collecting more field data, improving DEM's grid element size and coupling GIS with hydraulic flow model can improve the mudflow model.

REFERENCES :

COSTA.J.E, 1997, Hydraulic Modeling for Mudflow hazards at Cascades volcanos, *Environmental and Engineering Geoscience*, 3.1, pp 21-30.

http://www.lonelyplanet.com/dest/sea/graphics/map-indo.htm

JONES A.C., 1995., Improvement of volcanic hazards assessment tecques using GIS: a case study of Mount Etna, Sicily, Innovation in GIS2, Taylor and Francies.

LAENEN A AND HANSEN., 1988., Simulation of three lahars in the Mount St. Helens area, Washington, Using a One- Dimentional, Unsteady stream flow model.,*USGS*, Water Resources Invest. Rep. 88 - 4004, pp 20 .

MACEDONIO.G, PARESCHI.M.T., 1992., Numerical Simulation of some Mudflows from Mt. St. Helens, *Journal of Volcanology and Geothermal Research*, 54. 1-2, pp 65-80.

OPPENHEIMER, C., 1993, Infrared surveillance of crater lakes using satellite data. Journal of Volcanology and Geothermal Research, 55 117-128.

Public WorksResearch Institute., 1988., Technical Standard for measures against debrisflow, *Technical memorandum PWRI 2632*, Ministry of construction, Japan, 40p.

SIMKIN, T., AND SIEBERT, L., 1994, *Volcanoes of the World*, 2nd edition:Tucson, Geoscience Press, 349p.

SUMBERDAYA D., 1990., *G.Ijen*, Berkala vulkanologi edisi khusus, No.151, Departemen pertambangan danenergi, Republic Indonesia.

SURYO. I AND CLARKE M.C.G., 1985., The occurrence and mitigation of volcanic hazards in Indonesia as exemplified at the Mount Merapi, Mount Kelut and Mount Galunggung volcanoes, *Quarterly Journal of Engineering Geology* .,18: 79-98.

TAKAHASHI T., 1985., Debris flow: mechanics and hazard mitigation., *Proc. ROC-Japan Joint Seminar on Multiple hazards mitigation*, National Taiwan university , Taipei, pp. 1075-092.

USGS., 1998., Hazard posed by volcanoes,
http://volcanoes.usgs.gov/Hazards/What/Lahars/lahars.html.

VIGNAUX.M; WEIR.G.J., 1990., A General Model for Mt Ruaphehu Mudflows, *Bulletin of Volcanology*, 52.5, 381-390.

The 21st Asian Conference on Remote Sensing
December 4-8, 2000 Taipei, TAIWAN

Prospect for the Method of Urban Safety Analysis and Environmental Design

Osamu MURAO and Fumio YAMAZAKI

Institute of Industrial Science, University of Tokyo
4-6-1 Komaba, Meguro-ku, Tokyo, 153-8505
Tel: (81)-3-5452-6388, Fax: (81)-3-5452-6389
E-mail: murao@iis.u-tokyo.ac.jp
JAPAN

KEY WORDS: Information Technology, GIS, Digital City, Urban Simulation, Urban Safety Planning

ABSTRACT: In Japan, it is important to carry out urban planning considering natural disasters, because earthquakes occur frequently. However, except for few cases, cities in Japan have not been designed with any definite visions for urban safety based on previous research concerning natural disasters. It is necessary for the people in Japan to propose a future vision of a city from the urban safety point of view, as it has been plagued with many earthquakes throughout history. On the other hand, recent information technology enabled the improvement of real-time monitoring systems after the 1994 Northridge Earthquake and the 1995 Kobe Earthquake. The authors proposed a method of analyzing and designing a city based on the urban safety point of view in previous papers. This method, named as *MUSE* (*the Method of Urban Safety Analysis and Environmental Design*), is based on the theory of *The Image of the City* by Lynch (1961), and some urban physical elements are defined as parts of an organic system. In this paper the prospect for *MUSE* and the methodology to realize it are described. The proposed system is related to Information Technologies and we expect that *MUSE* will be applied to early earthquake damage assessment systems.

1. INTRODUCTION

Recent rapid development of information technologies, i.e., Internet, Mobile Computing, Remote Sensing, Virtual Reality, etc., have changed our social life in various fields. This remarkable innovation also affects the field of urban safety planning or disaster mitigation. Cooperating with these latest information technologies, some human activities for disaster mitigation could be shifted into a new paradigm. Especially, GIS technology will be an effective means, because the spatial viewpoint is indispensable not only for the field of physical environment like urban planning but also for human activities. In fact, a lot of researches with GIS have been carried out since the 1994 Northridge Earthquake and the standardization of spatial data infrastructure as ISO/TC211 is globally under development. In the field of architectural design, some architects (e.g., Frazer, 1995) have discussed new possibility of Cyber City or Cyber Architecture. However, the expected new concept of cyberspace might be only artistic expression on the monitor without awareness of urban problems in the real world. Linking the real world and the cyberspace together to solve the concrete urban problem, the new life style in the IT era will be realized. Based on the above social background and the previous research (e.g. Murao *et al.*, 2000), the present authors proposed a method named *MUSE* (*the Method of Urban Safety Analysis and Environmental Design*) to analyze a city from the viewpoint of urban safety (Murao and Yamazaki, 1999). This paper focuses on the prospect to realize *MUSE*.

2. OUTLINE OF "*MUSE* "

MUSE (*the Method of Urban Safety Analysis and Environmental Design*) is based on the theory of *The Image of the City* by Lynch (1961), and some urban physical elements are defined as parts of an organic system in GIS. This is a method to analyze or recognize urban phenomena. It will be able to simulate and design cities optimally according to each condition. The physical elements are classified into the following 10 types.

Element-0: Imaginary Walls
Element-I: Subjects (as Physical Dynamic Elements): people, bicycles, cars, trains, etc.
Element-II: Shapes (as Physical Static Elements)
- a. Paths (Leading Paths and Secondary Paths): streets, expressways, alleys, railways, etc.
- b. Edges: coastlines, riverbanks, long walls, edges of developed districts, etc.
- c. Cells: town blocks, etc.
- d. Voids: open spaces, public squares, parks, playgrounds, campuses, parking lots, etc.
- e. Cores: city halls, ward offices, elementary schools, hospitals, etc.

Element-III: Webs (as Systematic Elements): common ducts, lifelines, water supply, etc.
Element-IV: Nature (as Natural Elements): ponds, lakes, rivers, green belts, farms, etc.

With the classified spatial data for GIS, inventory and statistical data, and the latest information technologies (e.g., high quality computers, GPS, Remote Sensing, Virtual Reality, Augmented Reality, Ubiquitous Computing, Cyber Architecture, etc.), we hope to have remarkable improvement in the field of disaster mitigation (Figure 1).

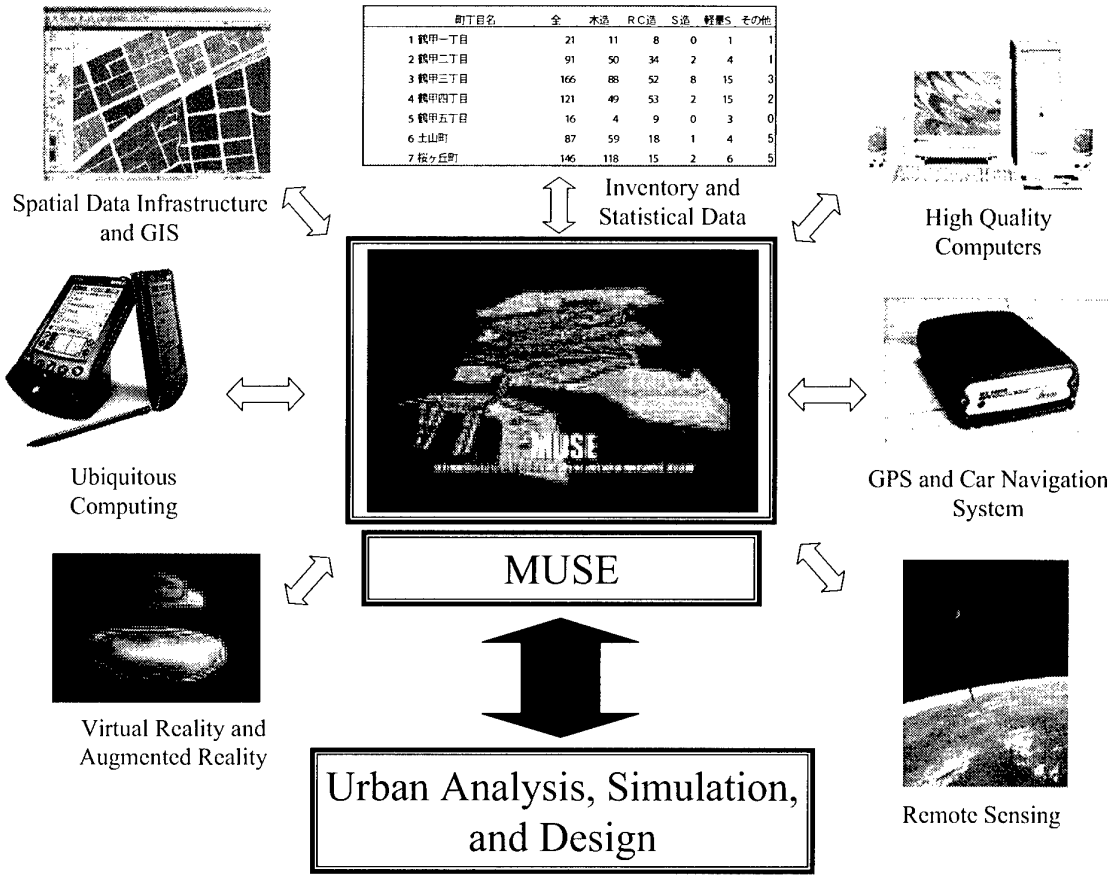


Figure 1 Cooperation between Information Technologies and *MUSE*

3. METHODOLOGY OF "*MUSE SYSTEM*"

3.1 Outline

The comprehensive system among *MUSE* and the information technologies to realize the vision (Figure 1) was named as *MUSE System*. This system consists of three fields, namely, *Semantics*, *Syntactics*, and *Pragmatics* (Figure 2). *Semantics* is the field in relation to the classification and the definition of spatial data. *Syntactics* deals with the relationship between the spatial data and other elements (i.e., time, location, and social systems). *Pragmatics* is the field in connection with the application of the information to the real social life for people.

3.2 *Semantics*

Semantics is the field that deals with the relationship between the digitized GIS spatial data and the physical elements of the city. In this stage, the physical elements and the spatial data are classified into some categories and the vocabulary of spatial data is defined clearly. For example, the element named "*Edge*" (coastlines, riverbanks, or long walls, etc.) is usually negative element that interrupts traffic activities (Figure 3). However, the element can be positive one to prevent fire spread in case of a big fire caused by an earthquake. The purpose of *Semantics* is to make a dictionary of urban spatial data which have some meanings depending upon circumstances. The standardization of spatial data infrastructure as ISO/TC211 is globally under development. GIS is an important tool to share the spatial information among users. Therefore, *Semantics* in *MUSE System* should be established in the global standardization.

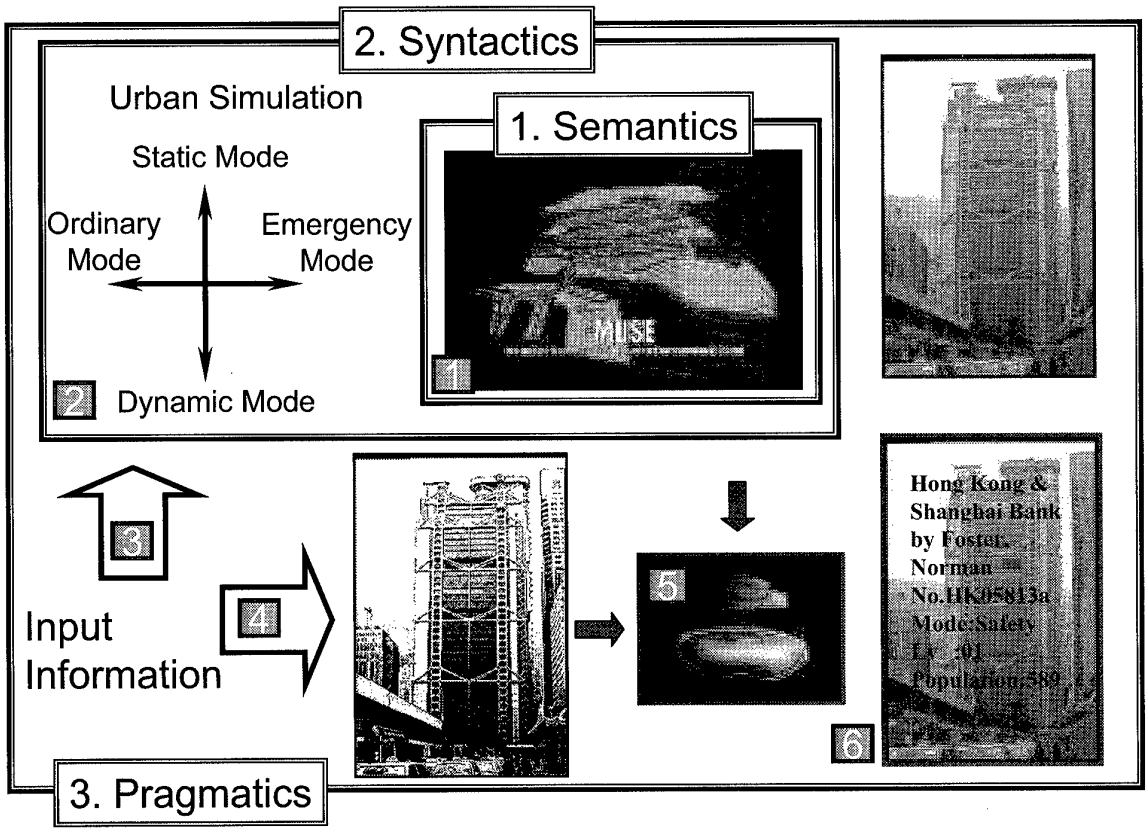


Figure 2 Process to realize *MUSE*

3.3 *Syntactics*

Syntactics is the field that deals with the relationship between the spatial data prescribed by *Semantics* and other elements, i.e., time, location, and social systems (e.g., economy or the laws and regulations). As a result, it will be possible to simulate the various urban phenomena as well as damage assessment of the city. Environmental Systems Research Institute, Inc. evaluates *GIS ModelBuilder*, which was developed for GIS simulation, as one of the most promising extended function in the next generation. Figure 4 (L) shows a flow chart of Erosion Hazard simulation including some ground condition by *GIS ModelBuilder*. The round shaped node represents a function to estimate each condition and each function can be changed for a more accurate and improved urban simulation according to the progress in the research field. The construction of the method to grasp the urban activities is a principal subject of *Syntactics*. There are two axes for the simulation in this stage as shown in Figure 2. One of them is the axis in connection with its use, the ordinary mode and the emergency mode. Another one is related to the time period to input data, the static mode and the dynamic mode. The static mode is used for the simulation with slow updating data like those for disaster management, which is not necessary to update data every day or every week. On the other hand, the dynamic mode is the real-time simulation in Internet or Ubiquitous-computing environment. The concept of the urban simulation will be a new method to recognize and design cities in the next century. For instance, a local government whose budget is limited can determine the optimal location of open space as a result of a fire spread simulation shown in Figure 4 (R). It is time to realize the symbioses of the Real City and the Invisible City with information technologies and spatial data infrastructure as Crane (1960) described 40 years ago.

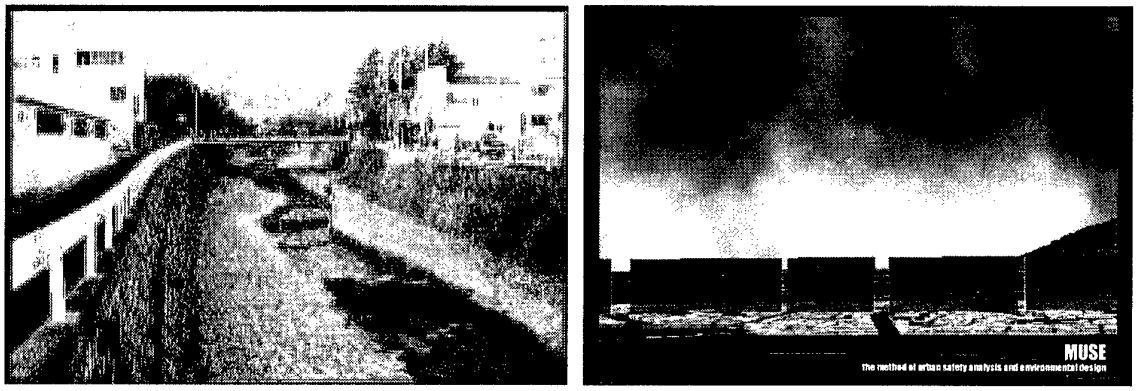


Figure 3 Meaning of "*Edge*"

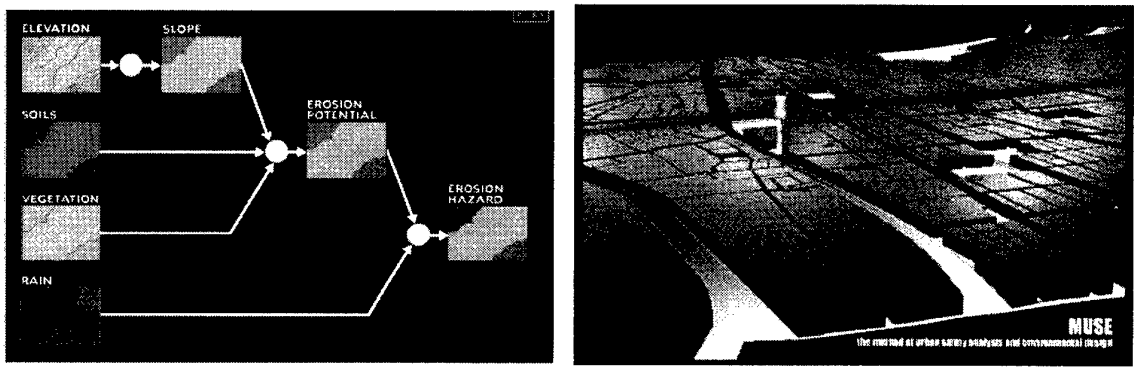
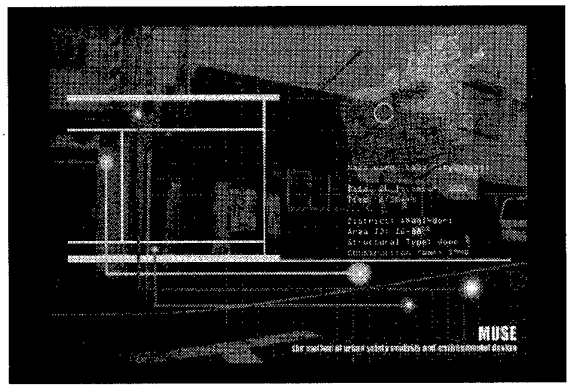


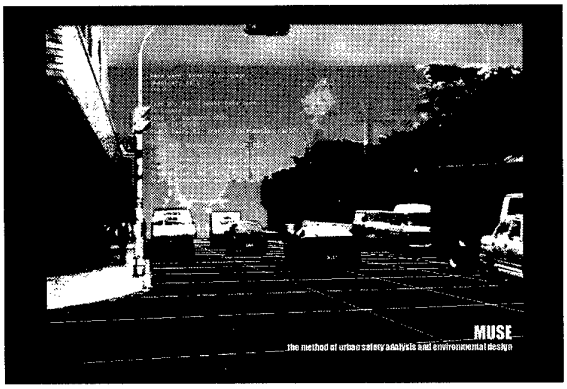
Figure 4 GIS ModelBuilder © 2000 ESRI (L) and Urban Simulation of Fire Spread (R)

3.4 *Pragmatics*

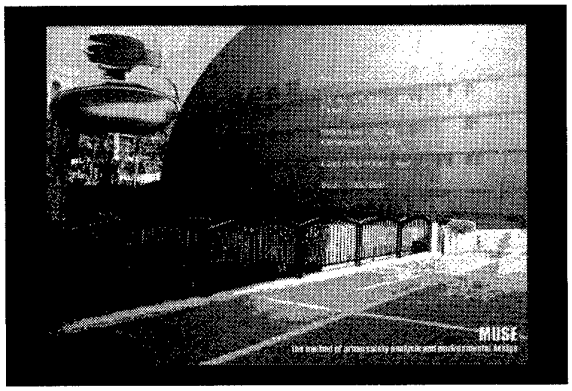
Syntactics is to recognize the social activities in a city through a computer monitor. How people deal with data or information in the social real life should be considered in *Pragmatics* field. One of the final goal of this stage might be realization of Augmented Reality (Feiner *et al.*, 1999) for disaster mitigation, in which people can get useful information of real objects in a person's presence through HMD (Head Mounted Display). Construction of a 3D Digital City Database is indispensable for it. One of the important subjects of this field is how automatically the spatial data could be updated according to the change of a city. Some information technologies like remote sensing, laser scanning, and positioning system can be helpful to solve the problem. The future vision in the field of disaster mitigation is shown in Figure 5. Figure 5 (a) is the utility data for residential buildings with its location projected on a monitor. Using this application, it is easier to find out the hidden damaged part of the utility after an earthquake. Figure 5 (b) shows the real-time traffic information on a car window based on the dynamic simulation described in 3.3. This will be useful for local governments or the public to grasp the traffic condition of a city. Figure 5 (c) shows the emergency information on a hospital just after an earthquake (e.g., the number of available beds, the number of doctors on duty, etc.). Figure 5 (d) is the image of the evacuation area led by HMD. The vision, which indicates a new relationship in the 21st century among information, human activities, and disaster mitigation, will be realized through the three stages by the linkage of the latest information technologies.



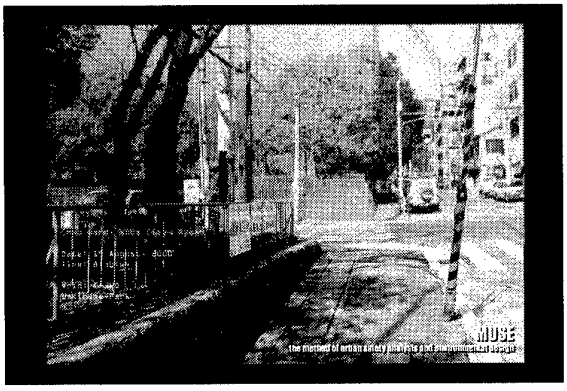
(a) Lifeline Data of House Projected on Monitor



(b) Traffic Information on a car window



(c) Emergency Information on Hospital



(d) Evacuation Area led by HMD

Figure 5 Application of *MUSE* to Urban Safety

4. CONCLUSIONS

The authors proposed a method named as *MUSE* (*the Method of Urban Safety Analysis and Environmental Design*) to analyze a city from the viewpoints of urban safety. In *MUSE*, some urban physical elements are defined as parts of an organic system in GIS to analyze or recognize urban phenomena. Also, a future vision in connection with disaster mitigation was suggested. In this paper the prospect for *MUSE* was described. The comprehensive system of *MUSE* and the information technologies to realize the vision was named *MUSE System*. This system consists of three fields, namely, *Semantics*, *Syntactics*, and *Pragmatics*. *Semantics* is the field in relation to the classification and the definition of spatial data. *Syntactics* deals with the relationship among the spatial data and other elements (i.e., time, location, and social systems). *Pragmatics* is the field in connection with the application of the information to the real social life for people. The vision, which indicates a new relationship in the 21st century among the information, human activities, and disaster mitigation, will be realized through the three stages by the linkage of the latest information technologies.

Acknowledgements

The authors would like to express their gratitude to Prof. Steven K. Feiner and Prof. Peter K. Allen of Columbia University, Federal Emergency Management Agency, Mr. Ronald T. Eguchi of ImageCat, Inc., Environmental Systems Research Institute, Inc., Pasco Corporation, Prof. Ryosuke Shibasaki of University of Tokyo, and The foundation for the promotion of Industrial Science, for the support of the investigations in this paper.

References

Crane, D., (1960). "City Symbolic," AIA.

Frazer, J. H., (1995). "The Architectural Relevance of Cyberspace," *Architectural Design: Architects in Cyberspace*, 76-81.

Höllerer, T., Feiner, S. and Pavlik J., (1999). "Situated Documentaries: Embedding Multimedia Presentations in the Real World," *Proceedings of ISWC '99 (International Symposium on Wearable Computers)*, 79-86.

Lynch, Kevin, (1960). *The Image of the City*, MIT Press.

Murao, O., Tanaka, H., and Yamazaki, F., (2000). "New Method for Building Collapse Risk Assessment Based on Damage Data Due to the 1995 Kobe Earthquake," *Proceedings of the 12th World Conference on Earthquake Engineering*, CD-ROM, No.2312, 8p, Auckland, New Zealand.

Murao, O., and Yamazaki, F., (1999). "Use of GIS for the Method of Urban Safety Analysis and Environmental Design," *Proceedings of the 20th Asian Conference on Remote Sensing*, Vol. 2, 951-956, Hong Kong.

The 21st Asian Conference on Remote Sensing
December 4-8, 2000 Taipei, TAIWAN

The Development of Forest Fire Forecasting System using Internet GIS and Satellite Remote Sensing

Myung-Hee Jo* Myung-Bo Lee**, Si-Young Lee**, Yun-Won, Jo* Seong-Ryul Baek*
*Department of Geodetic Engineering, Kyungil University
33 Buho-ri, Hayang-up. Kyungsan-si, Kyungsan bukdo, 712-701, Korea
Tel)+82-53-850-7312, Fax)+82-53-854-1272
mhjo@bear.kyungil.ac.kr, gerry@w3.ko, fosco@hanmail.net
** Div. Forest Environment, Korea Forest Research Institute, Tel)+82-2-9612-744
Fax)+82-2-9612-543, leemb@foa.go.kr,LSY925@chollian.net

KEY WORDS: Satellite Image, Forest Fire Hazard Index, Internet GIS

ABSTRACT

The purpose of this study is to develop the most effective method for a forest fire forecasting in small mountain through GIS and Remote Sensing. The study area was Young-chon area including all of the Kyung-sang Province, Korea. GIS DB was constructed based on factors of geographical and natural features those are necessary factors to forecast a forest fire. It was clarified that satellite image and some spatial data is very effective for developing the Graphic User Interface to forecast the forest fire using Internet GIS. In addition, the forest fire hazard area was prevented and managed effectively.

INTRODUCTION

Recently the human lives, fortune and the ecosystem have been deadly threatened by the many cases of forest fire and it's huge size. Even though there is trip of extinguish equipment, the main reason of this large sized forest fire is that there is limitation of traditional method and no more scientific way to predict these disasters.

In this paper, we present that the fatal damage by forest fire could be reduced if there are suitable predictions and rapid provision against forest fire using Internet GIS. This Internet GIS modeling is the most perfect way for forest fire forecasting system because forest fire has a movement in both in spatial and temporal.

CFFDRS(Canadian Forest Fire Danger Ration System) was developed for a prediction of forest fire in 1987 and GIMS(Geographical Information and Modeling System) was installed for a management of it by Kessell(1990). GIMS could assign a part by telling the shape of forest fire in real time and help the managers of forest fire have best decision against these disasters. In 1993 Gracia and Lee prepared a map for forest fire forecasting in Alberta after evaluating the main danger factors of forest fire.

In Korea, Y.H Cheong(1989) studied about predicting the dangerous rate of oxidation and S.Y Lee(1990) found out the relationship between the factor of environment and temperature of forest fire . K.C Lee(1998) constructed the modeling of suitability analysis about forest fire extinguish water tank using GIS .

The study purposes of this paper are as follows that the investigation into actual condition of forest fire in Young-chon area was first carried out and secondly constructed in to GIS DB. Danger index of forest fire was computed with the based on topographic and meteorological factor in this area and evaluated the relationship between these factors and forest fire. Finally, the network presentation system of that using Internet GIS, which is the main goal of this paper, was installed.

Review on Physical Factors of Forest Fire in Study Area

In the view of season, the number of forest fire increase in the spring and the winter because it is very dry and small amount of precipitation. 3,362 cases took places between 1990~1999 and the damaged area was 13991.43ha. Among them 2,069 cases happened between March and April and 883 cases occured in the winter. The main reasons of forest fire in this area have been composed of accidental fire(44%), ditch burn up(22%), visit tomb accident fire(7%), playing with fire(5%), etc(23%). 49% cases of them took places around 2 p . m ~ 6 p . m, 38% took places 11 a . m ~1 p . m, 9% took places 7 p . m ~ 4 a . m, 4% took places 5 a . m ~ 10 p . m in order.

In study area, 84.2% cases of forest fire happened from March. 21 to April 10.

The potential factors including aspect, elevation, slope, stream, vegetation, which can have an effect on forest fire were extracted for probability analysis.

Aspect is related to the amount of sunshine. In general, the cases of forest fire occur in area of south more than in the area of north because a southern exposure has higher burning point.

Actually, more than 40% of forest fire happened in aspect of south area while it doesn't happen in the other area. Therefore, the aspect is really related to forest fire. Comparing with previous forest fire, more than 90% cases of forest fire happened at 100m above the sea level. Most these disasters take places in lower area above the sea level. 65 % cases in entire forest fire occurred in between a slope of zero and a slope of twenty degrees. The rate of forest fire decrease remarkably as slope increases.

Stream is regarded as an important role not only to extinguish forest fire but also to provide moisture toward plants. The area far from stream has higher dangerous factors. Especially, the road can be immediate factor to forest fire because there are human beings.

Fuel, which is composed of the amount of precipitation, the humidity of air, the direction of the wind and temperature, is very related to season, and time.

In study area, the air is exceedingly dry in the winter and much precipitation is in the summer. Also, its north, west, east is consisted in a mountainous area, which is over 900 meters above the sea level. There are open field in its south area and cultivated fruit.

The Kum-ho river, which is joined with Nam-chun(Jaho-chun, Gokung-chun) and Buk-chun(Sinryung-chun, Gohyun-chon), is flowed in the middle of this study area. The size of this is 919 and 69% in this area is forests and crop fields and 18% is cultivated area.

In 1999 the number of a broad-leaved tree was twice than the number of a needle-leaf tree while the number of both was same. By analyzing Landsat TM satellite image data, the classes of trees are consist of 55% of Coniferous, 30% of Deciduous, 15% of Mixture forest.

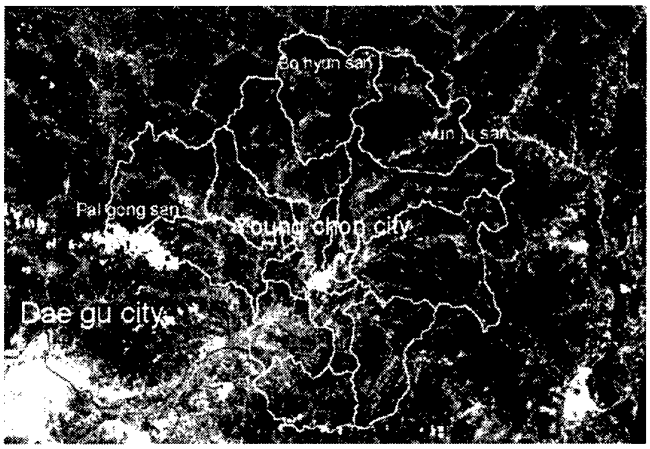


Figure 1. The location of study area

Materials and Methods

In this paper the classes of trees in this area were simply composed of Conifer, Deciduous, Mixed forest, and Agriculture. And the dimensions of damage area, the classification of vegetation and land classification map were found out by Landsat images.

The spatial data including topographic map, geologic map and aerial photo was used to make forest fire hazard index GIS DB. ERDAS IMAGINE 8.3 and Unix Arc/Info GIS tool for image processing and spatial analysis are used and Map Object 2.0 and Visual Basic 6.0 for Internet Network are needed. Virtual GIS is applied to realize forest fire hazard index on 3D terrain.

Topographies of three areas, which are called Hawsan, Hawnam, Jungang in Young-chon city, are analyzed. More than 60% of forest fire happened in between a slope of zero and a slope of twenty degrees and in aspect of south and southern west. Places of those disasters occurred between 100m and 350m above the sea level and close to road, which is far from river.

Table 1. Forest fire Summary

Area	Date	Temperature	Precipitation(mm)	Damage(ha)	Vegetation
A	1999/4/15	10.43	42.5	5	Conifer
C	1999/3/31	8.55	0	1.5	Conifer
G	1999/3/4	4.97	18.5	1.5	Deciduous

After analyzing above table1, the main factors which could affect forest fire, are needle-leaf trees the aspect of southern west and humidity.

Forest fire hazard index could be extracted by using average data acquired from an observation station based on three above factors and presented it in a contour line.

In general, predict modeling was used like density transfer, density regression, significance regression, discriminate function analysis, logistic regression. In this research, logistic regression was considered most suitable analysis because it could compute difference of a variable environment between occurrence spot, in addition nonoccurrence spot and applied to undetected area yield probability.

$$Zi = 3.754 + 0.231 \times(\text{slope}) + 0.324 \times(\text{elevation}) + 0.165\times(\text{aspect}) + 0.328 \times(\text{stream}) + 0.195 \times(\text{forest type}) + -0.017 \times(\text{agricultural pattern}) + -0.128 \times(\text{urban}) + 0.030 \times(\text{road}) + 0.872 \times(\text{rainfall}) + 0.652\times(\text{sunshine}) + 0.713\times(\text{moisture})$$

$$Pi = \exp(Zi) / (1 + \exp(Zi))$$

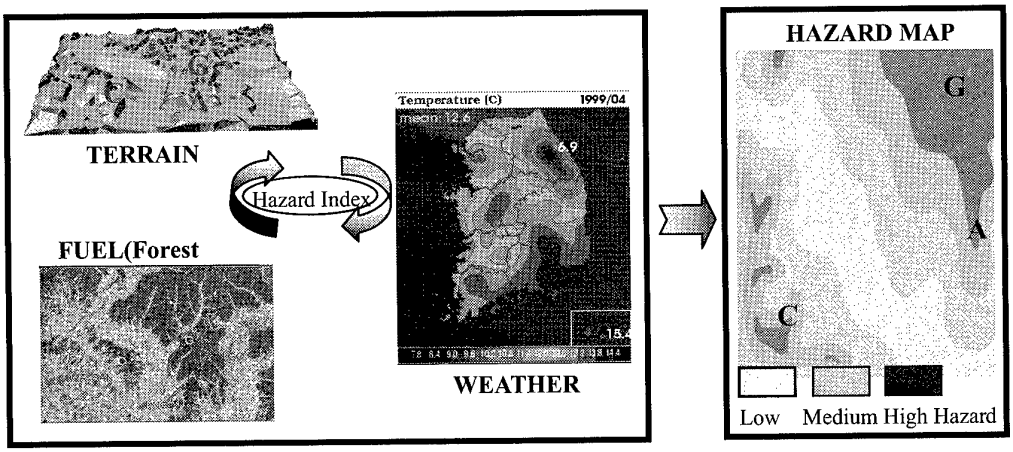


Figure 2. Hazard Map on Study Area

Forest fire hazard Index Forecast System using GIS

1) Development of Forecasting System

The purpose of this study is to develop the most effective method for a forest fire forecasting through GIS and Remote Sensing. In this study digital map was prepared and expressed numerically which includes factors of geographical and natural features, which are necessary factors to forecast a forest fire hazard index.

Fire potential requires collecting baseline vegetation information, daily to weekly monitoring of vegetation condition or vigor daily monitoring of weather conditions, and acquiring risk management information.

A computer-based model is to predict wild fire behavior across time and space. The computer model uses fuel type, weather conditions, slope, aspect and elevation to predict the direction, speed, and burn intensity of a wild fire across various landscapes. The model uses Geographic Information System (GIS) technology. The program is responsible for all the complex computations necessary for simulating fire behavior.

The model's user-interface is designed so advanced computer skills and GIS knowledge is not required to execute the model. Ease-of-use puts fire behavior prediction into the hands of fire managers where it can be most effectively applied. With fire damage growing every year, fire departments need better planning tools to minimize fire's impact.

The model is also a good analysis tool for resource managers. A Graphic User Interface (GUI) allows the user to easily specify and edit the data and parameters necessary to execute each simulation. Forest fire Danger Index Presentation System would be useful to managers, policy makers and scientists interested in mitigating and evaluating the effects of forest fire. Real time forest fire hazard information is offer to public welfare and administration business management.

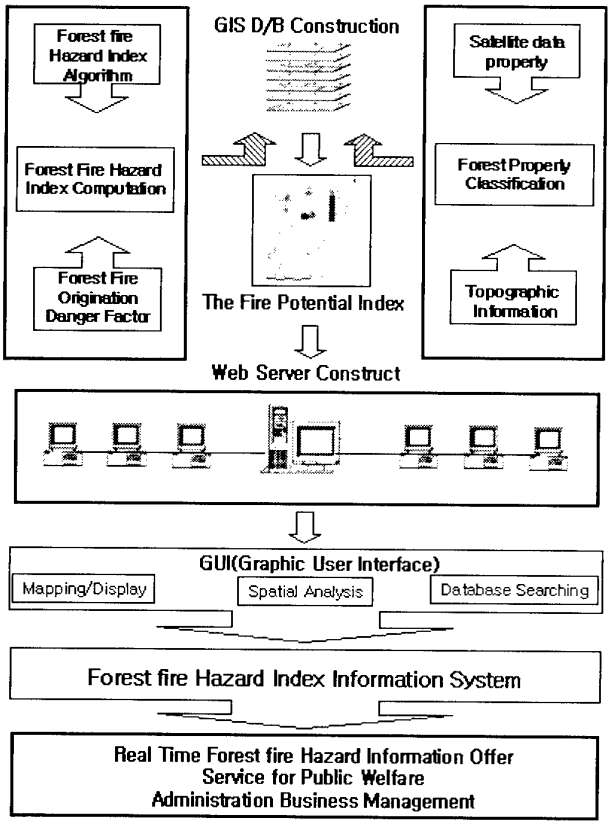


Figure 3. Procedure of Study Frame

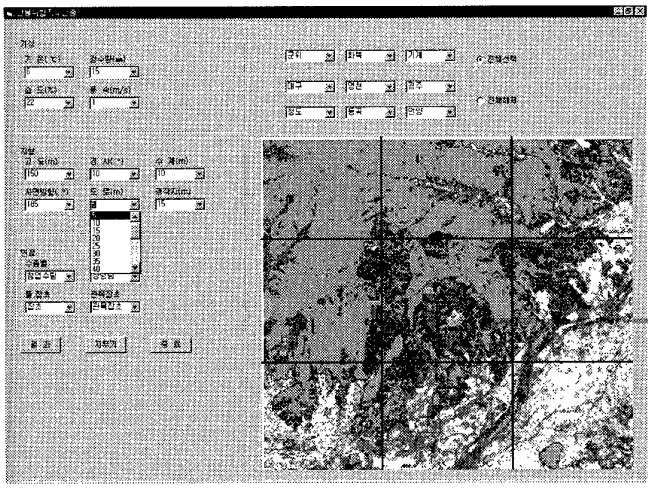


Figure 4. Forest Fire Hazard Index Presentation System

CONCLUSION

In conclusion, the information of forest in the specific area can be easily searched, analyzed and managed through Internet GIS and Remote Sensing. It makes possible for this forest fire forecasting system to predict and to prevent forest fire in effective and scientific because it can assume exact forest fire hazard index in real time and present in proper time. Especially forest fire hazard index was presented in real time integrated with meteorological data through internet web base to forest fire task officer and local citizens without time lagging. It also allows to analyze with spatial modeling and monitoring in the predicted area. Therefore it was clarified that the forecasting system using Web based GIS is prominent for management and prevention of forest fire.

REFERENCES

An, Sang-Hyun, 2000, A Forest fire prevention mechanism using Geographic Information System – The case of Uam Mt. In Chungju-, Chungbuk National University, Korea.45p.

Beck, J.A., 1989b, A geographical information and modeling system for the management of wildfire incidents, Proceedings, Urban and Regional Planning Information Systems, 17, p.474.

Chou, Y. H., 1990b, Modeling fire occurrence for wild land fire management: A GIS spatial analysis. In Proceedings of the GIS/LIS'90 Conference, November 7-10, 1990, Anaheim California, pp.440-449.

Donoghue, L.R., and Main, W. A., 1985, Some factors influencing wildfire occurrence and measurements of the prevention effectiveness, Journal of Environment, 20, pp.87-96.

Kim Y.S, Suh A.S, Jo M.H, 1998. Introduction to Remote Sensing, DongHwa Technology Publishing Co, 373p.

Kyung Choi, Hong Sub Lee, Ho Joong Youn, Jae Heun Kim, 1994, Selection of tree species to mitigate landslide hazard, Res. Int. No.491, pp.103-109.

Myung-Hee Jo. 1989. Land cover classification using Landsat TM image; The case of the Nak-Tong River mouth area, Ph.D.Thesis, Kyungpook National Univ.,Korea, 154p.

Myung-Hee Jo. 1995. A Geomorphologic study on coastal land classification using satellite remote sensing and GIS.

Piwower, J.M., Ledrew, E. F., and Dudycha, D. J., 1990, Integration of spatial data in vector and

raster formats in a geographic information system environment. Int.J.Geographical Information Systems, Vol.4, pp.429-444.

R.W.Klaver, A.Singh, Global Forest Fire Watch:Wildfire Potential,Detection,Monitoring and Assessment:http://www.usags.gov/

Si Young Lee, Yeon Ha Cheong, Bong Soo Lee, 1996, Analysis of the spread rate and behavior pattern of forest fire using digital topographic data. Vol.53, pp. 186-193.

Stephen R. Kessell, 1990, An Australian geographical information and modeling system for natural area management, Int.J. Geographical Information Systems, Vol.4, No.3, pp.429-444.

The Annual Report of Youngchon City: 1996,1997,1998,1999.

Yue Hong Chou, 1992, Management of wildfire with a geographical information system, Int.J.Geographical Information Systems, Vol.6, No.2, pp.123-140.

Yun-Jung Kim, 1996, A study on predictive modeling of Forest fire: The case of Puk'ansan National Park, Ewha Womans University, Korea.75p.

Yeon Ha Cheong, Si Young Lee, Yuk Cheol Yeom, 1994, Evaluation of forest fire warning period and estimation of forest fire danger rating index, Res. Int. No.49, pp.92-102.

CONTRIBUTION FORM REMOTE SENSING IN UPDATING BATHYMETRIC CHART

K. Abdullah , M. Z. MatJafri and Z. B. Din
Universiti Sains Malaysia
11800 Penang, Malaysia
Tel: 604-6577888 Fax: 604-6579150
E-mail: khirudd@usm.my, mjafri@usm.my

KEY WORDS: algorithm, bathymetry, remote sensing.

ABSTRACT

The study area selected is the Strait of Penang, located in the north western part of peninsular Malaysia. Surveys were conducted to measure new sounding points using a boat equipped with an echo sounder. The station locations were determined using a GPS system. The data were analysed and tidal corrections were applied to reduce the measured water heights to the chart datum. The tidal readings obtained from the nearest station were used for reference in the data analysis. A new suggested bathymetric chart was drawn based on the new sounding points. We attempted to employ satellite imagery as an aid to bathymetric charting. Cloud free scenes of Landsat TM and SPOT data acquired between January 1997 and February 1997 were available for use in the present study. Each subscene was rectified to the corresponding bathymetric chart. Image locations were related to map GCP coordinates through the second degree polynomial transformation equations. The pixel values at the sample locations were extracted and used as independent variables. Multiband water depth algorithm was used in the calibration analysis. Regression technique was used for calibration of the satellite signals for water depth measurement using the measured sounding points as dependent variables. The correlation coefficient and root-mean-square deviations were examined for each data set. The accuracy of each calibrated algorithm was further verified using other known sounding points. The respective calibrated algorithm was then applied to the coresponding image to generate a water depth map. The colour coded bathymetric map was used for visual interpretation and assessment of the present water depth pattern.

1.0 INTRODUCTION

Although the existing bathymetric charts were reprinted recently, they display water depth values which were measured decades ago. Oceanographers have often questioned the reliability of these charts. Costal erosion and siltation as well as activities like dredging and land reclaimation can cause deposition and erosion of the sea floor and hence changing the bottom topography. Therefore a resurvey of the present water depth pattern was conducted in an attempt to update the existing bathymetric chart.

In this present study the use of both the algorithms (using single-band, two-band ratio and three-band) and the proposed three-band methods were investigated in coastal areas of Malaysia. The aim of the study is to assess the accuracy provided by different types of satellite data in bathymetric mapping. TM and SPOT data were used in the present comparative analysis. The limitations faced by the remote sensing technique are discussed.

2.0 PHYSICAL PRINCIPLES OF WATER DEPTH DETERMINATION

The development of water depth determination techniques was based on the simple water reflection model which accounts for the major part of the signal received by a sensor over a clear shallow water (Lyzenga (1978)). According to this model, the radiance, L, in a single wavelength band can be written as

$$L = L_s + L_o R_b \exp(-KfZ) \quad (1)$$

where L_o is a constant which includes solar irradiance, the transmittance of the atmosphere and the water surface and the reduction of the radiance due to refraction at the water surface; L_s is the radiance observed over deep water (due to external reflection from the water surface, volume reflected radiance from the water column and scattering in the atmosphere); R_b is the bottom reflectance; K is the effective attenuation coefficient of water; f is a geometrical factor to account for path length through water and Z is the water depth. Other models developed by Benny and Dawson (1983), Stove (1985), Philpot (1989), and Lee et al. (1999) were also studied.

3.0 REGRESSION ALGORITHMS

As far as the regression is concerned the expression should be in the most simplified form. The single-band depth algorithms derived from the above model can be written in a common simplified form for channel i

$$Z = a_{oi} + a_{1i} X_i \quad (2)$$

where $X_i = \ln(L_i - L_{si})$, $a_{oi} = (1/K_i f)\ln(L_{oi} R_{bi})$ and $a_{1i} = -1/K_i f$

The above equation can be regressed linearly with in-situ water depths. The limitation with a single band method is that changes in the bottom reflectance within the area of interest will cause errors in the depth calculation. Predes and Spero (1983) derived the n-band/n-bottom type case as

$$Z = a_0 + a_1 X_1 + a_2 X_2 + \ldots + a_n X_n \quad (3)$$

We modified the above algorithm by writing equation (2) for 3 bands as simultaneous equations and finding the single expression for z for the 3-band case. The form of the series obtained:

$$Z = a_0 + a_1 X_1 + a_2 X_2 + a_3 X_3 + a_4 X_1 X_2 + a_5 X_1 X_3 + a_6 X_2 X_3 + a_7 X_1 X_2 X_3 + \ldots \quad (4)$$

For the present bathymetric application we used the series up to the term displayed above and the coefficients were determined by regression.

4.0 DATA FOR THE AREA UNDER INVESTIGATION

The study area is the shallow water region in the Straits of Penang, Malaysia (between latitudes 5.30° to 5.45° N and longitudes 100.30° to 100.40° E). Images scenes of SPOT and TM captured on 1 January 1997 and 28 February 1997 respectively, were selected for analysis. The bathymetric chart of Penang (chart 1366, 1:60000 scale, published at Taunton, England, revised in 1999) was used for reference. New depth sounding data measured using echo sounder were available. Tidal data corresponding to the scenes were acquired. Data on water quality parameters and other oceanic parameters were not available for reference.

5.0 DATA PROCESSING

5.1 Depth Points and Pixel Values for Calibration

The water depth measurements were corrected for tidal height variations and the readings were reduced to the level of the Lowest Astronomical Tide (Chart Datum). The tidal data relevant to the analysis of tidal correction were taken from the published tide tables (Royal Malaysian Navy, 1999). The number of points chosen for depth calibration and validation were 175 and 43 respectively.

The image pixel positions were related to the geographical coordinates through rectification to the bathymetric chart using selected ground control points and second-degree polynomial transformation equations. The locations of these sounding points were then transformed into image scan-line and column-numbers by using the corresponding calibrated transformation equations obtained from the rectification analysis. The pixel intensities (digital values) at these points were then obtained for bands 1, 2 and 3. For each pixel location, a 3 by 3 sample window was used for the extraction of the pixel value. The actual water height at any point during image acquisition was determined by adding the height of the tide above chart datum to the corrected depth obtained earlier. The data quality for bathymetric application using each data set was validated by observing the distribution of the data on the plot of pixel intensity versus depth (Figure 1).

5.2 Determination of Deep-water Radiance

One of the prerequisites of the algorithms listed above is the value of the deep-water radiance for each band. The procedure involved finding the pixel value of a deep-water area within the scene. The deep-water radiance is normally (but not always) characterized by the lowest digital number in each band.

Due to the high degree of uncertainty in obtaining these values from the image inspection approach, we determined this parameter by optimizing equation (2) through regression analysis. The iteration process determined the optimum value of L_{si}. This method was adopted in this study because the calibration accuracy was found to be better than the regression results using the deep-water radiance obtained by image inspection.

The results of the analysis gave the L_{si} values in terms of DNs for the first 3 bands at about 80, 25 and 8 for the TM data and the SPOT scene gave values of 60, 20, and 10 respectively.

5.3 Calibration Regression

A least squares minimization was performed to calculate the best values of the coefficients in the algorithm. The results using all the data points showed high RMS error due to the presence of many outliers that degraded the calibration accuracy. To minimize the root-mean-square (RMS) error, the points having high residuals were discarded. After a sufficient number of iterations to discard these outliers only 168 points were retained. The RMS deviation error and correlation coefficient, R, for each data set were noted.

Inspection of the regression results indicates that the accuracy increases from the single-band to the three-band algorithms. The proposed algorithm produced some improvement over the

conventional three-band method. This algorithm was used for further analyses. The results using the proposed algorithm are displayed in Table 1.

5.4 Validation of the Calibrated Algorithm

The validation data sets, which were not used in the calibration regression analysis, were then used for depth evaluation. Each calibrated algorithm was applied to the respective remotely sensed data set. Scatter plots of depths from chart versus calculated depths were made and the correlation coefficients determined (Table 2).

5.5 Generation of Water Depth Maps

The water depth readings from echo sounding were used to plot the suggested updated bathymetric map of the area (Figure 2). Assessment for the contribution of remote sensing data for bathymetric charting was made using the present data sets. Each calibrated algorithm was applied to the corresponding multispectral image on a pixel-by-pixel basis. The land and cloud pixels were masked out using the infrared bands. The density-sliced depth images were geometrically corrected to the same coordinate system of the generated bathymetric map. The generated maps were colour-coded for display of the different depth contours (Figure 2).

6.0 RESULTS AND DISCUSSION

The newly bathymetric map shows close similarity in depth patterns with the generated depth maps using remote sensing data. Observation of the plots of intensity versus depths and the results of calibration and validation for all the data sets reveal that TM and SPOT have comparable performances. TM and SPOT displayed nearly similar depth patterns. The principal error arose from the effect of water turbidity. Non-uniformity in the water turbidity and bottom reflectance caused additional complexities with this technique.

7.0 CONCLUSION

New depth information was obtained from the techniques employed in the present study. The results seggest that the existing bathymetric maps need to be updated. Remote sensing data can provide a valuable contribution in bathymetry. However, the environmental conditions may have a major influence in the accuracy of the technique.

Acknowledgment

This study is partially supported by the National Space Development Agency of Japan through the joint NASDA-ESCAP project entitled 'National Capacity building for sustainable environment and natural resources management through research and studies on the use of ADEOS data' and the Malaysian Government IRPA Grant no: 08-02-056011. Thanks are extended to Universiti Sains Malaysia.

References

Benny, A. H. and Dawson, G. J., 1983. Satellite imagery as an aid to bathymetric charting in the Red Sea. Cathographic Journal, 20: 5-16.

Lee, Z. P., Carder, K. L., Mobley, C. D., Steward, R. G., and Patch, J. S., 1999. Hyperspectral remote sensing for shallow waters: 2 . Deriving bottom depths and water properties by optimization. Applied Optics, 38: 3831-3843.

Lyzenga, D. R., 1978. Passive remote sensing techniques for mapping water depth and bottom features. Applied Optics, 17: 379-383

Peredes, J. M. and Spero, R. E., 1983. Water depth mapping from passive remote sensing under a generalized ratio assumption. Applied Optics, 22: 1134-1135.

Philpot, W. D., 1989. Bathymetric mapping with passive multispectral imagery. Applied Optics, 28: 1569-1579

Royal Malaysian Navy, 1999. Tide Tables, Vol. I, 2000. Hydrographic Branch, Royal Malaysian Navy.

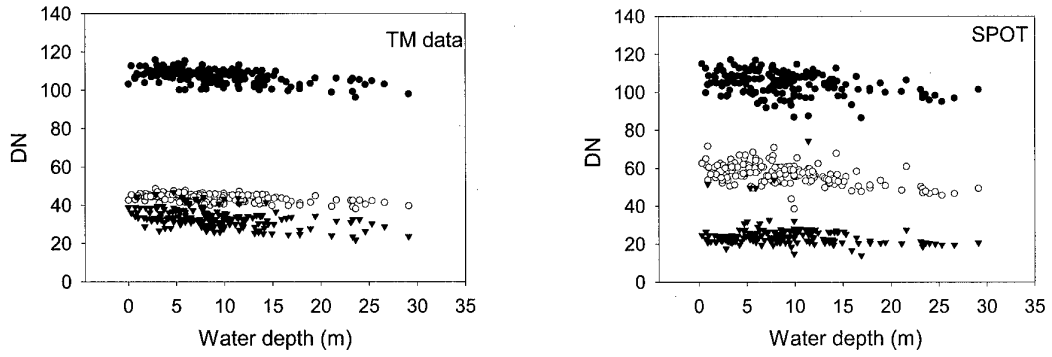
Stove, G. C., 1985. Use of high-resolution satellite imaging in optical and infrared wavebands as an aid to hydrographic charting and coastal engineering. Proceedings of the Technical Programme, Electronics in Oil and Gas, London, pp. 509-530.

Table 1 Calibration results for the data sets

		SPOT	TM
Calibration	R	0.59	0.57
	RMS (m)	4.7	4.6

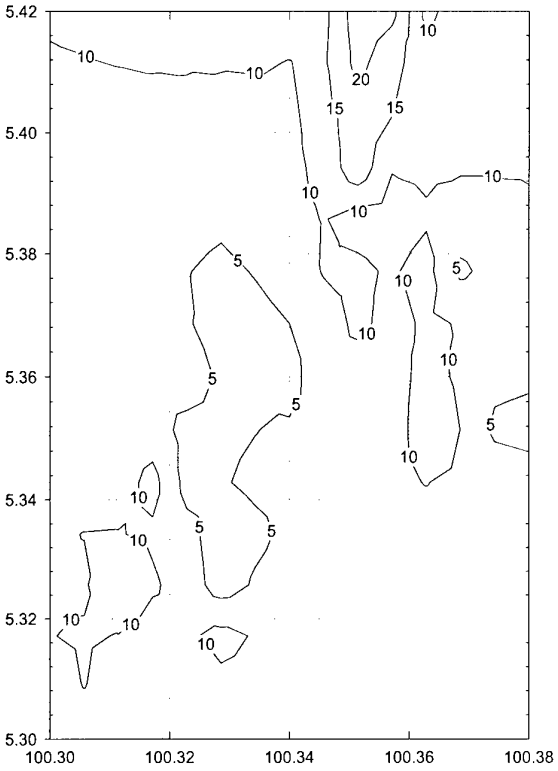
Table 2 Validation results for the data sets

		SPOT	TM
Validation	R	0.31	0.54
	RMS (m)	6.5	5.12

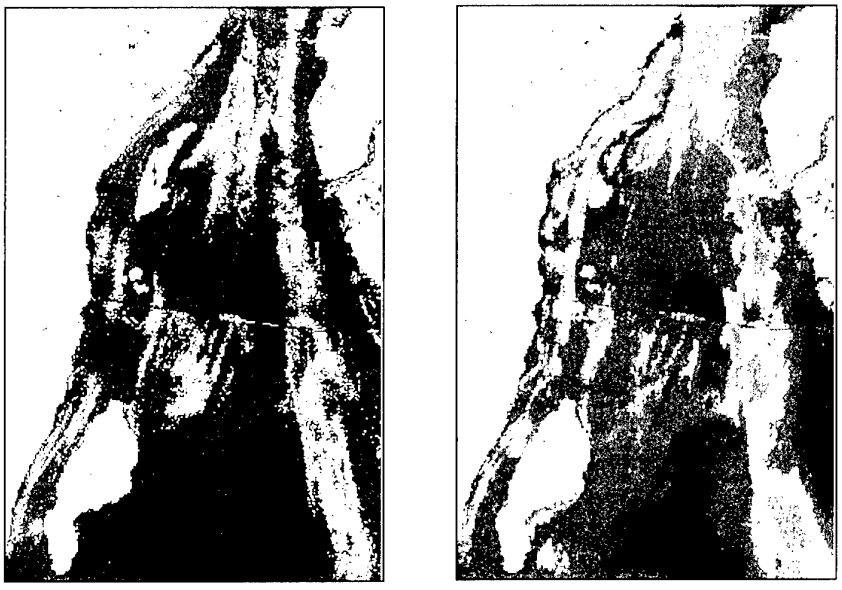


(a) (b)

Figure 1 Intensity versus depth for (a) TM and (b) SPOT data (solid circles for band 1, circle for band 2 and solid triangle for band 3)



(a)



(b) (c)

Figure 2 Bathymetic maps (a) using measured depth sounding points, (b) TM, and (c) SPOT data (colour code: blue 0-5m, green 5-10m, yellow 10-15m and orange >15m)

The 21st Asian Conference on Remote Sensing
December 4-8, 2000 Taipei, TAIWAN

REMOTE SENSING OF TOTAL SUSPENDED SOLIDS IN PENANG COASTAL WATERS, MALAYSIA

K. Abdullah, Z. B. Din, Y. Mahamod , R. Rainis, and M. Z. MatJafri
Universiti Sains Malaysia, 11800 Penang, Malaysia
Tel: 604-6577888 Fax: 604-6579150 E-mail: khirudd@usm.my

KEY WORDS: algorithm, regression, total suspended solids, Thematic Mapper

ABSTRACT

An attempt to estimate the concentration of total suspended solids (TSS) using Thematic Mapper (TM) data was carried out in the coastal waters of Penang. The algorithm used is based on the reflectance model which is a function of the inherent optical properties of water which can be related to its constituents concentrations. A multiple regression algorithm was derived using multi-band data for retrieval of the water constituent. The digital numbers coinciding with the sea truth locations were extracted and converted to radiance and exoatmospheric reflactence units. Solar angle and atmospheric corrections were performed on the data sets. These data were combined for multi-date regression analysis. The efficiency of the present algorithm versus other forms of algorithms was also investigated. Based on the observations of correlation coefficient and root-mean-square deviations with the sea-truth data, the results indicated the superiority of the proposed algorithm. The solar corrected data gave good results, and comparable accuracy was obtained with the atmospherically corrected data. The calibrated TSS algorithm was employed to generate water quality maps.

1.0 INTRODUCTION

Quantitative measurements from satellite remote sensing through analysis with coincident sea-truth data are rarely conducted in the equatorial region. The main reason for this drawback is the difficulty in obtaining cloud free scenes. In this study we attempted to use remote sensing data acquired simultaneously with the surface reference data. Thematic Mapper (TM) data were used because of the spatial resolution and availability of suitable bands for the present applications. Throughout 1999, only two TM scenes were successful acquired.

TM data have been widely used for water quality studies in coastal regions and in inland lakes (Ekstrand 1992, Ritchie et al. 1990, Baban 1993, Dekker and Peters 1993, Forster et al. 1993, Allee and Johnson 1999). To utilize the multi-spectral radiance responses detected by the sensor as a means of water quality monitoring, a model or algorithm is required to relate the TM signals to the scattering and absorption phenomena occurring within the sea.

The objectives of the study are (i) to develop remote sensing retrieval algorithms for total suspended solids (TSS) in coastal waters based on water optical model through regression with coincident sea-truth data and (ii) to perform data correction for multi-date analysis in order to establish calibrated algorithm for local applications using TM data.

2.0 STUDY AREA AND DATA ACQUISITION

The study area is the Penang Straits which is located within latitudes 100° 15' E to 100° 25'E and longitudes 5° 15'N to 5° 30'N. The corresponding satellite track for the TM scenes is 128/56. Based on the bathymetric map the water depth within the study may reach up to about 20 m.

There are two major channels within the straits, namely, the Eastern and Western channels with mean depths of about 10m and 8m respectively.

The water samples were collected from February to November 1999 on dates that the satellite was supposed to overpass the study area. Surface water samples for the determination of TSS concentration were collected using 1 liter polyethylene bottles and later analyzed in the laboratory using standard methods as proposed by Strickland and Parsons (1972). The TM scenes acquired on 2 February 1999 and 22 March 1999 were available for applications.

3.0 WATER OPTICAL MODEL

A physical model relating radiance from the water column and the concentrations of the water quality constituents provide the most effective way for analysing remotely sensed data for water quality studies. Reflectance is particularly dependent on inherent optical properties: the absorption coefficient and the backscattering coefficient. The irradiance reflectance just below the water surface, R(λ), is given by

$$R(\lambda) = 0.33 b_b(\lambda) / a(\lambda) \tag{1}$$

where λ is the spectral wavelength, b_b is the backscattering coefficient and a is the absorption coefficient (Kirk, 1984). The inherent optical properties are determined by the contents of the water. The contributions of the individual components to the overall properties are strictly additive (Gallegos and Correll, 1990).

For the case of two water quality components, i.e. chlorophyll, C, and suspended sediment, P, the simultaneous equations for the two channels can be expressed as

$$R(\lambda_1) = R_1 = 0.33 \frac{(0.5 b_{bw}(\lambda_1) + b_{bc}^*(\lambda_1) C + b_{bp}^*(\lambda_1) P)}{(a_w(\lambda_1) + a_c^*(\lambda_1) C + a_p^*(\lambda_1) P)} \tag{2a}$$

$$R(\lambda_2) = R_2 = 0.33 \frac{(0.5 b_{bw}(\lambda_2) + b_{bc}^*(\lambda_2) C + b_{bp}^*(\lambda_2) P)}{(a_w(\lambda_2) + a_c^*(\lambda_2) C + a_p^*(\lambda_2) P)} \tag{2b}$$

where $b_{bw}(i)$ is the backscattering coefficient of water, b_{bc}*and b_{bp}* are the specific backscattering coefficients of chlorophyll and sediment respectively, $a_w(i)$ is the absorption coefficient of water, a_c*(i) and a_p*(i) are the specific absorption coefficients of chlorophyll and sediment respectively (Gallie and Murtha,1992).

4.0 REGRESSION ALGORITHM

Solving the above simultaneous equations for TSS concentration yields the series consisting of the terms R_1 and R_2

$$P = a_0 + a_1 R_1 + a_2 R_2 + a_3 R_1 R_2 + a_4 R_1^2 + a_5 R_2^2 + a_6 R_1^2 R_2 + a_7 R_1 R_2^2 + a_8 R_1^2 R_2^2 + \ldots \tag{3}$$

where a_j, j = 0, 1, 2,... are the functions of the coefficients in equation (3) which are to be determined empirically using multiple regression analysis. The algorithm can be extended to the three-band method

$$P = e_o + e_1R_1 + e_2R_2 + e_3R_3 + e_4R_1R_2 + e_5R_1R_3 + e_6R_2R_3 + e_7R_1^2 + e_8R_2^2 + e_9R_3^2 \quad (4)$$

and the coefficients e_j are then empirically determined.

5.0 ANALYSIS OF TM DATA

A sub-scene for each date was extracted covering an image area of 1200 pixels by 1200 pixels for analysis. The images were rectified to the corresponding map (BA Chart no. 1366) to determine their geographical coordinates by using the second order polynomial coordinate transformation. The digital numbers (DN) for bands 1, 2, and 3 at the sample stations were extracted for analysis. These DNs were then converted to radiance unit and effective at satellite reflectance. The simple solar angle correction was performed to the data sets. The atmospheric correction based on the darkest pixel method was employed in the present study (Lathrop et al. 1991, Keiner and Yan (1998), Allee and Johnson 1999).

The relationship between the sea truth reference data (TSS) and the TM bands was first examined using the combined data from both image dates for multi-date analysis. Points situated in the shallow water areas and cloud pixels were removed. The TM signals were then regressed against the suspended solid concentrations using our developed algorithm. Other forms of water quality algorithms were also tested with these data sets and their accuracies were compared with that of the proposed algorithm. For each regression model the correlation coefficient, R, and the root-mean-square deviation, RMS, were noted.

Maps of these water quality parameters were then generated using the coefficients obtained from the regression analysis of our proposed algorithm. Land and cloud areas were masked out using the threshold values of band 4 and thermal band data. The water quality images were geometrically corrected through resampling process using the nearest neighbor method. Image smoothing was performed to each map using the median filter to remove random noise while preserving high frequency features (edges). The generated maps were colour-coded for visual interpretation.

6.0 RESULTS AND DISCUSSIONS

Figure 1 shows the plot of the relationship between TM signals versus TSS concentration. As the concentration increases, the response from each TM band also increases. Other investigators using remote sensing data in the visible channels for suspended sediment studies showed similar characteristics (Schiebe et al. 1992, Choubey and Subramaniam 1992). The trend suggests that the non-linear relation is preferred by the data set.

The single band method was found to be less accurate. The calibration results showed that when a single independent variable was used the polynomial form gave better accuracy than the simple linear model. The accuracy was observed to improve when higher order series were used. Generally the accuracy increased when more spectral bands and higher order series were included in the regression analysis. The proposed model used these criteria and therefore produced superior results using different sets of data transformations. Table 1 shows the comparative performance of the algorithms.

For this multi-date analysis, the use of combined raw data did not produce satisfactory results. Solar angle corrected radiance and exoatmospheric reflectance provided some improvement to

the results. Figure 2 shows the regression results using the proposed algorithm for TSS using the solar angle corrected radiance data. The results suggest that the atmospheric conditions for the two scenes were nearly the same. Atmospherically corrected data did not appear to improve the accuracy. The most probable cause of the error may be the incorrect choice of the clear deep water radiance for each TM band from the two acquired scenes.

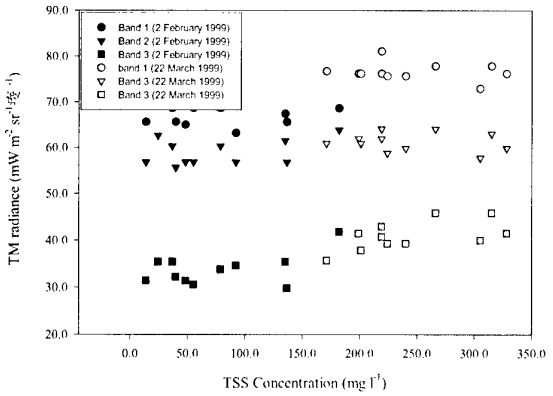


Figure 1 TM radiance versus TSS concentration.

Table 1 Regression results using different forms of algorithms for TSS and chlorophyll

Algorithm	R	RMS ($mg\ l^{-1}$)
$P=a_0 + a_1B_1 + a_2B_1^2 + a_3B_1^3$	0.80	54.91
$P=a_0 + a_1B_3 + a_2B_3^2 + a_3B_3^3$	0.85	48.94
$P=a_0 + a_1\ln B_1 + a_2\ln B_1^2 + a_3\ln B_1^3$	0.75	61.09
$P=a_0 + a_1\ln B_3 + a_2\ln B_3^2 + a_3\ln B33$	0.84	49.25
$P=a_0 + a_1(B_1/B_2) + a_2(B_1/B_2)^2 + a_3(B_1/B_2)^3$	0.78	57.05
$P=a_0 + a_1(B_2/B_3) + a_2(B_2/B_3)^2 + a_3(B_2/B_3)^3$	0.90	41.09
$P=a_0 + a_1\ln(B_1/B_2) + a_2\ln(B_1/B_2)^2 + a_3\ln(B_1/B_2)^3$	0.83	53.71
$P=a_0 + a_1\ln(B_2/B_3) + a_2\ln(B_2/B_3)^2 + a_3\ln(B_2/B_3)^3$	0.90	41.77
$P = a_0 + a_1B_1 + a_2B_2 + a_3B_1B_2 + a_4B_1^2 + a_5B_2^2 + a_6B_1^2B_2 + a_7B_1B_2^2 + a_8B_1^2B_2^2$	0.89	44.09
$P = a_0 + a_1B_1 + a_2B_2 + a_3B_3 + a_4B_1B_2 + a_5B_1B_3 + a_6B_2B_3 + a_7B_1^2 + a_8B_2^2 + a_9B_3^2$ (proposed)	0.95	28.17

The sediment concentration patterns are consistent with the local distribution pattern (Figure 3). Higher concentration areas are distributed near the river mouths and the shallow southern region of the channel. The plumes in the river mouths were created by river discharges. In the shallow water, the turbidity might be caused by bottom resuspension due to waves and wind actions. The concentration seems to be relatively lower in the deeper part of the sea. Based on the sea truth data as well as earlier reports (Din 1995), we are quite confident of the distribution shown. However, we are unable to establish the validity of the apparent higher concentration on the west coast of Penang Island because of the absence of sea truth data. Further sea truthing for the area will be done to confirm the values. The March TSS pattern was dominated by high concentration.

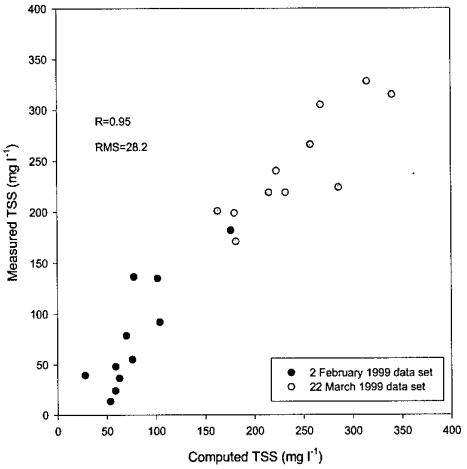


Figure 2 Regression results for TSS



(a) (b)

Figure 3 Distribution of TSS on (a) 2 February 1999 and (b) 22 March 1999 (colour code: blue 0-50, green 55-100, yellow 100-150,orange 150-200, red >200 mg l^{-1})

7.0 CONCLUSION

With the present constraints of having only two scenes, the proposed model was found to provide a useful multi-date TM water quality calibration model for the Penang Strait. The accuracy of the sea truth data played a very important role in determining the reliability of the calibrated algorithm and the quality of the generated water quality maps. The feasibility of applying the present techniques for operational use has to be further validated. Therefore more data will be required for this verification analysis.

Acknowledgements

This project was carried out using the Malaysian Government IRPA grant no.08-02-05-6011. We would like to thank the technical staff and research officer who participated in this project. Thanks are extended to MACRES and USM for support and encouragement

References

Allee, R. J. and Johnson, J. E., 1999. Use of satellite imagery to estimate surface chlorophyll-a and Secchi disc depth of Bull Shoals, Arkansas, USA, International Journal of Remote Sensing, 20, 1057-1072.

Baban, S. M., 1993. Detecting water quality parameters in the Norfolk Broads, U. K., using Landsat imagery. International Journal of Remote Sensing, 14: 1247-1267.

Choubey, V. K. and Subramaniam, V., 1992. Estimation of suspended solids using Indian Remote Sensing Satellite-1A data: a case study from Central India. International Journal of Remote Sensing, 13: 1473-1486

Dekker, A. G. and Peters, S. W. M., 1993. The use of Thematic Mapper for the analysis of eutrophic lakes: a case study in the Netherlands. International Journal of Remote Sensing, 14: 799-821.

Din, Z. B., 1995. Environmental impact assessment study of the proposed 275kV overhead cable crossing: Juru to Bayan Lepas. Final consultancy report submitted to the Tenaga National Berhad.

Ekstrand, S., 1992. Landsat TM based quantification of chlorophyll-a during algae blooms in coastal waters. International Journal of Remote Sensing, 13, 10, 1913-1926.

Forster, B. C. Xingwei, I. S., and Baide, X., 1993. Remote sensing of water quality parameters using landsat TM. International Journal of Remote Sensing, 14: 2759-2771.

Gallegos, C. L. and Correl, D. L., 1990. Modelling spectral diffuse attenuation,absorption and scattering coefficients in a turbid estuary. Limnology and Oceanography, 35, 1486-1502.

Gallie, E. A. and Murtha, P. A., 1992. Specific absorption and backscattering spectra for suspended minerals and chlorophyll-a in Chilko Lake, British Columbia. Remote Sensing of Environment, 39, 103-118.

Keiner, L. and Yan, X-H., 1998. A neural network model for estimating sea surface chlorophyll and sediments form Themitic Mapper imagery. Remote Sensing of Environment, 66: 153-165.

Kirk, J. T. O., 1984. Dependence of relationship between inherent and apparent optical properties of water on solar altitude. Limnology and Oceanography, 29, 350-356.

Lathrop, R. G., Lilliesand, T. T., and Yandel, B. S. 1991. Testing the utility of simple multi-date Thematic Mapper calibration algorithms for monitoring turbid inland waters. International Journal of Remote Sensing, 12: 2405-2063.

Ritchie, C. J., Cooper, C. M., and Schiebe, F. R., 1990. The relationship of MSS and TM digital data with suspended sediment, chlorophyll and temperature in Moon Lake, Mississipi. Remote Sensing of environment, 33, 137-148.

Schiebe, F. R., Harrington, J. A., and Ritchie, J. C., 1992. Remote sensing of suspended sediments: the Lake Chikot, Arkansas project. International Journal of Remote Sensing, 13: 1487-1509

Strickland, J. D. H. and Parsons, T. R., 1972. A practical handbook of seawater analysis.

FLOOD HAZARD MAP AND LAND DEVELOPMENT PRIORITY MAP DEVELOPED USING NOAA AVHRR AND GIS DATA

Dr. Md. Monirul Islam
Research Fellow, Tropical Marine Science Institute
National University of Singapore
14 Kent Ridge Road, Singapore 119223
Tel: 65 874 4649, Fax: 65 872 4067
E-mail: tmsmmi@nus.edu.sg
Singapore

Dr. Kimiteru Sado
Professor, Kitami Institute of Technology
165 Koen-cho, Kitami 090-8507
Tel. 81 157 269492, Fax. 81 157 239408
E-mail: sado@hp712.civil.kitami-it.ac.jp
Japan

KEY WORDS: NOAA AVHRR data, Flood-affected frequency, Population density, Flood hazard map, Land development priority map

ABSTRACT: In this paper flood hazard map and land development priority map for Bangladesh were developed using the flood events of 1988, 1995 and 1998 data with the digital data of physiographic divisions, geologic divisions, land cover classification and population density those were used as Geographical Information System (GIS) data. The techniques to construct a map for land development on the priority basis against the flood damages were described. Flood-affected frequency and flood depth were considered as hydraulic factors, and special attention were paid on population density for the land development priority map. Flood hazard assessment was undertaken using National Oceanographic and Atmospheric Administration (NOAA) Advanced Very High Resolution Radiometer (AVHRR) with GIS. Flood-affected frequency and flood depth were estimated using NOAA AVHRR images. Flood hazard ranks were categorized using the flood affect on land cover classifications, physiographic and geologic divisions.

1. INTRODUCTION

There have been many destructive floods in Bangladesh including very severe floods of 1987, 1988 and 1998. The 1988 flood set new record for flooded area while 1998 flood set new record for its long duration. In 1988, Bangladesh experienced one of the worst floods in living memory, and then the study team comprised a core group of international consultants provided by UNDP, the Asian Development Bank, the European Economic Community and the world bank (World Bank 1989) and local experts who investigated the flood damages and its remedy. Bangladesh lies in the downstream area of the three river basins of the Ganges, Brahmaputra and Meghna. The three mighty rivers the Ganges, Brahmaputra and Meghna, enter Bangladesh from India through northwest, north and northeast of the country, respectively. High magnitude of floods strike on a regular basis in these three river basins in Bangladesh, India and its peninsular (Bhattacharyya 1997; Islam & Sado 2000a;b; Kale & Pramod 1997; Kundzewich & Takeuchi 1999; Muramoto 1988) because of the passage of depression and cyclone storm during the monsoon season. Bangladesh has limited control over the Ganges, Brahmaputra and Meghna rivers, moreover, for adequate and timely flood forecasting, Bangladesh sometimes

depends on information from surrounding countries. The frequently occurring floods are very costly in terms of human hardship and economic loss. Therefore, the ability to estimate damages associated with the flood events are very important and necessary to evaluate future alternate flood control policies. In a round-table discussion following 1998 flood event, experts from different fields recommended the need for flood hazard maps for proper planning and management for future flood disaster (Nishat 1998). In our previous studies (Islam and Sado 2000 a; b) we have developed flood hazard maps only using 1988 event. Therefore, in this study we focus on the historical events of 1988 and 1998 severe floods and 1995 medium flood. NOAA AVHRR data are found very useful for monitoring large surface phenomena, such as floods, in the fields through out the world on local, regional and international scales while ERS, MOS, Landsat and SPOT has been used to observe regional or local floods. Furthermore, the routine measurement and the estimation of hydrological parameters including flood-related parameters could be useful in the areas ranging from global scale to local or regional scales, depending on the spatial resolution and recurrent period (Schultz 1994). The time of acquisition of satellite data does not generally coincide with the time of flood peak or maximum inundated area. The data and time of data collection and recurrent periods of satellite imaging are important for investigation of satellite data (Oberstadler et al. 1997). Therefore, in this paper result of analysis of NOAA AVHRR data, from the series of NOAA satellite 10 and 12, are used for the flood hazard assessment in Bangladesh and the construction of flood hazard map and land development priority map.

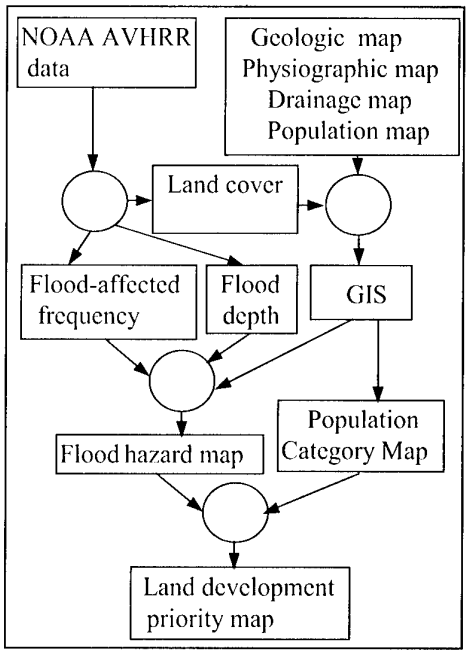


Figure 1. Schematic concept of model

2. FLOOD HAZARD ASSESSMENT

Study proved that the combination by land cover, physiography and geology is the best combination of GIS data for each of the flood hazard map performed for flood depth and flood-affected frequency (Islam & Sado 2000b). Therefore, flood hazard assessments were undertaken using land cover, physiographic and geologic features and drainage network data. Land cover classification was carried out using dry season's NOAA AVHRR image of 20 January 1988. Land cover data, drainage network data, physiographic and geologic features were used as GIS data. Flood depth and flood-affected frequency were used as hydraulic parameters of the floods. A model was considered for the assessment of the flood hazard, which is shown in Figure 1.

2.1 Flood-affected Frequency

Flood-affected frequency within the event of 1988, 1995 and 1998 were estimated by using the images of 18 September 1988, 31 October 1995 and 18 September 1998. The terminology of flood-affected frequency is determined for each pixel as the ratio of the number of NOAA images within the three flood events of 1988, 1995 and 1998, showing inundation to the total number of cloud free NOAA images available near to the peak flood time. The concept of the different degree of flood-affected frequency is shown in Figure 2. Inundated area that did not appear in any of the above mentioned three images (i.e. 8 in Fig.2) were considered to be a non-

hazard area and that which appeared in a single image (5, 6 or 7 in Fig. 2) was considered to be a low hazard area. The common inundated area that appeared in two images (2 or 3 or 4 in Fig. 2) and that which appeared in all three images (1 in Fig. 2) were considered to be medium and high hazard areas, respectively. Flood-affected frequency within the three events was categorized as non-hazard, low, medium and high according to their hazardous hit number of the floods.

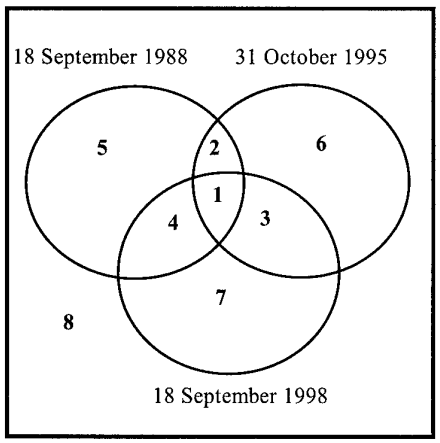


Figure 2: Schematic concept of flood-affected frequency for the flood events of 1988, 1995 and 1998

2.2 Flood Depth

Flood depths were classified as shallow, medium and deep by using the maximum likelihood method of supervised classification for the same images. Training areas for shallow, medium and deep flood were selected on NOAA AVHRR images of 18 September 1988, 31 October 1995 and 18 September 1998 according to the difference in colors and gray scales for different categories of depth. To measure the flood depth using remote sensing imagery is very difficult. The differences among the depths were understood after superimposing the NOAA images onto the digital elevation image of Bangladesh. Furthermore, the ranking for flood depth was categorized as no-flooding, shallow, medium and deep flood. Therefore, three flood depth maps were constructed for three flood events of 1988, 1995 and 1998 by using above-mentioned images, respectively.

2.3 Hazard Rank Assessment Through GIS for Flood Hazard Map

Flood hazard ranks were estimated based on a weighted score for land cover, physiography and geological data for each pixel of the land area of Bangladesh. A weighted score was estimated by

$$Weightedscore = 0.0 \times A + 1.0 \times B + 3.0 \times C + 5.0 \times D \quad (1)$$

where A, B, C and D represent the occupied area percentage by non-hazardous area, low, medium and high flood-affected frequency, respectively, for each category of land cover categories (9 categories), physiographic divisions (31 divisions) and geologic divisions (28 divisions) (Islam & Sado 2000b), when flood-affected frequency was considered to be a hydraulic factor. Similarly, A, B, C and D represent the occupied area percentage by non-flooded area, shallow, medium and deep flood, respectively, for each category of above mentioned GIS component, when flood depth was considered to be a hydraulic factor. The coefficients of 0.0, 1.0, 3.0 and 5.0 for A-D in equation (1) were used to describe the weight for flood damage. The acquired area percentage by non-hazardous, low, medium and high damaged areas only for the land cover categories are shown in Table 1 with calculated weighted score. Points for the categories of land cover were estimated on the basis of linear interpolation between 0 and 100, where 0 corresponds to the lowest (0) and 100 to the highest (230.21 in Table 1) weighted score. To quantify the flood hazard, the three rankings for flood damage (HR 1~3) were obtained from the allocated point. Hazard ranks were fixed according to the corresponding value of the points: points 0-33 corresponded to hazard rank 1, 33-66 rank 2 and 66-100 rank 3, as shown in Table 1. Similarly hazard ranks were determined using the same

algorithm for geologic divisions and physiographic divisions, using flood-affected frequency. Different four categories of flood depth were estimated independently for the images of 18 September 1988, 31 October 1995 and 18 September 1998. Hazard ranks were determined for each event using the above-mentioned algorithm for physiographic divisions, geologic divisions and land cover categories, using flood depth.

Table 1: Flood hazard ranks for land cover categories by using flood-affected frequency (Cat.: land cover category)

Cat.	A	B	C	D	Score	Points	HR
1	36.93	28.49	22.01	12.57	157.38	68.36	3
2	29.88	19.22	21.73	29.17	230.21	100.00	3
3	28.29	23.08	26.17	22.46	213.89	92.91	3
4	55.84	23.14	12.70	8.32	102.82	44.66	2
5	47.54	26.05	14.58	11.83	128.93	56.01	2
6	60.93	22.54	13.46	3.07	78.29	34.01	2
7	77.11	12.59	5.55	4.75	52.99	23.02	1
8	42.96	33.66	14.03	9.35	122.52	53.22	2
9	16.98	30.67	34.84	17.51	222.76	96.76	3

2.4 Development of Flood Hazard Map

Flood hazard maps were constructed by considering the interactive effect of flood damages onto the land cover categories, physiographic and geological divisions. The concept of the ranking matrix in three dimensional multiplication modes is shown in Figure 3.

Flood hazard map using flood-affected frequency as hydraulic factor: Flood-affected frequency consisted of four classes: non-hazardous, low, medium and high damaged areas. Hazard ranks were considered from 1 to 27 after combining the hazard ranks of land cover categories (HR 1-3), physiographic divisions (HR 1-3) and geologic divisions (HR 1-3) simultaneously, using the ranking matrix of three dimensional multiplication modes (Fig. 3).

Flood hazard map using flood depth as hydraulic factor: Flood depths consisted of four classes: non-flooded area, shallow, medium and deep flood. Initially three different hazard maps were developed for three above mentioned images by considering the interactive effect of land cover categories, physiographic divisions and geologic divisions onto the flood depth, using the ranking matrix (Fig. 3). Each hazard map consisted of hazard ranks from 1 to 27. Finally, hazard map of 1988 event for the flood depth was selected as a hazard map among the three hazard maps, because this hazard map shows the deviation in the marginal distribution toward higher ranks compared with other two hazard maps.

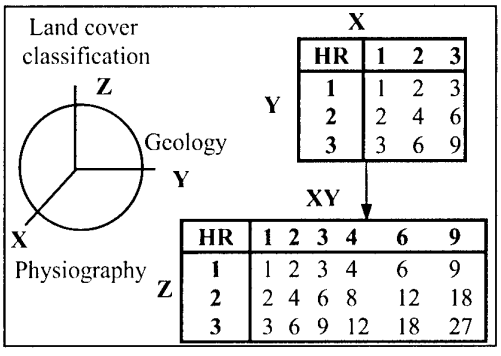


Figure 3: Concept of the ranking matrix

Interactive effect of flood-affected frequency and flood depth for the development of flood hazard map: Two flood hazard maps were developed for flood-affected frequency and flood depth, respectively, considering the flood hazard rank from 1 to 27. In these two hazard maps, 56.31% pixels exhibited the same hazard ranks and 43.69% were different, because flood-affected frequency and flood depth were considered independently. Comparing between the hazard maps of flood-affected frequency and flood depth, higher rank for a pixel was assigned for that pixel for the new developed hazard map. Watercourses were not included to the developed flood hazard map. Therefore, the drainage map was overlaid onto the hazard map, and final hazard map with watercourses is shown in Figure 4.

3. DEVELOPMENT PRIORITY MAP FOR FLOOD COUNTERMEASURE

The major cities of Bangladesh are extremely highly populated area. The planning of river works for flood countermeasure should be undertaken by considering the economical effects of the infrastructure and the importance of the concerned area. Therefore, using flood hazard map and population density map land development priority map was developed. Digital population data was prepared using population map of Bangladesh. Urban and industrial areas show high dense of population, while agricultural low land and agricultural flat-plain show low dense of population. According to the population density, the population digital data was categorized into five zones. The area which shows the population density 1 to 500 per square kilometer was considered as zone 1, similarly, the areas which show the population density 501 to 1000, 1001 to 2500, 2501 to 4000 and over 4000 were considered as zone 2, zone 3, zone 4 and zone 5, respectively. Similarly, hazard ranks of flood hazard map were categorized into five groups. Hazard rank 1, 2 and 3 is grouped as 1, then similarly, 4 and 6 is 2, 8 and 9 is 3, 12 and 18 is 4, and 27 is 5. This new hazard grouped map was superimposed with population digital categories map and finally the land development priority map was developed using the ranking matrix of two dimensional multiplication modes. Figure 5 shows the land development priority map for flood countermeasure based on pixels. The ranks of land development map are ranging from 1 to 25. Higher ranks indicate the higher priority has to be given for the development for flood countermeasure. This development priority map shows the rank of priority on the basis of pixel. Comparing between the hazard map (Fig. 4) and the development priority map (Fig. 5), it is understood that some high hazardous areas do not show the high rank for the development. The northeast part of the Meghna river and southwest lower parts of Bangladesh show high hazard ranks whereas development map shows the low ranks for the development of the same areas. Some part of Dhaka and Narayanganj districts show the higher development rank due to the high dense population. Dhaka is the capital city of Bangladesh. Study showed that Dhaka city was highly affected during the 1988 flood (Sado & Islam 1997).

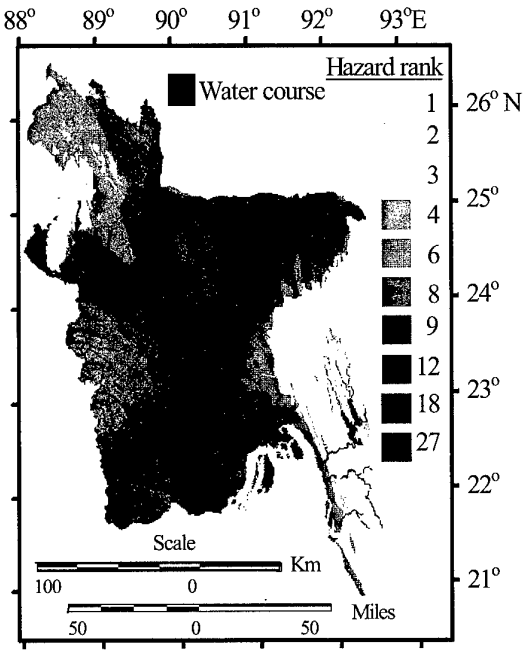
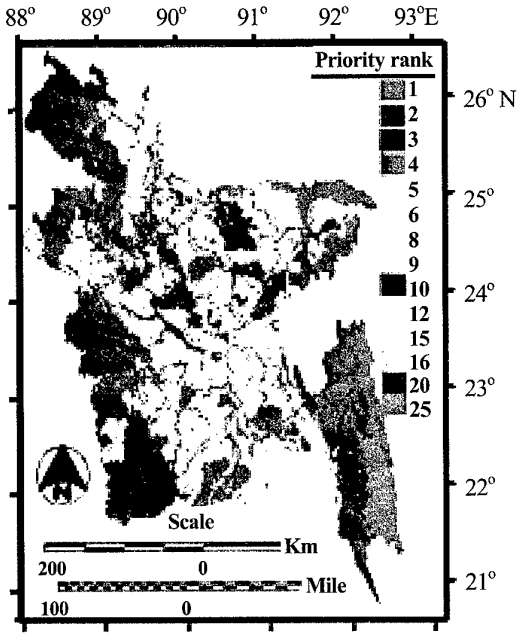


Figure 4: Flood hazard map



(Monochrome fig. produced from original color fig.)

Figure 5: Land development priority map

4. CONCLUSIONS

Flood hazard assessment were undertaken considering the interactive effect of flood-effected frequency and flood water depth, those were estimated from NOAA AVHRR images of 18 September 1988, 31 October 1995 and 18 September 1998, and finally a new flood hazard map for Bangladesh was developed. Flood hazard map represents the magnitude of flood damage for each pixel. Land development priority map for flood countermeasure were developed based on each pixel. Although flood hazard ranks for some urban areas are comparatively less than the hazard for some rural areas, development should be undertaken for those urban areas (higher dense populated area) on first priority basis. The results described in this study should provide helpful information for flood control planning and the construction and development of flood countermeasures. Flood hazard map and land development priority map also help the responsible authorities to better comprehend the inundation characteristics of the flood plains, the protection of which is their responsibility. Relief and aid operation can be performed by using flood hazard map for further future events.

REFERENCES

Bhattacharyya, N. N., 1997. Floods of the Brahmaputra river in India. Water International, 22(4), pp. 222-229.

Islam, M. M. & Sado, K., 2000a. Flood hazard assessment in Bangladesh using NOAA AVHRR data with geographical information system. Hydrol. Process. 14(3), pp. 605-620.

Islam, M. M. & Sado, K., 2000b. Development of a flood hazard maps of Bangladesh using NOAA-AVHRR images with GIS. Hydrological Science Journal, 45(3), pp. 337-356.

Kale, V. S. & Pramod, H., 1997. Flood hydrology and geomorphology of monsoon-dominated rivers: the Indian Peninsula. Water International, 22(4), pp. 259-265.

Kundzewich, Z. W. & Takeuchi, K., 1999. Flood protection and management: quo vadimus?. Hydrological Science Journal, 44(3), pp. 417-432.

Muramoto, Y., 1988. Investigation of the flood disaster caused by heavy rainfall in Bangladesh during the 1987 monsoon season. Report of Scientific Research for Natural Disaster, no. B-62-5, Ministry of Education, Tokyo, Japan.

Nishat, A., 1998. A discussion on flood management in Bangladesh. The 1998 Deluge-Developing Coping Capacities, Workshop on the 1998 flood, Nagorik Durjug Mokabela Uddogh, Dhaka, Bangladesh.

Oberstadler, R., Honsch, H. & Huth, D., 1997. Assessment of the mapping capabilities of ERS-1 SAR data for flood mapping: case study in Germany. Hydrol. Processes,11, pp. 1415-1426.

Sado, K. & Islam, M. M., 1997. Satellite remote sensing data analysis for flooded area and weather study: case study of Dhaka city, Bangladesh. J. Hydraul. Engng., JSCE, 41, pp. 945-950.

Schultz, G. A., (1994). Meso-scale modelling of runoff and water balance using remote sensing and other GIS data. Hydrol Sci. J. 39(2), pp. 121-141.

World Bank, 1989. Bangladesh Action Plan for Flood Control. 91, Asian Region, Country Department-1, World Bank, Washington DC, USA.

The 21st Asian Conference on Remote Sensing
December 4-8, 2000 Taipei, TAIWAN

USE OF LANDSAT IMAGES FOR THE IDENTIFICATION OF DAMAGE DUE TO THE 1999 KOCAELI, TURKEY EARTHQUAKE

Miguel Estrada, Fumio Yamazaki***
*Graduate Student, **Associate Professor
Institute of Industrial Science, The University of Tokyo
Bw304, 4-6-1 Komaba, Meguro-ku, Tokyo 153-8505
Tel: +81 (3) 5452-6388 Fax: +81 (3) 5452-6389
E-mail: miguel@rattle.iis.u-tokyo.ac.jp, yamazaki@iis.u-tokyo.ac.jp
JAPAN

Masashi Matsuoka
Chief Research Engineer, Earthquake Disaster Mitigation Research Center, RIKEN
2465-1 Mikiyama Miki, Hyogo 673-0433
Tel: +81 (794) 83-6632 Fax: +81 (794) 83-6695
E-mail: matsuoka@miki.riken.go.jp
JAPAN

KEY WORDS: The 1999 Kocaeli Earthquake, Building damage detection, subsidence, fire.

ABSTRACT: In this study, remote sensing satellite images are used to identify the affected areas due to the 1999 Kocaeli, Turkey Earthquake with a magnitude of 7.4. The aim of this study is to identify the hard-hit areas in different levels of damage, sunk areas into the sea and areas affected by fire. The analysis has been carried out in two different cities, Gölcük and Adapazari, where these types of damage were seen. The data that have been used are optical remote sensing images taken by Landsat/TM satellite on March 27 and August 18, 1999, before and after the earthquake, respectively. For the detection of burned and sunk areas a spectral comparison of the Landsat/TM is carried out. In order to detect the different levels of damages in the urban areas, a comparison of the ratio between different bands of the pre- and post-event images is conducted. In addition, principal components analysis is conducted for each one of the sets of images and later compared. In order to calibrate the results of these comparisons the product images are geographically corrected and mapped, afterwards they are compared with the ground truth data that are in a GIS system.

1. INTRODUCTION

The identification of damage due to large earthquakes is a vital issue to grasp the level and extension of the hard-hit areas. The evaluation can be conducted through a field reconnaissance survey. Even though, the field survey has a high accuracy it requires a lot of resources and time. In the event of large natural disasters, like a destructive earthquake, a fast assessment of the damaged areas is required to send off rescue teams and help. Also the awareness of the extension of damage can help to outline recovery plans. Recently remote sensing technology has become a tool in damage identification after the occurrence of natural disasters like floods, landslides or earthquakes (e.g. Matsuoka and Yamazaki, 1999). The identification of damage from a large area gives vital information that authorities can use to plan rescue procedures as well as to draw a general idea of the magnitude of the damage. The location of different types of damage like fire outbreak, ground settlement and building damage using optical remote sensing data is considered in this study.
In order to identify the different kinds of damage, the comparison of optical satellite images taken before and after the earthquake is conducted. In this study the area around Gölcük city in Turkey has been focused.

First, image-to-image registration was carried out to match the images. To detect the fire outbreak we compared the profiles along X-axis and Y-axis of the pre- and post-event images. For the detection of the sunken area the histograms of the infrared band are matched and then the result images are compared. For the detection of different levels of damage an analysis in the visible region is conducted as well as Principal Component Transformation (Yasuoka, 1990). Data for the 1999 Kocaeli Earthquake are: Date: August 17th, 1999. Time: 00:01:38.56 (UTC). Mw = 7.4. Epicenter: Lat. = 40.639N, Long. = 29.830E (Fig. 1). Hypocentral depth: 17 km. More than 200,000 buildings were lightly to heavily damaged. More than 17,000 people were killed and almost 44,000 were injured.



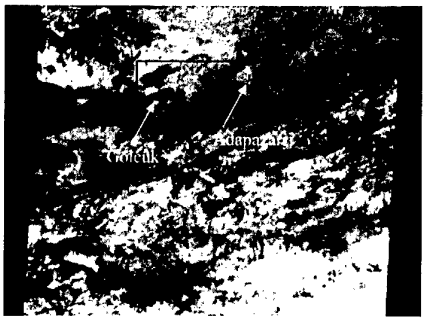
Figure 1. Map of Turkey and the epicenter of the earthquake.

2. LANDSAT/TM IMAGE

The data in this research are remote sensing images from Landsat/TM satellite taken over the affected area due to the earthquake. The images have been taken on 27 of March 1999, pre-event image, and on 18 of August 1999, for the post-event image. The composite color images of the pre-event and post-event (751) are shown in Figure 2(a) and 2(b), respectively. The images cover an area of 185 km by 154 km. Before making comparison, these two sets of images have to be registered; it means the pixels in both images must represent the same geographic location. To make an image-to-image registration one of them is chosen as a master to which the other, known as the slave, is to be registered. In this study the master image is the pre-event image and the slave image is the post-event image. The image registration has been conducted with the total area of the images and defining 250 ground control points deployed on the extension of the images. Rotation, scaling and translation method was used for warping the slave image and nearest-neighbor method was used for resampling.



(a) Pre-event image (99/03/27)

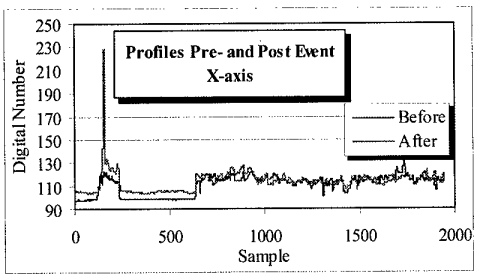


(b) Post-event image (99/08/18)

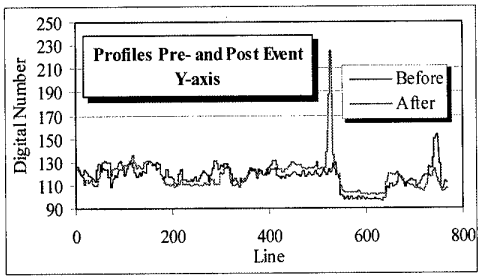
Figure 2. Composite color images (751). Raw images.

3. IDENTIFICATION OF DAMAGE CAUSED BY FIRE

To identify the areas affected by fire we compare the profiles of the pre- and post-event images. The profile represents the distribution of the digital number (DN) of certain band along a strip of the image. This strip can be taken over the X-axis or Y-axis. For this comparison the band 5 (mid infrared), band 6 (far infrared or thermal band) and band 7 (mid infrared) have been used. Figure 3 shows the profiles of the DN of band 6 along the X-axis and Y-axis.



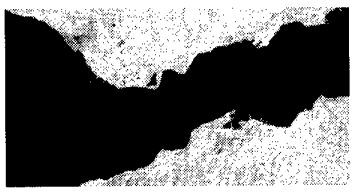
(a) Profile along X-axis.



(b) Profile along Y-axis.

Figure 3. Profiles of the pre- and post-event images of the band 6. Notice the peak values that represent the area around Tüpras refinery.

It can be observed (Figure 3) that there is a pattern in the profile before the earthquake as well in the after one. But in the region between sample 100 and sample 200, in the X-axis, and between the line 500 and 600, in the Y-axis, there are peak values, which represent the high temperature. Since the coordinates of this area are known, we can identify it in the image. This area corresponds to the Tüpras refinery, which suffered from a very large fire. Figure 4 shows the composite color image (752) as well as an aerial photo of the area around of the refinery.



(a) Pre-event



(b) Post-event



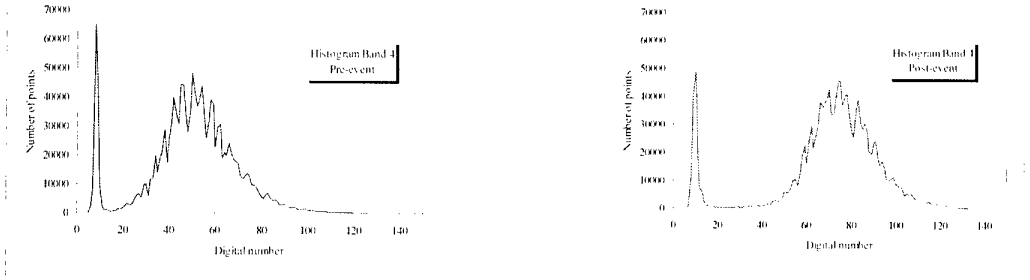
(c) Aerial photo

Figure 4. Color composite (752) images around Tüpras refinery.

4. IDENTIFICATION OF THE SUBSIDENCE

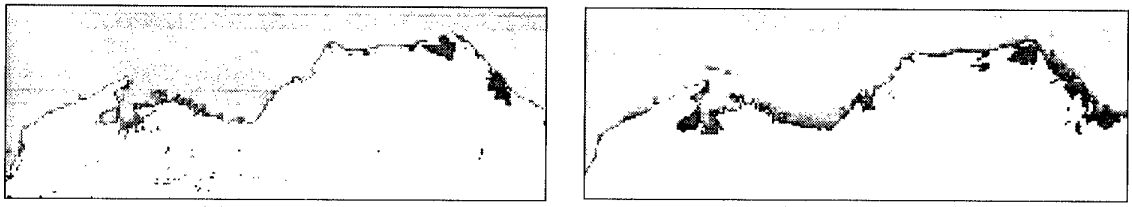
Remote sensing provides a straightforward means to map the extent of water bodies, to inventory an area occupied by open water, and to monitor changes in water bodies over time. Likewise, comparisons of shoreline positions before and after flooding, permits measurement of areas flooded, as well as determination of locations of flooded areas. Such information can be difficult to acquire by conventional means. Determination of the land-water body is usually easiest in the near-infrared region, where land, especially if vegetated, is bright and open water dark. In order to detect the sunken areas we have matched the histogram of the near-infrared band (band 4). By matching the histograms of the two images (pre- and post-event) we will obtain an apparent distribution of brightness as close as possible and will minimize the brightness value variations. Since the reflectance value of the water in the near infrared band is low, we match the histograms in the range 1 to 20 and obtain the images in Fig. 6. Comparing these two images, it can be seen that in the image of the post-event (Fig. 6 (b)) there are some areas that differ from those in the pre-event image. These differences represent the inundated area. Also it is possible to calculate the extension of the flooding, by counting the number of pixels that differ between these two images. In order to count the number of pixels that belong to water body we have used the 2-D scatter diagram. In this diagram we plot the distribution of reflectance of two bands, in this case band 4 vs. band 5. We define threshold values for the reflectance of the water, based on the values of training areas of water. Finally with the threshold values we make the selection in the 2-D scatter diagram. Finally we count the number

of pixels that fall into this 2-D range. The number of pixels that belong to water: Before: 8430 pixels, after: 9413 pixels, difference = 983 pixels. Total affected area (flooding) = 983 x 30 x 30 = 884,700 m^2, that correspond to red areas in the Figure 6 (b).



(a) Pre-event (b) Post-event

Figure 5. Histogram of the near infrared band



(a) Pre-event (b) Post-event

Figure 6. The coastline in Gölcük, after matching the histograms. The intense red in (b) shows the sunken areas.

5. IDENTIFICATION OF DIFFERENT LEVELS OF DAMAGE

5.1 Comparison in the Visible Range

As a first comparison for the detection and localization of damage we have conducted the comparison of the data in the visible range. For Landsat/TM satellite images bands 1, 2 and 3 cover the visible range. First we calculate de average of these first three bands by the formula:

$$BR_{avg}(i,j) = \sum_{k=1}^{3} BB_k(i,j) \Big/ 3 \tag{1}$$

where: $BB_k(i, j)$ is the digital number of the pixel (i, j) of the band k of the pre-event image. $BR_{avg}(i, j)$ is the averaged value of the pixel (i, j) of the pre-event image. This same formula is also applied to the post-event image. Then, we calculate the ratio between these two averaged images by Equation 2, where AR represents the averaged image after the event and R the ratio. Figure 7 shows the image obtained from this equation.

$$R(i,j) = AR_{avg}(i,j) \big/ BR_{avg}(i,j) \tag{2}$$

In the center of this image, the damaged area appears brighter and also the sunken area can be distinguished (in dark tones). This image is then compared with the ground truth data (AIJ, 1999) shown in Figure 8. As a result of this comparison we obtain the distribution of DN for the different levels of damage. Figure 9 shows 4 different sections: the sunken area (blue), low level damaged (green and turquoise) the section for level of damage 12.5% - 25% (yellow) and the section for high level of damage (read and orange).

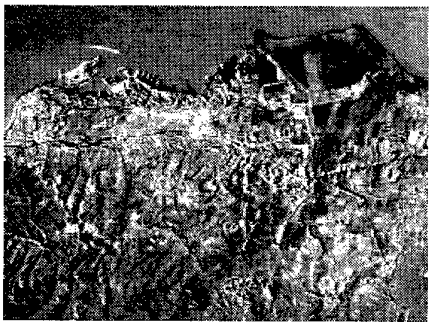


Figure 7. Ratio (after/before) of the average of the first three visible bands.

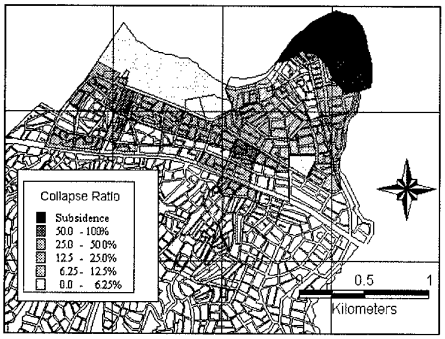


Figure 8. Damage distribution in Gölcük city by AIJ (1999).

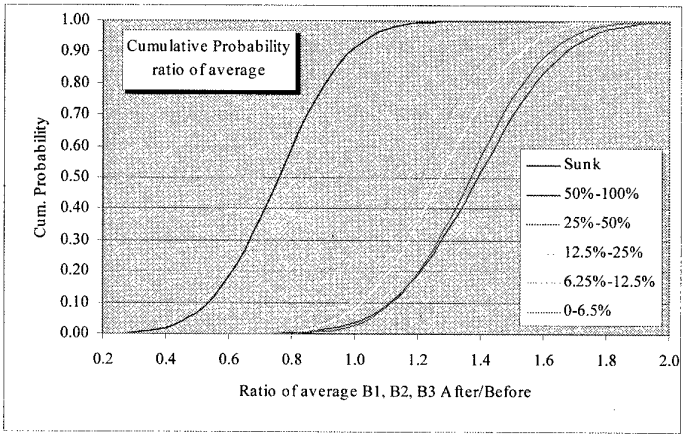


Figure 9. Cumulative probability of the ratio (after/before) of the averaged images.

5.2 Principal Component Analysis

The Principal Component Transformation is designed to reduce redundancy in multispectral data. The purpose is to compress all of the information contained in an original n-band data set into fewer n new bands or components. Let $L=\{L_1(DN_k), L_2(DN_k)\}$ be a combined set of $2n$ bands images composed of two different dates images and C_L be the variance-covariance matrix of L. Each principal component X_j is expressed as:

$$X_j = \sum_{k=1}^{n} \alpha_k L_1(DN_k) + \sum_{k=1}^{n} \beta_k L_2(DN_k) \tag{3}$$

where $\{\alpha_k, \beta_k\}$ is the normalized eigenvectors of the variance-covariance matrix C_L of L. Difference of the surface reflectance between two dates is evaluated by the following principal component:

$$D = \sum_{k=1}^{n} \alpha_k L_1(DN_k) + \sum_{k=1}^{n} \beta_k L_2(DN_k), (\alpha_k > 0, \beta_k < 0 \text{ for all } k) \tag{4}$$

In this case, by joining the 6 non-thermal bands of the pre- and post-event images we obtain the $2n$ set. In this study the 3rd principal component satisfies the condition given by Formula 4. Where the first 6 coefficients are positives and the lasts 6 are negative. It means, this principal component conveys the changes between the pre- and post-event images for this multitemporal set of images. The digital number of the pixels for the 3rd principal component image also follows the same distribution as shown in Figure 9. Based in the distribution of the digital

number and using the maximum likelihood classifier we obtain the spatial distribution of the damage for Gölcük as is shown in Figure 10. This figure shows the distribution of the different levels of damage from Level 1 (no damage) up to Level 5 (high level of damage) and the sunken area. Same procedures have been conducted for Adapazari city, however, in this case the classification has been performed in only 3 levels of damage (Figure 11): no damage (blue), extensive (green) and catastrophic (red).

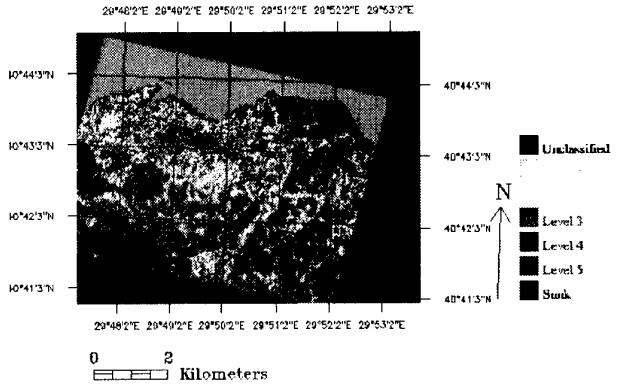


Figure 10. Spatial distribution of damage using the maximum likelihood classifier for Gölcük.

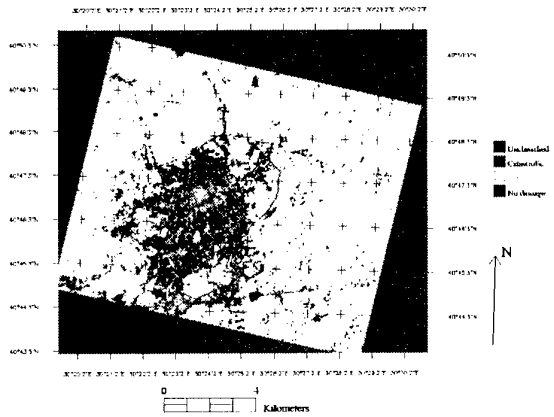


Figure 11. Spatial distribution of damage in Adapazari.

7. CONCLUSIONS

Damage detection due to The 1999 Kocaeli, Turkey earthquake was carried out using Landsat/TM images. Fire and sunken areas were successfully identified using the thermal band and the near infrared band, respectively. Different levels of building damage were recognized properly to some extent. It can be seen that the value of the digital number for the affected area increases with the increasing of damage level. This is due to the spread of debris after the earthquake. The debris has a higher reflectance in the visible region than the buildings in good condition. After using Principal Component Analysis we have found that in case of Landsat/TM images, principal component 3 conveys the changes in the multitemporal 12 non-thermal bands image.

REFERENCES

AIJ Reconnaissance Team, Kabeyasawa, T. et. al., 1999. Progress Report on Damage Investigation after Kocaeli Earthquake by Architectural Institute of Japan. Proc. ITU-IAHS International Conference on the Kocaeli Earthquake 17 August 1999.

Campbell, J. (1996). Introduction to Remote Sensing Second Edition. The Guilford Press. USA.

Matsuoka, M. and Yamazaki, F., 1998. Characteristics of Satellite Images of Damaged Areas due to the 1995 Kobe Earthquake. 2nd Conference on the Applications of Remote Sensing and GIS for Disaster Management.

Richards, J. and Jia, X., 1999. Remote Sensing Digital Image Analysis An Introduction Third Edition. Springer. Germany.

Mather, P., 1999. Computer Processing of Remotely-Sensed Images An Introduction Second Edition. John Wiley & Sons. England.

Yasuoka, Y., 1990. Digital Image Processing for Landcover Change Detection in Environmental Monitoring. National Institute for Environmental Studies. Japan.

NATURAL-SCIENTIFIC APPROACH FOR NATURAL CONSERVATION USING GIS

*Byungyang CHOI・**Takekazu KOYANAGI・***Yuji KUWAHARA・****Kunio SHIMA

*Graduate Student, Graduate School of Sciences and Engineering, Ibaraki University.
4-12-1Nakanarusawa-cho, Hitachi-city Ibaraki-ken, 316-8511 JAPAN
TEL: (81)-294-38-5165 FAX: (81)-294-38-5249
E-mail: ibaraki@hcs.ibaraki.ac.jp
**Professor, Department of Urban and Civil Engineering, Ibaraki University.
4-12-1Nakanarusawa-cho, Hitachi-city Ibaraki-ken, 316-8511 JAPAN
TEL: (81)-294-38-5165,FAX:(81)-294-38-5249
E-mail: koyanagi@civil.ibaraki.ac.jp
***Lecturer, Department of Urban and Civil Engineering, Ibaraki University.
4-12-1Nakanarusawa-cho, Hitachi-city Ibaraki-ken, 316-8511 JAPAN
TEL: (81)-294-38-5261,FAX:(81)-294-38-5249
E-mail: kuwahara@hcs.ibaraki.ac.jp
****Assistant, Department of Urban and Civil Engineering, Ibaraki University.
4-12-1Nakanarusawa-cho, Hitachi-city Ibaraki-ken, 316-8511 JAPAN
TEL: (81)-294-38-5175,FAX:(81)-294-38-5249
E-mail: shima@hcs.ibaraki.ac.jp

KEY WORDS: Natural-Scientific Approach, Vegetation, Grade of Vegetation Naturalness, Conservation

ABSTRACT: This study uses the vegetation in order to approach a diversity of the natural resource in the natural park of the Hakusan national park super forest road vicinity region. The natural scientific analysis was carried out using natural parameters such as soil, geology, and geography. It pick up the natural environment in which the protected grade of vegetation naturalness the utilize it. As a result of the overlay analysis, the study area came in grade 9 of the vegetation naturalness rank. It is because where Saseto-kurilensae-Fagion crenatae Fagion crenatae primary forest grows. About 40% of soil was Brown Forest Soils it was observed that the natural condition of the place with the high naturalness, protected the nature of the place which the slope was well over 30 degree. There were many Regosoils in the soil located in the landslide area, and there were some more over 30 degree on the slope. It was understood that there was landslide in relation to soil on slopes by the analysis. The vegetation of which the naturalness was higher than the azimuth was distributed in many for the west direction. This study was able to guess what it should consider in place, when it can grasp the difference between present and past by using latest data and data 10 years ago, in respect of the vegetation, and then it will attempt to protect conserve the natural environment at present. By this it was able to predict the flow of the natural environment, as it showed the possibility of spatially grasping role and importance of the natural vegetation.

1. INTRODUCTION

It was adopted convention on biological diversity of Earth Summit in 1992, and in Japan, it is promoting the

policy for the protection of biological diversity as an important problem. In addition, it carries out the examination on utilization and sustainable development, while it attempts natural protection and conservation for national land planning and regional development in Japan. The development or the utilization of the natural environment must be considered for protection and conservation of the biology, because it effects largely the survival of the biology. And, it is necessary to sufficiently grasp present state of natural environment in order to realize protection of biological diversity for the protection and conservation of the natural environment.

In the existing study, Harashina(1998) analyzed a habitat environment of the terrestrial mammalian of which the continuity of the forest is important, and Choi(1992) described the status of development and utilization for natural park.

In this study, it mainly examined the analysis of natural environment by the natural-scientific approach such as soil and geology, geography, and vegetation which is important natural component in order to protect original natural environment of natural park.

The study area(about 13000ha) is Hakusan super forest road vicinity located in Hakusan National Park, Japan(Fig. 1). It analyzed the natural environment using soil map, geological map, topographical map, existing vegetation map, and aerial photography in order to grasp the natural scientific data of the natural environment. The analysis of the natural environment utilized Geographic Information System.

2. OUTLINE OF THE STUDY AREA

The Hakusan National Park of 2702m altitude, which was designated in the 1955 as a Quasi-national Park, when the area became 47700ha it becomes the 20th national park in 1962. Afterwards, it set the park plan (protection plan and utilization plan), and about 38% of the park area became a special protection area.

The Hakusan super forest road of the study area belong to the district in 1967, and made the construction plan along Jadani of the Ojo river upstream, developed by Forest Development Corp. as a super forest road. It constructed this forest road from the Oguchi village of Ishikawa Prefecture to the Sirakawa village of Gifu Prefecture for the purpose of the development of Underdevelopment Forest Resources.

The study area is the mountainous zone of in the center of Hakusan. The climate the Sea of Japan influenced by the Siberia climate, and annual rainfall is pluvial snowy region where it reaches 2000-3000mm(Fig. 2). Hakusan has well protected well alpine zone and subalpine zone. It is the region of the naturalness primary forest of the rich Fagus crenate growth is

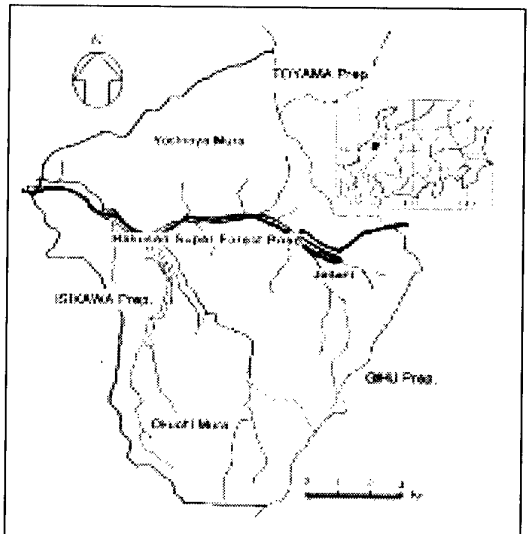


fig . 1 Location of Study Area


fig . 2 Topographical Map (3 D)

high. Though the plant community in the study area receives various effects according to temperature, snowfall and land condition, etc., the effect by the snow seems to be the biggest even in the interior.

This greatly divides the plant community in the study area, into forest and grassland. There are mainly Fagus crenate forest and Thuja standishii-Pius parviflora forest of the sub-alpine in the forest, altherbosa and artificial grassland are located in the grassland.

The animal of the study area is distributed as a center in respect to Hakusan region and Tedori river region. It protects the good natural environment for the inhabitant of the animal. There are many mountains and hilly area in which development has not been done to most of this region. Especially, Japanese macaque, Capricornis Crispus and Japanese black bear of large Mammalia, etc. that mainly inhabit the study area.

3. PURPOSE AND METHOD OF THE STUDY

Purpose of the Study: The vegetation is the important element, which constitutes the ecosystem, due to its disaster-preventing important ability and its scientific research importance to the location. And, it shows greatly difference on vegetation growth and recovery according to regionality and land condition.

The study area is necessary to protect the vegetation from conservation of the land resource because it is a region with severe environmental condition climatically and topographically, though primary forest of the beech with the high naturalness is an abounding region.

This purpose of this study shows natural environment spatially and analyzes the relevance from the transition of geography condition and vegetation to analyze present state of the vegetation. This study has two approach for analysis. One is the use of geography information data made from the aerial photograph in order to show the geography characteristics in the study area. The other is to spatially analyze and examine the vegetation transition using the existing vegetation maps of 1975 and 1985, with vegetation distribution and the diversity of vegetation. In a series of examination, it clarifies the relationship of primary information on the relevance between geography characteristics and vegetation distribution such as a slope and azimuth. On the basis of these it analyzed the spatial information to express various natural environment on.

Analysis Method: The low artificial vegetationGeographic information data used in this analysis are soil map, .geological map, topographical map, vegetation map, and aerial photography. It applied the statistical analysis by overlay technique, that classifies the relevance to the natural condition using ARC/INFO(Ver.8.0.1) developed in U.S.A. ESRI Co. in order to digitize all geographic information data in the analysis.

Soil map(Fig. 3) and geological map(Fig.4) utilized 1/200000 map of the Economic Planning Agency in

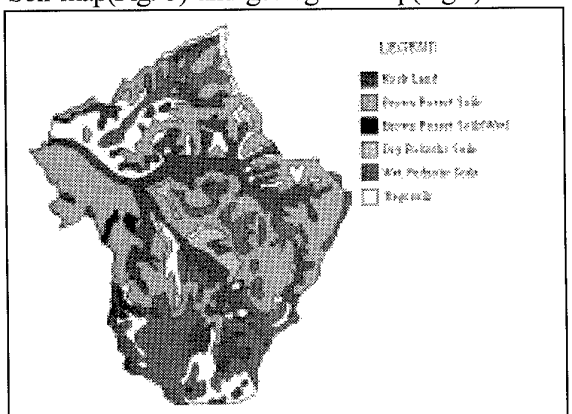


fig. 3 Soil Map

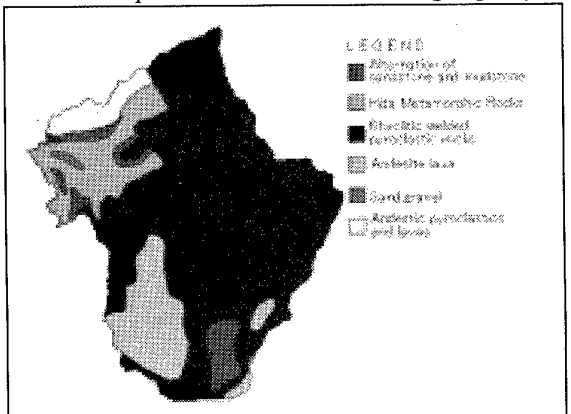


fig. 4 Geological Map

1974. The topographical map utilized 1/25000 map of Geographical Survey Inst., and the DEM made by using digitizer and TIN of ARC/INFO. The geomorphic area converted DEM into the UTM coordinate, and it made and computed slope figure (fig. 5), and azimuth figure (fig. 6) from the DEM. The vegetation map digitized existing vegetation map of 1/200000 of the first National Survey on the Natural Environment (1975, fig. 7) and 1/50000 of the third National Survey on the Natural Environment (1985, fig. 8) of the Environment Agency.

As the characteristics of the study area, the geography fluctuation is a frequent place of landslide and avalanche. Therefore, it digitized the delicate landscape evolution (landslide and slope failure) which could not be shown by topographical map, after it showed the information in topographical map using aerial photograph (1977)(Fig. 9). It showed spatially biological diversity of the natural environment on the basis of the analytical result.

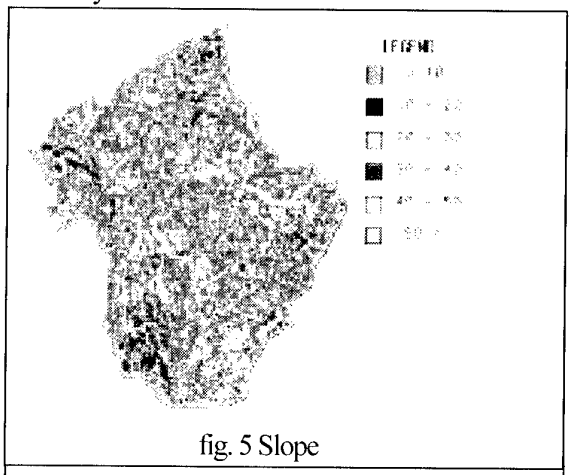


fig. 5 Slope

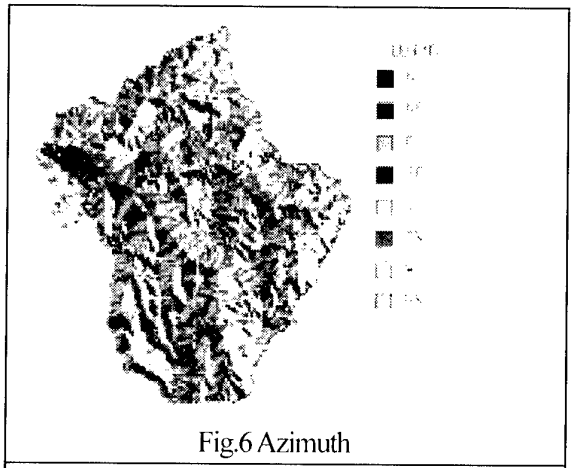


Fig.6 Azimuth

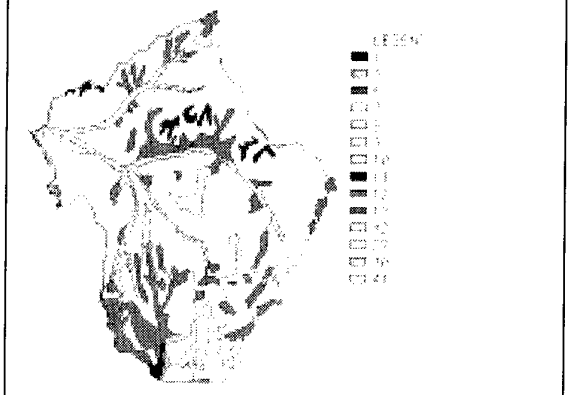


Fig. 7 Vegetation Map (1975)

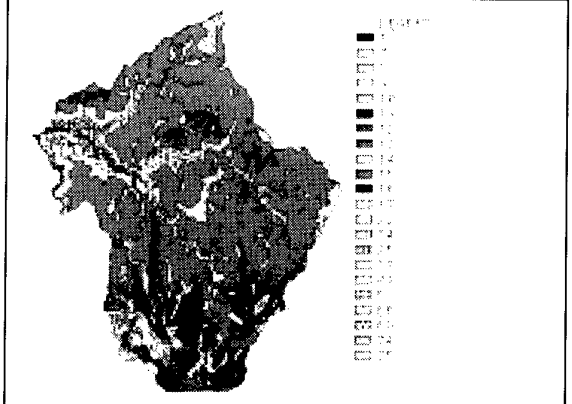


Fig. 8 Vegetation Map (1985)

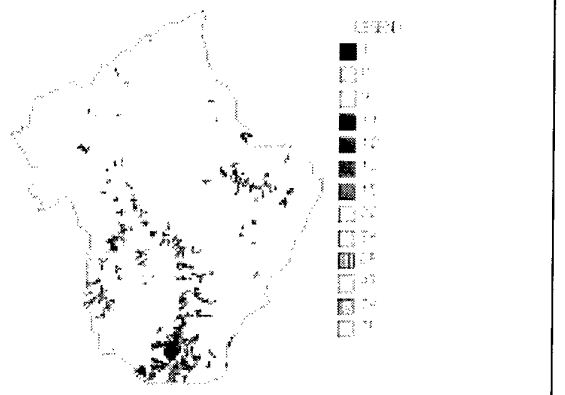


Fig. 9 Landslide Area

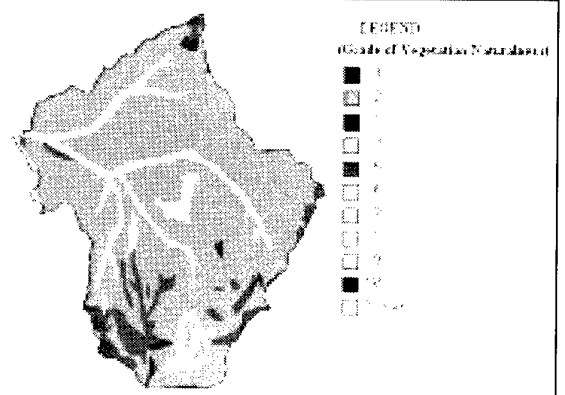


Fig. 10 Grade of Vegetation Naturalness (1975)

4. ANALYSIS OF NATURAL ENVIRONMENT

It grasps the place of which the naturalness is of high grade in vegetation, if it protects biological diversity of the natural park, it must be protected and maintained. Since it is the one index which shows ' of which degree remained, in this study, the naturalness which the ' land has used grade of vegetation naturalness (Table 1) for the analysis as the index which grasps natural environment.

Though vegetation 1975(fig. 10, table 2) was about 90% at naturalness 2(the low artificial vegetation), when it tried to analyze the transition of the vegetation, in 1985 (Fig. 11, table 3), showed about 80% of naturalness lowered. Fig. 12can confirms the difference. With the analysis of the grade of the vegetation naturalness, Saseto-kurilensae-Fagion crenatae was decreased, and was the result. However, the naturalness of the study area is yet high even in it.

There is the relation which is close with soil and slope, since it becomes a factor of landslide and avalanche. Saseto-kurilensae-Fagion crenatae of naturalness of 2 was widely distributed in Brown Forest Soils for old vegetation and new vegetation as the remarkable point in the analysis, and it occupied about 30-40% of the study area. In the old vegetation, Rock Land occupied about 20%, and in the new vegetation, Wet Podzolic Soils occupied about 20%. Regosoils occupied 30% on the soil of (450ha) in the landslide ground which was made from the aerial photography.

In the analysis of the geology, it could not regard noticed change as old vegetation or new vegetation.

Table1.Grade of Vegetation Naturalness Item

Naturalless	Definition
1	hardly the vegetation
2	the low artificial vegetation
3	planting forest from middle to sub tree
4	low or middle of the secondary grassland
5	high in the secondary grassland
6	the plantation
7	the secondary forest
8	almost a natural vegetation
9	natural vegetation of the multiple
10	natural vegetation of the simple species

Table 2. Vegetation Item (1975)

Legend	Vegetation
1	Vaccinio-Pinetum pumilae
3	Alpine tall herb stands
6	Abietum mariesii
7	Sasa spp.-Betula ermanii community
8	Alnus maximowiczil community
9	Sasa kurilensis community
10	Saseto-kurilensae-Fagion crenatae
11	Thuja standishii-Pius parviflora community
12	Polysticho-Pterocaryetum
13	Alnus pendula-Weigela hostensis community
27	Cryptomeria japonica plantation
40	Open water
41	Natural bare land
42	Sasa kurilensis community

Table 3. Vegetation Item (1985)

Legend	Vegetation
1	Vaccinio-Pinetum pumilae
7	Faurio-Caricetum blepharicarpae
8	Abies mariesii-Betula ermanii forest
9	Abietum mariesii
10	Abies mariesii-Fagus crenata community
11	Sasa spp.-Betula ermanii community
12	Alnus maximowiczil community
13	Trollio-Ranunculion acris japonicae
14	Sasa spp. community
15	Saseto-kurilensae-Fagion crenatae
16	Thuja standishii-Pius parviflora community
17	Polysticho-Pterocaryetum
22	Altherbosa
24	Fagus crenate-Quercus mongolica var.grosseserrata community
25	Castanea crenate-Quercus mongolica var.grosseserrata community
27	Miscanthion sinensis
47	Phragmitetum japonicae
53	Cryptomeria japonica,Chamaecyparis obtusa,Chamaecyparis pisifera plantation
66	Paddy-field weed communities
69	Urban and residential district with many trees
74	Open water
75	Natural bare land

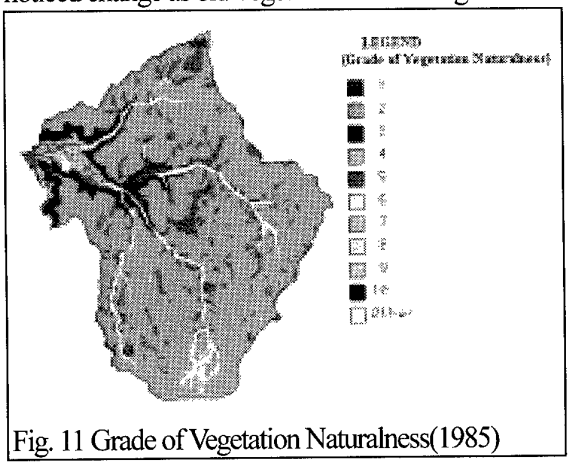


Fig. 11 Grade of Vegetation Naturalness(1985)

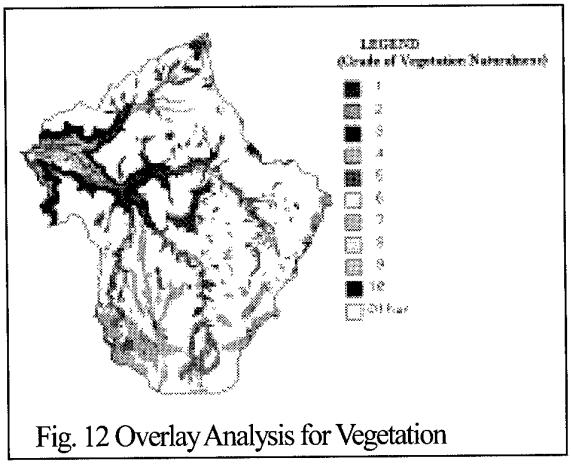


Fig. 12 Overlay Analysis for Vegetation

Rhvolotic Welded Phroclastic Rocks in which about 80% of Saseto-kurilensae-Fagion crenatae of the 2 grade of vegetation naturalness grew occupied about 60% of the whole area.

A slope of 30-50degree increases the danger of a land collapse in. In the analysis, it was distributed for slope 30 –50 degree of both of the naturalness of 2 for about 50%. Altherbosa and Natural bare land mainly existed in the geography condition of the study area in the place of over 30 of degree. However, there is seldom the danger, when noticing point separates from the rill parallel a little.

The landslide is frequent due to weather condition and geography condition. In the inclinatio in the landslide ground, the Regosoils soil saw over 15% over 40-50 degree. It seems that and, there is the relation here with geology (lternation of Sandstone and Mudstone).

The relation between sunshine and its duration which raises the plant is deep for the slope azimuth. The type of the vegetation is different from the speed of the growth by its direction. The azimuth was generally distributed for naturalness of 2, when it classifies the slope azimuth as 8, it regards the naturalness as a relation, since most vegetation is distributed for the naturalness of 2. Especially, 30% of Saseto-kurilensae-Fagion crenatae accupied the whole of west plane occupied whole about.

5. CONCLUSION

Saseto-kurilensae-Fagion crenatae Fagion crenatae primary forest which occupies most of the study area comes in at 9 grade of vegetation naturalness. It does not go, if 9 grade of vegetation naturalness does not try for the protection, since academically important vegetation, mainly grows. And, Brown Forest Soils of the forest productivity is usual, and it ought to avoid the modification of the soil, since the land productivity is low for Podzolic Soils. Though steep geography condition is the characteristics of the study area there was the danger in which the slope failure could be generated. Altherbosas, etc. grew by it, and it became the important inhabiting field of the animal. This study will propose natural resource in an attempt to protect conservation of a diversity of natural environment to be considered with the viewpoint in the approach for natural environment.

REFERENCES

Harashina, K. Tsynekawa, A. Takeuchi, K. and Takatsuki, S. (1999): Relationships between Connectivity of Forests and Distributions of Terrestrial Mammals in Honshu, Japan of the Japanese Institute of Landscape Architecture, Vol.62(5), 569-572.

Choi, B., Koyanagi, T. and Itoga, R.(1999): Fundamental on the natural Environmental Assessment and Environmental Consideration to Using GIS, Japan Soc. Environmental Systems Research, Vol.27, 549-554.

GIS Application on the Strategy for Sustainable Development in Phitsanulok Province

Vicharn Amarakul and Sirirat Sanyong
Faculty of Agriculture, Natural Resources and Environment, Naresuan University. Phitsanulok 65000. Thailand.
Tel: (6655)261000 ext.2750 ,Fax:(6655)261040 and E-mail: vicharn_a@hotmail.com

ABSTRACT

The strategy for sustainable development in Phitsanulok (SSDP) is integrated policy among government policy, people needs and natural resources potential. SSDP will be a tool for making decision on projects planning, government budget, the balance of using, developing rehabilitation and conservation natural resources and environment (NRE). The main idea of SSPD must be related on vertical and horizontal policy of nation, province and local. Integrated on natural resources and environment management is the main purpose on the good ecology for living and non-living things. Human is an important role on ecology change. Therefore, we should be clever management on socio-economic and environment. At the present, the government distributes their authority from center to local for human good living and increasing the efficiency of administration. The local stakeholders are important role for making decision on their get and lost benefit. The problems in each area is different, it need the special solve the solution. The stakeholders had took action for look sharp on problems, opportunities, vision, goals, targets, integrated of decisions, resolution of conflicts and implementation of management framework for sustainable development in their area for next 20 years (2002- 2021).

GIS and others information, Spatial planning or geographic planning, are the tools for planning and decision making on SSDP. Natural resources, infrastructure, social and economic data had been analyzed by using GIS. GIS will be a guideline management and decision on potential area where related with their goals. Data base system and the layers of map scale 1:50000, topography landuse river and waterbody infrastructure Administration Boundary etc., are using for NRE management. GIS is a tool for manipulation modification and update data, application program for analysis, display and query. GIS had been used as the tool for analysis weakness, strength, opportunities and threats. Spatial information will show locations, sizes and conflicts. Data collection and analyze for the target and criteria in each area should be correlate with objectives, management guidelines, zoning, and conflict analysis. Therefore, GIS could decrease the conflicts resolution on NRE management by making many options. Type of zoning mean conservation zone, rehabilitation zone, developing zone, agriculture zone and industries zone etc. All data base are the guidelines for stakeholders decide to get the highest benefit and not disturb the NRE. Therefore, the spatial data could be very quickly conclusion on GIS and realistic present to the stakeholders.

Introduction

The Strategy for Sustainable Development in Phitsanulok (SSDP) is the national policy of Thailand. Phitsanulok province is one province from eight provinces for pilot project to introduce the strategy for sustainable development. Phase I (year 1999 – 2001) for pilot strategy is promoting on Phitsanulok, Chaing-rai, Mahasarakhram, Ubon Ratchathani, Nakornnayok, Kanjanaburi, Phungua and Trang provinces. Phase II (year 2002 – 2006) will be promote to the remains of 67 provinces. SSDP project's budget and guidelines are supported by the Canadian International Development Agency : CIDA. Ministry of Interior under Government of Thailand had cooperated with Natural Resources and Environmental Management Project : NREM under CIDA for implementation the strategy which emphasis on

the integrated the three dimensions of government policy, people needs and natural resources potential. The intersection of the three dimensions will be the conclusion of sustainable development and management on natural and environmental resources for each area. Phitsanulok strategy for sustainable developments had been brain storming and creation by Phitsanulok's people, non government organizations, the representatives of all levels of government, the representative of private sectors and the local philosophers. Naresuan University staffs is a local university had a role as facilitators for conclusion the all of brain storming. The SSDP will be considered by the committee of Phitsanulok province's development for the last check.

1. General Information

Phitsanulok province located at the latitude 16° 21′ 23″ North to 17° 44′ 31″ North and longitude 99° 52′ 27″ East to 101° 4′ 34″ East. Phitsanulok province area is 10,815.85 square Kilometres and the driving distance between Bangkok and Phitsanulok is 377 kilometres.

The north side of this province connected with Num Prad district , Uttradit province and The People Democratic Republic of Loas. The south side connected with Muang Phichit and Sam Ngam district, province. The east side connected with Dan Zide district, Leoi . and Lom Gou district, province. The west side connected Sri Sam Rong, Sukothai province and Pran Ka Tai district, Kumphaengphet province.

The lower northern part of Thailand located on fertile land at the upper ChaoPhaya plain which consisted of 8 provinces; Phitsanulok, Phichit, Nakornsawan, Uthai Thani, Kumphaengphet, Sukothai, Uttradit and Phetchabun provinces. Phitsanulok province is the connection center for the center part, upper northern part and north-eastern part of Thailand. Therefore, the importance government offices for this region had been established on Phitsanulok province.The local governor is divided into 9 districts, 93 sub-districts, 947 villages, 13 municipality and 90 local communities. The occupation of the most of Phitsanulok's people are farmers which there are identified 59.45% for paddy field, 14.68% for services, 12.25% for commercial, 7.08% for constructions and 4.8% for industries sectors.

2. The guidelines of strategy for sustainable development in Phitsanulok province

The guidelines of strategy for sustainable development in Phitsanulok province are emphasized on the integrated the three dimensions.

2.1 The Policy and all Projects under Thai Government

The policy and project should be related on the vertical and horizontal levels. The vertical level is national policy, provincial policy and local policy. The horizontal level is cooperated the projects between ministries, departments and divisions.

2.2 Ecosystem approach

The living things and non-living things should be strand together as symbiosis in the ecological system. Therefore, the planning for the integrated on natural and environmental management for the proper use is the very important tool for natural conservation and environmental rehabilitation. The most the important factor effect to the ecology, environment, social and economic is human being. A planning and decision-making approach that is founded on ecological principles and recognizes that human intervention in the environment has significant effects across the whole connected natural system.

2.3 Public Participation

The provision of opportunity for general public during a planning process and to influence decisions resulting from a planning process. The public is all inclusive and includes individual citizens, all levels of government, non-government organizations, and the private sector. The stakeholders will be making decision on their benefit in the future. The problems in each area will been solved in different levels and situations by stakeholders. Equal and participation created the vision for the future 20 years.

3. The strategy for sustainable development in Phitsanulok province

The process of the strategy for sustainable development are:

Step 1. Establishment the team works and database
Step 2. Analysis on issues and opportunities
Step 3. Vision, goals, objectives and management guidelines
Step 4. Integrated of decision and resolution of conflicts
Step 5. Implementation of management framework for sustainable development

4. Geographic Information System :GIS

The application using by GIS and other database are the important tool for planning and decision making in the SSDP. GIS data base contained natural resources, infrastructure, economic and social map layers. Those maps were overlaid for spatial analysis the potential ability of the land to support renewable natural resources such as forestry, agriculture, wildlife, recreation and water production. In the other hand, spatial data could be used for problems and opportunities analysis. Spatial data could show the situation and size of problems and development opportunities. GIS is a tool for analysis target area, criteria, objectives, management guideline, zoning, resolution of conflicts and options in each area. The same area maybe implement more than one objectives. Finally, all stakeholders were satisfied and related with the potential ability of land.

Methodology

1. Data collection in terms of spatial data for target analysis, criteria in each area, management guidelines and zoning. (Fig 1.)

1.1 To keep the importance data in sequence for example boundary of country, boundaries of provinces and districts.

1.2 To mark the boundaries which correlate with the objectives for example protection zone applied the ecological boundary or physiological boundary, developing zone applied administrative and location boundary, production zone applied ability potential of natural resources boundaries or irrigation boundaries.

1.3 To group the spatial data which showed the same objectives for the advantage of processing, monitoring and evaluation.

2. Application the suitable activities for compatible uses on those geography. A geographical defined area in which compatible and non-compatible uses are prescribed. In integrated natural resources and management planning, zoning is used as means to implement the plan. In case of the strategy for sustainable development, some activities have much effect on environment. So, the Environmental Impact Assessment should be considered.

3. Criteria on land use management

The criteria on land use management could divide into 4 categories as following:

3.1 Protection zone

Protection zone or sensitive area is the areas and features (both terrestrial and aquatic) on all lands and waters, both public and private, including natural, social and cultural amenities which identified and described in the planning process and become prime protection areas to be avoided by development. These areas are normally buffered with a standard set-back zone and include restrictive uses to sustain the feature.

3.2 Production zone

Production zone meant the high productivity areas and quantity of resource that can be produced continuously over time and, at the same time, maintain ecosystem health.

3.3 Development zone

Development zone is identified for the compatible areas for social and economic which showed ineffective to the environment. A concept, it has made some profound changes in the attitudes as to how these finite resources are being development.

3.4 Multiple zone

Multiple zone is not protection, production and development zones but these zone have integrated activities. Multiple zone is the barrier buffer zone between protection, production and development zones.

Results and Conclusion

The strategy for sustainable development in Phitsanulok province had been analysed by brain storming from Phitsanulok 's people, ability potential of natural resources and all levels of government, private sectors and non government organizations. All stakeholders had created the vision, goals, objectives, targets, criteria, management guideline and resolution of conflicts by their consensus.

The strategy for sustainable development in Phitsanulok province for next 20 years (2002 - 2021) are arranged by zoning as follows. (Fig 2.)

1. Protection zone. The protection areas is 3,644.83 km^2 or 33.70 % , their criteria showed as table 1.
2. Production zone. The production areas is 3,309.35 km^2 or 30.60 % , their criteria showed as table 2.
3. Development zone. The development areas is 2,131.60 km^2 or 19.71 % , their criteria showed as table 3.
4. Multiple zone. The multiple areas is 1,730.07 km^2 or 16.00 % , their criteria for showed as table 4.

The proper or improper activities in each zones had been decision by all stakeholders 's consensus as table 5.

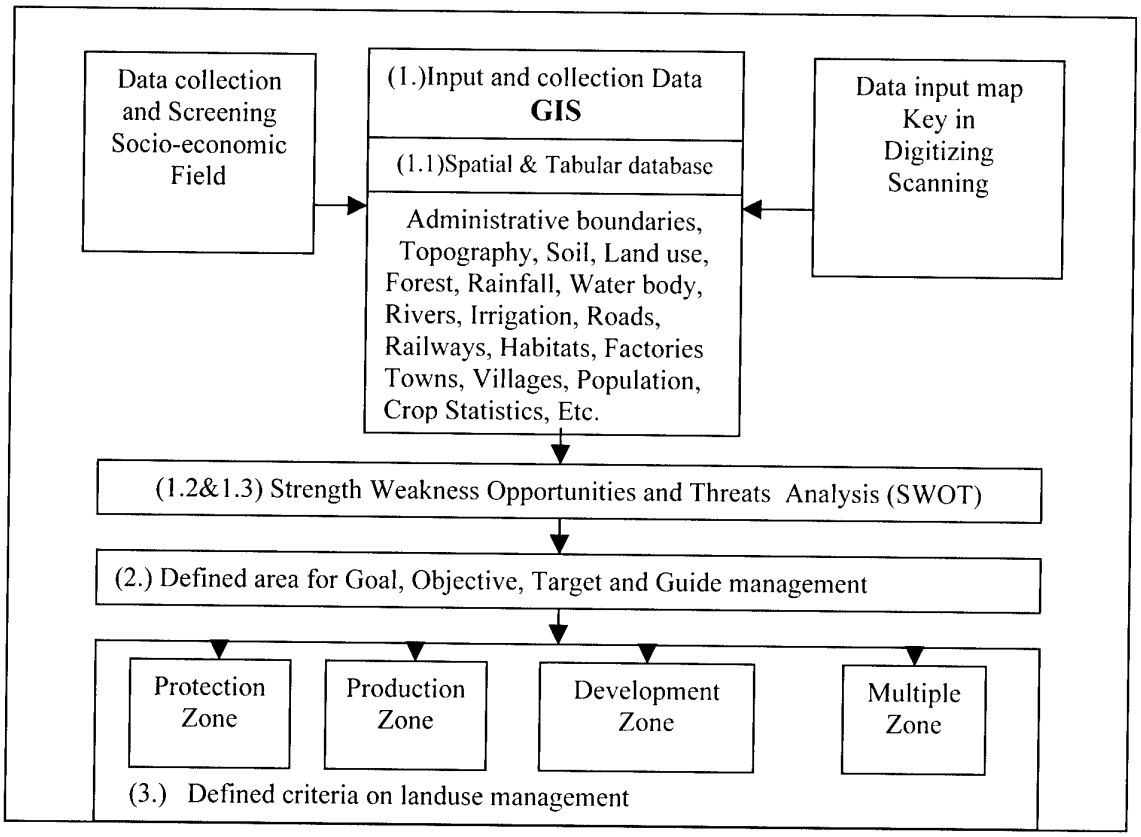


Fig 1. Diagram showed the strategy for sustainable development in Phitsanulok by using GIS

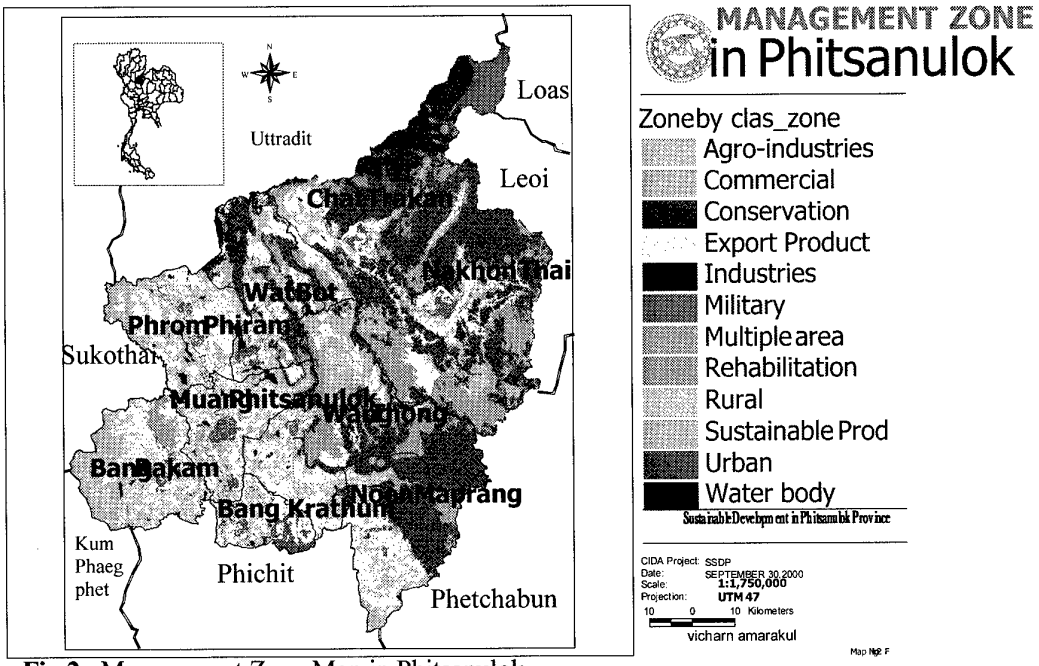


Fig 2. Management Zone Map in Phitsanulok

Table 1. Defined criteria on protection zone

Protection Zone	Criteria
Natural Parks, Wildlife Conservation Areas, Forestry Areas, etc.	Boundary under the law, government policy and people needs
Waterfall, Ancient history area, Eco tourism areas, etc.	Buffer distances 500 m.
Upper water shed area, Sensitive area, Deforestation area, Steep area more than 15 degree	High erosion area, forestry area, etc.
Sensitive area to environmental change	Terrestrial area adjacent to water bodies including lakes, rivers, ponds, wetlands. Buffer distances 100 m.
Rehabilitation area	To rehabilitate infertile soil, barren lands, land out of development zone

Table 2. Defined criteria on production zone

Production Zone	Criteria
High productivity area	Suitable soil group for agriculture
Irrigation area	Boundary of irrigation
Non irrigated area	Rainfed area
High value added crops an fruit trees	Existing land use map for fruit trees and vegetables
Land reformation	Deforestation area but suitable soil group for agriculture
Barren land need to rehabilitation for agriculture	Suitable soil group for agriculture
Agriculture area in forestry zone	Sustainable production
Fishery for commercial	Potential of land, natural resources
Animal Husbandry for commercial	Potential of land, natural resources

Table 3. Defined criteria on Development zone

Development Zone	Criteria
Urban, municipality, rural, village have population more than 500 persons.	Buffer distance 500 m. for sustainable development
Super high way, roads, streets, etc	Buffer distance 50 m. for main roads and 20 m. sub-roads. Indochina intersection region
Industry and agro-industry	Buffer distance 1,000 m. from urban and rural boundary for heavy industries
Airport	Infrastructure for international airport
Commercial center, transportation center, warehouse and cargo	Buffer distance not less than 500 m. from urban and rural boundary . Not produce water, air , and noise pollution
Mineral resources	Buffer distance not less than 1,000 m. Decision making was done by the stakeholder.

Table 4. Defined criteria on Multiple zone

Multiple Zone	Criteria
Military zone	Special area for military usage.
Buffer zone for protection areas	Buffer distance 100 m. from forestry boundary and 50 m. from water resources
Buffer zone for urban, street, industry, etc.	Criteria the same as development zone
Conflicts areas between government sector and people	Disagree on land use

Table 5 The suitable activities for each zones in Phitsanulok province.

Zones / Activities	Protection zone		Production zone		Development zone			Multiple zone
	Conservation	Rehabilitation	Export production	Sustainable production	Urban area	Rural area	Industries and commercial areas	Multiple using areas
Paddy field	Φ	♣	•	•	♣	•	•	♣
Field crop	Φ	♣	•	•	♣	•	♣	♣
Orchards / Trees	Φ	♣	♣	♣	♣	•	♣	•
Agro-forestry	Φ	♣	Φ	♣	Φ	♣	Φ	•
Community forestry	Φ	♣	Φ	•	♣	♣	♣	♣
forestry Production	Φ	♣	♣	♣	Φ	Φ	Φ	♣
Fishery	Φ	♣	•	•	♣	•	♣	•
Husbandry	Φ	♣	♣	•	Φ	♣	♣	Φ
Waste areas	Φ	♣	♣	♣	Φ	♣	♣	Φ
Heavy Industry	Φ	Φ	Φ	Φ	Φ	♣	♣	Φ
Medium Industry	Φ	Φ	Φ	Φ	Φ	♣	♣	Φ
Small Industry	Φ	Φ	♣	♣	♣	•	•	♣
Agro-industry	Φ	Φ	♣	♣	♣	•	•	♣
Public park[1/]	♣	♣	•	•	•	•	♣	♣
Tourism[2/]	Φ	Φ	♣	♣	•	•	♣	♣
Houses	Φ	♣	♣	♣	•	•	•	♣
Constructions	Φ	♣	♣	♣	♣	•	♣	♣

• Suitable activities

♣ Activities under control conditions.

Φ Not permit to do any activitie

[1/] Relaxation areas are not permitted to built any construction.

[2/]Tourism areas are permitted to construct hotels, car parks, etc

DYNAMIC SIMULATION OF LAND USE/COVER CHANGE BASED ON TIME SERIES SATELLITE IMAGES

Zhongchao Shi, Ryousuke Shibasaki
Center for Spatial Information Science(CSIS), The University of Tokyo
4-6-1 Komaba, Meguro-ku,Tokyo 153-8558
Tel. +81-3-5452-6413 Fax +81-3-5452-6414
Email : shizc@skl.iis.u-tokyo.ac.jp
shiba@skl.iis.u-tokyo.ac.jp
JAPAN

KEY WORDS : Dynamic, Land Use/Land Cover(LUCC), Change Detection

ABSTRACT : Land use and land cover of the earth are changing dramatically because of the human activities and natural disasters. To simulate the changes of land use/cover is significant for making a sustainable land use plan. In this paper, a method aiming at dynamic simulation and estimation of the land use/cover change (LUCC) is proposed, which includes following models: 1) Image classification model; 2) Data transformation model; 3) Change detection model.

1. INTRODUCTION

Land use and land cover of the earth are changing dramatically because of the human activities and natural disasters. In many areas, people are suffering from the deforestation, flooding, food shortage, green house affect, urban extension etc. Most of these environmental problems are related to LUCC changes. It is then important to master the LUCC change in order to make a sustainable global land use plan.

In 1993, the first LUCC/CPPC (Land use/Cover/Core Project Planning Committee) conference was held in Spain, which is a sign of international collaborative research in LUCC. In 1996, LUCC Open Science Meeting was held in Holland and the international LUCC project was started after that.

Satellite images have played an important role in LUCC project and LUCC change detection. Up to now, NOAA AVHRR time series images have been widely used for LUCC research because of their low cost. But, for the purpose of regional LUCC research, 1km resolution is insufficient. In our research, time series MSS and TM images are used for LUCC change detection. Many case studies have been carried out. But because of the page limitation, only two typical areas of our experimental results will be shown in this paper.

2. STUDY AREAS

China was selected for the case study because the LUCC of some areas of China changed a lot in the past three decades. As shown in Fig. 1, two places were selected in this paper. One is located in Inner Mongolia (Grassland) while another is close to Pearl River (Urban Extansion) in Guangdong province. Three images (1 MSS in 70's and two TMs in 80's and 90's respectively) for each area were utilized for the analysis (see Table 1).

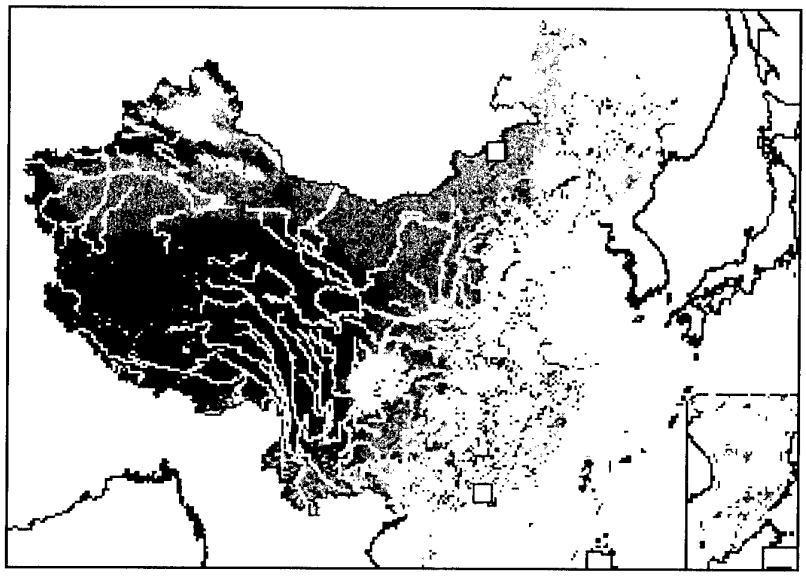


Fig.1 Study areas

Table 1. Image data

Area	Path/Row	Date (mm/dd/yy)	Sensor
Inner Mongolia	134/029	11/04/1973	Landsat MSS
	124/029	07/30/1987	Landsat TM
	124/029	09/25/1996	Landsat TM
Pearl River	131/044	02/10/1977	Landsat MSS
	122/044	12/10/1988	Landsat TM
	122/044	10/29/1994	Landsat TM

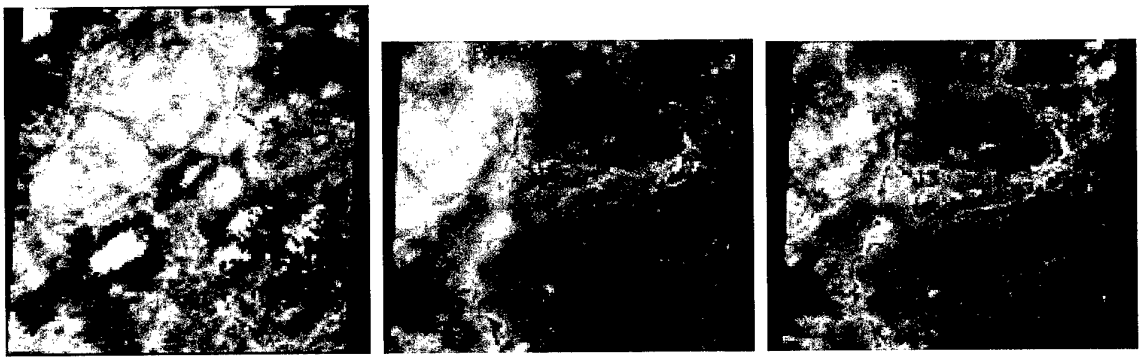
3. METHODOLOGY

Authors have proposed an arable land use change model in 1999. In this paper, we introduce a method, which can detect the changes of different type of the geo-objects. The procedures of the processing are:

1) Image classification. Maximum likelihood method integrated with NDVI and principle component analysis is mainly used in this model. A quantity of ground survey data is used for correcting and verifying the classification results.
2) Data transformation. This model is developed for high-quality overlapping of time series images for the purpose of change detection. In this research, since Landsat MSS and TM taken at different time were utilized, we have to adjust these images into one coordinate system and unify their resolution.
3) Change detection model. In different area, the major land use/cover types are different. For example, in Inner Mongolia, the grassland is the major LUCC type while in Pearl River region, there are a lot of cities, villages etc. We choose the major types of LUCC and find their changes in different research areas.

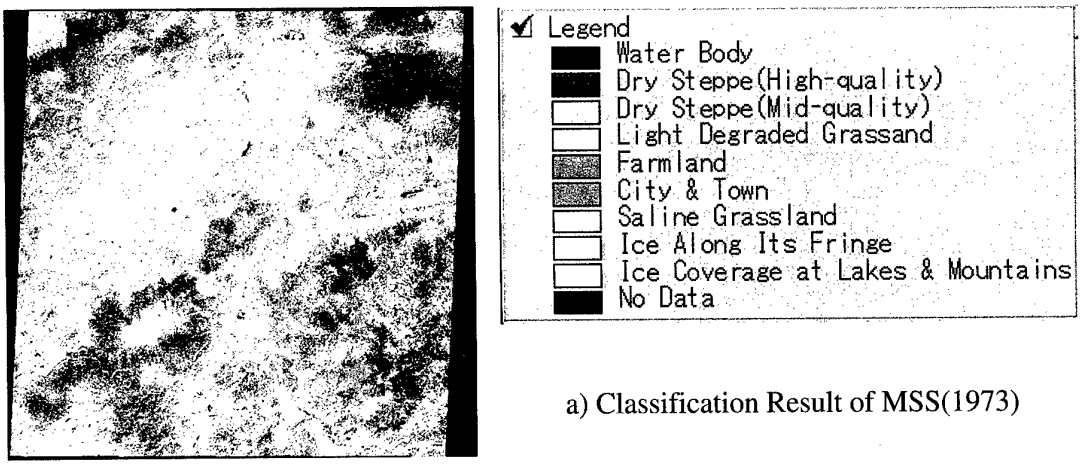
4. CASE STUDIES

Several case studies have been carried out according to the method introduced in former Chapter. We would like to show two of them because of the page limitation in this paper. Fig.2 shows three images used in Inner Mongolia. Fig.3 and Fig. 4 show the classification results and detected grassland changes, respectively.

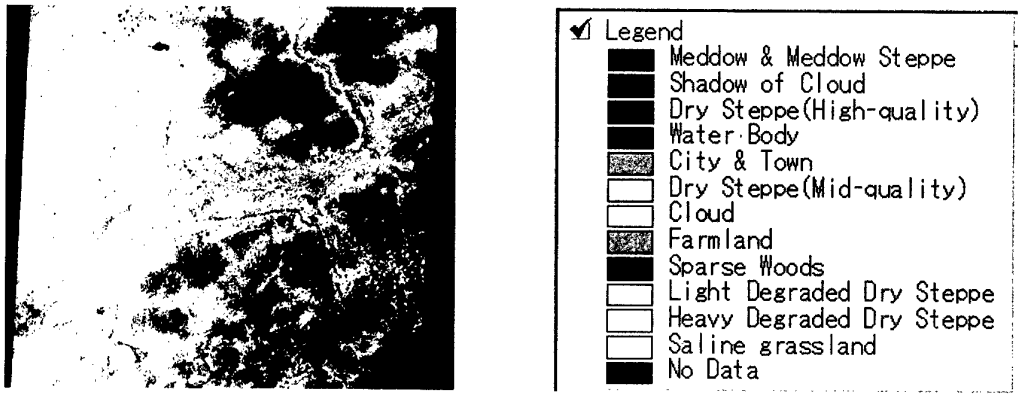


a) MSS image (1973) b)TM image(1987) c)TM image (1996)

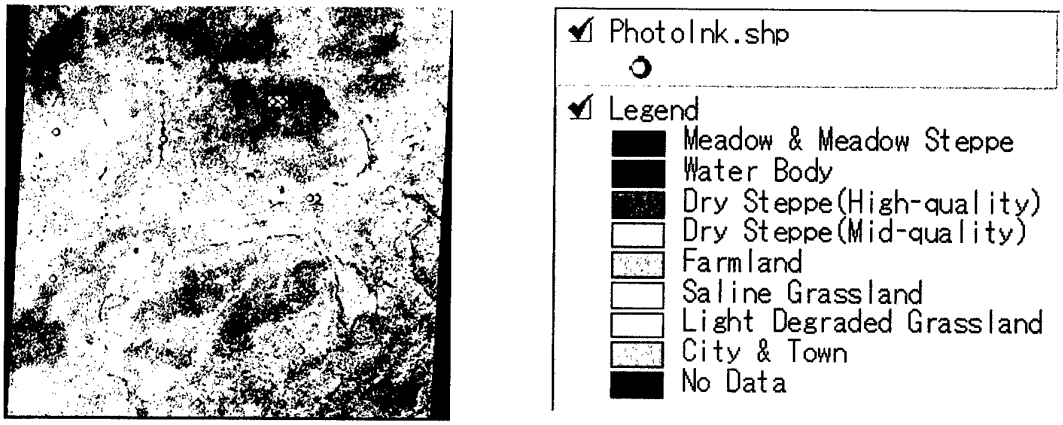
Fig.2 Three images of Inner Mongolia



a) Classification Result of MSS(1973)



b) Classification Result of TM(1987)



c) Classification Result of MSS(1973)

Fig.3 Classification results in Inner Mongolia area

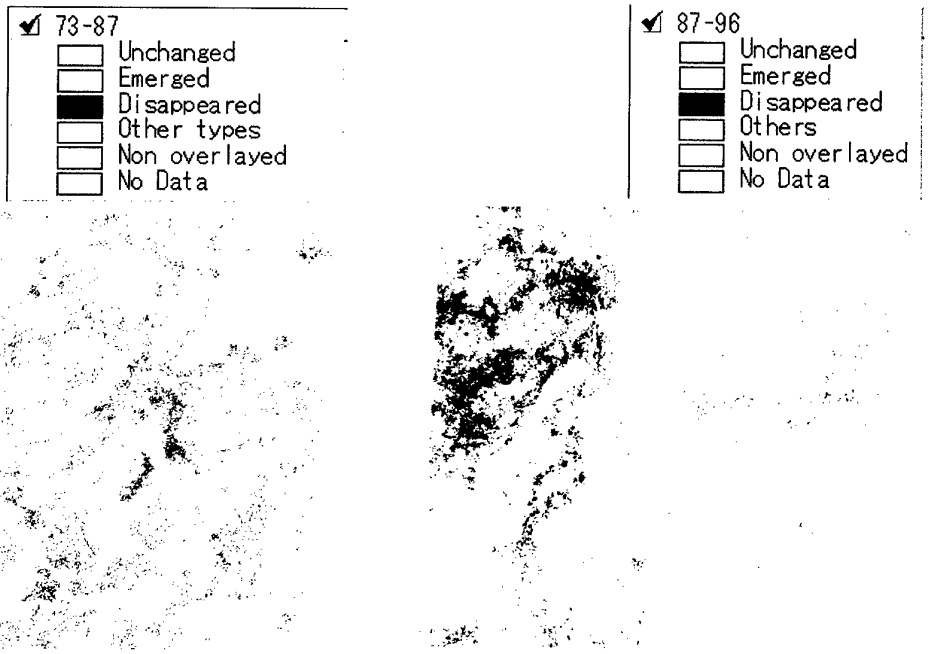


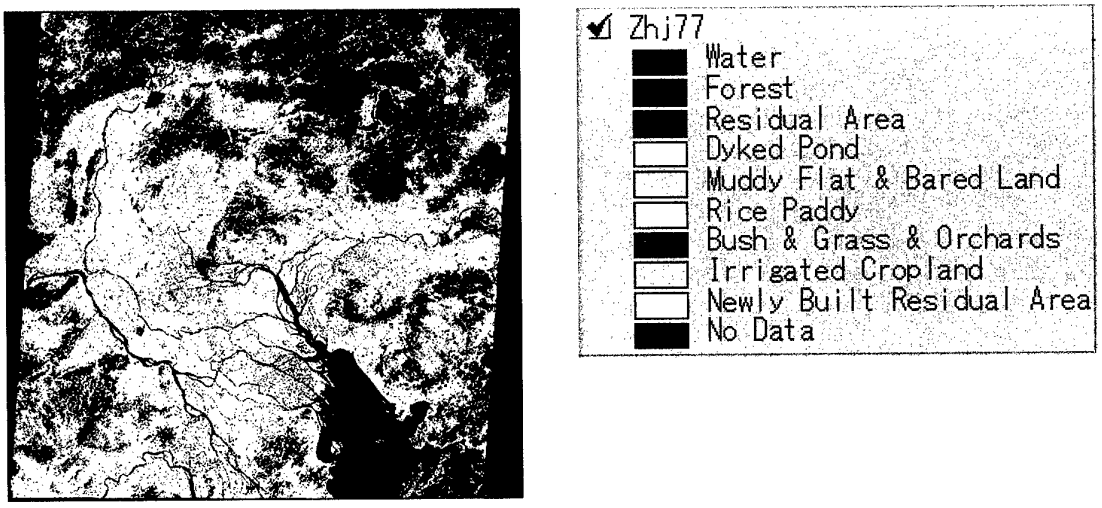
Fig.4 Detected grassland changes in Inner Mongolia area

Fig.5 shows three images used in Pearl River area. Fig.6 and Fig. 7 show the classification results and detected change of urbanization in that area, respectively.

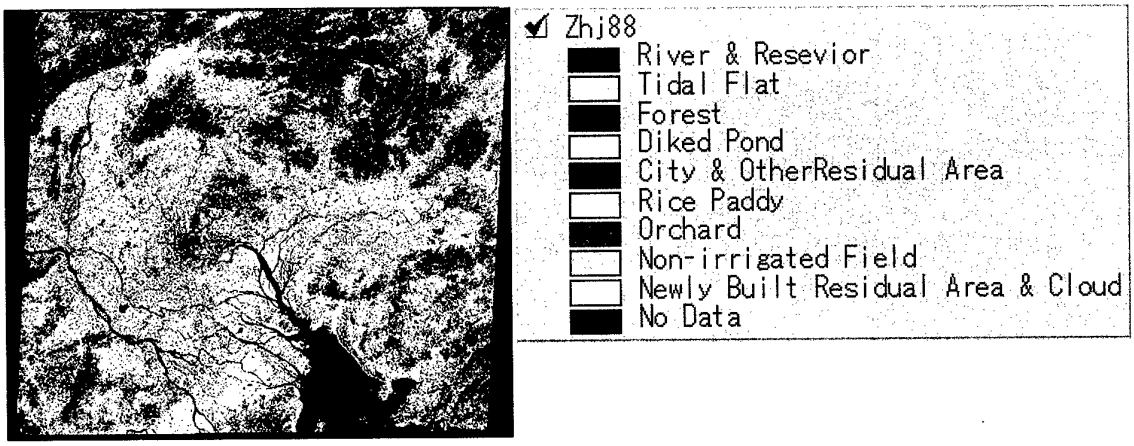


b) MSS image (1977) b)TM image(1988) c)TM image (1994)

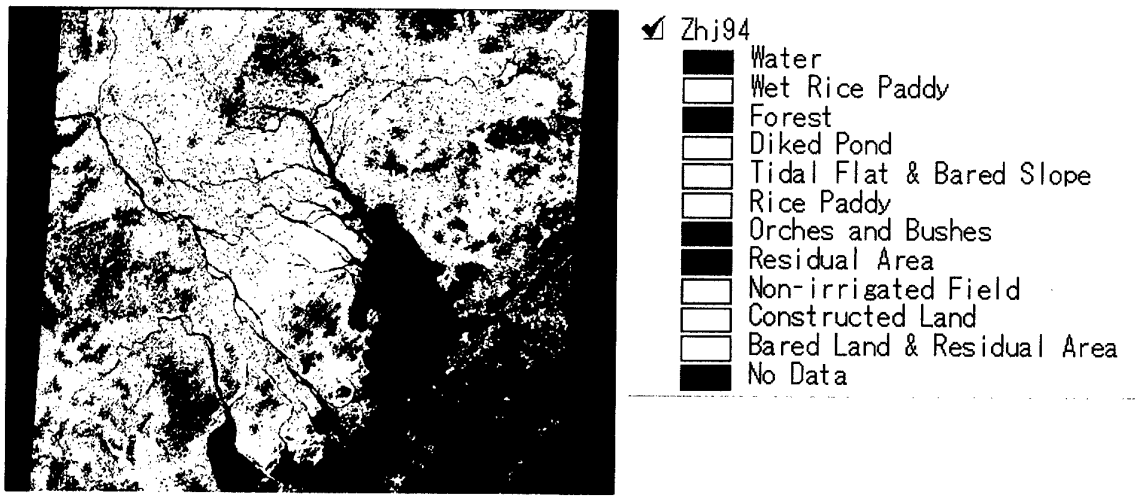
Fig.5 Three images of Pearl River area



a) Classification Result of MSS(1977)



b) Classification Result of TM(1988)



c) Classification Result of TM (1994)

Fig.6 Classification results in Pearl River area

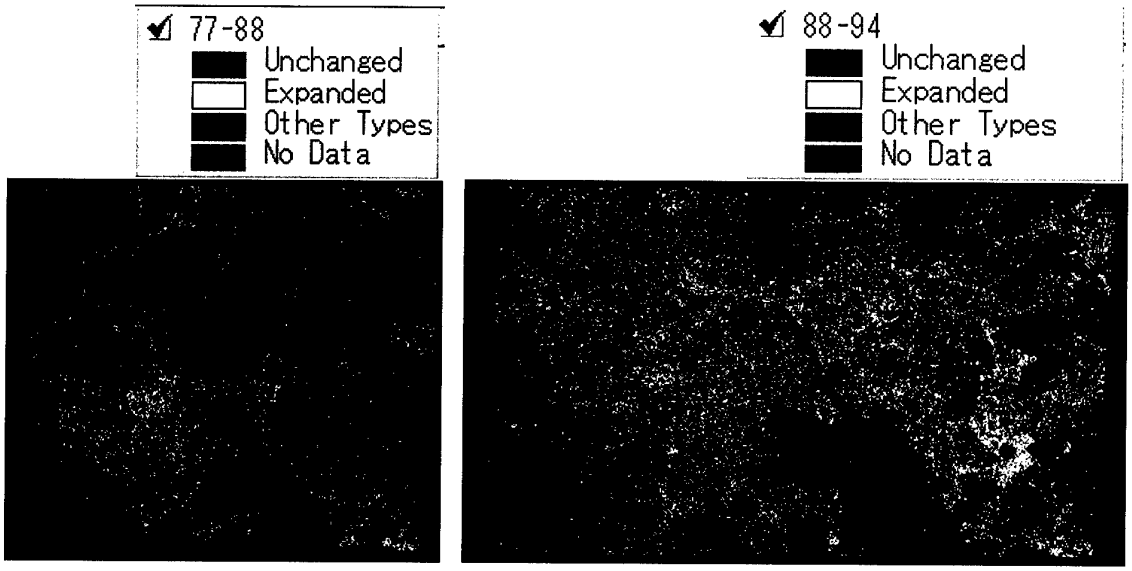


Fig.7 Detected urbanization regions in Pearl River area

5. CONCLUSIONS

In this paper, a method respect to LUCC change detection based upon time series Landsat images was introduced. By using time series Landsat images, the LUCC changes can be detected accurately. The LUCC change information is very important for decision making of sustainable land use planning in both national and regional levels.

6. REFERENCES

Z.C. Shi, H. Liu, R. Shibasaki, "A Practical Model For Estimating The Arable Land Change Of China Using Remotely Sensed Imagery," Proc. of ACRS'99, Nov. 1999, HongKong, pp. 753-758.

GROUNDWATER PREDICTION POTENTIAL ZONE IN LANGAT BASIN USING THE INTEGRATION OF REMOTE SENSING AND GIS

[1]Khairul Anam Musa, [2]Juhari Mat Akhir and [2]Ibrahim Abdullah

[1]Malaysian Centre for Remote Sensing (MACRES)
No.13, Jalan Tun Ismail, 50480 Kuala Lumpur
[2]Universiti Kebangsaan Malaysia, 43600 Bangi, Selangor
MALAYSIA

ABSTRACT

Groundwater constitutes an important source of water supply for various purposes, such as domestic industries and agriculture needs. In the hydrological cycle, groundwater occurs when surface water (rainfall) seeps to a greater depth filling the spaces between particles of soil or sediment or the fractures within rock. Groundwater flows very slowly in the subsurface toward points of discharge, including wells, springs, rivers, lakes, and the ocean. In this study, the integration of remote sensing and geographic information system (GIS) method were used to produce map that classified the groundwater potential zone to either very high, high, moderate, low or very low in terms of groundwater yield. Almost all alluvial plains have a high potential of groundwater occurrence. Meanwhile, in the hard rock areas, groundwater potential is in the high density lineament zones.

1.0 INTRODUCTION

Groundwater forms the part of the natural water cycle, which is present within underground strata. The principle sources of groundwater recharge are precipitation and stream flow (influent seepage) and those of discharge include effluent seepage into the streams and lakes, springs, evaporation and pumping (Gupta, 1991). Ground water cannot be seen directly from the earth's surface, so a variety of techniques can provide information concerning its potential occurrence. Geological methods, involving interpretation of geologic data and field reconnaissance, represent an important first step in any ground water investigation. Remote sensing data from aircraft or satellite has become an increasing valuable tool for understanding subsurface water condition (Todd, 1980). They are particularly useful, very detailed and also show up features which cannot be seen easily on the ground. The various surfacial parameters prepared from remotely sensed data and ancillary data can be integrated and analyzed through GIS to predict the potential of ground water zone.

2.0 OBJECTIVES

The objectives of this study are as follows:

i. To collect the ancillary data and to analyze the remote sensing data for getting information that is related to groundwater occurrence.
ii. To prepare difference thematic maps from the above information.
iii. To predict the groundwater potential zone through the various thematic maps using GIS technique.
iv. To develop a GIS model to identify groundwater potential zones.
v. To show the integration of remote sensing and GIS techniques for prediction of the groundwater potential zone in the study area.

3.0 STUDY AREA

Langat Basin is located in south of Selangor and north of Negeri Sembilan within latitude 2°40'U to 3°20'U and longitude 101°10'E to 102°00'E with the geographical area extent of around 2,394.38 km^2 (Figure 1).

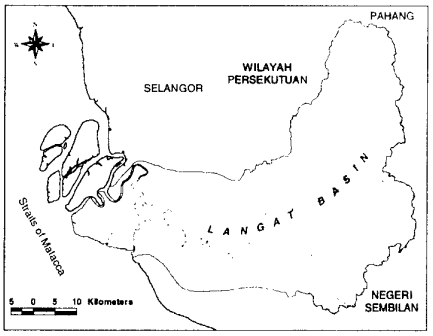


Figure 1: Map showing the location of the study area.

4.0 METHODOLOGY

In order to prepare the map showing potential zone for groundwater, five stages were applied; Source Data Collection, Image Processing, Building Database, Data Processing and Data Integration as outlined in Figure 2.

4.1 Source Data Collection

The Landsat TM data acquired on 6 March 1996 was collected together with the geological maps sheets 93, 94, 95, 101, 102 and 103 on 1:63,360 scale, prepared by the Minerals and Geoscience Department (JMG); topography maps sheets 3858, 3657, 3757, 3857, 3656, 3756, 3856, 3755 and 3855 on 1:50,000 scale, prepared by Survey and Mapping Department (JUPEM); rainfall data from 1982 to 1996 collected by the Meteorology Department of Malaysia, Drain and Drainage Department (JPS) and Universiti Kebangsaan Malaysia (UKM), soil series map of the study area on 1:150,000 scale, prepared by the Agriculture Department of Malaysia. In addition, hydrogeological map of Peninsular Malaysia on a scale of 1:500,000 and borehole data collected by the JMG were also utilized.

4.2 Satellite Data Analysis

The main task in this stage is to do an analysis and interpretation of satellite data, in order to produce basic maps such as structural and land use map in digital form. Basically, satellite data registration, correction and other image processing (such as enhancement, filtering, classification and other GIS process), together with field checking of the relevant area will be applied in this stage.

4.3 Spatial Database Building

The main task is to bring all the appropriate data (from stage 2 and existing relevant data) together into a GIS database. Basically, all the available spatial data will be assemble in the digital form, and properly registered to make sure the spatial component will overlap correctly. Digitizing of existing data and the relevant processing such as transformation and conversion between raster to vector, griding, buffer analysis, box calculating, interpolation and other format will also be conducted. This stage produces derived layers such as annual rainfall, lithology, lineament density, topography elevation, slope steepness, drainage density, land use and soil type.

4.4 Spatial Data Analysis.

This stage will process all the input layer from stage 2 and 3 in order to extract a spatial features which are relevant to the groundwater zone. This phase includes various analysis such as table analysis and classification, polygon classification and weight calculation. Polygons in each of the thematic layers were categorised depending on the recharge characteristics and suitable weightages were assigned (Table 1-8). The values of the weightage are based on Krishnamurthy et al. (1996 & 1997).

4.5 Data Integration

The final stage involves combining all thematic layers using the method that is modified from DRASTIC model, which is used to assess ground water pollution vulnerability by Environmental Protection Agency of the United State of America (Aller, 1985). The formula of the groundwater potential model (GP) as shown below:

$$GP = Rf + Lt + Ld + Lu + Te + Ss + Dd + St$$

where:

Rf:annual rainfall, Lt:lithology, Ld:lineament density, Lu:land use,

Te:topography elevation, Ss:slope steepness, Dd:drainage density and St:soil type.

The output is then reclassed into five groups such as very high, high, moderate, low and very low using the Quantile classification method (ESRI, 1996). The output that is produced is capable of being used for further investigations and assessments, especially at larger scale.

5.0 RESULT AND DISCUSSION

The ground water potential map of the Langat Basin area is shown in figure 3. In order to produce the map, a GIS model has been used, to integrate thematic maps such as annual rainfall, lithology, lineament density, land use, topography elevation, slope steepness, drainage density and soil type. Each thematic layer consists of a number of polygons, which correspond to different features. The polygons in each of the thematic layers have been categorized, depending on the suitability/relevance to the ground water potential, and suitable weights were assigned. Finally, all the thematic layers were integrated using the ground water potential model to derive the final derived layers. The score values of the area in the final map are shown Table 9.

Table 1 : Landuse

Landuse	Weight
Forest	20
Agriculture	40
Scrub	30
Wetland	50
Urban	10
Cleared Land	10
Water Body	60

Table 2: Lineament Density

Lineament Density (km/km^2)	Weight
> 0.0075	60
0.0055 – 0.0075	50
0.0035 – 0.0055	40
0.0015 – 0.0035	30
< 0.0015	20

Table 3: Annual Rainfall.

Annual Rainfall (mm)	Weight
2500 – 2750	70
2250 – 2500	60
2000 – 2250	50
1750 – 2000	40
1500 – 1750	30

Table 4 : Lithology.

Lithology	Weight
Alluvium	70
Limestone	40
Phylite-Schist-Quarzit	20
Quartz vein	5
Volcanic	30
Granite	10

Table 5 : Topography Elevation

Elevation (m)	Elevation Zone	Weight
< 20	Almost Flat Topography	50
20 – 100	Undulating Rolling Hilly	40
100 – 500	Hilly Steeply Disserted	35
500 – 1000	Steeply Dissected Mountainous	25
> 1000	Mountainous	10

Table 6 : Slope Steepness

% Slope	Slope Gradient	Slope Zone	Weight
0 – 7	0° - 3°	Almost Flat Topography	50
8 – 20	4° - 9°	Undulating Rolling Hilly	40
21 – 55	10° - 24°	Hilly Steeply Disserted	30
56 – 140	25° - 63°	Steeply Dissected Mountainous	20
> 140	> 63°	Mountainous	10

Table 7 : Drainage Density

Drainage Density (km/km^2)	Weight
> 0.0055	10
0.0040 – 0.0055	20
0.0025 – 0.0040	30
0.0010 – 0.0025	40
< 0.0010	50

Table 8 : Soil Type

Soil Series	Soil Type	Weight
Keranji	Clay	10
Melaka-Durian-Muncung	Gravel clay-silty clay-clay	20
Muncung-Seremban	Fine sandy clay	20
Prang	Clay	10
Regam-Jerangau	Coarse sandy clay-clay	30
Selangor-Kangkung	Clay	10
Serdang-Bugor-Muncung	Fine sandy clay loam-fine sandy clay-clay	30
Serdang-Kedah	Fine sandy clay loam	30
Urban Land	Sandy clay	30
Steep Land	Coarse sandy clay	40
Peat Land	Clay	10
Tanah Lombong	Sand	50
Telemung-Akob-Lanar Tempatan	Sandy loam-sandy clay	30

Table 9: Score values of the area polygons in the final map.

Score/value	Class of groundwater zone	Estimate of discharge rate
> 285	Very High	> 22 m^3/hour/well
260 – 380	High	18 – 22 m^3/hour/well
245 – 255	Moderate	14 – 18 m^3/hour/well
230 – 240	Low	10 – 14 m^3/hour/well
< 225	Very Low	< 10 m^3/hour/well

A summary of the results (Table 10), shows that almost all alluvial plains have high potential of groundwater occurrence. Where as, in steeply mountainous areas underlain by granite with low lineament density, the potential for groundwater is very low. Meanwhile in hard rock areas, the groundwater potential is high in areas with high lineament density and low drainage density.

Borehole data collected by the Minerals and Geoscience Department were used to compare the final results with the actual field data.

6.0 CONCLUSION

Based on this study, several conclusions can be made and they are:

i. The indicators of groundwater occurrences are related to the hydrological cycle and these are rainfall distribution, land use, soil types, lithology, geological structures, elevation, slope and drainage features of the area.

ii. Satellite data has been proven to be very informative and useful for surface study, especially in detecting a surface features and characteristics such as lineaments and land use.

iii. In order to predict the groundwater potential zones, different thematic maps have been prepared. These include annual rainfall distribution, land use, lithology, lineament density, topography elevation, slope steepness, drainage density and soil type.

iv. In subsurface study, remote sensing could be used more effectively if it is supported by the suitable GIS approach or techniques and good background knowledge of the related application.

v. Integrated assessment of thematic maps using a model developed based on GIS techniques is the most suitable method for groundwater potential prediction zoning.

vi. The methods and results of this study were effective only for groundwater zone prediction in hard rock terrain, but was less effective in the alluvium environment.

7.0 ACKNOWLEDGEMENT

The authors wish to thank Mr. Nik Nasruddin Mahmood (Director of MACRES), staff of MACRES and UKM for their comments and support in this project.

8.0 REFERENCES

Aller, L., Bennett, T., Lehr, J.H. & Petty, R.J. 1985. *DRASTIC: A Standard System for Evaluating Ground Water Pollution Potential Using Hydrogeologic Settings*. EPA/600/2-85/018, R.S. Kerr Environmental Research Laboratory, U.S. Environmental Protection Agency, Ada, Oklahoma.

Bonham-Carter, Graeme. 1994. *Geographic Information Systems For Geoscientist: Modelling with GIS*. Canada: Pergamon.

ESRI. 1996. *ArcView GIS, The Geographic Information System for everyone*: USA: Environmental Systems Research Institute.

Gupta, Ravi P. 1991. Remote Sensing Geology. New York: Springer-Verlag Berlin Heidelburg.

Krishnamurthy, J., Venkatesa Kumar, N., Jayaraman, V. & Manivel, M. 1996. *An approach to demarcate ground water potential zones through remote sensing and a geographical information system*. International Journal of Remote Sensing, 7, 1867-1884.

Krishnamurthy, J., Arul Mani, M., Jayaraman, V. & Manivel, M. 1997. *Selection of Sites for Artificial Recharge Towards Groundwater Development of Water Resource in India*. Proceeding of the 18th Asian Conference on Remote Sensing, Kuala Lumpur. 20 – 24 Oktober.

Todd, David K. 1980. Groundwater *Hydrology*. 2nd Edition. New York: John Wiley & Son.

Van Zuidam, R.A. 1979. *Terrain Analysis and Classification Using Aerial Photographs*. ITC Textbook of Photo Interpretation Vol. VII.

Table 10: Summary of the results.

Layers\Potential Zone	Very High	High	Moderate	Low	Very Low
Rainfall (mm)	M/L	H	VH	M	M/L/VL
Landuse	Agriculture/Water body/Wetland	Agriculture/Water body/Scrub	Forest	Agriculture	Forest/Cleared land/Urban
Soil Type	Clay	Fine sandy clay loam/Fine sandy clay/Clay	Coarse sandy clay / Sandy loam/Sandy clay/Clay	Gravel clay/Coarse sandy clay/Silty clay/Clay	Coarse sandy clay
Lithology	Alluvium	Phylite-Schist-Quarzit	Phylite-Schist-Quarzit/ Granite	Granite	Granite
Lineament Density (km/km²)	NE	VH	M/H	VL	L
Elevation(m)	<20	<20/20-100	20-100	20-100/100-500	100-500/>1000
Slope (%)	0-7/8-20	21-55	21-55/56-140	56-140	>140
Drainage Density (km/km²)	VL/L/M	VL/M	M/H	M/VH	L/M

Note :

	Rainfall (mm)	Lineament Density (km/km²)	Drainage Density (km/km²)
VL (Very Low)	1500-1750	<0.0015	<0.0010
L (Low)	1750-2000	0.0015-0.0035	0.0010-0.0025/
M (Moderate)	2000-2250	0.0035-0.0055	0.0025-0.0040
H (High)	2250-2500	0.0055-0.0075	0.0040-0.0055
VH (Very High)	2500-2700	>0.0075	>0.0055

NE – No Effect

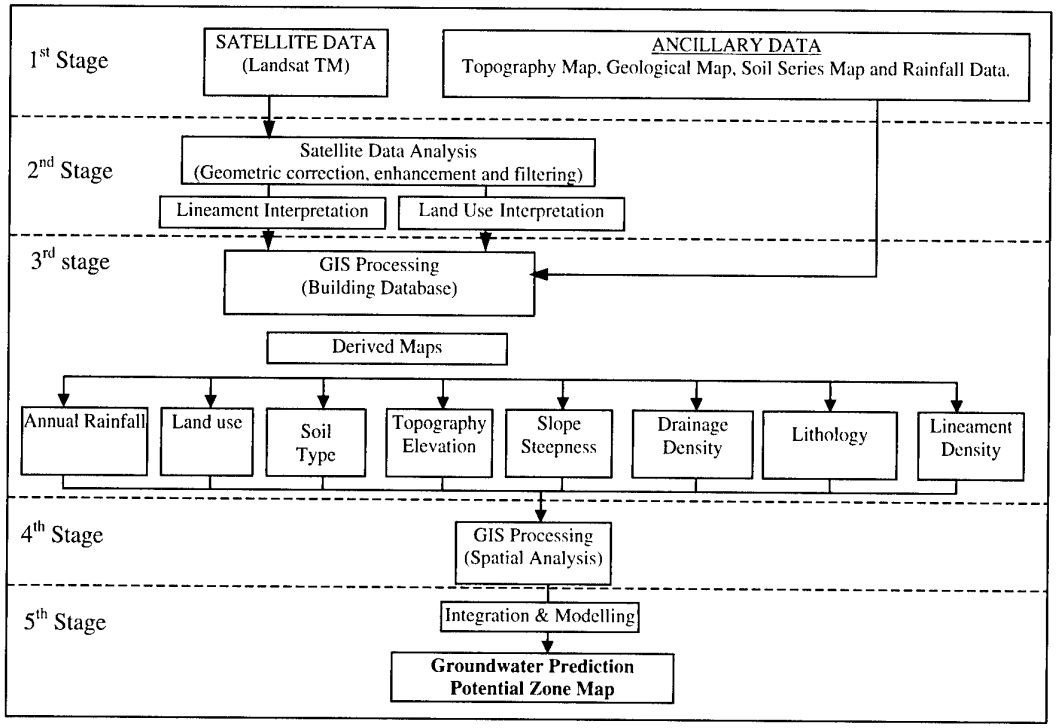


Figure 2 : Methodology flowchart for groundwater potential zone mapping.

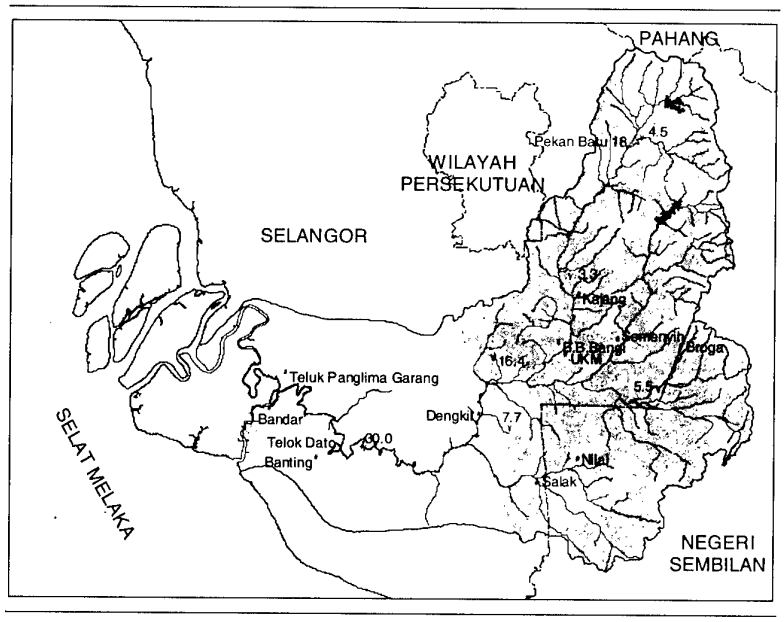


Figure 3: Groundwater potential map of the Langat Basin.